Aerodynamics of Bodies of Revolution

N. F. Krasnov

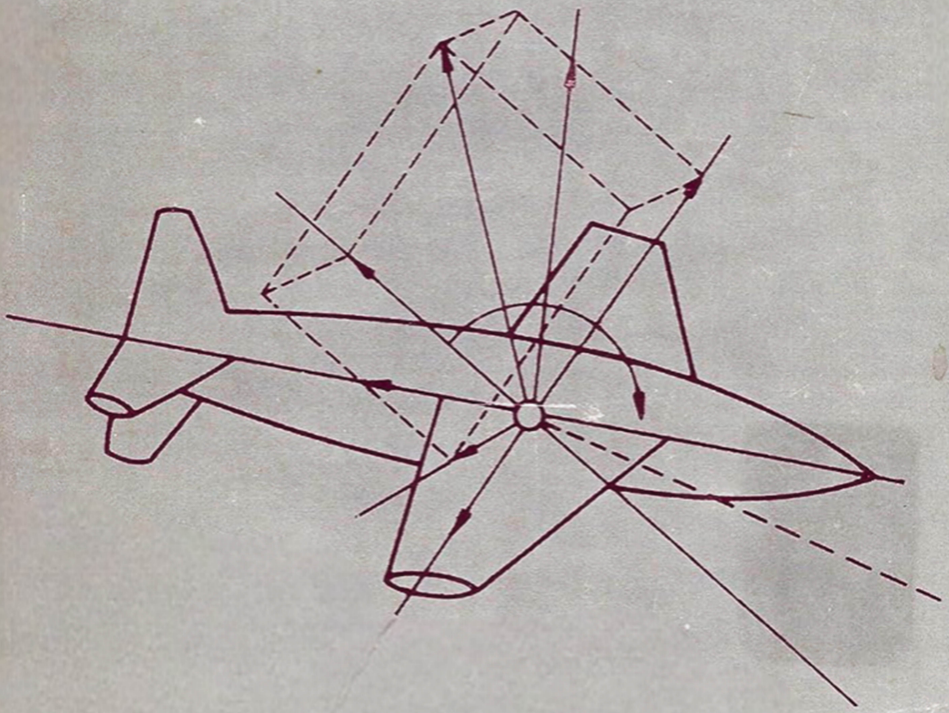

R-455-PR
June 1970

AERODYNAMICS OF BODIES OF REVOLUTION

N. F. KRASNOV

EDITED AND ANNOTATED BY DEANE N. MORRIS

A Report prepared for

UNITED STATES AIR FORCE PROJECT RAND

Rand
SANTA MONICA, CA. 90406

This research is supported by the United States Air Force under Project RAND—Contract No. F44620-67-C-0045—monitored by the Directorate of Operational Requirements and Development Plans, Deputy Chief of Staff, Research and Development, Hq USAF. Views or conclusions contained in this study should not be interpreted as representing the official opinion or policy of RAND or of the United States Air Force.

Aerodynamics of Bodies of Revolution

Aerodynamics of Bodies of Revolution

N. F. Krasnov

EDITED AND ANNOTATED BY

Deane N. Morris

The RAND Corporation
Santa Monica, California

Translated from the Second Russian Edition
by Joy B. Gazley, The RAND Corporation

American Elsevier Publishing Company, Inc.
NEW YORK · 1970

AMERICAN ELSEVIER PUBLISHING COMPANY, INC.
52 Vanderbilt Avenue, New York, N.Y. 10017

ELSEVIER PUBLISHING COMPANY, LTD.
Barking, Essex, England

ELSEVIER PUBLISHING COMPANY
335 Jan Van Galenstraat, P.O. Box 211
Amsterdam, The Netherlands

International Standard Book Number 0-444-00076-3

Library of Congress Card Number 73-116707

Copyright © 1970 by The RAND Corporation

All rights reserved.
No part of this publication may be reproduced,
stored in a retrieval system, or transmitted
in any form or by any means, electronic,
mechanical, photocopying, recording,
or otherwise, without the prior
written permission of the publisher,
American Elsevier Publishing Company, Inc.,
52 Vanderbilt Avenue, New York, N.Y. 10017.

Manufactured in the United States of America

Contents

EDITOR'S PREFACE xi

FOREWORD TO THE SECOND EDITION xv

PREFACE TO THE SECOND EDITION xvii

Chapter One

BASIC CONCEPTS AND EQUATIONS FOR THE AERODYNAMICS OF BODIES OF REVOLUTION

Editor's Introduction 1
1. Aerodynamic Forces and Moments 3
2. The Basic Features of Very High Velocity Gas Flow 30
3. The Basic Concepts and Equations for Determining the Flow Parameters 63
4. The Basic Relations for Determining Gas Parameters Behind a Shock Wave 101
5. Results from Boundary Layer and Heat Transfer Theory 140

Chapter Two

THE CONE IN SUPERSONIC FLOW

Editor's Introduction 161
6. Symmetrical Flow Around a Pointed Cone 163
7. The Circular Cone at an Angle of Attack 207

Chapter Three

THE METHOD OF CHARACTERISTICS

Editor's Introduction 237
8. The Calculation of Symmetric Potential Flows 239
9. The Calculation of Axially Symmetric Rotational Flow 270
10. The Method of Characteristics for the Calculation of Flow at Very High Temperatures 284
11. The Influence of the Boundary Layer on Inviscid Flow Parameters 297
12. Application of the Method of Characteristics to the Calculation of Flow Around a Body of Revolution at an Angle of Attack 303

Chapter Four

DRAG OF SLENDER BODIES OF REVOLUTION IN LINEARIZED FLOW

Editor's Introduction 333
13. Wave Drag 335
14. Skin Friction and Base Drag 379

Chapter Five

LIFT OF SLENDER BODIES OF REVOLUTION IN LINEARIZED FLOW

Editor's Introduction 403
15. Determination of the Normal Force Coefficient, Pitching Moment, and Center of Pressure 405
16. Unsteady Flow Around Slender Bodies of Revolution 443

Chapter Six

AERODYNAMICS OF BODIES OF REVOLUTION AT HYPERSONIC SPEEDS

Editor's Introduction 461
17. Symmetric Flow 463
18. Approximate Calculation of Aerodynamic Characteristics Based on Newtonian Flow Theory 498

Chapter Seven

AERODYNAMICS OF BLUNT BODIES OF REVOLUTION

Editor's Introduction 543
19. The Flow Characteristics of Blunt-Nosed Bodies 545
20. Inviscid Flow Around a Blunt Nose 549
21. Hypersonic Flow Around Slightly Blunted Cylindrical and Conical Bodies 586
22. Application of the Method of Characteristics to the Calculation of Flow Around Blunt Bodies of Revolution 612
23. Effect of Angle of Attack 621
24. Flow Around Blunt Bodies of Curved Shape 627
25. Nonequilibrium Effects on Inviscid Flow Around Blunt Bodies 642

Chapter Eight

SKIN FRICTION AND HEAT TRANSFER ON BLUNT BODIES

Editor's Introduction 661
26. Changes in Flow Characteristics Due to Blunting 663
27. Heat Flow on a Blunt Nose 683
28. Viscosity Effects on the External Flow Around a Blunt Body . 742

Chapter Nine

HEAT AND MASS TRANSFER FROM THE SURFACE OF A VEHICLE

Editor's Introduction 751
29. General Definitions 753
30. Calculation of the Heat of Ablation 764

Chapter Ten

AERODYNAMICS OF RAREFIED GASES

Editor's Introduction 779
31. The Limits of Applicability of Continuum Flow Theory 781
32. Free Molecule Flow 787
33. Friction and Heat Transfer in Slip Flow 808

Chapter Eleven

SIMILARITY LAWS AND AERODYNAMIC CHARACTERISTICS AT TRANSONIC VELOCITIES

Editor's Introduction 827
34. The Transonic Similarity Laws 829
35. Some Data on Transonic Flow Around Bodies of Revolution 840

Appendix
A. PARAMETERS OF AIR AT VARIOUS ALTITUDES 871
B. CONVERSION TABLE TO INTERNATIONAL UNIT SYSTEM (SI) 873

REFERENCES 875

BIBLIOGRAPHY OF THE SECOND EDITION 883

INDEX 887

Editor's Preface

The Russian text, entitled *Aerodinamika Tel Vrashcheniia*, was written by Nikolai F. Krasnov, Professor of Aeronautics at the Moscow Bauman Higher Technical Institute. The second, highly revised edition was published in 1964 by Mashinostroenie, Moscow, in an edition of 5000 copies.

The book, a comprehensive technical treatise on the aerodynamics of bodies of revolution from transonic to hypersonic speeds, covers all aspects of the subject, including transonic flow, linearized supersonic flow, the method of characteristics, flow around blunt bodies, hypersonic flow, Newtonian flow, rarefied gas and free-molecule flow, skin friction, heat transfer, and mass transfer. The author's general approach is to assume a knowledge of the basic equations of gas dynamics (presented but not derived in the text) and then to apply these equations to solve problems in the aerodynamics of bodies of revolution. The reader is provided with a detailed development of all of the important methods and techniques in modern aerodynamic theory. However, the author's ultimate intent is to present practical results and methods to be applied to engineering problems; the final results are usually in the form of working equations, graphs, tables, or detailed sequential calculation methods.

While much of the book is based on material that has already appeared in various forms in American or Soviet technical publications and texts, no book that collects, integrates, and summarizes this earlier work has previously existed in English. The nearest English text might be "Bodies of Revolution," Volume 3, Section 8 of the *Handbook of Supersonic Aerodynamics*, published by the Bureau of Naval Weapons in 1961, but the resemblance is only superficial. For this reason, it seemed that there would be sufficient interest in Krasnov's book within the academic and aeronautical engineering community in the United States and Great Britain to warrant a complete translation of the text.

A few comments are necessary concerning the editorial mechanics of the translation. While I have made a few changes in the symbols to agree with common U.S. usage, in general the symbols remain as in the original. The reader will notice a great deal of redundancy in the symbols, but this repetition seems almost unavoidable in a text of such broad coverage.

The original book did not contain a table of symbols, and it seemed that such a table would not be particularly useful in the translation, since the author has been careful to define possibly obscure symbols as they are used.

Numerous typographical errors have been found in the course of editing and checking the equations and these have usually been corrected without comment. Where there appeared to be errors of substance, the text has been corrected and a footnote used to explain the discrepancy. Unfortunately, I have been entirely unsuccessful in my repeated attempts to contact Professor Krasnov with regard to these anomalies.

A copy of the very sketchy bibliography found in the original text is included in the back of this book. Because the references listed are only occasionally keyed to the text material, the listing is practically useless as a reference guide. I have therefore tried to reference material that I could identify in each chapter; the results appear as the list of references at the end of the book. This attempt to amplify the references sometimes proved extremely difficult; at times I had the uncomfortable feeling that I had previously seen a certain analysis or figure, but finding the original sources was often a matter of luck. My apologies are due those authors who recognize their own work in the text and wonder why they have not been credited for it.

An editor's introduction is provided at the beginning of each chapter. The original purpose of these introductions was to provide a mechanism for editorial comment without the inconvenience of numerous editorial footnotes. Because an unfortunately long time has elapsed between the publication of the Russian text and this translation, however, these introductions have also proved to be an ideal vehicle for summarizing and referencing pertinent material that has appeared since 1964.

Mrs. Joy Gazley deserves tremendous credit for her translation of a lengthy and highly technical text; my task of technical editing was greatly simplified by her work. Mrs. Eleanor Harris was a dedicated perfectionist in the editorial production of the book. Mrs. Jo Sloan redrew most of the figures that appear in the translation. Others who contributed to the production of the book include Mrs. Nancy McNally Bryan, Mrs. Terry Fujikawa, and Mrs. Marjorie Behrens. Technical review

of certain chapters was provided by Jerome Aroesty, W. D. Gosch, Richard Schamberg, and R. L. Spicer.

Finally, I must give special acknowledgment to the dedication and perseverance of Mrs. Shirley Story Echols, who has typed the 850 pages of the text no less than three times as refined versions were produced. The excellence of her work is visible in all the pages of the book.

This work, as part of a continuing investigation of the state of the art in aerodynamics, was supported by the United States Air Force under Project RAND.

Deane N. Morris
November 1969

Foreword to the Second Edition

The second edition of this book introduces the most important results of the theoretical and experimental work on hypersonic aerodynamics that has been carried out since 1958, when the first edition appeared.

Among the new subjects discussed are the characteristics of gas flows at hypersonic speeds, the influence of dissociation and ionization of a gas on the flow behind a shock, the aerodynamics of blunt bodies of revolution, heat shielding and mass transfer from the surface of a body, and the aerodynamics of rarefied gases. The sections carried over from the first edition were revised and supplemented to take into account the latest theoretical and experimental data.

The book is intended as a textbook for engineering college students but will also be useful to engineers and scientists in industry.

Prof. N. S. Arzhanikov, Reviewer
Asst. Prof. Ia. M. Kotliar, Editor

VIII, which gives information on skin friction and heat transfer on blunt bodies. Current methods of calculating the flow around bodies of revolution with different shapes and degrees of blunting are presented, based on the concept that the flow field consists of an inviscid region and a boundary layer. Inviscid flow theory is used initially to calculate the forces and moments from the pressure distribution and to compute the skin friction and heat transfer to the wall. The perturbation effect of the boundary layer on the inviscid parameters is then calculated by introducing an effective thickness of the streamlined body.

In connection with the study of the aerodynamic problems of blunt axisymmetric bodies, a series of important advances should be noted. One is the use of the analogy with the unsteady motion of a gas under the action of a cylindrical piston in calculating the perturbed flow near a blunt body. G. G. Chernyi, correspondent-member of the Academy of Sciences, USSR, made a great contribution to the mathematical treatment of this analogy and obtained important practical results. Another obvious advance is O. M. Belotserkovskii's treatment of the method of calculating the flow over bodies of revolution with blunt noses of various shapes. The latter study is based on a method of integrating a system of differential equations on electronic computers, originally proposed by Academician A. A. Dorodnitsyn, which has resulted in the practical development of the method of characteristics to calculate the inviscid flow about axisymmetric bodies (among them, blunt-nosed bodies).

In addition to the discussion in the text of exact methods of calculating inviscid flow, a number of approximate methods are described, including the modified Newtonian theory developed in recent years. The formulas resulting from this theory give good results in calculating the pressure distribution around blunt noses of curved shape for a wide range of supersonic speeds.

Important new results in the field of heat transfer on blunt bodies are also discussed. The development of the theory of heat transfer on a curved surface, based on the previous history of the boundary layer and its physical-chemical processes, is a recent achievement.

Studies of perturbed flow caused by blunting have given rise to the concept of an inviscid, high-entropy layer of small velocities, whose properties can be determined. The proper utilization of the characteristics of this layer can result in a decrease in heat flow to the surface. Thus, in a sense, it is necessary to investigate blunting as a means of thermal shielding of aircraft. At the same time, the blunt nose itself undergoes very intense heating and consequently needs more heat shielding than the rest of the vehicle.

The most effective shielding requires the use of various coatings that ablate at suitable temperatures, thus absorbing energy. The development of the theory and of practical methods to calculate ablation characteristics also belong to the number of outstanding achievements of contemporary aerodynamics. The brief discussion of ablation problems in Chapter IX will enable the reader to familiarize himself with results pertaining to the elementary theory and to methods for calculating the mass loss of the superheated material.

Finally, as a result of the active development of space flight, it has become necessary to consider the discrete structure of the rarefied

medium when evaluating the interactions of the medium and a flight vehicle. The basic information on the aerodynamics of a rarefied gas is given in Chapter X.

The new edition provides a more comprehensive description of methods for calculating boundary-layer parameters as applied to the solution of problems of aerodynamic forces and of heat transfer and ablation. The section on the theoretical and experimental results of strong interaction between the fluid and the body has been thoroughly revised, and outdated material has been replaced by important results obtained in recent years.

It should be noted that the most substantially revised chapter deals with the aerodynamics of bodies of revolution at hypersonic speeds. Much of the material is discussed on the basis of the law of plane sections, proceeding from the analogy with the unsteady motion of a gas ahead of a piston. The application of this theory unifies many of the research results in the hypersonic aerodynamics of slender bodies of revolution. The section of this chapter that deals with the application of Newtonian theory was completely revised, and incorporates new data from refined versions of the theory.

Among the new subjects introduced in the second edition are the application of recent advances in the theory of hypersonic conical flow to the calculation of inviscid parameters on conical surfaces, the consideration of variable specific heat, dissociation, and ionization in skin friction and heat transfer analyses, and the use of the method of characteristics to calculate dissociated gas flows.

On the whole, the book acquaints teachers with the basic methods of solving problems of aerodynamics and with the most important conclusions that derive from the analysis of the flow processes of a gas in its various states. The applied character of the book makes it particularly useful for engineering calculations, but it can also be used for the detailed analysis of physical and chemical phenomena accompanying high-velocity gas flows around bodies.

Numerical data and the results of experimental research are quoted from domestic and foreign literature. To facilitate conversion of the dimensional units used for physical quantities into the new, recently adopted, international system (SI), a special conversion table is presented in Appendix B.

Chapter I

BASIC CONCEPTS AND EQUATIONS FOR THE AERODYNAMICS OF BODIES OF REVOLUTION

Editor's Introduction

THIS INTRODUCTORY CHAPTER *begins with a detailed development of the coefficients for the aerodynamic forces and moments on bodies of revolution and a summary of equations defining the geometric characteristics of typical body shapes. These results are unusual only in that they are seldom found collected together in the concise forms given here. It is notable, for example, that the frictional forces are included in the development of expressions for normal force and pitching moment and that the center of pressure is discussed as a basic aerodynamic parameter.*

Section 2 presents a well-organized summary of the effects of high temperature, dissociation, and ionization on the thermodynamics of gas flow. Much of the theoretical analysis in this section is derived from the basic work of Lighthill, Freeman, and Bray on the characteristics of an "ideal dissociating gas," but the graphical thermodynamic results are taken from the comprehensive calculations of Predvoditelev et al. Hilsenrath, Klein, and Woolley (AEDC-TR-59-20, 1959) have shown that the Soviet thermodynamic data are in excellent agreement with those of the National Bureau of Standards. The next two sections contain summaries of the basic equations of gas dynamics and the shock-wave equations, as specialized for bodies of revolution. This material is obviously not new, but it is impossible to find these equations collected together in such a form elsewhere. The standard texts by Sauer, Ferri, Shapiro, Liepmann and Roshko, and Schlichting contain most of these results in one form or another, but a considerable amount of cross-referencing is required to locate even an incomplete collection of the basic equations in cylindrical, spherical, and curvilinear coordinates (required for analyses of bodies of revolution). The simple extensions of the basic equations to flows with variable specific heats and to real gases are also useful.

The boundary layer and heat transfer theory in Section 5 is given a more superficial treatment than the topics discussed in other parts of the chapter. Crude approximations are used that are not consistent with the refinement and detail of other parts of the book. For example, although comprehensive results are readily available in the literature for the effects of Mach number and wall temperature on the laminar and turbulent skin friction coefficients, they are not mentioned in this

*section. The method of "effective" temperatures or enthalpies used by Krasnov is known to compare well with experiment, but, in the spirit of the rest of the book, considerably more graphical information could have been presented on the variation of the skin friction coefficient with Mach number and wall temperature. Furthermore, since Krasnov emphasizes the presentation of working formulas and graphs, he might have cited some relatively well-known analytical results that are as accurate as the effective-temperature method and that can be presented in convenient analytic or graphical form. For example, A. D. Young's relations for laminar skin friction on a flat plate (*Aeronautical Quarterly, *August 1949) are as sound theoretically as the effective-temperature method, and the results are comparable. Young's expression for the local laminar skin friction coefficient is*

$$\frac{c_{fL}}{c_{fL}^{0}} = \left(0.45 + 0.55\,\frac{i_w}{i_\delta} + 0.18\,\frac{rV_\delta^2}{2i_\delta}\right)^{(n-1)/2},$$

where n is the exponent in the power law for viscosity and the other symbols are as defined in Section 5 of the present text. This equation bears a strong resemblance to, and has the same origins as, the effective-temperature method.

*For turbulent flow on a flat plate, the theory of Van Driest (*J. Aero. Sci., *March 1951, and* Aero. Eng. Rev., *October 1956) can be used to develop a similar parameter for the local turbulent skin friction coefficient:*

$$\frac{c_{fT}}{c_{fT}^{0}} = \left(\frac{\sin^{-1}\Lambda_\delta}{\Gamma_\delta}\right)^{4/5}\left(\frac{i_w}{i_\delta}\right)^{n/5},$$

where $\Gamma_\delta = rV_\delta^2/2i_\delta$ *and*

$$\Lambda_\delta = \frac{(1 + \Gamma_\delta - i_w/i_\delta) - (1 - \Gamma_\delta - i_w/i_\delta)\sqrt{i_w/i_\delta}}{(1 + \Gamma_\delta - i_w/i_\delta)^2 + 4(i_w/i_\delta)\Gamma_\delta}\,(2\sqrt{\Gamma_\delta}).$$

These formulas can be plotted versus $V_\delta/\sqrt{i_\delta}$ *(or* M_δ*) and* i_w/i_δ *(or* T_w/T_δ*) and are recommended in preference to Krasnov's Eqs. (5.12) through (5.15) They are equivalent in validity, within the estimates of experimental accuracy, to the results of the effective-temperature method outlined in Section 5.*

The power law for viscosity is used in both of these expressions. Many other approximate formulas have been published in the literature, some using the more exact Sutherland law for viscosity and allowing a variable Prandtl number; in general, these are more complicated but no more accurate.

§ 1. *AERODYNAMIC FORCES AND MOMENTS*

THE FORCES ACTING ON A BODY MOVING IN A FLUID

THE EFFECT OF A FLUID MEDIUM on a body moving within it consists of pressure forces continuously distributed over the surface of the body, as well as shear forces due to the viscosity of the medium. All of these forces (Fig. 1) can be reduced to one principal vector $\bar{F}$ of aerodynamic forces and to a principal vector $\bar{M}$ of the moment of these forces about any designated point. The center of moments can be chosen

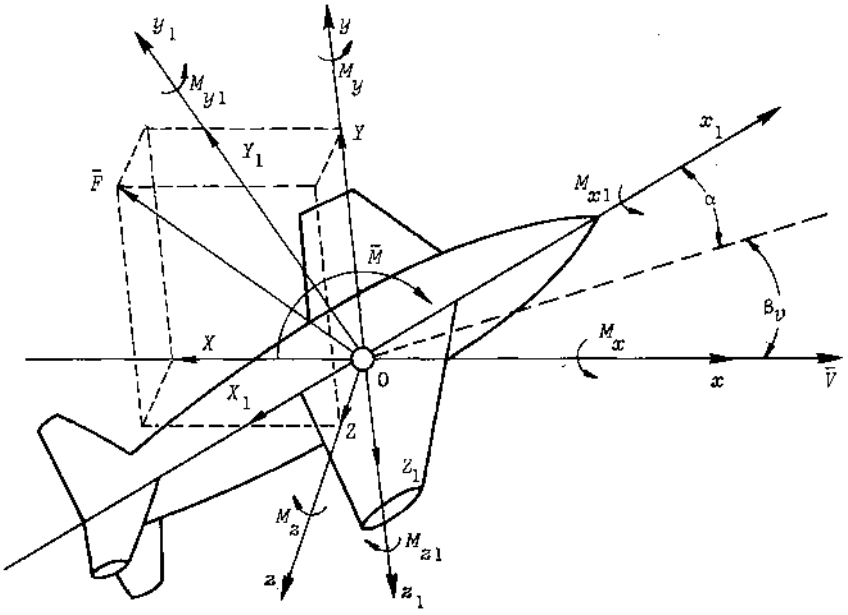

Fig. 1--Aerodynamic forces and moments on an aircraft in wind (x, y, z) and body (x_1, y_1, z_1) coordinate systems

as the center of gravity, the apex of the nose, etc. Engineering practice is usually not concerned with the vectors $\bar{F}$ and $\bar{M}$ but with their projections on the axes of some system of coordinates.

The projections of the vector $\bar{F}$ on the x, y, and z axes of the wind system of coordinates are designated as the drag D, the lift L, and the lateral force Z. The corresponding projections of the same vector on the x_1, y_1, and z_1 axes of the body system of coordinates are defined as the axial force (X_1 or A), the normal force (Y_1 or N), and the side force Z_1.

The projections of vector $\bar{M}$ on these or any other coordinate systems are identically designated and are distinguished by the subscripts; i.e., the components M_x and M_{x1} on the longitudinal axis are the rolling moments, the components M_y and M_{y1} on the vertical axis are the yawing moments, and the components M_z and M_{z1} on the lateral axis are the pitching moments. The magnitude and direction of the forces and the moments depend on the orientation of the body with respect to the velocity vector $\bar{V}_\infty$ (or, if dynamic motion is being investigated, with respect to the direction of the velocity of the incident flow). This orientation is determined by the angle of attack α, the angle between the axis Ox_1 and the projection of the vector $\bar{V}_\infty$ on the plane x_1Oy_1, and by the side slip angle β_V, the angle between the vector $\bar{V}_\infty$ and the plane x_1Oy_1.

In the study of the aerodynamics of bodies of revolution, it is convenient to choose the position of the vertical plane x_1Oy_1 of the body coordinate system in such a way that it is the plane of symmetry of the body itself; for $\beta_V = 0$ it will also be the plane of symmetry of the flow field around the body. When $\beta_V = 0$, both the longitudinal axis of the body Ox_1 and the velocity vector $\bar{V}_\infty$ (Fig. 2) will be located in the plane x_1Oy_1. Any other plane that passes through the longitudinal axis is called a meridian plane; it forms an angle with the vertical plane, called the meridian angle ϕ. In this notation, the vertical plane is defined as the zero meridian plane. Since the vector $\bar{V}_\infty$ is located in this plane, it can also be called the angle-of-attack plane.

When the vertical plane is chosen in this way, the vector $\bar{F}$ lies in the plane and the vector $\bar{M}$ is oriented normal to it. Consequently, the

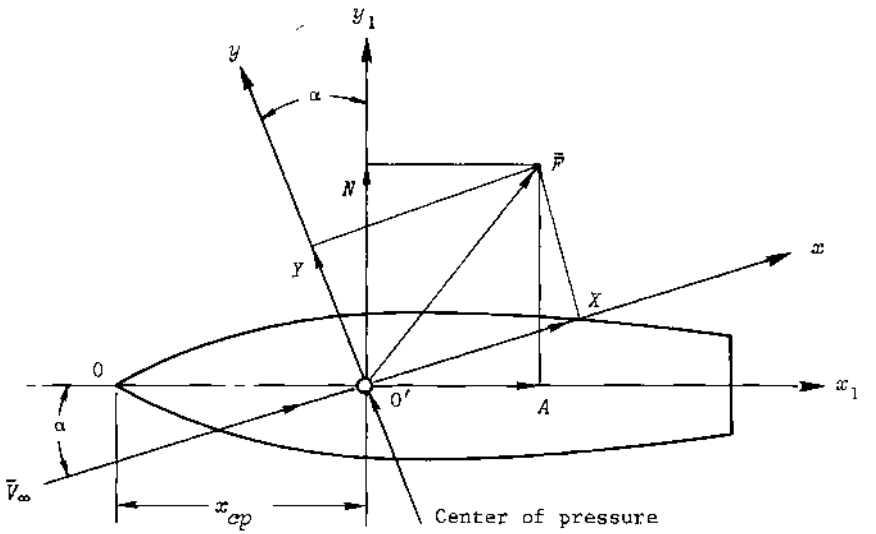

Fig. 2--Aerodynamic forces on a body of revolution in wind and body coordinate systems

motion of the body in the wind coordinate system will be determined by the drag D, the lift L, and the pitching moment M_z, or by the aerodynamic coefficients C_D, C_L, and C_m, respectively. In the body coordinate system, the motion of the body will be determined by the axial force A, the normal force N, and the pitching moment M_{z_1}, or by the respective aerodynamic coefficients C_A, C_N, and C_{m1}.

The drag and lift coefficients are related to the axial and normal force coefficients by the relations

$$C_D = C_A \cos \alpha + C_N \sin \alpha,$$
$$C_L = C_N \cos \alpha - C_A \sin \alpha. \tag{1.1}$$

In practice, it is more convenient to carry out aerodynamic calculations in the body coordinate system. Therefore, in what follows we shall operate with the coefficients C_N and C_A. The pitching moment

coefficient does not depend on the choice of the coordinate system, i.e., $C_m = C_{m_1}$, but is a function of the reference point about which the moment is calculated. As a rule, we shall henceforth make this calculation with reference to the nose of the body of revolution, rather than to the location of the center of gravity, which, generally speaking, varies in flight. In specific cases relating particularly to the oscillatory motion of the body of revolution, the pitching moment and its coefficient are more easily determined with reference to the center of gravity.

AXIAL FORCE COEFFICIENT

The axial force coefficient will be defined as the sum of three components:

$$C_A = C_{Ap} + C_{AB} + C_{Af}, \tag{1.2}$$

where C_{Ap} is the axial force coefficient due to pressure forces acting on the surface of the body; C_{AB} is the axial force coefficient due to base drag, which is a function of pressure acting on the base; and C_{Af} is the axial force coefficient due to skin friction.

To calculate these coefficients it is necessary to know the pressure distribution and the shear stress over the body surface. Consequently, a considerable portion of this work is devoted to these subjects. In this section we shall discuss the more general and comparatively simple problem of determining the components of axial force and the corresponding coefficients, assuming that the distributions of pressure and shear stress are known.

First, we shall examine the following problem. Let the pressure distribution along the surface of a body of revolution and the pressure, p_B, on the base section be known for a given angle of attack, α, and for given parameters of the incident flow (velocity $\vec{V}_\infty$, static pressure p_∞, and density ρ_∞). We need to find general expressions for the coefficients C_{AB} and C_{Ap} when the geometric shape of the body, specifically the equation of its generatrix, $r = f(x)$, is given.

The expression for the base drag coefficient is determined from the condition that the axial force resulting from the differential pressure $p_B - p_\infty$ acting on a base with an area S_B equals $(p_B - p_\infty)S_B$, and this force can be defined as

$$(p_B - p_\infty)S_B = -C_{AB}qS_{\text{mid}},$$

where $q = \rho_\infty V_\infty^2/2$ is the dynamic pressure, and S_{mid} is the area of the largest cross section of the body. Consequently, the base drag coefficient is

$$C_{AB} = -C_{pB}\bar{S}_B, \tag{1.3}$$

where $C_{pB} = (p_B - p_\infty)/q$ is the base pressure coefficient, and the base area ratio is defined as $\bar{S}_B = S_B/S_{\text{mid}}$. Thus, to determine C_{AB} it is necessary to know the base pressure coefficient, the formula for which will be presented later.

To find the general expression for the coefficient C_{Ap}, consider an element of the body surface with a width dx, located at a distance x from the nose (Fig. 3). A force equal to $(p - p_\infty)r\,d\phi\,ds$ acts on the portion of this element with an area $r\,d\phi\,ds$. The surface element ds is related to distance along the axis by $dx = ds\cos\delta$, where δ is the angle between the axis of the body and the tangent to the surface at a given point.

The magnitude of the axial force acting on the element of area is $dA_p = (p - p_\infty)r\,dx\,d\phi\sin\delta$. Remembering that $dx = ds\cos\delta$, and considering the symmetric character of the pressure distribution about the zero meridian plane, we obtain for the axial force

$$A_p = 2\int_0^l r\tan\delta\,dx\int_0^\pi (p - p_\infty)\,d\phi, \tag{1.4}$$

where l is the length of the body. The axial force is related to the coefficient C_{Ap} by the formula $A_p = C_{Ap}qS_{\text{mid}}$.

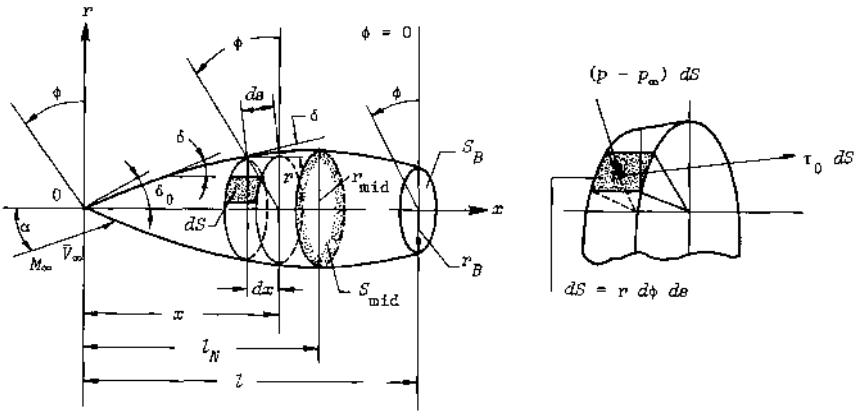

Fig. 3--Illustration of variables for determining the aerodynamic characteristics of a body of revolution

The reference cross-sectional area of the body is $S_{mid} = \pi r_{mid}^2$ (where r_{mid} is the radius of the midsection of the body), so that

$$C_{Ap} = \frac{4\lambda_l}{\pi} \int_0^1 \bar{r} \tan \delta \, d\bar{x} \int_0^{\pi} C_p \, d\phi, \tag{1.5}$$

where $\bar{r} = r/r_{mid}$, $\bar{x} = x/l$; $\lambda_l = l/2r_{mid}$, the fineness ratio of the body; and $C_p = (p - p_\infty)/q$, the pressure coefficient whose distribution is a function of the variables $x(r)$ and ϕ.

In the case of zero angle of attack, Eq. (1.5) is simplified:

$$C_{Ap} = 4\lambda_l \int_0^1 C_p \bar{r} \tan \delta \, d\bar{x}, \tag{1.6}$$

while the pressure coefficient now depends on only one variable, either x or r.

Now, let us assume that the distribution of the shear stress, τ_0, is known over the body surface; i.e., the magnitude of τ_0 as a function

of $x(r)$ and ϕ is known. We want to find the coefficient C_{Af} of the axial force due to friction. The axial component of the shear force acting on an elementary area, $dS = r\, d\phi\, ds$, is (see Fig. 3)

$$dA_f = \tau_0\, dS \cos\delta = \tau_0 r \cos\delta\, ds\, d\phi.$$

Since $dx = ds \cos\delta$, the integrated value of the axial component of the shear force acting on the surface area S_w is

$$A_f = \int_{S_w} \tau_0 \cos\delta\, dS = 2\int_0^l r\, dx \int_0^\pi \tau_0\, d\phi. \tag{1.7}$$

Let us introduce the local friction coefficient, defined as

$$c_{fx} = \frac{\tau_0}{q}. \tag{1.8}$$

Then the axial force coefficient C_{Af} is given by the expression

$$C_{Af} = \frac{A_f}{qS_{\text{mid}}} = \frac{2}{S_{\text{mid}}} \int_{S_w} c_{fx} \cos\delta\, dS = \frac{4\lambda_l}{\pi} \int_0^1 \bar{r}\, d\bar{x} \int_0^\pi c_{fx}\, d\phi. \tag{1.9}$$

In symmetric flow, the coefficient c_{fx} is only a function of the variable x:

$$C_{Af} = 4\lambda_l \int_0^1 c_{fx}\bar{r}\, d\bar{x}. \tag{1.9a}$$

NORMAL FORCE COEFFICIENT

In the same way as for the axial force, the total magnitude of the normal force depends on the distribution of pressure and shear stress over the body surface. Consequently, the normal force coefficient C_N can be represented by the sum

$$C_N = C_{Np} + C_{Nf}, \tag{1.10}$$

where C_{Np} is the component resulting from the action of pressure, and C_{Nf} is the component resulting from friction.

First, we shall derive the equation that determines the coefficient C_{Np} for a known pressure distribution. It is evident from Fig. 3 that the elementary value of the normal force is

$$dN_p = -(p - p_\infty) r \, d\phi \, ds \cos \phi \cos \delta.$$

Considering the symmetry of the pressure distribution, the value of the normal force is

$$N_p = -2 \int_0^l r \, dx \int_0^\pi (p - p_\infty) \cos \phi \, d\phi. \tag{1.11}$$

Then the normal force coefficient is

$$C_{Np} = \frac{N_p}{qS_{\text{mid}}} = -\frac{4\lambda_l}{\pi} \int_0^1 \bar{r} \, d\bar{x} \int_0^\pi C_p \cos \phi \, d\phi. \tag{1.12}$$

For zero angle of attack C_{Np} equals zero, since the pressure distribution is then independent of ϕ and the second integral in Eq. (1.12) reduces to zero.

It is known from experimental data that the influence of viscosity on the normal force becomes important for large fineness ratio bodies, and that this influence increases for large angles of attack and high velocities. It is possible to determine the component of the normal force coefficient C_{Nf} if the distribution of the shear stress τ_0 over the body surface is known. It is evident from Fig. 3 that the elementary value of the normal force due to viscosity is

$$dN_f = \tau_0 \sin \delta \cos \phi \, dS = \tau_0 r \sin \delta \cos \phi \, ds \, d\phi.$$

The total value of this force is

$$N_f = \int_{S_w} \tau_0 \sin \delta \cos \phi \, dS = 2 \int_0^l r \tan \delta \, dx \int_0^\pi \tau_0 \cos \phi \, d\phi. \quad (1.13)$$

and the normal force coefficient is

$$C_{Nf} = \frac{1}{qS_{\text{mid}}} \int_{S_w} \tau_0 \sin \delta \cos \phi \, dS = \frac{4\lambda l}{\pi} \int_0^1 \bar{r} \tan \delta \, d\bar{x} \int_0^\pi c_{fx} \cos \phi \, d\phi. \quad (1.14)$$

In the case of zero angle of attack, the local friction coefficient c_{fx} does not depend on the variable ϕ and, consequently, $C_{Nf} = 0$.

One particular application of the aerodynamic characteristics of bodies is for stress calculations, and an important part of such calculations is the determination of the bending stresses in various sections of the vehicle. For this purpose, it is necessary to know how the normal force is distributed longitudinally.

If we consider only the normal force due to pressure (which is the dominating influence in practical cases), the distribution of this force can be obtained from Eq. (1.11) in the form

$$\frac{dN_p}{dx} = -2 \int_0^\pi (p - p_\infty) r \cos \phi \, d\phi. \quad (1.15)$$

This equation gives the longitudinal distribution of the normal force; the corresponding distribution of the normal force coefficient is given by

$$\frac{dC_{Np}}{d\bar{x}} = -\frac{4\bar{r}\lambda l}{\pi} \int_0^\pi C_p \cos \phi \, d\phi. \quad (1.16)$$

The normal force distribution is also used to analyze the influence of various components of the body of revolution on the value of

the total normal force and the pitching moment. For example, it is evident from Fig. 4a that the nose of the body creates a positive normal force but the tail creates a negative force. As a consequence, a destabilizing moment results with reference to the center of gravity. The installation of a tail section in the form of a conical flare (Fig. 4b) or tail surfaces (Fig. 4c) results in the generation of a positive normal force at the rear and, consequently, in the occurrence of a stabilizing moment.

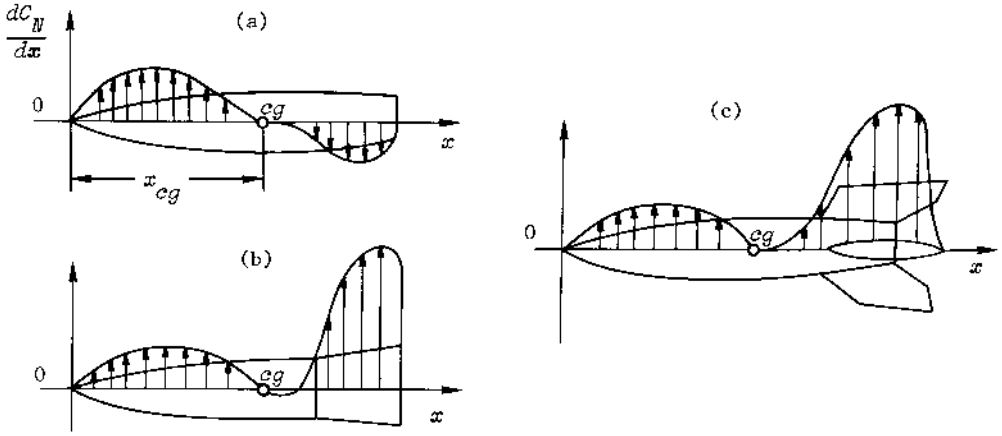

Fig. 4--Axial distribution of the normal force coefficient

PITCHING MOMENT COEFFICIENT AND CENTER OF PRESSURE

Moment Coefficient

The pitching moment coefficient depends on the same factors as the normal force coefficient. Therefore, the quantity C_m can be written

$$C_m = C_{mp} + C_{mf}, \tag{1.17}$$

where C_{mp} is the component of the moment coefficient that depends on pressure, and C_{mf} is the component caused by viscosity. In addition,

the magnitude of the quantity C_m depends on the point of reference.

Let us find the general expression for the components of this coefficient assuming that the nose of the body is chosen as the point of reference, or if the body is blunted, the leading point of the surface located on the axis. To determine the coefficient C_{mp}, we shall first find, with the help of Fig. 3, the elementary value of the moment of forces from the pressure acting on an area located at a distance x from the reference point:

$$dM_p = -x(p - p_\infty)r \cos\delta \cos\phi \, ds \, d\phi - r^2(p - p_\infty) \sin\delta \cos\phi \, ds \, d\phi.$$

Taking into account the symmetry of the pressure distribution about the zero meridian plane, integration of this equation gives

$$M_p = -2\int_0^l xr \, dx \int_0^\pi (p - p_\infty) \cos\phi \, d\phi$$

$$-2\int_0^l r^2 \tan\delta \, dx \int_0^\pi (p - p_\infty) \cos\phi \, d\phi, \qquad (1.18)$$

whence

$$C_{mp} = \frac{M_p}{qS_{\text{mid}}l} = -\frac{4\lambda_l}{\pi}\int_0^1 \bar{r}\bar{x} \, d\bar{x} \int_0^\pi C_p \cos\phi \, d\phi$$

$$-\frac{1}{\pi}\int_0^1 \bar{r}^2 \tan\delta \, d\bar{x} \int_0^\pi C_p \cos\phi \, d\phi. \qquad (1.19)$$

If the body is slender, the second terms in Eqs. (1.18) and (1.19) can be neglected.

To calculate the component of the moment coefficient depending on viscosity, we can write the expression for the elementary value of this moment:

$$dM_f = x\tau_0 \sin\delta \cos\phi \, dS - r\tau_0 \cos\delta \cos\phi \, dS$$

$$= x\tau_0 r \sin\delta \cos\phi \, ds \, d\phi - r^2\tau_0 \cos\delta \cos\phi \, ds \, d\phi.$$

Upon integration, the moment becomes

$$M_f = \int_{S_\omega} x\tau_0 \sin\delta\cos\phi\, dS - \int_{S_\omega} r\tau_0 \cos\delta\cos\phi\, dS$$
$$= 2\int_0^l xr\tan\delta\, dx\int_0^\pi \tau_0\cos\phi\, d\phi - 2\int_0^l r^2\, dx\int_0^\pi \tau_0\cos\phi\, d\phi. \tag{1.20}$$

Accordingly, the viscous component of the moment coefficient referenced to the maximum cross-sectional area of the body is

$$C_{mf} = \frac{4\lambda_l}{\pi}\int_0^1 \bar{x}\bar{r}\tan\delta\, d\bar{x}\int_0^\pi c_{fx}\cos\phi\, d\phi$$
$$- \frac{2}{\pi}\int_0^1 \bar{r}^2\, d\bar{x}\int_0^\pi c_{fx}\cos\phi\, d\phi. \tag{1.21}$$

Center of Pressure

We shall assume that the center of pressure is the same as the aerodynamic center and that it is the position along the axis of the body at which all of the normal force can be assumed to be concentrated in calculating the pitching moment. The coordinate of this point is determined by the equation $x_{cp} = M_z/N$. Substituting the corresponding aerodynamic coefficients for the pitching moment M_z and the normal force N, we obtain the following expression for the center-of-pressure coefficient:

$$\bar{x}_{cp} = \frac{x_{cp}}{l} = \frac{C_m}{C_N} = \frac{C_{mp} + C_{mf}}{C_{Np} + C_{Nf}}. \tag{1.22}$$

The value of this coefficient is independent of the location of the center of gravity.

When the angle of attack is small, the fineness ratio of the body and the crossflow velocity are comparatively unimportant, and C_{mf} and

C_{Nf} can be neglected; then the location of the center of pressure will depend only on the pressure distribution, i.e., $\bar{x}_{cp} = C_{mp}/C_{Np}$. Substituting Eqs. (1.12) and (1.19) for C_{Np} and C_{mp}, we obtain

$$\bar{x}_{cp} = \frac{\int_0^1 \bar{r}\bar{x}\, d\bar{x} \int_0^{\pi} C_p \cos\phi\, d\phi + \frac{1}{4\lambda_l} \int_0^1 \bar{r}^2 \tan\delta\, d\bar{x} \int_0^{\pi} C_p \cos\phi\, d\phi}{\int_0^1 \bar{r}\, d\bar{x} \int_0^{\pi} C_p \cos\phi\, d\phi}. \tag{1.23}$$

THE USE OF AERODYNAMIC CHARACTERISTICS FOR STABILITY STUDIES OF BODIES OF REVOLUTION IN FLIGHT

Static Stability

For a body in motion, an accidental disturbance (an initial bump when departing from the launcher, a gust of wind, a deviation of the propulsion system from its scheduled performance, etc.) causes a change in the angle of attack. The pitching moment that exists after the cessation of the disturbance results in a further variation in the angle of attack. If the angle α continues to increase, the moment is destabilizing. In this case, the change in the moment M_z (and correspondingly, in the coefficient C_m) will be the same as that of the angle of attack; i.e., the moment will increase. Consequently, for the range of α under consideration the derivative $\partial C_m/\partial\alpha = C_{m\alpha} > 0$. A body whose aerodynamic properties are characterized by the condition $C_{m\alpha} > 0$ will be statically unstable in flight. The center of pressure of such a body is located between the nose and the center of gravity.

On the other hand, if the derivative $C_{m\alpha} < 0$, the body is statically stable and the center of pressure is located behind the center of gravity. In this case the moment generated strives to decrease the absolute value of the angle of attack and to return the body to its initial position, i.e., to stabilize its flight.

If the derivative $C_{m\alpha} = 0$, the body is neutrally stable and the center of pressure coincides with the center of gravity.

The Aerodynamic Damping Moment

In the preceding derivations of the pitching moment M_z and pitching moment coefficient C_m, we were only interested in determining these quantities assuming that the pressure and shear stress distributions were known, but the conditions under which these distributions developed were not of concern. However, the previous history of the motion is of interest in the study of the aerodynamic properties of an actual vehicle in flight. At a given moment the angle of attack may have been attained under conditions where the body was moving translationally along a trajectory, with no rotation of the longitudinal axis about the center of gravity. On the other hand, it may have been reached by a combination of motion of the center of gravity and rotation about the lateral axis. The first case cannot be realized in actual flight since there is always some oscillatory motion of the body about the lateral axis. This case is observed only in wind tunnel testing, where it corresponds to steady flow over a model at a fixed angle of attack.

The second case is characteristic of actual flight; the body is oscillating and the flow around it is unsteady. This causes an additional moment of aerodynamic forces, called the damping moment.

Studies have shown that the damping moment M_{zd} is proportional to the angular velocity Ω of the body around its center of gravity and is determined from the equation

$$M_{zd} = m_z \rho_\infty V_\infty \Omega l^2 S_{\text{mid}}, \tag{1.24}$$

which defines m_z, the aerodynamic damping moment coefficient.

A case in which the direction of motion of the center of gravity remains practically unchanged can be examined as, for example, motion along a flat trajectory. Then the angular velocity can be expressed by the quantity $\dot{\alpha} = d\alpha/dt$, and the damping moment with reference to the center of gravity is given by the equation

$$M_{zd} = m_z \rho_\infty V_\infty l^2 S_{\text{mid}} \dot{\alpha}. \tag{1.25}$$

In wind tunnels this moment is usually calculated in terms of the

coefficient m_z, which can be found from force tests on models of bodies that are free to oscillate about their centers of gravity. In any case, whether the damping moment is evaluated by theoretical or experimental means, it can be used to determine the distribution of the additional pressure caused by the oscillation of the body in flow. In this case Eqs. (1.11) and (1.18) can be used to determine, respectively, the additional increment of normal force ΔN and pitching moment ΔM_z with respect to the nose. Then the damping moment with respect to the center of gravity is

$$M_{zd} = \Delta M_z - x_{cp}\,\Delta N. \tag{1.26}$$

The expression for the damping moment can also be written in the form

$$M_{zd} = C_m q S_{\text{mid}} l, \tag{1.27}$$

where the moment coefficient C_m, in accordance with Eq. (1.25), can be presented in the form

$$C_m = \frac{2m_z \dot{\alpha} l}{V_\infty}. \tag{1.28}$$

Since the coefficient m_z is independent of $\dot{\alpha}$, $C_m = (\partial C_m/\partial\dot{\alpha})\dot{\alpha}$, where the derivative is

$$\frac{\partial C_m}{\partial \dot{\alpha}} = C_{m\dot{\alpha}} = \frac{2m_z l}{V_\infty}. \tag{1.29}$$

Consequently,

$$M_{zd} = C_{m\dot{\alpha}} q S_{\text{mid}} l \dot{\alpha}. \tag{1.30}$$

The sign of the rotational derivative $C_{m\dot{\alpha}}$ is always negative, which

indicates that the damping moment tends to diminish the angular velocity of rotation.

Dynamic Stability

Analysis of the derivative $C_{m\alpha}$ allows us to determine whether or not a body is statically stable. However, this is not sufficient for evaluating the flight qualities of a moving body, since it does not describe the character of the body's motion after the cessation of the disturbance, nor does it define the values of the parameters that determine this motion. If we know only that $C_{m\alpha}$ is negative and that, therefore, the center of pressure is located behind the center of gravity, we can only reach a conclusion concerning the static stability. But we cannot determine from this the amplitude of the oscillation of the angle of attack at a given time, nor the way in which the angle of attack or other important aerodynamic parameters change with time. The theory of dynamic stability answers all of these and other questions.†

Just as $C_{m\alpha}$ or the center of pressure are criteria of static stability, there are criteria of dynamic stability that depend on the aerodynamic properties of a vehicle. One of these is the logarithmic decrement or damping constant, which is expressed in the form

$$\varepsilon = \lambda_1 T. \tag{1.31}$$

The value of this criterion depends on the damping coefficient

$$\lambda_1 = -C_{m\dot{\alpha}} q S_{\text{mid}} \frac{l}{2I}, \tag{1.32}$$

and the oscillation period

$$T = \frac{2\pi}{\left(-C_{m\alpha} q S_{\text{mid}} l/I - \lambda_1^2\right)^{\frac{1}{2}}}, \tag{1.33}$$

where I is the moment of inertia of the body.

†Editor's note: See, for example, B. Etkin, *Dynamics of Flight*, John Wiley & Sons, Inc., 1959.

The larger the damping constant, the stronger the influence of the damping, and the more rapidly the oscillations decay with time. With the damping constant as a criterion of dynamic stability, the time to decrease the oscillations to half amplitude is

$$t_2 = \frac{1}{\lambda_1} \log 2. \tag{1.34}$$

In practice it is usually desirable to design the vehicle so that the damping coefficient is large, although another of the stability parameters, the so-called oscillatory wavelength, increases somewhat thereby, which is undesirable. The oscillatory wavelength is defined as

$$\lambda = TV_\infty. \tag{1.35}$$

In practice one should attempt to decrease the oscillatory wavelength, and for this it is necessary to increase the stabilizing moment which, in its turn, leads to such favorable phenomena as a decrease in oscillatory amplitude.

At this point in the discussion, it should be remembered that in the case of an actual object that is controlled in flight, the aerodynamic properties of the vehicle, and particularly those properties that are determined by parameters of dynamic stability, need to be closely coordinated with the controllability of the flight vehicle.

GEOMETRY OF BODIES OF REVOLUTION

Pointed Bodies

In the subsequent examples that relate to determining aerodynamic characteristics, as a rule we shall examine shapes of axisymmetric bodies that are currently used in design.

Several shapes of bodies of revolution with pointed noses are shown in Fig. 5. The shapes are typical, incorporating three distinct parts, namely the forward (nose), middle, and rear (boattail or afterbody). The afterbody usually has a slender section, the area of which is more

or less the area of the middle cross section. It can be in the form of a frustum of a cone, of a portion of a body with a curved surface, and as a special case, the afterbody can be cylindrical.

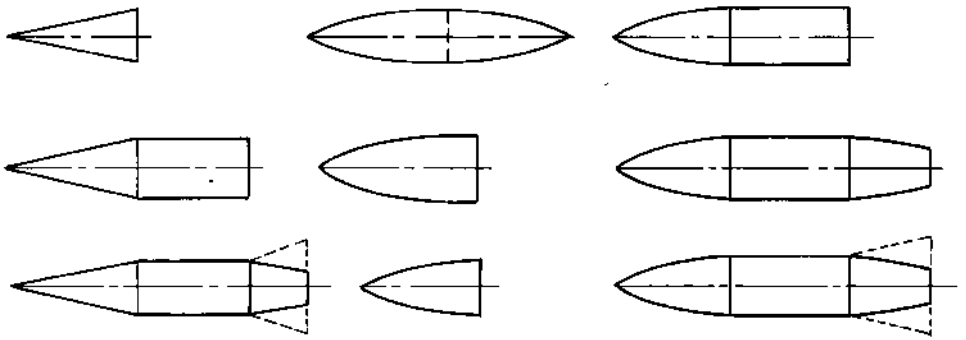

Fig. 5--Typical shapes of bodies of revolution with pointed noses

The midsection of the body can also have an arbitrary shape in the general case. Most frequently it is shaped in the form of a cylinder; sometimes it has the form of a conical frustum by means of a slight inclination of the generatrix.

The most common nose sections are in the form of cones, ogives, or parabolic bodies. The ogive nose has a generatrix that is a circular arc of a certain radius (Fig. 6). The nose section of a body may be joined to the cylindrical portion either tangentially or at some angle $\delta \neq 0$. In the first case, the ogival curve is called a tangent; in the second, a secant. The equation for an ogival curve in dimensionless form is

$$\bar{r} = 1 - 2\bar{R}\left\{1 - \left[1 - \frac{\lambda_N^2}{\bar{R}^2}(1 - \bar{x})^2\right]^{1/2}\right\}, \qquad (1.36)$$

where $\lambda_N = l_N/2r_{mid}$ is the fineness ratio of the nose (l_N is the nose length), and $\bar{R} = R/2r_{mid}$, $\bar{x} = x/l_N$, and $\bar{r} = r/r_{mid}$.

From Fig. 6 the relation between the fineness ratio λ_N and the

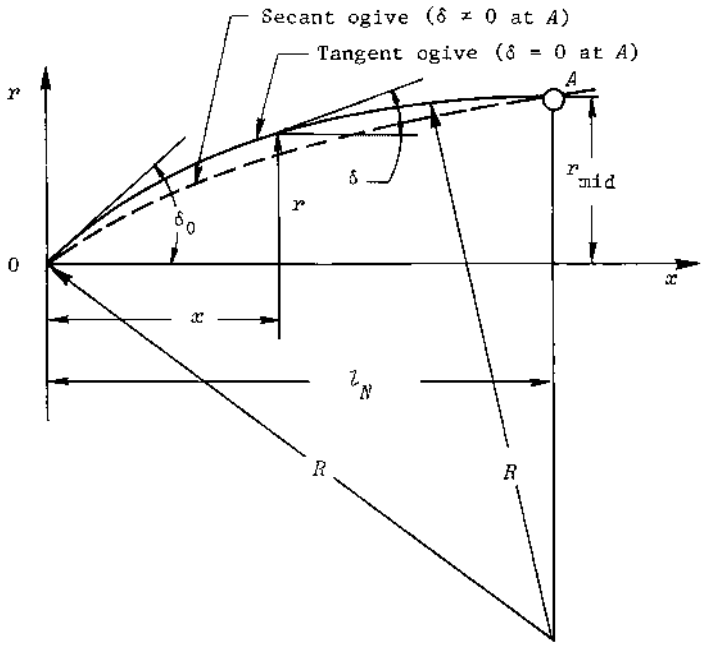

Fig. 6--Shape and geometric parameters of an ogive nose

dimensionless radius of curvature $\bar{R}$ of the ogive can be found directly:

$$\lambda_N = \sqrt{\bar{R} - 1/4}. \tag{1.37}$$

For an investigation of the flow around ogival surfaces, it is necessary to know how the slope of the surface varies along the body surface. To find this relation, Eq. (1.36) is differentiated:

$$\tan \delta = \frac{dr}{dx} = \frac{1}{2\lambda_N} \frac{d\bar{r}}{d\bar{x}}$$

$$= \frac{\lambda_N}{\bar{R}} (1 - \bar{x}) \left[1 - \frac{\lambda_N^2}{\bar{R}^2} (1 - \bar{x})^2 \right]^{-1/2}. \tag{1.38}$$

The tangent to the surface at the apex of the nose is given by

$$\tan \delta_N = \left(\frac{dr}{dx}\right)_{x=0} = \frac{\lambda_N/\bar{R}}{(1 - \lambda_N^2/\bar{R}^2)^{\frac{1}{2}}}$$

$$= \frac{\lambda_N}{\lambda_N^2 - \frac{1}{4}}. \tag{1.38a}$$

If the nose of the body is of parabolic shape rather than ogival, the body coordinates are given in the general case by the equation

$$r = x(a + bx + cx^2 + \ldots).$$

However, when the dimensionless radius of curvature $\bar{R}$ of the ogive noses defined by Eq. (1.36) becomes large, the body shape approaches that of a parabolic arc. For example, when $\bar{R} \geq 4$ the error in the coordinates is less than 3 percent. In these cases the constant $\frac{1}{4}$ in Eq. (1.37) can be neglected in comparison to $\bar{R}$, and we obtain the approximate relation $\bar{R} = \lambda_N^2$. Substituting this relation into Eq. (1.36) and simplifying, we obtain the dimensionless equation for a parabolic nose:

$$\bar{r} = \bar{x}(2 - \bar{x}). \tag{1.39}$$

The tangent of the angle of inclination between the axis of the body and the tangent to the surface is determined by differentiating Eq. (1.39):

$$\frac{dr}{dx} = \tan \delta = \frac{1}{\lambda_N}(1 - \bar{x}). \tag{1.40}$$

Hence the slope of the surface at the nose of the body is $(dr/dx)_{x=0} = \tan \delta_N = 1/\lambda_N$, and Eq. (1.40) can be rewritten as

$$\frac{dr}{dx} = (1 - \bar{x}) \tan \delta_N.$$

Similar to the ogive, the parabolic nose can be either a tangent or a secant.

A body with a parabolic shape has an important feature that results from Eq. (1.39): All such bodies are characterized by an identical longitudinal thickness distribution (Table 1). Among these bodies there may be geometrically similar bodies that differ in all of their linear dimensions by the same factor. Obviously, such bodies have identical fineness ratios and can be superposed one upon the other by means of an equivalent transformation, i.e., identical for all directions.

Table 1

THICKNESS DISTRIBUTION OF A PARABOLIC BODY

$\bar{x}$	0	0.2	0.4	0.6	0.8	1.0	1.2	1.4	1.6	1.8	2.0
$\bar{r}$	0	0.36	0.64	0.84	0.96	1.0	0.96	0.84	0.64	0.36	0

However, most parabolic bodies cannot be superposed by means of an equivalent transformation. Let us imagine two parabolic bodies of different fineness ratios. Having introduced a linear scale for the radial coordinate, the body can be deformed appropriately in the radial direction but this will not give complete congruence; another scale factor is required for the axial coordinate. Such an operation is called an affine transformation, and bodies with a parabolic shape are called affine-similar. Obviously, conical bodies, which are given by an equation in the dimensionless form $\bar{r} = \bar{x}$, are also characterized by an identical distribution of relative thicknesses and consequently will be affine-similar.

In contrast to parabolic and conical bodies, ogive noses have a lengthwise thickness distribution that varies with a change in the fineness ratio, as can be seen from Eq. (1.36). Consequently, it is impossible to transform one ogive nose into another by an affine mapping. Thus bodies with ogive noses are not affine-similar, with the exception of those cases in which the noses have an identical fineness ratio, i.e., that are geometrically similar. However, in those cases

in which the fineness ratio is large ($\lambda_N > 2$), the ogival shape differs negligibly from the parabolic, as was indicated. Therefore, the lengthwise distribution of relative thicknesses can be neglected in transforming one body into another, and most ogive noses can be considered affine-similar.

Blunt Bodies

Along with pointed bodies, blunt nose sections are widely used in practice. They are used primarily for very high speed flight, in which the basic requirement for the nose section is the capability of withstanding very high temperatures. However, quite often low-speed aircraft have a blunt nose shape depending on the structural characteristics, the purpose of the craft, etc.

One type of blunt nose is the so-called power-law shape, defined by the equation

$$r = r_{\text{mid}} \left(\frac{x}{l_N}\right)^n. \tag{1.41}$$

In the general case, when $0 < n < 1$, the nose is blunted. This is evident from the fact that the quantity $(dr/dx)_{x=0} = \infty$ for this range of n.

Aircraft with spherically blunted noses are quite common, but the shape of the remainder of the nose section behind the spherical tip can be either curved or linear (Fig. 7). The most common blunted bodies with a linear shape are in the form of cones. The equation for this shape is

$$r - r_N = (x - x_N) \tan \delta_c, \tag{1.42}$$

where $r_N = R_N \cos \delta_c$, $x_N = R_N \cot \delta_c \cos \delta_c$, and R_N and δ_c are the radius of the sphere and the cone angle, respectively. In the case of a cylindrical section tangent to a spherical nose (Fig. 8),

$$\delta_c = 0 \quad \text{and} \quad r = r_N = R_N.$$

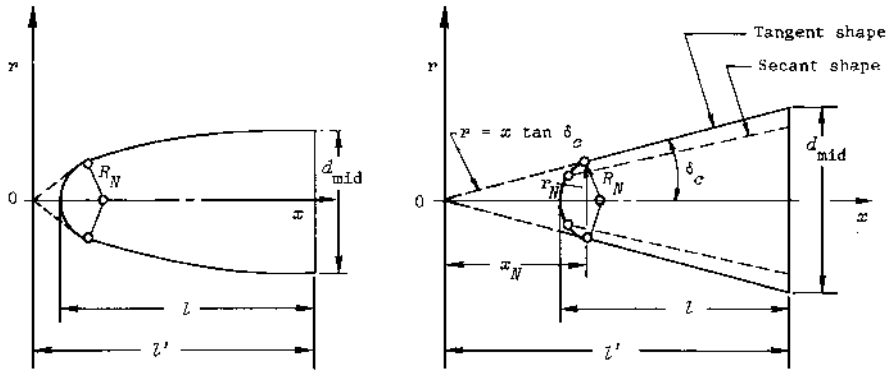

Fig. 7--Nose shapes with spherical nose caps

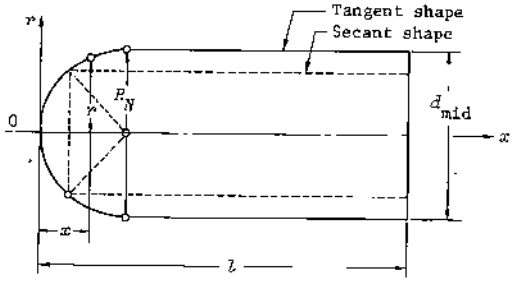

Fig. 8--Cylindrical body with a spherical nose

The equation for the spherical nose shape can be obtained from Eq. (1.36) by assuming $r_{mid} = l_N = R = R_N$. Then this equation takes the form

$$\bar{r}^2 = 1 - (1 - \bar{x})^2, \tag{1.43}$$

where now $\bar{r} = r/R_N$ and $\bar{x} = x/R_N$. The slope of the surface at a given point on the sphere is given by

$$\tan \delta = \frac{dr}{dx} = \frac{1 - \bar{x}}{\bar{r}}. \tag{1.44}$$

The spherical form of blunting includes two types of noses, in the form of secant and tangent spheres. The tangent spherical nose can be characterized by the radius of the sphere R_N. If this radius equals zero, the blunting is "nil" and, consequently, the nose is pointed (Fig. 9). The bluntness of the nose increases as the radius of the sphere increases for given values of r_{mid} and δ_c, with a maximum value of $R_N = r_{mid}/\cos \delta_c$.

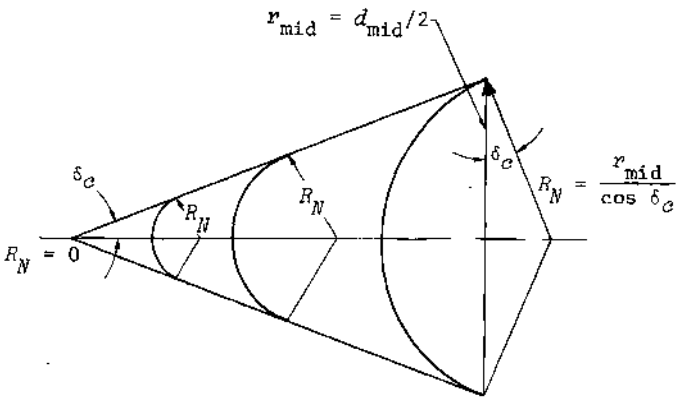

Fig. 9--Cone with varying degrees of spherical blunting

If we consider the base section of the nose to be, for example, a cone or a cylinder, the blunt nose constructed on this section with an arbitrary radius R_N has the form of a secant sphere (see Fig. 10). The smallest value of the spherical radius is $R_N = r_{mid}/\cos \delta_c$ or $R_N = r_{mid}$, i.e., the tangent sphere for a conical or a cylindrical body, respectively. The body with a flat nose corresponds to a spherical nose with an infinite radius. Therefore, the tangent spherical nose and the flat nose represent the limiting cases of an entire series of blunt nose shapes. Both of these shapes are of particular interest in aerodynamic research on blunt bodies of intermediate shape, because they make possible the evaluation of limiting values of the aerodynamic characteristics.

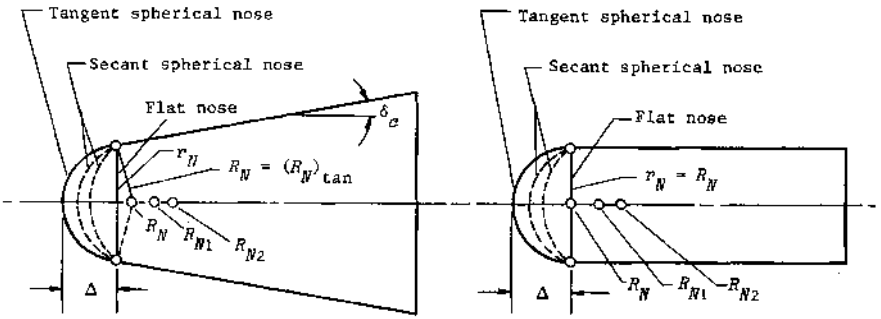

Fig. 10--Cone and cylinder with spherical and flat blunting

The spherical and the flat nose can also be considered as special cases of an elliptical surface. A cone and a cylinder with this type of blunting are shown in Fig. 11. The geometric characteristics of an elliptical nose are described by the major and minor axes and by the orientation of the axes. The special case of the major axis perpendicular to the axis of the body is illustrated in Fig. 11. When both axes are equal, the elliptical blunting becomes spherical, and when the minor axis is zero the elliptical surface degenerates into a plane.

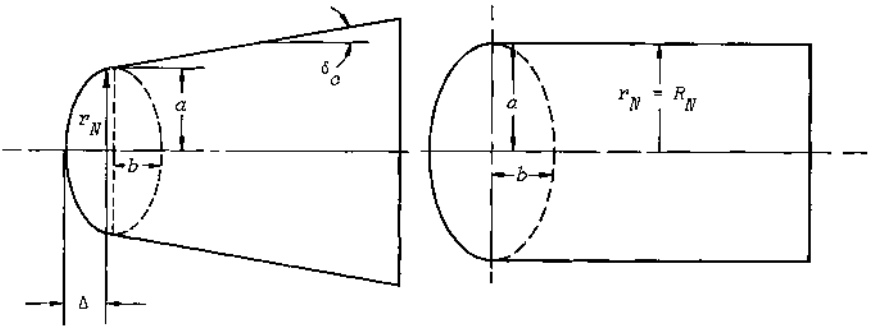

Fig. 11--Cone and cylinder with elliptical blunting

As with spherical blunting, an elliptical nose can be either secant or tangent. In the latter case, the radius r_N of the smaller end of the cone is not in general equal to the semiaxis adjoining it. This equality is strictly satisfied only in the case of a nose joined to a cylinder. However, it can be assumed to be approximately true for small cone angles.

Along with the forms of blunting already discussed, another common shape is shown in Fig. 12. The blunting consists of a flat end with a round bevel of radius r. When this radius is equal to $R_N = r_N/\cos \delta_c$, the blunting becomes a spherical shape; in the case of $r = 0$, the surface becomes a flat nose.

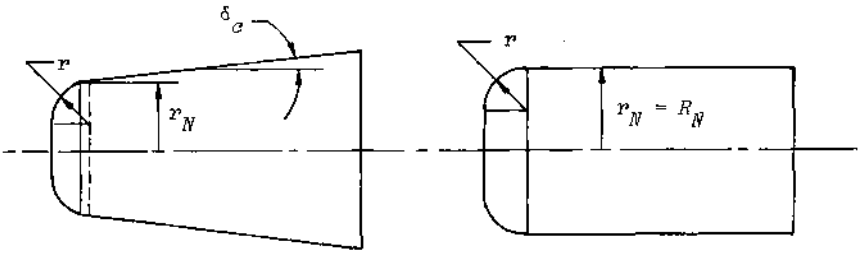

Fig. 12--Cone and cylinder with blunting in the form of a flat surface with a round bevel

The aerodynamic characteristics of blunted bodies of a given nose type depend on the degree of blunting, by which we henceforth shall mean the ratio of the radius of the base of the blunt tip r_N to the radius of the maximum cross section of the body r_{mid}. Of equal importance is the geometric parameter describing the blunt shape. For a spherical nose, this is represented by the parameter $(R_N)_{tan}/R_N$, where $(R_N)_{tan}$ is the radius of the tangent spherical nose; this ratio varies from zero to one. For an elliptical nose the geometric parameter can be the ratio of the semiaxis $\bar{b} = b/a$, which varies within the range $0 \leq \bar{b} \leq 1$ for the cylindrical body and $0 \leq \bar{b} < 1$ for the conical body.

For small angles δ_c of conical bodies, it is convenient to choose the depth Δ as one of the characteristic dimensions (see Fig. 10) and for the other, the radius r_N. Then the blunting parameter can be determined as the ratio $\bar{\Delta} = \Delta/r_N$, which will vary in the range $0 \leq \bar{\Delta} \leq 1$.

It is obvious from Fig. 12 that the quantity $\bar{r} = r/r_N$ can be chosen as the blunting parameter of a nose made in the form of a flat surface with a round bevel. This parameter will vary in the range $1 \leq \bar{r} \leq 0$ for cylindrical and conical bodies with small angles δ_c.

Of course, the variety of all of the bodies encountered in practice has not been exhausted by the forms of blunt and pointed noses discussed here. We have presented only the simplest typical forms which reflect that variety to some degree. It is important to note that theoretical solutions have been found for these shapes, and rather extensive experimental data have been obtained.

§ 2. *THE BASIC FEATURES OF VERY HIGH VELOCITY GAS FLOW*

THE VARIATION OF SPECIFIC HEATS WITH TEMPERATURE

BECAUSE OF THE GREAT INCREASE in aircraft speeds in recent years, it has become necessary to consider the effects of variations in the physical-chemical characteristics of air when studying the aerodynamics of gas flows at these speeds. In "ordinary" supersonic aerodynamics, compressibility is the dominant characteristic of the flow, and the effect of temperature on the thermodynamic properties of the gas, particularly the specific heat, can be neglected. At hypersonic speeds, however, the dominant effects are those due to high temperatures, arising either from strong shock waves in the flow field or from the viscous deceleration of the flow in the boundary layer. As the temperature increases, the specific heats of a gas increase, at first due to excitation of the translational and rotational degrees of freedom and, at higher temperatures, due to the excitation of the vibrational levels of the internal energy.

Studies of shock waves and of the boundary layer have shown that all the relationships of ordinary supersonic aerodynamics are valid as long as the flow conditions are such that the specific heat can be assumed to be constant and the equation of state for an ideal gas can be used, i.e., $p = \rho RT$, where R is the absolute gas constant and ρ and T are the density and temperature of the gas, respectively.

We must consider the variation in specific heat at temperatures lower than those for which the equation of state departs appreciably from that for a perfect gas. For example, the effects of the variation in specific heat due to temperature become significant for the transition through a normal shock wave at Mach numbers of 3 to 4. However, we can retain the equation of state for a perfect gas and that for the velocity of sound ($a^2 = \gamma RT$) up to Mach numbers of 6 or 7 ($\gamma = c_p/c_v$ is the adiabatic exponent, equal to the ratio of the specific heat c_p at constant pressure to the specific heat c_v at constant volume).

Thermodynamic tables or interpolation formulas can be used to find the actual specific heats as a function of temperature. Assuming that the specific heats vary linearly with temperature, empirical formulas for conditions of thermodynamic equilibrium are

$$c_p = 0.2317 + 0.000221T, \qquad c_v = 0.1647 + 0.000221T, \tag{2.1}$$

where c_p and c_v are given in kcal/kgf·deg. It is apparent that the adiabatic exponent γ can be determined easily from Eq. (2.1).

Another approximate estimate of the temperature influence on the specific heat at constant pressure is given by[2]

$$\frac{c_p}{c_{p_\infty}} = \left(\frac{T}{T_\infty}\right)^{\varphi}, \tag{2.2}$$

where the exponent in turn is a function of the temperature (Fig. 13). For $T > 1000°K$, this exponent can be assumed constant at $\varphi = 0.1$. In numerical calculations with $T_\infty = 288°K$ (i.e., room temperature), it is customary to assume that the specific heat $c_{p_\infty} = 0.24$ kcal/kgf·deg. The specific heats and adiabatic exponent can be calculated taking into account only the effect of temperature up to temperatures of 2000° to 2500°K, where the vibrational degrees of freedom are fully excited.

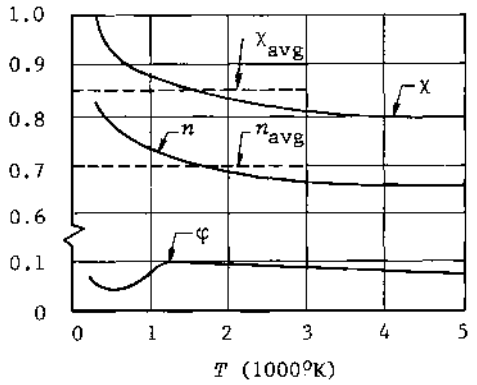

Fig. 13--Exponents in equations for specific heat, viscosity, and thermal conductivity

DISSOCIATION AND IONIZATION

The Thermodynamic Functions of Air at Very High Temperatures

At high temperatures air ceases to follow the equation of state of a perfect gas due to disarrangements in the molecular structure. The vibrational degrees of freedom being fully excited, further temperature increases provide enough energy for the atoms to overcome the intramolecular forces, resulting in the diatomic molecule breaking up into two monatomic molecules. This is called the dissociation process.

Dissociation is completed at a temperature of the order of 6000°K. At higher air temperatures, another process begins to develop and results in the ionization of the air; i.e., electrons escape from the atom because of the large influx of energy. The collision of molecules in thermal motion is the basic cause of ionization; therefore, such a process is called thermal ionization. Its intensity is in proportion to the increase in temperature and is obviously accompanied by an increase in the concentration of free electrons. The intensity of this process can be characterized by the degree of ionization, which is equal to the ratio of the number of ionized atoms to the total number of atoms present. Studies indicate that hydrogen and nitrogen, for example, are fully ionized (the degree of ionization equals unity) at 10,000° and 17,000°C, respectively, for a pressure of 1 atm.

The assumption of constant stagnation temperature, on which the usual shock-wave equations are based, is not valid with the existence of dissociation and ionization. Therefore, the equations must take into account the physical-chemical changes in air at high temperatures.

Important elements in the calculation of these flows are the determination of the thermodynamic properties and kinetic coefficients of the dissociated and ionized air, as well as its composition. Detailed data are now available on these parameters and coefficients, as well as on the composition of air under conditions of thermodynamic equilibrium at temperatures of 1000° to 20,000°K and pressures of 0.001 to 1000 atm. These data were obtained with the aid of electronic computers by a group of Soviet scientists under the leadership of Professor A. S. Predvoditelev of the Academy of Sciences USSR.[1,3] Calculations were made for temperatures of 1000° to 6000°K without including

ionization, since its influence in this temperature range is negligibly small, but the effect of ionization was taken into account in the calculations in the temperature range of 6000° to 20,000°K. The hypothetical mechanism of so-called single ionization[4] was used to simplify the calculations; with this approximation, air was fully ionized at T = 12,000°K and p = 0.001 atm.

Based on the results of these calculations, graphs of atomic and molecular concentrations have been plotted (Fig. 14) and the enthalpy-entropy diagram (i-S diagram) is presented in Fig. 15 as a function of pressure and temperature. These graphs are replotted in Fig. 16 with density and temperature as the independent variables, and in terms of the dimensionless enthalpy i/RT_∞ and the dimensionless entropy S/R.

Graphs such as Fig. 17, which permit the determination of the average molecular weight μ_{avg} of dissociated and ionized air depending

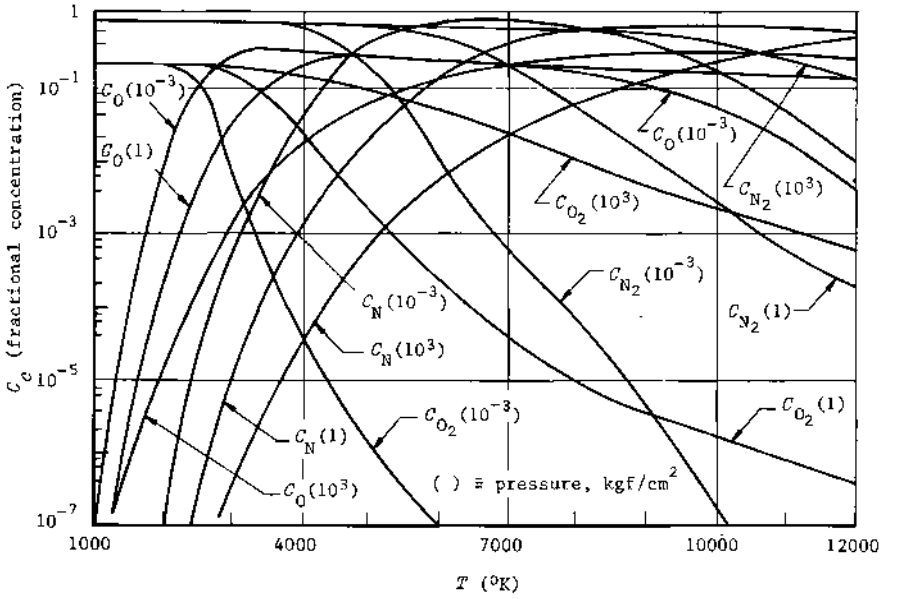

Fig. 14--Atomic and molecular concentrations of the components of air

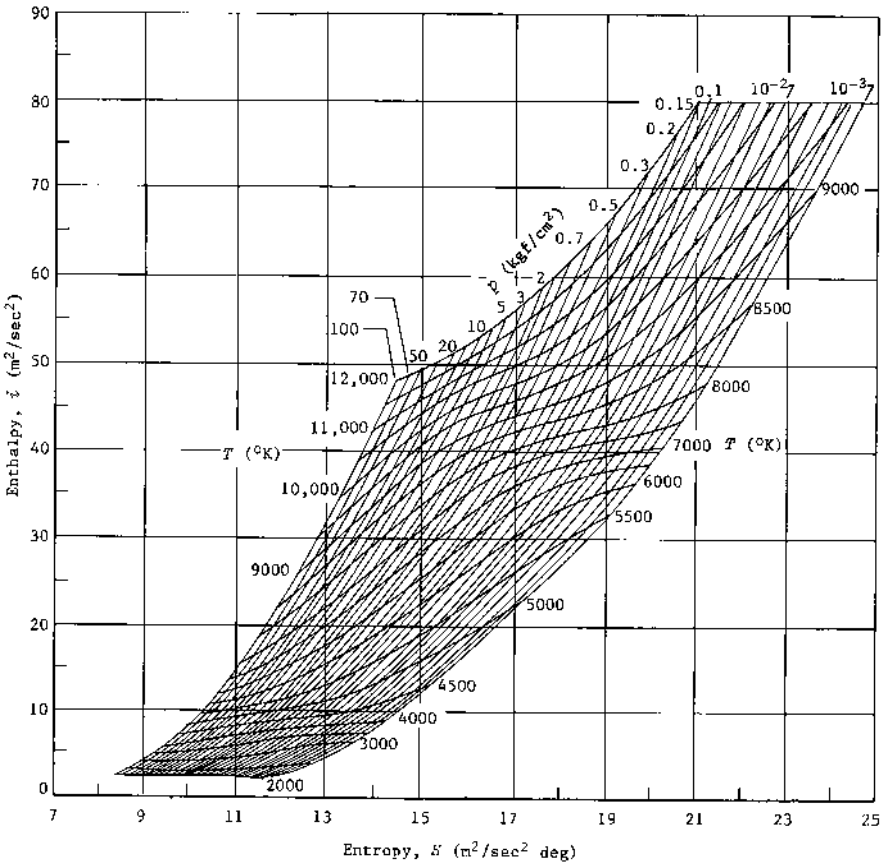

Fig. 15--Enthalpy-entropy diagram

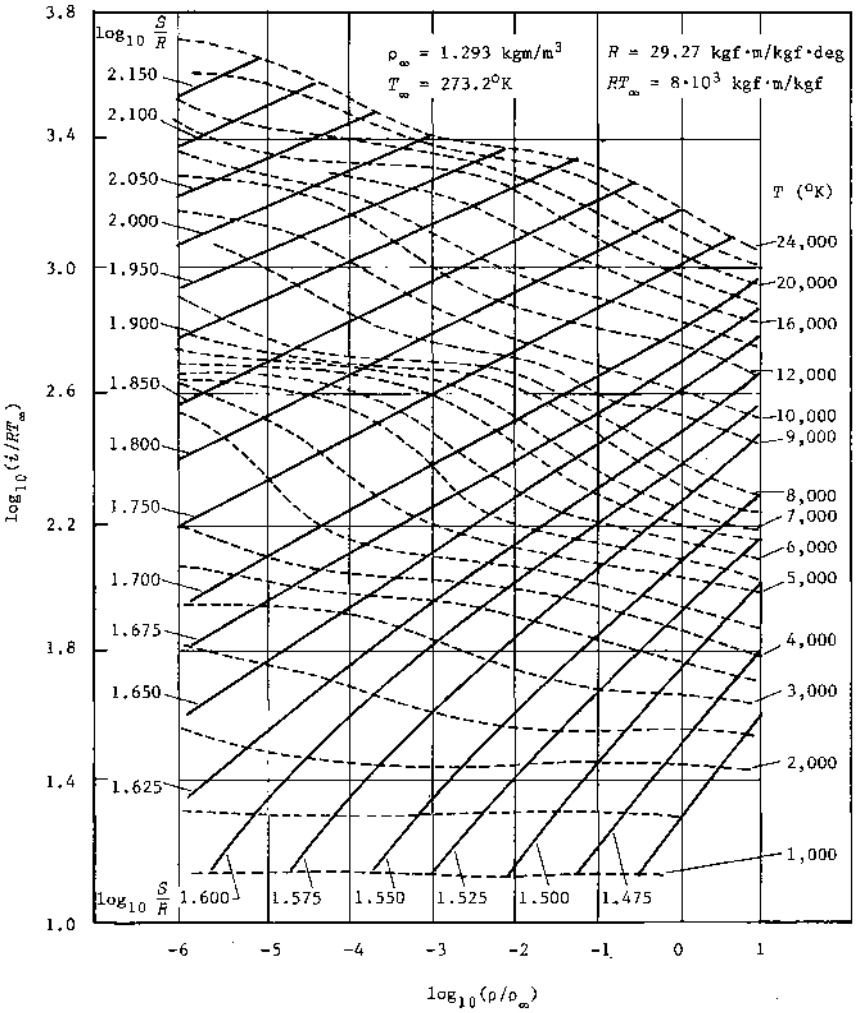

Fig. 16--Air parameters at high temperature in thermodynamic equilibrium

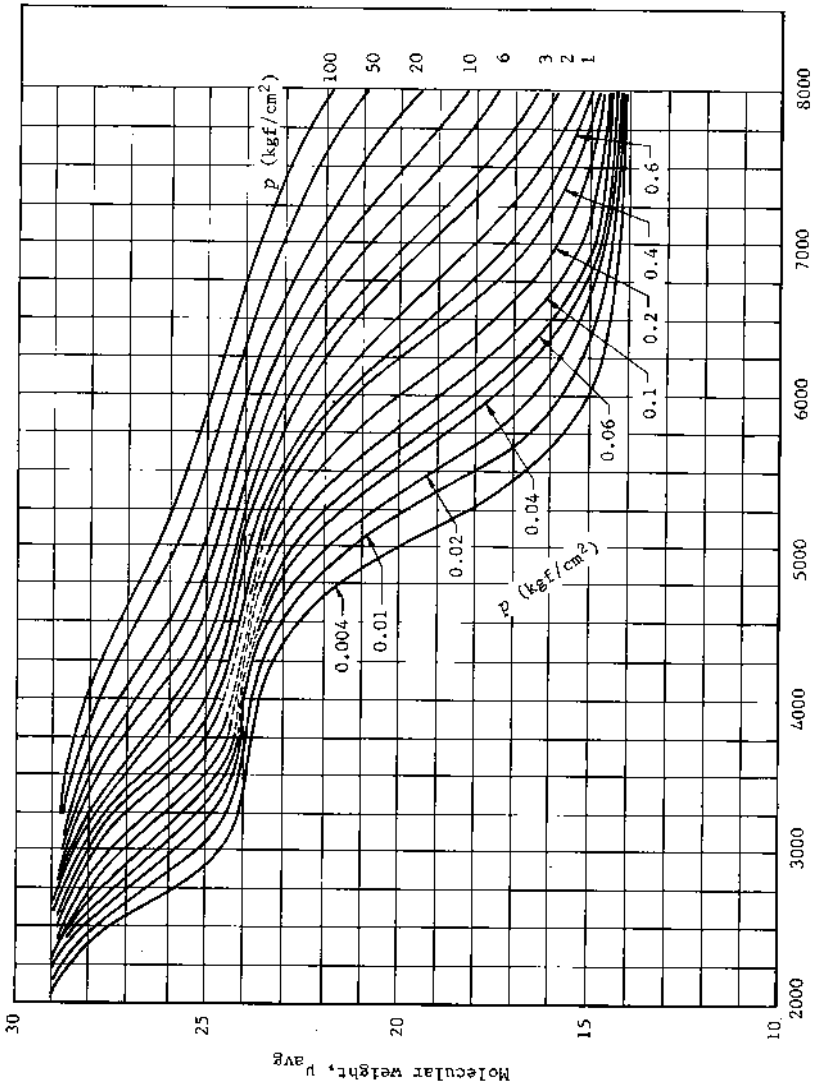

Fig. 17--Average molecular weight of air at high temperature

on temperature and pressure, are important for practical calculations. As is evident from the graph, the average molecular weight decreases with temperature, and three regions of sharp decrease can be noted. The first of these is caused by the dissociation of oxygen, the second by the dissociation of nitrogen, and the third by ionization.

It is possible to find the value of the velocity of sound as a function of temperature and pressure with the help of still another set of curves presented in Fig. 18.

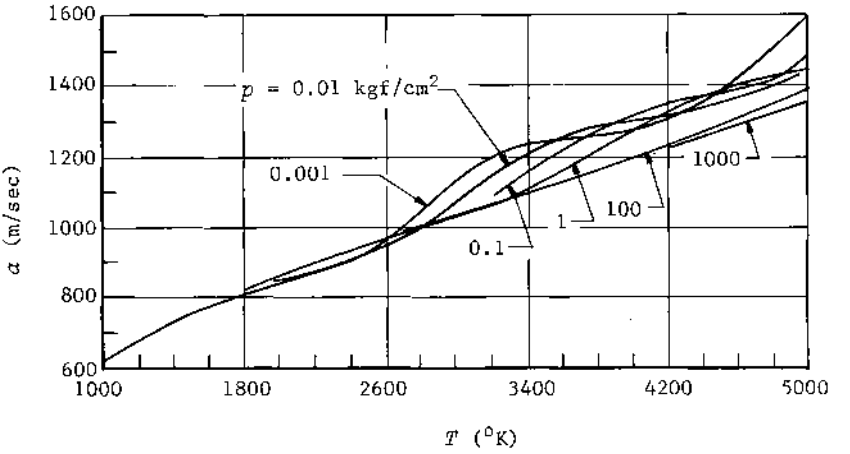

Fig. 18--Speed of sound in air at high temperature

The Kinetic Coefficients of Dissociated and Ionized Air

In friction and heat transfer research, it is necessary to know the values and the laws of variation of kinetic gas parameters such as the coefficients of viscosity μ and thermal conductivity λ. It has been established that, in the absence of dissociation, the viscosity of air depends only on temperature and, in practice, does not depend on pressure. The temperature relation can be presented in various forms. One example is the power relation, which has the form

$$\frac{\mu}{\mu_\infty} = \left(\frac{T}{T_\infty}\right)^n, \tag{2.3}$$

where the subscript ∞ denotes undisturbed flow parameters or in general an initial value of the quantity in question. The exponent n, in turn, depends on temperature (see Fig. 13). For comparatively small values of T, it can be assumed that $n = 0.76$ (or 3/4). According to Fig. 13, the average value is $n \approx 0.7$ for quite a wide temperature range, while the initial value of μ can be assumed to be $\mu_\infty = 1.82 \cdot 10^{-6}$ kgf·sec/m^2 at $T_\infty = 288°$K. For the so-called isothermal atmosphere, the initial conditions correspond to the values $T_\infty = 261°$K, $p_\infty = 1.058$ kgf/cm^2, $\rho_\infty = 0.125$ kgf·sec^2/m^4, and $\mu_\infty = 1.75 \cdot 10^{-6}$ kgf·sec/m^2.

In approximate calculations, it is possible to use Eq. (2.3) up to temperatures of the order of 2000° to 2300°K, i.e., until dissociation sets in. For temperatures less than 1500°K, the Sutherland equation gives somewhat better results (temperature in °K):

$$\frac{\mu}{\mu_\infty} = \left(\frac{T}{T_\infty}\right)^{1/2} \frac{1 + 111/T_\infty}{1 + 111/T}. \qquad (2.4)$$

As the temperature increases and dissociation begins, the viscosity of air begins to depend on pressure. Unfortunately, there are no experimental data on viscosity at high temperatures. Only theoretical results are available and furthermore, they are very approximate, having been deduced on the assumption that air is a binary mixture of molecular components (nitrogen, oxygen, and nitrogen oxide) and atomic components (nitrogen, oxygen, and argon). The results of these theoretical calculations[4] are presented in Fig. 19.

The viscosity of equilibrium air has been determined by several investigators (in particular Van Driest) assuming that the interaction potentials of all particles are equivalent. The results differ from the Sutherland equation by less than 10 percent up to 9000°K, and Eq. (2.4) could be used for estimating μ for dissociated air. However, it is better to use the more accurate Sutherland equation for partially dissociated air:

$$\frac{\mu}{\mu_\infty} = \left(\frac{T}{T_\infty}\right)^{1/2} \frac{1 + 111/T_\infty}{1 + 111/T} \left(\frac{1}{1 + 0.89 c_A/c_M} + \frac{1.42}{1 + 1.26 c_M/c_A}\right), \qquad (2.5)$$

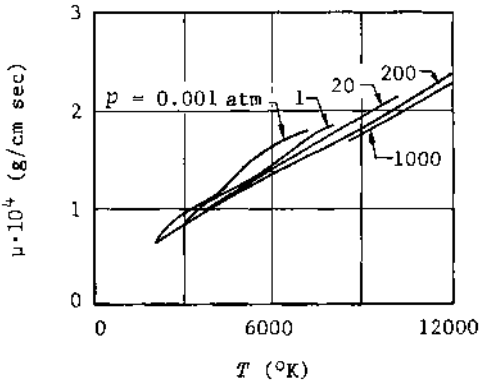

Fig. 19--Viscosity coefficient of air at high temperature

where c_M and c_A are the concentrations of molecules and atoms, respectively, for the binary mixture $c_M + c_A = 1$. In this case it is possible to replace the concentration by the degree of dissociation α, i.e., $c_A = \alpha$, $c_M = 1 - \alpha$.

Without dissociation $\alpha = 0$ and Eq. (2.5) converts to the usual Sutherland equation. For complete dissociation ($\alpha = 1$), the term in the second set of parentheses in Eq. (2.5) equals 1.42, which indicates a 42 percent increase in viscosity compared with an undissociated medium at the same temperature.

In the same way as viscosity, thermal conductivity does not, in practice, depend on pressure for temperatures up to 2000°K, and can be determined as a function of viscosity and specific heat from the equation

$$\frac{\lambda}{\lambda_\infty} = \frac{\mu}{\mu_\infty} \frac{c_p - 0.0374}{c_{p_\infty} - 0.0374}, \tag{2.6}$$

where the specific heats c_p and c_{p_∞} have the dimensions kcal/kgf·deg, and μ and λ have the dimensions kgf·sec/m^2 and kcal/m·sec·deg, respectively. The exponential equation is simpler:

$$\frac{\lambda}{\lambda_\infty} = \left(\frac{T}{T_\infty}\right)^\chi, \tag{2.7}$$

in which the exponent χ is a function of temperature as shown in Fig. 13. In approximate calculations, the average value $\chi = 0.85$ can be assumed. The coefficient λ_∞ can be taken for conditions of an isothermal atmosphere ($T_\infty = 261°K$), i.e., $\lambda_\infty = 5.53 \cdot 10^{-3}$ kcal/m·sec·deg. In solving practical problems it must be kept in mind that thermodynamic parameters such as specific heats vary significantly less with temperature than do the kinetic coefficients μ and λ.

At high temperatures, dissociation causes additional variations in the thermal conductivity coefficient, these effects being larger for the lower pressures. The simplest theoretical method for computing the thermal conductivity coefficient of air consists of representing the air as a reacting binary mixture of gases. The results obtained[4] are presented in Fig. 20.

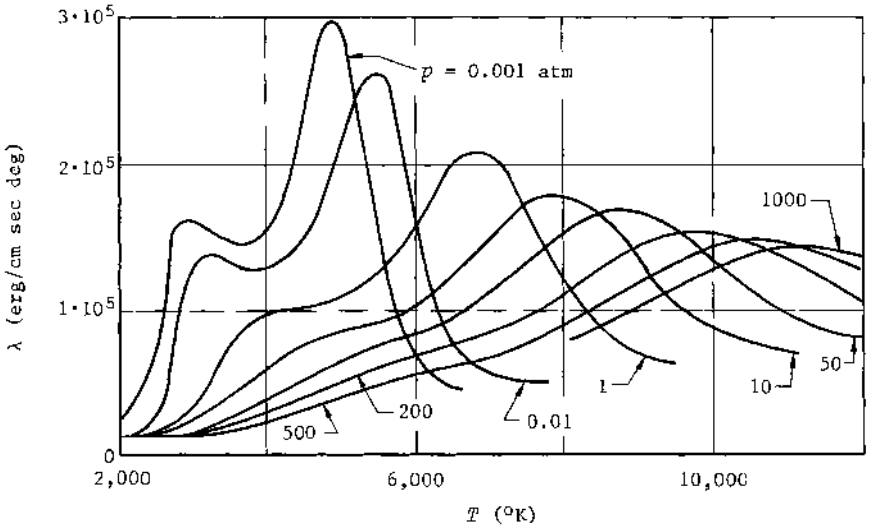

Fig. 20--Thermal conductivity coefficient of air at high temperature

The data on the state parameters and the kinetic characteristics of air presented in Ref. 5 will be found to be very useful in research on high temperature flows.

Basic Relations for a Diatomic Dissociating Gas

The information presented above pertained to dissociating air, which as a chemical medium is a complex mixture of diatomic and monatomic gases. Strictly speaking, this mixture is not a mechanical aggregate of various components, but a complex combination of chemically reacting substances. However, for practical purposes air can be represented as a conventional diatomic gas. Such a dissociating medium consists of symmetric molecules of one kind that are dissociating into two atoms as a result of double collisions. In turn, the atoms can recombine into a molecule by means of triple collisions. This scheme allows the study of the dissociation mechanism of a so-called ideal dissociating diatomic gas,[6] the concept of which requires the absence of ionization.

Naturally, the study of the dynamics of a dissociating gas is based on the establishment of specific assumptions that simplify the study of the dissociation phenomenon itself. One of these is the premise, which can be established in chemical thermodynamics, concerning the equilibrium of dissociation. This implies that in a chemical reaction defined, for example, by the simplest equation of the binary process,

$$A_2 \underset{r_R}{\overset{r_D}{\rightleftharpoons}} A + A, \tag{2.8}$$

the rates of the reactions from left to right, r_D, and from right to left, r_R (the rates of dissociation and recombination, respectively) are identical.

In most studies of dissociating flows, an initial limit is set on the degree of equilibrium dissociation. The degree of dissociation is defined as a value α that equals the ratio between the moles of fully dissociated gas and the initial number of moles of undissociated gas at a specific temperature and pressure (or density).

The calculation of the degree of dissociation of air can be simplified by examining air as a mechanical mixture consisting of pure dissociable components, i.e., nitrogen N_2 and oxygen O_2. In this

connection it is important to establish the conditions under which the chemical reaction of decomposition into atomic nitrogen and oxygen occurs. If we consider the chemical thermodynamics of an ideal dissociating diatomic gas (which includes nitrogen and oxygen), the relation for determining the degree of equilibrium dissociation is

$$\frac{\alpha^2}{1-\alpha} = \frac{\rho_d}{\rho} e^{-T_d/T}. \tag{2.9}$$

Equation (2.9) corresponds to the reaction indicated in Eq. (2.8), the degree of dissociation being determined by

$$\alpha = \frac{n_A}{n_A + 2n_{A_2}}, \tag{2.10}$$

where n_A is the number of atoms of the element A per unit volume, and n_{A_2} is the number of molecules of the gas A_2 in the same volume.

The quantities ρ_d and T_d in Eq. (2.9) are the characteristic density and temperature, respectively. Computations show that the characteristic temperature of dissociation for oxygen is T_d = 59,000°K, and for nitrogen T_d = 113,000°K. The characteristic density varies somewhat as a function of temperature (Table 2). Since this variation is very small, average values of 150 g/cc for oxygen and 130 g/cc for nitrogen can be assumed for ρ_d in approximate studies.

Equation (2.9) is plotted in Fig. 21, from which it is possible to estimate the degree of dissociation α for any dimensionless values

Table 2

CHARACTERISTIC PARAMETERS OF DISSOCIATION

Element	p_d atm	u_d kcal/kgf	u_d m^2/sec^2	V_d m/sec	ρ_d g/cm³	
					1000<T<7000°K	5000<T<7000°K
Oxygen	$2.3\cdot10^7$	$3.7\cdot10^3$	$1.5\cdot10^7$	$3.9\cdot10^3$	150	130
Nitrogen	$4.1\cdot10^7$	$8.0\cdot10^3$	$3.4\cdot10^7$	$5.8\cdot10^3$	130	125
Air	$3.7\cdot10^7$	$7.1\cdot10^3$	$3.0\cdot10^7$	$5.4\cdot10^3$	135	126

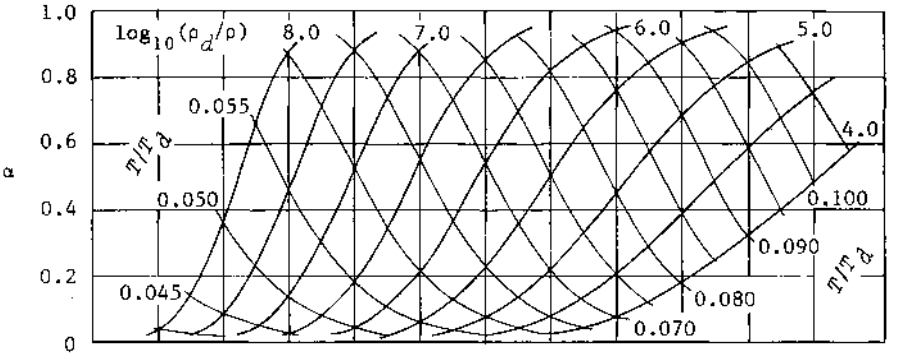

Fig. 21--Degree of dissociation of a diatomic gas as a function of temperature and density

of T/T_d and ρ/ρ_d. Similar sets of curves are presented in Figs. 22 and 23, which allow the determination of α from either ρ/ρ_d or T/T_d along with the relative enthalpy i/u_d, calculated from the so-called specific heat of dissociation u_d. The specific heat of dissociation is also called the characteristic energy of dissociation per unit mass (the energy of dissociation of one gram of A_2) and is determined from the equation

$$u_d = \frac{D}{2m_A}, \tag{2.11}$$

where m_A is the mass of the atom, and D is the energy of dissociation of a molecule of A_2. Approximate values of u_d are presented in Table 2, and more accurate values in Table 3.

Table 3

ENERGY OF DISSOCIATION OF NITROGEN AND OXYGEN

Units	Nitrogen	Oxygen
Electron volts/molecule	9.76	5.08
kcal/g-mole	225	117
kcal/kgf	8089	3686

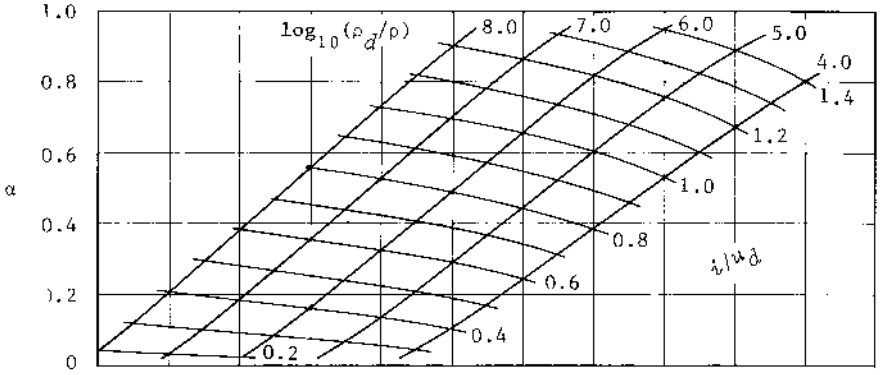

Fig. 22--Degree of dissociation of a diatomic gas as a function of enthalpy and density

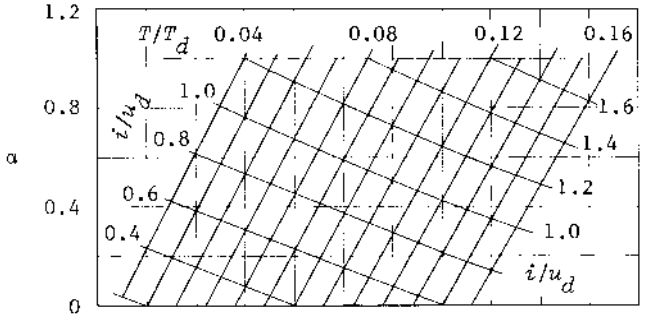

Fig. 23--Degree of dissociation of a diatomic gas as a function of temperature and enthalpy

In addition to the characteristic parameters already mentioned, we can define a characteristic pressure p_d and a characteristic velocity V_d, the concept of which is given below.

The equation of state for a gas mixture generated as the result of dissociation of diatomic molecules is obtained from the relations for the pressure of the mixture p and the partial pressures of the components p_i:

$$p = \sum_i p_i, \tag{2.12}$$

$$p_i = \rho_i T \frac{k}{m_i}, \tag{2.13}$$

where k is the gas constant with reference to one molecule (Boltzmann constant), and the subscript i designates the gas component. Henceforth, we shall describe the atomic component $i = 1$ by the subscript A and the molecular component $i = 2$ by the subscript M.

Since the concentration of the component is $c_i = \rho_i/\rho$, i.e., for atomic and molecular components, respectively, $c_1 = c_A = \alpha = \rho_A/\rho$, and $c_2 = c_M = 1 - \alpha = \rho_M/\rho$, we find the equation of state from Eqs. (2.12) and (2.13) on condition that $m_M = 2m_A$:

$$p = \frac{k}{2m_A} \rho T(1 + \alpha), \tag{2.14}$$

where $k/2m_A$ is the gas constant for 1 gm of component A_2 in the mixture.

Relating Eq. (2.14) to the state specified by the characteristic parameters, we obtain a relation for the characteristic pressure, $p_d = 0.5k\rho_d T_d/m_A$. Since the energy of dissociation of a molecule of A_2 equals $D = kT_d$, then

$$p_d = \frac{D\rho_d}{2m_A}.$$

The characteristic velocity is determined from the equation $V_d = u_d^{1/2}$. Values of p_d and V_d for oxygen and nitrogen are presented in Table 2.

Several thermodynamic equations for a diatomic dissociating gas will be of interest. In particular, the equation for the internal energy of a unit mass of gas has the form

$$u = \frac{3}{2} \frac{kT}{m_A} + \frac{D}{2} \frac{\alpha}{m_A}. \tag{2.15}$$

Dividing u and T by the corresponding characteristic parameters u_d and T_d, this equation can be written in the dimensionless form

$$\bar{u} = 3\bar{T} + \alpha, \tag{2.16}$$

where $\bar{u} = u/u_d$, $\bar{T} = T/T_d$. The equation for enthalpy can also be written in dimensionless form:

$$\bar{i} = \bar{u} + \frac{\bar{p}}{\bar{\rho}}, \tag{2.17}$$

in which $\bar{i} = i/u_d$, $\bar{p} = p/p_d$, and $\bar{\rho} = \rho/\rho_d$. Using the concept of dimensionless parameters, the equation of state (2.14) can also be reduced to dimensionless form:

$$\bar{p} = \bar{\rho}\bar{T}(1 + \alpha). \tag{2.18}$$

Introducing Eq. (2.16) for $\bar{u}$ into Eq. (2.17) and using Eq. (2.18), we obtain for the enthalpy

$$\bar{i} = \alpha + \frac{4 + \alpha}{1 + \alpha}\frac{\bar{p}}{\bar{\rho}}. \tag{2.17a}$$

Thus far we have examined an ideal dissociating diatomic gas. Considering a mixture of diatomic gases, these relations are inaccurate, strictly speaking, for determining gasdynamic and thermodynamic parameters, particularly the degree of ionization. Examining air as a mixture in which nitrogen predominates, we can conclude that at high temperatures nitrogen will exert a basic influence on all the chemical phenomena and on the related gasdynamic and thermodynamic processes. Under these conditions the representation of real air in the form of a model of a diatomic gas is valid not only because nitrogen dissociation will be the predominant process but also because the molecular weights of oxygen and nitrogen are very close. At the same time, the considerable disparity in the characteristic temperatures of nitrogen and oxygen (for nitrogen the characteristic temperature is twice as large as that of oxygen) separates the influence of the dissociation of O_2 on the entire dissociating mixture. Oxygen begins to dissociate at considerably lower temperatures than does nitrogen and is fully dissociated by the time nitrogen begins to dissociate.

If it is assumed that N_2 starts to dissociate at 3500°K, at this temperature the degree of dissociation of a diatomic model of air will be established by the relative mass of oxygen in the mixture, i.e., by the value 0.235.

For $T < 3500$°K, the degree of dissociation of the air model is

$$\alpha = 0.235\alpha_{O_2}, \tag{2.19}$$

where α_{O_2} is the degree of dissociation of pure oxygen. When the O_2 is completely dissociated, $\alpha_{O_2} = 1$, and for $T > 3500$°K the degree of dissociation of air is determined from the expression

$$\alpha = 0.235 + 0.765\alpha_{N_2}, \tag{2.20}$$

where α_{N_2} is the degree of dissociation of pure nitrogen, and the value 0.765 is determined by the fractional volume of N_2 in air. For fully dissociated air, $\alpha_{O_2} = \alpha_{N_2} = 1$ and, consequently, $\alpha = 1$.

Thus, for an approximate calculation of the degree of dissociation as well as of other parameters, a simplified mass composition of undissociated air is usually assumed, made up of 76.5 percent N_2 and 23.5 percent O_2 (although atmospheric air contains about 1 percent monatomic inert gases). In addition, it is possible to use an approximate method based on the determination of effective values of the characteristic parameters of the dissociation of air consistent with the mass fractions of nitrogen and oxygen. For example, the effective characteristic pressure of dissociation is found from the equation

$$p_d = p_{dN_2} r_{N_2} + p_{dO_2} r_{O_2}, \tag{2.21}$$

where $r_{N_2} = 0.765$, $r_{O_2} = 0.235$, and p_{dN_2} and p_{dO_2} are the characteristic pressures of the dissociation of nitrogen and oxygen, respectively. It is possible to calculate the effective values of the other characteristic parameters in an analogous manner. The effective values of p_d, u_d, and V_d calculated in this way are presented in Table 2. It should be

noted that these values are considerably greater than the corresponding values for oxygen because of higher energy of dissociation of nitrogen.

In calculating the degree of dissociation and other parameters for air, we can proceed from the assumption that all the equations presented above and relating to diatomic gases can be used, with the characteristic parameters obtained in accordance with the initial mass composition. Thus, air can be examined as a diatomic, ideal, dissociable gas, representing a mixture of N_2 and O_2, and the appropriate relations of chemical thermodynamics can be applied to it. However, the relations for an ideal dissociating gas reduce to an initial (undissociated) state that would correspond to a condition with excited vibrational energy levels and an adiabatic exponent $\gamma = 1.33$. Strictly speaking, such a gas does not exist under ordinary flight conditions, but the relationships presented above have practical value. Transition of the flow through the shock wave ahead of the body is a nonequilibrium process. Even for very high speeds and therefore high temperatures behind the shock wave, the flow is undissociated immediately behind the shock but the vibrational levels are excited. Thus, the properties of the real and the hypothetical gas are similar just behind the shock wave. The accuracy of the calculations increases as the flight velocity increases, since the gas behind the shock wave is heated to very high temperatures.

RELAXATION PHENOMENA

Nonequilibrium Flows

The methods examined above for calculating the thermodynamic parameters, taking into account the physical-chemical changes, are based on the assumption of equilibrium flow processes. This assumption involves conformity between the energy levels of the internal degrees of freedom and the parameters characteristic of the state of the gas. For example, at comparatively low temperatures (low velocities), equilibrium is established between the temperature and the vibrational degrees of freedom, which corresponds to equilibrium between the temperature and the specific heat. At high temperatures (large velocities), when the gas is dissociating, the equilibrium process is characterized by

adjustment between the degree of dissociation and the temperature and pressure. Finally, at still higher temperatures (very high velocities) equilibrium results from adjustments in the excitation of electron states and the degree of ionization.

If a sudden temperature change in an equilibrium flow can establish instantaneously the corresponding internal degrees of freedom, and if dissociation and ionization can be looked upon as manifestations of new degrees of freedom, there will be no lag in the establishment of degrees of freedom; i.e., the time for achieving equilibrium will be equal to zero. Essentially equilibrium conditions are observed in supersonic flow around bodies at Mach numbers of about 4 or 5 under conditions corresponding to altitudes of 10 to 15 km or less. Under these conditions, the maximum temperatures generated are of the order of 1000° to 1500°K. The main portion of the internal energy is transferred into translational and rotational degrees of freedom, which are established practically instantaneously by sudden temperature changes since only a few molecular collisions are sufficient to achieve equilibrium. For this reason, the translational and rotational degrees of freedom are usually called "active" degrees. With increases in velocity and, consequently, in temperature, a considerable portion of the internal energy is transferred into vibration, then dissociation, then excitation of the electron levels and ionization.

Real gas flow processes are such that these energy states are established more slowly than the translational and rotational states, since a considerably larger number of collisions are required for their establishment. Therefore, the vibrational and dissociational degrees are sometimes called "passive." The delay in achieving equilibrium, particularly for the passive degrees, is called relaxation. The time during which equilibrium is achieved (when conformity between the temperature and the energy level is established) is the relaxation time.

Relaxation processes are defined by the kind of degree of freedom that is becoming excited. If a sudden temperature variation gives rise to vibrations, the nonequilibrium process accompanying it is called vibrational relaxation. It is characterized by a delay in the variation of the specific heat with temperature. If the temperature is increased,

the specific heat is increased because of the change in the molecular motion from translation and rotation to translation, rotation, and vibration. The time required for the vibrational motion to reach equilibrium is called the vibrational relaxation time. A sudden temperature change in a dissociating gas results in a delay in the change in the degree of dissociation. This is explained by the fact that, particularly with a rapid temperature increase, the rate of generation of atoms exceeds the rate of disappearance; i.e., the dissociation rate is greater than the recombination rate. From the standpoint of energy, a relatively small number of collisions is required to produce dissociation; but to accomplish recombination, the comparatively infrequent occurrence of three particle collisions is necessary. The direct and reverse reaction rates become balanced in time; the time required to obtain an equilibrium concentration (or degree of dissociation) is called the dissociation relaxation time.

Vibrational and dissociational relaxation processes are of primary importance at temperatures up to approximately 10,000°K. Relaxation processes connected with the electronic states of molecules and atoms, as well as ionization, can be neglected below 10,000°K since very little of the internal energy is contributed to these degrees at these temperatures.

Nonequilibrium conditions have an important influence on the various processes accompanying gas flow at high velocities. In particular, vibrational and dissociational relaxation changes the gas parameters on passing through shock waves and in the flow around bodies, which, in turn, influences the friction and heat transfer processes and the pressure distribution.

Equations for Chemical Reaction Rates

The study of nonequilibrium flows involves the combined analysis of the laws of fluid motion and of chemical processes occurring at finite rates. Thus, the equation for chemical reaction rates must be added to the usual system of gasdynamic equations.

To simplify the analysis, we shall consider the simple binary reaction of dissociation and recombination of an ideal dissociating

diatomic gas, represented by Eq. (2.8). In this relation, the dissociation and recombination rates are not initially equal, and consequently, the chemical reaction occurs at a certain rate. Equilibrium is achieved only when the rate of molecule generation as a result of the recombination of atoms equals the dissociation rate of molecules into atoms. Rate means the number of molecules generated or decomposed per unit time. Thus, the actual reaction rate of the dissociation process is

$$\frac{d\alpha}{dt} = r_D - r_R, \tag{2.22}$$

where α is the degree of dissociation. To obtain general expressions for the dissociation and recombination rates, relationships from chemical kinetics must be used.

The recombination of two atoms A into a molecule A_2 on impact with a third particle B is expressed by $A + A + B \xrightarrow[k_R]{} A_2 + B$, where B is the particle carrying away the energy of recombination. The coefficient k_R is determined by the equation for the recombination rate

$$\left\{\frac{d[A]}{dt}\right\}_R = 2k_R[A]^2[B]. \tag{2.23}$$

The square brackets denote the concentration in moles/cm^3, and k_R has the dimensions cm^6/mole^2 sec.

It follows from Eq. (2.23) that the rate of recombination of atoms is proportional to the concentration of each of the components taking part in the triple collision.

For a binary mixture of atoms and molecules, the sum of the concentrations is $c_M + c_A = 1$. Consequently,

$$[A] = \frac{\rho c_A}{m_A}, \qquad [A_2] = \frac{\rho c_M}{m_M} = \frac{\rho(1 - c_A)}{2m_A},$$
$$[B] = [A] + [A_2] = \frac{\rho(1 + c_A)}{2m_A}, \tag{2.24}$$

where $c_A = \alpha$, and $c_M = 1 - \alpha$. Introducing Eq. (2.24) into Eq. (2.23), we obtain the relation for the recombination rate:

$$r_P = \left(\frac{d\alpha}{dt}\right)_R = k_R\left(\frac{\rho}{m_A}\right)^2 \alpha^2(1 + \alpha). \tag{2.25}$$

The dissociation reaction $A_2 + B \underset{k_D}{\longrightarrow} A + A + B$ represents the process of decomposition of a molecule as a result of a paired collision. Here k_D is the dissociation rate coefficient, and B is the second particle in a paired collision with a molecule transmitting the energy of dissociation to it. The rate of dissociation is

$$r_D = \left(\frac{d\alpha}{dt}\right)_D = \frac{1}{2} k_D\left(\frac{\rho}{m_A}\right)^2 (1 - \alpha^2). \tag{2.26}$$

Substituting Eqs. (2.25) and (2.26) into Eq. (2.22), we obtain

$$\frac{d\alpha}{dt} = \frac{1}{2} k_R\left(\frac{\rho}{m_A}\right)^2 (1 + \alpha)[K_p(1 - \alpha) - 2\alpha^2], \tag{2.27}$$

where $K_p = k_D/k_R$. This value is defined as a thermodynamic constant for equilibrium processes, but under certain circumstances the constant is also valid for nonequilibrium reactions. For the equilibrium case $d\alpha/dt = 0$ in Eq. (2.27), so that $K_p = 2\alpha_e^2/(1 - \alpha_e)$, where α_e is the equilibrium degree of dissociation. Making use of Eq. (2.9), we obtain

$$K_p = \frac{2\alpha_e^2}{1 - \alpha_e} = \frac{2\rho_d}{\rho} e^{-D/kT} = \frac{k_D}{k_R}.$$

Substituting this expression into Eq. (2.27) we find

$$\frac{d\alpha}{dt} = C\bar{\rho}\rho_d[(1 - \alpha)e^{-1/\bar{T}} - \bar{\rho}\alpha^2], \tag{2.28}$$

where

$$C = \frac{k_R}{m_A^2}(1 + \alpha)\rho_d. \tag{2.29}$$

As is evident from Eq. (2.28), it is important to know the recombination rate for the study of nonequilibrium flows. For this purpose, it is sufficient to determine the dissociation rate, since the thermodynamic equilibrium constant can be used.

Average experimental values of the recombination rate coefficient are presented in Fig. 24 for a pressure of about 1 atm. It is assumed that these values represent the lower limit of the recombination rate.

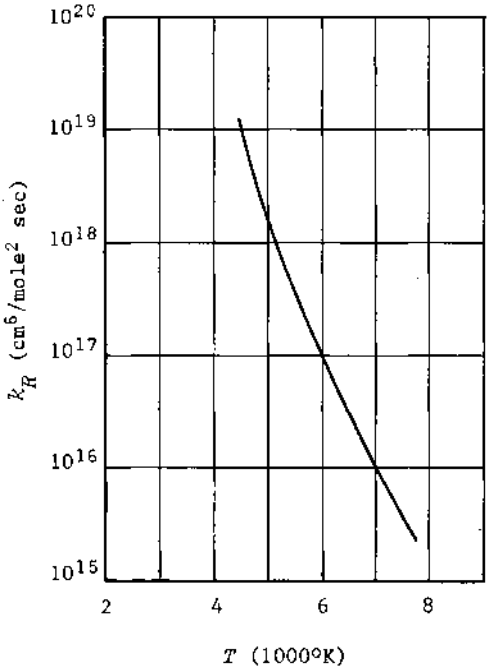

Fig. 24--Recombination rate coefficient of air

Relaxation Time

Equation (2.29) can be written in another form, again making use of the concept of an equilibrium constant applicable to conditions of

nonequilibrium and equilibrium flows. Replacing $(1/\bar{\rho})\exp(-1/\bar{T})$ by $\alpha_e^2/(1-\alpha_e)$ in Eq. (2.28) gives

$$\frac{d\alpha}{dx} = \frac{\alpha_e - \alpha}{Vt_D} \quad \text{or} \quad \frac{d\alpha}{d\bar{x}} = \alpha_e - \alpha, \tag{2.30}$$

where

$$\frac{1}{t_D} = C\bar{\rho}^2 p_d \left(\alpha + \frac{\alpha_e}{1-\alpha_e}\right), \qquad d\bar{x} = \frac{dx}{Vt_D}. \tag{2.31}$$

The parameter t_D is the relaxation time, whose determination is a very important problem in the physics of relaxation processes. It has been studied both theoretically and experimentally by means of shock tubes, where the nonequilibrium processes behind shock waves are artificially created by heating the gas to very high temperatures (of the order of 10,000°K) for a very short interval of time, measured in microseconds. Some of the experimental results for oxygen and nitrogen are presented in Fig. 25. It has been shown that the theoretical and experimental data for dissociational relaxation times agree very well, and it is evident from Fig. 25 that the experimental vibrational relaxation times are less than those for dissociation.

Analysis has indicated that the computed relaxation times for dissociation are less than those for recombination by approximately one order of magnitude. Therefore, to estimate relaxation effects it is more reliable to use the recombination times, although a rough estimate can also be made from the time of the direct reaction. The same may be said of vibrational relaxation, since the time of excitation to a given temperature is less than the damping time of vibrations in the reverse process of cooling from that temperature. An approximate expression can be used to estimate the recombination time of oxygen or nitrogen. For example:

$$t_D = 7.7\cdot 10^{-7} \frac{1}{\alpha(1-0.7\alpha)} \left(\frac{T_0}{T}\right)^{\frac{1}{2}} \left(\frac{\rho_0}{\rho}\right)^2, \tag{2.32}$$

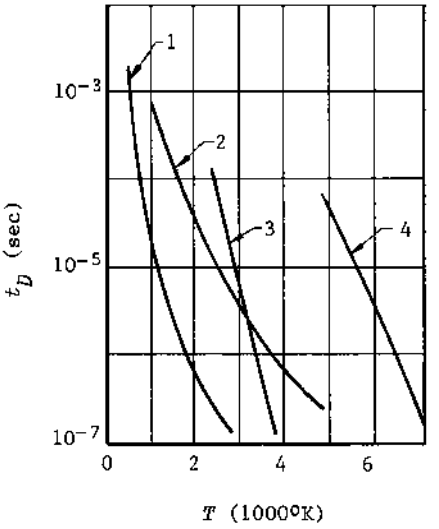

1,2 — Experimental vibrational relaxation times for O_2 and N_2, respectively

3,4 — Calculated relaxation times for dissociation of O_2 and N_2, respectively

Fig. 25--Relaxation times at standard atmospheric pressure

where the subscript 0 denotes the final values of the parameters. It is evident from Eq. (2.32) that the larger the initial density and temperature, the more rapidly the reaction proceeds and, consequently, the shorter the relaxation time. This would also indicate a decrease in t_d with an increase in pressure, which the curves of Fig. 26 corroborate; increasing the pressure by three orders of magnitude decreases the relaxation time by approximately ten times (the pressure p on the graph is divided by the sea level atmospheric pressure p_{SL}).

Studies have shown that the relaxation times for dissociation in air are less than in either nitrogen or oxygen. This is explained by the fact that dissociable air is not an additive mixture of components, but a complex composition of gases reacting among themselves.

Equilibrium Processes

There are difficulties connected with the analysis of gas flows, including nonequilibrium processes, because the rates of excitation and damping must be taken into account and, in the case of dissociation,

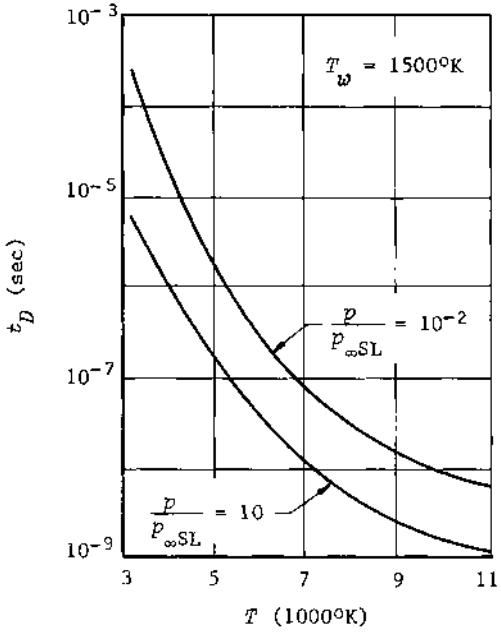

Fig. 26--Relaxation time for the dissociation of oxygen

the rates of the direct and reverse reactions. These rates have received little study and there are satisfactory data only for specific cases, so that the studies must be of a qualitative nature to a large degree. Equilibrium flow can be analyzed more reliably from both the qualitative and quantitative aspects.

The study of such flows shows that the flow regimes in which equilibrium is established differ for different degrees of freedom due to the unequal relaxation times and the different energy levels involved. In many cases the nonequilibrium process is such that the attainment of equilibrium in one degree of freedom will correspond to the onset of the relaxation phenomena of another, and there may be little overlap in the processes of establishing equilibrium for the various degrees of freedom. An approximate model of this process can be obtained on the basis of the "freezing" principle, whereby the equilibrium process is analyzed

for one or several degrees of freedom while the remaining degrees are not excited. As the temperature increases, equilibrium in the degrees of freedom occurs in the following order: translational, rotational and vibrational degrees, dissociation, excitation of the electronic states, and ionization. For example, the first two degrees of freedom can be assumed to be fully excited in order to examine the region in which vibrational equilibrium is achieved.

This method is unacceptable for several gases, particularly nitrogen at high temperatures, because ionization is begun before dissociation has been completed. This is explained by the fact that the dissociation and ionization energies of nitrogen differ from each other by a factor of only about one and a half. In this case, the regions in which equilibrium is achieved overlap. An analogous phenomenon is observed for air at comparatively low temperatures. It is evident from Fig. 25 that, for temperatures greater than 3200°K, the relaxation time for the dissociation of oxygen is less than the time for establishing vibrations in nitrogen. Thus, equilibrium in the dissociation of oxygen will be attained before vibrations in nitrogen have been fully excited.

DIFFUSION PHENOMENA IN THE BOUNDARY LAYER

The Diffusion Flow of Matter and Heat Transfer

In the study of the phenomena related to high velocity flow around bodies, it is necessary to deal with nonuniform heating, which leads to a three-dimensional distribution of both the temperature and the composition of the gas. The temperature gradients that arise generate a heat flux as a result of molecular thermal conductivity. The varying concentration of atoms resulting from dissociation of the gas leads to an additional transfer of energy by the diffusion of these atoms, which then release heat upon recombination. A flow of heat to the surface of the body results from these processes.

The transport of enthalpy by diffusion of certain components of the gas represents an unusual source of energy flux, which, however, can exceed the heat flow caused by thermal conductivity under specified conditions.

The heat flux generated by the recombination of diffusing atoms is

$$q_d = Qi_R, \tag{2.33}$$

where Q is the diffusional flow of matter, and i_R is the heat of recombination of atoms into molecules, the value of which obviously equals the heat of dissociation of the molecules of the components of air. (For nitrogen and oxygen, the values $i_R = u_d$ are presented in Table 3.)

In what follows we shall consider a simple binary mixture of atoms and molecules that is characterized by the coefficient of binary diffusion $\bar{D}$ (m^2/sec). Assuming that c is the mass concentration of the atomic component (or degree of dissociation), the diffusional flow of the atoms across the boundary layer is

$$Q = \rho \bar{D} \frac{\partial c}{\partial y}. \tag{2.34}$$

Influence of the Reaction Rate

Diffusional heat transfer depends on the reaction rate in the boundary layer. In the general case where the rates are finite, some recombination occurs in the gas itself but the remaining atoms diffuse to the wall. Thus, heat is released through the boundary layer as well as on the surface of the body.

The study of two special cases is of value in analyzing this process. The first of these is characterized by an infinite recombination rate, so that thermodynamic equilibrium is established at every point in the flow and there is no diffusion of matter to the wall. The chemical reaction and, consequently, the heat release occurs in the boundary layer itself. Therefore, the diffusional heat transfer is caused by the presence of a profile of equilibrium concentrations. In practical cases, flow conditions approximating such a hypothetical "equilibrium" boundary layer will occur when the rate of diffusion is negligibly small compared to the rate of dissociation and recombination (and in the case of ionization, the same is true for electron reactions).

In the second special case, recombination proceeds infinitely slowly; i.e., chemical reaction does not take place. Consequently, despite the

fact that the diffusion of atoms occurs, there is no recombination, and energy is not released in the boundary layer. In practice, this can occur if the time of the chemical reaction is large compared to the characteristic time of the motion of the particles. Such flows are called "frozen."

In frozen flow, the atoms generated by dissociation diffuse in the direction of the cold wall, where they recombine. The energy released thereby depends on the catalytic properties of the wall, which are defined by the rate of the catalytic recombination reaction.

Recombination at the Wall

The catalytic effect of the wall, in the general case, is characterized by finite rates of the catalytic recombination reaction. The wall has its greatest effect as a catalyst in the theoretical limiting case of infinitely rapid recombination. In the other limiting case, when the recombination rate is infinitesimally small, the wall is noncatalytic.

In general the rate of heat transfer to the wall is determined by the flow of matter in the steady state:

$$q_w = k_w(c_w\rho_w)^m, \tag{2.35}$$

where k_w is the rate constant of the catalytic wall reaction, and m is the exponent that takes into account the character of the catalytic reaction ($1 \leq m \leq 2$). For the special and simplest case of a reaction of the first order, we can choose $m = 1$.

According to the law of the conservation of mass (neglecting thermal diffusion),

$$q_w = k_w(c_w\rho_w)^m = \rho_w\bar{D}_w\left(\frac{\partial c}{\partial y}\right)_w. \tag{2.35a}$$

From Eq. (2.35) it follows that, in the limiting case of diffusion with an infinitely large recombination rate ($k_w \sim \infty$), atoms reach the surface even for conditions of zero concentration at the wall ($c_w \approx 0$). In the case of a noncatalytic wall ($k_w = 0$), the flow of atoms is zero because the concentration is always finite; consequently, the heat flux

due to diffusion is zero. In the first case catalysis proceeds infinitely fast; in the second, on the contrary, at a negligibly slow rate.

Conditions for the Occurrence of Equilibrium and "Frozen" Flows

The type of flow is determined by the average time, t_{dif}, for the diffusion of atoms to the wall and the average time, t_{chem}, of the life of the atom. If t_{dif} is significantly larger than t_{chem}, the chemical reaction occurs before the atom reaches the wall and local thermodynamic equilibrium exists in the boundary layer. Thus, $\bar{t}_{dif} = (t_{dif}/t_{chem}) \gg 1$ will be the condition for equilibrium. The relative time $\bar{t}_{dif}$ is called a recombination rate parameter.

The reaction proceeds so slowly at small values ($\bar{t}_{dif} \ll 1$) that recombination begins only at the wall, and the gas flow appears to be "frozen."

The diffusion time t_{dif} can be calculated as the time of transition of particles through the boundary layer to the wall. Difficulties arise in estimating the atomic lifetime because the chemical recombination process has not been studied sufficiently, but the time t_{chem} can be estimated approximately from Eq. (2.32), in which the parameters t_0 and ρ_0 are determined for an undissociated medium and t and ρ are determined for the gas dissociating in equilibrium at the external edge of the boundary layer. In order to estimate t_{dif}, we can use the expression

$$\bar{t}_{dif} = \frac{k_1 (p_0')^2}{(T_0')^{3.5} R_0^2 \tilde{\lambda}} \tag{2.36}$$

for calculating the relative time of diffusion. In this equation R_0 is the universal gas constant; p_0' and T_0' are evaluated at the stagnation point of the body; $\tilde{\lambda}$ is the velocity gradient at that point (which will be determined later); and k_1 is the recombination rate constant. There are very little data on the rate constant. Specifically, it is known that for the recombination of oxygen at $T = 300°K$, the product $k_1 T^{-1.5} = 5 \cdot 10^4$ cm^6/mole^2 sec.

Equation (2.36) shows that "frozen" flow exists at high altitudes

and at low flight velocities. Therefore, "freezing" restricts any increase in the recombination rate with ascent to altitude.

Thus far we have been discussing a gas that is in thermodynamic equilibrium at the outer edge of the boundary layer. However, particles approaching the edge of the layer in a rarefied medium may not be in an equilibrium state because of the large dissociational relaxation times. This complicates the analysis. The investigation can be simplified if it is assumed that dissociation is retarded at low density and low velocity and, thus, the flow will be "frozen." In this case, using a surface of noncatalytic material will retard the increase in thermal flux caused by diffusion. Some increase will occur because of the energy transferred by molecules that have not succeeded in dissociating.

The Criterion of the Catalytic Process

The so-called recombination (or catalytic) capability, $\gamma = N_r/N$, is used as the criterion of the catalytic process, where N is the total number of atoms hitting the surface per unit area per unit time, and N_r is the portion of atoms that recombine.[7]

According to Eq. (2.35), for $m = 1$, the number of recombining atoms is $N_r = Q_w/m_A = k_w c_w \rho_w / m_A$. The total number of atoms $N = p_A (2\pi m_A k T_w)^{-\frac{1}{2}}$. Since $p_A = n_A k T_w$ and $c_w \rho_w = n_A m_A$, the recombination capacity is

$$\gamma = \frac{N_r}{N} = k_w \left(\frac{2\pi m_A}{k T_w} \right)^{\frac{1}{2}}. \tag{2.37}$$

The experimental values of the catalytic capacity of pyrex glass (whose composition will be presented later) and several other materials are shown in Fig. 27. Curves for the constant k_w are plotted on the same graph. The study of oxygen recombination has shown that the catalytic capacity of the materials investigated is so low that the recombination rate parameter $k_w < 10$ cm/sec. Of course, the use of these materials as coatings can decrease the heat transfer to the surface. A large effect is obtained by using glass, but less from the chlorides, whose catalytic capacity varies greatly with temperature.

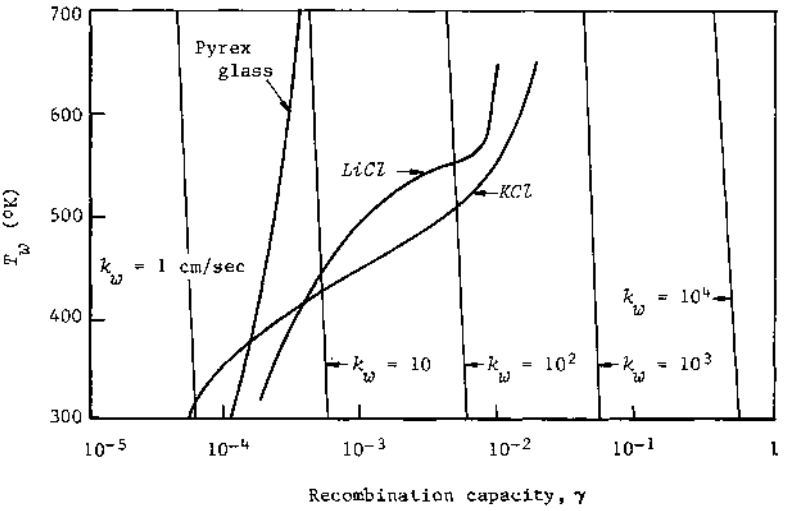

Fig. 27--Catalytic capacity of several materials

The recombination of nitrogen atoms has been studied on various metallic and nonmetallic surfaces. It was established that the majority of metals show a strong catalytic effect on atomic nitrogen, but nonmetallic materials have the opposite property, resulting in a low recombination capability with nitrogen. In particular, the recombination capacity $\gamma = 3 \cdot 10^{-5}$ for nitrogen at a partial pressure of 10^{-3} atm on pyrex glass.

The study of pure nitrogen and oxygen recombination is of important practical value since it permits an estimate of the expected catalytic effects in the study of heat transfer in air. But in addition it must be assumed that the recombination of an air mixture is accelerated because of intermediate reactions between oxygen and nitrogen; therefore, the total catalytic capacity increases and, as a consequence, the heat transfer is greater than the estimates that are based on the pure components.

§ 3. *THE BASIC CONCEPTS AND EQUATIONS FOR DETERMINING THE FLOW PARAMETERS*

THE SYSTEM OF BASIC EQUATIONS

ALL SPECIFIC PROBLEMS, including those concerning flow around a body of revolution, contain a series of unknowns. If we consider as unknowns four basic quantities, i.e., velocity, pressure, density, and temperature, we need a system of four independent equations to determine them.

It often proves expedient to convert this number of unknowns into a greater number, in which case the number of equations in the system increases correspondingly. For example, it is more convenient for the solution of a given problem to solve for the velocity components along the axes of a coordinate system instead of the total velocity. In general there will be three such components and, consequently, the number of equations in the system will increase to six. Instead of one equation of motion in vector form, three are written, each of which describes the motion with reference to a corresponding axis of the coordinates.

Along with the basic unknowns, other parameters usually enter the equations. These can be the friction stress, enthalpy, entropy, specific heats, velocity of sound, heat flow, etc. Then the system of equations is supplemented by a corresponding number of equations that link together the new unknowns.

The system of equations represents the most important flow laws in the most general form. Their derivation is based on a set of premises that define the physical character of the flow under investigation. The development of a model of the flow and of the processes that occur in it is a prerequisite to any aerodynamic analysis because it allows the maximum simplification of the equations. The model can be more or less complicated to correspond to the nature of the flow itself.

The Prandtl theory is an example of a physical model of this type, in which the flow around a body is considered to be inviscid outside of a thin boundary layer and viscous within it. This model simplifies the equations that are used to study the phenomena in both flow regimes.

A system of equations of the most general form is considered below, and the special cases that correspond to inviscid flow and boundary layer flow are also presented. Equations that reflect the various unique features (physical models) of actual flows are given in each of the special cases.

The Equation of Motion

General Form of the Equation of Motion. Let us consider the first equation of the system, the equation of motion of a fluid particle. Its derivation is based on the d'Alembert principle. Applying this principle to a particle of fluid in the form of an elementary parallelepiped (Fig. 28), an equation of motion is obtained with reference to the Cartesian coordinates x, y, z, in the following vector form:

$$\frac{d\bar{V}}{dt} = -\frac{1}{\rho}\,\text{grad}\,p + \frac{1}{\rho}\left(\frac{\partial \bar{\tau}_x}{\partial x} + \frac{\partial \bar{\tau}_y}{\partial y} + \frac{\partial \bar{\tau}_z}{\partial z}\right). \tag{3.1}$$

The vectors of the viscous surface forces, $\bar{\tau}_x$, $\bar{\tau}_y$, $\bar{\tau}_z$, can be written in the form

$$\bar{\tau}_k = p_{kx}i_1 + p_{ky}i_2 + p_{kz}i_3, \tag{3.2}$$

where k assumes the successive values x, y, z, and i_1, i_2, i_3 are unit vectors in the corresponding directions. The velocity vector is given by $V_x i_1 + V_y i_2 + V_z i_3$, where V_x, V_y, V_z are the components of that vector along the coordinate axes. The gradient of the pressure is

$$\text{grad}\,p = \frac{\partial p}{\partial x}\,i_1 + \frac{\partial p}{\partial y}\,i_2 + \frac{\partial p}{\partial z}\,i_3. \tag{3.3}$$

Equation (3.1) describes the general case of motion of a weightless, nonconductive, compressible, viscous gas in vector form.

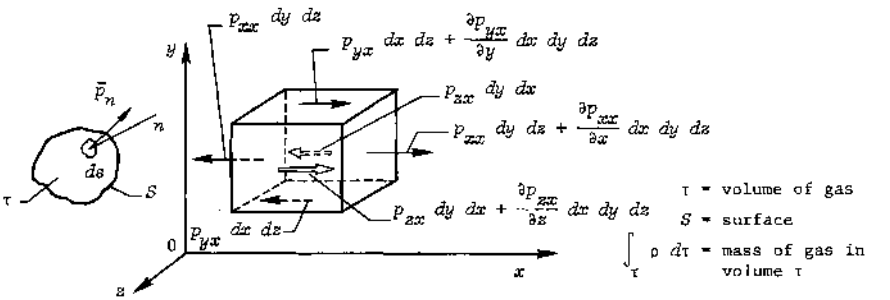

Fig. 28--Forces acting on an elemental volume of gas

Equation of Motion for a Perfect Fluid. A wide range of problems is associated with the calculation of the flow field around various bodies, including bodies of revolution, under conditions of inviscid flow. In actual cases, it is assumed that the flow outside the boundary layer is inviscid. Obviously, the equation of motion of an inviscid gas should not contain terms involving the viscosity. The equation of motion for a perfect fluid can be obtained from Eq. (3.1) by discarding the second term on the right side:

$$\frac{d\bar{V}}{dt} = -\frac{1}{\rho}\,\text{grad}\,p. \tag{3.4}$$

This equation is known as Euler's equation. In its derivation, no limitations were placed on the character of the rotational motion of the gas, so it also applies to the case of rotational flow.

For the investigation of flow around a body of revolution, it is convenient to use the Euler equation in either cylindrical or spherical coordinates. If x, r, and ϕ are the cylindrical coordinates (Fig. 29), the gradient of pressure in Eq. (3.4) is

$$\text{grad}\,p = \frac{\partial p}{\partial x}\,i_1 + \frac{\partial p}{\partial r}\,i_2 + \frac{1}{r}\,\frac{\partial p}{\partial \phi}\,i_3.$$

Designating the velocity components by V_x, V_r, and V_ϕ, the equation of

motion can be written in expanded form:

$$\frac{\partial V_x}{\partial t} + V_x \frac{\partial V_x}{\partial x} + V_r \frac{\partial V_x}{\partial r} + \frac{V_\phi}{r} \frac{\partial V_x}{\partial \phi} = -\frac{1}{\rho} \frac{\partial p}{\partial x},$$

$$\frac{\partial V_r}{\partial t} + V_x \frac{\partial V_r}{\partial x} + V_r \frac{\partial V_r}{\partial r} + \frac{V_\phi}{r} \frac{\partial V_r}{\partial \phi} - \frac{V_\phi^2}{r} = -\frac{1}{\rho} \frac{\partial p}{\partial r}, \tag{3.5}$$

$$\frac{\partial V_\phi}{\partial t} + V_x \frac{\partial V_\phi}{\partial x} + V_r \frac{\partial V_\phi}{\partial r} + \frac{V_\phi}{r} \frac{\partial V_\phi}{\partial \phi} + \frac{V_r V_\phi}{r} = -\frac{1}{\rho r} \frac{\partial p}{\partial \phi}.$$

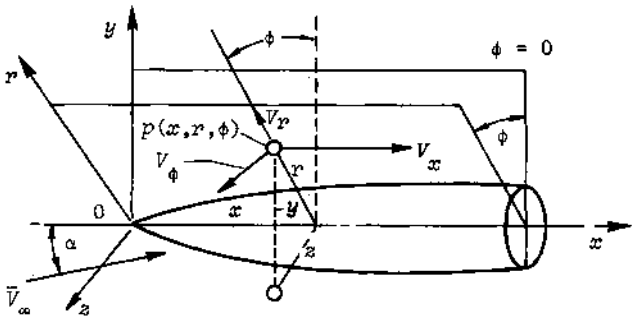

Fig. 29--Components of the local flow velocity in cylindrical coordinates

These equations can be used for the study of unsteady rotational flow around bodies of revolution of arbitrary shape at an angle of attack. In the case of steady flow, the equations take a simpler form because the partial derivatives with respect to time are eliminated. This system of equations for steady symmetric flow around a body of revolution can be simplified further:

$$V_x \frac{\partial V_x}{\partial x} + V_r \frac{\partial V_x}{\partial r} = -\frac{1}{\rho} \frac{\partial p}{\partial x},$$

$$V_x \frac{\partial V_r}{\partial x} + V_r \frac{\partial V_r}{\partial r} = -\frac{1}{\rho} \frac{\partial p}{\partial r}. \tag{3.6}$$

Another special form of the equation of motion comes from Eq. (3.4):

$$\frac{\partial V_r}{\partial t} + V_r \frac{\partial V_r}{\partial r} = -\frac{1}{\rho}\frac{\partial p}{\partial r}, \tag{3.7}$$

which describes the unsteady motion of a gas behind a cylindrical wave. This wave originates from the expansion of a piston, which can be considered a kind of impermeable, moving surface (Fig. 30). It will be shown later that an analogy exists between high velocity flow around a body and the flow of a gas when it is displaced by a piston. This analogy is used for the solution of a number of problems in hypersonic aerodynamics.

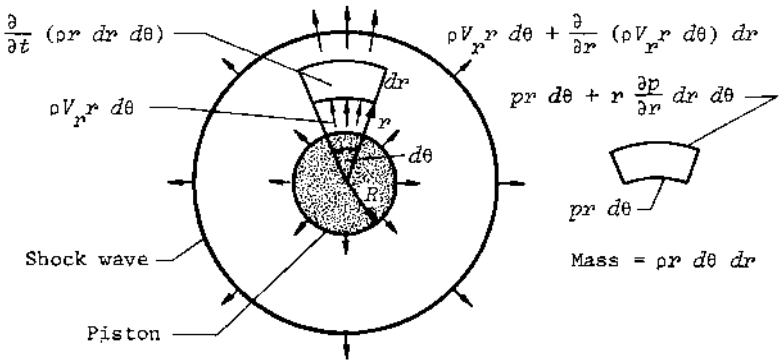

Fig. 30--Flow parameters behind a cylindrical shock wave

Let us now examine the equation of motion in the spherical coordinates r, Θ, ψ (Fig. 31), which is particularly useful for the study of supersonic flow around cones. To obtain this equation, we write the expression for the gradient of pressure in spherical coordinates:

$$\text{grad } p = \frac{\partial p}{\partial r} i_1 + \frac{1}{r}\frac{\partial p}{\partial \Theta} i_2 + \frac{1}{r \sin \Theta}\frac{\partial p}{\partial \psi} i_3.$$

Denoting the velocity components along the corresponding axes of the coordinate system by V_r, V_Θ, V_ψ, and assuming the special case of steady

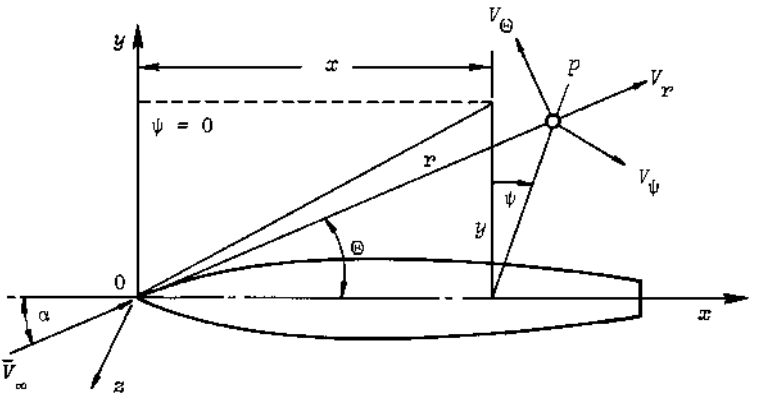

Fig. 31--Local velocity components in spherical coordinates

flow, we can write Eq. (3.4) in the expanded form:

$$V_r\frac{\partial V_r}{\partial r}+\frac{V_\Theta}{r}\frac{\partial V_r}{\partial\Theta}+\frac{V_\psi}{r\sin\Theta}\frac{\partial V_r}{\partial\psi}-\frac{V_\Theta^2+V_\psi^2}{r}=-\frac{1}{\rho}\frac{\partial p}{\partial r},$$

$$V_r\frac{\partial V_\Theta}{\partial r}+\frac{V_\Theta}{r}\frac{\partial V_\Theta}{\partial\Theta}+\frac{V_\psi}{r\sin\Theta}\frac{\partial V_\Theta}{\partial\psi}+\frac{V_rV_\Theta}{r}-\frac{V_\psi^2\cot\Theta}{r}=-\frac{1}{r\rho}\frac{\partial p}{\partial\Theta}, \qquad (3.8)$$

$$V_r\frac{\partial V_\psi}{\partial r}+\frac{V_\Theta}{r}\frac{\partial V_\psi}{\partial\Theta}+\frac{V_\psi}{r\sin\Theta}\frac{\partial V_\psi}{\partial\psi}+\frac{V_rV_\psi}{r}+\frac{V_\Theta V_\psi\cot\Theta}{r}=-\frac{1}{r\rho\sin\Theta}\frac{\partial p}{\partial\psi}.$$

For steady symmetric flow, the parameters do not depend on the variable ψ and Eq. (3.8) is simplified:

$$V_r\frac{\partial V_r}{\partial r}+\frac{V_\Theta}{r}\frac{\partial V_r}{\partial\Theta}-\frac{V_\Theta^2}{r}=-\frac{1}{\rho}\frac{\partial p}{\partial r},$$

$$V_r\frac{\partial V_\Theta}{\partial r}+\frac{V_\Theta}{r}\frac{\partial V_\Theta}{\partial\Theta}+\frac{V_rV_\Theta}{r}=-\frac{1}{r\rho}\frac{\partial p}{\partial\Theta}. \qquad (3.9)$$

Another popular system is the so-called normal (or natural) coordinate system[8] (Fig. 32). In the plane case or for axisymmetric flow,

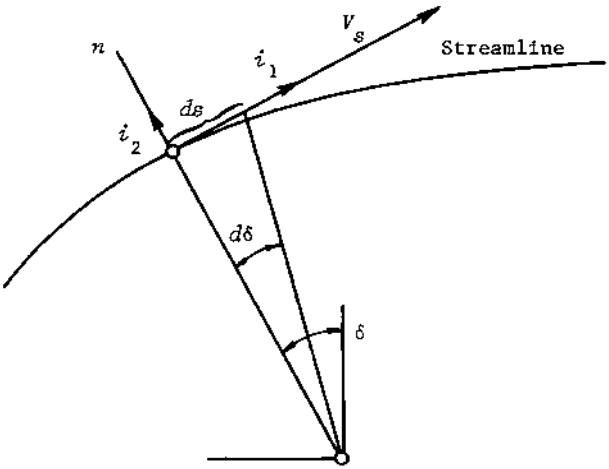

Fig. 32--Normal (natural) coordinate system

one of the axes of this system is tangent to the arc s of a streamline, and the other is directed along the perpendicular n to the streamline at a given point. The equation of motion with reference to the axes of the normal coordinate system can be obtained from Eq. (3.4) with the the gradient of pressure given by

$$\text{grad } p = \frac{\partial p}{\partial s} i_1 + \frac{\partial p}{\partial n} i_2$$

and the vector of total acceleration by

$$\frac{d\bar{V}}{dt} = W_s i_1 + W_n i_2.$$

The tangential component of acceleration for steady motion is $W_s = V_s(\partial V_s/\partial s)$ and the normal component is $W_n = V_s^2(\partial\delta/\partial s)$, where δ is the angle of inclination of the streamline. Consequently, the components of the equation of motion will take the form

$$V_s \frac{\partial V_s}{\partial s} = -\frac{1}{\rho}\frac{\partial p}{\partial s}, \qquad V_s^2 \frac{\partial \delta}{\partial s} = -\frac{1}{\rho}\frac{\partial p}{\partial n}. \tag{3.10}$$

Usually the curvilinear system of coordinates is employed in boundary layer theory. Such a system is also convenient to use in the study of flow in the thin layer of inviscid gas between the shock wave and the curved surface of a body at very high flight velocities. The location of the arbitrary point M in this system (Fig. 33) is determined by the distances y along the normal to the surface and x along the surface.

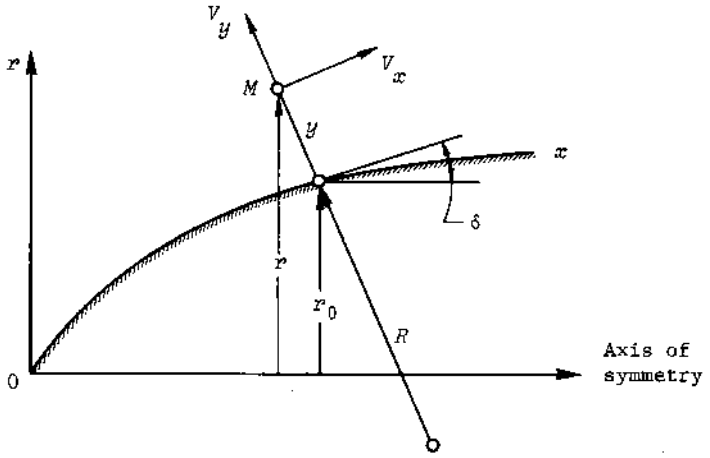

Fig. 33--Curvilinear coordinate system

For steady symmetric flow around a body of revolution, the equation of motion has the following form:

$$\frac{V_x}{1+y/R}\frac{\partial V_x}{\partial x}+V_y\frac{\partial V_x}{\partial y}+\frac{V_xV_y}{R+y}=-\frac{1}{1+y/R}\frac{1}{\rho}\frac{\partial p}{\partial x},$$

$$\frac{V_x}{1+y/R}\frac{\partial V_y}{\partial x}+V_y\frac{\partial V_y}{\partial y}-\frac{V_x^2}{R+y}=-\frac{1}{\rho}\frac{\partial p}{\partial y}, \tag{3.11}$$

where R is the radius of curvature of the body contour.

Equation of Motion in the Boundary Layer. Figure 34 illustrates the derivation of the equation of motion in the boundary layer. The

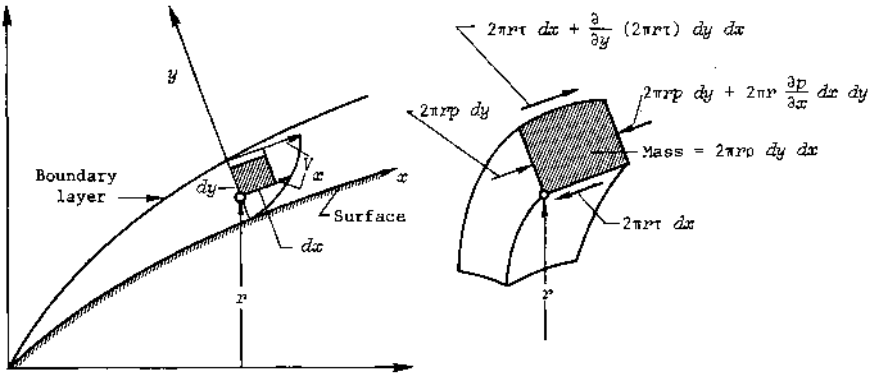

Fig. 34--Diagram of gas flow in the boundary layer

basis for this derivation is the important assumption that the boundary layer thickness δ is small compared to the linear dimensions of the body. If this condition is fulfilled, the pressure at various points in a cross section of the boundary layer is identical and equal to the value at the edge of the layer. Therefore, the forces acting on the end surfaces of the fluid element are not a function of viscosity and will be determined by the magnitude of this pressure. Because of the very small thickness of the boundary layer, the Coriolis acceleration can be neglected. Then the equation of motion in this layer will be

$$V_x \frac{\partial V_x}{\partial x} + V_y \frac{\partial V_x}{\partial y} = -\frac{1}{\rho}\frac{\partial p}{\partial x} + \frac{1}{rp}\frac{\partial (r\tau)}{\partial y}. \qquad (3.12)$$

This equation is adequate for the study of both laminar and turbulent boundary layers. If the mean turbulent layer is examined with no fluctuating components of the parameters, the quantities V_x, V_y, ρ, and p are assumed to be averaged in Eq. (3.12), and the frictional stress is determined from the expression $\tau = (\mu + \varepsilon)(\partial V_x/\partial y)$. In this expression, ε is the coefficient of turbulent viscosity (differing from μ, which is the coefficient of the usual molecular viscosity in the laminar boundary

layer). In the laminar boundary layer $\varepsilon = 0$, the friction is given by $\tau = \mu(\partial V_x/\partial y)$, and Eq. (3.12) is rewritten as

$$V_x \frac{\partial V_x}{\partial x} + V_y \frac{\partial V_x}{\partial y} = -\frac{1}{\rho}\frac{\partial p}{\partial x} + \frac{1}{r\rho}\frac{\partial}{\partial y}\left(\mu r \frac{\partial V_x}{\partial y}\right). \tag{3.12a}$$

In the general case when a gas undergoes physical and chemical changes, the coefficient μ varies across the boundary layer. If this variation is neglected (μ = const), Eq. (3.12a) is simplified.

The Continuity Equation

The Form of the Continuity Equation. The continuity equation, along with the equation of motion, is related to a number of basic aerodynamic equations. In mathematical form it reflects the hypothesis that a gas is a continuous medium. If the flow of a gas through a fixed element of volume is examined, according to this hypothesis the equation of continuity in the general form is written thus:

$$\frac{d\rho}{dt} + \rho \operatorname{div} \bar{V} = 0. \tag{3.13}$$

If the motion is examined with reference to Cartesian coordinates, the expression for the divergence of the velocity can be written in the form

$$\operatorname{div} \bar{V} = \frac{\partial V_x}{\partial x} + \frac{\partial V_y}{\partial y} + \frac{\partial V_z}{\partial z}.$$

Then the continuity equation for unsteady three-dimensional flow is written as

$$\frac{\partial \rho}{\partial t} + \frac{\partial(\rho V_x)}{\partial x} + \frac{\partial(\rho V_y)}{\partial y} + \frac{\partial(\rho V_z)}{\partial z} = 0. \tag{3.14}$$

To convert to cylindrical coordinates, we use the expression

$$\operatorname{div} \bar{V} = \frac{\partial V_x}{\partial x} + \frac{\partial V_r}{\partial r} + \frac{1}{r}\frac{\partial V_\phi}{\partial \phi} + \frac{V_r}{r}.$$

The continuity equation is then written as

$$r\frac{\partial \rho}{\partial t}+\frac{\partial(\rho r V_x)}{\partial x}+\frac{\partial(\rho r V_r)}{\partial r}+\frac{1}{r}\frac{\partial(\rho r V_\phi)}{\partial \phi}=0. \tag{3.15}$$

For symmetric flow around a body of revolution, the fourth term is dropped from the equation. Moreover, if the flow parameters are not functions of x, Eq. (3.15) takes the special form

$$r\frac{\partial \rho}{\partial t}+\frac{\partial(\rho r V_r)}{\partial r}=0. \tag{3.16}$$

This equation represents the condition of continuity of an unsteady flow of gas behind a cylindrical wave, and its derivation can be reproduced with the aid of Fig. 30.

Let us consider the continuity equation in spherical coordinates. For this purpose we can use the expression for divergence in spherical coordinates:

$$\operatorname{div}\vec{V}=\frac{1}{r^2}\frac{\partial(r^2V_r)}{\partial r}+\frac{1}{r\sin\Theta}\frac{\partial(V_\Theta\sin\Theta)}{\partial\Theta}+\frac{1}{r\sin\Theta}\frac{\partial V_\psi}{\partial\psi}.$$

The continuity equation in these coordinates for the case of unsteady flow can be obtained by substituting the expression for div $\vec{V}$ into Eq. (3.13). For the special case of steady flow, the equation has the form

$$\frac{1}{r^2}\frac{\partial(\rho r^2V_r)}{\partial r}+\frac{1}{r\sin\Theta}\frac{\partial(\rho V_\Theta\sin\Theta)}{\partial\Theta}+\frac{1}{r\sin\Theta}\frac{\partial(\rho V_\psi)}{\partial\psi}=0. \tag{3.17}$$

Equations for the study of supersonic steady flow around cones at an angle of attack can be derived from this equation. If the angle of attack is zero and the flow is symmetrical, Eq. (3.17) is simplified because the third term is dropped.

We can also present the continuity equation in a normal coordinate system (see Fig. 32) for the case of steady flow. This equation is obtained if the condition of the conservation of mass is written for the

flow of gas between two adjacent flow surfaces. The lines of intersection with the vertical meridian plane are streamlines. This condition permits us to obtain the equation of continuity:

$$\frac{\partial \delta}{\partial n} + \frac{\partial \log \rho}{\partial s} + \frac{\partial \log V_s}{\partial s} + \frac{\sin \delta}{r} = 0. \tag{3.18}$$

If we consider the curvilinear coordinate system (see Fig. 33), the equation of continuity for steady flow is written as

$$\frac{\partial(\rho r V_x)}{\partial x} + \frac{\partial\left[\rho r V_y (1 + y/R)\right]}{\partial y} = 0. \tag{3.19}$$

This equation can be simplified for investigating the boundary layer, keeping in mind that the thickness of the layer is small. Neglecting the quantity y/R compared with unity, we find

$$\frac{\partial(\rho r V_x)}{\partial x} + \frac{\partial(\rho r V_y)}{\partial y} = 0. \tag{3.19a}$$

Transformation of the Continuity Equation. In practice, the continuity equation is often modified to eliminate density. This is done with the aid of the equation of motion and the equation for the local velocity of sound, $a^2 = dp/d\rho$, which is valid in the absence of physical-chemical changes. Any system of coordinates can be used for the transformation.

If potential unsteady flow is investigated in a cylindrical coordinate system, the transformation of the continuity equation will be an equation in cylindrical coordinates for the velocity potential Φ:

$$(a^2 - \Phi_x^2)\Phi_{xx} + (a^2 - \Phi_r^2)\Phi_{rr} + \frac{\Phi_\phi}{r^2}\left(a^2 - \frac{\Phi_\phi^2}{r^2}\right) - \frac{2}{r^2}\Phi_{r\phi}\Phi_r\Phi_\phi - \frac{2}{r^2}\Phi_{x\phi}\Phi_x\Phi_\phi - 2\Phi_{xr}\Phi_x\Phi_r$$
$$+ \frac{1}{r}\Phi_r\left(a^2 + \frac{\Phi_\phi^2}{r^2}\right) - 2\Phi_x\Phi_{xt} - 2\Phi_r\Phi_{rt} - \frac{2}{r^2}\Phi_\phi\Phi_{\phi t} - \Phi_{tt} = 0, \tag{3.20}$$

where derivatives are $\Phi_x = \partial\Phi/\partial x$, $\Phi_{xx} = \partial^2\Phi/\partial x^2$, $\Phi_{x\phi} = \partial^2\Phi/\partial x \partial\phi$, etc.

The equation for the study of steady flow at an angle of attack is of practical interest and can be obtained by eliminating from Eq. (3.20) all terms containing partial derivatives with respect to time. If the flow is symmetrical, the terms containing derivatives with respect to ϕ also drop from the equation.

An equation obtained in an analogous manner is that for the velocity potential in spherical coordinates. This is used, for example, in studies of conical supersonic flows. The equation for steady flow has the form

$$\Phi_{rr}\left(1-\frac{\Phi_r^2}{a^2}\right)+\frac{\Phi_{\Theta\Theta}}{r^2}\left(1-\frac{\Phi_\Theta^2}{r^2a^2}\right)+\frac{\Phi_{\psi\psi}}{r^2\sin^2\Theta}\left(1-\frac{\Phi_\psi^2}{r^2a^2\sin^2\Theta}\right)$$
$$-\frac{2\Phi_\Theta\Phi_\psi\Phi_{\Theta\psi}}{r^2a^2\sin^2\Theta}-\frac{2\Phi_r\Phi_\Theta\Phi_{\Theta r}}{r^2a^2}-\frac{2\Phi_r\Phi_\psi\Phi_{r\psi}}{r^2a^2\sin^2\Theta}+\frac{\Phi_r}{r}\left(2+\frac{\Phi_\Theta^2\sin^2\Theta+\Phi_\psi^2}{r^2a^2\sin^2\Theta}\right)$$
$$+\frac{\Phi_\Theta\cot\Theta}{r^2}\left(1+\frac{\Phi_\psi^2}{r^2a^2\sin^2\Theta}\right)=0. \qquad (3.21)$$

Here as in Eq. (3.20), the single subscript on Φ denotes the first derivative and the double subscript denotes the second derivative of the velocity potential with reference to the corresponding independent variables. In the case of zero angle of attack, Eq. (3.21) takes on a simpler form because the derivatives with respect to ψ equal zero.

The equations presented for the velocity potential are fundamental in the aerodynamics of isentropic (irrotational) flows, the distinguishing characteristic of which is constant entropy, not only along but also across the streamlines. If viscosity is neglected, subsonic flow around a body of revolution possesses such a characteristic. Flow behind a straight shock wave will also be isentropic. In this case the entropy at any point along the shock is changed by the same value when the flow passes through it. Consequently, the entropy behind the shock from one streamline to another will not vary and the flow will remain potential.

A curved shock wave is generated by supersonic flow around a body with a curved shape. Transition through a curved shock causes a change in entropy at each streamline. It follows that, although the flow is

adiabatic, there will be an entropy change from one streamline to another. Consequently, such a flow will be isentropic along a streamline and nonisentropic in the direction normal to it. In other words, the flow behind a curved shock wave is rotational flow and, strictly speaking, it is impossible to study this type of flow with an equation in terms of the velocity potential. However, it has been shown that, in the case of low supersonic Mach numbers, the flow behind a curved shock wave can be approximated by an isentropic flow throughout, and therefore the equation for the velocity potential can be used. This approximation gives better results as the body becomes thinner.

The rotational character of the supersonic flow behind a curved shock wave must be considered for large Mach numbers or thick bodies, and also for significant deviations from symmetric flow. In these cases, the use of the equation for the velocity potential produces substantial errors. Therefore, for these calculations one should proceed from the general equation of continuity, transformed with the aid of the equation of motion so that density is eliminated from it (the pressure, which enters into the equation of motion, can be eliminated by the introduction of the velocity of sound: $dp/d\rho = a^2$).

Let us denote the form of the equations that can be obtained for different coordinate systems, keeping in mind that they are for the special case of steady symmetric flow:

In cylindrical coordinates:

$$\left(1 - \frac{V_x^2}{a^2}\right)\frac{\partial V_x}{\partial x} - \frac{V_x V_r}{a^2}\left(\frac{\partial V_x}{\partial r} + \frac{\partial V_r}{\partial x}\right) + \left(1 - \frac{V_r^2}{a^2}\right)\frac{\partial V_r}{\partial r} + \frac{V_r}{r} = 0; \quad (3.22)$$

In spherical coordinates:

$$\left(1 - \frac{V_r^2}{a^2}\right)\frac{\partial V_r}{\partial r} - \frac{2V_r V_\Theta}{a^2}\frac{\partial V_\Theta}{\partial r} + \frac{1}{r}\left(1 - \frac{V_\Theta^2}{a^2}\right)\frac{\partial V_\Theta}{\partial \Theta} + \frac{V_r}{r}\left(2 - \frac{V_\Theta^2}{a^2}\right) + \frac{V_\Theta}{r}\cot\Theta = 0; \quad (3.23)$$

In normal (natural) coordinates:

$$\frac{\partial \delta}{\partial n} + \left(1 - \frac{V_s^2}{a^2}\right)\frac{\partial \log V_s}{\partial s} + \frac{\sin \delta}{r} = 0. \qquad (3.24)$$

The Equation for the Stream Function. The stream function equation is widely used in theoretical research. It has the advantage, compared, for example, to Eq. (3.22), of having only one unknown, the stream function Ψ, instead of the two unknowns V_x and V_r.

The relation between the stream function Ψ and the velocity components V_r and V_x is obtained from the continuity equation, Eq. (3.15), for the condition of steady flow and axial symmetry:

$$\frac{\partial \Psi}{\partial x} = -\frac{r\rho}{\rho_0} V_r, \qquad \frac{\partial \Psi}{\partial r} = \frac{r\rho}{\rho_0} V_x, \qquad (3.25)$$

where ρ_0 is the stagnation density for isentropic flow.

Transforming Eq. (3.22) to the new variable Ψ, we obtain the equation for the stream function:

$$(a^2 - V_x^2)\Psi_{xx} + (a^2 - V_r^2)\Psi_{rr} - 2V_x V_r \Psi_{xr} - a^2 V_x (1 - \tilde{V}^2)^{1/(\gamma-1)}$$

$$= r^2 (a^2 - V^2)(1 - \tilde{V}^2)^{(\gamma+1)/(\gamma-1)} f(\Psi), \qquad (3.26)$$

where the derivatives are $\Psi_{xx} = \partial^2\Psi/\partial x^2$, $\Psi_{xr} = \partial^2\Psi/\partial x \partial r$, $\Psi_{rr} = \partial^2\Psi/\partial r^2$, and $\tilde{V} = V/V_{max}$, where V_{max} is the maximum velocity,† and $V = (V_x^2 + V_r^2)^{1/2}$. The function $f(\Psi)$ is

$$f(\Psi) = \frac{1}{\rho_0}\frac{dp_0}{d\Psi} = -\frac{1}{r}\left(\frac{\partial V_r}{\partial x} - \frac{\partial V_x}{\partial r}\right)(1 - \tilde{V}^2)^{-\gamma/(\gamma-1)}, \qquad (3.27)$$

and p_0 is the stagnation pressure for isentropic flow.

---

†Editor's note: The maximum velocity is defined as follows: $V_{max}^2 = 2\gamma(p_0/\rho_0)/(\gamma - 1)$, where p_0 and ρ_0 are stagnation pressure and stagnation density, respectively.

If the stagnation pressure does not change along the shock wave, $(dp_0/d\Psi) = 0$ and $f(\Psi) = 0$. In this case, Eq. (3.26) determines the stream function for potential (isentropic) flow.

In the region behind a curved shock wave, the total pressure varies from one streamline to another and $f(\Psi) \neq 0$. Then Eq. (3.26) describes nonisentropic (rotational) flow.

The change in total pressure across the streamlines is caused by the change in entropy, S, the expression for which is given in the form $S = c_v \log (p/\rho^\gamma) + \text{const}$. Since the process along the streamline is isentropic, it is obvious that in this equation

$$\frac{p}{\rho^\gamma} = \frac{p_0}{\rho_0^\gamma} = \left(\frac{p_0}{\rho_0}\right)^\gamma p_0^{1-\gamma}.$$

Substituting the value $(RT_0)^\gamma$ for the quantity $(p_0/\rho_0)^\gamma$ and considering the fact that the stagnation temperature T_0 is the same for all streamlines according to the law of conservation of energy, then, after calculating the derivative $dS/d\Psi$, we obtain

$$\frac{1}{p_0}\frac{dp_0}{d\Psi} = -\frac{\gamma}{(\gamma - 1)c_p}\frac{dS}{d\Psi}. \tag{3.28}$$

Using this equation, Eq. (3.26) can be transformed to one containing entropy.

The Diffusion Equation

The diffusion processes occurring in the boundary layer depend on the concentration distribution of the components of the gas. One of the relations for determining this is the diffusion equation. Like the continuity equation, the diffusion equation is an expression for the conservation of mass with the difference that it expresses the condition for the conservation of the diffusing components of the mixture.

If we first assume that there are no chemical reactions, the rate of production W_i of atoms or molecules as a result of dissociation or recombination is zero. Then, neglecting the diffusion flux in the

direction of the x-axis and also the thermal diffusion, we can obtain a continuity equation for the ith component of the mixture (or, as it is called, a diffusion equation) from Eq. (3.19a). This is obtained by replacing $\rho r V_x$ by the quantity $\rho r V_x c_i$ and $\rho r V_y$ by $\rho r V_y c_i - Q_i$, where Q_i is the diffusion flux across the boundary layer. If chemical reactions occur in the gas, resulting in the production of new particles or the disappearance of others, the term rW_i appears on the right side of the equation, and this takes into account the changes in that component. Thus, the equation for the diffusion of the ith component has the form

$$\frac{\partial(\rho r V_x c_i)}{\partial x} + \frac{\partial(\rho r V_y c_i)}{\partial y} = \frac{\partial}{\partial y}\left(\rho \bar{D} r \frac{\partial c_i}{\partial y}\right) + rW_i, \qquad (3.29)$$

where the diffusion coefficient $\bar{D}$ is a quantity that is identical for each pair of diffusing components of a binary mixture.

Equation (3.29) is simplified if the composition of the gas is "frozen" so that chemical reactions do not occur, in which case $W_i = 0$ can be assumed.

The diffusion equation can be converted from the concentration to the degree of dissociation α of a binary mixture by using the relation $c_A = \alpha$, $c_m = 1 - \alpha$. For the atomic component, the continuity equation has the form

$$\frac{\partial(\rho r V_x \alpha)}{\partial x} + \frac{\partial(\rho r V_y \alpha)}{\partial y} = \frac{\partial}{\partial y}\left(\rho \bar{D} r \frac{\partial \alpha}{\partial y}\right) + rW_A. \qquad (3.29a)$$

These equations can be applied to both the laminar and the turbulent boundary layer. In the first case, the quantity $\bar{D}$ is the coefficient of laminar diffusion $\bar{D}_L$ and is defined as a parameter of molecular transfer. In the second case the diffusion coefficient consists of the coefficients of laminar ($\bar{D}_L$) and turbulent ($\bar{D}_T$) diffusion; i.e., instead of $\bar{D}$ the quantity $\bar{D}_L + \bar{D}_T$ enters the equation.

The Momentum Equation

The General Form of the Equation. It is often convenient in gasdynamic research to use an equation based on the law of conservation

of momentum. Using again the elemental parallelepiped of Fig. 28 as the control volume, the net change in momentum per unit time in that volume must equal the sum of the external forces acting on the surfaces. The general form of the momentum equation is

$$-\operatorname{grad} p + \frac{\partial \bar{\tau}_x}{\partial x} + \frac{\partial \bar{\tau}_y}{\partial y} + \frac{\partial \bar{\tau}_z}{\partial z} = \frac{\partial (\rho \bar{V})}{\partial t} + \frac{\partial (\rho V_x \bar{V})}{\partial x} + \frac{\partial (\rho V_y \bar{V})}{\partial y} + \frac{\partial (\rho V_z \bar{V})}{\partial z}. \quad (3.30)$$

The Steady Motion of a Perfect Gas. In the case of steady motion of a perfect gas, the partial derivative with respect to time is equal to zero, and forces that depend on viscosity are omitted. Thus, Eq. (3.30) has the form

$$-\operatorname{grad} p = \frac{\partial (\rho V_x \bar{V})}{\partial x} + \frac{\partial (\rho V_y \bar{V})}{\partial y} + \frac{\partial (\rho V_z \bar{V})}{\partial z}. \quad (3.31)$$

The momentum equation for the one-dimensional flow of a gas in a channel of constant cross section is of practical interest. From Eq. (3.31) it follows that $dp/dx = -d(\rho V_x^2)/dx$ in this case. Integrating with respect to x between two arbitrary sections "1" and "2," we obtain

$$\rho_2 V_2^2 - \rho_1 V_1^2 = p_1 - p_2. \quad (3.32)$$

The left side of the equation represents the change in momentum, the right side the impulse of external force from the difference in pressure; therefore, Eq. (3.32) is called an impulse equation. If the quantity $\rho V^2 + p$ is defined as total impulse, Eq. (3.32) represents the law of conservation of impulse. The same quantity in the physical sense represents the total momentum of the gas in a given cross section, so that Eq. (3.32) is an equation for the conservation of momentum. This law as well as the two other laws of conservation of mass and of energy are fundamental to gasdynamic theory.

The Momentum Equation for the Boundary Layer. For the investigation of steady motion in a two-dimensional boundary layer, taking into account its small thickness, we can use the following simplified relation instead of Eq. (3.30) (in natural or curvilinear coordinates):

$$\frac{\partial(\rho V_x^2)}{\partial x} + \frac{\partial(\rho V_x V_y)}{\partial y} = -\frac{\partial p}{\partial x} + \frac{\partial \tau}{\partial y}. \tag{3.33}$$

From this equation, the integral form of the momentum equation can be derived, which is known in the literature as Karman's equation:

$$\frac{d}{dx}\int_0^\delta \rho V_x^2\, dy - V_\delta \frac{d}{dx}\int_0^\delta \rho V_x\, dy = -\delta \frac{dp}{dx} - \tau_0, \tag{3.34}$$

where τ_0 is the friction at the wall, and V_δ is the velocity at the edge of the boundary layer.

Applying Eq. (3.10) to the outer edge of the boundary layer, the pressure gradient is $dp/dx = -\rho_\delta V_\delta (dV_\delta/dx)$, where ρ_δ is the density at the edge of the layer; after some transformation, Eq. (3.34) becomes

$$\frac{d}{dx}\int_0^\delta \rho V_x V_\delta \left(1 - \frac{V_x}{V_\delta}\right) dy + \frac{dV_\delta}{dx}\int_0^\delta \rho_\delta V_\delta \left(1 - \frac{\rho V_x}{\rho_\delta V_\delta}\right) dy = \tau_0. \tag{3.35}$$

Based on the form of this equation we can define the following parameters:

$$\begin{aligned} \delta^* &= \int_0^\delta \left(1 - \frac{\rho V_x}{\rho_\delta V_\delta}\right) dy, \\ \theta &= \int_0^\delta \frac{\rho V_x}{\rho_\delta V_\delta}\left(1 - \frac{V_x}{V_\delta}\right) dy, \end{aligned} \tag{3.36}$$

which are called the displacement thickness and the momentum thickness, respectively.

The physical meaning of these parameters follows directly from Eq. (3.36). It is apparent that the displacement thickness characterizes the decrease in the flow rate, and the momentum thickness the decrease of momentum in the fluid, caused by the influence of viscosity.

It is possible to derive a similar integral relation for the boundary layer of a compressible fluid around a body of revolution by using the equations of motion, Eq. (3.12), and continuity, Eq. (3.19a):

$$\frac{d}{dx}\int_0^{\delta} \rho V_x V_\delta r\left(1 - \frac{V_x}{V_\delta}\right) dy + \frac{dV_\delta}{dx}\int_0^{\delta} \rho_\delta V_\delta r\left(1 - \frac{\rho V_x}{\rho_\delta V_\delta}\right) dy = (r\tau)_0. \qquad (3.37)$$

Equations (3.35) and (3.37) are general, and are applicable to both the laminar and the turbulent boundary layer.

The integral form of the momentum equations often can be used for calculating total aerodynamic characteristics such as the drag, lift, or moment acting on a body of revolution, thus avoiding the necessity of integrating the equations of motion to calculate the flow parameters.

The Energy Equation

The General Form of the Energy Equation. The energy equation is one of the fundamental equations of aerodynamics. It is a mathematical representation of the law of conservation of energy, which states that the change in the kinetic and internal energy of the moving particles is equal to the sum of the work done by external forces and the energy flux caused by external transfer of heat.

Let us assume that the external work is caused by surface forces arising from the normal pressure and the shear stress. Heat transfer occurs because of molecular thermal conduction, radiation, and gaseous diffusion. Then the energy equation for the mass of gas enclosed in an arbitrary volume τ (see Fig. 28) will have the form

$$\frac{d}{dt}\int_\tau \rho\left(\frac{V^2}{2} + u\right) d\tau = \int_S \bar{p}_n \bar{V}\, dS + \int_S q_T\, dS + \int_\tau \varepsilon\, d\tau + \int_S q_D\, dS, \quad (3.38)$$

where q_T and q_D are the heat rates caused by thermal conductivity and diffusion, respectively, through a unit surface; ε is the radiative heat flux of a unit mass per unit time; u is the internal energy of a unit mass of gas; and $\bar{p}_n$ is the vector of surface force.

Isentropic Flow. In considering the case of isentropic flow, the gas is assumed to be nonconductive and nonradiative; therefore, the heat flux equals zero. If it is also assumed that there is no diffusion, the last three terms are dropped from the right side of Eq. (3.38).

Replacing the remaining integral by the volume integral, with the condition that there is no friction and the surface force is caused only by the normal pressure, we obtain the equation $d(u + p/\rho + V^2/2)/dt = 0$. Integrating, and remembering that the enthalpy $i = u + p/\rho$, we obtain the energy equation for isentropic flow:

$$i + \frac{V^2}{2} = \text{const.} \tag{3.39}$$

According to the concept of the derivation, we have been tracking the motion of particles; therefore, the constant in Eq. (3.39) refers to a given streamline, along which the flow is isentropic. For a nonisentropic flow field, this constant can vary in passing from one streamline to another.

The enthalpy term in Eq. (3.39) can be replaced by the expression $i = [\gamma/(\gamma - 1)]p/\rho$. Furthermore, based on the integral form of the equation of motion, $V^2/2 = -\int dp/\rho + \text{const}$ along a streamline. As a result, we obtain the familiar adiabatic relation $p/\rho^\gamma = \text{const}$.

The Energy Equation for the Boundary Layer. First, we shall examine the energy equation for the laminar boundary layer with chemical reactions and diffusion occurring in it. We use the general Eq. (3.38) for this purpose. The thermal flux that appears there is due to molecular thermal conduction and is determined from $q_T = -\lambda(\partial T/\partial n)$. The amount of heat that can be transferred by gaseous diffusion is

$$q_D = \sum_i Q_i i_i = -\sum_i \rho \tilde{D} \frac{\partial c_i}{\partial n} i_i.$$

The enthalpy of the ith component is

$$i_i = \int_0^T c_{pi}\, dT + (i_{\text{chem}})_i = i_{ci} + (i_{\text{chem}})_i,$$

where c_{pi} is the specific heat of the component; $i_{ci} = \int_0^T c_{pi}\, dT$ is its enthalpy as a perfect gas; and $(i_{\text{chem}})_i$ is the chemical energy of formation of the component, which can be assumed to be equal to zero for

molecules. For atoms this quantity is negative and is given in the form $(i_{chem})_i = -i_R$, where i_R is the dissociation energy of a unit mass of the atomic components. Obviously, the enthalpy of the mixture of gases is $i = \sum_i c_i i_i$.

If Eq. (3.38) is related to the flow conditions in the boundary layer around a body of revolution and curvilinear coordinates are used, we obtain the energy equation in the form

$$\rho r \frac{d}{dt}\left(i + \frac{V^2}{2}\right) = \frac{\partial(\tau V_x r)}{\partial y} + \frac{\partial}{\partial y}\left(r\lambda \frac{\partial T}{\partial y}\right) - \sum_i i_i \frac{\partial(rq_i)}{\partial y}, \qquad (3.40)$$

where, for a binary mixture of atoms and molecules,

$$di = (c_p)_{avg}\, dT + \sum_i i_i\, dc_i, \qquad (3.40a)$$

and the average specific heat of the mixture is

$$(c_p)_{avg} = \sum_i (c_p)_i c_i = (c_p)_M c_M + (c_p)_A c_A.$$

The first term on the right is the molecular component of the average specific heat and the second is the atomic component.

Equation (3.40) can be rewritten using the expression for total enthalpy, $i_0 = i + V^2/2$:

$$\rho r \frac{di_0}{dt} = V_x \rho r \frac{\partial i_0}{\partial x} + V_y \rho r \frac{\partial i_0}{\partial y}$$

$$= \frac{\partial(\tau V_x r)}{\partial y} + \frac{\partial}{\partial y}\left(r\lambda \frac{\partial T}{\partial y}\right) + \sum_i \frac{\partial}{\partial y}\left(r\rho \bar{D} i_i \frac{\partial c_i}{\partial y}\right). \qquad (3.41)$$

The energy equation can be simplified by omitting the quantity r, which, within the limits of the boundary layer thickness, differs little from the radius of the body surface.

It follows from Eq. (3.41) that the variation in total enthalpy, $i_0 = u + V^2/2 + p/\rho$, depends on transfer processes in the gas that are

accompanied by an irreversible increase in entropy, which therefore identifies the nonisentropic character of the flow in the boundary layer. The first term on the right side defines the irreversible dissipation of heat due to friction caused by the transfer of momentum. The second term is related to the transfer of energy due to thermal conductivity, and the third term is related to the diffusion associated with chemical reactions. By their nature, transfer processes are dissipative, and the dissipated energy cannot be converted into kinetic energy because it is expended in overcoming the molecular bond forces.

Equation (3.41) can undergo further transformation if we investigate a binary mixture of two components for which the sum of the concentrations is $c_M + c_A = 1$ and, consequently, $(\partial c_M/\partial y) = -(\partial c_A/\partial y)$. Moreover, since the enthalpy of the mixture is $i = \sum_i i_i c_i$ and the average specific heat of the mixture is $(c_p)_{avg} = \sum_i c_i (c_p)_i$, it can be assumed that for a binary mixture

$$di = (c_p)_{avg}\, dT + (i_A - i_M)\, dc_A.$$

Hence it is possible to find the expression for the partial derivative $\partial T/\partial y$.

Substituting $\partial T/\partial y$ into Eq. (3.41) and drawing upon the continuity equation, Eq. (3.19a), to transform the right side, we obtain

$$\frac{\partial (\rho r V_x i_0)}{\partial x} + \frac{\partial (\rho r V_y i_0)}{\partial y} = \frac{\partial}{\partial y}\left(\frac{r\mu}{\mathrm{Pr}}\frac{\partial i_0}{\partial y}\right) + \frac{\partial}{\partial y}\left[r V_x \mu\left(1 - \frac{1}{\mathrm{Pr}}\right)\frac{\partial V_x}{\partial y}\right]$$
$$+ \frac{\partial}{\partial y}\left[r(i_A - i_M)\rho\bar{D}\left(1 - \frac{\mathrm{Sc}}{\mathrm{Pr}}\right)\frac{\partial c_A}{\partial y}\right], \qquad (3.42)$$

where $\mathrm{Pr} = \mu(c_p)_{avg}/\lambda$ is the Prandtl number and $\mathrm{Sc} = \mu/\rho\bar{D}$ is the Schmidt number. The ratio of these numbers is called the Lewis–Semenov number, $\mathrm{Le} = \mathrm{Pr}/\mathrm{Sc}$.

All these parameters represent physical properties of the gas and depend on the transfer coefficients. The Prandtl number, for example, is a function of the coefficients of viscosity and thermal conductivity; the viscosity coefficient μ represents those properties of the medium

on which the molecular transfer of momentum is dependent, and the coefficient λ is a measure of the intensity of molecular heat transfer. Thus, the Prandtl number indicates what portion of the kinetic energy is transformed into heat. For gases $Pr < 1$.

The Schmidt number defines the ratio between the kinetic energy of the particles and the energy transferred by means of diffusion. Just as for the Prandtl number, the Schmidt number is less than one for gases, and $Sc < Pr$.

The Lewis-Semenov parameter is the ratio of the intensity of heat transfer by mass exchange as a result of diffusion to the intensity of heat transfer by means of thermal conduction. In the general case, the Lewis-Semenov number is greater than one and, consequently, mass transfer of heat is greater than transfer by thermal conduction.

It is often assumed that the Prandtl and Schmidt numbers are equal. Then the Lewis-Semenov number $Le = 1$ and the intensities of both processes are identical. The last term on the right side of Eq. (3.42) is eliminated in this case, which implies the absence of the influence of diffusion in the boundary layer. Since the processes of thermal conduction and diffusion proceed with equal intensity, the excess chemical energy at the edge of the boundary layer is transformed entirely into heat at the wall. The more general case is characterized by $Pr > Sc$ in the boundary layer, so that $Le > 1$; this indicates an incomplete conversion of chemical energy into heat.

In addition to $Le = 1$, it can be assumed that $Pr = 1$. For this case Eq. (3.42) can be simplified still further, because the second term on the right is also eliminated. From physical considerations it follows that all the kinetic energy of the external flow is converted into heat at the wall.

Studies of the numerical values of the parameters discussed above are of important practical value. It has been established theoretically that the Schmidt number for a two-component atom-molecule mixture changes very little over a wide range of temperatures. For example, at 252°K the Schmidt number is 0.495, and at 3360°K it is 0.482. The same may also be said of the general character of the change in the Prandtl number, whose nominal value is approximately 0.71. If it is assumed that the Schmidt

number equals its average value, Sc = 0.49, the Lewis-Semenov parameter can be assumed constant and equal to

$$\mathrm{Le} = \frac{\mathrm{Pr}}{\mathrm{Sc}} = \frac{c_p \mu}{\lambda} \frac{\rho \bar{D}}{\mu} = \frac{\rho \bar{D} c_p}{\lambda} = \frac{0.71}{0.49} = 1.45.$$

According to the data at hand, this parameter depends only slightly on temperature up to values of $T = 9000°K$.

It is important to consider the particular form of Eq. (3.42) corresponding to the absence of diffusion. In this case, the equation will not have the third term on the right and it can be considered an energy equation for "frozen" flow; however, the total enthalpy i_0 that enters into other terms in the equation does not include the chemical energy capable of being released by the recombination of atoms.

It is possible to convert from total enthalpy i_0 to stagnation temperature if the specific heats are assumed constant, since then $i_0 = c_p T_0$. Thus, the energy equation for a dissociable gas neglecting diffusion will differ from the energy equation for a perfect gas only in that total enthalpy is used instead of stagnation temperature.

In the case of small velocities characterized by a negligible influence of compressibility and also by a negligibly small amount of heat released as a result of friction and conversion of kinetic energy, the energy equation takes the form

$$\rho V_x \frac{\partial T}{\partial x} + \rho V_y \frac{\partial T}{\partial y} = \frac{\lambda}{\rho c_p} \frac{\partial}{\partial y} \left(r \frac{\partial T}{\partial y} \right). \tag{3.43}$$

The energy equation presented for the laminar boundary layer can be converted to an equation for mean turbulent flow by certain modifications. It is necessary to add to the quantities that are functions of transfer parameters in Eq. (3.42) the corresponding quantities that are functions of the turbulent transfer parameters. For example, in the first term on the right, the quantity $\varepsilon/\mathrm{Pr}_T$ must be added to the term μ/Pr, where ε, as before, is the turbulent viscosity coefficient and $\mathrm{Pr}_T = \varepsilon (c_p)_{ave}/\lambda_T$ is the turbulent Prandtl number. The parameter λ_T is the turbulent thermal conductivity coefficient and is analogous

to the usual molecular thermal conductivity coefficient, so that the total coefficient of thermal conductivity is $\bar{\lambda} = \lambda + \lambda_T$. Introducing similar changes in the two other terms, we obtain the energy equation for the turbulent boundary layer:

$$\rho r \frac{di_0}{dt} = \frac{\partial}{\partial y}\left[r\left(\frac{\mu}{\mathrm{Pr}} + \frac{\varepsilon}{\mathrm{Pr}_T}\right)\frac{\partial i_0}{\partial y}\right] + \frac{\partial}{\partial y}\left\{r\left[\mu\left(1 - \frac{1}{\mathrm{Pr}}\right) + \varepsilon\left(1 - \frac{1}{\mathrm{Pr}_T}\right)\right]\frac{1}{2}\frac{\partial V_x^2}{\partial y}\right\} + \frac{\partial}{\partial y}\left\{r(i_A - i_M)\frac{\partial c_A}{\partial y}\left[\frac{\mu}{\mathrm{Pr}}(\mathrm{Le} - 1) + \frac{\varepsilon}{\mathrm{Pr}_T}(\mathrm{Le}_T - 1)\right]\right\}, \quad (3.44)$$

where the turbulent Lewis-Semenov number is $\mathrm{Le}_T = \rho \bar{D}_T (c_p)_{\mathrm{avg}} / \lambda_T$, and all the gasdynamic and thermodynamic parameters are taken as averages.

The calculation of the influence of diffusion is obtained from the solution of Eq. (3.44). Therefore, it is important to determine the turbulent Lewis-Semenov number. Some studies have indicated that Le_T can be assumed to be approximately equal to Le for laminar flow. A more accurate analysis indicates that the turbulent parameter is somewhat less than its laminar value, that is, closer to unity.

Some special cases of Eq. (3.44) are of practical value. One of these pertains to the absence of diffusion in the boundary layer, in which case the third term is eliminated from the right side. Essentially the same effect also occurs in the case where $\mathrm{Le} = \mathrm{Le}_T = 1$.

Additional simplification is attained for a perfect (nondissociable) gas because the stagnation temperature T_0 can be introduced instead of the total enthalpy i_0. Equation (3.44) takes an even simpler form when $\mathrm{Le} = \mathrm{Le}_T = \mathrm{Pr} = \mathrm{Pr}_T = 1$; retaining the total enthalpy i_0, this equation can be used for the approximate study of the dissociable turbulent boundary layer.

The Equation of State

The equation of state is also fundamental. For a real gas it can be written in the form

$$\frac{p}{\rho RT} = \varphi(p, T), \tag{3.45}$$

where R is the gas constant for a perfect gas, and the function φ, which depends on pressure and temperature, determines the deviation of the real gas properties from those of the perfect gas. If there is no deviation and $\varphi = 1$,

$$p = \rho RT. \tag{3.45a}$$

The function φ will deviate from unity as the physical-chemical properties of air change at either very high pressures or high temperatures. In the first case, intermolecular forces are important and increase as the temperature decreases; these phenomena are taken into account by the well-known Van der Waals' equation.

Of greater interest in aerodynamics are the processes connected with the second case, where dissociation and ionization occur as a result of large temperature increases. The function φ determines the value of the gas constant for an imperfect gas, i.e., $R_I = \varphi R$. Expressing R_I as a ratio of the universal gas constant R_0 to the molecular weight, we find the expression

$$\varphi(p, T) = \frac{(\mu_{avg})_0}{\mu_{avg}},$$

where the molecular weight in the numerator is that of undissociated air and in the denominator that of dissociated air. It is easy to see that $\varphi > 1$, since the average molecular weight of air decreases as the number of particles increases with dissociation.

Since the gas constant $R = R_0/(\mu_{avg})_0$, the equation of state for a dissociable gas is

$$p = \varphi\rho RT = \frac{(\mu_{avg})_0}{\mu_{avg}} \rho RT = \frac{R_0}{\mu_{avg}} \rho T. \tag{3.46}$$

In the special case of a dissociable diatomic gas, the function φ can be expressed by the concentration of the atomic component or, what

amounts to the same thing, by the degree of dissociation α. Let the mass concentration of an arbitrary component be c_i and its molecular weight be μ_i. Then the average molecular weight of the mixture μ_{ave} will be found from the relation $\mu_{avg} \Sigma (c_i/\mu_i) = 1$, in which the summation sign determines the number of moles of the mixture. For a diatomic dissociable gas,

$$\sum_i c_i = c_1 + c_2 = c_A + c_M = 1.$$

It is obvious that $c_A = \alpha$, $c_M = 1 - \alpha$, and $2\mu_A = \mu_M = (\mu_{avg})_0$. Since φ is defined as $(\mu_{avg})_0/\mu_{avg}$, it is given by $\varphi = 1 + \alpha$. After substituting φ in Eq. (3.46), the equation of state takes the form

$$p = (1 + \alpha)\rho RT, \tag{3.47}$$

where, according to Eq. (2.14), the gas constant is $R = k/2m_A$.

The Conservation of Entropy

In addition to the system of fundamental equations already presented, it is necessary to include the condition that the entropy along a given streamline remains constant for inviscid shock-free flows. This can be written as the scalar product of two vectors, i.e.,

$$\bar{V} \cdot \text{grad } S = 0. \tag{3.48}$$

According to this condition, the entropy gradient (the vector grad S) is normal to the direction of the tangent to the streamline at a given point. Equation (3.48) can be expanded if a specific coordinate system is used; for example, in a cylindrical system it would be

$$V_x \frac{\partial S}{\partial x} + V_r \frac{\partial S}{\partial r} + \frac{V_\phi}{r} \frac{\partial S}{\partial \phi} = 0. \tag{3.48a}$$

If another coordinate system is utilized, the vectors $\bar{V}$ and grad S must be written accordingly in expanded form and the scalar product must be found.

INITIAL AND BOUNDARY CONDITIONS

The solution of the differential equations describing the flow around bodies of revolution must conform to the initial and boundary conditions defined for that flow. The initial conditions are determined by the parameters at the initial moment of time of the motion, $t = t_0$; obviously, this condition is applicable only to unsteady flow.

Boundary conditions apply to the solution of any problem of gas motion and must be fulfilled at each moment of time of this motion, although they can be variable with time. As one example, the boundary conditions for pressure in steady supersonic flow about a body of revolution are determined first by the known pressure in the undisturbed flow ahead of the shock wave. Using the equation for a shock wave, the pressure immediately behind the shock can be established. The shock then acts as a boundary for the perturbed flow field around the body, and the pressure behind the shock serves as the boundary condition for the region between the shock and the body.

In the generalized case of ideal supersonic flow around bodies, the solutions of the equations must satisfy the conditions on the surface of the body, in the undisturbed (or incident) flow ahead of the shock wave, and immediately behind the shock. The conditions behind the shock wave will be considered in the next section. The other boundary conditions, those on the surface of the body and in the undisturbed flow, are discussed below.

The first condition is that the gas flow must move continuously along the surface of the body--often called the condition of continuous flow. At any given point on the surface, the velocity vector $\bar{V}$ is perpendicular to the direction of the normal to the surface, which is determined by the gradient of the function $F(x, r, \phi) = 0$, which represents the equation of the surface (for this case in cylindrical coordinates). In other words, the two vectors $\bar{V}$ and grad F must be perpendicular, and their scalar product is equal to zero; the boundary condition has the form

$$V_x \frac{\partial F}{\partial x} + V_r \frac{\partial F}{\partial r} + \frac{V_\phi}{r} \frac{\partial F}{\partial \phi} = 0. \tag{3.49}$$

Let us consider as an example a circular cone, the equation for which is $F(x, r) = r - bx = 0$ in cylindrical coordinates (the x-axis coincides with the axis of the cone). As a result of differentiaion with respect to r and x we obtain, respectively, $\partial F/\partial r = 1$, $\partial F/\partial x = -b$. Introducing these values into Eq. (3.49) and noting that $\partial F/\partial \phi = 0$, we obtain the condition of continuous flow in the form $V_r/V_x = b$, where b is the tangent of the cone half-angle. Thus, the condition of continuous flow around a cone consists of the coincidence of the flow direction with the generatrix of the cone.

From Eq. (3.49) it follows that for any body of revolution, if the x-axis is aligned with the axis of the body the condition of continuous flow is written in the form

$$V_x \frac{\partial F}{\partial x} + V_r \frac{\partial F}{\partial r} = 0, \tag{3.49a}$$

because, for a body of revolution, $\partial F/\partial \phi = 0$. If the equation for the surface is given as $F(x, r) = 0$, then $dF = (\partial F/\partial x)\, dx + (\partial F/\partial r)\, dr = 0$. After substitution of the derivative dr/dx found from this relation into Eq. (3.49a), we obtain the condition of continuous flow around a body of revolution with an arbitrary shape

$$\frac{V_r}{V_x} = \frac{dr}{dx}. \tag{3.50}$$

Spherical coordinates can also be studied. In this case the equation of the surface is $F(r, \Theta, \Psi) = 0$, with the angles Θ and Ψ measured from an arbitrary direction not coincident with the axis of the body of revolution. Then we can write the boundary condition, in analogy with Eq. (3.49), in the form

$$V_r \frac{\partial F}{\partial r} + \frac{V_\Theta}{r} \frac{\partial F}{\partial \Theta} + \frac{V_\Psi}{r \sin \Theta} \frac{\partial F}{\partial \Psi} = 0. \tag{3.51}$$

If the spherical system is chosen in such a way that the reference for the angles Θ and ψ is the axis of the body, the equation of the surface is written in the form $F(r, \Theta) = 0$ and Eq. (3.51) is simplified to

$$\frac{V_\Theta}{V_r} = r\frac{d\Theta}{dr}. \tag{3.51a}$$

The equation of a circular cone is Θ = const; hence the condition of continuous flow will be $V_\Theta = 0$. This demonstrates again that the direction of total velocity coincides with the generatrix of the cone.

In the study of potential flow, boundary conditions are imposed on the solution of the equations for the potential Φ. In accordance with the condition of continuous flow, the function Φ at the surface must satisfy the condition

$$\frac{\Phi_r}{\Phi_x} = \frac{dr}{dx}. \tag{3.52}$$

In actual cases this condition is often written in a somewhat different form. Let us consider, for example, flow around a body at an angle of attack, and let us find the velocity component of the incident flow with respect to the axes of a cylindrical system, which is easily done with the aid of the diagram in Fig. 35:

$$\begin{aligned} V_{x\infty} &= V_\infty \cos\alpha, \\ V_{r\infty} &= V_\infty \sin\alpha\cos\phi, \\ V_{\phi\infty} &= -V_\infty \sin\alpha\sin\phi. \end{aligned} \tag{3.53}$$

These relations permit the potential function for the incident (unperturbed) flow to be written in the form

$$\Phi_\infty = \varphi_\infty = xV_\infty \cos\alpha + rV_\infty \sin\alpha\cos\phi. \tag{3.54}$$

It is obvious that the velocity potential Φ of the perturbed flow must comply with this condition as well as with the condition at the surface of the body. This corresponds to the requirement that solutions for velocity components in unperturbed flow should satisfy the conditions given by Eq. (3.53).

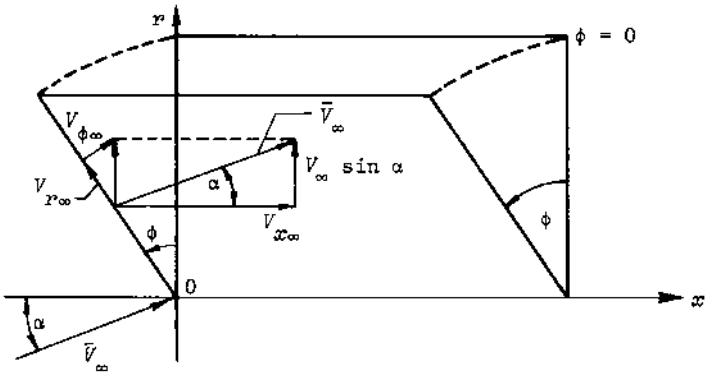

Fig. 35--Free-stream velocity components in cylindrical coordinates

If the perturbed potential function is in the form

$$\phi = xV_\infty \cos\alpha + rV_\infty \sin\alpha \cos\phi + \varphi(x, r, \phi), \tag{3.55}$$

according to Eq. (3.54) the additional potential $\varphi(x, r, \phi)$ must be equal to zero in the unperturbed flow. At the surface of the body itself, φ should satisfy the condition of continuous flow:

$$\frac{\phi_r}{\phi_x} = \frac{V_\infty \sin\alpha \cos\phi + \varphi_r(x, r, \phi)}{V_\infty \cos\alpha + \varphi_x(x, r, \phi)} = \frac{dr}{dx}, \tag{3.56}$$

where φ_r and φ_x are partial derivatives of φ with respect to r and x.

The boundary conditions illustrated above pertain to the case of ideal flow around a body. In the study of the flow of a viscous medium in the boundary layer, the solutions must satisfy the conditions at the wall and at the edge that effectively separates the viscous flow from the free stream or, as it is called, the outer edge of the boundary layer. The wall conditions result from the fact that the velocity equals zero; i.e., for $y = 0$ the components $V_x = V_y = 0$. At the outer edge, i.e., for $y = \delta$, the velocity V_x equals its value in the inviscid flow and the friction stress $\tau = 0$.

If the thermal processes in the boundary layer are being studied, conditions are defined at the wall and at the edge of the layer for

parameters that determine heat transfer; for example, one of these parameters is temperature, the solution for which must satisfy these conditions. The distribution of the thermal flux caused by thermal conductivity across the thickness of the layer must be such that its value equals zero at the edge of the layer.

In the study of diffusion phenomena, boundary conditions are imposed on the value of the concentration c_i. The solution for c_i must be such that, at the edge of the layer, it yields the value of concentration in the free stream, and for $y = 0$, the value at the wall.

With the help of the conditions indicated and using the boundary layer equations, it is possible to obtain various additional conditions that result from the physical premises and that can be applied to any problem.

ISENTROPIC FLOW

The Case of Constant Specific Heats

The calculation of isentropic flows is based on the Bernoulli equation

$$\frac{V^2}{2} + \int_{p_0}^{p} \frac{dp}{\rho} = 0. \tag{3.57}$$

The equation for the adiabatic curve, $dp = (\gamma p/\rho)\, d\rho$, can be used to calculate the integral. If the enthalpy, $i = c_p T = c_p p/\rho R$, is introduced, the equation takes the form $dp = \rho\, di$. After substitution in Eq. (3.57) and integration from the flow section with the enthalpy i to the section where the flow is completely stopped, as represented by the stagnation enthalpy i_0, we find

$$\frac{V^2}{2} + i = i_0. \tag{3.57a}$$

This equation was defined earlier as the equation for the conservation of energy. The enthalpy i_0 determines the total energy along a given streamline for isentropic flow and, in general, can vary across the

streamlines; however, in the case of uniform unperturbed flow the total enthalpy is constant. On the other hand, other stagnation parameters, particularly the pressure p_0 and density ρ_0, can change in passing from one streamline to another. This is characteristic of the flow behind a curved shock, for example, where the local parameters are proportional to the stagnation conditions.

The corresponding equations for the calculation of pressure, density, and temperature have the form

$$p = p_0 A^{\gamma/(\gamma-1)}, \qquad \rho = \rho_0 A^{1/(\gamma-1)}, \qquad T = T_0 A, \tag{3.58}$$

where the quantity A is determined from the expression $A = 1 - \widetilde{V}^2$. It is possible to convert this expression from the dimensionless velocity ratio, $\widetilde{V} = V/V_{max}$, to the local number $M = V/a$ or to relative velocity $\lambda = V/a^*$, where a^* is the critical velocity of sound. In the first case $A = 1/[1 + (\gamma - 1)M^2/2]$, in the second $A = [1 - (\gamma - 1)\lambda^2/(\gamma + 1)]$. It is evident from a comparison of these values that there is a connection between λ and M:

$$\lambda^2 = \frac{\frac{\gamma + 1}{2} M^2}{1 + \frac{\gamma - 1}{2} M^2}. \tag{3.59}$$

Comparing the other pair of expressions for A, the relation between $\widetilde{V}$ and M is

$$\widetilde{V} = \left(1 - \frac{1}{1 + \frac{\gamma - 1}{2} M^2}\right)^{\frac{1}{2}}. \tag{3.60}$$

From the equations presented, which are valid for all velocities, it is possible to obtain approximate relationships for those cases in which the local velocities are very great and $M \gg 1$. In these cases, naturally, M_∞ is also very large compared to unity. Consequently,

$$\frac{p}{p_\infty} = B^{2\gamma/(\gamma-1)}, \qquad \frac{\rho}{\rho_\infty} = B^{2/(\gamma-1)}, \qquad \frac{T}{T_\infty} = B^2, \tag{3.61}$$

where $B = M_\infty/M$. Equation (3.60) is also simplified to a certain extent:

$$\frac{\tilde{V}}{\tilde{V}_\infty} = \frac{V}{V_\infty} = 1 + \frac{1}{\gamma - 1}\left(\frac{1}{M_\infty^2} - \frac{1}{M^2}\right), \tag{3.62}$$

where $\tilde{V}_\infty = V_\infty/V_{max}$.

Isentropic Flow with Variable Specific Heats

In considering variable specific heats, it is assumed that the heating of the gas is not yet accompanied by dissociation, and the variation in specific heat is only a function of temperature and not of pressure. Consequently, the equation of state and the relation for the velocity of sound in a perfect gas are still valid.

To obtain the basic relations for isentropic flow we utilize the concept of average specific heat, which results from the following considerations. Using the equation $di = c_p\, dT$, the change in the enthalpy per unit weight of gas with a change in temperature in the range of values from T_x to T_y is

$$i_y - i_x = \int_{T_x}^{T_y} c_p\, dT.$$

The same change can be expressed by the average specific heat $(c_p)_m$ in the form $i_y - i_x = (c_p)_m(T_y - T_x)$, whence its value is found:

$$(c_p)_m = \frac{1}{T_y - T_x}\int_{T_x}^{T_y} c_p\, dT. \tag{3.63}$$

Instead of the value $(c_p)_m$, it is more convenient to use the dimensionless coefficient

$$\vartheta = \frac{(c_p)_m}{c_p}, \tag{3.64}$$

where c_p is the specific heat at the temperature T_x. Then the variation in enthalpy is

$$i_y - i_x = \theta c_p (T_y - T_x). \tag{3.65}$$

For isentropic flows, it is possible to introduce the so-called exponential specific heat $(c_p)_e$, which determines the ratio of pressures for the transition of a gas from the x-state to the y-state in accordance with the expression

$$\frac{p_y}{p_x} = \left(\frac{T_y}{T_x}\right)^{(c_p)_e/R}.$$

From this relation we obtain

$$(c_p)_e = \frac{R}{\log\,(T_y/T_x)} \log\left(\frac{p_y}{p_x}\right).$$

Since the relation $dp = (pc_p/RT)\,dT$ is valid for arbitrary points along a streamline, it can be integrated to give

$$\log\left(\frac{p_y}{p_x}\right) = \frac{1}{R}\int_{T_x}^{T_y} c_p \frac{dT}{T}.$$

Consequently,

$$(c_p)_e = \frac{1}{\log\,(T_y/T_x)} \int_{T_x}^{T_y} c_p \frac{dT}{T}. \tag{3.66}$$

In analogy with the coefficient of (3.64), let us introduce the dimensionless parameter

$$\theta_e = \frac{(c_p)_e}{c_p}, \tag{3.67}$$

and we shall write the expression $p_y/p_x = (T_y/T_x)^{\theta_e c_p/R}$. Having further assumed that the ratio $c_p/R = \gamma/(\gamma - 1)$ for the x-state, we find

$$\frac{p_y}{p_x} = \left(\frac{T_y}{T_x}\right)^{\theta_e \gamma/(\gamma-1)}, \tag{3.68}$$

where $\gamma = c_p/c_v$ is the ratio of specific heats at the temperature T_x. With the aid of the coefficients θ and θ_e, it is possible to obtain the relations for calculating the isentropic flow parameters. For this purpose let us write Eq. (3.57a) in the form $\theta_0 c_p (T_0 - T) = V^2/2$, where c_p is the specific heat at the temperature T, and the coefficient θ_0 is determined from Eq. (3.64). From the resulting expression, we find the relation for the temperature:

$$\frac{T}{T_0} = \frac{1}{1 + \dfrac{\gamma - 1}{2\theta_0} M^2}, \tag{3.69}$$

where the adiabatic exponent γ is determined at the temperature T. After substitution in Eq. (3.68) we find the expression for pressure:

$$\frac{p}{p_0} = \left(1 + \frac{\gamma - 1}{2\theta_0} M^2\right)^{-\theta_e \gamma/(\gamma-1)}. \tag{3.70}$$

Finally, using the equation of state it is possible to calculate the density:

$$\frac{\rho}{\rho_0} = \left(1 + \frac{\gamma - 1}{2\theta_0} M^2\right)^{1-\theta_e \gamma/(\gamma-1)}. \tag{3.71}$$

The coefficient θ_e is found from Eq. (3.67) for the temperature range T_0 to T.

The resulting expressions permit the determination of the stagnation parameters. Comparing their values with those obtained for constant specific heats, it can be noted that, for the same free-stream conditions, the stagnation density and pressure are larger but the stagnation temperature, on the other hand, is less. The decrease in temperature is caused by the redistribution of the internal energy with

heating in such a way that part of it goes into the excitation of the translational, rotational, and vibrational degrees of freedom.†

The Isentropic Flow of a Dissociating and Ionizing Gas

The calculation of the isentropic flow of a dissociating and ionizing gas is more complex because the thermodynamic parameters depend not only on temperature but also on pressure. Prepared tables or diagrams must be used to facilitate the calculation. The most important of these is the i-S diagram, two variants of which are presented in Figs. 15 and 16. Equation (3.39) is a supplement to the tables or diagrams. This equation permits the determination of the local velocity of the isentropic flow from a known enthalpy or, on the other hand, permits the calculation of the enthalpy from the velocity.

† Editor's note: I have not noticed the parameters θ and θ_e presented in Western literature. They seem useful enough to deserve a graph, although Krasnov does not show them. Consequently, they are plotted in Fig. 35a, using the data from the National Bureau of Standards Tables, Ref. 9.

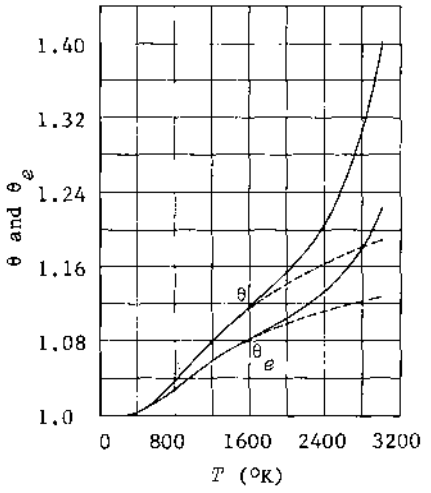

$$\theta = \frac{1}{c_{p0}(T - T_0)} \int_{T_0}^{T} c_p \, dT$$

$$\theta_e = \frac{1}{c_{p0} \log (T/T_0)} \int_{T_0}^{T} \frac{c_p}{T} \, dT$$

——— Real gas

------- Ideal gas

$T_0 = 290^\circ K$

$c_{p0} = 0.240$ cal/g°K

Fig. 35a--Specific heat ratios for air

§ 4. *THE BASIC RELATIONS FOR DETERMINING GAS PARAMETERS BEHIND A SHOCK WAVE*

IN THE AERODYNAMICS OF BODIES of revolution, the problem of the compression shock (or shock wave) is first and primarily associated with the determination of boundary conditions for the gas flow between the body surface and the wave. On the other hand, for the solution of the problem of flow around plane two-dimensional bodies (flat plates, plane wedges), the shock calculation is directly related to the calculation of the surface parameters, because the density, pressure, temperature, and other parameters (in the case of thermodynamic equilibrium) everywhere on the body surface will be the same as those behind the attached shock. However, in the case of a two-dimensional detached curved wave originating, for example, in front of a blunt plate of finite thickness or a blunt plane wedge, the shock-wave problem again acquires the significance of a boundary-condition problem.

THE OBLIQUE SHOCK-WAVE EQUATIONS

Let us investigate the general case in which the shock wave is curved and the gas behind it undergoes physical and chemical changes. The question of the rates of the physical and chemical changes is of great significance in the study of these shock waves, since the high temperatures existing behind the shock result in the excitation of vibrations, dissociation, and ionization, and create conditions for chemical reactions.

Part of the kinetic energy behind the shock wave is converted almost instantaneously into internal energy of the gas. Under these conditions it is usually impossible to disregard the fact that thermodynamic equilibrium is achieved over a finite period of time. The analysis of

such phenomena represents a complex problem and is connected, first of all, to the study of the mechanism of nonequilibrium processes and, in particular, to the knowledge of chemical reaction rates in air.

The simplest case is characterized by infinitely large rates of chemical and physical changes and, consequently, by the instantaneous establishment of thermodynamic equilibrium. Experimental research confirms that such processes are physically possible behind shock waves. The basic results examined below permit the calculation of the equilibrium parameters behind a shock wave. There are ten such unknown parameters in the case of a dissociable gas: pressure, p_2; density, ρ_2; temperature, T_2; velocity, V_2; enthalpy, i_2; entropy, S_2; the velocity of sound, a_2; the mean molecular weight $(\mu_{avg})_2$; and the wave angle, θ_s (or the deflection angle of the flow, δ_s). Consequently, a system of ten equations must be created. The parameters up to the shock wave will be known in these equations.

Before writing the equations, let us examine the diagram of a curved shock wave (Fig. 36), which can be described as an infinite series of oblique plane shocks. For one of these shocks, the surface of which is

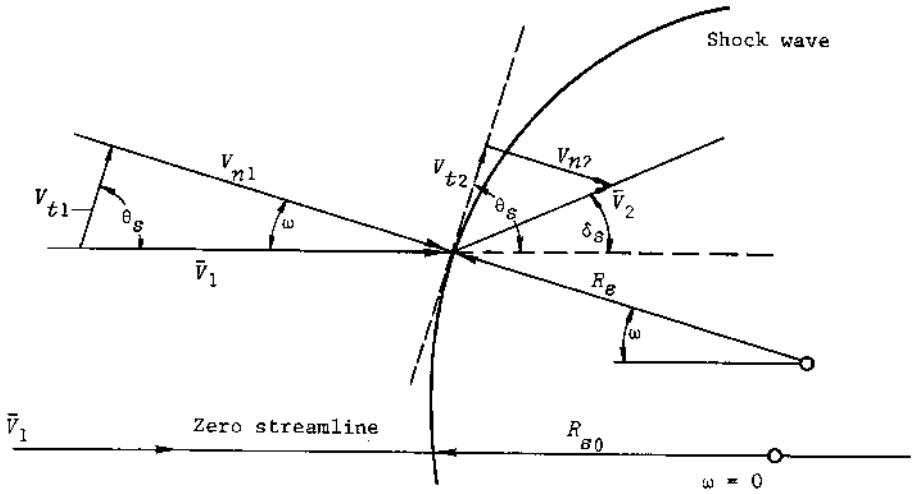

Fig. 36--Diagram of a curved shock wave

tangent to the surface of the curved wave, triangles of the flow velocities are plotted ahead of the shock (parameters with the subscript 1) and behind it (parameters with the subscript 2). From these triangles, it is not difficult to determine the auxiliary relationships for calculating the normal (subscript n) and tangential (subscript t) velocity components:

$$\begin{aligned} V_{t1} &= V_1 \cos \theta_s, \\ V_{n1} &= V_1 \sin \theta_s, \\ V_{t2} &= V_2 \cos (\theta_s - \delta_s), \\ V_{n2} &= V_2 \sin (\theta_s - \delta_s). \end{aligned} \tag{4.1}$$

In some cases it may be preferable to use the angle ω instead of θ_s, where ω is the angle between the free-stream velocity vector and the normal to the surface of the shock wave; it is clear from Fig. 36 that the substitution $\theta_s = \pi/2 - \omega$ can be made in Eq. (4.1). An important relation can be obtained from these results, namely,

$$\frac{V_{n1}}{V_{n2}} = \frac{\tan \theta_s}{\tan (\theta_s - \delta_s)}, \tag{4.2}$$

which is based on the fact that the tangential velocity components before and after the shock wave are equal, i.e., $V_{t1} = V_{t2}$. These relations can be considered the first two equations of the system. Three other equations are conservation equations: the equation for the conservation of mass,

$$\rho_1 V_{n1} = \rho_2 V_{n2}; \tag{4.3}$$

the impulse equation (the equation for the conservation of momentum in a direction normal to the wave surface),

$$p_1 + \rho_1 V_{n1}^2 = p_2 + \rho_2 V_{n2}^2; \tag{4.4}$$

and the equation for the conservation of energy,

$$i_1 + \frac{V_{n1}^2}{2} = i_2 + \frac{V_{n2}^2}{2}. \tag{4.5}$$

Four more equations of the system under consideration permit the determination of enthalpy, entropy, mean molecular weight, and the velocity of sound in a dissociable gas as general functions of pressure and temperature:

$$i_2 = f_1(p_2, T_2), \tag{4.6}$$

$$S_2 = f_2(p_2, T_2), \tag{4.7}$$

$$(\mu_{ave})_2 = f_3(p_2, T_2), \tag{4.8}$$

$$a_2 = f_4(p_2, T_2). \tag{4.9}$$

These relations are found using tables or graphs of the thermodynamic functions of air at high temperatures.

The tenth equation is obtained from the equation of state for conditions before and after the shock wave and has the form

$$p_2 - p_1 = R_0 \left[\frac{\rho_2 T_2}{(\mu_{avg})_2} - \frac{\rho_1 T_1}{(\mu_{avg})_1} \right]. \tag{4.10}$$

Let us present the basic parameters behind the shock wave in terms of the relative change of the normal components of velocity, i.e., by the quantities $\Delta V_n / V_{n1} = (V_{n1} - V_{n2})/V_{n1} = \Delta \bar{V}_n$:

$$\frac{\rho_1}{\rho_2} = 1 - \Delta \bar{V}_n, \tag{4.11}$$

$$\frac{p_2}{p_1} = 1 + \frac{\rho_1 V_{n1}^2}{p_1} \Delta \bar{V}_n, \tag{4.12}$$

where for an undissociated incident flow

$$\frac{\rho_1 V_{n1}^2}{p_1} = \gamma_1 M_{n1}^2.$$

For the temperature and enthalpy ratios we obtain

$$\frac{T_2}{T_1} = (1 + \gamma_1 M_{n1}^2 \, \Delta\bar{V}_n)(1 - \Delta\bar{V}_n) \frac{(\mu_{avg})_2}{(\mu_{avg})_1}, \tag{4.13}$$

$$\frac{i_2}{i_1} = 1 + \frac{V_{n1}^2}{2} \frac{\Delta\bar{V}_n}{i_1} (2 - \Delta\bar{V}_n). \tag{4.14}$$

The other parameters can also be expressed in terms of the quantity $\Delta\bar{V}_n$ and the known parameters of the incident flow. Since this quantity, according to Eq. (4.11), is determined by the ratio of densities ρ_2/ρ_1, the other ratios, i.e., Eqs. (4.12), (4.13), etc., can be presented as functions of ρ_2/ρ_1. In addition, instead of the quantities V_{n1} or M_{n1}, the values $V_{n1} = V_1 \sin \theta_s$ and $M_{n1} = M_1 \sin \theta_s$, respectively, can be introduced into the equation. Thus, the solution of the problem of an oblique shock with a known angle of inclination amounts to searching for the density ratio ρ_2/ρ_1, or what is the same thing, to the determination of the quantity $\Delta\bar{V}_n$. This is accomplished with the help of Eqs. (4.13) and (4.14), which can be written in the form

$$\Delta\bar{V}_n = A + \sqrt{A^2 - B}, \tag{4.15}$$

$$\Delta\bar{V}_n = 1 - \sqrt{1 - 2(i_2 - i_1)/V_{n1}^2}, \tag{4.16}$$

where

$$A = \frac{\gamma_1 M_{n1}^2 - 1}{2\gamma_1 M_{n1}^2}, \qquad B = \frac{1}{\gamma_1 M_{n1}^2} \left[\frac{T_2}{T_1} \frac{(\mu_{avg})_1}{(\mu_{avg})_2} - 1 \right]. \tag{4.17}$$

Equations (4.15) and (4.16) must be solved for $\Delta\bar{V}_n$ by the method of successive approximations.

THE SHOCK WAVE IN A GAS FLOW WITH CONSTANT SPECIFIC HEATS

The System of Equations

The system is simplified because the average molecular weight of air does not vary and specific heats remain constant. Such parameters as the velocity of sound and the enthalpy depend only on temperature. The entropy is determined from the thermodynamics of a perfect gas. On this basis, Eqs. (4.6) through (4.9) are written thus:

$$i_2 = c_p T_2, \qquad S_2 = c_v \log\left(\frac{p_2}{\rho_2^{\gamma}}\right), \qquad a_2^2 = \gamma R T_2,$$
$$(\mu_{avg})_2 = (\mu_{avg})_1 = \mu_{avg} = \text{const.} \tag{4.18}$$

Equation (4.10) is also simplified:

$$p_2 - p_1 = R(\rho_2 T_2 - \rho_1 T_1). \tag{4.19}$$

The form of Eqs. (4.2) through (4.5) remains the same.

Equations for the Calculation of Parameters

The simplified forms given by Eqs. (4.15) and (4.16) can be solved to obtain the following expression for the relative change in the normal velocity component:

$$\Delta\bar{V}_n = (1 - \varepsilon)\left(1 - \frac{1}{M_1^2 \sin^2\theta_s}\right), \tag{4.20}$$

where $\varepsilon = (\gamma - 1)/(\gamma + 1)$.

Substituting Eq. (4.20) into Eqs. (4.11) and (4.12), we obtain the following relations:

$$\frac{\rho_2}{\rho_1} = \frac{M_1^2 \sin^2\theta_s}{(1-\varepsilon) + \varepsilon M_1^2 \sin^2\theta_s}, \tag{4.21}$$

$$\frac{p_2}{p_1} = (1+\varepsilon)M_1^2 \sin^2\theta_s - \varepsilon, \tag{4.22}$$

with the aid of which equations for the calculation of other parameters can be found. In particular, the equation for the temperature ratio is obtained from the equation of state:

$$\frac{T_2}{T_1} = \frac{p_2}{p_1}\frac{\rho_1}{\rho_2}. \tag{4.23}$$

It is obvious that the enthalpy ratio is equal to the temperature ratio and also to the ratio of the square of the velocity of sound before and after the shock wave.

If $\theta_s = \pi/2$ is assumed in the ratios presented, they can be used for the calculation of the parameters behind a normal shock wave. For both the oblique and the normal shock, the relation between pressure and density is

$$\frac{p_2}{p_1} = \frac{\rho_2/\rho_1 - \varepsilon}{1 - \varepsilon\rho_2/\rho_1}. \tag{4.24}$$

This relation is called the Rankine-Hugoniot equation and is obtained from Eqs. (4.21) and (4.22) by eliminating the quantity $M_1 \sin\theta_s$.

Angles of Inclination of the Shock Wave and Velocity Vectors

From ratios (4.21) and (4.22) it follows that the parameters behind the shock wave depend not only on the Mach number M_1, but also on the angle of inclination of the shock wave θ_s. The value of this angle, in turn, is determined by the same Mach number M_1 and by the angle of deflection of the flow δ_s. The corresponding relation is obtained from Eqs. (4.2) and (4.20) and has the form

$$M_1^2 \sin^2\theta_s = \frac{(1-\varepsilon)\tan\theta_s}{\tan(\theta_s - \delta_s) - \varepsilon\tan\theta_s}. \qquad (4.25)$$

The relation between the angles θ_s and δ_s for different values of M_1 is presented graphically in Fig. 37. It will be noted that the shock-wave angle θ_s is double valued with respect to the deflection angle δ_s. In the area located to the left of the dashed curve, θ_s increases as δ_s is increased, but to the right of the dashed curve it decreases. This is caused by the varied shapes possible for the shock wave. If one examines the shock in front of a pointed body, in the first case the shock is attached to the nose. The angle of inclination of the shock wave increases in proportion to the increase in the body thickness and therefore to the increase in the angle of deflection of the flow. It can be seen in Fig. 37 that the angle δ_s can increase only up to a specific value that is a function of the Mach number M_1. This maximum angle is called the critical angle (δ_{cr}) of deflection (or turning) of the flow. The critical deflection angle is indicated in Fig. 37 by the dashed line. Analysis has shown that the flow behind an attached shock is stable in the sense of maintaining its shape as long as the deflection angle of the flow is less than critical everywhere behind the shock. In accordance with this, such flow is called subcritical.

As the thickness of the body is increased further, the deflection angle δ_s becomes equal to the critical value. With a further increase in thickness, the shock wave detaches from the nose, and a stable region of flow exists behind the detached shock, characterized by a deflection angle that is also less than critical. However, in contrast to subcritical flow, such a flow is called supercritical because the nose angle of the body exceeds the maximum value for which the shock wave can be attached.

The detached shock wave changes its shape completely, as is evident in the example of a cone in flow. While the flow is subcritical, the shock is attached to the apex, and the generatrix of its surface is a straight line. Flow around thick cones can become supercritical, in which case the shock wave detaches and takes on a curved shape. A normal shock wave is formed at the axis of flow, with an angle $\theta_s = \pi/2$.

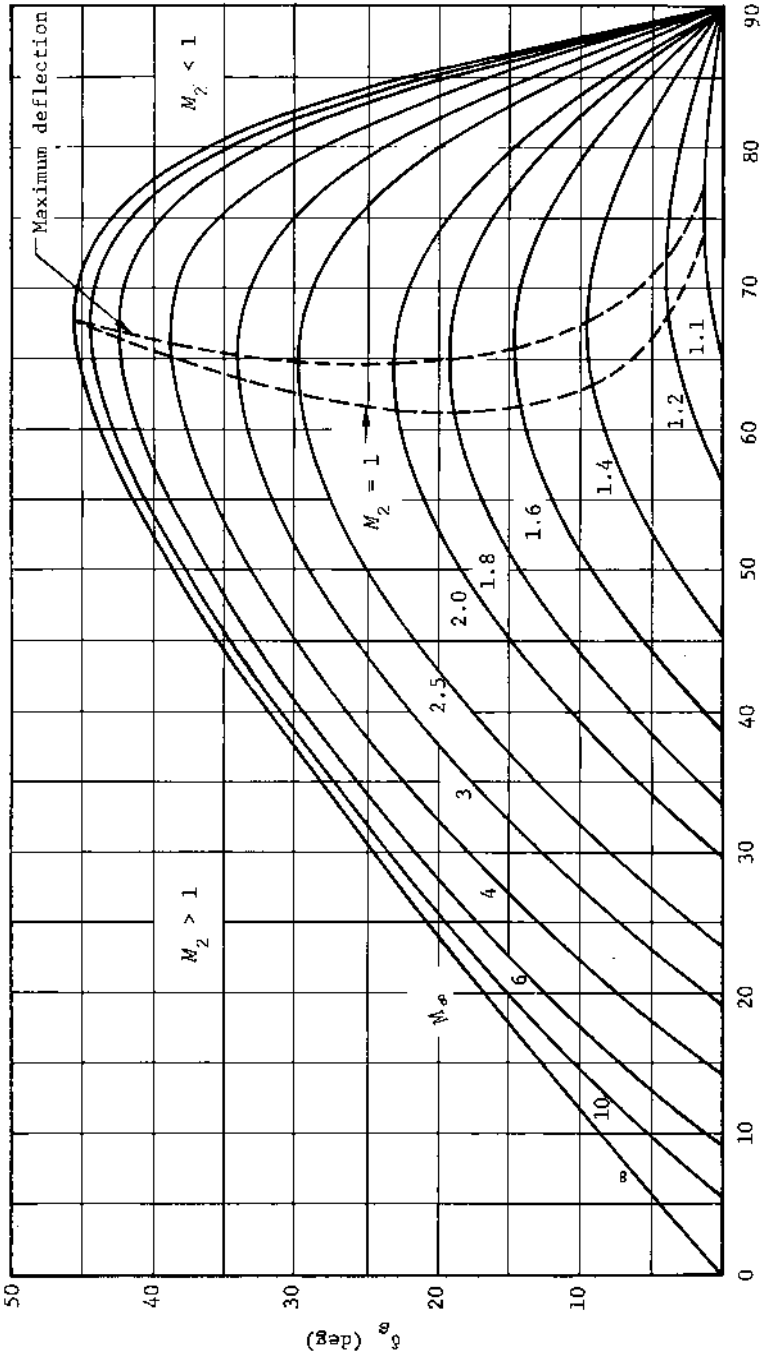

Fig. 37—Change in flow inclination as a function of shock-wave angle and Mach number

As one moves away from the axis, the angle of inclination of the shock decreases, but there will always be a region near the axis where the flow is supercritical. The variation in the deflection angle of the flow behind the shock wave has a different character. As can be seen from Fig. 37, the deflection angle δ_s is zero when passing through the normal shock on the axis. Moving away from the axis, the deflection angle increases as the shock-wave angle decreases in the supercritical region. At some point on the shock, the deflection angle reaches its critical value and then decreases. It follows from Eq. (4.25) that as δ_s approaches zero, the shock angle nears the value $\theta_s = \sin^{-1}(1/M_1)$. Thus the shock-wave angle for a given Mach number can vary within the range $\sin^{-1}(1/M_1) \leq \theta_s \leq \pi/2$. At the lower limit, the shock degenerates into a Mach wave and the flow deflection angle $\delta_s = 0$. At the upper limit, the wave is a normal shock and again the flow deflection $\delta_s = 0$. It is apparent in Fig. 37 that two different shock-wave angles can be found for the same deflection angle. The larger value of θ_s corresponds to a strong shock, behind which the flow is subsonic; the smaller value of θ_s corresponds to a weak shock with supersonic flow behind it (except for a small region near critical δ_s where the flow can be subsonic).

Let us consider the possible cases of supersonic flow around a pointed body, since in flow around blunted bodies there is only one type of flow, characterized by the development of a curved detached bow wave. As already indicated, the essential element of the calculation is the determination of the relation between the angles δ_s and θ_s. In addition to Eq. (4.25), the following relations are useful:

$$\tan(\theta_s - \delta_s) = \frac{\varepsilon p_2/p_1 + 1}{\varepsilon + p_2/p_1} \tan\theta_s, \tag{4.26}$$

$$\cot\delta_s = \frac{1 + \left(\frac{1}{1-\varepsilon} - \sin^2\theta_s\right)M_1^2}{M_1^2 \sin^2\theta_s - 1} \tan\theta_s. \tag{4.27}$$

If Eqs. (4.2) and (4.3) are modified in a corresponding manner, the relation between the angles θ_s and δ_s can also be expressed in terms

of the density ratio ρ_2/ρ_1:

$$\cot \theta_s = \left[\frac{1}{2}\left(1 - \frac{\rho_1}{\rho_2}\right) \pm \sqrt{\frac{1}{4}\left(1 - \frac{\rho_1}{\rho_2}\right)^2 - \frac{\rho_1}{\rho_2}\tan^2\delta_s}\right]\cot \delta_s, \quad (4.28)$$

where the different signs, in accordance with Fig. 37, determine two different solutions for the shock-wave angle.

The Mach Number and Velocity behind a Shock Wave

The Mach number M_2 is determined from the following expression:

$$M_2 \sin(\theta_s - \delta_s) = \sqrt{(1 - \varepsilon)/(\rho_2/\rho_1 - \varepsilon)}. \quad (4.29)$$

Eliminating δ_s by means of Eq. (4.27), we obtain the relation

$$M_2^2 = \frac{(1 - \varepsilon) + \varepsilon M_1^2}{(1 + \varepsilon)M_1^2 \sin^2\theta_s - \varepsilon} + \frac{(1 - \varepsilon)M_1^2 \cos^2\theta_s}{(1 - \varepsilon) + \varepsilon M_1^2 \sin^2\theta_s}. \quad (4.30)$$

To determine the velocity behind the shock wave, we can use the equation

$$\frac{V_2^2}{V_1^2} = \cos^2\theta_s + \left(\frac{\rho_1}{\rho_2}\right)^2 \sin^2\theta_s, \quad (4.31)$$

in which the density ratio can be replaced by Eq. (4.21).

Entropy and Total Pressure

The calculation of entropy and total pressure is an important practical result of shock-wave theory. The nonisentropic character of transition through the shock wave is manifested in an increase in entropy, because the process is thermodynamically irreversible. Losses in the shock wave are connected directly with this irreversible conversion of a portion of the total flow energy into internal energy. The increase in entropy is

$$S_2 - S_1 = c_v\left(\log \frac{p_2}{p_1} - \frac{1+\varepsilon}{1-\varepsilon} \log \frac{\rho_2}{\rho_1}\right). \tag{4.32}$$

There is a unique relation between the entropy change and the decrease in total pressure behind the shock wave. This relation is based on the use of the isentropic relations before and after the shock:

$$\frac{p_1}{\rho_1^\gamma} = \frac{p_0}{\rho_0^\gamma},$$

$$\frac{p_2}{\rho_2^\gamma} = \frac{p_0'}{(\rho_0')^\gamma},$$

where p_0, ρ_0 and p_0', ρ_0' are the stagnation pressure and density before and after the shock wave, respectively. Then the entropy difference can be written as

$$S_2 - S_1 = c_v \log\left[\frac{p_0'}{p_0}\left(\frac{\rho_0}{\rho_0'}\right)^\gamma\right] = c_v \log\left[\left(\frac{p_0'}{p_0}\right)^{1-\gamma}\left(\frac{T_0'}{T_0}\right)^\gamma\right].$$

Since the stagnation temperatures before and after the shock are equal, $T_0 = T_0'$, we obtain for total pressure

$$\frac{p_0'}{p_0} = \exp\left[-\frac{S_2 - S_1}{(\gamma - 1)c_v}\right]. \tag{4.33}$$

Substituting the entropy difference from Eq. (4.32) and using the relations given in Eqs. (4.21) and (4.22), the expression for the total pressure ratio becomes

$$\frac{p_0'}{p_0} = \frac{1}{\left[(1+\varepsilon)M_1^2 \sin^2\theta_s - \varepsilon\right]^{(1-\varepsilon)/2\varepsilon}\left(\varepsilon + \dfrac{1-\varepsilon}{M_1^2 \sin^2\theta_s}\right)^{(1+\varepsilon)/2\varepsilon}}. \tag{4.33a}$$

Analysis of these results shows that the ratio of total pressures across a shock wave, p_0'/p_0, is always less than one, and that the larger the shock angle at a given Mach number, i.e., the stronger the shock, the larger will be the loss in total pressure and hence the smaller the ratio p_0'/p_0. Referring to Eq. (3.58) for the ratio of static to total pressure (with p_0 replaced by p_0'), it follows that the local static pressure at the same velocity will be higher on a streamline located behind a weaker shock.

The Hodograph of Velocity

The analytical solution to the problem of determining the flow parameters behind an oblique shock was presented above. A graphical method based on the concept of the hodograph of velocity can also be used.

A hodograph of velocity is a curve representing the geometric location of the terminals of the velocity vectors behind the shock. The hodograph equation is obtained from the general relationship for an oblique shock wave and has the form

$$\frac{\lambda_W^2}{(\lambda_1 - \lambda_U)^2} = \frac{\lambda_1\lambda_U - 1}{(1 - \varepsilon)\lambda_1^2 + 1 - \lambda_1\lambda_U}, \tag{4.34}$$

where $\lambda_W = W_2/a^*$, $\lambda_U = U_2/a^*$, $\lambda_1 = V_1/a^*$, and W_2 and U_2 are the vertical and horizontal velocity components behind the shock, respectively.

Equation (4.34) is represented graphically by a curve known as a strophoid (Fig. 38). The two branches that stretch to infinity (to the right of point A) have no physical meaning because they correspond not to the shock wave but to a rarefaction wave. The part of the strophoid (to the left of point A) that has physical meaning is called a shock polar. A different shock polar corresponds to each value of λ_1 (or M_1), so that a family of polars can be constructed to the same scale for a series of Mach numbers.

The points A and B in Fig. 38 represent the ends of the velocity vectors before and after the shock wave, in terms of the dimensionless parameter λ. The direction of the shock is given by the normal to the

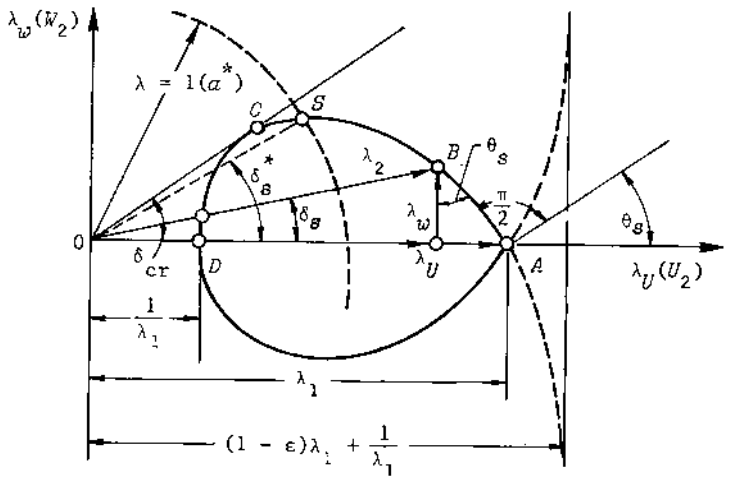

Fig. 38--The shock polar (strophoid)

straight line connecting points A and B. Thus, for a given shock angle θ_s, the direction and velocity of the flow behind the shock wave can be determined graphically from the shock polar. Conversely, the velocity behind the shock and the shock angle can be determined for a given flow deflection angle.

As the flow deflection angle decreases to zero, point B approaches point A, and the shock-wave slope approaches the value corresponding to an infinitesimal deflection. This angle is the slope of a Mach line and is given by the normal to the slope of the shock polar at A (Fig. 38). At the other end of the polar, the point D corresponds to a normal shock, with zero deflection of the flow and the smallest velocity behind the shock.

If an arc of a circle is constructed with a radius corresponding to the critical velocity of sound a^* (i.e., $\lambda = 1$), it divides the shock polar into a subsonic region on the left and a supersonic region on the right. A straight line from 0 at an angle δ_s intersects the polar at two points, B and E. These points represent in graphic form the two solutions to the oblique shock equations that were mentioned earlier. A weak shock corresponds to point B (greater velocity), and a strong shock to point E (lesser velocity). The weak shock is the one found

in practice in flow over bodies. As the deflection angle increases, it reaches a value δ_s^* corresponding to sonic flow behind the shock, and finally the angle δ_{cr}, where the line is tangent to the shock polar at point *C*. The latter angle is the maximum deflection angle of the flow and earlier was called the critical angle.

The Shock Wave at Hypersonic Velocities (Constant Specific Heats)

The relations for gas flow through a shock wave with constant specific heats can be simplified for very high velocities, for which the parameter $M_1 \sin \theta_s$ is much larger than one. For example, Eq. (4.21) is written as

$$\frac{\rho_2}{\rho_1} = \frac{1}{\varepsilon} = \frac{\gamma + 1}{\gamma - 1}. \tag{4.21a}$$

Equation (4.22) has the form

$$\frac{p_2}{p_1} = (1 + \varepsilon)K_s^2, \tag{4.22a}$$

where $K_s = M_1 \sin \theta_s$ or, for small wave angles, $K_s = M_1\theta_s$. The pressure coefficient behind the shock is found from the above equation:

$$C_{p2} = \frac{2(p_2 - p_1)}{\gamma p_1 M_1^2} = 2(1 - \varepsilon)\frac{K_s^2}{M_1^2}. \tag{4.35}$$

After simplification of Eq. (4.20), we obtain

$$\Delta\bar{V}_n = 1 - \varepsilon. \tag{4.20a}$$

Approximate equations can be obtained in a similar way for other parameters for hypersonic flow velocities.

These relations apply for very large values of K_s, i.e., where $K_s \to \infty$. It is of interest to develop these relations for cases where $K_s \gg 1$, but still small enough so that the free-stream Mach number has an effect on the parameters. Assuming that the shock-wave angle θ_s and

the flow deflection angle δ_s are small, we can use Eqs. (4.2), (4.3), (4.22), and (4.24) to derive an expression for the ratio of the angles:

$$\frac{\theta_s}{\delta_s} = \frac{K_s}{K} = \frac{1}{2(1-\varepsilon)}\left[1 + \sqrt{1 + 4(1-\varepsilon)^2/K^2}\right], \tag{4.36}$$

where the parameter $K = M_1\delta_s$ is the hypersonic similarity parameter based on the flow deflection angle behind the shock. This parameter is obviously the correct similarity parameter for the ratio θ_s/δ_s. Hypersonic flows will be similar in the sense that, for identical values of K, the ratios θ_s/δ_s will also be identical and independent of the absolute value of the quantities that characterize the flows.

For $K \to \infty$, this ratio approaches the limit

$$\frac{\theta_s}{\delta_s} = \frac{1}{1-\varepsilon}. \tag{4.36a}$$

Combining Eqs. (4.22) and (4.36), and assuming that $\sin\theta_s \approx \theta_s$, we obtain the approximate equation for the pressure coefficient:

$$\frac{C_{p2}}{\delta_s^2} = 2\frac{\theta_s}{\delta_s} = \frac{1}{1-\varepsilon}\left[1 + \sqrt{1 + 4(1-\varepsilon)^2/K^2}\right]. \tag{4.37}$$

The equation shows that K is the correct similarity parameter for the pressure coefficient. As $K \to \infty$, the pressure coefficient is given by

$$\frac{C_{p2}}{\delta_s^2} = \frac{2}{1-\varepsilon}. \tag{4.37a}$$

The similarity parameter K can be used to define other related parameters. For example, the quantity $\Delta\bar{V}_n$ can be expressed as a function of K based on Eq. (4.20):

$$\Delta\bar{V}_n = \frac{\delta_s}{\theta_s} = \frac{2(1-\varepsilon)}{1 + \sqrt{1 + 4(1-\varepsilon)^2/K^2}}. \tag{4.38}$$

It is evident that as $K \to \infty$ this quantity approaches the value given by Eq. (4.20a). The density ratio across the shock can be obtained from these results by using Eq. (4.11).

A simplified equation for the Mach number behind the shock M_2 can also be derived. Writing Eq. (4.30) in terms of the parameter K_s, and assuming that $\sin \theta_s \approx \theta_s$ and $\cos \theta_s \approx 1$, we obtain

$$M_2^2 = \frac{M_1^2/(1-\varepsilon)^2}{\left(\frac{1+\varepsilon}{1-\varepsilon} K_s^2 - \frac{\varepsilon}{1-\varepsilon}\right)\left(\frac{1}{K_s^2} + \frac{\varepsilon}{1-\varepsilon}\right)}, \tag{4.39}$$

where K_s is determined as a function of the similarity parameter K from Eq. (4.36).†

Some Relations for Curved Shock Waves

A curved shock always has at least one point at which a tangential plane is perpendicular to the direction of the velocity of incident flow. This point is called the "normal" part of the shock wave. We will designate the streamline passing through this point as the zero streamline. The flow proceeds without a change in direction and, consequently, the angle of inclination of the radius of curvature of the shock equals zero at this point.

Moving out along the shock wave, this angle increases, as does the deflection of the flow, even though the strength of the shock wave decreases. This trend differs in principle from that of an attached shock, where the strength of the wave increases with an increase in the deflection angle.

To determine the character of the change in the flow deflection angle along a curved shock, we can use the derivative

†Editor's note: Observe that, for large values of K_s, this reduces to a simpler expression:

$$\frac{M_2}{M_1} = \frac{1}{\sqrt{1 + \varepsilon(1+\varepsilon)K_s^2}},$$

and as $M_1 \to \infty$, $M_2 \to 1/\theta_s \sqrt{\varepsilon(1+\varepsilon)}$.

$$\frac{d\delta_s}{d\omega} = \frac{(1-\varepsilon)\{[(1+\varepsilon)\cos^4\omega - \cos^2\omega]M_1^4 + [2(1-\varepsilon)\cos^2\omega - 1]M^2 - (1-\varepsilon)\}}{(1-\varepsilon+\varepsilon M_1^2\cos^2\omega)^2 + (M_1^2\sin\omega\cos\omega)^2}, \tag{4.40}$$

which results from the differentiation of Eq. (4.27), with the shock angle θ_s replaced by $\theta_s = \pi/2 - \omega$.

Relations that permit the determination of the variation in the other parameters along a curved shock wave are important for the solution of the problem of flow around bodies. In particular, the relations

$$\frac{d(\log p)}{d\omega} = -\frac{2(1+\varepsilon)M_1^2\sin\omega\cos\omega}{(1+\varepsilon)M_1^2\cos^2\omega - \varepsilon}, \tag{4.41}$$

$$\frac{d(\log \rho)}{d\omega} = -\frac{2(1-\varepsilon)\tan\omega}{(1-\varepsilon)+\varepsilon M_1^2\cos^2\omega} \tag{4.42}$$

can be used for the calculation of pressure and density changes; they indicate that the pressure and density increase monotonically as they approach the zero streamline and have a maximum value at the apex of the wave, where $\omega = 0$, and where the derivatives $dp/d\omega = d\rho/d\omega = 0$.

The geometric properties of a curved shock wave can be described by the radius of curvature of the shock surface, R_s, and by its variation along the wave. Let the equation $r = f(x)$ represent, in general form, the equation of a shock wave in any meridian plane. The radius of curvature at an arbitrary point is

$$R_s = \frac{ds}{d\omega} = -\frac{[1+(r')^2]^{3/2}}{r''}, \tag{4.43}$$

where ds is an element of arc of the generatrix, $r' = dr/dx$, and $r'' = d^2r/dx^2$ where $r'' < 0$. Calculating the derivative with respect to ω, we find the expression

$$\frac{dR_s}{d\omega} = \frac{R_s\{[1+(r')^2]r''' - 3r'(r'')^2\}}{(r'')^2}, \tag{4.44}$$

which allows us to find the variation in the radius of curvature along the shock if its shape is known. Let us assume that the generatrix of the shock has the shape of a parabola, $x = ar^2$. Then the radius of curvature is

$$R_s = \frac{(4a^2r^2 + 1)^{3/2}}{2a}, \tag{4.43a}$$

and at the point $r = 0$, through which the zero streamline passes, the quantity $R_s = R_{s0} = \frac{1}{2}a$. For the parabolic shock, Eq. (4.44) takes the form

$$\frac{dR_s}{d\omega} = \frac{3rR_s}{R_{s0}}, \tag{4.44a}$$

where R_s is determined from Eq. (4.43a).

Experimental data show that the generatrix of a curved shock in the vicinity of the zero streamline can also be represented by a hyperbola:

$$\frac{x^2}{a^2} - \frac{r^2}{b^2} = 1$$

with the semiaxes a and b. In this case the radius of curvature is

$$R_s = R_{s0}\left[1 + \left(1 + \frac{a}{R_{sc}}\right)\frac{r^2}{aR_{s0}}\right]^{3/2}, \tag{4.45}$$

where $R_{s0} = b^2/a$ is the radius of curvature on the axis ($x = r = 0$). From Eq. (4.45) the derivative is

$$\frac{dR_s}{d\omega} = 3r\left(\frac{R_s}{R_{s0}}\right)\left(1 + \frac{R_{s0}}{a}\right)\left(1 + \frac{r^2}{aR_{s0}}\right)^{1/2}. \tag{4.46}$$

THE SHOCK WAVE IN A GAS FLOW WITH VARIABLE SPECIFIC HEATS

It will be assumed that dissociation does not occur, but the excitation of vibrational degrees of freedom due to increasing temperature

causes an increase in the specific heats of the gas. The variability of the specific heat has a strong influence on the flow behind the shock wave, and we must proceed from the more general system of Eqs. (4.2) through (4.10). Since there is no dissociation, it is possible to simplify some of these equations. Equation (4.6) can be written as

$$i_2 - i_1 = \theta_2 (c_p)_1 (T_2 - T_1), \tag{4.47}$$

where θ_2 is the coefficient calculated from Eq. (3.64) for the temperature range $T_2 - T_1$.

Equation (4.9) for the velocity of sound has the form

$$a_2^2 = \gamma_2 R T_2, \tag{4.48}$$

where γ_2 is the ratio of specific heats behind the shock wave. Equation (4.8) drops out of the system because the molecular weight of the gas does not change. The rest of the equations retain their previous form.

This form of the system of equations allows us to obtain a series of important relations for calculating the flow parameters. For example, one of these relations is the adiabatic equation for a shock wave, which has the form

$$\frac{\rho_2}{\rho_1} = \frac{1 + \Omega p_2/p_1}{\Omega + p_2/p_1}, \tag{4.49}$$

where the parameter

$$\Omega = \frac{2\gamma_1 \theta_2}{\gamma_1 - 1} - 1 \tag{4.50}$$

is a function of temperature. This parameter can be presented somewhat differently. Let us recall that the coefficient $\theta_2 = (c_p)_m/(c_p)_1$, where $(c_p)_m$ is evaluated as a mean for the temperature range $T_2 - T_1$. Keeping in mind that $c_p - c_v = R = \text{const}$, we obtain $\theta_2 = \gamma_m(\gamma_1 - 1)/\gamma_1(\gamma_m - 1)$ for this coefficient and therefore can write

$$\Omega = \frac{\gamma_m + 1}{\gamma_m - 1}, \tag{4.51}$$

where γ_m is the ratio of specific heats calculated from the specific heat $(c_p)_m$. After substituting Eq. (4.51) into Eq. (4.49), the latter assumes the same external form as the ordinary Rankine-Hugoniot equation. The difference lies in the fact that the variable quantity γ_m, which can be called an effective ratio of specific heats, enters into the new equation. It should be noted that this quantity differs from the value of the adiabatic exponent γ_2 behind the shock wave, and, on the basis of the approximation $\gamma_m = 0.5(\gamma_1 + \gamma_2)$, the value $\gamma_m > \gamma_2$.

In addition to Eq. (4.49), the relation between pressure and density can be determined with the aid of the equation

$$\frac{p_2}{p_1} - 1 = \frac{\rho_1 V_{n1}^2}{p_1}\left(1 - \frac{\rho_1}{\rho_2}\right) = \gamma_1 M_{n1}^2\left(1 - \frac{\rho_1}{\rho_2}\right), \tag{4.52}$$

which is obtained as a result of the combination of the momentum and mass flow equations. Eliminating the density ratio from Eq. (4.49) and (4.52), we can find the expression for pressure as a function of the parameter Ω and the normal Mach number $M_{n1} = M_1 \sin \theta_s$. Equation (4.49) can then be used to calculate the density behind the shock wave. Next, using the equation of state, the temperature ratio can be calculated from Eq. (4.23). The variability of the specific heat has an effect on the change in stagnation pressure compared with the case of constant specific heat. The equations presented above allow us to obtain the following relation for the stagnation pressure ratio:

$$\frac{p_0}{p_0'} = \frac{p_1}{p_2}\left(\frac{p_2}{p_1}\,\frac{\Omega + p_2/p_1}{1 + \Omega p_2/p_1}\right)^{\beta\gamma_1/(\gamma_1-1)}\left(\frac{T_0}{T_1}\right)^{\gamma_1(\theta_{e1}-\beta)/(\gamma_1-1)}, \tag{4.53}$$

where the coefficient θ_{e1} is found from Eq. (3.67) for the temperature range $T_0 - T_1$, and the coefficient

$$\beta = \frac{\gamma_1 - 1}{\gamma_2 - 1}\frac{\gamma_2}{\gamma_1}\theta_{e2}, \tag{4.54}$$

where θ_{e2} is determined from the same Eq. (3.67) but for the temperature range $T_0 - T_2$.

The expressions for the coefficients θ_{e1}, θ_{e2}, and β can be simplified if the flow behind a normal shock is considered, because the stagnation temperature differs very little from its value directly behind the shock wave. For this reason the respective specific heats and the adiabatic exponents will be nearly equal. It is possible to calculate that the ratio of specific heats, in the shock layer between the stagnation point and the shock wave, will be approximately constant and equal to γ_2 behind the shock. Then

$$\theta_{e1} = \theta_2 = \frac{\gamma_m}{\gamma_1}\frac{\gamma_1 - 1}{\gamma_m - 1},$$

$$\theta_{e2} = \frac{(c_p)_2}{(c_p)_1} = \frac{\gamma_2}{\gamma_1}\frac{\gamma_1 - 1}{\gamma_2 - 1}, \tag{4.55}$$

$$\beta = \left(\frac{\gamma_1 - 1}{\gamma_2 - 1}\frac{\gamma_2}{\gamma_1}\right)^2.$$

It follows from Eq. (4.53) that the stagnation pressure ahead of the shock wave will be larger than that behind it, i.e., $p_0 > p_0'$. The ratio p_0/p_0' differs, although not significantly, from the value obtained for constant specific heats. The stagnation temperatures are identical ahead of and behind the shock wave, in agreement with the energy equation, i.e., $T_0 = T_0'$. The absolute stagnation temperature can be found from Eq. (3.69).

The calculations for an oblique shock wave are related to the determination of the slope of the streamline behind it. The equation for this is

$$\tan(\theta_s - \delta_s) = \tan\theta_s \frac{\Omega + p_2/p_1}{1 + \Omega p_2/p_1}. \tag{4.56}$$

Computations can be made to determine the values γ_2, θ_2, θ_{e2}, Ω, and β from the relations above and the known parameters of the gas up to the shock wave, in particular, from the values M_1 and T_1. Since these parameters can be determined only if the temperature T_2 behind the shock wave is known, the solution as a whole is accomplished by means of successive approximations. Initially, the temperature T_2 is determined in a first approximation, assuming that the specific heats do not vary. From this temperature γ_2 is found, and then $(c_p)_2$ and $(c_p)_{e2}$ are computed from Eq. (3.63) and (3.66), respectively, for the temperature range $T_2 - T_1$; the coefficients θ_2 and θ_{e2} are found from Eqs. (3.64) and (3.67). Knowing the values γ_2, θ_2, θ_{e2}, it is possible to find the parameters Ω and β and to determine the temperature in the second approximation. After this the values of Ω, β, and the other coefficients are recalculated, and the remaining parameters behind the shock wave are computed.

The results of computations of the quantities γ_2, θ_2, Ω, β, and the parameter $\mu = (\gamma_1 - 1)/(\gamma_2 - 1)$ as a function of M_{n1} are presented in Fig. 39. It can be seen that the larger the Mach number M_{n1}, the

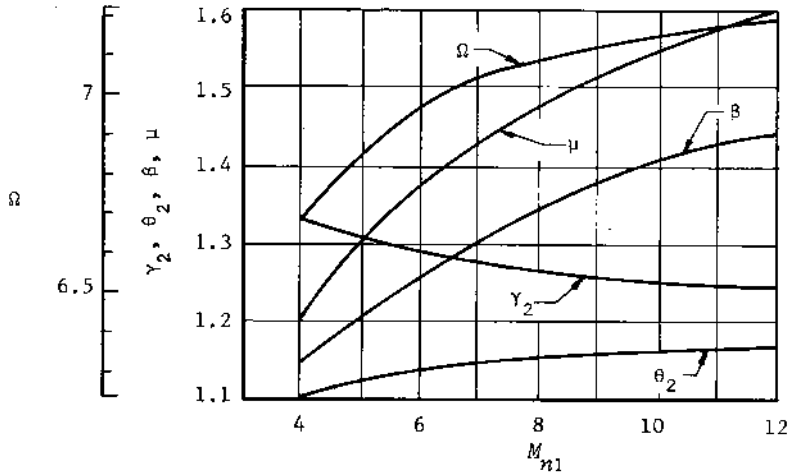

Fig. 39--Shock-wave parameters including the effect of variable specific heats

more the coefficients θ_2, μ, and β differ from unity, the more the values of γ_2 and Ω differ from the respective values 1.4 and 6 for unheated air, and thus the more significant is the influence of the variable specific heat on the gas parameters behind the shock wave. It should be kept in mind that the curves presented in Fig. 39 were calculated for a free-stream temperature of $T_1 = 288°K$. These curves must be recalculated for other temperatures. This results from the fact that the parameters behind the shock wave depend not only on the Mach number M_1, as in the case of constant specific heats, but also on temperature.

THE INFLUENCE OF DISSOCIATION AND IONIZATION ON THE GAS PARAMETERS BEHIND A SHOCK WAVE

The equation system (4.2) through (4.10) must be used in any shock-wave theory that includes the effects of dissociation and ionization. In solving the system, we shall assume that the gas undergoes no physical-chemical changes ahead of the shock wave. The various thermodynamic characteristics of dissociated and ionized gas behind the shock are considered to be known functions of pressure and temperature.

Solution of the Thermodynamic Functions of Air at Very High Temperatures

The solution of the shock-wave problem in a dissociated and ionized gas is accomplished by means of successive approximations. The initial conditions are represented by the air parameters at a given altitude H (pressure p_1, temperature T_1, density ρ_1, etc.) and by the magnitude of the normal velocity component V_{n1}. In this way a portion of an oblique shock is evaluated as though it were a normal shock.

In the first approximation we will choose $\Delta\bar{V}_n = 1$, which corresponds to assuming complete deceleration of the flow behind the shock wave ($V_{n2} = 0$). The pressure p_2 can then be found from Eq. (4.12) and the enthalpy i_2 from Eq. (4.14), the latter obviously being equal to the stagnation enthalpy i_0'. Then, the temperature T_2 can be determined from the i-S diagram in Fig. 15, and the average molecular weight $(\mu_{avg})_2$ from Fig. 17. Instead of the diagrams and graphs, the corresponding tables of the thermodynamic functions of air can be used, which will increase the accuracy of the calculations.

From the values, p_2, T_2, $(\mu_{avg})_2$, and the equation of state, the density ρ_2 can be determined and the value $\Delta\bar{V}_n$ can be refined by means of Eq. (4.11). Using the new value of $\Delta\bar{V}_n$ in the second approximation, we can recalculate the pressure and enthalpy from Eqs. (4.12) and (4.14) and determine improved values of temperature and average molecular weight from the tables or graphs. Finally, a second approximation to the density ρ_2 can be obtained from the equation of state. The successive approximations are concluded on achieving a given accuracy.

As an example, let us examine the parameters behind a shock wave with a velocity V_{n1} = 8.1 km/sec, somewhat exceeding orbital velocity, and with a pressure $p_{\infty H}$ = 0.01 kgf/cm^2, which corresponds to flight conditions at an altitude of approximately 31 km.

Since the calculation is conducted for the purpose of illustration, we shall use the graphs of the thermodynamic functions. The results of the calculation according to the method discussed are presented in Table 4 and show that there is only a small difference between the first and second approximations, the density ratio differing by approximately 2 percent. Consequently, for practical purposes, the calculation can be concluded with the second approximation. It should be noted, however, that for lesser flight velocities the quantity $\Delta\bar{V}_n$ differs more significantly from unity than in the example, and a greater number of approximations will be required.

As was shown in § 2 of this chapter, when dissociation and ionization are present the gas parameters behind a shock wave depend not only on temperature, as was the case for variable specific heats, but also depend on pressure. This dependence is represented graphically in Figs. 40 through 42.

Calculations of the temperature and density ratios were carried out for average values of temperature T_1 = 220°K and 350°K, which are equal to the probable minimum and maximum temperatures expected in the upper atmosphere based on yearly averages.

It is evident from Fig. 40 that dissociation and ionization cause a decrease in the equilibrium temperature compared with the case of constant specific heats (γ = 1.4) due to the absorption of energy in dissociation and ionization. This is particularly noticeable for the smaller ambient pressures.

Table 4

EXAMPLE CALCULATION OF FLOW PROPERTIES BEHIND A SHOCK WAVE AND AT A STAGNATION POINT

Initial Conditions

1	2	3	4	5	6	7
V_{n1} m/sec	H km	p_1 kgf/cm^2	$(\mu_{avg})_1$	T_1 °K	a_1 m/sec	M_{n1}
Chosen		Appendix A	Chosen	Appendix A		$\frac{(1)}{(6)}$
8100	31	0.01	29	236	310	26.1

First Approximation

8	9	10	11	12	13	14	15	16	17
$\frac{\Delta V_{n1}}{V_{n1}}$	i_2 m^2/sec^2	i_2 kcal/kgf	p_2 kgf/cm^2	T_2 °K	$(\mu_{avg})_2$	$\frac{p_2}{p_1}$	$\frac{T_2}{T_1}$	$\frac{(\mu_{avg})_2}{(\mu_{avg})_1}$	$\frac{\rho_2}{\rho_1}$
Assumed	$\frac{V_{n1}^2}{2}$	$\frac{(9)}{9.81 \cdot 427}$	$p_1(1+\gamma_1 M_{n1}^2)$	Fig. 15	Fig. 17	$\frac{(11)}{(3)}$	$\frac{(12)}{(5)}$	$\frac{(13)}{(4)}$	$\frac{(14)(16)}{(15)}$
1	$3.27 \cdot 10^7$	7820	9.53	8500	16.4	953	36	0.566	15

Second Approximation

18	19	20	21	22	23	24	25	26	27	28
$\frac{\Delta V_{n1}}{V_{n1}}$	p_2	i_2	T_2	$(\mu_{avg})_2$	$\frac{p_2}{p_1}$	$\frac{T_2}{T_1}$	$\frac{(\mu_{avg})_2}{(\mu_{avg})_1}$	$\frac{\rho_2}{\rho_1}$	a_2	S_2 kcal/kgf deg
Eq. (4.11)	Eq. (4.12)	Eq. (4.14)	Fig. 15	Fig. 17	$\frac{(19)}{(3)}$	$\frac{(22)}{(5)}$	$\frac{(22)}{(4)}$	$\frac{(19)(25)}{(23)}$	Fig. 18	Fig. 15
0.933	8.90	7670	8400	17	890	35.5	0.586	14.7	2200	3.37

Parameters at Stagnation Point

29	30	31	32	33	34	35	36	37	38
V_1	i_0'	$S_2 - S_0'$	p_0'	T_0'	$(\mu_{avg}')_0$	$\frac{P_0'}{p_1}$	$\frac{T_0'}{T_1}$	$\frac{(\mu_{avg}')_0}{(\mu_{avg})_1}$	$\frac{\rho_0'}{\rho_1}$
(1)	(10)	(28)	Fig. 15	Fig. 15	Fig. 17	$\frac{(32)}{(3)}$	$\frac{(33)}{(5)}$	$\frac{(34)}{(4)}$	$\frac{(35)(37)}{(38)}$
8100	7820	3.37	10	8520	17	1000	36.1	0.586	16.2

NOTE: The italic numbers in parentheses indicate the column of the specified value.

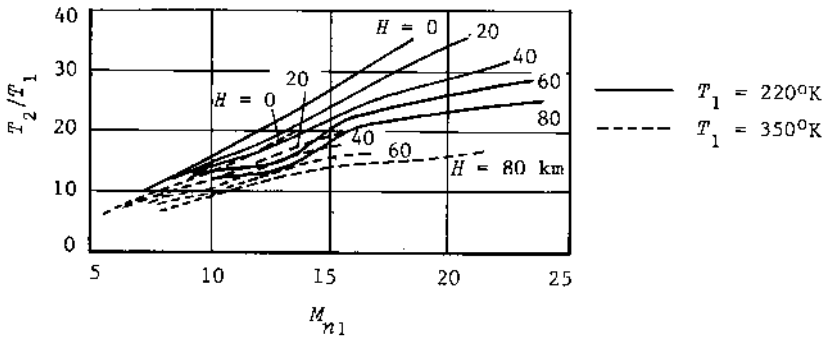

Fig. 40--Temperature ratio across a shock wave including the effects of dissociation and ionization

The density (Fig. 41), on the other hand, increases with increasing temperature and decreasing pressure, and the density ratio ρ_2/ρ_1 can far exceed the limiting value $\rho_2/\rho_1 = 6$ corresponding to $\gamma = 1.4 = \text{const}$. The pressure depends on the physical-chemical changes of air to a significantly lesser degree than do the other parameters. As is evident from Fig. 42, the pressure ratio p_2/p_1 is essentially a function of the

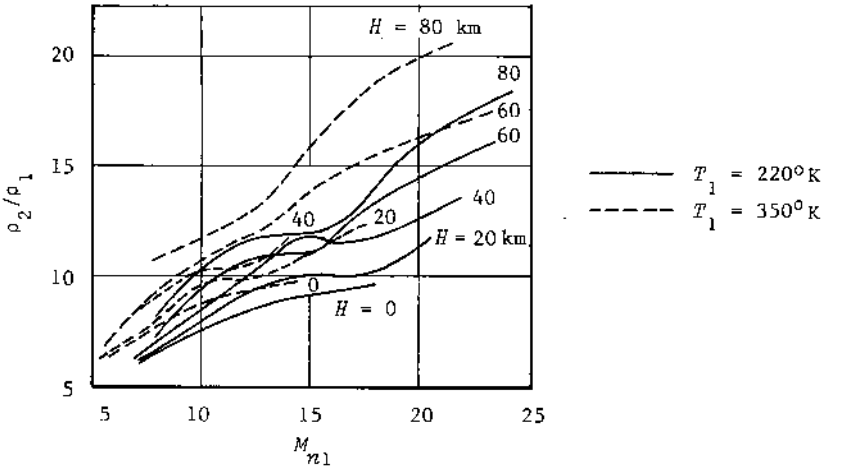

Fig. 41--Density ratio across a shock wave including the effects of dissociation and ionization

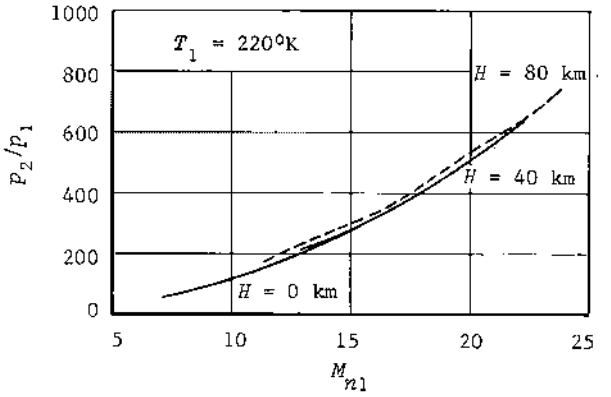

Fig. 42--Pressure ratio across a shock wave including the effects of dissociation and ionization

Mach number M_{n1} alone. The maximum value of the ratio cannot exceed the value given by $p_2/p_1 = 1 + \gamma_1 M_{n1}^2$, which is a function only of free-stream conditions and does not depend on the structure and physical-chemical properties of air behind the shock wave.

The method of calculation under consideration can apply equally to oblique and normal shock waves. This method is simplified when applied to a normal shock, since it is known beforehand that $\theta_s = \pi/2$ and $\delta_s = 0$. Therefore, the velocity V_1 is equal to V_{n1} and the Mach number $M_1 = M_{n1}$. Formally, one can eliminate the subscript n from the ratios presented above to apply the method to the normal shock wave. Some of the results calculated for a normal shock are presented in Table 4.

The calculations of gas parameters behind an oblique shock wave must be supplemented by the computation of the angle δ_s (or θ_s) and also of the Mach number M_1 (or the velocity V_1). For this purpose the following relations can be used:

$$\Delta\bar{V}_n = 1 - \frac{\tan(\theta_s - \delta_s)}{\tan\theta_s}, \qquad (4.57)$$

$$M_1 = \frac{M_{n1}}{\sin\theta_s}, \qquad V_1 = \frac{V_{n1}}{\sin\theta_s}.$$

From the first equation, either θ_s or δ_s can be determined as a function of $\Delta\bar{V}_n$ provided that the other angle is given. The velocity V_1 and Mach number M_1 are calculated from the other two equations. As an illustration, results of calculations of the parameters behind the shock are shown for V_{n1} = 8.1 km/sec (M_{n1} = 26.1) in Table 4. These results are given for a single value $\Delta\bar{V}_n$ = 0.933. Let us assume that they pertain to a shock wave with slope of, say, θ_s = 45°. Then, from the first equation of (4.57) we find the value δ_s = 41°10′ and the other two relations give V_1 = 11.45 km/sec and M_1 = 36.9.

For convenience in calculating, δ_s can be computed as a function of θ_s and $\Delta\bar{V}_n$ and tabulated or plotted. Then, for a given value of $\Delta\bar{V}_n$, corresponding to previously calculated values of the ratios p_2/p_1, ρ_2/ρ_1, etc., it is easy to obtain either angle for a specified value of the other.

One such result is illustrated in Fig. 43, which presents the

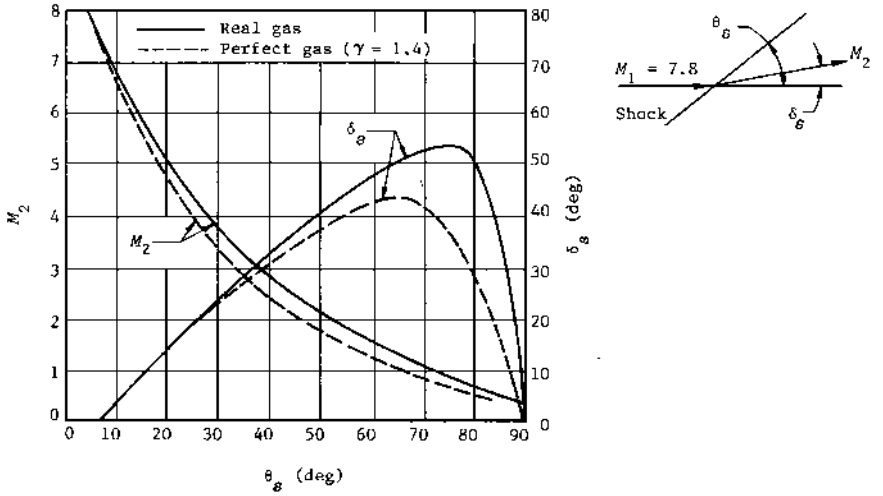

Fig. 43--Mach number and flow deflection behind an oblique shock wave for a real and a perfect gas

relation between δ_s and θ_s for $M_\infty = 7.8$, $T_\infty = 450°K$, and $p_\infty = 1.45 \cdot 10^{-3}$ kgf/cm^2. For $\theta_s > 30°$ the flow deflection angle for $\gamma = 1.4$ is less than for a real gas; for the real gas the maximum deflection angle is 54.5°, while for constant specific heats it is only 43.5°. Thus, the shock detaches later for a heated gas than for a cold gas.

It can be seen from Fig. 43 that the Mach number behind an oblique shock is less for constant specific heats ($\gamma = 1.4$) than in a real gas. However, the opposite is observed in the case of a normal shock, where the calculation that makes use of the properties of a real gas results in a decrease in the Mach number from 0.39 (for constant specific heats) to 0.30.

The calculated data for temperature, pressure, and density ratios behind an oblique shock wave, for the free-stream air parameters given above, are presented in Figs. 44 and 45. It is evident that a given shock angle results in a much higher density in a real gas than in a perfect gas.

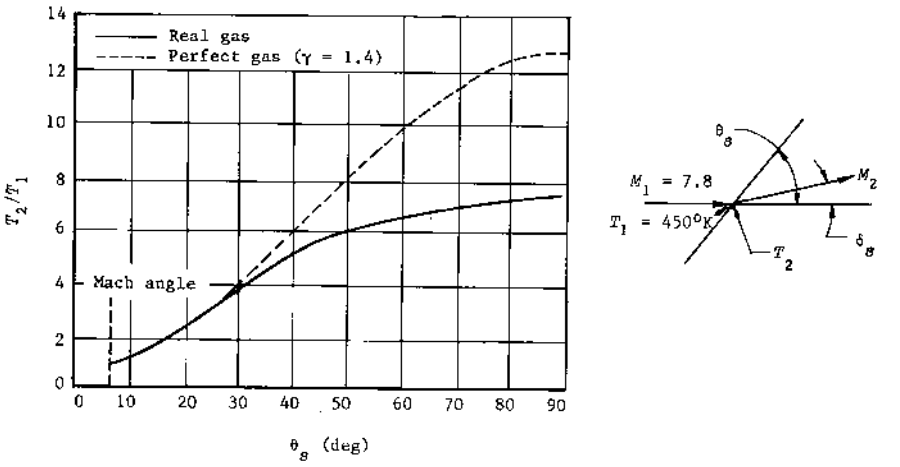

Fig. 44--Temperature ratio across an oblique shock wave for a real and a perfect gas

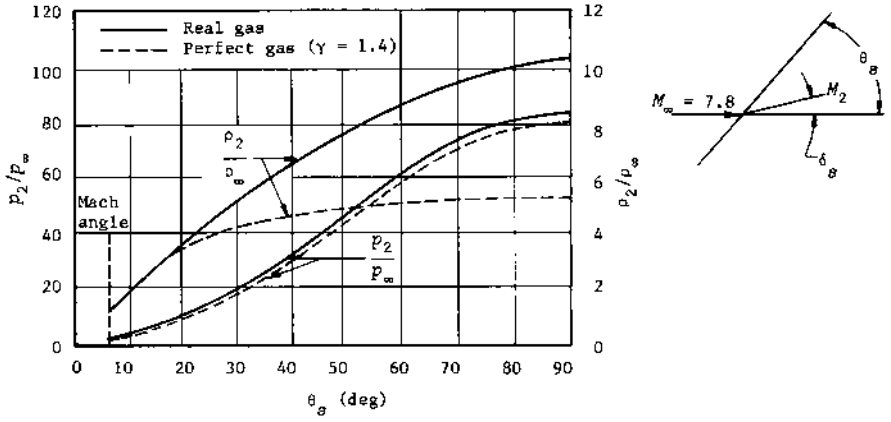

Fig. 45--Pressure and density ratios across an oblique shock wave for a real and a perfect gas

Calculation of Parameters at the Stagnation Point

An important practical application of normal shock-wave theory is for the calculation of parameters at the stagnation point of a blunt nose. The entropy S_2 can be determined from the values of i_2 and p_2 obtained from an i-S diagram (e.g., Fig. 15) or from a table of thermodynamic functions of air (including the effects of dissociation and ionization). Considering the zero streamline and assuming that the flow along it is isentropic, the entropy S_0' at the stagnation point is equal to the value S_2 behind the shock wave. Moreover, the enthalpy at the stagnation point is given by $i_0' = i_1 + 0.5V_1^2$. Knowing S_0' and i_0', the remaining parameters, i.e., p_0', T_0', ρ_0', etc., can be determined from the i-S diagram or thermodynamic tables.

The results of the calculation of gas parameters at the stagnation point by this method are presented in Table 4. These results correspond to flight conditions at an altitude of 31 km; the flow conditions change with altitude, and, thus, the stagnation parameters also change (see Fig. 46). These curves allow the determination of the temperature T_0' and the pressure p_0' as functions of the velocity V_1 and the flight altitude H.

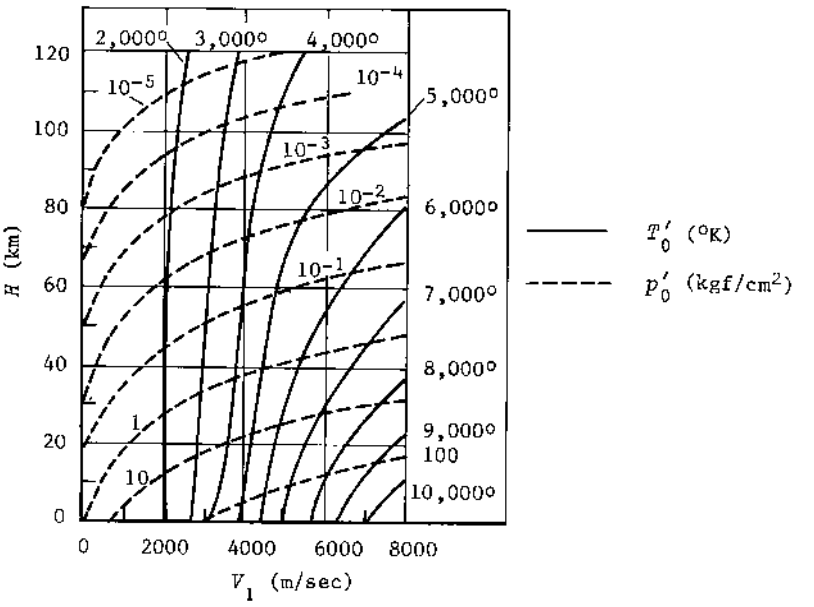

Fig. 46--Pressure and temperature at the stagnation point of a blunt nose

Because of the very high pressure at the stagnation point, which causes a lesser degree of dissociation, the temperature at this point will be the highest in comparison with other parts of the surface. This condition is explained by the fact that, in spite of the total stagnation of the flow at the wall by the boundary layer, the decreased pressure causes an increased degree of dissociation and as a result, less heating.

The Shock Wave in a Pure Dissociable Diatomic Gas

It is comparatively simple to investigate the parameters behind the shock wave using Eqs. (4.2) through (4.10) and the relations for determining the thermodynamic functions and the degree of dissociation of a pure dissociable diatomic gas. When we combine the energy equation, Eq. (4.5), and the equation for the enthalpy of a dissociating gas, Eq. (2.17a), we obtain

$$\alpha_1 + \frac{4 + \alpha_1}{1 + \alpha_1}\frac{\bar{p}_1}{\bar{\rho}_1} + \frac{\bar{V}_{n1}^2}{2} = \alpha_2 + \frac{4 + \alpha_2}{1 + \alpha_2}\frac{\bar{p}_2}{\bar{\rho}_2} + \frac{\bar{V}_{n2}^2}{2}, \tag{4.58}$$

in which the pressure and density are made dimensionless with respect to the characteristic parameters p_d and ρ_d, respectively, and the velocity with respect to the characteristic quantity V_d. Then the velocity ratio $\Delta\bar{V}_n = (V_{n1} - V_{n2})/V_{n1}$ can be calculated:

$$\Delta\bar{V}_n = \frac{3}{7 + \alpha_2}\left(1 + \sqrt{1 + \widetilde{D}/\bar{V}_{n1}^2}\right), \tag{4.59}$$

where

$$\widetilde{D} = \frac{2}{9}(7 + \alpha_2)(1 + \alpha_2)\alpha_2. \tag{4.60}$$

Equation (4.59) is obtained with the assumptions that the gas is undissociated ahead of the shock wave ($\alpha_1 = 0$), that the velocity V_{n1} is very large, that the static enthalpy i_1 of the free-stream flow can be neglected, and also that certain higher order terms are small enough to be neglected. For an undissociated gas ($\alpha_2 = 0$), Eq. (4.59) indicates that $\Delta\bar{V}_n = 6/7$. It is interesting that in ordinary shock theory this parameter approaches the value $\Delta\bar{V}_n = 2/(\gamma + 1)$ as $V_{n1} \to \infty$. For $\gamma = 1.33$ the quantity $\Delta\bar{V}_n = 6/7$ and for $\gamma = 1.4$, $\Delta\bar{V}_n = 5/6$; the difference between these results is approximately 3 percent.

From Eq. (4.59) it follows that it is necessary to know the degree of dissociation α_2 to determine the relative velocity change. Therefore, Eq. (4.59) must be solved together with Eq. (2.9), as well as the enthalpy relation

$$\bar{i}_2 = \frac{\bar{V}_{n1}^2}{2}\Delta\bar{V}_n(2 - \Delta\bar{V}_n), \tag{4.61}$$

where the enthalpy i_2 is divided by the specific energy u_d; $\bar{i}_2$ is related to the temperature ratio by

$$\bar{i}_2 = \bar{T}_2(4 + \alpha_2) + \alpha_2. \tag{4.62}$$

Calculations using these equations must be made by means of successive approximations. Assuming the velocity V_{n1} is known, we can choose a density ratio ρ_2/ρ_1 (or $\Delta\bar{V}_n$) for the first approximation. From the quantity $\Delta\bar{V}_n$, which we find from Eq. (4.11) if ρ_2/ρ_1 is chosen, the enthalpy $\bar{i}_2$ is calculated from Eq. (4.61). Then from this value and the density ratio ρ_2/ρ_d the degree of dissociation is determined as a first approximation from Fig. 22. Equation (4.59) can be used to calculate a new value of $\Delta\bar{V}_n$, after which the routine is repeated.

To illustrate, let us determine the diatomic gas parameters behind a shock wave on the condition that $V_{n1} = 1.5V_d$ (for nitrogen, $V_{n1} = 1.5 \cdot 5.8 = 8.7$ km/sec; for oxygen, $V_{n1} = 1.5 \cdot 3.9 = 5.85$ km/sec). First, we assign an expected value of $\rho_2/\rho_1 = 14$ and we find $\Delta\bar{V}_n = 1 - 1/14 = 0.929$. Then we calculate the value $\bar{i}_2 = 1.12$ from Eq. (4.61). Now, assuming that flight occurs at some altitude where the density $\rho_1 = 1.5 \cdot 10^{-7}\rho_d$, we find $\log_{10}(\rho_d/\rho_2) = 5.68$. From this value and from the value $\bar{i}_2 = 1.12$, using the graph in Fig. 22, we determine $\alpha_2 = 0.735$. The repeated calculation gives the same value for the degree of dissociation to the second decimal point.

The method discussed can be used for approximate estimates of the quantity α_2 and other air parameters behind the shock wave, although it relates only to pure dissociable diatomic gases. For calculations the characteristic dissociation parameters should be found for air as for a model gas consisting of a mixture of nitrogen and oxygen according to its components by mass. The process of the approximate estimation of parameters behind the shock wave is the same as for a diatomic gas.

Calculations for real air show that the actual parameters differ from those obtained by the method discussed above for a diatomic model of air. Thus, for the velocity $V_{n1} = 1.5V_d = 8.1$ km/sec, the density of real air behind the shock wave is $\rho_2 = 14.7\rho_1$, which is about 5 percent larger than the example investigated with a diatomic model of air.

RELAXATION EFFECTS IN SHOCK WAVES

The Physical Picture of the Nonequilibrium Process

When a gas passes through a shock wave, a part of the kinetic energy is transformed into the energy of active and passive degrees of

freedom. Equilibrium is established for the active degrees, translational and rotational, during a time commensurate with the transition time of the gas through the shock thickness. Since this time is very short, it can be assumed in practice that the establishment of the active degrees occurs instantaneously. Thus, the temperature behind the shock wave will be like that in a gas with constant specific heats.

The passive degrees of freedom are not excited directly behind the shock wave, because they have a finite relaxation time that is greater than the transition time through the thickness of a real shock wave. The temperature attained initially will decrease until the passive degrees (first vibration, then dissociation, excitation of the electronic levels, and finally ionization) achieve equilibrium. This process is accompanied by an increase in density and by some increase in pressure compared to an ideal gas. The degree of dissociation (and, at very high temperatures, the degree of ionization) also increases from zero just behind the shock to equilibrium values.

The Calculation of Nonequilibrium Flow behind a Normal Shock Wave

The problem involves the estimation of the extent of the nonequilibrium zone or, as it is called, the relaxation length, and also the determination of the nonequilibrium parameters behind the shock wave. For this purpose it is necessary to solve a system of equations for one-dimensional steady motion:

$$V \frac{dV}{dx} = -\frac{1}{\rho} \frac{dp}{dx}, \tag{4.63}$$

and also the equations of energy, Eq. (4.58), state, Eq. (2.18), and chemical reaction rate, Eq. (2.28).

This system of equations (using the notation introduced in § 2 of this chapter) has the form

$$\frac{1}{2} \frac{d\bar{V}^2}{d\bar{x}} + \frac{1}{\bar{\rho}} \frac{d\bar{p}}{d\bar{x}} = 0, \tag{4.64}$$

$$\alpha + \frac{4 + \alpha}{1 + \alpha} \frac{\bar{p}}{\bar{\rho}} + \frac{\bar{V}^2}{2} = \bar{i}_0, \tag{4.65}$$

$$\bar{p} = \bar{\rho}\bar{T}(1 + \alpha), \tag{4.66}$$

$$\bar{V}\frac{d\alpha}{d\bar{x}} = \bar{\varphi}\frac{\bar{V}_1\bar{c}^2}{\bar{\rho}_1^2}\left[(1 - \alpha)\frac{e^{-1/\bar{T}}}{\bar{\rho}} - \alpha^2\right], \tag{4.67}$$

where $\bar{x} = x/L$ (L is a characteristic linear dimension) and the parameter $\bar{\varphi}$ is defined as

$$\bar{\varphi} = \frac{C\rho_1^2 L}{\rho_d V_1}. \tag{4.68}$$

In place of Eq. (4.67), one of the expressions given in Eq. (2.30) can be used.

Equations (4.64) through (4.67) represent the case of nonequilibrium flow along an arbitrary streamline. If the "zero" streamline passing through a normal part of the shock wave is considered, the system is somewhat simplified. Instead of Eq. (4.64), the impulse equation for a strong shock wave can be used:

$$p + \rho V^2 = \rho_1 V_1^2. \tag{4.69}$$

Then one differential equation, either Eq. (4.67) or Eq. (2.30), remains, and the problem involves its solution together with the other equations of the system.

The initial conditions for the integration of Eq. (4.67) are determined by the parameters directly behind the shock wave, which are found from the theory of the ordinary shock-wave transition, i.e., with the assumption that dissociation is absent and consequently $\alpha = 0$ at $x = 0$. In this case the pressure along the "zero" streamline is considered constant and independent of nonequilibrium effects.

The results of a numerical integration with the additional condition of equilibrium with respect to the vibrational degrees of freedom[10] (the curve $t_v = 0$) are given in Fig. 47. Oxygen was chosen as a medium and its recombination-rate coefficient is $k_R = 8.4 \cdot 10^{14}$ cm^6/mole^2 sec according to experimental data. The curve in Fig. 47 allows us to estimate the nonequilibrium degree of dissociation in the relaxation zone

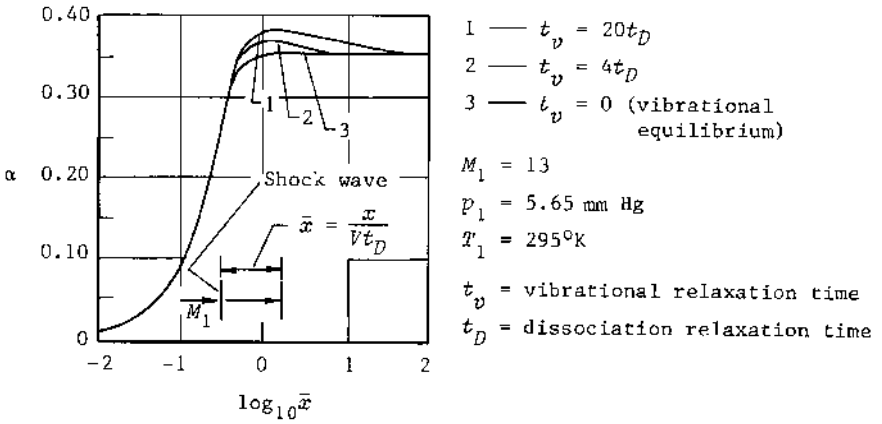

Fig. 47--Variation of the nonequilibrium degree of dissociation of oxygen behind a shock wave

as it increases from zero directly behind the shock wave up to the equilibrium value $\alpha = \alpha_e$ at the end of the relaxation length.

The graph in Fig. 48 illustrates the density change in the nonequilibrium region. In agreement with the character of the change in the degree of dissociation, the density increases from its value for a nondissociated gas to the value for equilibrium dissociation.

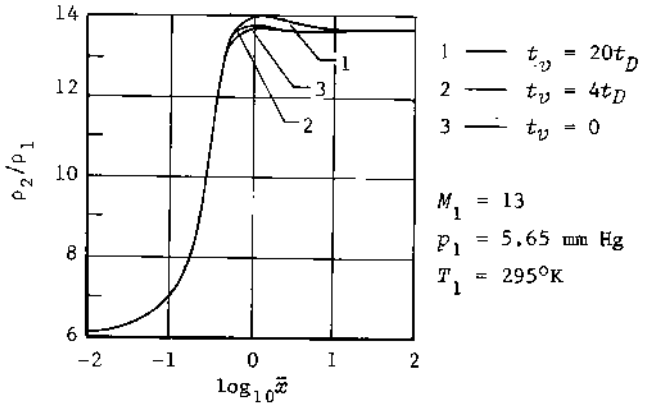

Fig. 48--Variation of the density ratio across a shock for nonequilibrium flow of oxygen

Figures 47 and 48 also show the curves ($t_v \neq 0$) taking into account the relaxation time t_v for the vibrational degrees of freedom. It should be noted that the vibrations of the atoms result in an increase in the degree of dissociation and in the density ratio compared with their equilibrium values (for $t_v = 0$). This is explained by the fact that if the vibrations do not attain equilibrium the unabsorbed part of the energy goes toward additional dissociation. Such a phenomenon is observed in the case where the vibrational relaxation time is greater than the dissociational relaxation time. This occurs for oxygen at approximately 3800°K.

Research has shown that these conditions are generally characteristic of very strong shock waves, behind which the process of vibrational excitation occurs more slowly than the chemical reactions. Moreover, the anomalous increase in the degree of dissociation and in the density in the relaxation zone occurs not only in a diatomic gas but also in air. When a temperature of the order of 4000°K is attained in nitrogen behind a shock wave, almost no vibrational excitation occurs and a corresponding part of the vibrational energy is absorbed by the oxygen, the result being an increase in the degree of dissociation and also in density.

Data concerning the degree of dissociation enable us to estimate the temperature, for example, from an approximate formula:

$$\bar{T} = \frac{\bar{i} - \alpha}{4 + \alpha}. \tag{4.70}$$

Assuming that $\bar{i} = 0.5\bar{V}_1^2$ for very high velocities, and using the data in Figs. 47 and 48, the temperature changes from 9700°K directly behind the shock wave ($\bar{x} = 0$) to the equilibrium value 3700°K. As has been mentioned, the results presented pertain to oxygen, inasmuch as the recombination rate k_R is known more reliably for this gas. However, for an approximate estimation of the influence of nonequilibrium effects on air flow, it is possible to use the same system of equations based on a diatomic model of air consisting of an additive mixture of oxygen and nitrogen. In this case, the coefficient C in Eq. (4.68) is determined

for oxygen, and all the remaining parameters (e.g., the degree of dissociation α, the characteristic density and pressure, etc.) are found for the diatomic model of air.

The temperature and density distribution of an air mixture of oxygen and nitrogen in the relaxation zone behind a shock wave at $M_1 = 14.2$, $T_1 = 300°K$, $p_1 = 1$ mm Hg is shown in Fig. 49. The solid curve is based on the assumption of instantaneous vibrational excitation, and the dashed line on no vibrational excitation. It follows from these results that vibrations play a considerable role. Without taking them into account, the temperature behind the shock wave equals 12,000°K, while for the totally excited state the temperature is significantly lower, 9770°K.

It is also evident from Fig. 49 that the extent of the nonequilibrium zone is relatively small, approximately 8 to 10 mm, and vibrational excitation is of practically no significance at the end of this zone. Therefore, in calculations of equilibrium dissociation, the vibrational excitation rate can be assumed infinitely large, thus considering the gas to be fully excited before the beginning of dissociation.

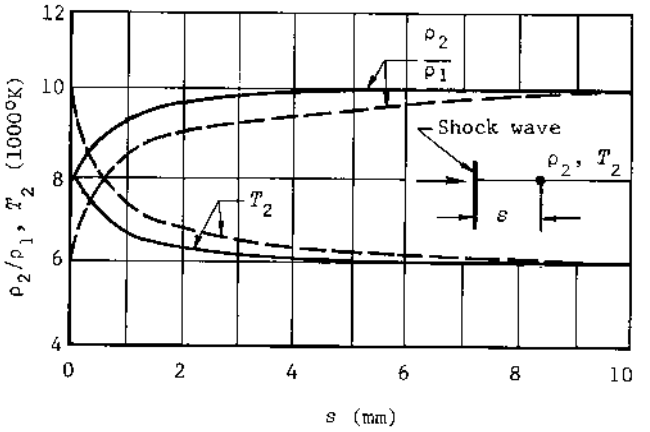

Fig. 49--Effect of nonequilibrium dissociation on density and temperature behind a shock

§ 5. *RESULTS FROM BOUNDARY LAYER AND HEAT TRANSFER THEORY*

THE BOUNDARY LAYER

The Incompressible Boundary Layer on a Flat Plate

THE MOST IMPORTANT RESULTS from boundary layer theory are methods of calculating the distribution of shear stresses on the body surface and such parameters as the boundary layer thickness, displacement thickness, and momentum loss.

In the general case when heat transfer in the boundary layer is considered, it is necessary to obtain simultaneous solutions for the viscous and heat transfer parameters, resulting in the determination of the heat flux distribution.

To simplify the study, the influence of heat transfer can be eliminated by examining the so-called insulated viscous boundary layer. Additional simplification results for the special case of an incompressible boundary layer on a thin plate. However, these simple results can be used for the approximate calculation of more complicated cases of boundary layer flow, including the effects of very high velocities, compressibility, heat transfer, and curved surfaces.

To obtain the fundamental relations for the incompressible boundary layer on a plate, the velocity profile laws for laminar and turbulent boundary layers can be used. Approximate expressions for these profiles are

$$\begin{aligned} \frac{V_x}{V_\delta} &= \frac{3}{2}\frac{y}{\delta} - \frac{1}{2}\frac{y^3}{\delta^3} + \ldots \qquad \text{(laminar)}, \\ \frac{V_x}{V_\delta} &= \left(\frac{y}{\delta}\right)^{1/7} \qquad \text{(turbulent)}, \end{aligned} \tag{5.1}$$

where V_x is the flow velocity at an arbitrary point in the layer, and V_δ is the velocity at the outer edge of the layer.

Using the integral relation given in Eq. (3.34), the following general relation is obtained for the relative thickness of the boundary layer:

$$\frac{\delta}{L} = A\bar{x}^m(\mathrm{Re})^n, \tag{5.2}$$

where L is the length of the plate, the dimensionless coordinate $\bar{x} = x/L$, and the Reynolds number is $\mathrm{Re} = V_\delta L/\nu$.

The friction stress at the wall, τ_w, is determined as a result of the substitution of Eqs. (5.1) and (5.2) in the formulas

$$\begin{aligned} \tau_w &= \mu\left(\frac{\partial V_x}{\partial y}\right)_{y=0}, \\ \tau_w &= 0.0225\rho_\delta V_\delta^2\left(\frac{\nu}{V_\delta\delta}\right)^{\frac{1}{4}}, \end{aligned} \tag{5.3}$$

the first of which pertains to the laminar, and the second to the turbulent boundary layer. As a result we obtain

$$\tau_w = B\rho_\delta V_\delta^2(\mathrm{Re}_x)^n, \tag{5.4}$$

where the local Reynolds number $\mathrm{Re}_x = V_\delta x/\nu$.

The local skin friction coefficient can be found from the shear stress at the wall by the relation

$$c_{fx}^0 = \frac{\tau_w}{q} = C(\mathrm{Re}_x)^n, \tag{5.5}$$

where $q = \rho_\delta V_\delta^2/2$.

Using Eq. (5.5), the average value of the skin friction coefficient is

$$c_f^0 = \int_0^1 c_{fx}^0\, d\bar{x} = D(\mathrm{Re})^n. \tag{5.6}$$

The values of the coefficients A, B, C, D, and the exponents m, n are presented in Table 5.

Table 5

VALUES OF THE COEFFICIENTS AND EXPONENTS IN THE EQUATIONS FOR THE BOUNDARY LAYER PARAMETERS

Boundary Layer	Coefficient					
	A	B	C	D	m	n
Laminar	4.65	0.332	0.664	1.32	1/2	-1/2
Turbulent	0.37	0.0289	0.0578	0.072	4/5	-1/5

Equation (5.6) is reliable for the turbulent skin friction coefficient c_{fT}^0 if the Reynolds number does not exceed about 10^6. Other relations give better results for larger Reynolds numbers. For example,† for Reynolds numbers in the range $10^6 < \mathrm{Re} < 10^9$

$$c_{fT}^0 = 0.427(\log_{10}\mathrm{Re} - 0.407)^{-2.46}. \tag{5.7}$$

For a similar range, $5\cdot10^6 < \mathrm{Re} < 10^{10}$, the following equation can also be used:

$$c_{fT}^0 = 0.043(\mathrm{Re})^{-0.167} \tag{5.8}$$

The relation

$$c_{fT}^0 = 0.032(\mathrm{Re})^{-0.145} \tag{5.9}$$

corresponds to Reynolds numbers in the range $2\cdot10^6 < \mathrm{Re} < 10^{10}$.

The Influence of Altitude

The effect of altitude appears in the change in Reynolds number with altitude. If at sea level $\mathrm{Re}_{SL} = M_\infty a_{SL} l/\nu_{SL}$ (where a_{SL} and ν_{SL}

†Editor's note: Schlichting[11] indicates the exponent in Eq. (5.7) is -2.64. This is probably a typographical error in the Russian text.

are the velocity of sound and the kinematic viscosity coefficient at sea level) and at a given altitude the Reynolds number is $\mathrm{Re} = M_\infty a l/\nu$, the latter can be written as

$$\mathrm{Re} = \mathrm{Re}_{SL}\, f_1(H) f_2(H) f_3(H), \tag{5.10}$$

where

$$f_1(H) = \frac{\rho}{\rho_{SL}}, \qquad f_2(H) = \frac{a}{a_{SL}}, \qquad f_3(H) = \frac{\mu_{SL}}{\mu} \tag{5.11}$$

are functions that determine the change in the density, velocity of sound, and coefficient of viscosity with altitude. The values of these functions can be determined from atmosphere tables (see Appendix A).

The Effect of Compressibility

Friction drag at high velocities depends on compressibility. This relation can be accounted for approximately if a correction, which is a function of the Mach number M_∞, is introduced into the incompressible equations presented above. For example, the equation for the laminar boundary layer takes the form

$$\frac{c_{fL}}{c_{fL}^0} = (1 + 0.03M_\infty^2)^{-\frac{1}{3}}, \tag{5.12}$$

and for the turbulent boundary layer

$$\frac{c_{fT}}{c_{fT}^0} = (1 + 0.12M_\infty^2)^{-\frac{1}{2}}, \tag{5.13}$$

where c_{fL} and c_{fT} are the laminar and turbulent skin friction coefficients for compressible flow.

Calculations based on these equations, as well as the experimental studies, show that the effect of compressibility is less for laminar friction than for the turbulent case. Comparisons of theory and experiment also show that Eq. (5.12) gives values that agree better with e experimental data than does the turbulent equation. Equation (5.13)

can be refined if the numerical coefficient for M_∞^2 is considered to be a function of the Reynolds number. The coefficient 0.12 shown above corresponds approximately to the value Re = 10^6, and the coefficient increases somewhat with an increase in Reynolds number. For example, a value of 0.18 is a better approximation for Reynolds numbers of the order of 10^8.

The relation proposed by A. A. Dorodnitsyn can be used instead of Eq. (5.13):

$$c_{fT} = \frac{0.472}{1 + 0.1M_\infty^2}\left[\log_{10}\mathrm{Re}\ (1 + 0.2M_\infty^2)^{-1.76}\right]^{-2.58} \tag{5.14}$$

or Luther's equation[12]

$$c_{fT} = \frac{0.0631\ \exp\ (-0.172M_\infty)}{(\mathrm{Re})^{0.182}}, \tag{5.15}$$

which gives more satisfactory results for Reynolds numbers that are in the range $10^6 < \mathrm{Re} < 10^{10}$.

All these equations are approximate and are derived on the basis of experimental studies of friction on plates. Therefore, it is natural that errors result when they are applied to bodies of revolution, the magnitude of the error depending on the shape of the body. For example, the error is small for a body with a curved profile, but increases in the case of a conical surface. Moreover, the errors depend on whether the boundary layer is laminar or turbulent; in the laminar case the error is large; in the turbulent, it is less. Therefore, it follows that the determination of the character of the flow in the boundary layer is an essential ingredient in the calculation of friction drag; we shall discuss this later.

THE INFLUENCE OF HIGH TEMPERATURES ON BOUNDARY LAYER FLOW

The presence of the Mach number in the equations presented above results from the fact that viscous drag in the boundary layer, coupled with increases in temperature, cause changes in the density of the gas, because the gas is basically a compressible medium. The temperature in

the layer increases with increased velocity, causing not only density variations but also significant changes in the thermodynamic properties and the kinetic coefficients of the gas in the boundary layer, as well as chemical reactions. These phenomena are decisively important in influencing the frictional and heat transfer processes in the boundary layer, but their computation is usually quite difficult. Therefore, trial attempts were made to discover comparatively simple approximate methods of calculating boundary layer parameters for very high flow velocities. One of these methods, examined below, is based on the use of relations that are externally similar to the incompressible relations.

There is always a region near the surface where the flow velocity is very small and, therefore, the gas is similar in character to an incompressible medium. If it is assumed that the flow in this region has a basic influence on the processes of friction and heat transfer, modified forms of the incompressible relations can be used for compressible boundary layer study. The difference involves the use of parameters in these relations that are functions of the local temperature in the boundary layer. Research has shown that satisfactory results are obtained if the calculation is carried out using the so-called effective temperature T^*. The local values of enthalpy, i^*, density, ρ^*, viscosity, μ^*, ν^*, etc. are also designated "effective" to correspond with the temperature.

Let us consider some relations for calculating the effective parameters of the boundary layer.

Laminar Boundary Layer

We will designate the parameters of an incompressible fluid by the subscripts "δ" and "inc" where they are connected with the relations presented above for the incompressible boundary layer. Introducing the effective parameters into these equations, we obtain relations that take into account the high temperatures. For example, the high-temperature boundary layer thickness is obtained from Eq. (5.2):

$$\delta = \delta_{inc}\left(\frac{\mu^*}{\mu_\delta}\frac{\rho_\delta}{\rho^*}\right)^{\frac{1}{2}}. \tag{5.16}$$

Following Eq. (5.4), the relation for the shear stress is

$$\tau_w = (\tau_w)_{inc} \frac{\delta}{\delta_{inc}} \frac{\rho^*}{\rho_\delta} = \left(\frac{\mu^* \rho^*}{\mu_\delta \rho_\delta}\right)^{\frac{1}{2}} (\tau_w)_{inc}. \tag{5.17}$$

It is evident that the ratio of the friction stresses equals the ratio of the local and of the average skin friction coefficients:

$$\frac{\tau_w}{(\tau_w)_{inc}} = \frac{c_{fx}}{(c_{fx})_{inc}} = \frac{c_f}{(c_f)_{inc}}. \tag{5.18}$$

From Eq. (5.16) it is apparent that the boundary layer thickness increases with an increase in temperature. The friction decreases despite the increase in viscosity, because the density, which decreases with the increase in temperature, has the dominating influence on friction. As a consequence, there is a decrease in the ability of the gas to resist shear.

Turbulent Boundary Layer

Introducing the effective parameters into the power law for velocity distribution (Eq. (5.1)) and Eqs. (5.2) to (5.6) for the other parameters of the incompressible boundary layer, the following equation for the turbulent boundary layer thickness results:

$$\delta = \delta_{inc} \left(\frac{\mu^*}{\mu_\delta} \frac{\rho_\delta}{\rho^*}\right)^{1/5}. \tag{5.19}$$

The external form of the equations for stress and for the friction coefficients is the same as that of Eqs. (5.17) and (5.18), but the thickness of the layer is now given by Eq. (5.19). Comparison shows that the increase in thickness is not as large in the turbulent boundary layer as in the laminar, so that the shear stress and the friction coefficients decrease more significantly.

It is known from incompressible boundary layer theory that the use of the 1/7 power law is limited to comparatively small Reynolds numbers, so its extension to the case of very high velocities requires verification and accurate definition. In this connection attempts were made to derive the necessary relations on the basis of the general equation for

the turbulent boundary layer. One result is the equation

$$c_{fx} = (c_{f_0})_x \left[2 \left(\frac{1 + \alpha_\delta}{1 + \alpha_w} \right)^{1/7} - 1 \right], \tag{5.20}$$

in which $(c_{f_0})_x$ is the local friction coefficient calculated for the local values M_δ, T_w/T_δ, and $\mathrm{Re} = V_\delta \rho_\delta \delta / \mu_\delta$, but without dissociation; α_δ and α_w are the degrees of dissociation at the outer edge of the boundary layer and at the wall. The latter quantities for air can be determined by assuming that air is a diatomic gas, with α_w based on the wall temperature.

The coefficient c_{f_0} can be calculated on the basis of the 1/7 power law for the effective temperature but without taking dissociation into account and with the assumption of constant specific heats. In all cases it is assumed that the wall temperature is given. Some data concerning the coefficient c_{f_0} are presented in Figs. 50 through 52. The friction coefficient c_f, including the effects of dissociation, can be calculated from Eq. (5.20), which is plotted in Fig. 53. From this figure it is apparent that the influence of dissociation results in an increase of 22 percent in the friction coefficient if $\alpha_\delta = 1$ and $\alpha_w = 0$, i.e., if the surface is catalytic and the atoms are fully recombined at the wall. In the other limiting case, dissociation results in a decrease of 22 percent in the friction coefficient when $\alpha_\delta = 0$ and $\alpha_w = 1$, corresponding to the case of a noncatalytic surface.

Effective Enthalpy (Temperature)

The formulas given above can be applied, in general, to any type of flow by use of the effective parameters. Because of their simplicity, they can provide at least a qualitative picture of the effects of various parameters, suitable for graphical presentation. For example, they can be applied to the flow along an adiabatic wall, i.e., a surface in thermal equilibrium with the boundary layer. If in addition the gas itself is not heat conducting, the variation in thermodynamic properties across the boundary layer will be adiabatic, and the equations will indicate the isolated effects of compressibility (i.e., Mach number) on the boundary layer parameters.

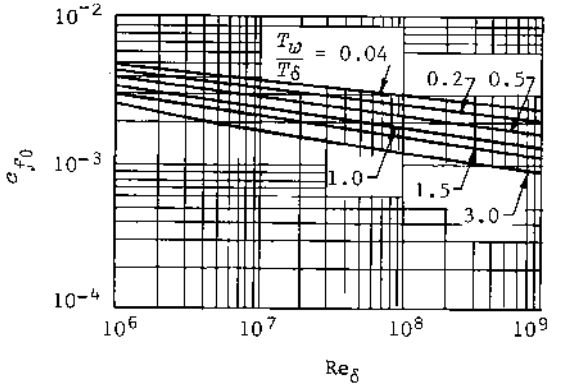

Fig. 50--Local friction coefficient on a plate in incompressible turbulent flow

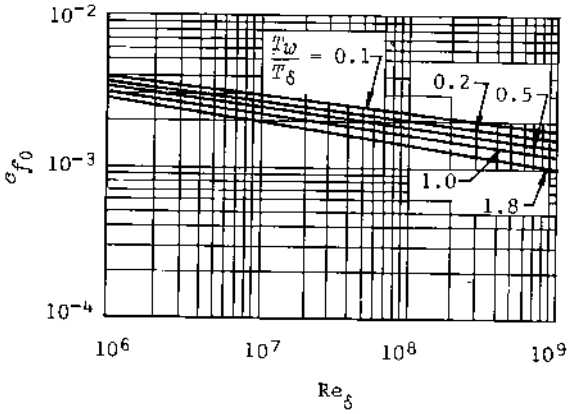

Fig. 51--Local friction coefficient on a plate without dissociation for M_δ = 2

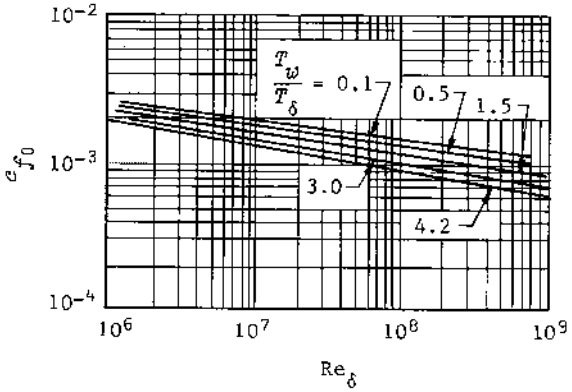

Fig. 52--Local friction coefficient on a plate without dissociation for $M_\delta = 4$

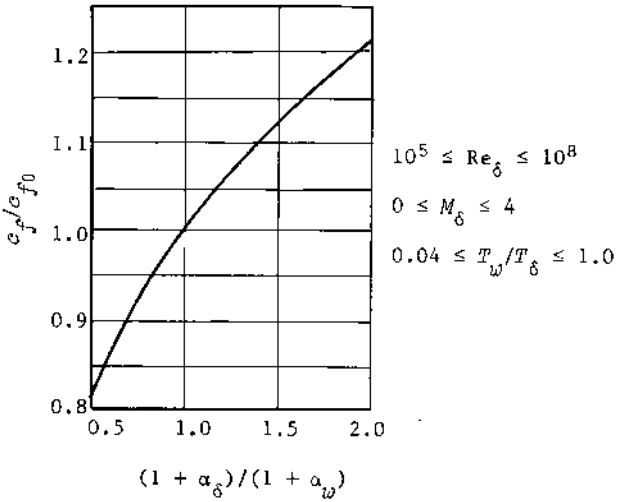

Fig. 53--Ratio of the friction coefficient on a plate with and without dissociation

Compressibility is the dominant effect at moderate flight velocities where the heating is small and density changes across the boundary layer are significant. Because of this, the assumption made previously that the gas in the boundary layer is incompressible is less valid for moderate velocities than it is for large velocities, where because of the high temperatures the gas becomes "stiffer" and acts more like an incompressible fluid. Therefore, the formulas containing the effective parameters are more valid in application to gas flow at hypersonic speeds. At these velocities it is particularly important to consider heat transfer between the wall and the boundary layer, and this should be included in the calculation of the effective parameters. A basic parameter that includes these effects is the effective enthalpy, which can be computed from Eckert's equation:

$$i^* = 0.5(i_w + i_\delta) + 0.22(i_r - i_\delta), \tag{5.21}$$

where i_w and i_δ are the gas enthalpies, respectively, at the wall and at the outer edge of the boundary layer, and i_r is the so-called recovery enthalpy.

Strictly speaking, the effective enthalpy as well as the other analogous parameters depend on the structure of the boundary layer and also on the Mach number M_∞. There are a series of relationships for calculating the quantity i^* separately for the laminar and the turbulent boundary layer and for various ranges of Mach number. Equation (5.21) has the advantage of being a universal relation, and can be used with well-known approximations for both laminar and turbulent flows over a rather wide range of free-stream Mach numbers.

The enthalpy at the wall is needed to calculate i^* from Eq. (5.21), and in most practical cases it will be known, since the surface temperature will be maintained at some specified level. If the surface temperature is changing because of heating from the boundary layer, i_w must be determined from simultaneous solutions for heat transfer between the wall and the gas.

Of the other parameters that enter into Eq. (5.21), the enthalpy, i_δ, at the outer edge of the layer is usually known from inviscid flow

solutions, and the recovery enthalpy is determined from the expression

$$i_r = i_\delta + r\frac{V_\delta^2}{2}, \tag{5.22}$$

in which r is called the recovery factor. The recovery factor is always less than unity for air, and as a result the recovery enthalpy is less than the stagnation enthalpy, i_0; this is in accord with Fourier's law, since heat flow from the wall to the outer edge of the boundary layer results in a temperature decrease. Studies show that the recovery factor can be calculated from the equation $r = \mathrm{Pr}^m$, in which $m = 1/2$ for laminar flow and $m = 1/3$ for turbulent flow. If the boundary layer calculation is carried out using the effective parameters, the expression $r^* = (\mathrm{Pr}^*)^m$ should be used, where the effective Prandtl number is $\mathrm{Pr}^* = c_p^*\mu^*/\lambda^*$.

Equation (5.21) can be used in the general case of a dissociable gas, since enthalpy instead of temperature is the basic parameter, and the enthalpy represents not only the thermal energy but also the energy expended on dissociation. If the heated gas in the boundary layer is not dissociating, it is better to substitute temperature for enthalpy, since the equations are simplified:

$$i_k - i_\delta = (c_p)_m(T_k - T_\delta), \tag{5.23}$$

where the enthalpy i_k can be the parameters i_r, i_w, or i^*, and the temperature T_k can be the quantities T_r, T_w, or T^*. The average specific heat $(c_p)_m$ is computed for the temperature range $T_k - T_\delta$. As a result of these substitutions, instead of Eq. (5.21) we obtain a similar formula for the effective temperature T^*, with the recovery temperature given by

$$T_r = T_\delta + \frac{r^*}{2}\frac{V_\delta^2}{(c_p)_m} = T_\delta\left(1 + \frac{\varkappa_\delta - 1}{2}r^*M_\delta^2\right), \tag{5.24}$$

where the average specific heat $(c_p)_m$ is determined for the temperature range $T_r - T_\delta$; $\varkappa_\delta$ is the adiabatic exponent at the outer edge of the boundary layer; M_δ is the Mach number at that edge, given by $M_\delta = V_\delta/a_\delta$

(the velocity of sound is $a_\delta = \sqrt{\gamma_\delta RT_\delta}$).† The thermodynamic functions and the kinetic coefficients are computed as functions of the effective temperature:

$$\frac{c_p^*}{c_{p_\infty}} = \left(\frac{T^*}{T_\infty}\right)^\psi, \qquad \frac{\mu^*}{\mu_\infty} = \left(\frac{T^*}{T_\infty}\right)^n, \qquad \frac{\lambda^*}{\lambda_\infty} = \left(\frac{T^*}{T_\infty}\right)^\chi. \tag{5.25}$$

HEAT TRANSFER

The Equation of Thermal Balance

This equation in the general form defines the total heat flux q_w going into heating the wall. Its value is equal to the difference between the heat flow into the surface, q_i, and the heat flow out, q_0; i.e., $q_w = q_i - q_0$. The thermal influx originates because of boundary layer heating caused by friction, solar and terrestrial radiation, heat from the equipment, etc. Since we shall henceforth examine only aerodynamic heating caused by processes that occur in the boundary layer, let us assume that the thermal influx equals the convective heat flow, which can be determined from the Newtonian equation:

$$q_i = q_c = h(T_r - T_w), \tag{5.26}$$

where h is the heat transfer coefficient, the determination of which is a problem of aerodynamic heat transfer theory. The net heat output is made up of thermal energy radiated by the heated surface, heat absorbed by the wall or by various cooling devices, etc. We shall consider here only heat removal by radiative transfer of energy and, later, by ablation from the surface. Then the emission is equal to the radiative flux, q_r, which is given by the Stefan-Boltzmann law:

†Editor's note: The second form of Eq. (5.24) is not consistent with the definition of $(c_p)_m$. Using Eqs. (3.64) and (3.65), it should be written as

$$T_r = T_\delta\left(1 + \frac{\gamma_\delta - 1}{2\theta_\delta} r^* M_\delta^2\right),$$

where $\theta_\delta = (c_p)_m / c_{p\delta}$.

$$q_0 = q_r = \varepsilon\sigma T_w^4, \tag{5.27}$$

where $\sigma = 1.37 \cdot 10^{-11}$ kcal/m^{2}sec°K^4 is the radiation coefficient of a completely black body, and ε is the emissivity of the surface.

Thus, the thermal flux to the wall is determined by the heat balance equation in the following form:

$$q_w = h(T_r - T_w) - \varepsilon\sigma T_w^4. \tag{5.28}$$

Let us assume that we are dealing with a thin skin that is instantaneously heated throughout its thickness. Then the heat absorbed by the skin is $q_w = c\gamma\delta(dT_w/dt)$, where c, γ, and δ are the specific heat, the specific weight, and the thickness of the skin material, respectively. If steady state conditions have been achieved, so that the wall temperature does not vary with time, $q_w = 0$ and Eq. (5.28) assumes the form

$$h(T_r - T_w) = \varepsilon\sigma T_w^4. \tag{5.28a}$$

The wall temperature determined by this equation is called the radiative equilibrium temperature and is designated $T_w = T_e$. This differs from the recovery temperature, which is, by definition, the surface temperature without radiation and internal cooling; therefore, the parameter T_r is sometimes called the adiabatic wall temperature. The temperature T_e represents an upper limit for the radiating surface that is reached when the radiation from the heated wall just balances the energy received from the boundary layer.

This temperature, T_e, is unrealistic for very large heat flow because it is so great that it cannot be attained without the destruction of the surface material (fusion, sublimation, combustion). However, in certain cases the radiation equilibrium temperature can occur in flight, e.g., on the surface of a glide vehicle where the kinetic energy is converted gradually to thermal energy. Under these circumstances, the intensity of the convective heat flow may be comparatively small, and all the energy absorbed can be reradiated at an equilibrium temperature that is safe for the design.

Equation (5.28a), the boundary layer relations presented earlier, together with the effective parameters form a system of equations, the solution of which enables us to find the wall temperature, the shear stress, etc.

Given the values of T_p and h/ε, it is possible to determine the radiative equilibrium temperature directly from Eq. (5.28a). The recovery temperature is assumed to be known and is given by $T_r \approx V_\infty^2/2c_p$ at sufficiently high velocities. The solution of Eq. (5.28a) is presented in Fig. 54. It can be concluded from the graph that reducing the ratio h/ε is the principal method of decreasing the radiative equilibrium temperature. This can be done first by increasing the emissivity. For this purpose, a special coating can be applied to the surface that increases ε to 0.7 or 0.8 and thereby increases the cooling by radiation. In those cases where a thin metal wall is heated to high temperatures, it is also possible to increase the emissivity to a value that is close to unity. In the second place, the heat transfer coefficient can be reduced; methods for accomplishing this reduction are discussed later.

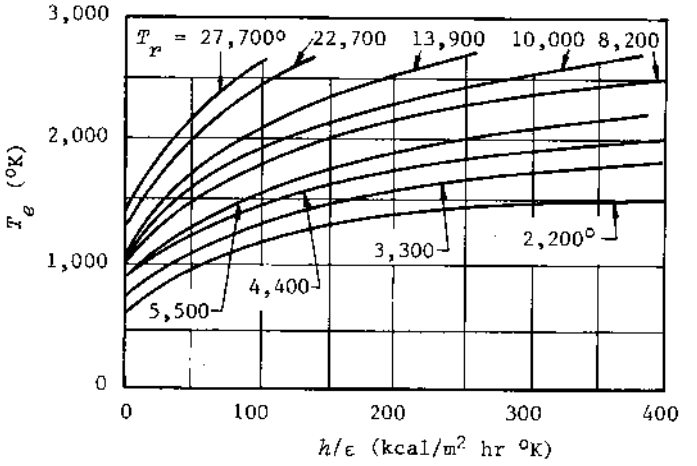

Fig. 54--Radiative equilibrium temperature as a function of the parameters h/ε and T_r

Approximate Solution for Equilibrium Temperature

The basic assumption in the method of solution lies in disregarding terms containing $T_r - T_e$ to the third and higher powers.[13] Such terms occur on the right side of Eq. (5.28a) if it is written in the form

$$\varepsilon\sigma T_e^4 = \varepsilon\sigma[T_r - (T_r - T_e)]^4,$$

and then the quantity in the square brackets is expanded in a binomial series. After simplification, the heat balance equation has the form

$$6\varepsilon\sigma T_r^2 T_e^2 + (h - 8\varepsilon\sigma T_r^3)T_e + 3\varepsilon\sigma T_r^4 - hT_r = 0.$$

Solving this equation for the temperature T_e, we find

$$T_e = \frac{8T_r^3 - \varphi + \sqrt{\varphi^2 + 8\varphi T_r^3 - 8T_r^6}}{12T_r^2}, \tag{5.29}$$

where $\varphi = h/\varepsilon\sigma$. If only the term with the difference $(T_r - T_e)$ is retained in the binomial expansion, Eq. (5.29) is simplified:

$$T_e = \frac{\varphi T_r + 3T_r^4}{4T_r^3 + \varphi}. \tag{5.29a}$$

It is possible to generalize these equations somewhat by considering the other sources of the energy supplied. For example, if the flow of solar radiation εG is taken into account by adding it into the left side of Eq. (5.28a), the quantity $24GT_r^2/\sigma$ must be added to the sum of the terms under the radical in Eq. (5.29), and the quantity G/σ must be added to the numerator in Eq. (5.29a).

The Relation between Skin Friction and Heat Transfer

Since the unknown quantity h enters into Eq. (5.29), this equation must be supplemented by a relation linking the heat transfer coefficient and the boundary layer parameters, i.e., the skin friction at the wall.

For this purpose, let us examine the equations of motion and energy, Eqs. (3.12) and (3.42). We assume that the boundary layer is laminar and is generated by supersonic flow around a conical surface. Since the static pressure is constant on a cone, then, assuming that the Prandtl and Schmidt numbers equal unity, these equations will have the form

$$\rho r V_x \frac{\partial V_x}{\partial x} + \rho r V_y \frac{\partial V_x}{\partial y} = \frac{\partial}{\partial y}\left(r\mu \frac{\partial V_x}{\partial y}\right),$$

$$\rho r V_x \frac{\partial i_0}{\partial x} + \rho r V_y \frac{\partial i_0}{\partial y} = \frac{\partial}{\partial y}\left(r\mu \frac{\partial i_0}{\partial y}\right).$$

Transforming to the variables $\bar{V}_x = V_x/V_\delta$, $\Theta = (i_0 - i_w)/(i_{0\delta} - i_w)$, it can be noted that the equations allow the solution $\bar{V}_x = \Theta$. Therefore, the boundary conditions for both parameters are identical: At the wall the values of $\bar{V}_x$ and Θ equal zero; at the edge of the boundary layer they equal unity. Consequently, the solutions of these equations must agree, i.e.,

$$\frac{i_0 - i_w}{i_{0\delta} - i_w} = \frac{V_x}{V_\delta}.$$

Considering the conditions at the wall where $(\partial i_0/\partial y)_w = (\partial i/\partial y)_w = [c_p(\partial T/\partial y)]_w$, and keeping in mind that the heat flux at the wall is given by

$$q = \left(\lambda \frac{\partial T}{\partial y}\right)_w \tag{5.30}$$

and the friction stress is $\tau_w = [\mu(\partial V_x/\partial y)]_w$, we obtain the following expression for the heat flux:

$$q = \frac{i_{0\delta} - i_w}{(c_p)_w}\left[\left(\frac{\lambda\tau}{\mu}\right)_w \frac{1}{V_\delta}\right]. \tag{5.31}$$

The quantity in the square brackets represents the local heat transfer coefficient h_x. On the other hand, it is known that the local friction

coefficient is $c_{fx} = 2\tau_w/(\rho_\delta V_\delta^2)$. Consequently, the relation between these two coefficients is

$$h_x = \frac{c_{fx}}{2} \frac{\rho_\delta V_\delta \lambda_w}{\mu_w}. \tag{5.32}$$

From this equation follow the relations for the two most important dimensionless heat transfer criteria, i.e., the local Nusselt number

$$\mathrm{Nu}_x = \frac{h_x x}{\lambda_w} = \frac{c_{fx}}{2} \mathrm{Re}_x, \tag{5.33}$$

where $\mathrm{Re}_x = \rho_\delta V_\delta x/\mu_w$, and the local Stanton number

$$\mathrm{St}_x = \frac{h_x}{\rho_\delta V_\delta c_{p\delta}} = \frac{c_{fx}}{2}. \tag{5.34}$$

It must be noted that the relation established between the friction and heat transfer parameters is approximate since in reality the Prandtl and Schmidt numbers differ from unity. The influence of these numbers can be taken into account if the expressions for the Nusselt and Stanton criteria are written in the form

$$\begin{aligned} \mathrm{Nu}_x &= \frac{1}{2} c_{fx} \mathrm{Re}_x f_1(\mathrm{Pr}, \mathrm{Sc}), \\ \mathrm{St}_x &= \frac{1}{2} c_{fx} f_2(\mathrm{Pr}, \mathrm{Sc}), \end{aligned} \tag{5.35}$$

where f_1 and f_2 are functions of the Prandtl and Schmidt numbers. The computation of the influence of these numbers when they differ from unity indicates, physically, that the excess chemical and kinetic energy is not completely converted into heat at the surface. The analytical form of the functions f_1 and f_2 is determined by solving the boundary layer equations for specific conditions. Research indicates that, if diffusion is neglected, $f_1 = (\mathrm{Pr})^{\frac{1}{3}}$ and $f_2 = (\mathrm{Pr})^{-\frac{2}{3}}$. Thus for local Stanton numbers, which will usually be used henceforth, we obtain the expression

$$St_x = \frac{c_{fx}}{2} f_2 = \frac{c_{fx}}{2} (Pr)^{-\frac{2}{3}}. \tag{5.34a}$$

The expression in terms of average values is identical to Eq. (5.34a) and is obtained simply by omitting the subscripts x. However, it must be assumed that the local and average Prandtl numbers are identical.

Equation (5.34a) is called the Reynolds analogy and is of great practical value since it indicates that the heat transfer parameter St_x is related directly to the skin friction coefficient and depends on the same variable, i.e., the Reynolds number Re_x. Accordingly, the quantity $f_2 = (Pr)^{-\frac{2}{3}}$ is called the Reynolds analogy parameter.

It has been shown that Eqs. (5.35) in their general form are also applicable to the turbulent boundary layer, with the difference that the friction coefficient must be computed from the corresponding relations. The parameter f_2 also should be calculated for turbulent flow conditions, but for practical purposes its value (without diffusion) can be assumed to be given approximately by $(Pr)^{-\frac{2}{3}}$.

To take the influence of the Prandtl number into account, it is convenient to convert from the stagnation enthalpy, $i_{0\delta} = i_\delta + 0.5V_\delta^2$, to the recovery enthalpy, i_r, in Eq. (5.31). Furthermore, if it is assumed that $c_{pw} \approx c_{p\delta}$, the heat flow is

$$q = \frac{h_x}{c_{p\delta}} (i_r - i_w). \tag{5.31a}$$

The heat transfer coefficient is found from the equation

$$h_x = St_x \rho_\delta V_\delta c_{p\delta}. \tag{5.36}$$

As presented, the relations above are suitable for the calculation of a highly cooled boundary layer. In other cases, where the gas is subject to a large amount of heating, the heat transfer must be calculated by using the effective parameters. Then,

$$St_x^* = \frac{c_{fx}}{2} f_2^*, \tag{5.37}$$

where the parameter $f_2^* = (\mathrm{Pr}^*)^{-\frac{2}{3}}$ and the coefficient c_{fx} is also found from the effective parameters. The local heat transfer coefficient is computed from the Stanton number

$$h_x = \mathrm{St}_x^* \rho_\delta v_\delta (c_p)_m, \tag{5.36a}$$

where $(c_p)_m$ is the average specific heat determined for the temperature range $T_r - T_w$. To calculate the heat flux, it is necessary to use Eq. (5.31a), with $(c_p)_m$ substituted for $c_{p\delta}$.

It should be noted that Eq. (5.31a) differs from Eq. (5.26) in that enthalpy enters into it instead of temperature. This makes its use feasible for a dissociable boundary layer.

The general equations for heat transfer can, as indicated earlier, be used both for laminar and for turbulent boundary layers. In the latter case, Eq. (5.20) can be used for c_{fx} in Eq. (5.37), resulting in

$$\mathrm{St}^* = \frac{(c_{f0})_x}{2}\left[\frac{c_{fx}}{(c_{f0})_x}\right] f_2^* = (\mathrm{Pr}^*)^{-\frac{2}{3}} \frac{(c_{f0})_x}{2}\left[2\left(\frac{1+\alpha_w}{1+\alpha_\delta}\right)^{1/7} - 1\right]. \tag{5.38}$$

The heat transfer will depend on diffusion, and this dependency is expressed by the fact the Schmidt number must enter into the corresponding relationships; these effects will be discussed in Chap. VIII.

Chapter II

THE CONE IN SUPERSONIC FLOW

Editor's Introduction

THE DISCUSSION *of the solution for conical flow of an ideal gas given in this chapter is similar to that in many gas dynamics texts, but is presented in considerably more than usual detail. The tables of conical-flow data are taken directly from Kopal.*(1) *It should be noted that Sims* (NASA SP-3004, *1964) has recalculated the supersonic flow field about cones for* $\gamma = 1.4$ *(instead of Kopal's value of* 1.405*) and for systematic increments in Mach number. Bertram* (NASA TN D-2339, *1964) has presented convenient and accurate graphs of the Kopal and Sims data for an ideal gas correlated by means of hypersonic similarity parameters.*

Surprisingly, Krasnov has not used the hypersonic similarity parameters for correlation purposes in the presentation and discussion of the solutions for conical flow in dissociated air, although Romig (Aero/Space Eng., *March 1959) has shown that the results of exact solutions for conical flow of dissociated air in equilibrium can be correlated by using these parameters. Romig presents graphs of the pressure ratio, density ratio, temperature, and velocity at the surface of cones as a function of both altitude and a parameter corresponding to the hypersonic similarity parameter* $M_\infty \sin \delta_c$. *A more complete set of similar graphs has recently been published by Hudgins* (Picatinny Arsenal Technical Memorandum 1493, *1965). Although the curves of density, temperature, and Mach number cannot be approximated conveniently by empirical formulas, some of the other parameters can be. For example, designating the hypersonic similarity parameter by* $K_1 = M_\infty \sin \delta_c$, *the shock wave angle can be determined from*

$$M_\infty \sin \theta_s = \left(1 + \frac{\gamma_\infty + 1}{2} K_1^2\right)^{\frac{1}{2}} \qquad (K_1 < 6)$$

$$M_\infty \sin \theta_s = \left[0.39 - 0.01 \log_{10}\left(\frac{p_\infty}{p_{SL}}\right)\right] + \left[1.03 + 0.005 \log_{10}\left(\frac{p_\infty}{p_{SL}}\right)\right] K_1 \qquad (K_1 > 6),$$

where the ideal gas formula (for $K_1 < 6$) was first published by Hord (NACA TN 3485, 1955). The pressure and enthalpy on the cone's surface can be approximated by

$$\frac{p_c}{p_\infty} = 1.493\ (K_1)^{1.98} + 1.302, \qquad \frac{i_c}{i_\infty} = 0.240\ (K_1)^{1.97} + 1.119,$$

and the surface velocity can then be calculated from

$$\frac{V_c^2}{V_\infty^2} = \frac{2}{(\gamma_\infty - 1)M_\infty^2}\left(1 + \frac{\gamma_\infty - 1}{2} M_\infty^2 - \frac{i_c}{i_\infty}\right).$$

An error appears in the development of the Mangler transformation (relating boundary layer characteristics on a cone to those on a flat plate) and persists into later chapters of the book. Krasnov defines the laminar boundary layer thickness on a cone as $\sqrt{3}$ times that on a flat plate, whereas the correct relation is $\delta_c = (1/\sqrt{3})\delta_{pl}$; a similar error was made in the case of the turbulent boundary layer. These errors have been corrected in Eqs. (6.26) and (6.27) and in Chapters III and VIII.

The lengthy table (Table 10), which gives the sample calculation of skin friction and heat transfer on a cone, appears anachronistic in this era of digital computers but is actually very useful as a "how-to-do-it" guide (this comment also applies to most of the sample calculation tables in the book).

Section 7 presents both the equations and a detailed exposition of the solution for a cone at angle of attack. The general approach is that of Stone and Kopal,[4,5] with the modifications of Young and Siska[6] presented almost verbatim. Sims (NASA SP-3007, 1964) has recalculated the flow fields about cones at small angles of attack using $\gamma = 1.4$ and body axes rather than wind axes. These results are much easier to use than the original calculations of Kopal[4].

An approximate method for the analysis of cones at angle of attack, based on the local-cone method, is discussed briefly at the end of the chapter. Several more recent semiempirical methods that give somewhat better agreement with experiment include that of Jacobs (J. Aero. Sci., December 1961) as modified by High and Blick (AIAA Journal, November 1964), and the method developed by Collingbourne, Crabtree, and Bartlett (Royal Aircraft Establishment TN Aero 2967, June 1964).

§ 6. *SYMMETRICAL FLOW AROUND A POINTED CONE*

CALCULATION OF PARAMETERS FOR IDEAL FLOW

System of Equations

THE PROBLEM OF FLOW around a pointed cone is one of the most important in the study of aerodynamics of bodies of revolution. Its solution is of great practical value because it not only permits the calculation of flow around the conical bodies themselves, but also is useful in the calculation of supersonic flow around pointed bodies of revolution with curved profiles. For example, the conical solution provides the initial values in the calculation of the flow parameters for pointed bodies of arbitrary shape. Furthermore, the results for symmetric flow around cones can be used to make approximate calculations of the pressure distribution on cones at angle of attack (the "local-cone" method). These same results are useful for comparative purposes in aerodynamic research on blunt cones.

In addition to exact methods, a series of approximate solutions have been developed for the flow around a cone and, particularly, for simple estimates of the pressure drag; some of these solutions apply only to slender cones in linearized supersonic flow or in flow at high Mach numbers. The exact solution considered below can in general be applied to cones of any angle in flows of any velocity. The basic condition that must be fulfilled is related to the maintenance of conical flow (defined below) around the body. The solutions are for inviscid flow, but the results can be used in the study of viscous flow for the determination of skin friction and heat transfer.

The problem is to calculate the flow properties between a cone with a semivertex angle δ_c and the conical shock wave in front of it.

Therefore, it is also necessary to determine θ_s, the angle of the conical shock (Fig. 55). For this purpose, let us consider a system of equations applicable to flow behind a shock wave when the gas is subject to physical and chemical changes due to the influence of high temperature. It will be assumed that thermodynamic equilibrium is established in the perturbed flow region.

Let us further assume that the gas parameters are constant on any intermediate conical surface (including those with angles $\theta = \theta_s$ and $\theta = \delta_c$) and change only from one surface to another. The flow described by such a solution is called conical. On the basis of this property, any partial derivative with respect to the r-coordinate (see Fig. 55) is equal to zero. Then from Eq. (3.9) the first two equations can be obtained:

$$\frac{dV_r}{d\theta} = V_\theta, \tag{6.1}$$

$$\rho V_\theta \frac{dV_\theta}{d\theta} + \rho V_r V_\theta + \frac{dp}{d\theta} = 0. \tag{6.2}$$

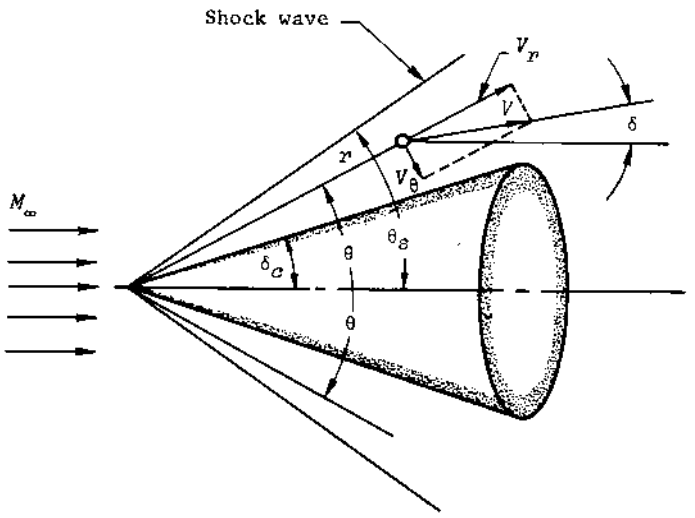

Fig. 55--Velocity components on an intermediate conical surface

To correspond with the number of unknowns, it is necessary to add to these two equations the continuity equation, Eq. (3.17), written in the form

$$2\rho V_r + \gamma_\theta \frac{d\rho}{d\theta} + \rho \frac{dV_\theta}{d\theta} + \rho V_\theta \cot \theta = 0, \tag{6.3}$$

and an expression derived from the equation of state, Eq. (3.46),

$$\frac{p}{p_s} = \frac{(\mu_{avg})_s}{\mu_{avg}} \frac{\rho}{\rho_s} \frac{T}{T_s}. \tag{6.4}$$

The energy equation, Eq. (3.39), appears as

$$i + \frac{V^2}{2} = i_s + \frac{V_s^2}{2}. \tag{6.5}$$

In these equations the subscript s denotes the parameters directly behind the shock wave. Equations (4.6) through (4.9) for calculating the enthalpy, entropy, average molecular weight, and the velocity of sound must also enter into the solution.

As presented, the system of equations is general enough to be used for the study of dissociable gas flow around a cone. The equations and their solution are simplified for the special case of flow without dissociation. Here, in turn, two cases can be investigated, that for constant specific heats and that for specific heat as a function of temperature.

Constant Specific Heats

The results obtained in the case of constant specific heats are of important practical value in themselves, and they can also be used for approximate estimates of several parameters (e.g., pressure) even when the flow is accompanied by significant heating of the gas. These results are of basic interest because they are simple enough to be generalized in tabular and graphical form.

The simplified system consists of Eq. (6.1) together with the following equation:

$$\frac{dV_\theta}{d\theta} = \frac{V_r(V_\theta^2/a^2 - 2) - V_0 \cot\theta}{1 - V_\theta^2/a^2}, \qquad (6.6)$$

where the velocity of sound is given by $a^2 = [(\gamma - 1)/2](V_{max}^2 - V_\theta^2)$. Equation (6.6) is obtained by combining Eqs. (6.2) and (6.3) and taking into account that $dp/d\theta = a^2(d\rho/d\theta)$.

The velocity distribution can be found from the simultaneous solution of the two differential equations Eqs. (6.1) and (6.6). This is sufficient for the complete solution of the problem, because the remaining gasdynamic parameters can be found from the velocities with the help of the other equations, and, as was shown in the analysis of shock waves, these equations are simplified considerably in a flow with constant specific heats.

The boundary conditions are determined by the conditions on the cone and behind the shock wave. The boundary condition at the cone requires that the velocity component normal to the surface, V_θ, be zero, so that

$$\frac{dV_r}{d\theta} = V_\theta = 0 \quad \text{for} \quad \theta = \delta = \delta_c.$$

Two conditions behind the shock wave are sufficient; the first of these is obtained from Fig. 56 and has the form

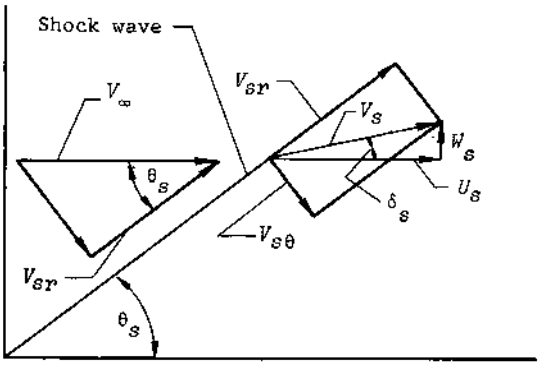

Fig. 56--Velocity components ahead of and behind a shock wave

$$V_{sr} = V_\infty \cos \theta_s. \tag{6.7}$$

The second condition can be obtained from Eq. (4.34) for the shock polar, which is written in the form†

$$\frac{W_s^2}{(V_\infty - U_s)^2} = \frac{(\gamma + 1)(V_\infty U_s - a^{*2})}{2V_\infty^2 + (\gamma + 1)(a^{*2} - \gamma_\infty U_s)}. \tag{6.8}$$

Referring to Fig. 56 and making use of Eq. (6.7), it can be determined that

$$\tan \theta_s = \frac{\gamma_\infty - U_s}{W_s}.$$

Therefore,

$$\tan^2 \theta_s = \frac{2V_\infty^2}{(\gamma + 1)(V_\infty U_s - a^{*2})} - 1. \tag{6.8a}$$

Using Fig. 56 and Eq. (6.7) again, the product $V_\infty U_s$ can be written as

$$V_\infty U_s = V_{sr}^2 + V_{sr} V_{s\theta} \tan \theta_s.$$

When this expression and Eq. (6.7) are substituted into Eq. (6.8a), the second boundary condition behind the shock is obtained:

$$\tan \theta_s = \frac{a^{*2} - \frac{\gamma - 1}{\gamma + 1} V_{sr}^2}{V_{sr} V_{s\theta}}. \tag{6.9}$$

Making the substitutions $\lambda_{sr} = V_{sr}/a^*$ and $\lambda_{s\theta} = V_{s\theta}/a^*$, we obtain

$$\tan \theta_s = \frac{1 - \frac{\gamma - 1}{\gamma + 1} \lambda_{sr}^2}{\lambda_{sr} \lambda_{s\theta}}. \tag{6.9a}$$

†Editor's note: The derivation leading to Eq. (6.9) has been rewritten, because that in the original text is confusing.

If the dimensionless velocities $\tilde{V}_{sr} = V_{sr}/V_{max}$ and $\tilde{V}_{s\theta} = V_{s\theta}/V_{max}$ are introduced by means of the formulas

$$\lambda_{sr} = \tilde{V}_{sr}\sqrt{\frac{\gamma+1}{\gamma-1}}, \qquad \lambda_{s\theta} = \tilde{V}_{s\theta}\sqrt{\frac{\gamma+1}{\gamma-1}},$$

Eq. (6.9) can be rewritten in the form

$$\tan\theta_s = \frac{\gamma-1}{\gamma+1}\frac{1-\tilde{V}_{sr}^2}{\tilde{V}_{sr}\tilde{V}_{s\theta}}. \tag{6.9b}$$

The calculations are begun by computing the parameters behind the shock, V_{sr} and $V_{s\theta}$, for a given free-stream velocity and shock angle, and by computing the velocity of sound a_s. Knowing these boundary conditions, the gas parameters on a series of intermediate conical surfaces can be found consecutively by numerical integration. The computations are completed when satisfactory boundary conditions are obtained on the cone. The angle θ must equal the angle of the cone δ_c, and the value λ_r will equal the total relative velocity on its surface. (A detailed explanation of the order of the calculation is presented later in this section.)

Analogous calculations can also be made starting with the boundary conditions on the cone. In this case it is necessary to know the angle δ_c and the relative velocity on the cone λ_c. When the boundary conditions (6.7) and (6.9) are satisfied, the numerical integration is completed. As a result, the gas parameters and also the slope of the shock wave in front of a given cone are found.

The Solution in the Form of a Taylor Series

A Taylor expansion can be used for the numerical calculation of flow around a cone. The expression for the radial velocity component with respect to the maximum velocity in the form of such a series is

$$\tilde{V}_r = \tilde{V}_c + \tilde{V}'_{cr}(\theta-\delta_c) + \ldots + \tilde{V}^{(n)}_{cr}\frac{(\theta-\delta_c)^n}{n!} + \ldots, \tag{6.10}$$

where $\tilde{V}_c$ is the dimensionless value of the total velocity on the cone,

and $\tilde{V}_{cr}^{(n)}$ is the value of the derivative $d^n\tilde{V}_r/d\theta^n$ on the surface of the cone.

All of these derivatives are determined from the known velocity on the cone. The first derivative $\tilde{V}'_{cr}$ is equal to zero, because the normal velocity component on the cone is $\tilde{V}_{c\theta} = \tilde{V}'_{cr} = 0$. From Eqs. (6.1) and (6.6) we can determine in a general form the expression for the second derivative:

$$\tilde{V}''_r = \frac{\tilde{V}_r(\tilde{V}'^2_r/\tilde{a}^2 - 2) - \tilde{V}'_r \cot\theta}{1 - \tilde{V}'^2_r/\tilde{a}^2}, \tag{6.11}$$

in which $\tilde{a} = a/V_{max}$. At the surface of the cone, $\theta = \delta_c$, $\tilde{V}_r = \tilde{V}_c$, $\tilde{V}'_r = \tilde{V}'_{cr} = 0$, and therefore $\tilde{V}''_{cr} = -2\tilde{V}_c$.

Using successive differentiation of Eq. (6.6), we can determine the third and higher derivatives. The series in Eq. (6.10) is then written as follows:

$$\frac{\tilde{V}_r}{\tilde{V}_c} = 1 - h^2 + a_3h^3 - a_4h^4 + \ldots, \tag{6.12}$$

where $h = \theta - \delta_c$, and the coefficients a_3 and a_4 are given for $\gamma = 1.4$ by

$$a_3 = \frac{1}{3}\cot\delta_c, \qquad a_4 = \frac{1}{12}\left(3\cot^2\delta_c + \frac{20\tilde{V}_c^2}{1 - \tilde{V}_c^2}\right). \tag{6.13}$$

Differentiating with respect to θ, we find the series that represents the normal velocity component:

$$\frac{\tilde{V}_\theta}{\tilde{V}_c} = -2h + 3a_3h^2 - 4a_4h^3. \tag{6.14}$$

Equations (6.12) and (6.14) enable us to compute the velocity components near the cone and to determine successively (step by step) the velocity components on the intermediate conical surfaces. For this purpose the series

$$\tilde{V}_{rh} = (\tilde{V}_r)_{h-1} + h(\tilde{V}'_r)_{h-1} + \ldots \tag{6.15}$$

can be used, where $\tilde{V}_{rh}$ is the radial velocity component on a conical surface with an angle of inclination $\theta + h$, $(\tilde{V}_r)_{h-1}$ is the same component on a neighboring intermediate cone with an angle θ, and $(\tilde{V}'_r)_{h-1}$ is the value of the first derivative on the same cone. In practical calculation it is better to use the average values of the velocity components and their derivatives:

$$(\tilde{V}'_r)_{h-1} = (\tilde{V}_\theta)_{h-1} = \frac{1}{2}\,[\tilde{V}_{\theta h} + (\tilde{V}_\theta)_{h-1}].$$

In analogy to Eq. (6.15), the expression for the derivative can be written

$$\tilde{V}'_{rh} = (\tilde{V}'_r)_{h-1} + h(\tilde{V}''_r)_{h-1} + \ldots. \tag{6.16}$$

The first and second derivatives on the right side of this expression can be determined from Eq. (6.6). Equation (6.16) then makes it possible to compute the normal velocity component on the intermediate conical surface:

$$\tilde{V}_{\theta h} = (\tilde{V}_\theta)_{h-1} + h(\tilde{V}''_r)_{h-1}. \tag{6.17}$$

The accuracy of the computation increases with a decrease in the magnitude of the interval $h = \Delta\theta$. It is apparent that the determination of the second derivative on the preceding conical surface from Eq. (6.11) is the basic operation in these computations.

The computations proceed from one conical surface to another, ending when the angle θ, obtained from the sum of δ_c and all the given intervals $h = \Delta\theta$, is equal to the value $\theta = \theta_s$, as calculated from Eq. (6.9b). This determines the slope of the shock and the values of $\tilde{V}_r = \tilde{V}_{sr}$, $\tilde{V}_\theta = \tilde{V}_{s\theta}$, the radial and normal velocity components behind the shock. Knowing $\tilde{V}_{sr}$ and the angle θ_s, the free-stream velocity can be calculated from Eq. (6.7).

Tables, Graphs, and Approximate Equations

The results of the numerical calculations of flow around cones are presented in a series of tables[1] offered below. In Table 6, values are presented for the radial and normal velocity components as functions of the angle θ for given values of the cone angle δ_c and Mach number M_∞. In Table 7, the surface velocity on the cone, the shock-wave angle, and the coefficient $K_D^* = C_{pc}/2$ are tabulated as functions of the cone angle and the free-stream Mach number.

The data presented in Table 8 give the minimum values of the free-stream Mach number for which flow between the cone and the shock remains supersonic. At lesser Mach numbers, subsonic regions appear and cause deviations from conical flow.

A visual presentation of the flow parameters can be given graphically. One of the graphs (Fig. 57) shows a family of curves representing the geometric position of the ends of the velocity vectors on the surface of the cone. These curves are similar to the shock polars discussed earlier, which gave the flow conditions behind a shock wave in graphical form. The surface velocity for a given cone angle and free-stream Mach number can be found geometrically from these curves, which are called "apple" curves because of their shape. For comparison, the corresponding shock polars are shown in the lower part of Fig. 57.

The slope of a line from point 0 tangent to the apple curve determines the critical angle of the cone $(\delta_c)_{cr}$. If the actual angle of the cone is larger than the critical angle, it is impossible to study the flow around the cone with the aid of this curve. Under actual conditions the shock wave detaches from the apex; such a flow is called supercritical. It can be verified easily from Fig. 57 that the critical angle of a cone is larger than that of a wedge (which is represented by the shock polars). It is also apparent that this angle is a function only of the relative velocity λ_∞ (or M_∞). This dependence is represented graphically in Fig. 58.

Thus, the apple curve makes it possible to determine graphically the velocity and, therefore, the other parameters for cone angles that are less than critical. These calculations do not provide the necessary accuracy for all values of $\delta_c < (\delta_c)_{cr}$, but only for those at which the

Table 6

VALUES OF THE RADIAL AND NORMAL VELOCITY COMPONENTS FOR SYMMETRIC SUPERSONIC FLOW ABOUT A CONE

$\delta_c = 10°$ $\tilde{V}_c = 0.55$ $M_\infty = 1.5956$ $\theta_s = 39.708°$			$\delta_c = 10°$ $\tilde{V}_c = 0.75$ $M_\infty = 2.7794$ $\theta_s = 23.101°$			$\delta_c = 10°$ $\tilde{V}_c = 0.85$ $M_\infty = 4.0748$ $\theta_s = 17.518°$		
$\theta°$	$\tilde{V}_r$	$\tilde{V}_\theta$	$\theta°$	$\tilde{V}_r$	$\tilde{V}_\theta$	$\theta°$	$\tilde{V}_r$	$\tilde{V}_\theta$
10	0.55000	-0.00000	10	0.75000	-0.00000	10	0.85000	-0.00000
14	0.54759	-0.06612	11	0.74987	-0.02503	11	0.84975	-0.02840
18	0.54103	-0.12048	12	0.74914	-0.04821	12	0.84902	-0.05485
22	0.53090	-0.16927	14	0.74670	-0.09085	13	0.84784	-0.08001
26	0.51748	-0.21473	16	0.74283	-0.13035	14	0.84623	-0.10436
30	0.50097	-0.25791	18	0.73762	-0.16806	15	0.84420	-0.12828
34	0.48150	-0.29954	20	0.73111	-0.20504	16	0.84175	-0.15222
38	0.45915	-0.34100	22	0.72330	-0.24283	17	0.83888	-0.17693
39.708	0.44871	-0.36093	23.101	0.71842	-0.26590	17.518	0.83722	-0.19058
$\delta_c = 10°$ $\tilde{V}_c = 0.97$ $M_\infty = 15.146$ $\theta_s = 11.568°$			$\delta_c = 20°$ $\tilde{V}_c = 0.50$ $M_\infty = 1.6531$ $\theta_s = 44.424°$			$\delta_c = 20°$ $\tilde{V}_c = 0.75$ $M_\infty = 3.3694$ $\theta_s = 28.180°$		
$\theta°$	$\tilde{V}_r$	$\tilde{V}_\theta$	$\theta°$	$\tilde{V}_r$	$\tilde{V}_\theta$	$\theta°$	$\tilde{V}_r$	$\tilde{V}_\theta$
10.0	0.97000	-0.00000	20	0.50000	-0.00000	20	0.75000	-0.00000
10.3	0.96998	-0.01002	24	0.49770	-0.06413	21	0.74978	-0.02561
10.5	0.96993	-0.01658	28	0.49118	-0.12155	22	0.74911	-0.05029
11.0	0.96972	-0.03279	32	0.48083	-0.17435	24	0.74652	-0.09780
11.5	0.96937	-0.04905	36	0.46690	-0.22451	26	0.74230	-0.14422
			40	0.44951	-0.27348	27	0.73958	-0.16958
11.568	0.96931	-0.05130	44.424	0.42626	-0.32985	28.180	0.73584	-0.19588

Table 6--continued

$\delta_c = 20°$ $\tilde{V}_c = 0.85$ $M_\infty = 5.5457$ $\theta_s = 24.433°$			$\delta_c = 20°$ $\tilde{V}_c = 0.90$ $M_\infty = 9.5928$ $\theta_s = 22.834°$			$\delta_c = 30°$ $\tilde{V}_c = 0.50$ $M_\infty = 2.0470$ $\theta_s = 47.414°$		
$\theta°$	$\tilde{V}_r$	$\tilde{V}_\theta$	$\theta°$	$\tilde{V}_r$	$\tilde{V}_\theta$	$\theta°$	$\tilde{V}_r$	$\tilde{V}_\theta$
20	0.85000	-0.00000	20.0	0.90000	-0.00000	30	0.50000	-0.00000
21	0.84975	-0.02906	20.5	0.89993	-0.01554	34	0.49764	-0.06633
22	0.84899	-0.05726	21.0	0.89973	-0.03082	38	0.49085	-0.12782
23	0.84775	-0.08508	22.0	0.89893	-0.06101	42	0.47986	-0.18677
24	0.84602	-0.11303	22.5	0.89833	-0.07614	46	0.46478	-0.24536
24.433	0.84512	-0.12534	22.834	0.89786	-0.08036	47.414	0.45847	-0.26663

$\delta_c = 30°$ $\tilde{V}_c = 0.65$ $M_\infty = 3.1617$ $\theta_s = 39.175°$			$\delta_c = 30°$ $\tilde{V}_c = 0.75$ $M_\infty = 5.0109$ $\theta_s = 35.631°$			$\delta_c = 30°$ $\tilde{V}_c = 0.83$ $M_\infty = 16.617$ $\theta_s = 33.444°$		
$\theta°$	$\tilde{V}_r$	$\tilde{V}_\theta$	$\theta°$	$\tilde{V}_r$	$\tilde{V}_\theta$	$\theta°$	$\tilde{V}_r$	$\tilde{V}_\theta$
30	0.65000	-0.00000	30	0.75000	-0.00000	30.0	0.83000	-0.00000
32	0.64922	-0.04420	31	0.74977	-0.02583	30.5	0.82994	-0.01437
34	0.64693	-0.08670	32	0.74910	-0.05111	31.0	0.82975	-0.02861
36	0.64318	-0.12832	33	0.74799	-0.07605	32.0	0.82901	-0.05676
38	0.63798	-0.16990	34	0.74645	-0.10086	33.0	0.82777	-0.08484
39.175	0.63424	-0.19477	35.631	0.74300	-0.14165	33.444	0.82706	-0.09741

Table 7

VALUES OF THE SURFACE VELOCITY, SHOCK-WAVE ANGLE, FREE-STREAM MACH NUMBER, AND DRAG COEFFICIENT FOR SYMMETRIC SUPERSONIC FLOW ABOUT A CONE

$\delta_c = 10°$				$\delta_c = 20°$			
$\tilde{V}_c$	$\theta_s°$	M_∞	K_D^*	$\tilde{V}_c$	$\theta_s°$	M_∞	K_D^*
0.40	68.653	1.0901	0.09222	0.35	68.507	1.2175	0.27059
0.41036	65.234	1.1162	0.08631	0.40	58.043	1.3144	0.22402
0.45	55.162	1.2330	0.07365	0.41036	56.235	1.3428	0.21721
0.50	46.309	1.4028	0.06510	0.45	50.281	1.4672	0.19733
0.55	39.708	1.5956	0.05941	0.50	44.424	1.6531	0.18032
0.60	34.452	1.8165	0.05498	0.55	39.835	1.8714	0.16805
0.65	30.091	2.0750	0.05129	0.60	36.124	2.1297	0.15852
0.70	26.363	2.3869	0.04803	0.65	33.045	2.4431	0.15076
0.75	23.101	2.7794	0.04506	0.70	30.435	2.8387	0.14420
0.80	20.184	3.3041	0.04226	0.75	28.180	3.3694	0.13853
0.85	17.518	4.0748	0.03948	0.80	26.199	4.1538	0.13347
0.90	15.013	5.4223	0.03669	0.85	24.433	5.5457	0.12888
0.95	12.566	9.0999	0.03370	0.90	22.834	9.5928	0.12470
0.98	11.059	37.064	0.03167	0.927	22.027	44.696	0.12254

$\delta_c = 30°$				$\delta_c = 40°$			
$\tilde{V}_c$	$\theta_s°$	M_∞	K_D^*	$\tilde{V}_c$	$\theta_s°$	M_∞	K_D^*
0.35	63.320	1.5164	0.40826	0.35	64.033	2.0242	0.54852
0.41036	55.514	1.6736	0.35942	0.40	59.431	2.2007	0.51526
0.50	47.414	2.0470	0.31958	0.41036	58.597	2.2486	0.50976
0.60	41.426	2.6863	0.29412	0.45	55.734	2.4673	0.49189
0.65	39.175	3.1617	0.28511	0.50	52.755	2.8389	0.47478
0.70	37.268	3.8497	0.27765	0.55	50.327	3.3691	0.46174
0.75	35.631	5.0109	0.27133	0.60	48.324	4.2019	0.45154
0.80	34.210	7.8599	0.26591	0.65	46.650	5.8336	0.44334
0.83	33.444	16.617	0.26302	0.70	45.235	13.101	0.43660

Table 8

VALUES OF THE SURFACE VELOCITY AND FREE-STREAM MACH NUMBER CORRESPONDING TO VARIOUS FLOW REGIMES FOR SUPERSONIC CONICAL FLOW

δ_c°	1	2a	2b	3a	3b
5	1.0129	1.0130	0.39779	1.0385	0.41036
7.5	1.0294	1.0298	0.38800	1.0737	0.41036
10	1.0588	1.0538	0.37846	1.1160	0.41036
12.5	1.0828	1.0848	0.37005	1.1645	0.41036
15	1.1193	1.1230	0.36328	1.2187	0.41036
17.5	1.1622	1.1688	0.35838	1.2781	0.41036
20	1.2115	1.2227	0.35538	1.3428	0.41036
22.5	1.2673	1.2853	0.35418	1.4135	0.41036
25	1.3301	1.3572	0.35459	1.4911	0.41036
30	1.4820	1.5336	0.35907	1.6736	0.41036
35	1.6814	1.7686	0.36644	1.9114	0.41036
40	1.9582	2.0995	0.37462	2.2486	0.41036
45	2.3821	2.6216	0.38240	2.7950	0.41036
50	3.1650	3.6791	0.38924	3.9569	0.41036

NOTES:
Col. 1: Minimum value of M_∞ for which conical flow is possible.
Col. 2a: Maximum value of M_∞ for completely subsonic flow between the cone and the shock wave.
Col. 2b: Dimensionless surface velocity, $\tilde{V}_c$, corresponding to M_∞ in Col. 2a.
Col. 3a: Minimum value of M_∞ for completely supersonic flow between the cone and the shock wave.
Col. 3b: Value of $\tilde{V}_c$ corresponding to M_∞ in Col. 3a.

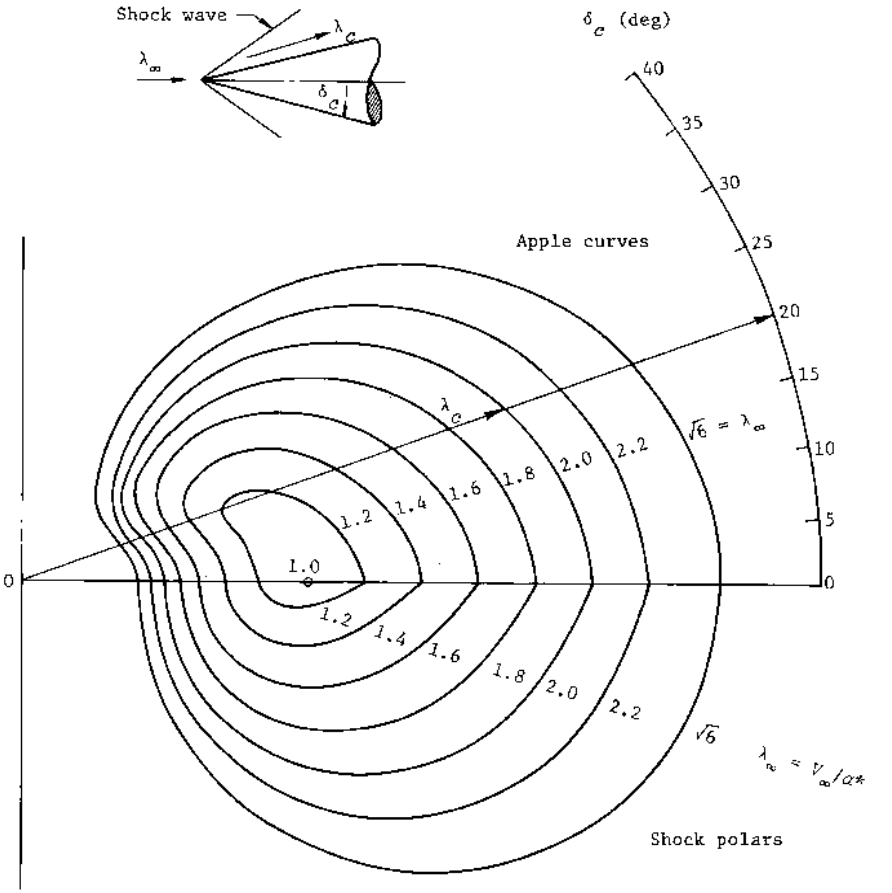

Fig. 57--Families of apple curves and shock polars

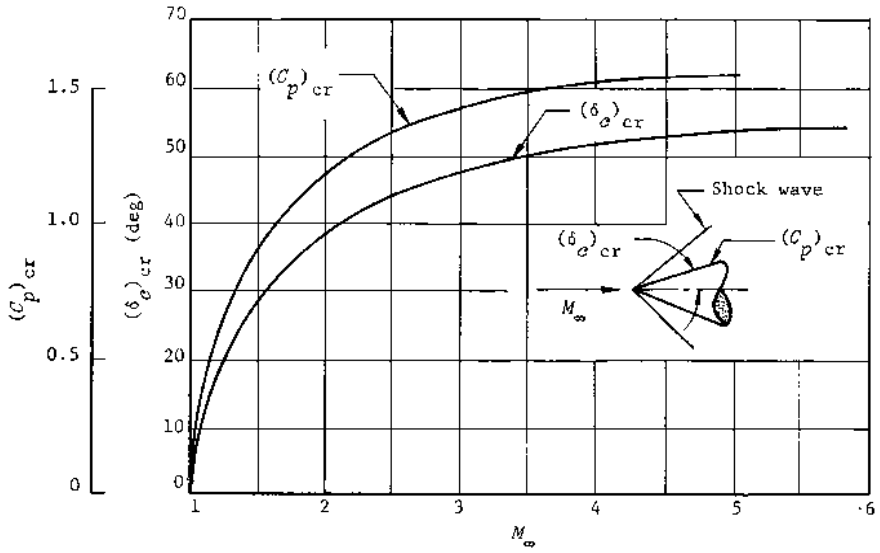

Fig. 58—The critical cone angle and corresponding pressure coefficient

flow between the cone and the shock is supersonic. (These limits on δ_c can be obtained by constructing an arc with the radius a^* in Fig. 57, or from Table 8.) It is apparent that two solutions correspond theoretically to every angle of the cone. One gives less velocity and larger slope of the shock; the other, on the contrary, gives a greater velocity and a lesser shock angle. The second solution corresponds to a stable flow behind the shock wave and is the only type of flow that is observed in practice.

In addition to the apple curves, the curves presented in Fig. 59 are convenient for approximate velocity calculations. Also useful is the graph in Fig. 60, which gives the shock-wave angle on a cone as a function of the cone angle and Mach number.

The determination of temperature, density, and pressure from the values of $\tilde{V}_c$ and ϑ_s is an important element in the calculation of ideal flow around a cone. The corresponding calculations are made with the aid of Eq. (3.58), which can be written in the following form:

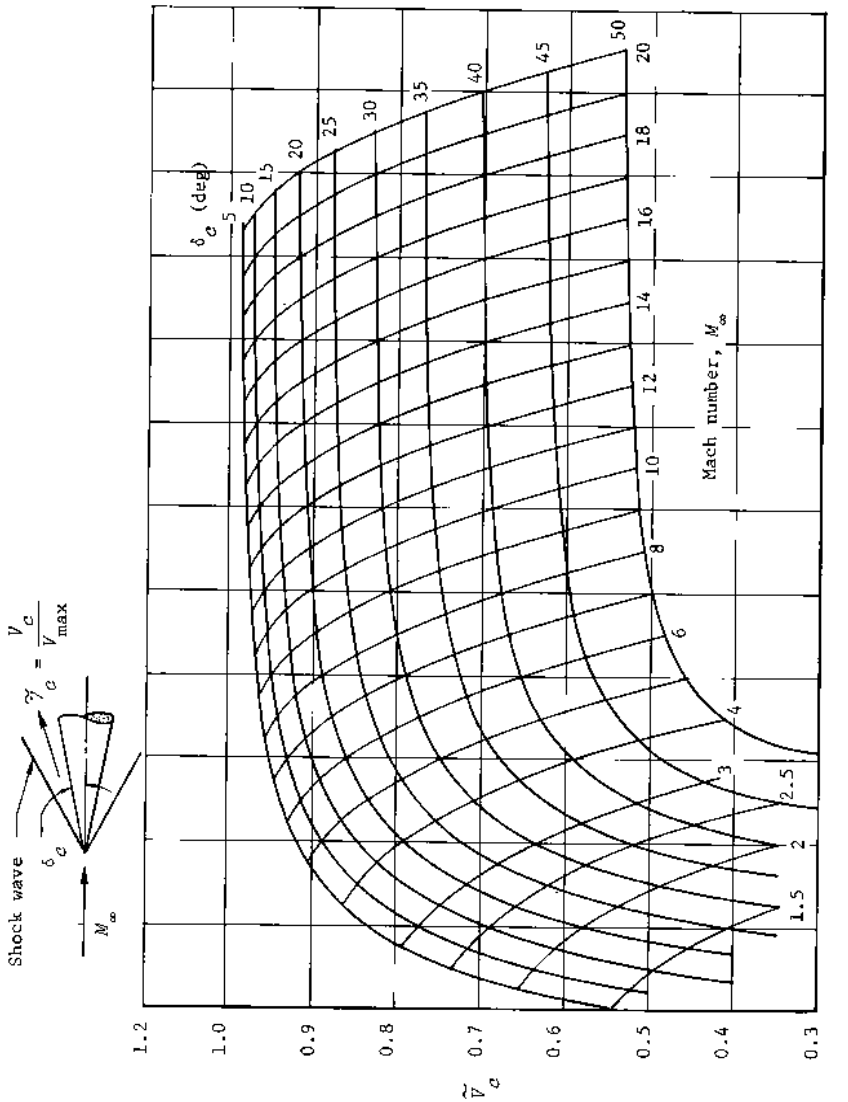

Fig. 58--Dimensionless velocity parameter on a cone in supersonic flow

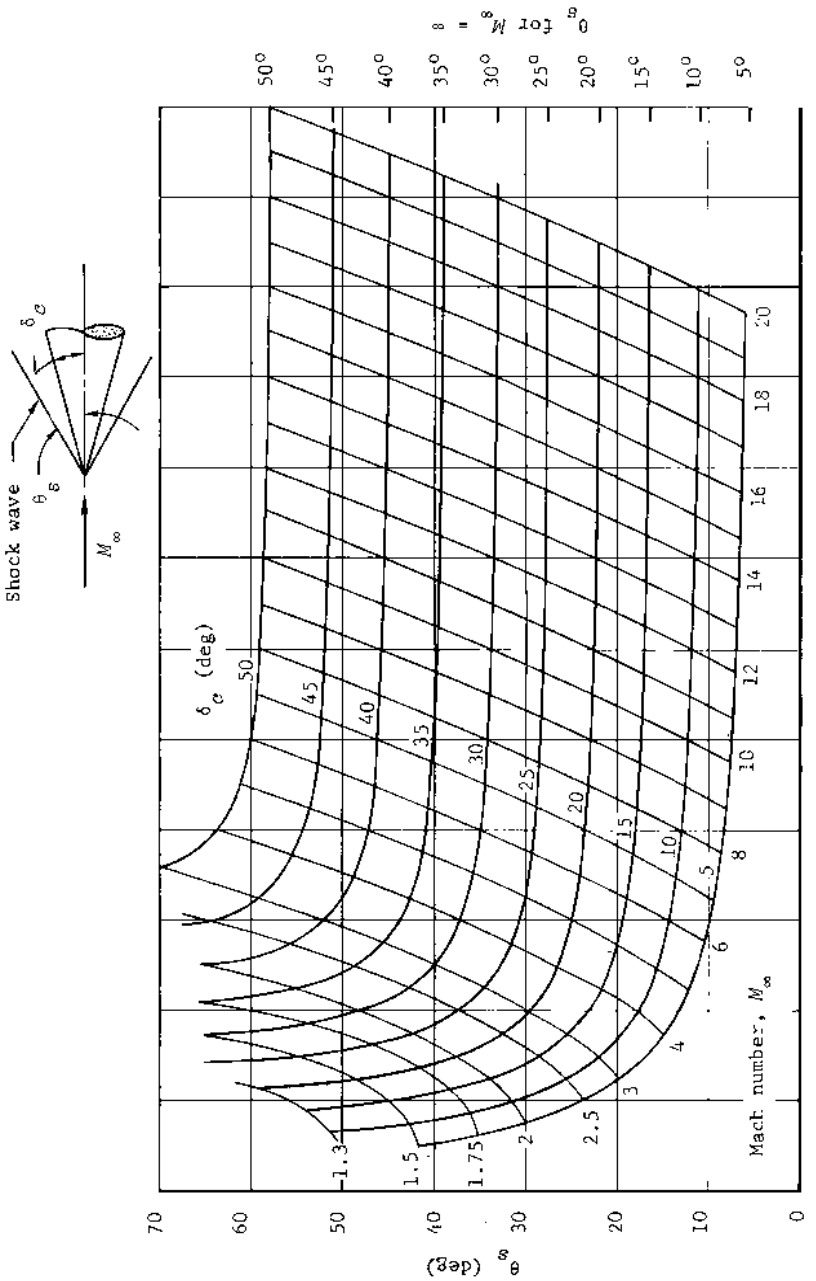

Fig. 60--Shock-wave angle for a cone in supersonic flow

$$\frac{T_c}{T_\infty} = (1 - \tilde{V}_c^2)\left(1 + \frac{\gamma - 1}{2} M_\infty^2\right),$$

$$\frac{p_c}{p_\infty} = \nu_0 \left(\frac{T_c}{T_\infty}\right)^{\gamma/(\gamma-1)}, \qquad (6.18)$$

$$\frac{\rho_c}{\rho_\infty} = \nu_0 \left(\frac{T_c}{T_\infty}\right)^{1/(\gamma-1)}.$$

The parameter $\nu_0 = p_0'/p_0$ is the ratio of the stagnation pressures behind and in front of the shock; it is determined as a function of the free-stream Mach number and shock angle from Eq. (4.33a), or as a function of M_∞ and cone angle from Fig. 61.

The pressure coefficient on the cone is given by $C_{pc} = (p_c - p_\infty)/q$ and, as follows from Eq. (1.6), it is equal to the wave drag coefficient (plotted in Fig. 62). Instead of the family of curves in this figure, we can use a so-called universal curve (Fig. 63). As is evident from the latter figure, the curve represents the relation between the function[†] $C_{pc}/\tan^2\delta_c + C_{pc}$ and the parameter $K_1 = \sqrt{M_\infty^2 - 1}\,\tan\delta_c$.

Thus, the graph in Fig. 63 represents the similarity law for cones. According to this law, the aerodynamic properties of a set of conical bodies, in flows with different free-stream Mach numbers such that the parameter K_1 is the same, will all be defined by the single quantity $C_{pc}/\tan^2\delta_c + C_{pc}$.

To determine the applicability of the similarity law with respect to the parameter K_1, the admissible error must be defined and the results compared with exact theory. Using this method, a shaded area is plotted in Fig. 64; outside of the shaded area, the use of the similarity law gives an error of less than 5 to 6 percent.[(2)]

As a result of evaluating data from exact theory, the following approximate equation for calculating the pressure coefficient on a cone can be recommended:

[†]Editor's note: The function representing the pressure coefficient can obviously be written as $C_{pc}/\sin^2\delta_c$, and the notation has been changed on Fig. 63. It is not clear why Krasnov uses the more awkward form.

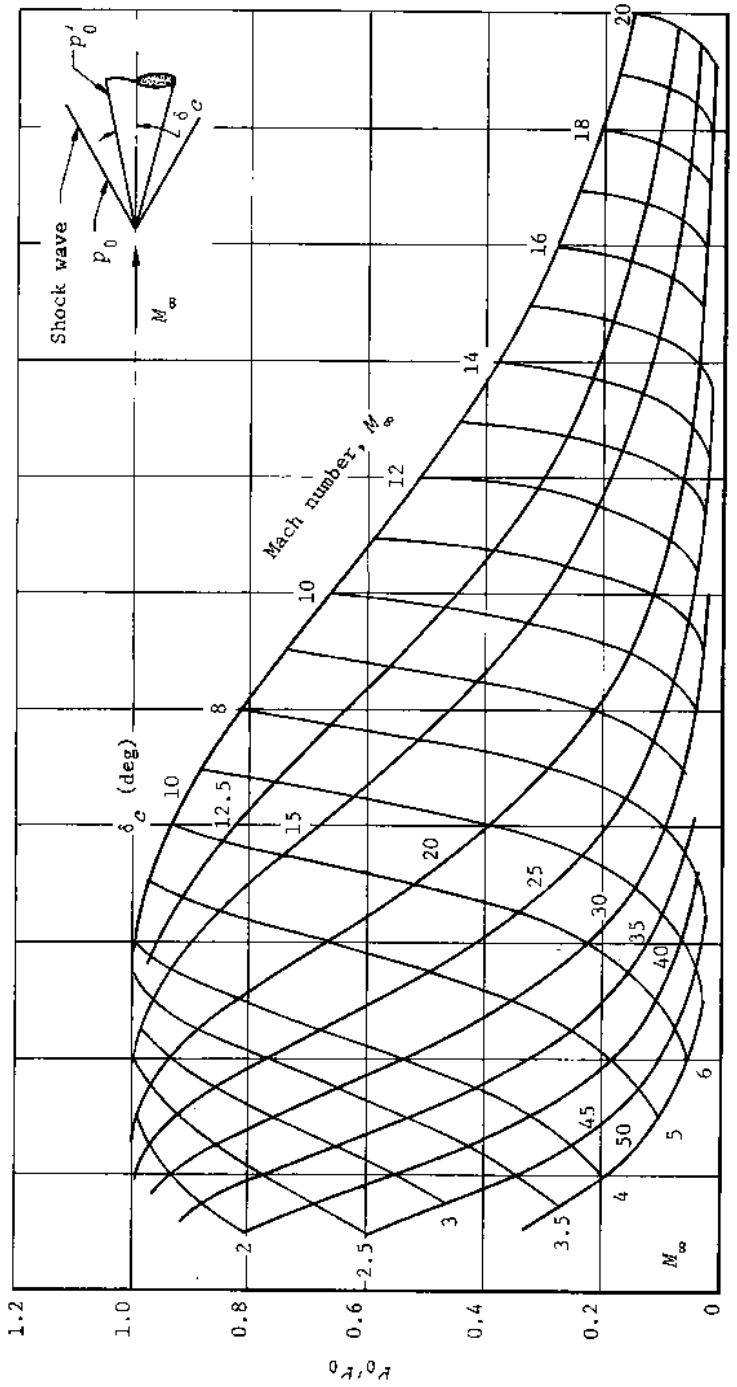

Fig. 61--Stagnation pressure ratio across a shock for supersonic flow about a cone

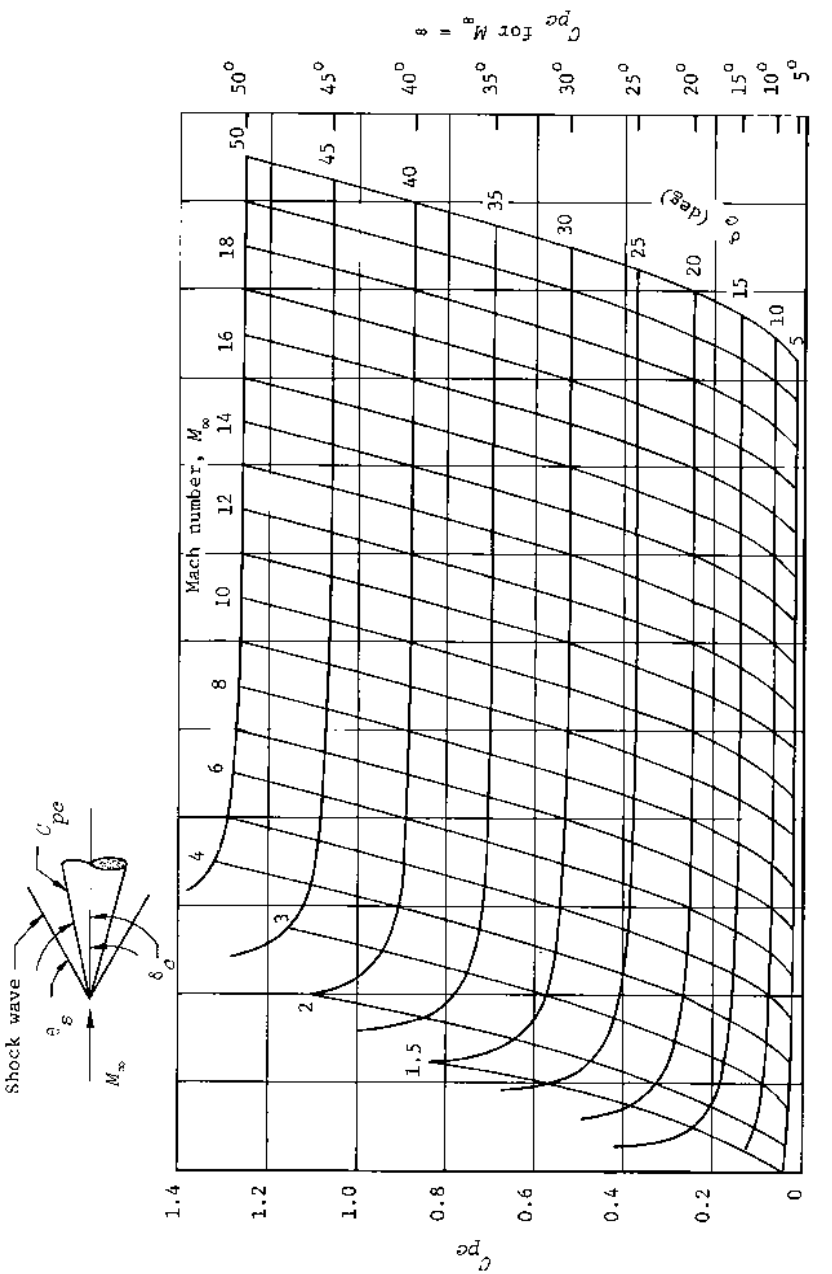

Fig. 62--Pressure coefficient on a cone in supersonic flow

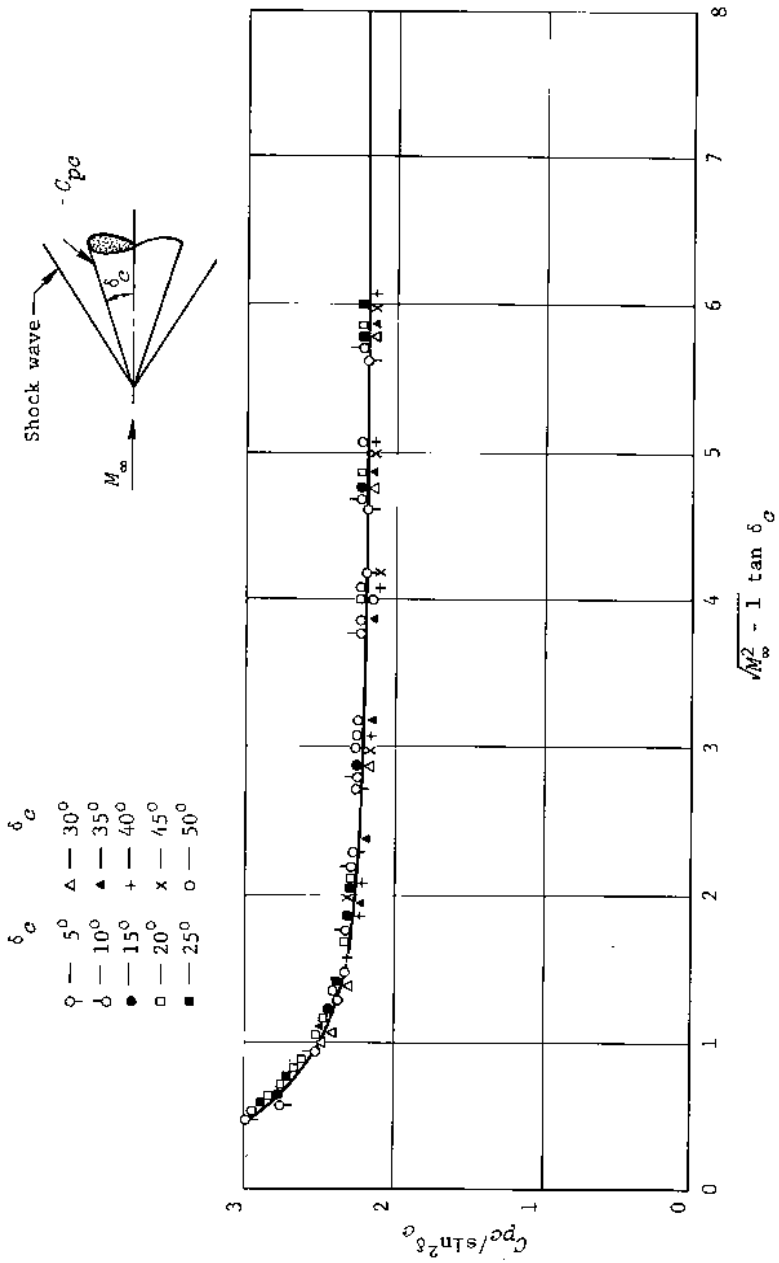

Fig. 63--Universal curve for the pressure coefficient on a cone

$$C_{pc} = C_{Dc} = \left(0.0016 + \frac{0.002}{M_\infty^2}\right)(\delta_c)^{1.7}, \qquad (6.19)$$

where δ_c is the semiapex angle of the cone in degrees. This equation is valid up to values of $\delta_c \leq 50°$ and $M_\infty \approx 8$. The lower limit for the parameters δ_c and M_∞ is determined by the values for which flow between the cone and the shock remains supersonic.

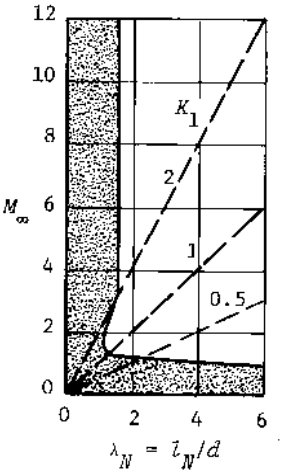

Fig. 64--Region of applicability of the similarity law

Another interesting method is based on the simplification of the numerical integration of Eq. (6.6). The possibility of simplifying this equation results from the fact that the velocity of sound in a perturbed region varies so slightly that it can be assumed constant and equal to its value directly behind the shock wave. The calculations made on this supposition have shown good accuracy; e.g., for $M_\infty = 3$ and $\theta_s = 28°11'$, the error in the determination of the cone angle, when it is compared with exact theory, is 0.08 percent and about 0.2 percent in the velocity on its surface.

The Case of Variable Specific Heats

The equation of state (6.4) must be added to Eqs. (6.1) through (6.3) and (6.5); it will be assumed that $(u_{avg})_s/v_{avg} = 1$. Another necessary relation is for enthalpy:

$$i - i_s = \bar{\theta} c_p (T - T_s), \tag{6.20}$$

in which $\bar{\theta}$ is found from Eq. (3.64) for the temperature range $T - T_s$. Finally, the equation for the velocity of sound must be used in the form $a^2 = \gamma RT$, where the ratio of specific heats γ is generally considered to be a variable function of temperature.

The sequence for the calculation of this type of flow is as follows. First, the oblique shock wave is calculated from a given value of the shock angle θ_s and from the known parameters T_∞ and V_∞ in front of the shock. Thus, the quantities V_{sr}, $V_{s\theta}$, p_s, ρ_s, T_s, i_s, $\bar{\theta}_s = (c_{pm})_s/c_p$, γ_s, and a_s^2 are found. From these quantities, the values of the derivatives are computed with the aid of Eqs. (6.1) and (6.6), and then the velocity components are computed on the adjacent conical surface with the angle $\theta_s - \Delta\theta$:

$$V_r = \left(\frac{dV_r}{d\theta}\right)_s \Delta\theta + V_{sr},$$

$$V_\theta = \left(\frac{dV_\theta}{d\theta}\right)_s \Delta\theta + V_{s\theta}.$$

The velocity components enable us to determine the total velocity $V = \sqrt{V_\theta^2 + V_r^2}$ from which the difference in enthalpy, $i - i_s$, is calculated using Eq. (6.5). If the coefficient $\bar{\theta}$ is now assumed equal to its value directly behind the shock wave, it is possible to find the temperature T from Eq. (6.20) and the pressure and density from

$$\frac{p}{p_s} = \left(\frac{T}{T_s}\right)^{\bar{\theta}} e^{\gamma/(\gamma-1)},$$

$$\frac{\rho}{\rho_s} = \frac{p}{p_s}\frac{T_s}{T}.$$

The coefficient $\bar{\theta}_e$ is determined from Eq. (3.67) for the temperature range $T - T_s$.

After the parameters are found for the conical surface with the angle $\theta_s - \Delta\theta$, the same procedure is applied to the next surface, defined by the angle $\theta_s - 2\Delta\theta$. The calculations are concluded when the normal velocity component equals zero for some angle $\theta_s - \Sigma\,\Delta\theta$. Then the conical surface will be that surface corresponding to the angle $\delta_c = \theta_s - \Sigma\,\Delta\theta$.

The calculations are simplified if we neglect the local variation of the specific heats and the adiabatic exponent in the flow field about the body. It can be assumed that they remain constant in the entire perturbed region and are equal to their corresponding values behind the shock wave. Then the velocity of sound is found from the equation

$$a^2 = a_s^2 + \frac{\gamma_s - 1}{2}(V_s^2 - V^2),$$

and the temperature, pressure, and density from the expressions

$$\frac{T}{T_s} = \frac{a^2}{a_s^2},$$

$$\frac{p}{p_s} = \left(\frac{T}{T_s}\right)^{\gamma_s/(\gamma_s-1)},$$

$$\frac{\rho}{\rho_s} = \left(\frac{T}{T_s}\right)^{1/(\gamma_s-1)}.$$

It is evident from the discussion that, in contrast to the case of constant specific heats, the conditions for conical flow of a heated gas with variable specific heats are dependent on not only the specific heat variation but also on the free-stream temperature T_∞.

The Influence of Dissociation and Ionization

Dissociation and ionization are accounted for by essentially the same calculation methods as for the case of variable specific heats.

Part of the equation system is used in its previous form, i.e., Eqs. (6.2), (6.4), (6.5), and (6.6). The difference involves the use of more general relations for determining the velocity of sound, the enthalpy, the entropy, and the average molecular weight. The calculation begins with the determination of the gas parameters behind the oblique shock for a given shock angle θ_s and for known values of p_∞, T_∞, and V_∞. Next, the first derivatives of the velocity components are computed from Eqs. (6.1) and (6.6) for conditions behind the shock. The velocity components V_r and V_θ and the enthalpy difference $i - i_s$ on the adjacent conical surface with an angle $\theta_s - \Delta\theta$ are calculated. Assuming that the flow behind the shock is isentropic in all areas and that the entropy $S = S_s = \text{const}$, and knowing i and S, it is possible to determine the pressure and temperature on this surface from the entropy diagram or from tables. From these values, the velocity of sound, the average molecular weight, and the density are determined. Making analogous calculations, the method proceeds to the next adjacent intermediate conical surface, etc. The computation is completed when the normal velocity component on one of the surfaces is equal to zero. The parameters obtained thereby will belong to the surface of the cone.

These parameters, as is apparent, depend not only on temperature, which was characteristic for the case of variable specific heats, but also on the pressure of the free-stream flow. Some of the results of calculations for high velocity flows around a cone are presented in Figs. 65 to 67. The character of the variation in these parameters with dissociation and ionization is the same on the cone surface as that directly behind the shock wave. The effects on pressure seem to be just as small; the temperature and density vary considerably and the thicker the cone, the larger the variation.

If the cone angle is small, these parameters are influenced little by the physical-chemical changes even at considerable velocities. For example, calculations show that at $M_\infty = 24$ the density ratio changes only slightly with altitude for cone angles up to 15° and, at $M_\infty = 10$ (Fig. 67), there is no effect of altitude for cone angles up to 35°. Thus, the range of angles within which the influence of high temperature is unimportant widens with a decrease in velocity. The same phenomenon is observed with a decrease in altitude.

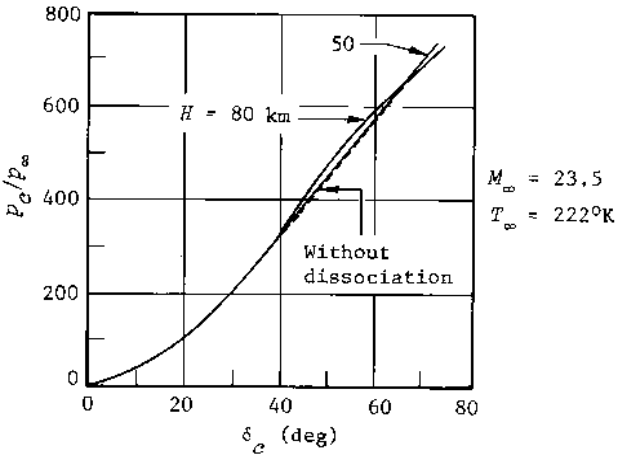

Fig. 65--Pressure ratio on a cone including dissociation effects

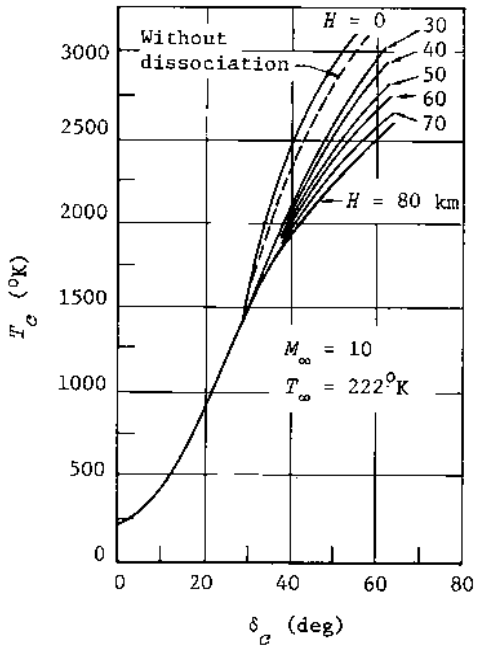

Fig. 66--Temperature on a cone including dissociation effects

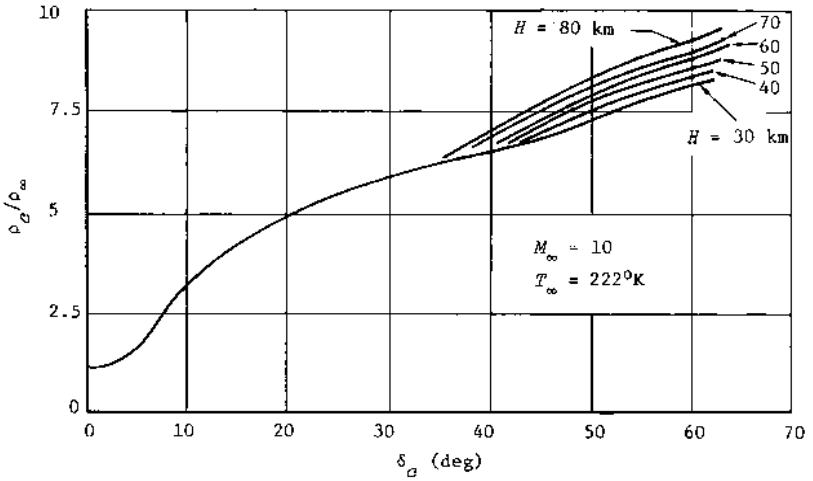

Fig. 67--Density ratio on a cone including dissociation effects

Cones with larger angles cause more intense heating and, therefore, more dissociation and ionization, which can have considerable influence on the flow parameters. This effect on the variation in shock-wave angle with Mach number for a 40° cone is shown in Fig. 68. The shock angle decreases in comparison with that observed for constant specific heats (γ = 1.4). This figure also shows the change in the angle θ_s calculated for a hypothetical perfect gas with an adiabatic exponent, γ = 1.2. It can be seen that the hypothetical gas method gives fair results at very high velocities. Thus, the flow parameters around a cone at very high velocities are basically determined by the physical-chemical properties of the gas behind the shock wave, and particularly by the ratio of specific heats.

These comments apply to such parameters as density, temperature, and shock-wave angle. The pressure, as already noted, is almost unchanged in comparison with a perfect gas. Its value depends almost wholly on the free-stream flow conditions, while the maximum excess pressure cannot exceed $\rho_\infty V_\infty^2$. The calculations from an assumed ratio of specific heats, γ = 1.2, give pressure values that are too low, as is evident from Fig. 69.

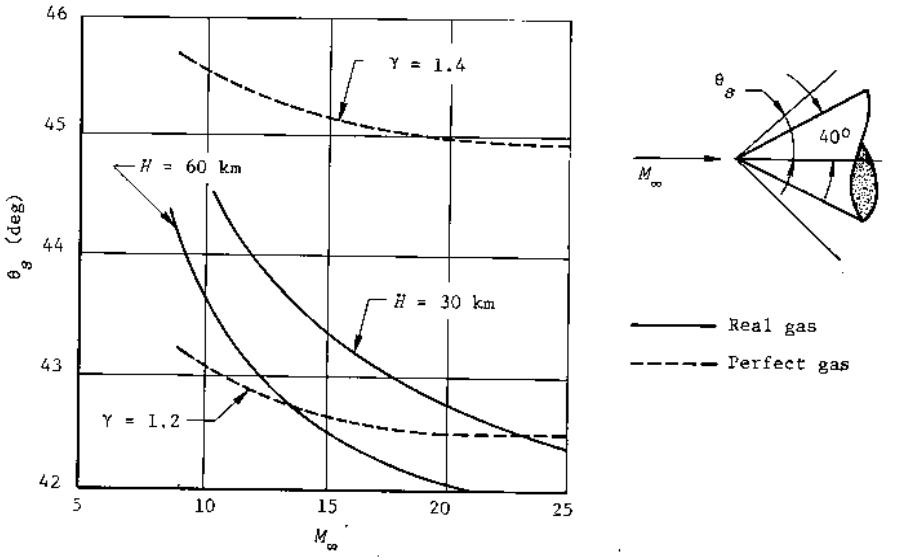

Fig. 68--Shock-wave angle on a cone for a real gas

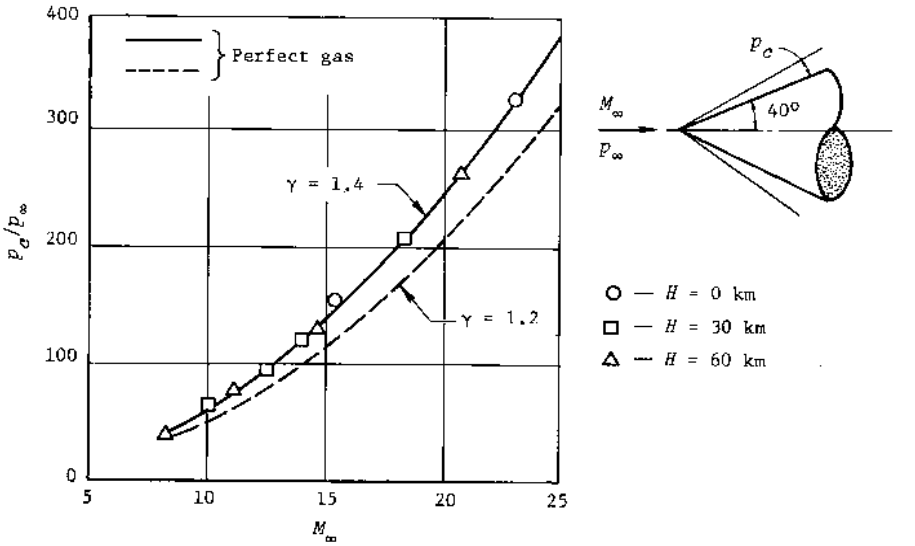

Fig. 69--Pressure ratio on a cone for a dissociated gas

Studies of real-gas flow around a cone can be simplified if a constant velocity of sound is assumed behind the shock wave. It was mentioned above that the results obtained on the basis of this assumption deviated little from the exact results in the case of constant specific heats. Numerical integration of Eq. (6.6) for $a = a_s = \text{const}$ showed that the agreement of the results for dissociating flow was even greater. For example, with typical conditions ($T_\infty = 288°K$, $p_\infty = 1$ kgf/cm^2) in front of a shock wave at an angle $\theta_s = 14°$ for $M_\infty = 14$, the error in determining the angle δ_c is 0.06 percent and in the velocity, 0.002 percent.

If the velocity of sound is constant, the problem reduces basically to the determination of the velocities on the intermediate conical surfaces. The calculation of such parameters as enthalpy, pressure, density, and temperature is made independently after the velocity field is found.

An illustration of the method is given in Table 9, where the data from Table 4 for conditions behind a shock have been used as initial

Table 9

SAMPLE CALCULATION FOR FLOW OVER A CONE INCLUDING THE EFFECTS OF DISSOCIATION AND IONIZATION

1	2	3	4	5	6
V_{n1} m/sec	$\theta_s^\circ = \theta_0$	$V_{\theta 0} = -V_{n2}$	V_{r0}	a_2 m/sec	S_2 kcal/kgf deg
Assumed		$-V_{n1}\left(1 - \frac{\Delta V_{n1}}{V_{n1}}\right)$	$V_{n1}/\tan\theta_s$	From Table 4	
8100	45°	−543	8100	2200	3.37

7	8	9	10	11	12	13
$\left(\frac{dV_\theta}{d\theta}\right)_0$	$\left(\frac{dV_r}{d\theta}\right)_0$	$\Delta\theta$	θ_1°	$V_{\theta 1}$	V_{n1}	V_1
Eq. (6.6)	Eq. (6.1)	Assumed	$\theta_s + \Delta\theta$	Eq. (6.17)	Eq. (6.15)	$V_{\theta 1}^2 + V_{r1}^2$
−16,150	−543	−0.005	44.714°	−462.2	8103	8110

conditions to calculate the flow parameters on a conical surface with an angle $\Delta\theta = -0.005$ radian = -0.286° less than the shock angle. The calculation sequence shown in Table 9 is continued for other intermediate conical surfaces with assigned intervals of $\Delta\theta = -0.005$ radian until the condition $V_\theta = 0$ is satisfied, which specifies the cone angle and the surface velocity.

To determine the remaining parameters on the intermediate surface, the enthalpy $i_i = i_\infty + 0.5(V_\infty^2 - V_i^2)$ is found from the velocity. In the example, $V_\infty = 8100/\sin 45° = 11{,}450$ m/sec, and i_∞ was assumed to be negligible. Then p_i, T_i, $(\mu_{avg})_i$, and ρ_i were determined from each of the values of i_i for $S_2 = 3.37$ kcal/kgf deg with the aid of the graphs or tables.

For rough calculations of flow around a cone, the equations can be simplified still further for very high velocity because of the proximity of the shock to the cone and, therefore, the thinness of the perturbed region of flow. The derivative $dV_\theta/d\theta$ varies only slightly in this region compared to its value directly behind the shock. For example, in the calculation above the values of the derivative on the cone and behind the shock differ by less than 5 percent. Thus, this derivative can be assumed constant and equal to its value behind the shock.

Again, because of the small size of the angle between the shock wave and the cone, the derivative $dV_r/d\theta$ can be replaced by its mean value, $dV_r/d\theta = 0.5V_{\theta s}$.

With these assumptions, the cone angle and the surface velocity can be determined directly:

$$\delta_c = \theta_s - |\Delta\theta|,$$
$$V_c = V_{rc} = V_{rs} - 0.5V_{\theta s}|\Delta\theta|, \tag{6.21}$$

where $|\Delta\theta| = V_{0s}/(dV_\theta/d\theta)_s$. For the calculation in Table 9, $V_{\theta s} = -543$ m/sec and $(dV_\theta/d\theta)_s = -16{,}150$ m/sec. Thus, $\Delta\theta = 0.0336$ radian = 1.93°, $\delta_c = 43.07°$, and $V_c = 8109$ m/sec. These data can be used as a first approximation in more accurate calculations. More detailed data on the parameters of dissociable air flow around a cone can be found in Ref. 3.

Nonequilibrium Effects

We have examined two cases of inviscid flow around a cone. One was for constant specific heats, the other for equilibrium dissociation and ionization in the entire region between the body and the shock. They can be considered as limiting cases, located at the boundaries of a region within which nonequilibrium gas flow predominates.

In the first case, the physical-chemical properties of the gas remain the same as those directly behind the shock wave, and the flow passes through the perturbed region with constant specific heats. Thus, the gas is considered "frozen" in the entire region, with no excitation of energy levels. As a further approximation, it can be assumed that the vibrational degrees of freedom directly behind the wave front reach equilibrium and then remain "frozen."

In the second case, the dissociable gas is assumed to be in equilibrium throughout the region. Research has shown that the values of the flow parameters are different in the two limiting cases. For example, in frozen flow the shock angle and the surface temperature are greater, but the density and pressure are less.

If the temperatures are not high enough for dissociation to develop, the limiting cases will be characterized, on the one hand, by frozen flow with constant specific heats and, on the other, by flow with excitation of the vibrational states in the entire region.

Thus, the limiting case of frozen flow can be considered with or without excitation of the vibrational levels to the values that they would have just behind the shock. At the same time, the limiting case of equilibrium flow will consist of equilibrium excitation of vibrations only or will also include equilibrium dissociation, depending on the temperature. Both limiting cases consist of conical flow, but the intermediate nonequilibrium flow is not conical. Of course, the study of the latter is much more complex.

For preliminary estimates, it can be assumed that the parameters vary from frozen flow values at the nose to equilibrium values at the end of the relaxation length, i.e,, the point at which an equilibrium degree of dissociation or vibrational equilibrium is attained. A diagram of this process is given in Fig. 70. The solid curves correspond

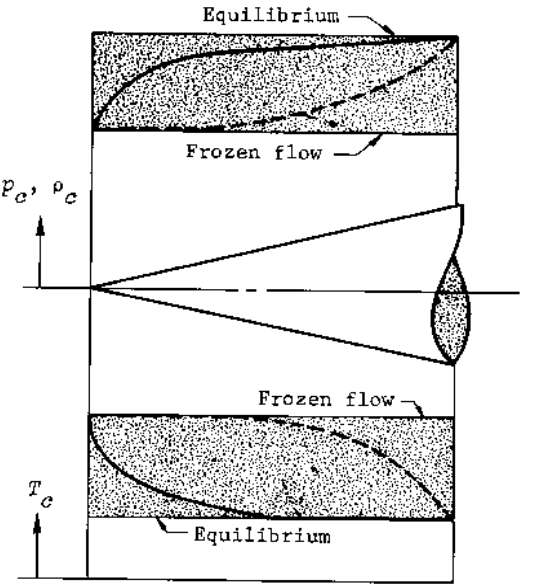

Fig. 70--Nonequilibrium parameters on a cone

to the case close to equilibrium in all regions and the dashed curves to the frozen case. The assumption of frozen flow is further justified when the vibrational relaxation time is less than the dissociation relaxation time. Therefore, the frozen case is more probable at high altitudes and the equilibrium case at low altitudes.

From this qualitative description it follows that nonequilibrium effects modify the aerodynamic characteristics. In particular, the drag is greater than that for frozen flow and less than that for equilibrium flow, but the differences are very small. If the nonequilibrium effects on lift were investigated, they might prove to be more significant than those on the drag forces.

FRICTION AND HEAT TRANSFER

Skin Friction

We can use the integral relationship of Eq. (3.37) to calculate the shear stress for viscous supersonic flow around a pointed cone.

Assuming that the gas parameters at the outer edge of the boundary layer are everywhere identical and, therefore, that the longitudinal pressure gradient and velocity gradient are zero, and also keeping in mind that $r = R + y \cos \delta_c$, this relation can be presented in the form

$$\frac{d}{dx}\int_0^{\delta}\frac{\rho V_x}{\rho_c V_c}(R + y\cos\delta_c)\left(1 - \frac{V_x}{V_c}\right)dy = \frac{R\tau_0}{\rho_c V_c^2},$$

where R is the distance from the axis to a point on the cone surface (Fig. 71), and τ_0 is the shear stress on the surface at this point.

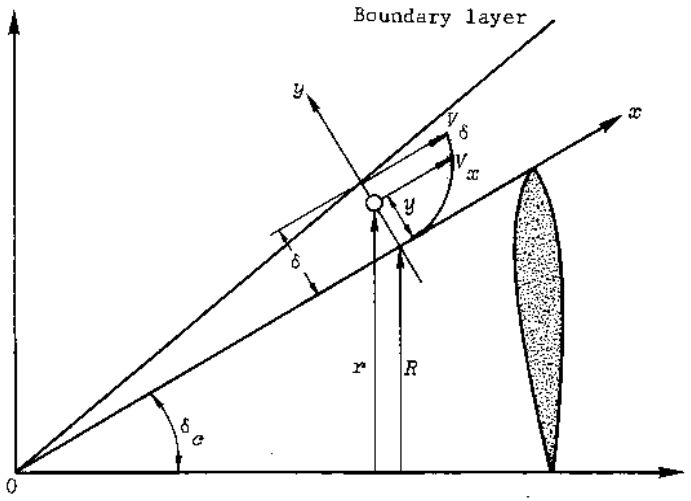

Fig. 71--The boundary layer on a cone

For a laminar boundary layer, the shear stress at any point in the boundary layer is given by $\tau = \mu(\partial V_x/\partial y)$; at a fixed distance x from the nose, the equation can be rewritten as $dy = (\mu/\tau)\, dV_x$. Assuming that $y \ll R$, the integral relationship is

$$\frac{d}{dx}\int_0^{\delta}\frac{\rho V_x}{\rho_c V_c}\frac{\mu}{\mu_c}\frac{R}{\tau}\left(1 - \frac{V_x}{V_c}\right)d\left(\frac{V_x}{V_c}\right) = \frac{R\tau_0}{\rho_c V_c^3 \mu_c}. \qquad (6.22)$$

In this equation, the velocity ratio is a function of the dimensionless coordinate y/δ; i.e., $V_x/V_e = f_1(y/\delta)$. Moreover, the shear stress distribution also conforms to a similarity law of the form $\tau/\tau_0 = f_2(y/\delta)$. These functions can be introduced into Eq. (6.22) in order to produce the integral

$$J = \int_0^{\delta} \frac{\rho V_x}{\rho_e V_e} \frac{\mu}{\mu_e} \frac{1 - f_1}{f_2} \, df_1,$$

which is independent of x (assuming that the wall temperature is uniform). As a result we obtain

$$J \frac{R}{\tau_0} \frac{d}{dx}\left(\frac{R}{\tau_0}\right) = \frac{R^2}{\rho_e V_e^3 \mu_e}. \tag{6.23}$$

If we consider a thin flat plate for which the flow parameters are assumed to be equal to the local values for a cone in ideal flow, then, after eliminating R from Eq. (6.23) and integrating, we find the shear stress on the surface:

$$(\tau_0)_{pl} = \left(\frac{J}{2} \frac{\rho_e V_e^3 \mu_e}{x}\right)^{\frac{1}{2}}.$$

A similar expression is obtained for a conical body as a result of integrating Eq. (6.23), given that $R = x \sin \delta_e$:

$$(\tau_0)_e = \sqrt{3} \left(\frac{J}{2} \frac{\rho_e V_e^3 \mu_e}{x}\right)^{\frac{1}{2}}.$$

From these two equations comes the important relation

$$(\tau_0)_e = \sqrt{3} \, (\tau_0)_{pl}, \tag{6.24}$$

according to which the shear stress on a cone is $\sqrt{3}$ larger than that on a plate. In applying this result, it should be remembered that $(\tau_0)_{pl}$ is calculated for the local flow parameters on the cone.

From Eq. (6.24), the local and average values of the skin friction coefficients are related by†

$$(c_{fx})_c = \sqrt{3}\,(c_{fx})_{pl},$$
$$(c_f)_c = \frac{2}{\sqrt{3}}\,(c_f)_{pl}. \tag{6.25}$$

These skin friction coefficients are based on the dynamic pressure of the local flow, $q_c = \rho_c V_c^2/2$. If they are converted to the free-stream dynamic pressure, the factor $\rho_c V_c^2/\rho_\infty V_\infty^2$ will appear on the right side of the equations.

An approximate formula can also be written for the relation between the boundary layer thicknesses on a cone and on a plate. Recalling that the skin friction coefficient for laminar flow is inversely proportional to the square root of the Reynolds number, the factor $\sqrt{3}$ appearing in Eq. (6.25) can be incorporated into the Reynolds number term. Thus, the local skin friction coefficient on a cone at a given Reynolds number and Mach number will be the same as that on a flat plate at the same Mach number but at a Reynolds number that is one-third of that for the cone. On this basis, the relation between the laminar boundary layer thicknesses on a cone and on a plate will be††

$$\delta_c = \frac{1}{\sqrt{3}}\,\delta_{pl}. \tag{6.26}$$

Studies of the turbulent boundary layer have shown that the boundary layer parameters on a cone are equal to their corresponding values on a plate for the same Mach number and surface temperature ratio when evaluated for a Reynolds number on the plate that is 2.2 times less than the Reynolds number on the cone (according to E. E. Solodkin). Using

---

†Editor's note: The expression for the average skin friction coefficient was given as $(c_f)_c = \sqrt{3}(c_f)_{pl}$ in the Russian text. The same error occurs several times later in the book.

††Editor's note: This equation was written as $\delta_c = \sqrt{3}\,\delta_{pl}$ in the Russian text. Similar errors were corrected in the expression for the turbulent boundary layer thickness in Eq. (6.27), and in Chapter VIII.

this factor with the 1/7 power law, the following relations are obtained:

$$(\tau_0)_c = A(\tau_0)_{pl}, \qquad (c_{fx})_c = A(c_{fx})_{pl}, \qquad \delta_c = \frac{1}{A}\,\delta_{pl}, \tag{6.27}$$

where $A = 1.17$. Compressibility and high temperature can be accounted for by using the effective parameters in the equations presented.

Heat Transfer

The local Stanton number can be calculated from Eq. (5.37), using the skin friction coefficient for a cone:

$$St_x^* = \frac{A}{2}\,(c_{fx})_{pl}(Pr^*)^{-\frac{2}{3}}, \tag{6.28}$$

where $A = \sqrt{3}$ for the laminar boundary layer, and $A = 1.17$ for the turbulent boundary layer. The corresponding heat transfer coefficient h_x is then computed from Eq. (5.36a). For those cases in which an equilibrium radiation temperature seems likely, the calculation of friction and heat transfer on a cone must be made by the method of successive approximations.

To illustrate, let us describe the calculation sequence for the friction and heat transfer parameters, assuming that the gas in the boundary layer is dissociated. (At very high velocities the gas can also be dissociated in the local inviscid flow region.) The calculation begins with the determination of the parameters of ideal flow around a cone, specifically the pressure p_c, density ρ_c, enthalpy i_c, velocity V_c (here we can replace the subscript c by the subscript δ). Next, depending on the type of flow in the boundary layer, the recovery factors $r_L^* = 0.85$ or $r_T^* = 0.90$ are assigned, the recovery temperature T_r is calculated, and the effective enthalpy i^* is computed from Eq. (5.21) for a surface temperature $T_w = T_r$. From the values of i^* and p_c, the effective temperature T^* is found with the aid of graphs or tables of thermodynamic functions. Using the equation of state, the density is given by $\rho^* = p_c \mu_{avg}^* / R_0 T^*$, where the average molecular weight μ_{avg}^* is calculated from the values of T^* and p_c.

In addition to these parameters, the viscosity μ^* must be calculated. The skin friction coefficient can be computed as a first approximation

from Eqs. (5.5), (5.17), and (5.18), the Stanton number from Eq. (6.28), and the heat transfer coefficient h from Eq. (5.36a).

The equilibrium radiation temperature $T = T_e$ is determined for the second approximation from Eq. (5.28a) and the heat flux from Eq. (5.26). It is possible to carry out the calculation after correcting the value of the heat transfer coefficient and the wall temperature to $T_w = T_e$.

In addition to the case of a dissociable gas, we can consider a gas in which no dissociation occurs and the specific heats are either functions of temperature or are constant. The molecular weight, therefore, does not change, and all of these calculations are considerably simplified.

EXAMPLE

Let us calculate the friction and heat transfer parameters on a 10° cone for flight conditions corresponding to an altitude of 30 km, a Mach number of 15, and the surface at the equilibrium radiation temperature.

First, the inviscid flow parameters are calculated; because the cone is slender, dissociation can be neglected in the local inviscid flow field. The results of this calculation are presented in Table 10.† After assigning a constant value to the Prandtl number of Pr = 0.71 (taking into account that in practice it depends little on temperature), we can determine the recovery enthalpy for the laminar and turbulent flows. Knowing i_r and the pressure p_δ, the recovery temperature can be found with the aid of graphs or tables of thermodynamic functions. Henceforth, we will assume that the values of i_r and T_r are constant. The friction and heat transfer parameters can now be calculated from the results for inviscid flow.

In Table 10, the calculations are made for two points on the cone. The coordinates of the first point are such that the local Reynolds number is $\mathrm{Re}_x = 5 \cdot 10^6$ and, therefore, the boundary layer remains laminar.

†Editor's note: The data given in Table 10 in the original Russian text contained numerous errors: in the equation numbers cited in the table, in the values obtained from graphs or tables, and in the arithmetic. Consequently, the entire table has been reworked. Most of the general comments that follow are not affected by these revisions.

Table 10

SAMPLE CALCULATION OF SKIN FRICTION AND HEAT TRANSFER ON A CONE

1	2	3	4	5	6	7	8	9
M_∞	H km	δ_c	K_i	K_ϑ	$\frac{p_\delta}{p_{\infty H}}$	$\frac{a_\delta^2}{a_{\infty H}^2} = \frac{T_\delta}{T_{\infty H}}$	$\frac{\rho_\delta}{\rho_{\infty H}}$	$\frac{c_{p\delta}}{(c_{p_\infty})_H}$
			$M_\infty \delta_c$	$M_\infty \theta_s$	Fig. 63	Eq. (6.18)	$\frac{(6)}{(7)}$	Eq. (2.2)
15	30	0.174	2.61	3.00	11.2	2.74	4.08	1.10

10	11	12	13	14	15	16
$\frac{\mu_\delta}{\mu_{\infty H}}$	Pr	$\frac{p_{\infty H}}{p_{\infty SL}}$	$\frac{\rho_{\infty H}}{\rho_{\infty SL}}$	$\frac{a_{\infty SL}}{a_{\infty H}} = \sqrt{\frac{T_{\infty SL}}{T_{\infty H}}}$	g m/sec^2	p_δ kgf/cm^2
Eq. (2.3)	Assumed	Standard Atmosphere (App. A)				$(6)\cdot(12)\cdot p_{\infty SL}$
2.02	0.71	0.0118	0.0145	1.11	9.72	0.132

17	18	19	20	21	22	23	24
$\frac{V_\delta}{V_{max}} = \bar{V}_\delta$	M_δ	$\frac{V_\delta}{V_\infty}$	V_∞ m/sec	V_δ m/sec	r_L	r_T	$i_r - i_\delta$ m^2/sec^2
Fig. 59	Eq. (3.60)[a]	$\frac{M_\delta}{M_\infty}(7)^{\frac{1}{2}}$	340 $\frac{M_\infty}{(14)}$	$(19)\cdot(20)$	$\sqrt{\text{Pr}}$	$\sqrt[3]{\text{Pr}}$	$r_L \frac{V_\delta^2}{2}$
0.975	10.40	1.145	$4.61\cdot10^3$	$5.29\cdot10^3$	0.845	0.890	$11.80\cdot10^6$

25	26	27	28	29	30	31
$i_r - i_\delta$ kcal/kgf	i_δ kcal/kgf	$\text{Re}_{\delta L}$	x_L m	$(c_{fx})_L$	St_{xL}	h_{xL} $\frac{\text{kcal}}{\text{m}^2 \text{ sec deg}}$
$\frac{(24)\cdot2.37\cdot10^{-2}}{g}$	$c_{p\delta}T_\delta$	Assumed	$\text{Re}_\delta \frac{\mu_\delta}{V_\delta \rho_\delta}$	Eqs. (5.5), (6.25)	Eq. (6.28)	$(30)c_{p\delta}\rho_\delta V_\delta$
$2.87\cdot10^3$	167	$5\cdot10^6$	0.382	$0.515\cdot10^{-3}$	$3.25\cdot10^{-4}$	$3.31\cdot10^{-2}$

[a] Editor's note: Calculated for $\gamma_\delta = 1.35$, corresponding to the $c_{p\delta}$ of Col. 9.

Table 10--continued

32	33	34	35	36	37	38	39
ϵ	$\frac{\bar{h}_{xL}}{\epsilon}\ \frac{\text{kcal}}{\text{m}^2\ \text{hr deg}}$	T_r °K	T_e °K	$\text{Re}_{\delta T}$	x_T, m	$(c_{fx})_T$	St_{xT}
Assumed	$3.6\cdot10^3\ \frac{(31)}{(32)}$	From i_r, p_δ, and Fig. 15	From (33), (34), and Fig. 54	Assumed	$20\cdot(28)$	Eqs. (5.5), (6.27)	Eq. (6.28)
0.8	149	5300	1700	10^8	7.64	$1.7\cdot10^{-3}$	$1.08\cdot10^{-3}$

40	41	42	43	44	45
$h_{xT}\ \frac{\text{kcal}}{\text{m}^2\ \text{sec deg}}$	$\frac{\bar{h}_{xT}}{\epsilon}\ \frac{\text{kcal}}{\text{m}^2\ \text{hr deg}}$	T_e °K	i_e kcal/kgf	i^* kcal/kgf	T^* °K
(39) $c_{p\delta}\rho_\delta V_\delta$	$3.6\cdot10^3\ \frac{(40)}{(32)}$	From (41), (34), and Fig. 54	From (35), (16), and Fig. 15	From (25), (26), (43), and Eq. (5.21)	From (44), (16), and Fig. 15
0.110	494	2300	450	940	2900

46	47	48	49	50	51
$\frac{T^*}{T_{\infty H}}$	$\frac{\rho^*}{\rho_{\infty H}}$	$\frac{c_p^*}{(c_{p\infty})_H}$	$\frac{\mu^*}{\mu_{\infty H}}$	$\frac{\rho^*}{\rho_\delta}$	$\frac{\mu^*}{\mu_\delta}$
$\frac{(45)}{288}\ (14)^2$	$(8)\ \frac{(7)}{(46)}$	From (46) and Eq. (2.2)	From (46) and Eq. (2.3)	$\frac{(47)}{(8)}$	$\frac{(49)}{(10)}$
12.5	0.89	1.287	5.90	0.218	2.92

52	53	54	55	56	57
$\frac{c_p^*}{c_{p\delta}}$	Re_L^*	$(c_{fx}^*)_L$	St_{xL}^*	$h_{xL}^*\ \frac{\text{kcal}}{\text{m}^2\ \text{sec deg}}$	$\frac{\bar{h}_{xL}^*}{\epsilon}\ \frac{\text{kcal}}{\text{m}^2\ \text{hr deg}}$
$\frac{(48)}{(9)}$	$\frac{(27)\cdot(50)}{(51)}$	$(29)\left(\frac{\text{Re}_\delta}{\text{Re}^*}\right)^{\frac{1}{2}}_L$	Eq. (6.28)	$(31)\ \frac{(55)}{(30)}\ (56)(52)$	$\frac{(56)}{(32)}\ 3.6\cdot10^3$
1.16	$0.374\cdot10^6$	$1.89\cdot10^{-3}$	$1.19\cdot10^{-3}$	$3.06\cdot10^{-2}$	138

Table 10--continued

58	Heat Flux	59	60	61	62	63
T_e °K	q $\frac{\text{kcal}}{\text{m}^2\ \text{sec}}$	i_e kcal/kgf	i^* kcal/kgf	T^* °K	$\frac{T^*}{T_{\infty H}}$	$\frac{\rho^*}{\rho_{\infty H}}$
From (57), (34), and Fig. 54	$h^*_{xL}(T_r - T_e)$	From (42), (18), and Fig. 15	From (25), (26), (59), and Eq. (5.21)	From (60), (18), and Fig. 15	$\frac{(61)}{288}$ $(14)^2$	(8) $\frac{(7)}{(62)}$
1650	112	610	1020	2950	12.8	0.87

64	65	66	67	68	69	70
$\frac{c^*_p}{(c_{p_\infty})_H}$	$\frac{\mu^*}{\mu_{\infty H}}$	$\frac{\rho^*}{\rho_\delta}$	$\frac{\mu^*}{\mu_\delta}$	$\frac{c^*_p}{c_{p\delta}}$	Re^*_T	$(c^*_{fx})_T$
From (62) and Eq. (2.2)	From (62) and Eq. (2.3)	$\frac{(63)}{(8)}$	$\frac{(65)}{(10)}$	$\frac{(64)}{(9)}$	$\frac{(36)(66)}{(67)}$	$(38)\left(\frac{\text{Re}_\delta}{\text{Re}^*}\right)^{\frac{1}{5}}_T$
1.29	6.00	0.214	2.97	1.18	$7.20\cdot10^6$	$2.87\cdot10^{-3}$

71	72	73	74	Heat Flux
St^*_{xT}	h^*_{xT} $\frac{\text{kcal}}{\text{m}^2\ \text{sec deg}}$	$\frac{h^*_{xT}}{c}$ $\frac{\text{kcal}}{\text{m}^2\ \text{hr deg}}$	T_e °K	q $\frac{\text{kcal}}{\text{m}^2\ \text{sec}}$
Eq. (6.28)	(40) $\frac{(71)}{(39)}$ (66)(68)	$\frac{(72)}{(32)}$ $3.6\cdot10^3$	From (73), (34), and Fig. 54	$h^*_{xT}(T_r - T_e)$
$1.81\cdot10^{-3}$	0.0466	210	1900	159

NOTES: The italic numbers in parentheses indicate the column of the specified value.

Cols. 27-35: Calculations of the inviscid parameters for a laminar boundary layer.

Cols. 36-42: Calculations of the inviscid parameters for a turbulent boundary layer.

Cols. 43-58: Calculations of the effective parameters for a laminar boundary layer.

Cols. 59-74: Calculations of the effective parameters for a turbulent boundary layer.

The other point is located farther back so that its Reynolds number is $Re_x = 10^8$ and the boundary layer is turbulent. The distances from the apex to these points, x_L and x_T, are determined from the inviscid flow parameters and from the given Reynolds numbers.

The calculation of skin friction and heat transfer is initially made using the known inviscid flow parameters around the cone. These results are modified by using the effective parameters to account for the effects of compressibility and heat transfer.

It is apparent from the results in Table 10 that the refined values of the skin friction coefficients and the Stanton numbers are very different from their values using the inviscid parameters, particularly for the laminar boundary layer. On the other hand, the heat transfer coefficients and the equilibrium radiation temperatures change only slightly, although the differences are more significant in the case of the turbulent boundary layer.

The increases in the local skin friction coefficients and in the Stanton numbers by a factor of 3 for the laminar and a factor of 1.5 for the turbulent boundary layer reflect the influence of compressibility and heat transfer, which were taken into account by the use of the effective parameters. As was indicated, the calculations were made on the assumption that the Prandtl number was constant. It is not difficult to include a variable Prandtl number using the effective parameters, which then modifies the values of i_r and T_r. However, calculations show that the results were not substantially improved.

Some of these results (e.g., the wall temperature) make it possible to obtain a more accurate definition of the length of the laminar boundary layer in the vicinity of the nose. As studies show (for more detail, see Chap. VIII, § 26), the transition Reynolds number is determined by the local Mach number M_δ and the wall temperature ratio T_w/T_r (which is equal to T_e/T_r in the present example), with Re_{tr} being roughly inversely proportional to T_w/T_r. From Fig. 258 (p. 674), the transition Reynolds number is $Re_{tr} = 3 \cdot 10^6$ for $M_\delta = 10.4$ and $T_w/T_r = 1$, i.e., for an uncooled "adiabatic" wall. In agreement with the hypothesis of proportionality in the example considered, the transition Reynolds number is $9.3 \cdot 10^6$ for the same Mach number $M_\delta = 10.4$ and for the wall temperature

ratio of the example, $T_w/T_r = T_e/T_r = 0.321$. Thus, the cooling of the wall caused by radiation led to a threefold increase, approximately, in the extent of the laminar boundary layer. In our example, the length of the laminar boundary layer along the cone is less than 1 m (more accurately $1.86 \cdot 0.382 = 0.712$ m). An analysis of the equilibrium radiation temperature shows that its value depends on the flow regime in the boundary layer and on the coordinate of the point on the surface. In the special case considered, this temperature equals 1650°K at a distance from the nose of 0.382 m, increasing with proximity to the apex.

Transition to a turbulent boundary layer causes an increase in the wall temperature. For example, at a distance $x_T = 7.64$ m the wall temperature is $T_w = T_e = 1900$°K. This is a very high temperature, at which a metallic skin would melt. The emissivity of the surface can be raised to cool the wall; however, difficulties are encountered in providing an emissivity of more than about 0.8. Therefore, the internal wall surface must be cooled or the skin must be protected by insulation.

The Temperature of an Insulated Wall, Cooled Internally. Let us consider the case of a wall consisting of an outer insulation and a skin, with thicknesses δ_{in} and δ_s, respectively. A certain amount of heat, q_c, is carried off from within with the help of a fluid coolant. The equation for thermal balance with steady state heat transfer is written in the form $q_w - q_{in} - q_c = 0$; i.e.,

$$\sigma T_w^4 = \frac{h}{\varepsilon}(T_r' - T_w), \tag{6.29}$$

where we have used the reduced recovery temperature $T_r' = T_r(1 - q_c/hT_r)$. In this equation, the heat absorbed by the insulation is zero, and it is assumed that the radiant energy flux to the wall is zero. The heat flux carried away by the coolant is usually set beforehand. Consequently, the problem of determining the equilibrium radiation temperature of the wall is solved in the same way as was shown in the example.

To estimate the expected reduction of this temperature, let us assume, for example, that $q_c = 30$ kcal/m^2 sec and investigate a point on the surface with the same coordinate $x_L = 0.382$, for which $h^*_{xL} = 3.06 \cdot 10^{-2}$ kcal/m^2 sec deg was calculated. From these data we find $q_c/h^*_{xL}T_r = 0.185$

and the reduced recovery temperature $T_r' = 4300°K$. Therefore, from Fig. 54, the equilibrium temperature of the wall is $T_w = T_e = 1550°K$; i.e., the temperature was successfully lowered 100°K by means of cooling.

The external and internal temperatures of the skin T_e and T_i, respectively, can be determined from the value found for T_w. The calculation is based on the assumption that for steady state heat transfer the heat flux through the insulation and skin is equal to that removed by the cooling system; therefore,

$$\lambda_{in}\left(\frac{\partial T}{\partial y}\right)_{in} = \lambda_s\left(\frac{\partial T}{\partial y}\right)_s = q_e,$$

which includes, of course, the coefficients of thermal conductivity of the insulation and skin materials. If it is assumed that their values are constant, the above relation can be integrated with respect to the insulation and skin thicknesses, resulting in

$$T_s = T_w - \frac{q_e\delta_{in}}{\lambda_{in}}, \qquad T_i = T_s - \frac{q_e\delta_s}{\lambda_s}. \tag{6.30}$$

Let us assume that a ceramic coating of a thickness $\delta_{in} = 10$ mm is chosen as the insulation. Since the thermal conductivity coefficient of this coating is $\lambda_{in} = 6\cdot10^{-4}$ kcal/m sec deg, the skin temperature is

$$T_s = 1550 - \frac{30\cdot10\cdot10^{-3}}{6\cdot10^{-4}} = 1050°K.$$

If the skin is made of metal, the temperature on its internal surface remains almost the same as on its external surface. For example, let the thickness of a steel skin be $\delta_s = 5$ mm. Since the thermal conductivity coefficient of steel is $\lambda_s = 1.08\cdot10^{-2}$ kcal/m sec deg, $T_i = 1036°K$, or a temperature drop across the skin of 14°.

The Temperature of a Thin Wall with Unsteady Heat Transfer. When the wall temperature varies with time, the heating process will differ from steady state heat transfer. If a thin metal skin with large thermal

conductivity is examined, the temperature gradient across its thickness can be neglected. Equation (5.28) can be used to calculate the wall temperature, with the heat flux $q_w = c\gamma\delta(dT_w/dt)$. Internal surface radiation will be neglected for this case, although the necessary correction can easily be made.

Thus, the problem is reduced to the solution of the differential equation, Eq. (5.28), for some initial temperature. For example, this can be the equilibrium radiation temperature at a constant velocity and altitude. At some given time, an unsteady portion of flight is begun (e.g., an acceleration or deceleration of the aircraft).

The free-stream Mach number is known from the trajectory calculations for the time $t + \Delta t$, where Δt is an arbitrary interval of time. The appropriate inviscid flow parameters can be computed, as well as the values of h_x and T_r, at a given point on the surface. Using these data, a first approximation can be computed for the derivative

$$c\gamma\delta\left(\frac{dT_w}{dt}\right)_1 = h(T_r - T_w) + \varepsilon\sigma T_w^4. \tag{6.31}$$

A corrected value for the wall temperature is given by

$$T_w^{(1)} = T_e + \Delta T = T_e + \left(\frac{dT_w}{dt}\right)_1 \Delta t.$$

By use of this temperature, a second approximation can be calculated for the values of h_x, T_r, T_e, the derivative in Eq. (6.31), and the wall temperature $T_w^{(2)}$. If the time interval has been chosen sufficiently small, it is usually only necessary to use the first approximation for Eq. (6.31).

The calculation method cited for unsteady heat transfer cannot be applied to materials of low heat conductivity nor to thick skins. In these cases, a large temperature gradient across the thickness of a thick wall or of a layer of insulation is a characteristic feature, and the temperature of the outer surface will be considerably higher than the average temperature.

§ 7. THE CIRCULAR CONE AT AN ANGLE OF ATTACK

THE EQUATION SYSTEM AND ITS SOLUTION

Conical Flow Equations

AS IN THE CASE of supersonic symmetric flow, flow around a cone at an angle of attack will possess the character of conical flow but with the difference that the parameters are not completely constant on a conical surface, but only along specific rectilinear rays. The parameters in such a flow generally vary on transition from one ray to another, all passing through the tip of the cone.

Let us examine a conical flow in a spherical system of coordinates r, θ, ϕ (Fig. 72), chosen so that the coordinate $r = 0$ coincides with the tip of the cone, the free-stream flow direction coincides with the

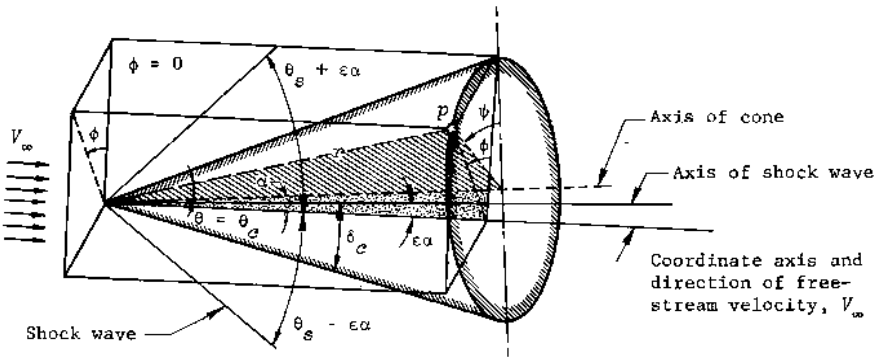

Fig. 72--Flow diagram for a cone at angle of attack

axis $\theta = 0$, and the plane passing through the free-stream velocity vector and the axis of symmetry of the cone corresponds to the meridian plane $\phi = 0$. In this coordinate system, the equation of the cone inclined to the velocity vector at an angle α (in Fig. 72 this angle is negative) is as follows:

$$\cos \theta_c \cos \alpha - \sin \theta_c \sin \alpha \cos \varphi = \cos \delta_c, \tag{7.1}$$

where θ_c is the spherical coordinate of the cone surface. According to the nature of conical flow, the flow parameters are independent of r but are functions of the variables θ, ϕ. Therefore, derivatives with respect to r do not appear in the flow equations. In studying symmetric flow past a cone, we used the fact that the flow was irrotational. For the general case of asymmetric conical supersonic flow, the flow is also isentropic in a plane $\phi = \text{const}$ because the intersection of this plane with the shock surface is a straight line, and the entropy does not change. This is true for all planes $\phi = \text{const}$, but since the slope of the shock wave is not the same for all planes, the entropy is not the same and is a function of the angle ϕ. Hence, it follows that asymmetric conical flow is nonisentropic and, in general, must be calculated allowing for the entropy variation from one plane $\phi = \text{const}$ to another.

The theoretical bases for the study of such flow are the equations of motion, Eq. (3.8), and continuity, Eq. (3.17). If the conical asymmetric flow is steady, these equations are

$$V_\theta \frac{\partial V_r}{\partial \theta} + \frac{V_\phi}{\sin \theta} \frac{\partial V_r}{\partial \phi} - V_\theta^2 - V_\phi^2 = 0,$$

$$V_\theta \frac{\partial V_\theta}{\partial \theta} + \frac{V_\phi}{\sin \theta} \frac{\partial V_\theta}{\partial \phi} + V_r V_\theta - V_\phi^2 \cot \theta = -\frac{1}{\rho} \frac{\partial p}{\partial \theta}, \tag{7.2}$$

$$V_\theta \frac{\partial V_\phi}{\partial \theta} + \frac{V_\phi}{\sin \theta} \frac{\partial V_\phi}{\partial \phi} + V_r V_\phi + V_\theta V_\phi \cot \theta = -\frac{1}{\rho \sin \theta} \frac{\partial p}{\partial \phi},$$

$$2\rho V_r \sin \theta + \frac{\partial(\rho V_\theta \sin \theta)}{\partial \theta} + \frac{\partial(\rho V_\phi)}{\partial \phi} = 0, \tag{7.3}$$

where V_r, V_θ, and V_ϕ are the velocity components corresponding to the spherical coordinate system selected.

From the nature of conical flow, it follows that the solutions for V_r, V_θ, V_ϕ, and also for p and ρ, will be independent of r. Therefore, we can seek solutions in the form

$$
\begin{aligned}
V_r &= V_r^0(\theta) - \alpha \sum_{n=0}^{\infty} x_n(\theta) \cos n\phi + \alpha^2 \sum_{n=0}^{\infty} \hat{u}_n(\theta) \cos n\phi + \ldots, \\
V_\theta &= V_\theta^0(\theta) - \alpha \sum_{n=0}^{\infty} y_n(\theta) \cos n\phi + \alpha^2 \sum_{n=0}^{\infty} \hat{v}_n(\theta) \cos n\phi + \ldots, \\
V_\phi &= -\alpha \sum_{n=0}^{\infty} z_n(\theta) \sin n\phi + \alpha^2 \sum_{n=0}^{\infty} \hat{w}_n(\theta) \sin n\phi + \ldots, \qquad (7.4) \\
p &= p^0(\theta) - \alpha \sum_{n=0}^{\infty} \eta_n(\theta) \cos n\phi + \alpha^2 \sum_{n=0}^{\infty} \hat{p}_n(\theta) \cos n\phi + \ldots, \\
\rho &= \rho^0(\theta) - \alpha \sum_{n=0}^{\infty} \xi_n(\theta) \cos n\phi + \alpha^2 \sum_{n=0}^{\infty} \hat{\rho}_n(\theta) \cos n\phi + \ldots,
\end{aligned}
$$

where $V_r^0(\theta)$, $V_\theta^0(\theta)$, $p^0(\theta)$, and $\rho^0(\theta)$ are the parameters for symmetric flow on an intermediate conical surface with angle θ.

Each of the expressions in Eq. (7.4) is a series in which the linear term with respect to angle of attack represents the first-order approximation and the quadratic term the second-order approximation of the complete solution. For small angles of attack, the parameters will differ little from their values in symmetric flow, and the influence of the angle of attack is represented adequately by the linear terms. When α increases, it becomes necessary to use the second-order terms in the calculation. Henceforth, we will limit the discussion to these approximations, assuming that the angle of attack does not exceed approximately

15°. Therefore, the coefficients x_n, y_n, z_n, η_n, and ξ_n in the first-order terms and the coefficients $\hat{u}_n$, $\hat{v}_n$, $\hat{w}_n$, $\hat{p}_n$, and $\hat{\rho}_n$ in the second-order terms can be considered as the quantities that determine the effect of the angle of attack. All of these coefficients are functions of one variable, θ; therefore, their solutions can be found from ordinary differential equations.

From Eq. (7.4) it follows that determination of the flow parameters for a cone at an angle of attack begins with the solution of the particular problem of symmetric flow around the same cone. This results in finding the values of V_r°, V_θ°, p°, and ρ° as functions of the angle θ. The effect of angle of attack is examined below for the first-order approximation and then for the second-order.

The First-order Approximation

The initial problem is the determination of the coefficients x_n, y_n, z_n, η_n, and ξ_n in Eq. (7.4) assuming that the squared or higher power terms are absent. Studies have shown that the solution will have physical meaning if the value $n = 1$ is assumed in the remaining linear terms. Then Eq. (7.4) is written

$$\begin{aligned} V_r &= V_r^\circ(\theta) - \alpha x(\theta) \cos\phi, \\ V_\theta &= V_\theta^\circ(\theta) - \alpha y(\theta) \cos\phi, \\ V_\phi &= -\alpha z(\theta) \sin\phi, \\ p &= p^\circ(\theta) - \alpha\eta(\theta) \cos\phi, \\ \rho &= \rho^\circ(\theta) - \alpha\xi(\theta) \cos\phi. \end{aligned} \tag{7.5}$$

The coefficients $x(\theta)$, $y(\theta)$, $z(\theta)$, $\eta(\theta)$, and $\xi(\theta)$ are the unknowns that must be evaluated in the solution of the first approximation.

This solution has much in common with that of the problem of symmetric flow around a cone. In the case of zero angle of attack, the problem requires the solution of Eq. (6.6). In the present case, the

differential equations are given by Eqs. (7.2) and (7.3), and their solutions are sought in the form of Eq. (7.5). In addition, the Bernoulli equation

$$\frac{V_r^2 + V_\theta^2 + V_\phi^2}{2} + \frac{\gamma}{\gamma - 1}\frac{p}{\rho} = \frac{V_{\max}^2}{2} \tag{7.6}$$

must be included, as well as an expression for the entropy. The latter reflects the fact that the finite change in entropy on passing through a shock wave is a function of the shock angle and therefore the coordinate ϕ. If the entropy expression is written in the form

$$\frac{1}{c_v}(S - S^0) = \log\frac{p}{p^0} - \gamma \log\frac{\rho}{\rho^0},$$

where S and S^0 are the corresponding values for asymmetric and symmetric flow past a cone, the condition mentioned above can be presented in the form

$$\log\left[\frac{p}{p^0}\left(\frac{\rho^0}{\rho}\right)^\gamma\right] = -\alpha d \cos\phi. \tag{7.7}$$

In this equation, the ratio $p^0/(\rho^0)^\gamma$ is a constant, since symmetric flow is totally isentropic; the coefficient d results from substituting Eq. (7.5) for p and ρ in Eq. (7.7). The resulting relation has the form

$$d = \frac{\eta}{p^0} - \frac{\gamma\xi}{\rho^0}. \tag{7.8}$$

Inserting Eq. (7.5) for the unknown parameters in Eqs. (7.2), (7.3), (7.6), and (7.7), after some transformation we obtain differential equations for x, y, and z of the form

$$\frac{x''}{d} + A\frac{x'}{d} + B\frac{x}{d} + C = 0. \tag{7.9}$$

This equation is used to determine the quantity x/d and is a basic equation in the first-order theory. It is a nonhomogeneous differential

equation of the second order with variable coefficients A, B, and C, which are functions of the unknown quantities V_r^o, V_θ^o, and also the angle θ.

The equation is integrated starting from the conditions at the shock wave for symmetric flow, $\theta = \theta_s$, until the conditions on the cone are satisfied; i.e., the normal velocity component equals zero for $\theta = \delta_c$ (θ is measured from the axis of the cone). As a result of the numerical calculations, x can be found as a function of θ, after which the other coefficients can be calculated.

The coefficients x, y, and z, referred to the maximum velocity V_{max}, and also the dimensionless quantities η/p^o and ξ/ρ^o, have been tabulated for a series of cone angles and free-stream Mach numbers;[4] part of these results are presented in Tables 11 and 12.† Using these tables, the velocity components, pressure, and density can be calculated from Eq. (7.5), and the axial and normal force components can be computed from the resulting pressure distribution.

It has been found that the value of the axial force component does not change from its value in symmetric flow. Therefore, to the first order the axial force coefficient is equal to the pressure coefficient on a cone at a zero angle of attack, C_{pc}, which is given by Eq. (6.19) or in Figs. 62 and 63. It is also possible to use Table 14 (see p. 220), in which values of the coefficient $K_D = (\pi/8)C_{pc}$ are presented.

The normal force coefficient C_{Np} can be calculated with the help of the quantity K_N presented in Table 12, where $C_{Np} = (8/\pi)\alpha K_N$. In turn, the quantity K_N is determined from the expression

$$K_N = \frac{N_p}{\rho_\infty V_\infty^2 d_{mid}^2 \alpha} = \frac{\pi \eta_c \cot \delta_c}{8 \rho_\infty V_\infty^2}, \qquad (7.10)$$

where η_c is the value of $\eta(\theta)$ at the surface of the cone.

In determining the shape of the shock wave, we have assumed that it is a circular cone with an apex angle equal to the angle of the conical

†Editor's note: Values of ξ/ρ^o are not tabulated in Tables 11 and 12. They can be found in the cited reference by Kopal, or the density can be computed from the Bernoulli equation, Eq. (7.6).

shock in symmetric flow. The axis of the conical shock is inclined to the direction of the free stream at an angle

$$\delta = -\varepsilon\alpha, \tag{7.11}$$

which is called the angle of attack of the shock wave. The coefficient ε that determines the magnitude of this angle is given in Tables 12 and 14.

The Second-order Approximation

It can be shown that the series in Eq. (7.4) have physical meaning to the second order if the equations are written in the form

$$\begin{aligned}
V_r &= V_r^0(\theta) - \alpha x(\theta)\cos\phi + \alpha^2[\hat{u}_0(\theta) + \hat{u}_2(\theta)\cos 2\phi],\\
V_\theta &= V_\theta^0(\theta) - \alpha y(\theta)\cos\phi + \alpha^2[\hat{v}_0(\theta) + \hat{v}_2(\theta)\cos 2\phi],\\
V_\phi &= -\alpha z(\theta)\sin\phi + \alpha^2\hat{w}_2(\theta)\sin 2\phi,\\
p &= p^0(\theta) - \alpha\eta(\theta)\cos\phi + \alpha^2[\hat{p}_0(\theta) + \hat{p}_2(\theta)\cos 2\phi],\\
\rho &= \rho^0(\theta) - \alpha\xi(\theta)\cos\phi + \alpha^2[\hat{\rho}_0(\theta) + \hat{\rho}_2(\theta)\cos 2\phi],
\end{aligned} \tag{7.12}$$

The coefficients $\hat{u}_0$, $\hat{u}_2$, $\hat{v}_0$, $\hat{v}_2$, $\hat{w}_2$, $\hat{p}_0$, $\hat{p}_2$, $\hat{\rho}_0$, and $\hat{\rho}_2$ are unknown in these expressions. The coefficients x, y, z, η, and ξ are assumed known because they were found in the first-order solution.

The unknown coefficients are determined in the same manner as for the first-order solution, i.e., by substituting Eq. (7.12) into Eqs. (7.2), (7.3), (7.6), and into the condition for entropy, which is now written as follows:

$$\log\left[\frac{p}{p^0}\left(\frac{\rho_0}{\rho}\right)^\gamma\right] = -\alpha d\cos\phi + \alpha^2(l_0 + l_2\cos 2\phi), \tag{7.13}$$

where l_0 and l_2 are coefficients that determine the entropy change to the second order. As a result of these substitutions we obtain a series

Table 11

COEFFICIENTS FOR THE FIRST APPROXIMATION OF THE FLOW FIELD ABOUT A CONE AT ANGLE OF ATTACK ($\gamma = 1.4$)

$\theta°$	x	y	z	η/p^0	$\theta°$	x	y	z	η/p^0
δ_c=10°, $\tilde{V}_c$=0.55, M_∞=1.5956, θ_s=39.708°					δ_c=10°, $\tilde{V}_c$=0.75, M_∞=2.7794, θ_s=23.101°				
10	-0.1737	1.1000	1.0003	0.9499	10	-0.1983	1.5000	1.1526	2.3365
14	-0.1168	0.6090	0.4834	1.0398	11	-0.1741	1.2825	0.9200	2.5590
18	-0.0823	0.4054	0.2666	0.9353	12	-0.1532	1.1213	0.7428	2.6616
22	-0.0582	0.2976	0.1553	0.8173	14	-0.1182	0.8991	0.4927	2.6942
26	-0.0399	0.2306	0.0910	0.7092	16	-0.0896	0.7534	0.3275	2.6287
30	-0.02549	0.1838	0.05101	0.6114	18	-0.0651	0.6512	0.2124	2.5631
34	-0.01398	0.1474	0.02501	0.5201	20	-0.0438	0.5783	0.1288	2.4449
38	-0.00478	0.1173	0.00777	0.4351	22	-0.0244	0.5397	0.0653	2.4471
39.708	-0.00133	0.1263	0.00209	0.4792	23.101	-0.0138	0.5839	0.0352	2.7520
δ_c=10°, $\tilde{V}_c$=0.85, M_∞=4.0748, θ_s=17.518°					δ_c=10°, $\tilde{V}_c$=0.97, M_∞=15.146, θ_s=11.568°				
10	-0.1971	1.7000	1.2027	3.9392	10.0	-0.1943	1.9400	1.7483	9.679
11	-0.1695	1.4750	0.9294	4.4054	10.3	-0.1844	1.8754	1.3784	10.768
12	-0.1452	1.3141	0.7279	4.6594	10.5	-0.1778	1.8407	1.2407	11.442
14	-0.1034	1.1047	0.4417	4.9033	11.0	-0.1620	1.7847	0.9667	13.095
16	-0.0670	0.9972	0.2480	5.1342	11.5	-0.1465	1.7815	0.7473	15.023
17.518	-0.0405	1.0411	0.1345	5.8849	11.568	-0.1444	1.7869	0.7199	15.344
δ_c=20°, $\tilde{V}_c$=0.50, M_∞=1.6531, θ_s=44.424°					δ_c=20°, $\tilde{V}_c$=0.75, M_∞=3.3694, θ_s=28.180°				
20	-0.2967	1.0000	0.8913	1.3347	20	-0.3396	1.5000	1.2299	3.0747
24	-0.2360	0.7633	0.5933	1.5078	21	-0.3142	1.4110	1.0276	3.3480
28	-0.1878	0.6287	0.4086	1.5353	22	-0.2902	1.3402	0.8881	3.5647
32	-0.1471	0.5440	0.2830	1.5181	24	-0.2453	1.2405	0.6661	3.9128
36	-0.1112	0.4887	0.1923	1.4951	26	-0.2031	1.1893	0.4912	4.2572
40	-0.0783	0.4567	0.1232	1.4985	27	-0.1823	1.1857	0.4158	4.4818
44.424	-0.0429	0.4826	0.0613	1.6978	28.180	-0.1577	1.2150	0.3340	4.8822

Table 11--continued

$\theta°$	x	y	z	T/p°	$\theta°$	x	y	z	η/p°
$\delta_c=20°$, $\tilde{V}_c=0.85$, $M_\infty=5.5457$, $\theta_s=24.433°$					$\delta_c=20°$, $\tilde{V}_c=0.90$, $M_\infty=9.5928$, $\theta_s=22.834°$				
20.0	-0.3637	1.7000	1.5511	4.1834	20.0	-0.3812	1.8000	1.7944	4.8835
21.0	-0.3348	1.6135	1.1830	4.7523	20.5	-0.3657	1.7550	1.4329	5.3772
22.0	-0.3072	1.5537	0.9697	5.2494	21.0	-0.3505	1.7197	1.2449	5.8409
23.0	-0.2804	1.5200	0.7954	5.7461	22.0	-0.3209	1.6812	0.9574	6.7719
24.0	-0.2540	1.5187	0.6454	6.3326	22.5	-0.3062	1.6810	0.8377	7.2957
24.433	-0.2424	1.5328	0.5861	6.6541	22.834	-0.2964	1.6907	0.7638	7.6966
$\delta_c=30°$, $\tilde{V}_c=0.50$, $M_\infty=2.0470$, $\theta_s=47.414°$					$\delta_c=30°$, $\tilde{V}_c=0.65$, $M_\infty=3.1617$, $\theta_s=39.175°$				
30	-0.4428	1.0000	1.0562	1.6540	30	-0.4904	1.3000	1.3576	2.3585
34	-0.3777	0.8765	0.7593	1.8888	32	-0.4464	1.2250	1.0367	2.6681
38	-0.3693	0.8056	0.5669	2.0316	34	-0.4046	1.1752	0.8429	2.9245
42	-0.2645	0.7707	0.4189	2.1630	36	-0.3641	1.1486	0.6831	3.1746
46	-0.2108	0.7765	0.2984	2.3711	38	-0.3241	1.1492	0.5475	3.4735
47.414	-0.1914	0.7966	0.2600	2.5039	39.175	-0.3004	1.1692	0.4755	3.7123
$\delta_c=30°$, $\tilde{V}_c=0.75$, $M_\infty=5.0109$, $\theta_s=35.631°$					$\delta_c=30°$, $\tilde{V}_c=0.83$, $M_\infty=16.617$, $\theta_s=33.444°$				
30	-0.5351	1.5000	1.6577	2.8717	30.0	-0.5786	1.6600	1.9575	3.3018
31	-0.5093	1.4590	1.3231	3.1651	30.5	-0.5641	1.6388	1.6026	3.5635
32	-0.4841	1.4277	1.1416	3.4351	31.0	-0.5499	1.6210	1.4294	3.8170
33	-0.4594	1.4069	0.9922	3.6985	32.0	-0.5218	1.5987	1.1664	4.3229
34	-0.4349	1.3976	0.8621	3.9737	33.0	-0.4939	1.5982	0.9563	4.8730
35.631	-0.3951	1.4150	0.6781	4.5161	33.444	-0.4815	1.6072	0.8737	5.1518

Table 12

COEFFICIENTS FOR THE FIRST APPROXIMATION OF THE SURFACE CONDITIONS ON A CONE AT ANGLE OF ATTACK ($\gamma = 1.4$)

$\tilde{V}_e$	M_∞	x	y	z	η/p°	d	ϵ	K_N
				$\delta_e = 10°$				
0.40	1.0901	-0.1406	0.8000	0.8098	0.4645	0	0.0884	0.7151
0.45	1.2330	-0.1523	0.9000	0.8771	0.5963	0	0.0753	0.7195
0.50	1.4028	-0.1635	1.0000	0.9417	0.7562	0	0.0886	0.7188
0.60	1.8165	-0.1825	1.2000	1.0515	1.1864	0.0002	0.1508	0.7152
0.70	2.3869	-0.1951	1.4000	1.1278	1.8515	0.0027	0.2630	0.7132
0.80	3.3041	-0.1990	1.6000	1.1731	2.9950	0.0295	0.4354	0.7168
0.90	5.4223	-0.1933	1.8000	1.2801	5.4019	0.3854	0.6902	0.7327
0.95	9.0999	-0.1915	1.9000	1.5256	7.981	2.010	0.8791	0.7518
0.97	15.146	-0.1943	1.9400	1.7483	9.679	5.041	0.9815	0.7650
0.98	37.064	-0.1975	1.9600	1.9130	10.739	9.366	1.0426	0.7737
				$\delta_e = 20°$				
0.35	1.2175	-0.2761	0.7000	0.8182	0.7535	0.0042	0.4748	0.6152
0.40	1.3144	-0.2786	0.8000	0.8247	0.9091	0.0046	0.4251	0.6238
0.45	1.4672	-0.2873	0.9000	0.8546	1.1054	0.0079	0.4444	0.6297
0.50	1.6531	-0.2967	1.0000	0.8913	1.3347	0.0152	0.4880	0.6348
0.60	2.1297	-0.3141	1.2000	0.9834	1.8979	0.0587	0.6017	0.6459
0.70	2.8387	-0.3305	1.4000	1.1254	2.5291	0.2099	0.7288	0.6596
0.80	4.1538	-0.3505	1.6000	1.3679	3.5875	0.7343	0.8644	0.6763
0.90	9.5928	-0.3812	1.8000	1.7944	4.8535	3.096	1.0161	0.6978
0.927	44.696	-0.3930	1.8540	1.9582	5.3170	5.124	1.0619	0.7050
				$\delta_e = 30°$				
0.35	1.5164	-0.4465	0.7000	0.9852	1.1080	0.0517	0.8434	0.5409
0.40	1.6404	-0.4320	0.8000	0.9662	1.2585	0.0684	0.7959	0.5397
0.45	1.8199	-0.4340	0.9000	0.9974	1.4458	0.1026	0.8001	0.5444
0.50	2.0470	-0.4428	1.0000	1.0562	1.6540	0.1597	0.8244	0.5506

Table 12--continued

$\tilde{V}_c$	M_∞	x	y	z	η/p°	d	ε	K_N
$\delta_c = 30°$								
0.60	2.6863	-0.4718	1.2000	1.2373	2.1134	0.3870	0.8942	0.5646
0.70	3.8497	-0.5115	1.4000	1.4975	2.6114	0.9151	0.9716	0.5785
0.80	7.8599	-0.5614	1.6000	1.8386	3.1368	2.235	1.0496	0.5919
0.83	16.617	-0.5786	1.6600	1.9575	3.3018	3.000	1.0728	0.5965

of differential equations with one independent variable, θ, whose solution enables us to calculate the unknown coefficient in each specific case.

The coefficients thus found have been tabulated in Table 13,[5] where the coefficients $\hat{u}_0$, $\hat{u}_2$, $\hat{v}_0$, $\hat{v}_2$, and $\hat{w}_2$ are referred to the maximum velocity, and, instead of coefficients for determining pressure and density, their dimensionless values $\hat{p}_0/p^\circ$, $\hat{p}_2/p^\circ$, $\hat{\rho}_0/\rho^\circ$, $\hat{\rho}_2/\rho^\circ$ are presented.†

From the second-order solution it is possible to refine the axial force coefficient. The normal force coefficient does not change in comparison to the first-order approximation, but the axial force coefficient becomes a function of the coefficient K_{D2}.†† The values of this coefficient are presented in Table 14. The shock wave changes its shape somewhat compared with the first-order approximation. The equation for the shock wave is written in the form

$$\theta = \theta_s - a\varepsilon \cos\phi + a^2(\mu_0 + \mu_2 \cos 2\phi). \qquad (7.14)$$

The coefficients μ_0 and μ_2 are also presented in Table 14. Equation (7.14) shows that the shock can be considered an approximately conical surface with the same angle at the tip as in the case of symmetric flow.

†Editor's note: Again, the density parameters are omitted. The Kopal tables can be referred to, or the density calculated from the Bernoulli equation.

††Editor's note: See Eq. (7.35) for the use of K_{D2}.

Table 13

COEFFICIENTS FOR THE SECOND APPROXIMATION OF THE FLOW FIELD ABOUT A CONE AT ANGLE OF ATTACK ($\gamma = 1.4$)

$\theta°$	$\hat{u}_0$	$\hat{u}_2$	$\hat{v}_0$	$\hat{v}_2$	$\hat{w}_2$	$\hat{p}_0/p^o$	$\hat{p}_2/p^o$
$\delta_c = 10°$, $\tilde{V}_c = 0.55$, $M_\infty = 1.5956$, $\theta_s = 39.708°$							
10	-0.0824	-0.7437	-0.174	8.704	8.568	-4.962	3.633
14	-0.0883	-0.3709	0.001	3.219	3.065	-0.866	3.963
18	-0.0836	-0.2134	0.118	1.565	1.380	0.143	2.948
22	-0.0731	-0.1309	0.172	0.886	0.698	0.510	2.155
26	-0.0603	-0.0819	0.197	0.553	0.374	0.672	1.600
30	-0.0461	-0.0503	0.208	0.369	0.201	0.751	1.207
34	-0.0312	-0.0287	0.215	0.259	0.103	0.801	0.926
38	-0.0157	-0.0132	0.223	0.194	0.043	0.867	0.742
39.708	-0.0089	-0.0078	0.226	0.175	0.026	0.892	0.711
$\delta_c = 10°$, $\tilde{V}_c = 0.75$, $M_\infty = 2.7794$, $\theta_s = 23.101°$							
10	-0.2025	-0.8673	-0.1987	10.568	9.176[a]	-11.091	7.328
11	-0.1995	-0.7176	-0.1651	7.916	7.419	-6.649	9.357
12	-0.1965	-0.5973	-0.0576	6.131	5.663	-3.818	9.987
14	-0.1934	-0.4261	0.1824	3.959	3.467	-0.507	9.647
16	-0.1832	-0.3110	0.3850	2.749	2.218	1.353	8.677
18	-0.1667	-0.2291	0.5489	2.011	1.459	2.580	7.667
20	-0.1451	-0.1678	0.6879	1.529	0.967	3.532	6.758
22	-0.1191	-0.1211	0.7750	1.137	0.640	4.257	5.769
23.101	-0.1066	-0.1041	0.8415	0.326	0.529	5.138	5.188
$\delta_c = 10°$, $\tilde{V}_c = 0.85$, $M_\infty = 4.0748$, $\theta_s = 17.518°$							
10	-0.3249	-0.8397[a]	-0.197	10.771	8.24[a]	-18.01	9.92
11	-0.3084	-0.7415	-0.123	8.079	7.03	-10.05	14.55
12	-0.3054	-0.6234	-0.099	6.251	5.52	-4.95	15.27
13	-0.3034	-0.5281	-0.091	4.963	4.35	-1.40	15.97
14	-0.2994	-0.4511	0.271	4.009	3.48	1.25	16.39
16	-0.2844	-0.3373	0.516	2.587	2.33	4.85	14.59
17.518	-0.2758	-0.2876	-0.397	0.638	1.87	7.71	12.21

Table 13--continued

$\theta°$	$\hat{u}_0$	$\hat{u}_2$	$\hat{v}_0$	$\hat{v}_2$	$\hat{w}_2$	$\hat{p}_0/p^0$	$\hat{p}_2/p^0$
$\delta_c = 20°$, $\tilde{V}_c = 0.50$, $M_\infty = 1.6531$, $\theta_s = 44.424°$							
20	-0.1822[b]	-0.5733[b]	-0.2967	3.544	3.176[b]	-3.244	2.227
24	-0.1780	-0.4193	-0.1806	2.061	1.996	-1.224	2.777
28	-0.1837	-0.3058	-0.0450	1.323	1.256	-0.252	2.596
32	-0.1821	-0.2299	0.0702	0.904	0.836	0.333	2.274
36	-0.1735	-0.1768	0.1668	0.639	0.581	0.752	1.944
40	-0.1590	-0.1392	0.2459	0.445	0.422	1.090	1.601
44.424	-0.1398	-0.1156	0.1534	0.050	0.326	0.916	0.505
$\delta_c = 20°$, $\tilde{V}_c = 0.60$, $M_\infty = 2.1297$, $\theta_s = 36.124°$							
20	-0.2695[b]	-0.6135[b]	-0.3141	3.829	3.025[c]	-4.51	2.63
24	-0.2449	-0.4667	-0.1936	2.237	2.091	-1.505	3.788
28	-0.2485	-0.3453	-0.0135	1.422	1.354	-0.014	3.665
32	-0.2433	-0.2654	0.1312	0.912	0.940	0.918	3.172
34	-0.2380	-0.2378	0.1542	0.664	0.810	1.185	2.722
36.124	-0.2346	-0.2208	-0.0653	0.149	0.726	0.657	1.291
$\delta_c = 20°$, $\tilde{V}_c = 0.70$, $M_\infty = 2.8387$, $\theta_s = 30.435°$							
20	-0.4203[d]	-0.6341[d]	-0.3305	3.953	1.609[b]	-6.42	2.84
22	-0.3377	-0.6140	-0.3327	3.045	2.499	-3.695	4.481
24	-0.3367	-0.5323	-0.2560	2.337	2.121	-1.901	5.076
26	-0.3407	-0.4638	-0.1693	1.795	1.782	-0.633	5.134
28	-0.3446	-0.4108	-0.1273	1.308	1.531	-0.227	4.759
30.435	-0.3534	-0.3718	-0.0601	0.382	1.353	-0.118	2.709

[a] For $\theta = 10.25°$.

[b] For $\theta = 20.25°$.

[c] For $\theta = 20.5°$.

[d] For $\theta = 20.125°$.

Table 14

COEFFICIENTS FOR THE SECOND APPROXIMATION OF THE SURFACE CONDITIONS ON A CONE AT ANGLE OF ATTACK ($\gamma = 1.4$)

$\bar{V}_c$	θ_s°	M_∞	K_D	K_N	ε	K_{D2}	μ_0	μ_2	d
				$\delta_c = 10°$					
0.40	68.653	1.0901	0.07243	0.7151	0.0884	0.28	0.25	0.03	0
0.45	55.162	1.2330	0.05784	0.7195	0.0753	0.53	0.14	0.06	0
0.50	46.309	1.4028	0.05113	0.7188	0.0886	0.91	0.15	0.10	0
0.55	39.708	1.5956	0.04666	0.7171	0.1140	1.43	0.23	0.16	0.0001
0.60	34.452	1.8165	0.04318	0.7152	0.1508	2.11	0.33	0.24	0.0002
0.65	30.091	2.0750	0.04028	0.7138	0.2001	3.04	0.43	0.34	0.0008
0.70	26.363	2.3869	0.03772	0.7132	0.2630	4.30	0.53	0.44	0.0027
0.75	23.101	2.7794	0.03539	0.7139	0.3408	6.10	0.61	0.55	0.0089
0.80	20.184	3.3041	0.03319	0.7168	0.4354	8.68	0.66	0.66	0.0295
0.85	17.518	4.0748	0.03101	0.7224	0.5495	12.34	0.71	0.77	0.1011
				$\delta_c = 15°$					
0.40	61.679	1.1916	0.12292	0.6682	0.2337	0.37	0.48	0.09	0.0004
0.45	51.757	1.3382	0.10428	0.6731	0.2408	0.64	0.39	0.15	0.0007
0.50	44.559	1.5144	0.09362	0.6752	0.2772	1.04	0.41	0.21	0.0016
0.55	39.043	1.7178	0.08614	0.6769	0.3287	1.57	0.45	0.28	0.0038
0.60	34.620	1.9541	0.08034	0.6793	0.3899	2.26	0.48	0.34	0.0091
0.65	30.959	2.2345	0.07557	0.6827	0.4585	3.13	0.50	0.40	0.0214
0.70	27.854	2.5787	0.07148	0.6874	0.5331	4.16	0.48	0.45	0.0492
0.75	25.163	3.0217	0.06785	0.6933	0.6130	5.33	0.42	0.51	0.1113
0.80	22.784	3.6345	0.06455	0.7009	0.6992	6.31	0.32	0.57	0.2521
				$\delta_c = 20°$					
0.35	68.507	1.2175	0.21723	0.6152	0.4748	1.34	2.66	0.04	0.0042
0.40	58.043	1.3144	0.17594	0.6238	0.4251	0.75	0.72	0.11	0.0046
0.45	50.281	1.4672	0.15498	0.6297	0.4444	0.69	0.55	0.17	0.0079
0.50	44.424	1.6531	0.14162	0.6348	0.4880	1.05	0.50	0.22	0.0152

Table 14--continued

$\tilde{V}_c$	θ_s°	M_∞	K_D	K_N	ϵ	K_{D2}	u_0	u_2	d
$\delta_c = 20^\circ$									
0.55	39.835	1.8714	0.13199	0.6401	0.5422	1.50	0.47	0.27	0.0301
0.60	36.124	2.1297	0.12650	0.6459	0.6017	2.01	0.43	0.31	0.0587
0.65	33.045	2.4431	0.11841	0.6524	0.6642	2.50	0.37	0.35	0.1120
0.70	30.435	2.8387	0.11325	0.6596	0.7288	2.82	0.29	0.40	0.2099
$\delta_c = 25^\circ$									
0.35	64.819	1.3503	0.26750	0.5787	0.6568	1.03	2.20	0.03	0.0173
0.40	56.636	1.4608	0.23078	0.5819	0.6483	0.43	0.81	0.09	0.0225
0.45	50.366	1.6236	0.20901	0.5879	0.6347	0.61	0.61	0.15	0.0362
0.50	45.507	1.8248	0.19428	0.5943	0.6714	0.85	0.49	0.20	0.0619
0.55	41.644	2.0665	0.18345	0.6014	0.7169	1.11	0.40	0.24	0.1064

Strictly speaking, the shock cone ceases to be circular in cross section, but the deviation from a circular cone is a function of the square of the angle of attack, so that it is slight for small α. The intersection of a plane normal to the cone axis with the shock surface forms a curve approximating an ellipse with a small eccentricity.

THE CALCULATION SEQUENCE FOR FLOW PARAMETERS†

Refinement of the Results of the Previous Calculations

The results calculated on the basis of Eq. (7.12) can be improved. The boundary conditions for symmetric flow were used in the integration of differential equations of the type of Eq. (7.9); i.e., it was assumed that the shock was undeflected (Fig. 73). Actually, the boundary conditions should be determined by the deflected shock surface (Fig. 74).

† Editor's note: Almost all of this section is taken directly from Young and Siska, Ref. 6.

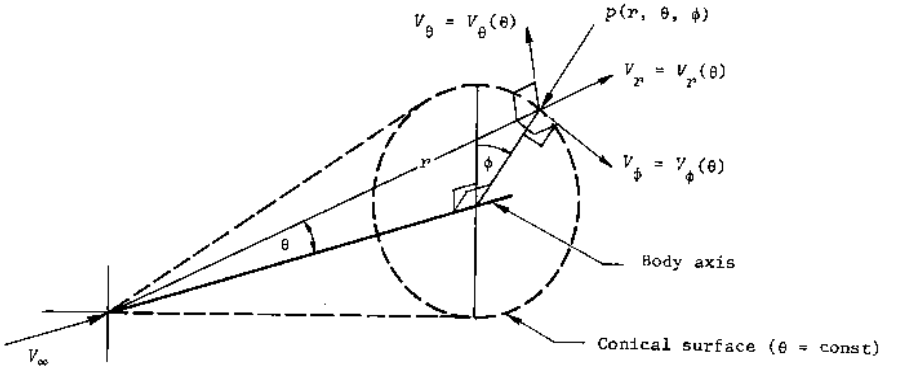

Fig. 73--Velocity components in spherical coordinates on an intermediate undeflected conical surface

Moreover, since the angles must now be read from the axis of flow (and not from the cone axis as previously), the cone surface itself appears inclined; the equation for the cone is expressed as follows:

$$\theta_c = \delta_c - \alpha \cos \phi - \frac{1}{2} \alpha^2 \cot \delta_c \sin^2 \phi. \qquad (7.14a)$$

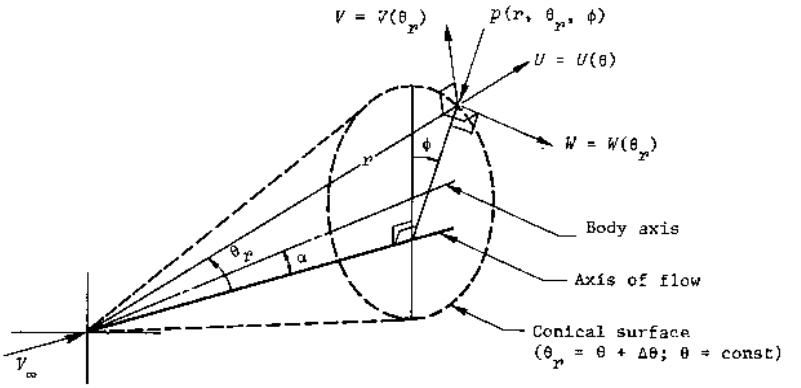

Fig. 74--Velocity components in spherical coordinates on an intermediate deflected conical surface

Hence it follows that the inclination angle of a meridian of the cone is

$$\Delta\theta_c = \theta_c - \delta_c = -\alpha \cos\phi - \frac{1}{2}\alpha^2 \cot\delta_c \sin^2\phi. \tag{7.15}$$

The inclination of the conical surface of the shock is found directly from Eq. (7.14) in the form

$$\Delta\theta_s = -\alpha\varepsilon \cos\phi + \alpha^2(\mu_0 + \mu_2 \cos 2\phi). \tag{7.15a}$$

The velocity components, the pressure, and the density on an intermediate deflected conical surface can be expressed by means of a Taylor expansion in the following form:

$$\begin{aligned}
U(\theta_r) &= V_r(\theta + \Delta\theta) = V_r(\theta) + V_r'(\theta)\,\Delta\theta + V_r''(\theta)\,\frac{(\Delta\theta)^2}{2} + \ldots,\\
V(\theta_r) &= V_\theta(\theta + \Delta\theta) = V_\theta(\theta) + V_\theta'(\theta)\,\Delta\theta + V_\theta''(\theta)\,\frac{(\Delta\theta)^2}{2} + \ldots,\\
W(\theta_r) &= V_\phi(\theta + \Delta\theta) = V_\phi(\theta) + V_\phi'(\theta)\,\Delta\theta + V_\phi''(\theta)\,\frac{(\Delta\theta)^2}{2} + \ldots,\\
p_r(\theta_r) &= p(\theta + \Delta\theta) = p(\theta) + p'(\theta)\,\Delta\theta + p''(\theta)\,\frac{(\Delta\theta)^2}{2} + \ldots,\\
\rho_r(\theta_r) &= \rho(\theta + \Delta\theta) = \rho(\theta) + \rho'(\theta)\,\Delta\theta + \rho''(\theta)\,\frac{(\Delta\theta)^2}{2} + \ldots,
\end{aligned} \tag{7.16}$$

where $V_r(\theta)$, $V_\theta(\theta)$, $V_\phi(\theta)$, $p(\theta)$, $\rho(\theta)$, and the first and second derivatives of these parameters with respect to θ are determined from Eq. (7.12). Equation (7.16) serves only to refine the results obtained from Eq. (7.12) and is used in an approximate form in practice. The increment $\Delta\theta$ is approximated in the expansions by

$$\Delta\theta = -\alpha \cos\phi - \frac{\alpha^2}{2} \cot\theta \sin^2\phi \qquad (\delta_c < \theta < \theta_s). \tag{7.17}$$

Thus, it is assumed that the shock remains a circular cone within a known approximation and is inclined to the flow at an angle $\varepsilon\alpha$. Substituting Eq. (7.17) into Eq. (7.16), introducing the flow parameters and their first and second derivatives, and eliminating the terms with α to the third and higher powers, we find the following relations for calculating the velocity components, the pressure, and the density on the intermediate conical surface ($\delta_c < \theta < \theta_s$):

$$U = V_r^0 - \alpha \cos\phi\,(x + V_\theta^0) + \alpha^2\left[\hat{u}_0 - \frac{1}{4}V_\theta^0 \cot\theta + \frac{1}{2}y + \frac{1}{4}(V_r^0)''\right] + \alpha^2\cos 2\phi\left[\hat{u}_2 + \frac{1}{4}V_\theta^0\cot\theta + \frac{1}{2}y + \frac{1}{4}(V_r)''\right], \tag{7.18}$$

$$V = V_0^0 - \alpha\cos\phi\left[y + (V_r^0)''\right] + \alpha^2\left[\hat{v}_0 - \frac{1}{4}(V_r^0)''\cot\theta + \frac{1}{2}y' + \frac{1}{4}(V_r^0)'''\right] + \alpha^2\cos 2\phi\left[\hat{v}_2 + \frac{1}{4}(V_r^0)''\cot\theta + \frac{1}{2}y + \frac{1}{4}(V_r^0)'''\right], \tag{7.19}$$

$$W = -\alpha z\sin\phi + \alpha^2\sin 2\phi\left(\hat{w}_2 + \frac{1}{2}z'\right), \tag{7.20}$$

$$p_r = p^0\left\{1 - \alpha\cos\phi\left[\frac{\eta}{p^0} + \frac{(p^0)'}{p^0}\right] + \alpha^2\left[\frac{\hat{p}_0}{p^0} - \frac{1}{4}\frac{(p^0)'}{p^0}\cot\theta + \frac{1}{2}\frac{\eta'}{p^0} + \frac{1}{4}\frac{(p^0)''}{p^0}\right] + \alpha^2\cos 2\phi\left[\frac{\hat{p}_2}{p^0} + \frac{1}{4}\frac{(p^0)'}{p^0}\cot\theta + \frac{1}{2}\frac{\eta'}{p^0} + \frac{1}{4}\frac{(p^0)''}{p^0}\right]\right\}, \tag{7.21}$$

$$\rho_r = \rho^0\left\{1 - \alpha\cos\phi\left[\frac{\xi}{\rho^0} + \frac{(\rho^0)'}{\rho^0}\right] + \alpha^2\left[\frac{\hat{\rho}_0}{\rho^0} - \frac{1}{4}\frac{(\rho^0)'}{\rho^0}\cot\theta + \frac{1}{2}\frac{\xi'}{\rho^0} + \frac{1}{4}\frac{(\rho^0)''}{\rho^0}\right] + \alpha^2\cos 2\phi\left[\frac{\hat{\rho}_2}{\rho^0} + \frac{1}{4}\frac{(\rho^0)'}{\rho^0}\cot\theta + \frac{1}{2}\frac{\xi}{\rho^0} + \frac{1}{4}\frac{(\rho^0)''}{\rho^0}\right]\right\}, \tag{7.22}$$

where the superscript o designates, as previously, symmetric flow parameters, and the primes indicate derivatives with respect to θ.

If Eqs. (7.18) through (7.22) are applied to conditions on the cone (the respective parameters will have the subscript c), they assume a simpler form:

$$U_c = V_c^0 - \alpha x_c \cos\phi + \alpha^2\left(\hat{u}_{0c} + \frac{V_c^0}{2}\right) + \alpha^2 \cos 2\phi\left(\hat{u}_{2c} + \frac{V_c^0}{2}\right), \tag{7.18a}$$

$$V_c = \alpha^2\left(\hat{v}_{0c} - x_c - \frac{z_c}{2}\csc\delta_c\right) + \alpha^2\cos 2\phi\left(\hat{v}_{2c} - V_c^0\cot\delta_c - x_c - \frac{z_c}{2}\csc\delta_c\right), \tag{7.19a}$$

$$W_c = -\alpha z_c \sin\phi + \alpha^2 \sin 2\phi\left(\hat{w}_{2c} - V_c^0\csc\delta_c - \frac{z_c}{2}\cot\delta_c\right), \tag{7.20a}$$

$$p_{rc} = p_c^0\left\{1 - \alpha\cos\phi\,\frac{\eta_c}{p_c^0} + \alpha^2\left[\frac{\hat{p}_{0c}}{p_c^0} + \frac{\gamma(V_c^0)^2}{2(a_c^0)^2}\right] + \alpha^2\cos 2\phi\left[\frac{\hat{p}_{2c}}{p_c^0} + \frac{\gamma(V_c^0)^2}{2(a_c^0)^2}\right]\right\}, \tag{7.21a}$$

$$\rho_{rc} = \rho_c^0\left\{1 - \alpha\cos\phi\,\frac{\xi_c}{\rho_c^0} + \alpha^2\left[\frac{\hat{\rho}_{0c}}{\rho_c^0} + \frac{(V_c^0)^2}{2(a_c^0)^2}\right] + \alpha^2\cos 2\phi\left[\frac{\hat{\rho}_{2c}}{\rho_c^0} + \frac{(V_c^0)^2}{2(a_c^0)^2}\right]\right\}. \tag{7.22a}$$

Corresponding relations, enabling us to calculate the parameters at the shock wave (subscript s), are as follows:

$$U_s = V_{sr}^0 - \alpha\cos\phi\,(x_s + \varepsilon\gamma_{s\theta}^0) + \alpha^2\left[\hat{u}_{0s} + \frac{\varepsilon}{2}y_s + \mu_{0s}V_{s\theta}^0 + \frac{\varepsilon^2}{4}(\gamma_{sr}^0)''\right] + \alpha^2\cos 2\phi\left[\hat{u}_{2s} + \frac{\varepsilon}{2}y_s + \mu_{2s}V_{s\theta}^0 + \frac{\varepsilon^2}{4}(V_{sr}^0)''\right], \tag{7.18b}$$

$$V_s = V^o_{s\theta} - \alpha \cos\phi \left[y_s + \varepsilon (V^o_{sr})'' \right] + \alpha^2 \left[\hat{v}_{0s} + \frac{\varepsilon}{2} y_s' + \mu_{0s} (V^o_{sr})'' + \frac{\varepsilon^2}{4} (V^o_{sr})''' \right]$$

$$+ \alpha^2 \cos 2\phi \left[\hat{v}_{2s} + \frac{\varepsilon}{2} y_s' + \mu_{2s} (V^o_{sr})'' + \frac{\varepsilon^2}{4} (V^o_{sr})''' \right], \tag{7.19b}$$

$$W_s = -\alpha z_s \sin\phi + \alpha^2 \sin 2\phi \left(\hat{w}_{2s} + \frac{\varepsilon}{2} z_s' \right), \tag{7.20b}$$

$$p_{rs} = p^o_s \left\{ 1 - \alpha \cos\phi \left[\frac{\eta_s}{p^o_s} + \varepsilon \frac{(p^o_s)'}{p^o_s} \right] + \alpha^2 \left[\frac{\hat{p}_{0s}}{p^o_s} + \frac{\varepsilon}{2} \frac{\eta_s'}{p^o_s} + \mu_{0s} \frac{(p^o_s)'}{p^o_s} + \frac{\varepsilon^2}{4} \frac{(p^o_s)''}{p^o_s} \right] \right.$$

$$\left. + \alpha^2 \cos 2\phi \left[\frac{\hat{p}_{2s}}{p^o_s} + \frac{\varepsilon}{2} \frac{\eta_s'}{p^o_s} + \mu_{2s} \frac{(p^o_s)'}{p^o_s} + \frac{\varepsilon^2}{4} \frac{(p^o_s)''}{p^o_s} \right] \right\}, \tag{7.21b}$$

$$\rho_{rs} = \rho^o_s \left\{ 1 - \alpha \cos\phi \left[\frac{\xi_s}{\rho^o_s} + \varepsilon \frac{(\rho^o_s)'}{\rho^o_s} \right] + \alpha^2 \left[\frac{\hat{\rho}_{0s}}{\rho^o_s} + \frac{\varepsilon}{2} \frac{\xi_s'}{\rho^o_s} + \mu_{0s} \frac{(\rho^o_s)'}{\rho^o_s} + \frac{\varepsilon^2}{4} \frac{(\rho^o_s)''}{\rho^o_s} \right] \right.$$

$$\left. + \alpha^2 \cos 2\phi \left[\frac{\hat{\rho}_{2s}}{\rho^o_s} + \frac{\varepsilon}{2} \frac{\xi_s}{\rho^o_s} + \mu_{2s} \frac{(\rho^o_s)'}{\rho^o_s} + \frac{\varepsilon^2}{4} \frac{(\rho^o_s)''}{\rho^o_s} \right] \right\}. \tag{7.22b}$$

The derivatives with respect to θ that appear in these expressions are as follows:

$$(V^o_r)' = V^o_\theta, \tag{7.23a}$$

$$(V^o_r)'' = \frac{(a^o)^2 (2V^o_r + V^o_\theta \cot\theta) - V^o_r (V^o_\theta)^2}{(a^o)^2 - (V^o_\theta)^2}, \tag{7.23b}$$

$$(V_r^o)''' = \frac{1}{(a^o)^2 - (\gamma_\theta^o)^2}\left\{(a^o)^2\left[V_\theta^o \csc^2\theta - 2V_\theta^o - (V_r^o)''\cot\theta\right]\right.$$
$$\left. + 2V_\theta^o(V_r^o)''\left[V_r^o + (\gamma_r^o)''\right] + (V_\theta^o)^3 + \frac{(\gamma-1)(\gamma_\theta^o)^3}{(a^o)^2}\left[V_r^o + (V_r^o)''\right]^2\right\}, \quad (7.23c)$$

$$y = x', \quad (7.24a)$$

$$y' = \frac{(a^o)^2}{(a^o)^2 - (\gamma_\theta^o)^2}\left\{-y\cot\theta + \frac{2V_\theta^o y}{(a^o)^2}\left[V_r^o + (V_r^o)''\right] - x\left[2 - \left(\frac{V_\theta^o}{a^o}\right)^2\right]\right.$$
$$\left. - z\csc\theta + \frac{\gamma-1}{(a^o)^4}(V_\theta^o)^2\left[V_r^o + (V_r^o)''\right](V_r^o x + V_\theta^o y)\right\}, \quad (7.24b)$$

$$z' = -y\csc\theta - z\left(\cot\theta + \frac{V_r^o}{V_\theta^o}\right) - \frac{\csc\theta}{V_\theta^o}\left[V_r^o x + \frac{(a^o)^2 d}{\gamma(\gamma-1)}\right], \quad (7.25)$$

$$\frac{(p^o)'}{p^o} = -\frac{\gamma V_\theta^o}{(a^o)^2}\left[V_r^o + (V_r^o)''\right], \quad (7.26a)$$

$$\frac{(p^o)''}{p^o} = -\frac{\gamma(V_r^o)''}{(a^o)^2}\left[V_r^o + (V_r^o)''\right] + \frac{\gamma(\gamma_\theta^o)^2}{(a^o)^4}\left[V_r^o + (V_r^o)''\right]^2 - \frac{\gamma V_\theta^o}{(a^o)^2}\left[\gamma_\theta^o + (V_r^o)'''\right], \quad (7.26b)$$

$$\frac{(\rho^o)'}{\rho^o} = -\frac{V_\theta^o}{(a^o)^2}\left[V_r^o + (V_r^o)''\right], \quad (7.27a)$$

$$\frac{(\rho^o)''}{\rho^o} = -\frac{(V_r^o)''}{(a^o)^2}\left[V_r^o + (V_r^o)''\right] - \frac{V_\theta^o}{(a^o)^2}\left[V_\theta^o + (V_r^o)'''\right]$$
$$+ (2-\gamma)\frac{(V_\theta^o)^2}{(a^o)^4}\left[\gamma_r^o + (V_r^o)''\right]^2, \quad (7.27b)$$

$$\frac{\eta'}{p^o} = \frac{\gamma V_\theta^o \left[V_r^o + (V_r^o)''\right]}{(a^o)^2} \left[-\frac{\eta}{p^o} - \frac{\gamma - 1}{(a^o)^2}(V_r^o x + V_\theta^o y) - \frac{x + y'}{V_r^o + (V_r^o)''} \right]$$

$$- \frac{\gamma y \left[V_r^o + (V_r^o)''\right]}{(a^o)^2}, \tag{7.28a}$$

$$\frac{\xi'}{\rho^o} = \frac{V_\theta^o \left[V_r^o + (V_r^o)''\right]}{(a^o)^2} \left[-\frac{\xi}{\rho^o} - \frac{\gamma - 1}{(a^o)^2}(V_r^o x + V_\theta^o y) - \frac{x + y'}{V_r^o + (V_r^o)''} \right]$$

$$- \frac{y \left[V_r^o + (V_r^o)''\right]}{(a^o)^2}. \tag{7.28b}$$

Calculation of the Aerodynamic Coefficients

In calculating the aerodynamic forces, it is convenient to use the body-axis coordinate system (r, Θ, ψ) rather than the wind-axis system (r, θ, ϕ) in which the relations above were written. The velocity components in this system are shown in Fig. 75. The transfer of the axes can be made with the help of the equation

$$\cot \phi = \cos \alpha \cot \psi - \sin \alpha \cot \Theta \csc \psi, \tag{7.29}$$

from which the following approximate relations can be obtained:

$$\begin{aligned} \alpha \cos \phi &\approx \alpha \cos \psi - \frac{\alpha^2}{2} \cot \Theta + \frac{\alpha^2}{2} \cot \Theta \cos 2\psi, \\ \alpha \sin \phi &\approx \alpha \sin \psi + \frac{\alpha^2}{2} \cot \Theta \sin 2\psi, \\ \alpha^2 \cos 2\phi &\approx \alpha^2 \cos 2\psi, \\ \alpha^2 \sin 2\phi &\approx \alpha^2 \sin 2\psi. \end{aligned} \tag{7.30}$$

With the aid of these relations, Eqs. (7.18a) through (7.22a) for the velocity components and the pressure are transformed to

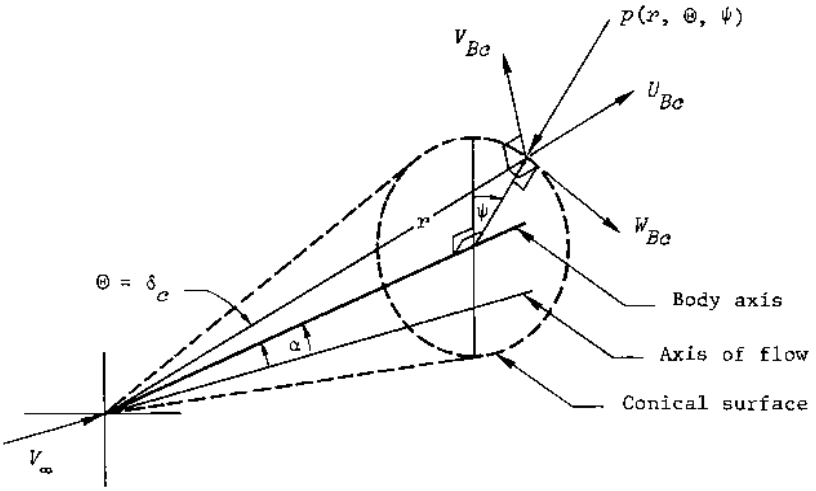

Fig. 75--Velocity components in the body-axis system of coordinates

$$U_{Bc} = V_c^o - \alpha x_c \cos\psi + \alpha^2\left(\hat{u}_{0c} + \frac{x_c}{2}\cot\delta_c + \frac{V_c^o}{2}\right) + \alpha^2\cos 2\psi\left(\hat{u}_{2c} - \frac{x_c}{2}\cot\delta_c + \frac{V_c^o}{2}\right),$$

$$V_{Bc} = 0, \tag{7.31}$$

$$W_{Bc} = -\alpha z_c \sin\psi + \alpha^2 \sin 2\psi\left(\hat{\omega}_{2c} - V_c^o \csc\delta_c - z_c\cot\delta_c\right),$$

$$p_{Bc} = p_c^o\left\{1 - \alpha\cos\psi\,\frac{\eta_c}{p_c^o} + \alpha^2\left[\frac{\hat{p}_{0c}}{p_c^o} + \frac{\gamma(V_c^o)^2}{2(a_c^o)^2} + \frac{\cot\delta_c}{2}\frac{\eta_c}{p_c^o}\right] + \alpha^2\cos 2\psi\left[\frac{\hat{p}_{2c}}{p_c^o} + \frac{\gamma(V_c^o)^2}{2(a_c^o)^2} - \frac{\cot\delta_c}{2}\frac{\eta_c}{p_c^o}\right]\right\}. \tag{7.32}$$

The flow parameters at the surface of the cone are designated by the subscript B in these equations.

The equality $V_{Bc} = 0$ comes from the condition of continuous flow, according to which there is no flow normal to the surface of the cone.

The relation for density can be obtained from Eq. (7.22a) after substitution of Eq. (7.30) with $\Theta = \delta_c$. The density can also be found using the Bernoulli equation with the known values of U_{Bc}, W_{Bc}, and p_{Bc}. The temperature is determined from the equation of state.

The calculation agrees well with experimental data. This is particularly evident in Fig. 76, which presents data on the variation of p_{Bc}/p_∞ for two cones with angles of 10° and 15° for $M_\infty = 2$ and $\alpha = 12.2°$.

Knowing the pressure on the cone, the pressure coefficient can be computed from $C_{pc} = 2(p_{Bc} - p_\infty)/\gamma p_\infty M_\infty^2$. Then the axial and normal force coefficients are obtained from Eqs. (1.5) and (1.12):

$$C_{Ap} = \frac{8A_p}{\pi d_{\text{mid}}^2 \gamma p_\infty M_\infty^2} = \left\{ \frac{p_c^\circ}{p_\infty} \left[1 + \alpha^2 \left(\frac{\hat{p}_{0c}}{p_c^\circ} + \frac{\cot \delta_c}{2} \frac{\eta_c}{p_c^\circ} + \frac{\gamma (V_c^\circ)^2}{2(a_c^\circ)^2} \right) \right] - 1 \right\} \frac{2}{\gamma M_\infty^2}, \tag{7.33}$$

$$C_{Np} = \frac{8N_p}{\pi d_{\text{mid}}^2 \gamma p_\infty M_\infty^2} = \frac{\alpha}{\gamma M_\infty^2} \frac{p_c^\circ}{p_\infty} \frac{\eta_c}{p_c^\circ} \cot \delta_c. \tag{7.34}$$

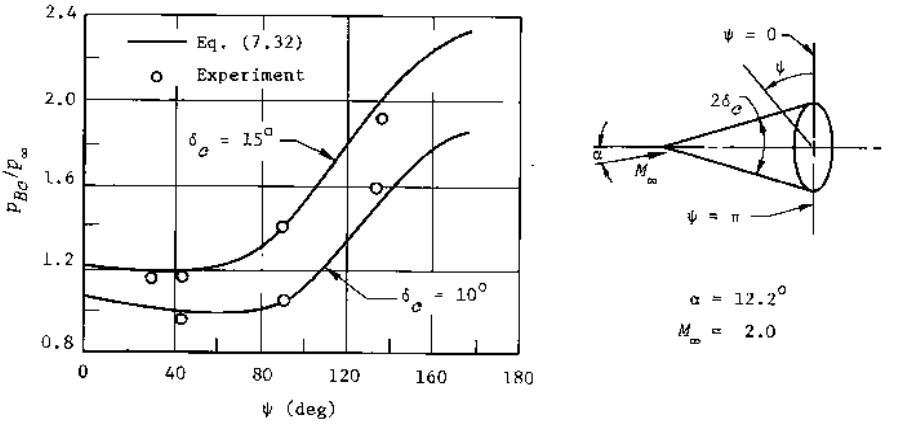

Fig. 76--Pressure distribution about a cone in asymmetric flow

As is evident from comparison with Eq. (7.10), the normal force coefficient is the same as in the first-order approximation. The axial force coefficient C_{Ap} is different because of the quadratic term in α, and its value can be calculated with the help of Table 14. Listed there are the coefficient K_D which determines the quantity $C_{pc} = (8/\pi)K_D$ for symmetric flow and the coefficient K_{D2} which accounts for the second-order effect of angle of attack on the axial force coefficient. The axial force coefficient is computed from

$$C_{Ap} = \frac{8}{\pi} K_D + \alpha^2 \left\{ \left(\frac{8}{\pi} K_D + \frac{2}{\gamma M_\infty^2} \right) \left[K_{D2} - \frac{\gamma V_c^0 x_c d}{2(\gamma - 1)(a_c^0)^2} + \frac{1}{2} \right] - \frac{8}{\pi} K_N \right\}. \quad (7.35)$$

The variation with angle of attack of the axial force coefficient, as calculated from Eq. (7.35), is shown in Fig. 77. As is evident, the theoretical data agree satisfactorily with the experimental results.

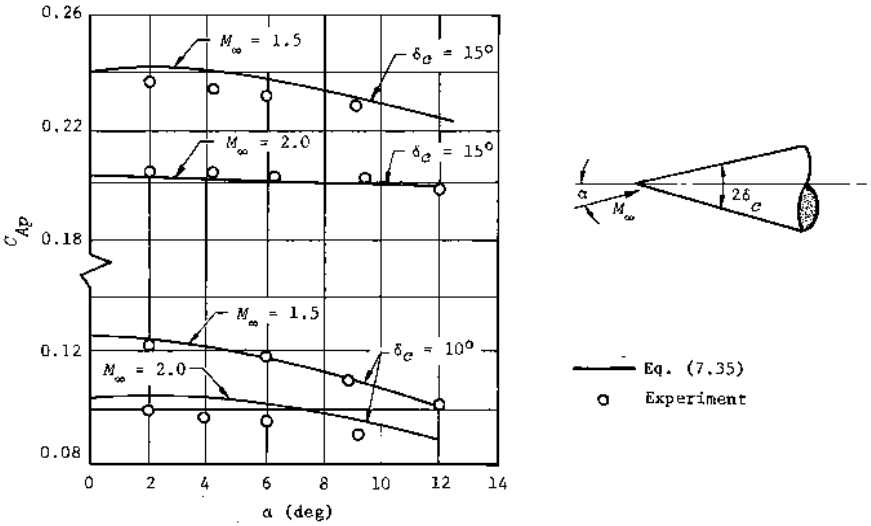

Fig. 77--Variation in axial force coefficient on a cone with angle of attack

Equations for the wave drag and lift coefficient can be derived from those for C_{Np} and C_{Ap}:

$$C_{Dp} = \frac{8}{\pi} K_D + \alpha^2 \left[(K_{D2} - \widetilde{K}) \left(\frac{8}{\pi} K_D + \frac{2}{\gamma M_\infty^2} \right) + \frac{1}{\gamma M_\infty^2} \right], \tag{7.36}$$

$$C_{Lp} = \frac{8}{\pi} (K_N - K_D)\alpha, \tag{7.37}$$

where

$$\widetilde{K} = \frac{\gamma V_c^o x_c d}{2(\gamma - 1)(a_c^o)^2}.$$

Analysis shows that the wave drag coefficient depends very little on the quantity $\widetilde{K}$ for normal supersonic Mach numbers; however, for large Mach numbers, its influence is significant.

With the aid of Eqs. (7.32) and (1.19), the relation for calculating the pitching moment coefficient can be found:

$$C_{mp} = \frac{2}{3} \frac{\alpha}{\gamma M_\infty^2} \left(\frac{p_c^o}{p_\infty} \right) \left(\frac{\eta_c}{p_c^o} \right) (1 + \tan^2 \delta_c) \cot \delta_c. \tag{7.38}$$

The center of pressure is determined from the values of C_{mp} and C_{Np}:

$$\bar{x}_{cp} = \frac{C_{mp}}{C_{Np}} = \frac{2}{3} (1 + \tan^2 \delta_c). \tag{7.39}$$

The Equation for the Shock-wave Surface

The equation for the shock-wave surface determines the angle of inclination of a shock-wave element in a given meridian plane. If this angle is measured from the cone axis, Eq. (7.14) must be transformed from wind-axis coordinates (r, θ, φ) to body-axis coordinates (r, Θ, ψ). The result is

$$\Theta = \theta_s + \alpha(1 - \varepsilon) \cos \psi + \alpha^2 \left(\mu_0 + \mu_2 \cos 2\psi - \frac{1 - 2\varepsilon}{2} \cot \theta_s \sin^2 \psi \right). \tag{7.40}$$

The two rays of the shock surface that lie in the vertical plane of symmetry ($\psi = 0$ and π) are of particular interest. The slopes of these rays are given by the relations

$$\begin{aligned} \Theta_{\psi=0} &= \theta_c + (1 - \varepsilon)\alpha + (\mu_0 + \mu_2)\alpha^2, \\ \Theta_{\psi=\pi} &= \theta_s - (1 - \varepsilon)\alpha + (\mu_0 + \mu_2)\alpha^2, \end{aligned} \tag{7.41}$$

in which the absolute value of α must be used. The first relation pertains to the ray lying on the shadow side ($\psi = 0$) and the second to the ray lying on the windward side ($\psi = \pi$).†

Instead of these relations for determining the location of the two rays mentioned, it is possible to use the equation obtained by A. L. Gonor:(7)

$$\Theta_{\psi=\pi,0} = \delta_c + \frac{\gamma - 1}{\gamma + 1} \frac{\tan(\delta_c \pm \alpha)}{t^2} \left[(1 + t) \log (1 + t) - t\right] \times \left[1 + \frac{2}{(\gamma - 1)M_\infty^2 \sin^2(\delta_c \pm \alpha)}\right], \tag{7.42}$$

where

$$t = \pm \frac{\sin \alpha}{\sin \delta_c \cos (\delta_c \pm \alpha)}.$$

In these expressions, the upper sign corresponds to the windward side of the cone ($\Theta = \Theta_{\psi=\pi}$) and the lower sign to the leeward or shadow side ($\Theta = \Theta_{\psi=0}$).

---

†Editor's note: Equations (7.40) and (7.41) are incorrect in the original text. In order to transform Eq. (7.14) from wind-axis to body-axis coordinates, it is necessary to use Eq. (7.29) or (7.30) to replace ϕ with ψ, and an additional relation between θ and Θ. The latter can be obtained by comparing the geometrical relations in Figs. 73 and 75, resulting in the following expression:

$$\sin^2\theta = \sin^2\Theta \sin^2\psi + (\sin \Theta \cos \psi - \cos \Theta \tan \alpha)^2 \cos^2\alpha.$$

An analysis of Eq. (7.42) shows an interesting feature in the relative positions of the shock wave with increasing Mach number. Up to a certain M_∞, the inclination of the shock wave is less on the windward side than on the shadow side. The two angles gradually approach each other with an increase in velocity, and at a specific Mach number the shock wave has the shape of a conical surface with an approximately circular cross section. At this moment, the effect of the asymmetric flow, which appears as a deformation in the wave surface, seems to disappear. With a further increase in M_∞, the wave shape is again deformed, but in a different way: It more closely approximates a cone on the shadow side than on the windward side. The shape of the wave does not correspond now to the usual concept.

This phenomenon is observed for all cones, and for thicker cones it appears at a lesser velocity. For example, the shock wave changes shape at M_∞ somewhat less than four for a cone with $\delta_c = 40°$.

APPROXIMATE METHOD OF CALCULATION

It is possible to use the results obtained for zero angle of attack to estimate the surface parameters of a cone in asymmetric flow. Let us assume that each generatrix of a cone that is inclined at some angle of attack corresponds to the generatrix of an equivalent cone in a given symmetrical flow. The latter cone is constructed on the basis of a local slope θ_c to the direction of the incident flow and is called a "local cone."

The parameters on the surface of the local cone are determined from the results of symmetric flow theory, and these parameters are then assumed to apply to the corresponding ray on the actual deflected cone. It is apparent that the fundamental element in the calculation is the determination of the angle of the local cone. Its value could be obtained from Eq. (7.14a), but the results of the calculation of flow parameters from this value of the angle θ_c do not quite agree with the exact data. In this case better agreement is obtained if we base the calculation on an angle θ_c determined from

$$\theta_c = \delta_c - \alpha \cos \psi - \frac{\alpha^2}{2} \cot \delta_c \sin^2 \psi, \tag{7.43}$$

which gives the same values for $\psi = 0$ and π as Eq. (7.14a), but somewhat smaller values for intermediate ψ.

During the calculation, the angles ψ are assigned, the corresponding values of θ_c are determined for specific values of δ_c and α, and, knowing M_∞, the parameters on the deflected cone are determined from the theory for symmetric flow. Thus, the calculation results in a relation between the cone parameters and the angle ψ. In addition, it is possible to find the approximate parameters on the shock wave, as well as its slope.

The degree of error in this method can be estimated by comparison with exact theory or with experimental data. Obviously, the results should coincide on the generatrices corresponding to the zero meridian plane (ϕ and $\psi = 0$ or π), because there is no lateral flow in that plane (the velocity component $V_\phi = 0$) and the derivatives of the other parameters with respect to ϕ are zero; i.e., $dV_r/d\phi$, $dV_\theta/d\phi$, and $d\rho/d\phi$, as Eq. (7.12) indicates. Consequently, the equation system for flow will be similar to that in the symmetric case, and the parameters will be the same.

A discrepancy between the calculated and actual values of the parameters is observed at corresponding points on the surface for the intermediate generatrices (ψ differing from 0 and π) because of the cross-flow caused by the lack of symmetry, which is not accounted for in the local-cone method. For example, for $M_\infty = 2$ and $\alpha = 12.2°$ with a 15° cone, the greatest error in the pressure calculations is 10 percent, although it is only half as large for $M_\infty = 4$. The accuracy also increases with a decrease in the angle of attack. Therefore, it is advisable to use this method for rather high velocities and comparatively small angles of attack.

This method is of great practical interest because it permits the rather rapid and simple estimation of the distribution of the flow parameters in the more complicated cases of asymmetric flow with dissociation or with variable specific heats; however, this requires a corresponding knowledge of the simpler case of symmetric flow around a cone for the same conditions.

This method can also be used for calculating the friction and heat transfer parameters. If the parameters of the inviscid asymmetric flow

are specified, an approximate calculation can be made, from the relations for the symmetric case, of the boundary layer and heat transfer parameters at an arbitrary meridian plane with an angle ψ by assuming that the ray located in this plane belongs to the local cone.

Chapter III

THE METHOD OF CHARACTERISTICS

Editor's Introduction

THIS CHAPTER CONTAINS *a number of detailed descriptions of the numerical calculations required to apply the method of characteristics to various problems. Irrotational flow is discussed in Section 9, rotational flow of a real gas in Section 10, and flow over a body at angle of attack in Section 12. The numerical techniques discussed in these sections are written for manual calculations and are not particularly useful for application to digital computer solutions. However, the discussion represents a good summary of the method of characteristics and its application to a broad range of problems, and the rather tedious details, if followed carefully, give the reader a clear picture of the mechanics of the method and the differences between the various types of solutions--as, for example, between those for potential and rotational flow.*

*Similar discussions in American technical literature are provided in the comprehensive and detailed series of monographs by Isenberg (*USAF AMC Technical Reports F-TR-1173A-ND, F-TR-1173B-ND, *and* F-TR-1173C-ND, *December 1947) and, for example, in the textbooks by Ferri (*Elements of Aerodynamics of Supersonic Flows, *1949, and Section G of* General Theory of High Speed Aerodynamics, *1954). However, these were also prepared before the advent of digital computers, and their descriptions of the numerical methods are thus obsolete as well. Most aerospace firms now have digital computer programs for solutions of axisymmetric flow field problems by the method of characteristics. Typical of these programs is that developed by Inouye, Rakich, and Lomax (*NASA TN D-2970, *1965); although the complete program is written for blunt-nosed bodies, it can be readily applied to pointed bodies by using the appropriate starting conditions. To the editor's knowledge, there are no operational computer programs for characteristics solutions about a body of revolution at an angle of attack. This problem may be academic, of course, since at any appreciable angle of attack the flow separates from the lee side of the body and inviscid solutions become useless.*

*A number of approximate methods and formulas are discussed at the end of Section 8, including two forms of the tangent-cone method attributed to an unpublished paper by Vallander. The hypothesis of identical pressures corresponds to the most commonly used method; the hypothesis of identical velocities has been discussed by Ehret (*NACA TN 2764, *1952), but was not developed to the extent given here. The latter method is*

quite easy to apply, and appears to be fairly accurate at the lower supersonic Mach numbers. Other approximate methods that might have been cited include Van Dyke's second-order supersonic theory (J. Aero. Sci., March 1951, and NACA TN 2744, 1952) and the second-order shock expansion method of Syvertson and Dennis (NACA Report 1328, 1957), both of which give accurate results (see editor's paper, J. Aero. Sci., July 1961). Neither of these theories, however, leads to simple analytic formulas.

In the editor's paper cited above, general curves are presented for the pressure drag coefficients of conical and ogive noses for Mach numbers from one to infinity, correlated by the hypersonic similarity parameters. The curves are based on calculations by transonic flow theory, second-order supersonic flow theory, the second-order shock expansion method, exact conical theory, and the method of characteristics. Summary graphs for the two nose shapes are reproduced below.

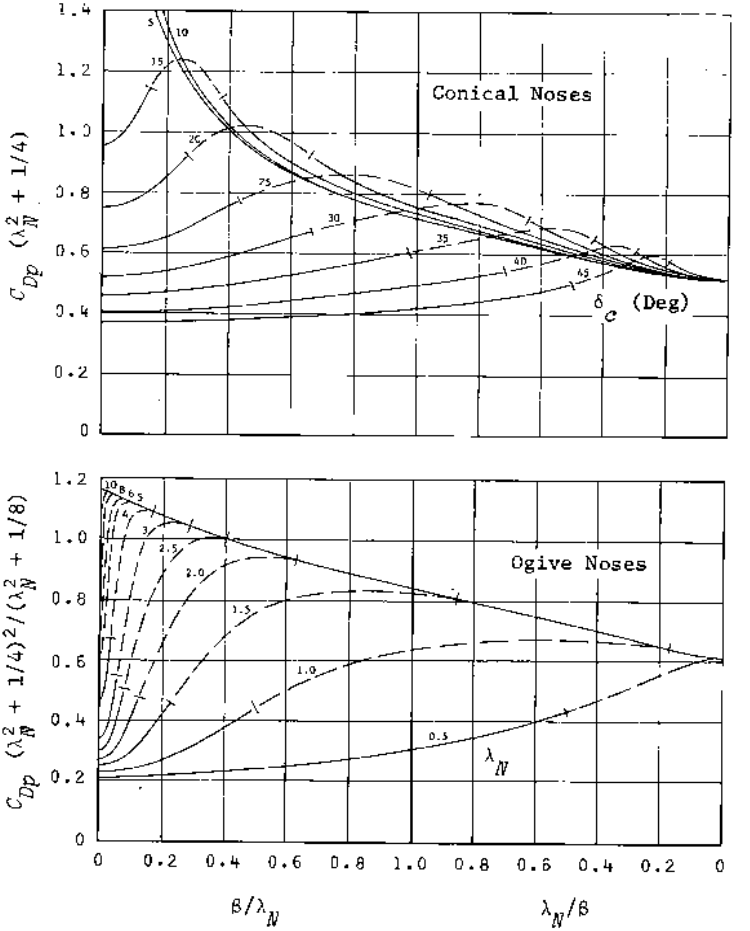

§ 8. *THE CALCULATION OF SYMMETRIC POTENTIAL FLOWS*

EQUATIONS FOR THE METHOD OF CHARACTERISTICS

General Definitions

THE METHOD OF CHARACTERISTICS occupies an important position among the methods used in supersonic aerodynamics. Without dwelling in detail on the mathematical theory, which is discussed in many specialized works, let us examine the application of this method to the problems of flow around bodies of revolution. All gasdynamic problems can be divided into two fundamental groups: The first group consists of problems of gas flows with small perturbations, investigated on the basis of linearized equations; the second group consists of problems of a more general case of motion, characterized by nonlinear equations.

The first group of problems is considered in Chaps. IV and V; their solution, as we shall see, is greatly simplified because only linearized equations are involved. The solution of problems of the second group is more complicated because of the nonlinear character of the corresponding equations. The solution of that part of the problem related to the calculation of flow around slender pointed bodies for very large free-stream Mach numbers can be facilitated by the fact that the equations of motion can be somewhat simplified even though their nonlinear character is maintained. These simplified nonlinear equations are based on the theory of small perturbations. For nonslender bodies or slender bodies with blunt noses, small perturbation theory becomes useless, and it is necessary to proceed from the usual nonlinear equations. Steady symmetric potential flows around bodies of revolution can be studied for Mach numbers for which the perturbed flow is considered irrotational. Equation (3.20) is used for the velocity potential, on condition that the derivatives

with respect to ϕ and t are dropped. The character of the flow diverges increasingly from potential flow as the Mach number increases, and the influence of vorticity becomes an essential factor. Therefore, Eq. (3.26) must be used for the stream function in the study of rotational flow around an axisymmetric body. Asymmetric potential flow can be examined using the same Eq. (3.20) for the velocity potential, but retaining the derivatives with respect to ϕ. If the flow around bodies is of a more general character, it must be studied using a system of equations (motion, continuity, etc.) that represent that character of the flow.

The method of characteristics enables us to solve equations, either graphically or numerically, for the velocity potential and stream function. We may also solve the equations of motion in general form and thus calculate gas flow behind any stationary shock wave provided that this flow is supersonic. It should be noted, however, that the flow behind the shock need not be everywhere supersonic to use the method of characteristics in its general form. Some variants of this method have been developed that permit the calculation of the subsonic flow regions that appear, in particular, between a detached shock wave and the blunt nose of an axisymmetric body. These methods are not investigated in the present work, but can be studied in specialized literature.

The method of characteristics may be considered as an expression of the exact theory of motion of a gaseous medium, because it employs the general nonlinear relations that describe flows with large perturbations. In practice, the use of the method of characteristics is based on the graphical and numerical integration of equations that determine the laws of variation of parameters along particular lines or characteristics, and involves a series of approximations from which these parameters are determined step by step in a certain region. The prescribed accuracy of the calculation is attained by the choice of the interval of integration and by the number of approximations. The computation is accelerated significantly by using electronic computers.

The Cauchy Problem

The method of characteristics has been especially developed in its application to steady supersonic symmetric rotational or irrotational

flows. Through its use, Eq. (3.20) for the velocity potential Φ and Eq. (3.26) for the stream function Ψ can be solved as linear with respect to the second partial derivatives and as nonlinear with respect to the first derivatives. Such equations are called quasilinear.

The solutions $\Phi = \Phi(x, r)$ and $\Psi = \Psi(x, r)$ are geometrically represented by integral surfaces in a space that can be specified either by the coordinate systems x, r, Φ or x, r, Ψ. In these systems, the plane x, r is considered primary and is called the physical plane or the plane of independent variables. Geometrically, it coincides with the meridian plane passing through the axis of the body of revolution.

The desired functions and also their derivatives can be located at points in the physical plane as a result of the solution of Eqs. (3.20) and (3.26). The solutions will be uniquely determined if they conform to additional specified conditions. The conditions in the Cauchy problem are the establishment of the values of the required function $\Phi(x, r)$, or $\Psi(x, r)$, and of one of its first derivatives $\Phi_x(\Psi_x)$, or $\Phi_r(\Psi_r)$ (the so-called initial Cauchy data), on an initial curve AB (Fig. 78). It

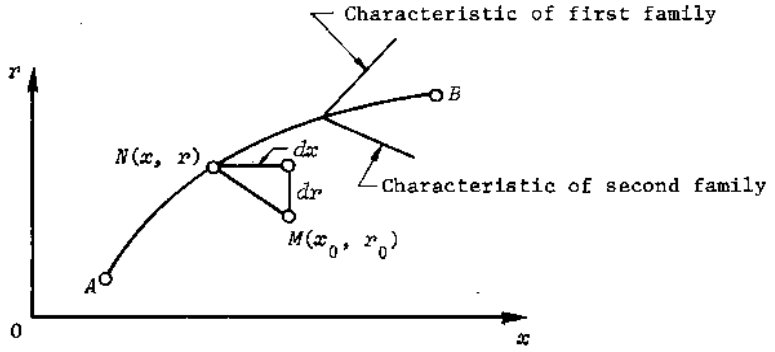

Fig. 78--Initial conditions

should be noted that the establishment of the function itself and one of its first derivatives (e.g., Φ_r on the AB curve) automatically determines the other derivative (e.g., Φ_x), as can be seen from

$$\frac{d}{dx}\Phi[x, r(x)] = \frac{\partial}{\partial x}\Phi[x, r(x)] + \frac{dr}{dx}\frac{\partial}{\partial r}\Phi[x, r(x)],$$

where it is assumed that the AB curve is prescribed by the equation $r = r(x)$. Therefore, the initial conditions consist essentially of the establishment of the values of the required functions and their first derivatives on the initial curve AB. The solution of the Cauchy problem requires the discovery of a function Φ (or Ψ) that satisfies the given equation and the initial conditions in the vicinity of the initial curve.

From the geometrical point of view, the Cauchy problem involves the determination of an integral three-dimensional surface in x, r, Φ (or x, r, Ψ) space that passes through a three-dimensional curve. Professor F. I. Frankl has solved the Cauchy problem as applied to supersonic symmetric flows and in connection with this has developed a corresponding method of characteristics.[1]

To investigate the Cauchy problem, let us represent Eqs. (3.20) and (3.26) in the following general form:

$$Au + 2Bs + Ct + H = 0, \tag{8.1}$$

where $u = \Phi_{xx}$ (or Ψ_{xx}), $s = \Phi_{xr}$ (or Ψ_{xr}), and $t = \Phi_{rr}$ (or Ψ_{rr}) are the second partial derivatives. The values A, B, and C are equal to the coefficients for the corresponding second partial derivatives in Eqs. (3.20) or (3.26).

Let us seek the solution of Eq. (8.1) in the vicinity of the required curve in the form of a series:

$$\Phi = \Phi(x, r) + \sum_{n=1}^{\infty} \frac{1}{n!} \left[(\Delta x)^n \frac{\partial^n \Phi}{\partial x^n} + n(\Delta x)^{n-1} \Delta r \frac{\partial^n \Phi}{\partial x^{n-1} \partial r} \right.$$

$$\left. + \frac{n(n-1)}{1 \cdot 2} (\Delta x)^{n-2} (\Delta r)^2 \frac{\partial^n \Phi}{\partial x^{n-2} \partial r^2} + \ldots + (\Delta r)^n \frac{\partial^n \Phi}{\partial r^n} \right], \tag{8.2}$$

where $\Delta x = x_0 - x$, $\Delta r = r_0 - r$, and the stream function Ψ can appear instead of Φ. This expansion gives the required solution if the values of the function Φ (or Ψ) and their derivatives of any order are known and also lie on the prescribed curve. Since the first derivatives

$p = \Phi_x$ (or Ψ_x) and $q = \Phi_y$ (or Ψ_y) are assigned on this curve, it is necessary to find the values of the second derivatives and also derivatives of a higher order. (We shall not dwell on the question of the existence of these derivatives.) Thus, the solution of the Cauchy problem amounts specifically to the discovery of conditions for which the determination of the leading derivatives of a prescribed curve is possible.

For this purpose, let us first consider the second derivatives and find the equations by which they may be determined. Since there are three derivatives, u, s, and t, just as many independent equations are needed to determine them. The first of these is Eq. (8.1), which we will examine on the initial curve AB. The two others are obtained from the following relationships, also considered along the initial curve:

$$\begin{aligned} dp &= \frac{\partial p}{\partial x}\,dx + \frac{\partial p}{\partial y}\,dy = u\,dx + s\,dy, \\ dq &= \frac{\partial q}{\partial x}\,dx + \frac{\partial q}{\partial y}\,dy = s\,dx + t\,dy. \end{aligned} \tag{8.3}$$

Hence, the equation system for determining the second derivatives is written

$$\begin{aligned} Au + 2Bs + Ct + H &= 0, \\ dx\,u + dy\,s + 0t - dp &= 0, \\ 0u + dx\,s + dy\,t - dq &= 0. \end{aligned} \tag{8.4}$$

If we introduce the symbols Δ, Δ_u, Δ_s, and Δ_t, respectively, for the principal and partial determinants of the system, the second derivatives on the curve are determined from the relations

$$u = \frac{\Delta_u}{\Delta}, \qquad s = \frac{\Delta_s}{\Delta}, \qquad t = \frac{\Delta_t}{\Delta}. \tag{8.4a}$$

From these relations it follows that if the principal determinant Δ is not equal to zero on AB, the derivatives u, s, and t are uniquely determined. If, however, the curve AB is such that this determinant equals zero along it, i.e.,

$$\Delta = \begin{vmatrix} A & 2B & C \\ dx & dr & 0 \\ 0 & dx & dr \end{vmatrix} = 0,$$

and, consequently,

$$A\left(\frac{dr}{dx}\right)^2 - 2B\frac{dr}{dx} + C = 0, \tag{8.5}$$

the second derivatives are either not completely determined by Φ, p, and q, or are not determined uniquely. Such a case will always occur if Eq. (8.5) is satisfied at each point on the curve or, in effect, if the following equality is fulfilled:

$$\left(\frac{dr}{dx}\right)_{1,2} = r'_{1,2} = \frac{1}{A}\left(B \pm \sqrt{B^2 - AC}\right). \tag{8.5a}$$

It is apparent that Eq. (8.5a) gives equations in differential form for two families of real curves if $B^2 - AC > 0$. Such curves, for each point of which the principal determinant of the system (8.4) equals zero, are called characteristics, and Eq. (8.5) is called a characteristic equation.

From what has been said, we arrive at the condition for which the unique determination of the second derivatives on the initial curve is possible: No element of the arc of this curve should coincide with the characteristics. It can be shown that the same condition, $\Delta \neq 0$, applies to the unique determination of the higher derivatives that enter the series in Eq. (8.2). Consequently, if $\Delta \neq 0$, all the coefficients in Eq. (8.2) are determined uniquely from the data on the initial curve.

The case in which the curve AB coincides with one of the characteristics occupies a fundamental position in supersonic flow theory. Not only does the major determinant of Eq. (8.4) equal zero along the curve but the partial determinants do also: $\Delta_u = \Delta_s = \Delta_t = 0$. It can be shown that, if the determinants Δ and Δ_t equal zero, the other two determinants automatically equal zero. In the case considered it follows

from Eq. (8.4a) that the system has finite, although not unique, solutions. The equations

$$\Delta = 0, \qquad \Delta_t = \begin{vmatrix} A & 2B & H \\ dx & dr & dp \\ 0 & dx & dq \end{vmatrix} = 0,$$

in expanded form are

$$A(r')^2 - 2Br' + C = 0, \tag{8.5a}$$

$$A(r'\,dq - dp) - 2B\,dq + H\,dx = 0. \tag{8.6}$$

These equations are called the compatibility relations. The first represents two sets of characteristics in the physical plane, x-r, and the second, two sets of curves in the hodograph plane, p-q. The corresponding characteristics of both sets are commonly called conjugate.

Equation (8.6) is the condition that must be satisfied by the values of the first derivatives, p and q, of the desired function on the initial curve AB when this curve is a characteristic. Thus, a distinguishing feature of characteristics is that the initial conditions can be assigned arbitrarily along a curve that is not a characteristic, but it is then impossible to assign arbitrary conditions to the characteristics of this curve. As we see, every point on the characteristics in the x-r plane corresponds to a specific point on the characteristics in the p-q plane. This relationship, as will subsequently be evident, permits the use of characteristics in the calculation of gas flows.

The Occurrence of Characteristics

The method of characteristics is of practical interest in the case where the expression $B^2 - AC > 0$, so that the roots of Eq. (8.5a) give two different sets of real characteristics. In this case, Eq. (8.1) will be of hyperbolic type. It is not difficult to show that the gas flow described by this equation must be supersonic. In fact, if we

replace the coefficients A, B, and C in the inequality $B^2 - AC > 0$ by their values according to Eq. (3.20), we find that $B^2 - AC = a^2(V^2 - a^2)$. Hence, it is evident that the condition $B^2 - AC > 0$ is fulfilled when the flow velocity is supersonic, i.e., $V > a$.

For such a flow, the two sets of conjugate characteristics in the physical plane are determined by the different real roots, $\lambda_{1,2} = dr/dx$, of Eq. (8.5a):

$$\lambda_{1,2} = \left(\frac{dr}{dx}\right)_{1,2} = \frac{1}{V_x^2 - a^2}\left(V_x V_r \pm a\sqrt{V^2 - a^2}\right), \qquad (8.7)$$

where the subscript 1 is for the first set of characteristics and the subscript 2 is for the second.

The physical meaning of these characteristics can be established by defining an angle μ between the velocity vector at some point in the flow and the direction of the characteristic at the same point (Fig. 79). This angle can be found from Eq. (8.7) using a local coordinate system x_1, r_1, with the origin at point A and with the horizontal axis x_1 coinciding with the direction of the velocity vector $\bar{V}$. For this condition,

1 — Direction of first-family characteristic at point A
2 — First-family characteristic
3 — Direction of second-family characteristic at point A
4 — Second-family characteristic

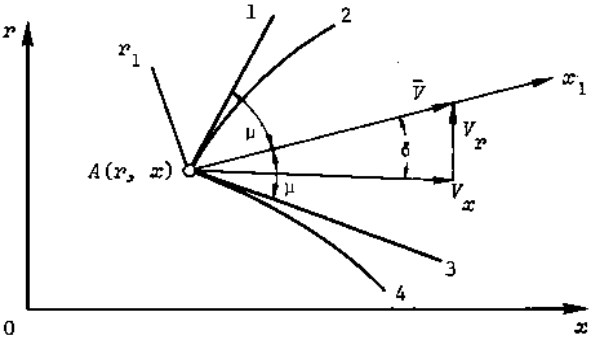

Fig. 79--Physical meaning of the characteristics

$V_x = V$, $V_r = 0$, and therefore

$$\lambda_{1,2} = \tan \mu_{1,2} = \pm \frac{1}{\sqrt{M^2 - 1}}. \tag{8.8}$$

Thus, at each point of the characteristic, the angle between its direction and the velocity vector equals the slope of the Mach line. This means the characteristic itself is a Mach line.

In a given case, all of these considerations pertain to any one meridian plane ϕ = const. The characteristic (the Mach line) in this plane must be considered as the line of intersection of the characteristic surface of a given family with the meridian plane. The characteristic surface itself represents an envelope of Mach cones with apexes at the points that are the sources of these perturbations. Every region of supersonic gas flow around a body is occupied by two families of characteristic surfaces. Moreover, each of them can be considered a Mach wave. The intersection of such surfaces with the meridian plane gives two families of lines covering the whole x-r plane, and they can be considered as Mach lines or Mach waves on the plane.

The Characteristics in the Hodograph Plane

If we substitute the first root of the characteristic equation ($r' = \lambda_1$) for the value r' in Eq. (8.6), the latter will represent the first family of characteristics in the p-q plane. An analogous substitution of the second root, $r' = \lambda_2$, gives the equation for the second family of characteristics in the same plane. The equations thus obtained for the conjugate characteristics can be transformed after utilizing the nature of the roots of Eq. (8.5b), according to which $2B - A\lambda_{1,2} = A\lambda_{2,1}$. Introducing this relation into Eq. (8.6), we obtain

$$A(dp + \lambda_{2,1}\, dq) + H\, dx = 0, \tag{8.6a}$$

where, in this equation, subscript 2 corresponds to the first family of characteristics and subscript 1 to the second.

The Solution of Problems by the Method of Characteristics

The information presented concerning the theory of characteristics is sufficient to determine, either graphically or numerically, the parameters of supersonic flow. Examining the general scheme of the calculation, it is possible to assume that q and p are the radial (V_r) and axial (V_x) velocity components, respectively. The problem of flow around a body of revolution will be formulated as that of the problem of determining the velocity field. Moreover, its solution consists of the solution of two special problems. The first of these is related to the determination of the velocities at the point of intersection of the characteristics of different families that emerge from two closely located points at which the velocities are known. The second problem involves the calculation of the velocity at the intersection of a solid wall with a characteristic, provided that the latter is drawn from a point lying close to the wall and that the velocity at this point is known.

For a clearer representation, we will illustrate the method for the solution of these problems by means of graphical constructions. The detailed method will be described later in the text in the form of numerical calculations.

Let us consider the first problem. According to the conditions, the velocity is known at two adjacent points, A and B, in the physical plane (Fig. 80a), and we wish to find the velocity at point C, where elements of the characteristics of the first and second families intersect. For this purpose, elements $A'C'$ and $B'C'$ of the conjugate characteristics must be constructed in the p-q plane. The coordinates of point C' at their intersection determine the velocity components at point C.

In the second problem, the velocity at point B (Fig. 80b), which lies on the intersection of the wall with the element of the characteristic DB, is also found with the help of the p-q plane. In this case, a characteristic element of the same family must be drawn through the corresponding point D' to the intersection at point B' with the straight line $0'B'$, which is inclined to the axis V_x at an angle δ equal to the slope of a tangent to the wall at point B. As a result, the velocity components at point B will be determined by the coordinates of point B'.

1 — Characteristic element of second family

2 — Characteristic element of first family

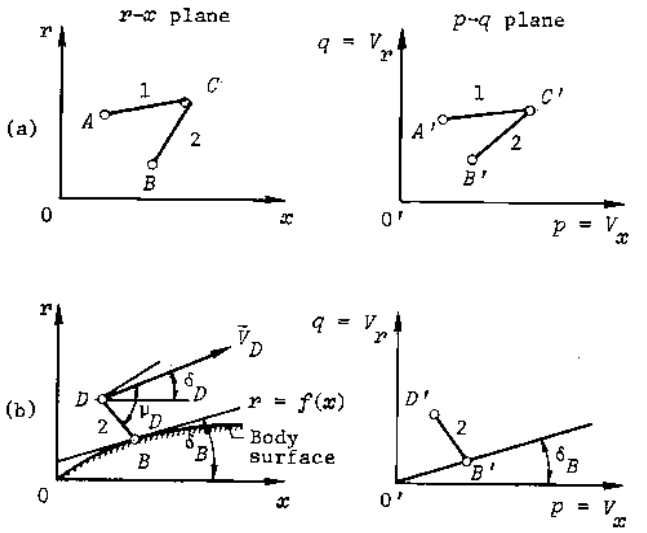

Fig. 80--Method of calculating the flow velocity

Moreover, the total velocity vector coincides with the direction of the tangent to the profile of the wall.

In numerical calculations, the solution of the characteristics equations by finite differences is substituted for these graphical constructions. As a result, the coordinates of the intersection points of corresponding characteristics are found. These coordinates determine the location of new flow points in the x-r plane and the velocity components at this point in the V_x-V_r plane (or hodograph plane). A truly graphical method can also be used to solve the problem.

THE ANALYTICAL METHOD OF FLOW CALCULATION

Transformation of the Characteristic Equations

The analytical calculation method[2] is based on the use of several transformed equations for the characteristics in the hodograph plane. These are obtained from the equations for conjugate characteristics (8.6a):

$$\frac{dV_x}{dx} + \lambda_{2,1}\frac{dV_r}{dx} + \frac{H}{A} = 0, \tag{8.6b}$$

where, in agreement with Eq. (3.20), $H = -a^2V_r/r$ and $A = V_x^2 - a^2$. To make the transformations, we introduce the variables V and δ by the relations $V_x = V\cos\delta$ and $V_r = V\sin\delta$. Equation (8.6b) takes the form

$$\frac{dV}{V} + d\delta\,\frac{\sin\delta - \lambda_{2,1}\cos\delta}{\cos\delta + \lambda_{2,1}\sin\delta} + \frac{dx}{r}\,\frac{\sin\delta\sin^2\mu}{(\sin^2\mu - \cos^2\delta)(\cos\delta + \lambda_{2,1}\sin\delta)} = 0. \tag{8.9}$$

The equation for the conjugate characteristics in the physical plane for symmetric potential flow can be written in the form (Fig. 79)

$$\lambda_{1,2} = \left(\frac{dr}{dx}\right)_{1,2} = \tan(\delta \pm \mu), \tag{8.10}$$

where the upper sign corresponds to the characteristic of the first family and the lower sign to the second family. Thus, the angular coefficients that enter into Eq. (8.9) are determined from the expressions $\lambda_{2,1} = \tan(\delta \mp \mu)$, in which the minus sign pertains to the characteristic of the first family and the plus to the second. Taking this into account, Eq. (8.9) for the conjugate characteristics will be

$$\frac{dV}{V} \mp \tan\mu\,d\delta - \frac{dx}{r}\,\frac{\sin\mu\sin\delta\tan\mu}{\cos(\delta \pm \mu)} = 0, \tag{8.9a}$$

where, as before, the upper sign corresponds to characteristics of the first family and the lower to the second family.

For calculating three-dimensional symmetric flows by the method of characteristics, we can make use of the characteristics of two-dimensional plane supersonic flow in the hodograph plane. To demonstrate, we write the characteristics equation, Eq. (8.9a), in the form

$$\cot\mu\,\frac{dV}{V} \mp d\delta - \frac{dx}{r}\,\frac{\sin\mu\sin\delta}{\cos(\delta \pm \mu)} = 0, \tag{8.9b}$$

and introduce a new variable

$$\omega = \int_{a^*}^{V} \cot \mu \frac{dV}{V} = \int_{1}^{\lambda} \cot \mu \frac{d\lambda}{\lambda}, \tag{8.11}$$

which represents an angle. In this expression, the value $d\lambda/\lambda$ is determined from Eq. (3.59):

$$\frac{d\lambda}{\lambda} = \frac{dM}{M\left(1 + \frac{\gamma - 1}{2} M^2\right)}.$$

Substituting this equation into Eq. (8.11), along with the relation $\cot \mu = \sqrt{M^2 - 1}$, and integrating from $M = 1$ to an arbitrary value of M greater than 1, we find

$$\omega = \sqrt{\frac{\gamma + 1}{\gamma - 1}} \arctan \sqrt{\frac{\gamma - 1}{\gamma + 1}(M^2 - 1)} - \arctan \sqrt{M^2 - 1}. \tag{8.11a}$$

From this expression it is evident that the angle ω is only a function of the Mach number. If we introduce the relative velocity $\lambda = V/a^*$, ω can also be represented as a function of λ.

Equation (8.9b) can be transformed to the variable ω. Then, if the last term is neglected, we obtain the equations for the characteristics of a two-dimensional flow in the hodograph plane, $\delta = \pm\omega(\lambda) + \delta_{1,2}$, in which $\delta_{1,2}$ are the integration constants. These equations correspond geometrically to two sets of curves, i.e., to characteristics that are epicycloids and are located in a ring, the internal radius of which is $\lambda = 1$ and the external is $\lambda = [(\gamma + 1)/(\gamma - 1)]^{\frac{1}{2}}$. The constant δ_1 and the plus sign in front of the function $\omega(\lambda)$ correspond to an epicycloid (a characteristic) of the first family and the constant δ_2 and the minus sign to the second family.

The form of these characteristics does not depend on the boundary conditions and is identical for all gas flows; therefore, it is advantageous to construct first a mesh of epicycloids. On such a graph in polar coordinates (Fig. 81), the angle δ and the relative velocity λ

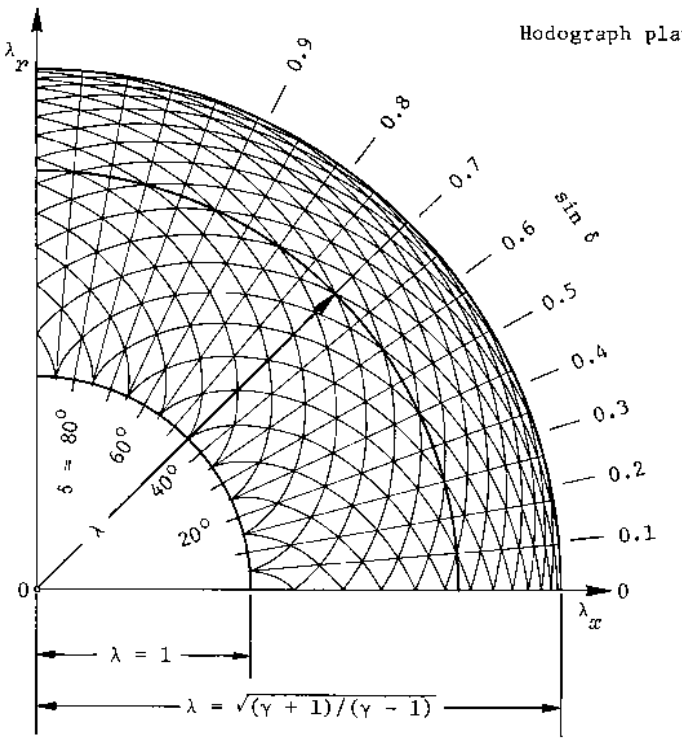

Fig. 81--The family of epicycloids

are the coordinates of the epicycloid. In using the graph, it should be noted that an increase in velocity, equivalent to an expansion of the flow, corresponds to a greater absolute value of the angle δ, i.e., to a greater deflection of the flow from its original direction.

The slope of the velocity vector is determined directly by the angle ω, whose physical meaning can be established from the equation $\delta = \pm\omega(\lambda) + \delta_{1,2}$. It is the angle of deflection of the flow for isentropic expansion from $M = 1$ to the state corresponding to the Mach number that is the upper limit in the integral for ω in Eq. (8.11). Thus, the angle $\delta = \pm\omega$ determines the total deflection of the flow in an expansion from the state characterized by $M = 1$. The angle of the deflection of the flow starting from a Mach number greater than one can

be determined in the following manner. Let us assume that the Mach number M_1 of the supersonic flow in some section is known. As a result of expansion, the Mach number is increased and reaches a value $M_2 > M_1$. Corresponding to these Mach numbers are the angles ω_1 and ω_2 of the deflection of the flow from an initial direction of the flow with $M = 1$. These angles can be determined graphically by means of one of the epicycloids or from the expressions $|\delta_1| = \omega_1(M_1)$ and $|\delta_2| = \omega_2(M_2)$. Then the angle of deflection from the direction corresponding to $M = M_1$ equals $\Delta\delta = |\delta_2 - \delta_1| = \omega_2 - \omega_1$.

The calculation for the flow parameters can be carried out in any order; i.e., the local Mach number M_2 can be determined from the known value of M_1 and from the value of the angle $\Delta\delta$ of the deflection of the flow from the initial direction. To facilitate such calculations, the values of the function $\omega = \omega(M)$ are presented in Table 15 as a function of Mach number, as computed from Eq. (8.11a) for $\gamma = 1.4$. The slope of the Mach lines, calculated from the formula $\mu = \arcsin(1/M)$, are presented in the same table.

Despite the fact that the relation between the deflection angle of the flow and the Mach number is established only for plane flow, the properties of an epicycloid can be used to calculate three-dimensional, symmetric, supersonic flows by writing Eq. (8.9b) in terms of ω:

$$d(\omega \mp \delta) - \frac{dx}{r}\frac{\sin\mu\sin\delta}{\cos(\delta \pm \mu)} = 0. \qquad (8.12)$$

To these equations must be added Eq. (8.10) for the conjugate characteristics in the physical plane.

The Technique of Numerical Calculation

Let us suppose that we must solve the first of the problems formulated above; i.e., from the known velocities at points A and B (see Figs. 80-82), we must find the velocity at the intersection of the characteristic elements at point C.

Let the Mach numbers M_A, M_B, and M_C correspond to the velocities at points A, B, and C. The other parameters at these points are denoted

Table 15

PRANDTL-MEYER ANGLE AND MACH ANGLE FOR SUPERSONIC FLOW ($\gamma = 1.4$)

M	$\omega°$	$\mu°$	M	$\omega°$	$\mu°$	M	$\omega°$	$\mu°$
1.00	0.000	90.000						
1.10	1.336	65.380	4.10	67.082	14.117	7.10	91.491	8.097
1.20	3.558	56.443	4.20	68.333	13.774	7.20	91.997	7.984
1.30	6.170	50.285	4.30	69.541	13.448	7.30	92.490	7.873
1.40	8.987	45.585	4.40	70.706	13.137	7.40	92.970	7.776
1.50	11.905	41.810	4.50	71.832	12.814	7.50	93.440	7.662
1.60	14.861	38.682	4.60	72.919	12.556	7.60	93.898	7.561
1.70	17.810	36.032	4.70	73.970	12.284	7.70	94.345	7.462
1.80	20.725	33.749	4.80	74.986	12.025	7.80	94.781	7.366
1.90	23.586	31.757	4.90	75.969	11.776	7.90	95.208	7.272
2.00	26.380	30.000	5.00	76.920	11.537	8.00	95.625	7.181
2.10	29.097	28.437	5.10	77.841	11.308	8.20	96.430	7.005
2.20	31.732	27.036	5.20	78.732	11.087	8.40	97.200	6.837
2.30	34.283	25.771	5.30	79.596	10.876	8.60	97.936	6.677
2.40	36.746	24.624	5.40	80.433	10.672	8.80	98.642	6.525
2.50	39.124	23.578	5.50	81.245	10.476	9.00	99.318	6.379
2.60	41.415	22.620	5.60	82.032	10.287	9.20	99.967	6.240
2.70	43.621	21.738	5.70	82.796	10.104	9.40	100.589	6.107
2.80	45.746	20.925	5.80	83.537	9.928	9.60	101.188	5.979
2.90	47.790	20.171	5.90	84.256	9.758	9.80	101.763	5.857
3.00	49.757	19.471	6.00	84.955	9.594	10.00	102.316	5.739
3.10	51.650	18.819	6.10	85.635	9.435	10.20	102.849	5.626
3.20	53.470	18.210	6.20	86.296	9.282	10.40	103.362	5.518
3.30	55.222	17.640	6.30	86.937	9.133	10.60	103.857	5.413
3.40	56.907	17.105	6.40	87.561	8.989	10.80	104.335	5.313
3.50	58.530	16.602	6.50	88.168	8.850	11.00	104.796	5.216
3.60	60.091	16.128	6.60	88.759	8.715	11.20	105.241	5.123
3.70	61.595	15.680	6.70	89.335	8.584	11.40	105.671	5.032
3.80	63.044	15.258	6.80	89.895	8.457	11.60	106.087	4.945
3.90	64.440	14.857	6.90	90.441	8.333	11.80	106.489	4.861
4.00	65.785	14.478	7.00	90.973	8.213	12.00	106.879	4.780

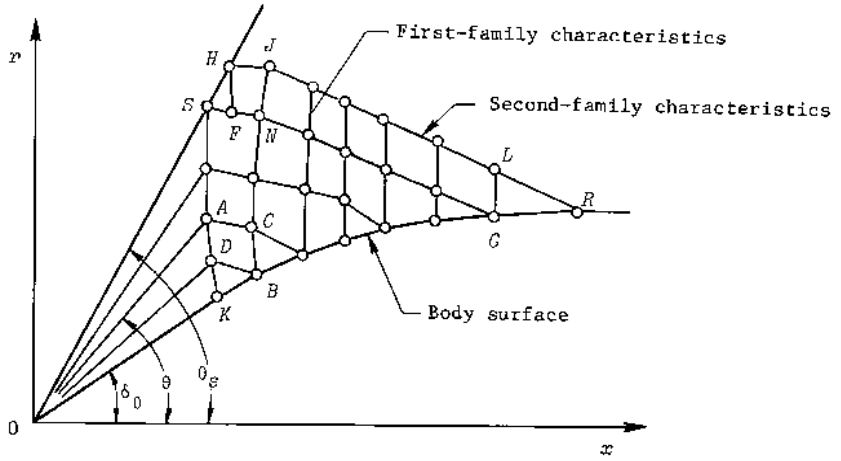

Fig. 82--Characteristic net for supersonic flow about a body of revolution

with subscripts in a similar manner. The unknowns will be the parameters at point C, specifically the angle δ_C, the Mach number M_C, and the coordinates x_C and r_C.

All the numerical calculations are based on the characteristic equations, Eqs. (8.10) and (8.12), which must be written in finite-difference form. To determine the coordinates x_C and r_C, Eq. (8.10) is written in the form of finite differences:

$$r_C - r_B = (x_C - x_B) \tan (\delta_B + \mu_B),$$

$$r_C - r_A = (x_C - x_A) \tan (\delta_A - \mu_A).$$

The coordinates x_C and r_C are found as a result of solving this system of equations.

To determine the Mach number M_C and the angle δ_C at point C, Eq. (8.12) for the conjugate characteristics in the hodograph plane must be written in finite-difference form. The equations, which correspond to the elements BC and AC of the characteristics of the first and second families of curves, have the form

$$\Delta\omega_B - \Delta\delta_B - \frac{x_C - x_B}{r_B} l_B = 0, \tag{8.13}$$

$$\Delta\omega_A + \Delta\delta_A - \frac{x_C - x_A}{r_A} m_A = 0, \tag{8.14}$$

where the coefficients l_B and m_A are computed from the expressions

$$l = \frac{\sin\mu \sin\delta}{\cos(\delta + \mu)}, \qquad m = \frac{\sin\mu \sin\delta}{\cos(\delta - \mu)} \tag{8.15}$$

for the values of the angles μ and δ at the points B and A, respectively. Thus, Eqs. (8.13) and (8.14) are written on the assumption that the coefficients l and m remain constant along the characteristic elements and are equal to their values at the initial points A and B.

The increments $\Delta\omega_B$, $\Delta\omega_A$, $\Delta\delta_B$, and $\Delta\delta_A$ are the unknowns in these equations. The number of unknowns can be reduced to two if it is noted that

$$\begin{aligned} \Delta\omega_B &= \Delta\omega_A + \omega_A - \omega_B, \\ \Delta\delta_B &= \Delta\delta_A + \delta_A - \delta_B. \end{aligned} \tag{8.16}$$

Then Eq. (8.14) can be converted to the form

$$\Delta\omega_B + \Delta\delta_B - \omega_A + \omega_B - \delta_A + \delta_B - \frac{x_C - x_A}{r_A} m_A = 0. \tag{8.14a}$$

Solving this equation and Eq. (8.13) for the increment $\Delta\delta_B$, we get

$$\Delta\delta_B = \frac{1}{2}\left[\frac{x_C - x_A}{r_A} m_A - \frac{x_C - x_B}{r_B} l_B + (\omega_A - \omega_B) + (\delta_A - \delta_B)\right]. \tag{8.17}$$

From this value of $\Delta\delta_B$, we can find the second unknown quantity:

$$\Delta\omega_B = \Delta\delta_B + \frac{x_C - x_B}{r_B} l_B. \tag{8.18}$$

At this point is is possible to compute the angles $\delta_C = \delta_B + \Delta\delta_B$ and $\omega_C = \omega_B + \Delta\omega_B$. The Mach number M_C and the Mach angle μ_C can be determined from the quantity ω_C with the help of Table 15. Other parameters may be found if required, e.g., the density, temperature, etc. The parameters thus computed represent a first approximation, because the coefficients l and m along the characteristic elements, and also the radial coordinates, are assumed constant and equal to their corresponding values at points A and B. These parameters can be refined if averages between the quantities given at points A and B, and those obtained at point C in the first approximation, are substituted into Eqs. (8.13) and (8.14) instead of l_B, m_A, r_B, and r_A. The approximation process can be repeated until a given accuracy is attained.

A decreased distance between points A and B can ensure the necessary accuracy in the second, or even in the first, approximation. In making the calculations it should be remembered that the initial points, A and B, cannot be located on the same characteristic.

Let us now investigate the numerical calculation by the method of characteristics for the second problem formulated above. This problem involves the determination of the velocity at point B, which is located on the intersection of the characteristic element DB (of the second family of curves) with the surface of the body of revolution (see Figs. 80-82). The magnitude and direction of the velocity at point D and the coordinates of the point are known. We can determine the velocity at point B directly with the help of Eq. (8.12) written in finite-difference form:

$$\Delta\omega_D + \Delta\delta_D - \frac{x_B - x_D}{r_D} m_D \approx 0. \qquad (8.19)$$

In this equation the increment $\Delta\delta_D = \delta_B - \delta_D$ is the difference of the slopes of the velocity vectors at points B and D. Furthermore, we can determine δ_B from the condition of continuous flow along the surface, $\tan \delta_B = (dr/dx)_B$, and the equation for the body shape, $r = f(x)$. The coordinates x_B and r_B are found from the simultaneous solution of the equations

$$r_B - r_D = (x_B - x_D) \tan (\delta_D - \mu_D), \qquad r_B = f(x_B).$$

After computing the third term in Eq. (8.19), it is possible to determine $\Delta\omega_D$ to find the angle $\omega_B = \Delta\omega_D + \omega_D$ and to calculate the Mach number M_B and the Mach angle μ_B.

The Calculation of Flow around a Pointed Body of Revolution

The calculation of flow around a pointed body usually begins with the determination of the conical flow around the apex for which, in the case of small curvature of the nose, it is possible to substitute a cone. (In Fig. 82, point K is the end of the cone.) The velocity and the angles ω, μ, and δ are found as a result of the calculation on the rays OD, OA, etc. of the intermediate conical surfaces (including the rays of the cone OK and the shock wave OS). Selection of the angles θ of the intermediate cones is arbitrary as long as the interval $\Delta\theta$ is sufficiently small to ensure the required accuracy.

It is advisable to follow the calculations by means of a graphical construction of the mesh of the characteristics, similar to that presented in Fig. 82. First, the element KD of a characteristic of the first family is constructed by means of the data known at point K, i.e., the angles μ_K and δ_K. The terminal point D of the element is the point of its intersection with the adjacent conical ray OD. Its coordinates are found as the result of the joint solution of the equations

$$r_K - r_D = (x_K - x_D) \tan (\delta_K + \mu_K), \qquad r_D = x_D \tan \theta_D.$$

The coordinates are found in a similar manner for the remaining points of the first-family characteristic KS, which is the edge of the conical flow. To obtain more accurate data, the calculation of the coordinates can be carried out for average values of the angles δ and μ between the adjacent points K and D, D and A, etc.

In addition to the coordinates at every point on this characteristic, including the point S of its intersection with the shock, the value and direction of the velocity (Mach number M and angles ω, μ, and δ) will be known. The problem amounts to determining the velocity field in the area between the characteristic and the surface of the body.

The solution of this problem is made up of solutions to the two

special problems that were mentioned above. First, the parameters are calculated at point B, lying at the intersection of the body and the element DB of the characteristic of the second family (second problem). Next, from the velocity found at point B and from the parameters at point A, which are known from the solution of the cone problem, the computation is made for the parameters at point C, which lies at the intersection of element AC of the second-family characteristic and the element BC of the first-family characteristic (first problem). In the process, the angles δ and ω are determined and the local Mach number and the angle μ are found from the value of ω. These calculations can be carried out with the help of Table 15. Analogous computations permit the determination of the parameters at all points of the second series, including point N.

Further calculation involves finding the parameters at the intersection with the shock of the element of the characteristic drawn through point N. In practice, to obtain a better approximation, the characteristic is not drawn from point N but from point F, located between points N and S. With this construction of the characteristic, the element adjacent to the shock wave proves to be quite small.

The coordinates at point F and also the other parameters (M, ω, μ, and δ) are computed from their known values at points S and N by linear interpolation. It is then possible to formulate equations for the element FH of the first-family characteristic in the physical plane and also for the element of the corresponding characteristic of the same family in the hodograph plane.

Solving the equation for the characteristic in the x-r plane together with the equation for a planar shock wave, we can find the coordinates of the point H in the first approximation. To determine the velocity at this point, it is necessary to consider both the conditions on the characteristic and the conditions on the shock wave, because point H is located on the shock surface. The characteristic FH approaching the shock is from its nature a rarefaction wave originating on the body surface, and it therefore decreases the intensity and slope of the shock wave. Thus, the entropy varies along the shock and the flow is rotational. If the vorticity is slight, the shape of the shock and the velocity behind it can be determined from shock theory and from the

equations for the characteristics in potential flow. Assuming that this condition holds in the present case, we can find the parameters at point H. One of the unknown parameters is the slope of the velocity vector δ_H, which can be determined from the change in the angle δ along the element FH in the form $\delta_H = \Delta\delta_F + \delta_F$.

Let us assume that the angle δ also varies by the quantity $\Delta\delta_F$ along the shock element SH, so that the corresponding increment in Mach number is equal to $\Delta M_{\delta_F} = (dM/d\delta)_{\delta_F} \Delta\delta_F$.

If it is assumed that the deflection of flow behind the shock at point S is the same as at point F (i.e., it is determined by the angle δ_F), it is possible to compute the corresponding Mach number M_S from this deflection† and find the Mach number at point H in a first approximation:

$$M_H = M_S + \left(\frac{dM}{d\delta}\right)_{\delta_F} \Delta\delta_F. \tag{8.20}$$

The derivative $(dM/d\delta)_{\delta_F}$ can be calculated from shock-wave theory:

$$\frac{dM}{d\delta} = \frac{dM}{d\delta_S} = -M\left[\cot(\theta_S - \delta_S)\left(\frac{d\theta_S}{d\delta_S} - 1\right) + \frac{\gamma+1}{4} M^2 \sin^2(\theta_S - \delta_S) \frac{d}{d\delta_S}\left(\frac{\rho_2}{\rho_1}\right)\right]. \tag{8.21}$$

The two derivatives on the right side of Eq. (8.21) are, in turn, determined from the equations

$$\frac{d}{d\delta_S}\left(\frac{\rho_2}{\rho_1}\right) = 2\frac{\rho_2}{\rho_1}\cot\theta_S\left(1 - \frac{\gamma-1}{\gamma+1}\frac{\rho_2}{\rho_1}\right)\frac{d\theta_S}{d\delta_S}, \tag{8.22}$$

$$\frac{d\theta_S}{d\delta_S} = -\frac{\rho_2/\rho_1}{\dfrac{\cos^2(\theta_S - \delta_S)}{\cos^2\theta_S} - \dfrac{\rho_2}{\rho_1} - 2\cos^2(\theta_S - \delta_S)\left(1 - \dfrac{\gamma-1}{\gamma+1}\dfrac{\rho_2}{\rho_1}\right)}. \tag{8.23}$$

The change in Mach number along the characteristic from point F to point H, i.e., the value $\Delta M_F = M_H - M_F$, can be obtained from Eq. (8.20):

†Editor's note: The quantities M_S and δ_S will be known from conical shock theory.

$$\Delta M_F = M_S + \left(\frac{dM}{d\delta}\right)_{\delta_F} \Delta\delta_F - M_F. \tag{8.24}$$

Converting from Mach number to the angle ω, Eq. (8.24) can be replaced by

$$\Delta\omega_F = \omega_S + \left(\frac{d\omega}{d\delta}\right)_{\delta_F} \Delta\delta_F - \omega_F, \tag{8.25}$$

where $(d\omega/d\delta)_{\delta_F}$ is given by

$$\frac{d\omega}{d\delta} = g(M)\,\frac{dM}{d\delta}. \tag{8.26}$$

The function $g(M)$, in turn, is determined from

$$g(M) = \frac{d\omega}{dM} = \frac{\sqrt{M^2 - 1}}{M\left(1 + \dfrac{\gamma - 1}{2} M^2\right)}. \tag{8.27}$$

Using Eq. (8.12) for the first-family characteristic element FH and solving together with Eq. (8.25), we find

$$\Delta\delta_F = \frac{\omega_F - \omega_S + \dfrac{x_H - x_F}{r_F}\, l_F}{(d\omega/d\delta)_{\delta_F} - 1},$$

$$\Delta\omega_F = \Delta\delta_F + \frac{x_H - x_F}{r_F}\, l_F. \tag{8.28}$$

The angle ω_H at point H can be calculated from the quantity $\Delta\omega_F$ and then used to find M_H and the Mach angle μ_H. The angle $\delta_H = \Delta\delta_F + \delta_F$ is calculated at the same point, and a second approximation to the slope of the shock is obtained. It is apparent that the shock angle will be less than that for a conical shock, the decrease being caused by the weakening of the shock, as was noted.

Having completed the calculation for point H, the calculation for the following series of points is begun, as before. Accordingly, the

velocity (or Mach number) field is determined for the flow around a pointed body of revolution with any shape that is given in the form of a smooth curve.

From the Mach number at the intersection points of the characteristics with the body surface, it is possible to find other parameters, e.g., temperature, density, and pressure. For example, at point B,

$$\frac{T_B}{T_0} = \frac{1}{1 + \frac{\gamma - 1}{2} M_B^2},$$

$$\frac{\rho_B}{\rho_0} = \nu_0 \left(\frac{T_B}{T_0}\right)^{1/(\gamma-1)}, \qquad \frac{p_B}{p_0} = \nu_0 \left(\frac{T_B}{T_0}\right)^{\gamma/(\gamma-1)},$$

where T_0, ρ_0, and p_0 are the isentropic stagnation values and can be determined from

$$\frac{T_0}{T_\infty} = 1 + \frac{\gamma - 1}{2} M_\infty^2, \qquad \frac{\rho_0}{\rho_\infty} = \left(\frac{T_0}{T_\infty}\right)^{1/(\gamma-1)}, \qquad \frac{p_0}{p_\infty} = \left(\frac{T_0}{T_\infty}\right)^{\gamma/(\gamma-1)}.$$

The coefficient $\nu_0 = p_0'/p_0$ is the stagnation pressure ratio before and after the shock and can be found either from Fig. 62 (p. 182) for the cone angle $\delta_c = \delta_0$ and the Mach number M_∞, or from Eq. (4.33a) for M_∞ and the angle of the conical shock θ_s. From the absolute value of the static pressure, the pressure coefficient can be calculated from $C_{pB} = (1/\gamma M_\infty^2)[(p_B/p_0)(p_0/p_\infty) - 1]$.

The pressure distribution, computed by the method of characteristics for a parabolic body of revolution with a fineness ratio $\lambda_N = 3.8$ for $M_\infty = 2.0$, 3.0, and 3.92, is illustrated in Fig. 83. In Fig. 84, data are presented for the nose pressure drag coefficient, obtained from the pressure distribution around a body of the same parabolic form (after Frankl).†

† Editor's note: The curves in Figs. 83 and 84 of the original text do not agree with the correct values for the pressure distribution and pressure drag coefficient of parabolic noses. They have been redrawn correctly here.

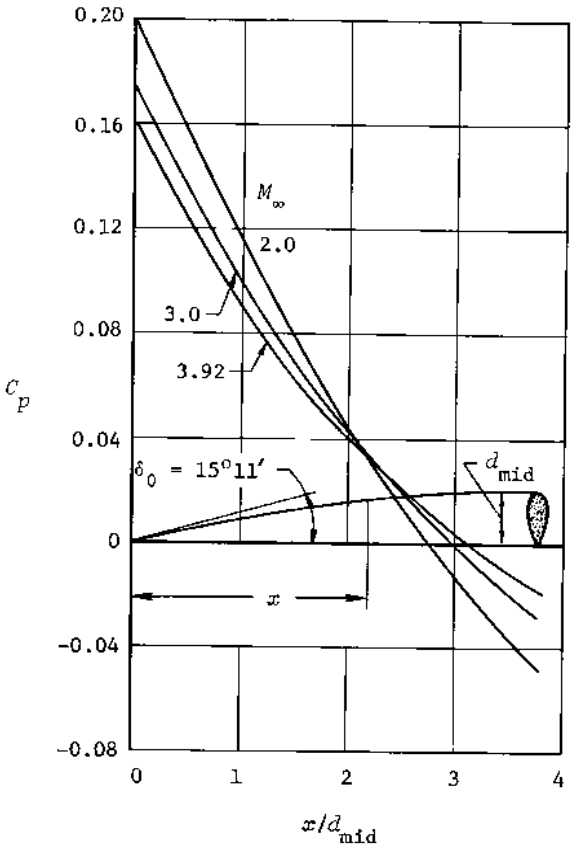

Fig. 83--Pressure distributions calculated by the method of characteristics for a parabolic body of revolution

APPROXIMATE CALCULATION OF FLOW

Equations for Ogive Noses

If it is necessary to make quick calculations and to obtain rough data on the parameters, there are simpler methods and approximate relations that can be used in place of the time-consuming method of characteristics. Several of these methods have been developed as a result of processing data from calculations by the method of characteristics or from experiments.

One of these relations is a semiempirical equation (see Ref. 3)

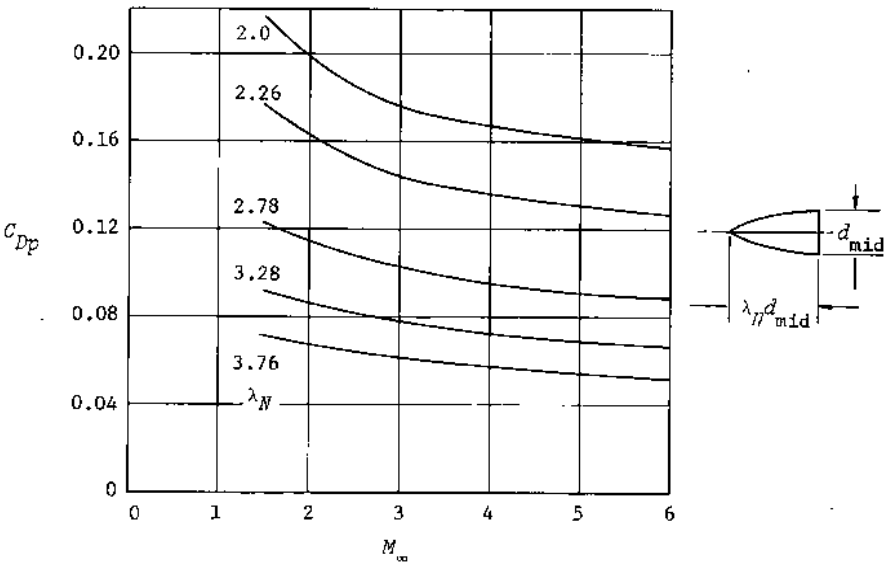

Fig. 84--Pressure drag coefficients for a parabolic body of revolution, calculated by the method of characteristics

for the calculation of the pressure drag coefficient for ogive noses with half-angles at the vertex of $10° \leq \delta_c \leq 45°$ for a Mach number range of $1.5 \leq M_\infty \leq 3.5$:

$$C_{Dp} = C_{pc}\left[1 - \frac{196\lambda_N^2 - 16}{14(M_\infty + 18)\lambda_N^2}\right], \tag{8.29}$$

where C_{pc} is the pressure coefficient at the apex, and λ_N is the fineness ratio of the nose of the body of revolution, which can be determined from Eq. (1.37) or from the expression $\lambda_N = 1/[2 \tan (\delta_c/2)]$.

The Method of Local Cones

The approximate method of local cones has been proposed by several investigators; the most detailed treatment is by Soviet scientist S. V. Vallander.(4) The pressure coefficient at some point A on the surface

of a body in a flow with a Mach number M_∞ is assumed to be the same as that on a local cone with an angle δ in a flow with the same free-stream Mach number (Fig. 85). The cone is tangent to the surface of

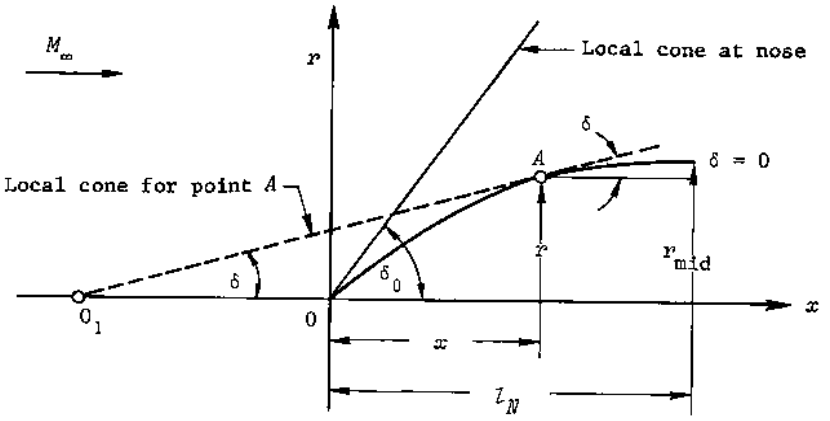

Fig. 85--Diagram for the method of local cones

the body at the point in question; therefore, the method of local cones is often called the method of tangent cones. By the nature of the method, all of the results for supersonic flow around cones can be used for the calculation of the pressure distribution.

Instead of specifying that the local pressure is the same as that on the tangent cone, it can be assumed that the local velocities are the same at the point under consideration on the body. The pressure p_v is then determined from the first relation of Eq. (3.58), in which the velocity is a known function of M_∞ and the angle of the local cone δ, and the stagnation pressure $p_0 = p_0'$ is a function of M_∞ and the nose angle δ_0. From the pressure p_v, the pressure coefficient can be calculated from the usual relation $C_{pv} = (2/\gamma M_\infty^2)(p_v/p_\infty - 1)$.

The calculation is somewhat unwieldy on the basis of the hypothesis of identical velocities. However, it can be simplified by assuming that the local velocities are the same by either method, in which case the relation between the pressure coefficients is given by

$$C_{pv} = C_{pp}\bar{v} + \frac{2(\bar{v} - 1)}{\gamma M_\infty^2}, \tag{8.30}$$

where C_{pp} is the pressure coefficient corresponding to the hypothesis of identical pressures. The quantity $\bar{v}$ is determined as the ratio ν_0/ν, where $\nu = p_0''/p_0$ is calculated from the stagnation pressure p_0'' for a local cone with an angle δ, and $\nu_0 = p_0'/p_0$ is determined from the stagnation pressure p_0' for a cone with the angle δ_0.

Thus, to calculate the pressure coefficient C_{pv}, it is first necessary to find the value C_{pp} on the local cone (e.g., from Eq. (6.19)) and next determine the coefficients ν, ν_0, and the ratio $\bar{v} = \nu_0/\nu$.

It is apparent that this ratio equals unity at the apex, while at the end of the nose (where $\delta = 0$) its value is $\bar{v} = \nu_0$, which is less than unity. From the form of Eq. (8.30), it follows that the pressure coefficient C_{pv} can be zero at some station on the nose and negative further downstream. Thus, the hypothesis of identical velocities gives more valid results than does the equal pressure method for moderate Mach numbers, for which a region of negative pressure coefficients is known to exist on the rear part of the nose, either from experimental results or by exact calculations. The values of the coefficients C_{pv} and C_{pp} approach each other near the apex and, for $x = r = 0$, they are identical.

The variation of the pressure coefficient C_{pv} with $\tan \delta_0$ and $\tan \delta$ is shown in Figs. 86 and 87 for two values of the free-stream Mach number, $M_\infty = 2$ and 5. Knowing the distribution of pressure from C_{pv}, it is possible to determine the corresponding pressure drag coefficient $(C_{Dp})_v$. Its value can also be calculated approximately by using Eq. (1.6) and Eq. (8.30) for the relation between C_{pv} and C_{pp}:

$$(C_{Dp}')_v = 2\int_0^1 \left[C_{pp}\bar{v} + \frac{2(\bar{v} - 1)}{\gamma M_\infty^2}\right] \bar{r}\, d\bar{r}, \tag{8.31}$$

where $\bar{r} = r/r_B$. This equation determines the pressure drag coefficient with respect to a base area with a radius r_B that, in general, may be different from the maximum radius of the nose, i.e., $r_B \leq r_{mid}$. The

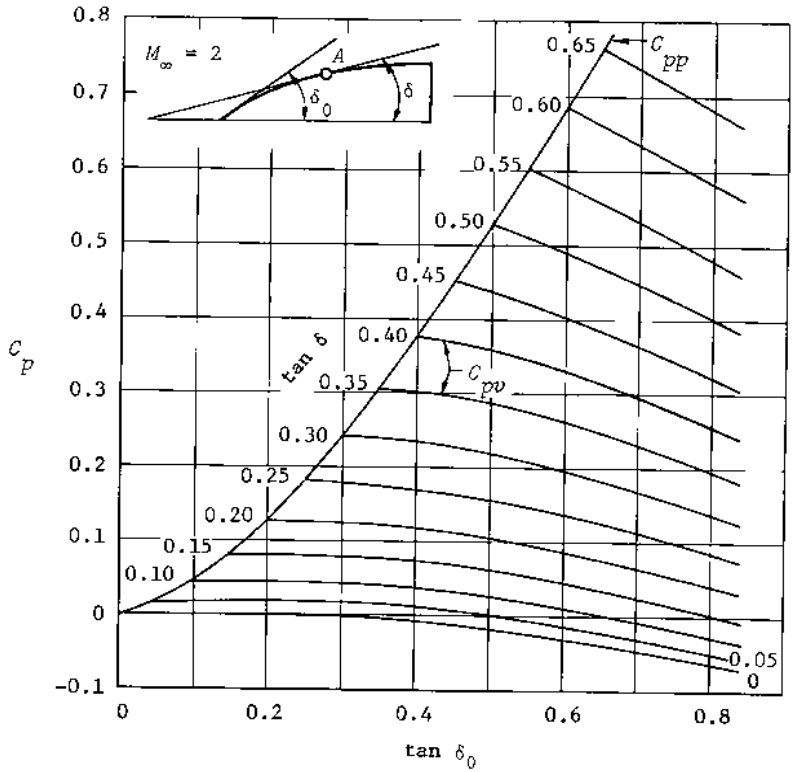

Fig. 86--Graph for calculation of the pressure distribution based on the hypotheses of identical pressures and velocities ($M_\infty = 2$)

equation can be simplified if we examine the special case where the function $\bar{\nu}$ varies little along the body. Then the quantity $\bar{\nu}$ can be replaced by its average value, and Eq. (8.31) has the form

$$(C'_{Dp})_v = (C'_{Dp})_p \bar{\nu}_{avg} + \frac{2(\bar{\nu}_{avg} - 1)}{\gamma M_\infty^2}, \qquad (8.31a)$$

where $(C'_{Dp})_p$ is the drag coefficient with respect to the area of the base section πr_B^2 and is computed on the basis of the hypothesis of identical pressures. This coefficient is determined from Eq. (1.6) with $C_p = C_{pp}$.

Equation (8.31a) is approximately valid for values of $\bar{\nu}$ within the

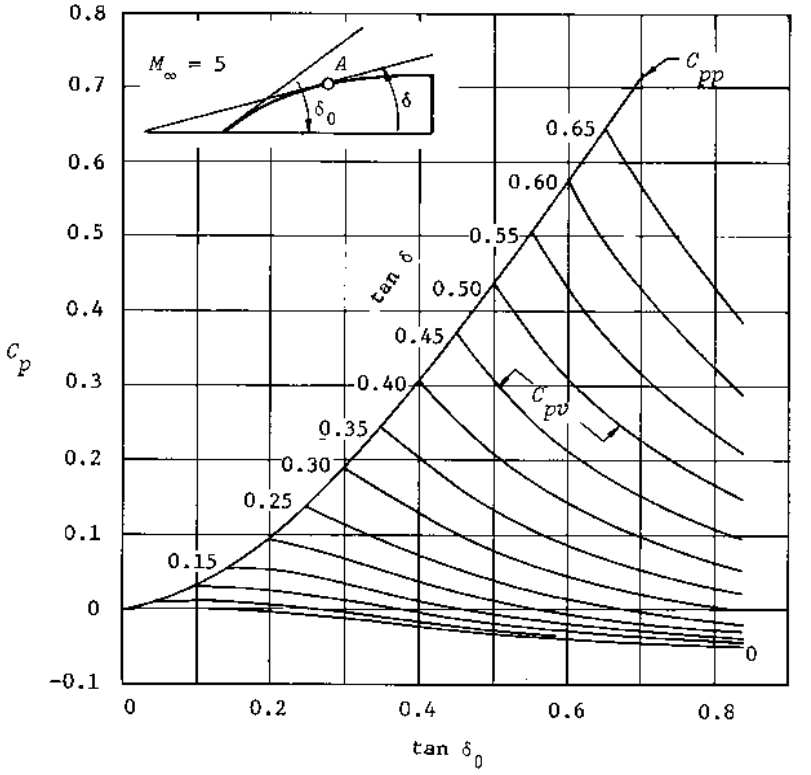

Fig. 87--Graph for calculation of the pressure distribution based on the hypotheses of identical pressures and velocities ($M_\infty = 5$)

limits $0.8 \leq \bar{v} \leq 1$. If this condition is not fulfilled, the general Eq. (8.31) must be used. Even in this case, however, the calculation can be simplified. It has been found that the distribution of the function $\bar{v}$ along parabolic or ogival noses can be represented approximately by the equation

$$\bar{v} = v_0 + (1 - v_0)(1 - \bar{x})^2, \tag{8.32}$$

where $\bar{x} = x/l_N$. Moreover, the pressure coefficient C_{pp} can be estimated from the expression $C_{pp} = C_{pa}(1 - \bar{x})^{1.47}$, in which C_{pa} is the pressure coefficient at the apex of the body. Then Eq. (8.31) can be written as

$$(C'_{Dp})_v = (C'_{Dp})_p - 0.667\bar{r}_B(1 - \nu_0)\left[(1 - 0.552\bar{r}_B + 0.068\bar{r}_B^2 - 0.189\bar{r}_B^3)C_{pc} + \frac{1.43}{M_\infty^2}\right], \tag{8.33}$$

where $\bar{r}_B = r_B/r_{mid}$. In the case of a nose for which $r_B = r_{mid}$, this equation has the form

$$(C_{Dp})_v = (C_{Dp})_p - 0.667(1 - \nu_0)\left(0.327C_{pc} + \frac{1.43}{M_\infty^2}\right). \tag{8.33a}$$

The coefficients $(C_{Dp})_v$ and $(C_{Dp})_p$ are based on the area πr_{mid}^2. For parabolic noses the latter coefficient can be approximated by

$$(C_{Dp})_p = 0.415C_{pc}. \tag{8.34}$$

If the value of the coefficient is based on the area πr_B^2 of some arbitrary section,

$$(C'_{Dp})_p = C_{pc}(1 - 0.490\bar{r}_B + 0.056\bar{r}_B^2 - 0.151\bar{r}_B^3). \tag{8.34a}$$

Comparison with the method of characteristics and with experimental data indicates that Eq. (8.33a) can be used in those cases in which the free-stream Mach number lies in the range $2 < M_\infty \leq 6$ to 7 and the fineness ratio λ_N is less than about 2 to 2.2, i.e., for rather thick bodies of revolution. Equation (8.34) gives results that are too large for these conditions; for example, for a parabolic nose with a fineness ratio of 2 and $M_\infty = 2$, the value of C_{Dp} calculated from this equation is almost twice as large as that calculated by the method of characteristics. More satisfactory data are obtained from Eq. (8.34) if an empirical parameter dependent on M_∞ is substituted in place of the numerical coefficient 0.415. The pressure drag coefficient then has the form

$$C_{Dp} = \frac{0.08(15.5 + M_\infty)}{3 + M_\infty} C_{pc}. \tag{8.35}$$

This expression is suitable for nose fineness ratios greater than 2.5 and for $1.5 \leq M_\infty \leq 6$.

§ 9. *THE CALCULATION OF AXIALLY SYMMETRIC ROTATIONAL FLOW*

GENERAL FORM OF THE EQUATIONS FOR THE CHARACTERISTICS

WITH AN INCREASE in the free-stream Mach number, the intensity of the curved shock wave in front of the body increases so much that it becomes necessary to take into account the rotational character of the flow. We must develop, in a manner similar to that used for potential flow, a system of characteristics that allows a numerical solution of the differential equation (3.26) for the stream function and that thereby permits the calculation of the rotational flow in the region between the shock and the body.

The coefficients for the second partial derivatives and the forcing function have the following values:

$$A = V_x^2 - a^2, \qquad B = V_x V_r, \qquad C = V_r^2 - a^2,$$

$$H = a^2 V_x (1 - \tilde{V}^2)^{1/(\gamma-1)} + r^2 (a^2 - V^2)(1 - \tilde{V}^2)^{(\gamma+1)/(\gamma-1)} f(\Psi). \tag{9.1}$$

The function $f(\Psi)$, given in Eq. (3.27), is determined by the value of the rotation $\partial V_r/\partial x - \partial V_x/\partial r$. In turn, the relation for the rotation term is known from gas dynamics:

$$\frac{\partial V_r}{\partial x} - \frac{\partial V_x}{\partial r} = \frac{a^2}{V} \frac{1}{\gamma R} \frac{dS}{dn}, \tag{9.2}$$

which indicates the dependence of the rotation on the entropy gradient normal to the streamline, i.e., on the derivative dS/dn. Consequently, the function $f(\Psi)$ can be presented in the form

$$f(\Psi) = -\frac{\gamma - 1}{2\gamma R}\frac{V_{max}}{r\tilde{V}(1 - \tilde{V}^2)^{1/(\gamma-1)}}\frac{dS}{dn}. \tag{9.3}$$

The coefficients A, B, and C in Eq. (9.1) are the same as those in Eq. (3.22) for the velocity potential in axisymmetric flow. Therefore, the equations for the characteristics of rotational flow in the physical plane (x, r) will be the same as those for potential flow. As to the hodograph plane (p, q), the form of the characteristic equations is changed as follows:

$$\frac{dp}{dx} + \lambda_{2,1}\frac{dq}{dx} + \frac{H}{A} = 0, \tag{9.4}$$

where, in agreement with Eq. (3.25),

$$\begin{aligned} p &= \Psi_x = -rV_r(1 - \tilde{V}^2)^{1/(\gamma-1)}, \\ q &= \Psi_r = rV_x(1 - \tilde{V}^2)^{1/(\gamma-1)}, \end{aligned} \tag{9.5}$$

and the angular coefficients are $\lambda_{2,1} = \tan(\delta \mp \mu)$.

Let us transform Eq. (9.4) to such a form that it determines the characteristics in the hodograph plane V_x, V_r. For this purpose, we find the ratio H/A that enters into Eq. (9.4) and calculate the derivatives dp/dx, dq/dx from Eq. (9.5). Substituting the results into Eq. (9.4), we obtain

$$\lambda_{2,1}(\lambda_{2,1}\tilde{V}_x - \tilde{V}_r) - \frac{2r\tilde{V}}{\gamma - 1}\frac{\lambda_{2,1}\tilde{V}_x - \tilde{V}_r}{1 - \tilde{V}^2}\frac{d\tilde{V}}{dx} - \frac{a^2\tilde{V}_x}{a^2 - \gamma_x^2} + r\left(\lambda_{2,1}\frac{d\tilde{V}_x}{dx} - \frac{d\tilde{V}_r}{dx}\right)$$

$$- \frac{r(\gamma - 1)}{2\gamma R}\frac{a^2(1 - \tilde{V}^2)(M^2 - 1)}{\tilde{V}(a^2 - V_x^2)}\frac{dS}{dn} = 0, \tag{9.6}$$

where the velocity components are divided by the maximum velocity, i.e., $\tilde{V}_x = V_x/V_{max}$, $\tilde{V}_r = V_r/V_{max}$.

For subsequent transformation, let us introduce the polar coordinates

δ and V, which can be determined by the expressions $V_x = V\cos\delta$, $V_r = V\sin\delta$. The following expressions result:

$$\frac{d\tilde{V}}{\tilde{V}} + d\delta\,\frac{(\lambda_{2,1}\sin\delta + \cos\delta)\tan^2\mu}{\lambda_{2,1}\cos\delta - \sin\delta} - \frac{dx}{r}\left[\lambda_{1,2}\tan^2\mu - \frac{\sin^2\mu\tan^2\mu\cos\delta}{(\sin^2\mu - \cos^2\delta)(\lambda_{2,1}\cos\delta - \sin\delta)}\right] + \frac{dx}{\gamma R}\,\frac{\sin^4\mu}{(\sin^2\mu - \cos^2\delta)(\lambda_{2,1}\cos\delta - \sin\delta)}\,\frac{dS}{dn} = 0. \tag{9.7}$$

In these equations, it is possible to carry out a number of other trigonometric transformations that take into account the substitution of $\lambda_{2,1} = \tan(\delta \mp \mu)$. Combining the result with the equations for the characteristics in the physical plane, we obtain the entire system of equations for the conjugate characteristics of axisymmetric rotational flow:

$$\frac{dr}{dx} = \tan(\delta \pm \mu),$$

$$\frac{d\tilde{V}}{\tilde{V}} \mp \tan\mu\,d\delta - \frac{dx}{r}\,\frac{\sin\delta\sin\mu\tan\mu}{\cos(\delta \pm \mu)} \pm \frac{dx}{\gamma R}\,\frac{\sin^3\mu}{\cos(\delta \pm \mu)}\,\frac{dS}{dn} = 0. \tag{9.8}$$

These equations for the characteristics in the hodograph plane can be transformed in a manner similar to those for potential flow so that they include the angle ω, which can be determined from Eq. (8.11). Then Eq. (9.8), in expanded form, is written as follows:

For the first family:

$$\frac{dr}{dx} = \tan(\delta + \mu),$$

$$d(\omega - \delta) - \frac{dx}{r}\,l + \frac{dx}{\gamma R}\,\frac{dS}{dn}\,e = 0; \tag{9.9}$$

For the second family:

$$\frac{dr}{dx} = \tan(\delta - \mu),$$
$$d(\omega + \delta) - \frac{dx}{r} m - \frac{dx}{\gamma R} \frac{dS}{dn} t = 0; \tag{9.10}$$

where

$$l = \frac{\sin\delta \sin\mu}{\cos(\delta + \mu)}, \qquad m = \frac{\sin\delta \sin\mu}{\cos(\delta - \mu)},$$
$$e = \frac{\sin^2\mu \cos\mu}{\cos(\delta + \mu)}, \qquad t = \frac{\sin^2\mu \cos\mu}{\cos(\delta - \mu)}. \tag{9.11}$$

Instead of the entropy gradient in the equations for the characteristics in the hodograph plane, the stagnation pressure gradient dp_0'/dn can be introduced, using the following relation:

$$\frac{dS}{dn} = -\frac{R}{p_0'} \frac{dp_0'}{dn} = -R \frac{d \log p_0'}{dn}. \tag{9.12}$$

THE NUMERICAL METHOD OF CALCULATION

The Calculation of Entropy and Stagnation Pressure

The equations for the characteristics of rotational flow differ from the corresponding equations for potential flow only by the inclusion of an additional term depending on the entropy variation across the streamline. Therefore, in addition to the variables that relate to isentropic flow, it is necessary to calculate, step by step, the entropy of the gas flow and its variation from one streamline to another.

Let us assume that the velocity components and the other gas parameters, including the entropy S_A and S_B (Fig. 88), are known at points A and B located on different streamlines. Assuming that the entropy varies linearly between A and B, the change in entropy per unit distance normal to the streamlines is

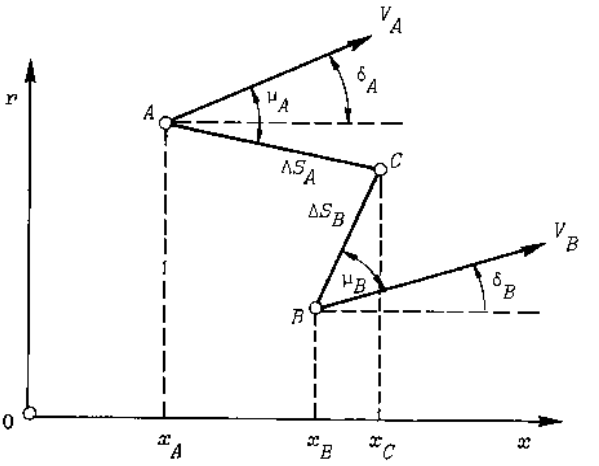

Fig. 88--Calculation of the velocity, including entropy changes

$$\frac{\Delta S}{\Delta n} = \frac{S_A - S_B}{(AC)\sin\mu_A + (BC)\sin\mu_B},$$

where

$$AC = \frac{x_C - x_A}{\cos(\delta_A - \mu_A)}, \qquad BC = \frac{x_C - x_B}{\cos(\delta_B + \mu_B)}.$$

Introducing the notation

$$\begin{aligned} e &= (x_C - x_A)\sin\mu_A\cos(\delta_B + \mu_B), \\ f &= (x_C - x_B)\sin\mu_B\cos(\delta_A - \mu_A), \end{aligned} \tag{9.13}$$

we obtain

$$\frac{\Delta S}{\Delta n} = \frac{(S_A - S_B)\cos(\delta_B + \mu_B)\cos(\delta_A - \mu_A)}{f + e}. \tag{9.14}$$

The absolute value of the entropy is determined from the relation

$$S_C = \Delta S_B + S_B = \left(\frac{\Delta S}{\Delta n}\right) BC \sin \mu_B + S_B = \frac{(S_A - S_B)f}{f + e} + S_B. \qquad (9.15)$$

The stagnation pressure gradient along the normal to the streamline is given by an equation analogous to Eq. (9.14):

$$\frac{\Delta p_0'}{\Delta n} = \frac{(p_{0A}' - p_{0B}') \cos (\delta_B + \mu_B) \cos (\delta_A - \mu_A)}{f + e}, \qquad (9.16)$$

where p_{0A}' and p_{0B}' are the stagnation pressures at points A and B. The sign of the ratio, $\Delta p_0'/\Delta n$, depends on the character of the variation in stagnation pressure along the normal from A to B. In the case of flow around an axisymmetric body with a curved bow shock, the stagnation pressure decreases as the body surface is approached. If point B is located close to the surface, the value $\Delta p_0'/\Delta n = (p_{0A}' - p_{0B}')/\Delta n$ is positive because the stagnation pressure p_{0B}' is less at this point than at point A. The stagnation pressure at point C, which lies on the intersection of the characteristics of the two families through points A and B, is calculated from an expression similar to Eq. (9.15):

$$p_{0C}' = p_{0B}' + \frac{(p_{0A}' - p_{0B}')f}{f + e}. \qquad (9.17)$$

Numerical Calculation Procedure

The numerical calculation procedure is, in principle, the same as that for potential flow. If the parameters at two adjacent points A and B are known, it is necessary to use finite-difference equations to determine the velocity at point C (Fig. 88). Equation (9.10) is used to find the variation of the parameters along the element AC for characteristics of the second family, and Eq. (9.9) for characteristics of the first family along BC.

Using the respective equations for characteristics in the hodograph plane and solving for the increment $\Delta\delta_B$, we obtain the expression

$$\Delta\delta_B = \frac{1}{2}\left[\frac{x_C - x_A}{r_A} m_A - \frac{x_C - x_B}{r_B} l_B - \frac{x_C - x_A}{\gamma p'_{0A}} \frac{\Delta p'_0}{\Delta n} t_A \right.$$

$$\left. - \frac{x_C - x_B}{\gamma p'_{0B}} \frac{\Delta p'_0}{\Delta n} c_B - (\omega_B - \omega_A) - (\delta_B - \delta_A)\right], \qquad (9.18)$$

which allows the calculation of the change in inclination of the velocity vector from B to C. In this expression, the coefficients m_A, l_B, t_A, and c_B are found from Eqs. (9.11), evaluated at points A and B. To determine x_C, a system of finite-difference equations must be formulated for the characteristics of both families of curves in the physical plane. As a result of the solution of these equations, the other coordinate r_C is computed along with x_C.

From the increment $\Delta\delta_B$, we can calculate

$$\Delta\omega_B = \Delta\delta_B + \frac{x_C - x_B}{r_B} l_B + \frac{x_C - x_B}{\gamma p'_{0B}} \frac{\Delta p'_0}{\Delta n} c_B \qquad (9.19)$$

and the angles $\delta_C = \Delta\delta_B + \delta_B$ and $\omega_C = \Delta\omega_B + \omega_B$. The latter value allows us to find the local Mach number at point C, from which the remaining parameters can be calculated, i.e., the pressure, density, and temperature. Thus, proceeding from point to point, the velocity field in rotational flow is calculated.

In the example above for flow around a body of revolution with a conical element (see Fig. 82), rotational flow will be observed behind the shock beginning at point S, which lies at the end of the conical part. The lower edge of the rotational region coincides with the second-family characteristic SG that begins at that point. The flow will be potential in that portion of the flow bounded by this characteristic and by the conical shock, and the calculation of the velocity field can be made by the characteristics method for potential flow.

In the area above the curve SG, it is necessary to use the characteristics theory for rotational flow. As an example, let us show how to calculate the velocity at point H (see Fig. 82), which is located on the curved part of the shock. The rotational character of the flow results

in changes in the flow parameters compared to potential flow. In the example in § 8, the influence of vortices was not taken into account, because the flow was assumed to be approximately irrotational.

First, let us compute the quantity $(1/p_0')\Delta p_0'/\Delta n$ along the curved portion of the shock wave SH and assume that the variation in stagnation pressure will be the same from point F to point H. The stagnation pressure p_{0S}' at point S can be found from Eq. (4.33a) for the known values of free-stream Mach number and angle of the conical shock. Assuming that the deflection of the flow behind the shock wave at point H equals the inclination of the velocity vector at point F, we can find, as previously, the slope of the shock wave θ_{sH} and calculate the stagnation pressure p_{0H}'.

The distance between the points F and H along the normal to the streamline is

$$\Delta n = (FH) \sin \mu_F = \frac{x_H - x_F}{\cos (\delta_F + \mu_F)} \sin \mu_F,$$

and the variation of the stagnation pressure along this increment is

$$\frac{1}{p_{0F}'} \frac{\Delta p_0'}{\Delta n} = \frac{1}{p_{0S}'} \frac{p_{0H}' - p_{0S}'}{\Delta n}.$$

Since point H lies on the shock wave, the flow parameters there are determined by combining Eq. (8.24) and the equation for the first family of characteristics. Thus, the increment of flow deflection $\Delta\delta_F$ is obtained from an expression similar to Eq. (8.28), except that there will be an additional term to account for the influence of vorticity:

$$\Delta\delta_F = \frac{\omega_F - \omega_S + \dfrac{x_H - x_F}{r_F} l_F - \dfrac{x_H - x_F}{\gamma p_{0F}'} \dfrac{\Delta p_0'}{\Delta n} c_F}{(d\omega/d\delta)_{\delta_F} - 1}. \tag{9.20}$$

Using Eq. (9.19), we can compute the increment $\Delta\omega_F$, and calculate the angle ω_H and the Mach number M_H. The deflection angle $\delta_H = \Delta\delta_F + \delta_F$ and M_H are used to find the slope θ_{sH} of the shock at point H, and as a result, it is possible to refine the stagnation pressure ratio p_{0H}'/p_0.

We can proceed to the calculation of the parameters at the adjacent point J (see Fig. 82) in the same way as at point C of the example described above (see Fig. 88). The relations presented in this example will be correct if we convert from the designations for points A, B, and C to the corresponding designations for points H, N, and J.

Thus, the coordinates of the points H, J, ..., L of the second-family characteristic are determined step by step, along with the gas-dynamic parameters. From the parameters found at point L, the velocity and other parameters at point R located on the surface of the body can be determined. The geometric coordinates at R are calculated from the joint solution of the equations for the body surface and the straight line drawn through the point L at an angle $\delta_L - \mu_L$. The inclination of the velocity vector at R is equal to the slope of a tangent to the body surface at R. The stagnation pressure p'_{0R} is also known and will be the same as that at points K, B, ..., G, which belong to the same streamline. Therefore, the variation in stagnation pressure along the characteristic LR is

$$\left(\frac{1}{p'_0}\frac{\Delta p'_0}{\Delta n}\right)_L = \frac{[(p'_0/p_0)_L - (p'_0/p_0)_R]\cos(\delta_L - \mu_L)}{(p'_0/p_0)_L (x_R - x_L)\sin\mu_L}. \qquad (9.21)^{\dagger}$$

Using the equation for the second-family characteristic, we find

$$\Delta\omega_L = -\Delta\delta_L + \frac{x_R - x_L}{r_L} m_L - \frac{x_R - x_L}{\gamma}\left(\frac{1}{p'_0}\frac{\Delta p'_0}{\Delta n}\right)_L t_L. \qquad (9.22)^{\dagger}$$

Since $\omega_R = \Delta\omega_L + \omega_L$, the Mach number, pressure, and other parameters at R can be calculated, including the effects of rotational flow.

Studies show that these effects are significant at high velocities. For example, the pressure drag of a parabolic nose with a fineness ratio of 5 at a value of $K_1 = M_\infty/\lambda_N = 1$ is increased 5 percent by including the effects of rotation. For $K_1 = 4$, i.e., $M_\infty = 20$, it is increased more than 25 percent. From the physical point of view, the cause of

---

†Editor's note: Equations (9.21) and (9.22) appear to be wrong in the original text and have been revised.

the increased drag is due to the fact that an additional part of the kinetic energy of the flow is irreversibly consumed by the generation of vortices.

The pressure distributions calculated by the method of characteristics[5] for two bodies with parabolic noses for a value of the parameter $K_1 = M_\infty \tan \delta_0 = M_\infty/\lambda_N = 2$ are presented in Fig. 89. The increase in pressure due to rotational flow is clearly evident from the graph. This effect must be taken into account in practical cases beginning approximately at $K_1 = 1.2$ to 1.5; at lesser values of K_1, the effect of rotation can be neglected.

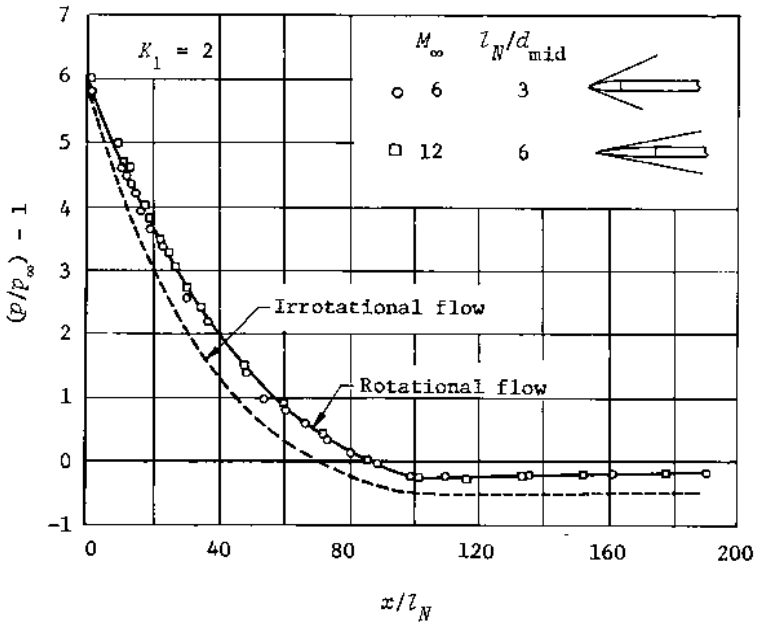

Fig. 89--Pressure distribution on a parabolic body of revolution with rotational and irrotational flow behind the shock

The graph in Fig. 89 confirms the validity of the similarity law with respect to the parameter K_1 not only with reference to cones but also for affine-similar bodies of revolution with a curved generatrix,

such as bodies of parabolic shape. It is evident that the flow around the two bodies is characterized by one curve for the pressure ratio, because K_1 was the same in each case.

The similarity law with respect to the parameter K_1 is of great practical value. In fact, instead of experimenting with various models, it is possible to carry out tests with one body, thereby obtaining data on the pressure distribution for a series of values of the parameter K_1. According to the similarity law, these data can be extended to a whole family of affine bodies. For example, if the results in Fig. 89 are obtained at $M_\infty = 6$ for a body with a nose fineness ratio of 3 so that $K_1 = 2$, it is evident from the figure that the curve is also valid for another body with a fineness ratio $\lambda_N = 6$ at $M_\infty = 12$, i.e., for the same value $K_1 = 2$. Using the similarity law, it is possible to relate the results obtained to a body with $\lambda_N = 5$ at $M_\infty = 10$, etc. However, in a given case the results are limited to a single value of the parameter $K_1 = 2$. Similar curves can be established for other values of K_1, using either experimental or calculated data. Results are presented in Fig. 90 for calculations by the method of characteristics of the pressure ratio for slender cylindrical bodies with parabolic noses for $K_1 = 1$ and 0.5.

It should be noted that another important consequence of the similarity law is that test results can be obtained at lesser Mach numbers if high velocity facilities are not available. The experiment must be carried out with thicker affine-similar models to maintain the given parameter K_1. For example, instead of an experiment at $M_\infty = 12$ on a model with $\lambda_N = 6$, the experiment is conducted on a model twice as thick ($\lambda_N = 3$) at a Mach number of 6.

The area of applicability of the similarity law for parabolic noses can be ascertained from an analysis of the possible use of this law for conical noses. Figure 64 (p. 184) can be used after modifying the fineness ratio along the horizontal axis. It should be noted that for identical angles, δ_0 and δ_c, the fineness ratio of the parabolic nose will be twice as large as that of a cone. Thus, the rearranged graph (Fig. 91), with its scale maintained, will be compressed along the horizontal axis. Calculations[5] by the method of characteristics of the pressure distribution around slender cylindrical bodies of revolution with parabolic

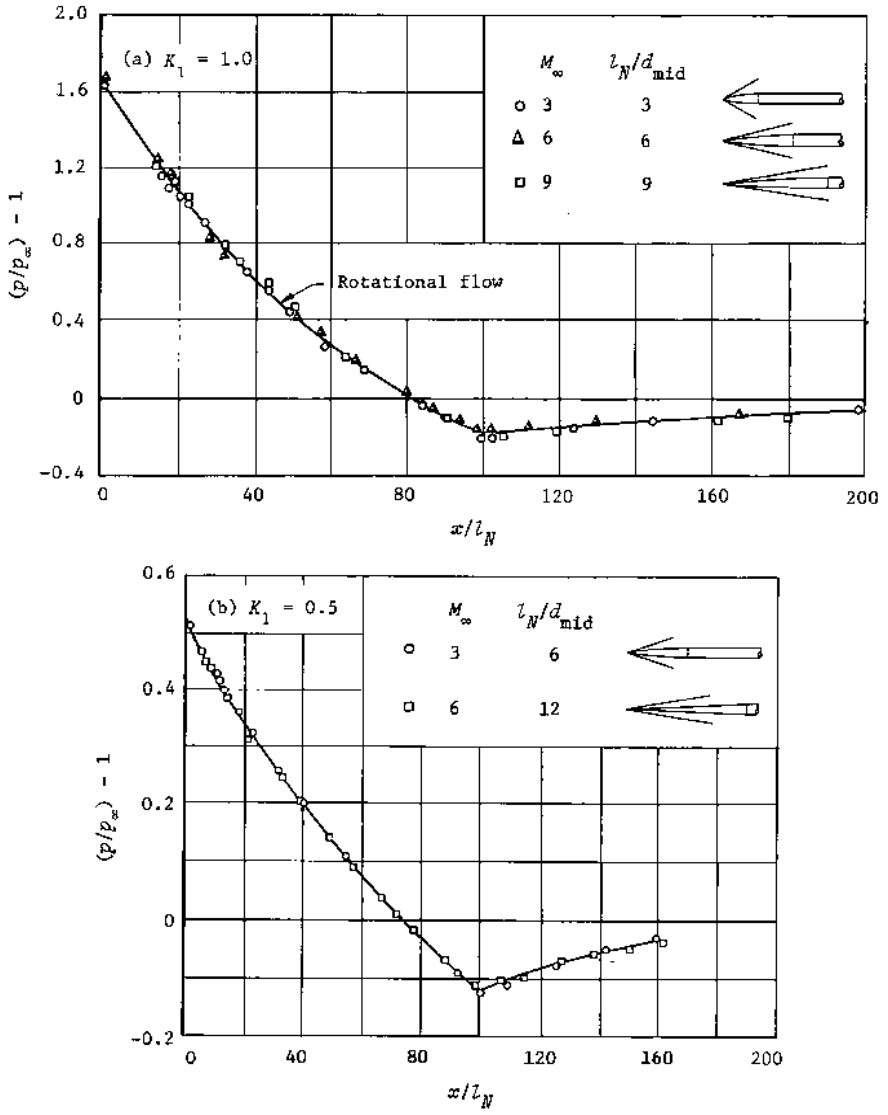

Fig. 90--Pressure distribution on a parabolic body of revolution for two values of the similarity parameter K_1

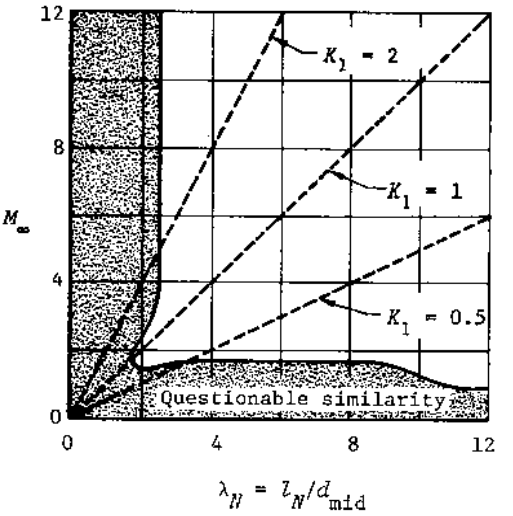

Fig. 91--Region of validity of the similarity law for slender parabolic or ogival bodies

(or ogival) noses have been carried out according to the limits of applicability of the similarity law, as established by Fig. 91. The results of these calculations are presented in a general form in Fig. 92.

In the study of the effect of rotational flow, it has been shown that increases in the flight velocity require taking into account, in the calculation of the inviscid flow field, the influence of factors that could be neglected at lesser velocities. However, experiment and theory also show that at high velocities it is necessary to consider not only the effects of rotational flow but also the influence of such factors as the boundary layer and the various effects observed in it (compressibility, dissociation, and heat transfer between the wall and the gas). A significant influence is also exerted by vibrational excitation and dissociation of air, which can originate at very high flow velocities due to the significant temperature increase in the inviscid flow region between the shock wave and the body surface. The calculation can also be made by the method of characteristics in this region for a gas undergoing physical-chemical changes.

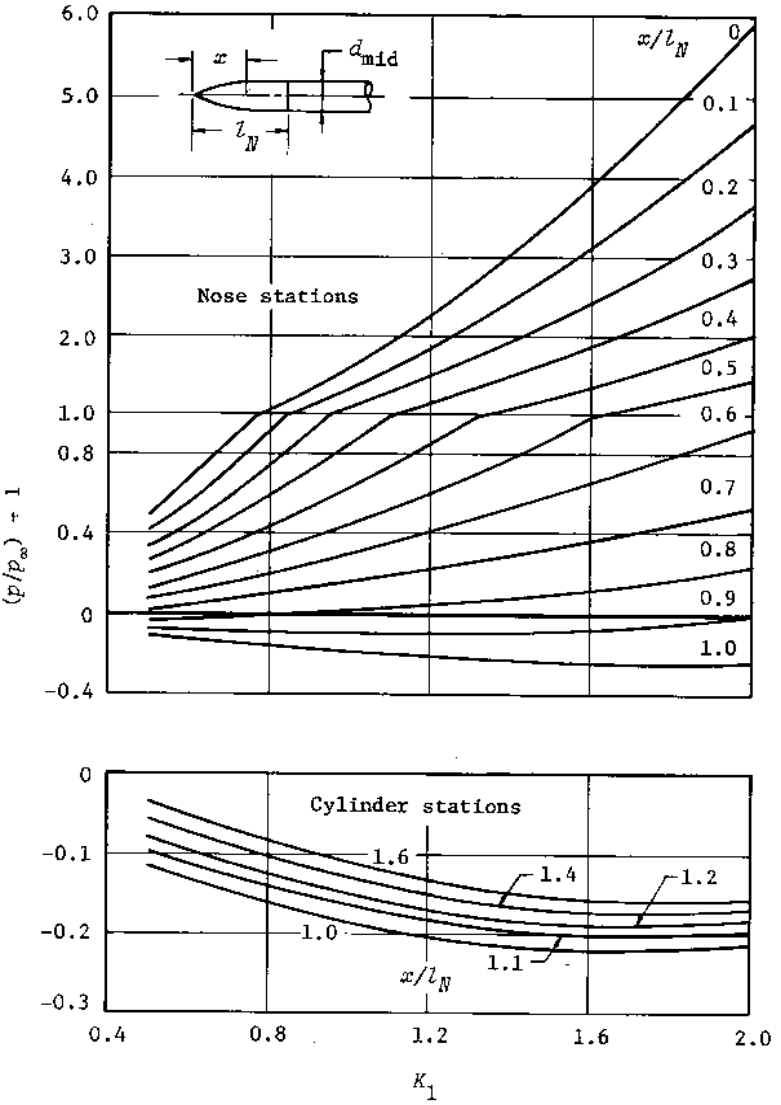

Fig. 92--Pressure distribution on slender cylindrical bodies with parabolic (ogival) noses

§ 10. *THE METHOD OF CHARACTERISTICS FOR THE CALCULATION OF FLOW AT VERY HIGH TEMPERATURES*

THE GENERAL RELATIONS FOR THE CHARACTERISTICS

Nonisentropic (Rotational) Flow

LET US CONSIDER A GAS FLOW under conditions of very high temperature, but without friction and heat transfer.[6] It will be assumed that the pressure is not very large and that it is possible to use the equation of state given by Eq. (3.46). In addition, we shall consider that the processes of excitation of the vibrational degrees of freedom and of dissociation and ionization are in equilibrium. In other words, it is assumed that the relaxation times of these processes are negligibly small compared with the characteristic time of the change in the flow parameters, so that at each point in the flow field the processes assume values corresponding to the local temperature and pressure.

Considering the flow in one of the meridian planes, and using a natural coordinate system (see Fig. 32, p. 69), we can write a relation for the rate of change of flow inclination that is valid along both families of characteristics:

$$\frac{d\delta}{ds} = \frac{\partial \delta}{\partial s} \mp \frac{1}{\sqrt{M^2 - 1}} \frac{\partial \delta}{\partial n}. \tag{10.1}$$

The partial derivatives can be replaced by expressions obtained from Eqs. (3.10) and (3.18), resulting in

$$\frac{d\delta}{ds} = -\frac{1}{\rho \gamma^2} \frac{\partial p}{\partial n} \pm \frac{1}{\rho} \frac{1}{\sqrt{M^2 - 1}} \frac{\partial \rho}{\partial s} \mp \frac{1}{\rho V^2} \frac{1}{\sqrt{M^2 - 1}} \frac{\partial p}{\partial s} \pm \frac{\sin \delta}{r} \frac{1}{\sqrt{M^2 - 1}}.$$

Substituting the expression

$$\frac{\partial p}{\partial n} = \sqrt{M^2 - 1}\left(+\frac{dp}{ds} \pm \frac{\partial p}{\partial s}\right)$$

and noting that $a^2 = (\partial p/\partial s)(\partial s/\partial \rho)$, we find

$$\pm \frac{d\delta}{ds} = \frac{\sqrt{M^2 - 1}}{\rho V^2}\frac{dp}{ds} + \frac{\sin\delta}{r}\frac{1}{\sqrt{M^2 - 1}}.$$

Rewriting the total derivative dp/ds by using the relations for entropy $T\,dS = di - dp/\rho$ and enthalpy $di = -V\,dV$, we obtain

$$\pm \frac{d\delta}{ds} = -\sqrt{M^2 - 1}\,\frac{1}{V}\frac{dV}{ds} + \frac{\sin\delta}{r}\frac{1}{\sqrt{M^2 - 1}} - \frac{T\sqrt{M^2 - 1}}{V^2}\frac{dS}{ds}. \qquad (10.2)$$

An expression for the velocity differential can be obtained from the energy equation, Eq. (3.39):

$$\frac{dV}{V} = \frac{1}{2}\,d\,\log\left(\frac{M^2}{2i/a^2 + M^2}\right) = \frac{1}{2}\frac{(2i/a^2)\,dM^2}{M^2(2i/a^2 + M^2)} - \frac{1}{2}\frac{d(2i/a^2)}{2i/a^2 + M^2}. \qquad (10.3)$$

Next we introduce a new variable in the form of an angle:

$$\omega = \sqrt{1 + 2i/a^2}\ \arctan\sqrt{\frac{M^2 - 1}{1 + 2i/a^2}} - \arctan\sqrt{M^2 - 1}. \qquad (10.4)$$

The set of curves corresponding to this equation is shown in Fig. 93. It is apparent that the ratio $2i/a^2 = 2/(\gamma - 1)$ for constant specific heats, so that Eq. (10.4) reduces to the familiar Eq. (8.11a) for epicycloids, which represent characteristics in the hodograph plane for the case of no physical-chemical reactions.

To further transform Eq. (10.2), we write the expression for the differential:

$$d\omega = \frac{\partial\omega}{\partial M^2}\,dM^2 + \frac{\partial\omega}{\partial(2i/a^2)}\,d\left(\frac{2i}{a^2}\right). \qquad (10.5)$$

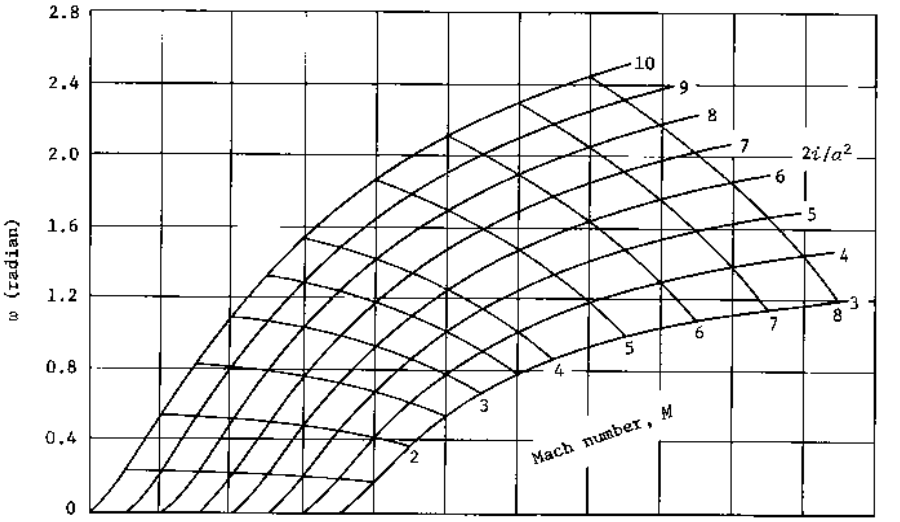

Fig. 93--Dependence of the function ω on Mach number and the ratio $2i/a^2$

The first partial derivative can be obtained from Eq. (10.4) as

$$\frac{\partial \omega}{\partial M^2} = \frac{1}{2M^2} \frac{2i}{a^2} \frac{\sqrt{M^2 - 1}}{2i/a^2 + M^2}. \tag{10.6}$$

This derivative can be determined graphically from Fig. 94, where curves are presented for the function $\partial\omega/\partial M$, which is related to Eq. (10.6) by $\partial\omega/\partial M = 2M(\partial\omega/\partial M^2)$. Transforming Eq. (10.2) with the help of Eqs. (10.3) through (10.6), we obtain the equation for the characteristics:

$$d(\omega \pm \delta) = \left[2 \frac{\partial \omega}{\partial (2i/a^2)} + \frac{\sqrt{M^2 - 1}}{2i/a^2 + M^2} \right] d\left(\frac{i}{a^2}\right)$$

$$+ \frac{\sin \delta}{r} \frac{d\vartheta}{\sqrt{M^2 - 1}} - \frac{\sqrt{M^2 - 1}}{V^2} T \, dS, \tag{10.7}$$

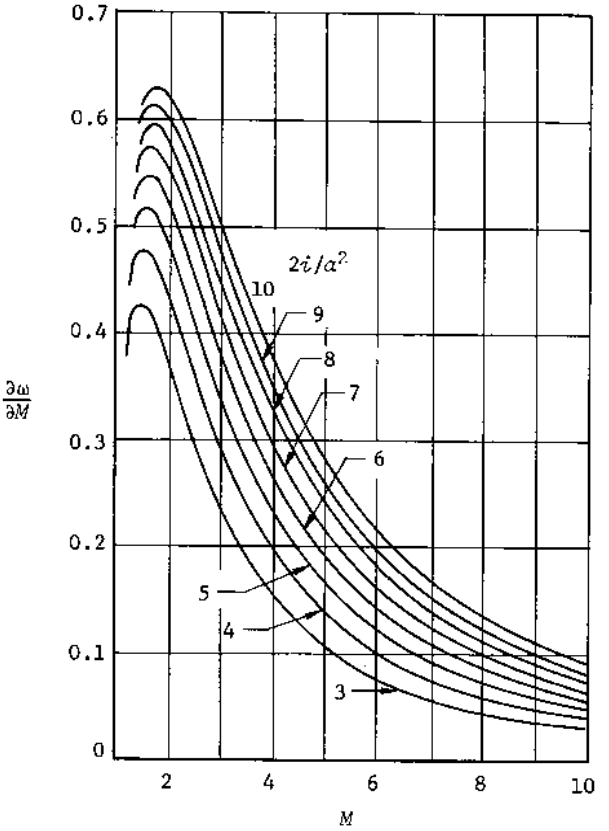

Fig. 94--The derivative $\partial\omega/\partial M$ as a function of Mach number and the ratio $2i/a^2$

where the partial derivative is

$$\frac{\partial\omega}{\partial(2i/a^2)} = \frac{1}{2\sqrt{1 + 2i/a^2}} \arctan \sqrt{\frac{M^2 - 1}{1 + 2i/a^2}} - \frac{\sqrt{M^2 - 1}}{2(2i/a^2 + M^2)}. \quad (10.8)$$

Curves for this derivative are presented in Fig. 95.

The last two terms on the right side of Eq. (10.7) can be written in another form by replacing the element of arc ds of the streamline (Fig. 96) by the equation

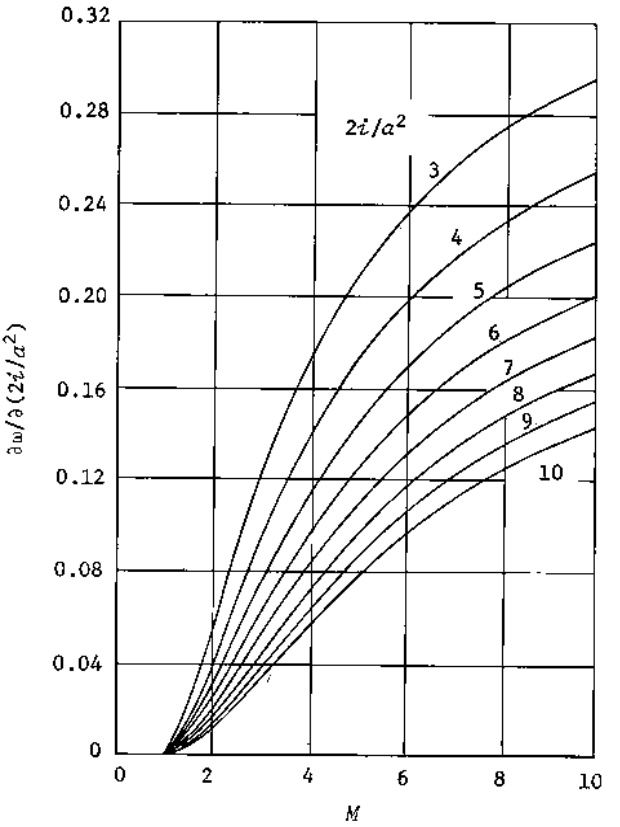

Fig. 95--The derivative $\partial\omega/\partial(2i/a^2)$ as a function of Mach number and the ratio $2i/a^2$

$$ds = \frac{dx \cos \mu}{\cos (\delta \mp \mu)}.$$

The equation for the velocity of sound will be used in the form $a^2 = \bar{\varphi}RT$, where $\bar{\varphi}$ is a parameter depending on pressure and temperature. Using the relation along a characteristic

$$\frac{dn}{ds} = \pm \frac{1}{\sqrt{M^2 - 1}} = \pm \tan \mu$$

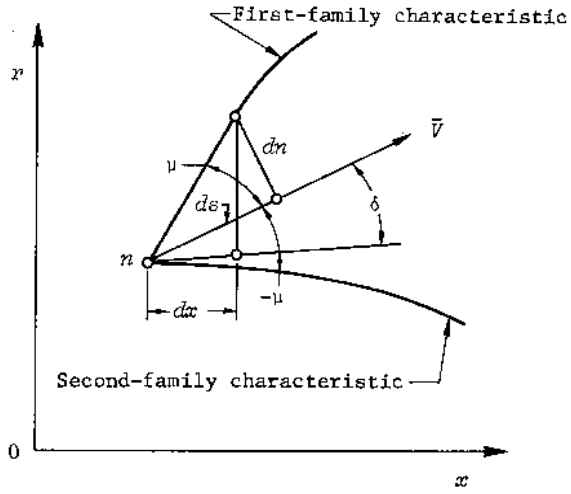

Fig. 96--Geometric relationships for streamlines and characteristics

and Eq. (10.8), it is possible to rewrite the last two terms of Eq. (10.7):

$$d(\omega \pm \delta) = D\, d\left(\frac{i}{a^2}\right) + \frac{\sin\delta \sin\mu}{\cos(\delta \mp \mu)} \frac{dx}{r} \mp \frac{\sin^2\mu \cos\mu}{\cos(\delta + \mu)} \frac{d\bar{S}}{dn} \frac{dx}{\bar{\varphi}}. \qquad (10.9)$$

The function D, presented graphically in Fig. 97, has the form

$$D = \frac{1}{\sqrt{1 + 2i/a^2}} \arctan \sqrt{\frac{M^2 - 1}{1 + 2i/a^2}} \qquad (10.10)$$

and the dimensionless entropy $\bar{S} = S/R$.[†] The upper sign in Eq. (10.9)

[†]Editor's note: An error in Eq. (10.7), carried over from the original reference[6] to the Russian text, has been corrected here. It occurs in the sign within the square brackets of the equation and results in a superfluous term in the expression for D, namely,

$$-\frac{2 \sin\mu \cos\mu}{1 + (2i/a^2)\sin^2\mu}.$$

Thus, Fig. 97 of the original text is incorrect and has been redrawn in this edition.

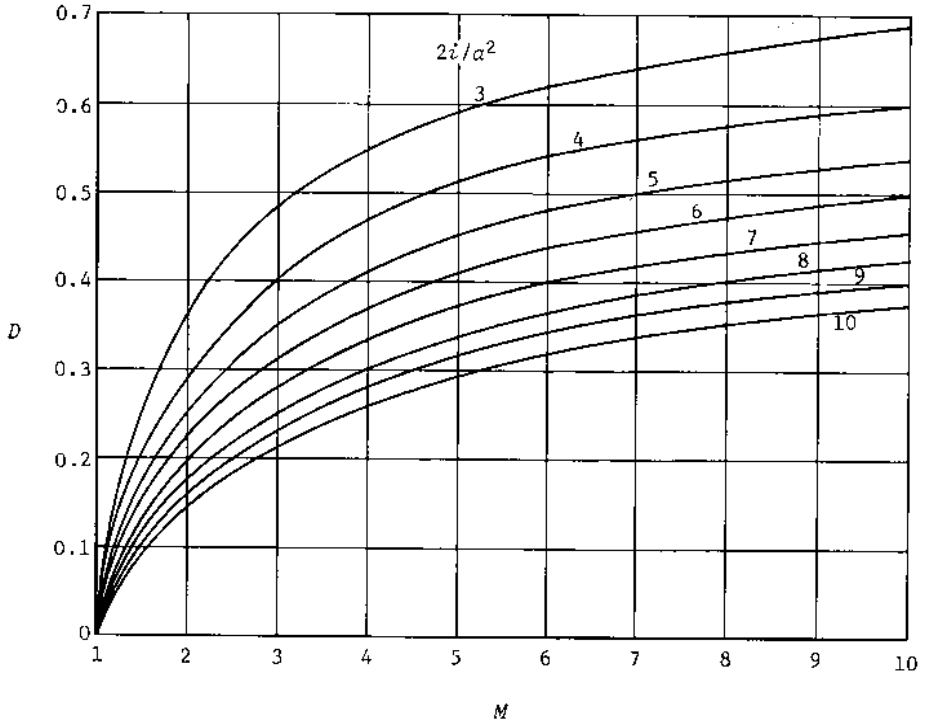

Fig. 97--Graph of the function D for dissociable flow

corresponds to characteristics of the second family, and the lower sign to the first family.

Equation (10.9) must be used in combination with the determination of the enthalpy, entropy, and velocity of sound of a dissociable gas as functions of temperature and pressure. The special graphs or tables of the thermodynamic functions of air are again used. The ratio $2i/a^2$ can be obtained from the thermodynamic tables and is plotted in Fig. 98. In the special case of a heated but undissociated gas, this ratio depends only on temperature:

$$\frac{2i}{a^2} = \frac{1}{\gamma_2 - 1}\left[\left(\frac{\gamma_2 - 1}{\gamma_1 - 1}\frac{\gamma_1}{\gamma_2} + 1\right) + \frac{T_1}{T_2}\left(\frac{\gamma_2 - 1}{\gamma_1 - 1}\frac{\gamma_1}{\gamma_2} - 1\right)\right], \qquad (10.11)$$

where γ_1 and γ_2 are determined as functions of T_1 and T_2, respectively,

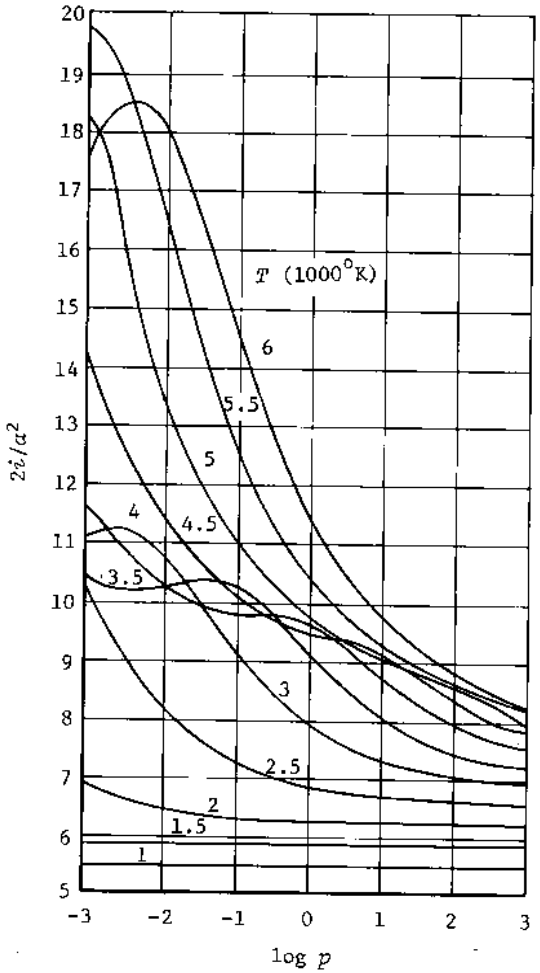

Fig. 98--The ratio $2i/a^2$ in a dissociable gas

and the velocity of sound is also a function of temperature given by $a^2 = \gamma_2 RT_2$. Thus, in this case the coefficient $\bar{\varphi} = \gamma_2$.

The entropy of a dissociable gas is determined from the known values of pressure and temperature with the aid of graphs or thermodynamic tables. In isentropic flow, the entropy remains constant along streamlines. Therefore, it is sufficient to find its value at any one point

on the streamline, e.g., directly behind the shock where both temperature and pressure can be calculated by taking into account variable specific heats and dissociation.

If the shape of the shock wave has been previously determined (e.g., in a wind tunnel by optical methods), the preliminary calculation of temperature and pressure and, therefore, of entropy and other parameters is simplified because the shock slope is known at each point.

Irrotational Dissociable Flow

Since the entropy in irrotational flow is identical everywhere, Eq. (10.9) for the characteristics can be rewritten in a simpler form:

$$d(\omega \pm \delta) = D\, d\left(\frac{i}{a^2}\right) + \frac{\sin\delta \sin\mu}{\cos(\delta \mp \mu)} \frac{dx}{r}. \tag{10.12}$$

Instead of this equation, we can use an equation obtained[7] as a result of a simple transformation of Eq. (10.2). This conversion results from the condition that $di = -V\,dV$ for the uniform flow and, for isentropic perturbed flow, this same differential is $di = dp/\rho$. Consequently, $dV/V = -dp/(\rho V^2)$. Under these conditions, it can be assumed that all parameters are functions of the local Mach number or, in effect, of the Mach angle μ. Then the equations for the characteristics can be presented in the following form:

$$\pm d\delta - f(\mu)\, d\mu = \frac{\sin\delta \sin\mu}{\cos(\delta \mp \mu)} \frac{dx}{r}, \tag{10.13}$$

where

$$f(\mu) = \frac{\sin\mu \cos\mu}{a^2} \frac{di}{d\mu}. \tag{10.14}$$

The equations for the characteristics in the physical plane remain as before.

For numerical calculations, the equations for the characteristics are represented in a finite-difference form and the resulting system is solved by an iteration method. This system differs from the corresponding system for a perfect gas by the presence of the function $f(\mu)$. For

an ideal gas,

$$f(\mu) = f^{0}(\mu) = \frac{1 + \cos 2\mu}{\gamma - \cos 2\mu}. \tag{10.15}$$

For a real gas, $f(\mu)$ must be determined by Eq. (10.14) and, as is evident, cannot be represented in an explicit form. In the calculations of real-gas flows, it is convenient to replace $f(\mu)$ by the ratio $z(\mu) = f(\mu)/f^{0}(\mu)$, which equals unity for a perfect gas.

Therefore, the determination of the local value of the function $z(\mu)$ is an essential element of the calculations. Knowing the conditions in the free stream, the entropy behind the shock wave is computed, and, for a given series of possible values of the velocity, V_0, V_1, ..., V_i, V_{i+1}, a corresponding series of enthalpies is calculated:

$$i_i = i_0 + 0.5V_0^2 - 0.5V_i^2.$$

From the entropy and enthalpy, the pressure, temperature, and velocity of sound are determined with the help of the tables or graphs of thermodynamic functions, and the Mach number M_i and the Mach angle μ_i can be computed at a given point. From the resulting data, a curve of $i(\mu)$ is plotted, the derivative $di/d\mu$ determined, and $f(\mu)$ and $z(\mu)$ computed.

THE METHOD FOR CALCULATING ROTATIONAL DISSOCIABLE FLOW AROUND A BODY OF REVOLUTION

The principal part of the calculation of rotational dissociable flow is the same as that for flow with constant specific heats. First, the conical flow of a dissociable gas around the conical tip is found, and the initial characteristic *KS* of the first family (see Fig. 82) is determined. Thus, all the parameters along this characteristic will be known. From these parameters can be calculated the auxiliary values, such as the ratio $2i/a^2$, the coefficient $\bar{\varphi}$, and the function D. According to the diagram in Fig. 82, the calculation begins with the computation of the parameters at point B, which lies on the intersection of the body surface with an element of the characteristic of the second family. For this element, the form of the finite-difference equation is as follows:

$$\Delta\omega_D + \Delta\delta_D = D\,\Delta\left(\frac{i}{a^2}\right)_D - t_D\frac{x_B - x_D}{\bar{\varphi}_D}\left(\frac{\Delta\bar{S}}{\Delta n}\right)_D + m_D\frac{x_B - x_D}{r_D}. \qquad (10.16)$$

The coordinates x_B and r_B are easily determined by a joint solution of the equations for the element of the characteristic in the x-r plane and the generatrix of the body. Therefore, the difference of the angles, $\Delta\delta_D = \delta_B - \delta_D$, can be assumed known, and the other quantities in Eq. (10.16) for point D are also known. In addition to the unknown $\Delta\omega_D$, there is still another unknown increment, $\Delta(i/a^2)$. Thus, in contrast to the case of constant specific heats, it is necessary to know how the ratio i/a^2 varies from one point to another. To determine the difference $\Delta(i/a^2)_D$, which in the present case is given by the change in the ratio i/a^2 from point D to point B, let us proceed from the entropy S_B known at point B. Assuming the pressure p_B is equal to the average of the pressures at points K and D, we can determine the enthalpy i_B and the speed of sound a_B from the values p_B and S_B with the help of the thermodynamic tables and graphs. Then the ratio $(i/a^2)_B$ and the increment $\Delta(i/a^2)_D$ can be computed. Knowing this value, the increment $\Delta\omega_D$ can be found from Eq. (10.16), and the absolute value of the angle ω_B and the Mach number M_B at the point B can be computed. It should be noted that the second term on the right side of Eq. (10.16) can be assumed equal to zero, since the flow is potential in the particular region in question.

The transition to point C, which lies at the junction of the elements AC and BC of the characteristics of the second and first families, is related to the simultaneous solution of Eq. (10.16) for the element AC (with $D = A$ and $B = C$) and of an equation for the element BC. The latter is obtained from Eq. (10.9), rewritten in finite-difference form, by retaining the lower signs. The general form of this equation will be like that of Eq. (10.16), with appropriate changes in signs. The subscripts D and B are replaced by B and C, respectively.

The determination of the ratio $(i/a^2)_C$ at point C is a basic element of the calculation. We must keep in mind that, since the flow for the present is potential, the entropy is the same as that at the adjacent points A and B. In a first approximation, assuming the pressure p_C is the average between the values at points A and B, it is possible

to find the quantity $(i/a^2)_C$ from the entropy S_B and compute the increments $\Delta(i/a^2)_A$ and $\Delta(i/a^2)_B$. The calculation of the parameters of the points of the first family, beginning at point B, is concluded with their determination at point H on the shock wave. For this purpose, we use the equation for the characteristic element FH of the first family and the equation for the shock wave. The term that takes into account the entropy variation from point F to point H must be retained in the characteristic equation. The shock equation remains the same as Eq. (8.25), but the derivative $d\omega/d\delta$ for a dissociable gas is impossible to write in explicit form. It can be written as

$$\frac{d\omega}{d\delta} = \frac{\partial\omega}{\partial M}\frac{dM}{d\delta} + \frac{\partial\omega}{\partial(2i/a^2)}\frac{d(2i/a^2)}{d\delta}. \qquad (10.17)$$

The derivatives $\partial\omega/\partial M$ and $\partial\omega/\partial(2i/a^2)$ can be determined from the graphs in Figs. 94 and 95 or from Eqs. (10.6) and (10.8). The derivatives $dM/d\delta$ and $d(2i/a^2)/d\delta$ can also be found graphically or numerically. The necessary tables or graphs can be constructed beforehand for a range of free-stream flight conditions (Mach number M_∞ and altitude H) by computing the local Mach number and enthalpy parameter $2i/a^2$ behind a shock wave as functions of the flow deflection δ and evaluating the derivatives with respect to δ. After calculating the parameters at point H, we pass to the adjacent point J. Since J is located in a rotational region, it is necessary to solve the equations for the elements HJ and NJ taking into account the entropy change to determine the parameters in this region. As at the other points, we determine the ratio (i/a^2), for which purpose an interpolation formula can be used for the entropy at point J:

$$S_J = S_N + (S_H - S_N)\frac{\delta n}{\Delta n},$$

where δn is the distance between the streamlines passing through points J and N. Having computed the pressure at point J from an analogous interpolation equation, we can find, from the values S_J and p_J, the enthalpy and the velocity of sound at this point to calculate the ratio $(i/a^2)_J$ and then the respective differences. The calculation results

in the determination of the Mach number M_J, from which the local enthalpy is recalculated: $i_J = i_0 - V_J^2/2$, where $V_J = M_J a_J$.

From the known entropy and the refined enthalpy, and with the aid of tables and graphs of the thermodynamic functions, the other flow parameters can be found, i.e., the density and temperature and a second approximation for the pressure. The latter can be determined from the equation of state, if the average molecular weight of the air and the temperature and density are known.

This method of calculation permits the step-by-step determination of the parameters in an equilibrium dissociable flow field bounded by a curved shock wave, where the shock shape is gradually built in the process of the calculation and has a stepwise form. The shock wave in such a flow is located closer to the body compared with that in an undissociated flow, because it is possible to compress the gas to a higher density.

§ 11. *THE INFLUENCE OF THE BOUNDARY LAYER ON INVISCID FLOW PARAMETERS*

LET US EXAMINE THE QUESTION of how to take into account, approximately, the influence of viscosity on the parameters of high-velocity inviscid flow. It should be noted that a hypothesis exists in the theory of gas dynamics of a viscous medium on the lack of a reciprocal influence of the boundary layer on the free stream. According to this hypothesis, the same static pressure is measured on the body surface as in the free stream if the boundary layer thicknesses are small compared to the linear dimensions of the body. Thus, it follows that the calculation of pressures can be carried out disregarding the viscous property of the gas. However, it is known that the longer the body, the greater the boundary layer thickness, and the less reliable will be the hypothesis concerning the lack of reciprocal influence. Moreover, the boundary layer thickness can increase due to the influence of compressibility and high temperature, which also increase the effect of viscosity. In such cases, the pressure calculation on the surface as well as the calculation of the other flow parameters must be made considering the influence of viscosity. In principle, this could be done if Euler's equations were replaced by equations of motion derived taking into account the real properties of the gas. However, to carry out such a calculation in practice is extremely difficult. Therefore, a simpler approximate method is suggested that permits accounting for the variation in the parameters of an inviscid flow due to the presence of a boundary layer on the surface.

This method is based on the assumption that it is possible to replace the real body by a fictitious (apparent) body with a profile increased in lateral dimension by the apparent displacement thickness (see Eq. (3.36)). The thickness is assumed to be a layer across which

flows an amount of gas (per unit time and with the free-stream velocity) equal to the decrease in the flow rate across the entire thickness of the boundary layer. The apparent thickness characterizes, as it were, the decrease in the local velocity of an inviscid flow over the surface of a body with a boundary layer.

Because the effects of viscosity and the decrease in the gas flow rate connected with it are limited by the dimensions of displacement thickness, the flow beyond the limits of this layer can be considered inviscid and the calculation of the parameters proceeds from Euler's equations. Obviously, this calculation must be carried out on the basis of the boundary conditions on the surface of the apparent body; and the radius of such a body, in comparison with the actual body, can be assumed to be increased by approximately the displacement thickness.

The pressure on the surface of the apparent body, found as a result of the calculation, will be the same as the pressure that occurs on the surface of the real body in a viscous flow. The velocity, density, temperature, and other parameters thus calculated will equal their respective values at the edge of the layer.

It is clear from the foregoing discussion that, in calculating the inviscid parameters including the effects of the boundary layer, it is first necessary to find the law of the variation of the displacement thickness along the length of the body and to introduce a correction into the equation for the body shape. We can use the results of supersonic boundary layer theory for flat plates and cones. In the general case, these results are associated with the use of effective parameters.

To obtain the necessary relationships, first let us find the expressions for the apparent displacement thickness of an incompressible boundary layer on a plate. Assuming that $\rho = \rho_\delta$ in Eq. (3.36), we can substitute the ratio V_x/V_δ for the laminar and turbulent boundary layers from Eq. (5.1). Integrating, we obtain the expression $(\delta^*_{\text{inc}})_L = 3\delta/8$ for the displacement thickness of the laminar layer and $(\delta^*_{\text{inc}})_T = \delta/8$ for the turbulent layer. Introducing into these expressions the corresponding equations for the boundary layer thickness, we obtain

$$\delta^*_{\text{inc}} = B\left(\frac{\nu_\delta}{V_\delta \rho_\delta}\right)^n x^m, \tag{11.1}$$

where $B = 1.74$, $n = m = 1/2$ for the laminar layer; and $B = 0.046$, $n = 1/5$, $m = 4/5$ for the turbulent layer. Transforming to the effective parameters, we find

$$\delta^* = \delta^*_{\text{inc}} \left(\frac{\mu^*}{\mu_\delta}\right)^n \left(\frac{\rho_\delta}{\rho^*}\right)^n. \tag{11.2}$$

If we consider a cone in supersonic viscous flow, the displacement thicknesses can be computed from the equation

$$\delta^*_c = A\delta^*, \tag{11.3}$$

in which $A = 1.73$ for the laminar boundary layer, and $A = 1.17$ for the turbulent boundary layer.

Thus, the radius of the apparent body is $r_\delta = r + \delta^* \cos \delta_c$. The relative thickness is determined from the expression

$$\delta^* = \bar{A} P^n x^m, \tag{11.4}$$

where

$$P = \frac{\mu^*}{\mu_\delta} \frac{\rho_\delta}{\rho^*} \frac{\mu_\delta}{\rho_\delta V_\delta},$$

while $\bar{A} = 3.01$ for the laminar layer, and $\bar{A} = 0.054$ for the turbulent layer. In this equation, the x-coordinate represents the distance along a ray of the cone from the tip to an arbitrary section in the boundary layer and is given by $x = r/\sin \delta_c$.

It is clear that the apparent body differs from a cone and has a curved generatrix. However, to simplify the calculations, it is expedient to assume that the surface is conical. An average increment, $\Delta\delta = \delta^*/L$, can be computed, where the displacement thickness is determined from Eq. (11.4) for $x_c = L$, i.e., for the boundary layer profile at the base. Then the angle of the apparent cone is $\delta_{c\delta} = \delta_c + \Delta\delta$, and all the calculations of the inviscid parameters on the cone are made using this angle.

Let us now consider an axisymmetric body of arbitrary shape. A version of the local-cone method can be used to calculate the generatrix

of an apparent body corresponding to a given shape and to the flow conditions. Assuming that the nose of the body is a conical element of a small length, x_1 (Fig. 99), the displacement thickness at its end is

$$\delta_1^* = \bar{A} P_1^n x_1^m, \tag{11.5}$$

where P_1 is calculated for the parameters on the conical nose.

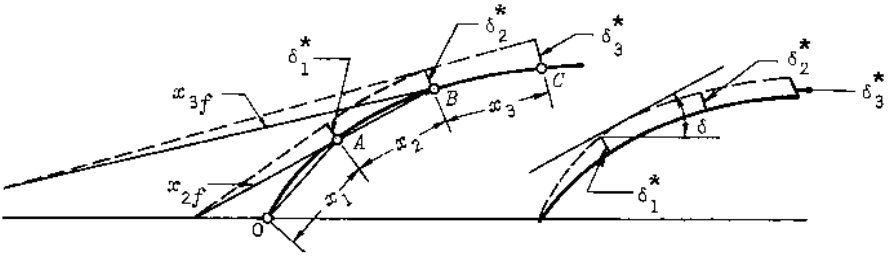

Fig. 99--Diagram for calculation of the relative displacement thickness

A frustum of a cone with a generatrix of length x_2 is substituted for the following small section of the curved surface, assuming that it is the continuation of a fictitious conical body with a generatrix of length x_{2f}. At the beginning of this fictitious cone, the relative thickness equals δ_1^* and is computed from Eq. (11.5). Consequently, we have the expression $\delta_1^* = \bar{A} P_2^n x_{2f}^m$ for the fictitious cone, from which the length x_{2f} of its generatrix can be found. The function P_2 is calculated from the parameters on the second section. Knowing the generatrix length, $x_{2f} + x_2$, of the fictitious cone corresponding to the second section, the displacement thickness at point B on the body surface (see Fig. 99) can be calculated approximately:

$$\delta_2^* = \bar{A} P_2^n (x_{2f} + x_2)^m.$$

The displacement thickness at point C can be computed analogously:

$$\delta_3^* = \bar{A} P_3^n (x_{3f} + x_3)^m,$$

where the function P_3 is found from the parameters on the third section, and the length x_{3f} of the fictitious cone is calculated with the help of the expression

$$\delta_2^* = \bar{A}P_2^n(x_{2f} + x_2)^m = \bar{A}P_3^n x_{3f}^m.$$

These relations can be written in a general form for the relative thickness at the ith section:

$$\delta_i^* = \bar{A}P_i^n(x_{if} + x_i)^m, \tag{11.6}$$

where the generatrix length of the fictitious cone, x_{if}, is found from the condition

$$\delta_{i-1}^* = \bar{A}P_{i-1}^n[(x_{i-1})_f + x_{i-1}]^m = \bar{A}P_i^n x_{if}^m. \tag{11.7}$$

To obtain the coordinate of a point on the surface of the apparent body, the same expression as before can be used, $r_\delta = r + \delta^* \cos\delta$.

The method of calculation involves the simultaneous solution of two problems: The first is the determination of the inviscid flow parameters, the second the calculation of the friction and heat transfer parameters. In the latter case, the wall temperature can be assigned a specific value, or the equilibrium radiation temperature can be determined as one part of the solution.

To simplify the calculation, the influence of heat transfer and high temperature on the thermodynamic characteristics and the kinetic coefficients of the gas can be neglected. Then the effect of the high velocities amounts to a compressibility influence on the boundary layer thickness and, therefore, on the inviscid flow parameters.

Obviously, this influence will be minimal if the effect of the Mach number is not considered. The relations for the relative thickness of an incompressible boundary layer can be assumed for an approximate estimate of the inviscid parameters. In a series of cases for an axisymmetric body of curved shape, good agreement with test data has been obtained, even when the calculation was made using the equations for a flat plate. This is evident in Fig. 100a, where data are presented on the pressure distribution obtained in a wind tunnel with a "cold" flow.

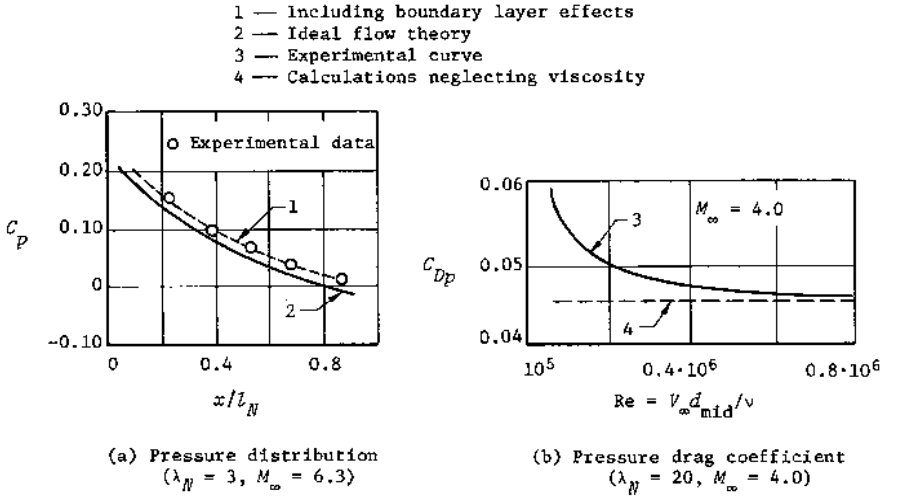

(a) Pressure distribution (λ_N = 3, M_∞ = 6.3)

(b) Pressure drag coefficient (λ_N = 20, M_∞ = 4.0)

Fig. 100--Influence of the boundary layer on pressure distribution and wave drag of a parabolic body

Such satisfactory agreement of the theoretical and experimental results is to some degree explained by the fact that the temperature of the air flow is low and, therefore, the various physical-chemical reactions are not encountered. On the whole, these results can be explained by the nature of the theory itself and also by the favorable choice of premises.

It should be noted, however, that similar experiments in "cold" wind tunnels with a highly rarefied flow in the test section are greatly affected. Because the gas is at low density, the boundary layer is quite thick, and the pressures measured on the body surface are modified by the viscous effects. Thus, these experiments allow the influence of the boundary layer on the flow parameters to be observed.

When compared to inviscid theory, the wave drag can increase quite substantially because of the effects of viscosity. This is evident in Fig. 100b, where data are presented on the axial force coefficient for an ogive nose.[8] In general, the increase in wave drag is greatest at the low Reynolds numbers accompanying rarefied gas flow and for bodies of very high fineness ratios.

§ 12. *APPLICATION OF THE METHOD OF CHARACTERISTICS TO THE CALCULATION OF FLOW AROUND A BODY OF REVOLUTION AT AN ANGLE OF ATTACK*

THE CHARACTERISTICS EQUATION

THE PROBLEM OF POTENTIAL FLOW around a body of revolution at an angle of attack is associated with the integration of differential Eq. (3.20) for the velocity potential in asymmetric flow. The numerical solution of this equation can be accomplished by using characteristics, since, for $U > a$, Eq. (3.20) is a second-order partial differential equation of hyperbolic type. Therefore, characteristics exist that, in contrast to the symmetric case, are surfaces of asymmetric shape. The equations for these surfaces are best obtained by returning to the symmetric case and writing the equations for the characteristics in a different form from Eq. (8.5), and then extending them to asymmetric flow.

The equation for the characteristics can be written in the general form $g(x, r) = 0$. Along each characteristic represented by this equation, there exists the identity

$$\frac{\partial g}{\partial x}\,dx + \frac{\partial g}{\partial r}\,dr = 0, \tag{12.1}$$

with the help of which Eq. (8.5) for the conjugate characteristics (in the physical plane) can be converted to the following form:

$$A\left(\frac{\partial g}{\partial x}\right)^2 + 2B\,\frac{\partial g}{\partial x}\,\frac{\partial g}{\partial r} + C\left(\frac{\partial g}{\partial r}\right)^2 = 0. \tag{12.2}$$

Introducing the designations

$$A = a_{11}, \qquad B = a_{12}, \qquad C = a_{22}, \tag{12.3}$$

Equation (12.2) can be written in another form:

$$\sum a_{ik} g_i' g_k' = 0, \tag{12.4}$$

where the partial derivatives g_i' and g_k' are computed according to the indices of the coefficients a_{ik}. For example, if the indices i and k are 1 and 2, respectively, i.e., $a_{ik} = a_{12}$, then $g_i' = \partial g/\partial x$ and $g_k' = \partial g/\partial r$, etc. Moreover, it is assumed that $a_{ik} = a_{ki}$.

Equation (12.4) can be easily converted to the form of Eq. (8.5). In fact, let $r = f(x)$ represent the equations for the characteristics, so that $g(x, r) = r - f(x)$. Then

$$\frac{\partial g}{\partial x} = -\frac{\partial f}{\partial x} = -\frac{dr}{dx}, \qquad \frac{\partial g}{\partial r} = 1. \tag{12.5}$$

Introducing these values for the partial derivatives into Eq. (12.4), we obtain the same equation as Eq. (8.5) but written in terms of the coefficients a_{ik}, namely,

$$a_{11}\left(\frac{dr}{dx}\right)^2 - 2a_{12}\frac{dr}{dx} + a_{22} = 0. \tag{12.6}$$

Equation (12.4) also represents the equations for characteristics applicable to all processes that are described by quasilinear second-order partial differential equations with three or more independent variables, i.e., equations of the form $\Sigma\, a_{ik}\partial^2\Phi/\partial x_i \partial x_k = 0$.

In the study of potential flow processes around an axisymmetric body at an angle of attack, it is necessary to deal with an unknown function, the velocity potential Φ, which depends on such variables as x, r, and ϕ. At the same time, the characteristics represent surfaces belonging to a family described in the general form by the equation $r = f(x, \phi)$. Hence, $g(x, r, \phi) = r - f(x, \phi)$ and therefore

$$\frac{\partial g}{\partial x} = -\frac{\partial f}{\partial x} = -r_x', \qquad \frac{\partial g}{\partial r} = 1, \qquad \frac{\partial g}{\partial \phi} = -\frac{\partial f}{\partial \phi} = -r_\phi'. \tag{12.7}$$

Using these relationships, Eq. (12.4) for the characteristics is presented

in the following form:[2]

$$a_{11}(r'_x)^2 - a_{12}r'_x + a_{22} + a_{13}r'_x r'_\phi - a_{23}r'_\phi + a_{33}(r'_\phi)^2 = 0, \qquad (12.8)$$

where the coefficients a_{ik} are determined from Eq. (3.20), with the derivatives with respect to t set equal to zero, and have the form

$$a_{11} = 1 - \frac{V_x^2}{a^2}, \quad a_{12} = \frac{-2V_x V_r}{a^2}, \quad a_{22} = 1 - \frac{V_r^2}{a^2},$$
$$a_{13} = \frac{-2V_x V_r}{ra^2}, \quad a_{23} = \frac{-2V_r V_\phi}{ra^2}, \quad a_{33} = \frac{1}{r^2}\left(1 - \frac{V_\phi^2}{a^2}\right). \qquad (12.9)$$

It was established in the study of symmetric flow that the characteristic surface is a surface of revolution and coincides with the symmetric Mach wave. If the flow is not symmetric, the characteristic surfaces are also unsymmetric, but they still represent surfaces along which perturbations are propagated. Thus, the characteristic surfaces should be considered as envelopes of cones of perturbation with apexes at the points that are the sources of these perturbations.

The intersection of this surface with two planes is usually investigated in the study of asymmetric flow around a body of revolution. One of these is the meridian plane; the other is a plane normal to the longitudinal axis of the body. The lines of intersection with the meridian plane are a pair of conjugate characteristics. The lines of intersection with the transverse plane are of auxiliary character and used for the construction of a three-dimensional characteristics mesh.

COMPATIBILITY CONDITIONS

In calculations by the method of characteristics, it is necessary to use both Eq. (12.8) for the characteristic surface $r = f(x, \phi)$ and the equation analogous to that for the characteristics in the hodograph plane of symmetric flow. The symmetric flow equation was obtained by equating the major determinant Δ of Eq. (8.4) to zero after substituting the free terms of Eqs. (8.4) in place of the coefficients of t.

The similar equation for asymmetric flow can be obtained by determining the second partial derivatives u and s in terms of t from Eq. (8.3) and substituting them into Eq. (8.1). Thus, we obtain

$$A\frac{dV_x}{dx} + \frac{dV_r}{dx}(2B - Ar') + H + t[A(r')^2 - 2Br' + C] = 0. \tag{12.10}$$

The term in brackets is equal to zero from Eq. (8.5b), and the equation for the characteristics in the hodograph plane becomes

$$\frac{dV_x}{dx} + \frac{2B - Ar'}{A}\frac{dV_r}{dx} + \frac{H}{A} = 0, \tag{12.11}$$

which is also the condition of compatibility in the hodograph plane.

The Compatibility Conditions for the Asymmetric Case in the Meridian Plane

Let us consider first the intersection of the characteristic surfaces with the meridian planes. The compatibility conditions can be represented in the form of equations that determine the variation in flow parameters along the corresponding lines of intersection. Each of these lines of intersection is designated by σ, where the curve σ_1 is a characteristic of the first family, and the curve σ_2 is a characteristic of the second family. Along each curve, the following relations are valid:

$$\begin{aligned} dV_x &= \frac{\partial V_x}{\partial x}dx + \frac{\partial V_x}{\partial r}dr, \\ dV_r &= \frac{\partial V_r}{\partial x}dx + \frac{\partial V_r}{\partial r}dr, \\ dV_\phi &= \frac{\partial V_\phi}{\partial x}dx + \frac{\partial V_\phi}{\partial r}dr. \end{aligned} \tag{12.12}$$

The velocity components can be replaced by the potential function Φ, and at the same time we will introduce the designation $p_{ik} = \Phi_{ik}$. For example,

the value $p_{ik} = p_{12}$ will represent the second partial derivative Φ_{xr}, the value $p_{ii} = p_{11}$ the derivative Φ_{xx}, etc. In agreement with this designation, Eq. (12.12) can be presented in the form

$$\begin{aligned} dV_x &= (p_{11} + p_{12}r'_x)\ dx, \\ dV_r &= (p_{12} + p_{22}r'_x)\ dx, \\ d(rV_\phi) &= (p_{13} + p_{23}r'_x)\ dx. \end{aligned} \tag{12.13}$$

To determine the curve of the intersection of the meridian plane ϕ = const with the characteristic surface of the first family, let us introduce a notation similar to that used in the symmetric flow case:

$$\lambda_1 = r'_x = \left(\frac{dr}{dx}\right)_{\phi=\text{const}}. \tag{12.14}$$

Following the method used to obtain the compatibility conditions in the symmetric case, the partial derivatives are determined from Eq. (12.13):

$$\begin{aligned} p_{12} &= \frac{dV_x}{dx} - p_{22}\lambda_1, \\ p_{13} &= \frac{d(rV_\phi)}{dx} - \lambda_1 p_{23}, \\ p_{11} &= \frac{dV_x}{dx} - \lambda_1 \frac{dV_r}{dx} + \lambda_1^2 p_{22}. \end{aligned} \tag{12.15}$$

Introducing the velocity-potential derivatives, Eq. (8.1) can be written as

$$a_{11}\frac{dV_x}{dx} + (a_{12} - a_{11}\lambda_1)\frac{dV_r}{dx} + a_{13}\frac{d(rV_\phi)}{dx} + \frac{V_r}{r}a_{44} + E_1 = 0, \tag{12.16}$$

where the coefficient $a_{44} = 1 + V_\phi^2/a^2$ and E_1 is given by

$$E_1 = p_{22}(a_{11}\lambda_1^2 - a_{12}\lambda_1 + a_{22}) + p_{23}(a_{23} - a_{13}\lambda_1) + a_{33}p_{33}. \quad (12.17)$$

Conditions in the Plane Normal to the Axis

The partial derivatives p_{22}, p_{23}, and p_{33} are unknowns that must be eliminated. For this purpose, we shall consider the intersection of the characteristic surface with a plane normal to the x-axis. Let τ_1 and τ_2 be the lines of intersection of this plane, x = const, with the characteristic surfaces of the first and second families, respectively. The element $d\tau_1$ of the intersection curve for the characteristic surface of the first family can be determined from the expression

$$(d\tau_1)^2 = (dr)^2 + (r\,d\phi)^2. \quad (12.18)$$

Along this curve the following relations are valid:

$$\frac{dV_\phi}{d\tau_1} = \frac{\partial V_\phi}{\partial \phi}\frac{d\phi}{d\tau_1} + \frac{\partial V_\phi}{\partial r}\frac{dr}{d\tau_1},$$

$$\frac{dV_r}{d\tau_1} = \frac{\partial V_r}{\partial \phi}\frac{d\phi}{d\tau_1} + \frac{\partial V_r}{\partial r}\frac{dr}{d\tau_1}.$$

Introducing the potential function Φ in terms of the parameter p by the relation $p_{ik} = \Phi_{ik}$, and also a new coefficient,

$$k = r'_\phi = \left(\frac{dr}{d\phi}\right)_{x=\text{const}}, \quad (12.19)$$

these relations for the derivatives can be presented in the form

$$\frac{d(rV_\phi)}{d\tau_1} = (p_{33} + kp_{23})\frac{d\phi}{d\tau_1},$$

$$\frac{dV_r}{d\tau_1} = (p_{23} + kp_{22})\frac{d\phi}{d\tau_1}. \quad (12.20)$$

The derivative $d\phi/d\tau_1$ is eliminated by using Eq. (12.18):

$$\frac{d\phi}{d\tau_1} = \frac{1}{r\sqrt{1 + k^2/r^2}}.$$

As a result we obtain

$$\begin{aligned} p_{23} + kp_{22} &= r\sqrt{1 + k^2/r^2}\,\frac{dV_r}{d\tau_1}, \\ p_{33} - k^2 p_{22} &= r\sqrt{1 + k^2/r^2}\left[\frac{d(rV_\phi)}{d\tau_1} - k\,\frac{dV_r}{d\tau_1}\right]. \end{aligned} \tag{12.21}$$

These relations can be used for the conversion of Eq. (12.16). First, let us rewrite the characteristics equation (12.8); by the addition and subtraction of equal terms, it is reduced to the form

$$E_1 = (p_{22}k + p_{23})(a_{23} - a_{13}\lambda_1) + a_{33}(p_{33} - k^2 p_{22}),$$

where E_1 is given by Eq. (12.17). Introducing Eq. (12.21) into this expression, we obtain

$$E_1 = r\sqrt{1 + k^2/r^2}\left[\frac{dV_r}{d\tau_1}(a_{23} - \lambda_1 a_{13} - ka_{33}) + a_{33}\,\frac{d(rV_\phi)}{d\tau_1}\right]. \tag{12.22}$$

It is evident that the unknown derivatives p_{22}, p_{23}, and p_{33} are not present in this expression and, therefore, are also not in the characteristics equation (12.16).

Equations analogous to Eqs. (12.16), (12.14), and (12.19) can be obtained corresponding to conditions at the intersection of the second-family characteristic surfaces with the same plane, ϕ = const:

$$a_{11}\frac{dV_x}{dx} + (a_{12} - a_{11}\lambda_2)\frac{dV_r}{dx} + a_{13}\frac{d(rV_\phi)}{dx} + \frac{V_r}{r}a_{44} + E_2 = 0, \tag{12.23}$$

$$\lambda_2 = \left(\frac{dr}{dx}\right)_{\phi=\text{const}}, \qquad k = \left(\frac{dr}{d\phi}\right)_{x=\text{const}}. \tag{12.24}$$

The function E_2, corresponding to the intersection line σ_2 of the characteristic surface, is determined in the same way as the function E_1 in Eq. (12.22).

Equations (12.16) and (12.23) represent the compatibility conditions in the meridian plane. The angular coefficients λ_1 and λ_2 determine the slope of the conjugate characteristics (corresponding to the curves σ_1 and σ_2) at each point and are calculated by the solution of Eq. (12.8), which can be written in the form

$$a_{11}\lambda^2 + F\lambda + D = 0, \tag{12.8a}$$

where

$$F = a_{13}k - a_{12}, \qquad D = a_{22} - a_{23}k + a_{33}k^2.$$

The roots of Eq. (12.8a) are

$$\lambda_{1,2} = -\frac{F}{2a_{11}} \pm \frac{1}{2a_{11}}\sqrt{F^2 - 4Da_{11}}. \tag{12.25}$$

Using the nature of these roots,

$$\lambda_1 + \lambda_2 = -\frac{a_{13}k - a_{12}}{a_{11}},$$

it is possible to rewrite Eqs. (12.16) and (12.23):

First family:

$$a_{11}\frac{dV_x}{dx} + (a_{11}\lambda_2 + a_{13}k)\frac{dV_r}{dx} + a_{13}\frac{d(rV_\phi)}{dx} + \frac{V_r}{r}a_{44} + E_1 = 0; \tag{12.16a}$$

Second family:

$$a_{11}\frac{dV_x}{dx} + (a_{11}\lambda_1 + a_{13}k)\frac{dV_r}{dx} + a_{13}\frac{d(rV_\phi)}{dx} + \frac{V_r}{r}a_{44} + E_2 = 0. \tag{12.23a}$$

The Compatibility Conditions in the Plane Normal to the Axis

Equations (12.16a) and (12.23a) determine the velocity variation along the characteristics in the meridian plane. However, for the solution of the three-dimensional problem, it is also necessary to know how the flow parameters change in passing from one meridian plane to another, i.e., depending on the angle ϕ. Therefore, we must examine the relations that determine the velocity variation along the intersection lines of the characteristic surfaces with the plane $x = \text{const}$.

Let us consider the intersection of a characteristic surface of the first family and the curve τ_1 along which this intersection occurs. For each point on the curve, the following relations are valid:

$$dV_x = \frac{\partial V_x}{\partial r}\,dr + \frac{\partial V_x}{\partial \phi}\,d\phi = (p_{12}k + p_{13})\,d\phi,$$

$$d(rV_\phi) = \frac{\partial (rV_\phi)}{\partial r}\,dr + \frac{\partial (rV_\phi)}{\partial \phi}\,d\phi = (p_{23}k + p_{33})\,d\phi,$$

$$dV_r = \frac{\partial V_r}{\partial r}\,dr + \frac{\partial V_r}{\partial \phi}\,d\phi = (p_{22}k + p_{23})\,d\phi.$$

Using these relations, the expressions for the partial derivatives are

$$p_{13} = \frac{dV_x}{d\phi} - p_{12}k,$$

$$p_{23} = \frac{dV_r}{d\phi} - p_{22}k,$$

$$p_{33} = \frac{d(rV_\phi)}{d\phi} - k\,\frac{dV_r}{d\phi} + k^2 p_{22}.$$

Introducing these derivatives into Eq. (3.20) for the velocity potential, we obtain

$$a_{13}\frac{dV_x}{d\phi} + (a_{23} - a_{33}k)\frac{dV_r}{d\phi} + a_{33}\frac{d(rV_\phi)}{d\phi} + \frac{V_r}{r}a_{44} + G_i = 0, \qquad (12.26)$$

where

$$G_1 = p_{22}(a_{33}k^2 - a_{23}k + a_{22}) + p_{12}(a_{12} - a_{13}k) + p_{11}a_{11}. \qquad (12.27)$$

The derivatives p_{22}, p_{12}, and p_{11} must be eliminated from the expression for the function G_1. For this purpose, we investigate the meridian plane ϕ = const and the curve σ_1 along which this plane intersects the characteristic surface of the first family. The element of the arc of the curve $d\sigma_1$ is computed from the differential expression

$$(d\sigma_1)^2 = (dx)^2 + (dr)^2,$$

from which it is also possible to find the derivative

$$\frac{d\sigma_1}{dx} = \sqrt{1 + \lambda_1^2}. \qquad (12.28)$$

Along the curve in question, the following relations are valid:

$$\frac{dV_x}{d\sigma_1} = \frac{\partial V_x}{\partial x}\frac{dx}{d\sigma_1} + \frac{\partial V_x}{\partial r}\frac{dr}{d\sigma_1} = (p_{11} + p_{12}\lambda_1)\frac{dx}{d\sigma_1},$$

$$\frac{dV_r}{d\sigma_1} = \frac{\partial V_r}{\partial x}\frac{dx}{d\sigma_1} + \frac{\partial V_r}{\partial r}\frac{dr}{d\sigma_1} = (p_{12} + p_{22}\lambda_1)\frac{dx}{d\sigma_1}.$$

Using these expressions and Eq. (12.28), it is possible to find

$$\begin{aligned} p_{12} + p_{22}\lambda_1 &= \sqrt{1 + \lambda_1^2}\,\frac{dV_r}{d\sigma_1}, \\ p_{11} - p_{22}\lambda_1^2 &= \sqrt{1 + \lambda_1^2}\left(\frac{dV_x}{d\sigma_1} - \lambda_1\frac{dV_r}{d\sigma_1}\right). \end{aligned} \qquad (12.29)$$

Adding and subtracting equal terms to Eq. (12.5) transforms it as follows:

$$G_1 = a_{11}(p_{11} - p_{22}\lambda_1^2) + (p_{12} + p_{22}\lambda_1)(a_{12} - a_{13}k).$$

Introducing Eq. (12.29), we obtain

$$G_1 = \sqrt{1 + \lambda_1^2}\left[a_{11}\frac{dV_x}{d\sigma_1} + \frac{dV_r}{d\sigma_1}(a_{12} - a_{13}k - a_{11}\lambda_1)\right]. \qquad (12.30)$$

An equation similar to Eq. (12.26) can be written for the curve σ_2, which is the intersection line of the plane x = const with the characteristic surface of the second family. The only difference lies in the fact that a function G_2 enters in place of G_1. In turn, this function is computed from Eq. (12.30) in which the angular coefficient λ_2 must be substituted for λ_1.

METHOD OF CALCULATION OF ASYMMETRIC FLOW AROUND A BODY OF REVOLUTION

The Construction of a Characteristic Surface

Equations (12.8), (12.16a), (12.23a), and (12.26) permit the calculation of three-dimensional supersonic flow around a body of revolution at an angle of attack if the initial conditions on any characteristic surface are known. These conditions can be determined if the fore part of the body of revolution is assumed to be a sufficiently small conical length and the asymmetric flow around such a cone is calculated.

Figure 101 shows a body of revolution, the fore part of which is in the form of a cone. The curve AA' separates the conical element of the body from the remaining curved profile. Since the flow around the

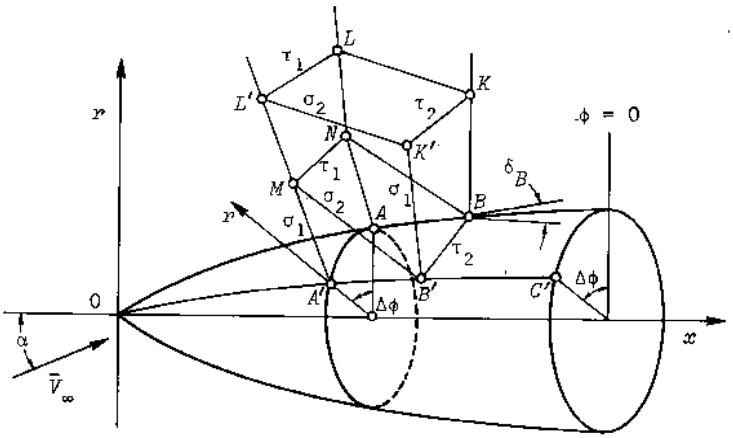

Fig. 101--Diagram for the calculation of asymmetric flow

conical portion at an angle of attack is known (it can be calculated by the methods presented in Chap. II), the flow parameters are known at points A and A' on the curve AA'. The flow behind this curve changes direction, expanding somewhat thereby and leading to the generation of a perturbation that is propagated downstream along a characteristic surface.

If the characteristic surface is known, the calculation of the expanding flow amounts to the determination of the velocity field between it and the curved surface of the body of revolution. Therefore, the first stage of the calculation is the construction of the characteristic surface. To do this, we must first determine the surface's intersection with the meridian plane.

Every such plane intersects the characteristic surface along a line that passes through some arbitrary point located on the curve AA'. The zero meridian plane $\phi = 0$ intersects the characteristic surface along the characteristic ANL of the first family. The element of this characteristic passing through point A is determined by the equation

$$r = r_A + \lambda_1(x - x_A), \tag{12.31}$$

in which λ_1 is the angular coefficient at this point. Since we are considering a body of revolution, the coordinate is constant along the curve AA' and $k = r'_\phi = 0$. Therefore, the angular coefficient λ_1 is determined from the characteristics equation (12.8a) for $k = 0$. In other words, it is possible to use Eq. (8.5) from the symmetric case. Because the normal velocity $V_\phi = 0$ at all points of the zero meridian plane, including point A, the roots of the equation, $\lambda_{1,2}$, are functions only of the components V_x and V_r, and are given by Eq. (8.5a).

The angular coefficients of the characteristics at the points on the curve AA' are determined from Eq. (8.5a) for all meridian planes, since $k = r'_\phi = 0$. Therefore, an element of the characteristic surface can be constructed in the vicinity of this curve. It should be emphasized that to each value of the angle ϕ of the meridian plane there corresponds a different value of the angular coefficient λ_1, because of the velocity change along the curve AA'.

Let us consider the intersection of the characteristic surface with the planes normal to the body axis and located at distances $x = x_1$ and $x = x_A$. At the same time, we shall assume that the distance between these planes is small; it is possible to assume that the angular coefficients λ_1 in a given meridian plane are identical, although they vary as a function of the angle ϕ. The coordinates r in the plane $x = x_1$ for each of the values of this angle can be computed from Eq. (12.31), thus finding the curve MN of the intersection of the characteristic surface with the plane $x = x_1$.

Since the coordinates r of this curve are now known, we can determine the value $k = (r'_\phi)_{x1}$ and then find, with the aid of Eq. (12.8a), a new value of the angular coefficient $\lambda_1(\phi)$ at the corresponding point of the curve MN. Finding the values $\lambda_1(\phi)$ along this curve, it is possible to draw the elements of the characteristics ML', NL, etc. from points M and N as well as from other points lying between them. As a result, a second element of the characteristic surface $MNLL'$ is generated.

Continuing the construction, the characteristic surface of the first family of curves can be determined. This surface is limited from below by the curve AA' located on the body, and from above by the curve that represents the intersection of the characteristic surface with the surface of the shock wave.

Having completed the construction, the velocity field between the characteristic surface and the body of revolution can be determined.

The Velocity on the Surface of the Body in the Plane $\phi = 0$

Let us consider the point N on a characteristic surface of the first family. From the known value of the angular coefficient λ_2 at this point, we can construct a tangent to the characteristic surface of the second family in the plane $\phi = 0$. Point B is the point of intersection of an element of this tangent with the surface of the body of revolution. One of the velocity components at B, i.e., the normal component $V_{\phi B}$, is known and is equal to zero. Moreover, from the continuous flow condition, $V_{rB}/V_{xB} = \tan \delta_B$ is the known ratio between the two other components. Therefore, only one additional equation is needed and this is Eq. (12.23a) for the characteristics of the second family. Converting this equation

to finite differences, we obtain

$$\Delta V_{xB} + \lambda_{1N}\Delta V_{rB} + \frac{1}{a_{11N}}\left(\frac{V_{rN}}{r_N}a_{44N} + E_{2N}\right)(x_B - x_N) = 0, \quad (12.32)$$

where

$$\Delta V_{xB} = V_{xB} - V_{xN},$$

$$\Delta V_{rB} = V_{rB} - V_{rN}.$$

The continuous flow relation gives

$$\Delta V_{rB} = \Delta V_{xB}\tan\delta_B + V_{xN}\tan\delta_B - V_{rN}. \quad (12.33)$$

Introducing this expression into Eq. (12.32), we obtain the relation for determining the velocity change along element NB:

$$\Delta V_{xB} = -\frac{\lambda_{1N}(V_{xN}\tan\delta_B - V_{rN})}{1 + \lambda_{1N}\tan\delta_B} - \frac{(A_N + E_{2N})(x_B - x_N)}{a_{11N}(1 + \lambda_{1N}\tan\delta_B)}, \quad (12.34)$$

where the function $A_N = V_{rN}a_{44N}/r_N$.

Having computed the velocity increment ΔV_{xB}, the difference ΔV_{rB} can be found from Eq. (12.33). The velocity components at point B are given by $V_{xB} = V_{xN} + \Delta V_{xB}$ and $V_{rB} = V_{rN} + \Delta V_{rB}$. It is assumed that the velocity components at point N are known from the conditions on the characteristic surface of the first family. Knowing the velocity at point B, the tangent BK to the characteristic surface of the first family can be drawn through point B in the plane $\phi = 0$.

The Velocity on the Body Surface at Points Lying in the Meridian Plane $\phi = \Delta\phi$

Let us consider the intersections of the characteristic surface and of the body of revolution with the meridian plane $\phi = \Delta\phi$. A tangent MB' to the second-family characteristic, having an angle determined by the coefficient λ_2, can be drawn from point M in the meridian plane to the

intersection with the body surface at point B'. This construction can be repeated at other points along the line MN to generate the curve BB', which represents the intersection of the element of the second-family characteristic surface $MB'BN$ with the body. In approximate calculations, it can be assumed that the curve BB' is a circumferential arc and therefore is located in a plane normal to the body axis.

The velocity at point B' is calculated from the equations for the variation in the velocity components along the curves MB' and BB'. (In Fig. 101, the first curve is designated σ_2, the second, τ_2.)

The finite-difference form of the equation for MB' is obtained from Eq. (12.23a):

$$\Delta V_{xB'} + \frac{ka_{13M} + \lambda_{1M}a_{11M}}{a_{11M}} \Delta V_{rB'} + \frac{a_{13M}}{a_{11M}} \Delta(rV_\phi)_{B'} + \frac{A_M + E_{2M}}{a_{11M}} \Delta x_{B'} = 0, \tag{12.35}$$

where

$$\Delta V_{xB'} = V_{xB'} - V_{xM}, \qquad \Delta V_{rB'} = V_{rB'} - V_{rM}, \qquad \Delta(rV_\phi)_{B'} = (rV_\phi)_{B'} - (rV_\phi)_M. \tag{12.36}$$

The equation for curve BB' is obtained from Eq. (12.26) after transformation to finite differences:

$$\Delta' V_{xB'} + \frac{a_{23B}}{a_{13B}} \Delta' V_{rB'} + \frac{a_{33B}}{a_{13B}} \Delta'(rV_\phi)_{B'} + \frac{A_B + G_{1B}}{a_{13B}} \Delta\phi = 0, \tag{12.37}$$

where

$$\Delta' V_{xB'} = V_{xB'} - V_{xB}, \qquad \Delta' V_{rB'} = V_{rB'} - V_{rB}, \qquad \Delta'(rV_\phi)_{B'} = (rV_\phi)_B. \tag{12.38}$$

The difference $\Delta\phi = \phi_{B'} - \phi_B = \phi_{B'}$ in Eq. (12.37) must be sufficiently small. It should also be noted that the quantity k is absent in this equation because the coordinate r is constant along the curve BB' and, consequently, $k = 0$.

In addition to Eqs. (12.35) and (12.37), we must include the continuous flow condition at point B', having the form $V_{rB'} = V_{xB'} \tan \delta_{B'}$.

In these three equations, there are six unknowns. The number of unknowns can be reduced to three by writing Eq. (12.38) in the following form:

$$\Delta' V_{xB'} = \Delta V_{xB'} + V_{xM} - V_{xB},$$

$$\Delta' V_{rB'} = \Delta V_{rB'} + V_{rM} - V_{xB}, \tag{12.39}$$

$$\Delta' (rV_\phi)_{B'} = \Delta (rV_\phi)_{B'} + (rV_\phi)_M.$$

The continuous flow condition can be written in a different form:

$$\Delta V_{rB'} = \Delta V_{xB'} \tan \delta_{B'} + V_{xM} \tan \delta_{B'} - V_{rM}. \tag{12.40}$$

Combining Eqs. (12.35) and (12.37) with (12.39) and using Eq. (12.40), the following system is obtained for determining the three unknowns:

$$\begin{aligned} \Delta V_{xB'} + F_\tau^1 \Delta V_{rB'} + F_\tau^2 \Delta (rV_\phi)_{B'} + F_\tau^3 &= 0, \\ \Delta V_{xB'} + F_\sigma^1 \Delta V_{rB'} + F_\sigma^2 \Delta (rV_\phi)_{B'} + F_\sigma^3 &= 0, \\ \Delta V_{xB'} + F_\beta^1 \Delta V_{rB'} + F_\beta^3 &= 0. \end{aligned} \tag{12.41}$$

The functions $F^1_{\tau(\sigma,\beta)}$ are determined by the expressions

$$F_\tau^1 = \frac{a_{23B}}{a_{13B}}, \qquad F_\tau^2 = \frac{a_{33B}}{a_{13B}},$$

$$F_\tau^3 = V_{xM} - V_{xB} + \frac{a_{23B}}{a_{13B}} (V_{rM} - V_{rB}) + \frac{a_{33B}}{a_{13B}} (rV_\phi)_M + \frac{A_B + G_{2B}}{a_{13B}} \Delta\phi,$$

$$F_\sigma^1 = \frac{1}{a_{11M}} (ka_{13M} + \lambda_{1M} a_{11M}), \tag{12.42}$$

$$F_\sigma^2 = \frac{a_{13M}}{a_{11M}}, \qquad F_\sigma^3 = \frac{A_M + G_{2B}}{a_{11M}},$$

$$F_\beta^1 = -\frac{1}{\tan \delta_B}, \qquad F_\beta^3 = V_{xM} - \frac{V_{rM}}{\tan \delta_B}.$$

Solving Eqs. (12.41) for the increment $\Delta V_{rB'}$, we obtain

$$\Delta V_{rB'} = \frac{F_\beta^3(F_\sigma^2 - F_\tau^2) - F_\sigma^2 F_\tau^3 - F_\tau^2 F_\sigma^3}{F_\sigma^2(F_\tau^1 - F_\beta^1) - F_\tau^2(F_\sigma^1 - F_\beta^1)}. \tag{12.43}$$

Knowing this value, the increment $\Delta V_{xB'}$ can be determined from the third equation of (12.41), and the quantity $\Delta(rV_\phi)_{B'}$ from the second equation. Now the velocity components at point B' can be computed:

$$\begin{aligned} V_{xB'} &= V_{xM} + \Delta V_{xB'}, \\ V_{rB'} &= V_{rM} + \Delta V_{rB'}, \\ V_{\phi B'} &= \frac{1}{r_{B'}}\,[(rV_\phi)_M + \Delta(rV_\phi)_{B'}]. \end{aligned} \tag{12.44}$$

From the known velocities at points B and B' we can determine the angular coefficients of the elements of the characteristics located in the meridian planes $\phi = 0$ and $\phi = \Delta\phi$. Constructing these elements, we can then find the line KK' of the intersection of the two elements of the characteristic surfaces of the first and second families.

The Velocity at Points Located on the Line KK'

To find the velocities at the points K and K', a corresponding system of equations for the characteristics must be set up and solved for each of them. Let us consider first the point K. Since it lies in the zero meridian plane, the normal velocity component is zero. To compute the other components, Eqs. (12.16a) and (12.23a) are transformed to finite differences and written to conform to the conditions along the elements BK and LK, respectively:

$$\begin{aligned} a_{11B}\,\Delta' V_{xK} + a_{11B}\lambda_{2B}\,\Delta' V_{rK} + (A_B + E_{1B})(x_K - x_B) &= 0, \\ a_{11L}\,\Delta V_{xK} + a_{11L}\lambda_{1L}\,\Delta V_{rK} + (A_L + E_{2L})(x_K - x_L) &= 0. \end{aligned} \tag{12.45}$$

The velocity-component increments along the characteristic elements LK and BK have the form

$$\begin{aligned} \Delta' V_{xK} &= \Delta V_{xK} + V_{xL} - V_{xB}, \\ \Delta' V_{rK} &= \Delta V_{rK} + V_{rL} - V_{rB}. \end{aligned} \tag{12.46}$$

Introducing these relations into the first equation of Eq. (12.45), the increments ΔV_{xK} and ΔV_{rK} can be found, and then the velocity components at point K can be computed: $V_{xK} = \Delta V_{xK} + V_{xL}$, $V_{rK} = \Delta V_{rK} + V_{rL}$.

Let us examine point K', which lies on the intersection of the elements $B'K'$ and $L'K'$ of the characteristics of the first and second families, respectively, and the line $K'K$, which represents the intersection of two elements of characteristic surfaces of different families. Hence, three equations are required to calculate the velocity at point K', each of which determines the velocity variation along the lines $L'K'$, $B'K'$, and KK':

$$\begin{aligned} &a_{11L'}\,\Delta V_{xK'} + (a_{11L'}\lambda_{1L'} + a_{13L'}k)\,\Delta V_{rK'} + a_{13L'}\,\Delta(rV_\phi)_{K'} \\ &\qquad + (A_{L'} + E_{2L'})(x_{K'} - x_{L'}) = 0, \\ &a_{11B'}\,\Delta' V_{xK'} + (a_{11B'}\lambda_{2B'} + a_{13B'}k)\,\Delta' V_{rK'} + a_{13B'}\,\Delta'(rV_\phi)_{K'} \\ &\qquad + (A_{B'} + E_{1B'})(x_{K'} - x_{B'}) = 0, \\ &a_{13K}\,\Delta'' V_{xK'} + (a_{23K} - a_{33K}k)\,\Delta'' V_{rK'} \\ &\qquad + a_{33K}\,\Delta''(rV_\phi)_{K'} + (A_K + G_{1K})\,\Delta\phi = 0. \end{aligned} \tag{12.47}$$

The quantity $k(\phi)$ in these equations is computed from

$$k(\phi) = \frac{\lambda_\phi - \lambda_{\phi=0}}{\Delta\phi}\,\Delta x.$$

For example, the corresponding quantity for element $L'K'$ is

$$k(\phi) = \frac{\lambda_{2L'} - \lambda_{2L}}{\Delta\phi}\,(x_{K'} - x_{L'}).$$

In Eqs. (12.47), there are nine unknowns. However, by a simple transformation analogous to that which was used above, the number of these unknowns can be decreased to three. For example, the increments $\Delta' V_i$ and $\Delta'' V_i$ can be expressed in terms of the increment ΔV_i:

$$\begin{aligned} \Delta' V_i &= \Delta V_i + V_{iL'} - V_{iB'}, \\ \Delta'' V_i &= \Delta V_i + V_{iL'} - V_{iK}. \end{aligned} \tag{12.48}$$

The subscript i indicates the velocity component in question. For example, if it is the axial component at point K', $i = x$ and

$$\Delta' V_{xK'} = \Delta V_{xK'} + V_{xL'} - V_{xB'},$$

$$\Delta'' V_{xK'} = \Delta V_{xK'} + V_{xL'} - V_{xK}.$$

After the substitution of Eqs. (12.48) into the last two equations of Eqs. (12.47), there remain only three unknown quantities, i.e., $\Delta V_{xK'}$, $\Delta V_{rK'}$, and $\Delta(rV_\phi)_{K'}$. After determining these, it is possible to compute the velocity components at point K'. For example, the axial component is $V_{xK'} = \Delta V_{xK'} + V_{xL'}$.

It should be noted that to compute the functions E and G that enter into Eq. (12.47), the velocity increment on a unit length of the element must be known, i.e., the values $\Delta V_r/\Delta\sigma$, $\Delta V_x/\Delta\sigma$, $\Delta V_r/\Delta\tau$, and $\Delta(rV_\phi)/\Delta\tau$. For example, the computation of the function E_{2L} requires the determination of the ratio $\Delta(rV_\phi)/\Delta\tau$ from the values rV_ϕ at the points L and L' of the element LL', with the help of the equation

$$\frac{\Delta(rV_\phi)_{L'}}{\Delta\tau_{L'}} = \frac{(rV_\phi)_{L'} - (rV_\phi)_L}{LL'},$$

where the length of the element $LL' = \Delta\tau_{L'}$. In the particular case

under consideration, the quantity $(rV_\phi)_L = 0$, because the normal velocity component $V_{\phi L} = 0$ at point L in the zero meridian plane.

Using the known velocities at points K and K' in the characteristics equation (12.8a), the angular coefficients λ_1, λ_2 can be determined and the tangents drawn to the characteristic surfaces of both families of curves in the planes $\phi = 0$, $\phi = \Delta\phi$. Continuing the calculations and constructions, it is possible to determine step by step the parameters of potential flow around a body of revolution at an angle of attack.

EXPERIMENTAL DATA AND APPROXIMATE METHODS OF CALCULATING THE FLOW AROUND A BODY OF REVOLUTION AT AN ANGLE OF ATTACK

Combination of Conical Flows and Expansion Flows

The complication and intricacy of calculations using the method of characteristics emphasize the need for widespread experimental research and for the development of approximate methods of calculating asymmetric flow around a body of revolution. One of these is the method of combining the calculation of conical flows and two-dimensional expansions.† For application to asymmetric flow around a pointed body of revolution, this method is based on using the Mach number and other parameters at the nose in each meridian plane from the solution for the flow around a cone at an angle of attack; the flow behind the nose in each meridian plane is then calculated as though it were a two-dimensional supersonic expansion, usually called a Prandtl-Meyer expansion.

To perform this calculation, it is necessary to use the properties and the analytical relations for the characteristics of two-dimensional flow. These are geometrically represented by epicycloids, as has been indicated. For each point on an epicycloid, there are specific values of Mach number and of flow deflection angle in an isentropic expansion from the initial state of flow at $M = 1$. The latter state represents the critical regime characterized by a local pressure p^*. Hence, a specific value of the pressure ratio p/p^* corresponds to each point of the epicycloid because the ratio depends only on the local Mach number, as is indicated by the equation

†Editor's note: In American literature called the generalized shock-expansion method, or the conical shock-expansion method.

$$\frac{p}{p^*} = \left[\frac{(\gamma + 1)/2}{1 + \frac{\gamma - 1}{2} M^2}\right]^{\gamma/(\gamma-1)}. \tag{12.49}$$

This equation can also be used to calculate the pressure at any section that follows an isentropic expansion or compression from an initial state at an arbitrary local Mach number. Suppose that the initial station is located behind the shock wave on the conical nose, where the stream is deflected from the direction of the incident flow by an angle δ_0 and the local Mach number $M = M_2$. We wish to find the pressure at a point on the surface located in a given meridian plane. At this point the angle δ between the tangent to the profile and the direction of the free-stream velocity vector is known.

First, solving the problem for asymmetric flow around a cone, we can find the value of the Mach number M_2 and, from Eq. (8.11a) or Table 15, the corresponding angle ω_2. Then the total turning angle ω is obtained as the sum of the turning angle ω_2 and the local (absolute) angle of deflection $\delta_0 - \delta$. From the value of $\omega = \omega_2 + (\delta_0 - \delta)$, the local Mach number can be found from Table 15 and the pressure ratio p/p^* from Eq. (12.49). The pressure coefficient is given by

$$C_p = \frac{2p^*}{\gamma p_\infty M_\infty^2}\left(\frac{p}{p^*} - \frac{p_\infty}{p^*}\right). \tag{12.50}$$

Compared with experimental data, on the whole this approximate calculation gives satisfactory results and is more accurate the larger the Mach number M_∞ and the larger the similarity parameter $K_1 = M_\infty/\lambda_N$. This is evident in Fig. 102, where results are presented for the pressure distribution around two ogive noses with fineness ratios of 3 and 5 for $M_\infty = 5.05$ and angles of attack of 5° and 15°.[9] The theory and experiment agree better for the larger value of the parameter $K_1 = 1.68$, i.e., for the body with a fineness ratio of 3. For the nose with a fineness ratio of 5 ($K_1 = 1.01$), the numerical calculation gives values somewhat too low on the upper side of the body compared with the experimental results. However, on the whole the theoretical data are fairly good. This is true in practice for all values of $K_1 > 1$, although, as has been

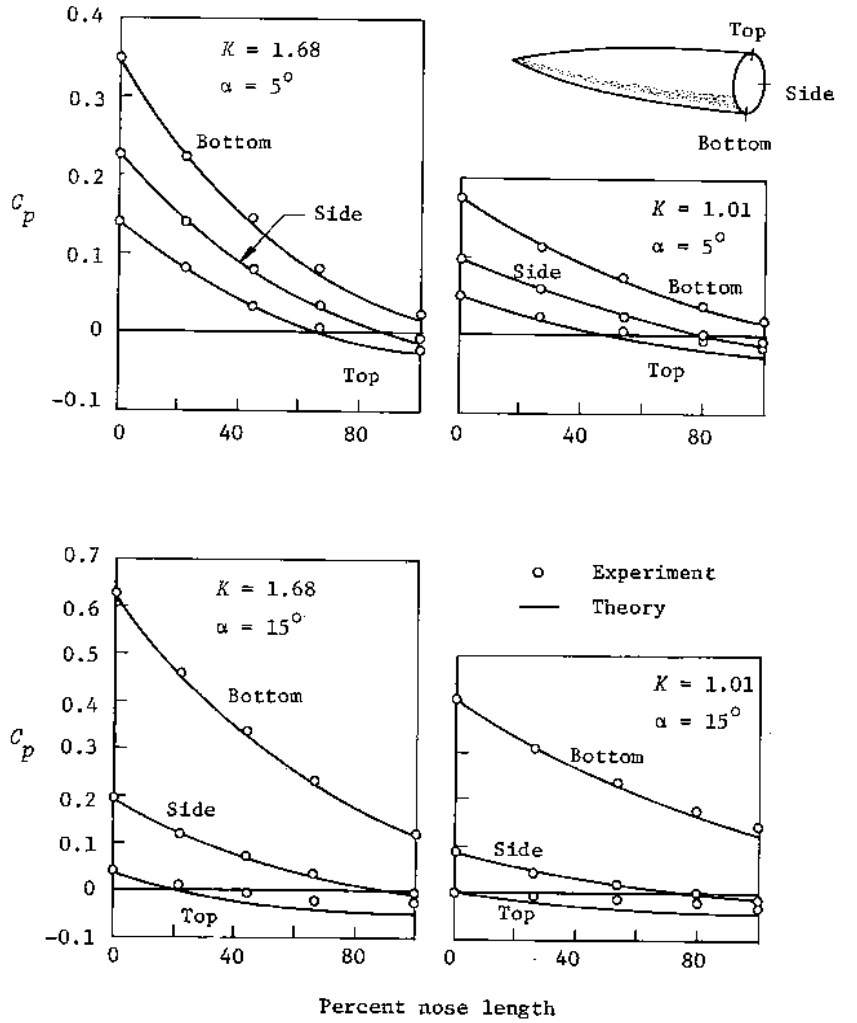

Fig. 102--Pressure distribution on parabolic noses with fineness ratios of 3 and 5 at M_∞ = 5.05

stated, the accuracy of the calculations decreases as the similarity parameter decreases. If this parameter is less than unity, as a rule the approximate calculation proves to be unacceptable.

From a comparison of calculations with test data, it is also possible to reach the conclusion that the approximate method gives better

results for smaller angles of attack. The discrepancy in the pressure distribution between theoretical calculations and experiment for large α is due to the influence of viscosity on the crossflow, especially on the upper side of the body, which is not taken into account by the approximate theory. This effect increases with an increase in the free-stream Mach number. The reliability of the method of combining conical and expansion flows can be tested further by comparing theoretical and experimental data for a shock wave. Shock-wave shapes in the vertical plane of symmetry have been calculated for two bodies of revolution with fineness ratios of 3 and 5 for $M_\infty = 5.05$ at an angle of attack of 10°, and their shape was photographed in a test of models in a wind tunnel.(9) From the comparative data presented in Fig. 103, good agreement of the theoretical and experimental results is evident. The shapes of shock waves calculated for a circular cone with an angle δ_0 are also shown on the figure. It is apparent that the conical shock is close to the actual shock profile on the upper side.

For a total evaluation of the approximate method, it is advisable to compare the normal force coefficients found experimentally and theoretically. As can be seen in Fig. 104, the agreement is satisfactory; however, a better correspondence of theory and experiment is observed for the larger value of the similarity parameter. It can be shown that the approximate method has the same accuracy in the estimation of the longitudinal force coefficient as for the determination of the normal force coefficient.

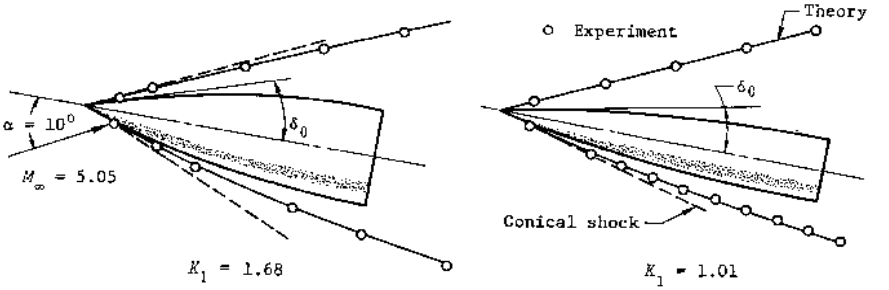

Fig. 103--Shock waves for a parabolic nose at angle of attack

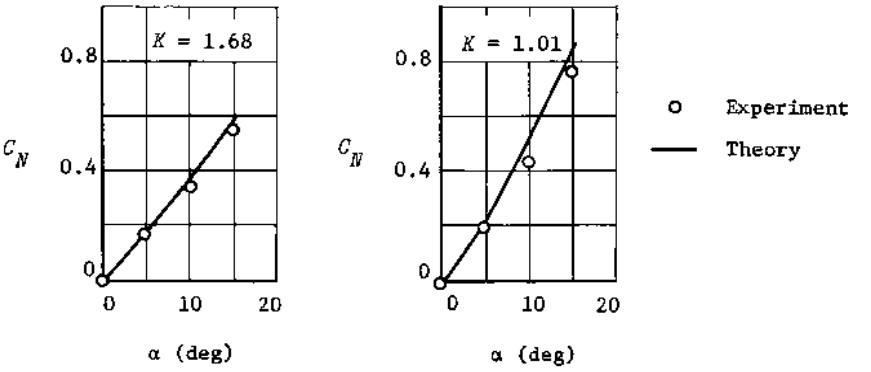

Fig. 104--Normal force coefficient for a parabolic nose at $M_\infty = 5.05$

The Determination of the Local Mach Number

A slightly different method for calculating the local Mach number in combined conical and expansion flows is advantageous when computing machines are used for the calculations. The relation for the difference of the angles of the flow deflection at the tip and at an arbitrary point on the surface can be represented in the form

$$\omega - \omega_2 = f(M) - f(M_2) = \delta_0 - \delta,$$

where the functions $f(M) = \omega$ and $f(M_2) = \omega_2$ are determined from Eq. (8.11a) as a function of the corresponding Mach number. Further, the derivative $g(M) = d\omega/dM$ can be determined from Eq. (8.27) as a function of the Mach number. Consequently,

$$\delta_0 - \delta = \int_{M_2}^{M} g(M)\, dM,$$

so that, in the first approximation, the local Mach number is

$$M^{(1)} = M_2 + \frac{\delta_0 - \delta}{g(M_2)}. \qquad (12.51)$$

The second approximation is based on the value found for $M^{(1)}$:

$$M^{(2)} = M^{(1)} + \frac{F - f[M^{(1)}]}{g[M^{(1)}]}, \tag{12.52}$$

where the function $F = f(M_2) + \delta_0 - \delta$. The approximation process, which is always converging, is continued until a given accuracy is attained.

In the general form, the expression for the nth approximation is

$$M^{(n)} = M^{(n-1)} + \frac{F - f[M^{(n-1)}]}{g[M^{(n-1)}]}, \tag{12.53}$$

where n varies in the range $1 \leq n < \infty$. The Mach number $M^{(0)} = M_2$ corresponds to the value $n = 0$.

The Method of Local Cones

The method of local cones, as applied to the calculation of asymmetric flow around a body of revolution with an arbitrary shape, consists of the following. It is assumed that a line tangent to the profile at some point on the surface (Fig. 105) is also the generatrix of a cone in a symmetric unperturbed flow. The angle of this cone can be

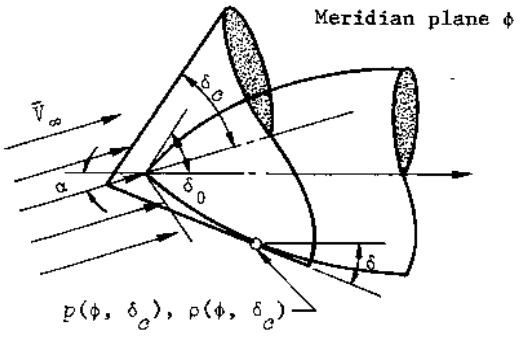

Fig. 105--The method of local cones for asymmetric flow

determined from

$$\delta_c = \delta - \alpha \cos \phi + \frac{\alpha^2}{2} \cot \delta \sin^2 \phi, \qquad (12.54)$$

in which δ is the angle between the tangent to the surface and the axis of the body. If the parameters on the cone are determined for $\alpha = 0$, then, according to the concept of the method of local cones, these parameters will be the same as those for the real flow at the point under consideration on the surface at a given angle of attack.

Comparison of the calculations with experimental data shows that it is necessary to employ the hypothesis of identical velocities in using the local-cone method for computing the parameters on the surface of pointed bodies of revolution having noses of small fineness ratio for $M_\infty = 3$ to 4 and lower at small angles of attack. From the velocities found on the basis of this hypothesis, the pressure and density are calculated taking into account the entropy of the stream flowing in the meridian plane under consideration through a shock wave at the tip.

The hypothesis of identical pressures gives better results for high velocities. The velocity and the density can then be determined from the pressure, accounting for variations in entropy.

Strictly speaking, the use of the local-cone method is only valid up to the point where the tangent to the surface is parallel to the direction of the incident flow, in which case the angle of the local cone is zero. The local slope corresponding to a value of $\delta_c = 0$ is obtained from Eq. (12.54):

$$\delta = \alpha \cos \phi - \frac{\alpha^2}{2} \cot \delta \sin^2 \phi. \qquad (12.55)$$

At points on the surface determined by this angle, the pressure will be equal to the free-stream static pressure according to the identical-pressure hypothesis. However, if the calculation is made on the basis of the hypothesis of identical velocities, the velocity at that point is equal to the free-stream velocity.

The local-cone method can be used for rough estimates of flow parameters beyond the indicated boundaries, in the so-called shadow zone. This can be done by arbitrarily calculating a local cone with a negative angle δ_c from Eq. (12.54). Then the pressure coefficient, based

on the absolute value of δ_c, must be considered negative in sign at the given point in the shadow zone.

Influence of Angle of Attack on Nose Drag

It can be assumed that the nose drag varies quadratically with α up to angles of attack of 15° to 20°, and the effect of angle of attack is different for different bodies. This is apparent from the experimental data in Fig. 106, which shows the effect of angle of attack on

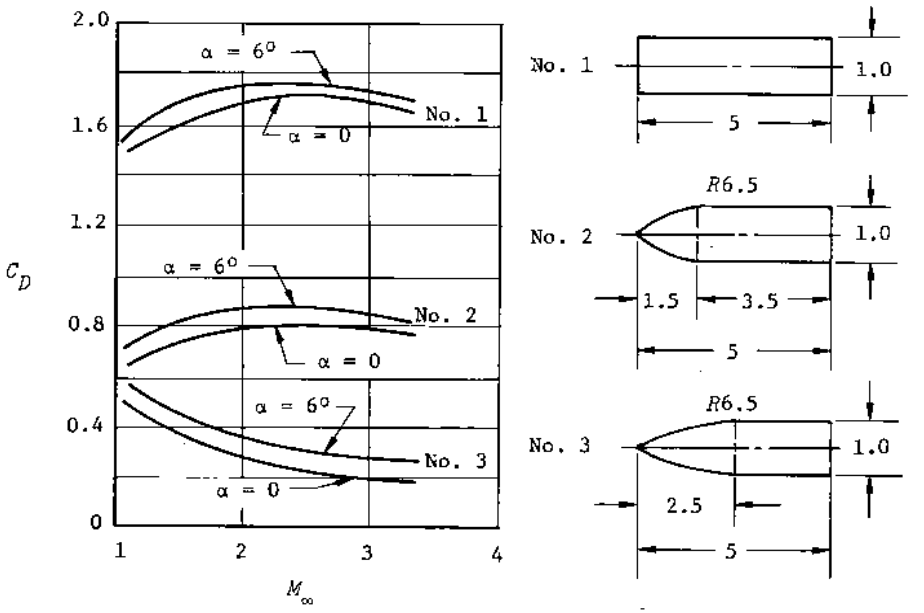

Fig. 106--Effect of angle of attack and body shape on the nose drag coefficient

the nose drag coefficient of three bodies of different shape. Although the absolute values of the variation of the coefficient C_D are almost identical for all three bodies (increasing slightly for the tapered shapes), the relative increment is significantly larger for the pointed bodies. For example, the absolute increments of the drag coefficient for bodies Nos. 2 and 3 in Fig. 106 are approximately identical and equal to 0.1 for $M_\infty = 2$ at an angle of attack of 6°. However, the relative

increment of the less pointed body (No. 2) is approximately 10 percent, but that for the more slender body (No. 3) is 25 percent. If we consider the cylindrical body with a flat face (No. 1), the relative increment of the drag is only about 5 percent for approximately the same absolute change in C_D.

The effect of asymmetric flow becomes more significant as the angle of attack is increased. This is evident in Fig. 107a, where results are

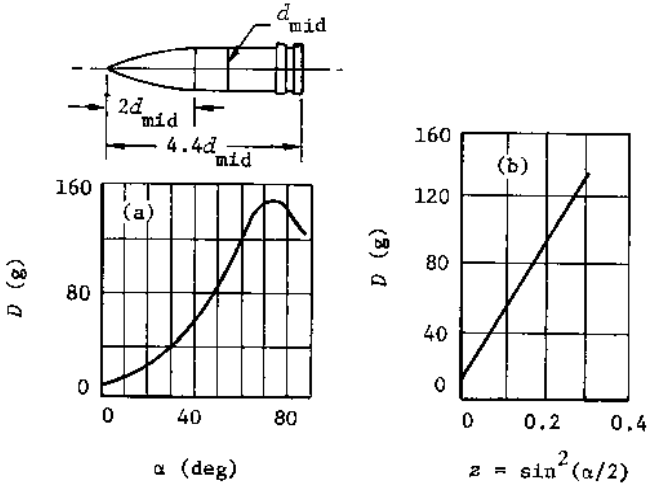

Fig. 107--Variation of the nose drag with angle of attack at low velocities

presented for a wind-tunnel test of a model of a projectile at low speed for angles of attack up to almost 90°, i.e., essentially for flow normal to the axis. The curve at the left shows the variation in drag (in grams) with angle of attack. Obviously, the angle of attack influences the drag significantly; even at $\alpha = 15°$, the drag is increased by a factor of almost two. A maximum is attained at an angle of attack of approximately 75°. The reduction in drag above 75° is caused, apparently, by a decrease in separation of the flow behind the base. Because of this the base drag is decreased and, consequently, the total drag. If the drag curve is redrawn as a function of $z = \sin^2(\alpha/2)$ (Fig. 107b), it appears

that up to large angles of attack ($\alpha \approx 65°$, $0 \leq z \leq 0.3$) the nose drag and therefore the drag coefficient are linear functions of z.

Studies at supersonic velocities also indicate that for $M_\infty > 1.4$ the nose drag coefficient changes linearly with z according to the equation

$$C_D = C_{D0}(1 + \varepsilon z), \tag{12.56}$$

in which C_{D0} is the nose drag coefficient at zero angle of attack and ε is a coefficient that depends on the shape of the body and the velocity. The experiments show that the dependence on velocity is slight and in practice ε can be assumed to be constant for a rather wide range of Mach numbers. For a pointed projectile of caliber 12.7 mm in the range $1.5 \leq M_\infty \leq 2.2$, the average value of $\varepsilon = 87$, and for a missile of caliber 20 mm in approximately the same range, $\varepsilon = 80$. Equation (12.56) was confirmed on the basis of experimental firings at velocities of more than 450 m/sec and for values $0 \leq z \leq 0.1$ ($0 \leq \alpha \leq 37°$). The linear relation does not hold at lesser velocities and a more general relationship should be used:

$$C_D = C_{D0}(1 + a_1 z + a_2 z^2 \ldots), \tag{12.57}$$

in which terms with second and even higher powers of z must be taken into account, depending on the flow conditions.

The equations presented for the nose drag coefficient apply to the case of rather large angles of attack. If the angle of attack is small (0° to 5°), Eq. (1.1) can be used for approximate calculations, which gives $C_D = C_A + C_N\alpha$ for small angles of attack. Experimental and theoretical research indicates that the axial force coefficient varies insignificantly with angle of attack. For example, in wind-tunnel tests it has been established that, with a change in the angle of attack from 0° to 5°, C_A increases by approximately 2 to 2.5 percent for a model in the form of a cylinder with a conical nose. Therefore, the axial force coefficient in the first approximation can be assumed constant and equal to C_{A0} for zero angle of attack. Then the equation for the drag coefficient is simplified:

$$C_D = C_{A_0} + C_N \alpha . \tag{12.58}$$

Thus, the calculation of C_D for asymmetric flow is dependent on the preliminary computation of both the axial force coefficient for $\alpha = 0$ and the normal force coefficient for the given angle of attack.

Chapter IV

DRAG OF SLENDER BODIES OF REVOLUTION IN LINEARIZED FLOW

Editor's Introduction

THE FIRST SECTION IN THIS CHAPTER *contains a standard and fairly complete derivation of the linearized equations of motion and the first-order equations for the pressure and velocity distribution on the surface of a body of revolution. The usual method of sources and a power series expression for the shape of the body are used, but an unusual method of solution is described. The formulas and functions defined and presented in Eqs. (13.30) through (13.39) and in Table 16 do not appear in Western technical literature on linearized theory. The definitive first-order method of solution in the American literature is that described by Van Dyke in* NACA TN 2744 *(1952), in conjunction with a method for calculating second-order supersonic flow about a body of revolution. Krasnov makes only passing reference to the Van Dyke second-order theory, omitting discussion "because of its complexity." This is unfortunate, since second-order supersonic theory is the only accurate method of calculation for pointed bodies of revolution (short of characteristics solutions) for the lower supersonic Mach numbers (see the editor's survey article,* J. Aero. Sci., *July 1961). Krasnov also pays very little attention to slender-body theory, which has been the subject of extensive study in the West, particularly by the British (see, for example, Ward,* Linearized Theory of Steady High-Speed Flow, *1955).*

The so-called universal curve for the pressure drag coefficient of parabolic noses presented in Fig. 122 is similar to that illustrated in the Introduction to Chapter III, although there are sufficient differences to suggest that it has been derived independently.

*The treatment of boattail effects is rather extensive in terms of summary curves of the inviscid pressure drag coefficient, although there is little discussion of the details of the flow or the pressure distributions over the boattail and no mention of the complex viscous interactions that can produce strong effects on the theoretical inviscid solutions. Actually, no adequate general treatment of the flow fields about the boattails of bodies of revolution is available. The only general results for the inviscid pressure drag coefficient on conical boattails are those of the editor (op. cit.) and of Jack (*NACA TN 2972, *1953), and it is not apparent that the curves in Fig. 119 are derived from these references. The similar results for parabolic boattails in*

Fig. 125 also appear to be independently derived, and they agree well with the editor's correlation of second-order calculations (op. cit.). The method of correlating the pressure coefficients for boattails of arbitrary shape shown in Figs. 123 and 124 appears to be new; if sufficiently accurate, it could prove to be very useful. However, inadequate detail is provided to verify the analytical basis of the method, and no reference is cited.

*Section 14, concerned with skin friction and base drag, is disappointing both in content and detail. The discussion of skin friction drag consists of a few isolated experimental curves and relatively crude approximate formulas which, while sufficient for initial estimates, are not consistent with the quality of other parts of the text. Allen and Monta (*NASA TN D-4193, *October 1967) present a method for predicting the turbulent boundary layer characteristics on pointed bodies of revolution. Jackson and Smith (*NASA TN D-5046, *March 1969) combine a similar method for the turbulent boundary layer with the second-order shock expansion theory to calculate the total drag of pointed bodies.*

That part of Section 14 dealing with base drag is similarly inadequate. The one curve that is presented for base pressure coefficient as a function of Mach number (Fig. 136) is for a body with no boattail and with stabilizing fins near the base (see Spahr and Dickey, NACA TN 2360, *April 1951), but these special conditions are not noted in the text. Although there is still no generally accepted method available for calculating the base pressure on axially symmetric bodies of arbitrary shape, there is a well substantiated empirical curve for base pressure coefficient as a function of Mach number for bodies of revolution without boattail (reproduced below). In addition, the semi-empirical theories of Chapman (*NACA Report 1051, *1951), Love (*NACA TN 3819, *January 1957), and Korst (*J. Appl. Mech., *1956) provide alternative, and usually comparable, methods for estimating the effects of boattail and Reynolds number on the base pressure. A review and critique of the state of knowledge of base pressure on bodies of revolution is given by Sedney (*Ballistic Research Laboratories Report 1337, *October 1966).*

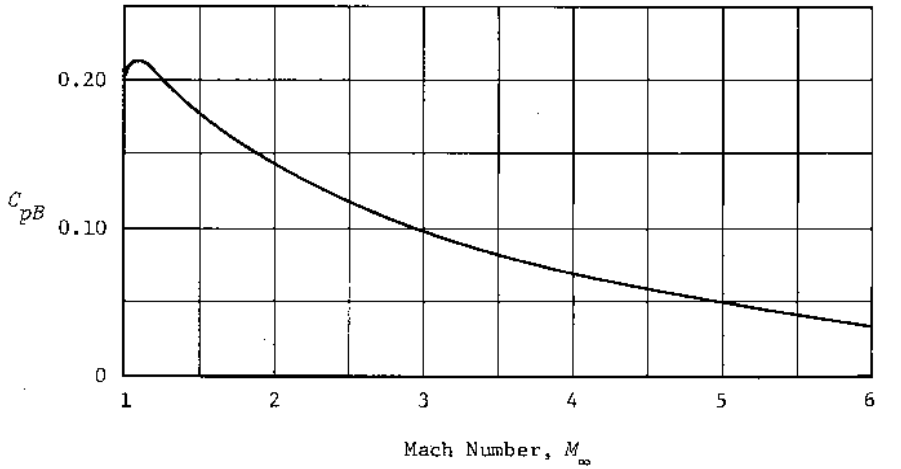

§ 13. *WAVE DRAG*

CALCULATION OF THE PRESSURE DISTRIBUTION IN SYMMETRIC FLOW

Linearization of the Equations

THE AERODYNAMIC EQUATIONS presented previously apply to the case of a perturbed flow for which the parameters differ significantly from the corresponding free-stream parameters. These equations can be applied to bodies of revolution with arbitrary shape and at angle of attack; in general, the differential equations are nonlinear.

The case of a slender body at a small angle of attack is often encountered in practice. The perturbed flow around such bodies differs little from the free stream, and the differential equations can be simplified to linear equations with constant coefficients. This operation is called linearization. The slightly perturbed flow described by such simplified equations is often called linearized flow.

Since the basic assumption for linearized flow is that the parameters do not differ significantly from those in the free stream, they can be expressed by the following relations:

$$\vec{V} = \vec{V}_\infty + \vec{V}', \qquad a = a_\infty + a', \qquad p = p_\infty + p', \qquad \rho = \rho_\infty + \rho',$$

where the subscript ∞ designates the free-stream parameters, and the prime designates small perturbation parameters.

Similar relations can be written for the other parameters, including entropy. If the entropy of the unperturbed flow is designated S_∞, the entropy in the linearized perturbed flow is given by $S = S_\infty + S'$, where S' is the perturbation entropy resulting from the perturbed flow. The increase in entropy can be shown to be so small that it can be

neglected, so that in practice linearized flow is considered isentropic in all regions. Therefore, it is assumed that the curved shock in front of a slender, pointed, axisymmetric body degenerates into a wave of infinitely small intensity, called a Mach wave.

The isentropic flow behind such a wave can be characterized by a potential function $\Phi = \varphi_\infty + \varphi$, consisting of the free-stream potential and the perturbation potential φ. The simplification of Eq. (3.20) for the velocity potential in cylindrical coordinates is based on the fact that the perturbation velocity components $V_x' = \partial\varphi/\partial x$, $V_r' = \partial\varphi/\partial r$, and $V_\phi' = (1/r)\,\partial\varphi/\partial\phi$ are small compared to the velocity of the incident flow. As a result, terms that contain the quantities V_x', V_r', and V_ϕ' to higher powers than the first can be neglected and the equation is simplified.

If unsteady asymmetric flow is considered, the linearized equation for the velocity potential has the form

$$(a_\infty^2 - V_\infty^2)\varphi_{xx} + a_\infty^2\varphi_{rr} + \frac{1}{r^2}\,a_\infty^2\varphi_{\phi\phi} + \frac{1}{r}\,a_\infty^2\varphi_r - 2V_\infty\varphi_{xt} - \varphi_{tt} = 0. \quad (13.1)$$

The subscripts on φ designate corresponding partial derivatives; e.g., $\varphi_x = \partial\varphi/\partial x$, $\varphi_{xx} = \partial^2\varphi/\partial x^2$, $\varphi_{xt} = \partial^2\varphi/\partial x\,\partial t$, etc.

Equation (13.1) is used for the study of unsteady flow around slender axisymmetric bodies, inclined at a small angle of attack. If the flow is steady, the partial derivatives with respect to time are eliminated from this equation and it has the form

$$(a_\infty^2 - V_\infty^2)\varphi_{xx} + a_\infty^2\varphi_{rr} + \frac{1}{r}\,a_\infty^2\varphi_r + \frac{1}{r^2}\,a_\infty^2\varphi_{\phi\phi} = 0. \quad (13.2)$$

Finally, the linearized equation for symmetric flow is even simpler:

$$(a_\infty^2 - V_\infty^2)\varphi_{xx} + a_\infty^2\varphi_{rr} + \frac{1}{r}\,a_\infty^2\varphi_r = 0. \quad (13.3)$$

Equations (13.1) through (13.3) comprise the theoretical basis of the aerodynamics of linearized flows around bodies of revolution. The perturbation potential φ is determined as a result of the solution of these equations.

The boundary conditions that these solutions must satisfy are somewhat simplified compared to the general case. The boundary condition at the surface of the body can be obtained by representing the unknown potential function in the form

$$\Phi = xV_\infty\left(1 - \frac{\alpha^2}{2}\right) + rV_\infty\alpha\cos\phi + \varphi(x, r, \phi, t). \tag{13.4}$$

Equation (13.4) is obtained from Eq. (3.55), in which terms up to order α^2 have been retained in the expansions for the trigonometric functions. The function $\varphi(x, r, \phi, t)$ must be zero in unperturbed flow.

Computing the derivatives from the total potential function Φ, we find the expression for the velocity components of the perturbed flow:

$$\begin{aligned} V_x &= V_\infty\left(1 - \frac{\alpha^2}{2}\right) + \varphi_x, \\ V_r &= \alpha V_\infty\cos\phi + \varphi_r, \\ V_\phi &= -\alpha V_\infty\sin\phi + \frac{1}{r}\varphi_\phi. \end{aligned} \tag{13.5}$$

Neglecting the term $\alpha^2/2$ compared with unity, we obtain the condition for continuous flow, Eq. (3.52), at an angle of attack in the form

$$[V_\infty + \varphi_x(x, r, \phi, t)]\frac{dr}{dx} = \alpha V_\infty\cos\phi + \varphi_r(x, r, \phi, t). \tag{13.6}$$

If the flow is symmetrical, Eq. (13.6) is simplified:

$$[V_\infty + \varphi_x(x, r, t)]\frac{dr}{dx} = \varphi_r(x, r, t). \tag{13.6a}$$

The velocity potential of linearized flow around a body of revolution at an angle of attack can be presented in the form of the sum of three components: the free-stream potential φ_∞, the perturbation potential for symmetric flow $\varphi_1(x, r, t)$, and a second perturbation potential due to the lack of symmetry $\varphi_2(x, r, \phi, t)$.

In linearized flow theory φ_1 and φ_2 are considered to be functions which, as solutions of the equations of motion, define flows that are

independent of each other. Therefore, boundary conditions can be found separately for each function; for example, the solution for φ_1 must satisfy Eq. (13.6a) for symmetric flow. The solution for φ_2 must satisfy the boundary condition at the surface of the body as given by Eq. (13.6). However, it is possible to obtain the continuous flow condition in a simpler form. Equation (13.6) can be rewritten in the following manner:

$$(V_\infty + \varphi_{1x} + \varphi_{2x})\frac{dr}{dx} = \alpha V_\infty \cos\phi + \varphi_{1r} + \varphi_{2r}, \tag{13.7}$$

where $\varphi_{1x} = \partial\varphi_1/\partial x$, $\varphi_{2x} = \partial\varphi_2/\partial x$, etc. Replacing φ_x and φ_r in Eq. (13.6a) by φ_{1x} and φ_{1r}, respectively, and disregarding the higher order term $(dr/dx)\varphi_{2x}$ in Eq. (13.7), we obtain from Eq. (13.7) the boundary condition for asymmetric flow:

$$V_{2r} = -\alpha V_\infty \cos\phi. \tag{13.7a}$$

In other words, the perturbation potential φ_2 must be such that the radial velocity component of the incident flow disappears at the surface of the body.

The Method of Sources

The calculation of the flow parameters around a slender body in linearized flow for the case of steady flow at an angle of attack is based on the use of Eq. (13.2) for the perturbation potential φ. It was indicated above that the solution of this equation is sought as the sum of two perturbation potentials: that for symmetric flow $\varphi_1(x, r)$ and that for the lack of symmetry $\varphi_2(x, r, \phi)$. Using Eqs. (13.3) and (13.2) for φ_1 and φ_2, respectively, we obtain

$$(1 - M_\infty^2)\varphi_{1xx} + \varphi_{1rr} + \frac{\varphi_{1r}}{r} = 0, \tag{13.3a}$$

$$(1 - M_\infty^2)\varphi_{2xx} + \varphi_{2rr} + \frac{1}{r^2}\varphi_{2\phi\phi} + \frac{1}{r}\varphi_{2r} = 0. \tag{13.8}$$

Thus, the parameters for asymmetric flow around a body of revolution can be found if two essentially independent problems are solved: the problem

of flow around a body at a zero angle of attack, and the problem of perturbation flow due to the lack of symmetry.

It can be shown that the solution of the second problem is obtained with the help of the solution of the first; i.e., there is an interrelation between φ_1 and φ_2. To show this relation, the equation for symmetric flow is differentiated with respect to r:

$$(1 - M_\infty^2)\frac{\partial^2}{\partial x^2}\left(\frac{\partial \varphi_1}{\partial r}\right) + \frac{\partial^2}{\partial r^2}\left(\frac{\partial \varphi_1}{\partial r}\right) - \frac{1}{r^2}\frac{\partial \varphi_1}{\partial r} + \frac{1}{r}\frac{\partial^2 \varphi_1}{\partial r^2} = 0.$$

On comparison with Eq. (13.8), it is apparent that the function φ_2 can be related to φ_1 by

$$\varphi_2 = -\frac{\partial \varphi_1}{\partial r}\cos\phi. \tag{13.9}$$

Hence the solution of Eq. (13.3a) for $\varphi_1(x, r)$ must be chosen so that the potential $\varphi_2(x, r, \phi)$ satisfies the boundary condition of Eq. (13.7a). Consequently, the total perturbation potential for asymmetric flow is

$$\varphi = \varphi_1 - \frac{\partial \varphi_1}{\partial r}\cos\phi. \tag{13.10}$$

We have considered the case of steady flow. However, Eq. (13.9) for φ_2 can also be applied to unsteady flow, as would be apparent if the more general Eq. (13.1) had been used initially.

After having determined the total value of the perturbation potential, including the effect of the boundary conditions, the velocities can be calculated, and the pressure evaluated from the Bernoulli equation:

$$\frac{\gamma}{\gamma - 1}\frac{p}{\rho} + \frac{V^2}{2} + \varphi_t = \frac{\gamma}{\gamma - 1}\frac{p_\infty}{\rho_\infty} + \frac{V_\infty^2}{2}.$$

Since the square of the total velocity $V^2 = (V_\infty \cos\alpha + V_x')^2 + V_r^2 + V_\phi^2$, and the density $\rho = \rho_\infty(p/p_\infty)^{1/\gamma}$, then, after substitution and transformation of the Bernoulli equation, we obtain

$$\frac{p}{p_\infty} = \left[1 - (\gamma - 1)M_\infty^2\left(\frac{V_x'}{V_\infty}\cos\alpha + \frac{V_r^2}{2V_\infty^2} + \frac{V_\phi^2}{2V_\infty^2} + \frac{\varphi_t}{V_\infty^2} + \frac{V_x'^2}{2V_\infty^2} - \frac{\sin^2\alpha}{2}\right)\right]^{\gamma/(\gamma-1)}.$$

In this equation, the second term in the square brackets is less than unity, and the right-hand side of the equation can be expanded in a binomial series. Retaining only the first two terms in the expansion, neglecting the quantity $V_x'^2/2V_\infty^2$ compared with the other terms, and assuming small angles of attack, we obtain

$$\frac{p}{p_\infty} = 1 - \gamma M_\infty^2\left(\frac{V_x'}{V_\infty} + \frac{V_r^2}{2V_\infty^2} + \frac{V_\phi^2}{2V_\infty^2} + \frac{\varphi_t}{V_\infty^2} - \frac{\alpha^2}{2}\right).$$

Then the expression for the pressure coefficient is

$$C_p = -2\left(\frac{V_x'}{V_\infty} + \frac{V_r^2}{2V_\infty^2} + \frac{V_\phi^2}{2V_\infty^2} + \frac{\varphi_t}{V_\infty^2} - \frac{\alpha^2}{2}\right). \tag{13.11}$$

From the boundary condition given by Eq. (13.6a), the velocity component V_r can be approximated by $V_\infty(dr/dx)$. Making this substitution, and replacing V_x' and V_ϕ by the corresponding components of the perturbation potential, we find

$$C_p = -\frac{2}{V_\infty^2}\left[V_\infty\varphi_x + \frac{\gamma_\infty^2}{2}\left(\frac{dr}{dx}\right)^2 + \frac{1}{2}\left(\frac{\varphi_\phi}{r} - \alpha V_\infty \sin\phi\right)^2 + \varphi_t - \frac{\alpha^2 V_\infty^2}{2}\right]. \tag{13.11a}$$

The pressure coefficient can be presented as the sum of two components, i.e., $C_p = C_{p1} + C_{p2}$. The component C_{p1} is determined by the conditions for symmetric flow:

$$C_{p1} = -\frac{2}{V_\infty^2}\left[V_\infty\varphi_{1x} + \frac{V_\infty^2}{2}\left(\frac{dr}{dx}\right)^2 + \varphi_{1t}\right]. \tag{13.12}$$

The component C_{p2} is determined from the crossflow, which depends on the angle of attack:

$$C_{p2} = -\frac{2}{V_\infty^2}\left[V_\infty\varphi_{2x} + \frac{1}{2}\left(\frac{\varphi_{2\phi}}{r} - \alpha V_\infty \sin\phi\right)^2 + \varphi_{2t} - \frac{\alpha^2 V_\infty^2}{2}\right]. \tag{13.13}$$

If the flow is steady, the partial derivatives with respect to time

in these expressions are zero. When the symmetric component of flow is steady, the pressure coefficient is

$$C_{p1} = -2\left[\bar{\varphi}_{1x} + \frac{1}{2}\left(\frac{dr}{dx}\right)^2\right], \tag{13.14}$$

where $\bar{\varphi}_{1x} = \varphi_{1x}/V_\infty$. Even though the symmetric component of flow is steady, the crossflow may be unsteady, and this component of the pressure coefficient must be calculated from Eq. (13.13). If, however, the crossflow is also steady, then

$$C_{p2} = -2\left[\bar{\varphi}_{2x} + \frac{1}{2}\left(\frac{\bar{\varphi}_{2\phi}}{r} - \alpha \sin \phi\right)^2 - \frac{\alpha^2}{2}\right], \tag{13.15}$$

where the bar indicates that the derivatives of the potential have been made dimensionless by dividing by V_∞.

Equation (13.13) for C_{p2} can be simplified by determining φ_2 from Eq. (13.9) and using the boundary condition of Eq. (13.7a) to estimate the ratio $\varphi_{2\phi}/r$. Let us write Eq. (13.9) in the form

$$\varphi_2 = -\frac{1}{r}\left[r\left(\frac{\partial \varphi_1}{\partial r}\right)\right]\cos \phi.$$

It will be shown later in this section that the quantity $\partial\varphi_1/\partial r = V_{1r}$ has the form $f(x)/r$ for small r, so that the product rV_{1r} approaches the limiting value $f(x)$ as $r \to 0$. Differentiating Eq. (13.9) with respect to ϕ, we find that for sufficiently small r

$$V_{2\phi} = \frac{\varphi_{2\phi}}{r} = \frac{1}{r^2} f(x) \sin \phi. \tag{13.16}$$

When the derivative is computed with respect to r, the radial perturbation velocity component for $r \to 0$ is given by

$$V_{2r} = \varphi_{2r} = \frac{1}{r^2} f(x) \cos \phi. \tag{13.17}$$

According to Eq. (13.7a), this component equals $-\alpha V_\infty \cos \phi$ on the body surface. Therefore, the function $f(x) = -\alpha V_\infty r^2$ and $\varphi_{2\phi}/r = -\alpha V_\infty \sin \phi$.

Substituting this expression into Eq. (13.13), we obtain

$$C_{p2} = -2\left[\bar{\varphi}_{2x} + \frac{\alpha^2}{2}(4\sin^2\phi - 1) + \bar{\varphi}_{2t}\right], \qquad (13.13a)$$

where the derivative $\bar{\varphi}_{2t} = \varphi_{2t}/V_\infty^2$.

The total value of the pressure coefficient for asymmetric unsteady flow is

$$C_p = -2\left[\bar{\varphi}_{1x} + \frac{1}{2}\left(\frac{dr}{dx}\right)^2 - \bar{\varphi}_{1rx}\cos\phi + \frac{\alpha^2}{2}(4\sin^2\phi - 1) + \bar{\varphi}_{2t}\right], \qquad (13.11a)$$

where $\bar{\varphi}_{1rx} = \varphi_{1rx}/V_\infty$. For steady flow

$$C_{p2} = -2\left[-\bar{\varphi}_{1rx}\cos\phi + \frac{\alpha^2}{2}(4\sin^2\phi - 1)\right], \qquad (13.15a)$$

and the total value of the pressure coefficient is

$$C_p = -2\left[\bar{\varphi}_{1x} + \frac{1}{2}\left(\frac{dr}{dx}\right)^2 - \bar{\varphi}_{1rx}\cos\phi + \frac{\alpha^2}{2}(4\sin^2\phi - 1)\right], \qquad (13.18)$$

where the derivatives φ_{1x} and φ_{1rx} depend only on the variables x and r.

When this expression is substituted into Eq. (1.5), it will be noted that the basic component of the axial force coefficient does not depend on the angle of attack and is determined by the symmetric flow conditions. The additional quantity results from the asymmetry of the flow and depends on the square of the angle of attack.

If terms of the second order in α can be neglected, the axial force coefficient can be calculated from the pressure distribution resulting from the symmetric component of the flow about the body of revolution. Thus, in this case the wave drag coefficient is equal to the axial force coefficient.

From these results, it follows that the problem of linearized flow around a slender body can be solved if the perturbation velocity potential φ_1 for symmetric flow is found. The value of the potential is used directly for calculating velocity and pressure distributions, and also

for calculating the wave drag at zero angle of attack. This can be verified by the fact that the expression

$$\varphi_1 = \int_0^{x-\beta r} \frac{f(\xi)\, d\xi}{\sqrt{(x-\xi)^2 - \beta^2 r^2}} \tag{13.19}$$

actually satisfies Eq. (13.3), where

$$\beta = \sqrt{M_\infty^2 - 1}.$$

This equation is the basis of the source method, according to which a system of sources distributed continuously along the body axis is substituted for the body in the flow, and φ_1 represents the potential of those sources.

The law for the distribution of the source intensities, i.e., the form of the function $f(\xi)$, must be such that one of the streamlines of the flow coincides with the surface of the body as a result of the combination of the unperturbed flow and the flow from these sources. Thus, the potential function φ_1 must satisfy the continuous flow condition.

In using the method of sources, it must be kept in mind that the perturbations from the sources in supersonic flow are propagated only within the perturbation cones with vertices at the sources. Thus, if we consider a system of sources continuously distributed along the body axis (Fig. 108), the velocity and the other parameters at a point $A(x, r)$ can be determined by those perturbations that proceed from the sources located upstream, beginning with the point $\xi = x - \beta y$ and ending at the point $\xi = x = 0$. At the point $\xi = x = 0$ the source intensity equals zero, since it is assumed that for $\xi \leq 0$ perturbations do not occur. This is the reason for the integration limits in Eq. (13.19). The shape of the curve $f(\xi)$ (or $f(x)$), which represents the distribution of the source intensities for a slender body of arbitrary shape, is presented in Fig. 108. This curve indicates the continuous character of small perturbations in linearized flow.

To find a general relation for velocity and pressure, Eq. (13.19) can be transformed with the help of a new variable of integration:

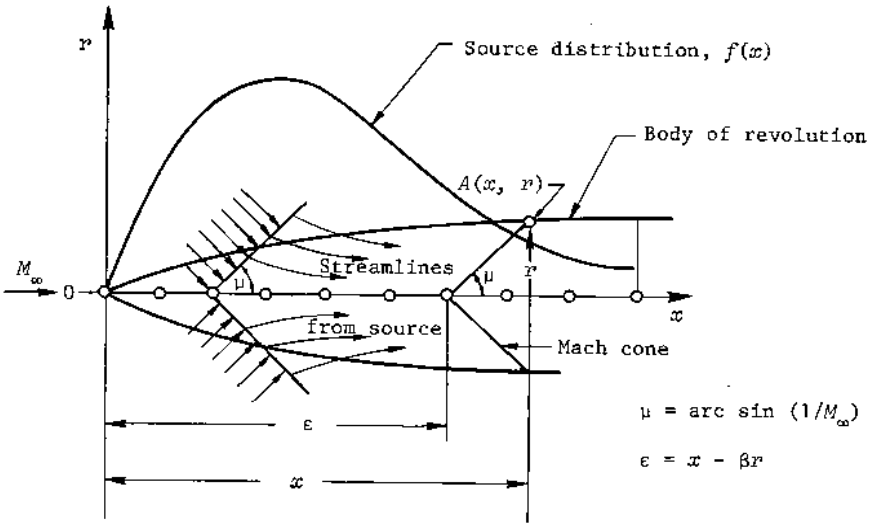

Fig. 108--Distribution of sources on the axis of a body of revolution

$$z = \operatorname{arc\,cosh} \frac{x - \xi}{\beta r}. \tag{13.20}$$

Taking into account that

$$\cosh z = \frac{x - \xi}{\beta r}, \qquad \xi = x - \beta r \cosh z, \qquad d\xi = -\beta r \sinh z \, dz,$$

Eq. (13.19) becomes

$$\varphi_1 = \int_0^{\operatorname{arc\,cosh} x/\beta r} f(x - \beta r \cosh z)\, dz. \tag{13.21}$$

Differentiating φ_1 with respect to x and r and assuming a source intensity at the tip $f(\xi) = f(0) = 0$, the velocity components are

$$\varphi_{1x} = V_x' = \int_0^{\operatorname{arc\,cosh} x/\beta r} \dot{f}(x - \beta r \cosh z)\, dz, \tag{13.22}$$

$$\varphi_{1r} = V_r = -\beta \int_0^{\operatorname{arc\,cosh} x/\beta r} \dot{f}(x - \beta r \cosh z) \cosh z \, dz, \tag{13.23}$$

where $\dot{f}$ is the total derivative of the function f with respect to the argument $(x - \beta r \cosh z)$.

The Method for Calculating Flow Parameters

A number of practical procedures for the calculation of linearized flow parameters around an axisymmetric body have been developed on the basis of the method of sources. To illustrate, Eq. (13.23) can be converted back to the variable ξ by means of Eq. (13.20):

$$V_r = \frac{1}{r} \int_{x-\beta r}^{0} \frac{\dot{f}(\xi)(x - \xi)\, d\xi}{\sqrt{(x - \xi)^2 - \beta^2 r^2}}. \tag{13.24}$$

Setting r to zero in the integrand, the limiting value for the radial velocity component becomes

$$V_r = -\frac{1}{r} f(x). \tag{13.25}$$

This expression has already been used to determine the order of magnitude of rV_r near the axis. It is obvious that the function used above differs only in sign from that entering into Eq. (13.16).

Assuming that the velocity component on the surface of a very slender body is determined to the first order by Eq. (13.25) and using the condition of continuous flow, the equation for the distribution of source intensities for such a body is

$$f(x) = -r \frac{dr}{dx}. \tag{13.26}$$

Differentiating this function with respect to x, the derivative is

$$\dot{f}(x) = -\left[\left(\frac{dr}{dx}\right)^2 + r \frac{d^2 r}{dx^2}\right]. \tag{13.27}$$

Let us assume that the equation for the curved generatrix is given in the form of a series

$$r = \sum_{n=0}^{t} e_n x^{n+1}. \tag{13.28}$$

If this expression for r is introduced into Eq. (13.27) and the terms are arranged in powers of x, the following general form results for the derivative:

$$\dot{f}(x) = -\sum_{m=0}^{k} d_m x^m. \tag{13.29}$$

This expression can be considered to be a first approximation for the derivative of the distribution function of source intensities in the case of an arbitrary body of revolution. This relation can be made more precise by introducing into Eq. (13.29) some correction factors, a_0 and a_1, which can be determined during the solution of the problem itself. Replacing the variable x by ξ, the function $\dot{f}(\xi)$ becomes

$$\dot{f}(\xi) = -\left(a_0 + a_1 \sum_{m=1}^{k} d_m \xi^m\right). \tag{13.30}$$

Substituting this expression into Eq. (13.23), we obtain for the radial velocity component

$$V_r = \beta(a_0 i_r^0 + \eta a_1), \tag{13.31}$$

where

$$\begin{aligned} i_r^0 &= \int_0^{\operatorname{arc\,cosh} u} \cosh z \, dz, \\ \eta &= \int_0^{\operatorname{arc\,cosh} u} \sum_{m=1}^{k} d_m (x - \beta r \cosh z)^m \cosh z \, dz, \\ u &= \frac{x}{\beta r}. \end{aligned} \tag{13.32}$$

An analogous relation can be found for the axial component of the perturbation velocity by substituting Eq. (13.30) into Eq. (13.22):

$$-V_x' = a_0 i_x^0 + a_1 \psi, \tag{13.33}$$

where

$$i_x^0 = \int_0^{\operatorname{arc\,cosh} u} dz,$$

$$\psi = \int_0^{\operatorname{arc\,cosh} u} \sum_{m=1}^{k} d_m(x - \beta r \cosh z)^m \, dz. \tag{13.34}$$

Equations (13.32) and (13.34) contain integrals of the form

$$I_n = \int_0^{\operatorname{arc\,cosh} u} (\cosh z)^n \, dz. \tag{13.35}$$

If the value of k is limited to 3, functions of the form i_r^n and i_x^n appear in Eqs. (13.31) and (13.33), defined by the expressions

$$i_r^0 = I_1, \qquad i_r^1 = uI_1 - I_2,$$

$$i_r^2 = u^2 I_1 - 2uI_2 + I_3, \qquad i_r^3 = u^3 I_1 - 3u^2 I_2 + 3uI_3 - I_4,$$

$$i_x^0 = I_0, \qquad i_x^1 = uI_0 - I_1, \tag{13.36}$$

$$i_x^2 = u^2 I_0 - 2uI_1 + I_2, \qquad i_x^3 = u^3 I_0 - 3u^2 I_1 + 3uI_2 - I_3.$$

From Eqs. (13.35) and (13.36), it follows that the functions i_r^n and i_x^n depend only on the parameter u. These functions, calculated for values of u from 1 to 8.8, are presented in Table 16.

To determine the coefficients a_0 and a_1, the continuous flow condition at a given point on the body must be used:

$$\frac{dr}{dx} = \frac{V_r}{1 + V_x} = \frac{\beta(a_0 i_r^0 + a_1 \eta)}{1 - (a_0 i_x^0 + a_1 \psi)}. \tag{13.37}$$

The coefficient a_0 can be found directly from Eq. (13.37) by relating this condition to the leading conical element of the body. For a cone

Table 16

VALUES OF THE FUNCTIONS $i_r^n(u)$ *AND* $i_x^n(u)$

u	i_r^0	i_r^1	i_r^2	i_r^3	i_x^0	i_x^1	i_x^2	i_x^3
1.0	0	0	0	0	0	0	0	0
1.1	0.4582	0.0303	0.0026	0.0004	0.4435	0.0298	0.0019	0.0001
1.2	0.6633	0.0856	0.0109	0.0015	0.6223	0.0838	0.0149	0.0071
1.3	0.8312	0.1256	0.0383	0.0096	0.7567	0.1527	0.0392	0.0095
1.4	0.9804	0.2526	0.0794	0.0281	0.8673	0.2342	0.0753	0.0254
1.6	1.249	0.4756	0.2230	0.1124	1.047	0.4265	0.2068	0.2412
1.8	1.450	0.7166	0.4137	0.2949	1.177	0.6690	0.4875	0.4631
2.0	1.732	1.073	0.8296	0.6950	1.317	0.9024	0.7314	0.6332
2.4	2.182	1.857	1.990	2.326	1.522	1.472	1.675	2.030
2.8	2.615	2.816	3.846	5.946	1.690	2.116	3.107	4.854
3.2	3.040	3.948	6.543	11.90	1.831	2.820	5.076	9.701
3.6	3.458	5.247	10.21	21.84	1.954	3.578	7.634	17.28
4.0	3.873	6.714	14.98	36.84	2.064	4.382	10.81	28.28
4.4	4.286	8.348	21.00	58.31	2.162	5.227	14.65	43.46
4.8	4.694	10.14	28.37	87.74	2.251	6.111	19.19	63.76
5.2	5.103	12.10	37.26	127.0	2.333	7.028	24.44	89.85
5.6	5.510	14.22	47.78	177.9	2.408	7.976	30.44	122.7
6.0	5.916	16.51	60.07	242.4	2.478	8.953	37.21	163.2
6.4	6.322	18.96	74.25	322.8	2.544	9.958	44.77	212.3
6.8	6.726	21.56	90.44	421.4	2.605	10.99	53.17	271.1
7.2	7.130	24.34	108.8	540.7	2.663	12.04	62.37	340.2
7.6	7.534	27.27	129.4	683.4	2.717	13.12	72.43	421.0
8.0	7.937	30.36	152.5	852.2	2.769	14.22	83.37	514.5
8.4	8.341	33.62	178.1	1050.4	2.818	15.33	95.18	621.4
8.8	8.743	37.04	206.3	1280.6	2.865	16.47	107.9	743.3

$k = m = 1$ and, consequently, $\eta = \psi = 0$; thus, we obtain the equation

$$a_0 = \frac{(dr/dx)_0}{(dr/dx)_0 (i_x^0)_0 + \beta (i_r^0)_0}. \tag{13.38}$$

The quantities $(i_r^0)_0$ and $(i_x^0)_0$ can be determined from Eqs. (13.32) and (13.34) by setting the parameter $u = u_0 = 1/\beta\delta_0$ at the conical tip ($x = r = 0$):

$$\begin{aligned} (i_r^0)_0 &= \sqrt{u_0^2 - 1}, \\ (i_x^0)_0 &= \operatorname{arc\,cosh} u_0. \end{aligned} \tag{13.36a}$$

Since the coefficient a_0 is known and remains the same for all points on the body, in practice only the coefficient a_1 turns out to be unknown and must be calculated each time from Eq. (13.37) at the point under consideration on the surface. Solving Eq. (13.37) for a_1, we obtain

$$a_1 = \frac{dr/dx - a_0 [(dr/dx) i_x^0 + \beta i_r^0]}{\beta\eta + (dr/dx)\psi}, \tag{13.39}$$

where the values of the functions i_x^0, i_r^0, η, and ψ are found for the value of u at that point.

When the coefficients a_0 and a_1 have been found, the perturbation velocity components can be determined and the pressure coefficient computed from Eq. (13.14).

For illustration, let us consider the application of the proposed method to the calculation of flow around a parabolic body of revolution. In this case, the derivative $\dot{f}$ can be determined from the equation $\bar{r} = \bar{x}(2 - \bar{x})$ and Eqs. (13.27) and (13.30):

$$\dot{f}(\xi) = -\left[a_0 + a_1\left(\xi - \frac{\xi^2}{2}\right)\right]. \tag{13.40}$$

Comparing Eqs. (13.30) and (13.40), we see that $\sum_{m=1}^{k} d_m \xi^m = \xi - \xi^2/2$. Noting that the variable $\xi = x - \beta r \cosh z$ and substituting Eq. (13.40)

in Eqs. (13.32) and (13.34), the functions η and ψ can be written as follows:

$$\eta = \bar{m}\left(i_r^1 - \frac{\bar{m}i_r^2}{2}\right),$$
$$\psi = \bar{m}\left(i_x^1 - \frac{\bar{m}i_x^2}{2}\right), \tag{13.41}$$

where $\bar{m} = \beta\bar{r}/2\lambda_N$ and $\bar{r} = r/r_{mid}$. The auxiliary functions i_r^2 and i_x^2 can be determined from the parameter u either by means of Eqs. (13.32) and (13.34) or from Table 16.

After the values of η and ψ are determined, the coefficient a_1 can be calculated for a given point from Eq. (13.39). Using a_1, the component of the perturbation velocity $V_x' = \varphi_{1x}$ can be evaluated from Eq. (13.33) and the pressure coefficient calculated from Eq. (13.14). It should be noted that the component of the pressure coefficient $\Delta C_{pl} = -(dr/dx)^2$ can be found in advance if the body shape is known. For example, for a parabolic nose, $\Delta C_{pl} = -\delta_0^2(1 - \bar{x})^2$.

The pressure distribution calculated by this method is presented in Fig. 109, along with a curve obtained by the method of local cones for comparison. The curves are close to each other over most of the body. Experimental data for the pressures on the body agree somewhat

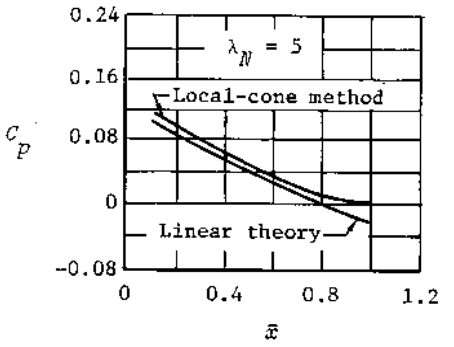

Fig. 109--Pressure distribution on a parabolic body of revolution for $M_\infty = 2.6$

better with the calculation by the linearized method than with the calculation by the method of local cones.

This method can be used for the approximate calculation of flow around an axisymmetric body that is a combination of various elements, e.g., one consisting of a nose and a cylindrical part. At the rear, it may be joined to a converging boattail or to a section of another shape.

The pressure distribution calculated for the cylindrical part of a body is presented in Fig. 110. As is evident, the pressure along the cylindrical section increases downstream; however, the flow around a converging afterbody is accompanied by a continued expansion over most of the boattail.

The curves for the pressure distribution on a body of revolution with a parabolic nose, regardless of the Mach number, will be similar in shape to those presented in Figs. 111 through 113. The data on these figures are for a Mach number of 1.5 and show the effect of various afterbody shapes. Also shown in the figures are calculations for the same body shapes by the method of characteristics and by the method of local cones, using Eq. (6.19).

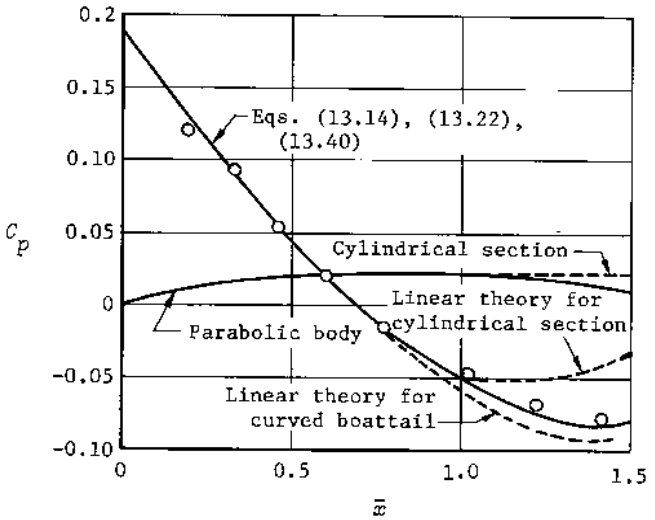

Fig. 110--Pressure distribution on a body of revolution at $M_\infty = 1.87$

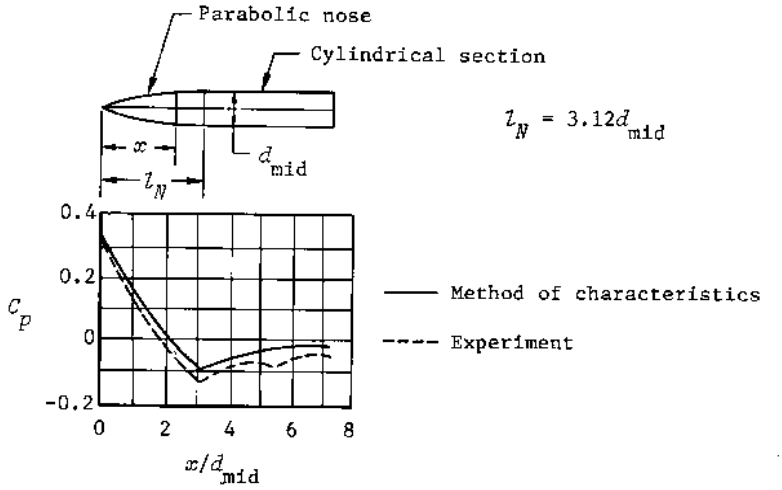

Fig. 111--Pressure distribution on a body with a parabolic nose and a cylindrical afterbody

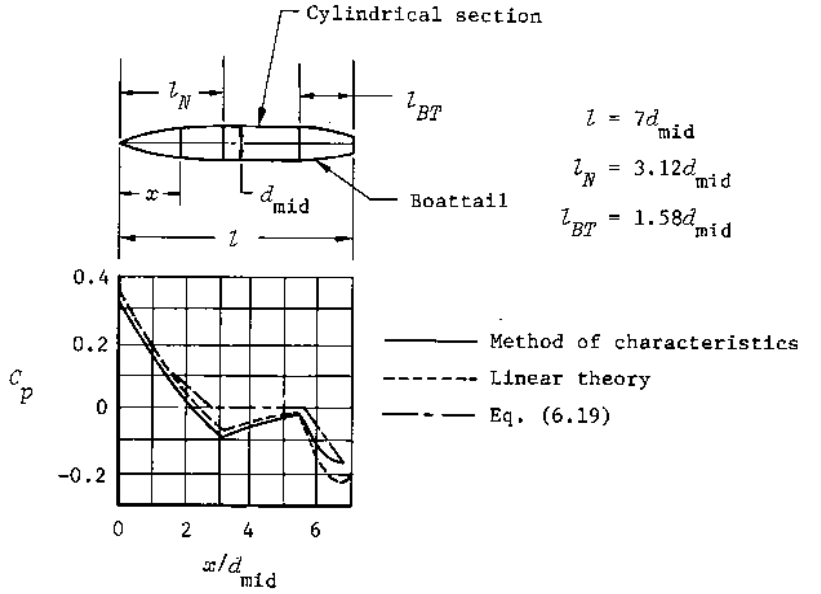

Fig. 112--Pressure distribution on a body with a parabolic nose, a cylindrical midsection, and a boattail

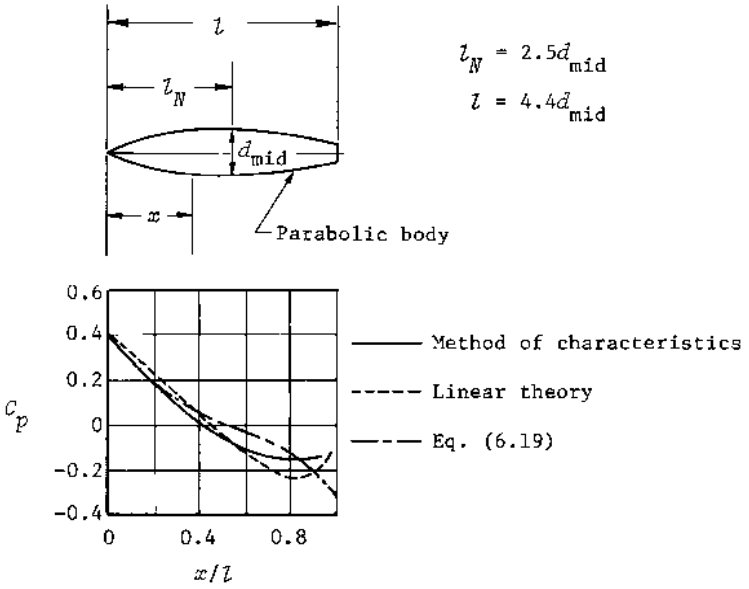

Fig. 113--Pressure distribution on a parabolic body of revolution without a cylindrical midsection

From Figs. 111 and 112 it is apparent that the pressure approaches the free-stream pressure on the cylindrical section and is essentially equal to this value at a little more than two diameters behind the start of the constant section. A reduction in pressure is observed over the boattail, but not for the entire length; it can be seen that the pressure increases somewhat in the vicinity of the base section or of the pointed tail.

The accuracy of the proposed method for calculation of linearized flow increases with increasing slenderness of the body. For very slender bodies, it is not necessary to introduce the correction factors a_0 and a_1 into Eq. (13.29) for the function $\dot{f}(x)$. In this case we proceed from Eq. (13.26), which can be rewritten in the form

$$f(x) = -\frac{1}{2\pi}\frac{dS(x)}{dx} = -\frac{S'(x)}{2\pi}, \qquad (13.42)$$

where $S(x) = \pi r^2$ is the local cross-sectional area of the slender body.

Then the derivative is

$$\dot{f}(x) = -\frac{1}{2\pi}\frac{d^2S(x)}{dx^2} = -\frac{S''(x)}{2\pi}. \tag{13.43}$$

Transforming to the variable ξ, where $\xi = x - \beta r \cosh z$, and substituting the resultant expression for $\dot{f}(\xi)$ into Eq. (13.22), we obtain

$$V_x' = -\frac{1}{2\pi}\int_0^{\operatorname{arc\,cosh} u} S''(x - \beta r \cosh z)\, dz. \tag{13.44}$$

If the shape of the body is given, it is possible to find the function S, to determine its second derivative S'', and to compute the integral in Eq. (13.44), which gives the perturbation velocity component. For example, for a parabolic nose the equation of the nose shape is, in dimensional form,

$$r = \frac{x}{2\lambda_N}\left(2 - \frac{x}{l_N}\right).$$

The cross-sectional area and the second derivative of S will have the following forms (with the substitution of ξ for x):

$$\begin{aligned} S(\xi) &= \frac{\pi}{4\lambda_N^2}\left(4\xi^2 - \frac{4\xi^3}{l_N} + \frac{\xi^4}{l_N^2}\right), \\ S''(\xi) &= \frac{\pi}{\lambda_N^2}\left(2 - \frac{6\xi}{l_N} + \frac{3\xi^2}{l_N^2}\right). \end{aligned} \tag{13.45}$$

Replacing ξ by $x - \beta r \cosh z$ in the expression for the second derivative and substituting this into Eq. (13.44), we obtain after integration

$$V_x' = -\frac{\Omega_2}{2\pi}, \tag{13.46}$$

where

$$\Omega_2 = \int_0^{\operatorname{arc\,cosh} u} S''(x - \beta r \cosh z)\, dz = \frac{\pi}{\lambda_N^2}\left(2i_x^0 - \frac{6\bar{x}i_x^1}{u} + \frac{3\bar{x}^2 i_x^2}{u^2}\right). \tag{13.47}$$

The difference in the results of the two methods proposed can be observed if, for example, the axial velocity components on the conical tip are compared. These components are determined from Eq. (13.33) for the first method and from Eq. (13.46) for the second method; they are, respectively,

$$-V_x' = \frac{\delta_0 \left(i_x^0\right)_0}{\delta_0 \left(i_x^0\right)_0 + \beta \left(i_r^0\right)_0}, \qquad -V_x' = \frac{\left(i_x^0\right)_0}{\lambda_N^2} = \delta_0^2 \left(i_x^0\right)_0. \tag{13.48}$$

The second expression can be obtained from the first if the cone is very slender. In this case, the term $\delta_0 (i_x^0)_0$ in the denominator is much smaller than the second term and can be neglected. The second term assumes the form $\beta (i_r^0)_0 \approx 1/\delta_0$ for small values of δ_0.

Equations (13.48) make it possible to estimate the order of magnitude of the perturbation in the flow around a slender cone. The additional perturbation velocity component is of the order of δ_0^2, i.e., of the square of the cone angle. In the general case of an arbitrary shape, this component is of the order of magnitude of τ^2, i.e., the square of a small dimensionless geometric parameter of the body. The radial component of the perturbed velocity, from the continuous flow condition $V_r = dr/dx$, is of the order of τ, so that the perturbation is less by one order of magnitude in the longitudinal direction than in the lateral direction. Therefore, the terms that contain squares of the perturbations in the transverse direction should be retained in Eq. (13.14) for pressure.

The Similarity Laws for Pressure Functions and Drag Coefficients

The relation for the pressure coefficient can be written in the following form:

$$C_p = \frac{\Omega_2}{\tau} - \left(\frac{dr}{dx}\right)^2. \tag{13.49}$$

It is evident from Eq. (13.47) that Ω_2 for a given point with coordinate

$\bar{x}$ is a function of the parameter $u = x/\beta r$ and of the fineness ratio λ_N, which in turn determines the angle δ_0 at the nose ($\delta_0 = 1/\lambda_N$). The parameter u can be written in a general form as $u = u_0 h(\bar{x})$; e.g., for a parabolic shape, the function is $h(\bar{x}) = 2/(2 - \bar{x})$.

The general equation for the pressure coefficient is

$$C_p = \delta_0^2 N(u_0, \bar{x}), \tag{13.50}$$

where N is a function of the parameter u_0 and of the dimensionless coordinate $\bar{x}$.

The general relation for the wave drag coefficient is obtained from Eq. (1.6):

$$C_{Dp} = \delta_0^2 D(u_0), \tag{13.51}$$

where D is a function of u_0 only.

The general form of Eqs. (13.50) and (13.51) results in the following conclusion on the similarity of flows around bodies of revolution. If these flows are characterized by identical values of u_0, the ratio C_p/δ_0^2 will be identical at corresponding points on the body, as indicated by Eq. (13.50). Such flows are also called similar. It follows from Eq. (13.51) that, for similar flows, the axial forces are related in such a way that C_{Dp}/δ_0^2 will be identical. Thus, the similarity parameter for these flows is $u_0 = 1/\beta\delta_0 = 1/\delta_0(M_\infty^2 - 1)^{\frac{1}{2}}$.

If it is assumed that the nose angle δ_0 is inversely proportional to the fineness ratio of the body, i.e., $\delta_0 \sim 1/\lambda_l$, Eq. (13.51) can be written in the form $C_{Dp} = D(u_0)/\lambda_l^2$, and the similarity parameter is defined as $u_0 = \lambda_l/(M_\infty^2 - 1)^{\frac{1}{2}}$. For example, for a body of revolution with a parabolic shape, the fineness ratio of the nose section is $\lambda_N = 1/\delta_0$; it follows that $C_{Dp} = D(u_0)/\lambda_N^2$ and $u_0 = \lambda_N/(M_\infty^2 - 1)^{\frac{1}{2}}$.

Equation (13.50) can be presented in a somewhat different form for those cases where M_∞ is sufficiently large that it can be assumed that $(M_\infty^2 - 1)^{\frac{1}{2}} \approx M_\infty$. Let us define a similarity parameter $K_1 = M_\infty/\lambda_N = M_\infty\delta_0$. Multiplying Eq. (13.50) by $(\gamma/2)M_\infty^2$, the relation for the pressure function can be rewritten as

$$\frac{p}{p_\infty} - 1 = N_1(K_1, \bar{x}).$$

Thus, at a given point $\bar{x}$, the pressure function depends only on the parameter K_1.

The similarity law based on this parameter is confirmed by the results of calculations of pressure distributions by the method of characteristics. These results are presented in Fig. 114 in the form of curves for two bodies with parabolic noses for which the flow conditions result in the same value of the similarity parameter ($K_1 = 0.5$). It is evident from the figure that the pressure distributions on the surfaces of both bodies are identical.

The pressure distributions over the same body for three values of the parameter K_1 are presented in Fig. 115. Comparison with the method

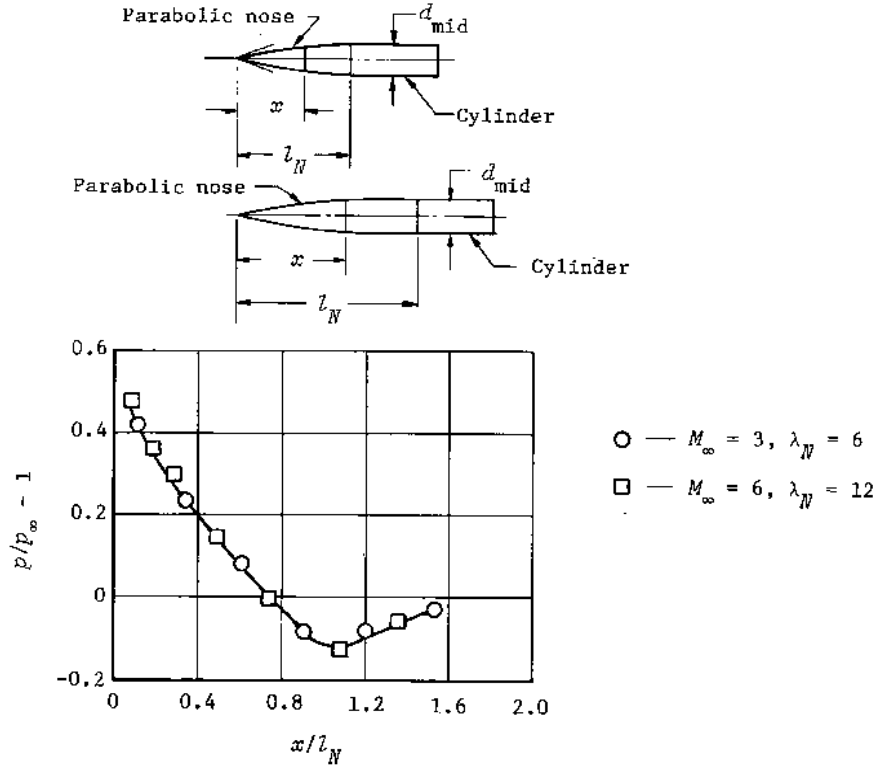

Fig. 114--Pressure distributions for two bodies with identical similarity parameters

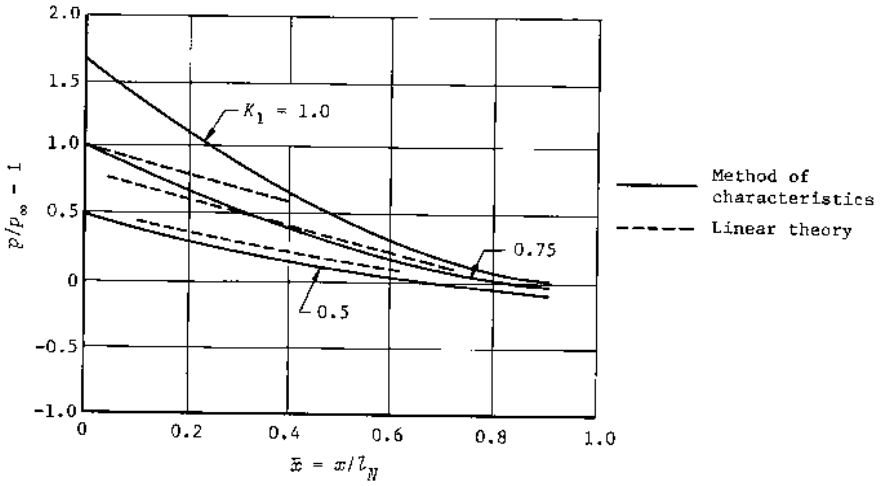

Fig. 115--Comparisons of pressure distribution by the method of characteristics and by linearized theory

of characteristics shows that satisfactory results are obtained from linearized theory only when K_1 is less than unity.

The similarity law based on this parameter is generally questionable for those combinations of free-stream Mach number and fineness ratio corresponding to the limits of application of linearized theory. These limits can be established from Eq. (13.48) for the axial component of the perturbation velocity on a cone. Obviously, if $u_0 < 1$, this equation is no longer valid because imaginary values are obtained in Eq. (13.36a).

Whenever u_0 approaches one, Eq. (13.48) also gives unrealistic results, and in the limit $u_0 = 1$ the equation becomes indeterminate. Therefore, calculations by linearized theory give satisfactory results only for conditions at which u_0 is considerably larger than unity. Hence, the use of the similarity law is obviously doubtful in cases where u_0 differs little from 1. However, the quantity u_0 can still be defined as a function of the combination of the two parameters, i.e., the fineness ratio of the nose and the free-stream Mach number.

Physically, the region of doubtful similarity of flows corresponds to the divergence of the real flow from linearized flow. If the fineness ratio is decreased, i.e., the body becomes thicker, or if the Mach number increases for the same fineness ratio, the flow differs increasingly from linearized flow. To maintain linearized flow characteristics for large Mach numbers, it is necessary to increase the fineness ratio so that the inequality $\lambda_N > M_\infty$ is maintained. Then the similarity parameter will always be greater than unity.

It follows from the expression $u_0 = 1/\beta\delta_0$ that, if the body of revolution is sufficiently slender (i.e., the fineness ratio is large), u_0 will always be greater than 1 for small supersonic Mach numbers. But as $M_\infty \to 1$, as Eq. (13.48) indicates, the absolute value of the perturbation velocity approaches infinity, which is physically impossible. Thus, to apply the theory of linearized flow and the similarity laws requires the simultaneous fulfillment of two inequalities, $\lambda_N > (M_\infty^2 - 1)^{\frac{1}{2}}$ and $M_\infty > 1$.

The region of possible application of linearized flow theory and the similarity laws is shown in Fig. 91, where the shaded area corresponds to doubtful similarity. According to these data, it is not recommended that linearized calculations be made for small fineness ratios, $\lambda_N < 2$, and small Mach numbers. In practical cases, Mach numbers of not less than $M_\infty = 1.4$ to 1.5 should be chosen.

The similarity parameter K_1 for pressure also determines the similarity for wave drag, and the application of the similarity law must satisfy the same requirements for the maintenance of linearized flow. After multiplying both sides of Eq. (13.51) by M_∞^2, we obtain the general expression for the drag function $M_\infty^2 C_{Dp} = H(K_1)$, where H is a function depending only on the parameter K_1. This expression shows that if the flows around two or more bodies of revolution of different fineness ratio have the same value of K_1, each of these bodies will have the same value of the function $M_\infty^2 C_{Dp}$.

DETERMINATION OF THE WAVE DRAG COEFFICIENT

The Wave Drag of a Slender Cone

Equation (13.48) for the axial component of the perturbation velocity on a cone enables us to determine the pressure and, consequently,

the wave drag coefficient. From Eq. (13.14), we find

$$C_{pc} = C_{Dp} = 2(i_x^0)_c A - \delta_c^2, \tag{13.52}$$

where $A = 1/[(i_x^0)_c + (\beta/\delta_c)(i_r^0)_c]$ and the functions $(i_x^0)_c$ and $(i_r^0)_c$ are calculated from Eq. (13.36a) with $u_0 = 1/\beta\delta_c$.

Equation (13.52) can be simplified somewhat for $u_0 > 3$:

$$C_{pc} = C_{Dp} = \delta_c^2[4.606 \log_{10}(2u_0) - 1]. \tag{13.52a}$$

Calculations of the wave drag coefficient by Eq. (13.52) are compared with exact theory in Fig. 116. Good agreement of the results are

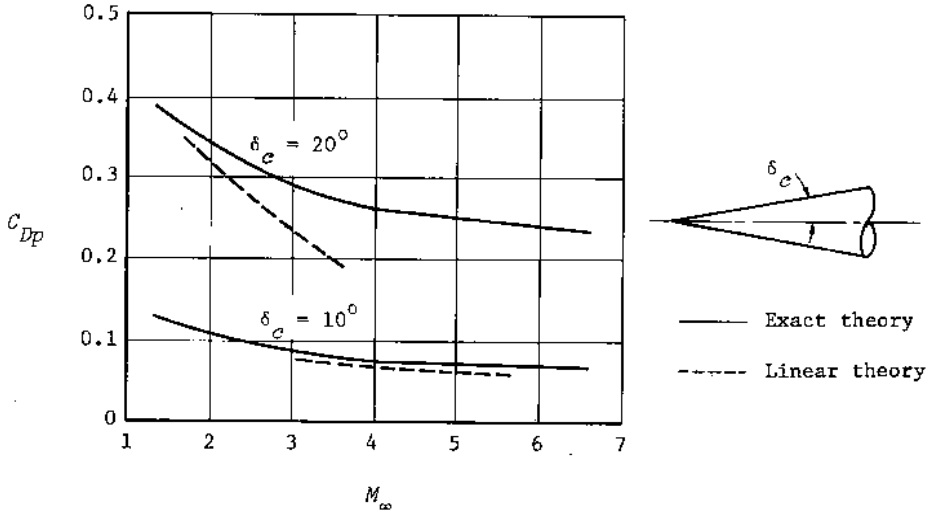

Fig. 116--Pressure drag coefficient for cones by exact and linearized theories

observed for slender bodies up to large Mach numbers. However, a considerable discrepancy is indicated at comparatively small Mach numbers for the thicker bodies, as is evident in Fig. 116 for the 20° cone. Obviously, the flow around such a cone deviates significantly from linearized flow. Therefore, in using linearized theory for flow calculations, it is necessary to stay within the limits indicated earlier for

determining the Mach numbers and nose angles for which linearized flow is valid. If these limits are exceeded, the linearized solution, which is essentially a first approximation, will give an increasingly large error. In such cases, more accurate results can be achieved by using the general equations of motion, or, in special cases, the equations for the velocity potential in which second-order terms are retained. These equations, derived by Van Dyke, comprise the theoretical basis of the method of flow calculation in the second approximation.[1] We omit a detailed discussion of this method because of its complexity and present only the equation for calculating the pressure coefficient on a cone by second-order theory:†

$$C_{pc} = C_{Dp} = \delta_c^2[4.606 \log_{10}(2u_0) - 1] + \frac{\delta_c^2}{u_0}\left[15.9 \log_{10}^2(2u_0) - 11.52 \log_{10}(2u_0) + \frac{113}{20}\right]. \qquad (13.53)$$

This equation can be compared with the first-order result of Eq. (13.52a).

Wave Drag of Bodies of Revolution Composed of Conical Elements

Several possible types of axisymmetric bodies composed of separate conical elements are presented in Fig. 117. In general, the calculation of the wave drag coefficient of bodies of this type is dependent on the estimation of the pressure distribution on their surface. In Fig. 118, experimental data are presented for the pressure distribution at $M_\infty = 2$. These data were obtained from wind-tunnel tests of a body of revolution consisting of a conical nose, a cylindrical midsection, and an afterbody in the form of a frustum of a cone. Approximately the same results are obtained from calculations by linearized theory.

One of the important and difficult aspects of the theoretical calculations is the determination of flow parameters, particularly the pressure, on the surface of the afterbody. For example, a negative pressure

†Editor's note: This is the formula given by Broderick[2] for cones using second-order slender-body theory. Van Dyke's results reduce to the same formula when the slender-body assumption is made.

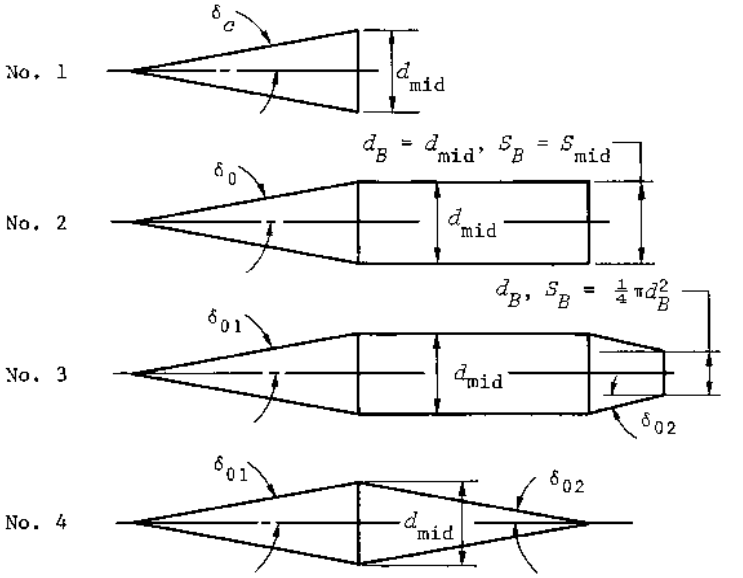

Fig. 117--Shapes of bodies composed of conical sections

coefficient in this region can lead to a significant increase in the total drag.

The difficulty in the calculation is due to the fact that the flow around the afterbody can be determined only if the flow parameters are computed over the entire body, including the cylindrical section. Such a complete calculation can be made either by linearized theory or by the method of characteristics. However, the calculation requires a large expenditure of time. In practice, simple methods for the approximate estimation of flow parameters on the afterbody are necessary, particularly for pressure, which make it possible to find the total drag, including the effect of the afterbody.

Equation (6.19) can be used for the nose drag coefficient, since it has been shown earlier that it gives almost exact results for this case. Figure 118 indicates that the actual value of the pressure coefficient on the conical afterbody is somewhat less than that obtained from Eq. (6.19). Therefore, the pressure distribution found from this

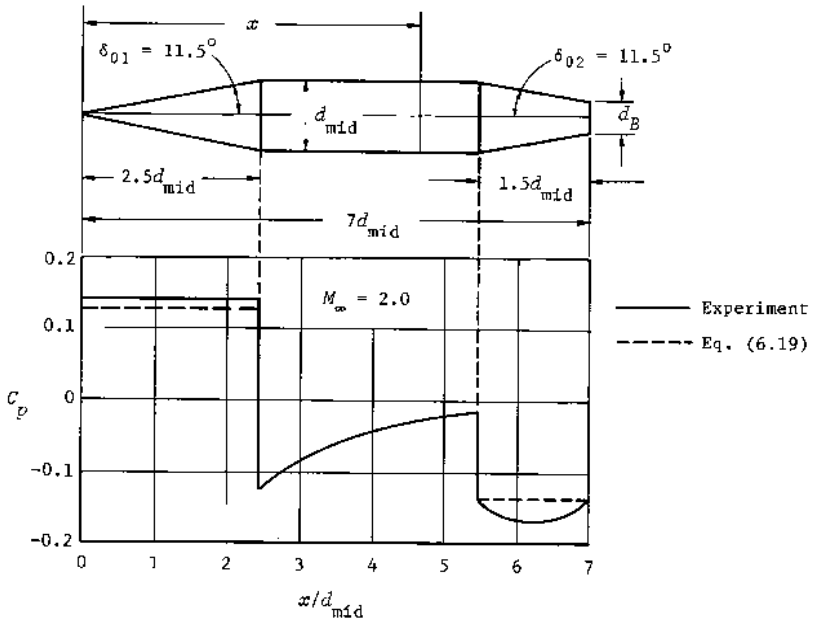

Fig. 118--Pressure distribution on a body with a conical nose and conical boattail

equation must be regarded as an approximate estimate of the actual case. The use of Eq. (6.19) enables us to find a comparatively simple--even though quite approximate--relation for estimating the wave drag coefficient of bodies consisting of conical elements.

Let us assume that C_{p1} and C_{p2} are the pressure coefficients on the nose cone and tail cone, respectively, and that the dimensionless quantity $\bar{S}_B$ determines the taper of the afterbody, defined as $\bar{S}_B = S_B/S_{mid} = (d_B/d_{mid})^2$. Then, using Eq. (1.6), we obtain the following simple relation:

$$C_{Dp} = C_{p1} + C_{p2}(1 - \bar{S}_B), \tag{13.54}$$

in which the first term is the drag of the nose cone $C_{Dp}^{N} = C_{p1}$, and the second term is the afterbody drag $C_{Dp}^{BT} = C_{p2}(1 - \bar{S}_B)$. Introducing into

Eq. (13.54) the expressions for C_{p1} and C_{p2} from Eq. (6.19), we find

$$C_{Dp} = 0.002\left(0.8 + \frac{1}{M_\infty^2}\right)[(\delta_{01}^\circ)^{1.7} + (\delta_{02}^\circ)^{1.7}(1 - \bar{S}_B)], \qquad (13.54a)$$

where δ_{01}° and δ_{02}° are the angles in degrees of the nose and tail cones, respectively. The part of the drag that applies to the afterbody can be separated from the right side of Eq. (13.54a):

$$C_{Dp}^{BT} = 0.002\left(0.8 + \frac{1}{M_\infty^2}\right)(\delta_{02}^\circ)^{1.7}(1 - \bar{S}_B). \qquad (13.55)$$

The boattail drag coefficient can also be determined from the results presented in Fig. 119. One of the sets of curves is obtained from linearized theory, the other from the more exact second-order theory. All the results are based on the assumption that the conical afterbodies are sufficiently far downstream from the nose that the pressure and velocity at the start of the afterbody have returned to their free-stream values.

To use the curves in Fig. 119, it is first necessary to calculate the fineness ratio of the afterbody from the formula $\lambda_{BT} = l_{BT}/d_{mid}$ or from the expression $\lambda_{BT} = (1 - \bar{S}_B^{\frac{1}{2}})/2\delta_{02}$, and then compute the parameter $(1/2\lambda_{BT})\sqrt{M_\infty^2 - 1}$. The boattail or afterbody drag coefficient can be determined from the parameter $4\lambda_{BT}^2 C_{Dp}^{BT}$ shown in the figure.

Results shown in Fig. 119 indicate that Eq. (13.55) would give better results if it were modified empirically to the form

$$C_{Dp}^{BT} = 0.002\left(0.8 + \frac{1}{M_\infty^2}\right)(\delta_{02}^\circ)^{1.7}\sqrt{1 - \bar{S}_B}. \qquad (13.56)$$

Adding the nose drag

$$C_{Dp}^{N} = 0.002\left(0.8 + \frac{1}{M_\infty^2}\right)(\delta_{01}^\circ)^{1.7},$$

we obtain the following equation for the total pressure drag coefficient:

$$C_{Dp} = C_{Dp}^{N}\left[1 + \left(\frac{\delta_{02}}{\delta_{01}}\right)^{1.7}\sqrt{1 - \bar{S}_B}\right]. \qquad (13.57)$$

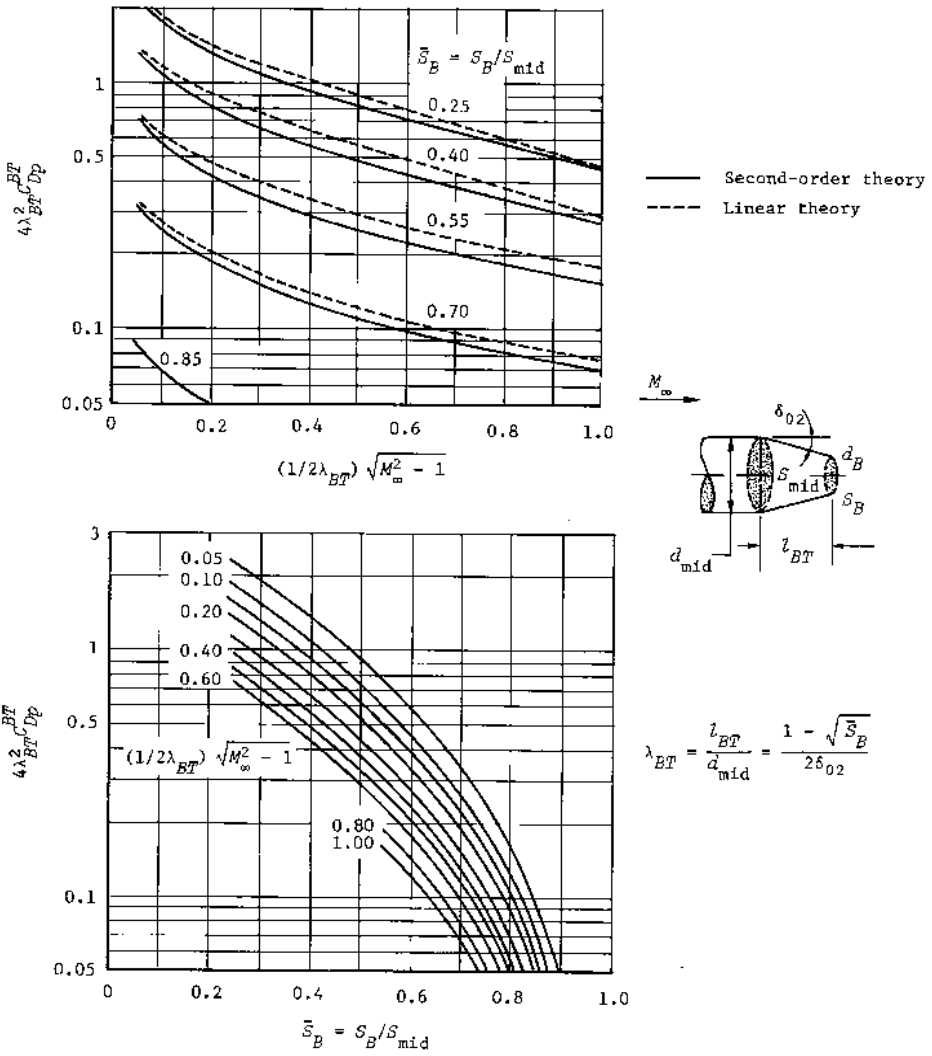

Fig. 119--Curves for the pressure drag coefficient of a conical boattail

If the nose and tail cones have identical angles, $\delta_{01} = \delta_{02}$, Eq. (13.57) takes the form

$$C_{Dp} = 0.002\left(0.8 + \frac{1}{M_\infty^2}\right)(\delta_{01}^\circ)^{1.7}\left(1 + \sqrt{1 - \bar{S}_B}\right). \qquad (13.57a)$$

In general, afterbodies can expand as well as taper, in which case the base area is larger than the area of the midsection. Consequently, the drag coefficient of the body increases as the angle and fineness ratio of the flare become greater.

The study of the drag component that originates due to a flared afterbody is a complex problem. If the flare angle is not too large, it is sometimes possible to use the method of characteristics. If the angle is large, only experimental methods are sufficiently reliable for flow studies. However, for rough estimates of the values of the flow parameters, the method of local cones can be used, assuming that the gas moves with the free-stream velocity in front of the conical flare. According to this method, the drag is determined as though the afterbody were part of a complete cone with the same slope as the flare. The wave drag coefficient of the conical afterbody then will depend on the fineness ratio of the tail cone $\lambda_{BT} = l_{BT}/d_{mid}$ (or on the flare angle δ_{02}), on the ratio $\bar{S}_B$, and on the Mach number M_∞. The wave drag coefficient of flared afterbodies is shown in Fig. 120, for which it is first necessary to compute $\lambda_{BT} = (\bar{S}_B^{\frac{1}{2}} - 1)/2 \tan \delta_{02}$.

The Wave Drag of a Slender Body of Revolution with an Arbitrary Shape

The general case of the calculation of the wave drag coefficient requires the computation of the pressure distribution and the subsequent use of Eq. (1.6). Typical shapes for which the general method of calculation provides accurate results are illustrated in Fig. 121. In addition, just as in the case of bodies composed of conical elements, it is possible to establish approximate relations that permit the comparatively simple estimation of the wave drag coefficient of bodies of revolution of arbitrary shape.

Noses of Various Shapes. It can be seen from Fig. 121 that the body nose plays a dual role. It can be a complete flying object in

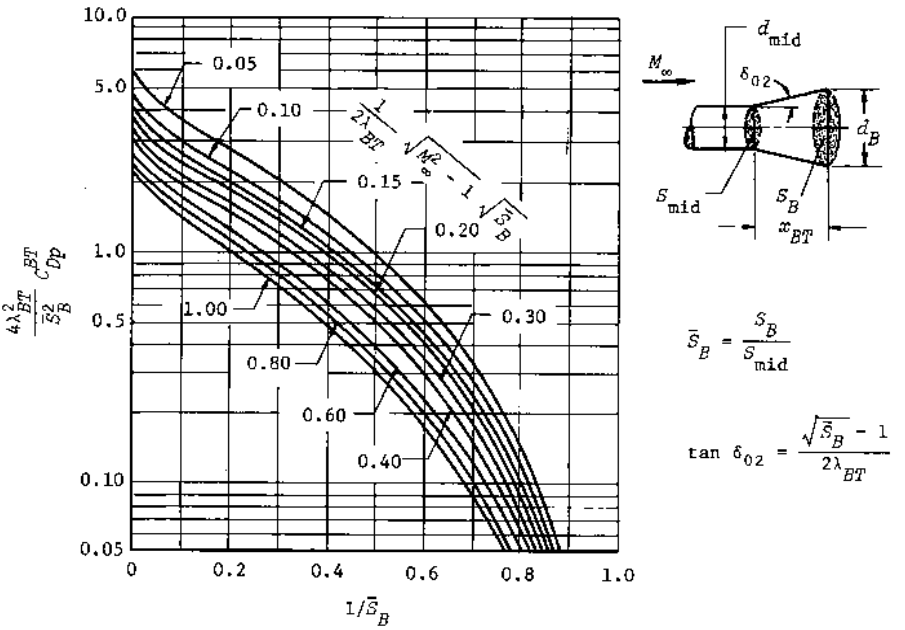

Fig. 120--Curves for the approximate estimation of the pressure drag coefficient of conical flares

itself (Fig. 121, Model Nos. 1 and 2) or it can be the fore part of a composite body (Fig. 121, Model Nos. 3 through 6). In the latter case, the nose drag is a part of the total drag of the entire body.

The nose drag can be calculated by means of the method of local cones, and it should be noted that in the case of linearized flow the results are the same for the two hypotheses of identical pressures or identical velocities. In general, if the velocities on the local cones are identical in both hypotheses, the pressures will differ because of the different stagnation pressures behind the shock waves. As already indicated, the stagnation pressure will be larger for a local cone using the hypothesis of identical pressures, so the static pressure on the local cone will also be larger. In the case of a slender, pointed body in linearized flow, the bow shock wave is transformed into a Mach wave behind which the stagnation pressure is the same as in the unperturbed flow.

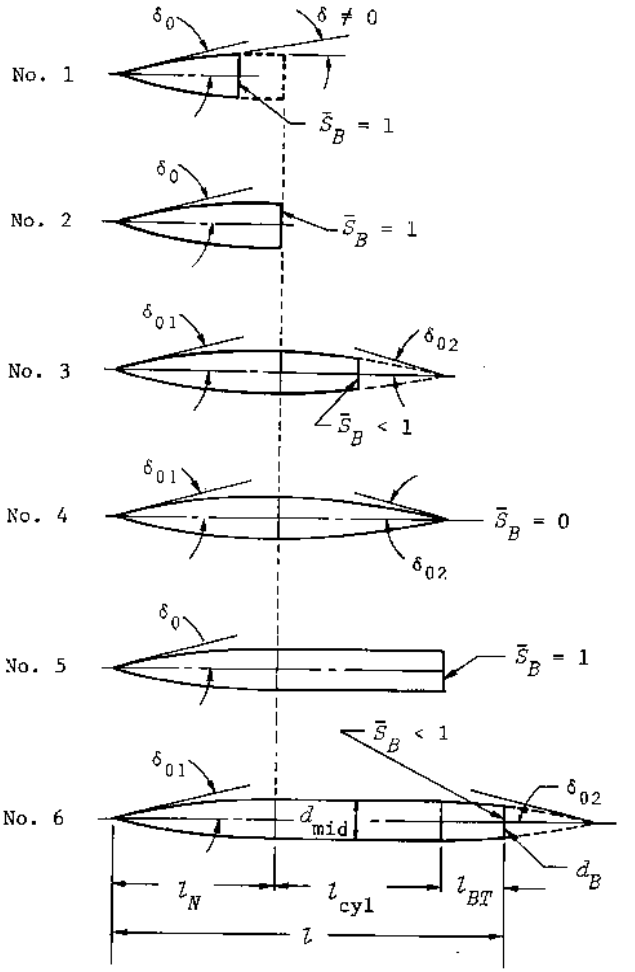

Fig. 121--Shapes of bodies of arbitrary profile

Therefore, both variants of the method of local cones will give identical results, and the relations for linearized flow around a slender cone can be used to calculate the pressure distribution.

Let us consider the case where the parameter u_0 and the Mach number M_∞ are rather large, and the nose has a parabolic shape with a local slope given by $\delta = \delta_0(1 - \bar{x})$. Equation (13.52a) enables us to find

the approximate relation for the pressure coefficient on a local cone:

$$M_\infty^2 C_p = 2K_1^2(1 - \bar{x})^2 \log\left[\frac{2}{K_1(1 - \bar{x})}\right] - K_1^2(1 - \bar{x})^2, \qquad (13.58)$$

where $K_1 = M_\infty \delta_0$. The pressure drag coefficient of the nose can be obtained by performing the integration in Eq. (1.6), resulting in

$$M_\infty^2 C_{Dp} = K_1^2\left[\frac{2}{3}\log\left(\frac{2}{K_1}\right) - \frac{1}{18}\right]. \qquad (13.59)$$

Thus, the drag function depends only on the similarity parameter $K_1 = M_\infty \delta_0$. Equation (13.59) is useful for approximate calculations at conditions that are represented graphically in Fig. 91. This expression was obtained for a complete (i.e., a tangent) nose, such as Model No. 2 in Fig. 121. However, it is not difficult to obtain an analogous relation for a shortened or secant nose (Model No. 1, Fig. 121).

In addition to Eq. (13.59), the expressions given by Eqs. (8.33) and (8.34) can be used for the calculation of the pressure drag of a parabolic or ogival nose. As was mentioned earlier, Eq. (8.34) gives values for the pressure drag coefficient that are too large, and a correction factor φ can be introduced:

$$C_{Dp} = 0.415\varphi C_{pc}. \qquad (13.60)$$

Comparison with exact data shows that the coefficient φ can be assumed equal to 0.8.†

Various graphs can also be used with the analytical equations to determine the drag. One such graph is the so-called universal curve shown in Fig. 122, which relates the function $4\lambda_N^2 C_{Dp}$ to the parameter $(1/2\lambda_N)\sqrt{M_\infty^2 - 1}$. Obviously, this is a similarity relation. The universal curve is compared with results from the method of characteristics in Fig. 122, indicating that the similarity law gives good results.

†Editor's note: Notice that Eq. (8.35) gives another form of the correction factor that would appear to be more accurate for general use.

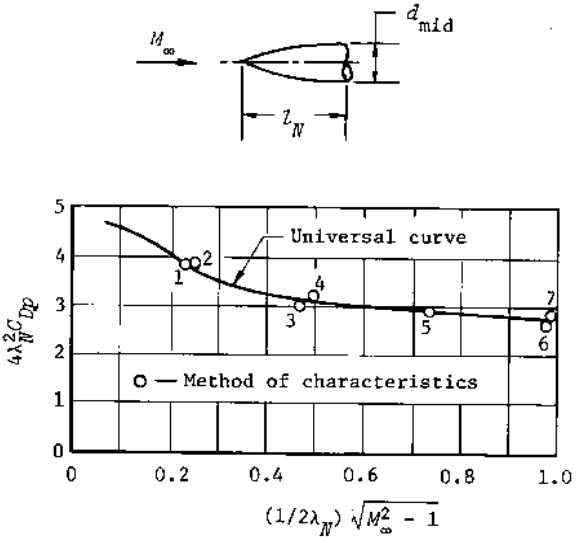

Model No.	$1/2\lambda_N$	M_∞
1	0.0833	3.0
2	0.0417	6.0
3	0.1667	3.0
4	0.0556	9.0
5	0.1250	6.0
6	0.1667	6.0
7	0.0833	12.0

Fig. 122--Universal curve for the pressure drag coefficient of a parabolic nose

Effect of Boattailing on the Drag. It has already been noted that the effect of boattailing can be taken into account if the pressure distribution on the afterbody is known. The calculation is simplified if the center cylindrical section is rather long, since the velocity on the cylinder at its junction with the boattail is essentially equal to the free-stream velocity. This will not be true if the cylindrical section is short, in which case the problem of flow around the afterbody is considerably more complicated.

Both in this case and in others, the flow calculation for the afterbody can be made by the method of characteristics. The results have shown that the pressure coefficient at a given point on the afterbody depends on the local slope of the surface, tan δ, and on the ratio of the coordinates, r/x (Fig. 123). The coordinate x is the distance from the point in question to the intersection with the body axis of a Mach line drawn through the origin of the boattail.

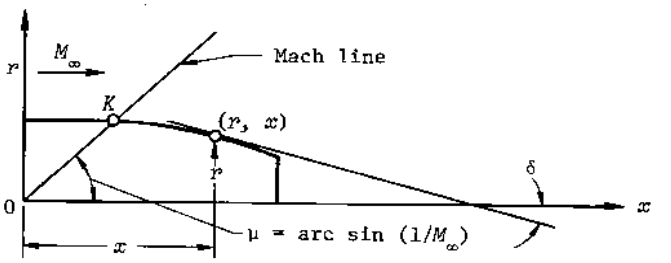

Fig. 123--Geometric parameters of an afterbody of arbitrary shape

Curves for the pressure coefficient on the afterbody as a function of the parameters tan δ and r/x are presented in Fig. 124 for a series of free-stream Mach numbers. These results are valid only for those cases in which the cylindrical portion of the bodies is sufficiently long.

If the geometric shape of the body is known and the Mach number is given, the pressure distribution can be found from Fig. 124 and the boattail drag coefficient computed. An analysis of the results showed that generalized graphs could be constructed that would enable the calculation of C_{Dp}^{BT} rather rapidly and reliably. Graphs for a parabolic afterbody are presented in Fig. 125. From these graphs, it is evident that the boattail drag coefficient depends on the fineness ratio of the boattail, $\lambda_{BT} = l_{BT}/d_{\text{mid}}$ (l_{BT} is the length of the afterbody), on the taper of the base $\bar{S}_B$, and on the free-stream Mach number. The drag parameter $4\lambda_{BT}^2 C_{Dp}^{BT}$ is a function of the two parameters $(1/2\lambda_{BT})\sqrt{M_\infty^2 - 1}$ and $\bar{S}_B$. It is easy to show that the parameter $\bar{S}_B$ depends on the fineness ratio of the actual boattail, λ_{BT}, and on the fineness ratio, $\lambda_N = l_N/d_{\text{mid}} = 1/\tan \delta_{02}$, of a fictitious parabolic nose resulting from the extension of the afterbody to a point, as shown in Fig. 125. The corresponding relation has the form $\bar{S}_B = (1 - \lambda_{BT}^2/\lambda_N^2)^2$.

In addition to the method of characteristics and the graphical data, the method of local cones can be used for approximate estimates of the pressure drag on the boattail. One of the relations for this purpose is Eq. (6.19) for the pressure coefficient on a cone. Assuming that

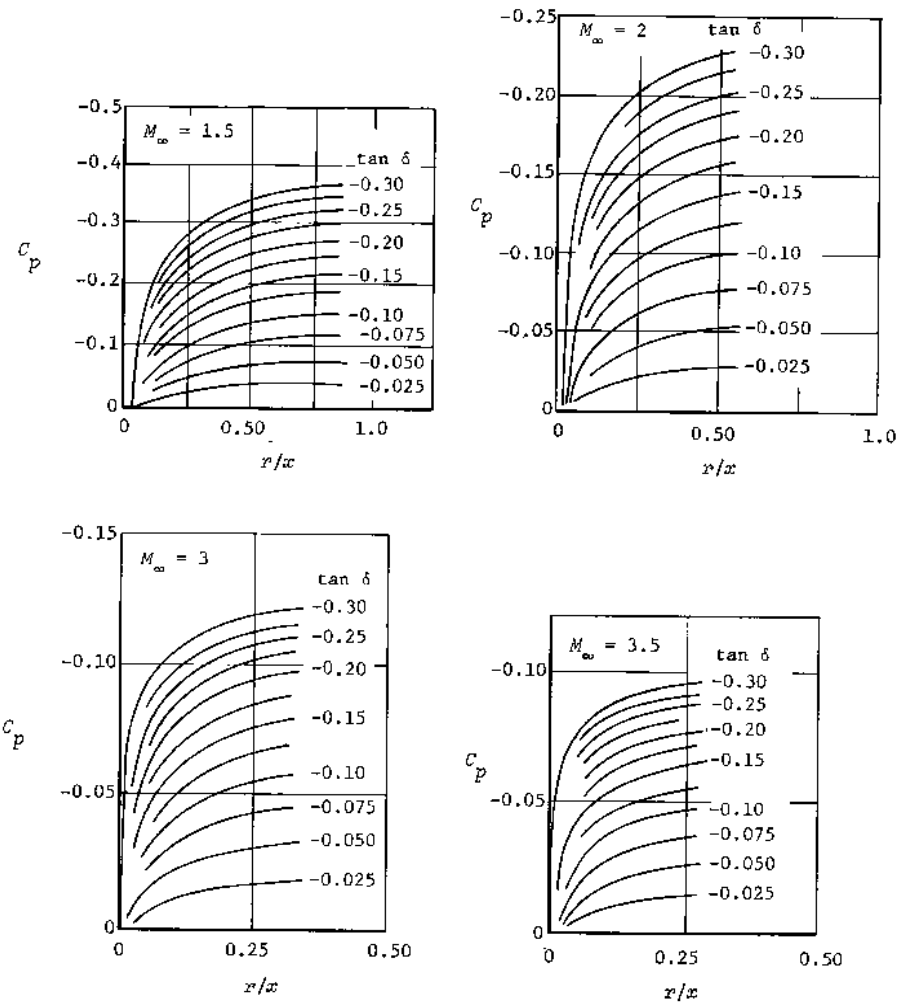

Fig. 124--Pressure distribution on the boattail of a body of revolution

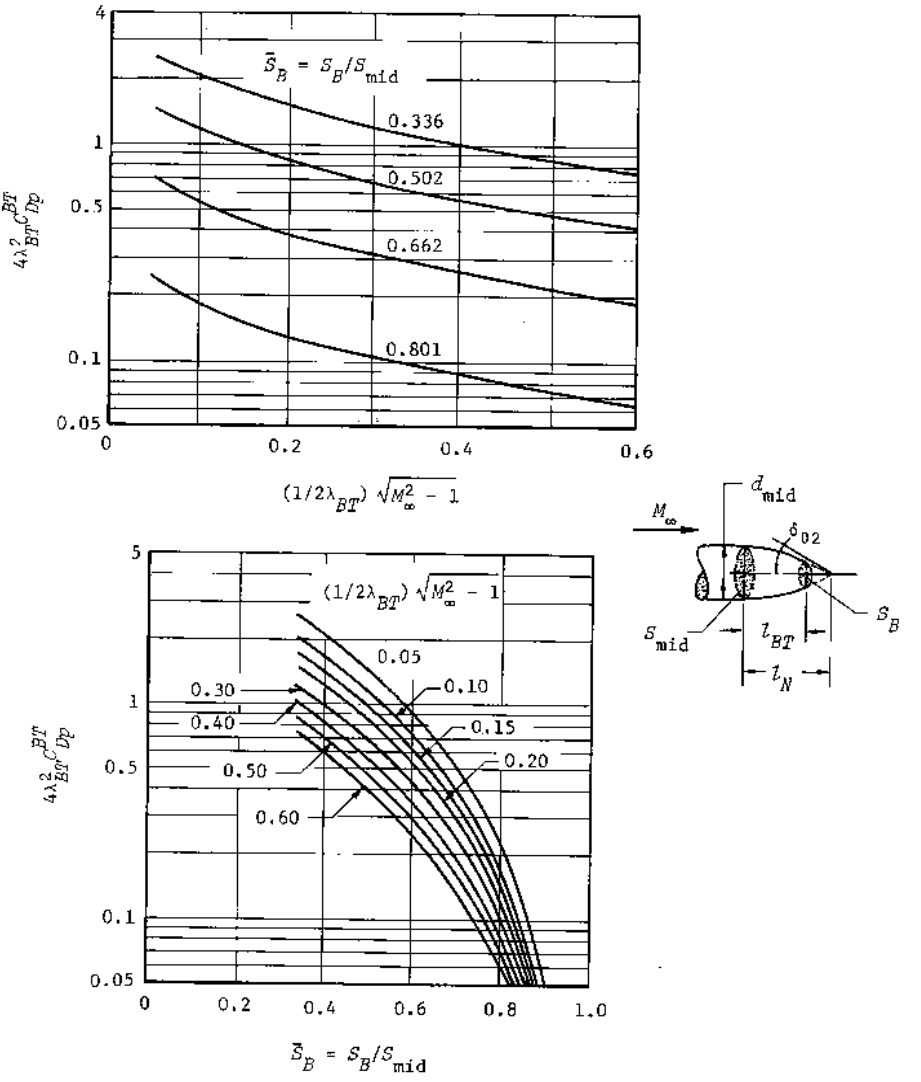

Fig. 125--Curves for the pressure drag coefficient of a parabolic boattail

the angle δ_c in Eq. (6.19) is variable in value and equal at each point on the surface to the slope of the tangent to the surface, the pressure coefficient can be estimated at this point. The pressure coefficient must be considered negative in sign. The results differ from those obtained by the method of characteristics, although they are of the same order of magnitude. Therefore, the results of the local-cone method must be considered rough approximations.

However, it is possible, considering the simplicity of the method of local cones, to attempt to correct these relations by using the accurate results of the method of characteristics. Assume that the afterbody of a given body has a parabolic shape. The fineness ratio of a fictitious nose with the same shape as the boattail is λ_N and the apex angle δ_{02} (Fig. 121, Model Nos. 3, 4, and 6). If C_{p2} is the pressure coefficient on the afterbody (negative in sign) and $\bar{S}_B$ is the taper, the boattail pressure drag coefficient is given by Eq. (1.6) as

$$C_{Dp}^{BT} = \int_{\bar{S}_B}^{1} C_{p2}\, d\bar{r}^2.$$

Substituting Eq. (6.19) for C_{p2} in this equation (replacing δ_c by $\delta = 57.3\delta_0(1 - \bar{x})$) and correcting the resulting relation with data from the method of characteristics, we obtain the following approximate equation:

$$C_{Dp}^{BT} = 0.4C_{pc2}\left[1 - 2.41\bar{S}_B^{4/3}\left(1 - 0.49\bar{S}_B^{1/2} + 0.056\bar{S}_B - 0.151\bar{S}_B^{3/2}\right)\right], \quad (13.61)$$

where C_{pc2} is the pressure coefficient on a cone with an angle δ_{02}.

Combining Eqs. (13.60) and (13.61), the total wave drag coefficient for a body with nose and tail sections of parabolic shape is

$$C_{Dp} = 0.332C_{pc1} + 0.4C_{pc2}\left[1 - 2.41\bar{S}_B^{4/3}\left(1 - 0.49\bar{S}_B^{1/2} + 0.056\bar{S}_B - 0.151\bar{S}_B^{3/2}\right)\right], \quad (13.62)$$

where the pressure coefficient C_{pc1} is computed for a cone with an angle δ_{01}.

When the boattail of the body is a cone with base taper $\bar{S}_B$, the total pressure drag coefficient is computed from the simpler equation:

$$C_{Dp} = 0.332C_{pc1} + C_{pc2}\sqrt{1 - \bar{S}_B}, \tag{13.63}$$

in which the coefficient C_{pc2} is found from the known angle δ_{02} of the conical element.

Extremely Slender Bodies of Revolution. The relations presented above for the pressure drag pertain to slender bodies, the parameters of which depend to some extent on the free-stream Mach number. Research has shown that this dependence decreases proportionally as the body becomes more slender. In the theoretical limit as $r \to 0$, the perturbed supersonic flow no longer is a function of compressibility. In practice, this obviously corresponds to an extremely slender body with a large fineness ratio.

The limiting case in question is studied in aerodynamics as a special subject usually called "slender-body theory."[3] According to this theory, the relation for the pressure drag coefficient is found in the following manner. Using Eq. (13.14) for the pressure coefficient and Eq. (13.22) for the axial component of the perturbation velocity, we obtain from Eq. (1.6)

$$C_{Dp} = 8\lambda_l \int_0^1 \bar{r}\left[\int_0^{x-\beta r} \frac{\dot{f}(\xi)\, d\xi}{\sqrt{(x-\xi)^2 - \beta^2 r^2}} - \frac{1}{2}\left(\frac{dr}{dx}\right)^2\right] \tan\delta\, d\bar{x}.$$

Converting to the limit $r \to 0$ in this expression and assuming that the slope of the profile at the base is equal to zero, we obtain the Kármán equation for the wave drag coefficient:

$$C_{Dp} = \frac{2\lambda_N^2}{\pi^2} \int_0^1 \int_0^1 S''(\bar{\xi}) S''(\bar{x}) \log \frac{1}{|\bar{x} - \bar{\xi}|}\, d\bar{x}\, d\bar{\xi}, \tag{13.64}$$

in which the dimensionless quantities are $\bar{\xi} = \xi/l_N$, $\bar{x} = x/l_N$. Since $S = \pi r^2$, Eq. (13.64) can be rewritten as

$$C_{Dp} = \frac{1}{8\lambda_N^2} \int_0^1 \int_0^1 \frac{d^2}{d\bar{\xi}^2}\left[\bar{r}^2(\bar{\xi})\right] \frac{d^2}{d\bar{x}^2}\left[\bar{r}^2(\bar{x})\right] \log \frac{1}{|\bar{x} - \bar{\xi}|}\, d\bar{x}\, d\bar{\xi}. \tag{13.64a}$$

As an example, let us compute the wave drag of a slender parabolic

nose from this equation. From the equation for the body shape, the second derivative is

$$\frac{d^2}{d\bar{x}^2}\left[r^2(\bar{x})\right] = 4(2 - 6\bar{x} + 3\bar{x}^2).$$

Introducing this derivative into Eq. (13.64a), we find

$$C_{Dp} = \frac{2}{\lambda_N^2}\int_0^1\int_0^1 (2 - 6\bar{\xi} + 3\bar{\xi}^2)(2 - 6\bar{x} + 3\bar{x}^2)\log\frac{1}{|\bar{x} - \bar{\xi}|}\,d\bar{x}\,d\bar{\xi}.$$

As a result of computing the double integral, we obtain

$$C_{Dp} = 1.17\lambda_N^2. \tag{13.65}$$

It is evident from this expression that the wave drag does not depend on the Mach number for a very slender body of revolution and that it is a function of the fineness ratio only.

The Shape of an Axisymmetric Body with Minimum Pressure Drag

A proper selection of the shape of a body of revolution can be made so that the pressure drag for the stated conditions is minimum. The following equation for the shape of a body having minimum pressure drag is found on the basis of linearized theory:

$$\bar{r} = 2\left[\sqrt{1 - \bar{x}^2} - \bar{x}^2 \operatorname{arc\,cosh}\left(\frac{1}{\bar{x}}\right)\right]^{\frac{1}{2}}, \tag{13.66}$$

where $\bar{r} = r/r_{mid}$, $\bar{x} = x/2l_N$. It can be shown that this equation produces symmetrical bodies that are slightly blunted at both ends. Despite this blunting, the drag turns out to be minimum because of the significant pressure decrease due to the overexpansion of the flow behind the blunted nose.

It should be noted that the shape of a nose with a generatrix described by Eq. (13.66) differs from an ordinary parabola only in the vicinity of the nose (Fig. 126).

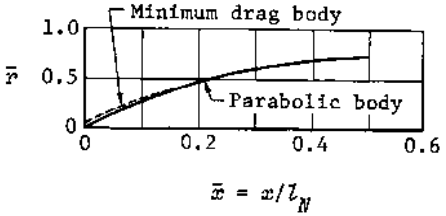

Fig. 126--Comparison of the profiles of a body with minimum wave drag and a parabolic nose

In addition to the rule for constructing an optimum shape based on the use of Eq. (13.66), several other recommendations can be made. The contour of a body having an approximate minimum-drag shape can be constructed from a parabolic shape in the following way. First a parabolic nose is constructed with a fineness ratio λ_N' that is $\sqrt{2}$ times larger than the required value λ_N (Fig. 127). Then the leading part of the body is cut off at the given fineness ratio λ_N. After rounding off the apex by means of a radius of $0.1d_{mid}$, a nose with minimum wave drag results.

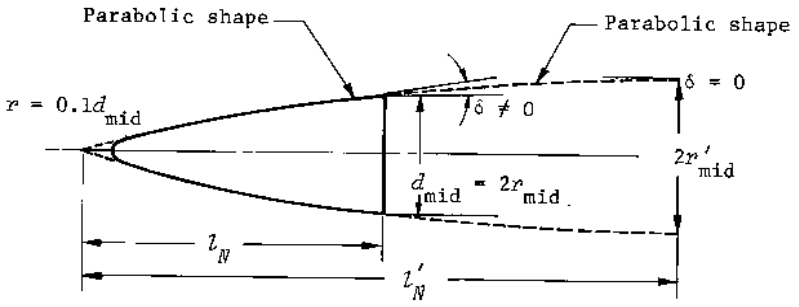

Fig. 127--Diagram for the construction of a body with minimum wave drag

Experiments show that a body with an optimized shape and a fineness ratio of 3 has one-half the wave drag of a cone of the same length. However, the difference between the drag coefficients of a body with optimum shape and a body in the form of a tangential parabolic nose is

comparatively slight, as might be expected since the bodies are similar in shape. The nose of optimum shape has a wave drag that is smaller by approximately 7 percent.

§ 14. *SKIN FRICTION AND BASE DRAG*

THE SKIN FRICTION COEFFICIENT

Fore Drag

IT HAS ALREADY BEEN POINTED OUT that the total drag of a body of revolution can be presented in the form of the sum of three components, i.e., drag due to pressure (wave drag), friction drag, and base drag. It is convenient to consider the fore drag as consisting of the sum of both the skin friction drag and the wave drag and to treat the base drag separately.

In general, the drag depends on the angle of attack. For a wide range of angles, the dependence has a quadratic character of the form $C_D = C_{D0} + a\alpha^2$, where C_{D0} is the drag coefficient for $\alpha = 0$ and a is a constant coefficient. It is obvious from this equation that the influence of angle of attack is considerable at sufficiently large angles. If linearized flow at small angles of attack is considered, the second term in this quadratic relation can be neglected. Then $C_D = C_{D0}$, i.e., the drag coefficient for small angles of attack equals the drag coefficient for symmetric flow, correct to the first order in α.

The total drag coefficient will be written as

$$C_D = C_{Dp} + C_{Df} + C_{DB}, \tag{14.1}$$

in which the first two terms, the pressure drag coefficient and the friction drag coefficient, determine the fore drag coefficient, and the third term is the base drag coefficient.

Let us examine some of the results of experiments in the study of the fore drag of cylindrical bodies with ogival and conical noses and

compare them with theoretical calculations. In the calculations, the pressure drag of the cone was determined from the theory of flow around a cone and the drag of the ogive nose by the method of characteristics. The friction drag coefficient was calculated from the equations

$$(C^{\circ}_{Df})_L = (C^{\circ}_{Df})'_L \frac{S_w}{S_{\text{mid}}},$$
$$(C^{\circ}_{Df})_T = (C^{\circ}_{Df})'_T \frac{S_w}{S_{\text{mid}}}, \tag{14.2}$$

which convert the skin friction coefficients from values based on the wetted area S_w to those based on the area of the midsection S_{mid}. The computation was made using the relations for a flat plate without accounting for the effects of compressibility. However, the actual experimental states of the boundary layer were considered: In two cases the boundary layer was completely laminar or completely turbulent, and in the third case, it was mixed. In the third case, a model of a body of revolution was used that had a band of roughness located at a given distance from the tip.

The equation for the friction drag coefficient of a mixed boundary layer has the following form:

$$C^{\circ}_{Df} = (\bar{C}^{\circ}_{Df})_L \frac{S_L}{S_{\text{mid}}} + (C^{\circ}_{Df})'_T \frac{S_w}{S_{\text{mid}}} - (\bar{C}^{\circ}_{Df})_T \frac{S_L}{S_{\text{mid}}}, \tag{14.3}$$

where $(\bar{C}^{\circ}_{Df})_L$ and $(\bar{C}^{\circ}_{Df})_T$ are the friction coefficients in the incompressible laminar and turbulent boundary layers, calculated from the equation for a flat plate. The calculation was made for a Reynolds number based on the distance x_L from the tip to the roughness band. This distance determines the portion of the wetted area S_L over which laminar flow exists. The parameter $(C^{\circ}_{Df})'_T$ is the turbulent friction coefficient calculated for the Reynolds number based on the total model length.

The most important questions in the experiments concerned determining the character of the flow in the boundary layer (laminar or turbulent) and investigating the processes of transition and separation of

the boundary layer. Answers to these questions are of great value, because they make possible not only accurate calculations of the friction drag, but also predictions of the effects of viscosity on other flow processes, such as the degree of expansion at the base and the resulting base drag.

For practical purposes it is important to be able to predict the extent of the laminar boundary layer; this is discussed in more detail in Chap. VIII. The presentation here is limited to the results of the wind-tunnel determination of the transition Reynolds number for $M_\infty = 1.5$ on smooth axisymmetric models. On the basis of comparison between the experimental data and the theoretical calculations of the fore drag (Fig. 128), it can be established that the boundary layer remains laminar approximately up to a Reynolds number of $6.5 \cdot 10^6$. However, it is probable that this value is too low, because premature transition from

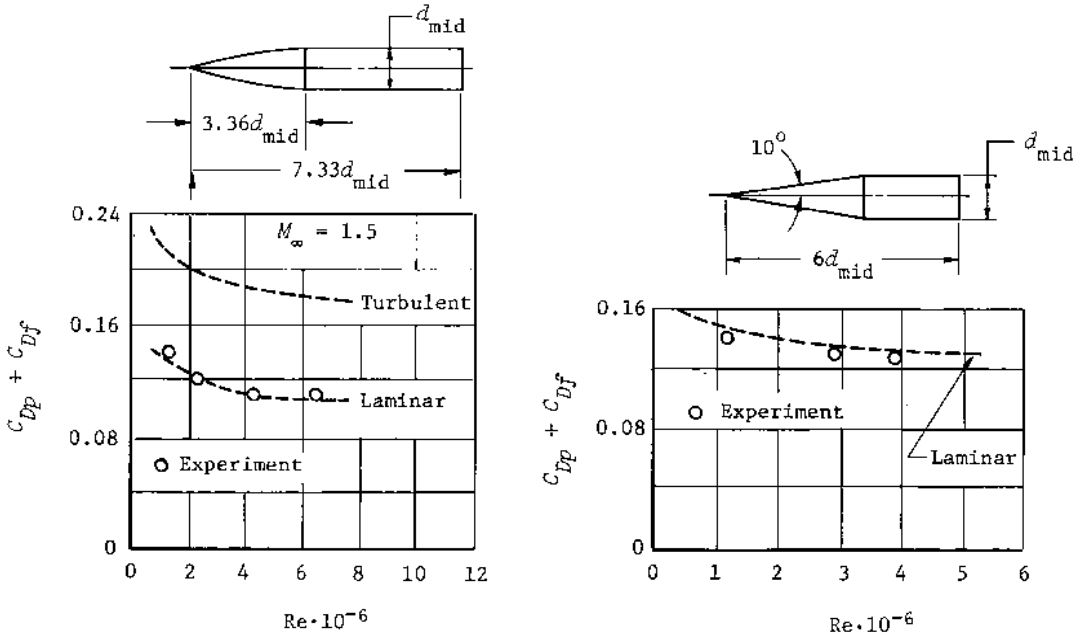

Fig. 128--Variation of the fore drag coefficient with Reynolds number

laminar to turbulent flow has been observed in these experiments. This is due to the interaction with the boundary layer of the bow wave reflected from the tunnel wall. Under actual flight conditions, the extent of laminar flow and the corresponding transition Reynolds number will be larger than those observed in the wind tunnel due to the absence of external disturbances.

A turbulent boundary layer was created on the models by means of artificial roughness, which promoted early transition to turbulent flow. In these experiments, as one might expect, an increase in fore drag was observed, caused not only by the existence of the turbulent boundary layer, but also by some increase in the pressure drag due to the band of roughness. For small Reynolds numbers, the results of the experiments indicate that when the boundary layer remains laminar regardless of the presence of the roughness band, the additional pressure drag caused by the roughness is small (see Fig. 129). However, after attaining the transition Reynolds number, which is less than that for a smooth model, a sharp increase in nose drag is observed for the banded model. This is primarily associated with the generation of turbulent friction on a significant portion of the model surface. The fore drag in the turbulent regime is approximately 20 percent higher than that for laminar flow for practically the entire range of Reynolds numbers investigated.

An important result from the experiments is the possibility of using the equations derived for a flat plate with an incompressible

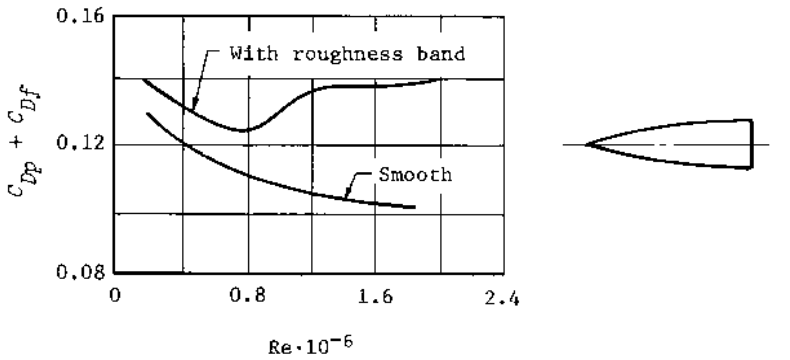

Fig. 129--Effect of surface roughness on the fore drag coefficient

boundary layer for the calculation of friction drag at low supersonic velocities. This is verified by the relatively good agreement of the theoretical and experimental values of fore drag for $M_\infty = 1.5$ in the Reynolds number range in question.

The influence of compressibility becomes larger as the velocity increases, and this can be taken into account by using the equations presented earlier for the friction on a plate, including the effects of Mach number. For example, if the skin friction coefficient is determined from Eqs. (5.6) and (5.9), and Eqs. (5.12) and (5.13) are used to account for compressibility, then, assuming that the transition Reynolds number is $6.5 \cdot 10^6$, we obtain an approximate relation for calculating the friction coefficient of a mixed laminar and turbulent layer:

$$C_{Df} = \left[\frac{4.96 \cdot 10^{-4}}{(1 + 0.03M_\infty^2)^{\frac{1}{3}}} \frac{S_L}{S_w} + \frac{0.032}{\sqrt{1 + 0.12M_\infty^2}} \left(\frac{1}{\mathrm{Re}^{0.145}} - \frac{0.1S_L}{S_w} \right) \right] \frac{S_w}{S_{\mathrm{mid}}}. \quad (14.4)$$

Further improvement of the results requires taking into account the influence of the shape of the body surface. A simplified method of friction calculation for long slender bodies involves the substitution of an equivalent cone for the nose section and a cylinder for the remaining portion. The flow parameters on both sections are considered constant and equal to the linearized flow parameters on the cone and the free-stream flow parameters on the cylinder.

The angle of the equivalent cone can be determined from the equation $\delta_{ce} = \int_0^1 \delta \, d\bar{x}$. In the special case of a parabolic nose, $\delta_{ce} = \delta_0/2$. For the equivalent cone-cylinder body, the total friction drag coefficient is

$$C_{Df} = A(C_f)_c^{\mathrm{pl}} \frac{\rho_c V_c^2}{\rho_\infty V_\infty^2} \frac{S_w^N}{S_{\mathrm{mid}}} + B(C_f)_{\mathrm{cyl}}^{\mathrm{pl}} \frac{S_w^{\mathrm{cyl}}}{S_{\mathrm{mid}}}, \quad (14.5)$$

where A equals $\sqrt{3}$ and 1.17[†] for laminar and turbulent boundary layers,

[†]Editor's note: These values are incorrect. They apply to the *local* skin friction coefficient only. The correct factors for *average* coefficients are $2\sqrt{3}/3$ and 1.02.

respectively, S_w^N is the wetted area of the real nose section, and S_w^{cyl} is the wetted area of the remaining section of the body. The coefficient B can be determined experimentally, but it can be assumed that $B \approx 1$ for approximate calculations.

The coefficient $(C_f)_e^{pl}$ in Eq. (14.5) is calculated from the expression for a flat plate but using the parameters on the equivalent cone. To calculate the friction coefficient on the cylinder, $(C_f)_{cyl}^{pl}$, the boundary layer thickness at the start of the cylinder must equal that at the end of the cone. A fictitious starting length of cylinder x_ϕ can be determined that produces the required thickness; then, equating the expressions for the thicknesses, this length is

$$x_\phi = x_{ce}\left(\frac{V_\infty}{V_e}\frac{\rho_\infty}{\rho_e}\frac{\mu_e}{\mu_\infty}\right)^n, \tag{14.6}$$

where x_{ce} is the length of the generatrix of the equivalent cone and the exponent $n = 1$ and 0.25 for the laminar and turbulent layers, respectively. The skin friction coefficient can now be determined:

$$(C_f)_{cyl}^{pl} = \frac{x_\phi + x_{cyl}}{x_{cyl}}(C_f)_{\phi+cyl} - \frac{x_\phi}{x_{cyl}}(C_f)_\phi, \tag{14.7}$$

where the coefficient $(C_f)_{\phi+cyl}$ is calculated for the length $x_\phi + x_{cyl}$, and $(C_f)_\phi$ is calculated for the fictitious length x_ϕ.

The direct effects of compressibility (i.e., of Mach number) and the relations using effective parameters for very high velocities can be included in the calculation of the friction coefficient.

For the computation of heat transfer parameters, it is necessary to convert to local friction coefficients, which are expressed as

$$C_{fx} = A(C_{fx})_e^{pl}, \qquad C_{fx} = B(C_{fx})_{cyl}^{pl} \tag{14.8}$$

for the equivalent cone and the cylinder, respectively.† The coefficient

†Editor's note: The values given previously for A are correct in this equation, i.e., $\sqrt{3}$ and 1.17 for laminar and turbulent flow, respectively.

$(C_{fx})^{pl}_{cyl}$ is calculated from the length $x_\phi + x$, where x is the distance from the beginning of the cylindrical section.

As we have noted previously, the equations for the heat transfer and skin friction parameters are solved simultaneously with the equation for the wall temperature. Therefore, the skin friction coefficient can be corrected for the effects of surface temperature during the heat transfer calculation. It is not necessary to consider physical-chemical processes in the boundary layer, since only comparatively low flow velocities can be studied by linearized flow theory; this simplifies the calculations.

The Influence of Flow Separation on Fore Drag

Flow around a body can be accompanied by separation of the flow. The study of this phenomenon is of considerable interest because separation causes a marked change in flow conditions and, consequently, in the aerodynamic characteristics of the body. Studies indicate that the point of separation and the degree of detachment of the boundary layer depend on the Reynolds number; as the Reynolds number increases, the separation point moves downstream and the degree of separation decreases. For a body of revolution with a tapered boattail, the laminar boundary layer separates for small Reynolds numbers at the start of the afterbody and is accompanied by an increase in pressure on the boattail, resulting in a reduction in fore drag compared with unseparated flow.

Under these conditions, the theoretical and experimental results for the pressure distribution do not agree, because the theory (e.g., the characteristics method) does not account for the effects of separation. This is confirmed by the data presented in Fig. 130a for the body with a boattail; it can be seen that the calculated decrease in pressure drag approaches the experimental values as the Reynolds number increases, indicating that the region of separated flow is contracting. At sufficiently high Reynolds numbers, the flow can remain completely attached, and better agreement is observed between the theoretical and experimental results. The data obtained for Model No. 1 (without a boattail) are shown in Fig. 130a. The agreement of theory and experiment is satisfactory over the entire Reynolds number range under study

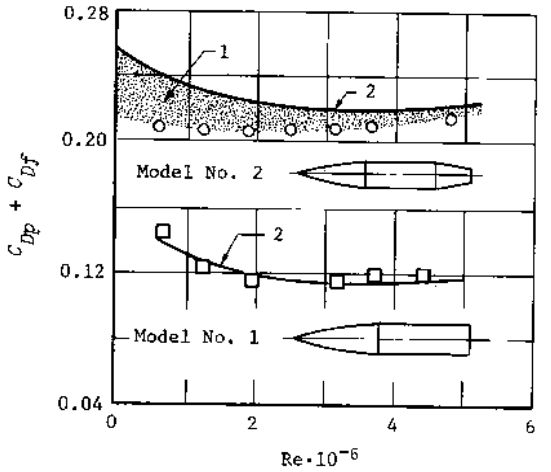

(a) Smooth model

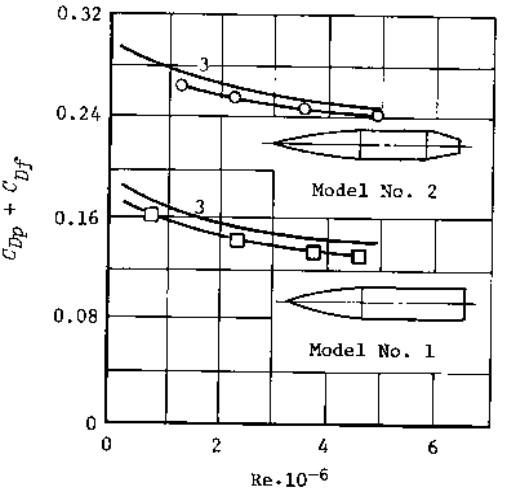

(b) Rough model

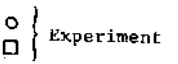

1 — Region of difference between experiment and calculation for a laminar boundary layer

2 — Theoretical $C_{Dp} + C_{Df}$, laminar

3 — Theoretical $C_{Dp} + C_{Df}$, turbulent

Fig. 130--Calculated and experimental fore drag coefficients as a function of Reynolds number

because there is no separation. The decrease in fore drag with the increase in Reynolds number is due to the reduction in the skin friction coefficient.

In Fig. 130b, experimental results are presented for the same models but with a band of roughness. First, it can be seen that the theoretical results are verified concerning the increase in the turbulent friction coefficient over the laminar value. Furthermore, the calculated and experimental data are in good agreement for the roughened Model No. 2 with a turbulent boundary layer, which indicates that flow separation did not occur over the converging afterbody.

Thus, the studies show that for bodies of revolution with a converging afterbody, calculations of the fore drag are more reliable with a completely turbulent boundary layer or with an unseparated laminar boundary layer.

BASE DRAG

Subsonic Velocities

As was stated earlier, the axial component of the pressure force is separated into two parts for convenience in investigation. One of these depends on the pressure distribution over the surface; the other, on rarefaction in the base region. The latter is usually called the base force and is equal to the base drag in symmetric flow. If there is an angle of attack the two forces differ, but if the angle is small the difference is slight and can be neglected in practice.

The phenomenon of the development of a low-pressure region at the base of a body has much in common with the processes involved in a jet pump. In this case the role of the pump is played by the external flow, which ejects the air occupying the stagnant region at the base of the body. As a result, a decrease in pressure occurs at the base.

Surveys show that the base pressure (and base drag) depends to a great extent on the surface condition of the body and on its length and taper. The properties of the boundary layer at the base are determined by these same factors, as has been shown. Therefore, there should be a relationship between the base pressure and skin friction.

It has been established by observation that the boundary layer in the vicinity of the base section acts like a cylindrical partition that separates the external flow from the internal cavity located at the base. In this way the boundary layer tends to decrease the suction effect, i.e., the ejection action of the external flow on the air in the base region, resulting in a decrease in rarefaction at the base. Thus, a specific relation exists between the boundary layer thickness and the base pressure. At the same time, the thickness of the boundary layer also determines the local friction coefficient. Therefore, the coefficient $(C_{Df})_B = \bar{C}_{Df}(S_w/S_B)$ can be introduced as a parameter in the analysis of base pressure, where $(C_{Df})_B$ is the skin friction coefficient based on the base area, and $\bar{C}_{Df}$ is the same coefficient based on the wetted area of the body.

The experimental data shown in Fig. 131 enable us to establish the following relation between the coefficient $(C_{Df})_B$ and the base pressure coefficient:[4]

$$C_{pB} = -\frac{0.029}{\sqrt{(C_{Df})_B}}. \tag{14.9}$$

Introducing the friction coefficient $C_{Df} = \bar{C}_{Df}(S_w/S_{\text{mid}})$, based on the midsection area, the expression for the base drag coefficient with reference area S_{mid} becomes

$$C_{DB} = \frac{0.029}{\sqrt{C_{Df}}}\left(\frac{d_B}{d_{\text{mid}}}\right)^3. \tag{14.10}$$

It follows from this equation that the base drag coefficient decreases with an increase in C_{Df} since the boundary layer becomes thicker as the skin friction increases. This thickened layer at the base section, playing the role of an insulating jacket, weakens the ejection action of the external flow. As a result, the rarefaction at the base is decreased, and the base drag decreases.

The experimental data in Fig. 132 indicate the possibility of using Eqs. (14.9) or (14.10) for approximate calculations of base pressure and drag not only in the case of purely subsonic velocities but also in the transonic flow region, i.e., for Mach numbers of the order of unity.

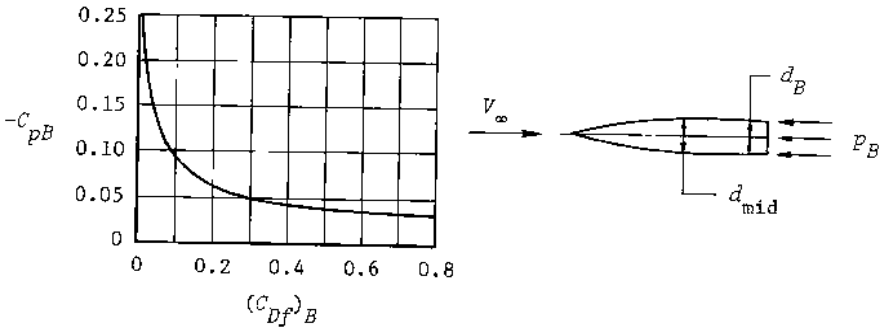

Fig. 131--Experimental data on the base pressure coefficient at subsonic speeds

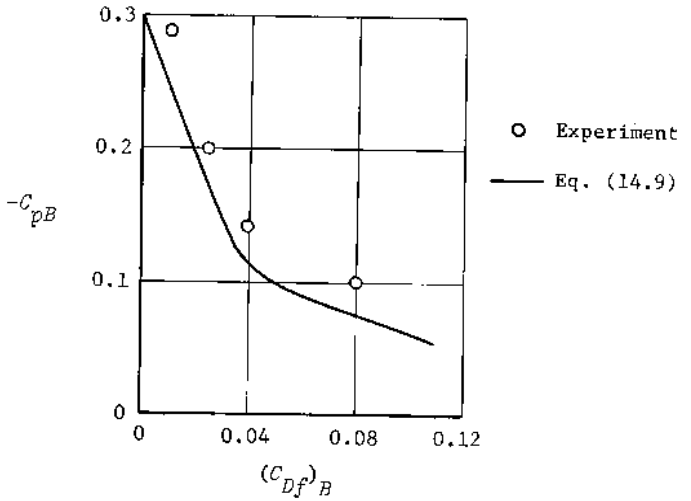

Fig. 132--Base pressure coefficient at transonic speeds

Supersonic Velocities

The flow diagram in Fig. 133 helps to clarify the character of the formation of base pressures at supersonic velocities. The existence of shock waves in the vicinity of the tail indicates that the base pressure depends to a certain extent on the formation and intensity of these shocks. Generally, the pressure change at the base is caused not only

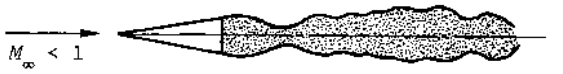

(a) Subsonic flow

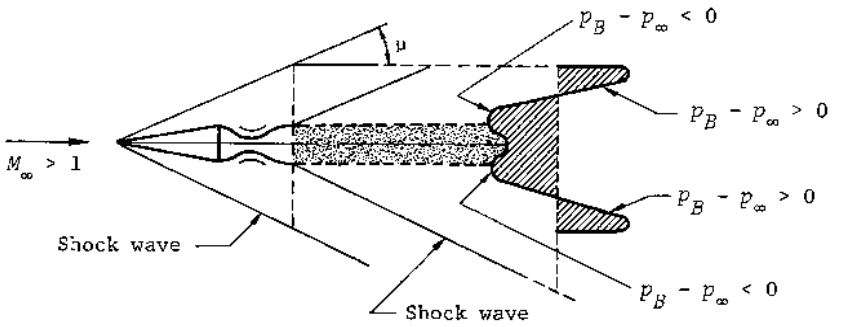

(b) Supersonic flow

Fig. 133--Flow diagram and pressure distribution behind the base of a missile

by the ejection action of the external flow (similar to that observed at subsonic velocities), but also by the compression behind the rear shock.

Experiments have shown the wave to be an oblique shock that develops because of the inward deflection of the flow behind the base. The flow must then be turned outward again because of the vortical wake extending behind the body, which acts somewhat as a solid wall in the flow field. The geometric spreading of the wake is less at supersonic velocities than at subsonic.

As with $M_\infty < 1$, the base pressure in supersonic flow is generally a function of the shape and geometric parameters of the body and the state of the boundary layer. In turn, the state of the boundary layer is determined by means of the Reynolds number, which influences the processes occurring at the base, including the generation of positive or negative relative pressures.

Experimental data can be used to establish the trend of the effects of Reynolds number on base pressure for the same type of boundary layer.

In the case of a laminar boundary layer, for example, the base pressure is a strong function of Reynolds number (Fig. 134a), but the dependence is not the same for bodies of a different shape. As can be seen in the figure, the base pressure coefficient of models without boattailing increases in absolute value by 60 percent, while for other models with various degrees of taper it more than doubles for the range of Reynolds numbers investigated.

The dependence of the base pressure on Reynolds number is comparatively slight for fully developed turbulent flow (Fig. 134b). However, as with the laminar regime, the body shape has a strong influence on the base pressure. For example, a lower pressure occurs on the base of models with a cylindrical afterbody than on models with a boattail. Moreover, if the taper is sufficient the pressure can even exceed the free-stream static pressure (see Fig. 134, Model No. 5). These results have been explained by means of a photographic study of the flow in the base region. It was shown that a strong shock wave originated in front of the base, and the resultant compression produced an increase in the base pressure.

A comparison of the results in Figs. 134a and 134b reveals that the base pressure is higher for turbulent flow than for laminar. For bodies with a boattail, this is due in large measure to the presence of strong tail shock waves. For bodies without taper, the pressure is increased due to the more intensive intermixing behind the base.

Additional investigations of the influence of viscosity on the base pressure have been made for models of varying length without boattails. The experimental data (Fig. 135) show that the base pressure is larger for the longer bodies. This same result was obtained in the more general case of a long body with an increasing fineness ratio.

Other experimental results make it possible to determine the influence of several other factors on base pressure. For example, it has been shown that the base pressure depends very little on the shape of the nose for bodies of rather high fineness ratios at supersonic velocities. Furthermore, the pressure remains practically the same at various points on the base section. The same studies showed that the base pressure of slender bodies is almost independent of angle of attack for small angles (approximately up to $\alpha \leq 5°$).

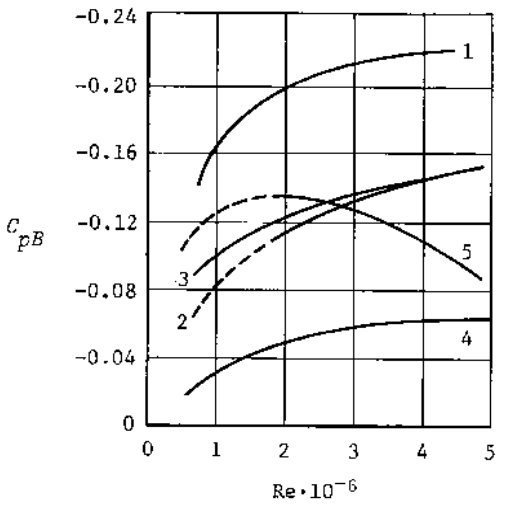

(a) Smooth model (laminar flow)

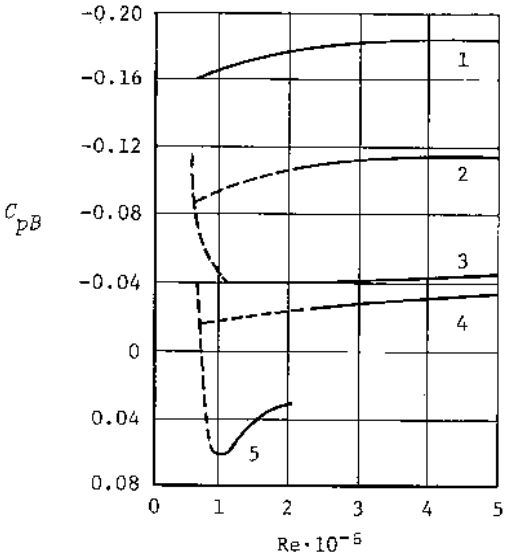

(b) Rough model (turbulent flow)

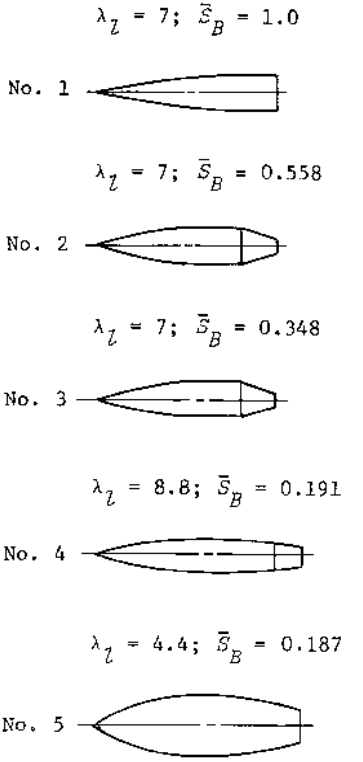
$\lambda_l = 7$; $\bar{S}_B = 1.0$
No. 1
$\lambda_l = 7$; $\bar{S}_B = 0.558$
No. 2
$\lambda_l = 7$; $\bar{S}_B = 0.348$
No. 3
$\lambda_l = 8.8$; $\bar{S}_B = 0.191$
No. 4
$\lambda_l = 4.4$; $\bar{S}_B = 0.187$
No. 5

Fig. 134--Variation of base pressure coefficient with Reynolds number

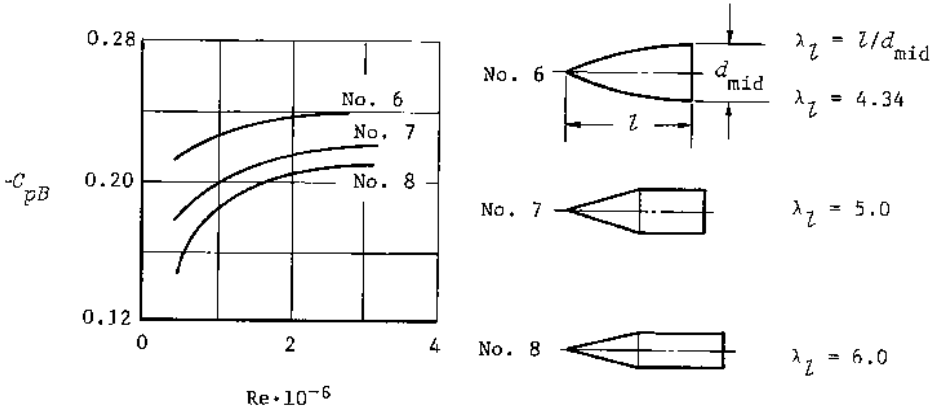

Fig. 135--Variation of base pressure coefficient with Reynolds number for models with different fineness ratios

The qualitative picture of the change in base pressure and the experimental data enable us to obtain several relations for approximate estimates of the base pressure and base drag coefficients. Theoretically, the limiting value of the base pressure coefficient is determined by that for an absolute vacuum, which for $\gamma = 1.4$ is given by

$$(C_{pB})_{vac} = -\frac{1.43}{M_\infty^2}. \tag{14.11}$$

In addition to the theoretical curve obtained from Eq. (14.11), experimental data are presented in Fig. 136 showing that the base pressure coefficient differs considerably from its limiting value under actual conditions. However, it appears that part of the experimental curve can be expressed by

$$C_{pB} = -k_B(C_{pB})_{vac}, \tag{14.12}$$

in which k_B is a correction factor. Studies show that k_B depends not only on M_∞ but also on the shape of the body, its fineness ratio, the Reynolds number, and the state of the boundary layer. The coefficient k_B becomes larger with an increase in M_∞ because of the increased rarefaction at the base.

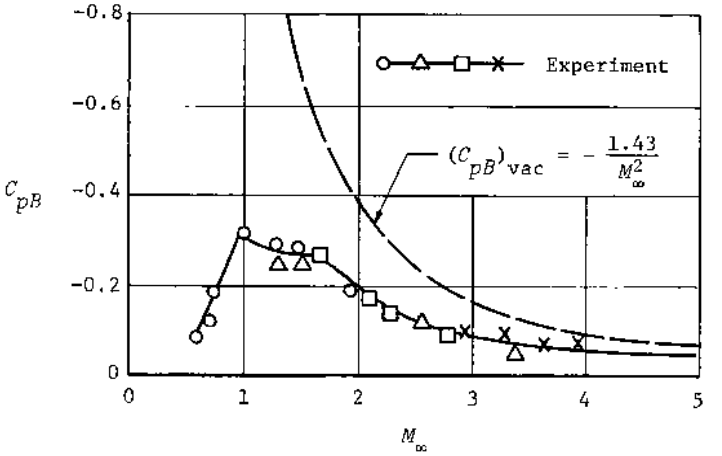

Fig. 136--Experimental and theoretical data for the base pressure coefficient

An analysis of the experimental data on the influence of the shape and the fineness ratio of the body leads to the conclusion that, with an increase in fineness ratio or a decrease in the base area ratio $\bar{S}_B$, the coefficient k_B decreases. The effect of fineness ratio on base pressure is the same as that discussed above for subsonic velocities, wherein the boundary layer on the body shields the base area from the ejector action of the free stream, resulting in less pressure decrease behind the body. The thickness of the boundary layer relative to the body diameter increases in proportion to the fineness ratio of the body, so that the base pressure increases and the coefficient k_B decreases. Thus, k_B can be considered a function of the fineness ratio of the body. In the case of a body with a boattail, this effect increases with the degree of taper. The combined effects of fineness ratio and boattail on the base pressure can be estimated by assuming that the coefficient k_B is a function of an effective fineness ratio defined as $\lambda_{eff} = \lambda_l/\bar{S}_B$.

The turbulent boundary layer can be used to derive a specific relation for k_B. It was mentioned above that the base pressure depends little on the Reynolds number in the case of a turbulent boundary layer; therefore, as a first approximation it can be assumed that k_B is also independent of the Reynolds number.

It is also known that the shape of the body, particularly the configuration of the afterbody, has an influence on the base pressure even for identical tapering. This effect is most pronounced for small values of $\bar{S}_B$ and is associated with the formation of a shock wave rather than with viscosity. However, in most practical cases the boattailing is equivalent to values of $\bar{S}_B$ of 0.4 or more. Then, assuming that the afterbody is sufficiently streamlined so that the average slope of the contour does not exceed 8° to 10°, the base pressure can be estimated as a function of the boundary layer thickness at the base. In this case, the base pressure coefficient depends only on the effective fineness ratio at a given Mach number. On the basis of the experimental data, an empirical equation for estimating the coefficient k_B can be written as

$$k_B = 0.8K_1(2 - K_1),$$

in which $K_1 = M_\infty/\lambda_{eff}$ represents the similarity parameter calculated from the value of the effective fineness ratio. Then, the base drag coefficient is

$$C_{DB} = \frac{1.144K_1(2 - K_1)\bar{S}_B}{M_\infty^2}. \tag{14.13}$$

This relation reflects the fact, noted above, that the pressure at the base decreases with an increase in Mach number. In practice, an absolute vacuum occurs at the base for high Mach numbers, corresponding to values of the similarity parameter $K_1 \gg 1$, and the base drag coefficient can be calculated from the equation

$$C_{DB} = \frac{1.43\bar{S}_B}{M_\infty^2}. \tag{14.13a}$$

In other cases, when $K_1 \leq 1$, the calculation is made from Eq. (14.13). It should be emphasized that this equation is applicable only to pointed bodies of revolution with rather large fineness ratios and with a boattail taper not less than $\bar{S}_B = 0.4$ to 0.5.

Because these formulas for C_{DB} are based on agreement with turbulent

boundary layer experiments, they are suitable only for order of magnitude estimates when applied to the laminar regime. Experimental measurements on wind-tunnel models are usually used in those cases where more accurate information on the base pressure is required.

For example, experimental studies were made of the base pressure on a body of revolution with an operating nozzle, i.e., under conditions corresponding to an operating rocket engine. In these studies, it was established that the pressure on the base of the body depends substantially on the pressure at the exit section of the nozzle for a given free-stream Mach number. The greater the pressure at the exit section, the greater the pressure on the base.

The base pressure also depends on the parameters of the incident flow--its velocity and static pressure. During the investigation of this dependence, the following characteristics were observed:

1. For a pressure of 1 kgf/cm^2 at the nozzle exit and a static pressure in the tunnel of 0.4 kgf/cm^2 (M_∞ = 1.87), the pressure on the annulus was less than static.
2. When the nozzle exit pressure was maintained at 1 kgf/cm^2 and the tunnel static pressure lowered to 0.16 kgf/cm^2 (increasing M_∞ to 2.5), the excess pressure on the annulus was zero.
3. When the static pressure in the tunnel was reduced still more, reaching 0.1 kgf/cm^2 (the flow in the tunnel was accelerated to M_∞ = 3), the pressure on the annulus was greater than the free-stream static value. The flow velocity in the tunnel was equal to or slightly greater than the velocity in the exhaust jet from the nozzle. The resultant difference between the values of static pressure at the nozzle exit and in the tunnel caused intermixing of gas at the base and an increase in base pressure.

The first of the phenomena described occurs in practice for an operating engine when the pressure at the nozzle exit equals the static pressure in the flow or does not differ significantly from it. If the pressure at the nozzle exit is less than the free-stream pressure, the resultant expansion can be even greater than that which occurs with a nonoperating engine.

From these results, it is evident how complex the investigations of the phenomena at the base can be in the presence of an expanding rocket jet. As yet, it is impossible to state any kind of an analytical method for the quantitative estimate of base pressure in this case. However, for the special case of an engine nozzle operating at conditions near those of the calculations above, Eq. (14.13) can be used for an approximate estimate of the base drag coefficient after substituting for $\bar{S}_B$ the value $\bar{S}_{an} = S_{an}/S_{mid}$, where S_{an} is the area of the base annulus or, in general, the area of that part of the base not occupied by the nozzle.

The influence of angle of attack on base pressure has been studied under experimental conditions and was shown to be insignificant for small angles of attack for both jet on and jet off. In both cases, a tendency toward some reduction in pressure with increasing angle of attack has been observed.

TOTAL DRAG

The determination of the total drag coefficient of a body of revolution amounts to the computation of its separate components with the subsequent summation. Generally, the total drag coefficient for a zero angle of attack is a function of body shape, Mach number, Reynolds number, and the state of the boundary layer. The curves in Fig. 137 indicate the character of this dependence on the last two factors. Comparing these curves with the base pressure measurements in Fig. 134, it appears that base drag is usually the largest component of the total drag in the case of a laminar boundary layer, although in the case of the body with the largest amount of boattailing the predominant component is the fore drag.

In the case of turbulent flow, the drag of Model No. 1 is less than for laminar flow, despite the increase in the friction coefficient, because of the sharp reduction in base drag. The total drag coefficient of Model Nos. 2, 3, and 4 is increased somewhat in comparison with laminar flow because the friction drag increase is greater than the reduction in base drag.

Thus, the necessity for accounting for the state of the boundary layer in calculating the total drag is evident from the experimental

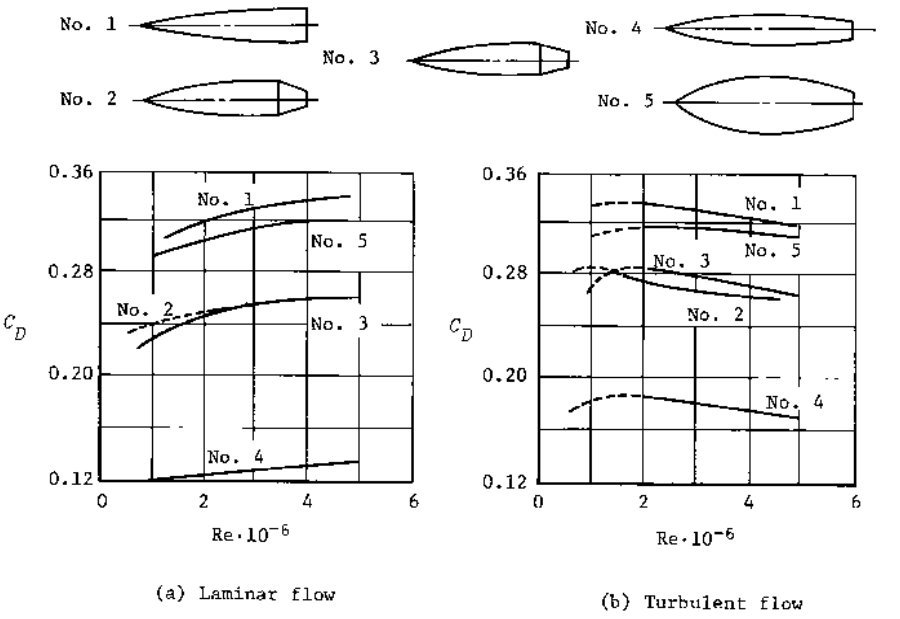

Fig. 137--Total drag coefficient as a function of Reynolds number at $M_\infty = 1.5$

data. As another example, the total drag for Model No. 2 at Re = $2 \cdot 10^6$ for a turbulent boundary layer is larger by 15 percent than for the laminar regime, due to the dissimilar character of the flow separation in the two cases and also to the different values of the components of drag due to pressure and friction. Evidently, despite the increase in base drag in the laminar regime, the total drag is reduced as a result of the decrease in skin friction.

Thus, the calculation of the fore drag must begin with the determination of the type of boundary layer, laminar or turbulent. It can be assumed that the transition Reynolds number is approximately $6.5 \cdot 10^6$. It must be kept in mind that the boundary layer on the body surface will generally be mixed: On the front part, it will be laminar, and on the remaining portion, including the afterbody, it will be turbulent.

The geometric extent of the laminar boundary layer is defined by the area ratio S_L/S_w, which appears in Eq. (14.4). If it is assumed

that $S_L/S_w \approx x_L/l$, then for $Re_{tr} = 6.5 \cdot 10^5$, the area ratio $S_L/S_w = 6.5 \cdot 10^6\ Re^{-1}$, where $Re = V_\infty l/\nu$ is based on the total length of the body l. It should be remembered that this estimate of the state of the boundary layer must be considered an approximation to the actual flow regimes.

As yet, there are no valid experimental data, based on actual tests in the atmosphere at various altitudes, for the determination of dependable criteria for estimating the extent of the laminar boundary layer. Therefore, in practical cases, the aerodynamic calculation must be made on the basis of transition Reynolds numbers obtained in wind tunnels. However, this probably represents the lower limit of the actual transition Reynolds number because flow around a body in motion in the atmosphere is considerably more favorable than that in a wind tunnel where, as was mentioned earlier, premature turbulence results from the interaction between the boundary layer and the shock waves reflected from the tunnel wall. Therefore, it must be assumed that the laminar layer on the fore part of the body will extend farther under natural conditions than it does on a wind-tunnel model.

In addition, it has been established experimentally that the stability of the laminar regime increases with an increase in Mach number and, consequently, the transition Reynolds number increases. The value of $Re_{tr} = 6.5 \cdot 10^6$ used above was obtained for a Mach number of about 2. Thus, for Mach numbers less or greater than 2, the values of Re_{tr} will be correspondingly smaller or larger.

The methods discussed for the calculation of the components of drag and their sum are confirmed by experimental research. The particular flow conditions can be reproduced in aerodynamic facilities, and the test results can then be compared with the theoretical results. A comparison is presented in Fig. 138 of data obtained for a completely turbulent boundary layer, and it is evident that the theoretical results are close to the experimental data for symmetric flow. Experimental curves for tests at angle of attack are plotted in the same figure. The drag increases with an increase in α, but at small angles of attack, e.g., $\alpha = 2°$, the increase is negligibly small.

Using the data of Fig. 138, it can be verified that the additional drag due to asymmetric flow depends on the square of the angle of attack.

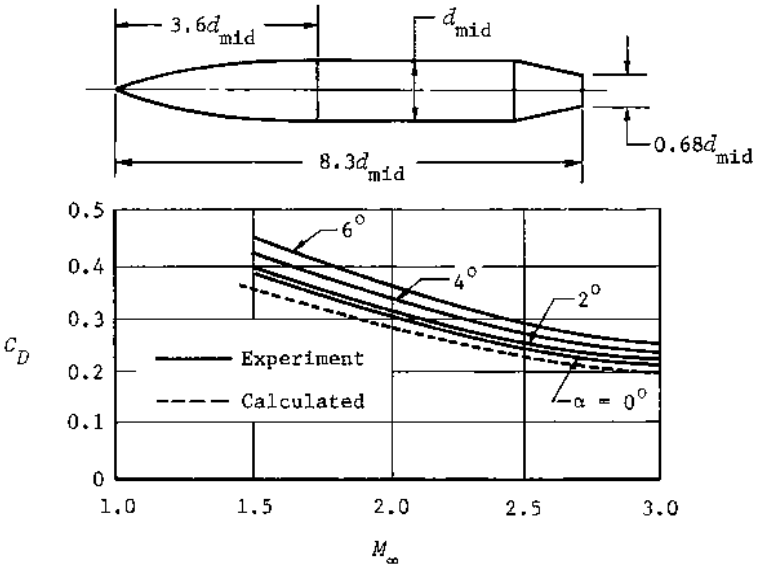

Fig. 138--Total drag coefficient as a function of Mach number for a turbulent boundary layer

As already noted, the major component of the drag coefficient is determined by the axial force coefficient C_A, which can be considered independent of the angle of attack and equal to the drag coefficient in symmetric flow.

In testing models in wind tunnels, the quantity C_A is measured directly using aerodynamic balances. The measurements allow us to verify a series of assumptions that can be used in practical calculations, e.g., the hypothesis that the axial force coefficient is independent of angle of attack for small α.

Also important is the confirmation of the assumption concerning the small influence of both the geometric shape and the dimensions of the composite parts of a body of revolution on the axial force in specific cases. For example, if the length of the cylindrical part of the body is sufficiently great (8 to 10 diameters and greater), the nose shape has practically no influence on the value of C_A. If the fineness ratio

of the nose is large, it is not an important variable in determining the drag. However, the nose section does influence the value of C_A for nose fineness ratios less than 1.5 to 2 for conical noses and 3 to 4 for parabolic noses, and with further decreases in the fineness ratio the effects increase noticeably. The increase in drag for small fineness ratios can be attributed to the formation of a detached shock wave at the appropriate velocity.

If the drag coefficient of a rather long body is plotted as a function of the nose fineness ratio, the drag coefficient decreases rapidly as the fineness ratio varies from 0 (blunt body) to 1.5 to 2 and then decreases very little for further increases in fineness ratio. This is due to the fact that the pressure drag on a nose of large fineness ratio is a very small component of the overall balance of forces acting on the body. Therefore, variations in nose drag do not have an important influence on the total drag, the major components of which are base drag and skin friction drag.

Chapter V

LIFT OF SLENDER BODIES OF REVOLUTION IN LINEARIZED FLOW

Editor's Introduction

THE BASIC RELATIONS FOR LINEARIZED FLOW *about a body of revolution at angle of attack are developed in Section 15 by extending the method used for symmetrical flow in Section 13, which produces a group of tabulated functions related to those of the previous chapter. These solutions appear to be equivalent in accuracy to those of Van Dyke.*[3]

Although Krasnov discusses the additional normal force induced on a cylinder following a pointed nose, he gives no quantitative data on this effect and implies that it can usually be neglected in practice. Actually, the increase in the initial normal force slope due to the addition of a cylinder behind the nose can be quite significant, as has been shown by Syvertson and Dennis.[1] *For example, for a cone with a fineness ratio of 3 at a Mach number of 3, the addition of a cylinder five diameters long increases the initial normal force slope* ($\partial C_N/\partial\alpha$ *at* $\alpha = 0$) *from* 1.83 *to* 3.21 *per radian. For an ogive nose of the same fineness ratio and for the same conditions, the change is from* 2.19 *to* 3.18 *per radian. Syvertson and Dennis detail the methods for calculating these effects and present numerous summary charts for the normal force slope and the center-of-pressure coefficient at* $\alpha = 0$ *for cone-cylinders and ogive-cylinders.*

The discussion of viscous crossflow is similar to that of Allen and Perkins (NACA Report 1048, *1951). Some later developments in the crossflow theory also deserve mention. For example, Kelly* (J. Aero. Sci., *August 1954), Perkins and Jorgensen* (NACA TN 3716, *May 1956), Phythian and Dommett* (J. Royal Aero. Soc., *July 1958), and Mello* (J. Aero. Sci., *March 1959) have tried to improve the basic theory of Allen and Perkins by using the analogy between the separated flow about an inclined body of revolution and the impulsive development of flow about a circular cylinder. The results of Jorgensen and Perkins* (NACA RM A55E31, *August 1955) and of Mello indicate that a pair of vortices form on the lee side of the body, and that these vortices move forward on the body as the angle of attack increases. The approximate location of the origin of the vortices is shown in the figure below, where* x_{sep} *is measured from the nose-cylinder junction. Although the data in the cited references do not indicate that the vortices extend onto the nose, this would be expected at the higher angles of attack, particularly for noses of high*

fineness ratio. The recent results of Sarpkaya (AIAA J., March 1966) provide definitive values for the time variation of the drag coefficient of a circular cylinder starting impulsively from rest. A summary curve from Sarpkaya's article is shown below, transformed into the coordinates of the inclined body of revolution. These results can be applied to the estimation of normal force by replacing the coefficient c in Eq. (15.30) by c_{dc} and rewriting the equation as

$$C_{Nf} = \frac{2 \sin^2 \alpha}{\pi r_{mid}^2} \int_{x_{sep}}^{l} c_{dc}\, r\, dx. \qquad (15.30a)$$

A similar change should be made in the equation for pitching moment on page 439.

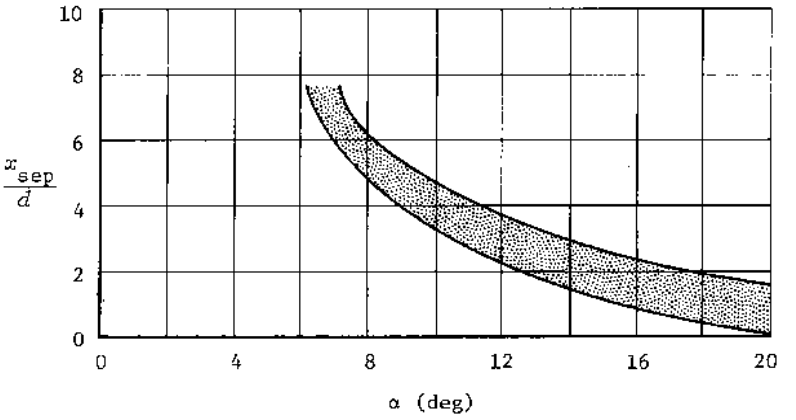

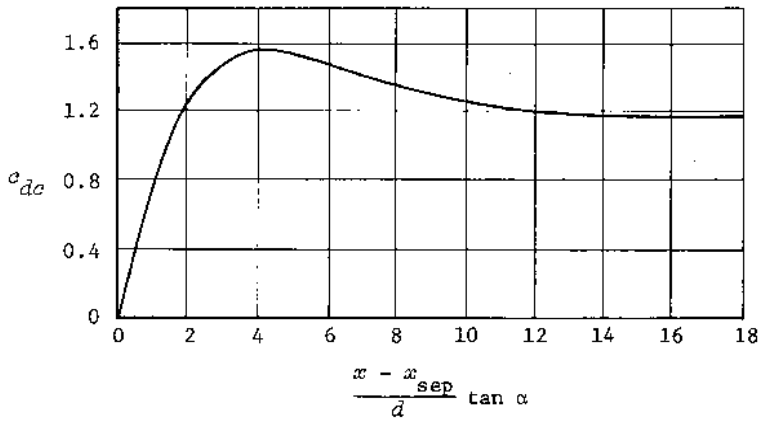

§ 15. *DETERMINATION OF THE NORMAL FORCE COEFFICIENT, PITCHING MOMENT, AND CENTER OF PRESSURE*

PRESSURE DISTRIBUTION IN ASYMMETRIC FLOW

Basic Relations

THE BASIC PROBLEM in asymmetric flow involves the determination of the additional pressure coefficient C_{p2} that results from the unsymmetric nature of the flow. In turn, this depends on the solution of the differential equation, Eq. (13.2), for the perturbation potential φ_2 of the crossflow, which is given in general form by Eq. (13.9). The total value of the pressure coefficient in asymmetric flow is $C_p = C_{p1} + C_{p2}$, where C_{p1} depends only on the variables x and r, and C_{p2} depends additionally on the variable ϕ.

The normal force coefficient in linearized flow is given by Eq. (1.12):

$$C_{Np} = -\frac{4\lambda_l}{\pi}\int_0^1 \bar{r}\, d\bar{x}\int_0^{\pi} C_{p2}\cos\phi\, d\phi. \tag{15.1}$$

Thus, the normal force coefficient depends only on the asymmetric flow conditions. It is necessary to find the distribution of C_{p2} to determine the normal force coefficient, and, as was noted, this is related to the computation of the perturbation potential φ_2. The expression for this potential can be derived from Eqs. (13.9) and (13.23) as

$$\varphi_2 = \beta\cos\phi\int_0^{\operatorname{arc\,cosh} x/\beta r} \hat{f}(x - \beta r\cosh z)\cosh z\, dz. \tag{15.2}$$

Changing from the variable z to $\zeta = x - \beta r\cosh z$ in this expression

and introducing the notation $m(\xi) = \dot{f}(\xi)$, we obtain

$$\varphi_2 = \frac{\cos\phi}{r} \int_0^{x-\beta r} \frac{m(\xi)(x-\xi)\,d\xi}{\sqrt{(x-\xi)^2 - \beta^2 r^2}}. \tag{15.3}$$

The physical interpretation of Eq. (15.3) involves the assumption that the body can be replaced by a system of doublets distributed along its axis. The additional perturbation of the doublets is assumed to be equivalent to the perturbation introduced into the flow by the body. The quantity φ_2 represents the potential of the doublets and the function m defines their distribution. In replacing the body by doublets distributed along its axis, the nature of the propagation of disturbances in supersonic flow must be considered; i.e., the perturbations are propagated only downstream within the limits of the cone of disturbance.

The solution for inclined flow is obtained by selecting the function m so that the potential φ_2 satisfies the boundary condition given by Eq. (13.7a) on the body surface.

The basic relations for asymmetric flow can be developed from Eq. (15.2) by first replacing $\dot{f}$ by m and using the symbol $u = x/\beta r$:

$$\varphi_2 = \beta \cos\phi \int_0^{\operatorname{arc\,cosh} u} m(x - \beta r \cosh z) \cosh z\, dz. \tag{15.2a}$$

Differentiating Eq. (15.2a), first with respect to x and then with respect to r, we find

$$\varphi_{2x} = V_x' = \beta \cos\phi \int_0^{\operatorname{arc\,cosh} u} \dot{m}(x - \beta r \cosh z) \cosh z\, dz, \tag{15.4}$$

$$\varphi_{2r} = V_r = -\beta^2 \cos\phi \int_0^{\operatorname{arc\,cosh} u} \dot{m}(x - \beta r \cosh z) \cosh^2 z\, dz, \tag{15.5}$$

where $\dot{m}$ is the derivative of m with respect to the argument $x - \beta r \cosh z$.

For simplicity, we will assume that the perturbation velocities are made dimensionless with respect to the free-stream velocity V_∞. Comparing Eq. (15.5) with Eq. (13.7a) for the boundary condition, we obtain

the equation

$$\alpha = \beta^2 \int_0^{\operatorname{arc\,cosh} u} \dot{m}(x - \beta r \cosh z) \cosh^2 z \, dz, \tag{15.6}$$

which can be used to determine the function $m(\xi)$.

The pressure coefficient corresponding to the crossflow is obtained from Eq. (13.13a) and Eq. (15.4) for the additional axial velocity component:

$$C_{p2} = -2\beta \cos \phi \int_0^{\operatorname{arc\,cosh} u} \dot{m}(x - \beta r \cosh z) \cosh z \, dz - \alpha^2(4 \sin^2\phi - 1). \tag{15.7}$$

The quadratic term in α improves the accuracy of this expression for the pressure coefficient; if the angle of attack is very small, this term can be neglected, giving

$$C_{p2} = -2\beta \cos \phi \int_0^{\operatorname{arc\,cosh} u} \dot{m}(x - \beta r \cosh z) \cosh z \, dz. \tag{15.7a}$$

The Calculation of the Flow Parameters

One method of calculation is based on the use, as a first approximation, of the distribution law of doublets along the axis of a very slender body. The form of the function $m(x)$ is found from the condition of continuous crossflow as given by Eq. (15.5). Converting to the variable $\xi = x - \beta r \cosh z$, we obtain

$$\int_0^{x-\beta r} \frac{\dot{m}(\xi)(x - \xi)^2 \, d\xi}{\sqrt{(x - \xi)^2 - \beta^2 r^2}} = \alpha r^2.$$

For very slender bodies (for which r is very small), the integral can be assumed, in a first approximation, to be equal to its value for $r \to 0$. Then $\alpha r^2 = \int_0^x \dot{m}(\xi)(x - \xi) \, d\xi$. Integrating by parts, and noting that $m(0) = 0$ at the tip, we obtain the equation $\int_0^x m \, dx = \alpha r^2$. From this we can find the distribution law of the doublets along the axis of a very slender body in the form $m = 2\alpha r(dr/dx)$. It is of interest that this law has the same form as the law of the distribution of sources.

This relation for m can be used for the flow calculation of a body that is less slender in the same way as was done in § 13 with the first approximation for the distribution of sources in the symmetrical case. As an illustration, let us consider the case of flow around a parabolic body. Using the expression obtained above for the function m, we can find the derivative $\dot{m}(\xi)$. Correcting this expression by introducing the constant coefficients a_0 and a_1, we obtain

$$\dot{m}(\xi) = \alpha\left[a_0 + a_1\left(\xi - \frac{\xi^2}{2}\right)\right]. \tag{15.8}$$

Converting from ξ to z and setting $\bar{m} = \beta r$, we find

$$\dot{m}(x - \beta r\cos z) = \alpha\left\{a_0 + a_1\bar{m}(u - \cos z)\left[1 - \frac{1}{2}\bar{m}(u - \cos z)\right]\right\}. \tag{15.9}$$

Introducing this expression for $\dot{m}$ into Eq. (15.6) and integrating, we obtain a second approximation to the continuous flow condition:

$$a_0 j_r^0 + a_1\left(j_r^1 - \frac{1}{2}\bar{m}j_r^2\right) = \frac{1}{\beta}. \tag{15.10}$$

The coefficient a_0 can be determined from Eq. (15.10) for conditions at the conical tip ($x = \xi = 0$), and a_1 is found by evaluating the boundary condition at an arbitrary point on the surface. As a result we find the equations

$$a_0 = \frac{1}{\beta(j_r^0)_0}, \qquad a_1 = \frac{\frac{1}{\beta} - a_0 j_r^0}{j_r^1 - \frac{1}{2}\bar{m}j_r^2}. \tag{15.11}$$

In Eqs. (15.10) and (15.11), j_r^n represents a function that depends only on the parameter $u = x/\beta r$. In the special case for the conical tip, the function $(j_r^0)_0$ depends on the parameter $u = u_0 = 1/\beta\delta_0$.

To obtain the relation for the axial component of the perturbation velocity in the crossflow, Eq. (15.9) can be substituted into Eq. (15.4) and the result integrated to give

$$V_x' = \frac{\alpha \cos \phi}{8} \left\{ \frac{j_x^0}{(j_r^0)_0} + \frac{j_x^1 - \frac{1}{2}\bar{m} j_x^2}{j_r^1 - \frac{1}{2}\bar{m} j_r^2} \left[1 - \frac{j_r^0}{(j_r^0)_0} \right] \right\}, \tag{15.12}$$

where j_x^n is a function of the same parameter u. The functions j_r^n and j_x^n are analogous to the functions i_r^n and i_x^n investigated in the study of symmetric flow.

Including terms to the third power in ξ in Eq. (15.8) for $\dot{m}(\xi)$, we obtain relations for Eqs. (15.4) and (15.5) that contain the functions

$$\begin{aligned} j_x^0 &= I_1, \qquad j_x^1 = uI_1 - I_2, \qquad j_x^2 = u^2 I_1 - 2uI_2 + I_3, \\ j_x^3 &= u^3 I_1 - 3u^2 I_2 + 3uI_3 - I_4, \end{aligned} \tag{15.13}$$

$$\begin{aligned} j_r^0 &= I_2, \qquad j_r^1 = uI_2 - I_3, \qquad j_r^2 = u^2 I_2 - 2uI_3 + I_4, \\ j_r^3 &= u^3 I_2 - 3u^2 I_3 + 3uI_4 - I_5, \end{aligned} \tag{15.14}$$

where the function I_n represents an integral of the form of Eq. (13.35). It will be noticed that the functions j_x^n are identical to the corresponding functions i_r^n introduced in the symmetric case. The values of the other functions j_r^n have been calculated from Eqs. (15.14) as a function of u and are presented in Table 17. In Tables 16 and 17 the functions are tabulated for values of u up to 8.8. Applications to long slender bodies at low Mach numbers may require additional values of u, in which case the functions must be computed from Eqs. (13.36), (15.13), and (15.14) and added to the tables.

The determination of the additional velocity component V_x' for given values of α and $\cos \phi$ from Eq. (15.12) requires the computation of the functions j_x^n, j_r^n, and the parameter $\bar{m}$ at the point in question, as well as the quantity $(j_r^0)_0$ at the tip of the cone. The additional value of the pressure coefficient can be found from

$$C_{p2} = -2\alpha \left(\frac{V_x'}{\alpha \cos \phi} \right) \cos \phi - \alpha^2 (4 \sin^2 \phi - 1), \tag{15.15}$$

Table 17

VALUES OF THE FUNCTIONS $j_r^n(u)$

u	j_r^0	j_r^1	j_r^2	j_r^3
1	0.0000	0.0000	0.0000	0.0000
1.1	0.4736	$0.3090 \cdot 10^{-1}$	$0.2300 \cdot 10^{-2}$	$0.1173 \cdot 10^{-3}$
1.2	0.7090	0.8394	$0.1450 \cdot 10^{-1}$	$0.3326 \cdot 10^{-2}$
1.3	0.8824	$0.1719 \cdot 10^{0}$	0.4021	$0.1031 \cdot 10^{-1}$
1.4	$0.1120 \cdot 10$	0.2688	$0.8462 \cdot 10^{-1}$	0.2862
1.6	0.1523	0.5378	$0.2446 \cdot 10^{0}$	$0.1191 \cdot 10^{0}$
1.8	0.1894	$0.8758 \cdot 10^{0}$	0.5519	0.4409
2.0	0.2391	$0.1317 \cdot 10$	$0.9632 \cdot 10^{0}$	$0.7850 \cdot 10^{0}$
2.4	0.3380	0.2467	$0.2450 \cdot 10$	$0.2740 \cdot 10$
2.8	0.4506	0.4039	0.5024	$0.7103 \cdot 10$
3.2	0.5780	0.6092	$0.9040 \cdot 10$	$0.1538 \cdot 10^{2}$
3.6	0.7202	$0.8682 \cdot 10$	$0.1491 \cdot 10^{2}$	0.2954
4.0	$0.8778 \cdot 10$	$0.1187 \cdot 10^{2}$	0.2309	0.5209
4.4	$0.1051 \cdot 10^{2}$	0.1573	0.3409	$0.8609 \cdot 10^{2}$
4.8	0.1239	0.2030	0.4844	$0.1330 \cdot 10^{3}$
5.2	0.1443	0.2566	0.6678	0.2040
5.6	0.1663	0.3187	$0.8974 \cdot 10^{2}$	0.2974
6.0	0.1899	0.3899	$0.1180 \cdot 10^{3}$	0.4214
6.4	0.2150	0.4708	0.1524	0.5831
6.8	0.2417	0.5621	0.1936	$0.7899 \cdot 10^{3}$
7.2	0.2700	0.6644	0.2426	$0.1051 \cdot 10^{4}$
7.6	0.2999	0.7783	0.3002	0.1376
8.0	0.3313	$0.9045 \cdot 10^{2}$	0.3674	0.1779
8.4	0.3644	$0.1044 \cdot 10^{3}$	0.4453	0.2262
8.8	$0.3990 \cdot 10^{2}$	$0.1196 \cdot 10^{3}$	$0.5348 \cdot 10^{3}$	$0.2849 \cdot 10^{4}$

where the ratio $V'_x/(\alpha \cos \phi)$ is independent of $\alpha \cos \phi$ and is determined from Eq. (15.12).

This method of calculation for asymmetric flow can be simplified, as in the symmetric case, by using the results of the theory of flow around very slender bodies. This theory is based on the assumption that, in determining the distribution law for doublets (e.g., in the form of Eq. (15.8)), there is no need for correction through use of the coefficients a_0 and a_1. The function m can then be represented in the form $m = (a/\pi)S'(x)$ and its derivative as $\dot{m} = (a/\pi)S''(x)$ for very slender bodies. Accordingly, the additional axial velocity component is

$$V'_x = \frac{\beta\alpha}{\pi} \cos \phi \int_0^{\operatorname{arc\,cosh} u} S''(x - \beta r \cosh z) \cosh z \, dz. \quad (15.16)$$

Let us consider the use of this relation for the calculation of the flow around a body of revolution with a parabolic shape, for which the second derivative S'' is given by Eq. (13.45). Substituting this expression under the integral of Eq. (15.16), we obtain

$$V'_x = \frac{\beta\alpha}{\pi} \Omega_3 \cos \phi, \quad (15.17)$$

where

$$\Omega_3 = \int_0^{\operatorname{arc\,cosh} u} S''(x - \beta r \cosh z) \cosh z \, dz$$

$$= \frac{\pi}{\lambda_N^2} \left(2\dot{\imath}_r^0 - \frac{6\bar{x}\dot{\imath}_r^1}{u} + \frac{3\bar{x}^2\dot{\imath}_r^2}{u^2} \right). \quad (15.18)$$

To compare the results obtained from Eqs. (15.12) and (15.17), let us compute the values of V'_x at the conical tip. The corresponding expressions are written (with $\delta_0 = 1/\lambda_N$):

$$V'_x = \frac{\alpha}{\beta} \frac{(\dot{\imath}_r^0)_0}{(\dot{\jmath}_r^0)_0} \cos \phi, \qquad V'_x = 2\beta\alpha\delta_0^2 (\dot{\imath}_r^0)_0 \cos \phi, \quad (15.19)$$

where

$$(i_r^0)_0 = \sqrt{u_0^2 - 1}, \qquad (j_r^0)_0 = \frac{1}{2}\left(u_0\sqrt{u_0^2 - 1} + \operatorname{arc\,cosh} u_0\right). \quad (15.20)$$

Comparison shows that the second equation for V_x' in Eq. (15.19) can be obtained from the first for a sufficiently slender cone, when the function $(j_r^0)_0$ can be approximated by $u_0^2/2$. The first relation for V_x' is a better approximation for the solution of the asymmetric flow problem.

Equation (15.19) also enables us to estimate the order of magnitude of the additional axial velocity component for asymmetric flow. In particular, it follows from the second equation for V_x' that, since $(i_r^0)_0 \sim u_0 = 1/\beta\delta_0$, the axial component is of the order of $V_x' \sim \alpha\delta_0$. This result for a cone can be extended to any slender body, indicating that the additional perturbation velocity component is of the order $V_x' \sim \alpha\tau$. Thus, the perturbations in the axial direction are of second order compared to unity.

The experimental data confirm the rather satisfactory results obtainable by this method of calculation. This is particularly evident in Fig. 139, where the results of the calculation of the function $V_x'/(\alpha \cos \phi)$ by Eq. (15.12) are compared with experimental data at a meridian angle $\phi = 30°$. An analysis of the results indicates that this equation can be used to estimate velocity and pressure even on the boattail of a body. Available data confirm the possibility of similar calculations for other tail shapes (e.g., flared or cylindrical shapes as shown in Fig. 140), although the afterbody should be slightly flared or convergent to maintain the linearized character of the flow.

The Similarity Law

According to Eq. (15.17), the function $V_x'/(\alpha \cos \phi)$ depends only on the parameter u at a given point. In § 13 it was shown that this parameter, in turn, was a function of its value u_0 at the cone tip and a function of the variable $\bar{x}$, i.e., $u = u_0 h(\bar{x})$. Since the function $(j_r^0)_0$ depends on the same parameter, u_0, we can write the general expression for the additional pressure coefficient from Eqs. (15.15) and (15.17):

$$C_{p2} = -2\alpha\delta_0 G(u_0, \bar{x}) \cos \phi - \alpha^2(4 \sin^2\phi - 1), \quad (15.21)$$

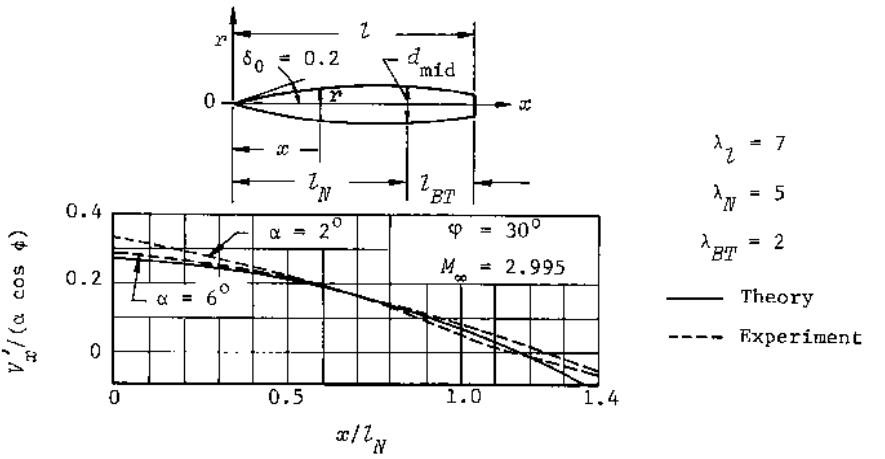

Fig. 139--Longitudinal distribution of $V'_x/(\alpha \cos \phi)$ on a parabolic body of revolution

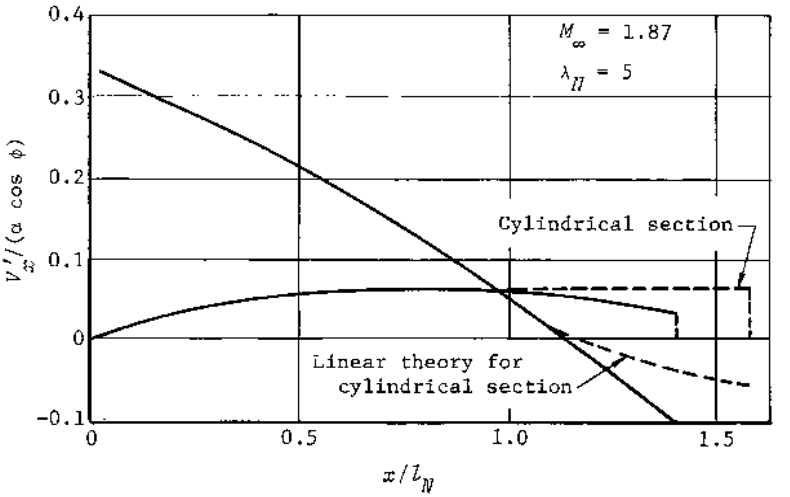

Fig. 140--Longitudinal distribution of $V'_x/(\alpha \cos \phi)$ on a body of revolution

where C is a function dependent on u_0 for a given point on the surface.

For the case of a high Mach number and a parabolic body with fineness ratio $\lambda_N = 1/\delta_0$, Eq. (15.21) can be written as

$$\frac{p_2}{p_\infty} - 1 = \alpha\lambda_N K_1^2 B_1(K_1, \bar{x}) \cos\phi - \frac{\gamma}{2}(\alpha\lambda_N)^2 K_1^2(4\sin^2\phi - 1), \quad (15.22)$$

where B_1 is a function of the body station and the parameter K_1. After designating the parameter $\alpha\lambda_N$ by K_2, Eq. (15.22) can be written in the general form

$$\frac{p_2}{p_\infty} - 1 = B(K_1, K_2, \bar{x}, \phi). \quad (15.22a)$$

It is evident from this equation that the pressure at a given point depends on the parameters K_1 and K_2, which are the similarity parameters for flows around slender bodies of revolution at an angle of attack.

According to Eqs. (1.12) and (1.19), the normal force and pitching moment coefficients will depend on these same parameters:

$$M_\infty^2 C_{Np} = E(K_1, K_2), \qquad M_\infty^2 C_{mp} = F(K_1, K_2). \quad (15.23)$$

DETERMINATION OF THE NORMAL FORCE COEFFICIENT

Body of Revolution of Arbitrary Shape

If the distribution of the additional pressure coefficient C_{p2} is known for asymmetric flow, the normal force coefficient can be computed. Using Eq. (15.1) and observing that $\int_0^\pi (4\sin^2\phi - 1)\cos\phi\, d\phi = 0$, we obtain

$$C_{Np} = 4\lambda_N \alpha \int_0^{l/l_N} \frac{V_x'}{\alpha\cos\phi} \bar{r}\, d\bar{x}, \quad (15.24)$$

where $\bar{x} = x/l_N$. For the special case of a parabolic body, this equation can be converted to the form

$$C_{Np} = 4\lambda_N \alpha \int_0^{t_l} \frac{V'_x}{\alpha \cos \phi}\, dt, \tag{15.24a}$$

where $t = \bar{x}^2(1 - \bar{x}/3)$.

The integrals that enter into this equation can be determined numerically or graphically. As an example, let us find the coefficient C_{Np} of the body for which the distribution of the function $V'_x/(\alpha \cos \phi)$ is presented in Fig. 140. The graphical integration (Fig. 141) gives the value $C_{Np} = 2\alpha$. It can be seen from the figure that the afterbody creates a negative normal force, which would decrease (in magnitude) if the tail were a straight cylinder.

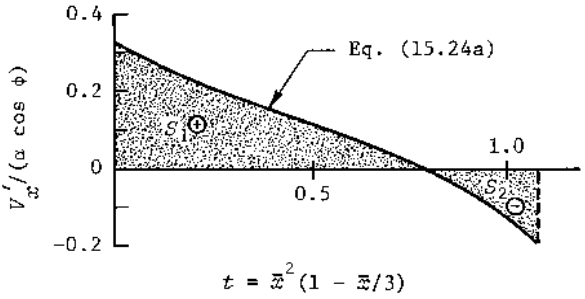

Fig. 141--Graphical integration for the normal force coefficient

The change in the function $V'_x/(\alpha \cos \phi)$ along the body is of practical interest. This function determines the elemental value of the normal force coefficient with respect to a unit length of the body according to the equation

$$\frac{V'_x}{\alpha \cos \phi} = \frac{1}{4\alpha\lambda_N \bar{r}} \frac{dC_{Np}}{d\bar{x}}. \tag{15.25}$$

From Fig. 142, it can be seen that, at a length of about two diameters from the end of the nose, the elemental value of the normal force coefficient is equal to zero, and then becomes negative on the afterbody,

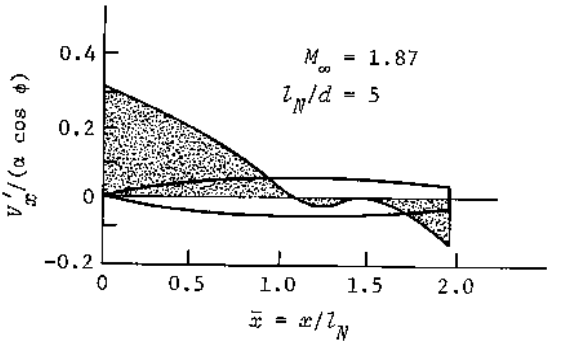

Fig. 142--Longitudinal distribution of $V_x'/(\alpha \cos \phi)$ for a segmented body of revolution

increasing negatively toward the base. In practice, the influence of the cylindrical midsection on the normal force is slight. The effect of the afterbody can be important in those cases where the length and taper are sufficiently great.

Studies show that the normal force coefficient of slender bodies at small angles of attack is almost independent of Mach number and fineness ratio. For example, the results of tests on two bodies with nose fineness ratios of 3 and 5 at a Mach number of 5.05 are shown in Fig. 143. It is evident that C_{N_p} varies very little, although a small tendency toward an increase in the normal force coefficients is observed with an increase in the fineness ratio. The data presented in Fig. 143 indicate an almost linear dependence of C_{N_p} on angle of attack, approximating the form

$$C_{N_p} = 2\alpha. \tag{15.26}$$

It is noteworthy that linearized theory for very slender bodies of revolution gives this same value for the normal force coefficient. To show this, we must find the distribution of the pressure coefficient in the limiting case of an infinitely slender body, i.e., for $r \to 0$. This limiting case is considered in slender-body theory, as was noted previously. According to this theory, the pressure coefficient is given by the limiting value of C_{p_2} as $r \to 0$:

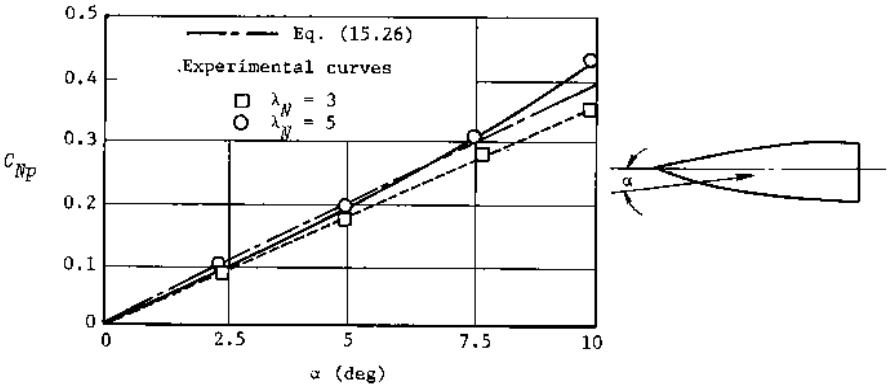

Fig. 143--Variation of normal force coefficient with angle of attack for $M_\infty = 5.05$

$$C_{p2} = -\frac{2\cos\phi}{r} m - \alpha^2(4\sin^2\phi - 1).$$

Since $m = 2\alpha r(dr/dx)$, the pressure coefficient is

$$C_{p2} = -4\alpha\cos\phi\frac{dr}{dx} - \alpha^2(4\sin^2\phi - 1). \tag{15.27}$$

Using this expression in Eq. (15.1), we obtain the relation

$$C_{Np} = 2\alpha\bar{S}_B, \tag{15.28}$$

which, in the absence of boattailing ($\bar{S}_B = 1$), agrees with Eq. (15.26).

Thus, slender-body theory gives the same linear dependence of the normal force coefficient on the angle of attack as was observed experimentally. Physically, this theory also correctly reflects the influence of the afterbody shape, which involves a decrease in C_{Np} with boattailing ($\bar{S}_B < 1$). It should be noted that the same experimental investigations showed that, for actual bodies that are not very slender, C_{Np} is more nearly proportional to the relative base diameter $\bar{d}_B$ than to the area ratio $\bar{S}_B$. Keeping this in mind, we shall nevertheless use the theoretical result of Eq. (15.28) in future discussions.

It has been shown in other studies that Eq. (15.26) can be used for approximate estimates of the normal force coefficients of comparatively short, slender bodies with fineness ratios of the order of 3 to 5.

The determination of the normal force coefficient of a body of revolution, representing the combination of a nose of some shape, an intermediate cylinder, and an afterbody, is of more interest for problems of a practical nature. If a body has a cylindrical afterbody, the nose is the major lifting element. Therefore, the normal force coefficient will depend on the geometric characteristics of the nose. Experiments show, for example, that the normal force coefficient increases with an increase in the fineness ratio of the nose, although the variation is slight for small changes in the geometric characteristics of rather pointed noses. The dependence of this coefficient on the shape of the pointed nose of bodies with cylindrical sections of identical relative lengths also has been verified experimentally. For example, the normal force coefficient is somewhat larger for a body with a parabolic nose than for a body with a conical nose of the same fineness ratio.

This dependence also results from the influence of the nose on the flow around the cylindrical section adjacent to it. A parabolic or ogival nose at high Mach numbers produces an additional negative normal force at a cylinder length of 2 to 3 diameters. Conversely, an additional positive normal force originates at the same length in the case of a conical nose, as is evident from Fig. 144. This force on the cylinder is due to the fact that a positive excess pressure is created on the lower portion and a negative excess pressure on the upper part. Although the pressure differential practically disappears at a distance of approximately three diameters behind the nose, the lifting portion of the cylinder creates an additional normal force larger than that in the case of a cylinder with a parabolic nose. The additional force is small enough in the latter case that it can be neglected in practice, but it can be significant for a body with a conical nose.†

Therefore, the normal force coefficient for cylindrical bodies with

†Editor's note: These effects can be evaluated both analytically and graphically from the results of the second-order shock-expansion theory of Syvertson and Dennis.(1)

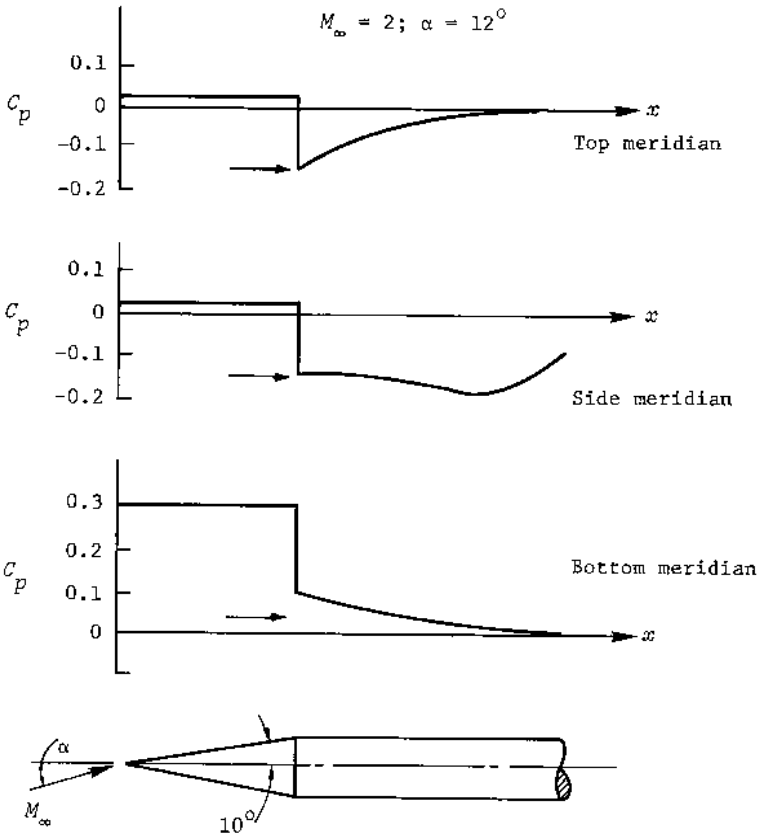

Fig. 144--Supersonic pressure distribution on a cone cylinder

parabolic or ogival noses can be calculated from Eq. (15.26). Based on comparisons with experiment, the same equation can be used for bodies with conical noses. Probably the agreement results from the fact that the decrease in the normal force on the cone, in comparison with a parabolic nose, is balanced by the increase on the cylindrical section.

If a cylindrical body is followed by an afterbody of some shape other than a cylinder, an additional normal force component occurs as the result of the redistribution of pressure on it. This component reduces the total

normal force if the afterbody converges ($\bar{S}_B < 1$) and results in an increase if the afterbody expands. Experimental research has shown that the normal force of the entire body including the afterbody can be estimated approximately from Eq. (15.28) in both cases. This formula does not account for the effects of Mach number on C_{Np}. Test data indicate some increase in the normal force coefficient with increasing Mach number, but the dependence is not large.

Effects of Viscosity

The estimate of normal force presented above does not account for the influence of friction. While this is justified for short bodies, the effects can be substantial for long bodies. In this case, an additional normal force originates as a result of flow separation on the upper part of the body, which corresponds to a cylinder in a crossflow of a viscous fluid with velocity $V_\infty \sin \alpha$ (Fig. 145).

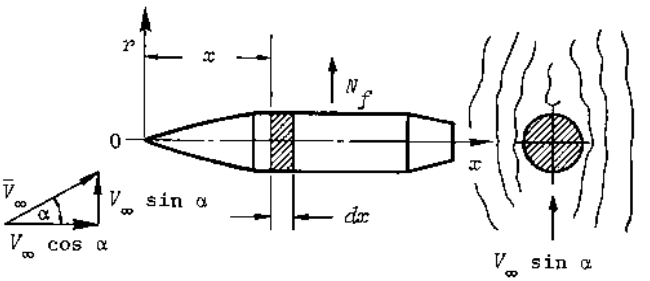

Fig. 145--Viscous crossflow at angle of attack

However, this phenomenon does not occur over the entire length. Observations have shown that the crossflow around the nose is essentially unseparated. Therefore, its influence on the creation of an additional normal force due to viscosity is significantly less than the influence of the cylinder and the afterbody.

For a surface element of length dx (see Fig. 145), the normal force due to viscosity is

$$dN_f = c\,\frac{\rho_\infty (V_\infty \sin\alpha)^2}{2}\,2r\,dx = \frac{\rho_\infty V_\infty^2}{2}\,\pi r_{\text{mid}}^2\,dC_{Nf}, \tag{15.29}$$

where c is a coefficient that can be determined by the flow conditions in the boundary layer. According to this expression,

$$dC_{Nf} = c\,\frac{2r}{\pi r_{\text{mid}}^2}\sin^2\alpha\,dx.$$

Integrating from l_n to l, we obtain

$$C_{Nf} = c\,\frac{2\sin^2\alpha}{\pi r_{\text{mid}}^2}\int_{l_N}^{l} r\,dx. \tag{15.30}$$

It should be noted that the point on the cylinder where flow separation begins, and thus where conditions occur leading to the creation of an additional normal force, is not necessarily exactly at the end of the nose. Consequently, the lower limit of the integral in Eq. (15.30) may be somewhat larger than l_N. However, since there are no reliable experimental or theoretical data on the location of this point, it can be assumed that the entire surface of the body behind the nose section is lifting.

If there is a tail section, there is no special need to calculate exactly the integral in Eq. (15.30), although it is not difficult to do. It is quite adequate to substitute a cylinder with a fineness ratio $\lambda_{BT} = l_{BT}/d_{\text{mid}}$ for the tail in this case. Accordingly,

$$C_{Nf} = c\,\frac{4}{\pi}\,(\lambda_{\text{cyl}} + \lambda_{BT})\sin^2\alpha, \tag{15.31}$$

where $\lambda_{\text{cyl}} = (l - l_N - l_{BT})/d_{\text{mid}}$ is the fineness ratio of the cylindrical part of the body. At small angles of attack, this equation can be approximated by

$$C_{Nf} = c\,\frac{4}{\pi}\,(\lambda_{\text{cyl}} + \lambda_{BT})\alpha^2. \tag{15.31a}$$

The value of the coefficient c depends on whether the boundary layer is

turbulent or laminar and on the Reynolds number, which can be computed from the expression $\mathrm{Re} = V_\infty d_{\mathrm{mid}}/\nu$. It has been established experimentally that c approximately equals 1 to 1.2 for laminar flow at $\mathrm{Re} = 5 \cdot 10^2$ to $2 \cdot 10^5$. As long as no other data are available, we can use this value for rough calculations at other Reynolds numbers and for turbulent flow.

The results of the calculation of $C_{Nf}/\sin^2\alpha$ from Eq. (15.31) are presented in Fig. 146a, and it can be seen that they agree well with the experimental data. Using these results for the normal force due to viscosity, the total normal force coefficient is given by

$$C_N = 2\bar{S}_B\alpha + c\,\frac{4}{\pi}\,(\lambda_{\mathrm{cyl}} + \lambda_{BT})\alpha^2. \qquad (15.32)$$

The values are somewhat low compared with experimental data, although they are reasonably close. Figure 146b presents experimental results indicating the effects of body fineness ratio and nose shape on the normal force coefficient of a cylindrical body of revolution.[2]

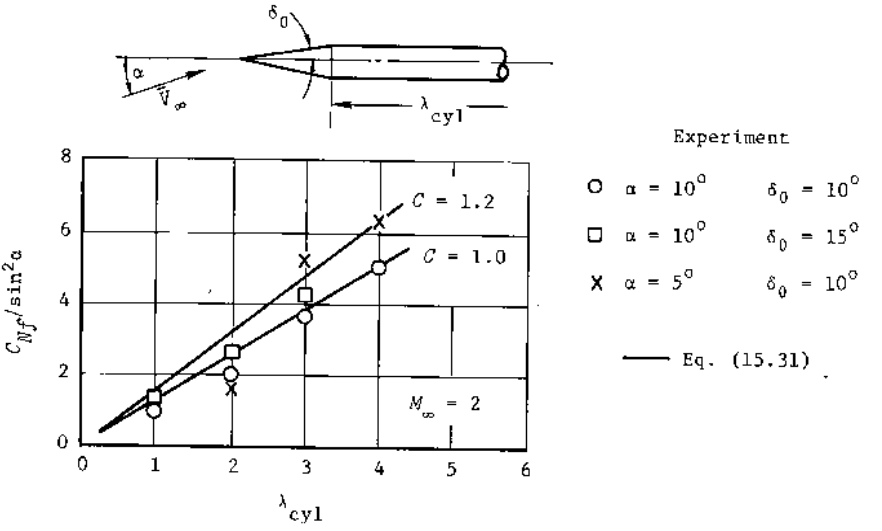

Fig. 146a--Variation of $C_{Nf}/\sin^2\alpha$ with the fineness ratio of the cylindrical section

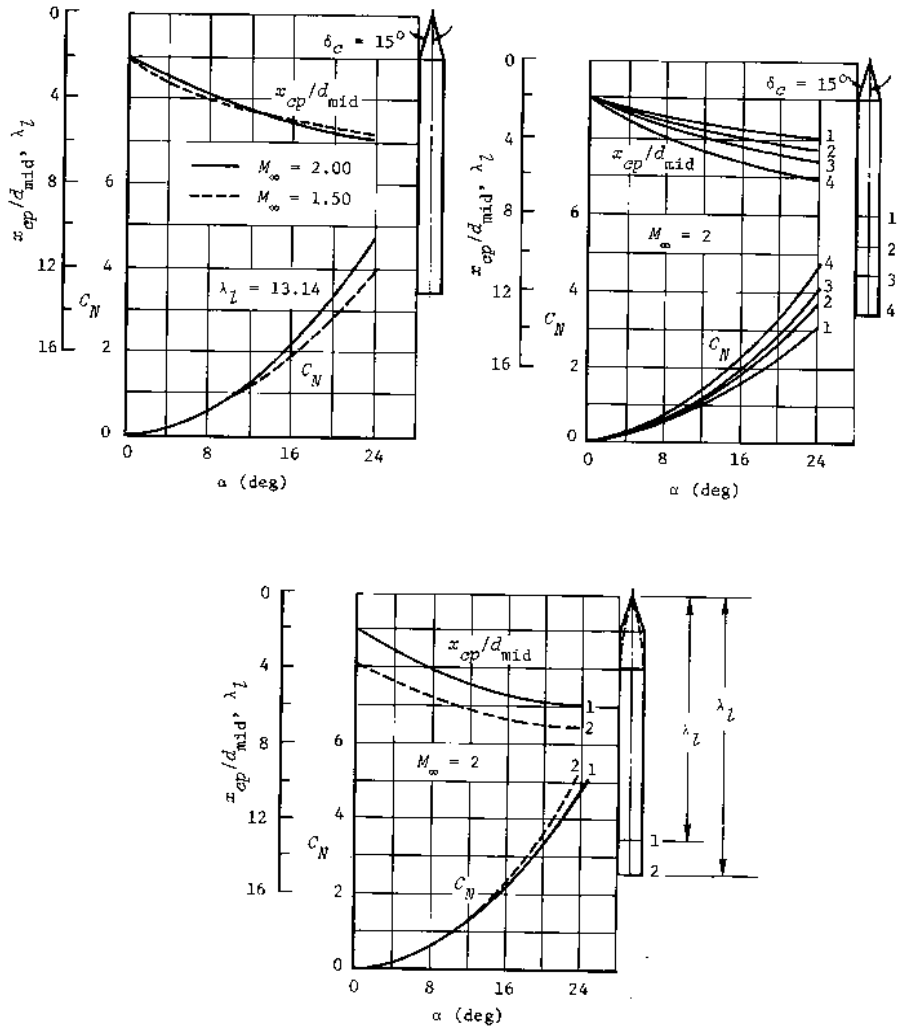

Fig. 146b--Normal force coefficient and center of pressure for bodies with cylindrical sections

The Normal Force Coefficient of a Slender Cone

The distribution of the additional pressure coefficient can be obtained by combining Eqs. (15.15) and (15.19):

$$C_{p2} = -\frac{2\alpha}{\beta}\frac{(i_r^0)_c}{(j_r^0)_c}\cos\phi - \alpha^2(4\sin^2\phi - 1), \qquad (15.33)$$

where the subscript 0 has been replaced by the subscript c. After substituting this expression for C_{p2} into Eq. (15.1), we find

$$C_{Np} = \frac{\alpha}{\beta\delta_c}\frac{(i_r^0)_c}{(j_r^0)_c}. \qquad (15.34)$$

This equation is based on the results of the solution of the linearized equation for the velocity potential and, therefore, is only valid for slender cones at low Mach numbers. Thus, Eq. (15.34) must be considered a first approximation to the correct value of C_{Np}.

A second-order approximation, applicable to a larger range of cone angles and Mach numbers, can be expressed by the partial derivative $\partial C_{Np}/\partial\alpha$:[3]

$$\frac{\partial C_{Np}}{\partial\alpha} = 2 - \delta_c^2\left(2M_\infty^2\log\frac{2}{\beta\delta_c} - 3M_\infty^2 + 2\right). \qquad (15.35)$$

Results of the calculation of the normal force slope by several methods are compared in Fig. 147 with exact theory.

The substantial difference in the results of the first approximation for linearized flow, Eq. (15.34), compared with the exact data for $M_\infty > 5$ is due to the nonlinear character of the flow at these high Mach numbers. The second-order approximation shows better agreement, but the best approximation is the value $\partial C_{Np}/\partial\alpha = 2$ from slender-body theory. The accuracy of this value increases with increasing Mach number, which indicates a decrease in the influence of compressibility in high velocity flows around cones.

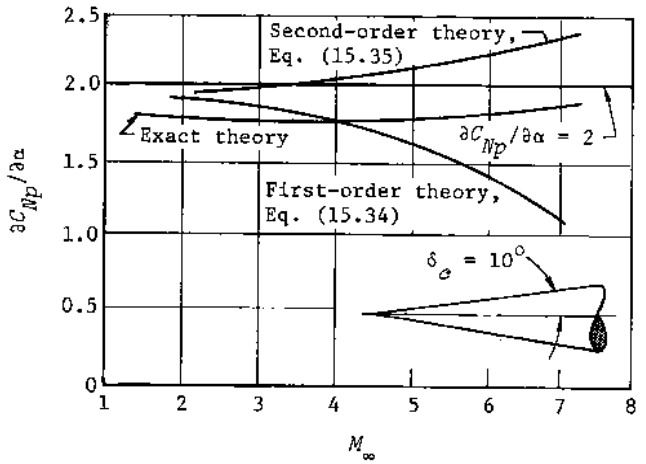

Fig. 147--Normal force slope for a slender cone

CALCULATION OF THE PITCHING MOMENT COEFFICIENT

Body of Arbitrary Shape

If the influence of viscosity is neglected, the moment coefficient depends on the distribution of the additional pressure, and on the location of the reference point about which the moment is computed. It will be assumed that the apex of the body with the coordinates $x = r = 0$ is the reference point. The pitching moment with respect to the apex is represented in general form by Eq. (1.18), and the corresponding coefficient C_{mp} by Eq. (1.19), where the reference length is the total length of the body l. The moment coefficient C'_{mp}, based on any other characteristic length (e.g., the length of the nose l_N), can be obtained from

$$C'_{mp} = C_{mp}\frac{l}{l_N} = C_{mp}\frac{\lambda_l}{\lambda_N}.$$

The expression for the moment coefficient based on the total length of the body can be obtained from Eq. (1.19) by using Eq. (15.15) for C_{p2}:

$$C_{mp} = \frac{4\lambda_N^2\alpha}{\lambda_l}\int_0^{l/l_N}\frac{V'_{\bar{x}}}{\alpha\cos\phi}\,\bar{r}\bar{x}\,d\bar{x}. \qquad (15.36)$$

In the special case of a parabolic body, this equation can be written as

$$C_{mp} = \frac{4\lambda_N^2 \alpha}{\lambda_l} \int_0^{L_l} \frac{V'_x}{\alpha \cos \phi} \, dL, \tag{15.36a}$$

where $L = \bar{x}^3(\frac{2}{3} - \bar{x}/4)$. To compute the moment coefficient using Eq. (15.36a), it is necessary to evaluate the function $V'_x/(\alpha \cos \phi)$ as a function of L and then use either numerical or graphical integration (Fig. 148). According to the results presented in the figure, the afterbody decreases the stabilizing moment of the nose by approximately 20 percent.

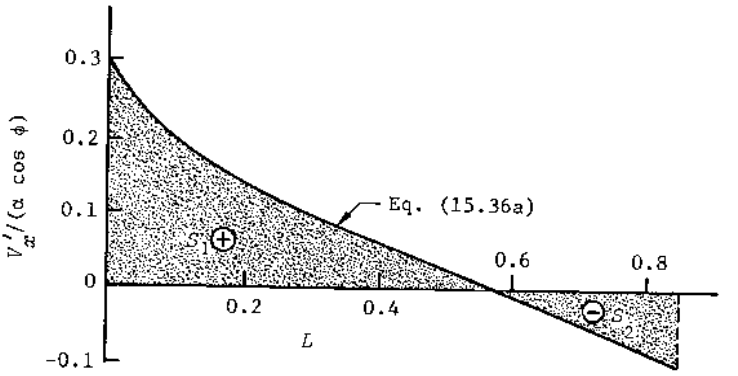

Fig. 148--Graphical integration for the moment coefficient

A graph of the function $(V'_x/\alpha \cos \phi)\bar{r}$ against $\bar{x}$ can also be used to determine the pitching moment coefficient. According to Eq. (15.36), the moment coefficient is proportional to the static moment about the ordinate axis of the area between the curve represented by the equation $f(\bar{x}) = \bar{r}(V'_x/\alpha \cos \phi)$ and the $\bar{x}$-axis. The area is usually divided into several sections, and the quantity C_{mp} is found as the sum of the static moments of the areas of these sections.

The Moment Coefficient of a Cone

Using Eq. (15.33) for the additional pressure coefficient on a cone, the moment coefficient can be determined from Eq. (15.36):

$$C_{mp} = \frac{2}{3}\frac{\alpha}{\beta\delta_c}\frac{(i_r^0)_c}{(j_r^0)_c}. \tag{15.37}$$

The moment coefficient of a parabolic nose is approximately the same as that of a cone, and studies have shown that similar results are observed for noses of nonparabolic shape.

The Moment Coefficient of Very Slender Bodies

If Eq. (15.27) is introduced into Eq. (1.19), we obtain the following relation:

$$C_{mp} = \frac{4\alpha}{lr_{\text{mid}}^2}\left(\int_0^{r_{\text{mid}}} xr\,dr + \int_{r_{\text{mid}}}^{r_B} xr\,dr\right).$$

Integrating by parts, we find

$$C_{mp} = 2\alpha\left(\bar{S}_B - \frac{l_N}{l}\int_0^{l/l_N}\bar{r}^2\,d\bar{x}\right) = 2\alpha\left(\bar{S}_B - \frac{W_T}{W_{\text{cyl}}}\right), \tag{15.38}$$

where W_T is the volume of the body, and W_{cyl} is the volume of a cylinder with base equal to the maximum cross-sectional area and length equal to the length of the body.

Equation (15.38) is useful mostly for order of magnitude estimates of the moment coefficient of actual slender bodies. Fairly satisfactory results are obtained from this equation for slender bodies of arbitrary shape without boattails; the equation also gives a fair approximation for slender conical noses. For example, for a cone with $\bar{S}_B = 1$ and $W_T/W_{\text{cyl}} = \frac{1}{3}$, the resultant value of $C_{mp} = 1.33\alpha$ is close to the rather good result for C_{mp} of 1.27α that is obtained from Eq. (15.37) at $M_\infty = 1.87$ for a cone angle of 0.1 radian.

The data presented in Fig. 149 also show that the derivative $\partial C_{mp}/\partial\alpha$ calculated from Eq. (15.38) for the same cone agrees well with exact theory. It is evident from the results of the exact theory that $\partial C_{mp}/\partial\alpha$ is almost independent of Mach number for slender cones.

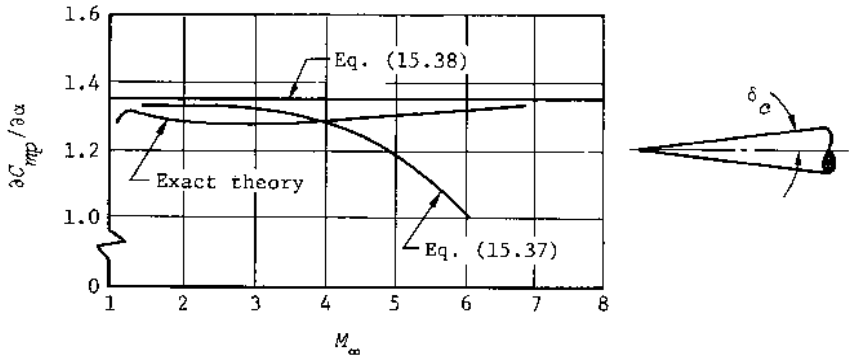

Fig. 149--Pitching moment slope for a slender cone

Effects of Viscosity

The equations presented above for the moment coefficient do not account for the influence of the viscosity of the flow. In general, however, this coefficient is a function of viscosity, as a result of the basic influence of the separation of the crossflow on the normal force.

The moment about the apex caused by the viscous crossflow forces acting on the body aft of the nose can be computed from Eq. (15.29) by considering the elemental moment on a body segment of a length dx (Fig. 150):

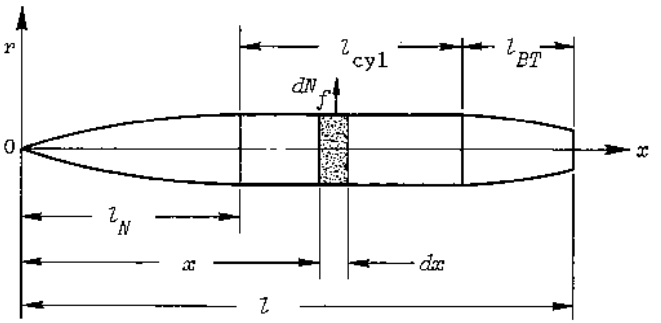

Fig. 150--Effect of viscosity on the moment coefficient

$$dM_f = x\,dN_f = c\,\frac{\rho_\infty (V_\infty \sin\alpha)^2}{2}\,2rx\,dx = \frac{\rho_\infty V_\infty^2}{2}\,\pi r_{mid}^2 l\,dC_{mf},$$

whence

$$C_{mf} = \frac{2}{\pi}\,\frac{c\,\sin^2\alpha}{l r_{mid}^2}\int_{l_N}^{l} rx\,dx.$$

If the afterbody is short, it can be replaced by a cylinder in calculating the moment coefficient induced by viscosity. This simplifies the equation, which, for small angles of attack, has the form

$$C_{mf} = \frac{2}{\pi}\,c\left(\lambda_l - \frac{\lambda_N^2}{\lambda_l}\right)\alpha^2. \tag{15.39}$$

The total moment coefficient is the sum of the pressure components from Eq. (15.38) and the viscous components from Eq. (15.39). Thus, with an afterbody, the moment coefficient is

$$C_m = 2\alpha\left(\bar{S}_B - \frac{W_T}{W_{cyl}}\right) + \frac{2}{\pi}\,c\alpha^2\left(\lambda_l - \frac{\lambda_N^2}{\lambda_l}\right). \tag{15.40}$$

In general, this equation is only valid for estimating the order of magnitude of the moment coefficient of actual body shapes, as was the corresponding expression for the normal force coefficient. However, in the special case of a cylindrical body with a conical nose, Eq. (15.40) gives a satisfactory approximation. For example, for a body consisting of a cone with a fineness ratio of 2.5 and a cylinder with a fineness ratio of 10, the calculated value differs from the experimental value by only 7 to 8 percent. In those cases where Eq. (15.40) does not provide the necessary accuracy, reliable data can be obtained only by using a more accurate theoretical analysis or by experimental means.

Another method of determining the moment coefficient is based on its computation from known values of the normal force coefficient and the center of pressure, using the equation

$$C_m = C_N \bar{x}_{cp}. \tag{15.41}$$

DETERMINATION OF THE CENTER OF PRESSURE

The Cone and Body of Revolution of Arbitrary Shape

It follows from Eq. (1.23) that the center of pressure of a slender cone (neglecting viscosity) is located two-thirds of the distance from the apex to the base of the cone. This is usually assumed to be the location of the center of pressure of a slender cone, because the influence of friction is negligibly small unless the cone is very long or the angle of attack is large.†

Considering only the contribution of the pressure forces for a body of arbitrary shape, the center-of-pressure coefficient is determined from Eqs. (1.22) or (1.23). For linearized flow this results in

$$\bar{x}_{cp} = \frac{\lambda_N}{\lambda_l} \frac{\int_0^{l/l_N} (V_x'/\alpha \cos\phi)\bar{r}\bar{x}\, d\bar{x}}{\int_0^{l/l_N} (V_x'/\alpha \cos\phi)\bar{r}\, d\bar{x}}. \tag{15.42}$$

This equation is suitable for comparatively short bodies for which the viscosity effects are small. Since $V_x'/(\alpha \cos\phi)$ is not a function of angle of attack, the center of pressure is also independent of α.

The center-of-pressure coefficient can be calculated from Eq. (15.42) by a graphical integration of the areas under the curves for $f_1(\bar{x}) = (V_x'/\alpha \cos\phi)\bar{r}$ and $f_2(\bar{x}) = (V_x'/\alpha \cos\phi)\bar{r}\bar{x}$. It can also be found by determining the center of gravity of the area bounded by the curve $f_1(\bar{x}) = (V_x'/\alpha \cos\phi)\bar{r}$, since the integral in the numerator of Eq. (15.42) is simply the static moment of the area represented by the integral in the denominator. The ratio of this static moment to its area is given by the abscissa of its center of gravity $\bar{x}_c$. Then the center-of-pressure coefficient is determined from $\bar{x}_{cp} = \bar{x}_c \lambda_N/\lambda_l$. A diagram for determining the center of pressure by this method is presented in Fig. 151 for the specific example of a parabolic body at $M_\infty = 1.87$. A graph such as that in Fig. 151 also makes it possible to find the change in center of pressure as the body is shortened. The center of gravity ($\bar{x}_c'$) of the

†Editor's note: However, see Eq. (7.39) for a more exact expression for the center of pressure of a cone.

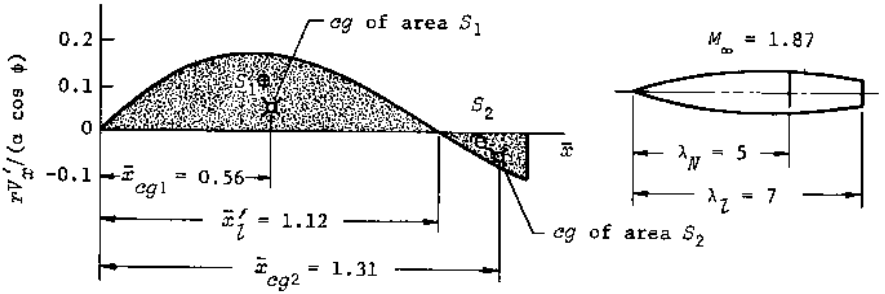

Fig. 151--Calculation of the center of pressure by the method of static moments

sectional part of the area is found, and the new center of pressure is determined from $\bar{x}_{cp} = \bar{x}'_c \lambda_N / \lambda'_l$, where λ'_l is the fineness ratio of the shortened body.

As a result of parametric calculations for the center of pressure of parabolic forebodies with fineness ratios up to approximately 5, an empirical formula can be written:

$$\bar{x}_{cp} = \frac{2}{3} - 0.01(11 + u_0)\bar{x}, \tag{15.43}$$

where $u_0 = 1/\beta\delta_0$. The center-of-pressure coefficient computed from this equation is based on the length of the particular forebody, i.e., $\bar{x}_{cp} = x_{cp}/x$ (see Fig. 152). The dimensionless quantity $\bar{x}$ is defined as $\bar{x} = x/l_N$ and should lie within the limits $0 \le \bar{x} \le$ (1.1 to 1.15). Thus, Eq. (15.43) is valid for shortened and for lengthened forebodies (in comparison with tangential noses, for which $x = l_N$). According to Eq. (15.43), the center of pressure moves aft as the nose is shortened. For the limit of $x \to 0$, it is indicated that $\bar{x}_{cp} = \frac{2}{3}$, as would be expected since the curved nose degenerates into a cone at the apex. It must be kept in mind that Eq. (15.43) applies only in the case of flow of a linearized character.

It is evident from this equation that, in general, the center of pressure is a function of Mach number; as M_∞ increases, the center of pressure shifts somewhat toward the base of the body, resulting in an improvement in the static stability. This is due to the fact that the pressure ratio at the end of the nose increases with increased velocity,

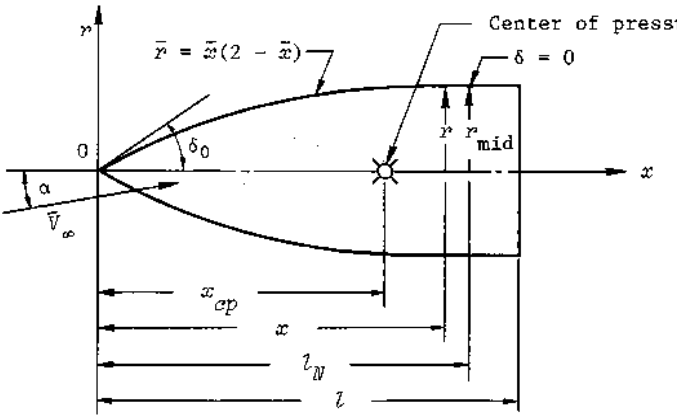

Fig. 152--Geometric parameters for calculating the center of pressure

and the destablizing effect of the afterbody is lessened. At $M_\infty = 2.5$ to 3 the rarefaction practically disappears and for $M_\infty > 2.5$ to 3 there is a positive excess pressure. Therefore, the aft part of the body begins to play the role of a stabilizer.

The opposite phenomenon can be observed for M_∞ of 1 to 1.5 and less, because the center of pressure moves toward the nose of the body. This is caused by the fact that the normal force on the fore part of the body increases more than that on the afterbody.

Although the Mach number has an influence on the location of the center of pressure, in practice it is small, as Eq. (15.43) and experimental data indicate.

Stabilization of Nose Shapes

A conical nose or a nose with an arbitrary shape is statically stable if the center of pressure is located behind the center of gravity, i.e., nearer to the base of the body. The stable nose is said to have a positive static margin, since the difference $(x_{cp} - x_{cg}) > 0$. The static margin $(\bar{x}_g)$ is quantitatively defined as a percentage from the relation

$$\bar{x}_g = \frac{x_{cp} - x_{cg}}{l_N} \cdot 100\%.$$

To guarantee the necessary static margin for a given nose shape, i.e., for a given location of the center of pressure, it is obviously possible to weight the nose section and thereby shift the center of gravity toward the nose. It is also possible to obtain a positive static margin by shifting the center of pressure toward the base of the body. Among the aerodynamic methods that can be used for this purpose, stabilization by means of tail surfaces is most widely used.* The stabilizing tail surface, located near the base of the body, creates an additional force that causes the center of pressure to move toward the base. The center of gravity also moves in the same direction due to the added weight of the stabilizer, but this shift is insignificant.

Among the other methods, stabilization by the use of stabilizing skirts occupies an important place. This technique can be described for a body of revolution in the form of a solid conical nose. Since its center of gravity is located at $\frac{3}{4}l_N$ from the nose (Fig. 153a), and the center of pressure is at $\frac{2}{3}l_N$, such a body in flight will obviously be statically unstable. In this case, the static margin is negative and equal to

$$\bar{x}_s = (\bar{x}_{cp} - \bar{x}_{cg}) \cdot 100\% = \left(\frac{2}{3} - \frac{3}{4}\right) \cdot 100\% = -8.34\%.$$

Let us attach a stabilizing skirt to the base of the conical body. It can be either a hollow frustum of a cone representing a continuation of the basic body (Fig. 153b), or a conical frustum with a lesser slope (Fig. 153c), or a hollow cylinder (Fig. 153d). Each of these versions of stabilizing devices has its own particular design application.

The simplest configuration for calculating the static margin is the conical skirt that is a continuation of the basic cone. It can be assumed that the location of the center of gravity of the entire stabilized body does not vary, since the weight of the skirt is insignificant, and its dimensionless coordinate is

*Another common stabilization technique uses a device for imparting a rotational motion to the body around its longitudinal axis, providing so-called gyroscopic (or spin) stabilization; this method is not examined in the present book.

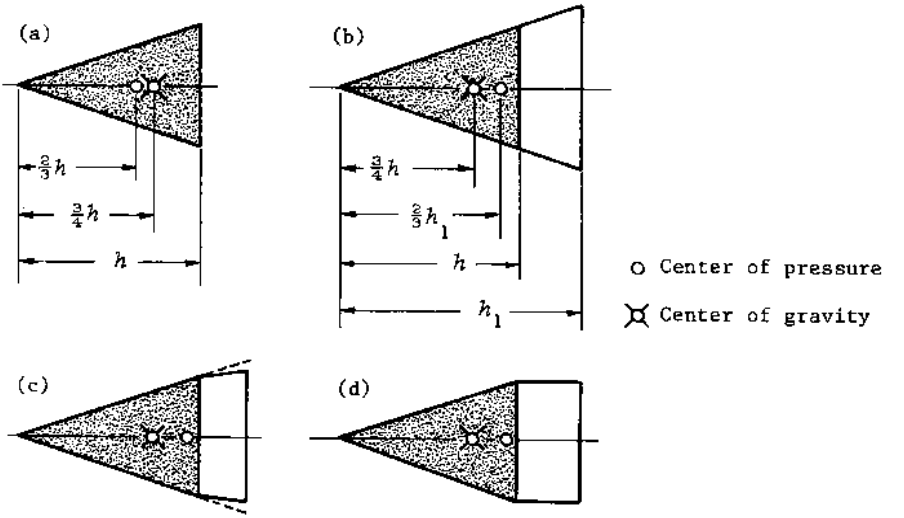

Fig. 153--Center of pressure and center of gravity for a conical body with and without a stabilizing flare

$$\bar{x}_{cg} = \frac{x_{cg}}{h_1} = \frac{3}{4}\frac{h}{h_1},$$

where h is the length of the basic nose, and h_1 is the length of the entire body including the stabilizing skirt. The center of pressure is at a distance $2h_1/3$ from the tip, so that the center-of-pressure coefficient is $\frac{2}{3}$ and the static margin $\bar{x}_s = (2/3)[1 - (9/8)(h/h_1)]\cdot 100\%$.

A value of h_1 can be selected so that the center of pressure is located between the base and the center of gravity, and the static margin is positive. In practice, the static margin is usually chosen to lie within the range of 8% to 10%. For example, for a static margin $\bar{x}_s = 10\%$,

$$\frac{h}{h_1} = \frac{8}{9}\left(1 - \frac{3}{2}\frac{10}{100}\right) = 0.76.$$

Thus, the stabilizing skirt is approximately one-quarter of the length of the entire body.

A similar stabilization method using a conical skirt can also be applied to a curved nose shape (Fig. 154). The body shown in Fig. 154a consists of a secant ogive and a conical skirt tangent to the base of the ogive. Experiments show that the center-of-pressure coefficient equals about 0.5 to 0.55 for values of h_1 of the order of $1.5h$ to $2h$.

The center of pressure depends slightly on Mach number, angle of attack, and the length of the stabilizing skirt. It moves somewhat to the rear with either an increase in the angle of attack or an increase in skirt length. The normal force coefficient of this shape is almost independent of Mach number and is given approximately by $C_N = 2.5\alpha$ to 3α.

The nose shape shown in Fig. 154b consists of a tangent ogive and a flared conical skirt. For a nose fineness ratio of 3.5 to 5, a flare with a fineness ratio of 1.5 to 2.5, and a relative base diameter of $\bar{d}_B = 1.5$ to 1.8, the center-of-pressure coefficient $\bar{x}_{cp} = x_{cp}/h_1$ approximately equals 0.55 to 0.60 (the lesser values correspond to shorter, narrower flares).

As with the conical nose, the length of the body with a stabilizing skirt (h_1) can be selected for given values of the nose length (h) and the center of gravity (x_{cg}) to provide a specified static margin.

The Center of Pressure of Long Bodies

In the case where a rather long center section is attached to the nose, viscosity is an important factor in determining the location of

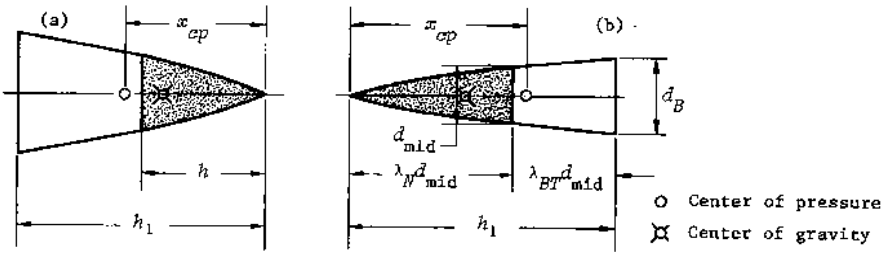

Fig. 154--Center of pressure and center of gravity for an arbitrary body with a stabilizing flare

the center of pressure. As was explained previously, the influence of viscosity increases with angle of attack. As a result of viscous effects, the center of pressure is displaced toward the base, resulting in an increase in static stability.

Let us examine the case in which a conical nose with a fineness ratio λ_N is joined to a cylinder of length $\lambda_{cyl} d_{mid}$, which is then followed by a converging or expanding afterbody with fineness ratio $\lambda_{BT} = l_{BT}/d_{mid}$. An approximate estimate of the center-of-pressure coefficient is given by the equation

$$\bar{x}_{cp} = \frac{2(\bar{S}_B - W_T/W_{cyl}) + c(2/\pi)(\lambda_l - \lambda_N^2/\lambda_l)\alpha}{2\bar{S}_B + c(4/\pi)(\lambda_{cyl} + \lambda_{BT})\alpha}. \tag{15.44}$$

Equation (15.44) should be used only for preliminary estimates of the center of pressure, since some of the terms in the equation are quite approximate. In general, calculations by Eq. (15.44) will locate the center of pressure slightly further aft than the correct values. The best results are obtained from Eq. (15.44) when there is no boattail, so that $\bar{S}_B = 1$ and $\lambda_{BT} = 0$. Furthermore, the expression is applicable primarily to bodies for which λ_{cyl} is greater than about 1.5 to 2. It can be seen from an inspection of the equation that a tapered boattail causes a decrease in $\bar{x}_{cp}$, resulting in a destabilizing effect. On the other hand, a flared boattail produces a stabilizing moment and shifts the center of pressure toward the base. As the Mach number increases, experiments have shown that the center of pressure moves forward for a body with a flared afterbody. For example, in the case of one body with a flare at the rear, the center of pressure at $M_\infty = 4$ was 7 percent less than at $M_\infty = 2$. Thus, increasing Mach number results in some destabilizing effects. As the angle of attack approaches zero, the effects of viscosity in Eq. (15.44) become negligible, and the center of pressure is determined only by the characteristics of the nose section.

An approximate calculation of the center of pressure of a body of arbitrary shape can also be carried out by using the known aerodynamic coefficients of the specific elements of the body. This can be illustrated by an example for the body of revolution shown in Fig. 155. The body is divided into sections, assuming that the normal force and its

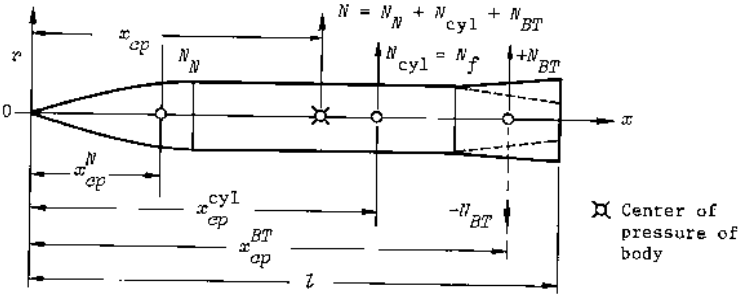

Fig. 155--Normal forces on a body without a tail

point of application is known for each section. The sum of the moments of forces with respect to the point 0 is equal to the product of the total normal force N and the distance x_{cp}, which represents the distance from the nose to the center of pressure of the entire body. This can be written as

$$Nx_{cp} = N_N x^N_{cp} + N_{cyl} x^{cyl}_{cp} \pm N_{BT} x^{BT}_{cp},$$

where the indices N, cyl, and BT designate the normal force and the coordinate of its point of application for the nose, the cylinder, and the tail, respectively. N_{cyl} is the normal force due to viscosity acting on the cylindrical section of the body, i.e., $N_{cyl} = N_f$. Taking into account that $N = N_N + N_{cyl} \pm N_{BT}$, and replacing the forces by coefficients for both the entire body and each of its elements, the center-of-pressure coefficient of the entire body is given by

$$\bar{x}_{cp} = \frac{1}{C_N} (C^N_N \bar{x}^N_{cp} + C^{cyl}_N \bar{x}^{cyl}_{cp} \pm C^{BT}_N \bar{x}^{BT}_{cp}), \qquad (15.45)$$

where the total normal force coefficient is $C_N = C^N_N + C^{cyl}_N \pm C^{BT}_N$. The plus sign corresponds to an expanding afterbody, which produces a stabilizing effect, and the minus sign to a tapered boattail, which creates a normal force negative in sign. The dimensionless coordinates $\bar{x}^N_{cp} = x^N_{cp}/l$, etc., have been used in Eq. (15.45).

If the body of revolution consists of a number of elements, the

general equation for the calculation of the center-of-pressure coefficient has the form

$$\bar{x}_{cp} = \frac{x_{cp}}{l} = \frac{\Sigma\ (C_N)_i(\bar{x}_{cp})_i}{\Sigma\ (C_N)_i}. \tag{15.46}$$

Let us consider how the specific quantities in this equation are determined. The normal force coefficient of the entire body (C_N) is computed from Eq. (15.32). The value C_N^N for the nose section must be computed taking into account its influence on the cylinder behind it. In this case, it is recommended that the computation be made for $C_N^N = 3\alpha$. The coordinate of the center of pressure of this part of the body (x_{cp}^N) should also include the effects of the nose on the cylinder. Since the part of the cylinder adjacent to the nose usually carries a positive load, the effective center of pressure is shifted aft compared with its location on an isolated nose. For conical noses with a cylinder, for example, this shift is approximately 5 to 10 percent. Consequently, in computing the center of pressure for a nose with an adjacent cylindrical section, it can be assumed that its value is $x_{cp}^N = \frac{2}{3}(1.05 \text{ to } 1.10)x_N$; i.e., in this case the dimensionless coordinate is

$$\bar{x}_{cp}^N = \frac{x_{cp}^N}{l} = \frac{2}{3}\frac{\lambda_N}{\lambda_l}\ (1.05 \text{ to } 1.10). \tag{51.47}$$

For a parabolic nose, the calculation is made from the usual equation $\bar{x}_{cp}^N = \bar{x}_{cp}(\lambda_N/\lambda_l)$. If the nose is joined tangentially to the cylindrical part, the coefficient $\bar{x}_{cp}$ is assumed to be given by Eq. (15.43). If, however, the nose is not tangent, the value obtained from Eq. (15.43) must be increased by approximately 5 to 10 percent since the cylinder behind the nose carries a significant load, as in the case of the cylinder behind a conical nose.

The normal force coefficient caused by viscous crossflow on the cylindrical part of the body can be determined from the equation

$$C_N^{cyl} = C_{Nf} = \frac{4}{\pi}\sigma\alpha^2(\lambda_l - \lambda_N), \tag{15.48}$$

assuming that the afterbody gives the same component due to friction

as a cylindrical portion of equal length. The center of pressure can be estimated by assuming that the normal force of the body in crossflow is distributed uniformly along a segment of a length $\lambda_l - \lambda_N$, so that the center of pressure is located in the middle; i.e.,

$$\bar{x}_{cp}^{cyl} = \frac{x_{cp}^{cyl}}{l} = \frac{1}{2}\left(1 + \frac{\lambda_N}{\lambda_l}\right). \tag{15.49}$$

The absolute value of the normal force coefficient produced by an expanding or converging tail section in inviscid flow is obtained from Eq. (15.28):

$$C_N^{BT} = 2\alpha(\bar{S}_B - 1). \tag{15.50}$$

Assuming that the point of application of the normal force is located in the middle of the afterbody, as a first approximation, the center of pressure is

$$\bar{x}_{cp}^{BT} = \frac{x_{cp}^{BT}}{l} = 1 - \frac{1}{2}\frac{\lambda_{BT}}{\lambda_l}. \tag{15.51}$$

Somewhat better results are obtained from these calculation methods if there is no boattail. The results then compare favorably with the experimental data presented in Fig. 146b, for example.

The Stabilization of Long Bodies

The stabilization of long bodies of revolution, as with short bodies, can be achieved through use of tail surfaces or other aerodynamic devices. If the normal force coefficient of the tail surface, C_N^T, is based on the area of the midsection of the body and if the center of pressure, $\bar{x}_{cp}^T = x_{cp}^T/l$, is also known, then, according to the diagram presented in Fig. 156, the center-of-pressure coefficient of the configuration is

$$\bar{x}_{cp} = \frac{C_N^B \bar{x}_{cp}^B + C_N^T \bar{x}_{cp}^T}{C_N^B + C_N^T}, \tag{15.52}$$

where C_N^B and C_N^T are the normal force coefficients of the body and tail

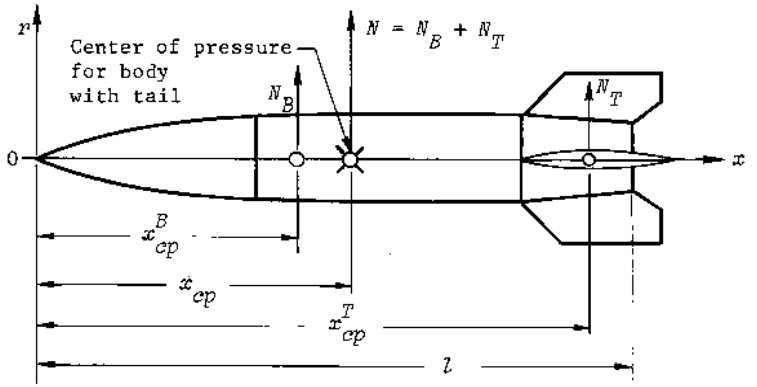

Fig. 156--Normal forces on a body with a tail

surface, and $\bar{x}_{cp}^B$ and $\bar{x}_{cp}^T$ are the coefficients of the centers of pressure of the body and tail. The normal force coefficient of the body is determined from the general equation $C_N^B = C_N^N + C_N^{cyl} + C_N^{BT}$, as was described earlier. The center of pressure of the body is given by Eq. (15.45).

In general, the aerodynamic characteristics of the body are affected by the presence of the tail surfaces and, conversely, the aerodynamics of the tail are influenced by the flow around the body. Thus, strictly speaking, it is necessary to account for the mutual interference of the body and tail surfaces to make the calculations. A rough estimate of the stability margin of a body with tail surfaces can be made by computing the normal force coefficients and centers of pressure of the body and tail separately, neglecting interference. For example, in preliminary calculations the center of pressure of the tail surface can be assumed to be located at the midpoint of its mean aerodynamic chord.

By the proper selection of the tail area, it is possible to obtain a center of pressure for the configuration in a location behind the center of gravity, and, thereby, a positive stability margin is guaranteed. If the static margin is assigned, the required area of the stabilizer can be selected for the design. For a given static margin $\bar{x}_s$, the center of pressure of the configuration is related to the center of gravity of the body and tail combination by the relation $\bar{x}_{cp} = \bar{x}_{cg} + \bar{x}_s/100$.

The general expression for C_N^T can be written in the following form: $C_N^T = (C_N^T)'(S_T/S_{mid})$, where $(C_N^T)'$ is the normal force coefficient of the tail based on the tail area. To account approximately for interference effects between the tail and the body, part of the planform area of the afterbody between the two halves of the tail surface (the covered-up area) can be included in the area S_T.

Using Eq. (15.52), the ratio of the required tail area (accounting for the covered-up area) to the area of the midsection of the body can be expressed as

$$\bar{S}_T = \frac{S_T}{S_{mid}} = \frac{C_N^B(\bar{x}_{cg} + 0.01\bar{x}_s - \bar{x}_{cp}^B)}{(C_N^T)'(\bar{x}_{cp}^T - 0.01\bar{x}_s - \bar{x}_{cg})}. \tag{15.53}$$

Setting the static margin at 8 to 10 percent, the required tail area ratio for stability can be found from this equation.

The use of a conical flare is another very effective method of stabilization. As with the tail surface, it creates a lift that is positive in sign, and, in the same way, shifts the center of pressure toward the base of the body. Equation (15.45) can be used to determine the center of pressure for this stabilization method. After replacing the coefficients C_N^N and C_N^{BT} by their values (e.g., according to the equations $C_N^N = 2\alpha$ and $C_N^{BT} = 2\alpha(\bar{S}_B - 1)$), we obtain

$$\bar{x}_{cp} = \frac{2\alpha\bar{x}_{cp}^N + C_N^{cyl}\bar{x}_{cp}^{cyl} + 2\alpha(\bar{S}_B - 1)\bar{x}_{cp}^{BT}}{2\alpha\bar{S}_B + C_N^{cyl}}. \tag{15.54}$$

Using this expression with a given static margin and a selected tail length, we can find the required flare of the afterbody, i.e., the value of the dimensionless area $\bar{S}_B$:

$$\bar{S}_B = \frac{2\alpha(\bar{x}_{cp}^{BT} - \bar{x}_{cp}^N) + C_N^{cyl}(\bar{x}_{cg} + 0.01\bar{x}_s - \bar{x}_{cp}^{cyl})}{2\alpha(\bar{x}_{cp}^{BT} - \bar{x}_{cg} - 0.01\bar{x}_s)}. \tag{15.55}$$

It can be seen from this equation that $\bar{S}_B$ has the largest value at very small angles of attack ($\alpha \to 0$) for fixed values of the other parameters.

Obviously, the greatest slope of the conical flare corresponds to this value for a given tail length. Therefore, the stabilizing cone could be more slender with an increase in the angle of attack. Of course, the final selection of the geometric dimensions of the flare must be based on guaranteeing a given static margin at small angles of attack.

Let us consider still another method of stabilization. The so-called subcaliber stabilization method involves the use of fins located at the base section, but with the maximum span of the fins less than or equal to the largest diameter of the body. A variant is the cellular stabilization method, in which longitudinal channels (cells) are made in the cylindrical afterbody over part of its length, the bulkheads between the channels being, in effect, small stabilizers.

Experiments with pointed bodies with a length of the order of 8 diameters have shown that with cellular stabilization the center of pressure can be shifted toward the base by more than 30 percent compared with its location for an unstabilized body. The advantage of this technique is that a significant backward shift of the center of pressure is achieved without a change in the external dimensions of the body. The selection of the parameters of cellular stabilization is based on experimental data in each case, and we can only present here some preliminary recommendations. For example, the length of the cell can be chosen as about 1.5 to 2 diameters, the number of cells 10 to 12, and their depth 0.1 to 0.15 diameters. For a pointed body of revolution with a length of 6 to 8 diameters, the center of pressure is $\bar{x}_{cp} \approx 0.5$ to 0.52 according to wind-tunnel tests.

§ 16. *UNSTEADY FLOW AROUND SLENDER BODIES OF REVOLUTION*

BASIC RELATIONS

General Discussion

THUS FAR, WE HAVE CONSIDERED the aerodynamic characteristics of slender bodies in steady supersonic flow. However, it is well known that an aircraft or missile in flight undergoes acceleration or deceleration and incurs oscillations of various kinds. In the case of pitching motion, this is equivalent to an unsteady flow of the air stream and usually results in a change in the aerodynamic characteristics of the body. In the case of axial accelerating supersonic flow, the pressure on the body surface increases, resulting in an increase in drag. However, research has shown that the effects of acceleration are insignificant, and in practical cases the drag can be considered invariant.

The determination of the aerodynamic characteristics of bodies in unsteady crossflows is of special interest, because the variation in aerodynamic properties is more substantial in this case than for an unsteady axial flow. The investigation of these properties is closely connected with the study of the dynamic stability of bodies of revolution.

One of the most important problems of this study is the determination of the so-called dynamic derivatives of the coefficients of the aerodynamic forces and moments, in other words, the dynamic stability derivatives. The solution of this problem for the special case of linearized unsteady flow around a body is investigated in this section.[4] As in the case of steady flow, the solution is based on the use of the method of sources, except that the body is replaced by a system of unsteady sources (or sinks) and doublets.

Let us assume that in a linearized supersonic flow at a Mach number

M_∞, there exists a crossflow with a velocity $W(x, t)$, dependent on the time t and the coordinate x of an arbitrary cross section of a body of revolution (Fig. 157). Since W is a function of time, the crossflow can be unsteady. According to the method of sources, the velocity potential of such a flow can be considered as the potential of the unsteady sources and doublets, the respective strength and moment of which vary with time.

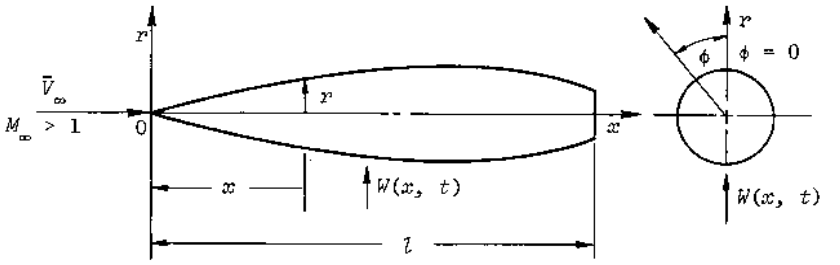

Fig. 157--Unsteady flow around a body of revolution

The velocity potential of the unsteady sources and doublets, distributed along the axis of a slender body, is determined from the linearized equation, Eq. (13.1). The integral of this equation is found in the form of the sum of two potentials: φ_1, the symmetric flow potential, which cannot produce perturbations leading to the formation of a normal force; and φ_2, the perturbation potential due to lack of symmetry, which results in a normal force. As in the case of steady flow, the solution for the perturbation potential φ_2 is found in the form of Eq. (13.9). The solution for φ_1 is the integral of the linearized equation for unsteady flow:

$$\beta^2\varphi_{1xx} - \varphi_{1rr} - \frac{1}{r}\varphi_{1r} + \frac{2M_\infty}{a_\infty}\varphi_{1xt} + \frac{\varphi_{1tt}}{a_\infty^2} = 0. \qquad (16.1)$$

The Potential of an Unsteady Source or Sink

Let the solution of Eq. (16.1) be written in the form

$$\varphi_1 = -\eta(x, r)\exp\left[i\omega\left(t - \frac{xM_\infty}{\beta^2 a_\infty}\right)\right], \qquad (16.2)$$

where ω is the angular frequency of oscillation of the body in pitch, and $\eta(x, r)$ is a function depending on the variables x and r. Along the line $x = 0$ there are no disturbances, which corresponds analytically to the condition $\eta(0, r) = \eta_x(0, r) = 0$.

After the substitution of Eq. (16.2) into Eq. (16.1), the differential equation converts to the form

$$\eta_{rr} + \frac{1}{r}\eta_r - \beta^2\eta_{xx} - \frac{\omega^2}{a_\infty^2\beta^4}\eta = 0, \tag{16.3}$$

where the subscripts x and r indicate the corresponding partial derivatives of the function η.

Equation (16.3) can be solved by an operational method based on Laplace transforms. As applied to the present case, this method involves the solution not of the original function $\eta(x, r)$ itself but of its so-called transform. The transformation of the function $\eta(x, r)$ with respect to the variable x is accomplished by multiplying η by the exponential function $\exp(-sx)$ and integrating with respect to x between the limits of 0 to ∞. As a result, we obtain

$$\bar{\eta}(s, r) = \int_0^\infty \eta(x, r) \exp(-sx)\, dx, \tag{16.4}$$

where $\bar{\eta}(s, r)$ is the Laplace transform of the function $\eta(x, r)$, and s is a complex quantity that is the operator of the transformation.

As a result of using the Laplace transformation given by Eq. (16.4), we obtain the following ordinary differential equation for the transform $\bar{\eta}$:

$$\frac{d^2\bar{\eta}}{dr^2} + \frac{1}{r}\frac{d\bar{\eta}}{dr} - \beta^2\left(s^2 + \frac{\omega^2}{a_\infty^2\beta^4}\right)\bar{\eta} = 0. \tag{16.5}$$

It is apparent from the form of Eq. (16.5) that the transformation has decreased the number of variables to one, and thereby enabled us to convert from an equation in partial derivatives, Eq. (16.3), to an ordinary differential equation, Eq. (16.5). Equation (16.5) is related to one of the forms of the Bessel equation and has as a solution

$$\bar{\eta} = K_0\left[\beta r\left(s^2 + \frac{\omega^2}{a_\infty^2\beta^4}\right)^{\frac{1}{2}}\right], \tag{16.6}$$

where K_0 is called the MacDonald function.†

After finding the transform $\bar{\eta}$, we can find the original η by using the inverse Laplace transformation. Referring to the specialized literature, where methods are cited for finding the original of a function from its transform, the final expression for the function η can be written:

$$\eta(x, r) = \frac{\cos\left[(\omega/a_\infty\beta^2)(x^2 - \beta^2r^2)^{\frac{1}{2}}\right]}{(x^2 - \beta^2r^2)^{\frac{1}{2}}}. \tag{16.7}$$

On the basis of Eqs. (16.2) and (16.7), we obtain the relation for the potential of an unsteady point source:

$$\varphi_1 = -\frac{\exp\left[i\omega\left(t - \frac{M_\infty x}{a_\infty\beta^2}\right)\right]\cos\left[\frac{\omega}{a_\infty\beta^2}(x^2 - \beta^2r^2)^{\frac{1}{2}}\right]}{(x^2 - \beta^2r^2)^{\frac{1}{2}}}. \tag{16.8}$$

If sources with a variable intensity $f(\xi)$ are located continuously along the x-axis, Eq. (16.8) has the integral form

$$\varphi_1 = \exp(i\omega t)\int_0^{x-\beta r}\frac{f(\xi)\exp\left[-\frac{i\omega M_\infty}{a_\infty\beta^2}(x - \xi)\right]\cos\left\{\frac{\omega}{a_\infty\beta^2}\left[(x - \xi)^2 - \beta^2r^2\right]^{\frac{1}{2}}\right\}d\xi}{\left[(x - \xi)^2 - \beta^2r^2\right]^{\frac{1}{2}}}, \tag{16.9}$$

where the minus sign in Eq. (16.8) is included in the definition of the function $f(\xi)$. The angular frequency ω is the characteristic parameter indicating unsteady flow in Eq. (16.9). If $\omega = 0$, the flow is steady and the potential function of Eq. (16.9) coincides with that of Eq. (13.19).

†Editor's note: This is usually referred to as a modified Bessel function of the second kind of order zero.

The Potential of an Unsteady Doublet

Differentiating the potential function φ_1 with respect to r and using Eq. (13.9), we find the additional potential φ_2 of an unsteady doublet. Before differentiating, however, it is necessary to convert Eq. (16.9) to the variable $z = \text{arc cosh } [(x - \xi)/\beta r]$. Then, differentiating with resepct to r and converting back to the variable ξ, we obtain an expression for the potential of continuously distributed, unsteady doublets with a variable moment:

$$\varphi_2 = \exp(i\omega t)\cos\phi\left[\frac{\omega}{r a_\infty \beta^2}\int_0^{x-\beta r} f(\xi)\exp\left[-\frac{i\omega M_\infty}{a_\infty \beta^2}(x-\xi)\right]\sin\left\{\frac{\omega}{a_\infty \beta^2}[(x-\xi)^2-\beta^2 r^2]^{\frac{1}{2}}\right\}d\xi\right.$$

$$+\int_0^{x-\beta r}\frac{\dot{f}(\xi)(x-\xi)\exp\left[-\frac{i\omega M_\infty}{a_\infty \beta^2}(x-\xi)\right]\cos\left\{\frac{\omega}{a_\infty \beta^2}[(x-\xi)^2-\beta^2 r^2]^{\frac{1}{2}}\right\}d\xi}{r[(x-\xi)^2-\beta^2 r^2]^{\frac{1}{2}}}$$

$$\left.+\frac{i\omega M_\infty}{a_\infty \beta^2 r}\int_0^{x-\beta r}\frac{f(\xi)(x-\xi)\exp\left[-\frac{i\omega M_\infty}{a_\infty \beta^2}(x-\xi)\right]\cos\left\{\frac{\omega}{a_\infty \beta^2}[(x-\xi)^2-\beta^2 r^2]^{\frac{1}{2}}\right\}d\xi}{[(x-\xi)^2-\beta^2 r^2]^{\frac{1}{2}}}\right]. \tag{16.10}$$

If $\omega = 0$ and $\dot{f}(\xi)$ is set equal to $m(\xi)$, we obtain Eq. (15.3) for the potential of steady doublets.

Boundary Conditions

The boundary condition necessary for the determination of the function $f(\xi)$ in Eq. (16.10) is obtained from the continuous flow condition, which specifies that the potential of an unsteady doublet must be such that the normal velocity component disappears on the surface of the body, or, neglecting its slight thickness, on the x-axis. Thus, a condition analogous to Eq. (13.7a) must be fulfilled:

$$\frac{\partial \varphi_2}{\partial r} = -W(x, t) \cos \phi. \tag{16.11}$$

This condition has various forms depending on the particular type of body motion.

One such possible case of motion is of practical interest in connection with studies of oscillatory stability. Let us assume that the body performs harmonic oscillations with respect to the lateral axis that passes through the center of gravity (Fig. 158a) in accordance with the equation

$$\alpha = \alpha_0 \exp(i\omega t), \tag{16.12}$$

where α_0 is the initial amplitude and is equal to the angle of attack at $t = 0$.

The oscillations of the body in pitch cause the formation of an unsteady perturbed flow, whose transverse component of velocity on the x-axis is

$$W(x, t) = V_\infty \alpha_0 \exp(i\omega t) + (x - x_{cg})\left(\frac{d\alpha}{dt}\right)$$

$$= \alpha_0 [V_\infty + i\omega(x - x_{cg})] \exp(i\omega t). \tag{16.13}$$

Consequently, the boundary condition Eq. (16.11) takes the form

$$\frac{\partial \varphi_2}{\partial r} = -\alpha_0 [V_\infty + i\omega(x - x_{cg})] \exp(i\omega t) \cos \phi. \tag{16.11a}$$

This condition serves to determine the law of the distribution of sources, i.e., the form of the function $f(\xi)$.

In the case of a very slender body, the form of this function can be found in the following way. First, Eq. (16.10) is transformed to the variable $z = \operatorname{arc\,cosh}[(x - \xi)/\beta r]$ and the partial derivative φ_{2r} is computed. After transforming back to ξ, the expression is evaluated in the limit as $r \to 0$. The specific value of the partial derivative φ_{2r} for $r \to 0$, which is treated in slender-body theory for the case of unsteady flow, is as follows:

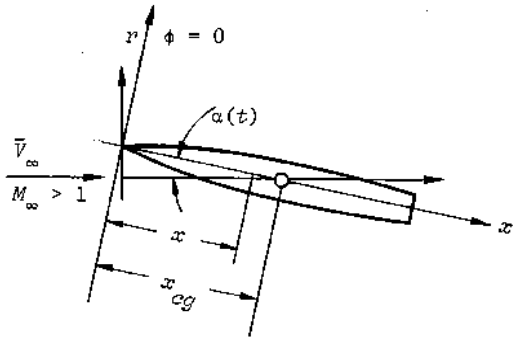

(a) Harmonic oscillation about *cg*

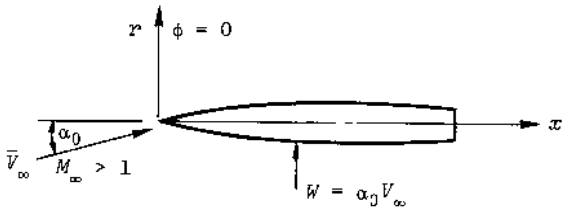

(b) Constant angle of attack

Fig. 158--Asymmetric flow around a body of revolution

$$\frac{\partial \varphi_2}{\partial r} = -\frac{\pi f(x)}{S(x)} \exp(i\omega t) \cos\phi, \tag{16.14}$$

where $S(x) = \pi r^2$ is the area of the cross section at a distance x from the apex of the body.

The Determination of the Aerodynamic Coefficients

The expression for the potential function and the boundary condition must be supplemented by the general relations that determine the aerodynamic coefficients. For example, one of these is Eq. (13.13) for the additional pressure coefficient that appears as a result of an unsteady crossflow. In place of Eq. (13.13) for C_{p2}, the expression for

this coefficient from Eq. (13.13a) is introduced under the integral of Eq. (15.1) to obtain the relation for the normal force coefficient:

$$C_{Np} = -\frac{\pi}{S_{\text{mid}}} \int_0^l \frac{C'_{p2}}{\cos \phi} r \, dx, \tag{16.15}$$

where $C'_{p2} = -2(\bar{\varphi}_{2x} + \bar{\varphi}_{2t})$, and $\bar{\varphi}_{2x} = \varphi_{2x}/V_\infty$, $\bar{\varphi}_{2t} = \varphi_{2t}/V_\infty^2$.

The relation for the moment coefficient about the axis that passes through the center of gravity is obtained from Eq. (1.19) in the form

$$C_{mp} = -\frac{2}{lS_{\text{mid}}} \int_0^l \int_0^\pi C'_{p2} r(x_{cg} - x) \cos \phi \, d\phi \, dx,$$

whence

$$C_{mp} = C_{Np}\left(\frac{x_{cg}}{l}\right) + \frac{\pi}{lS_{\text{mid}}} \int_0^l \frac{C'_{p2}}{\cos \phi} rx \, dx. \tag{16.16}$$

The expression for the axial force coefficient, as follows from Eqs. (1.6) and (13.13a), does not change compared with steady flow.

AERODYNAMIC COEFFICIENTS FOR LOW-FREQUENCY OSCILLATIONS

The General Equation for the Potential Function

The determination of the aerodynamic characteristics of a body of revolution in unsteady supersonic flow is simplified for low-frequency oscillations in pitch. If Eq. (16.10) is written in the form of a power series in the parameter $k = M_\infty \omega r/\beta V_\infty$, which is called a reduced harmonic frequency, it can be verified that the unsteady flow potential can, with sufficient accuracy, be presented in the form of a linear relation of the parameter k for frequencies of the order of $a_\infty \beta/l$. Converting to the variable $z = \text{arc cosh}\,[(x - \xi)/\beta r]$, the first approximation is

$$\varphi_2 = \beta \cos \phi \exp(i\omega t)\left[\int_0^{\text{arc cosh } u} \dot{f}(x - \beta r \cosh z) \cosh z \, dz - iM_\infty k \int_0^{\text{arc cosh } u} \dot{f}(x - \beta r \cosh z) \, dz\right]. \tag{16.17}$$

It will be noted that if we set $k = 0$ in Eq. (16.17) and replace $\dot{f}(x - \beta r \cosh z)$ by $m(x - \beta r \cosh z)$, the expression reduces to Eq. (15.2a) for the velocity potential of a steady crossflow.

The derivatives of φ_2 with respect to x and t are required for the determination of the pressure coefficient. Assuming that $\dot{f} = m$, as previously, we obtain

$$\varphi_{2x} = \beta \cos \phi \exp(i\omega t)\left[\int_0^{\operatorname{arc\,cosh} u} \dot{m}(x - \beta r \cosh z) \cosh z \, dz - iM_\infty k \int_0^{\operatorname{arc\,cosh} u} \dot{m}(x - \beta r \cosh z)\, dz\right], \tag{16.18}$$

$$\varphi_{2t} = \beta i\omega \cos \phi \exp(i\omega t)\left[\int_0^{\operatorname{arc\,cosh} u} m(x - \beta r \cosh z) \cosh z \, dz - iM_\infty k \int_0^{\operatorname{arc\,cosh} u} m(x - \beta r \cosh z)\, dz\right]. \tag{16.19}$$

The forms of the functions m and $\dot{m}$ are determined from the boundary condition by combining Eqs. (16.11a) and (16.14). The function $f(\xi)$ is given by

$$f(\xi) = \frac{S(\xi)}{\pi} \alpha_0 [V_\infty + i\omega(\xi - x_{cg})]. \tag{16.20}$$

Computing the first and second derivatives, we find

$$m(\xi) = \frac{S'(\xi)}{\pi} \alpha_0 [V_\infty + i\omega(\xi - x_{cg})] + \frac{S(\xi)}{\pi} i\omega\alpha_0, \tag{16.21}$$

$$\dot{m}(\xi) = \frac{S''(\xi)}{\pi} \alpha_0 [V_\infty + i\omega(\xi - x_{cg})] + \frac{2S'(\xi)}{\pi} i\omega\alpha_0. \tag{16.22}$$

Aerodynamic Coefficients

Equations (16.21) and (16.22) can be converted to the variable $z = \operatorname{arc\,cosh}[(x - \xi)/\beta r]$ and substituted into Eqs. (16.18) and (16.19).

Evaluating the integrals and using Eq. (13.13a), we obtain the expression

$$C'_{p2} = -\frac{2\beta \cos\phi}{\pi}\left[\left(\alpha - \frac{\dot{\alpha}x_{cg}}{V_\infty}\right)\Omega_3 + \frac{\dot{\alpha}l}{V_\infty}(\Omega_4 + 3\Omega_1) - \frac{\dot{\alpha}rM_\infty^2}{\beta V_\infty}\Omega_2\right], \quad (16.23)$$

where the functions Ω_2 and Ω_3 are given by Eqs. (13.47) and (15.18), respectively. The functions Ω_1 and Ω_4 are defined by

$$\Omega_1 = \frac{1}{l}\int_0^{\text{arc cosh } u} S'(x - \beta r \cosh z)\cosh z\, dz, \quad (16.24)$$

$$\Omega_4 = \frac{1}{l}\int_0^{\text{arc cosh } u} S''(x - \beta r \cosh z)(x - \beta r \cosh z)\cosh z\, dz. \quad (16.25)$$

The normal force coefficient and the pitching moment coefficient are obtained by substituting Eq. (16.23) into Eqs. (16.15) and (16.16):

$$C_{Np} = \frac{2\beta}{S_{\text{mid}}}\int_0^l \left[\left(\alpha - \frac{\dot{\alpha}x_{cg}}{V_\infty}\right)\Omega_3 + \frac{\dot{\alpha}l}{V_\infty}(\Omega_4 + 3\Omega_1) - \frac{\dot{\alpha}rM_\infty^2}{\beta V_\infty}\Omega_2\right] r\, dx, \quad (16.26)$$

$$C_{mp} = C_{Np}\left(\frac{x_{cg}}{l}\right) - \frac{2\beta}{lS_{\text{mid}}}\int_0^l \left[\left(\alpha - \frac{\dot{\alpha}x_{cg}}{V_\infty}\right)\Omega_3 + \frac{\dot{\alpha}l}{V_\infty}(\Omega_4 + 3\Omega_1) - \frac{\dot{\alpha}rM_\infty^2}{\beta V_\infty}\Omega_2\right] rx\, dx. \quad (16.27)$$

The coefficients C_{Np} and C_{mp} for very slender bodies can be determined from these expressions if the functions Ω_n are replaced by the corresponding relations from slender-body theory. To obtain these relations, it is necessary to convert to the variable $\xi = x - \beta r \cosh z$ in the expressions for Ω_n, and then to evaluate them in the limit as $r \to 0$. Equations (16.26) and (16.27) reduce to

$$C_{Np} = 2\alpha\bar{S}_B + 2\bar{S}_B \frac{\dot{\alpha} l}{V_\infty}\left(1 - \frac{x_{cg}}{l} + \frac{W_T}{lS_B}\right), \tag{16.28}$$

$$C_{mp} = 2\alpha\bar{S}_B\left(\frac{x_{cg}}{l} + \frac{W_T}{lS_B} - 1\right) - 2\bar{S}_B \frac{\dot{\alpha} l}{V_\infty}\left(1 - \frac{x_{cg}}{l}\right)^2. \tag{16.29}$$

The dynamic stability derivatives can be defined in the following way:

$$C_{Np\dot{\alpha}} = \frac{V_\infty}{l}\frac{\partial C_{Np}}{\partial \dot{\alpha}}, \qquad C_{mp\dot{\alpha}} = \frac{V_\infty}{l}\frac{\partial C_{mp}}{\partial \dot{\alpha}}. \tag{16.30}$$

From Eqs. (16.26) through (16.30), we obtain

$$C_{Np\dot{\alpha}} = \frac{2\beta}{lS_{\text{mid}}}\int_0^l \left[l(\Omega_4 + 3\Omega_1) - \frac{rM_\infty^2}{\beta}\Omega_2 - x_{cg}\Omega_3\right] r\, dx, \tag{16.26a}$$

$$C_{mp\dot{\alpha}} = \left(\frac{x_{cg}}{l}\right) C_{Np\dot{\alpha}} - \frac{2\beta}{l^2 S_{\text{mid}}}\int_0^l \left[l(\Omega_4 + 3\Omega_1) - \frac{rM_\infty^2}{\beta}\Omega_2 - x_{cg}\Omega_3\right] rx\, dx, \tag{16.27a}$$

$$C_{Np\dot{\alpha}} = 2\bar{S}_B\left(1 - \frac{x_{cg}}{l} + \frac{W_T}{lS_B}\right), \tag{16.28a}$$

$$C_{mp\dot{\alpha}} = -2\bar{S}_B\left(1 - \frac{x_{cg}}{l}\right)^2. \tag{16.29a}$$

The derivatives given by Eqs. (16.27a) and (16.29a) represent the damping moment coefficient on which depend the parameters of dynamic oscillatory stability discussed in § 1.

The Aerodynamic Coefficients and Their Static (Angular) Derivatives for the Motion of a Body at a Constant Angle of Attack

The pitching motion in steady flow, i.e., with $\dot{\alpha} = 0$ (Fig. 158b), was thoroughly examined in § 15. This case will be considered here for comparison with the unsteady flow results and also as a generalization

of the previous results. Assuming that $f(\xi) = [S(\xi)/\pi]V_\infty\alpha_0$, so that $\dot{m} = [S''(\xi)/\pi]V_\infty\alpha_0$, Eq. (16.23) for the additional pressure coefficient reduces to

$$C'_{p_2} = -\frac{2\beta\alpha_0 \cos\phi}{\pi}\Omega_3. \tag{16.31}$$

The relations for the normal force and moment coefficients then become

$$C_{Np} = \frac{2\beta\alpha_0}{S_{\text{mid}}}\int_0^l \Omega_3 r\,dx, \tag{16.32}$$

$$C_{mp} = C_{Np}\left(\frac{x_{cg}}{l}\right) - \frac{2\beta\alpha_0}{lS_{\text{mid}}}\int_0^l \Omega_3 rx\,dx. \tag{16.33}$$

Thus, the static derivatives $C_{Np\alpha} = \partial C_{Np}/\partial\alpha_0$ and $C_{mp\alpha} = \partial C_{mp}/\partial\alpha_0$ are determined by the following equations:

$$C_{Np\alpha} = \frac{2\beta}{S_{\text{mid}}}\int_0^l \Omega_3 r\,dx, \tag{16.34}$$

$$C_{mp\alpha} = C_{Np\alpha}\left(\frac{x_{cg}}{l}\right) - \frac{2\beta}{lS_{\text{mid}}}\int_0^l \Omega_3 rx\,dx. \tag{16.35}$$

Using slender-body theory, the following equations correspond to these expressions:

$$C_{Np\alpha} = 2\bar{S}_B, \tag{16.34a}$$

$$C_{mp\alpha} = 2\bar{S}_B\left(\frac{x_{cg}}{l} + \frac{W_T}{lS_B} - 1\right). \tag{16.35a}$$

The stability derivatives for unsteady and steady flow are thus defined. The total values of the aerodynamic coefficients can be computed from the following general relations:

$$C_0 = \alpha_0 C_\alpha, \qquad C = C_0 + \frac{\dot{\alpha} l}{V_\infty} C_{\dot{\alpha}}, \tag{16.36}$$

in which C_0 is the normal force or pitching moment coefficient for motion at a constant angle of attack, and C_α and $C_{\dot{\alpha}}$ are the corresponding derivatives of these coefficients.†

From these results it is possible to estimate, qualitatively, the influence on stability of oscillations of a body of revolution. It can be seen that this type of motion leads to a decrease of the moment about the center of gravity, which is equivalent to a damping effect. It should be noted that the damping in an actual case is greater than that obtained from slender-body theory.

Relations for Parabolic Bodies

Specific relations can be obtained for slender parabolic bodies by calculating the functions Ω_n with the use of the equation for a parabola, $r = (x/2\lambda_N)(2 - x/l_N)$. Then Eqs. (16.24) and (16.25) become

$$\Omega_1 = \frac{\pi l_N}{\lambda_N^2 l}\left[2\left(\frac{\bar{x}}{u}\right) i_r^1 - 3\left(\frac{\bar{x}}{u}\right)^2 i_r^2 + \left(\frac{\bar{x}}{u}\right)^3 i_r^3\right], \tag{16.37}$$

$$\Omega_4 = \frac{\pi l_N}{\lambda_N^2 l}\left[2\left(\frac{\bar{x}}{u}\right) i_r^1 - 6\left(\frac{\bar{x}}{u}\right)^2 i_r^2 + 3\left(\frac{\bar{x}}{u}\right)^3 i_r^3\right]. \tag{16.38}$$

These expressions for Ω_n make it relatively simple to calculate the additional pressure coefficient C_{p2} and the resultant stability derivatives.

To determine the stability derivatives using slender-body theory, the volume of the parabolic body must first be found:

$$W_T = \frac{\pi l^3}{4\lambda_N^2}\left[\frac{4}{3} - \frac{l}{l_N}\left(1 - \frac{1}{5}\frac{l}{l_N}\right)\right].$$

†Editor's note: These expressions have already been given in complete form in Eqs. (16.28) and (16.29).

As an illustration, the stability derivatives for a parabolic body with a fineness ratio $\lambda_l = 8$, a base taper of $\bar{s}_B = 0.41$, a length of 8 m, and with its center of gravity at 5 m, are presented in Figs. 159 and 160.[4] The absolute values of all the derivatives increase with an increase in M_∞. Since $C_{mp\dot{\alpha}}$ becomes more negative, the damping effect becomes stronger as the velocity increases, so that oscillations are damped more rapidly.

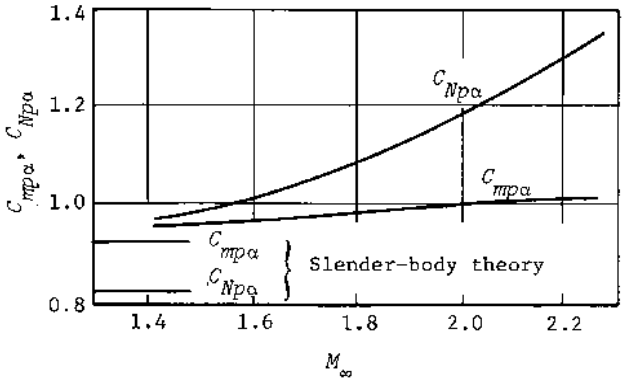

Fig. 159--Variation of the stability derivatives with Mach number for a constant angle of attack

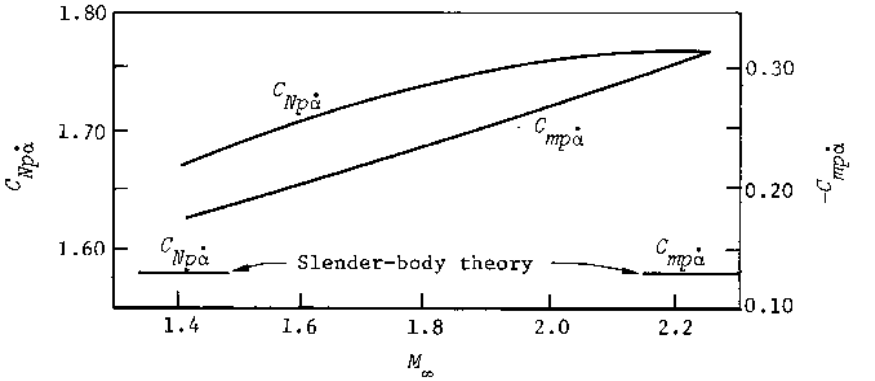

Fig. 160--Variation of the stability derivatives with Mach number for harmonic oscillations

The generation of a damping moment under oscillatory conditions causes a backward shift of the center of pressure compared with its position for motion at constant angle of attack. This effect can be illustrated by calculating the coordinates of the center of pressure for harmonic oscillation of the body discussed above with an angular velocity $\dot{\alpha} = 2$ radians/sec, and for motion at a constant angle of attack $\alpha_0 = 0.1$ radian at $M_\infty = 2$.

Using the graphs in Figs. 159 and 160, $C_{Np\alpha} = 1.18$, $C_{mp\alpha} = 1.0$, $C_{Np\dot{\alpha}} = 1.76$, and $C_{mp\dot{\alpha}} = -0.257$. Using Eq. (16.36), the coefficients are $C_{Np} = 0.118 + 0.041 = 0.159$, and $C_{mp} = 0.1 - 0.006 = 0.094$. Thus, the center of pressure is at a distance $x_{cp} = (0.094/0.159)l = 0.529l$ ahead of the center of gravity.

Without oscillations, $x_{cp} = (0.1/0.118)l = 0.848l$ ahead of the center of gravity, or about 40 percent more unstable.

From an analysis of the results of the example for a body with boattailing ($\bar{S}_B = 0.41$), it is apparent that this type of afterbody worsens the instability characteristics, not only for motion at a constant angle of attack but also for oscillations in pitch about the center of gravity.

This can also be demonstrated by comparing the stability derivatives of the two bodies shown in Fig. 161. One is the parabolic body discussed above, whose profile is defined by the equation $r = 0.2x(1 - 0.1x/d_{mid})$. The other body has the same parabolic nose to a length of five diameters,

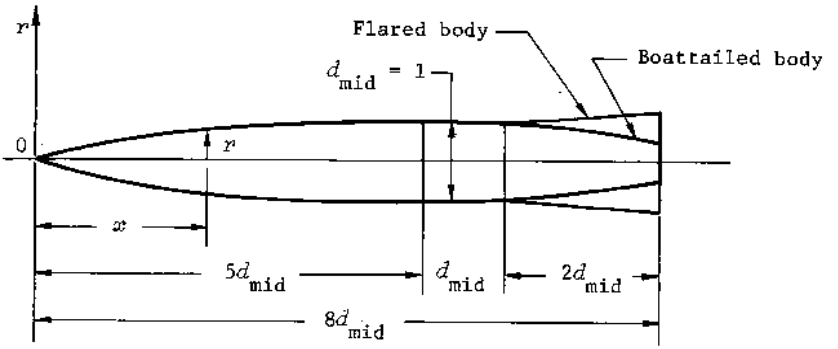

Fig. 161--Bodies used in sample calculation of stability derivatives

followed by a short cylindrical section one diameter in length ($\lambda_{cyl} = 1$), and finally an expanding conical tail section two diameters in length ($\lambda_{BT} = 2$) with a base area ratio $\bar{S}_B = 1.82$.

The stability derivatives have been calculated for these two bodies from the equations based on slender-body theory, and the results are presented in Table 18.[4] It is evident from these data that the body with the flare has a center of pressure located farther back and thus has better static stability characteristics. The flared body has a smaller value of $C_{mp\alpha}$ and a larger value of $C_{Np\alpha}$ than does the body with a boattailed afterbody. Both bodies are damped in oscillatory motion, although the value of $C_{mp\dot{\alpha}}$ for the body with a boattail is less than that of the body with a flare, and thus the boattail provides less damping than the flare. These results indicate the possibility of using aerodynamic stability characteristics to determine the proper choice of the shape of the afterbody.

Table 18

STABILITY DERIVATIVES ACCORDING TO SLENDER-BODY THEORY

Body Shape	Stability Derivatives			
	$C_{Np\alpha}$	$C_{mp\alpha}$	$C_{Np\dot{\alpha}}$	$C_{mp\dot{\alpha}}$
With boattail	0.82	0.93	1.58	-0.13
With flare	3.63	0.15	3.08	-0.59

Stability Characteristics of a Cone

The derivatives of the cross-sectional area of a cone with respect to x are $S' = 2\pi r\delta_c$ and $S'' = 2\pi\delta_c^2$, so the functions Ω_n are given by

$$\Omega_1 = \Omega_4 = 2\pi\delta_c^3\beta i_r^1 \frac{x}{l}, \qquad \Omega_2 = 2\pi\delta_c^2 i_x^0, \qquad \Omega_3 = 2\pi\delta_c^2 i_r^0. \tag{16.39}$$

The stability derivatives of a cone can be found from these values of Ω_n, assuming that the cone oscillates about its center of gravity, located at a distance $3l/4$ from the apex.

Introducing Eq. (16.39) into Eqs. (16.26a) and (16.27a), we find

$$C_{Np\dot{\alpha}} = 4\beta\delta_c^2\left(\frac{4}{3}\beta i_r^1 - \frac{1}{3}\frac{M_\infty^2}{\beta} i_x^0 - \frac{3}{8}\frac{i_r^0}{\delta_c}\right), \tag{16.40}$$

$$C_{mp\dot{\alpha}} = -\frac{1}{8}\beta\delta_c i_r^0. \tag{16.41}$$

The corresponding relations from slender-body theory are

$$C_{Np\dot{\alpha}} = 1.17, \qquad C_{mp\dot{\alpha}} = -0.125. \tag{16.42}$$

The motion of a cone at a constant angle of attack can be examined for comparison. In this case, the stability derivatives are determined using Eqs. (16.34) and (16.35):

$$C_{N\alpha} = 2\beta\delta_c i_r^0, \qquad C_{m\alpha} = \frac{1}{6}\beta\delta_c i_r^0. \tag{16.43}$$

Slender-body theory (Eqs. (16.34a) and (16.35a)) gives the following expressions:

$$C_{N\alpha} = 2, \qquad C_{m\alpha} = \frac{1}{6}. \tag{16.44}$$

As an example, let us find the stability derivatives of a cone for $\beta = 2.5$ ($M_\infty^2 = 7.25$) and $\delta_c = 0.1$. The parameter $u_0 = 1/\beta\delta_c = 4$ for these data. Using Table 16 (p. 348), we can find $i_x^0 = 2.064$, $i_r^0 = 3.873$, and $i_r^1 = 6.714$. According to Eqs. (16.40) and (16.41), the derivatives are $C_{Np\dot{\alpha}} = 0.58$ and $C_{mp\dot{\alpha}} = -0.121$. In the case of the motion of a cone at a constant angle of attack, the derivatives are calculated from Eqs. (16.43) and are $C_{Np\alpha} = 1.936$, $C_{mp\alpha} = 0.161$.

Thus, the analysis for a cone leads to the same results as that for the parabolic body. When the cone oscillates about its center of gravity, a damping moment is produced that causes damping of the oscillations and increases the static stability.

Chapter VI

AERODYNAMICS OF BODIES OF REVOLUTION AT HYPERSONIC SPEEDS

Editor's Introduction

THE BASIC RELATIONS *given in this chapter for calculating the pressures on cones in hypersonic flow are similar to those found in many current texts. The development of the equations for the flow about slender pointed bodies follows the hypersonic small disturbance theory of Van Dyke*[2] *in most details.*

*Two approximate methods applicable to hypersonic flow are discussed briefly in Section 17: the method of local cones and the shock expansion method. The shock expansion method has been described in more detail by Eggers and Savin (*NACA TN 2579, *December 1951) and Savin (*NACA TN 3349, *April 1955). Although it would have been appropriate to discuss it here, Krasnov does not mention the second-order shock expansion method of Syvertson and Dennis (*NACA Report 1328, *1957), which was referenced in the Introductions to Chapters 3 and 5. This method gives accurate predictions for the axial pressure distribution on a cylindrical midsection as well as on the nose. An approximate method for estimating the pressure distribution and pressure drag on a boattail is outlined at the end of Section 17. Staylor and Goldberg (*NASA TN D-2761, *May 1965) have shown that methods similar to this, or even characteristics solutions, are in poor agreement with experimental data for short boattails, thick boundary layers, or high Mach numbers. Under these conditions better agreement is obtained by assuming that the flow expands from sonic speed at the start of the boattail by a Prandtl-Meyer expansion. On the basis of their results, it appears that the pressure distribution along a boattail can be estimated fairly accurately by using the higher value of the pressure calculated by either (1) the sonic expansion method or (2) a more exact theory such as the method of characteristics or Van Dyke's second-order theory.*

*Abramovskii, Kovaleva and Avrakhov (*Gidroaeromekhanika, *1967) have published detailed equations for calculating the pressure distribution and shock wave shape on conical flares by using the second-order shock expansion method. Their results agree well with those obtained from the method of characteristics.*

Much of the Newtonian flow theory in Section 18 is based on the work of Crimminger, Williams, and Young.[4] *In addition to these results, a number of recent reports have presented comprehensive tables or graphs for the Newtonian aerodynamics of various shapes. For example, Rainey has published charts for calculating the pressures and*

forces on arbitrary bodies of revolution (NASA TN D-176, *December 1959*), *and Wells and Armstrong give extensive tables for conic and spheric components of bodies* (NASA TR R-127, *1962*). *An excellent collection of equations and charts for aerodynamic forces, moments, and stability derivatives is presented by Clark and Trimmer* (AEDC-TDR-64-25, *March 1964*); *emphasis is placed on components of lifting configurations, but many of the results are applicable to bodies of revolution. Since all of these reports are intended for application to general configurations for a variety of angular conditions, they are necessarily rather complicated to use; it is desirable to have simpler results for specific body shapes. Penland* (NASA TN D-2283, *May 1964*) *has prepared a series of accurate graphs for the aerodynamic force and moment coefficients of sharp cones for angles of attack from* 0 *to* 180 *deg. Mayo has presented similar data for ogive noses in tabular form* (NASA TN D-3337, *March 1966*). *It should be noted that the two sets of results are not directly comparable, since Penland includes the base of the cone in his calculations while Mayo calculates only the forces acting on the forebody. The stability derivatives of cones and cone cylinders according to Newtonian theory have been derived and discussed by Charwat* (Jet Propulsion, *August 1957*) *and Tobak and Wehrend* (NACA TN 3788, *September 1956*).

Seiff (NASA TN D-1304, *May 1962*) *has shown that the pressures at hypersonic speeds on a flared afterbody are grossly inaccurate when predicted by conventional Newtonian flow theory based on free-stream conditions, particularly when the body has a blunt nose. More accurate results are obtained if the pressures on the flare are calculated by considering it as a secondary flow field embedded in the shock layer, that is, by using Newtonian impact theory based on the local flow conditions at the beginning of the flare. The pressure coefficient on a conical flare is*

$$C_{pBT} = C_{pj} + \frac{q_j}{q_\infty} (C_{pBT})_N$$

where C_{pj} *and* q_j *are the pressure coefficient and dynamic pressure at the start of the flare, and* $(C_{pBT})_N$ *is the pressure coefficient for the flare by the usual (free-stream) Newtonian theory.*

Newtonian flow theory has been applied extensively in calculations of the pressure distribution and aerodynamic forces on blunt-nosed bodies of revolution; this subject is discussed in the next chapter.

§ 17. *SYMMETRIC FLOW*

CALCULATION OF THE FLOW AROUND CONES AT HYPERSONIC MACH NUMBERS

Shock-wave Angle

A COMPARATIVELY SIMPLE APPROXIMATE SOLUTION for hypersonic flow around a cone can be found from the series equations for the velocity components (see § 6). At hypersonic speeds, the shock is close to the cone surface and the difference of the angles $\theta_s - \delta_c$ is sufficiently small that Eqs. (6.12) and (6.14) can be used for the direct calculation of the velocity components behind the shock wave:

$$\tilde{V}_{sr} = \tilde{V}_c\left[1 - (\theta_s - \delta_c)^2 + \frac{1}{3}(\theta_s - \delta_c)^3 \cot \delta_c - \ldots\right], \qquad (17.1)$$

$$\tilde{V}_{s\theta} = \tilde{V}_c[-2(\theta_s - \delta_c) + (\theta_s - \delta_c)^2 \cot \delta_c - \ldots]. \qquad (17.2)$$

To use these relations for calculating the shock-wave angle, it is first necessary to combine Eq. (4.3) for the conservation of mass with Eq. (4.21):

$$-\frac{\tilde{V}_{\infty\theta}}{\tilde{V}_{s\theta}} = \frac{[(\gamma + 1)/2]M_\infty^2 \sin^2\theta_s}{1 + [(\gamma - 1)/2]M_\infty^2 \sin^2\theta_s}. \qquad (17.3)$$

The velocity component of the incident flow normal to the shock is $\tilde{V}_{\infty\theta} = \tilde{V}_\infty \sin \theta_s$, and, using Eq. (6.7), Eq. (17.3) can be converted to

$$-\frac{\tilde{V}_{sr}}{\tilde{V}_{s\theta}} = \frac{[(\gamma + 1)/4]M_\infty^2 \sin 2\theta_s}{1 + [(\gamma - 1)/2]M_\infty^2 \sin^2\theta_s}. \qquad (17.3a)$$

In this expression, both $\sin 2\theta_s$ and $\sin^2\theta_s$ can be written in the form of series. If it is assumed that the third term in the expansion for $\sin 2\theta_s$ can be neglected if it does not exceed 0.02, the shock angle cannot exceed 24° to 25°. Consequently, the Mach number M_∞ cannot be less than some limiting value for a given cone angle.

Let us assume that $\theta_s \leq 24°$ to 25° corresponds to flow around a cone with such a small angle δ_c that the shock degenerates into a Mach wave. In this case, the free-stream Mach number is determined by the condition $M_\infty = 1/\sin\theta_s \geq 2.5$ to 3. The allowable Mach number must increase in proportion to the increase in cone angle, since the condition $\theta_s \leq 24°$ to 25° can only be maintained in this manner. For example, the Mach number should not be less than 6 for $\delta_c = 20°$ and $\theta_s = 24°$.

Using Eqs. (17.1) and (17.2) in Eq. (17.3a), and replacing $\sin 2\theta_s$ and $\sin^2\theta_s$ by their series expansions, results in

$$\frac{1 - (\theta_s - \delta_c)^2}{(\theta_s - \delta_c)[2 - (\theta_s - \delta_c)\cot\delta_c]} = \frac{(\gamma + 1)M_\infty^2\theta_s(3 - 2\theta_s^2)}{6 + (\gamma - 1)M_\infty^2\theta_s^2(3 - \theta_s^2)}. \tag{17.4}$$

In principle, this equation can be used to determine the cone angles corresponding to various combinations of M_∞ and θ_s. However, Eq. (17.4) can be further simplified by assuming that the shock-wave angle and the difference $\theta_s - \delta_c$ are both small compared with unity. Then, with good approximation, Eq. (17.4) can be written as

$$\frac{1}{M_\infty(\theta_s - \delta_c)} = \frac{2(\gamma + 1)M_\infty\theta_s}{2 + (\gamma - 1)M_\infty^2\theta_s^2}. \tag{17.4a}$$

Solving this equation for $M_\infty\theta_s$, to be designated by K_0, we obtain

$$K_0 = M_\infty\theta_s = \frac{\gamma + 1}{\gamma + 3}K_1 + \sqrt{\left(\frac{\gamma + 1}{\gamma + 3}\right)^2 K_1^2 + \frac{2}{\gamma + 3}}, \tag{17.5}$$

where the parameter $K_1 = M_\infty\delta_c$. It is apparent from Eq. (17.5) that K_1 is the similarity parameter for determining the shock angle θ_s since

all cones will have identical values of K_0 for different combinations of δ_c and M_∞ as long as K_1 is the same.

Flow Parameters at the Cone Surface and Wave Drag

The pressure ratio at the surface of a cone can be expressed by $p_c/p_\infty = (p_c/p_s)(p_s/p_\infty)$, where p_s/p_∞ is found from Eq. (4.22), and p_c/p_s can be calculated from the adiabatic equation $p_c/p_s = (a_c/a_s)^{2\gamma/(\gamma-1)}$. The velocity of sound on the cone and behind the shock wave are given by

$$a_c^2 = \frac{\gamma - 1}{2}(V_{max}^2 - V_c^2), \qquad a_s^2 = \frac{\gamma - 1}{2}[V_{max}^2 - (V_{s\theta}^2 + V_{sr}^2)],$$

from which we get

$$\frac{a_c^2}{a_s^2} = 1 + \frac{\gamma - 1}{2}\frac{V_{sr}^2}{a_s^2}\left(1 + \frac{V_{s\theta}^2}{V_{sr}^2} - \frac{V_c^2}{V_{sr}^2}\right). \tag{17.6}$$

For small values of $\theta_s - \delta_c$, Eqs. (17.1) and (17.2) give the following ratios:

$$\begin{aligned} \frac{V_c^2}{V_{sr}^2} &= 1 + 2(\theta_s - \delta_c)^2 + \ldots, \\ \frac{V_{s\theta}^2}{V_{sr}^2} &= 4(\theta_s - \delta_c)^2[1 + 2(\theta_s - \delta_c)^2 + \ldots]. \end{aligned} \tag{17.7}$$

Noting that $V_{sr} = V_\infty \cos\theta_s$, and substituting Eq. (17.7) into Eq. (17.6), we obtain the relation

$$\frac{a_c^2}{a_s^2} = 1 + (\gamma - 1)(K_0 - K_1)^2\frac{a_\infty^2}{a_s^2}, \tag{17.8}$$

in which the ratio a_∞^2/a_s^2 can be determined from Eqs. (4.21) through (4.23) in the form

$$\frac{a_\infty^2}{a_s^2} = \frac{\frac{\gamma+1}{2}K_0^2}{\left(\frac{2\gamma}{\gamma+1}K_0^2 - \frac{\gamma-1}{\gamma+1}\right)\left(1 + \frac{\gamma-1}{2}K_0^2\right)}. \tag{17.9}$$

Introducing Eq. (17.8) into the adiabatic equation, the ratio of the pressures on the cone and behind the shock is

$$\frac{p_c}{p_s} = 1 + \gamma\left(\frac{a_\infty}{a_s}\right)^2 (K_0 - K_1)^2. \tag{17.10}$$

From Eqs. (4.22), (17.9), and (17.10), the equation for pressure on the cone relative to the static pressure of the unperturbed flow is

$$\frac{p_c}{p_\infty} = \frac{2\gamma}{\gamma+1}(K_0^2 - 1) + (K_0 - K_1)^2 \frac{\gamma(\gamma+1)K_0^2}{2 + (\gamma-1)K_0^2} + 1. \tag{17.11}$$

Using this equation, the pressure coefficient on the cone can be computed from $C_{pc} = (2/\gamma M_\infty^2)(p_c/p_\infty - 1)$. This coefficient is exactly equal to the wave drag coefficient of the cone.

The similarity parameter for the drag coefficient is[1]

$$C_{pc}M_\infty^2 = C_{Dp}M_\infty^2 = \frac{4}{\gamma+1}(K_0^2 - 1) + (K_0 - K_1)^2 \frac{2(\gamma+1)K_0^2}{2 + (\gamma-1)K_0^2}. \tag{17.12}$$

In reality, the drag function is only a function of the parameter K_1, since K_0 is, in turn, a function of K_1 as given by Eq. (17.5). Thus, flows at very high Mach numbers around cones are similar in the sense that the drag functions will be identical for identical values of the similarity parameter K_1.

Equation (17.12) is awkward to use because the intermediate parameter K_0 has to be determined. The following approximate relation is more convenient for calculations:

$$C_{pc}M_\infty^2 = C_{Dp}M_\infty^2 = \frac{2(\gamma+1)(\gamma+7)}{(\gamma+3)^2}K_1^2\left(1 + \frac{1}{5\gamma K_1^{3/2}}\right), \tag{17.13}$$

which, for $\gamma = 1.4$, has the form

$$C_{pc}M_\infty^2 = C_{Dp}M_\infty^2 = 2.091K_1^2\left(1 + \frac{0.143}{K_1^{3/2}}\right). \tag{17.13a}$$

As follows from their derivation, Eqs. (17.5) and (17.12) become more exact for large Mach numbers when the shock wave lies close to the surface of the slender cone. This is evident in Fig. 162a, where Eq. (17.12) is compared with exact calculations of the wave drag coefficient.[1] The agreement is generally better for values of K_1 that are greater than one, although satisfactory results are obtained for K_1 less than one for very slender cones (e.g., for $\delta_c = 5°$).

The shock-wave angle calculated by Eq. (17.5) agrees well with the exact results (Fig. 162b), starting at $K_1 = 0.5$ to 0.6. The curve in Fig. 162b corresponding to the equation $K_0 = 1.093K_1$ is obtained from Eq. (17.5) in the limit as $M_\infty \to \infty$:

$$K_0 = \frac{2(\gamma + 1)}{\gamma + 3} K_1. \tag{17.14}$$

For $\gamma = 1.4$, we obtain $K_0 = 1.093K_1$.

The drag function given in Eq. (17.13) can also be evaluated in the limit as $M_\infty \to \infty$, resulting in

$$C_{pc}M_\infty^2 = C_{Dp}M_\infty^2 = \frac{2(\gamma + 1)(\gamma + 7)}{(\gamma + 3)^2} K_1^2. \tag{17.15}$$

Assuming that $\gamma = 1.4$, we obtain the special case $C_{Dp}M_\infty^2 = 2.091K_1^2$, which is also plotted in Fig. 162b.

Estimate of the Magnitude of the Perturbations for a Slender Cone

The relations obtained above permit an estimate of the magnitude of the perturbations for hypersonic flow around a cone. The velocity at the surface of the cone can be obtained from Eq. (17.1), assuming that $V_{sr} = V_\infty(1 - \delta_c^2/2)$:

$$V_c = V_\infty\left[1 + (\theta_c - \delta_c)^2 - \frac{\delta_c^2}{2}\right]. \tag{17.16}$$

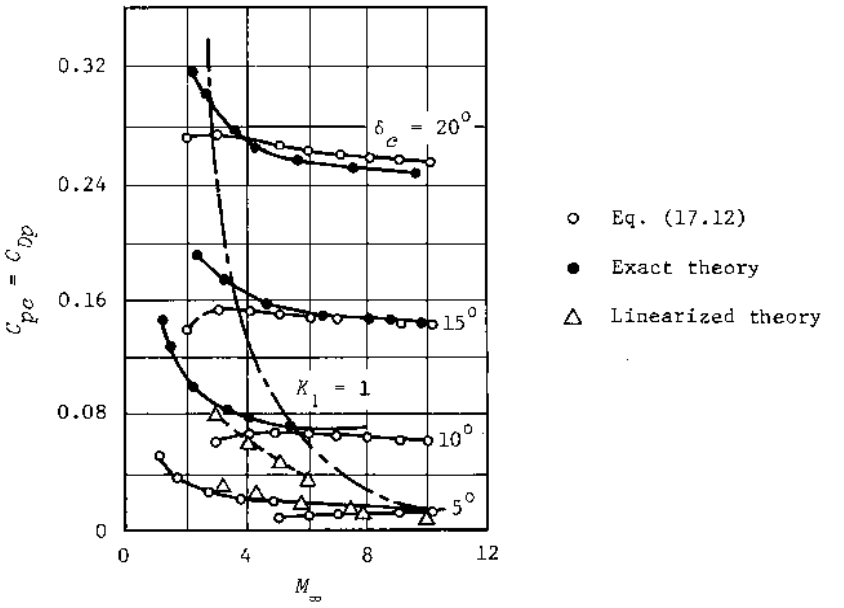

(a) Pressure drag coefficient

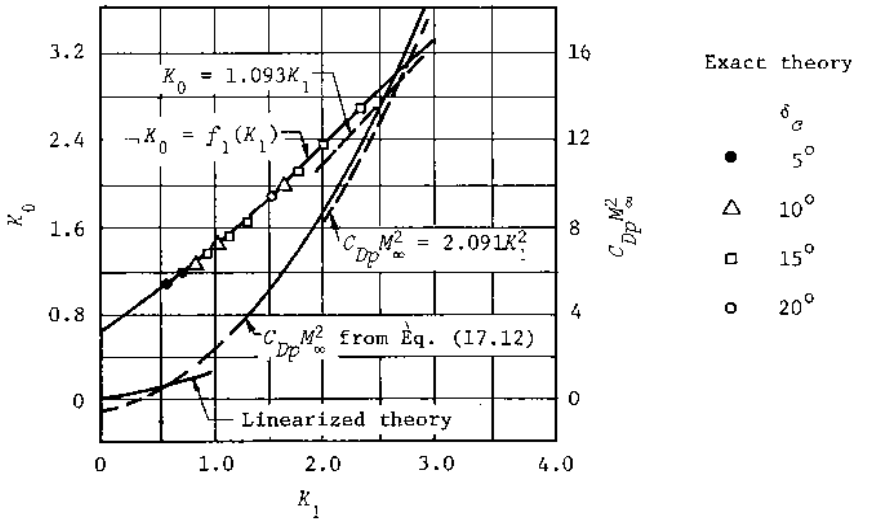

(b) Similarity parameters

Fig. 162--The flow characteristics around a cone calculated by various methods

It follows from this expression that the vertical velocity component is $V_r = V_c \sin \delta_c \sim V_\infty \delta_c$; the horizontal component is $V_x = V_c \cos \delta_c \sim V_c$. Therefore, the axial component of the perturbation velocity, equal to $V_\infty[(\theta_s - \delta_c)^2 - \delta_c^2/2]$, will be an order of magnitude less than the vertical component.

Hence, the compression process occurring in a gas flowing around a cone is basically caused by a displacement of air particles transverse to the flow, whereas the character of the flow in the longitudinal direction changes very little. Neglecting this change in velocity, i.e., assuming that the longitudinal component is equal to the free-stream velocity, we can assume that the process of displacing particles occurs only in a plane normal to the cone axis. This process is a particular example of the law of plane sections.

The limiting value of the shock-wave angle is given by $\theta_s = 1.093\delta_c$ for $\gamma = 1.4$, and the velocity on the cone will be $V_c \approx V_\infty(1 - 0.5\delta_c^2)$. Hence, the longitudinal perturbation is approximately equal to $-0.5V_\infty\delta_c^2$, and varies as the square of the small parameter δ_c. Instead of the angle, the reciprocal of the fineness ratio (i.e., $1/\lambda_c$) can be chosen as the small parameter.

If the designation τ is introduced for the small parameter in the general case, then, on the basis of the estimate of perturbations obtained for conditions on the cone, the longitudinal disturbance at an arbitrary point is of the order $V_\infty\tau^2$ and the transverse disturbance is of the order $V_\infty\tau$.

Equation (17.13) can be used to estimate the pressure perturbations. The pressure coefficient on a cone is of the order of $C_{pc} \sim \delta_c^2$, and, consequently, the absolute pressure is $p_c \sim p_\infty M_\infty^2 \delta_c^2$. Thus, the pressure at any point in the flow around the cone is of the order $p_\infty M_\infty^2 \tau^2$, which will considerably exceed the pressure in the undisturbed flow.

The density perturbations can be estimated on the basis of Eq. (4.21). Because very high velocities are under consideration, when $M_\infty \theta_s = K_0 \gg 1$, it can be concluded that the density in the perturbed flow is approximately of the same order as that in the undisturbed flow.†

†Editor's note: Equations (4.21) or (4.21a) indicate that the density ratio is of the order of 1/c.

Despite the large perturbations of pressure and density, the problem of hypersonic flow around a cone has been successfully simplified, and relatively simple relations have been obtained. This is possible because of the smallness of the velocity perturbations.

It should be noted that the estimates of perturbations examined above can be extended to the case of flow around any slender body of arbitrary shape. Thus, as for the cone, simplified analytic solutions can be obtained for the problem of hypersonic flow over slender bodies.

EQUATIONS FOR FLOW AROUND SLENDER BODIES IN HYPERSONIC FLOW

Simplification of the Equations

The above simplification of the problem of flow around slender bodies of revolution is related to the basic simplification of the aerodynamic equations for hypersonic velocities. This differs substantially from the linearization of the equations for small Mach numbers. It has been shown that the linearized equations are also derived on the assumption that the velocity perturbations are small. However, since the Mach number is small, terms containing perturbations to the first and higher powers are discarded in the coefficients of the equations, i.e., terms of the order of τ, τ^2, and so on (e.g., $M_\infty\tau < 1$ and $M_\infty^2\tau^2 \ll 1$).

The flow picture corresponding to this case is presented in Fig. 163. A feature of linearized flow is that the thickness of the body is small compared with the distance between the body and the shock wave. On the other hand, at hypersonic velocities the shock is located close to the body, and the influence of the shock on the region of perturbed flow is greater than in the case of linearized flow. Although the disturbances are also small, the product $M_\infty\tau$ can be of the order of unity. In this case, it is not possible to neglect terms containing the first power of τ if it appears in the form $M_\infty\tau$, since their order is the same as that of the remaining terms in the equation. The equations can be simplified by discarding terms of the order of τ^2 and higher when the small parameter τ enters independently, but not when it is together with M_∞. Despite these simplifications, the system of flow equations remains nonlinear. This nonlinearity is an essential characteristic of the equations for gas flow at large Mach numbers.

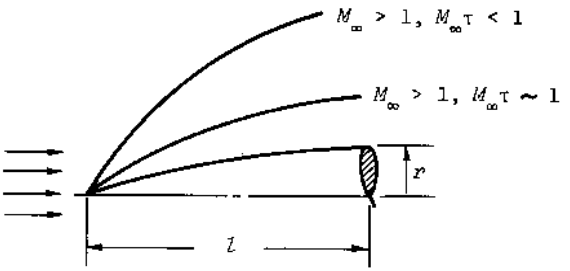

Fig. 163--Diagram of flow around a slender body of revolution

The equations for steady symmetric flow can be simplified[2,3] by introducing the dimensionless coordinates ξ and η, defined as

$$x = l_N\xi, \qquad r = \tau l_N\eta. \tag{17.17}$$

This is an affine transformation based on an appraisal of the extent of the region of perturbed flow, which is constrained to a thin supersonic layer near the body at hypersonic flow velocities. Thus, the longitudinal and radial coordinates will be of the orders of l_N and τl_N, respectively, and the actual coordinates x and r are given by Eq. (17.17).

Consistent with the estimates of the perturbations of velocity, pressure, and density made above, it is possible to write

$$V_x = V_\infty[1 + \tau^2\bar{V}_\xi(\xi, \eta)], \qquad V_r = V_\infty\tau\bar{V}_\eta(\xi, \eta), \tag{17.18}$$

$$p = p_\infty\gamma M_\infty^2\tau^2\bar{p}(\xi, \eta), \qquad \rho = \rho_\infty\bar{\rho}(\xi, \eta), \tag{17.19}$$

where $\bar{V}_\xi$, $\bar{V}_\eta$, $\bar{p}$, and $\bar{\rho}$ are new dimensionless variables on which the actual values of velocity, pressure, and density depend.

Equations (17.17) through (17.19) can be substituted into the equations of motion, Eq. (3.6), and continuity, Eq. (3.15), for steady symmetric flow. Using the condition of the conservation of entropy, Eq. (3.48), and neglecting terms of order τ^2, we obtain the following approximate equations:

$$\frac{\partial \bar{V}_\eta}{\partial \xi} + \bar{V}_\eta \frac{\partial \bar{V}_\eta}{\partial \eta} = -\frac{1}{\bar{\rho}} \frac{\partial \bar{p}}{\partial \eta}, \tag{17.20}$$

$$\frac{\partial \bar{\rho}}{\partial \xi} + \frac{\partial (\bar{\rho} \bar{V}_\eta)}{\partial \eta} + \frac{\bar{\delta} \bar{V}_\eta}{\eta} = 0, \tag{17.21}$$

$$\frac{\partial}{\partial \xi} \left(\frac{\bar{p}}{\bar{\rho}^\gamma} \right) + \bar{V}_\eta \frac{\partial}{\partial \eta} \left(\frac{\bar{p}}{\bar{\rho}^\gamma} \right) = 0. \tag{17.22}$$

These equations constitute the basis of small disturbance theory for the study of hypersonic flow around slender bodies of revolution. They apply to nonisentropic (nonpotential) flow and in particular to the case of rotational flow behind a shock wave.

The Law of Plane Sections

A particular application of the law of plane sections was illustrated for the special case of flow around a slender cone, but the law extends to a broad class of flows at high velocities. As was pointed out earlier, the effects of this principle are indicated by the fact that (to order δ_c^2) a body moving at a very high velocity induces only a lateral displacement of particles. The character of the motion is similar to that resulting from the expulsion of gas by the radial expansion of a flat cylindrical piston. Hence, it is possible to draw an analogy between the two-dimensional unsteady motion of a gas ahead of an expanding piston and the steady flow around a cone.

Suppose that, at the time $t = 0$, a piston (Fig. 164) instantly begins expanding radially with an initial velocity V, creating ahead of itself a plane cylindrical shock wave, the front of which travels at a velocity D. The distances $R = Vt$ and $R = Dt$ traversed by the piston and the shock wave, respectively, are represented in the plane R–t by straight lines corresponding to the surfaces of the cone and the shock wave in the physical plane r–x. Thus, the unsteady two-dimensional flow ahead of a piston expanding uniformly corresponds to steady flow around a cone.

In using this analogy, the physical coordinate x corresponds to

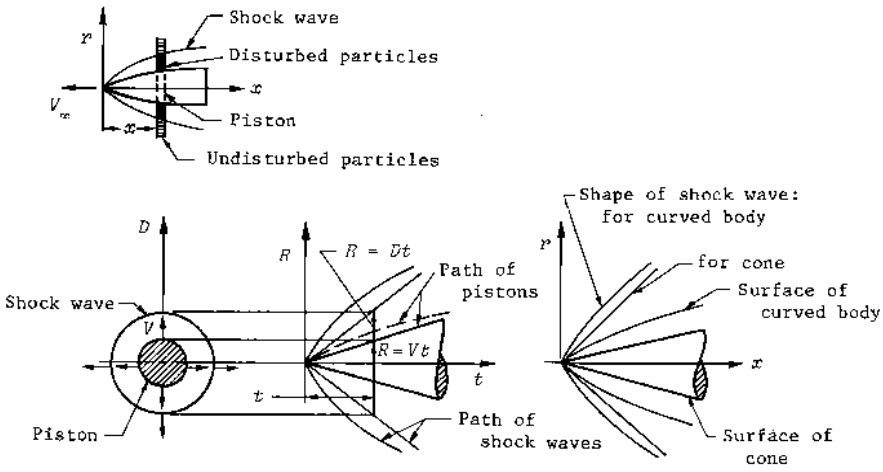

Fig. 164--The piston analogy

the time t. If the piston expands nonuniformly according to an arbitrary law $R(t)$, the trace of the motion of the piston and the shock wave in the R-t plane corresponds to the curved shapes of the body and shock in the r-x plane (see Fig. 164). Thus, unsteady two-dimensional flow ahead of a piston with nonuniform expansion is analogous to steady flow around a body with a curved shape. This comprises the generalized law of plane sections and results directly from the analogy to piston motion. Flow calculations by this law are correct to order of τ^2.

The law of plane sections, which is represented schematically in Fig. 164, becomes clearer if we consider an irrotational system involving a stationary gas and a moving body. Let us isolate from this medium a layer of particles located in a cross section perpendicular to the direction of the motion. An observer located in this section will note that the motion of the body passing through the layer of particles separates them and forces them to move only in the two-dimensional cross section. It is apparent that the body surface, which is an impermeable sliding wall for the particles of gas, plays the role of the piston.

If the generatrix of the body is given by the equation $r = f(x)$ and

the time is interpreted as $t = x/V_\infty$, the relation for the variation in the piston radius is of the form $R = f(tV_\infty)$. If differentiated with respect to t, the velocity of expansion of the piston is $V_p = \partial R/\partial t$.

In the case of a cone, $r = x\delta_c$, and, consequently, $R = V_\infty \delta_c t$ and $V_p = dR/dt = V_\infty \delta_c$. The latter expression indicates that the hypersonic similarity law results directly from the law of plane sections. In fact, the perturbed velocity of the particles on the surface of a cone, coinciding with the expansion velocity of the piston in the equivalent problem, will be the same if the product $V_\infty \delta_c$ is maintained. For various values of V_∞ and δ_c, the steady flow around a cone (or the equivalent unsteady motion of a gas ahead of a plane cylindrical piston) will differ only in linear scale. Since the conical body is affine-similar, analogous conclusions can be extended to other affine-similar bodies, particularly to parabolic bodies of revolution.

We have examined the law of plane sections, resulting from the analogy to piston motion, in terms of the physical concepts of the flow process. The same law can be derived from formal considerations by showing that Eqs. (3.7) and (3.16) for the radial unsteady motion of a gas behind a plane cylindrical shock are equivalent to Eqs. (17.20) and (17.21) for steady flow around a slender body at hypersonic speeds. To do this, Eqs. (3.7) and (3.16) must be converted to the new variables ξ, η, which are related to r and x by $r = \tau l_N \eta$ and $t = x/V_\infty = (l_N/V_\infty)\xi$. Equations (17.20) through (17.22), which are fundamental to small perturbation theory are, at the same time, the mathematical expression of the law of plane sections.

The Boundary Conditions

The solutions of Eqs. (17.20) through (17.22) must satisfy the boundary conditions on the body surface and in the free stream. If the equation $r = \tau b(x)$ of a body of revolution is known (Fig. 165), the conditions at the surface of the body can be written as

$$\bar{V}_\eta = \frac{db(\xi)}{d\xi} = b'(\xi) \quad \text{for} \quad \eta = b(\xi). \tag{17.23}$$

The condition for the free stream is

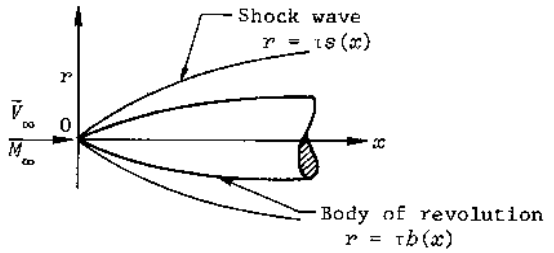

Fig. 165--Supersonic flow over a body of revolution

$$\bar{V}_\xi \to 0, \qquad \bar{V}_\eta \to 0, \qquad \bar{p} \to \frac{1}{\gamma M_\infty^2 \tau^2}, \qquad \bar{\rho} \to 1 \quad \text{for} \quad \xi \to \infty. \tag{17.24}$$

In addition, the conditions at the shock wave must also be fulfilled, where the shock surface can be described by the equation $r = \tau s(x)$. For example, the condition that the function $\bar{V}_\eta$ must satisfy can be determined from Eq. (4.20) for an oblique shock. The expression for the variation in the normal velocity component through the shock is given by

$$\frac{V_{n1} - V_{n2}}{V_{n1}} = \frac{2}{\gamma + 1}\left(1 - \frac{1}{M_\infty^2 \sin^2 \theta_s}\right).$$

The normal velocity components ahead of and behind the shock are $V_{n1} = V_{n\infty} = V_\infty \sin \theta_s$ and $V_{n2} = V_\tau \tan(\theta_s - \delta_s)$, so that

$$\frac{V_\infty \sin \theta_s - V_\tau \tan(\theta_s - \delta_s)}{V_\infty \sin \theta_s} = \frac{2}{\gamma + 1}\left(1 - \frac{1}{M_\infty^2 \sin^2 \theta_s}\right).$$

Since very large Mach numbers are being considered for which the shock angles are small, it can be assumed that $V_\tau = V_\infty \cos \theta_s \approx V_\infty$, and the sine and tangent can be replaced by the angle. As a result, we obtain

$$\frac{V_\infty \theta_s - V_\infty(\theta_s - \delta_s)}{V_\infty \theta_s} = \frac{2}{\gamma + 1}\left(1 - \frac{1}{K_0^2}\right).$$

It is apparent that the quantity $V_\infty \theta_s$ in this expression represents the radial velocity component V_r directly behind the shock wave, which can be written as

$$V_r = V_\infty \tau \bar{V}_\eta = \frac{V_\infty \theta_s \bar{V}_\eta}{s'(x)},$$

where, in accordance with the equation of the shock $r = \tau s(x)$, the small parameter is

$$\tau = \frac{dr/dx}{ds(x)/dx} = \frac{\theta_s}{s'(x)}.$$

Introducing $K_0 = M_\infty \theta_s$ and substituting the new variable ξ for x, the following condition is obtained for the function $\bar{V}_\eta$:

$$\bar{V}_\eta = \frac{2}{\gamma + 1} \frac{K_0^2 - 1}{K_0^2} s'(\xi). \tag{17.25}$$

The conditions on the shock wave for the functions $\bar{\rho}$ and $\bar{p}$ are obtained from Eqs. (4.21) and (4.22) by substituting $\rho_2/\rho_1 = \rho/\rho_\infty = \bar{\rho}$ into the first equation and

$$\frac{p_2}{p_1} = \gamma M_\infty^2 \tau^2 \bar{p} = \bar{p} \frac{\gamma K_0^2}{[s'(x)]^2}$$

into the second equation. Converting from x to ξ, we obtain

$$\bar{p} = \frac{2\gamma K_0^2 - (\gamma - 1)}{\gamma(\gamma + 1)K_0^2} [s'(\xi)]^2, \qquad \bar{\rho} = \frac{(\gamma + 1)K_0^2}{2 + (\gamma - 1)K_0^2}. \tag{17.26}$$

The Equation for the Stream Function

The solution of problems concerning flow around axisymmetric bodies of curved shape requires the determination of the entropy change from one streamline to another behind the shock wave. To facilitate the solution of similar problems for flow at hypersonic speeds, the equations obtained above can be converted to the stream function Ψ, which is determined from

Eqs. (3.25). Replacing ρ_0 by ρ_∞ in these equations, converting to the new variables η, ξ, and including in the stream function constants for the given conditions of V_∞, τ, and l_N, we obtain for small perturbations

$$\Psi_\eta = \frac{\partial \Psi}{\partial \eta} = \eta \bar{\rho}, \qquad \Psi_\xi = \frac{\partial \Psi}{\partial \xi} = -\eta \bar{\rho} \bar{V}_\Gamma. \tag{17.27}$$

Thus,

$$\bar{V}_\eta = -\frac{\Psi_\xi}{\Psi_\eta}, \qquad \bar{\rho} = \frac{\Psi_\eta}{\eta}. \tag{17.28}$$

These expressions can be substituted into Eq. (17.20), in which the derivative $\partial \bar{p}/\partial \eta$ is written as

$$\frac{\partial \bar{p}}{\partial \eta} = \frac{\partial}{\partial \eta}(\omega \bar{\rho}^\gamma) = \frac{\partial \omega}{\partial \eta} \bar{\rho}^\gamma + \gamma \omega \bar{\rho}^{\gamma-1} \frac{\partial \bar{\rho}}{\partial \eta} = \frac{d\omega}{d\Psi} \frac{\partial \Psi}{\partial \eta} \bar{\rho}^\gamma + \gamma \omega \bar{\rho}^{\gamma-1} \frac{\partial \bar{\rho}}{\partial \eta}.$$

The parameter $\omega = \bar{p}/\bar{\rho}^\gamma$ depends on the entropy change from one streamline to another and thus is a function of Ψ, i.e., $\omega = f(\Psi)$.

Designating the derivative $d\omega/d\Psi$ by ω' and replacing $\bar{\rho}$ by Eq. (17.28), we obtain

$$\frac{\partial \bar{p}}{\partial \eta} = \omega' \Psi_\eta \left(\frac{\Psi_\eta}{\eta}\right)^\gamma - \gamma \omega \left(\frac{\Psi_\eta}{\eta}\right)^{\gamma-1} \frac{\Psi_{\eta\eta}\eta - \Psi_\eta}{\eta^2}.$$

The equation for the stream function becomes

$$\Psi_\eta^2 \Psi_{\xi\xi} - 2\Psi_\xi \Psi_\eta \Psi_{\xi\eta} + \Psi_\xi^2 \Psi_{\eta\eta} = \frac{\Psi_\eta^{\gamma+1}}{\eta^{\gamma-1}} \left[\gamma \omega \left(\Psi_{\eta\eta} - \frac{\Psi_\eta}{\eta}\right) + \omega' \Psi_\eta^2\right]. \tag{17.29}$$

The pressure is determined by the expression

$$\bar{p} = \omega \bar{\rho}^\gamma = \omega \left(\frac{\Psi_\Gamma}{\eta}\right)^\gamma. \tag{17.30}$$

THE CALCULATION OF FLOW AROUND A SLENDER POINTED BODY OF CURVED SHAPE

One of the calculation methods that we shall investigate is based on the solution of Eq. (17.29) for the stream function. The solution cited here is not general, but can be used to calculate the parameters

in the vicinity of the tip. This limitation results from the complex form of the equation for the stream function, for which no general integral has yet been found.

The special solution is obtained by first finding the solution of the equation for flow around a conical tip with an angle δ_0 (Fig. 166).

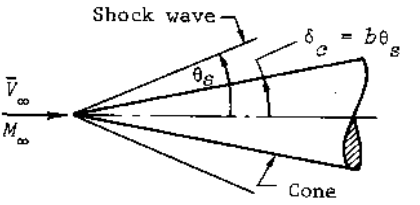

Fig. 166--The nose angle and shock-wave angle for a cone

In this case, as we shall see, the equation is solved exactly. Next, after examining a small region of the curved surface and knowing the stream function for flow around a cone, we find a new solution of Eq. (17.29), in which the influence of the curvature of the surface is taken into account to a first approximation. After this, the problem can be solved in the second approximation, which obviously broadens the region in which the solution for the stream function can be determined.

The Solution for a Cone

The flow around a cone is characterized by constant entropy in all regions behind the shock wave, so that the derivative ω' in Eq. (17.29) is zero. Moreover, the flow around a cone is conical, and the stream function can be written in the form

$$\Psi(\xi, \eta) = \xi^2 f(\theta), \tag{17.31}$$

where θ is the relative angle of the intermediate conical surface, defined as $\theta = r/(\theta_s x) = \eta/\xi$. Thus, the shock angle θ_s can be considered to be the small parameter that was designated by τ above.

The fact that the stream function, Eq. (17.31), actually corresponds to conical flow can be verified if the derivative $\Psi_\eta = \xi(df/d\theta)$, for example, is determined and equated to its value Ψ_η according to Eq. (17.27). As a result we find that one of the flow parameters, the dimensionless density $\bar{\rho}$, has a constant value on a conical surface of angle θ.

Introducing Eq. (17.31) into Eq. (17.29), an ordinary nonlinear differential equation is obtained:

$$4f^2f'' - 2f(f')^2 = \gamma\omega_0 \frac{(f')^{\gamma+1}}{\theta^{\gamma-1}}\left(f'' - \frac{f'}{\theta}\right), \tag{17.32}$$

in which f' and f'' are the first and second derivatives with respect to θ, and ω_0 is the constant value of the ratio $\bar{p}/\bar{\rho}^\gamma$ behind the shock wave. The latter is determined from Eqs. (4.21) and (4.22):

$$\omega_0 = \frac{2\gamma K_0^2 - (\gamma - 1)}{\gamma(\gamma + 1)K_0^2}\left[\frac{2 + (\gamma - 1)K_0^2}{(\gamma + 1)K_0^2}\right]^\gamma. \tag{17.33}$$

The solution of Eq. (17.29) must satisfy the boundary conditions at the shock wave, which are obtained from Eqs. (17.26), (17.27), (17.31), and (17.33). For example, the conditions for $f(\theta)$ and its derivative $f'(\theta)$ are found in the following manner. Using Eqs. (17.27) and (17.31), the derivative $\Psi_\eta = \xi f'(\theta) = \eta\bar{\rho}$, so that $f'(\theta) = \eta\bar{\rho}/\xi$. The function $f(\theta)$ is determined from Eqs. (17.27), (17.29), and (17.31) in the form

$$f(\theta) = \frac{1}{2}f'(\theta)\left(\theta + \frac{\Psi_\xi}{\Psi_\eta}\right) = \frac{1}{2}\theta\bar{\rho}(\theta - \bar{V}_\eta).$$

The parameters $\bar{V}_\eta$ and $\bar{\rho}$ are given by Eqs. (17.25) and (17.26). Setting $\theta = 1$, we obtain the conditions at the shock wave:

$$f(1) = \frac{1}{2}, \qquad f'(1) = \frac{(\gamma + 1)K_0^2}{2 + (\gamma - 1)K_0^2}. \tag{17.34}$$

The continuous flow condition requires that the stream function on the body surface be zero. If the equation for the cone is given in the form $r = \vartheta_s bx$, this condition is written as $f(b) = 0$.

The calculation of the flow around a cone is made in the following manner. Assigning a value to K_0, the values of the functions ω_0 and $f'(1)$ are determined. Equation (17.32) is numerically integrated from the conditions at the shock wave to the conditions on the cone surface. The resulting value $\delta_c = b\theta_s$ is the angle of the cone that produces a shock wave of angle ϑ_s for the assumed value of K_0. The calculation can then be repeated for other values of K_0. In addition to the angle δ_c, the value of the derivative f' is found on the surface of the cone, which enables us to calculate the pressure coefficient from the equation

$$\frac{C_{pc}}{\delta_c^2} = \frac{2(p_c - p_\infty)}{\gamma p_\infty K_1^2} = 2\left[\frac{\omega_0}{b^2}\left(\frac{f'}{\theta}\right)^\gamma - \frac{1}{\gamma K_1^2}\right]. \qquad (17.35)$$

This expression is obtained from Eqs. (17.19), (17.30), and (17.31) for the condition that $\tau = \theta_s$ and $\delta_c^2 = b^2\theta_s^2$. The parameter K_1 in Eq. (17.35) is defined as before: $K_1 = M_\infty \delta_c$. A curve for C_{pc}/δ_c^2 as a function of K_1 from Eq. (17.35) is compared with exact theory in Fig. 167.

The results of small disturbance theory also agree well with the approximate theory presented earlier in this chapter.

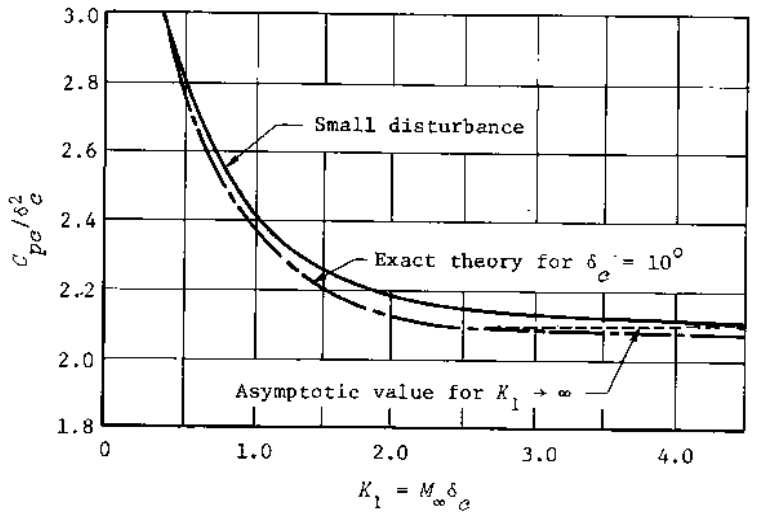

Fig. 167--Pressure coefficient on a cone at hypersonic speeds

First Approximation for Curvature

Let us assume that an axisymmetric body and its shock wave are represented, respectively, by the equations

$$r = \theta_0\left(bx + \frac{1}{2}\,cx^2\right), \qquad r = \theta_0\left(x + \frac{1}{2}\,lcx^2\right), \tag{17.36}$$

where θ_0 is the shock-wave angle at the tip (Fig. 168).

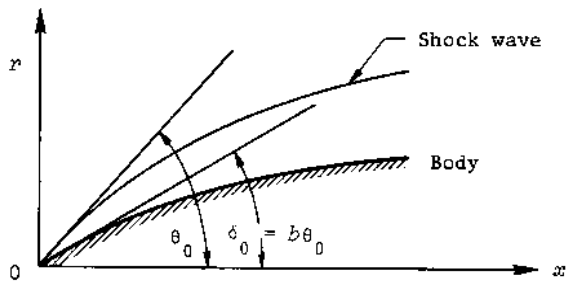

Fig. 168--The nose angle and the shock-wave angle for an arbitrary body of revolution

In the solution of Eq. (17.29) for a curved surface, the conditions on Ψ and ω directly behind the shock wave are determined by using Eqs. (17.26), (17.27), and (17.33). These conditions will depend on the local shock angle but can be simplified by expanding the functions in the region of the nose into series in terms of the parameter $K = M_\infty\theta_s$, calculated from the local shock angle. The parameter K_0 is constant and defined as $K_0 = M_\infty\theta_0$.

The conditions for the stream function directly behind the shock wave are determined by means of the derivatives Ψ_ξ and Ψ_η. Let us investigate how the initial condition for the derivative Ψ_ξ is found, keeping in mind that the calculation for Ψ_η will be similar. First, it will be noted from Eqs. (17.25) through (17.27) that Ψ_ξ depends on the value of the parameter K. Expanding this function in a series in terms of K in the vicinity of the tip and terminating with the second term in the expansion, we find

$$\Psi_\xi = \Psi_\xi(K_0) + \left.\frac{\partial \Psi_\xi}{\partial K}\right|_{K=K_0} dK.$$

The value of $\Psi_\xi(K_0)$ can be determined with the help of Eqs. (17.25) through (17.27). Noting that

$$s'(\xi) = \frac{1}{\theta_c}\frac{dr}{dx} = \frac{K}{K_0},$$

the function Ψ_ξ has the following form:

$$\Psi_\xi = -\frac{2\eta(K^2 - 1)}{2 + (\gamma - 1)K^2}\frac{K}{K_0}. \tag{17.37}$$

Setting $K = K_0$, we can find the value of $\Psi_\xi(K_0)$.

To find the derivative $(\partial\Psi_\xi/\partial K)_{K=K_0}$, it is necessary to differentiate Eq. (17.37) with respect to K and set $K = K_0$.

Finally, the differential can be obtained from Eq. (17.36):

$$dK = M_\infty(\theta_s - \theta_0) = K_0 \, l\sigma\xi.$$

The derivative Ψ_ξ at the shock wave can be written as

$$\Psi_\xi = -\eta\frac{2(K_0^2 - 1)}{2 + (\gamma - 1)K_0^2}\left\{1 + \frac{(\gamma - 1)K_0^4 + (\gamma + 5)K_0^2 - 2}{(K_0^2 - 1)[2 + (\gamma - 1)K_0^2]}\, l\sigma\xi\right\}. \tag{17.38}$$

The initial condition for the derivative Ψ_η can be obtained similarly:

$$\Psi_\eta = \eta\frac{(\gamma + 1)K_0^2}{2 + (\gamma - 1)K_0^2}\left[1 + \frac{4}{2 + (\gamma - 1)K_0^2}\, l\sigma\xi\right]. \tag{17.39}$$

The initial condition for ω is

$$\omega = \frac{\bar{p}}{\bar{\rho}^\gamma} = \frac{2\gamma K_0^2 - (\gamma - 1)}{\gamma(\gamma + 1)K_0^2}\left[\frac{2 + (\gamma - 1)K_0^2}{(\gamma + 1)K_0^2}\right]^\gamma\left\{1 + \frac{4\gamma(\gamma - 1)(K_0^2 - 1)^2}{[2\gamma K_0^2 - (\gamma - 1)][2 + (\gamma - 1)K_0^2]}\, l\sigma\xi\right\}. \tag{17.40}$$

As in the problem of a cone, the form of the solution for the stream function must be defined. Let us assume that this solution is determined basically by the value of the stream function for the conical tip with an angle $\delta_0 = b\theta_0$ and take the influence of curvature into account to a first approximation by a linear correction. Accordingly, we seek a solution in the form

$$\Psi(\xi, \eta) = \xi^2 f(\theta) - \varepsilon\xi^3 g(\theta), \tag{17.41}$$

where $g(\theta)$ is a function that accounts for the influence of the curvature. The solution must satisfy the boundary condition at the conical shock surface, for which $f(1) = \frac{1}{2}$. Assuming that $g(1) = 0$, this gives

$$\Psi = \frac{\eta^2}{2} = \frac{\xi^2}{2}.$$

The entropy function ω can be represented in the form of a series, retaining only the second term:

$$\omega(\Psi) = \omega_0(1 + \omega_1 \varepsilon\sigma \sqrt{2\Psi}), \tag{17.42}$$

where ω_0 is given by Eq. (17.33) and

$$\omega_1 = \frac{4\gamma(\gamma - 1)(K_0^2 - 1)^2}{[2\gamma K_0^2 - (\gamma - 1)][2 + (\gamma - 1)K_0^2]}. \tag{17.43}$$

Introducing Eqs. (17.41) and (17.42) into Eq. (17.29) and grouping the terms by identical powers of ξ, we obtain two equations. One of these is a nonlinear equation for the function $f(\theta)$, identical to Eq. (17.32) for a cone; the other is a linear equation for the function $g(\theta)$ having the form

$$Dg'' = A + Bg + Cg', \tag{17.44}$$

where g' and g'' are derivatives of the function $g(\theta)$ with respect to θ.

The coefficients in the latter equation are determined by the following expressions:

$$A = \omega_0\omega_1 \frac{(f')^{\gamma+1}}{\theta^{\gamma-1}}\left[\frac{(f')^2}{\sqrt{2f}} - \gamma\sqrt{2f}\left(\frac{f'}{\theta} - f''\right)\right],$$

$$B = 12ff'',$$

$$C = \gamma\omega_0 \frac{(f')^{\gamma+1}}{\theta^{\gamma-1}}\left[\frac{\gamma+2}{\theta} - (\gamma+1)\frac{f''}{f'}\right] - 8ff', \tag{17.45}$$

$$D = \gamma\omega_0 \frac{(f')^{\gamma+1}}{\theta^{\gamma-1}} - 4f^2.$$

Equation (17.44) can be integrated numerically. Setting $\theta = 1$ in Eqs. (17.38), (17.39), and (17.41), we obtain the conditions at the shock wave that the functions $g(\theta)$ and $g'(\theta)$ must satisfy:

$$g(1) = \frac{K_0^2 - 1}{2 + (\gamma - 1)K_0^2},$$

$$g'(1) = -K_0^2 \frac{(\gamma - 1)K_0^2 + 2(2\gamma + 3)}{[2 + (\gamma - 1)K_0^2]^2}. \tag{17.46}$$

The same values of K_0 chosen for the calculation of flow around a cone can be used for the numerical calculations. The integration is made from the known conditions on the shock wave using the same intervals that were used in the case of the cone. As a result, we find the function g and its derivative g' for each value of θ including $0 = b$, which corresponds to conditions on the conical nose.

The function g can also be found in the form of a series in the small parameter $\varepsilon = (\vartheta - b)/b$:

$$g(\theta) = \sum_{n=0}^{\infty} a_n b^n \varepsilon^n + b^{\frac{3}{2}}\varepsilon^{\frac{3}{2}} \sum_{n=0}^{\infty} c_n b^n \varepsilon^n. \tag{17.47}$$

Retaining terms containing ε to the fourth power, the required solution can be obtained from Eq. (17.44):

$$g(\theta) = \frac{2\sqrt{2}}{3\gamma}\omega_1[b\varepsilon f'(b)]^{\frac{3}{2}}\left[1 + \frac{3}{4}\varepsilon - \left(\frac{59}{70}\lambda - \frac{3}{32}\right)\varepsilon^2\right]$$

$$+ g(b)[1 + 2\lambda\varepsilon^3 - \lambda(1 + 2\lambda)\varepsilon^4]$$

$$+ g'(b)b\varepsilon\left(1 + \frac{1}{2}\varepsilon - \frac{3 - \gamma}{3}\lambda\varepsilon^2 + \frac{3 - \gamma}{6}\lambda\varepsilon^3\right), \qquad (17.48)$$

where

$$\lambda = \frac{b^{\gamma+1}}{\gamma\omega_0[f'(b)]^{\gamma-1}}. \qquad (17.49)$$

After the functions f and g and their derivatives are determined, the shock-wave shape can be found, and the pressure can be calculated for the first approximation.

The shape of the shock wave, as is evident from Eq. (17.36), is determined by the coefficient l, which is the ratio of the shock curvature to the curvature of the body profile. This coefficient is found from Eq. (17.41) by imposing the condition that the stream function on the body surface equals zero:

$$l = \frac{f'(b)}{2g(b)}. \qquad (17.50)$$

The pressure coefficient equals its value on the cone, plus a correction that is linear with respect to x, and depends on the initial pressure gradient. The value of this gradient is

$$\left.\frac{\partial C_p}{\partial x}\right|_b = -\frac{[f'(b)]^\gamma}{M_\infty^2 b^{\gamma-1}\delta_0^2}\frac{g'(b)}{g(b)}\delta_0 R_0'', \qquad (17.51)$$

where R_0'' is the curvature of the generatrix at the tip of the body.

Calculated results for the value of l and for the initial pressure gradient are presented in Figs. 169 and 170, respectively. The coefficient l can be approximated by the following relation:

$$l = 0.959 - 0.515K_1^{(-1.5+0.4/K_1)}. \qquad (17.52)$$

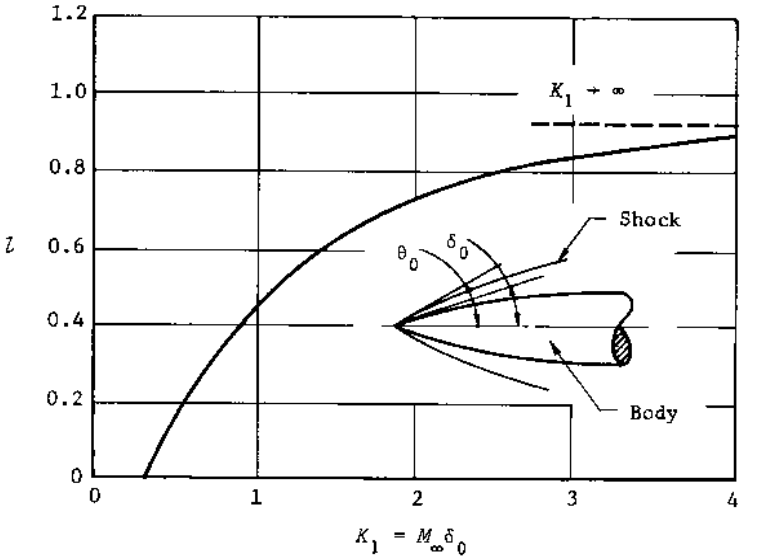

Fig. 169--Ratio of the curvatures of the shock wave and the body

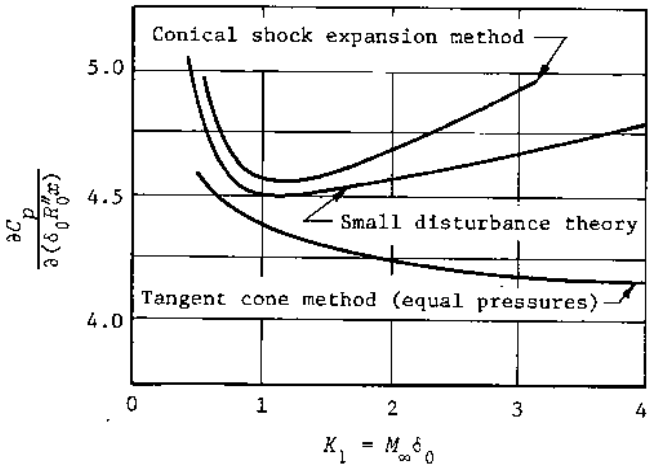

Fig. 170--Initial pressure gradient calculated by several methods

An approximation for the initial pressure gradient can be made from

$$\frac{\partial C_p}{\partial(\delta_0 R_0'' x)} = 4.929 - 0.429K_1^{-\frac{3}{2}} - \frac{0.645(K_1 - 1)}{K_1^2}. \tag{17.53}$$

Both equations give satisfactory results in the range $0.5 \leq K_1 \leq \infty$.

The pressure distribution can be obtained by an expansion in a power series in x. Terminating with the linear term, we find

$$C_p = C_{pc} + \frac{\partial C_p}{\partial x} x \quad \text{or} \quad C_p = C_{pc} + \delta_0 R_0'' \frac{\partial C_p}{\partial(\delta_0 R_0'' x)} x, \tag{17.54}$$

where C_{pc} is the pressure coefficient on the conical nose from Eq. (17.35), and $\partial C_p/\partial(\delta_0 R_0'' x)$ can be determined from Eq. (17.53). The curvature R_0'' is found from the equation for the body shape, written in the form

$$r = \delta_0 x + \frac{1}{2} R_0'' x^2.$$

The shape of the shock surface is determined from Eq. (17.36), which can be written somewhat differently, i.e.,

$$r = \theta_0 x + \frac{l}{2} R_0'' x^2,$$

where the coefficient l can be obtained from Eq. (17.52).

As an example, let us find the form of the shock wave and the pressure distribution near the tip of a parabolic body of revolution. For a parabolic shape, the nose angle is given by $\delta_0 = 1/\lambda_N$, and the curvature is

$$R_0'' = \frac{d^2 r}{dx^2} = -\frac{1}{l_N \lambda_N} = -\frac{\delta_0}{l_N}.$$

The equation for the shock can be written in the form

$$\bar{r} = \bar{x}\left(\frac{2K_0}{K_1} - l\bar{x}\right).$$

Equation (17.54) is used to determine the pressure distribution:

$$\frac{C_p}{\delta_0^2} = \frac{C_{pc}}{\delta_0^2} - \frac{\partial C_p}{\partial(\delta_0 R_0'' x)}\,\bar{x}.$$

It is apparent that the shape of the shock wave and the pressure coefficient at the surface are functions only of the parameter $K_1 = M_\infty \delta_0$, since K_0 and l are also dependent on K_1.

The Second Approximation

Calculation of the second approximation is concerned with discovering a more accurate expression for the stream function than Eq. (17.31). Let us assume that the equation for the body is given in the form

$$r = \theta_0\left(bx + \frac{1}{2}\,cx^2 + \frac{1}{6}\,dx^3\right), \tag{17.55}$$

and the equation for the shock wave is

$$r = \theta_0\left[x + \frac{1}{2}\,lcx^2 + \frac{1}{6}\,(md + nc^2)x^3\right]. \tag{17.56}$$

We rewrite Eq. (17.55) in new variables:

$$\tilde{r} = \eta - \frac{1}{2}\,c\xi^2 - \frac{1}{6}\,d\xi^3 = bx, \tag{17.55a}$$

where $\tilde{r} = bx$ is a new radial coordinate. The angle of the conical surface corresponding to it, the so-called conical coordinate, is $\tilde{\theta} = \tilde{r}/x = b$. Assuming that the flow parameters are functions of this coordinate, the stream function can be sought in the following form:

$$\psi = \xi^2 f(\tilde{\theta}) - c\xi^3 \tilde{g}(\tilde{\theta}) - \xi^4[c^2 \tilde{j}(\tilde{\theta}) + d\tilde{h}(\tilde{\theta})], \tag{17.57}$$

where

$$\tilde{g}(\tilde{\theta}) = lg(\tilde{\theta}) - \frac{1}{2}\,f'(\tilde{\theta}), \qquad \tilde{h}(\tilde{\theta}) = mh(\tilde{\theta}) - \frac{1}{6}\,f'(\tilde{\theta}),$$
$$\tilde{j}(\tilde{\theta}) = l^2 j(\tilde{\theta}) + nh(\tilde{\theta}) + \frac{1}{2}\,lg'(\tilde{\theta}) - \frac{1}{8}\,f''(\tilde{\theta}). \tag{17.58}$$

Substituting Eq. (17.57) into Eq. (17.29), and using the definitions of Eq. (17.58), we obtain an equation of the type of Eq. (17.32) for the function f, and of Eq. (17.44) for the function g. In addition, the equations for determining the functions $h(\tilde{0})$ and $j(\tilde{\vartheta})$ are

$$Dh'' = E + Fh + Gh',$$
$$Dj'' = I + Fj + Gj', \tag{17.59}$$

where the coefficient D is given by Eq. (17.45). The coefficients E, F, G, and I, which depend on f and its first and second derivatives, are found using Eqs. (17.32) and (17.44). In addition, the coefficient I depends on the function g and on its first and second derivatives. The expressions for these coefficients are unwieldy and are not presented here.† We limit ourselves to an examination of results that can be used directly for calculations.

The values of h and j can be determined from the numerical solution of Eq. (17.59) and the stream function evaluated by Eq. (17.57). After this, the pressure coefficient can be calculated:

$$\frac{C_p}{\delta_0^2} = \frac{2}{\gamma K_1^2}\left[\gamma\omega_0 K_0^2\left(\frac{\psi}{\eta}\right)_b^{\gamma} - 1\right]. \tag{17.60}$$

Equation (17.55) can be converted to the form

$$r = R_0'x + \frac{1}{2}R_0''x^2 + \frac{1}{6}R_0'''x^3, \tag{17.55b}$$

where $R_0^{(n)}$ is the value of the derivative d^nR/dx^n at the point $x = r = 0$. Then the pressure coefficient can be written in the form of a series:

$$C_p = (R_0')^2\frac{C_{pe}}{(R_0')^2} + R_0'R_0''\left[\frac{\partial C_p}{\partial(R_0'R_0''x)}\right]x + \frac{1}{2}\left[(R_0'')^2\frac{\partial^2 C_p}{\partial(R_0''x)^2} + R_0'R_0'''\frac{\partial^2 C_p}{\partial(R_0'x)\partial(R_0'''x)}\right]x^2. \tag{17.61}$$

†Editor's note: See Ref. 3 for these expressions.

The quantities $C_{pe}/(R_0')^2 = C_{pe}/\delta_0^2$ and $\partial C_p/\partial(R_0'R_0''x)$ can be determined by Eqs. (17.35) and (17.51), or from the approximations given by Eqs. (17.13) and (17.53), respectively.

The second derivatives in Eq. (17.61) have the following form:

$$\frac{\partial^2 C_p}{\partial(R_0''x)^2} = 2\gamma\omega_0\left(\frac{f_b'}{b}\right)^{\gamma}\left[\frac{\gamma-1}{4}\frac{(g_b')^2}{g_b^2} - \frac{\lambda}{2b^2} - 2n\frac{j_b'}{j_b} - 2l^2\frac{h_b'}{f_b'}\right], \qquad (17.62)$$

where λ is given by Eq. (17.49),

$$n = \frac{1}{8}f_b'' - \frac{1}{2}lg_b' - \frac{l^2h_b}{j_b},$$

and

$$\frac{\partial^2 C_p}{\partial(R_0'x)\partial(R_0'''x)} = -\frac{2}{3}\frac{\gamma\omega_0}{b}\left(\frac{f_b'}{b}\right)^{\gamma}\frac{j_b'}{j_b}. \qquad (17.63)$$

In these expressions, the subscript b corresponds to conditions on the body surface. Graphs of the derivatives given by Eqs. (17.62) and (17.63) are presented in Fig. 171.

If the body is of parabolic shape with an equation $\bar{r} = \bar{x}(2 - \bar{x})$, then $R_0''' = 0$ and only the second derivative $\partial^2 C_p/\partial(R_0''x)^2$ is needed. On the basis of Fig. 171, this can be approximated by

$$\frac{\partial^2 C_p}{\partial(R_0''x)^2} = 13.7 - \frac{K_1^{\frac{3}{2}} + 30K_1^{\frac{1}{2}} - b}{K_1^2}. \qquad (17.64)$$

This equation gives satisfactory results for K_1 in the range $1 \le K_1 \le \infty$ when the coefficient $b = 22.5$ and for the range $0.5 \le K_1 < 1$ when $b = 19.2$.

The results obtained for the pressure distribution are very close to those from the method of characteristics including rotational effects. This is explained by the fact that the small perturbation theory under discussion reflects the essential features of supersonic flow involving an entropy gradient behind the shock wave. The determination of the second derivative, using Eq. (17.64), allows for broadening the region

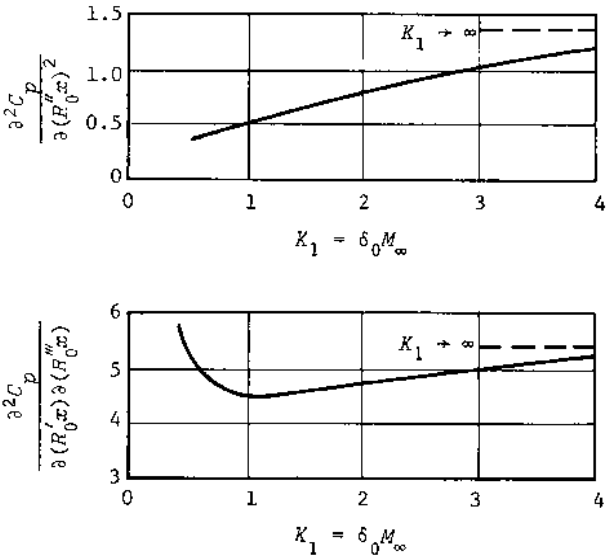

Fig. 171--Second derivative of the pressure coefficient

in which the pressure distribution is computed. However, it should be remembered that such a calculation does not totally represent the character of the pressure distribution on the whole surface of the body.†

To supplement the results obtained from small perturbation theory, we shall examine some approximate methods for the calculation of flow around bodies and compare the data obtained by these methods with the results of small perturbation theory to estimate their accuracy.

APPROXIMATE METHODS OF CALCULATING HYPERSONIC FLOW AROUND BODIES OF REVOLUTION

The Method of Local Cones

If we consider the local-cone method based on the hypothesis of identical pressures, Eq. (17.13a) can be used for the calculation of the

†Editor's note: The results are taken directly from Ref. 3, and Van Dyke shows very poor agreement for the second approximation on the aft portion of an ogive nose.

pressure distribution around a body of arbitrary shape if the parameter K_1 is determined for the angle of the local cone δ. As an example, consider the calculation of the flow around a slender parabolic body of revolution, the local slope of which is $\delta = \delta_0(1 - \bar{x})$. Using Eq. (17.13a), the equation for the pressure distribution on the body can be approximated by

$$\frac{C_p}{\delta_c^2} = 2.091\left[(1 - \bar{x})^2 + \frac{0.143}{K_1^{\frac{3}{2}}}(1 - \bar{x})^{\frac{1}{2}}\right], \tag{17.65}$$

where $K_1 = M_\infty \delta_c$ is determined for the local cone at the tip.

In using this equation, the limits of applicability of Eq. (17.13a) must be taken into account, since, strictly speaking, the calculations are valid only for those points on the body surface for which the local values of $K_1 = M_\infty \delta$ exceed 0.5 to 1.0. The results are doubtful for those sections of the nose where $\bar{x}$ is close to unity, since the slope of the local cone is small and, consequently, $K_1 <$ (0.5 to 1.0). The approximate method will always indicate a pressure coefficient of zero at the end of the nose, where $\bar{x} = 1$.

Since the character of the pressure distribution depends on the initial pressure gradient, it is of interest to compare the values of the first derivatives of the pressure coefficient at the tip from Eq. (17.65) with those from small disturbance theory (i.e., Eq. (17.53)). Differentiating Eq. (17.65), we obtain

$$\frac{\partial C_p}{\partial\left(\delta_0^2 \bar{x}\right)} = -4.182\left(1 + \frac{0.036}{K_1^{\frac{3}{2}}}\right). \tag{17.66}$$

The initial pressure gradient calculated from this equation is compared with small disturbance theory in Fig. 170. It is apparent that the accuracy of the calculation by the method of local cones decreases with an increase in the parameter K_1.

The equations for the pressure distributions in the vicinity of the tip for the special values $K_1 = 1$ and 2 are

$$K_1 = 1: \quad \frac{C_p}{\delta_0^2} = 2.40 - 4.50\bar{x} + 2.60\bar{x}^2, \qquad \frac{C_p}{\delta_0^2} = 2.40 - 4.38\bar{x} + 2.19\bar{x}^2,$$

$$K_1 = 2: \quad \frac{C_p}{\delta_0^2} = 2.20 - 4.62\bar{x} + 4.02\bar{x}^2, \qquad \frac{C_p}{\delta_0^2} = 2.20 - 4.25\bar{x} + 2.19\bar{x}^2.$$

The equations on the left result from the theory of small disturbances, those on the right from the method of local cones.

From a comparison of these equations, it follows that some overestimation of pressure is inherent in the method of local cones. The same conclusion results from comparing this method with experimental data and with the method of characteristics (Fig. 172). It is evident from this figure, however, that the difference in the results is slight, and the method of local cones can be used for approximate calculations.

This conclusion also applies to the pressure drag coefficient. The approximate relation for drag can be obtained if Eq. (17.65) is introduced into Eq. (1.6) and the result integrated:

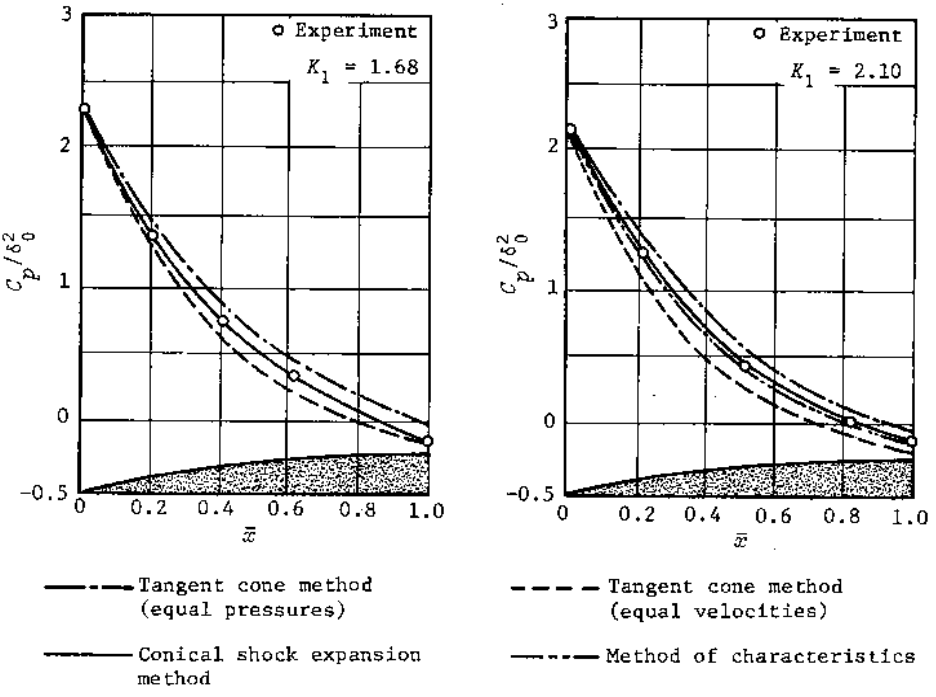

Fig. 172--Pressure distribution on a body of revolution at hypersonic speeds

$$\frac{C_{Dp}}{\delta_0^2} = 0.697 + \frac{0.213}{K_1^{\frac{3}{2}}}. \tag{17.67}$$

If the variant of the method of local cones based on the hypothesis of identical velocities is used, comparison shows that the calculated pressures are too low for large Mach numbers (Fig. 172).

Shock Expansion Theory

The basic principles of shock expansion theory were outlined in the discussion of the problem of asymmetric supersonic flow around a body of revolution. In applying this method to hypersonic velocities, a series of simplifications can be made. First, Eq. (8.11a) for the function ω can be written in an integral form for very high Mach numbers:

$$\omega = \frac{2}{\gamma - 1} \int_1^M \frac{dM}{M^2},$$

which, after integration, gives

$$\omega = -\frac{2}{\gamma - 1}\left(\frac{1}{M} - 1\right). \tag{17.68}$$

For flow conditions directly behind the shock wave on a conical nose, we obtain

$$\omega_2 = -\frac{2}{\gamma - 1}\left(\frac{1}{M_2} - 1\right).$$

The difference $\omega - \omega_2$ determines the deflection angle of the flow $\Delta\delta$ from the conditions at the nose to those at an arbitrary point on the body where the Mach number is M:

$$\omega - \omega_2 = \Delta\delta = -\frac{2}{\gamma - 1}\left(\frac{1}{M} - \frac{1}{M_2}\right). \tag{17.69}$$

This expression can be used in place of the complicated Eq. (8.11a) or Table 15 for the calculation of the local Mach number.

The remaining parameters, such as pressure, temperature, density,

speed of sound, and flow velocity, are calculated from the Mach number using the simplified Eqs. (3.61) and (3.62), into which it is necessary to substitute parameters with the subscript 2 in place of the corresponding values with the subscript ∞. For example, the relation for the pressure coefficient can be obtained from Eq. (3.61):

$$\frac{C_p}{\delta_0^2} = \left(\frac{M_2}{M}\right)^{2\gamma/(\gamma-1)} \left(\frac{C_{pe}}{\delta_0^2} + \frac{2}{\gamma K_1^2}\right) - \frac{2}{\gamma K_1^2}. \tag{17.70}$$

The Mach number M_2 in this equation and Eq. (17.69) can be determined from simplified formulas.

The practical application of the method is best illustrated by a specific example. The problem is to calculate the flow around a pointed body of revolution with a nose angle of $\delta_0 = 0.2$ radian for $M_\infty = 10$ (or $K_1 = 2$). First, we find M_2 directly behind the shock on a conical nose. If $\gamma = 1.4$, Eq. (17.5) indicates that $K_0 = M_\infty \theta_s = 2.38$, and from Eq. (4.39) we can compute $M_2 = 6.73$. It is now possible to calculate the necessary parameters at any point on the surface of the body.

Let us find the Mach number and the pressure at the point where the slope is $\delta = 0.1 = 5.73°$. In this case, the flow is deflected through an angle $\Delta\delta = \delta_0 - \delta = 0.1$, and from Eq. (17.69) the local Mach number is 7.83. The quantity C_{pe}/δ_0^2 at the conical tip is calculated from Eq. (17.13a) and is equal to 2.2. Then, from Eq. (17.70), $C_p/\delta_0^2 = 0.543$ for the point selected.

If a point further aft is investigated, for which $\delta = 0$, the calculation gives $M = 9.27$. The corresponding pressure coefficient parameter is $C_p/\delta_0^2 = -0.085$ and is negative. This indicates that the shock expansion method can lead to a negative value of the pressure coefficient in some regions, in agreement with experimental measurements. Thus, the shock expansion method will result in better general agreement than will the method of local cones with both small disturbance theory and the method of characteristics.

This conclusion is confirmed by the data in Fig. 170, where it is evident that the initial slope of the curve calculated by the shock

expansion method is closer to the results of small disturbance theory than is the method of local cones.

Satisfactory results of the shock expansion method are additionally confirmed in Fig. 172, where experimental data and pressure distributions calculated according to the method of characteristics are also shown.

Estimates of the Flow Parameters on a Converging Afterbody

The Mach number on the afterbody can be estimated in the same way as on the nose. Let us assume that the afterbody of a body of revolution is tapered and has an arbitrary shape with a smooth profile. Since the slope δ_{BT} of this section is known at every point, the total deflection angle of the flow from the conditions at the nose is known and is equal to $\Delta\delta = \delta_0 - \delta_{BT}$, where δ_{BT} is negative in sign.

The subsequent calculation is analogous to that discussed above, and for illustration, we shall continue with the example. Let us assume, specifically, that the value of the angle $\delta_{BT} = -0.1$. In this case, $\Delta\delta = 0.2 - (-0.1) = 0.3$ and, according to Eq. (17.69), the Mach number at the point in question equals 11.4. From Eq. (17.70), $C_p/\delta_0^2 = -0.293$, and the expansion is increased due to the effect of the boattail.

After calculating the pressure distribution in this manner, the boattail pressure drag can be computed from the formula

$$C_{Dp}^{BT} = \int_0^{\bar{r}_B^2} |C_p| \, d\bar{r}^2.$$

If the above example is applied to the frustum of a cone with an angle $\delta_{BT} = -0.1$, the pressure coefficient on the boattail is $C_p = -0.293\delta_0^2$ and is constant according to this method. Thus,

$$C_{Dp}^{BT} = 0.293\delta_0^2(1 - \bar{S}_B).$$

The shock expansion method for the estimate of flow parameters around the boattail section of a body must only be used after considering the familiar caution that the method does not take into account all the complex processes of three-dimensional flow around the forward

sections, particularly around the intermediate cylinder. These processes are accompanied by the interaction of the flow with the shock wave.

Another deficiency in the method is that it does not take into account the previous history of the motion of the gas particles. How the particle was moved to a given place is not important; only the position of the particle itself need be known. Thus, the parameters at any point on the surface of the body with a fixed tip angle δ_0 are assumed to be completely independent of the surface shape if the slope of the point in question is maintained constant.

As to the cylindrical midsection, the method lacks the potentiality for even an approximate picture of the flow around it. Consequently, only very rough preliminary estimates of the flow around the aft section of a body can be obtained. For example, the method can be used to estimate the flow deflection angle at which the absolute pressure falls to zero on the surface of the converging afterbody. In this case, obviously, the pressure coefficient is $C_p = -2/\gamma M_\infty^2$. As is evident from Eq. (17.70), this limiting value is attained as $M \to \infty$, which can occur (according to Eq. (17.69)) when the angle of deflection of the flow $\Delta\delta \to 2/(\gamma - 1)M_2$. If the angle of deflection is larger than this limiting value, the flow breaks away, and an almost absolute vacuum develops in the zone of detachment. Experimental research on axisymmetric bodies shows that such phenomena are observed under actual conditions for somewhat lesser angles of deflection.

§ 18. *APPROXIMATE CALCULATION OF AERODYNAMIC CHARACTERISTICS BASED ON NEWTONIAN FLOW THEORY*

AXIAL FORCE COEFFICIENT

Newtonian Flow Theory; Pressure Coefficient on a Cone

THE CONCEPT OF "NEWTONIAN DRAG" or "Newtonian flow" is usually associated with Newton's attempt to calculate the force of resistance from the loss of total momentum by the particles impinging on the largest cross section of the body. In the case of subsonic and moderately supersonic velocities, later research has established that the effective aerodynamic forces do not follow the Newtonian hypothesis even when the momentum loss is determined only by the normal component of the unperturbed velocity, i.e., taking into account the local slope of the body surface at the point in question. The excess pressure on any area calculated according to this momentum loss, i.e., on the basis of some modified theory of Newtonian flow, differs substantially from the real excess pressure.

As a result of the study of the flow around a cone, it should be noted, however, that this difference decreases with an increase in supersonic velocity. Actually, as follows from Eq. (17.15), the limiting value of the pressure coefficient on a cone is

$$C_{pc} = \frac{2(\gamma + 1)(\gamma + 7)}{(\gamma + 3)^2}\,\delta_c^2,$$

which, for $\gamma = 1.4$, gives $C_{pc} = 2.091\delta_c^2$.

Let us examine the flow around the same cone on the basis of Newtonian flow theory, which states that gas particles reach the surface

without experiencing disturbances (Fig. 173). On collision with the surface and loss of that part of the momentum associated with the undisturbed velocity component normal to the surface of the body, an excess pressure results:

$$p - p_\infty = \rho_\infty V_\infty^2 \delta_c^2,$$

from which the pressure coefficient is $C_{pc} = 2\delta_c^2$. This limiting value differs only by 4 percent from the previous value, which indicates that Newtonian flow agrees well with real flow at hypersonic velocities.

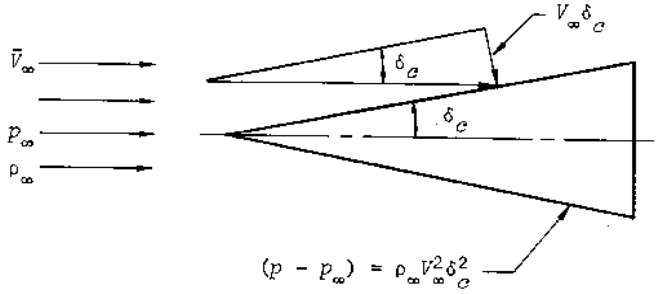

Fig. 173--Flow over a body according to Newtonian theory

The physical basis of this analogy results from the energy equation $0.5V_\infty^2 + i_\infty = \text{const}$. Obviously, at very high velocities, the enthalpy of the flow is small compared with the kinetic energy. Under such conditions, therefore, particle interactions have a relatively slight influence, and the gas can be considered, to a known approximation, to consist of atoms and molecules independent of each other. This flow model approximates the picture of Newtonian flow.

It is interesting to note that the analogy will be complete if a hypothetical flow with $\gamma = c_p/c_v = 1$ is examined instead of the actual flow. In fact, the limiting value of the pressure coefficient on a cone in such a flow is

$$C_{pc} = \frac{2(\gamma + 1)(\gamma + 7)}{(\gamma + 3)^2} \delta_c^2 = 2\delta_c^2,$$

i.e., a limiting value exactly equal to the value from Newtonian flow.

The shape of the shock wave can be determined for $\gamma = 1$ from Eq. (17.14), which gives the wave angle as $\theta_c = \delta_c$. Thus, the shock wave in Newtonian flow follows the surface closely. This analogy is the basis for using Newtonian flow theory to estimate approximately the pressure and aerodynamic coefficients of a body of revolution in a real flow at very high Mach numbers. As we shall note later, measures to refine Newtonian flow theory have been taken to obtain more accurate results, leading to the so-called modified Newtonian theory.

The Pressure Coefficient on the Surface of a Body of Revolution of Arbitrary Shape

Let us examine a body traveling at an angle of attack (Fig. 174). At very high free-stream Mach numbers approaching infinity, it can be assumed that the flow around the body can be calculated from Newtonian

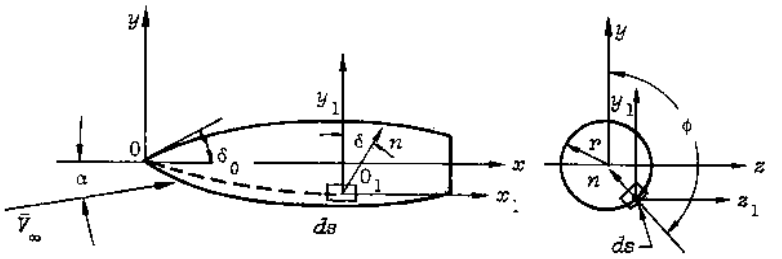

Fig. 174--Orientation of an elemental area on the surface of a body of revolution

flow theory, in accordance with which excess pressure occurs due to the deceleration of the particles in a direction normal to the body surface.[4] In the process of deceleration, the velocity component normal to the surface changes in value from $V_\infty \cos \eta$ to zero, and the excess pressure at this point is

$$p - p_\infty = \rho_\infty (V_\infty \cos \eta)^2, \qquad (18.1)$$

where η is the angle between the normal to the body surface and the

direction of the vector $\bar{V}_\infty$. To determine the angle η, an element dS of the body surface in an arbitrary section is selected, and a local coordinate system, x_1, y_1, z_1, is defined, centered at this element and parallel to the basic coordinate system, x, y, z.

It follows from Fig. 175 that the projection of O_1B in the direction of the normal n will be the segment $O_1E = (O_1B)\cos\eta$, which is

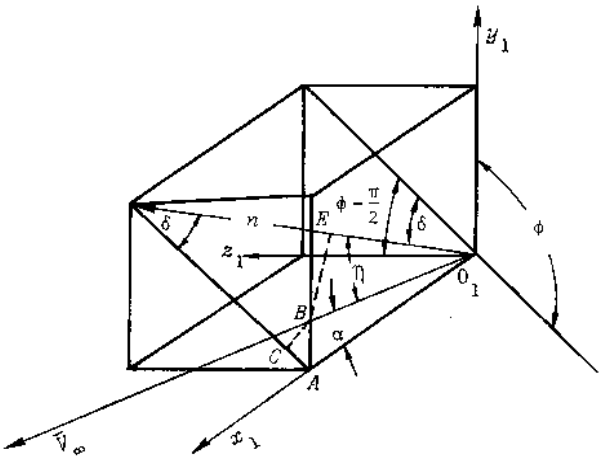

Fig. 175--Relation between the normal to an area and the free-stream direction

also equal to the projection of the broken line O_1ACB in the same direction. Thus, $O_1E = (O_1A)_n + (AC)_n + (CB)_n$. The figure indicates that

$$(O_1A)_n = (O_1B)\cos\alpha\sin\delta,$$

$$(AC)_n = -(O_1B)\sin\alpha\cos\phi\cos\delta,$$

$$(CB)_n = 0,$$

and, therefore,

$$\cos\eta = \cos\alpha\sin\delta - \sin\alpha\cos\phi\cos\delta. \qquad (18.2)$$

After calculating the normal velocity component $V_\infty \cos \gamma$, the limiting value of the pressure coefficient can be found from Eq. (18.1):

$$C_p = 2 \cos^2 \eta = 2(\cos \alpha \sin \delta - \sin \alpha \cos \phi \cos \delta)^2. \qquad (18.3)$$

For small angles of attack and slender bodies of revolution, we have

$$C_p = 2(\delta - \alpha \cos \phi)^2. \qquad (18.3a)$$

These equations enable us to determine the pressure coefficient for any area of the body having a positive slope. At those points on the body where the particle velocity V_∞ is tangent to the surface, i.e., $\eta = \pi/2$, the excess pressure is equal to zero because there is no loss of momentum. In this case, the particles slide, as it were, across the surface. The coordinates of these points can be found from Eqs. (18.3) or (18.3a). Assuming that $C_p = 0$, the angle $\delta = \alpha \cos \phi$. This equation represents the so-called curve of zero excess pressure (Fig. 176). From this line

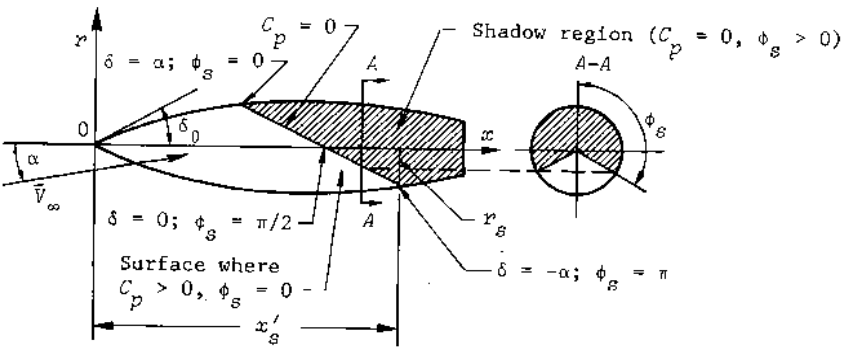

Fig. 176--The shadow region on a body of revolution

downstream, there is no deceleration of the flow by the body surface. Under actual conditions, a rarefaction should occur in the shadow region, and thus the pressure coefficient would be negative.

In Newtonian flow, it is obvious that at infinitely large free-stream Mach numbers the pressure coefficient in the shadow zone is equal

to zero, since

$$\lim_{M_\infty \to \infty} C_p = \lim_{M_\infty \to \infty} \left[\frac{2}{\gamma M_\infty^2} \left(\frac{p}{p_\infty} - 1 \right) \right] = 0.$$

Consequently, if the angle δ in Eq. (18.3a) is equal to or less than $\alpha \cos \phi$, the pressure coefficient can be assumed equal to zero.

For an arbitrary area with a positive local angle δ, in the case of symmetric flow, the pressure coefficient is determined by the equations

$$C_p = 2 \sin^2 \delta \quad \text{or} \quad C_p = 2\delta^2, \tag{18.4}$$

if the angle δ is small. At those points where $\delta \leq 0$, the pressure coefficient should be assumed equal to zero.

As an example, let us determine the pressure coefficient for flow around a slender parabolic body of revolution. Since the local slope of the surface is $\delta = \delta_0(1 - \bar{x})$ for this parabolic body, it follows that $C_p = 2\delta_0^2(1 - \bar{x})^2$. The pressure distribution calculated from this equation is shown in Fig. 177, along with a calculation by the method of characteristics for $M_\infty = 8$. A comparison of the results discloses a tendency toward some underestimation of the pressure calculated by Newtonian flow theory.

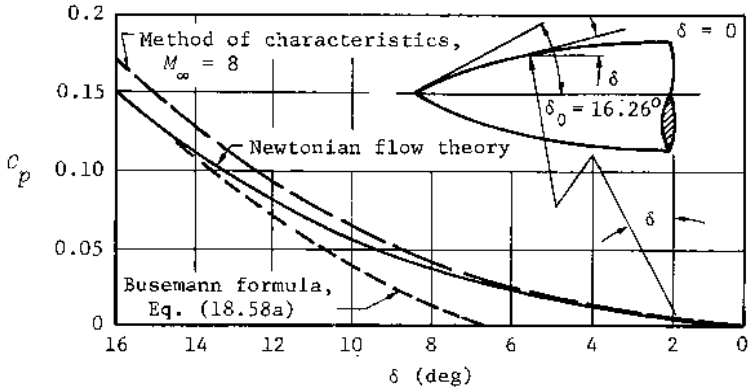

Fig. 177--Pressure distribution on a parabolic nose

An improvement in this theory results from what is called modified Newtonian theory, according to which the pressure coefficient is calculated from

$$C_p = C_{p0}\left(\frac{\sin\delta\cos\alpha - \cos\phi\sin\alpha\cos\delta}{\sin\delta_0\cos\alpha - \cos\phi\sin\alpha\cos\delta_0}\right)^2, \tag{18.5}$$

or, if the angles α and δ are small, from the expression

$$C_p = C_{p0}\left(\frac{\delta - \alpha\cos\phi}{\delta_0 - \alpha\cos\phi}\right)^2, \tag{18.5a}$$

where $C_{p0} = f(\alpha, \phi)$ is the pressure coefficient on a conical nose and is calculated from the usual theory of supersonic asymmetric flow around a cone. For given values of δ_0 and M_∞, C_{p0} is a function of the angles α and ϕ.

In the case of a zero angle of attack, Eqs. (18.5) and (18.5a) are simplified:

$$C_p = C_{p0}\frac{\sin^2\delta}{\sin^2\delta_0}, \qquad C_p = C_{p0}\frac{\delta^2}{\delta_0^2}, \tag{18.6}$$

where $C_{p0} = C_p^0$ is no longer dependent on α and ϕ and is a constant for given flow conditions.

It is apparent that the equations presented give exact results for the conical tip and, moreover, they improve the values of the pressure coefficient for other points on the body surface, compensating for the underestimation mentioned above. In those cases when the velocities are so great that the pressure is essentially independent of M_∞, similar results can be obtained by replacing the coefficient 2 in Eq. (18.3) by

$$\tilde{C}_p(\gamma) = \frac{2(\gamma + 1)(\gamma + 7)}{(\gamma + 3)^2}. \tag{18.7}$$

In particular, for a slender body, Eq. (18.3a) can be written in the form

$$C_p = \tilde{C}_p(\gamma)(\delta - \alpha\cos\phi)^2. \tag{18.8}$$

Calculation of the Axial Force Coefficient for Asymmetric Flow around a Slender Body

Introducing Eq. (18.5a) into Eq. (1.6), the axial force coefficient is given by

$$C_{Ap} = 4 \int_0^{\bar{x}_s'} \lambda_N \frac{A(\phi_s)}{\pi} \bar{r} \tan \delta \, d\bar{x}, \tag{18.9}$$

where the function

$$A(\phi_s) = \int_{\phi_s}^{\pi} \frac{C_{p0}(\delta - \alpha \cos \phi)^2}{(\delta_0 - \alpha \cos \phi)^2} d\phi. \tag{18.10}$$

If Eq. (18.8) is used, this function is simplified:

$$A(\phi_s) = \tilde{C}_p(\gamma) \int_{\phi_s}^{\pi} (\delta - \alpha \cos \phi)^2 \, d\phi. \tag{18.11}$$

After integration, this equation becomes

$$A(\phi_s) = \tilde{C}_p(\gamma) \left[(\pi - \phi_s) \left(\delta^2 + \frac{\alpha^2}{2} \right) + \alpha \sin \phi_s \left(2\delta - \frac{\alpha}{2} \cos \phi_s \right) \right]. \tag{18.11a}$$

The limits of integration ϕ_s and $\bar{x}_s'$ (or, in dimensional form, x_s') depend on the geometric shape of the body and the angle of attack, which are determined by specifying the boundaries of the shadow region on the body in which the particles do not collide with the body. The boundary of this region (see Fig. 176) is determined by a curve on which the pressure coefficient is equal to zero, which establishes the values of the limits ϕ_s and x_s' (or of the corresponding coordinate r_s). Thus, the value of the angle ϕ_s is found from the condition $\cos \phi_s = \delta/\alpha$.†

The calculation of the quantity x_s', representing the distance from the tip to the point on the bottom meridian at which the pressure is equal to zero, is based on the condition $\delta = -\alpha$, which leads to the following equation for the determination of x_s' (or r_s):

†Editor's note: The limit is given more accurately by Eq. (18.5) as $\cos \varphi_s = \tan \delta / \tan \alpha$.

$$\left(\frac{dr}{dx}\right)_{x=x_s'} = -\alpha. \tag{18.12}$$

Two possible cases of flow must be considered in computing the limits. The first case is characterized by an angle of attack less than the angle δ_0 of the tip of the body (Fig. 176). In this case, the local slope δ is equal to α when $\phi_s = 0$. As ϕ_s increases, the local slope corresponding to this limiting value becomes less than the angle of attack, and for $\phi_s = \pi/2$, the local slope is $\delta = 0$; similarly, for $\phi_s = \pi$, the corresponding local slope is $\delta = -\alpha$. For a cylindrical shape, $\delta = 0$ and ϕ_s is always $\pi/2$. The form of the function $A(\phi_s)$, represented by Eqs. (18.11) and (18.11a), is considerably simplified for these two values of δ. For example, for $\delta = 0$ and $\phi_s = \pi/2$, Eq. (18.11a) indicates that $A(\phi_s)/\tilde{C}_p(\gamma) = \pi\alpha^2/2$, and for $\delta = -\alpha$ and $\phi_s = \pi$, $A(\phi_s) = 0$. The limit x_s' is determined by the location of the point on the lower meridian where the shadow zone begins and, as is evident in Fig. 176, in general the value x_s' differs from the total length of the body.

In the second case, the angle of attack is equal to or greater than the nose angle of the body (Fig. 178). In this case, if $\alpha = \delta_0$, obviously the value $\phi_s = 0$ corresponds to a point at the tip, and the shadow area, in which $\phi_s > 0$ everywhere, begins directly behind it. For the case shown in Fig. 178, this region extends to the base, so that the coordinate $x_s' = l$.

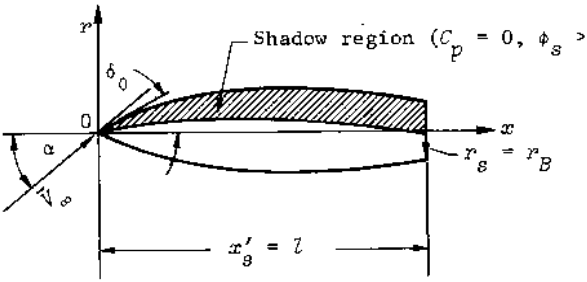

Fig. 178--Shadow region on a body for angles of attack greater than the apex angle

The pressure coefficient $C_{p0}(\alpha, \phi)$ at the nose tip in both the first and second cases can be determined by the method of local cones. In practice, the axial force coefficient can be determined from Eq. (18.9) either by numerical or graphical integration. In the latter case, it is convenient to construct a table of values of the integrand as a function of $\bar{x} = x/l_N$. Then a curve, restricted by the limiting coordinate $\bar{x} = \bar{x}_s'$ and representing the change in this function, is constructed from the data in the table. The area between the curve and the $\bar{x}$-axis multiplied by the corresponding scale determines the axial force coefficient.

If the body does not have a boattail, Eq. (18.9) can be written as

$$C_{Ap} = \int_0^1 \frac{A(\phi_s)}{\pi} d\bar{r}^2. \qquad (18.9a)$$

In this equation, the upper limit of the integral is one, because on a body with an untapered afterbody the pressure is equal to or greater than zero all the way to the base.

The graphical integration in a given case consists of the construction of a graph of the function $f_1(\bar{r}^2) = A(\phi_s)/\pi$ versus $\bar{r}^2$ and the determination of the area under the curve (Fig. 179).

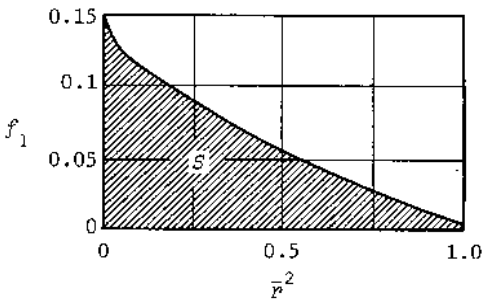

Fig. 179--Graphical integration for the pressure drag

The Axial Force Coefficient at Zero Angle of Attack

At zero angle of attack, the function in Eq. (18.9) is represented by $A(\phi_s) = (C_p^0/\delta_0^2)\delta^2\pi$, and the equation for the axial force coefficient

takes the form

$$C_{Ap} = C_{Dp} = \frac{2C_p^o}{\delta_0^2} \int_0^1 \delta^2 \bar{r}\, d\bar{r}. \tag{18.13}$$

In this equation, the upper limit of the integral is determined by the fact that the shadow zone begins at the largest cross section of the body (Fig. 180).

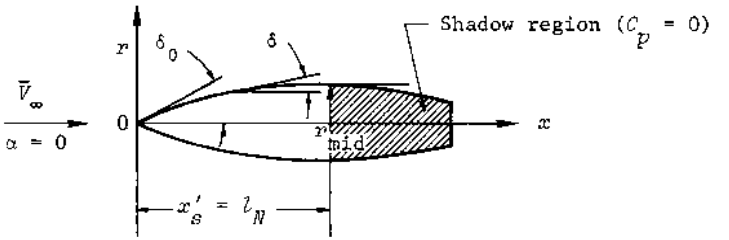

Fig. 180--The shadow region on a body in symmetric flow

For a parabolic body of revolution, $\delta = \delta_0 \sqrt{1 - \bar{r}}$, and Eq. (18.13) can be integrated to give $C_{Ap} = C_p^o/3$. Thus, the drag coefficient for a parabolic nose is one-third of its value for a conical nose of the same initial angle. If it is assumed that $C_p^o = \tilde{C}_p(\gamma)\delta_0^2$, the axial force coefficient is $C_{Ap} = 0.697\delta_0^2$ for $\gamma = 1.4$.

The expression for the drag coefficient of an ogive nose takes the form

$$C_{Ap} = \frac{C_p^o}{3} \frac{\lambda_N^2 + 0.125}{\lambda_N^2}. \tag{18.14}$$

For a body of arbitrary thickness ratio, the pressure coefficient on the tip for the limiting case of $M \to \infty$ is

$$C_p^o = \tilde{C}_p(\gamma) \sin^2\delta_0 = \frac{2(\gamma + 1)(\gamma + 7)}{(\gamma + 3)^2} \sin^2\delta_0, \tag{18.15}$$

where $\sin^2\delta_0 = \lambda_N^2/(\lambda_N^2 + 0.25)^2$ for an ogival nose. Consequently,

$$C_{Ap} = \frac{2(\gamma + 1)(\gamma + 7)}{3(\gamma + 3)^2} \frac{\lambda_N^2 + 0.125}{(\lambda_N^2 + 0.25)^2}. \qquad (18.16)$$

For large fineness ratios, the fraction on the right side is approximately equal to $1/\lambda_N^2$, and Eq. (18.16) coincides with the corresponding expression for a parabolic nose.

The Axial Force Coefficient for a Slender Cone

In Chap. II, the solution of the problem of asymmetric flow around a cone and, particularly, the calculation of the axial force were described in detail, so it is not necessary to apply modified Newtonian theory to this case. However, it is of interest to find a limiting solution for the axial force coefficient using Newtonian flow theory.

Since $\delta = \delta_c$ and is constant for a cone, the function $A(\phi_s)$, determined from Eq. (18.11), will be constant. Then

$$C_{Ap} = \frac{A(\phi_s)}{\pi}. \qquad (18.17)$$

If the cone angle is larger than the angle of attack, the shadow zone does not exist, the angle $\phi_s = 0$, and

$$A(\phi_s) = A(0) = \pi \tilde{C}_p(\gamma)\left(\delta_c^2 + \frac{\alpha^2}{2}\right).$$

If the cone angle is less than the angle of attack (second case considered earlier), a shadow zone exists on the top (see Fig. 181) and the

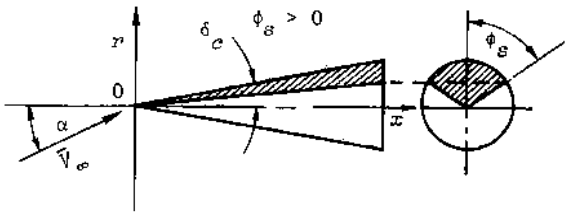

Fig. 181--The shadow region on a cone for angles of attack greater than the cone angle

function $A(\phi_s)$ must be determined from Eq. (18.11a). For zero angle of attack, the axial force coefficient $C_{Ap} = C_{Dp} = \widetilde{C}_p(\gamma)\delta_c^2$, and for $\gamma = 1.4$ this gives the quantity $2.091\delta_c^2$ already obtained above.

The Influence of Expansion of the Flow in the Shadow Zone

Thus far we have considered, relatively speaking, a pure "Newtonian flow," in which the pressure coefficient for the shadow zone is assumed to be equal to zero. The axial force coefficient in this limiting case is determined from Eq. (18.9). However, for a deviation from the limiting case, when the Mach number is large but finite, the axial force coefficient will differ from that obtained from Eq. (18.9). One of the reasons is that this equation does not allow for the influence of an expansion in the shadow zone. The results can be refined if a more general expression is used for the axial force coefficient, one that accounts for effects in the shadow zone:

$$C_{Ap} = \frac{2}{\pi r_{\text{mid}}^2} \int_0^l \int_0^{\pi} C_p r \tan\delta \, dx \, d\phi. \tag{18.18}$$

For convenience, let us present this coefficient in the form of the sum of two components, i.e.,

$$C_{Ap} = (C_{Ap})_N + \Delta C_{Ap}, \tag{18.19}$$

where $(C_{Ap})_N$ is the axial force coefficient that occurs due to impact, and ΔC_{Ap} is the additional drag coefficient caused by the influence of expansion in the shadow zone. The value of $(C_{Ap})_N$ is computed from Eq. (18.9). The additional drag coefficient is calculated from the following expression:

$$\Delta C_{Ap} = \frac{2}{\pi r_{\text{mid}}^2} \int_{x_s''}^l \int_0^{\phi_s} C_{pe} r \tan\delta \, dx \, d\phi, \tag{18.20}$$

which is obtained by allowing the integration for the axial force coefficient to be continued into the shadow zone. In this expression, the lower limit x_s'' is equal to the distance from the tip to the beginning

of the shadow zone on the upper side of the body. The pressure coefficient C_{pe} in this zone is determined from $C_{pe} = (2/\gamma M_\infty^2)(p_e/p_\infty - 1)$ and in general will be a variable quantity.

For an approximate estimate of the influence of the shadow zone, assume that $C_{pe} = -2/\gamma M_\infty^2$ and that it is constant at all points, which amounts to assuming a vacuum in the shadow zone ($p_e = 0$). Consequently, we obtain

$$\Delta C_{Ap} = -\frac{4}{\gamma M_\infty^2 \pi r_{\text{mid}}^2} \int_{x_s''}^{l} \phi_s r \tan\delta \, dx. \tag{18.21}$$

For a cone, the integration for the shadow zone is made from 0 to l, resulting in

$$\Delta C_{Ap} = -\frac{2}{\gamma M_\infty^2} \frac{\phi_s}{\tau}, \tag{18.21a}$$

so that the total axial force decreases somewhat. If there is no shadow zone ($\phi_s = 0$), the additional axial force disappears.

The shadow region totally encloses the afterbody of a body with a curved profile at zero angle of attack. In this case, since $x_s'' = l_N$ and $\phi_s = \pi$,

$$\Delta C_{Ap} = \frac{2}{\gamma M_\infty^2}(1 - \bar{r}_B^2), \tag{18.21b}$$

and the axial force increases somewhat.

The Shape of a Nose Section with Minimum Drag

The shape of a body of revolution having minimum drag at hypersonic speeds can be determined from Newton's equation, $p = \rho_\infty V_\infty^2 \sin^2\delta$. Using Eq. (1.6) and the relation $p = \rho_\infty V_\infty^2 (dr/ds)^2$, the expression for the pressure drag in symmetric flow can be written

$$D_p = 2\rho_\infty V_\infty^2 \pi \int_0^r r\left(\frac{dr}{ds}\right)^2 dr. \tag{18.22}$$

The problem involves the determination of the equation $r = f(x)$ for

which the function D_p is a minimum. The problem has been solved[5] subject to the constraints that the surface area S and the volume W be constant, i.e.,

$$S = 2\pi \int_0^s r\, ds = \text{const}, \qquad W = \pi \int_0^x r^2\, dx = \text{const}.$$

This is a variational problem with constant parameters, whose solution consists of the determination of the unconditional extremes of the function

$$\int_0^s \left[r\left(\frac{dr}{ds}\right)^3 + \lambda_1 r + \lambda_2 r^2 \left(\frac{dx}{ds}\right) \right] ds,$$

or

$$\int_0^s \left[r\left(\frac{dr}{ds}\right)^3 + \lambda_1 r + \lambda_2 r^2 \sqrt{1 - (dr/ds)^2} \right] ds,$$

where λ_1 and λ_2 are constants called Lagrangian multipliers.

Euler's equation for the latter function is

$$\frac{d}{ds}\left(\frac{\partial F}{\partial r'}\right) - \frac{\partial F}{\partial r} = 0, \tag{18.23}$$

in which

$$F\left(r, \frac{dr}{ds}\right) = r\left(\frac{dr}{ds}\right)^3 + \lambda_1 r + \lambda_2 r^2 \sqrt{1 - (dr/ds)^2}, \tag{18.24}$$

which is the solution for the minimum. After substituting Eq. (18.24) into Eq. (18.23), and taking into account that $\partial F/\partial s = 0$, this equation has the form

$$-\left(\frac{dr}{ds}\right)^3 + \frac{\lambda_2 r/2}{\sqrt{1 - (dr/ds)^2}} + \frac{\lambda_1}{2} = 0.$$

The constants λ_1 and λ_2 can be determined from the conditions that, for $r = 0$ the derivative $(dr/ds)_0 = \sin \delta_0$, and for $r = r_{mid}$ the derivative is equal to zero. As a result, the equation for the minimum shape is

$$\left(\frac{dr}{ds}\right)^3 = \sin^3\delta_0 \left[1 - \frac{r/r_{mid}}{\sqrt{1 - (dr/ds)^2}}\right]. \qquad (18.25)$$

Considering the local slope $u = dr/ds$ as a parameter in this equation, the radial coordinate of the body can be obtained from

$$\frac{r}{r_{mid}} = \sqrt{1 - u^2}\left(1 - \frac{u^3}{\sin^3\delta_0}\right). \qquad (18.25a)$$

The equation for the calculation of the other coordinate, x, is written as

$$\frac{dx}{dr} = \sqrt{(ds/dr)^2 - 1} = \frac{1}{u}\sqrt{1 - u^2}. \qquad (18.26)$$

By using Eq. (18.25a), this expression can be integrated from the point $r = r_{mid}$, $x = l_N$ to an arbitrary point with the coordinates x, r:

$$\int_{l_N}^{x} dx = \int_{r_{mid}}^{r} \frac{1}{u}\sqrt{1 - u^2}\, dr,$$

or

$$x = -r_{mid}\left(u + \frac{3u^2}{2\sin^3\delta_0} - \frac{u^4}{\sin^3\delta_0}\right) + l_N. \qquad (18.27)$$

At $x = 0$, the slope is $u = \sin\delta_0$, so that the length of the nose is

$$l_N = \frac{3}{2}\frac{r_{mid}}{\sin\delta_0}.$$

Equations (18.25a) and (18.27) represent the coordinates of a body of revolution of minimum drag in parametric form. A family of such shapes, constructed for various values of the angle δ_0, is presented in Fig. 182.

Using the parametric equations for the minimum shape, an expression can be obtained for the drag, and also for the surface area and volume

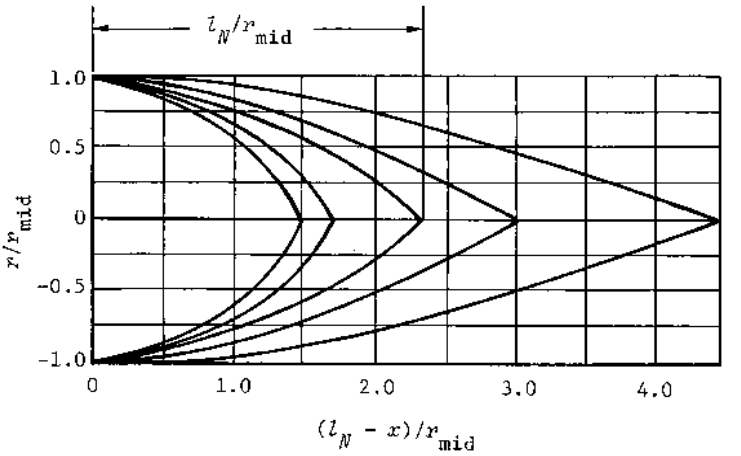

Fig. 182--Nose shapes for minimum drag at hypersonic speeds

of the body. Introducing Eq. (18.25a) into Eq. (18.22), we obtain

$$D_p = 2\rho_\infty V_\infty^2 \pi \int_{\sin\delta_0}^{0} r\left(\frac{dr}{ds}\right)^2 \frac{dr}{du}\, du$$

$$= \frac{9}{10}\,\rho_\infty V_\infty^2 \pi r_{mid}^2 \sin^2\delta_0\left(\frac{1}{2} - \frac{1}{7}\sin^2\delta_c\right). \tag{18.28}$$

Hence the drag coefficient is

$$C_{Dp} = \frac{2D_p}{\rho_\infty V_\infty^2 \pi r_{mid}^2} = \frac{9}{10}\sin^2\delta_0\left(1 - \frac{2}{7}\sin^2\delta_0\right). \tag{18.28a}$$

The equations for the surface area and the volume are obtained in the following form:

$$S = \frac{9\pi r_{mid}^2}{70\sin\delta_0}\,(14 + 5\sin^2\delta_0),$$

$$W = \frac{27\pi r_{mid}^3}{280\sin\delta_0}\,(7 + 2\sin^2\delta_0). \tag{18.29}$$

The variation of the minimum drag with nose angle is shown in Fig. 183. The dimensionless quantities l_N/r_{mid}, S/r^2_{mid}, and W/r^3_{mid} are also plotted in the figure. These curves and also the graphs in Fig. 182 show that the slope of the meridian approximates very closely an ogival curve. The optimum nose is slightly longer than an ogive nose with the same value of δ_0 and is slightly more conical near the tip.

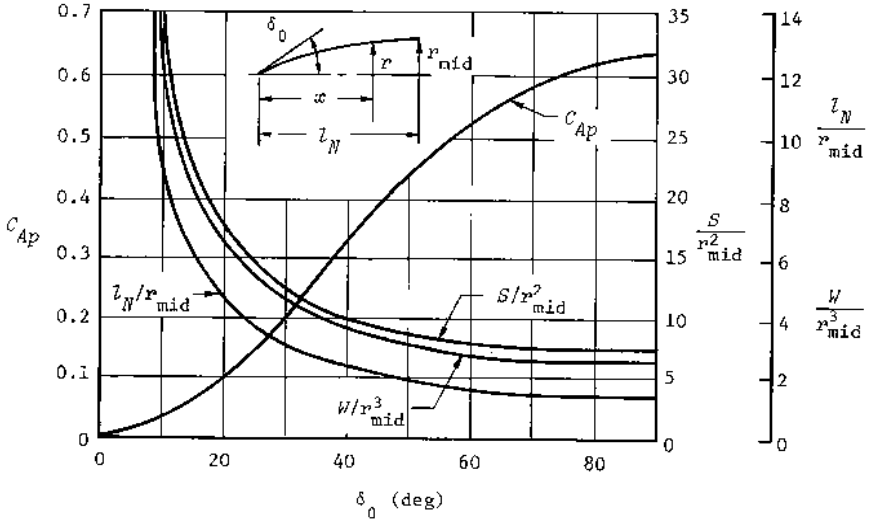

Fig. 183--The drag, length, surface area, and volume of noses with minimum pressure drag

These results can be extended to lower Mach numbers if modified Newtonian theory is used, according to which the absolute pressure is

$$p = p_\infty + (p_c - p_\infty)\frac{\sin^2\delta}{\sin^2\delta_0}, \tag{18.30}$$

where p_c is the pressure on a conical nose.

NORMAL FORCE COEFFICIENT

Body of Revolution of Arbitrary Shape

The absolute value of the normal force coefficient is obtained by substituting Eq. (18.5a) for the pressure coefficient into Eq. (1.12):

$$C_{Np} = \frac{2}{\pi r_{\text{mid}}^2} \int_0^{x_s'} B(\phi_s) r \, dx, \tag{18.31}$$

where the function

$$B(\phi_s) = -\int_{\phi_s}^{\pi} \frac{C_{p0}(\delta - \alpha \cos \phi)^2 \cos \phi}{(\delta_0 - \alpha \cos \phi)^2} d\phi, \tag{18.32}$$

and the upper limit x_s' represents the distance from the tip to the point on the body where the shadow zone reaches the lower meridian ($\phi_s = \pi$).

If Eq. (18.8) is used for the pressure coefficient, the function $B(\phi_s)$ can be found in explicit form, since the integral can be computed. This function is

$$B(\phi_s) = -\tilde{C}_p(\gamma)\left[\alpha \sin \phi_s \left(\delta \cos \phi_s + \frac{\alpha}{3} \sin^2 \phi_s\right)\right.$$

$$\left. - \sin \phi_s (\alpha^2 + \delta^2) - \alpha\delta(\pi - \phi_s)\right]. \tag{18.33}$$

The limit x_s' must be computed for the two cases presented earlier. For the first of these cases, Eq. (18.33) is greatly simplified. It was indicated that as long as $\alpha \leq \delta$, the value of $\phi_s = 0$, so that $|B(\phi_s)| = |B(0)| = \tilde{C}_p(\gamma)\alpha\delta\pi$.

When the angle δ is less than α, $\phi_s > 0$, and the shadow region begins directly behind the apex; in this case, the function $B(\phi_s)$ must be calculated from Eq. (18.33). If $\delta = 0$, $\phi_s = \pi/2$ and $|B(\phi_s)| = |B(\pi/2)| = 2\alpha^2\tilde{C}_p(\gamma)/3$. If $\delta = -\alpha$, $\phi_s = \pi$ and $|B(\phi_s)| = |B(\pi)| = 0$.

The application of these equations can be illustrated by calculating the normal force on a parabolic nose with a cylindrical afterbody. Equation (18.31) for the normal force coefficient is written as follows:

$$C_{Np} = \int_0^{\bar{x}_s'} f_2(\bar{x})\ d\bar{x}, \tag{18.31a}$$

where the function

$$f_2(\bar{x}) = \frac{4\lambda_N B(\phi_s)}{\pi}\,\bar{r}.$$

If graphical integration is used, the values of f_2 are calculated for several stations, a graph of this function is constructed, and the area under the curve is determined. A plot of this type is shown in Fig. 184. It is apparent that f_2 is constant on the cylindrical section,

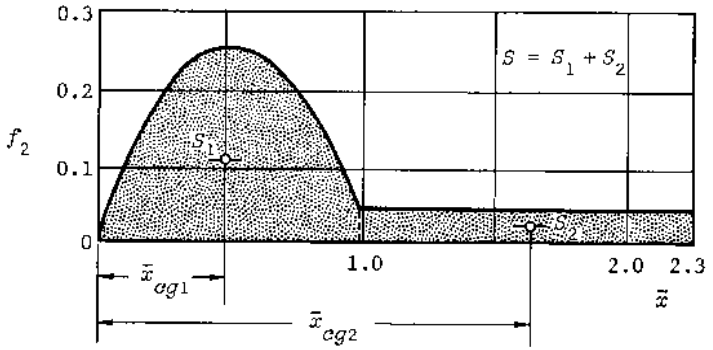

Fig. 184--Graphical integration for the normal force coefficient

since $\delta = 0$ everywhere, and thus $\phi_s = \pi/2$ and $B(\phi_s) = 2\alpha^2\tilde{C}_p(\gamma)/3$. Using these results in Eq. (18.31), the normal force coefficient for the cylindrical section is given by the simple relation

$$C_{Np}^{cyl} = \frac{8}{3\pi}\,\tilde{C}_p(\gamma)\lambda_{cyl}\alpha^2. \tag{18.34}$$

The corresponding calculations for the curved nose section can also be simplified if the flow regime is restricted to small angles of attack for which the influence of the shadow zone is negligibly small. In this

case, introducing the expression $B(\phi_s) = \tilde{C}_p(\gamma)\alpha\delta\pi$ into Eq. (18.31), we obtain

$$C_{Np} = \tilde{C}_p(\gamma)\alpha. \tag{18.31b}$$

The Normal Force Coefficient of a Slender Cone

The function $B(\phi_s)$ is constant for a cone, and Eq. (18.31) yields the following relation:

$$C_{Np} = \frac{B(\phi_s)}{\pi\delta_c}. \tag{18.35}$$

Using Eq. (18.33) for the function $B(\phi_s)$, Eq. (18.35) can be written in specific forms for special cases. For the first case, $\alpha \leq \delta_c$ and $\phi_s = 0$, and thus $|B(\phi_s)| = |B(0)| = \tilde{C}_p(\gamma)\alpha\delta_c\pi$. Then

$$C_{Np} = \tilde{C}_p(\gamma)\alpha. \tag{18.36}$$

This equation can be extended to the case of arbitrary magnitudes of the angles α and δ_c:

$$C_{Np} = \frac{\tilde{C}_p(\gamma)}{2}\cos^2\delta_c \sin 2\alpha. \tag{18.37}$$

In turn, from this equation, it is possible to find the initial slope of the curve $C_{Np}(\alpha)$:

$$\left(\frac{\partial C_{Np}}{\partial\alpha}\right)_{\alpha=0} = \tilde{C}_p(\gamma)\cos^2\delta_c. \tag{18.38}$$

For a slender cone at small angles of attack and for $\gamma = 1$, the last equation gives the value $(\partial C_{Np}/\partial\alpha)_{\alpha=0} = 2$, which is the same as for linearized flow. Consequently, it can be assumed that the normal force coefficient and its derivative are weak functions of M_∞ for the entire range of small to very high Mach numbers. This conclusion is confirmed by the results of exact calculations of the parameter $(1/\cos^2\delta_c)(\partial C_N/\partial\alpha)_{\alpha=0}$ for cones, as shown in Fig. 185.[4] It can be seen that the influence of

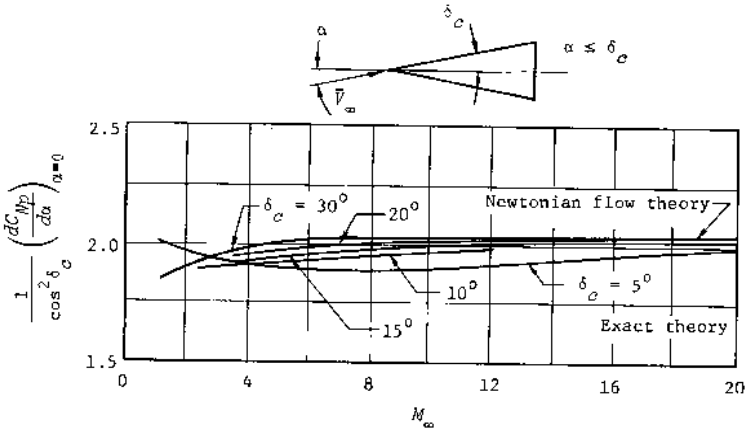

Fig. 185--Slope of the normal force coefficient for cones

Mach number diminishes as the cone angle increases, and it is almost negligible at the higher Mach numbers. It should be noted that the estimation of the normal force coefficient by Newtonian theory agrees better with the exact data if it is assumed that $\gamma = 1$ in the calculation of the quantity $\tilde{C}_p(\gamma)$.

In the second case for $\alpha > \delta_c$, the quantity $\phi_s > 0$ and the value of $B(\phi_s)$ must be computed from Eqs. (18.32) or (18.33).

Effect of Expansion of the Flow in the Shadow Zone

To estimate the normal force coefficient allowing for the effect of expansion in the shadow zone, a more general expression than Eq. (18.31) must be used:

$$C_{Np} = \frac{2}{\pi r_{mid}^2} \int_0^l \int_0^\pi C_p r \cos\phi \, dx \, d\phi. \qquad (18.39)$$

The normal force coefficient can be presented in the form of the sum of two components:

$$C_{Np} = (C_{Np})_N + \Delta C_{Np}, \tag{18.40}$$

where $(C_{Np})_N$ is calculated according to Eq. (18.31) from the Newtonian condition, and ΔC_{Np} for the shadow region is determined by using Eq. (18.39). Let us assume, as before, that $C_{pe} = (2/\gamma M_\infty^2)(p_e/p_\infty - 1)$ is the same everywhere in the shadow zone. Substituting this expression into Eq. (18.39), we find

$$\Delta C_{Np} = \frac{4}{\gamma M_\infty^2 \pi r_{\text{mid}}^2}\left(\frac{p_e}{p_\infty} - 1\right)\int_{x_s''}^{l}\int_0^{\phi_s} r\cos\phi\, d\phi\, dx. \tag{18.41}$$

Knowing the body shape in the shadow zone and the boundaries of this region, it is possible to determine ΔC_{Np}. In particular, the absolute value for a cone is[†]

$$|\Delta C_{Np}| = \frac{2}{\gamma M_\infty^2 \pi \delta_c}\left[1 - \frac{(p_e)_c}{p_\infty}\right]\sqrt{1 - \delta_c^2/\alpha^2}. \tag{18.42}$$

For a cylinder, for which $r = r_{\text{mid}}$ and $\phi_s = \pi/2$, the result is

$$|\Delta C_{Np}| = \frac{8\lambda_{\text{cyl}}}{\gamma M_\infty^2 \pi}\left[1 - \frac{(p_e)_{\text{cyl}}}{p_\infty}\right]. \tag{18.43}$$

The expansion in the shadow zone will have its greatest effect with a complete vacuum, i.e., when $(p_e)_c$ and $(p_e)_{\text{cyl}}$ are zero everywhere in this zone, so that $C_{pe} = C_{pe}^c = C_{pe}^{\text{cyl}} = -2/\gamma M_\infty^2$.

The results of the calculation[4] of the normal force coefficient for a body of revolution at $\alpha = 5°$ and $10°$ are shown in Fig. 186. The body consisted of a cone and a cylinder, and the calculation took into account the corrections computed from Eqs. (18.42) and (18.43) for a vacuum in the shadow zone as well as for a pressure coefficient of zero in that region. It is apparent that the experimental data are located between the calculations with and without the correction. It should

[†]Editor's note: For a cone with $\alpha > \delta_c$, the limit ϕ_s is obtained from $\cos\phi_s = \tan\delta_c/\tan\alpha \approx \delta_c/\alpha$, and $x_s'' = 0$.

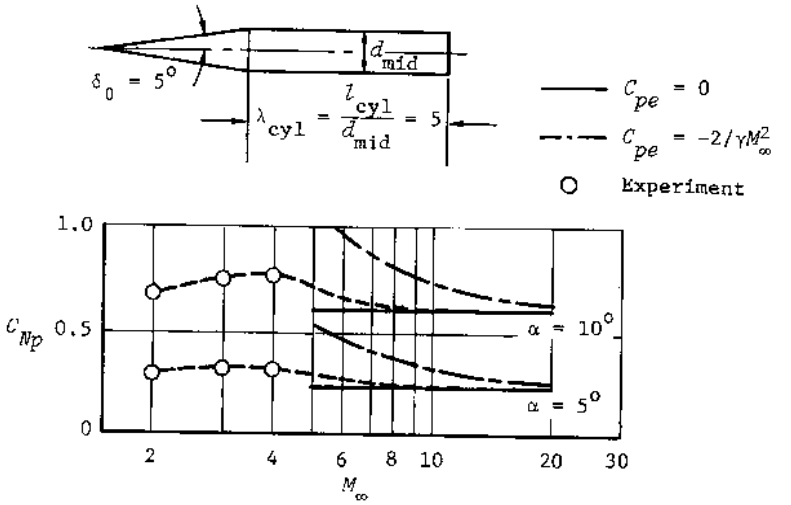

Fig. 186--Effect of expansion in the shadow zone on the normal force coefficient

also be noted that the influence of the shadow zone weakens with a decrease in the angle of attack.

It can be seen from Fig. 186 that, for an angle of attack of 5°, i.e., the same as the cone angle, the experimental curve is quite close to the curve for Newtonian theory without the correction for expansion. This is explained by the absence of a shadow zone on the cone and also by the small influence of the shadow zone on the cylinder.

Influence of the Cylindrical Portion of the Body on the Normal Force Coefficient

Calculations and experiments indicate that the effect of the cylindrical section is a function of nose shape and Mach number.[4] Figure 187 shows the variation in the derivative of the normal force coefficient with respect to distance along the axis of the body. This sketch can be used to estimate the role of the cylindrical section in the formation of the normal force on the entire body.

For relatively small supersonic velocities (M_∞ = 2 to 3), the local normal force coefficient decreases downstream and becomes equal to zero

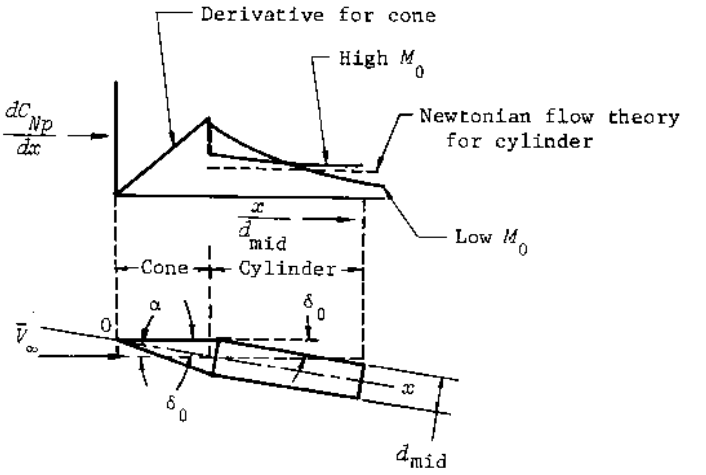

Fig. 187--Variation of $\partial C_{Np}/\partial x$ along the axis

at a distance of approximately 2 to 2.5 diameters from the cone-cylinder junction. For Mach numbers in the range $3 < M_\infty < 6$, the distribution of the local normal force coefficient flattens out, but its average value is larger. A further increase in Mach number is followed by continually less change in the normal force coefficient, and its value quite clearly tends toward a constant that can be determined approximately from Newtonian theory.

First let us discuss some general characteristics of the initial slope of C_{Np} with α, which will aid in estimating the influence of the cylindrical section for large Mach numbers. The normal force coefficient of a body of the shape represented in Fig. 188 can be given in the form of a general relation:

$$C_{Np} = f\left(\delta_0, \frac{l_a}{d_{mid}}, \frac{d_B}{d_{mid}}, M_\infty, \alpha\right).$$

In the case of an entirely cylindrical afterbody, i.e., $l_a = l_{cyl}$ and $d_B = d_{mid}$, this reduces to the form

$$C_{Np} = f\left(\delta_0, \frac{l_{cyl}}{d_{mid}}, M_\infty, \alpha\right).$$

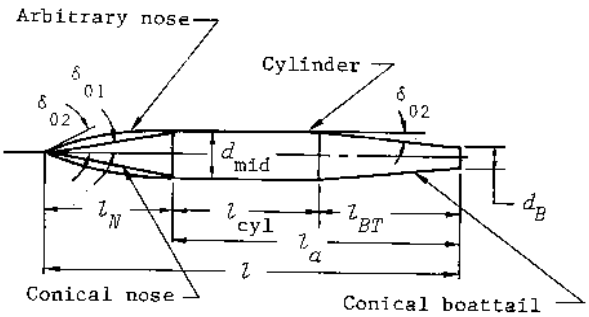

Fig. 188--Geometric parameters of a body of revolution with a cylindrical midsection

If the angle of attack is small, C_{Np} can be considered to be a linear function of α, and the expression for the normal force coefficient can be written in the form $C_{Np} = \alpha(\partial C_{Np}/\partial\alpha)_{\alpha=0}$, where the derivative is

$$\left(\frac{\partial C_{Np}}{\partial \alpha}\right)_{\alpha=0} = \varphi\left(\delta_0, \frac{l_{cyl}}{d_{mid}}, M_\infty\right).$$

Returning to Eq. (18.38) and Fig. 185, it is apparent that the normal force coefficient varies approximately as $\cos^2\delta_0$. For a slender body with δ_0 not exceeding about 10° to 15°, the effect of the nose angle will be small, and it can be assumed that

$$\left(\frac{\partial C_{Np}}{\partial \alpha}\right)_{\alpha=0} = \varphi\left(\frac{l_{cyl}}{d_{mid}}, M_\infty\right).$$

This assumed functional relation was compared with experiments on two bodies having cylindrical boattails and a conical and an ogive nose. The experimental results are presented in Fig. 189, indicating that the slope of the normal force coefficient is practically identical for both models when the length of the cylindrical section reaches about three diameters. The initial slope of the curve for C_{Np} is independent of the fineness ratio of the cylinder for cylinder lengths corresponding to λ_{cyl} of 8 to 9. The experimental data indicate that the slope of the

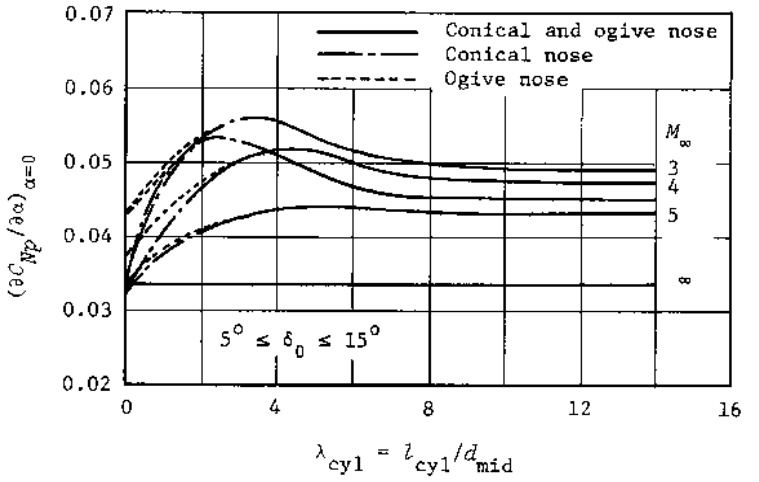

Fig. 189--Slope of the normal force coefficient of a body with a cylindrical aft section and a slender pointed nose

curve decreases with an increase in M_∞, and for M_∞ greater than about 8 the slope of the curve is equal to that predicted by Newtonian theory for a cone. This agrees with the conclusion drawn from Eq. (18.34), i.e., that the cylindrical section does not contribute to the initial slope for $M_\infty \to \infty$.

The Nonlinear Relation of Normal Force and Angle of Attack

If the slope of the curve of the normal force coefficient is not a function of the angle of attack, C_{Np} can be computed from the graph in Fig. 189. However, the normal force coefficient is no longer a linear function of α as the angle of attack increases. This deviation from the linear law can be taken into account by means of the equation

$$C_{Np} = \left(\frac{\partial C_{Np}}{\partial \alpha}\right)_{\alpha=0} \alpha + \Delta C_{Np}, \qquad (18.44)$$

in which the additional term ΔC_{Np} includes the nonlinear effects.

A curve based on experimental data is shown in Fig. 190. For angles of attack less than 15°, C_{Np} is proportional to α^2. Thus, the

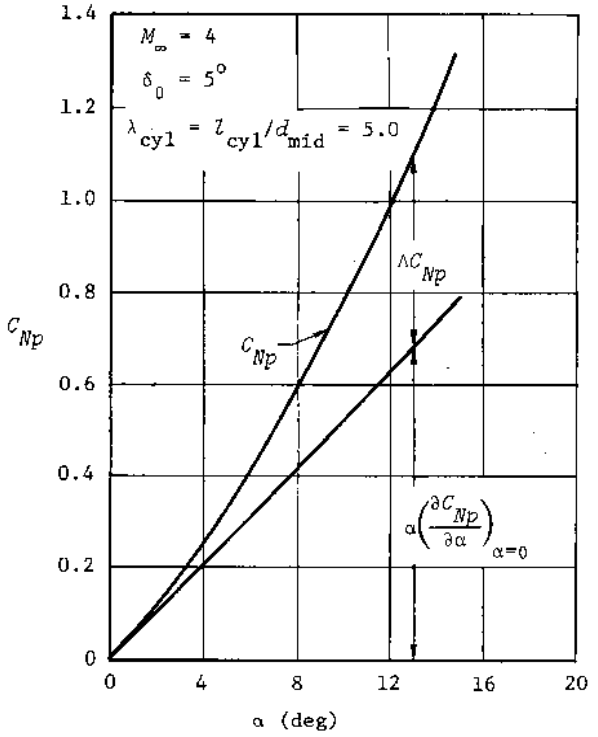

Fig. 190--Variation of the normal force coefficient and its components with angle of attack

parameter $\Delta C_{Np}/\alpha^2$ is a function of the geometric dimensions of the cylinder and the flow velocity but is independent of the angle of attack. Based on experimental data, curves can be constructed (Fig. 191) that indicate the variation of the parameter $\Delta C_{Np}/\alpha^2$ with M_∞ and with the fineness ratio of the cylindrical section of the body. A limiting line based on Eq. (18.34) is also shown in the figure.

Having curves for $(\partial C_{Np}/\partial\alpha)_{\alpha=0}$ and $\Delta C_{Np}/\alpha^2$ (Figs. 189 and 191), it is possible to estimate approximately the normal force coefficient at very high Mach numbers. In practice, after assigning an angle of attack, we must find the values of the initial slope of the curve of the normal force coefficient for several Mach numbers from Fig. 189. Then the value of ΔC_{Np} can be determined from Fig. 191 and C_{Np} calculated from Eq. (18.44).

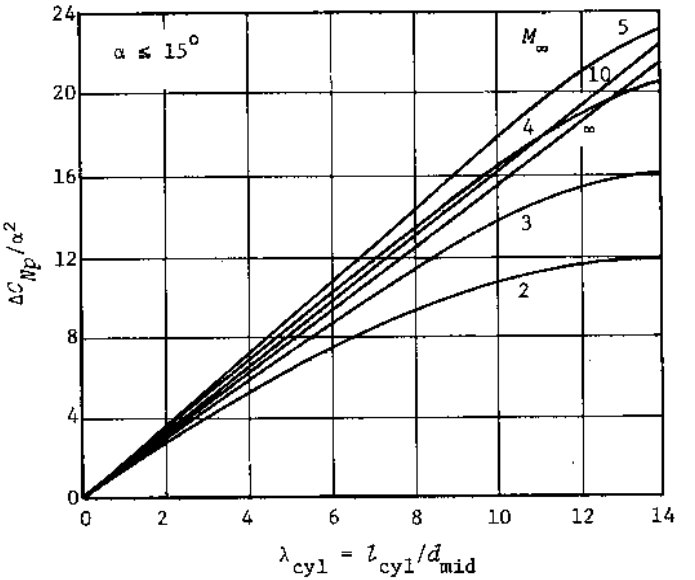

Fig. 191--Variation of $\Delta C_{Np}/\alpha^2$ with cylinder length and Mach number

A curve can be constructed from these values and then extrapolated so that, at M_∞ = 15 to 20, it approaches the value from Newtonian theory (the straight line in Fig. 186). The extrapolated curve can be used to estimate the normal force coefficient for intermediate values of M_∞.

The Effect of a Boattail on the Normal Force Coefficient

The influence of the boattail can be estimated for large Mach numbers using the experimentally determined curve shown in Fig. 192.[4] This curve represents the function

$$f(M_\infty) = \frac{\Delta(\partial C_{Np}/\partial\alpha)_{\alpha=0}}{1 - d_B/d_{mid}},$$

where $\Delta(\partial C_{Np}/\partial\alpha)_{\alpha=0}$ is the increment in the initial derivative of the normal force coefficient with respect to α. Physically, the curve reflects a phenomenon often observed in experiments; i.e., the normal

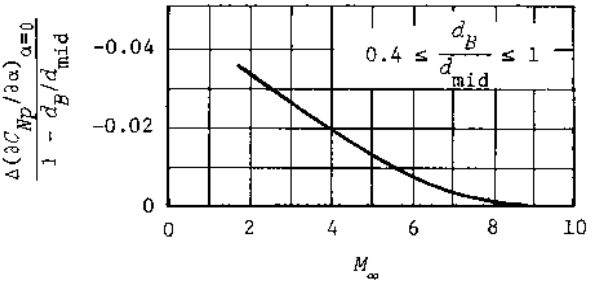

Fig. 193--Decrease in slope of the normal force coefficient for a body with a boattail

force slope decreases in an approximately linear manner with a decrease in the ratio d_B/d_{mid} in the range $0.4 \le (d_B/d_{mid}) \le 1.0$. This is a result of the destabilizing effect of the afterbody, as was noted in § 15. It has also been established experimentally that the slope or shape of the boattail plays a lesser role in the variation of the value of C_{Np} than does the magnitude of the base taper.

It follows from Fig. 192 that the effect of the boattail is substantial at low velocities. This agrees with the results of linearized theory, which indicate that the normal force coefficient of a body is zero for complete taper ($d_B/d_{mid} = 0$). The effect of the boattail disappears at M_∞ of 8 to 9, according to Fig. 192. This result is also predicted by Newtonian theory when the angle of attack is small enough that the boattail lies in the shadow zone. At larger angles, a stabilizing effect occurs when the boattail emerges from the shadow zone, producing a pressure region.

PITCHING MOMENT COEFFICIENT AND CENTER OF PRESSURE

The Approximate Estimation of the Moment Coefficient

Substituting Eq. (18.5a) for the pressure coefficient into Eq. (1.19), we find

$$C_{mp} = \frac{4\lambda_N}{\pi} \int_0^{\bar{x}_s'} \bar{x}\bar{r}B(\phi_s)\, d\bar{x}, \qquad (18.45)$$

where the characteristic length for the moment coefficient is the nose length, and $\bar{x} = x/l_N$. The function $B(\phi_s)$ is determined from Eqs. (18.32) or (18.33).

For a parabolic nose, Eq. (18.45) can be presented in the form

$$C_{mp} = \frac{4\lambda_N}{\pi} \int_0^{\bar{l}_s} B(\phi_s)\, d\bar{l}, \tag{18.45a}$$

where $\bar{l} = \bar{x}^3(\frac{2}{3} - \bar{x}/4)$, and the upper limit $\bar{l}_s$ is calculated from the coordinate $\bar{x}_s'$ of the point on the lower meridian at the beginning of the shadow region.

The method of graphical computation of the integral in Eq. (18.45a) can be used to determine the moment coefficient. The function

$$f_3(\bar{l}) = \frac{4\lambda_N}{\pi} B(\phi_s)$$

is evaluated by using the results for $B(\phi_s)$ obtained in the course of the previous calculations for the normal force coefficient. After constructing a graph of f_3 versus $\bar{l}$ (Fig. 193) and determining the area under the curve, the moment coefficient can be calculated. Figure 193 is plotted only for the nose section, giving the coefficient C_{mp}^N of the nose relative to the nose length l_N.

The calculation for the moment coefficient of the nose can be simplified if we use the assumption made in obtaining Eq. (18.31b). The expression for C_{mp}^N takes the form of the following equation:

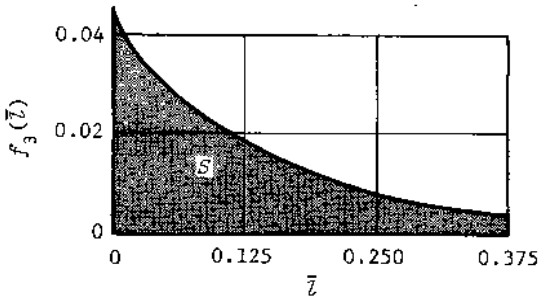

Fig. 193--Graphical integration for the moment coefficient

$$C_{mp}^{N} = \widetilde{C}_p(\gamma)\left(1 - \frac{W_N}{l_N S_{\text{mid}}}\right)\alpha, \tag{18.45b}$$

where W_N is the volume of the nose.

The equation for the moment coefficient of a cylindrical section C_{mp}^{cyl} can be derived directly, in view of which there is little necessity for constructing a graph of f_3 for this section of the body.

The equation for $B(\phi_s)$ found earlier for a cylinder is $B(\phi_s) = 2\widetilde{C}_p(\gamma)\alpha^2/3$. Introducing this expression into Eq. (18.45) and setting $\lambda_N = \lambda_{\text{cyl}}$, $\bar{r} = 1$, $\bar{x}_s' = 1$ for the case in question, we obtain

$$(C_{mp}')^{\text{cyl}} = \frac{4\widetilde{C}_p(\gamma)}{3\pi}\lambda_{\text{cyl}}\alpha^2. \tag{18.46}$$

The length of the cylindrical section is the characteristic dimension, and the value of the coefficient $(C_{mp}')^{\text{cyl}}$ obtained from this equation corresponds to the moment calculated relative to a point at the forward end of the cylinder. If the moment of forces acting on the cylindrical section is calculated with respect to another point located at a distance x from the front of the cylinder, the corresponding value of the coefficient based on the same length l_{cyl} will be

$$C_{mp}^{\text{cyl}} = \frac{4\widetilde{C}_p(\gamma)}{3\pi}\lambda_{\text{cyl}}\alpha^2\left(1 + \frac{2x}{l_{\text{cyl}}}\right). \tag{18.47}$$

If the moment coefficient is based on any other characteristic length, a corresponding change must be made in Eq. (18.47). Choosing the characteristic dimension as the total length l, and computing the moment with respect to the tip, the moment coefficient for the cylindrical portion of a body with a curved nose shape is given by

$$C_{mp}^{\text{cyl}} = \frac{8\widetilde{C}_p(\gamma)}{3\pi}\lambda_{\text{cyl}}\alpha^2\left(1 + \frac{\lambda_{\text{cyl}}}{2\lambda_N}\right)\frac{\lambda_N}{\lambda_l}. \tag{18.48}$$

Combining this expression with the moment coefficient for the nose section, also based on the length of the entire body, the total moment coefficient is

$$C_{mp} = C_{mp}^{cyl} + C_{mp}^{N} \frac{\lambda_N}{\lambda_l}.$$

This coefficient can also be determined by using the graph constructed for the estimation of the normal force coefficient (a special form of this graph was presented in Fig. 184). Based on Eq. (18.45), the moment coefficient can be computed as the static moment of the area under the curve of the function f_2. For convenience, this area is divided into sections for which we can easily find the center of gravity, calculate the static moments of these sections, and then sum them up. For example, the area in Fig. 184 can be divided into a section under a curve resembling a parabola and into a section in the form of a rectangle corresponding to the cylindrical part of the body. The coordinates of the centers of gravity, $\bar{x}_{cg1}$ and $\bar{x}_{cg2}$, corresponding to the first and second sections, can be found directly from the graph. If the area of each of the sections is known (S_1 and S_2), the static moment becomes $\mu_s(S_1\bar{x}_{cg1} + S_2\bar{x}_{cg2})$. In this expression, μ_s is the scale factor for the area assumed on the sketch. Consequently, the moment coefficient with respect to the length of the body is determined from the following expression:

$$C_{mp} = \mu_s(S_1\bar{x}_{cg1} + S_2\bar{x}_{cg2}) \frac{\lambda_N}{\lambda_l}.$$

The Moment Coefficient for a Cone

Since the function $B(\phi_s)$ is constant for a cone, the moment coefficient is

$$C_{mp} = \frac{2}{3} \frac{B(\phi_s)}{\pi\delta_c}. \tag{18.49}$$

If the function $B(\phi_s)$ is computed from Eq. (18.33), then, in the first case of flow ($\alpha \leq \delta_c$, $\phi_s = 0$), the moment coefficient is

$$C_{mp} = \frac{2}{3} \tilde{C}_p(\gamma)\alpha. \tag{18.50}$$

In the second case ($\alpha > \delta_c$, $\phi_s > 0$), the value of $B(\phi_s)$ must be calculated from Eq. (18.33) and the moment coefficient from Eq. (18.49).

Cone-cylinder Body

The expression for the moment coefficient acting on a cone-cylinder is derived rather simply, since the moment coefficients are known individually for the cone and for the cylinder. If we select the length of the body l as the characteristic dimension and use Eq. (18.33) for the function $B(\phi_s)$, we find

$$C_{mp} = \widetilde{C}_p(\gamma)\left[\frac{2}{3}\frac{B(\phi_s)}{\pi\delta_0\widetilde{C}_p(\gamma)} + \frac{8}{3\pi}\lambda_{cyl}\alpha^2\left(1 + \frac{\lambda_{cyl}}{2\lambda_N}\right)\right]\frac{\lambda_N}{\lambda_l}. \qquad (18.51)$$

In the case of $\alpha \leq \delta_0$, it can be assumed that $B(\phi_s) = \widetilde{C}_p(\gamma)\alpha\delta_0\pi$.

Approximate Estimation of the Center of Pressure

The center-of-pressure coefficient is equal to the ratio of the moment coefficient to the normal force coefficient. Using Eqs. (18.31) and (18.45) and neglecting the influence of the shadow zone, we obtain the following expression for $\bar{x}_{cp}$:

$$\bar{x}_{cp} = \frac{\int_0^{\widetilde{x}_s'} \bar{x}\bar{r}B(\phi_s)\,d\bar{x}}{\int_0^{\widetilde{x}_s'} \bar{r}B(\phi_s)\,d\bar{x}}, \qquad (18.52)$$

where $\widetilde{x}_s' = x_s'/l$.

The center of pressure can be calculated for each specific case by means of a graphical computation of the integrals in Eq. (18.52). If the coefficients C_{mp} and C_{Np} have been calculated previously, $\bar{x}_{cp}$ can be computed directly. The center of pressure can also be found by determining the center of gravity of the area located between the $\bar{x}$-axis and the graph of the function

$$f_2(\bar{x}) = \frac{4\lambda_N}{\pi}\bar{r}B(\phi_s) \quad \text{or} \quad f_4(\bar{x}) = B(\phi_s)\bar{r}.$$

As noted above, such a graph is constructed for the purpose of determining the normal force coefficient. From Fig. 184, the center-of-pressure coefficient is found from the equation

$$\bar{x}_{cp} = \frac{\mu_s(S_1\bar{x}_{cg1} + S_2\bar{x}_{cg2})}{\mu_s(S_1 + S_2)}\frac{\lambda_N}{\lambda_l}, \tag{18.53}$$

where $\bar{x}_{cp}$ is based on the length of the body l.

Approximate Equations for the Center of Pressure

Along with the practical procedures considered above for estimating the limiting values of $\bar{x}_{cp}$ at hypersonic speeds, various approximate relations can be recommended. One of these can be obtained from Eqs. (18.31b) and (18.45b) in the form

$$\bar{x}_{cp} = 1 - \frac{W_T}{lS_{\text{mid}}}. \tag{18.54}$$

This equation can only be used for flow conditions for which Eqs. (18.31b) and (18.45b) are valid, and the body cannot have a boattail.

The center of pressure for an ogival or parabolic body of revolution (Fig. 194b) can be determined approximately from the equation

$$\bar{x}_{cp} = \frac{x_{cp}}{l} = \frac{0.67 - 0.75\bar{l} + 0.20\bar{l}^2}{1 - \bar{l} + 0.25\bar{l}^2}, \tag{18.54a}$$

where $\bar{l} = l/l_N$. This equation can be used for the case of $\alpha < \delta_c$ and $0 \leq \bar{l} <$ (1.1 to 1.2). The body in question can have a short tapered afterbody.

If a cylinder is substituted for the afterbody (see Fig. 194a), the center of pressure for the resulting body can be calculated from another equation:

$$\bar{x}_{cp} = \frac{x_{cp}}{l} = \frac{0.73 + 0.67\alpha\lambda_N(\bar{l}^2 - 1)}{\bar{l}[1.57 + 1.33\alpha\lambda_N(\bar{l} - 1)]}. \tag{18.55}$$

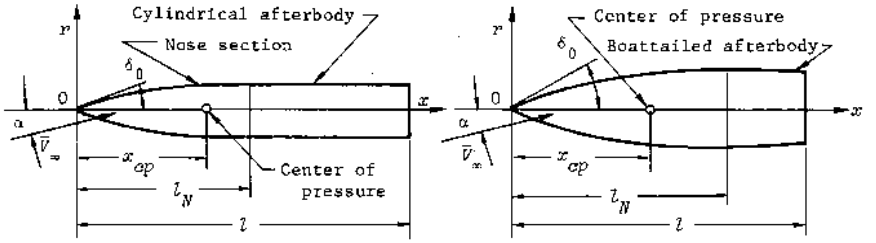

(a) Parabolic (ogive) nose and cylindrical afterbody

(b) Parabolic (ogive) contour with boattailed afterbody

Fig. 194--The shape and geometric parameters of bodies with pointed noses

Using this equation, it is necessary to satisfy the conditions $\alpha < \delta_0$ and $\bar{l} \geq 1$, while for $\bar{l} = 1$ we obtain the same value, $\bar{x}_{cp} = 0.47$, as is given by Eq. (18.54a). It should be noted that, with an increase in body length, the center of pressure shifts toward the base and tends toward a limiting position of $\bar{x}_{cp} = 0.50$ for $\bar{l} \to \infty$.

Equation (18.52) can be used to determine the center of pressure of a cone. Since $B(\phi_s)$ is constant for a cone, it cancels out of the equation. After performing the integration, the center of pressure is located at $\bar{x}_{cp} = \frac{2}{3}$. The same value is obtained from Eq. (18.54a) as the limiting position of the center of pressure for a curved nose as the nose length approaches zero. If a cylinder is attached to the conical nose, the center of pressure can be calculated from the equation

$$\bar{x}_{cp} = \frac{x_{cp}}{l} = \frac{0.67\lambda_N + 0.81\alpha\lambda_{cyl}(\lambda_N + 0.5\lambda_{cyl})}{(1 + 0.81\alpha\lambda_{cyl})\lambda_l}. \qquad (18.56)$$

For $\lambda_{cyl} = 0$, i.e., the case without a cylindrical section, we obtain $\bar{x}_{cp} = 0.67$ for a plain cone. When the cylinder is very long, the center-of-pressure coefficient tends toward the limiting value $\bar{x}_{cp} = 0.5$.

Comparing two bodies of the same fineness ratio but with conical and parabolic (or ogival) noses, it can be concluded from Eqs. (18.55) and (18.56) that the center of pressure of the conical body is characteristically located farther to the rear.

The Center of Pressure as a Function of Mach Number

The equations above give limiting values of the center of pressure that practically coincide with those corresponding to finite but large Mach numbers, of the order of 15 to 20. For lesser Mach numbers, the center of pressure can be calculated as follows. Assuming that the given body consists of several elements, Eq. (15.45) can be used to calculate the value of $\bar{x}_{cp}$. The normal force coefficient of the nose is determined from the graph in Fig. 189, and the normal force coefficient of the cylinder is found from Fig. 191, assuming that C_{Np}^{cyl} is equal to the correction ΔC_{Np}. Finally, the component for the afterbody C_{Np}^{BT} can be found from Fig. 192 as a function of M_∞ and d_B/d_{mid}.

In accordance with Eq. (15.45), it is necessary to determine the coordinates of the center of pressure of each element. In approximate calculations, the center of pressure of the nose can be assumed to be located at a distance $x_{cp} \approx 0.5l_N$ for a curved nose, and at a distance $x_{cp} = 0.67l_N$ for a conical nose. The centers of pressure of the cylindrical and tail sections can be assumed to be located in the middle of these sections of the body.

After these values have been computed for a series of Mach numbers, a curve can be constructed and extrapolated to fair into the results from Newtonian theory at $M_\infty = 15$ to 20. An analysis of the effect of Mach number indicates that as the Mach number decreases, the center-of-pressure coefficient also decreases, and the center of pressure is located closer to the tip compared with the limiting case for $M_\infty \to \infty$.

The aft movement of the center of pressure with an increase in velocity is caused by the increase in the stabilizing moment of the cylinder, as a result of the fact that a continually larger part of the cylinder is creating a positive normal force. In the limiting case of $M_\infty \to \infty$, the entire cylinder is "operating," in a manner of speaking, and the center of the load on the cylinder is located far aft of the tip. On the other hand, a considerable part of the cylinder carries practically no load at lesser Mach numbers. Up to M_∞ of 2 to 3, a finite normal force exists only to a length of approximately 2 to 2.5 diameters, in which case less stabilizing influence of the cylindrical section is observed. This is caused, on the one hand, by less normal force,

and on the other, by a more forward shift of the center of pressure. Therefore, it can be shown that, for identical locations of the center of gravity, a body with a long cylindrical section is statically stable at very high velocities and unstable at lesser velocities.

The discussion has been concerned only with the determination of the aerodynamic characteristics as functions of the normal pressure distribution on the lateral surface. The total values of these characteristics will also be functions of the base pressure. If Newtonian theory is followed strictly, the base pressure coefficient must be assumed to be zero as $M_\infty \to \infty$. The base section is in the shadow zone and does not have an influence on the aerodynamic coefficients. However, for finite but large Mach numbers, the effects of base pressure can be estimated approximately in the same way as was recommended for the consideration of flow expansion in the shadow zone on the lateral surface of the body, i.e., by assuming that the pressure at the base is zero for large Mach numbers. Consequently, the base pressure coefficient is $C_{pB} = -2/\gamma M_\infty^2$, and the axial force coefficient is $C_{AB} = (2/\gamma M_\infty^2)\bar{S}_B$.

THE EFFECT OF CENTRIFUGAL FORCES

According to the Newtonian theory, or, as it is still called, the Newtonian corpuscular theory, aerodynamic forces arise as a result of the collision of gas particles with the surface. Thus, the fundamental concept of this theory is concerned with the effects of these collisions. A similar phenomenon is observed on the transition of a gas through a shock wave.

It was noted above that Newtonian theory agrees completely with the theory of shock transition in the limiting hypothetical case of $\gamma \to 1$ and $M_\infty \to \infty$, when the shock wave is adjacent to the surface and the thickness of the compressed layer of gas is infinitesimally small. In fact, it follows from Eqs. (4.22) and (17.13) that, for $\gamma \to 1$ and $M_1 = M_\infty \to \infty$, the pressure coefficient on a cone or a wedge tends toward $C_p = 2 \sin^2\delta$, i.e., toward the same value as that from Newtonian theory. Under actual flow conditions, the shock cannot fit the surface closely. Consequently, after experiencing collision on transition across the shock wave, the particles continue in motion along a curved trajectory.

The result is that the pressure on the surface of body differs from the pressure directly behind the shock.

In principle, the same phenomenon occurs in the hypothetical flow at $M_\infty \to \infty$, $\gamma = 1$. The gas particles, passing through the shock wave next to the body, continue their motion in an infinitely thin layer along so-called geodesic lines of the surface. The velocity of this motion, V_2, can be determined by assuming that $\gamma = 1$ and $M_1 \to \infty$. Then $\Delta V_n / V_{n1} = 1$ and, consequently, $V_{n2} = 0$ and $V_2 = V_1 \cos \delta$.

Motion along a curved trajectory creates a centrifugal force that changes the pressure on the body surface compared with that resulting from Newtonian theory, the latter being equal to the pressure directly behind the shock wave. Thus, the difference in pressures at corresponding points on the surface of the body and directly behind the shock wave is equal to the pressure caused by the centrifugal force.

The value of this force is equal to $\rho_2 V_2^2 / R$, where the mass of particles passing through the shock per unit volume is equal to the density ρ_2, the centrifugal acceleration is V_2^2/R, and R is the radius of curvature of the flow contour. Therefore, the differential value of the pressure created by this force in a layer of thickness dn is $(\rho_2 V_2^2/R)\, dn$. The product $\rho_2\, dn$ can be obtained from the conservation of mass, i.e., $2\pi r \rho_2 V_2\, dn = \rho_1 V_1\, dS$, and the resulting expression integrated to obtain the difference in pressures. Then the pressure on the body surface is given by

$$p = \rho_1 V_1^2 \left(\sin^2 \delta + \frac{1}{2\pi r R} \int_0^S \cos \delta \, dS \right). \tag{18.57}$$

This relation, derived by Busemann, determines the pressure not only as a function of the local slope of the surface with respect to the direction of flow, but also as a function of the shape of the surface between the given section and the apex of the body.

However, it is possible to neglect the influence of the shape of the forward section for slender bodies with surface slopes that are everywhere small. This is based on the fact that if $\cos \delta \approx 1$ is assumed in Eq. (18.57), we have

$$p = \rho_1 V_1^2 \left(\delta^2 + \frac{1}{2} \frac{r}{R} \right). \tag{18.57a}$$

If the slender-body value is substituted for the radius of curvature, i.e., if it is assumed that $R = 1/(d^2r/dx^2)$, the relation for the pressure coefficient is

$$C_p = 2\left(\delta^2 + \frac{r}{2}\frac{d^2r}{dx^2}\right). \tag{18.58}$$

This relation can be written more accurately by basing it on the results of modified Newtonian theory:

$$C_p = \frac{C_{p0}}{\delta_0^2}\left(\delta^2 + \frac{r}{2}\frac{d^2r}{dx^2}\right). \tag{18.58a}$$

In the special case of a slender body with a parabolic shape,

$$R = -\frac{1}{\lambda_N l_N}, \qquad r = r_{mid}\bar{x}(2 - \bar{x}), \qquad \delta = \delta_0(1 - \bar{x}), \qquad \delta_0 = \frac{1}{\lambda_N}.$$

Therefore,

$$C_p = C_{p0}\left[(1 - \bar{x})^2 - \frac{\bar{x}}{4}(2 - \bar{x})\right]. \tag{18.59}$$

From this equation, it is evident that the centrifugal forces result in a decrease in pressure. Physically, this is explained by the fact that, in attempting to repel the particles from the surface, the centrifugal forces attenuate their collisions. As a result, calculations from Eq. (18.59) show significant expansion at the end of the body. However, experimental data and theoretical studies by the method of characteristics do not confirm these results. In fact, the expansion practically disappears at large Mach numbers, and the pressure is very close to that obtained by modified Newtonian theory.

Thus, correcting for the effects of centrifugal forces worsens Newtonian theory in the case of a body of revolution with a convex surface. As was shown earlier, Newtonian theory predicts a pressure somewhat too low compared with that obtained behind a real shock wave, since, for $\gamma = 1.4$, the wave does not lie against the surface and its angle is larger than that assumed in the theory. The effect of the centrifugal force is to decrease the pressure even more, resulting in a further divergence from the actual values.

In the actual flow, on the other hand, the pressure decrease due to centrifugal force near the surface tends to balance the pressure increase behind the real shock wave, resulting in relatively good accuracy of the Newtonian equation. Therefore, Newtonian theory without the inclusion of centrifugal forces should be used for aerodynamic calculations of bodies with convex surfaces for $\gamma = 1.4$.

However, for bodies with concave surfaces, each of the two effects acts in the same direction. As a result, the pressure behind the shock is increased even more due to centrifugal forces. Flow around such bodies must be calculated according to the Busemann theory, as is confirmed by comparison with experimental data.

In some cases, the Newtonian equation will also give incorrect predictions for the flow over convex bodies. This situation can occur when the shock wave lies very close to the body, so that the pressure behind the shock and the pressure calculated from Newtonian theory are nearly the same. Then the pressure decrease due to centrifugal forces must be included. This condition will occur for $M_\infty \to \infty$ and $\gamma \to 1$, when the wave and the body surface coincide in the limit. Consequently, the accuracy of the Busemann equation increases for hot air flow ($\gamma < 1.4$) around convex bodies at very large Mach numbers. In the limit as $M_\infty \to \infty$ and $\gamma \to 1$, when the density in the shock layer becomes infinite, the Busemann equation gives the exact value for the pressure.

THE SIMILARITY LAW FOR ASYMMETRIC FLOW

It has been previously established that, at hypersonic velocities and zero angle of attack, the similarity law is determined by the parameter $K_1 = \delta_0 M_\infty$, where the small parameter δ_0 is either the cone angle, the slope of the body at the tip, or the thickness ratio of the body. For example, the pressure coefficient at an arbitrary point on the body surface is $C_p = \delta_0^2 f(K_1, \bar{x})$, a function only of the parameter K_1 and of the dimensionless coordinate of the point. The drag coefficient is $C_{Dp} = \delta_0^2 F(K_1)$, a function only of the parameter K_1.

In asymmetric flow the aerodynamic coefficients are functions of the angle of attack. It can be demonstrated that flow around bodies is still similar and that the aerodynamic coefficients are identical

if, in addition to K_1, a second parameter $K_2 = \alpha/\delta_0$ is maintained constant. Let us use Eq. (18.5a), defining the pressure coefficient on the conical tip by the method of local cones in the form $C_{p0} = \delta_c^2 \varphi_p(K_1)$. If the angle of the local cone is written as $\delta_c = \delta_0 - \alpha \cos \phi$ for small angles of attack, we obtain

$$C_{p0} = (\delta_0 - \alpha \cos \phi)^2 \varphi_p(K_1).$$

Therefore, Eq. (18.5a) is written in the form

$$\frac{C_p}{\delta_0^2} = \varphi_p(K_1)\left(\frac{\delta}{\delta_0} - K_2 \cos \phi\right)^2. \tag{18.60}$$

It follows that if the equality of the parameters K_2 and K_1 is maintained for two affine-similar bodies, the quantities C_p/δ_0^2 will be identical at corresponding surface points with the same values of ϕ and δ/δ_0.

Substituting Eq. (18.60) into Eq. (1.6), we obtain the general form of the equation for the axial force coefficient:

$$\frac{C_{Ap}}{\delta_0^2} = \varphi_A(K_1, K_2). \tag{18.61}$$

To obtain the corresponding relation for the normal force coefficient, a similar substitution can be made in Eq. (1.12). It should be observed that the coordinate r in this equation will be less than x by an order of magnitude, i.e., $r \sim \delta_0 x$ (in the same way as $r_{mid} \sim \delta_0 l_N$ or $r_{mid} \sim \delta_0 l$). A general relation for the normal force coefficient is found by integrating Eq. (1.12):

$$\frac{C_{Np}}{\delta_0} = \varphi_N(K_1, K_2). \tag{18.62}$$

Thus, the family of affine-similar bodies in flows in which both K_1 and K_2 are identical is characterized by constant values of C_{Ap}/δ_0^2 and C_{Np}/δ_0.

In the limiting case as $M_\infty \to \infty$ ($K_1 \to \infty$), only the quantity K_2 remains as the similarity parameter for the aerodynamic coefficients. For

example, this is evident in the case of a cone, for which the pressure coefficient is

$$c_p = \tilde{c}_p(\gamma)\delta_c^2\left(1 - \frac{\alpha}{\delta_c}\cos\phi\right)^2, \tag{18.63}$$

and, according to Eqs. (18.17) and (18.36),

$$\frac{c_{Ap}}{\delta_c^2} = \tilde{c}_p(\gamma)\left(1 + \frac{\alpha^2}{2\delta_c^2}\right),$$

$$\frac{c_{Np}}{\delta_c} = \tilde{c}_p(\gamma)\,\frac{\alpha}{\delta_c}. \tag{18.64}$$

The similarity law with respect to the parameters K_1 and K_2 is verified by experimental data. These data indicate that the similarity law is valid even at small values of K_1, although the law itself was derived on the basis that the Mach number was large enough to ensure that $K_1 > 1$ even for small values of δ_0.

In Fig. 195, experimental data are presented for the pressure distribution as a function of angle of attack on the surfaces of two cones with angles of 0.166 and 0.102 radian for $M_\infty = 2.75$ and 4.46, respectively. The product $M_\infty\delta_c$ gives an identical value of $K_1 = 0.455$ for both bodies. In the experiments, the pressure was measured at points corresponding to the angles $\phi = 0°$, 45°, 90°, 135°, and 180°, and the function $p_c/p_\infty - 1$ is plotted for each of the cones as a function of the parameter K_2. As is evident from the graph, the values of the pressure function for corresponding points on both cones are defined by practically the same curve. Some divergence is observed at large values of the parameter K_2 on the upper side of the cone, which is due to flow separation at high angles of attack. This is not taken into account by the similarity law.

Thus, in using the similarity law with respect to K_2, it must be kept in mind that similarity is limited to small angles of attack. In practice, the similarity law is valid with respect to K_1 for a rather wide range of Mach numbers, and this range can be expanded to lower values of M_∞ if the parameter $M_\infty\delta_0$ is replaced by $K_1 = \delta_0\sqrt{M_\infty^2 - 1}$.

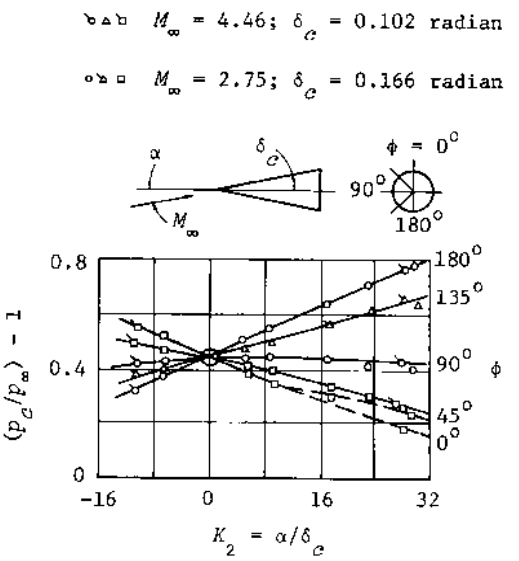

Fig. 195--Pressure distribution on a cone at angle of attack

Chapter VII

AERODYNAMICS OF BLUNT BODIES OF REVOLUTION

Editor's Introduction

A COMPREHENSIVE REVIEW *of theoretical and numerical methods for calculating inviscid flow over blunt bodies is contained in Hayes and Probstein* (Hypersonic Flow Theory, *1966). More detailed descriptions of numerical methods of solution are given by Belotserkovskii* (NASA TT F-453, *June 1967), with emphasis on the direct method developed by himself and Dorodnitsyn (that discussed in the present book). Methods are described for flows of an ideal gas, flows with equilibrium and nonequilibrium dissociation and ionization, and flows of a radiating gas.*

Traugott (J. Aero. Sci., *May 1960) has developed general relations for the radius of curvature of the shock wave and the velocity gradient at the stagnation point in the form of similarity parameters:*

$$\tilde{s}_0[1 + (r_N/R_N)\bar{s}_0] = \Gamma(\gamma, M_\infty), \qquad \frac{\bar{s}_0}{1 + (r_N/R_N)\bar{s}_0}\left(\frac{r_N}{V_\infty}\right)\left(\frac{dV_x}{dx}\right)_0 = \Pi(\gamma, M_\infty).$$

The improved formulas for shock detachment distance on spherical noses given in the footnote on p. 572 of Section 20 can be used to establish the values of the similarity parameters Γ *and* Π. *If the shock detachment parameter* $\bar{s}_0$ *is known for a given nose shape, as from Eqs. (20.43), (20.49), or (20.50), it is easy to determine the curvature of the shock* ($\bar{R}_{s0} = \bar{s}_0/\tilde{s}_0$) *and the velocity gradient for the given nose shape. For example, for a flat nose* $R_N \to \infty$ *and* $(\tilde{s}_0)_f = [1 + (\bar{s}_0)_{sph}](\tilde{s}_0)_{sph}$. *Then*

$$(\bar{R}_{s0})_f = \frac{1.03(1 + \sqrt{8\bar{\rho}/3})}{(1 + 0.78\bar{\rho})\sqrt{\bar{\rho}(1 - \bar{\rho})}} \tag{20.45a}$$

$$\left(\frac{dV_x}{dx}\right)_f = \frac{(\bar{s}_0)_{sph}}{(\bar{s}_0)_f[1 + (\bar{s}_0)_{sph}]}\left(\frac{dV_x}{dx}\right)_{sph}, \tag{20.45b}$$

where $(dV_x/dx)_{sph}$ *is calculated for a sphere with radius* r_N. *The parametric equations cannot be used for flat noses with rounded corners as* $\bar{r} \to 1$, *since the radius of curvature of the body at the stagnation point changes discontinuously from infinity to* r_N *at* $\bar{r} = 1$. *Clearly, higher order terms must be retained in the solution at this singularity.*

Theoretical calculations for blunt noses have recently been published by Inouye, Marvin, and Sinclair (NASA TN D-4397, February 1968) for flat-faced cylinders with rounded corners, and by South (NASA TN D-4563, May 1968) for spherical segment noses and other blunt shapes with sonic corners. The latter include very blunt cones with and without spherical tips, for which the shock is detached even with a pointed nose.

The well known curve of Chernyi (Fig. 225), which indicates that the drag of a blunt cone can be less than that of a sharp cone at hypersonic speeds, has been shown to be misleading by Chushkin (USSR Computational Math. and Math. Phys., 1962) and by Cleary (NASA TN D-2969, August 1965), on the basis of more exact calculations. Their results indicate that the pressure drag coefficients of blunt cones are always greater than those of the equivalent pointed cones and that Chernyi's result is due to the approximate nature of his theory.

Several reports are now available that present the results of detailed numerical calculations of the flow about spherically blunted cones of the type discussed briefly in Section 22. The original work is that of Chushkin and Shulishnina (USSR Computation Center Monograph, 1961, translated in AVCO Tech. Memo RAD-TM-62-63, September 1962), which has been retabulated and replotted by Ellett (Sandia Corporation SC-RR-64-1796, January 1965). Similar calculations are presented by Cleary (op. cit.) with emphasis on the flow properties in the inviscid shock layer. Roberts, Lewis, and Reed (AEDC-TR-66-121, August 1966) have independently calculated results similar to those of Chushkin and Shulishnina, but for different ranges of the variables and in more detailed graphical form.

The "universal" curve for pressure distribution on blunt cones presented in Fig. 225 appears to give a reasonable agreement with experimental data. However, the numerical solutions cited above provide a large amount of accurate data for correlation, and better parameters than Krasnov's empirical ones could be used. For example, Greenberg (J. Aero. Sci., March 1962) proposes the variables p/p_{o} and $[(p_{o}/p_{o})/\sqrt{C_{D_N}}](x/D_N)$ as basic correlation parameters, and indicates good agreement with experimental data. The numerical solutions for sphere-cones and sphere-cylinders also correlate well with the experimental data shown by Greenberg and with the equation of Van Hise (NASA TR R-78, 1960). The pressures near the junction with the blunt tip are not correlated by these parameters, but the pressure ratio at the junction (p_j/p_{o}) can be obtained from the numerical solutions and plotted in a manner similar to that suggested by Traugott (J. Aero. Sci., April 1962). There is no general method available for predicting the transition from the junction pressure to the correlation curve, but the curve can usually be faired through this region.

At the end of Section 24, Krasnov mentions the technique of matching a Prandtl-Meyer expansion to a Newtonian pressure distribution, as suggested originally by Lees and Kubota.[8] Useful curves for this method are given by Wagner (J. Aero. Sci., December 1959). Although the results are an improvement over Newtonian theory, they still differ considerably from those given by the numerical solutions cited above.

An excellent correlation of the normal force coefficient and the pitching moment coefficient at angle of attack for blunt cones at hypersonic speeds has been published by Whitfield and Wolny (AEDC-TDR-62-166, August 1962, and AIAA J., February 1963).

§ 19. *THE FLOW CHARACTERISTICS OF BLUNT-NOSED BODIES*

SOME DATA CONCERNING THE AERODYNAMICS of bodies of revolution with blunt noses are presented in this chapter. These bodies are important for practical application to hypersonic flight in the atmosphere because the total heat load to the nose is less compared with pointed bodies, and less mass is lost.

A diagram of the flow around a blunt body of arbitrary shape is presented in Fig. 196. A detached shock wave is generated ahead of the body with variable intensity at various points on its surface, as indicated by the local slope of the wave. Far from the nose, where the slope is $\mu_\infty = \arcsin(1/M_\infty)$, the shock wave degenerates into an ordinary Mach wave of infinitesimally small strength. The maximum strength will occur at the axis of the wave where $\theta_s = \pi/2$. Since the angle θ_s differs little from $\pi/2$ in the vicinity of the nose, the strength of the shock in this region is close to that of a normal shock.

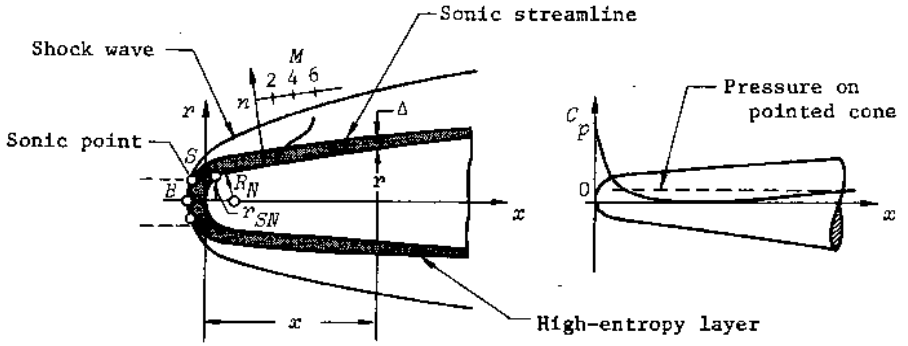

Fig. 196--Flow diagram for a blunt body

The transition of the gas particles through such a strong shock wave is accompanied by a considerable loss of total pressure and by an increase in entropy. As a result, the body surface is covered by a high-entropy layer of gas. The entropy in the various streamlines in this layer depends on the region of the shock wave through which the streamline passed. Obviously, the largest entropy is on the axial streamline, which passes through the apex of the wave (the normal shock) and coincides with the surface of the body.

The shock angle decreases with distance from the axis, and the entropy decreases in comparison with its value on the axial streamline. The velocity losses are greatest directly behind the normal part of the shock, and these losses decrease with distance along the curved surface of the shock. Thus, the farther the streamline is from the axis, the greater the local velocity. A similar picture of velocity distribution also exists at an arbitrary flow section behind the nose, due to the unequal degree of deceleration at various points on the shock wave (Fig. 196).

Thus, a region of small velocities exists near the surface, which has a pronounced effect on the development of the boundary layer. For example, the skin friction decreases due to the velocity decrease in the boundary layer. In addition, the flow regimes in the boundary layer around a blunt body differ in comparison with a pointed body. The laminar boundary layer becomes turbulent considerably farther downstream due to a decrease in the local Reynolds number, which can be calculated from the velocity at the edge of the layer. Since the extent of the laminar boundary layer increases, there is a significant reduction in friction, which results in a decrease in the thermal flux from the heated gas to the surface.

The reduction in heat flux can be interpreted as resulting from the increase in entropy of the gas on passing through the shock wave. Therefore, the effect of the use of blunting that we have discussed is called the entropy effect.

It should be noted that the physical interpretation of the entropy effect is not limited to a decrease in velocity at the external edge of the boundary layer; the density also decreases along with the decrease

in velocity. To illustrate, let us use some data for the pressure distribution on a blunt cone. It is evident from Fig. 196 that the pressure on the surface, except for the local region around the nose, is lower than that on a pointed body, and that the region of lower pressures extends for several bluntness diameters downstream. A section then follows where the pressure coefficient is almost the same as that on the pointed body. The equation for density can be written in the form $\rho = \rho_0'(p/p_0')^{1/\gamma}$ or $\rho = \rho_0 \nu^{(\gamma-1)/\gamma}(p/p_0)^{1/\gamma}$, where $\nu = p_0/p_0'$ is the stagnation pressure ratio across the shock in the vicinity of the nose. Obviously, the quantity ν will be considerably less for those streamlines that pass through the shock close to its normal portion than it is for a pointed cone. Therefore, if it is assumed that the ratio p/p_0 is approximately equal to its value for a pointed cone, the density on the blunt body will be less than on the cone, and the pressure reduction due to the blunting effect on the forward part of the body will increase this difference.

It is true that cases exist in which the local pressure is greater than that on a pointed cone (e.g., for cones with flat blunting). However, the effect of the entropy increase is dominant and, as a result, the density is still decreased.

In addition, the increase in entropy in comparison with the pointed body also leads to a temperature increase at the external edge of the boundary layer. This results in an effect opposite to that of the high-entropy layer and to some increase in the thermal flux from the boundary layer to the wall. However, the total entropy effect is usually dominant and results in a decrease in the heat flow with the proper choice of the degree and the shape of the blunting.

It is possible that the pressure drag can decrease in comparison with a pointed body if the blunting is slight and the axisymmetric body is fairly slender. The drag reduction is due to the net effect of the decreased pressure on a considerable portion of the body despite the pressure increase on the blunt nose. However, the chief effect of the use of blunting does not lie in a reduction of the drag. This reduction, even if attained, is generally small. The fundamental advantage in using a blunt body is the substantial decrease in friction. Specifically, this

provides for the dissipation into the atmosphere of a significant amount of heat in the form of losses in the bow shock wave and also in the form of other losses (local shock waves, trailing shocks, vortices, etc.). As a consequence, the heat flow to the wall is significantly reduced, and for blunt bodies it can constitute only a few percent of the total kinetic energy of the flow.

However, the importance of such research is not only due to the intentional use of blunt bodies. Actually, all bodies of revolution are blunted to some degree because it is impossible, in a practical sense, to achieve a perfectly pointed nose. Blunting can result from accidental mechanical effects, or the nose can be blunted by melting in the case of motion of a body with very high velocity in a dense gaseous medium.

§ 20. *INVISCID FLOW AROUND A BLUNT NOSE*

GENERAL SOLUTION FOR A NOSE OF ARBITRARY SHAPE

THE STUDY OF THE AERODYNAMICS of a complete blunt body is dependent on the investigation of the flow about the blunt nose itself. The results of these investigations are fundamental to the calculation of the flow parameters on the remaining part of the body. In addition, they are of value in themselves because it is then possible to determine the aerodynamic characteristics of an isolated blunt nose. The total aerodynamic characteristics can be specified by the summation of the components for the nose and the remaining parts.

Although the flow around the aft part of the body depends on the amount and type of blunting, the flow conditions around the nose itself are determined only by its shape or, more accurately, by the shape of the section of the nose up to the sonic point on its surface. Thus, it follows that the problem of flow around a blunt nose can be solved independently of the rest of the body.

We shall consider first the inviscid flow field. In addition to determining the basic pressure field, the solution to this problem is of value because it enables us to establish the basic flow conditions outside the boundary layer, which are necessary for the investigation of friction and heat transfer processes in the boundary layer.

A series of methods for solving the problem of flow around a blunt body have already been developed. A considerable number of authors have based their methods on a given shape and location of a shock found from experiment, for example. Then the inverse problem was solved: A system of nonlinear, partial differential equations was integrated approximately for known boundary conditions on the curved shock wave, and the

flow around the blunt surface was thus calculated. At the same time, the shape of the nose itself was determined.

Academician A. A. Dorodnitsyn proposed a method for the integration of a system of partial differential equations that reduces to the numerical solution of an approximate system of ordinary differential equations in a given region.[1] In particular, this method can be used when the boundary of the region is unknown, e.g., a curved shock wave in front of a blunt surface. Hence, the shape and location of the wave are determined in the process of solving the problem of flow around the nose.

Using this method, O. M. Belotserkovskii[2] has calculated the flow around blunt bodies of revolution with detached shock waves on an electronic computer. More detailed information concerning Dorodnitsyn's method and its application for the solution of these problems is available in the specialized literature. We shall examine briefly the mechanics of this solution and show some results obtained on the computer.

It is convenient to use a system of equations in spherical coordinates (Fig. 197) to calculate the mixed rotational flow that exists between the curved shock wave and a blunt nose of arbitrary shape. Since symmetric flow is considered, the equations of motion, Eq. (3.9), continuity, Eq. (3.17), and isentropic flow, Eq. (3.48), are simplified.

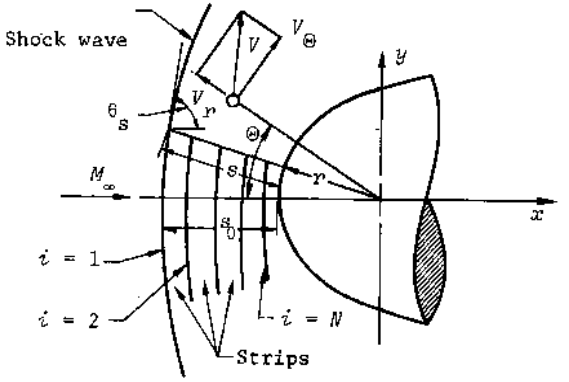

Fig. 197--Flow around a blunt nose and the region of integration

It is also convenient to transform the equation of motion with the help of the Bernoulli equation and to introduce the stream function Ψ. Then the whole system of equations has the following form:

$$\frac{\partial[\bar{r}^2(\bar{p} + \bar{\rho}\bar{V}_r^2)\sin\Theta]}{\partial\bar{r}} + \frac{\partial[\bar{r}\bar{\rho}\bar{V}_\Theta\bar{V}_r\sin\Theta]}{\partial\Theta} = \bar{r}(2\bar{p} + \bar{\rho}\bar{V}_\Theta^2)\sin\Theta,$$

$$\frac{\partial(\bar{r}^2\tau\bar{V}_r\sin\Theta)}{\partial\bar{r}} + \frac{\partial(\bar{r}\tau\bar{V}_\Theta\sin\Theta)}{\partial\Theta} = 0, \tag{20.1}$$

$$\frac{\partial\Psi}{\partial\Theta} = \bar{r}\bar{\rho}\left(\bar{V}_\Theta\frac{d\bar{r}}{d\Theta} - \bar{r}\bar{V}_r\right)\sin\Theta,$$

$$\varphi = \varphi(\Psi),$$

where

$$\tau = \left[\frac{\gamma-1}{2\gamma}(1 - \bar{V}^2)\right]^{1/(\gamma-1)}, \qquad \varphi = \frac{\bar{p}}{\bar{\rho}^\gamma},$$

$$\bar{p} = \frac{\gamma-1}{2\gamma}\bar{\rho}(1 - \bar{V}^2), \qquad \bar{\rho} = \frac{\tau}{\varphi^{1/(\gamma-1)}}. \tag{20.2}$$

The dimensionless parameters are defined as $\bar{V} = V/V_{max}$, $\bar{\rho} = \rho/\rho_\infty$, $\bar{p} = p/\rho_\infty V_{max}^2$, and $\bar{r} = r/l$, where l is a characteristic linear dimension of the body. The entropy function φ varies from one streamline to another; i.e., it varies with the stream function Ψ and is determined from the relation $S = c_v \log\varphi$.

The unknown quantities $\bar{V}_r$, $\bar{V}_\Theta$, φ, and Ψ can be calculated from the system of four equations given in Eq. (20.1). The solution must satisfy the boundary conditions on the surfaces of the nose and the shock wave. On the surface of a blunt nose whose equation is $r = r_0(\Theta)$, the boundary conditions are

$$\bar{V}_r = \frac{\bar{V}_\Theta}{r_0}\frac{dr_0}{d\Theta}, \qquad \Psi = 0, \qquad \varphi = \varphi(0) = \text{const}. \tag{20.3}$$

The entropy function can be found for the conditions behind the normal part of the shock and can be written in the form

$$\varphi(0) = \frac{2}{\gamma + 1}\left(\frac{\gamma - 1}{\gamma + 1}\right)^{\gamma} \frac{1}{\tilde{V}_\infty^{2\gamma}}\left[\tilde{V}_\infty^2 - \frac{(\gamma - 1)^2}{4\gamma}(1 - \tilde{V}_\infty^2)\right]. \tag{20.4}$$

The boundary conditions on a shock specified by $r = r_0(\Theta) + s(\Theta)$ (where s is the distance along a radial line $\Theta = \text{const}$ from the body to the shock) are found from the theory of a curved shock wave and have the form†

$$\begin{aligned}
\tilde{V}_r &= \tilde{V}_y \sin\Theta - \tilde{V}_x \cos\Theta,\\
\tilde{V}_\Theta &= \tilde{V}_x \sin\Theta + \tilde{V}_y \cos\Theta,\\
\tilde{V}_x &= \frac{2\tilde{V}_\infty}{\gamma + 1}\left(\cos^2\theta_s + \frac{\gamma - 1}{2\tilde{V}_\infty^2}\right),\\
\tilde{V}_y &= (\tilde{V}_\infty - \tilde{V}_x)\cot\theta_s,\\
\bar{p} &= \frac{2}{\gamma + 1}\left[\tilde{V}_\infty^2 \sin^2\theta_s - \frac{(\gamma - 1)^2}{4\gamma}(1 - \tilde{V}_\infty^2)\right],\\
\bar{\rho} &= \frac{\gamma + 1}{\gamma - 1}\frac{\tilde{V}_\infty^2 \sin^2\theta_s}{1 - \tilde{V}_\infty^2 \cos^2\theta_s},\\
\Psi \equiv \Psi_\infty &= \frac{(\bar{r}_0 + \bar{s})^2}{2}\tilde{V}_\infty \sin^2\Theta.
\end{aligned} \tag{20.5}$$

The boundary condition for the entropy function is found from the expressions for $\bar{p}$ and $\bar{\rho}$.

Equation (20.1) can be solved by means of the Dorodnitsyn method.

†Editor's note: Several of these equations have been revised from those in the original text, and a number of errors have been corrected.

According to this method, $N - 1$ lines are drawn between the body and the shock with equations

$$r = r_i(\Theta) = r_0(\Theta) + \xi_i s(\Theta),$$

where $\xi_i = (N - i + 1)/N$ and $i = 2, 3, \ldots, N$. Thus, these lines partition the area for integration; i.e., the perturbed portion of the flow between the body and the shock is divided into N strips (Fig. 197). The first two equations of Eq. (20.1) can then be integrated with respect to r along an arbitrary radial line $\Theta = \text{const}$ from the body to the edge of each of the strips, i.e., between the limits r_0 and r_i.

As a result, $2N$ independent integral relations are derived. The remaining two equations in Eq. (20.1) are written for conditions along each of the $N - 1$ intermediate lines, $r = r_i(\Theta)$, thus increasing the number of equations in the system to $4N - 2$. If we add the relation on the shock,

$$\frac{ds}{d\Theta} = -(r_0 + s) \cot(\theta_s + \Theta) - \frac{dr_0}{d\Theta}, \tag{20.6}$$

which can be derived from the condition $dy/dx = \tan \theta_s$, the system will consist of $4N - 1$ equations.

It should be noted that the first $2N$ equations contain integral terms resulting from the integration of the first two equations of Eq. (20.1) between the limits r_0 and r_i. If the integrands are denoted by $f(r, \Theta)$, the integrals can be computed by approximating the functions f with polynomials of the form

$$f(r, \Theta) = \sum_{m=0}^{N} a_m \left(\frac{r - r_0}{s}\right)^m, \tag{20.7}$$

where the coefficients $a_m(\Theta)$ are linear functions of the values of f at the boundaries of the strips.

After integration, we obtain a system of $4N - 1$ approximate equations, which can be solved for the derivatives with respect to Θ of the unknown functions $\tilde{V}_{ri}$, $\tilde{V}_{\Theta i}$, ψ_i, s, θ_s, and $\tilde{V}_{\Theta 0}$, resulting in a system of ordinary differential equations. These can then be solved numerically, using the boundary conditions for $\Theta = 0$ (i.e., on the axis of

symmetry), where $\widetilde{V}_{\Theta 0} = \widetilde{V}_{\theta i} = 0$, $\Psi_i = 0$, $\theta_s = \pi/2$, and $\varphi = \varphi_1(0)$, and the boundary conditions on the so-called singular line, the points of which are located in the vicinity of the sonic line where $V_0 = a^*$. Thus, the flow around bodies with detached shocks can be calculated for bodies with different types of blunting, e.g., in the shape of a sphere, a flat surface, a curved surface with a discontinuity, etc.

The effectiveness of the method is dependent on the use of high-speed electronic computers for the numerical integration, from which final results can be obtained with any required degree of accuracy. These results enable us to make judgments concerning the shape and location of the shock wave and concerning the magnitude and character of the distribution of the flow parameters between the shock wave and the blunt nose. We shall present below some of the results obtained on the basis of this method of integral relations.

The calculation scheme presented according to the Dorodnitsyn method does not take into account the variations in the physical-chemical properties of the air behind the shock wave for very high velocities. This can lead to inaccurate results for the shape and location of the shock wave and to inaccurate values of density, but it is claimed that the pressures are comparatively accurate. Some questions associated with the solution of the problem of flow near the blunt nose taking into account the effect of variable specific heats and dissociation are discussed in the next section.

SPHERICAL NOSES

Solution in the Vicinity of the Stagnation Point

For a more complete idea of the character of the flow around blunt bodies, let us examine separately the flow with a detached shock wave, first in front of a sphere and then in front of a flat surface. The study of the flow in the vicinity of the stagnation point on a spherical nose is of interest primarily because the heat transfer is largest at that point. It is shown below that the heat flow is a function of the initial velocity gradient along the spherical surface, which can be found from the solution for the inviscid flow around a blunt nose. In

addition, the solution of the problem of flow in the vicinity of the stagnation point enables us to determine the standoff distance of the shock wave and the distribution of the gas dynamic parameters in this local region. In general, the solution can be obtained taking into account the physical-chemical changes in the gas.

The solution to this problem can be obtained[3] by using the equations of motion, Eq. (3.11), and continuity, Eq. (3.19), in a curvilinear orthogonal system. The origin of the coordinates of this system coincides with the stagnation point, the coordinate x is measured along the surface, and the coordinate y is measured along the normal to the surface (Fig. 198).

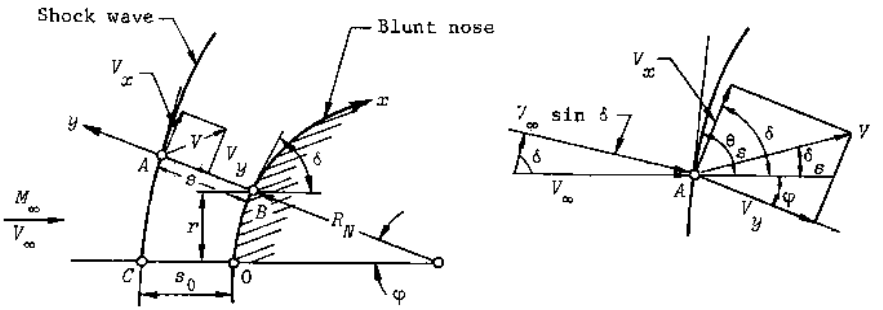

Fig. 198--Velocity components in curvilinear coordinates

If it is assumed that only the region in the vicinity of the stagnation point is being considered and that the incident flow has a very high supersonic velocity, the original complex equations can be simplified. In fact, for these conditions, the flow behind the shock wave can be assumed incompressible, since the Mach number M_2 differs little from the value $\sqrt{(\gamma - 1)/2\gamma}$, corresponding to the case of limiting flow (for $M_\infty \to \infty$), behind a normal shock. Therefore, the density in this region can be assumed constant and equal to $\rho \approx \rho_\infty/\bar{\rho}$, where $\bar{\rho} = \rho_\infty/\rho_s$, ρ_s is the density behind a normal shock wave (or at the stagnation point),

and a constant value for ρ can be used in the equations of motion and continuity.†

Since, in this case, large velocities are considered, the shock will lie very close to the surface of the body. The region of perturbed flow is contained in a thin layer of thickness δ, which is very small compared with the radius of curvature R_N of the body in the vicinity of the stagnation point.

Therefore, if it is assumed that $s/R_N \ll 1$, $y/R_N \ll 1$ also, since $0 \leq y \leq s$. Thus, the quantity $y/R \approx y/R_N$ can be neglected with respect to unity in the flow equations. In addition, the third terms on the left side of Eqs. (3.11) can be neglected, since they are also of a lesser order due to the fact that $y \ll R$, $x \ll R$. Finally, the continuity equation for conditions in the vicinity of the stagnation point can be simplified if it is assumed that $r \approx x$.

If all of these simplifications are taken into account, Eqs. (3.11) and (3.19) take the form

$$V_x \frac{\partial V_x}{\partial x} + V_y \frac{\partial V_x}{\partial y} = -\frac{\bar{\rho}}{\rho_\infty} \frac{\partial p}{\partial x}, \tag{20.8}$$

$$V_x \frac{\partial V_y}{\partial x} + V_y \frac{\partial V_y}{\partial y} = -\frac{\bar{\rho}}{\rho_\infty} \frac{\partial p}{\partial y}, \tag{20.9}$$

$$\frac{\partial (V_x x)}{\partial x} + \frac{\partial (V_y x)}{\partial y} = 0. \tag{20.10}$$

The solution of these equations must satisfy the conditions at an arbitrary point on the body surface, where the normal velocity component $V_y = 0$ for $y = 0$, and at the stagnation point, where $V_x = V_y = 0$ for $y = x = 0$. In addition, the solution must satisfy the flow conditions behind the shock wave. These conditions, written for the velocity components at point A, located at a distance s from the surface, have the form (see Fig. 198)

†Editor's note: Note that this definition of $\bar{\rho}$ is inverted from that defined in connection with Eq. (20.2). For the remainder of this section, $\bar{\rho}$ is defined as $\bar{\rho} = \rho_\infty/\rho$.

$$V_x = V \cos(\delta - \delta_s), \qquad V_y = -V \sin(\delta - \delta_s). \tag{20.11}$$

The total velocity and pressure at point A are obtained from Eqs. (4.31) and (4.12), assuming that $\rho = \rho_\infty/\bar{\rho}$ directly behind the shock:

$$\frac{V}{V_\infty} = \sqrt{\bar{\rho}^2 \sin^2\theta_s + \cos^2\theta_s}, \tag{20.12}$$

$$\frac{p}{p_\infty} = 1 + \gamma M_\infty^2 (1 - \bar{\rho}) \sin^2\theta_s. \tag{20.13}$$

The pressure and density can be eliminated from Eqs. (20.8) and (20.9) by differentiation with respect to y and x, respectively. Equating the results and including Eq. (20.10), we obtain

$$\frac{\xi V_x}{x} = V_x \frac{\partial \xi}{\partial x} + V_y \frac{\partial \xi}{\partial y}, \tag{20.14}$$

where the vorticity $\xi = \partial V_x/\partial y - \partial V_y/\partial x$ is known from Stokes' theorem for rotational flow. Thus, the problem lies in a search for solutions of Eqs. (20.10) and (20.14), in terms of V_x and V_y, that satisfy the boundary conditions indicated above.

Let us assume that the solution for V_x in the vicinity of the axis ($x = 0$) can be represented in the form of a series:

$$V_x = a_0(y) + a_1(y)x + a_2(y)x^2 + \ldots,$$

in which x is assumed to be small. Since the velocity component V_x must be equal in absolute value but opposite in sign for plus and minus values of x, only terms with odd exponents of x remain in the expansion; i.e.,

$$V_x = a_1(y)x + a_3(y)x^3 + \ldots.$$

As x approaches zero, only the first term need be considered, resulting in the expression $V_x = a_1(y)x$. Further, let us introduce the function

$$F(y) = \int_0^y a_1(y)\, dy,$$

so that $F'(y) = a_1(y)$ and $F(0) = 0$. Then V_x can be rewritten as

$$V_x = xF'(y). \tag{20.15}$$

From the continuity equation, Eq. (20.10), the other velocity component is

$$V_y = -2F(y) + f(x).$$

But from the boundary condition at the surface $V_y(x, 0) = 0$. Then $-2F(0) + f(x) = 0$, and since $F(0) = 0$, $f(x) = 0$. Therefore,

$$V_y = -2F(y). \tag{20.16}$$

Introducing these relations into Eq. (20.14), we obtain

$$F'''(y) = 0, \tag{20.17}$$

which has the general solution

$$-\frac{V_y}{2} = F(y) = C_0 + C_1 y + C_2 y^2. \tag{20.18}$$

Since $F(0) = 0$, $C_0 = 0$. The other two coefficients can be determined by using the conditions on the shock near the stagnation point at $x \to 0$. At point C, we get

$$V_y = -2(C_1 s_0 + C_2 s_0^2) = V_c \quad \text{and} \quad \theta_s = \frac{\pi}{2},$$

and $V_c = -\bar{\rho} V_\infty$ from Eq. (20.12). Therefore,

$$C_1 s_0 + C_2 s_0^2 = \frac{\bar{\rho} V_\infty}{2}. \tag{20.19}$$

On the other hand,

$$V_x = xF'(y) = x(C_1 + 2C_2 y). \tag{20.20}$$

The value of V_x behind the shock wave can be determined from Eqs. (20.11) and (20.12). In the limit as $x \to 0$, we obtain

$$\lim_{x\to 0} \frac{\cos(\delta - \delta_s)}{x} = \frac{C_1 + 2C_2 s_0}{\bar{\rho} V_\infty}.$$

The limit on the left side can be computed in the following way. It is evident from Fig. 198 that the angle $\delta - \delta_s = \pi/2 - (\varphi + \delta_s)$ at an arbitrary point. Therefore, $\cos(\delta - \delta_s) = \sin(\varphi + \delta_s)$, and for small values of φ and δ_s it can be assumed that $\sin(\varphi + \delta_s) \approx \varphi + \delta_s$. Then

$$\lim_{x\to 0} \frac{\cos(\delta - \delta_s)}{x} = \lim_{x\to 0} \frac{\varphi + \delta_s}{x} = \frac{1}{R_N} + \frac{1}{R_{s0}} \left(\frac{\delta_s}{\omega}\right)_{x\to 0},$$

where ω is the angle between the vector representing the radius of curvature of the shock and the axis of flow, and R_{s0} is the radius of curvature of the shock wave at the axis. The ratio

$$\left(\frac{\delta_s}{\omega}\right)_{x\to 0} = \left(\frac{d\delta_s}{d\omega}\right)_{\delta_s \to 0}$$

is equal to $1/\bar{\rho} - 1$, which can be obtained from Eq. (4.2) by substituting $\Delta V_n / V_{n1} = 1 - \bar{\rho}$ and $\vartheta_s = \pi/2 - \omega$, and taking the limit as $\omega \to 0$.

Assuming that R_N is approximately equal to R_{s0}, we get

$$C_1 + 2C_2 s_0 = \frac{V_\infty}{R_{s0}}. \tag{20.21}$$

Another relation must be added to Eqs. (20.19) and (20.21), since they contain three unknown constants, C_1, C_2, and s_0. This relation results from the expression for vorticity behind the shock wave. Using Eq. (20.20) and the boundary conditions on the body surface, we obtain the relation $\xi = \partial V_x / \partial y = 2C_2 x$. On the other hand, from the theory for curved shock waves it is known that the vorticity is given by

$$\xi = 2C_2 x = \frac{V_\infty (1 - \bar{\rho})^2 \sin\theta_s \cos\theta_s}{\sin(\theta_s - \delta_s)\sqrt{\bar{\rho}^2 \sin^2\theta_s + \cos^2\theta_s}} \frac{d\theta_s}{dx}.$$

The coefficient C_2 can be obtained from this expression by determining the limit as $x \to 0$:

$$C_2 = \frac{(1 - \bar{\rho})^2}{2} \frac{V_\infty}{\bar{\rho} R_{sc}}. \tag{20.22}$$

If we substitute the coefficient C_2 into Eqs. (20.19) and (20.21) and solve them jointly, we obtain the coefficient C_1 and the detachment distance s_0 as follows:

$$C_1 = \mp \sqrt{1 - \Delta^2} \frac{V_\infty}{R_{s0}}, \tag{20.23}$$

$$s_0 = \frac{1 \pm \sqrt{1 - \Delta^2}}{\Delta^2} \bar{\rho} R_{s0}, \tag{20.24}$$

where $\Delta = 1 - \bar{\rho}$.

The Initial Velocity Gradient and Velocity Distribution

There are two possible solutions for the gas parameters in the vicinity of a blunt surface, as indicated by the plus and minus signs in the equations above. It can be shown that the lower sign corresponds to the physically real process. In fact, it follows from Eq. (20.20) that at the surface of the body, where $y = 0$, the velocity is $V_x = C_1 x$, or from Eq. (20.23),

$$V_x = \mp \sqrt{1 - \Delta^2} \frac{V_\infty}{R_{s0}} x.$$

Since for $x > 0$ or $x < 0$ the velocity V_x must be correspondingly positive or negative, it is apparent that the lower sign must be used, and this applies also to Eqs. (20.23) and (20.24). Then the velocity components can be determined using the expressions for C_1 and C_2:

$$\frac{V_y}{V_\infty} = -2\bar{\rho}y\left(\frac{\sqrt{1+\Delta^2}}{\bar{\rho}R_{s0}} + \frac{\Delta^2}{2\bar{\rho}^2R_{s0}^2}\cdot y\right), \tag{20.25}$$

$$\frac{V_x}{V_\infty} = \bar{\rho}x\left(\frac{\sqrt{1-\Delta^2}}{\bar{\rho}R_{s0}} + \frac{\Delta^2}{\bar{\rho}^2R_{s0}^2}\, y\right), \tag{20.26}$$

where $\bar{\rho}R_{s0}$ is given as a function of ε_0 by Eq. (20.24).

On the surface of the nose ($y = 0$), the total velocity is equal to the component V_x and is given by

$$\frac{V}{V_\infty} = \frac{V_x}{V_\infty} = \bar{\rho}x\,\frac{\sqrt{1-\Delta^2}}{\bar{\rho}R_{s0}}. \tag{20.26a}$$

Hence, it is evident that V_x varies linearly in the vicinity of the stagnation point on the body surface.

As already noted, it is necessary to know the value of the gradient of the velocity V_x on the surface for the heat transfer problem. According to Eq. (20.26a), this is

$$\left(\frac{\partial V_x}{\partial x}\right)_{y=0} = \tilde{\lambda} = \frac{V_\infty}{R_{s0}}\sqrt{1-\Delta^2}. \tag{20.27}$$

Experimental studies have shown that this relation, obtained from an analysis of very high velocity flow, can be used for approximate calculations at relatively small velocities. This is illustrated in Fig. 199, where experimental values of the dimensionless velocity gradient $\tilde{\lambda}D_N/V_\infty$ are presented.[3]

Obviously, Eq. (20.26a) can be rewritten as $V_x = \tilde{\lambda}x$ and the angle φ can be introduced, where φ is related to x by the expression $x = \varphi R_N$. Then $V_x = \tilde{\lambda}R_N\varphi$, which implies a linear dependence of V_x on φ. Although this relation is obtained from an analysis of hypersonic flow over a small region of the nose, experimental research has shown that a linear velocity variation is valid for a relatively large part of the curved surface, and at comparatively small Mach numbers.

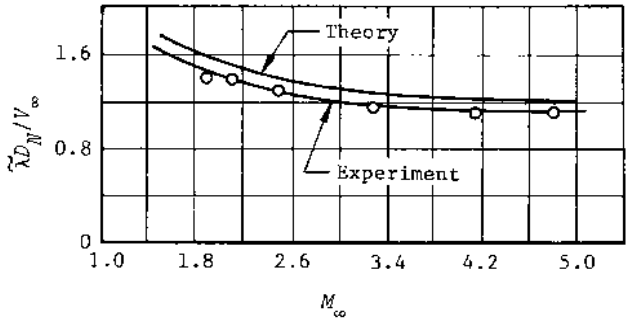

Fig. 199--Velocity gradient at the stagnation point

This is confirmed by the data in Fig. 200, where the dimensionless velocity $V_x/\tilde{\lambda}D_N$ is shown for a hemispherical nose. These values were determined by wind-tunnel measurements at four different Mach numbers. Linearity is maintained up to values of φ of 45° to 50°, and the results deviate only slightly from linear even at the largest angles.

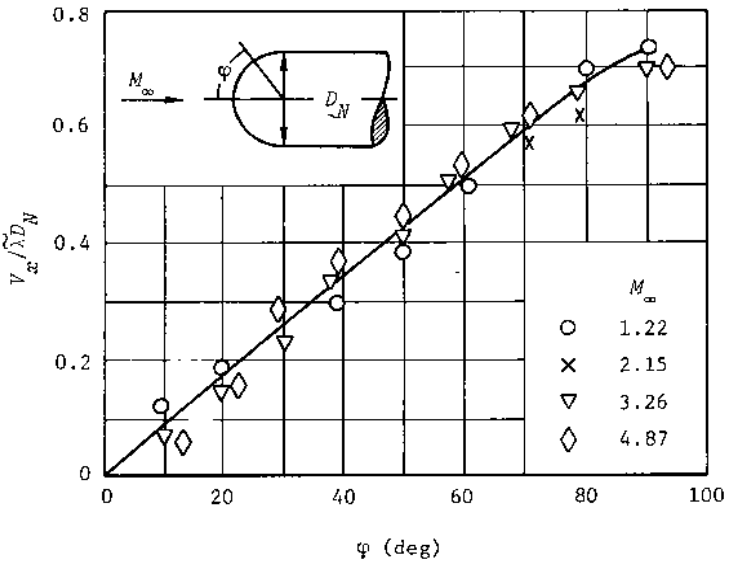

Fig. 200--Velocity distribution on a hemisphere

The equation for this linear law, $V_x = \tilde{\lambda} R_N \varphi$, can be written in the form $V_x = \bar{\lambda} V_\infty \bar{x}$, where $\bar{x} = x/D_N$, and $\bar{\lambda} = D_N \tilde{\lambda}/V_\infty$. The experimental and theoretical data are compared in Fig. 201. The velocity gradient can be found from the approximate relation

$$\tilde{\lambda} = \left(\frac{\partial V_x}{\partial x}\right)_{\substack{x=0 \\ y=0}} = \frac{1}{R_N}\sqrt{\frac{2(p_0' - p_\infty)}{\rho_0'}}, \tag{20.27a}$$

which is obtained in the following way. The velocity distribution over the spherical nose is related to the local static pressure by the expression for isentropic flow behind a shock wave:

$$\frac{V_x^2}{V_\infty^2} = \left(1 + \frac{2}{\gamma_\infty - 1}\frac{1}{M_\infty^2}\right)\left[1 - \left(\frac{p}{p_0'}\right)^{(\bar{\gamma}-1)/\bar{\gamma}}\right], \tag{20.28}$$

where γ_∞ is the ratio of specific heats in the unperturbed flow, and $\bar{\gamma}$ is the average ratio of specific heats behind the shock wave, which is of the order of 1.1 to 1.2 at very high temperatures. The pressure ratio in Eq. (20.28) can be determined from the Newtonian equation:

$$\frac{p}{p_0'} = \cos^2\varphi + \frac{p_\infty}{p_0'}\sin^2\varphi, \tag{20.29}$$

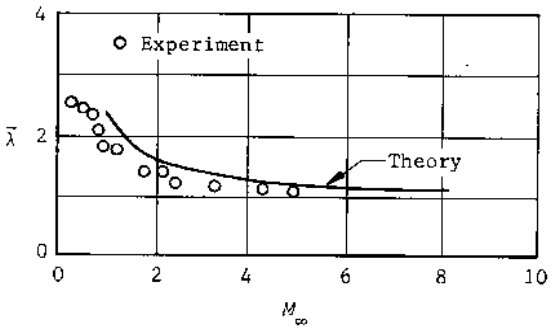

Fig. 201--Velocity gradient at the stagnation point as a function of Mach number

where it can be assumed that p_∞/p_0' is approximately equal to $1/\gamma_\infty M_\infty^2$ at sufficiently high Mach numbers. Equation (20.28) can be simplified for the velocity and velocity gradient in the vicinity of the stagnation point:

$$\frac{V_x}{V_\infty} = \bar{K}\varphi, \qquad \left(\frac{1}{V_\infty}\frac{dV_x}{d\varphi}\right)_{\varphi=0} = \bar{K}, \tag{20.30}$$

where

$$\bar{K} = \sqrt{\frac{\bar{\gamma}-1}{\bar{\gamma}}\left(1+\frac{2}{\gamma_\infty-1}\frac{1}{M_\infty^2}\right)\left(1-\frac{1}{\gamma_\infty M_\infty^2}\right)}. \tag{20.31}$$

For hypersonic velocities, the terms that are inversely proportional to M_∞^2 can be set equal to zero, which amounts to assuming that the flow in the vicinity of the stagnation point is incompressible, so that the stagnation pressure can be approximated by $p_0' = p + \rho_0' V_x^2/2$. The static pressure can be replaced by Eq. (20.29), in which, since φ is small, it can be assumed that $\cos\varphi \approx 1$ and $\sin\varphi \approx \varphi \approx x/R_N$. Differentiating V_x with respect to x, we obtain Eq. (20.27a) for the velocity gradient. For larger velocities, p_∞ can be neglected with respect to p_0' under the radical in Eq. (20.27a).

It is of interest to estimate the dimensions of the region of incompressible flow and the distance to the sonic point on the sphere. Equation (20.28) for isentropic flow can be used, assuming that the flow begins from the stagnation point. The conditions at this point can be assumed to be the same as those directly behind the normal portion of the shock. For example, the region of undissociated incompressible flow for $\gamma = 1.4$, $M_\infty = 5.1$, and $\bar{\rho} = 0.2$ is shown schematically in Fig. 202, assuming that the region is bounded by a local Mach number of 0.3. The angle to the point on the spherical nose where the local Mach number is 0.3 is shown as a function of free-stream Mach number in Fig. 203.

These results agree well with data for the sonic points on a sphere (Fig. 204) obtained by O. M. Belotserkovskii on an electronic computer.[2] Figure 204 also gives an idea of the shape of the sonic lines and the location of the sonic points on the shock wave for various Mach numbers.

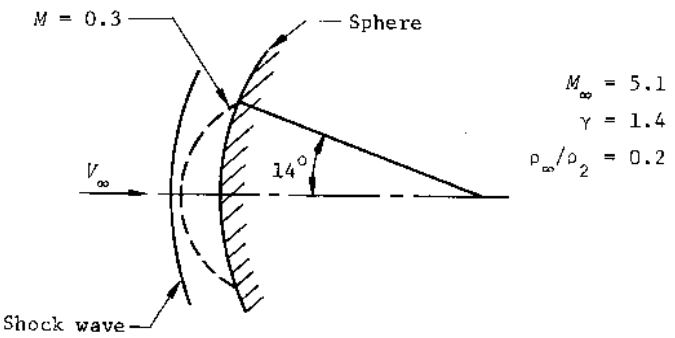

Fig. 202--Region of incompressible flow in the vicinity of a sphere

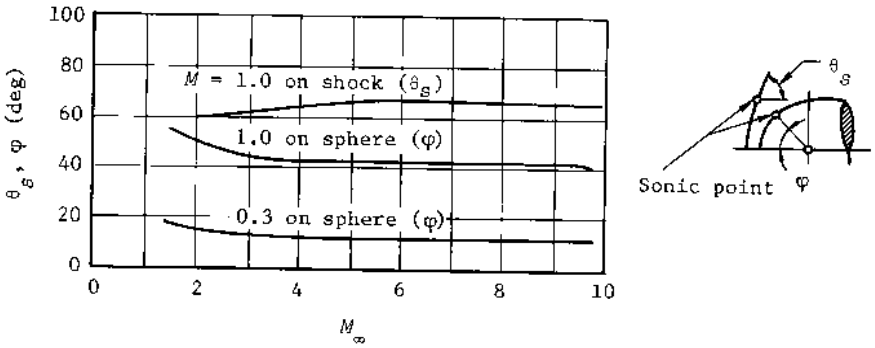

Fig. 203--Angular distance to the end of the incompressible region and to the sonic point on the surface and the shock

The shock angles corresponding to these points are shown in Fig. 203. It should be noted that, under real conditions, the regions of incompressible and subsonic compressible flows will be less than those calculated here, because either the vibrational motions of the molecules or dissociation behind the shock wave at high velocities will result in a reduction in temperature and a decrease in the velocity of sound. Consequently, the local Mach numbers increase for the same velocity on the sphere and the points for $M = 0.3$ and $M = 1$ are shifted over.

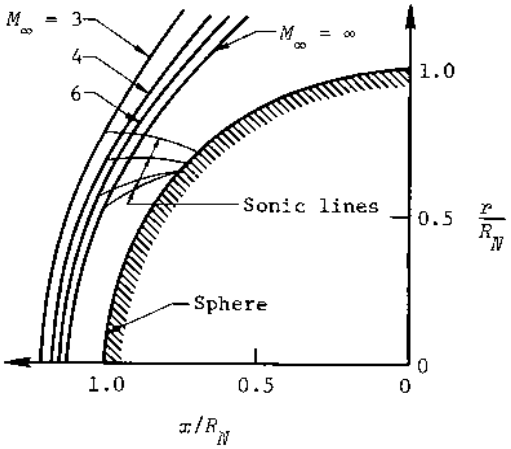

Fig. 204--Shock waves and sonic lines ahead of a sphere

The Pressure Distribution and Drag Coefficient

The results obtained for velocity allow the determination of the pressure distribution in the thin shock layer in the vicinity of the axis and also on the body surface close to the stagnation point. Using the incompressible Bernoulli equation, we obtain the pressure coefficient at an arbitrary point in the shock layer:

$$C_p = \frac{2(p - p_\infty)}{\rho_\infty V_\infty^2} = C_{pA} + \frac{1}{\rho}\left[\left(\frac{V_A}{V_\infty}\right)^2 - \left(\frac{V_y}{V_\infty}\right)^2 - \left(\frac{V_x}{V_\infty}\right)^2\right]. \qquad (20.32)$$

Since the layer is thin, the pressure coefficient C_{pA} and the velocity directly behind the shock wave at a point on its curved surface can be replaced, approximately, by the values C_{pC} and V_C, respectively, behind the normal portion at point C (Fig. 198). These values follow from Eqs. (20.13) and (20.12):

$$C_{pC} = 2(1 - \bar{\delta}) = 2\Delta, \qquad V_C = V_\infty \bar{\delta}.$$

For conditions on the axial (or what is called the zero) streamline,

C_{pA} equals C_{pC} exactly, and $V_A = V_C$. In this case, the pressure coefficient at an arbitrary point on the zero streamline (where $V_x = 0$) is

$$C_p = 2\Delta + \bar{\rho}\left[1 - \left(\frac{V_y}{\bar{\rho}V_\infty}\right)^2\right], \tag{20.33}$$

where $V_y/\bar{\rho}V_\infty$ is derived from Eq. (20.25). After assigning various values to y/s_0, we can calculate the pressure coefficient at each point on the axial streamline. For example, at the stagnation point on the surface, where $V_y = 0$, the pressure coefficient is

$$C_{p0} = 2 - \bar{\rho}. \tag{20.34}$$

Thus, in going from the shock wave to the stagnation point on the body, the gas undergoes an additional compression, and the pressure coefficient changes from $C_{pC} = 2(1 - \bar{\rho})$ to the larger value $C_{p0} = 2 - \bar{\rho}$. The nature of this change is shown in Fig. 205.

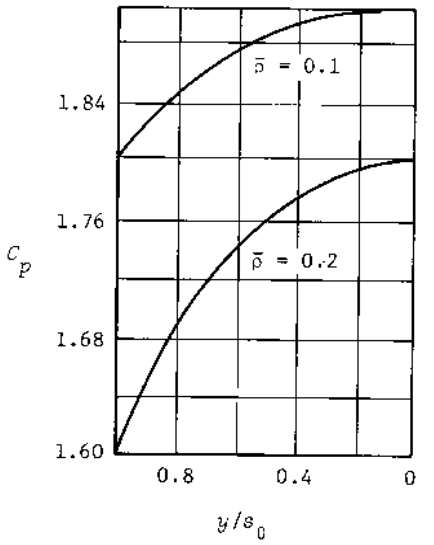

Fig. 205--Variation of the pressure coefficient along the axial streamline

It is apparent that the density ratio $\bar{\rho}$ is the only parameter that determines the value of the pressure coefficient, and the smaller $\bar{\rho}$ is, the larger the coefficient and the lesser the degree of compression. Thus, the pressure in the perturbed flow is distributed more uniformly either for very high velocity cold flow, in which the gas is strongly heated in the shock layer and $\bar{\rho}$ is rather small, or for lesser velocities of a preheated gas (which also results in a decrease in $\bar{\rho}$).

The pressure distribution on the surface of the body in the vicinity of the stagnation point can be calculated from Eq. (20.32) by setting $V_y = 0$ and $V_x = \tilde{\lambda}x$:

$$C_p = 2\Delta + \bar{\rho}\left[1 - \left(\frac{\tilde{\lambda}x}{\bar{\rho}V_\infty}\right)^2\right].$$

Substituting the value of the gradient $\tilde{\lambda}$ from Eq. (20.27) and assuming that $R_{s0} = R_N$, we obtain

$$C_p = (2 - \bar{\rho})\left[1 - \left(\frac{x}{R_N}\right)^2\right] = C_{p0}\left[1 - \left(\frac{x}{R_N}\right)^2\right]. \qquad (20.35)$$

This equation is derived for small values of x. However, studies show that, after a simple transformation, it can be extended to apply to a fairly large part of the body surface. In fact, since $x/R_N \approx \varphi \approx \sin\varphi$, $C_p = (2 - \bar{\rho})\cos^2\varphi$. The quantity $2 - \bar{\rho}$ is the pressure coefficient C_{p0} at the stagnation point, so that $C_p = C_{p0}\cos^2\varphi$, and we arrive at the modified Newtonian equation.

Experimental results and theoretical studies show that this equation predicts, with sufficient accuracy, the pressure distribution on practically the entire surface of the hemisphere, although the accuracy decreases somewhat at the end of the blunt nose.

Figure 206 presents for comparison experimental and theoretical data for a hemispherical nose at $M_\infty = 5.8$.[4] The theoretical data were calculated by the method of integral relations discussed earlier, using an electronic computer. It is evident that the Newtonian theory gives results somewhat lower than the experimental data only on a small part of the nose near the junction of the hemisphere and the cylinder.

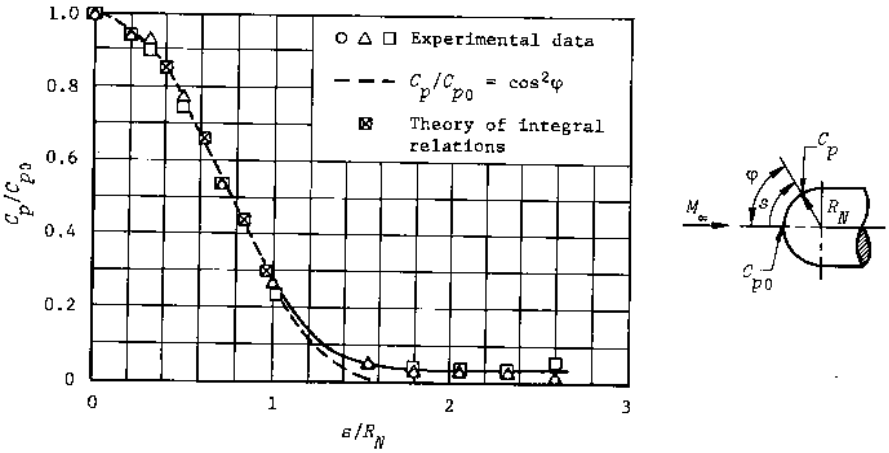

Fig. 206--Pressure distribution on a hemisphere cylinder

The good accuracy of the Newtonian equation allows it to be used for the calculation of the pressure drag coefficient of a spherical nose. According to Eq. (1.6), the drag coefficient with respect to the area πR_N^2 is

$$c_{Dp} = \int_0^{\sin^2\varphi} c_p \, d(\sin^2\varphi).$$

Introducing $c_p = c_{p0} \cos^2\varphi$ and integrating, we find

$$c_{Dp} = c_{p0} \sin^2\varphi\left(1 - \frac{\sin^2\varphi}{2}\right). \qquad (20.36)$$

Thus, the drag coefficient of a hemisphere is $c_{Dp} = c_{p0}/2$. The experiments (Fig. 207) agree well with Eq. (20.36), showing that its accuracy increases with an increase in velocity.

It is evident that it is necessary to find the pressure coefficient at the stagnation point to determine the drag coefficient of a hemisphere, or of a part of it. We already know how to determine its value taking

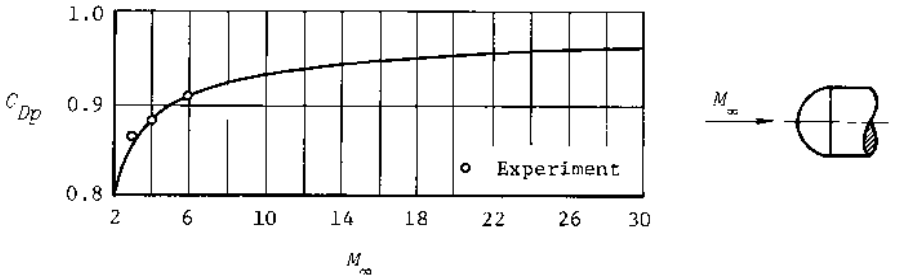

Fig. 207--Pressure drag coefficient of a hemisphere

dissociation and ionization into account. Particularly in approximate calculations, it is possible to find the density ratio $\bar{\rho} = \rho_\infty/\rho_2$ behind the normal portion of the shock by considering the physical-chemical changes and to compute the pressure coefficient from Eq. (20.34).

It should be noted that the calculations indicated are made on the assumption of equilibrium dissociation and ionization behind the shock wave. Strictly speaking, they are inapplicable in cases where flows of real gases are accompanied by relaxation processes.

Detachment Distance and Shape of the Shock Wave

The value of the detachment distance ε_0 can be determined from Eq. (20.24), which was derived for the case of very large velocities, when it can be assumed that $R_{s0} = R_N$, and for which experiments indicate that $\bar{\rho} \leq 0.1$. However, the same equation can be used for lesser velocities (larger $\bar{\rho}$) when $R_{s0} > R_N$, but in this case the relative value of the detachment distance $\tilde{\varepsilon}_0 = \varepsilon_0/R_{s0}$ is derived from Eq. (20.24). To determine the absolute value of ε_0, it is necessary to find R_{s0}. For given conditions of the incident flow, R_{s0} is a function of the radius of the sphere, and research shows that it is a linear function of R_N. If it is assumed that the shock is concentric with the sphere at the axis, $\bar{R}_{s0} = R_{s0}/R_N = 1/(1 - \tilde{\varepsilon}_0)$. Experiments indicate, however, that the radii are not concentric, particularly at the lower Mach numbers. Better results are obtained if the following relation is used:

$$\bar{R}_{s0} = \frac{R_{s0}}{R_N} = \frac{1}{(1 - \tilde{\varepsilon}_0)^2}. \qquad (20.37)$$

Then the detachment distance relative to the radius of the spherical nose can be calculated from the equation

$$\bar{s}_0 = \frac{s_0}{R_N} = \tilde{s}_0 \bar{R}_{s0} = \frac{\tilde{s}_0}{(1 - \tilde{s}_0)^2}. \qquad (20.38)$$

Figure 208 gives the results of calculations from Eqs. (20.38) and (20.24).

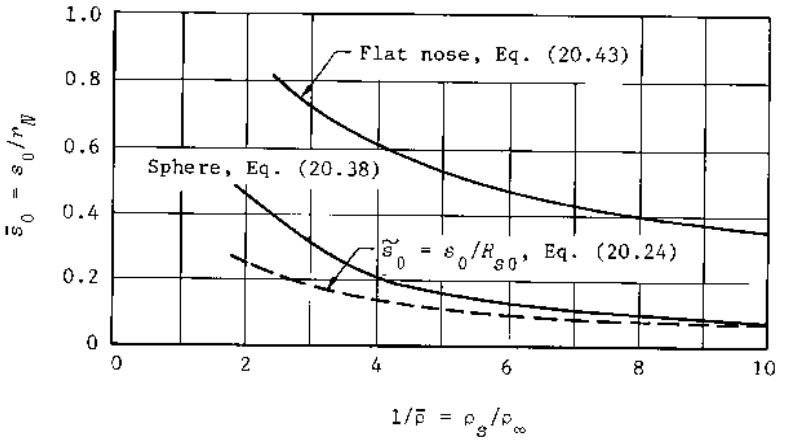

Fig. 208--Dimensionless shock-detachment distance for a sphere and a flat nose

For values of $\bar{\rho} < 0.5$, the relative detachment distance can be calculated approximately from the empirical relation[5]

$$\bar{s}_0 = \frac{2}{3} \frac{\bar{\rho}}{1 - \bar{\rho}}. \qquad (20.39)$$

To construct the shock in front of a blunt nose, it is necessary to know the shape of the shock wave as well as its standoff distance. Studies show that it can be assumed, with sufficient accuracy, that the shock has the shape of a circle with radius R_{s0} or a parabola

$$x = -s_0 + \frac{r^2}{2R_{s0}}.$$

A shock wave constructed in this way agrees closely with experimental shapes for a wide range of Mach numbers, and the approximation improves as the Mach number increases. The curve for the change in the radius, R_{s0}, as calculated from Eqs. (20.37) and (20.24), is given in Fig. 209.†

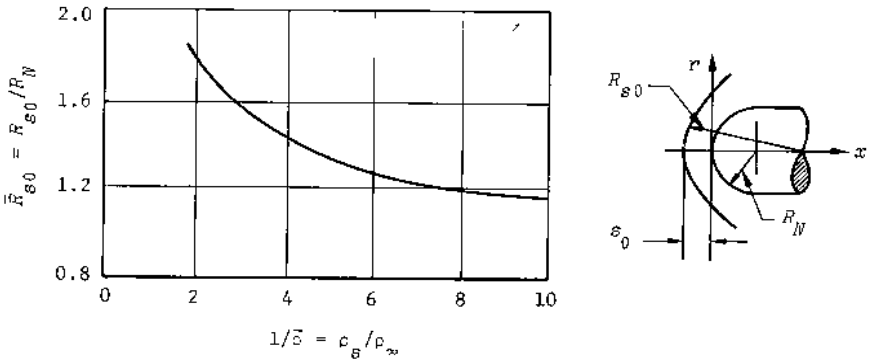

Fig. 209--Radius of curvature of a shock wave ahead of a sphere

Knowing the shape of the shock wave, it is possible to determine the parameters directly behind it at any point. For example, the distribution of M_2 can be found, and from this the point where $M_2 = 1$ can be located. For a dissociable gas, a series of values are assigned to $\omega = \pi/2 - \theta_s$, and the solution for an oblique shock is obtained for each of these values, accounting for dissociation. At the same time, the local values of V_2 and a_2, and therefore M_2, are determined. The value $M_2 = 1$ will correspond to one of the given angles $\omega = \omega'$. The distance from the axis to the point on the shock wave at which $M_2 = 1$ is approximately equal to $r = R_{s0} \sin \omega'$. Ordinary oblique shock theory, particularly Eq. (4.29), can be used to estimate the value of r. By choosing

†Editor's note: Recent calculations by Inouye[6] for equilibrium flow about spheres have indicated that the following equations give better correlations than the formulas in the text:

$$\tilde{\varepsilon}_0 = \bar{\rho}/(1 + \sqrt{8\bar{\rho}/3}), \qquad \bar{\varepsilon}_0 = 0.78\bar{\varepsilon}, \qquad \bar{R}_{s0} = 0.78\,(1 + \sqrt{8\bar{\rho}/3}).$$

The first equation is from Hayes and Probstein[7] and the second is from Seiff.[8]

a series of angles θ_s, we can find the value of θ_s for which $M_2 = 1$ as a function of M_∞. A graph of the variation of θ_s for $\gamma = 1.4$ calculated by this method is presented in Fig. 203.

FLAT NOSES

Pressure Distribution and Drag Coefficient

Calculations of the pressure distribution over a flat nose in symmetric flow, made on an electronic computer, are compared with experimental results in Fig. 210. An analysis of these results enables us to

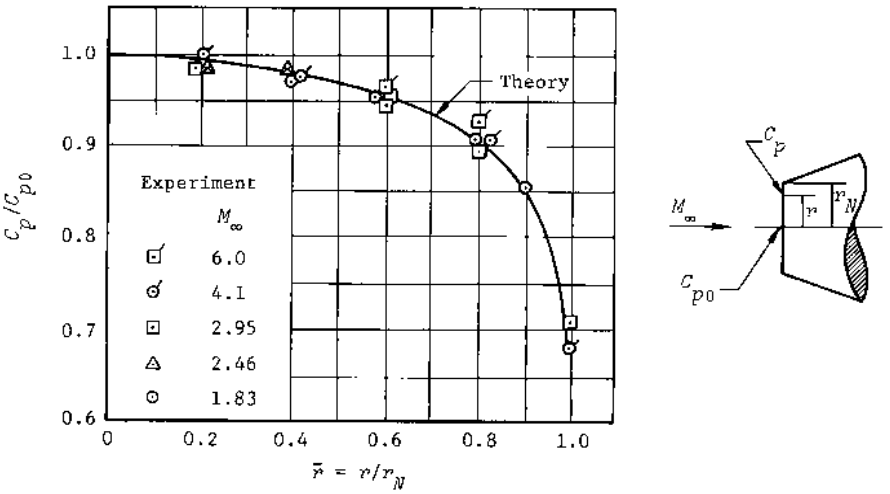

Fig. 210--Pressure distribution on a flat nose

determine the general relation for the variation of the pressure coefficient in the form $C_p = C_{p0} f(\bar{r})$. The dimensionless quantity $\bar{r}$ is equal to the ratio of the radial distance r to an arbitrary point on the flat surface to the nose radius r_N; $f(\bar{r})$ is a universal function varying only with $\bar{r}$, and C_{p0} is the pressure coefficient at the center of the nose, which coincides with the stagnation point. According to this rule, the

ratio C_p/C_{p0} is independent of the flow conditions in the free stream and of the absolute dimensions of the nose, and is determined only by the relative coordinate $\bar{r}$. With these results, the pressure drag coefficient of the flat nose can be derived from

$$C_{Dp} = C_{p0} \int_0^1 f(\bar{r})\, d\bar{r}^2.$$

Assuming that the universal function $f(\bar{r})$ is applicable for any velocity and is given in the form of the curve in Fig. 210, we can compute the integral and obtain the following relation:

$$C_{Dp} = 0.915 C_{p0}. \tag{20.40}$$

As is evident, the drag coefficient of the flat nose is almost twice as large as that of the hemisphere. Equation (20.40) is plotted in Fig. 211, where the effects of dissociation have been included in the calculation of C_{p0}. The available experimental results (see Fig. 211) confirm the accuracy of Eq. (20.40). Unfortunately, there are no valid data for very high velocities, but it is expected that the theoretical results from Eq. (20.40) will be satisfactory for such velocities.

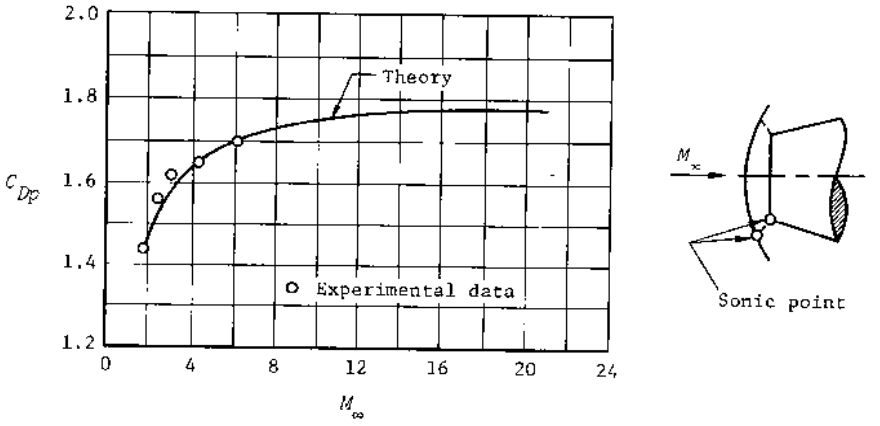

Fig. 211--Pressure drag coefficient of a flat nose

In addition to Eq. (20.40) for very high velocities, other approximate theoretical relations for the pressure coefficient and the pressure drag can be derived from an analysis of the pressure distribution directly behind the shock wave. The results of the analysis show that the pressure distributions behind the shock and on the surface are similar for comparatively low velocities, although in a small peripheral region the pressure directly behind the shock wave is somewhat lower than at corresponding points on the body surface.

The curves for pressure distribution converge with an increase in Mach number as the difference in the pressures caused by the additional compression from the shock to the body is decreased. This difference has been shown to be given by the ratio $C_{p0}/C_{ps} = (2 - \bar{\rho})/2(1 - \bar{\rho})$ on the axial streamline.

The difference disappears in the hypothetical case of $\gamma \to 1$ and $M_\infty \to \infty$, when the shock lies next to the surface of the nose. Thus, in this case, the conditions are identical for all the points on the flat surface. It can be assumed that these identical conditions are approximately maintained for a real flow at very high velocities. Consequently, the pressure coefficients on the flat surface, compared with their values at corresponding points directly behind the shock, are increased by the factor C_{p0}/C_{ps}.

Using Eq. (20.13) and assuming that the shock surface is spherical, we obtain the pressure coefficient:

$$C_p = (2 - \bar{\rho})\left(1 - \frac{\bar{r}^2}{\bar{R}_{s0}^2}\right). \tag{20.41}$$

This expression is identical with Eq. (20.35) for a curved nose when $R_{s0} = R_N$. From Eq. (1.6), the pressure drag coefficient is

$$C_{Dp} = (2 - \bar{\rho})\left(1 - \frac{1}{2\bar{R}_{s0}^2}\right). \tag{20.42}$$

In the limiting case of $\gamma \to 1$ and $M_\infty \to \infty$, the shock lies next to the surface, and $R_{s0} = \infty$ and $\bar{\rho} = 0$. Then $C_p = C_{Dp} = 2$, which agrees with the results of Newtonian theory. For actual flow conditions, it is

necessary to know the radius of curvature of the shock at the axis for the calculation of C_p and C_{Dp}. The determination of this radius is examined below.

The Detachment Distance and Shape of the Bow Shock Wave

Measurements of the detachment distance in various aerodynamic facilities have shown that it is proportional to the radius of the flat nose, r_N, as well as being a function of the free-stream velocity and the state of the gas. The latter factors determine the density variation behind the shock wave.

In the general case of a dissociated and ionized gas, it can be assumed that the distance from the shock to the body, relative to the radius r_N, will be a function of the density ratio across the normal part of the shock, $\bar{\rho} = \rho_\infty/\rho_s$, as in the case of a spherical nose. However, the standoff distance from a flat face is greater than that from a sphere. A preliminary estimate leads to the conclusion that, if the value of $\bar{s}_0 = s_0/r_N$ is of the order of the density ratio $\bar{\rho}$ for a spherical nose, its value in the case of a flat face is $\bar{s}_0 \sim \sqrt{\bar{\rho}}$.

An empirical expression for the relative detachment distance can be established from experimental data in the form[5]

$$\bar{s}_0 = \frac{s_0}{r_N} = 1.03\sqrt{\bar{\rho}/(1-\bar{\rho})}. \tag{20.43}$$

The radius of curvature of the shock wave at the axis, which determines its shape in the vicinity of the flat nose, is also proportional to the radius of the flat face. The relative value of the radius of curvature $\bar{R}_{s0} = R_{s0}/r_N$ can be written as $(\bar{R}_{s0})_f = (\bar{s}_0/\tilde{s}_0)_f$, where $\tilde{s}_0 = s_0/R_{s0}$ and the subscript f denotes parameters for a flat nose. The analogous relation for a sphere is $(\bar{R}_{s0})_{sph} = (\bar{s}_0/\tilde{s}_0)_{sph}$. Experimental studies show that the values of the relative detachment distances $\tilde{s}_0$ for a sphere and a flat nose are approximately the same, so that the ratios $\bar{s}_0/\bar{R}_{s0}$ will also be the same. Thus, the dimensionless radius of curvature for the flat nose is related to that for a sphere by the following equation:

$$(\bar{R}_{s0})_f = \frac{(\bar{\varepsilon}_0)_f}{(\bar{\varepsilon}_0)_{sph}} (\bar{R}_{s0})_{sph}. \tag{20.44}$$

The detachment distance for a flat nose is obtained from Eq. (20.43), and the quantities $(\bar{\varepsilon}_0)_{sph}$ and $(\bar{R}_{s0})_{sph}$ are determined from Eqs. (20.39) and (20.37), respectively.

Equation (20.44) can be simplified if it is assumed that the shock wave is concentric with the sphere, in which case

$$(\bar{R}_{sc})_{sph} = 1 + (\bar{\varepsilon}_0)_{sph}.$$

Using Eqs. (20.39) and (20.43), we find for the flat face

$$\bar{R}_{s0} = 0.52 \frac{3 - \bar{\rho}}{\sqrt{\bar{\rho}(1 - \bar{\rho})}}. \tag{20.45}$$

This relation is plotted in Fig. 212. It is apparent from Eq. (20.45) that as $\bar{\rho} \to 0$ the value of $\bar{R}_{s0} \to \infty$, because the shock wave comes into contact with the flat surface of the nose in the limit.†

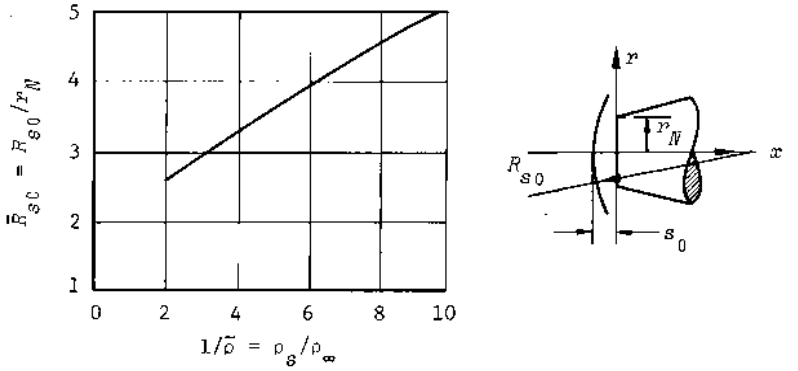

Fig. 212--Radius of curvature of a shock wave ahead of a flat nose

†Editor's note: See comments in Introduction to chapter.

The location of the sonic point on the shock wave can be determined by the methods discussed earlier for the flow around a sphere. The location of this point on the surface of the flat face can be found from the following considerations: Assume that the flow around the nose occurs in a convergent channel bounded by the shock wave and by the nose surface, and that the flow is subsonic since the sonic point on the shock wave is located outside the edge of the flat face. Therefore, the velocity of the gas in the converging channel increases. Since the narrowest section of the channel is bounded by the sharp corner of the nose, the flow at points lying on this corner will attain the velocity of sound. Experimental studies confirm this conclusion.

Since the velocity is sonic at the shoulder, the local Mach number is $M = 1$ and the pressure can be determined at this point. If it is assumed that the flow is isentropic along the streamline between the stagnation point and the sonic point, the expression for pressure is

$$\frac{p^*}{p_0'} = \left(\frac{2}{\gamma_2 + 1}\right)^{\gamma_2/(\gamma_2-1)},$$

where γ_2 is the ratio of specific heats calculated for conditions behind a normal shock. At small velocities, $\gamma_2 = \gamma_1$ and the pressure can be determined from the usual equation for p^* at a sonic point. At large velocities, it is necessary to take into account the variation in specific heats. If it is assumed that $\bar{\rho} = (\gamma_2 - 1)/(\gamma_2 + 1)$, the approximate expression for the ratio of the pressure coefficients can be presented in the form

$$\frac{C_p^*}{C_{p0}} = \frac{1 - \bar{\rho}}{2}.$$

According to this equation, the pressure coefficient at the corner of the flat nose is about one-half that at the stagnation point.

The Velocity Gradient at the Stagnation Point

The heat flux to the surface at the stagnation point is a function of the velocity gradient. It has been shown that the velocity gradient

for a sphere is inversely proportional to the radius of curvature of the surface R_N. Therefore, the velocity gradient decreases with an increase in this radius and is zero in the limit for flat blunting. However, studies show that the value of the gradient at the stagnation point of a flat nose differs from zero. On this basis, it can be assumed that the flat face has an influence on the flow that is similar to that of a spherical surface with a radius of curvature R_{Ne}. This is confirmed by observations of the shape of the shock wave. It is possible to select an equivalent radius, R_{Ne}, for which the curvature of the shock at the axis will be approximately identical with that in front of a flat nose. Thus,

$$r_N(\bar{R}_{s0})_f = R_{Ne}(\bar{R}_{s0})_{sph},$$

and the equivalent radius is

$$R_{Ne} = r_N \frac{(\bar{R}_{s0})_f}{(\bar{R}_{s0})_{sph}}. \tag{20.46}$$

From Eq. (20.27a), the velocity gradient at the stagnation point of a sphere with an equivalent radius R_{Ne} is:

$$\left(\frac{\partial V_x}{\partial x}\right)_{\substack{x=0 \\ y=0}} = \frac{1}{J}\frac{r_N}{R_{Ne}}, \tag{20.47}$$

where

$$J = \frac{r_N}{\sqrt{(2p_0'/\rho_0')(1 - p_\infty/p_0')}}.$$

The value of the velocity gradient determined from Eq. (20.47) is assumed to be the same as that at the stagnation point of the flat nose. This assumption, of course, is not exact and should be checked additionally by means of experimental research. The scanty data (Fig. 213) indicate that Eq. (20.47) gives a fairly accurate solution at high velocities.†

†Editor's note: See comments in Introduction to Chapter.

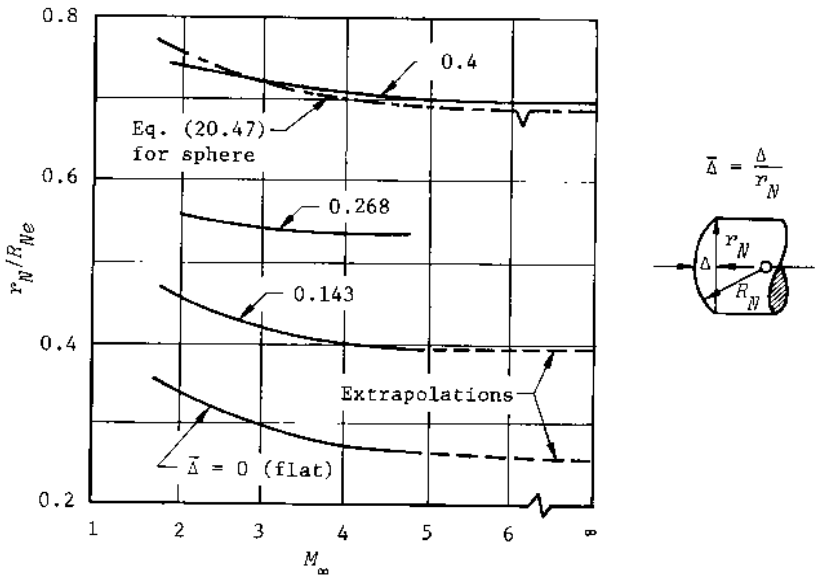

Fig. 213--Equivalent radius of a blunt nose

OTHER BLUNT NOSE SHAPES

Pressure Distribution and Drag

The spherical and flat-face blunting examined above should be considered as two limiting types of blunting between which lie noses of an intermediate form. For example, one can consider flat blunting with a curved bevel (rounded off) (see Fig. 12, p. 28) and blunting by means of a spherical segment with a radius larger than that of a hemisphere (see Fig. 10, p. 27). Studies show[9] that the shape and radius of curvature of the corner of the body exert an influence on the pressure distribution upstream into the subsonic region.

For flat noses with rounded edges, the effective parameter is the relative radius of curvature $\bar{r} = r/r_N$; for a nose composed of a spherical segment, it is the dimensionless radius of the sphere $\bar{r} = R_N/r_N$ (or the dimensionless height of the segment $\bar{\Delta} = \Delta/r_N$). For the second type of nose, the position of the corner influences the flow, since the sonic point is located there.

Typical pressure distributions are shown in Fig. 214, from which it is evident that the effect of the curvature results in a reduction in pressure in comparison with a flat nose, even for the nose with a partial flat portion. It is also possible to determine the pressure variation on a spherical-segment nose compared with that on a flat face and on a hemisphere. As the radius of curvature of the segment decreases, the pressure distribution approaches that for a hemisphere. However, sonic velocity must be maintained at the sharp corner, so that the pressure distribution is a function of both the local shape of the body and the location of the sonic point.

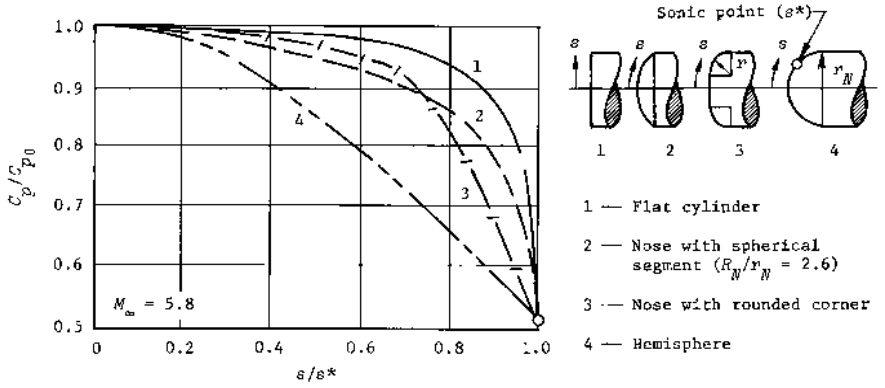

Fig. 214--Pressure distributions on blunt noses of various shapes

When the surface at the corner point has the same slope as it has at the sonic point on a hemisphere, i.e., an angle of approximately 45°, the pressure distribution is identical with that on the similar portion of a hemisphere. The character of the pressure distribution does not change with a further decrease in the radius of the segment, since perturbations will not penetrate into the subsonic region from the corner where the velocity is now supersonic.

The ratio of the pressure coefficients given in Fig. 214 depends relatively weakly on the free-stream Mach number. This was evident

earlier in the examples of flow around a hemisphere and a flat face. Curves based on experimental data are shown in Fig. 215 for the pressure distribution over the surface of a spherical segment with an angle of 26.21° for M_∞ = 2.01 and 4.76.[9] The sonic point is located at the corner for this nose.

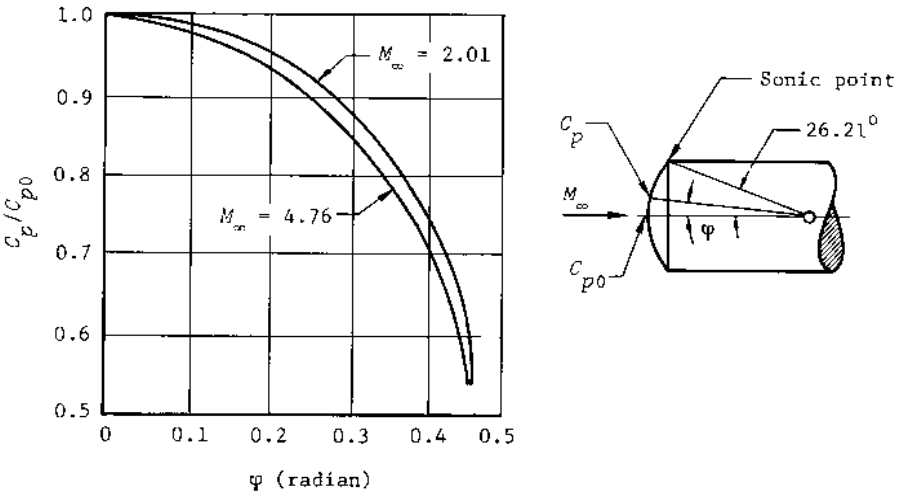

Fig. 215--Pressure distribution on a spherical segment

Experimental studies at medium Mach numbers indicate that the pressure drag coefficient for a flat nose with rounded corners is a linear function of the parameter $\bar{r}$ and can be represented in the form

$$c_{Dp} = (c_{Dp})_f - [(c_{Dp})_f - (c_{Dp})_{sph}]\bar{r}. \qquad (20.48)$$

It can be assumed that this relation is also valid at high velocities. Equation (20.48) can be extended approximately to blunt nose bodies in the form of a spherical segment with a radius of curvature greater than r_N, and also to bodies in the shape of an ellipse, although, strictly speaking, the experiments show some deviation from the linear relation.

In using Eq. (20.48) in these two cases, we must replace the parameter $\bar{r}$ by $\bar{\Delta}$ and $\bar{b}$, respectively.

Detachment Distance and Radius of Curvature of the Shock

Similar linear relations can be written for the relative detachment distance of the shock wave in front of a rounded-off nose. The variation of the dimensionless standoff distance $\bar{s}_0 = s_0/r_N$ with the blunting parameter $\bar{r} = r/r_N$ for $M_\infty = 5.8$ is shown in Fig. 216, based on experimental data. It is evident that the shape of the body surface in the sonic region has a strong influence on the detachment and curvature of the shock wave.

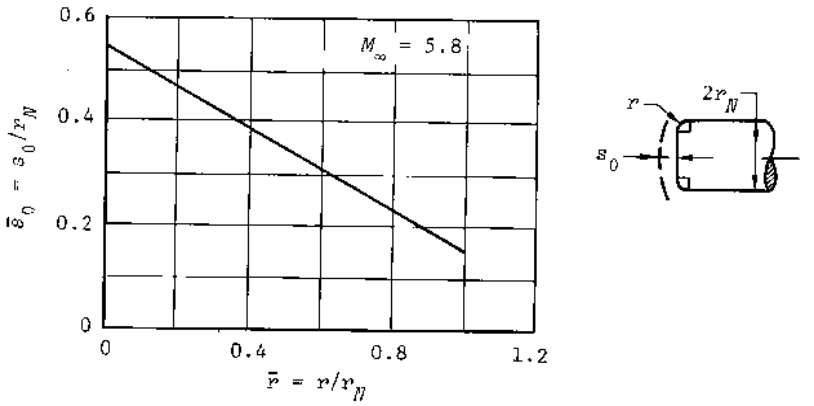

Fig. 216--Dimensionless shock-detachment distance for a flat nose with a curved bevel

Assuming that this variation is valid for arbitrary values of M_∞, we can write a general expression for estimating the detachment distance as follows:

$$\bar{s}_0 = (\bar{s}_0)_f - [(\bar{s}_0)_f - (\bar{s}_0)_{sph}]\bar{r}. \qquad (20.49)$$

A similar type of variation is observed for blunt noses consisting of spherical segments. In Fig. 217 are shown experimental data obtained

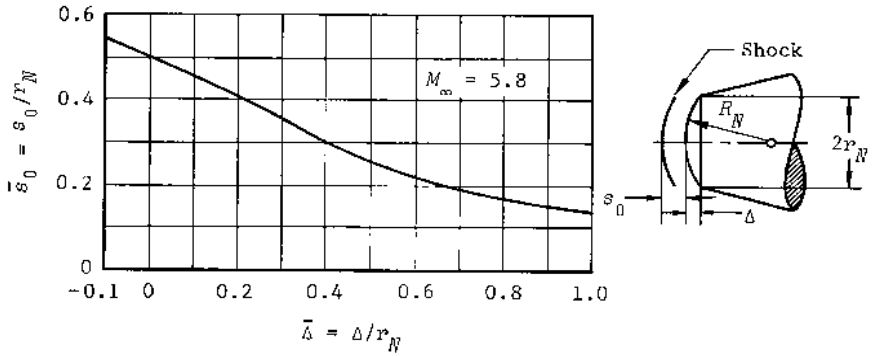

Fig. 217--Dimensionless shock-detachment distance for a blunt spherical segment

at $M_\infty = 5.8$ on models with both convex and concave noses. It is apparent that there is a practically linear relation for values of $\bar{\Delta}$ between -0.1 and 0.45. In this range of $\bar{\Delta}$, the flow velocity is sonic at the corner, and the nose is similar to a flat nose. As the value of $\bar{\Delta}$ increases, a continually greater part of the spherical surface is located downstream of the sonic point, the effect of the nose shape on the detachment distance is reduced, and the variation becomes nonlinear.

On the basis of these results, an approximate relation for the relative detachment distance in the range $-0.1 \leq \bar{\Delta} \leq 0.45$ can be presented in the following form:

$$\bar{s}_0 = (\bar{s}_0)_f - \frac{20}{9}\left[(\bar{s}_0)_f - A\right]\bar{\Delta}, \qquad (20.50)$$

where A is the value of the relative detachment distance at $\bar{\Delta} = 0.45$. According to experimental data, this quantity can be assumed to be approximately equal to $A = 2(\bar{s}_0)_{sph}$.

Experimental studies also enable us to establish the approximate nature of the relation for the radius of curvature of the shock at the axis. For bodies with a rounded corner, this relation is of a hyperbolic character in the entire region $0 \leq \bar{r} \leq 1$. The corresponding empirical relation is

$$\bar{R}_{s0} = \frac{R_{s0}}{r_N} = \frac{(\bar{R}_{s0})_f (\bar{R}_{s0})_{sph}}{(\bar{R}_{s0})_{sph} + [(\bar{R}_{s0})_f - (\bar{R}_{s0})_{sph}]\bar{r}}. \qquad (20.51)$$

For blunting in the shape of a spherical segment, the relative radius is an inverse function of the parameter $\bar{\Delta}$ for the case of an almost flat nose ($-0.1 \leq \bar{\Delta} \leq 0.45$). In this range of $\bar{\Delta}$, the radius of curvature can be represented in the form

$$\bar{R}_{sc} = \frac{9(\bar{R}_{s0})_f B}{9B + 20[(\bar{R}_{s0})_f - B]\bar{\Delta}}, \qquad (20.52)$$

where B is the value of $\bar{R}_{s0}$ at $\bar{\Delta} = 0.45$ and is approximately equal to 1.8 to 2 times $(\bar{R}_{s0})_{sph}$.

The Equivalent Spherical Radius and the Velocity Gradient at the Stagnation Point

The equivalent spherical radius and the velocity gradient are computed in the same way as in the study of flow around a flat nose. The equivalent radius of a sphere corresponding to a given nose is determined from Eq. (20.46), in which the numerator can be calculated from Eqs. (20.51) or (20.52).

The velocity gradient at the stagnation point is determined from Eq. (20.47) after the equivalent radius is found. Because of the many assumptions, these results are only approximate, and it is recommended that they be checked and refined with experiments. Results of such studies at low Mach numbers are presented in Fig. 213. Here, it is evident that Eq. (20.47) agrees well with the experimental data for a spherical segment with $\bar{\Delta} = 0.4$, although in this case the flow is still sonic at the corner. (The largest value of $\bar{\Delta}$ for which the corner velocity is sonic is 0.45.) The available data show that Eq. (20.47) can be used to calculate the velocity gradient at the stagnation point of spherical-segment noses for values of $\bar{\Delta}$ up to about 0.3 to 0.35.†

†Editor's note: See comments in Introduction to Chapter.

§ 21. *HYPERSONIC FLOW AROUND SLIGHTLY BLUNTED CYLINDRICAL AND CONICAL BODIES*

ANALOGY WITH THE UNSTEADY MOTION OF A PISTON

Effect of Small Blunting

STUDIES SHOW THAT THE INFLUENCE of a slight amount of blunting on the flow around the entire body is not the same for different conditions and is particularly a function of the free-stream velocity. Thus, it can be established from experiments that this effect is insignificant at moderate Mach numbers and affects only a small area of the body in the vicinity of the nose. The effect of blunting increases substantially at hypersonic flight velocities, as can be illustrated by comparing the order of magnitude of the drag of a blunt tip with a diameter $2R_N$ and the drag of the remaining portion of the body, e.g., a cone with a length L and a cone angle δ_c.

According to Newtonian theory, the drag of the spherical tip is of the order of $\rho_\infty V_\infty^2 (2R_N)^2/2$, and the drag for the remaining part of the body is of the order of $\rho_\infty V_\infty^2 (\delta_c L)^2 \delta_c^2/2$. For both portions of the body to have the same drag, the dimensions of the body must be of the order of $L/2R_N \sim 1/\delta_c^2$.[†] These considerations indicate the sizable influence of slight blunting on the character of the flow in a perturbed region tens and hundreds of blunting diameters in length. The thinner the body, the farther this region extends and, consequently, the more important is the blunting influence.

It should be noted that the blunting effect is also a function of the type of body; for example, the effect is significantly greater for

[†]Editor's note: In other words, the ratio of the nose radius to the cone base radius, R_N/r_{mid}, need only be of the order of $\delta_c/2$.

two-dimensional profiles than for three-dimensional bodies of revolution. The drag of a blunt two-dimensional profile always increases in comparison with a pointed profile, and this increase can be extremely large. However, the drag of bodies of revolution may not only not increase but, to the contrary, may even decrease.

It follows from physical considerations that the character of the flow around the body will be a function of the degree of blunting, which can be described by means of the ratio $2R_N/L$. It is obvious that the degree of blunting and the corresponding effect for a specific shape must agree with the methods of analysis for flow around blunt bodies. However, if the blunting parameter is small ($2R_N/L \ll 1$), the analysis can be carried out on the assumption that the body remains pointed and the effect of bluntness is replaced by the effect on the surrounding flow of the concentrated force acting on the blunted portion.

Professor G. G. Chernyi[10] solved the problem by using the analogy between steady flow around a cone and the unsteady motion of the gas behind the cylindrical shock wave originating in front of a piston. According to this analogy, the perturbed flow around a cone is equivalent (in a lateral plane stationary with respect to the body) to the gas flow in front of a piston. For observers located in this plane, the flow is similar to the flow that originates in the propagation of an explosion wave.

Thus, the perturbed flow around a cone is analogous to the flow generated in the explosion of a long linear cylindrical charge at a moment of time, $t = 0$. In the case of a cone, the initial energy of the gas is assumed equal to its value in the unperturbed flow, since the pointed nose does not exert a strong force on the gas in front of the explosion (or in front of the piston). However, when the body is blunt, the force is not negligible, but is equal to the pressure drag of the blunt nose. This force acts on the gas to produce work and transmits to the gas an energy E. Thus, the initial energy per unit length of the linear charge is identified with the nose drag.

For axially symmetric flow about a blunt body, the equivalent problem of the motion of a cylindrical piston can be formulated in the following way: In an undisturbed gas, an explosion occurs along a straight line at an initial moment of time; as a result, a specific energy E is

transmitted to the gas. At the same moment of time, a cylindrical piston starts expanding radially in the gas from the line of the explosion with a velocity V. The problem is solved by determining the resultant motion of the gas ahead of the piston, which gives the shape of the shock wave in front of the blunt cone and also the pressure distribution on its surface for the equivalent problem of steady flow.

To convert from one problem to the other, it is necessary to assume

$$E = D = C_{DN} \frac{\rho_\infty V_\infty^2}{2} \pi R_N^2, \qquad t = \frac{x}{V_\infty}, \qquad V = V_\infty \tan \delta_c, \qquad (21.1)$$

where C_{DN} is the drag coefficient of the blunt portion.

Thus, in the general case, the problem of flow around a blunt cone amounts to the problem of an explosion with the subsequent expansion of a piston. It should be noted that this analogy relates to a flow region not too close to the nose of the body, where the perturbed velocity in the longitudinal direction is small and, therefore, the law of plane sections is valid.

The System of Equations

Problems of the type discussed above can be solved more conveniently by using equations in the Lagrangian form rather than in the Euler form (see Chap. I). In this form, the equations correspond to the motion of a discrete particle. If, as in our case, one-dimensional radial motion of a piston is being considered, the solution of these equations determines the coordinates r and the parameters of state of the particle for any moment of time t.

If the coordinate of the particle is r_1 at the initial moment of time $t = 0$, the instantaneous coordinate r will be a function of time t and of the initial value r_1, i.e., $r = f(r_1, t)$. The parameters of state for their known initial values (e.g., density ρ_∞, pressure p_∞, entropy S_∞, etc.) are also functions of the initial coordinate r_1 and the time t. The basic equations can be derived in Lagrangian form using Fig. 30 (p. 67). If we equate to zero the sum of the inertial forces $(\partial V_r/\partial t)\rho(2\pi r\, dr \cdot 1)$ and the pressure $(\partial p/\partial r)(2\pi r \cdot 1)$ that are acting on a particle with a volume $2\pi r\, dr \cdot 1$, we obtain the equation of motion:

$$\frac{\partial V_r}{\partial t} = \frac{\partial^2 r}{\partial t^2} = -\frac{1}{\rho}\frac{\partial p}{\partial r}. \tag{21.2}$$

The continuity equation is derived from the condition of the conservation of mass of a particle in motion. According to this condition, if the mass was $\rho_\infty(2\pi r\, dr \cdot 1)$ at the initial moment of time, it will remain the same at any time t; therefore

$$2\pi r\rho\, dr = 2\pi r_1 \rho_\infty\, dr_1.$$

Since this condition is valid at any moment of time, the total derivative dr/dr_1 can be replaced by the partial derivative $\partial r/\partial r_1$. The continuity equation takes the form

$$\frac{\partial r}{\partial r_1} = \frac{\rho_\infty r_1}{\rho r}. \tag{21.3}$$

If the Lagrangian variable $m = \rho_\infty r_1^2/2$ is introduced, the equations of motion and continuity become

$$\frac{\partial V_r}{\partial t} = -r\frac{\partial p}{\partial m}, \tag{21.2a}$$

$$\frac{\partial r}{\partial m} = \frac{1}{\rho r}. \tag{21.3a}$$

These equations are solved for the condition of isentropic flow ahead of the piston. In mathematical form, the condition of constant entropy of the particle is stated as

$$\frac{\partial S}{\partial t} = 0 \quad \text{or} \quad \frac{\partial}{\partial t}\left(\frac{p}{\rho^\gamma}\right) = 0. \tag{21.4}$$

The first expression pertains to the more general case in which physical-chemical changes can occur in the gas; the second expression corresponds to isentropic flow with constant specific heats.

The energy equation relative to the same conditions behind a cylindrical shock wave must be added to these equations. It is written

on the basis of the law of conservation of energy. If the motion of gas ahead of a piston after an explosion is considered, the total (kinetic and internal) energy of the flowing gas at each moment of time is equal to the sum of the energy produced per unit length of the explosion E, the initial energy E_1, and the work of expansion of the piston. Thus,

$$\int_{r_0}^{r} \left(\frac{V_r^2}{2} + u\right)\rho(2\pi r\, dr) = E + \int_0^r \rho u_\infty (2\pi r\, dr) + \int_0^r p(2\pi r\, dr), \quad (21.5)$$

where u and u_∞ are the specific internal energies, with dimensions of the square of the velocity; p is the pressure of the gas on the piston; and r_0 and r are the distances to the piston and shock wave, respectively.

For the case of constant specific heats, $u = c_v T = [1/(\gamma - 1)]p/\rho$. Noting that $V_r = \partial r/\partial t$ and $r_1 \rho_\infty\, dr_1 = r\rho\, dr$, we find

$$\int_{r_0}^{r} \left[\frac{1}{2}\left(\frac{\partial r}{\partial t}\right)^2 + \frac{1}{\gamma - 1}\frac{p}{\rho}\right]\rho r\, dr = \frac{E}{2\pi} + \frac{p_\infty r^2}{2(\gamma - 1)} + \int_0^r pr\, dr. \quad (21.5a)$$

The momentum equation, together with the energy equation, is particularly useful in solving the problem of the motion of gas ahead of a cylindrical piston, and can be obtained from Eq. (21.2) in the form

$$\rho r \frac{\partial V_r}{\partial t}\, dr = -\frac{\partial p}{\partial r}\, r\, dr.$$

After integration across the thickness of the perturbed layer, we find

$$\int_{r_0}^{r} \frac{\partial V_r}{\partial t}\, \rho r\, dr = -\int_{p_\infty}^{p} r\, dp. \quad (21.6)$$

FLOW AROUND A BLUNT CYLINDER

The solution of the equivalent problem of the unsteady motion of a cylindrical piston enables us to calculate the flow around a blunt cylinder. In the statement of the problem, it is assumed that the

explosive charge distributed along the straight line transmits an initial energy E to the gas. The motion of the gas originating as a result of this explosion corresponds to the condition when the piston velocity is $V = 0$. In general, the parameters that define this motion behind the shock wave are the initial pressure p_∞, the initial density ρ_∞, the explosion energy E (the work with respect to a unit length), the ratio of specific heats γ, the distance r from the line of the explosion, and the time t. The dimensionless characteristics of the perturbed flow (e.g., the relative pressure) will be functions of dimensionless combinations of these parameters.

One of these parameters, the adiabatic ratio γ, is already a dimensionless quantity, so the dimensionless combinations must be composed of the remaining five parameters. Since there are three independent dimensions, it is possible to construct two independent dimensionless combinations, i.e., $p_\infty^{\frac{1}{2}} r / E^{\frac{1}{2}}$ and $p_\infty t / (\rho_\infty E)^{\frac{1}{2}}$.

Thus, the flow parameters behind the shock wave, in dimensionless form, will be functions of these three dimensionless parameters. The latter two can be transformed by using Eq. (21.1), and the system of dimensionless parameters takes the form

$$\gamma, \qquad \frac{1}{M_\infty \sqrt{C_{DN}}} \frac{r}{D_N}, \qquad \frac{1}{M_\infty^2 \sqrt{C_{DN}}} \frac{x}{D_N}. \tag{21.7}$$

Hence, it follows that the shape of the bow wave in front of a blunt cylinder is determined by the following general functional relation:

$$\frac{1}{M_\infty \sqrt{C_{DN}}} \frac{r_s}{D_N} = F\left(\gamma, \frac{1}{M_\infty^2 \sqrt{C_{DN}}} \frac{x}{D_N}\right). \tag{21.8}$$

The general relation for the pressure distribution on the surface of a cylinder is found from the condition $r = 0$ and has the form

$$\frac{\Delta p}{p_\infty} = F\left(\gamma, \frac{1}{M_\infty^2 \sqrt{C_{DN}}} \frac{x}{D_N}\right). \tag{21.9}$$

Equations (21.8) and (21.9) have been obtained on the basis of dimensional analysis, and do not give specific expressions for the quantities involved. Nevertheless, they are of great practical value since they reveal an extremely important relation between these quantities, and the dimensionless parameters can be considered as similarity parameters. Therefore, the relations presented are used as the theoretical foundation for experimental studies, in which it is assumed that the similarity parameters are

$$\frac{1}{M_\infty^2 \sqrt{C_{DN}}} \frac{x}{D_N} \quad \text{and} \quad \gamma.$$

The existence of such parameters permits the generalization of particular experimental results to include a group of similar flows around cylindrical blunt bodies.

As an example, experimental data[11] on the pressure distribution obtained in a wind-tunnel test of a cylindrical model with a hemispherical nose at $M_\infty = 7.7$ and $\gamma = 1.4$ are shown in Fig. 218a. To generalize these data, the parameter $(x/D_N)/M_\infty^2 \sqrt{C_{DN}}$ is calculated, where C_{DN} is that for a hemisphere at $M_\infty = 7.7$. The pressure ratio is plotted against this similarity parameter in Fig. 218b, which can be used for pressure calculations for arbitrary Mach numbers. An analogous graph that generalizes the experimental results of a study of shock-wave shape made at the same conditions ($\gamma = 1.4$, $M_\infty = 7.7$) is presented in Fig. 219.

In certain cases, the general Eqs. (21.8) and (21.9) can be converted to a more specific form. This is possible, for example, for very high velocities when the initial gas pressure p_∞ is negligibly small compared with the pressure behind a very strong shock wave. In this case, p_∞ can be dropped from the similarity parameters, and the pressure on the cylinder can be represented in the form

$$\Delta p \approx p = P(\gamma, \rho_\infty, E, t).$$

It is apparent that the last three functional parameters contain the three independent dimensions and it is possible to form a dimensionless

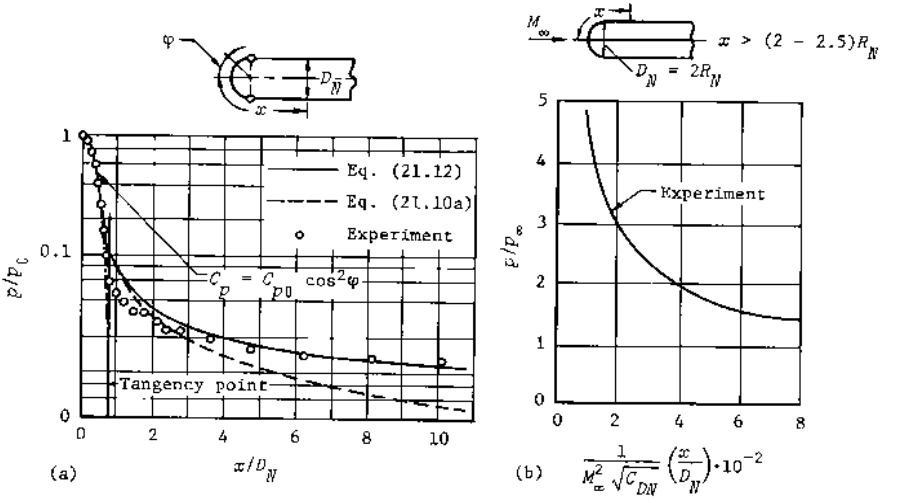

Fig. 218--Pressure distribution on a cylinder with a hemispherical nose

combination from them. If the techniques of dimensional analysis are used, the relation is

$$\Delta p = f_1(\gamma)\rho_\infty^x E^y t^z,$$

where $f_1(\gamma)$ is a function depending on the ratio of specific heats. After making substitutions from Eqs. (21.1) for E and t, we can write this expression as

$$\Delta p = f(\gamma)\rho_\infty^x\left(C_{DN}\frac{\rho_\infty V_\infty^2}{2}\frac{\pi D_N^2}{4}\right)^y\left(\frac{x}{V_\infty}\right)^z.$$

The exponents are determined by comparing the exponents on each side of the functional equation, i.e.,

$$ML^{-1}T^{-2} = [ML^{-3}]^x[MLT^{-2}]^y[T]^z,$$

where M, L, and T are the independent dimensions of mass, length, and

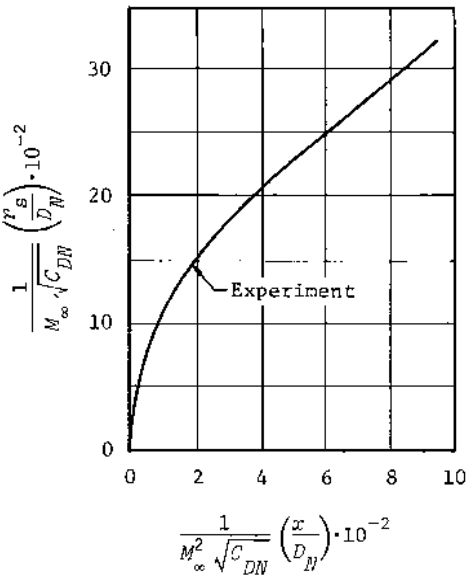

Fig. 219--Shape of the shock wave ahead of a cylinder with a hemispherical nose

time, respectively. Hence, we find that $x = y = \frac{1}{2}$ and $z = -1$. Therefore,

$$\frac{2\Delta p}{\rho_\infty V_\infty^2} = C_p = f(\gamma)\sqrt{C_{DN}}\left(\frac{D_N}{x}\right). \tag{21.10}$$

An analogous relation can be obtained for the coordinates of the shock wave. After first writing the general expression for the radial distance to the shock in the form $r_s = R(\gamma, \rho_\infty, E, t)$, we can use dimensional analysis in the same way as before. Thus, the radial dimension of the shock wave is written as

$$r_s = \varphi_1(\gamma)\rho_\infty^x E^y t^z,$$

where $\varphi_1(\gamma)$ is a function of γ. The equation for r_s in dimensionless coordinates is

$$\frac{r_s}{D_N} = \varphi(\gamma) C_{DN}^{\frac{1}{4}} \left(\frac{x}{D_N}\right)^{\frac{1}{2}}. \tag{21.11}$$

The functions $f(\gamma)$ and $\varphi(\gamma)$ in Eqs. (21.10) and (21.11) can be determined from the exact solution of the problem of the strong explosion of a linear charge. The numerical values obtained for these functions are presented graphically in Fig. 220. If this curve for $\gamma = 1.4$ and

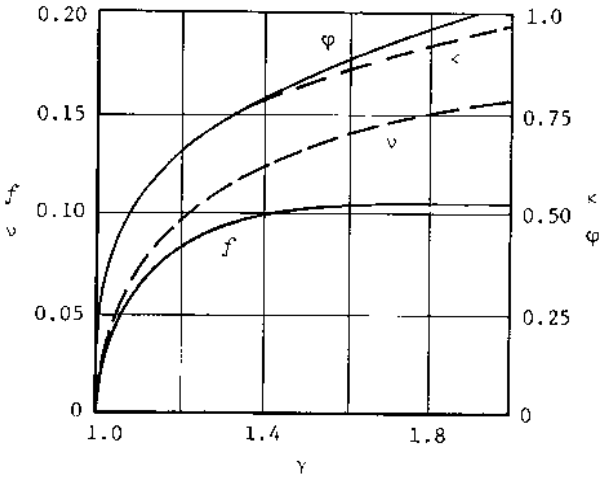

Fig. 220--Coefficients for calculating the pressure distribution and shock-wave shape

a value of $C_{DN} = 0.94$ in Eq. (21.10) are used, the expression for the pressure ratio becomes

$$\frac{p}{p_\infty} = 0.066 M_\infty^2 \left(\frac{D_N}{x}\right). \tag{21.10a}$$

It should be kept in mind that this equation, as well as the more general Eq. (21.10), is a first approximation, since the effect of the initial pressure is not considered. Attempts have been made to take this effect into account,[12] and a more accurate equation is

$$\frac{p}{p_\infty} = 0.066M_\infty^2\left(\frac{D_N}{x}\right) + 0.405 + \frac{0.155}{M_\infty^2}\left(\frac{x}{D_N}\right). \qquad (21.12)$$

As is evident from Fig. 218, the calculation from this equation agrees better with the experiment.

Equation (21.12), relating to a cylinder with a spherical nose, can be extended to a cylindrical body with an arbitrary form of blunting. For the case of $\gamma = 1.4$, the generalized equation will have the form

$$\frac{p}{p_\infty} = 0.069M_\infty^2\sqrt{C_{DN}}\left(\frac{D_N}{x}\right) + 0.405 + 0.150\frac{1}{M_\infty^2\sqrt{C_{DN}}}\left(\frac{x}{D_N}\right). \qquad (21.13)$$

If the cylinder has a spherical nose for which $C_{DN} = 0.94$, this equation reduces to Eq. (21.12).

Analogous relations are obtained for determining the shape of the shock wave. For the value of $\varphi(\gamma)$ for $\gamma = 1.4$ from Fig. 220 and for $C_{DN} = 0.94$, as previously, we obtain from Eq. (21.11) the equation for the first approximation for the radial distance to a point on the shock wave around a cylinder with a spherical nose:

$$\frac{r_s}{D_N} = 0.78\sqrt{x/D_N}. \qquad (21.11a)$$

A more accurate relation, taking into account the effect of the back pressure,[12] is written as

$$\frac{r_s}{D_N} = 0.78\sqrt{x/D_N}\left[1 + \frac{1.62}{M_\infty^2}\left(\frac{x}{D_N}\right) - \frac{6.17}{M_\infty^4}\left(\frac{x}{D_N}\right)^2\right]. \qquad (21.14)$$

For the general case when the blunting in front of the cylinder is of arbitrary shape, the relation is

$$\frac{r_s}{D_N} = 0.795C_{DN}^{\frac{1}{4}}\sqrt{x/D_N}\left[1 + \frac{1.57}{M_\infty^2\sqrt{C_{DN}}}\left(\frac{x}{D_N}\right) - \frac{5.80}{M_\infty^4 C_{DN}}\left(\frac{x}{D_N}\right)^2\right]. \qquad (21.15)$$

In using Eqs. (21.10) through (21.15), it should be remembered that

they give satisfactory results starting at about one body radius behind the end of the nose. Corresponding values of x measured from the stagnation point of the nose (Fig. 218) should be selected so that x/R_N is greater than about 2 to 2.5.

FLOW AROUND A SLENDER CONE WITH SMALL BLUNTING

The Basic Equations and the Method of Solution for Infinite Mach Number

The flow around a slender cone at hypersonic velocity can be studied by using the analogy from the problem of unsteady motion of a gas with a cylindrical shock wave.[10] If it is assumed that at these velocities the gas layer between the piston and the shock is extremely thin, the energy equation, Eq. (21.5a), can be simplified somewhat:

$$\frac{r^2}{4}\rho_\infty\left(\frac{\partial r}{\partial t}\right)^2 + \frac{(r^2 - r_0^2)p}{2(\gamma - 1)} = \frac{E}{2\pi} + \frac{p_\infty r^2}{2(\gamma - 1)} + \int_0^r pr_0\, dr_0. \qquad (21.5b)$$

The momentum equation, Eq. (21.6), can also be simplified. Since the perturbed layer is assumed to be thin, this equation is written as

$$\rho_\infty \frac{\partial r}{\partial t}\frac{r^2}{2} = \int_0^t (p - p_\infty) r\, dt. \qquad (21.6a)$$

In these equations, let us assume that the quantity $\partial r/\partial t = \dot{r}$ is constant in the entire perturbed region and is equal to the velocity of of the particles directly behind the shock wave, keeping in mind that this velocity can be determined from shock-wave theory. In steady shock-wave theory, the relative change in velocity is determined by the expression

$$\frac{V_\infty - V_2}{V_\infty} = \frac{2}{\gamma + 1}\left(1 - \frac{a_\infty^2}{V_\infty^2}\right).$$

Reversing the motion so that the shock wave travels into the steady flow with a velocity $V_\infty = D = \dot{r}_s$, we find the equation for the velocity of the particles behind the shock:

$$\dot{r} = V_\infty - V_2 = \frac{2}{\gamma + 1}\left(\dot{r}_s - \frac{a_\infty^2}{\dot{r}_s}\right), \tag{21.16}$$

which takes into account the initial pressure of the gas.

Furthermore, since the perturbed layer is thin, it can be assumed that the coordinate r equals the distance to the shock r_s. The radius of the piston is $r_0 = Ut$, where U is the velocity of expansion of the piston. Using Eq. (21.16) for $\dot{r}$ in Eqs. (21.5b) and (21.6a) and assuming that $r = r_s$ and $r_0 = Ut$, we can convert the resulting equations to dimensionless form by defining a characteristic length $L = (E/\pi\rho_\infty U^2)^{\frac{1}{2}}$ and a characteristic time L/U. Thus,

$$\frac{1}{2} r_s^2\left(\frac{2}{\gamma + 1}\right)^2\left(\dot{r}_s - \frac{1}{K_1^2 \dot{r}_s}\right)^2 + \frac{r_s^2 - t^2}{\gamma - 1}\left(\Delta p + \frac{1}{\gamma K_1^2}\right)$$

$$= 1 + \frac{r_s^2}{\gamma - 1}\frac{1}{\gamma K_1^2} + 2\int_0^t \left(\Delta p + \frac{1}{\gamma K_1^2}\right)t\, dt, \tag{21.17}$$

$$\frac{2}{\gamma + 1} r_s^2\left(\dot{r}_s - \frac{1}{K_1^2 \dot{r}_s}\right) = 2\int_0^t r_s\, \Delta p\, dt, \tag{21.18}$$

where $\Delta p = (p - p_\infty)/(\rho_\infty U^2)$, and K_1 is the similarity parameter defined as $M_\infty \tan \delta_c = U\sqrt{\rho_\infty/\gamma p_\infty}$. In general, the solution of these equations for arbitrary values of t can be obtained by numerical integration.

Let us consider the limiting case when $K_1 \to \infty$. It will be assumed that the time t is small, so that the initial energy of the gas in the perturbed region and the work of expansion of the piston will also be small compared with the energy released in the explosion. In this case, Eqs. (21.17) and (21.18) are simplified still further:

$$\frac{1}{2}\left(\frac{2}{\gamma + 1}\right)^2 r_s^2 \dot{r}_s^2 + \frac{r_s^2}{\gamma - 1}\Delta p = 1, \tag{21.17a}$$

$$\frac{2}{\gamma + 1} r_s^2 \dot{r}_s = 2\int_0^t r_s\, \Delta p\, dt. \tag{21.18a}$$

Eliminating Δp from these equations results in a single equation:

$$\frac{1}{2}\left(\frac{2}{\gamma+1}\right)^2 r_s^2 \dot{r}_s^2 + \frac{r_s}{\gamma^2-1}\frac{d(r_s^2\dot{r}_s)}{dt} = 1. \tag{21.19}$$

This equation has the solution

$$r_s = \left[\frac{4(\gamma+1)^2(\gamma-1)}{3\gamma-1}\right]^{\frac{1}{4}} t^{\frac{1}{2}}, \tag{21.20}$$

from which the coordinates of the shock wave can be computed. The pressure can be found by substituting Eq. (21.20) into Eq. (21.17a):

$$\Delta p = \left[\frac{\gamma-1}{4(3\gamma-1)}\right]^{\frac{1}{2}} \frac{1}{t}. \tag{21.21}$$

Converting to dimensional parameters and using Eq. (21.1), we obtain the relations for the shape of the shock wave and the pressure distribution on the cone surface:

$$\frac{r_s}{D_N} = \kappa C_{DN}^{\frac{1}{4}} \left(\frac{x}{D_N}\right)^{\frac{1}{2}}, \tag{21.20a}$$

$$C_p = \frac{2(p-p_\infty)}{\rho_\infty V_\infty^2} = \nu\sqrt{C_{DN}}\left(\frac{D_N}{x}\right), \tag{21.21a}$$

in which the coefficients are

$$\kappa = \frac{1}{2}\left[\frac{8(\gamma+1)^2(\gamma-1)}{3\gamma-1}\right]^{\frac{1}{4}}, \qquad \nu = \left[\frac{\gamma-1}{8(3\gamma-1)}\right]^{\frac{1}{2}}.$$

It is apparent that Eqs. (21.20a) and (21.21a) differ from the corresponding relations for a cylindrical body only by the values of the coefficients κ and ν, which are graphically presented in Fig. 220.

Equation (21.21a) can be used to determine some of the characteristics of the pressure variation on a blunt cone. According to this equation, the pressure coefficient has an infinitely large value at the

stagnation point, but decreases rapidly with distance from the nose, and at some distance the pressure is considerably less than that on a pointed cone. These trends are observed, for example, on a cone with a spherical nose. For comparison, assume that the pressure coefficient on a pointed cone is given by Newtonian theory as $C_p = 2\delta_c^2$, and the drag coefficient of the spherical nose is $C_{DN} = 1$. Assuming that $\nu = 0.125$ for $\gamma = 1.4$, we obtain

$$\frac{C_p}{C_{pc}} = \frac{0.0625}{\delta_c^2}\left(\frac{D_N}{x}\right).$$

If the cone angle is 0.1 radian, then $C_p/C_{pc} = 6.25(D_N/x)$, and the pressure on a blunt cone becomes less than on a pointed cone at a distance $x > 6.25D_N$ from the nose. This qualitative characteristic for the limiting case $K_1 = \infty$ is also maintained, as research shows, for finite values of the parameter K_1, even for values of K_1 of the order of unity.

Equation (21.21a) is not valid along the entire surface of a cone and only applies for comparatively small values of x, corresponding to a small time t. Analytical research and experimental data show that at large values of t, i.e., at a considerable distance from the nose, both the pressure coefficient and the shock angle tend toward the values for a pointed cone.

The peculiarities noted in the pressure distribution are evident in Fig. 221, where the results of wind-tunnel tests[13] at $M_\infty = 6.85$ are presented for a blunt, flat-nosed cone with $\delta_c = 10°$. It can be noted that the minimum pressure is attained at a distance of approximately 10 bluntness diameters downstream, and the restoration of pressure to the value on a pointed cone occurs at a length 10 times greater.

The slope of the shock wave also varies according to the character noted for the pressure distribution. The shock-wave angle at the same experimental conditions is presented in Fig. 222, where it is evident that, at a length of approximately $20D_N$, the angle reaches a minimum and, at distances of approximately $50D_N$, the slope of the shock wave becomes the same as that on a pointed cone.

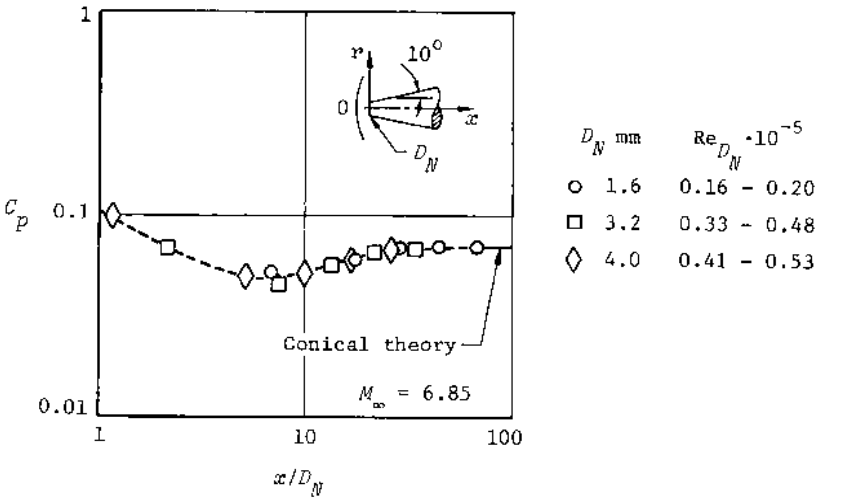

Fig. 221--Pressure distribution on a cone with a flat nose

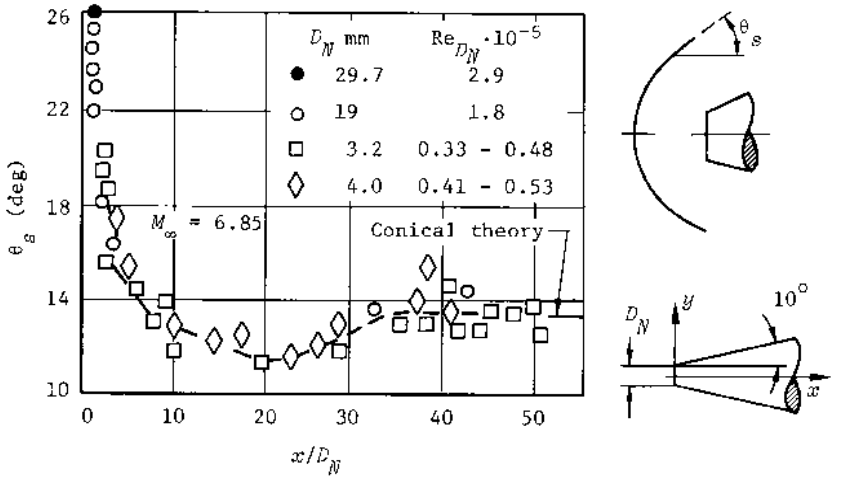

Fig. 222--Shock angle for a cone with a flat nose

The decreased pressure on a substantial part of the blunt cone can result in less drag than for a pointed cone. In Fig. 223, a graph is presented for the calculation of the drag of a blunt cone.[10] It is evident from the graph that the drag becomes minimum at a certain cone length. The reason for the existence of a minimum drag can be visualized. As the length of the body is decreased from that for the minimum, the drag will increase because of the growing influence of the blunt nose. As the length is increased, the drag will approach that for a sharp cone. If the drag is less than the sharp cone value at some intermediate point, a minimum must exist.

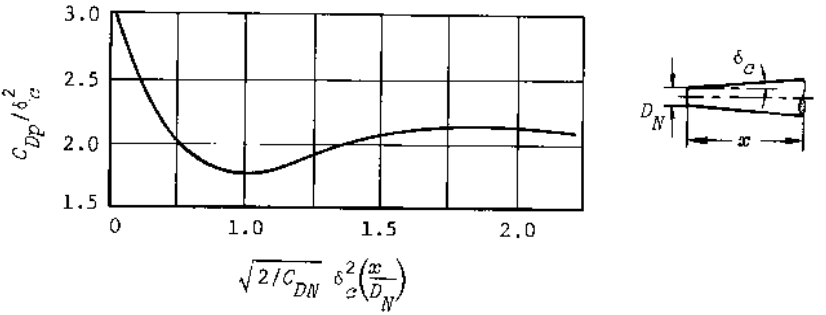

Fig. 223--Drag coefficient of a slender blunt cone

According to the data of Fig. 223, a minimum in the drag curve occurs at a relative cone length of

$$\frac{x}{D_N} = \frac{0.96}{\delta_c^2}\ \sqrt{C_{DN}/2}.$$

For example, for a cone with a spherical nose ($C_{DN} = 1$) and an angle $\delta_c = 0.1$, a minimum is located at $x/D_N = 68$, and the minimum drag is approximately 10 percent less than that for a pointed cone. When the cone is not extremely long, the drag of slightly blunt cones at hypersonic velocities is practically the same as for pointed cones.

The Similarity Law for Arbitrary Mach Numbers

The considerations presented above concerning the character of flow around blunt bodies can be used to develop the similarity law for the flow around blunt cones. The general relations for the flow around a blunt cylinder were derived by using the dimensionless parameters in Eq. (21.7). For a slender blunt cone it is necessary to include the cone angle δ_c in the set of parameters that define the motion. As in the case of flow around a pointed cone, this can be done by adding the similarity parameter $K_1 = M_\infty \delta_c$ to the number of dimensionless parameters on which the flow depends. These dimensionless parameters then determine the dimensionless characteristics of the flow.

From Newtonian theory, the order of magnitude of the excess pressure on the cone is $p - p_\infty \sim \rho_\infty V_\infty^2 \delta_c^2$, and the actual value of the excess pressure can be defined as $p - p_\infty = \rho_\infty V_\infty^2 \delta_c^2 \tilde{p}$, where $\tilde{p}$ is a dimensionless characteristic parameter for pressure. Therefore, the pressure coefficient on the cone surface is given by the general relation

$$\frac{C_p}{\delta_c^2} = \frac{2(p - p_\infty)}{\rho_\infty V_\infty^2 \delta_c^2} = P(x_*, K_1, \gamma), \tag{21.22}$$

where the function P is equal to $2\tilde{p}$ and is a function of γ, K_1, and a parameter

$$x_* = \frac{1}{M_\infty^2 \sqrt{C_{DN}}} \left(\frac{x}{D_N}\right) = \frac{1}{K_3} \left(\frac{x}{D_N}\right), \tag{21.23}$$

which can be considered as a dimensionless longitudinal coordinate. As previously noted, the longitudinal station must be at least one nose radius downstream of the end of the blunt tip. Henceforth, the coordinate x will be measured along the axis of the body from the base of the blunt tip for conical blunt bodies, so that it can be assumed that $x > R_N$.

In analogy to Eq. (21.8), the similarity law for the radial coordinate of the shock wave is

$$\frac{1}{M_\infty^2\sqrt{C_{DN}}}\frac{1}{\delta_c}\frac{r_s}{D_N} = \vartheta(x_*, K_1, \gamma), \qquad (21.24)$$

where the limits of validity of the similarity law can be extended by replacing δ_c by tan δ_c.

According to the similarity law for flow around slightly blunted cones having different values of δ_c and D_N, the dimensionless quantities in Eqs. (21.22) and (21.24) will be identical for equal relative coordinates x/D_N if the value of the following similarity parameters are maintained the same:

$$K_1 = M_\infty \tan \delta_c, \qquad K_3 = M_\infty^2\sqrt{C_{DN}}.$$

Thus, the parameter K_3 represents the specific characteristics of the flow around a blunt nose.

The similarity law can be extended to blunt bodies of arbitrary shape that are related by an affine transformation. In this case, instead of the angle δ_c, it is necessary to introduce another parameter representing the relative thickness of the body.

To obtain a more specific relation for the general forms given in Eqs. (21.22) and (21.24), experimental results for some particular conditions must be used. Data for the pressure distribution around cones with spherical noses and cone angles from 10° to 40° are presented in Fig. 224 for $\gamma = 1.4$ and $M_\infty = 6$. However, according to the similarity law, the five curves can be reduced to a single curve if selected new variables are introduced. The similarity law of Eq. (21.22) serves as a guide in selecting these variables. Of course, the equation obtained on the basis of experimental data may differ from its form in Eq. (21.22), since the theoretical form was based on a series of assumptions. Analysis of the experimental data shows that $K_1^{0.2}C_p/(\tan \delta_c)^{1.8}$ should be used for the pressure parameter, and the argument should be expressed as

$$\tilde{x} = \frac{K_1^{\frac{3}{2}}}{M_\infty^2\sqrt{C_{DN}}}\left(\frac{x}{D_N}\right).$$

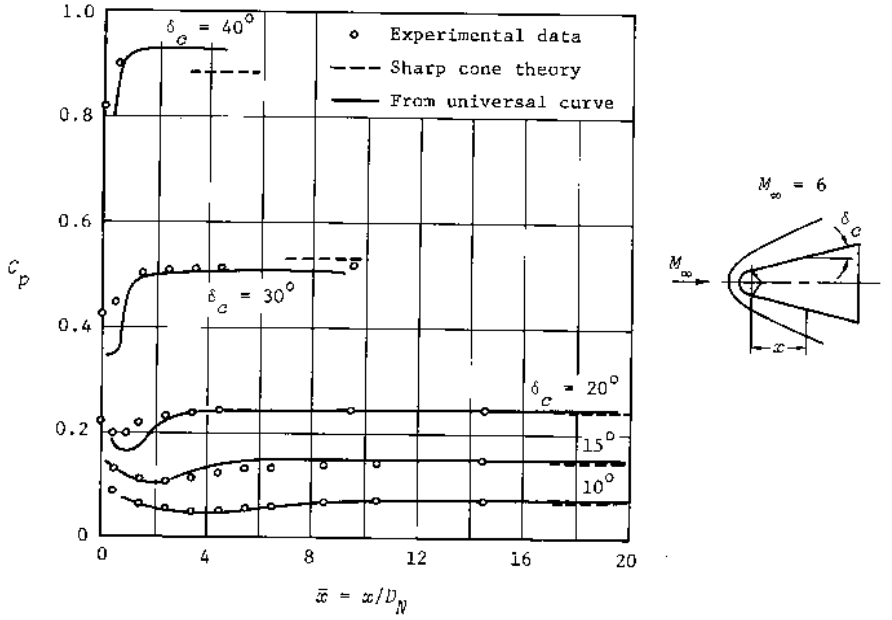

Fig. 224--Pressure distribution on a cone with a spherical nose

Thus, the expression for the similarity law is written in the form

$$\frac{K_1^{0.2} c_p}{(\tan \delta_c)^{1.8}} = P(\tilde{x}), \tag{21.25}$$

where $\tilde{x}$ can be treated as a conditional relative coordinate. It is evident that this expression differs significantly from the general relation given by Eq. (21.22).

In the special case under consideration, $C_{DN} = 0.91$ for $M_\infty = 6$ (see Fig. 207) and $M_\infty^2 \sqrt{C_{DN}} = 34.4$. Thus,

$$\frac{K_1^{0.2} c_p}{(\tan \delta_c)^{1.8}} = P(\tilde{x}) = P\left(\frac{K_1^{1.8}}{34.4} \frac{x}{D_N}\right). \tag{21.26}$$

The average universal curve, constructed on the basis of this relation and using the experimental data presented in Fig. 224, is shown in Fig. 225. According to the similarity law, this curve can be used for the calculation of pressure, not only on the surface of a spherically blunted cone, but also for blunting in the form of a flat face. In the latter case, the correct value of the nose drag coefficient should be chosen.

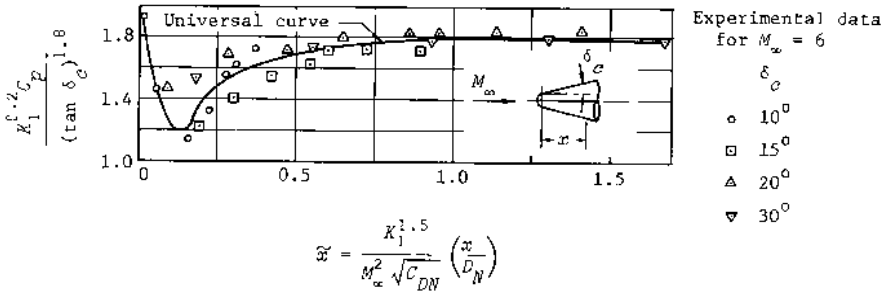

Fig. 225--Universal curve for the pressure distribution on blunt cones

Pressures on cones with different blunting can be compared by using this curve. For example, let us consider the same case of a 10° cone at a free-stream Mach number of 6. Since $C_{DN} = 0.91$ for the spherical nose and $C_{DN} = 1.7$ for the flat face, the corresponding values of $K_1^{1.5}/M_\infty \sqrt{C_{DN}}$ are 0.0317 and 0.0232. For a station on the body with the relative coordinate $\bar{x} = x/D_N = 10$, the conditional coordinate $\tilde{x} = 0.317$ and 0.232. Then from the curve in Fig. 225, the values of $K_1^{0.2} C_p/(\tan \delta_c)^{1.8}$ are 1.55 and 1.40. Since $K_1^{0.2}/(\tan \delta_c)^{1.8} = 23$, the pressure coefficients will be 0.0675 and 0.0608, respectively. From this example, it is evident that the pressure at corresponding points on a blunt cone with a flat nose is somewhat less than on a cone with a spherical nose.

Results are presented in Figs. 224 and 226 for the theoretical calculation of the pressure coefficient using the universal curve for cones with spherical noses and flat noses. The experimental data are also plotted for comparison. The data presented in these graphs pertain to cones at a fixed Mach number with different cone angles. The effect of

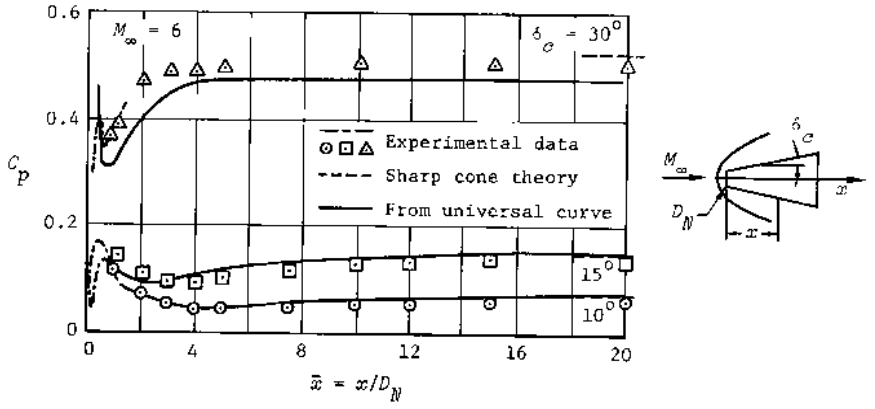

Fig. 226--Pressure distribution on a cone with a flat nose

Mach number on the pressure distribution around a specific cone is shown in Fig. 227. It is apparent that the larger the velocity, the more significant is the region of reduced pressures compared with the pointed cone. This indicates a basic advantage in the use of blunt bodies at very high Mach numbers: The decrease in local density associated with the reduction in pressure contributes to a large decrease in heat flux. In addition, the decrease in pressure aids in reducing the drag.

The similarity law derived above relates to cones with blunt noses of arbitrary shape. However, it is not valid for the entire surface of the body; for example, in the vicinity of the nose the results deviate considerably from the experimental data. Nevertheless, in the vicinity of a spherical nose the similarity law and, in particular, the universal curve, correctly specify the general character of the pressure change, according to which the pressure decreases gradually beginning at the stagnation point of the nose, reaches a minimum at some point downstream, and increases again to approach the value for a pointed cone.

On the other hand, a more complex phenomenon, which cannot be represented by the similarity law, is observed in flow around a cone in the vicinity of a flat face. Observations show that flow separation occurs directly behind the corner, and as a consequence a stagnant region develops (Fig. 228). The supersonic flow is diverted around this zone

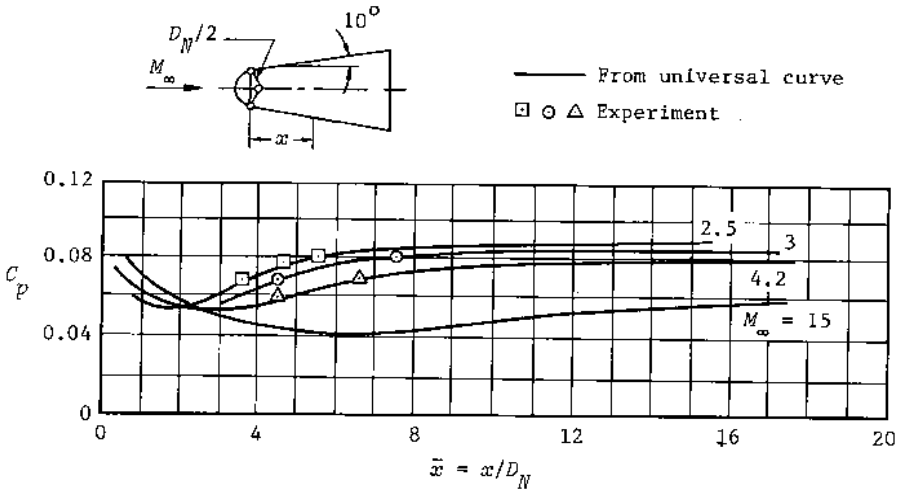

Fig. 227--Pressure distribution on a cone with a spherical nose

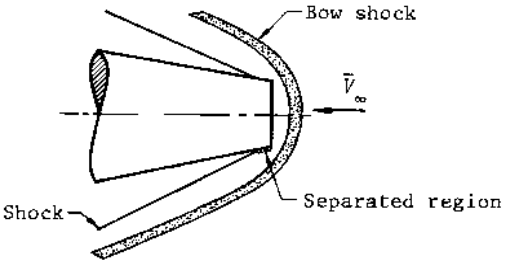

Fig. 228--Flow around a cone with a flat nose

and eventually reattaches itself to the surface. The deflection is accompanied by the development of a local shock wave. This illustrates one of the peculiar features of flow around a body with a flat nose.

It is natural that such a peculiarity leads to a change in the character of the pressure distribution in comparison with that on a spherical nose (see Fig. 226). The pressure decrease due to the expansion of flow directly behind the corner changes to a rapid increase, as the flow

passes through the local shock wave. After achieving some maximum, the pressure begins to decrease again. From this point on, the pressure variation is of the same character as that on a cone with a spherical nose. Thus, with the exception of a small region in the vicinity of the nose, the pressure distributions for both forms of blunting are similar, which permits the use of only one similarity law.

For convenience in practice, the similarity law can be applied arbitrarily to the region indicated, since this region is comparatively small for a sufficiently long body and the effect on the total pressure drag is very small.

The total pressure drag is calculated as the sum of the nose drag and the drag of the remainder of the body, i.e.,

$$D = \frac{1}{2}\rho_\infty \gamma_\infty^2 \pi R_N^2 C_{DN} + 2\pi \int_{r_N}^{r_{mid}} (p - p_\infty) r \, dr, \tag{21.27}$$

where C_{DN} is the nose drag coefficient calculated from Eq. (20.36). From this equation, the drag is calculated for the portion of the sphere extending to a central angle of $\varphi = \arcsin(r_N/R_N)$, which in turn can be determined by the radial coordinate to the junction of the spherical nose and the aft part of the body. Thus, the total drag coefficient is

$$C_D = C_{DN}\bar{R}_N^2 + 2\int_{\bar{r}_N}^{1} C_p \bar{r} \, d\bar{r}, \tag{21.28}$$

where $\bar{R}_N = R_N/r_{mid}$, $\bar{r} = r/r_{mid}$, and $\bar{r}_N = r_N/r_{mid}$. Introducing into Eq. (21.28) the expression for C_p obtained from Eq. (21.26) and substituting

$$\bar{r} = \bar{r}_N(1 + 2\bar{x}\tan\delta_c),$$

where $\bar{x} = x/D_N$, we obtain

$$C_D = C_{DN}\bar{R}_N^2 + 4\bar{r}_N^2 \frac{(\tan\delta_c)^{2.8}}{K_1^{0.2}} \frac{M_\infty^2\sqrt{C_{DN}}}{K_1^{1.5}} \left(\int_0^{\tilde{x}} P \, d\tilde{x} + \frac{M_\infty^2\sqrt{C_{DN}}}{K_1^{1.5}} \tan\delta_c \int_0^{\tilde{x}^2} P \, d\tilde{x}^2 \right). \tag{21.29}$$

In the case of a spherical nose, the coordinate $\bar{x}$ is calculated from the length x measured from its junction point with the cone. In this same case, the dimensionless radius $\bar{r}_N = \bar{R}_N \cos \delta_c$, but for a flat nose it should be assumed that $\bar{R}_N = \bar{r}_N$. The integrals

$$\int_0^{\bar{x}} P \, d\bar{x}, \qquad \int_0^{\bar{x}^2} P \, d\bar{x}^2,$$

which enter into Eq. (21.29), can be computed graphically from the universal curve of Fig. 225. The drag coefficients given by Eq. (21.29) for the special case of a cone with an angle $\delta_c = 10°$ and $M_\infty = 6$ are presented in Fig. 229. The experimental data are also plotted for comparison.

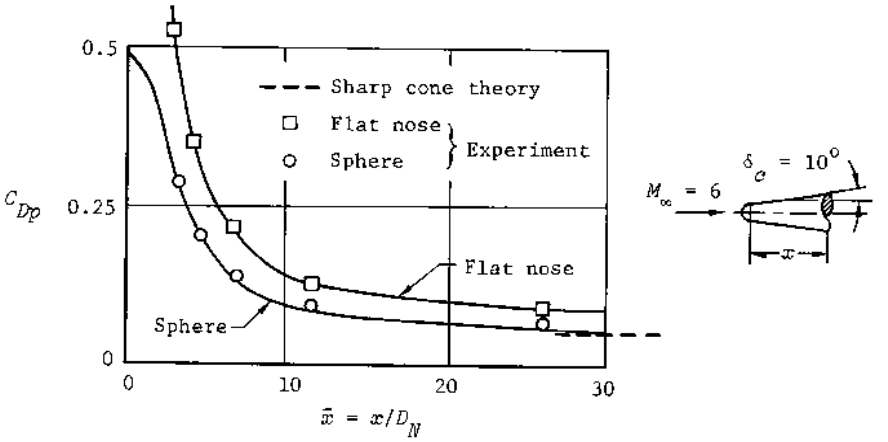

Fig. 229--Pressure drag coefficient of blunt cones

An analysis of the experimental results indicates the difference in the pressure variation for flow around slender and thick blunt bodies (see Figs. 224 and 226). In the case of slender bodies, the pressure on the cone section is considerably less than that on a pointed cone and it recovers comparatively slowly to the pressure on the pointed cone as the distance from the nose increases. However, for flow around a thick cone, the difference in pressure is sharply reduced, and the recovery process is practically completed close to the blunted portion.

This is quite evident in Fig. 224, for example, where experimental data are presented for $M_\infty = 6$ around a 40° cone with a spherical nose. At a distance somewhat larger than the blunting diameter from the stagnation point, the pressure on the conical section almost equals its value on a pointed cone. This indicates the practical possibility of estimating the pressure on the conical part of the body from the theory of flow around a pointed cone.

It is evident from the data presented in Fig. 230 that modified Newtonian theory ($C_p = C_{p0} \cos^2\varphi$) gives a good approximation to the experimental data both on the spherical nose and on the small conical portion in its vicinity.[14]

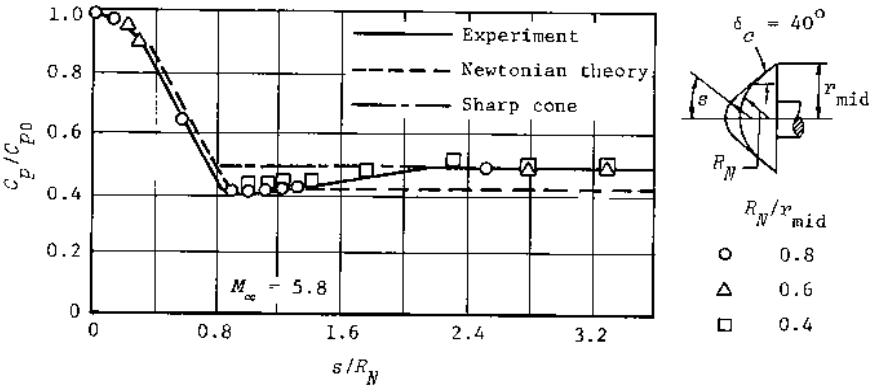

Fig. 230--Pressure distribution on a blunt cone with a spherical nose

§ 22. *APPLICATION OF THE METHOD OF CHARACTERISTICS TO THE CALCULATION OF FLOW AROUND BLUNT BODIES OF REVOLUTION*

THE CHARACTERISTICS EQUATIONS

THE THEORETICAL METHODS discussed above are applicable to the study of hypersonic flow around blunt bodies, but in practical cases it is also necessary to calculate the flow in the supersonic region downstream of the blunt nose. The method of characteristics can be used in this region, provided that the equations include the effects of the vorticity created by the curved shock wave in front of the body.

Therefore, Eqs. (9.9) and (9.10) are the basic equations for the conjugate characteristics of the supersonic rotational flow. In principle, for given boundary conditions, it is possible to calculate the flow parameters numerically and step-by-step in the region between the body surface and the shock wave. However, the method of characteristics has been extremely difficult to apply to practical computations, and because of the great expenditure of time for calculations, it had not been used widely in practice until recently. With the advent of electronic computers, this is no longer a problem. It has been shown, however, that the use of computers for solving the universally accepted equations (Eqs. (9.9) and (9.10)) for the characteristics was ineffective. These equations were not adapted to machine calculation, since a whole series of functions (e.g., exponential and trigonometric) entered into them and these required an additional expenditure of machine time in their computation. In addition, the programming was complicated. Thus, it became necessary to modify the basic equations and adapt them to effective machine calculation. P. I. Chushkin[15] accomplished this work and also carried out machine calculations for supersonic flow around a series of conical bodies with spherical noses.

To modify Eqs. (9.9) and (9.10), it is advantageous first to convert them to the new variables

$$\beta = \cot \mu = \sqrt{M^2 - 1}, \qquad \xi = \tan \delta, \qquad S = \log\left(\frac{\bar{p}}{\bar{\rho}^{\gamma}}\right),$$

where

$$\bar{\rho} = \frac{\rho}{\rho_\infty}, \qquad \bar{p} = \frac{p}{\rho_\infty a^{*2}}.$$

Then Eqs. (9.9) and (9.10) for the conjugate characteristics in the physical plane and the hodograph plane are written as

First family:

$$\frac{dx}{dr} = \frac{\beta - \xi}{\beta\xi + 1} \equiv m, \tag{22.1}$$

$$d\xi + K\, d\beta + L\, dr - P\, dS = 0; \tag{22.2}$$

Second family:

$$\frac{dr}{dx} = \frac{\beta\xi - 1}{\beta + \xi} \equiv n, \tag{22.3}$$

$$d\xi - K\, d\beta - N\, dx + P\, dS = 0, \tag{22.4}$$

where

$$K = -\frac{2\beta^2(\xi^2 + 1)}{(\gamma + 1)(\beta^2 + 1)(\varepsilon\beta^2 + 1)}, \qquad L = \frac{\xi(\xi^2 + 1)}{r(\beta\xi + 1)},$$

$$N = \frac{\xi(\xi^2 + 1)}{r(\beta + \xi)}, \qquad P = \frac{\beta(\xi^2 + 1)}{\gamma(\gamma - 1)(\beta^2 + 1)},$$

and $\varepsilon = (\gamma - 1)/(\gamma + 1)$.

It is convenient in the calculation of the entropy term to express

it by the stream function Ψ, at the same time rewriting Eq. (3.25) and the entropy relation in terms of the new variables β and ξ. In addition, it is useful to replace Ψ by a modified stream function ψ, defined by

$$d\psi = \left(\gamma e^{S}\right)^{1/(\gamma-1)} d\Psi.$$

If the differential $d\Psi$ is written in the form

$$d\Psi = \Psi_x\, dx + \Psi_r\, dr,$$

and Eq. (3.25) is substituted for the partial derivatives Ψ_x and Ψ_r, the equation for the modified stream function in terms of the variables β and ξ is

$$\frac{d\psi}{dx} = -\frac{r\sqrt{(\beta^2+1)(\xi^2+1)}}{(\beta+\xi)(\varepsilon\beta^2+1)^{1/2\varepsilon}} \equiv q. \tag{22.5}$$

Since isentropic flow is considered, both ψ and the entropy are constant on a given streamline, so that the relation between ψ and S obtained from the conditions behind the shock wave can be used.

The system consisting of Eqs. (22.1) through (22.5) and the equation relating S and ψ can be solved numerically. Each of the equations is represented, as already noted, in a finite-difference form, and the equations can then be solved by the method of successive approximations.

The solution of the two basic cases illustrated in Fig. 80 is the same as for the ordinary method of characteristics described in Chap. III. The third problem, concerned with the computation of the point H on the shock wave (see Fig. 82), can be solved in the following manner. At point H, the location of which is as yet unknown, an arbitrary value of the shock wave angle θ_{sH} is selected, somewhat less than at the adjacent point F. Then from the relations behind the shock wave, the following values can be determined:

$$\bar{\rho}_H = \frac{\bar{\rho}_0 \tan^2\theta_{sH}}{1 - \varepsilon\bar{\rho}_0 + \tan^2\theta_{sH}}, \qquad \bar{\rho}_0 = \frac{(\gamma+1)M_\infty^2}{2 + (\gamma-1)M_\infty^2},$$

$$\beta_H^2 = \frac{\bar{\rho}_0(\tan^2\theta_{sH} + \bar{\rho}_H^2) - \bar{\rho}_H^2(1 + \tan^2\theta_{sH})}{\bar{\rho}_H^2(1 + \tan^2\theta_{sH}) - \varepsilon\bar{\rho}_0(\tan^2\theta_{sH} + \bar{\rho}_H^2)},$$

$$\xi_H = \frac{(\bar{\rho}_H - 1)\tan\theta_{sH}}{\tan^2\theta_{sH} + \bar{\rho}_H},$$

$$S = \log\left\{\frac{1}{\bar{\rho}_H^{\gamma}}\left[\frac{2}{\gamma+1}\frac{\bar{\rho}_0\tan^2\theta_{sH}}{1+\tan^2\theta_{sH}} - \frac{\gamma-1}{2\gamma}(1 - c\bar{\rho}_0)\right]\right\}.$$

The coordinates x_H and r_H are found from an iterative solution of the equation for the first family of characteristics, in the form $\Delta x = m\Delta r$, and a parabolic equation representing the shock segment FH. The approximation is completed when the equation for the first-family characteristic is satisfied:

$$\xi_H - \xi_N + K_N(\beta_H - \beta_N) + L_N(r_H - r_N) - P_N(S_H - S_N) = 0.$$

The modified stream function at point H is

$$\psi_H = \psi_F + \gamma^{1/(\gamma-1)}\frac{\bar{\rho}_C^{\frac{1}{2}}}{4}\left(\exp\frac{S_F}{\gamma-1} + \exp\frac{S_H}{\gamma-1}\right)(r_H^2 - r_F^2).$$

BOUNDARY CONDITIONS

It is necessary to know the flow parameters on an initial curve to determine all the parameters in the flow field in the region between this curve, the surface of the body, and the shock wave. The shock shape is gradually constructed during the solution. For a body with a spherical nose, the initial data may be known along the normal to the spherical surface (AB) located in a completely supersonic region close to the sonic line CD (Fig. 231). These data can be determined by various methods; one of the most accurate is the method of integral relations described earlier.

An approximate method can also be used, in which a shock wave is

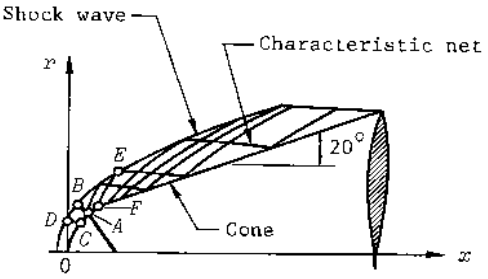

Fig. 231--Characteristics net for a blunt cone

constructed around the spherical nose with the equation $r^2 = 2R_{sc}(x + s_0)$. Then, close to the sonic point on the sphere, an arbitrary point A is selected through which passes a normal to the surface, AB (Fig. 232). The distribution of a parameter along the normal can be approximated by the polynomial

$$\Pi = \sum_{n=0}^{n} a_n \bar{y}^n, \tag{22.6}$$

in which $\bar{y} = y/s$, and s is the thickness of the shock layer at the section in question. The independent variable $\bar{y}$ varies from zero at the wall to unity at the shock wave.

At sufficiently high velocities and, therefore, small shock-layer thicknesses, the polynomial can be limited to three terms, i.e., a quadratic relation

$$\Pi = a_0 + a_1\bar{y} + a_2\bar{y}^2. \tag{22.6a}$$

The coefficient a_0 is determined from the wall condition at $\bar{y} = 0$, where the parameters at the wall can be calculated approximately from modified Newtonian theory or found experimentally. The two other coefficients can be determined from the shock-wave conditions at $\bar{y} = 1$ and the known value of the derivative $\partial\Pi/\partial y$ at point B ($\bar{y} = 1$) or A ($\bar{y} = 0$). This derivative enables us to find the coefficient $a_1 = (\partial\Pi/\partial\bar{y})_{\bar{y}=0}$.

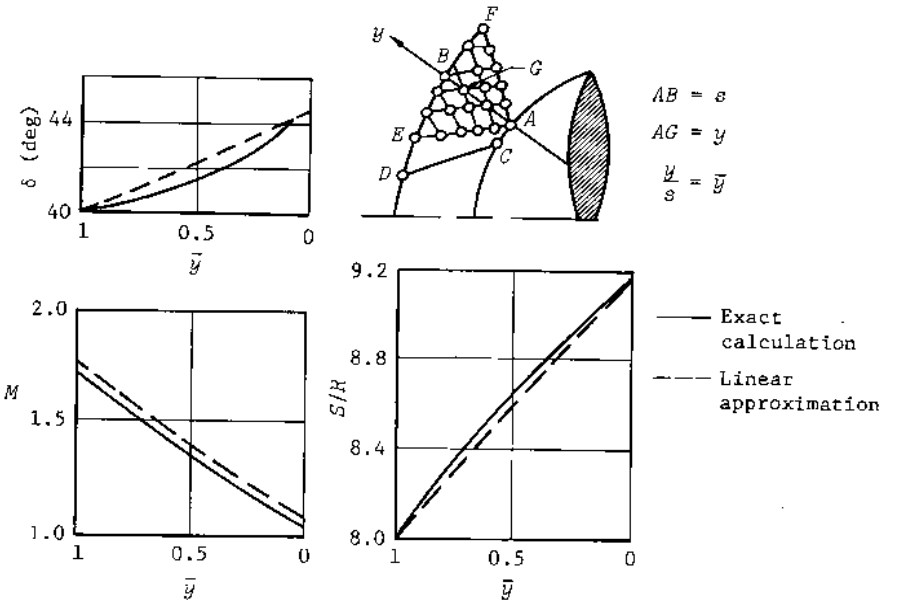

Fig. 232--Distribution of flow parameters across the shock layer

Results of the calculation of the distribution of some of the parameters are shown in Fig. 232, e.g., the Mach number, flow angle, and the dimensionless entropy S/R. It is evident that these results are close to those obtained from the parabolic relations given by Eq. (22.6a).

If the velocity of the incident flow is very large, the shock layer is very thin and the distribution is almost linear, so that it can be assumed that $a_2 = 0$ in Eq. (22.6a). In this case, the coefficient a_1 is equal to the value of the parameter in question at point B on the shock wave.† In Fig. 232, where data are presented for $M_\infty = 20$, it is evident that the parameters actually do approach a linear variation:

$$\Pi = a_0 + a_1\bar{y}.$$

†Editor's note: The coefficient a_1 is actually equal to the difference between the values behind the shock and on the surface.

The method of characteristics can be used directly to determine the initial data along a normal by choosing a row of points along an arbitrary arc, *EF*, of the given shock wave (Fig. 232). Since the parameters are known at each of these points, the equations for the characteristics can be solved to determine the grid in this region. The flow parameters at the junctions of the grid are then known in the region between the arc *EF* and the conjugate characteristics *EA* and *FA*, and the parameters can be found along the normal *AB*. The results presented in Fig. 232 were obtained in this way.

METHOD OF COMPUTATION AND SOME RESULTS

When a row of points has been determined along the selected normal, and at each of these points the flow parameters are known, the finite-difference form of the characteristics equations can be used to compute the parameters at the points of the first row close to the normal. The upper point of this row is located at the intersection of a first-family characteristic with the shock-wave surface, and the lower point lies at the intersection of the second-family characteristic with the body surface. All the remaining points lie at the intersection of the conjugate characteristics issuing from the adjacent points on the normal. The coordinates and parameters at the points of the following row are found in a similar way. Calculations on an electronic computer were produced by the method described for flow around a series of cones with spherical noses and different velocities. The cone angles were $\delta_c = 0°$, $20°$, $30°$, $40°$, and the Mach numbers were $M_\infty = 3$, 4, 6, 10, and ∞. The normal segment *AB* was divided into 48 spaces. Figure 231 shows a flow diagram around a blunt cone with a cone angle of $20°$ at $M_\infty = 6$ and gives some idea of the shape of the shock wave and of the characteristics network.

The calculation by the method of characteristics, accompanied by the construction of a network of characteristics, enables us not only to obtain the quantitative results but also to explain some phenomena observed in experiments. Among these is the frequent appearance of a second shock between a spherically blunted body and the bow shock wave. Shadowgraphs show that this discontinuity is, as it were, suspended above the surface, which is also indicated by the calculations, since

characteristics of the same family, issuing from points on the surface located close to one another, intersect at the place where the discontinuity originates. The surface points lie in the vicinity of the junction between the nose cap and the body.

This discontinuity is caused by the appreciable compression of the supersonic flow as it passes from a curved to a straight surface. Thus, the accumulation of the perturbations results in the development of a local "hanging" shock, which is apparent in the shadowgraphs.

In Fig. 231, the first-family characteristic issuing from the junction point of the sphere and the cone is *EF*, which is a boundary for that part of the flow directly affected by the flow around the spherical nose. Behind this part of the flow, there begins a region resulting from not only the influence of the sphere but also the basic part of the body. Thus, in many ways, the characteristic *EF* is analogous to the characteristic *KS* in Fig. 82, which separated the conical flow from that around a curved surface.

The pressure distribution on a 20° spherically blunt cone was computed on an electronic computer by the method of characteristics for three Mach numbers and the results are given in Fig. 233. The pressure

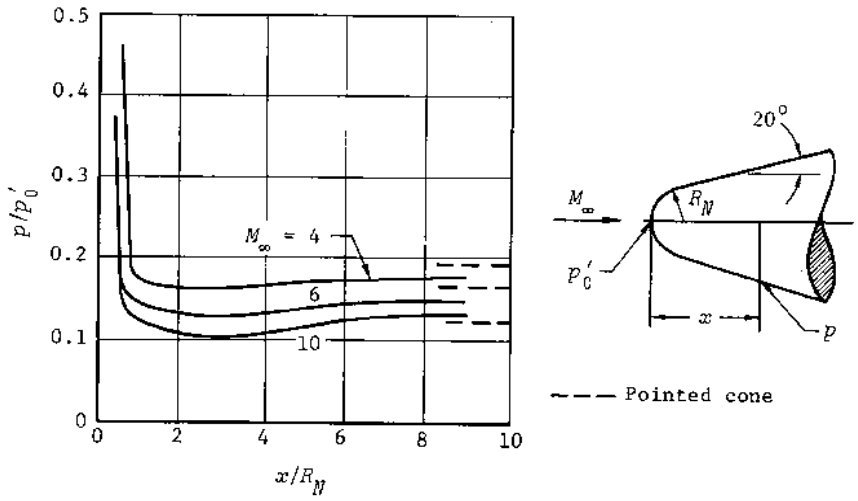

Fig. 233--Pressure distribution on a blunt cone

on a pointed cone is indicated by the dashed line for comparison. It is evident that blunting decreases the pressure over part of the cone, and the relative magnitude of the reduction increases with Mach number.

For low velocities, the flow around the conical part of the body differs little from flow over a pointed cone. This indicates the possibility of calculating the drag of a blunt cone by using the sum of the drag of the blunt nose and the remainder of the cone, on which the pressure is assumed to be equal to that on a pointed cone.

The same conclusion can also be reached in the case of a thick blunt body, for which the pressure distribution differs little at any velocity from the corresponding distribution on a pointed body, if we exclude the small area of the conical surface immediately behind the nose where the pressure changes considerably.

§ 23. *EFFECT OF ANGLE OF ATTACK*

STUDIES OF THE FLOW around blunt cones at angle of attack show that the basic characteristics of the pressure variation along different meridian planes are the same as those for zero angle of attack. This is evident, for example, from the experimental results[14] for a cone with a spherical nose at $M_\infty = 5.8$ and angles of attack of 4° and 8° (Fig. 234). On the upper and lower meridians of the cone, the pressure gradually decreases from the stagnation point, reaching a minimum at some distance from the nose. After this it increases to a value close to that which occurs in flow around a pointed cone.

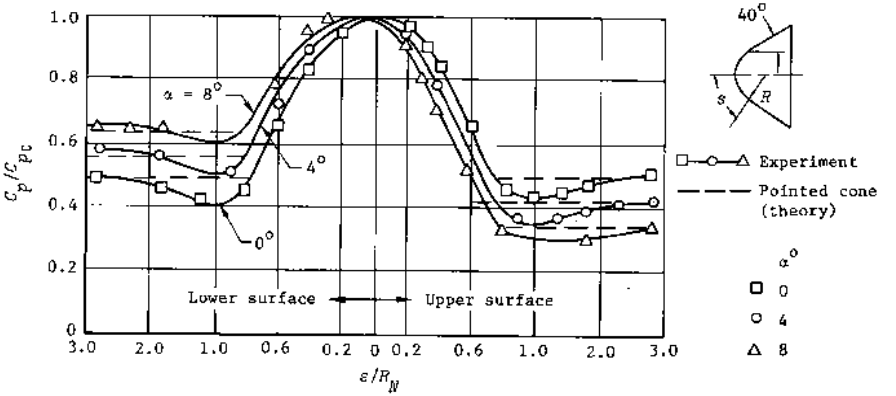

Fig. 234--Pressure distribution for asymmetric flow around a cone with a spherical nose

It is worth noting that the coordinates of the minimum in the pressure for small angles of attack are approximately identical with those for symmetric flow. This permits us to assume that the similarity law for the symmetric case can be used as the basis for the study of asymmetric flow.

Two universal curves have been constructed from the experimental data for blunt cones at $\alpha = 4°$ for two values of the meridian angle, $\phi = 0$ and π (Fig. 235). Approximate equations can be written for these curves in the form†

$$P = P_{\alpha=0} - \alpha B \cos \phi + \alpha^2 (C \cos 2\phi + D) + \ldots . \qquad (23.1)$$

Since the coefficients B, C, and D are independent of the angle of attack, known results of measurements or the calculations of the pressure distribution along three arbitrary meridians at a given angle of attack can be used for their determination. Equation (23.1) is simplified if it is applied only to meridian angles of zero, $\pi/2$, and π, since the coefficient D can be neglected compared with C for these cases. The coefficients B and C have been calculated from the experimental data shown in Fig. 235 by solving Eq. (23.1) for the meridians $\phi = 0$ and $\phi = \pi$ and assuming that $D = 0$.

Equation (23.1) can be used as an approximation for asymmetric flow, but it should be noted that the pressure distribution for flow around blunt cones at high velocities is quite sensitive even to small angles of attack. For a 10° blunt cone, an angle of attack of 0.5° results in a pressure change of 15 percent, compared with 10 percent for a pointed cone. The angle of attack of 4° used above is large enough to obtain reliable values of the coefficients from Eq. (23.1), although some improvement in the results is attained by retaining the other nonlinear term in the equation. The coefficients B and C are presented in Fig. 236, and these values can be used for preliminary estimates of the pressure. However, it is advisable to refine the coefficients when additional accurate experimental or theoretical data are available.

---

†Editor's note: The parameter P is as defined in Eq. (21.25). It is plotted versus $\bar{x}$ in Fig. 235, where $\bar{x}$ is defined in connection with Eq. (21.25). $P_{\alpha=0}$ is presented in Fig. 225.

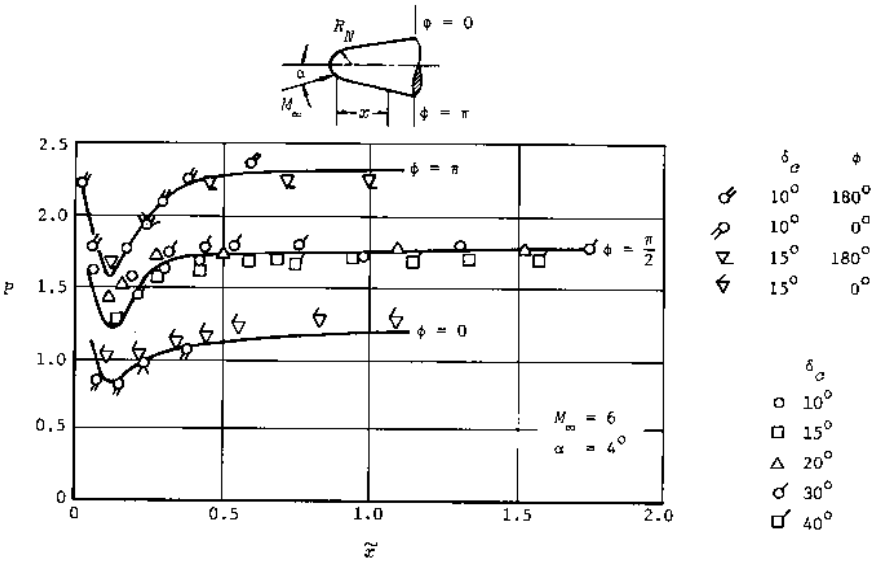

Fig. 235--Universal curves for the pressure distribution at angle of attack on blunt cones with spherical noses

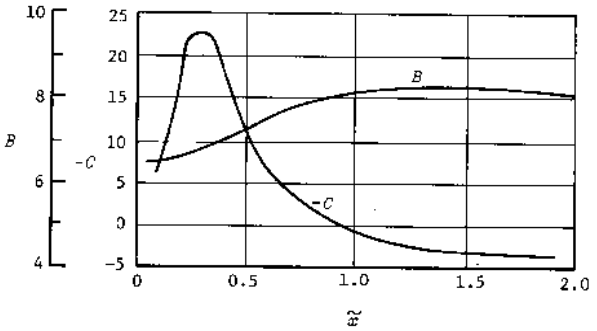

Fig. 236--Coefficients for calculating the pressure distribution at angle of attack

The accuracy of the results is increased as the angle of attack approaches zero. For very small values of α, only the second term in Eq. (23.1) is necessary, resulting in

$$P = P_{\alpha=0} - \alpha B \cos \phi. \tag{23.2}$$

This equation together with the data in Fig. 236 for B makes it possible to estimate very simply, for example, the location of the center of pressure. It will be assumed that the pressure distribution on the blunt tip in asymmetric flow does not have much influence on the change in the location of the center of pressure. Thus, the coordinate x will be measured from the beginning of the conical part of the body. Equations (1.12) and (1.19) are used for the normal force and moment coefficients, and Eq. (1.22) for the center of pressure. Making the following substitutions

$$r = r_N + x \tan \delta_c,$$

$$C_p = \frac{(\tan \delta_c)^{1.8}}{K_1^{0.2}} P(\bar{x}),$$

we obtain for the center-of-pressure coefficient

$$\bar{x}_{cp} = \frac{3F_1 N^2 \tan \delta_c + 6F_2 N(1 + \tan^2 \delta_c) + 4F_3 \tan \delta_c (2 + \tan^2 \delta_c)}{12(F_1 N + F_2 \tan \delta_c)\bar{x}}, \tag{23.3}$$

where

$$N = \frac{K_1^{1.5}}{M_\infty^2 \sqrt{C_{DN}}}, \tag{23.4}$$

$$F_1 = \int_0^{\bar{x}} B \, d\bar{x}, \qquad F_2 = \int_0^{\bar{x}^2} B \, d\bar{x}^2, \qquad F_3 = \int_0^{\bar{x}^3} B \, d\bar{x}^3. \tag{23.5}$$

The integrals of Eq. (23.5) can be determined numerically or graphically from the data of Fig. 236.†

For small cone angles ($\tan \delta_c \ll 1$), Eq. (23.3) is simplified:

$$\bar{x}_{cp} = \frac{3F_2 N + 4F_3 \delta_c}{6(F_1 N + F_2 \delta_c)\bar{x}}. \tag{23.3a}$$

The calculated variation of the center-of-pressure coefficient with length for blunted cones is compared with experiment in Fig. 237.

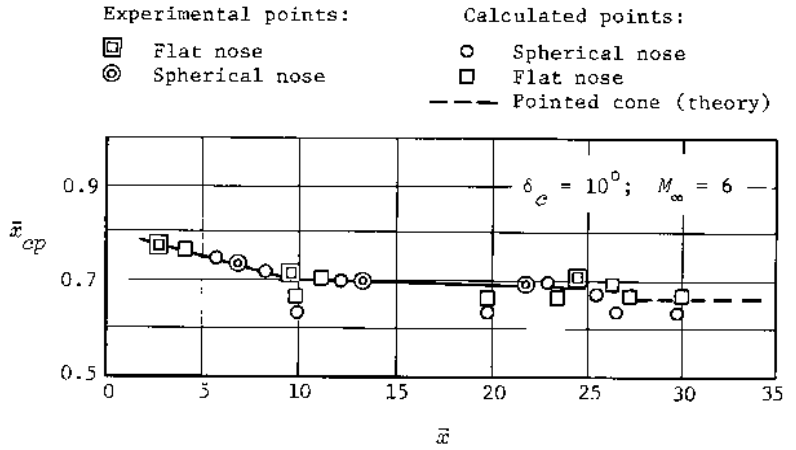

Fig. 237--Center of pressure of a blunt cone

The center of pressure of a blunt nose at hypersonic speeds can be determined from Newtonian theory, still retaining the assumption that the blunt tip exerts a negligibly small influence. Then the nose length l_N will be measured from the base of the blunt tip. If the radius of the initial cross section at this point is designated by r_N, the expressions for the normal force and moment coefficients of the blunt nose, corresponding to Eqs. (18.31b) and (18.45b), will be

†Editor's note: The definition of $\bar{x}$ in the above equations is that given with Eq. (21.25), i.e., $\bar{x} = Nx/D_N$. It must not be confused with that used in Eqs. (1.12) and (1.19), where $\bar{x}$ is defined as x/l.

$$C_{Np} = a\tilde{p}(\gamma)\left(1 - \frac{r_N^2}{r_{\text{mid}}^2}\right),$$

$$C_{mp} = a\tilde{p}(\gamma)\left(1 - \frac{W_N}{l_N S_{\text{mid}}}\right). \tag{23.6}$$

The relation for the center of pressure becomes

$$\bar{x}_{cp} = \frac{1 - W_N/l_N S_{\text{mid}}}{1 - r_N^2/r_{\text{mid}}^2}. \tag{23.7}$$

This equation applies not only to a thin slender conical nose but also to a slender body of arbitrary shape. For a thick body, the general expression, Eq. (1.23), must be used for $\bar{x}_{cp}$.

§ 24. *FLOW AROUND BLUNT BODIES OF CURVED SHAPE*

THE GENERAL SOLUTION

THE PROBLEM OF FLOW around certain blunt bodies with curved profiles, such as those defined in the form of a power law (Eq. 1.41), can be solved theoretically. The solution can be obtained by using the law of plane sections, the equation for which results from the analogy with the unsteady motion of a gas around a cylindrical piston. The general form of this one-dimensional motion is described by Eqs. (21.2a) and (21.3a). The solution of the equations can be found by expanding the required function into a power series in $\varepsilon = (\gamma - 1)/(\gamma + 1)$, as shown by Chernyi.[10] For an explanation of this method, let us return to the equations that determine the gas parameters behind the shock wave.

As was shown in §4, these relations, particularly Eq. (4.12) for pressure, express the required parameters in terms of the density ratio ρ_1/ρ_2. With an increase in velocity the density ratio decreases, and in the limiting case as $M_\infty \to \infty$, the value of $\rho_1/\rho_2 = \varepsilon$ for constant specific heats.

If the physical-chemical changes behind the shock wave are taken into account, the value of ρ_1/ρ_2 will be even less. Thus, a layer of compressed gas develops between the shock wave and the body in which the perturbed parameters will be of the same order of magnitude as those immediately behind the shock; i.e., the density ratio in the free stream is the determining parameter. The larger the velocity, the stronger the shock and the thinner the layer in which the compression occurs.

This perturbed region of gas behind the shock can be examined as a type of boundary layer, in which basic changes occur in the pressure of the gas. In the special case of infinitely large compression in this layer, i.e., $\rho_1/\rho_2 = 0$, the excess gas pressure behind the wave

is $p_2 - p_1 = \rho_\infty V_\infty^2 \sin^2\delta$, and agrees with the value obtained from Newtonian theory. The thickness of the layer becomes infinitesimally small. In reality, the pressure differs from this limiting case, and the criterion of the difference is the parameter ρ_1/ρ_2. Therefore, it is possible to seek the solution of the problem of gas flow in the thin layer near the shock in the form of a power series in the parameter ρ_1/ρ_2. The value of the small parameter can be assumed to be $\rho_1/\rho_2 = \varepsilon$ for an ideal gas with constant specific heats. Incidentally, it can be seen from the equations of §4 that the gas parameters behind the shock wave are completely defined by the parameter ε.

The solutions to Eqs. (21.2a), (21.3a), and (21.4) can be obtained by using the expansions†

$$r = r_0 + \varepsilon r_1 + \ldots,$$

$$p = p_0 + \varepsilon p_1 + \ldots, \tag{24.1}$$

$$\rho = \frac{\rho_0}{\varepsilon} + \rho_1 + \ldots.$$

Using these series and designating $\partial r_0/\partial t = \dot{r}_0$ and $\partial^2 r_0/\partial t^2 = \ddot{r}_0$, we obtain a new set of equations:

$$\frac{\partial r_0}{\partial m} = 0, \qquad \ddot{r}_0 = -r_0 \frac{\partial p_0}{\partial m}, \qquad \frac{\partial}{\partial t}\left(\frac{p_0}{\rho_0^\gamma}\right) = 0, \tag{24.2}$$

which determine the form of the functions r_0, p_0, and ρ_0. Integrating the equations, we get

$$r_0 = r_0(t), \qquad p_0 = P(t) - \frac{\ddot{r}_0}{r_0} m, \qquad p_0^{1/\gamma} = \zeta_0(m)\rho_0, \tag{24.3}$$

where $r_0(t)$, $P(t)$, and $\zeta_0(m)$ are arbitrary functions. From these results, we obtain another set of equations that r_1, p_1, and ρ_1 must satisfy:

†Editor's note: It should be noted that the r_1 used here is simply the second coefficient in the expansion, whereas r_1 denotes the initial condition for r in §21.

$$\frac{\partial r_1}{\partial m} = \frac{1}{\rho_0 r_0}, \qquad r_0 \frac{\partial p_1}{\partial m} = \frac{\ddot{r}_0}{r_0} r_1 - \frac{\partial^2 r_1}{\partial t^2}, \qquad \frac{\partial}{\partial t}\left(\frac{p_1}{p_0} - \gamma \frac{\rho_1}{\rho_0}\right) = 0. \quad (24.4)$$

The integration of these equations gives the following expressions for these functions:

$$r_1 = \frac{1}{r_0}\int_{m^*}^{m} \frac{\zeta_0(m)}{p_0^{1/\gamma}}\, dm + r_1^*(t), \qquad \rho_1 = \frac{\rho_0}{\gamma}\left[\frac{p_1}{p_0} - \zeta_1(m)\right],$$

$$p_1 = \frac{\ddot{r}_0}{r_0^2}\int_{m^*}^{m} r_1\, dm - \frac{1}{r_0}\int_{m^*}^{m} \frac{\partial^2 r_1}{\partial t^2}\, dm + p_1^*(t), \quad (24.5)$$

where $r_1^*(t)$, $p_1^*(t)$, and $\zeta_1(m)$ are arbitrary functions; the lower limit of the integrals (m^*) is also selected arbitrarily.

The conditions on the shock wave and on the surface of the piston must be used to determine the arbitrary functions. The conditions on the shock wave, moving with the velocity D with respect to the undisturbed flow, have the form

$$m = \frac{1}{2}\rho_\infty r_s^2,$$

$$p_s = (1 - \varepsilon)\rho_\infty D^2 - \varepsilon p_\infty, \quad (24.6)$$

$$\rho_s = \frac{\rho_\infty}{\varepsilon + (1 - \varepsilon)a_\infty^2/D^2}.$$

The correct choice of $r_0(t)$ is such that it agrees with the law of shock-wave propagation; i.e., it is given by $r_0 = r_s(t)$. The velocity of this propagation will be $D = \partial r_s/\partial t = \dot{r}_s$. For this choice, obviously, the function $r_1 = 0$ on the shock wave.

The conditions on the shock wave that the other terms in the expansion must satisfy are obtained if Eqs. (24.6) for p_s and ρ_s are equated to their respective values in Eq. (24.1). As a result, we obtain

$$p_0 = \rho_\infty \dot{r}_s^2, \qquad p_1 = -p_\infty - \rho_\infty \dot{r}_s^2,$$

$$\rho_0 = \frac{\varepsilon \rho_\infty}{\varepsilon + (1 - \varepsilon) a_\infty^2 / \dot{r}_s^2}, \qquad \rho_1 = 0. \tag{24.7}$$

The arbitrary functions in Eqs. (24.3) and (24.5) can now be determined from these conditions. For example, if we substitute $p_0 = \rho_\infty \dot{r}_s^2$ and $m = \rho_\infty r_s^2/2$ into the second expression of Eq. (24.3), we find the following function:

$$P(t) = \rho_\infty \dot{r}_s^2 + \frac{1}{2} \rho_\infty r_s \ddot{r}_s.$$

The other functions can be found in a similar manner. After substituting these functions into Eq. (24.3) and after simple transformations, we can determine the quantitites p_0 and ρ_0:

$$p_0 = \rho_\infty \dot{r}_s^2 + \frac{1}{2} \rho_\infty r_s \ddot{r}_s - \frac{\ddot{r}_s}{r_s} m,$$

$$\rho_0 = \rho_\infty \frac{(p_0/\rho_\infty \dot{r}^2)^{1/\gamma}}{1 + 2a_\infty^2/(\gamma - 1)\dot{r}^2}, \tag{24.8}$$

where $\dot{r} = \partial r/\partial \tau$ is a function of the new variable τ. If t corresponds to the instant in time when the particle crosses the shock wave, so that $m = m^* = \rho_\infty r_s^2/2$, τ is defined as the instant in time when the particle is at a distance r from the axis and the Lagrangian variable m is given by $m = \rho_\infty r^2/2$.

Equations for the functions r_1, p_1, and ρ_1 are obtained in the same way and have the form

$$r = \frac{1}{r_s} \int_{m^*}^{m} \frac{[1 + 2a_\infty^2/(\gamma - 1)\dot{r}^2]\dot{r}^{2/\gamma}\, dm}{\rho_\infty (\dot{r}_s^2 + r_s \ddot{r}_s/2 - m\ddot{r}_s/\rho_\infty r_s)^{1/\gamma}}, \tag{24.9a}$$

$$p_1 = \frac{\ddot{r}_s}{r_s^2}\int_{m^*}^{m} r_1\,dm - \frac{1}{r_s}\int_{m^*}^{m}\frac{\partial^2 r_1}{\partial t^2}\,dm - p_\infty - \rho_\infty r_s^2, \tag{24.9b}$$

$$\rho_1 = \frac{\rho_0}{\gamma}\left(1 + \frac{p_1}{p_0} + \frac{a_\infty^2}{\gamma \dot{r}^2}\right). \tag{24.9c}$$

Since the shape of the body is usually specified by the law for the motion of the piston, $r_N(t)$, it is necessary to relate r_s to r_N by an additional condition. Neglecting terms of the second and higher orders, we obtain

$$r = r_s + \varepsilon r_1 = r_N,$$

so that

$$r_s = r_N - \varepsilon\left|r_1\right|_{m^*}^{0}, \tag{24.10}$$

where $\left|r_1\right|_{m^*}^{0}$ is determined from Eq. (24.9a) by setting the upper limit of the integral equal to zero (the condition on the piston). Note that in Eq. (24.9a) the quantity r_s on the right side can be replaced by r_N, since when Eq. (24.10) is substituted for r_s, a term of order ε^2 results, which can be neglected.

FLOW AROUND A POINTED CONE

It is evident from the relations presented above that the solution is found in the form of functions that can be determined in turn by the law of motion of the shock wave, i.e., by the relation for r_s. An expression for this law for flow around a cone can be obtained by dimensional analysis.

Analysis of the phenomenon of shock-wave propagation indicates that the shock-wave velocity $D = \partial r_s/\partial t$ is a function of the variable t and of the dimensional variables p_∞ and ρ_∞, i.e.,

$$\frac{\partial r_s}{\partial t} = f(t,\ p_\infty,\ \rho_\infty).$$

It is apparent that all of these quantities have independent dimensions, so that it is possible to write

$$\frac{\partial r_s}{\partial t} = A t^n p_\infty^m \rho_\infty^k,$$

where A is a constant. It can be shown by dimensional analysis that the exponents n, m, and k are equal to $n = 0$, $m = 0.5$, and $k = -0.5$. Thus, the shock is propagated with a constant velocity

$$\frac{\partial r_s}{\partial t} = D = A \sqrt{p_\infty/\rho_\infty}.$$

If t is replaced by x/V_∞ in agreement with the law of plane sections, $\partial r_s/\partial x = D/V_\infty$. Thus, a shock-wave velocity equal to D corresponds to flow around a pointed cone with an attached shock wave whose angle is given by

$$\frac{\partial r_s}{\partial x} = \tan \theta_s = \frac{D}{V_\infty}.$$

The law of motion for the shock wave is expressed in the form $r_s = Dt$, where $D = V_\infty \tan \theta_s$. The form of the law of motion for the piston must correspond to the equation of the cone, $r = x \tan \delta_c$, and is given by $r = Ut$, where the velocity of the piston is $U = V_\infty \tan \delta_c$. If we substitute the expressions $r_s = Dt$ and $r = Ut$ into Eq. (24.8), we find a relation for p_0 and ρ_0:

$$p_0 = \rho_\infty D^2, \qquad \rho_0 = \frac{\rho_\infty}{1 + 2a_\infty^2/(\gamma - 1)D^2}. \tag{24.11}$$

A similar substitution into Eq. (24.9) gives the following relation for r_1:

$$r_1 = \frac{Dt}{2}\left(1 + \frac{2}{\gamma - 1}\frac{a_\infty^2}{D^2}\right)(\bar{m} - 1) = \frac{Dt}{2}\left(1 + \frac{2}{\gamma - 1}\frac{a_\infty^2}{D^2}\right)\left(\frac{r^2}{r_s^2} - 1\right), \tag{24.12}$$

where $\bar{m} = m/m^*$. Noting that $m^* = \rho_\infty D^2 t^2/2$, we can compute the second derivative:

$$\frac{\partial^2 r_s}{\partial t^2} = \frac{2m}{Dt^3 \rho_\infty}\left(1 + \frac{2}{\gamma - 1}\frac{a_\infty^2}{D^2}\right).$$

Substituting this derivative into Eq. (24.9) for p_1 and using the definitions $m = \rho_\infty r^2/2$ and $m^* = \rho_\infty r_s^2/2$, we obtain

$$p_1 = \frac{\rho_\infty D^2}{4}\left(1 + \frac{2}{\gamma - 1}\frac{a_\infty^2}{D^2}\right)\left(1 - \frac{r^4}{r_s^4}\right) - p_\infty - \rho_\infty D^2. \tag{24.13}$$

Finally, with Eqs. (24.11) and (24.13), Eq. (24.9c) gives a relation for ρ_1:

$$\rho_1 = \frac{\rho_\infty}{4\gamma}\left(1 - \frac{r^4}{r_s^4}\right). \tag{24.14}$$

To determine the relation between the velocities of the piston U and of the wave D, we must first set $m = 0$ in Eq. (24.12), resulting in

$$r_1 = -\frac{Dt}{2}\left(1 + \frac{2}{\gamma - 1}\frac{a_\infty^2}{D^2}\right).$$

Substituting this result with $r_s = Dt$ and $r = Ut$ into Eq. (24.12), we obtain

$$U = D\left[1 - \frac{\gamma - 1}{2(\gamma + 1)}\left(1 + \frac{2}{\gamma - 1}\frac{a_\infty^2}{D^2}\right)\right]. \tag{24.15}$$

This relation can be converted to an expression for the relation between the cone angle and the shock angle for hypersonic flow velocities, since

$$\frac{U}{a_\infty} = \frac{V_\infty}{a_\infty}\tan\delta_c = K_1, \qquad \frac{D}{a_\infty} = \frac{V_\infty}{a_\infty}\tan\theta_s = K_0.$$

Thus,

$$K_1 = K_0\left[1 - \frac{\gamma - 1}{2(\gamma + 1)}\left(1 + \frac{2}{\gamma - 1}\frac{1}{K_0^2}\right)\right]. \tag{24.16}$$

This equation agrees with the relation derived previously in Eq. (17.4a), and the expression for the pressure coefficient on the cone (obtained

from $p = p_0 + \varepsilon p_1$ by substituting Eqs. (24.11) and (24.13)) is identical with Eq. (17.11).

The relations for the dimensionless gas parameters at an arbitrary point between the wave and the cone are determined only as a function of the ratio r/r_s (see Eqs. (24.13) and (24.14)). Thus, unsteady motion ahead of a cylindrical piston, which is equivalent to steady flow around a cone, possesses the characteristic that the spatial distribution of the flow parameters remains the same with changes in time. This type of motion is called similar. It is evident from the discussion that, in the given case, similar motion also occurs when the initial pressure of the gas, p_∞, is included.

FLOW AROUND A POWER LAW BODY

In the example of flow around a cone, it was possible to obtain a closed-form solution. In the equivalent problem of the expansion of a piston, this solution describes the similar motion behind a cylindrical shock wave, which accounts for the ambient pressure p_∞. In addition, an analytical solution can be obtained for another form of similar motion that corresponds to the flow around a body with a particular curved shape.

Let us assume that the pressure in front of the shock wave can be neglected at hypersonic velocities, for which $a_\infty/D \ll 1$. The shock velocity is determined by the expression

$$\frac{\partial r_s}{\partial t} = f(t, \rho_\infty)$$

and

$$\frac{\partial r_s}{\partial t} = Bt^n \rho_\infty^m,$$

where B is a constant. The product of this constant and ρ_∞^m is also constant and can be designated by C_1. Then the propagation velocity of the shock is written as

$$\frac{\partial r_s}{\partial t} = D = C_1 t^n,$$

and the law of motion is

$$r_s = \frac{C_1}{n+1} t^{n+1}. \tag{24.17}$$

It should be noted that the constant C_1 has the dimensions $[L]/[T]^{n+1}$.

In analogy to the expression for r_s, the relation for the law of piston expansion is

$$r_N = \frac{C}{n+1} t^{n+1}. \tag{24.18}$$

Replacing t by x/V_∞, we obtain the equation for the profile of the body:

$$r_N = \frac{C}{n+1} \left(\frac{x}{V_\infty}\right)^{n+1}. \tag{24.18a}$$

In the special case of $n = 0$, we obtain the equation for a cone.

Using Eq. (24.17) for r_s and the corresponding relation

$$r = \frac{C_1}{n+1} \tau^{n+1}, \tag{24.17a}$$

we can evaluate the functions that are represented in general form by Eqs. (24.8) and (24.9). Assuming that α_∞/D is negligible, we obtain

$$\begin{aligned} p_0 &= \rho_\infty D^2 \left[1 + \frac{n}{2(n+1)} (1 - \bar{m})\right], \\ \rho_0 &= \rho_\infty^{(\gamma-1)/\gamma} \left(\frac{p_0}{C_1^2 \tau^{2n}}\right)^{1/\gamma}. \end{aligned} \tag{24.19}$$

The relations given by Eq. (24.9) are obtained in a similar manner:

$$r_1 = -\frac{r_s}{2} J(\bar{m}), \tag{24.20a}$$

$$p_1 = \rho_\infty D^2 \left\{\bar{m}^2 J'(\bar{m}) - \frac{1}{2}\left(\frac{n}{n+1} + \frac{3}{2}\right) \bar{m} J(\bar{m}) - \left[\frac{n}{2(n+1)} + \frac{3}{2}\right] \int_{\bar{m}}^{1} J(\bar{m})\, d\bar{m}\right\}, \tag{24.20b}$$

$$\rho_1 = \frac{\rho_0}{\gamma} \left(\frac{p_1}{p_0} + 1\right), \tag{24.20c}$$

where

$$J(\bar{m}) = \int_{\bar{m}}^{1} \left[\frac{\bar{m}^{n/(n+1)}}{1 + \frac{n}{2(n+1)}(1 - \bar{m})} \right]^{1/\gamma} d\bar{m}, \qquad (24.21)$$

and $J'(\bar{m}) = dJ/d\bar{m}$. It is evident from Eqs. (24.19) and (24.20) that the motion under consideration is, in fact, of a similar character because all the dimensionless parameters are determined by the one dimensionless quantity $\bar{m}$.

The laws of piston motion and of shock-wave motion are related by the coefficients C and C_1, which can be obtained from Eq. (24.10) and Eq. (24.20):

$$\frac{r_N}{r_s} = \frac{C}{C_1} = 1 - \frac{\varepsilon}{2} J(0). \qquad (24.22)$$

Equation (24.22) gives the ratio between the coordinates of the body surface and the shock wave and is plotted in Fig. 238.

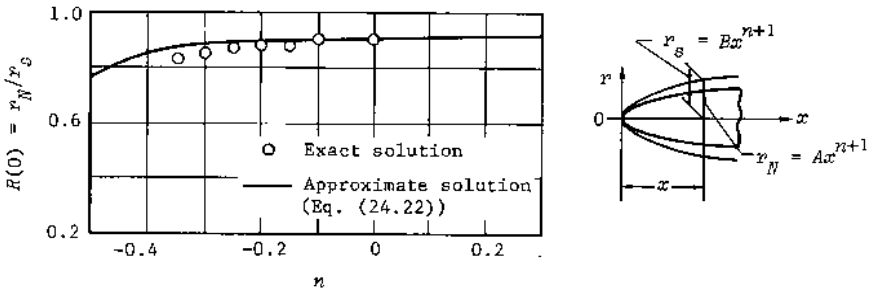

Fig. 238--Ratio of the coordinates for a power law body and its shock wave

Relations for the flow parameters in the perturbed layer between the shock wave and the body can be found by using Eqs. (24.19), (24.20), and (24.1). For example, the pressure at the surface ($\bar{m} = 0$) is

$$p_N = \rho_\infty D^2 \left[1 + \frac{n}{2(n+1)} - \frac{\varepsilon}{2} \left(\frac{n}{n+1} + 3 \right) \int_0^1 J(\bar{m})\, d\bar{m} \right] = p_s P(0), \qquad (24.23)$$

where the pressure directly behind the shock wave is

$$p_s = \frac{2}{\gamma + 1} \rho_\infty D^2,$$

and the function $P(\bar{m}) = P(0) = p_N/p_s$. This pressure ratio is presented in Fig. 239. The drag of a power law body can be determined from the equation

$$C_D qS = 2\pi \int_0^{r_N} p_N r_N \, dr_N$$

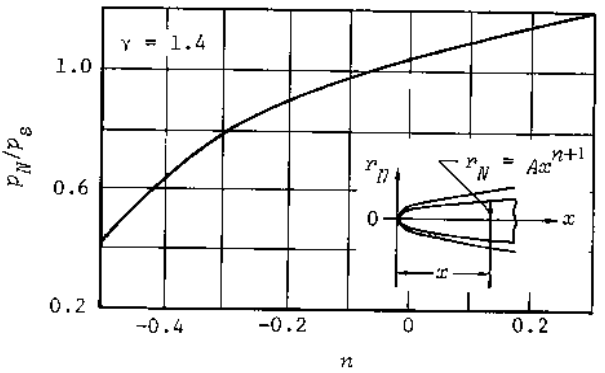

Fig. 239--Ratio of the surface pressure on a power law body to the pressure behind the shock wave

and the expression for pressure

$$p_N = p_s P(0) = \frac{2}{\gamma + 1} \rho_\infty D^2 P(0) = \frac{2}{\gamma + 1} \rho_\infty C_1^2 t^{2n} P(0).$$

The product $C_1^2 t^{2n}$ can be replaced by a function of r_s and r_N by using Eqs. (24.17) and (24.18). Then, performing the integration indicated above, we obtain

$$C_D qS = \frac{4\pi}{\gamma + 1} \rho_\infty C^2 \frac{P(0)}{R^2(0)} \left(\frac{n+1}{C}\right)^{2n/(n+1)} \frac{n+1}{2(2n+1)} r_N^{2+2n/(n+1)} \Bigg|_0^{r_N}, \quad (24.24)$$

where $R(\bar{m}) = R(0) = r_N/r_s$ is the function calculated from Eq. (24.22). To calculate the drag, it is necessary to know not only the free-stream flow parameters, but also the shape of the power law body. The latter is specified by the maximum radius r_{mid}, the exponent n, and the constant C. The fineness ratio $\lambda_N = l_N/2r_{mid}$ can be used instead of C, so that the equation for the body is written as

$$r_N = Ax^{n+1} = \frac{x^{n+1}}{2\lambda_N^{n+1}(2r_{mid})^n}.$$

After determining the value of A from this equation, the coefficient C is obtained from Eq. (24.18a) as $C = A(n+1)V_\infty^{n+1}$.

It follows from Eq. (24.24) that solutions do not exist for all values of the exponent n in Eq. (24.17), i.e., for all power law shapes. In particular, it is evident that the value of the integral

$$r_N^{2+2n/(n+1)}\Big|_0^{r_N}$$

diverges for $n/(n+1) \leq -1$ and the drag becomes infinite, which is not valid. The drag given by Eq. (24.24) will be finite for bodies with values of $n > -\frac{1}{2}$, and for $n < -\frac{1}{2}$ a similar solution does not exist. This means that the distribution of parameters in transverse planes between the body and the shock wave does not possess the property of similarity, and, therefore, it is impossible to express the pressure, density, and velocity in the form

$$\frac{P(r)}{P(0)} = f\left(\frac{r}{r_s}\right).$$

In this case the flow at a given station must be, to some degree, a function of the previous history of the flow, which in turn must be determined by the geometric shape of the body.

It follows from Eq. (24.18a) that, for $n > -\frac{1}{2}$, this equation represents both pointed bodies ($n \geq 0$) and blunt bodies. Since solutions were assumed to be given by the series in Eq. (24.1) and were limited to the

first order in $\epsilon = (\gamma - 1)/(\gamma + 1)$, Eq. (24.24) is approximate and can be used only for values of n somewhat larger than $-\frac{1}{2}$. This is evident in Fig. 240, in which a curve is plotted for the variation of the drag coefficient

$$C_D = \frac{1}{\gamma + 1} \frac{(n + 1)^3}{2n + 1} \frac{P(0)}{R^2(0)} \frac{1}{\lambda^2}, \tag{24.25}$$

where the reference area is $S = \pi r_N^2$, and the fineness ratio $\lambda = l_N/2r_N$. Equation (24.25) is derived from Eq. (24.24) by setting the integral equal to zero at the lower limit and choosing the constant to be

$$C = (n + 1) \frac{r_N}{t^{n+1}} = (n + 1) r_N \left(\frac{V_\infty}{x}\right)^{n+1}.$$

A comparison with the results of the exact solution (see Fig. 240) indicates that the accuracy of Eq. (24.25) decreases near values of $n = -\frac{1}{2}$. The same situation can be noted with respect to the shape of the shock wave as given by Eq. (24.22), which is compared with exact theory in Fig. 238.

The results in Fig. 240 indicate that the minimum value of $C_D\lambda^2$

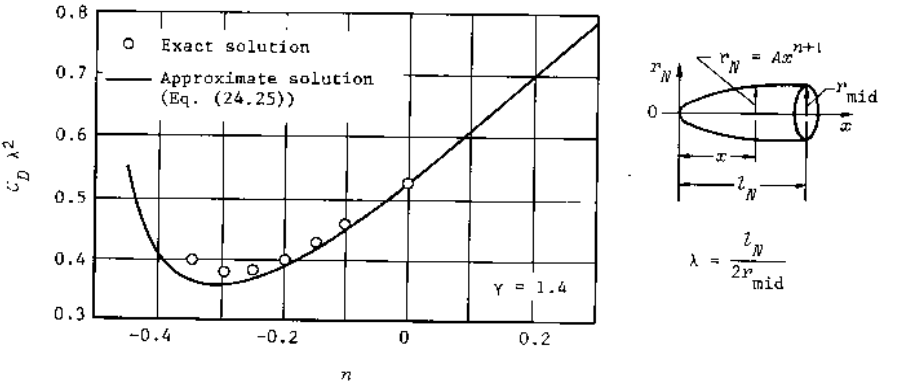

Fig. 240--Drag coefficients of power law bodies

is equal to 0.38 at approximately $n = -0.29$, and for a cone $C_D\lambda^2 = 0.52$, which is larger by 37 percent. Thus, at very high velocities, a blunt body of revolution with a curved generatrix, which is better from the standpoint of heating, is also advantageous in having less drag than a cone.

The relations obtained above pertain to the case in which terms of the order of ε are taken into account in Eq. (24.1). Of course, these relations are simplified if only the main terms are used.[16] For example, Eqs. (24.22) and (24.23) take the form

$$R(0) = \frac{r_N}{r_s} = \frac{C}{C_1} = 1, \tag{24.22a}$$

$$p_N = \rho_\infty D^2\left[1 + \frac{n}{2(n+1)}\right] = p_s P(0), \tag{24.23a}$$

and Eq. (24.25) for the drag coefficient is

$$C_D = \frac{(n+1)^2}{4(2n+1)}\,\frac{3n+2}{\lambda^2}. \tag{24.25a}$$

The minimum C_D for a fixed fineness ratio λ is obtained for $n = -\frac{1}{3}$. The minimum

$$C_D = \frac{1}{3\lambda^2} \tag{24.26}$$

is less than that given for a cone by Newtonian theory, $C_D = \frac{1}{2}\lambda^2$.

THE APPLICATION OF THE NEWTONIAN EQUATION

The pressure given by Eq. (24.23) applies to points on the surface of a power law body located at some distance from the blunt nose. Another method must be used for points on the blunt nose. It was noted that modified Newtonian theory gives satisfactory results in calculating the pressure distribution around a spherical nose. Research shows that these results can be applied to bodies of any curved shape. This is particularly evident in Fig. 241, where experimental data for the pressure

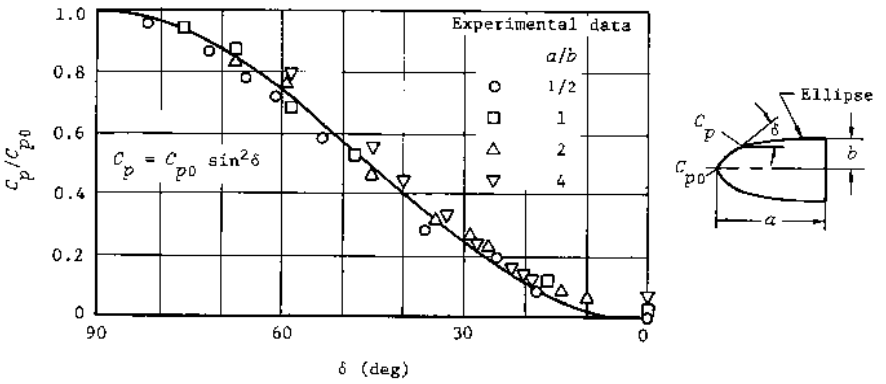

Fig. 241--Comparison of the theoretical and experimental pressure distributions around an ellipsoid

distribution over a symmetric ellipsoid are compared with the results of calculations by the equation $C_p = C_{p0} \sin^2\delta$.

The Newtonian equation can also be applied with the same success to blunt power law bodies. Comparison shows that better agreement of the experimental and theoretical results is observed for large supersonic velocities. However, Newtonian theory gives an approximation sufficiently satisfactory for practical purposes even for comparatively small velocities, as is verified by the data obtained in wind tunnels at $M_\infty = 4$ in Fig. 241.

The data indicate that the pressure measured at the rear of the nose is relatively large. The calculated results can be improved somewhat by "splicing" the pressure distribution obtained from the Newtonian equation on the forward part of the body to a pressure distribution over the aft part from a Prandtl-Meyer expansion. The Prandtl-Meyer theory can also be spliced to the calculation based on the law of plane sections, i.e., with Eq. (24.23).

§ 25. *NONEQUILIBRIUM EFFECTS ON INVISCID FLOW AROUND BLUNT BODIES*

NONEQUILIBRIUM FLOW IN REGIONS OF GREAT OVEREXPANSION AND SMALL PRESSURE GRADIENTS

Flow Regions around Blunt Bodies

THREE DIFFERENT REGIONS can be distinguished in the flow over a blunt body (Fig. 242). The first of these regions is directly adjacent to the blunt nose between the axis and the sonic line. The pressure in this region is almost constant, and is approximately equal to the stagnation pressure. Initially, the gas will be in a state of nonequilibrium dissociation after passing through the shock wave, but it will be assumed that it can return rapidly to an equilibrium state specified by an average value of pressure and enthalpy in this region. We shall consider nonequilibrium flow in this region in somewhat more detail later in this section.

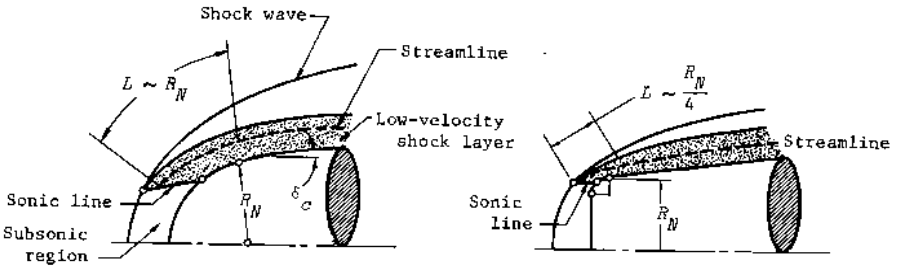

Fig. 242--Diagram of flow around blunt bodies

The second flow region begins at the sonic line and is characterized by a rapid decrease in pressure. It terminates behind the nose in a flow with a positive, zero, or negative pressure gradient, depending on the shape of the body. In the region of significant expansion, the state of the dissociating gas does not have time to reach equilibrium. Therefore, thermodynamic nonequilibrium is an important characteristic of the gas flow in this region.

Finally, in the third flow region over the aft part of the body, the pressure changes are small, and the gas tends toward equilibrium.

Thus, the nonequilibrium state must be considered in calculating inviscid flow. However, research has shown that there is little difference in the pressure between the nonequilibrium and the equilibrium state. Therefore, the effects of nonequilibrium molecular dissociation on such inviscid flow parameters as the degree of dissociation, the density, and the temperature can be estimated by assuming that the pressure distribution is independent of the dissociated state of the gas.

Calculation of Nonequilibrium Flow

The calculation of the flow parameters requires the integration of the system of equations given in Eqs. (4.64) through (4.67) for certain given constants and boundary conditions. The results presented below[17] were obtained using the values $C = 6 \cdot 10^{14}$ cm^3/g sec and $\rho_d = 125$ g/cm^3. The boundary conditions for the integration of the equations were the conditions on the sonic line, which were determined for a given flight velocity V_∞ and altitude H on the basis of equilibrium flow in the region of the stagnation point.

The streamline along which the nonequilibrium flow parameters were computed was located downstream of the sonic region. It was assumed that the pressure on this streamline was determined by a one-dimensional expansion as given by Prandtl-Meyer theory. It was also assumed that the length of the streamline having this pressure distribution would be of the order of the radius of a spherical nose, or one-fourth the radius of a flat face (or of a slightly curved face). The dimension assumed for the initial supersonic expansion also determines the characteristic length in Eq. (4.68) for $\bar{\varphi}$.

The pressure distribution is shown in Fig. 243, calculated on the basis of Prandtl-Meyer theory for a streamline passing through an expansion fan originating at the sonic point. In the present case, the radius of curvature of the streamline is assumed to be constant and approximately equal to the radius of curvature of the surface; the expansion angle is $\nu = \bar{x} = x/R_N$.

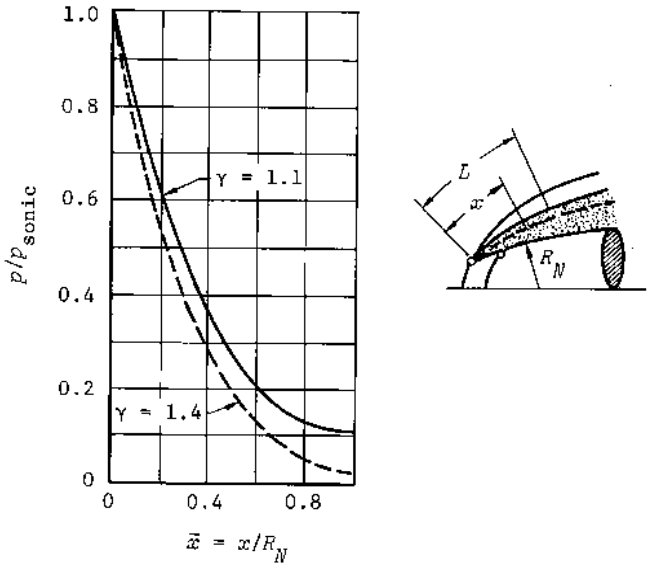

Fig. 243--Pressure distribution along a streamline for a Prandtl-Meyer expansion

Some results of the numerical integration of Eqs. (4.64) through (4.67) for various altitudes and flight velocities[17] are presented in Figs. 244 through 248. In each case the calculations were made for several values of the characteristic length L (corresponding to different values of the parameter $\bar{\varphi}$).

The character of the variation in nonequilibrium dissociation can be determined from Fig. 244. In addition, curves are shown for the variation in the equilibrium degree of dissociation for real air (B) and a model of a diatomic gas (A). It should be noted that the values of the

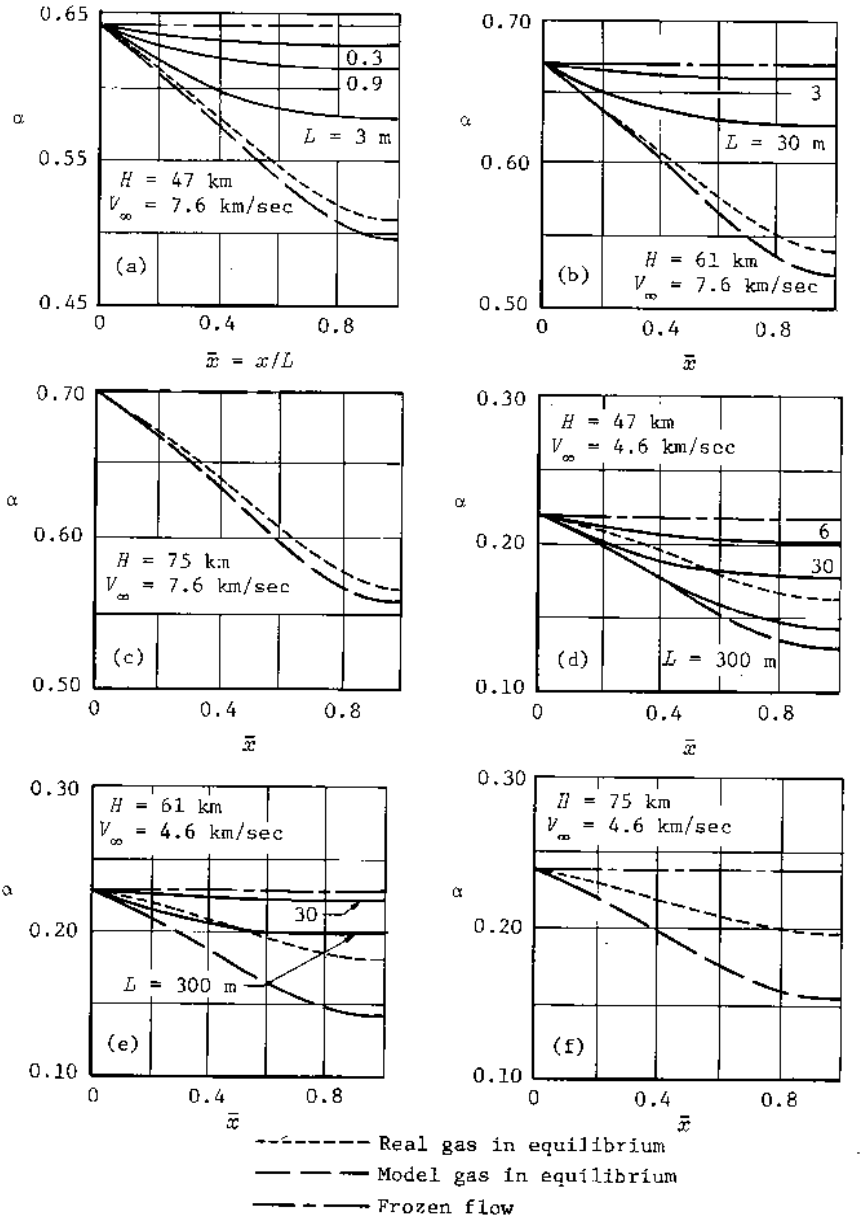

Fig. 244--Nonequilibrium effects on the degree of dissociation along a streamline

equilibrium degree of dissociation for the model gas are in good agreement with those for air at the higher velocity (7.6 km/sec). In the case of the nonequilibrium calculations, the change in the degree of dissociation along the streamline compared with the initial equilibrium value α_{0e} is generally quite small even for rather large values of L. This state of the gas is referred to as being close to "frozen." The frozen state is characterized by the fact that no reactions occur in the gas, and therefore its chemical state does not change.

In practical cases, the flow can be considered frozen if the state of the gas differs from the initial state by no more than about 5 percent. The state of the gas can also be defined by comparing the change in the degree of dissociation with the maximum possible change. If α_1 is the nonequilibrium degree of dissociation at the end of the region of expansion, the gas can be assumed to be in the frozen state if

$$\bar{\alpha}_1 = \frac{\alpha_1 - \alpha_{1e}}{\alpha_{0e} - \alpha_{1e}} \geq 0.95,$$

where α_{1e} is the equilibrium degree of dissociation at the end of the same region. If $\bar{\alpha}_1$ is less than about 0.05, the flow can be considered to be in equilibrium.

Returning to Fig. 244, it should be noted that flow in the expansion region near a blunt body will be practically frozen at altitudes higher than 47 km for flight velocities of 5 to 8 km/sec. For a fixed flight velocity and length L the flow becomes more frozen as the altitude increases, and for a fixed altitude and length the flow becomes more frozen with a decrease in velocity. An increase in freezing is also observed for a decrease in the characteristic length L. This is due to the decrease in the time a particle of gas remains in the expansion zone, during which time only a few atoms succeed in recombining.

From the results presented in Figs. 245 and 246, it follows that the deviation from equilibrium is caused by a reduction in density and an increase in temperature, which also leads to substantial changes in the local Reynolds number. However, the calculations show that the deviation from equilibrium flow has a small effect on the pressure.

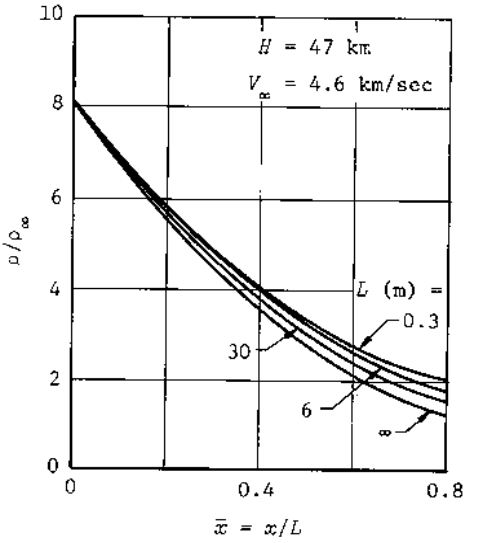

Fig. 245--Density ratio for nonequilibrium flow of a diatomic gas

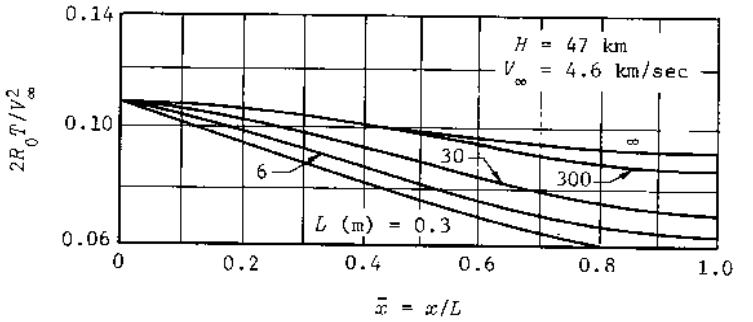

Fig. 246--Temperature distribution for nonequilibrium flow of a diatomic gas

Curves for the nonequilibrium dissociation parameter $\tilde{\alpha}_1$ as a function of $\bar{\varphi}$ are presented in Fig. 247. For the frozen state $\bar{\varphi} < 0.001$, and for the equilibrium state $\bar{\varphi} > 1$.

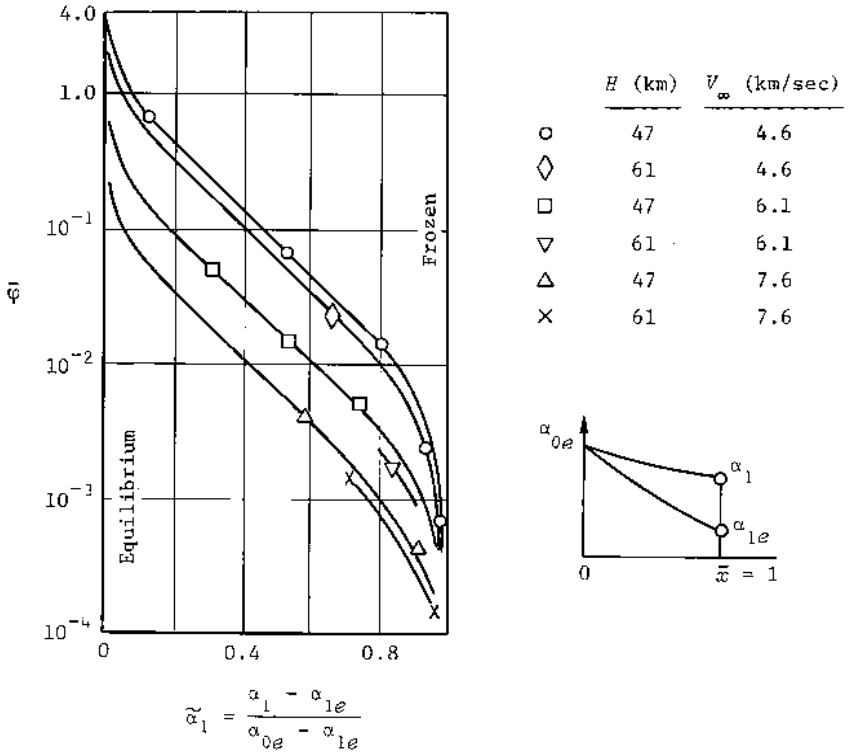

Fig. 247--The nonequilibrium dissociation parameter for various flow conditions

After the expansion, the flow enters a region of slowly changing pressure, which to simplify the analysis can be assumed to be a region of constant pressure. If a conical section lies behind the blunt nose, the pressure is actually almost constant. In this region of constant pressure, the gas particles are able to return to an equilibrium state, with constant values of enthalpy and pressure. During this transition the nonequilibrium parameters can be determined from the integration of Eq. (4.67). The initial conditions can be considered to be the frozen parameters at the end of the section of supersonic expansion discussed above (the length is measured from that station). The results show that, at velocities of 4.6 to 7.6 km/sec, the flow in the section behind the nose continues to remain frozen at a distance of more than 6 to 9 m.

This distance corresponds to an altitude of 45 to 47 km and increases for higher altitudes. For example, at H = 61 km, L increases to 30 m.

Some results of the calculation for an altitude of 47 km are presented in Fig. 248. It is evident that the approach to equilibrium conditions occurs more rapidly at the higher velocities.

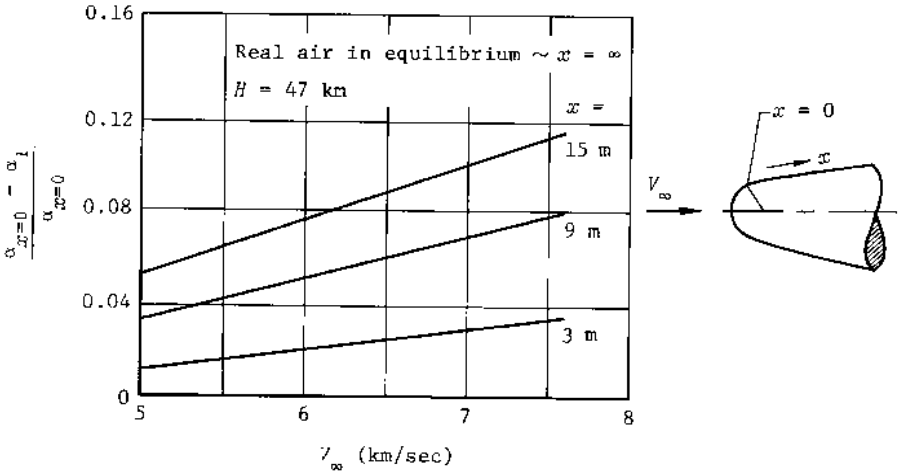

Fig. 248--Degree of dissociation along a streamline near a conical surface with constant pressure

The phenomenon of frozen flow is observed not only in the region with a zero pressure gradient but to an even greater degree in flow with a negative pressure gradient, such as that over a cylinder following a blunt nose. This is because the pressure reduction is accompanied by a decrease in density, and the term on the right side of Eq. (4.67) that represents recombination varies approximately proportionally to the square of the density.

The following conclusions can be reached from this discussion of nonequilibrium flow around a blunt body. Since the entire region of flow stemming from the strong part of the shock wave continues to remain frozen along almost the whole length of a blunt body, the inviscid flow parameters along a streamline in this shock layer can be calculated from isentropic flow conditions for γ_2 = 1.1 to 1.2 (the exact value of

γ_2 can be calculated for the stagnation conditions). The temperature and density at a given point can be found from the expressions

$$\frac{T}{T_0'} = \left(\frac{p}{p_0'}\right)^{(\gamma_2-1)/\gamma_2}, \qquad \frac{\rho}{\rho_0'} = \left(\frac{p}{p_0'}\right)^{1/\gamma_2}. \tag{25.1}$$

These approximate results for nonequilibrium flow around blunt bodies can be used in the calculation of friction and heat transfer parameters. It is apparent that the local temperature in the boundary layer will be higher, and the density and Reynolds number will be lower, than the corresponding values for equilibrium flow.

ESTIMATES OF NONEQUILIBRIUM EFFECTS IN THE VICINITY OF BLUNT BODIES

Nonequilibrium Effects between a Normal Shock and the Stagnation Point

We assumed above that thermodynamic equilibrium was established in the vicinity of the blunt nose. Strictly speaking, this premise is only valid for specific flight conditions and pertains to that part of the decelerated flow that is adjacent to the blunt surface.

In the region close to the shock wave, the flow will always be in a nonequilibrium state. It is necessary to estimate the extent of this region and to determine whether it includes the stagnation region on the body. For this purpose, the relaxation length x_D can be used. It is evident from Fig. 47 that equilibrium is attained at approximately $\bar{x} = 1$. Therefore, an expression for the relaxation length can be obtained from the second part of Eq. (2.31):

$$x_D = \int_0^1 V t_D \, d\bar{x}.$$

If average values of V and t_D are assumed on the portion of the streamline between the shock and the body, the relaxation length is

$$x_D = V t_D. \tag{25.2}$$

The time t_D can be determined from Eq. (2.31), if it is assumed that

$\rho_d = 130$ g/cm^3 for a diatomic model of air. Then the product $C\rho_d$ is

$$\bar{C} = C\rho_D = 6\cdot10^{14}\cdot130 \text{ sec}^{-1} = 7.8\cdot10^{16} \text{ sec}^{-1}.$$

The density can be assumed equal to the average value $\bar{\rho} = 0.5(\bar{\rho}_2 + \bar{\rho}_e)$, where $\bar{\rho}_2$ and $\bar{\rho}_e$ are the dimensionless densities behind the shock (for $\alpha = 0$) and for equilibrium, respectively.† Finally, setting $\alpha = 0.5\alpha_e$ in Eq. (2.31), we obtain an approximate estimate of the relaxation time:

$$t_D = \frac{2.8\cdot10^{-7}(1 - \alpha_e)}{\alpha_e(3 - \alpha_e)[f_\rho(H)\tilde{\rho}]^2}, \tag{25.3}$$

where $f_\rho(H) = \rho_{\infty H}/\rho_{\infty SL}$ is a function of altitude, and the density ratio $\tilde{\rho} = \rho/\rho_{\infty H}$ is determined as the average $\tilde{\rho} = 0.5(\tilde{\rho}_2 + \tilde{\rho}_e)$. The time t_D given by Eq. (25.3) is also called the characteristic reaction time.

As an example, let us calculate t_D for flight conditions at an altitude of 30 km and a velocity of 8.1 km/sec, for which it was shown in §4 that $\tilde{\rho}_e = 14$ and $\alpha_e = 0.735$. Then $\tilde{\rho} = 0.5(14 + 6) = 10$ and the altitude function $f_\rho(H) = 1.45\cdot10^{-2}$, so that

$$t_D = \frac{2.8\cdot10^{-7}(1 - 0.735)}{0.735(3 - 0.735)(1.45\cdot10^{-2}\cdot10)^2} = 2.1\cdot10^{-6} \text{ sec}.$$

The relaxation time of nitrogen and oxygen can be estimated approximately with the aid of Fig. 25 or Eq. (2.32), with the temperature T computed as an average between the values directly behind the shock ($\alpha = 0$) and in the equilibrium state ($\alpha = \alpha_e$).

To determine the relaxation length, we assume that the average velocity along the axial streamline $V = 0.5V_0$, where V_0 is the velocity directly behind the normal portion of the detached shock. Therefore,

$$x_D \approx 0.5V_0 t_D. \tag{25.2a}$$

†Editor's note: Here $\bar{\rho}$ is defined as in §4, i.e., $\bar{\rho} = \rho/\rho_d$. In §20, recall that $\bar{\rho} = \rho_\infty/\rho$, which is defined here as $1/\tilde{\rho}$.

If this length is less than the distance s_0 between the shock and the body, the relaxation zone is located close to the wave and does not include the body surface.

Thus, the condition of equilibrium in the vicinity of the nose will be $x_D \ll s_0$ or $0.5V_0 t_D \ll s_0$. This can also be expressed as an inequality $t_D \ll 2s_0/V_0$, where the term on the right represents the characteristic time t_{s0} that the particles remain in the region of nonequilibrium reaction (the "dwell" time). If this time is substantially larger than the characteristic reaction time, i.e., if $t_{s0} \gg t_D$, the gas particle attains equilibrium before it reaches the surface.

To illustrate, let us turn to the earlier example. For a value of $\tilde{\rho} = 10$, the dimensionless detachment distance is given by Eq. (20.39) as $\bar{s}_0 = 0.074$.† If it is assumed that $R_N = 0.5$ m, the absolute distance between the shock and the body is $s_0 = 37$ mm. The velocity behind the shock wave†† is $V_0 = 1350$ m/sec from Eq. (4.11), so that the characteristic dwell time is

$$t_{s0} = \frac{2s_0}{V_0} = \frac{2 \cdot 37 \cdot 10^{-3}}{1350} = 5.5 \cdot 10^{-5} \text{ sec.}$$

Thus, in this example, the relaxation time is approximately 26 times less than the dwell time. In other words, the extent of the relaxation zone is about 1/26 of the distance between the shock and the body and extends for only about 1.5 mm behind the shock wave.

It is apparent from Eq. (25.3) that the relaxation time increases with an increase in altitude and, thus, the extent of the nonequilibrium zone is increased; e.g., with an increase in altitude to 40 km, the time t_D increases by a factor of 23 and the relaxation length is 35 mm.

The basic parameter for estimates of the flow regime is the ratio of the relaxation time to the dwell time, i.e., $\bar{t}_D = t_D/t_{s0}$. Since $t_{s0} = 2s_0/V_0$ and $s_0 = \bar{s}_0 R_N$, the ratio of the characteristic times is

$$\bar{t}_D = \frac{t_D V_0}{2\bar{s}_0 R_N}. \tag{25.4}$$

†Editor's note: See the previous note.

††Editor's note: Calculated for $\tilde{\rho} = 6$.

The parameter $\bar{\varepsilon}_0 = \varepsilon_c/R_N$ is a function of the density ratio behind and ahead of the normal shock, as given, for example, by Eq. (20.39).

The quantity $R_N\bar{t}_D$ is shown in Fig. 249 as a function of Mach number and altitude, as calculated from Eqs. (25.3) and (25.4) for oxygen, if it is assumed that the dissociation of O_2 occurs at a wall temperature of 1500°K. Thus, the quantity $R_N\bar{t}_D$ can be determined as a function of M_∞ and H and then, for a given radius of sphere in meters, the flow regime can be estimated. For example, if $\bar{t}_D$ is less than 0.1 to 0.01, the region can be assumed to be in equilibrium.

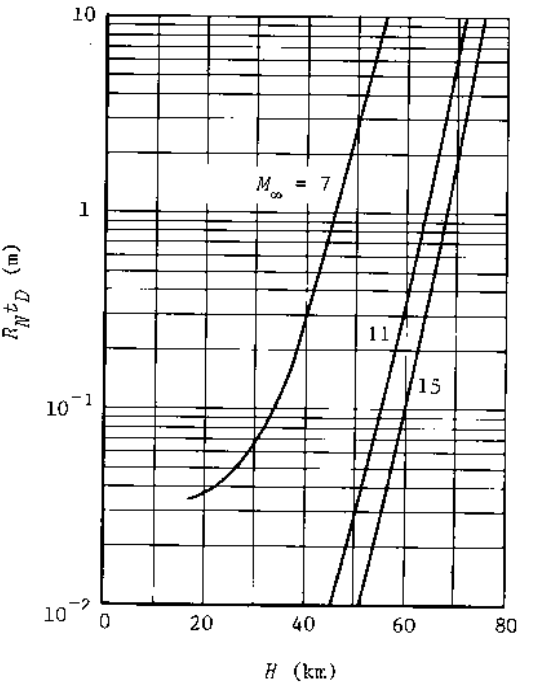

Fig. 249--Ratio of the relaxation time to the dwell time in the reaction zone

It must be kept in mind that the data in Fig. 249 represent a rather rough approximation even for oxygen, since the average temperature between the body and the shock is higher than T_w. Therefore, these data

can be used only to establish a qualitative picture of the flow. Similar graphs can be constructed taking into account all of the factors, which can then be used for quantitative estimates of the nonequilibrium effects.

Effects of Nonequilibrium on the Position and Shape of the Shock Wave

A hot gas layer will exist between the shock and the body for all cases of high velocity flow over a blunt body, and some region of nonequilibrium flow will always occur. This region will affect the shape and location of the shock wave. After examining the following two limiting cases, a qualitative estimate of this effect can be given.

The first case is characterized by completely frozen flow behind the shock wave; the gas behaves as a medium with constant specific heats corresponding to the instant accommodation of the vibrational degrees of freedom behind the shock wave. However, the greatest effect results if these degrees of freedom remain undisturbed. In the second limiting case, the gas is in a compressed layer under conditions of equilibrium dissociation. In the first case the shock lies farthest from the stagnation point and in the second case it is located closest to that point. Real nonequilibrium flows are bounded by these limiting cases, and the shock waves are located at intermediate positions.

These flows can be described by a nonequilibrium parameter that can be determined in the following way. From Eq. (4.67) it follows that, for flow conditions behind a normal shock, the quantity $1/Cp_\infty$ can be considered as a time scale for dissociation, and the parameter V_∞/Cp_∞ as a scale of length for the flow. Then, the ratio of a linear dimension of the body to the linear scale of the flow can be used as a dimensionless parameter for nonequilibrium flow.

The linear dimension for a sphere can be chosen as its diameter D_N, and the nonequilibrium parameter in this case is

$$\Lambda = \frac{D_N Cp_\infty}{V_\infty}. \tag{25.5}$$

If Λ equals zero, the flow is undissociated (frozen), which results from an infinitely slow chemical reaction. Large values of Λ correspond to rapid reactions and, therefore, dissociation begins close to the shock

and includes almost the entire region between the shock and the body. For $\Lambda \to \infty$, equilibrium is reached immediately behind the shock.

To analyze the flow between the shock wave and the body, a local value of Λ can be used, calculated from the local velocity on the zero streamline; i.e.,

$$\lambda = \frac{D_N C \rho_\infty}{V}. \tag{25.5a}$$

At the stagnation point, where $V = 0$, we obtain $\lambda = \infty$, and the dissociation is in equilibrium. This is because of the very low velocity near the stagnation point, which allows sufficient time for thermodynamic equilibrium to be established.

The extent of the nonequilibrium region can be estimated from the average velocity along the zero streamline, as was done above. If it is assumed that there is equilibrium flow on the body surface, the distribution of the concentrations of the atomic components along the normal to the wall are represented qualitatively by a gradual decrease in the direction of the shock wave, where the degree of dissociation is set equal to zero.

A theoretical profile of the concentrations can be calculated by a simultaneous solution of the flow equations and Eq. (4.67) in the vicinity of the stagnation point. Profiles for several special cases are presented in Fig. 250.

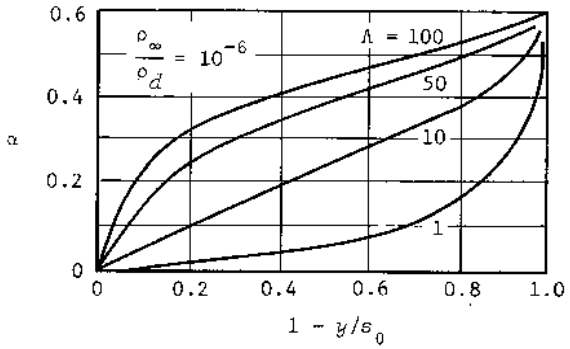

Fig. 250--Degree of dissociation along the axial streamline between the shock wave and the stagnation point

One of the results of the solution is the determination of the distance from the shock to the body. The variation in the relative displacement distance as a function of the nonequilibrium parameter Λ is presented in Fig. 251. It can be noted that the displacement in the two limiting cases, i.e., in frozen and equilibrium flows, can differ by a factor of two. The variation in the radius of curvature of the shock wave at the axis has approximately the same character.

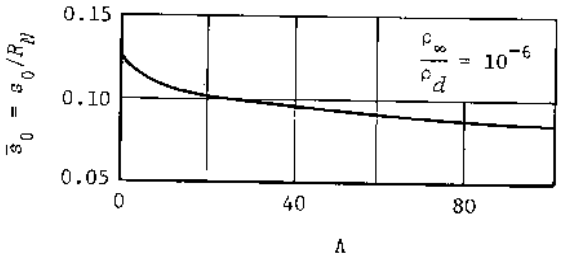

Fig. 251--Dimensionless shock-detachment distance as a function of the nonequilibrium parameter

The Case of Nonequilibrium at the Surface

The ratio of the characteristic times can be used for a preliminary estimate of the conditions for which chemical reactions occur at the wall. It is obvious that these reactions occur only for $\bar{t}_D \geq 1$, i.e., when the atoms reach the surface before they react. To estimate the extent of the length along the surface where chemical reactions take place, it is necessary to compare the characteristic time of the reaction with the characteristic dwell time of the particles in the nonequilibrium region in question. The dwell time is also a function of $d\alpha/dt$, which determines the rate of change in the degree of dissociation resulting from the disappearance of atoms due to recombination. The time of this disappearance is equal to the characteristic dwell time in the reaction zone and is determined from the equation

$$\frac{dt}{d\alpha} = \frac{1}{V}\frac{dx}{d\alpha}.$$

For an approximate estimate, it can be assumed that $dx/d\alpha \sim L/\alpha_0$, where α_0 is the nonequilibrium degree of dissociation at the stagnation point. Therefore, the dwell time can be represented in the form $L/\alpha_0 V$, where V is the velocity of a particle along the surface near the stagnation point. Assuming that this velocity is of the same order of magnitude as the average velocity between the wave and the body, $0.5V_0$, we get the ratio of the characteristic times:

$$\bar{t}_L = \frac{t_D V \alpha_0}{L} = \frac{t_D V_0 \alpha_0}{2L}, \tag{25.6}$$

which can be rewritten as

$$\bar{L}\bar{t}_L = \bar{t}_D \alpha_0 \bar{s}_0, \tag{25.6a}$$

where $\bar{L} = L/R_N$. In the zone of reaction, $\bar{t}_L \geq 1$, and the length of this region from the stagnation point is given by

$$\bar{L} = \bar{t}_D \alpha_0 \bar{s}_0. \tag{25.7}$$

As an illustration, the example used previously can be analyzed for an altitude of 50 km instead of 30 km. The density ratio (or the altitude function f_ρ) is decreased by a factor of 19 compared with that for 30 km, and the relaxation time is increased by the factor $(19)^2 = 361$. Therefore, the ratio of the characteristic times is $\bar{t}_D = 361/26 = 14$. For $\bar{s}_0 = 0.074$ and $\alpha_0 = 0.5$, we obtain $\bar{L} = 14 \cdot 0.5 \cdot 0.074 = 0.52$, and the length of the nonequilibrium zone is $L = 0.26$ m for a sphere with $R_N = 0.5$ m.

Over this length of the surface, atoms enter the boundary layer without having entered into chemical reactions. The process of recombination is completed in the boundary layer, producing well-known effects on the friction and heat transfer. However, it should be stressed that, in general, the pressure distribution is not altered by the nonequilibrium effects.

A more accurate definition of the flow regime in the stagnation zone (at the stagnation point and in some region downstream) provides

an estimate of the change in density and temperature if the flow in this region is not in equilibrium. The temperature increases and the density decreases at the outer edge of the boundaty layer compared with the equilibrium state. It can be assumed that, despite the temperature increase, the heat flux to the surface decreases somewhat due to the lower density.

All of the calculations so far have been made on the assumption that the recombination-rate parameter k_R is not a function of temperature. However, temperature actually has considerable influence on this parameter, and according to some experimental data for oxygen[17]

$$k_R = 8.4 \cdot 10^{14} \left(\frac{3500}{T}\right)^2 \text{ cm}^6/\text{mole}^2 \text{ sec.} \tag{25.8}$$

This temperature factor can be applied to the expression for the relaxation time, resulting in a corrected relaxation time:

$$\bar{t}_D' = \bar{t}_D \left(\frac{T}{3500}\right)^2. \tag{25.9}$$

Relaxation Effects for Expansion from Equilibrium Conditions at the Stagnation Point

In the case considered above, the nonequilibrium region included part of the surface of the body. Another case of interest is that for which the air in the vicinity of the stagnation point is in thermodynamic equilibrium. However, this equilibrium can be disturbed as the flow expands over the surface, because the inert degrees of freedom will not have time to adjust to the rapid changes in temperature and pressure.

This type of nonequilibrium flow will be frozen in the sense that the expansion occurs only with the participation of the active degrees of freedom and with fixed (frozen) thermodynamic parameters, i.e., with the specific heat and degree of dissociation established by the condition of thermodynamic equilibrium at the stagnation point. Therefore, the temperature of the isentropic expanding flow is determined by the translational and rotational degrees of freedom and will be less than for equilibrium conditions. As the particles continue on their paths,

relaxation effects in the gas will increase the internal energy as the inert degrees of freedom begin to adjust, and the temperature will increase compared with that for frozen flow. Since the heat input is irreversible, this process is accompanied by an increase in entropy.

An equilibrium flow of gas can also be maintained for a slow flow over the surface in the vicinity of the stagnation point, i.e., when the relaxation times of the inert degrees of freedom are small compared with the characteristic times of the process. The characteristic time can be written in the form

$$\Delta t = \frac{dt}{dT} T. \tag{25.10}$$

This expression represents a quantity inversely proportional to the rate of change of temperature in an adiabatic flow of a gas along a streamline.

If Δt is considerably larger than the maximum relaxation time t_D of the inert degrees of freedom, equilibrium can be maintained. The condition for maintaining equilibrium can be given, for example, in the form of an inequality $t_D/\Delta t < 10^{-3}$.

To determine the equilibrium region in the vicinity of the stagnation point, it is necessary to calculate the ratio $t_D/\Delta t$ for various points on the surface and to compare it with the value above. For this purpose, the temperature distribution as well as the velocity along the surface are calculated for equilibrium conditions.

Assuming that the velocity varies approximately linearly with time, we can find the variation of temperature with time and, therefore, compute the value Δt at each point. The distribution of $t_D/\Delta t$ is presented in Fig. 252 for flow around a sphere with R_N = 0.61 m. The gas used was nitrogen at M_∞ = 24 for conditions corresponding to an altitude of 37 km. For a maximum value of $t_D/\Delta t = 10^{-3}$, it is apparent that equilibrium flow for both the inert degrees of freedom, vibration, and recombination occurs only up to values of the central angle φ less than 30°. For larger values, equilibrium is not possible, and the gas flows as a frozen medium.

Calculations show that the local Reynolds number and Mach number of the frozen and equilibrium flows differ little, although the temperature in the frozen flow is 20 percent less than in equilibrium flow for the example in question.

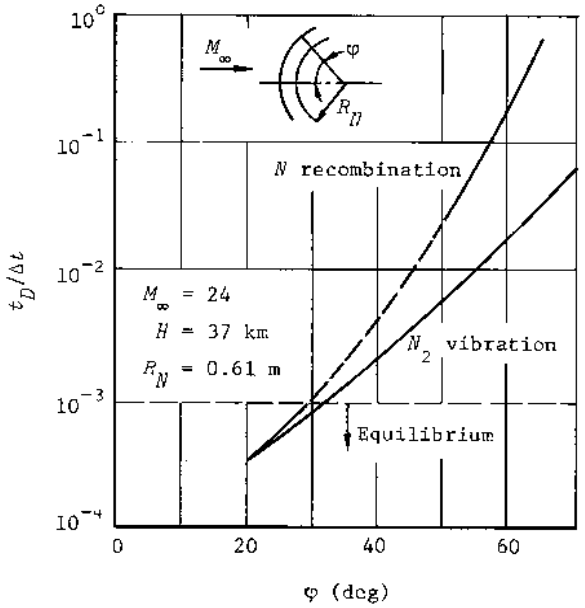

Fig. 252--Equilibrium and frozen flow regions around a sphere

Chapter VIII

SKIN FRICTION AND HEAT TRANSFER ON BLUNT BODIES

Editor's Introduction

MOST OF THE FIRST SECTION (§ 26) *of this chapter consists of a summary of the analysis of Moeckel*[1] *on the effects of bluntness in delaying boundary layer transition. The results provide an estimate of the bluntness required to delay transition to the point at which the thickness of the boundary layer and the entropy layer are equal. Wilson (*J. Spacecraft and Rockets, *July-August 1965) has solved the more general problem of the growth of a laminar boundary layer on a blunted cone, giving results for the effect of blunting on skin friction, heat transfer, and the flow conditions at the outer edge of the boundary layer. The local skin friction and heat transfer are reduced significantly by the slight blunting of the nose. The decay of the entropy layer far back on the body (discussed qualitatively at the end of Section 26) is also calculated by Wilson, and the effect of this decay on the heat transfer and skin friction is evaluated (discussed briefly on pp. 723-724).*

*Formulas for heat transfer at the stagnation point are given in Section 27, and the effects of nonequilibrium chemistry are discussed briefly on pp. 690-691. Tong (*AIAA J., *April 1965) shows that the nonequilibrium-flow Stanton numbers for noncatalytic and fully catalytic surfaces lie on the same curve if the enthalpy at the wall is defined as* $i_w = i_D c_w + (i_w)_0$, *where* $(i_w)_0$ *is the wall enthalpy with no dissociation. Tong gives correlation curves for determining the atom concentration* c_w *for a noncatalytic wall. Inger (*J. Spacecraft and Rockets, *March 1966) presents a relatively simple analytical method for predicting the effects of nonequilibrium dissociation on heat transfer to bodies with arbitrary surface catalyticity. The method is applicable downstream on the body as well as at the stagnation point.*

*Radiative heat transfer from the high temperature shock layer about the nose of a blunt body has been the subject of extensive study in recent years, particularly with regard to radiation cooling and self-absorption of radiation in shock layers. Representative of these studies are those of Hoshizaki and Wilson (*AIAA J., *January 1967) and Hoshizaki and Lasher (*AIAA J., *August 1968). They show that the combined effects of radiation cooling and self-absorption result in a significant reduction in the radiative flux to the surface, but have little effect on convective heat transfer; the total heating rate at the surface is almost*

independent of nose radius. Ablation products of typical ablator materials (particularly carbon atoms) can produce a substantial reduction in radiative heat transfer at the surface. Anderson (AIAA J., *November 1968) has published a simple and reasonably accurate method for estimating radiative heat transfer with radiation cooling and self-absorption.*

A very general computer solution for the laminar boundary layer has been developed by Smith and co-workers and described in a series of papers; see for example, Smith and Clutter (AIAA J., *April 1965) and Smith and Jaffe* (AIAA J., *April 1966). The method is valid for nonequilibrium dissociating air with finite reaction rates for axisymmetric or two-dimensional flow over surfaces with arbitrary catalyticity.*

Experimental data for turbulent heat transfer on blunt and sharp-nosed bodies of revolution have been correlated by Zoby and Sullivan (NASA TN D-3802, *January 1967); the results confirm the validity of Eqs. (27.76) to (27.78). Simple empirical formulas based on the results of Ref. 9 have been proposed by Arthur, Schultz, and Guard* (J. Spacecraft and Rockets, *October 1966).*

Experimental results for the drag of blunted cones at high Mach numbers have been used by Whitfield and Griffith (AIAA J., *October 1964) to evaluate theoretical estimates of viscous contributions to the drag. The major contributions resulted from the usual skin friction drag and the effects of transverse curvature, boundary layer displacement effects being small.*

§ 26. *CHANGES IN FLOW CHARACTERISTICS DUE TO BLUNTING*

THICKNESS OF THE INVISCID LAYER AT LOW VELOCITIES

AS HAS BEEN MENTIONED previously, the most important effect of blunting appears as a decrease in local Reynolds numbers, resulting in an aft movement of the transition point from laminar to turbulent flow, and thus in a reduction in friction and heat transfer.

The decrease in Reynolds number is caused by the fact that the boundary layer is located in a flow region of lesser velocity than on a pointed body due to the strong shock wave in front of the blunt body. Since this causes the transition point to shift toward the base of the body, the heat flux will be less. If the maximum reduction in heat transfer were required, the blunting would have to be such that the laminar layer completely covered the surface, i.e., such that the transition point lay at the base of the body. It should be noted that a large length of laminar flow is only possible for absolutely smooth surfaces.

The location of the transition point is determined by the transition Reynolds number Re_{tr}, which in turn can be determined from the velocity V_δ at the outer edge of the boundary layer. Therefore, for completely laminar flow, the blunting should be sufficient so that the flow in the high-entropy "inviscid" layer† (covering the boundary layer) has the necessary value of V_δ at the end of the body.

Studies[1] have shown that the outer edge of the high-entropy inviscid layer lies approximately on the streamline passing through the sonic point on a detached shock wave (Fig. 196). The location of the sonic point on the shock can be calculated for the general case including dissociation, as was discussed earlier. If the radial coordinate

†Editor's note: This is often called the entropy layer in American literature. We will continue to use the Russian term.

of this point is r_S, the rate of flow of gas through a cross section with an area πr_S^2 will be $\rho_\infty V_\infty \pi r_S^2$. The same amount of gas flows through the low Reynolds number layer having a thickness Δ (Fig. 196). In what follows we will neglect the effect of the boundary layer on the extent of the high-entropy layer. The thickness Δ corresponds to a section of the body with a radius r, so that

$$\rho_\infty V_\infty r_S^2 = 2\rho V r \Delta,$$

whence the thickness of the inviscid layer is

$$\Delta = \frac{1}{2} \frac{\rho_\infty}{\rho} \frac{r_S^2}{r} \frac{V_\infty}{V}, \tag{26.1}$$

where ρ and V are the density and velocity at the section under consideration, calculated for inviscid flow along the surface. Although these parameters should be determined including the effect of blunting, the calculations can sometimes be simplified if the pressure at some distance from the blunt nose is assumed to be the same as that on a pointed body. This was evident in the case of flow around a blunt cone.

The local density, temperature, enthalpy, and speed of sound can be determined at a given cross section from the local pressure and entropy behind the normal part of the shock wave by using the graphs or tables of the thermodynamic functions of air. Next, using the equation $i_0 = i + V^2/2$, we can compute the local velocity and Mach number. Thus, the influence of dissociation or the variation of the specific heat of the gas on passing through the shock wave can be considered.

The gasdynamic and thermodynamic parameters at stations far downstream from the nose can be computed with sufficient accuracy by using the relations for isentropic gas flow with constant specific heats. In this case, the equations for velocity, Mach number, and density have the following form:

$$\frac{V^2}{V_\infty^2} = \frac{1 - \left(\frac{p}{p_0} \frac{p_0}{p_0'}\right)^{(\gamma-1)/\gamma}}{1 - \left(\frac{p_\infty}{p_0}\right)^{(\gamma-1)/\gamma}}, \tag{26.2}$$

$$M^2 = \frac{2}{\gamma - 1}\left[\left(\frac{p_0'}{p_0}\frac{p_0}{p}\right)^{(\gamma-1)/\gamma} - 1\right], \tag{26.3}$$

$$\frac{\rho}{\rho_\infty} = \frac{\dfrac{\rho_0}{\rho_\infty}\dfrac{p_0'}{p_0}}{\left(1 + \dfrac{\gamma - 1}{2}M^2\right)^{1/(\gamma-1)}}. \tag{26.4}$$

To increase the accuracy of the calculations, the stagnation pressure can be selected as an average between the values at the points B and S (Fig. 196, p. 545), the first of which is located directly behind the normal part of the shock wave and the second at the sonic point.

It is apparent that the difference in the values of the parameters on the surfaces of pointed and blunt bodies is caused by unequal losses in total pressure through the shock wave. Since the shock in the vicinity of the nose is stronger in front of a blunt body, the value of p_0' will be less than for a pointed body. Then the local velocities, Mach numbers, and densities will also be less, as can be determined from Eqs. (26.2) through (26.4). The local Mach numbers on a blunt cone have been calculated from Eq. (26.3) assuming that the pressure is the same as on a pointed conical surface; the results are shown in Fig. 253.

If the relations for velocity and density are introduced into Eq. (26.1), the thickness of the low Reynolds number layer can be determined as a function of the body station provided the location of the sonic point on the shock wave is known. The cross-sectional area of this layer is equal to $2\pi r\Delta$. Shown in Fig. 254 is the ratio of the areas

$$\frac{F_S}{F_{SN}} = \frac{2\pi r\Delta}{\pi r_{SN}^2} = \frac{r_S^2}{r_{SN}^2}\frac{\rho_\infty}{\rho}\frac{V_\infty}{V}, \tag{26.1a}$$

where r_{SN} is the radial coordinate of the sonic point on the surface of a spherical nose. It was assumed in these calculations that the radius to this point is twice as large as that to the sonic point on the shock wave; i.e., the ratio r_S^2/r_{SN}^2 in Eq. (26.1a) is equal to 0.25.

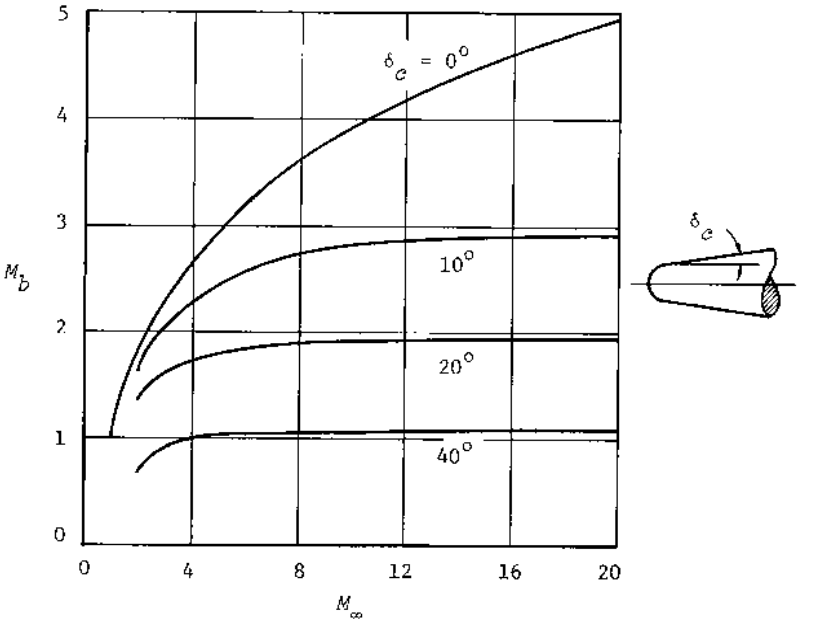

Fig. 253--Mach number on the surface of blunt cones in inviscid flow

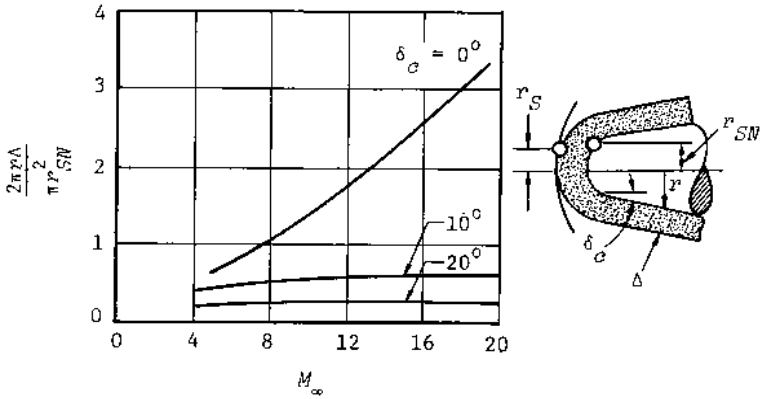

Fig. 254--Ratio of the area of the low-velocity layer on cones to the area πr_{SN}^2

It is evident from Fig. 254 that, for the assumptions made, the area ratio represented by this expression is of the order of unity for spherically blunted cones with small angles δ_c. If cones with flat noses are considered, it is clear from physical considerations that the low-velocity layer will be somewhat thicker. If it is assumed that the coordinates of the sonic points on the flat nose and the shock wave are approximately identical, i.e., $r_S = r_{SN} = R_N$, the area ratio F_S/F_{SN} will be four times larger than for a cone with a spherical nose, according to Eq. (26.1a). Thus, for the calculation of the thickness of the low-velocity layer, Eq. (26.1) can be used or, if the relation for the area ratio F_S/F_{SN} is given, it can be determined from

$$\Delta = \frac{F_S}{F_{SN}} \frac{r_{SN}^2}{2r}. \tag{26.5}$$

THE CALCULATION OF THE REQUIRED BLUNTING

The bluntness required (in terms of the radius r_{SN}) to maintain laminar flow to a given station can be estimated by imposing the condition that the thickness of the laminar layer at the transition point, i.e., for the required transition Reynolds number, be equal to the thickness of the inviscid low-velocity layer. Therefore, the conditions are

$$\delta_L = \frac{1}{2} \frac{\rho_\infty}{\rho} \frac{r_S^2}{r_{tr}} \frac{V_\infty}{\gamma},$$

$$\delta_L = \frac{F_S}{F_{SN}} \frac{r_{SN}^2}{2r_{tr}}, \tag{26.6}$$

where r_{tr} is the radius of the blunt cone at the transition point.

In particular, it follows from the second equation of Eq. (26.6) that if $F_S/F_{SN} \approx 1$, the coordinate r_{SN} should be of the order of $\sqrt{2r_{tr}\delta_L}$, which is the geometric mean of the diameter of the body and the thickness of the boundary layer at the transition point.

The thickness of the laminar layer at the transition point on the surface of a blunt cone can be determined from the transition Reynolds number Re^*_{tr} and the equation for a flat plate

$$\frac{\delta_L^{pl}}{x_{tr}} = \frac{4.64}{\sqrt{\mathrm{Re}^*_{tr}}},$$

in which x_{tr} is the distance to the transition point, and the transition Reynolds number $\mathrm{Re}^*_{tr} = Vx_{tr}\rho^*/\mu^*$ is calculated in the general case from the effective parameters of inviscid flow. Since the transition Reynolds number is usually assumed to be a known quantity, the length of the laminar portion can be calculated as $x_{tr} = \mu^*\mathrm{Re}^*_{tr}/V\rho^*$, and the thickness of the boundary layer at the transition point is

$$\delta_L = \frac{1}{\sqrt{3}}\delta_L^{pl} = \frac{1}{\sqrt{3}}x_{tr}\left(\frac{\delta_L^{pl}}{x_{tr}}\right). \tag{26.7}$$

For the case of constant specific heats, the equation for the calculation of the required blunting takes the form

$$\Pi = \frac{r_{SN}^2}{x_{tr}r_{tr}} = \frac{16.1}{\sqrt{\mathrm{Re}^*_{tr}}}\frac{p_0'}{p_0}\left(\frac{1+\frac{\gamma-1}{2}M_\infty^2}{1+\frac{\gamma-1}{2}M^2}\right)^{\frac{\gamma+1}{2(\gamma-1)}}\frac{M}{M_\infty}\frac{r_{SN}^2}{r_S^2}. \tag{26.8}$$

As was indicated, Re^*_{tr} is usually given in this equation and the ratios p_0'/p_0, r_{SN}^2/r_S^2, and the Mach number M on the blunt cone are determined from the known value of M_∞. In the case of rough calculations, r_{SN}/r_S can be assumed equal to 2 and 1, respectively, for a spherical and a flat nose.

The radius r_{tr} in Eq. (26.8) can be written in the form

$$r_{tr} = r_N + x_{tr}\sin\delta_c,$$

where r_N is the radius of the body at the tangency point between the spherical tip and the conical afterbody. In turn, the coordinate x_{tr} is determined from the given transition Reynolds number. To simplify

the calculations, it is possible to use the inviscid flow parameters obtained without considering the effective temperature instead of the effective parameters μ^* and ρ^*.

After determining the quantity Π and the coordinate x_{tr}, we can compute the required blunting r_{SN} or, more precisely, the coordinate of the sonic point on the nose, from

$$r_{SN}^2 = \Pi x_{tr}(r_N + x_{tr} \sin \delta_c). \tag{26.8a}$$

For a flat nose, this coordinate gives the magnitude of the radius of the flat surface, since $r_{SN} = r_N$, but for a spherical nose the radius is found from $R_N = r_{SN}/\sin \varphi$, where the angle φ is the location of the sonic point on a sphere (see Fig. 203, p. 565).

THE INFLUENCE OF BLUNTING ON THE EXTENT OF THE LAMINAR BOUNDARY LAYER

It is of interest to estimate the relative movement of the transition point due to blunting, if we assume that the transition Reynolds numbers are identical for pointed and blunt bodies (denoted by the subscripts p and b). For equal Reynolds numbers,

$$\left(\frac{V\rho x}{\mu}\right)_p = \left(\frac{V\rho x}{\mu}\right)_b,$$

and the relative shift of the transition point is

$$\frac{(x_{tr})_b}{(x_{tr})_p} = \left(\frac{V\rho}{\mu}\right)_p \left(\frac{\mu}{V\rho}\right)_b,$$

where all the parameters entering into this equation pertain to the transition point. However, for conical bodies the local flow parameters are constant along the surfaces, so the right-hand side of the previous expression simply represents the ratio of the local Reynolds numbers at a given station x:

$$\frac{(x_{tr})_b}{(x_{tr})_c} = \left(\frac{V\rho x}{\mu}\right)_c \left(\frac{\mu}{V\rho x}\right)_b = \frac{\mathrm{Re}_c}{\mathrm{Re}_b}. \tag{26.9}$$

The subscripts c and b now refer to pointed and blunt cones, respectively. Thus, the ratio of the transition points with and without blunting is directly proportional to the ratio of the local Reynolds numbers for the pointed and blunt cones:

$$\frac{\mathrm{Re}_c}{\mathrm{Re}_b} = \frac{V_c}{V_b}\frac{\rho_c}{\rho_b}\frac{\mu_b}{\mu_c}.$$

Let us assume that $\mu_b/\mu_c = (T_b/T_c)^n$ and that the pressures on the pointed and blunt cones are identical, so that $\rho_c/\rho_b = T_b/T_c$. Noting that

$$T = \frac{T_0}{1 + \frac{\gamma - 1}{2} M^2},$$

we obtain for the ratio of the Reynolds numbers

$$\frac{\mathrm{Re}_c}{\mathrm{Re}_b} = \frac{M_c}{M_b}\left[\frac{1 + \frac{\gamma - 1}{2} M_c^2}{1 + \frac{\gamma - 1}{2} M_b^2}\right]^{n+\frac{1}{2}}. \qquad (26.10)$$

The reciprocal of this ratio, which indicates the decrease in local Reynolds number due to blunting, is presented in Fig. 255. It is evident that a substantial decrease in local Reynolds number and, consequently, a considerable aft movement of the transition point, are characteristic of slender cones, and these effects are more significant for large Mach numbers. For example, according to the data in Fig. 255 for a blunt 10° cone at $M_\infty = 8$ and 15, the extent of the laminar boundary layer is increased by a factor of approximately 10 to 30.

SOME DATA ON THE TRANSITION REYNOLDS NUMBER

As we have seen, it is necessary to know at least a tentative value of the transition Reynolds number for the calculation of the required blunting. Unfortunately, there are as yet no theoretical methods for calculating this value, because at present the very nature of turbulence is not clear. Therefore, the estimation of Re_{tr} must be based

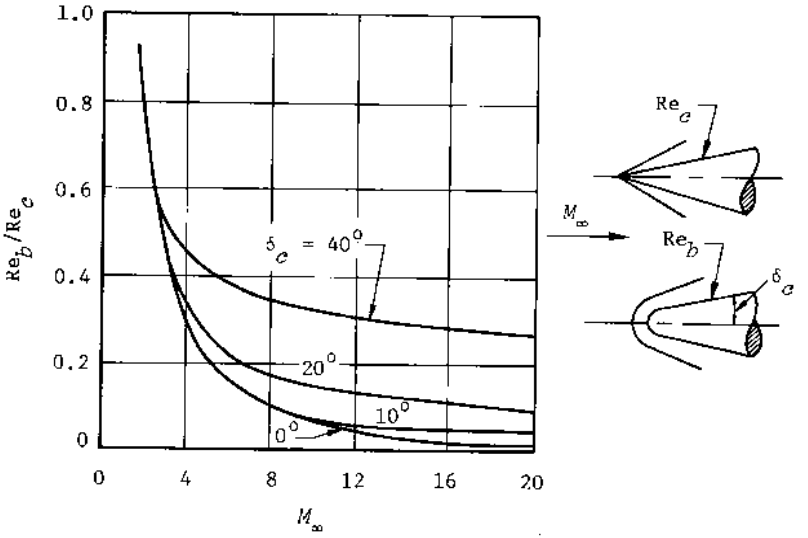

Fig. 255--Ratio of the Reynolds numbers on blunt and pointed cones

on available experimental data, which enable us to make a quantitative estimate and also to analyze, qualitatively, the phenomenon of laminar boundary layer stability and the process of transition to turbulence.

For example, it has been established that one of the main reasons for turbulence is the instability of the laminar boundary layer at large Reynolds numbers. The accidental formation of perturbations in the boundary layer due to the turbulence of the external flow or the roughness of the surface are not damped at large Reynolds numbers, making the boundary layer turbulent. Therefore, to maintain laminar flow, it is advisable to maintain a smooth surface.

If it is taken into account that the turbulence of the external flow under flight conditions in the atmosphere is negligibly small, it is possible to increase the transition Reynolds number considerably for a smooth wall. Nevertheless, an unstable condition remains, and it is desirable to take other measures to stabilize the laminar boundary layer. It has been noted that if the wall is cooled, the stability of the layer increases, because the density of the gas increases with a reduction in the gas temperature close to the surface and, consequently, the kinetic energy

of the gas increases. It is apparent that particles with large energy are less subject to the influence of perturbing pulsations. At the same time, it is worth noting that at very high velocities the Reynolds number plays a less significant role as the criterion of stability compared with such parameters as the relative temperature of the wall T_w/T_δ (T_w/T_∞ or T_w/T_r) and the Mach number M_δ at the outside edge of the boundary layer (or for a given body, M_∞).

Theoretical studies[1] enable us to determine the values of the relative wall temperature and local Mach number required for complete stability of the laminar boundary layer (Fig. 256). It is evident from

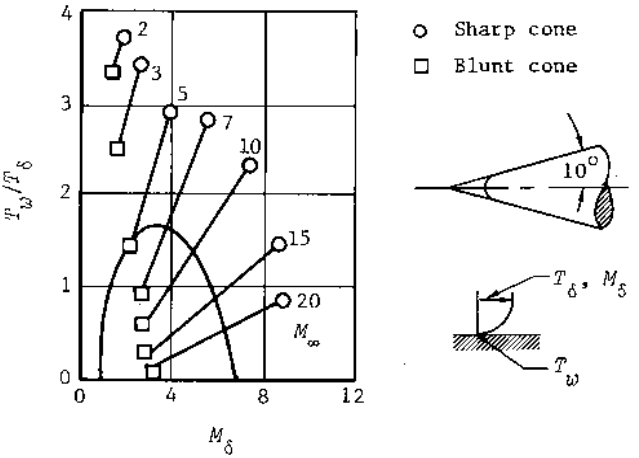

Fig. 256--Effect of blunting on the stability of the laminar boundary layer

Fig. 256 that the boundary layer cannot be stabilized at $M_\delta > 8$ irrespective of the intensity of the cooling. It can also be noted that the stability boundaries are broadened with a decrease in the ratio T_w/T_δ. Hence it follows that a decrease in speed of the local external flow, which is accompanied by a decrease in M_δ and an increase in T_δ, will be a stabilizing influence (if, at the same time, the wall temperature remains constant due to proper cooling). It was mentioned above that this can occur when a blunt instead of a pointed body is used.

Thus, blunting is an important means of stabilizing a laminar boundary layer, since it shifts the conditions at the external edge of the boundary layer from the unstable region toward the zone of stability, as Fig. 256 shows.

It should be noted that the region of instability located outside the curve in Fig. 256 is not necessarily a region of complete turbulence. Turbulent bursts are characteristic of the laminar layer in this region. Their formation is related to the inception of transition from laminar to turbulent flow. The transition is completed at the transition Reynolds number.

The experimental results obtained by Van Driest[2] for a fixed Reynolds number are presented in Fig. 257. The experimental model was a

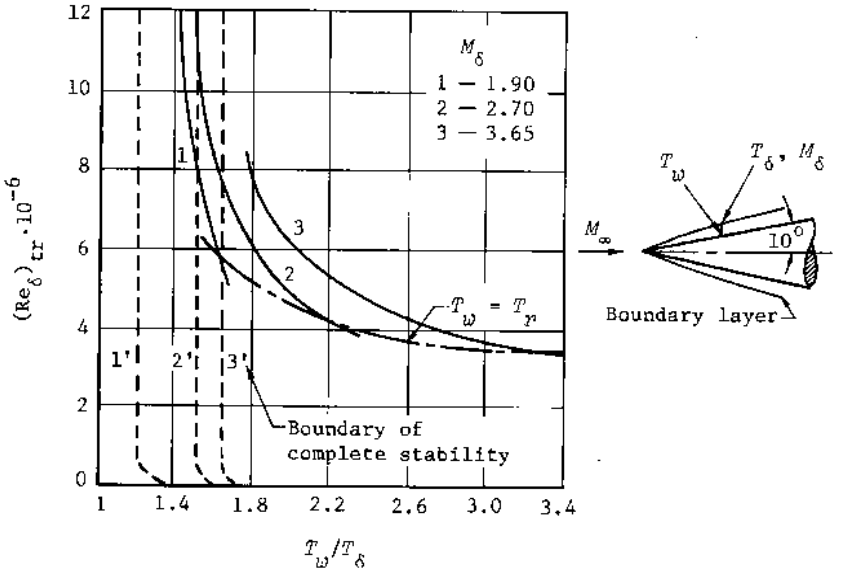

Fig. 257--Experimental data on the transition Reynolds number

pointed cone and was cooled from within, which ensured a variation in the ratio T_w/T_δ. The tests were conducted for various Mach numbers. Also presented in Fig. 257 are the theoretical curves 1′, 2′, and 3′ for the variation in the critical Reynolds numbers, corresponding to

the boundaries of complete stability. An analysis of the curves shows that the transition Reynolds number increases with a decrease in the wall temperature, while the character of this variation is a function of M_δ.

To show this relation, the curves are replotted in Fig. 258 so that the ratio T_w/T_r is represented as a parameter. First, it should

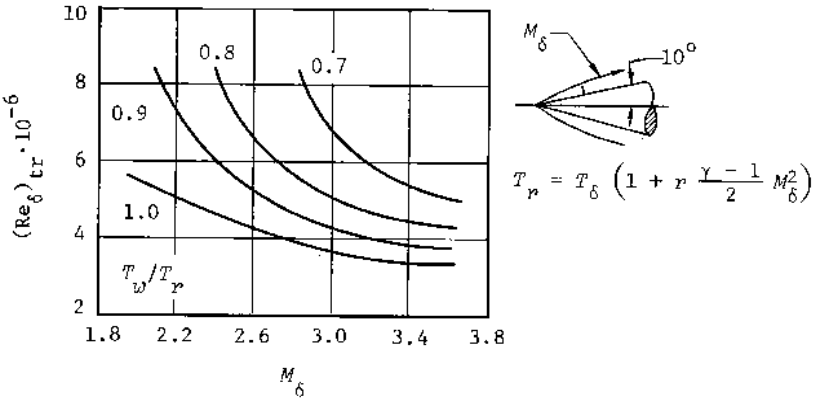

Fig. 258--Experimental data on the transition Reynolds number

be noted that the transition Reynolds number remains practically constant for M_δ greater than about 3.8. For a cooled surface ($T_w/T_r < 1$), the transition Reynolds number increases, and the estimate of the variation in Re_{tr} can be based on the fact that it is approximately inversely proportional to the relative temperature of the wall T_w/T_r, which can in turn be determined from the expression

$$\frac{T_w}{T_r} = \frac{T_w/T_\delta}{1 + r \frac{\gamma - 1}{2} M_\delta^2}.$$

The pressure gradient along the wall is known to have an influence on Re_{tr}. For example, a negative gradient is favorable for an increase in stability and, thus, for an increase in the critical and transition

Reynolds numbers. On the other hand, with a pressure increase in the direction of flow (i.e., a positive gradient), conditions are created for premature turbulence and the value of Re_{tr} decreases. The curve in Fig. 259 is for subsonic velocities and allows an estimate of the influence of the longitudinal pressure gradient on the transition Reynolds number. This curve is calculated from the empirical equation

$$\frac{(Re_{tr})_p}{(Re_{tr})_0} = \frac{1}{(1 - 0.048\lambda)^2},$$

where $\lambda = -18x\, dC_{p\delta}/dx$, and the pressure coefficient at the edge of the layer is $C_{p\delta} = 2p/\rho_\delta V_\delta^2$.

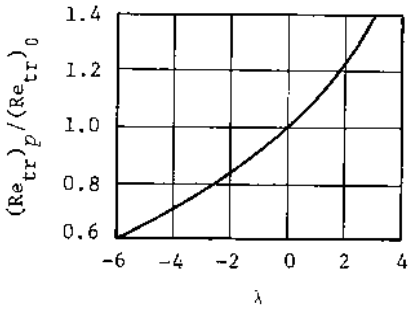

Fig. 259--Effect of longitudinal pressure gradient on the transition Reynolds number

If we consider flow around a blunt body (e.g., a cone), we find regions with various types of pressure variation on the surface. Directly behind the stagnation point, the pressure decreases and, therefore, a negative pressure gradient is established, favorable to stabilization of the laminar boundary layer. A deceleration of the flow begins at some distance from the nose, resulting in a positive pressure gradient. Generally speaking, this leads to a decrease in stability, although in practice the effect is small. Nevertheless, it is expedient to allow for this influence in the final selection of the blunting dimension by increasing it compared with the calculated dimension.

EXAMPLE

Let us calculate the location of the transition point for $M_\infty = 10$ on the smooth surface of a spherically blunted 10° cone. The Mach number on the blunt cone is determined from Fig. 253 as $M_B = 2.8$. From Fig. 258 the transition Reynolds number is $8.7 \cdot 10^6$, if it is assumed that the relative wall temperature $T_w/T_r = 0.7$, which corresponds to the ratio

$$\frac{T_w}{T_\delta} = 0.7\left(1 + \frac{\gamma - 1}{2} r M_B^2\right) = 0.7[1 + 0.169(2.8)^2] = 1.58.$$

The location of the transition point on a sharp 10° cone is determined from the equation

$$x_{tr} = \mathrm{Re}_{tr}\left(\frac{M_\infty}{M_c}\frac{\nu_\infty}{V_\infty}\right)\left[\frac{1 + \frac{\gamma - 1}{2} M_c^2}{1 + \frac{\gamma - 1}{2} M_\infty^2}\right]^{\frac{\gamma+1}{2(\gamma-1)} - n} \tag{26.11}$$

For a 10° cone, the local Mach number is $M_c = 7.6$. For flight at an altitude of approximately 24 km, the kinematic viscosity coefficient is given in Appendix A as $\nu_\infty = 0.2991 \cdot 10^{-3}$. Assuming that $n = 1$, we obtain the value $x_{tr} = 0.438$ m from Eq. (26.11).

To determine the corresponding length for the blunt cone, the decrease in the local Reynolds number can be estimated from Fig. 255, i.e., $\mathrm{Re}_b/\mathrm{Re}_c = 0.071$. Then the transition point on the blunt cone is located at

$$x_{tr} = \frac{0.438}{0.071} = 6.2 \text{ m}.$$

The radial coordinate of the sonic point on the shock wave (r_S) can be obtained from the equation for the shock wave, $x = -s_0 + r^2/2R_{s0}$, giving

$$\frac{r_S}{R_N} = \frac{R_{s0}/R_N}{(dr/dx)_S}.$$

The dimensionless radius of curvature of the shock, R_{s0}/R_N, is a function of the static density ratio ρ_s/ρ_∞ across a normal shock. For low altitudes at $M_\infty = 10$, the density ratio $\rho_s/\rho_\infty = 7.4$, including the effects

of dissociation (Fig. 41). The shock wave curvature is obtained from Fig. 209 or from the approximate equation in the footnote on p. 572 as $R_{sS}/R_N = 1.20$. The shock wave angle at the sonic point is determined from Fig. 203 as $\theta_{sS} = 67.5°$, and $(dr/dx)_S = \tan \theta_{sS} = 2.41$. Therefore, $r_S/R_N = 1.2/2.41 \approx 0.5$. From Fig. 203, the angular coordinate of the sonic point on the sphere is $\varphi_{SN} = 42.5°$, from which the dimensionless radial coordinate to the sonic point on the body is obtained as $r_{SN}/R_N = \sin \varphi_{SN} = 0.676$. Thus, the ratio of the coordinates of the sonic points is $r_{SN}/r_S = 0.676/0.5 = 1.35$.

The stagnation pressure ratio p_0'/p_0 can be assumed to be the average between the values at the apex and at the sonic point on the shock. Using Eq. (4.33a) and Mach number components normal to the shock of $M_\infty = 10$ and $M_\infty \sin \theta_s = 10 \sin 67.5° = 9.24$, we can compute the ratio of the stagnation pressure behind the shock to that in front as the average:

$$\frac{p_c'}{p_c} = \frac{3.14 + 4.52}{2} \cdot 10^{-3} = 3.83 \cdot 10^{-3}.$$

As a result of substituting these values into Eq. (26.8), we find the value of the function Π:

$$\Pi = \frac{r_{SN}^2}{x_{tr} r_{tr}} = 5.95 \cdot 10^{-3}.$$

The radius of the body at the tangency point is related to the radius at the sonic point by $r_N = r_{SN} \cos \delta_c / \sin \varphi_{SN}$. Substituting this expression into Eq. (26.8a) and solving the result for r_{SN}, we obtain the radial coordinate to the sonic point on the spherical nose:

$$r_{SN} = \frac{\Pi x_{tr} \cos \delta_c}{2 \sin \varphi_{SN}} + \sqrt{\left(\frac{\Pi x_{tr} \cos \delta_c}{2 \sin \varphi_{SN}}\right)^2 + \Pi x_{tr}^2 \sin \delta_c}.$$

Using the numerical values calculated above, we obtain $r_{SN} = 22.9$ cm. The radius of the spherical blunting is then

$$R_N = \frac{r_{SN}}{\sin \varphi_{SN}} = 33.9 \text{ cm}.$$

The body radius at the transition point is 1.4 m, and the ratio of the cross-sectional area of the blunt nose to the cross-sectional area of the cone at the transition point is approximately $\bar{S}_{sph} = 0.06$. If the transition point is located at the base, the entire surface of the cone is covered by the laminar boundary layer, and the total heat flux corresponds to that for completely laminar flow.

This example can be simplified if part of the shock wave is represented in the form of a circular arc with a radius R_{sc}. Obviously, the accuracy of this approximation increases with an increase in Mach number. In this case,

$$r_S = R_{sc} \sin \omega_S = R_{sc} \cos \theta_{cS}, \qquad r_{SN} = R_N \sin \varphi_{SN}.$$

Therefore,

$$\frac{r_{SN}}{r_S} = \frac{R_N}{R_{sc}} \frac{\sin \varphi_{SN}}{\cos \theta_{cS}} = 1.47.$$

The blunting parameters then can be calculated from these data.

INFLUENCE OF THE BOUNDARY LAYER

The required blunting computed by the method described above can be refined if the effect of the displacement thickness of the boundary layer is taken into account. In fact, it follows from physical considerations that the effect of viscosity on the flow can be accounted for, as was noted earlier, if we consider inviscid flow around an arbitrary body with the lateral dimensions increased by a displacement thickness δ_L^*. Thus, the low-velocity layer is displaced by a value of δ_L^*, and the calculation of the required blunting must be based on

$$\Delta = \delta_L - \delta_L^*.$$

The estimation of the displacement thickness can be based on the relation for boundary layer thickness; i.e., it is assumed that on a cone

$$(\delta_L^*)^c = \frac{1}{\sqrt{3}} (\delta_L^*)^{pl}.$$

In turn, the displacement thickness $(\delta_L^*)^{pl}$, calculated from the effective parameters, can be found from the equation for incompressible flow; i.e.,

$$(\delta_L^*)^{pl} = \frac{3}{8} \delta_L^{pl}. \tag{26.12}$$

Thus, if the influence of the displacement thickness is taken into account, the relation for a blunt cone is given by

$$\Delta = \delta_L - \delta_L^* = 0.361 x_{tr} \left(\frac{\delta_L^{pl}}{x_{tr}} \right). \tag{26.13}$$

Comparing this with Eq. (26.7), we can conclude that the required blunting is decreased by the effects of the boundary layer displacement.

EFFECTS OF VARIOUS ASSUMPTIONS IN THE THEORY OF THE INVISCID LAYER

A number of assumptions have been made to simplify the study of the flow processes involved in the important concept of the high-entropy, low-velocity, inviscid layer. One of these assumptions is based on the fact that the velocities and other flow parameters across a given section of the high-entropy layer are taken as constants. Actually, all these parameters vary and, strictly speaking, the influence of this variation on the formation of the boundary layer should be taken into account, particularly the influence of the velocity gradient occurring in the high-entropy layer. The assumption of constant flow properties is warranted in those cases where the thickness of the low-velocity inviscid layer is small compared with the boundary layer thickness, and, therefore, the influence of the transverse velocity gradient is insignificant. In this case the boundary layer develops in that section of the inviscid layer where the flow parameters are almost constant.

The second assumption results from the neglect of the interaction between the inviscid high-entropy layer and the viscous boundary layer. This assumption is warranted for those regions where the boundary layer

thickness is small. However, as was shown, this interaction can be taken into account by a simple method if the concept of the relative displacement thickness is used.

It was noted above that we estimated the effect of blunting on the location of the transition point assuming that the transition Reynolds number for pointed and blunt cones remained identical. There are very few experimental data to support this assumption, although what data do exist tend to confirm the hypothesis to some degree. However, there are still insufficient experimental data to validate any assumptions in the calculation of transition Reynolds numbers. The results available show that on a blunt surface, the transition point varies with the longitudinal pressure gradient and with surface roughness.

Finally, let us indicate one more premise, concerned with the invariability of the profile shape in the inviscid layer. In reality, a deformation of this profile occurs downstream and is caused by the decay of the low-velocity inviscid layer due to the continual entry into it of a large amount of air with low entropy. This decay of the high-entropy flow is equivalent to an effective decrease in blunting. Thus, the flow conditions at a great distance from the nose should approach those for the flow behind the conical shock existing for zero blunting. Therefore, the heat transfer must increase downstream. In regions closer to the nose, the predominant stagnation conditions are those behind a normal shock, and the heat transfer is low.

The approximate picture of the velocity variation along the body is presented in Fig. 260, where the velocity at the outer edge of the boundary layer has been calculated for various conditions. The dashed curves result from conditions behind conical and normal shocks. The velocities computed by considering the curvature of the shock are shown by solid lines and were calculated in the following way. The mass flow of gas through a section of the boundary layer was found on the basis of an approximate estimate of the thickness of the layer at the given station. The portion of the curved shock wave corresponding to this mass flow was determined, and the average value of the stagnation pressure was calculated. The velocity was computed from this average and the value of the local static pressure.

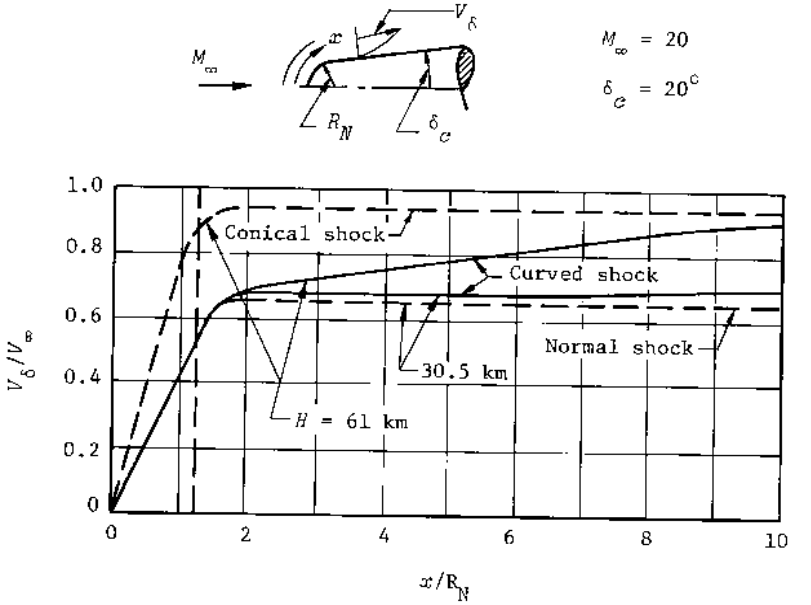

Fig. 260--Velocity distribution at the outer edge of the boundary layer for a spherically blunted cone

It is evident from Fig. 260 that, for an altitude of 30.5 km and a conical surface length of $x = 10R_N$, the velocity differs little from that calculated using the normal part of the shock. However, when the altitude is doubled, the difference becomes substantial, and the velocity computed by the indicated method is almost equal to that on a pointed cone. Here also the dissipation effect emerges, essentially leading to a decay of the inviscid layer of low velocities. If this effect were taken into account in practical calculations of optimum blunting, the blunting initially obtained would be increased somewhat.

Several studies have indicated that, for flight at comparatively low altitudes, dissipation of the low-velocity layer can be neglected for lengths of the laminar boundary layer of the order of 1000δ.

From this discussion, it is apparent that the results of the calculation of the low-velocity inviscid layer will differ somewhat from the actual values because of the simplifying assumptions used in the

calculations. Therefore, the quantitative estimate presented above for the thickness of the inviscid layer and for the coordinate of the transition point should be considered preliminary and, before making final practical recommendations, the calculated parameters obtained should be tested experimentally.

§ 27. *HEAT FLOW ON A BLUNT NOSE*

GENERAL SOLUTION FOR THE LAMINAR BOUNDARY LAYER ON THE CURVED SURFACE OF A NOSE FOR EQUILIBRIUM DISSOCIATION

FLOW CONDITIONS on a blunt nose are characterized by low velocities due to the abrupt deceleration of the flow through the bow shock. Negative pressure gradients are also characteristic of the flow. Therefore, the boundary layer in the majority of practical cases is laminar, and the heat transfer is defined by the processes in a laminar layer.

In the case of thermodynamic equilibrium, heat transfer is caused only by molecular thermal conductivity and, therefore, the heat flow to the surface is

$$q = \frac{k_w}{c_{pw}} \left(\frac{\partial i}{\partial y}\right)_w. \tag{27.1}$$

This expression applies to an arbitrary point on the surface of a spherical nose, including the stagnation point. The value of the heat flux at the point in question is a function of the local inviscid wall parameters and of the processes occurring in the boundary layer itself. The longitudinal pressure gradient also has considerable influence. In addition, the heat transfer is determined by processes that occur in the boundary layer upstream of the section under consideration. In other words, the heat flow to the wall is related to the previous history of the motion of the gas.

To take this previous history into account, it can be shown[3] that it is advantageous to introduce a new variable:

$$\xi = \int_0^x \rho_\delta V_\delta \mu_\delta r^2 \, dx. \tag{27.2}$$

Since ξ is a measure of the distance along the surface from the stagnation point, the parameters at a given section of the boundary layer will be functions of ξ. The heat transfer is determined by the variation of these parameters with thickness, as are the integral (or average) characteristics of the boundary layer.

The integral $\int_0^y (\rho/\rho_\delta)\, dy$ is introduced as a relative coordinate corresponding to the coordinate y at a point in the cross section of the boundary layer. Based on the dependence of the parameters in the boundary layer on the processes in the preceding sections of flow, it is necessary to relate $\int_0^y (\rho/\rho_\delta)\, dy$ to ξ by defining a new variable:

$$\eta = \frac{r\rho_\delta V_\delta}{\sqrt{2\xi}} \int_0^y \frac{\rho}{\rho_\delta}\, dy. \tag{27.3}$$

Studies have shown that similar solutions can be found representing a family of velocity and enthalpy profiles depending only on the parameter η. For example, if we introduce the stream function, which is defined by

$$\frac{\partial \Psi}{\partial y} = \rho V_x r, \qquad \frac{\partial \Psi}{\partial x} = -\rho V_y r, \tag{27.4}$$

and convert to the variables ξ and η, it can be shown that the stream function will depend on these new variables in the following way:

$$\Psi(\xi, \eta) = \sqrt{2\xi}\, f(\eta). \tag{27.5}$$

The relation for the velocity ratio V_x/V_δ is determined from Eqs. (27.4) and (27.5),

$$\frac{V_x}{V_\delta} = \frac{df}{d\eta} = f'(\eta), \tag{27.6}$$

and the enthalpy ratio is defined by a function $g(\eta)$:

$$\frac{i_0}{i_r} = g(\eta), \tag{27.7}$$

where

$$i_0 = i + \frac{V_x^2}{2}.$$

Using these results, we can transform the equations of motion, Eq. (3.33), and energy, Eq. (3.41), to the new variables ξ and η (neglecting the concentration gradient):

$$(Cf'')' + ff'' + \beta\left[\frac{\rho_\delta}{\rho} - (f')^2\right] = 0, \tag{27.8}$$

$$\left(\frac{Cg'}{\mathrm{Pr}}\right)' + fg' + \frac{V_\delta^2}{2i_r}\left[2C\left(1 - \frac{1}{\mathrm{Pr}}\right)f'f''\right]' = 0, \tag{27.9}$$

where

$$C = \frac{\rho\mu}{\rho_\delta\mu_\delta}, \qquad \beta = \frac{2\xi}{V_\delta}\frac{dV_\delta}{d\xi}.$$

For large supersonic velocities, it can be assumed that the density ratio $\rho_\delta/\rho \approx g(\eta)$, and that C is equal to unity. The study is also simplified if we assume that $\mathrm{Pr} \approx 1$ and that β, which is a function of the velocity gradient, is constant. Based on these assumptions, Eqs. (27.8) and (27.9) are simplified:

$$f''' + ff'' + \beta[g - (f')^2] = 0, \tag{27.8a}$$

$$g'' + fg' = 0. \tag{27.9a}$$

Thus, the equations obtained reflect local similarity, in the sense that the dimensionless velocity V_x/V_δ and enthalpy i_0/i_r are identical at points in different flows for which the parameter η, the similarity parameter, is the same.

Solving the system of ordinary differential equations, Eqs. (27.8a) and (27.9a) (for the proper boundary conditions), we can find the functions $f(\eta)$ and $g(\eta)$ and their derivatives and thereby determine the flow parameters V_x/V_δ, i_0/i_r, etc.

Specifically, studies have shown that the value of the derivative $g'(\eta)$ on a cooled wall, i.e., for $\eta = 0$, in the case of very high velocities can be expressed with sufficient accuracy by the relation†

$$g'(0) = \frac{1}{2}\,\mathrm{Pr}^{\frac{1}{3}}, \tag{27.10}$$

in which the Prandtl number is an average value for the given section of the layer. The cooled wall is characterized by the fact that the density ratio $\rho_w/\rho_\delta \gg 1$ on the surface.

The equation for heat flow, Eq. (27.1), can be transformed to the variable η and, with Eqs. (27.7) and (27.10), written as

$$q = \frac{k_w}{\bar{c}_{pw}}\, i_r \left(\frac{\partial g}{\partial \eta}\right)_w \left(\frac{\partial \eta}{\partial y}\right)_w = \frac{1}{2}\,\frac{k_w}{\bar{c}_{pw}}\,\frac{\rho_w V_\delta r i_r}{\sqrt{2\xi}}\,\mathrm{Pr}^{\frac{1}{3}}. \tag{27.11}$$

Assuming that $\rho_w \mu_w = \rho_\delta \mu_\delta$, we obtain

$$\frac{\rho_\delta \mu_\delta}{\rho_0' \mu_0'} = \frac{p}{p_0'}\,\frac{\omega_\delta}{\omega_0'}, \tag{27.12}$$

where $\omega = \mu/RT$. At high temperatures, the value of this function varies little with the thickness of the boundary layer, and it can be assumed that the values at the edge of the boundary layer and at the stagnation point are identical, i.e., $\omega_\delta = \omega_0'$. Therefore, only the ratio p/p_0' is a variable on the right side of Eq. (27.12).

Using Eq. (27.2) for ξ and taking into account that $\mathrm{Pr} = \bar{c}_{pw}\mu_w/k_w$, we obtain the heat flow as follows:

$$q = \frac{1}{2\,\mathrm{Pr}^{\frac{2}{3}}}\,\sqrt{V_\infty \rho_0' \mu_0'}\; i_r F(x), \tag{27.13}$$

where

$$F(x) = \frac{\sqrt{2}}{2}\,\frac{(p/p_0')(V_\delta/V_\infty) r}{\left[\int_0^x (p/p_0')(V_\delta/V_\infty) r^2\, dx\right]^{\frac{1}{2}}}. \tag{27.14}$$

†Editor's note: The more precise expression is $g'(0) = 0.47\,\mathrm{Pr}^{\frac{1}{3}}$.

It will be observed that the dimensions of i_r in Eq. (27.13) should be kcal m/kgf sec^2 to allow the proper units for the heat transfer rate.

STAGNATION POINT

Equilibrium Dissociation

Calculations of the heat transfer over the surface of a blunt nose are dependent on the determination of the heat transfer rate at the stagnation point. Conditions at this point are also of particular interest because the heat transfer rate is usually greater at the stagnation point than at any other point on the nose. The heat transfer rate at the stagnation point is given by Eq. (27.13), where $F(x)$ is computed for conditions in the vicinity of the stagnation point:

$$V_\delta = \tilde{\lambda} x = \frac{\bar{\lambda} V_\infty x}{D_N}, \qquad \frac{\rho}{\rho_0'} = \text{const} \approx 1, \qquad r = x.$$

The absolute value of the function is

$$|F(x)|_0 = \sqrt{2\tilde{\lambda}/V_\infty},$$

and Eq. (27.13) has the form

$$q_0 = \frac{0.664}{\mathrm{Pr}^{\frac{2}{3}}} (\tilde{\lambda}\rho_0'\mu_0')^{\frac{1}{2}} i_r. \tag{27.15}$$

This expression is obtained for a supercooled surface on which the temperature T_w and the enthalpy i_w are negligibly small compared with the corresponding values of T_r and i_r. In cases where the cooling does not ensure a sufficiently low wall temperature, e.g., for the dissipation of heat by radiation only when a comparatively high equilibrium radiation temperature is established, it is necessary to account for i_w. Studies have shown[4] that for the case of a heated wall, the equation for q_0 retains basically the same form as Eq. (27.15), but the quantity $(i_r - i_w)$ enters into the new equation instead of i_r, as well as the supplementary coefficient

$$\left(\frac{\rho_\omega \mu_\omega}{\rho'_0 \mu'_0}\right)^{1/10} = (\bar{\rho}_\omega \bar{\mu}_\omega)^{1/10},$$

which takes into account the variation of the parameters across the boundary layer in the vicinity of the stagnation point. Moreover, it has been established that better results are obtained if the coefficient 0.664 is changed to 0.763. If these changes are made, then, in the general case of a heated wall, the equation for the heat transfer can be presented in the following form:

$$q_0 = \frac{0.763}{\mathrm{Pr}^{\frac{2}{3}}} (\tilde{\lambda} \rho'_0 \mu'_0)^{\frac{1}{2}} (i_r - i_\omega)(\bar{\rho}_\omega \bar{\mu}_\omega)^{1/10}. \qquad (27.16)$$

The variation in the quantity $1/\bar{\rho}_\omega \bar{\mu}_\omega$ as a function of wall temperature is shown in Fig. 261. It is apparent that the heat flux does not increase significantly over its value for a cooled surface even for an insulated wall (for which $T_\omega = T_r$), since the heat transfer varies only with the $\frac{1}{10}$ power of the parameter.

Equation (27.16) indicates that at high velocities, when dissociation has a considerable influence on heat transfer processes, the heat

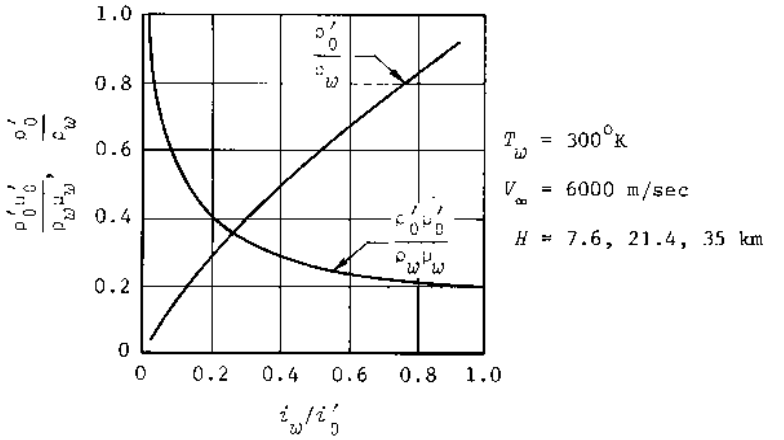

Fig. 261--Variation in density and the product $\rho\mu$ *in the boundary layer near the stagnation point*

transfer is a function of the enthalpy rather than the temperature. At these velocities, the recovery enthalpy i_r can be computed from $i_r = V_\infty^2/2$. In a wind tunnel, the enthalpy is determined from the gas temperature in the stagnation chamber and, in a shock tube, from the equation $i_r = u_s^2$, in which u_s is the velocity of the shock wave. In Eq. (27.16), it is possible to convert from an enthalpy difference to a temperature difference if we substitute

$$i_r - i_w = \bar{c}_{pw}(T_r - T_w),$$

where the specific heat $\bar{c}_{pw}$ is calculated as an average between the values on cooled and insulated walls having temperatures of T_w and T_r, respectively.

It should be noted that the equations for the calculation of the heat transfer rate pertain to the case of steady motion of a body on a trajectory. If the velocity is not constant, the expression

$$\frac{d\bar{q}_0}{dt} = h_l(T_r - T_w)_l = q_{0l} \tag{27.17}$$

can be used for an approximate estimate of the heat flux at a point l on the trajectory, where q_{0l} is given by Eqs. (27.15) or (27.16), for example. The total amount of heat transferred to the stagnation point during an interval of time $t_2 - t_1$ is

$$\bar{q}_0 = \int_{t_1}^{t_2} \frac{d\bar{q}_0}{dt}\, dt = \int_{t_1}^{t_2} h_l(T_r - T_w)_l\, dt. \tag{27.18}$$

It follows from the equations presented that the heat flow to the wall is a function of the parameters at the external edge of the boundary layer. The parameters are determined from the flow conditions at the stagnation point of the spherical nose.

With an increase in flight velocity, it becomes increasingly necessary to consider the effects of dissociation of the gas in front of the blunt body. At very high Mach numbers, a large part of the kinetic energy of the moving gas is converted into heat in the vicinity of the stagnation point. For example, at a velocity of 8 km/sec, almost 8000

kcal are generated by 1 kg of air, i.e., an amount sufficient for the dissociation of a large portion of the nitrogen and oxygen molecules.

Of course, the variation in the chemical composition of air at high temperatures changes the heat transfer conditions. The chemical composition must be considered in the calculation of the parameters at the outer edge of the boundary layer, e.g., the longitudinal velocity gradient $\tilde{\lambda}$, the density ρ_0', and the viscosity μ_0'. These calculations are similar to the computation of these parameters behind a normal shock. Knowing the entropy on the zero streamline and the stagnation enthalpy, we can compute p_0', T_0', ρ_0', and the other parameters at the stagnation point necessary in Eqs. (27.15) or (27.16).

An analysis of the numerical results of the calculation for hypersonic velocities enables us to obtain the following approximate equation for the calculation of the heat flux at the stagnation point:[5]

$$q_0 = \frac{31,500}{\sqrt{R_N}} \sqrt{\frac{\rho_{\infty H}}{\rho_{\infty SL}}} \left(\frac{V_\infty}{V_C}\right)^{3.25} \left(1 - \frac{i_w}{i_r}\right)^3 \quad \text{kcal/m}^2 \text{ sec}, \qquad (27.19)$$

in which V_C is the orbital velocity, equal to 7.93 km/sec; $\rho_{\infty H}$ and $\rho_{\infty ST.}$ are the atmospheric densities at altitude H and at sea level, respectively; and R_N is the radius of the sphere in meters. The recovery enthalpy can be assumed equal to the stagnation enthalpy.

Equation (27.19) is obtained on the assumption of equilibrium dissociation in the boundary layer. However, research has shown that it can also be used at high velocities where the flow in the boundary layer on a catalytic surface is in a nonequilibrium state. In this case, the recombination of atoms is accelerated by the catalytic effect of the wall (e.g., a metal skin) and is accompanied by the generation of heat that is almost equal to the heat of dissociation. At the same time, the processes occurring in the boundary layer, although not in equilibrium, are nevertheless close to equilibrium. Thus, Eq. (27.19) accounts not only for heat conduction but also for the transfer of heat by diffusion due to the recombination of atoms at the wall.

If the surface of the sphere is noncatalytic (e.g., a nonmetallic

surface), Eq. (27.19) will give values of the heat flux that are too high. In this case, the equation will become increasingly inaccurate as the altitude increases, i.e., as the gas deviates from the equilibrium state.

From a practical viewpoint, the use of a noncatalytic surface can be advantageous since it decreases the heat transfer. In this case, the low rate of recombination peculiar to these chemical reactions under ordinary conditions is not affected by the noncatalytic surface, and the heat absorbed by the dissociation process can be considerable.

In calculations in which these equations are used, it is assumed that the enthalpy or wall temperature is known. For example, a specific value can be assigned, thus setting a cooling requirement. In particular, it is possible to examine the case of a strongly cooled surface when the quantity i_w/i_r can be neglected in comparison with unity. In other cases, it is possible to assign a maximum allowable skin temperature. In addition, the heat flux to the surface can be calculated, assuming that it is equal to the heat emitted by radiation from the surface. By selecting a value for the emissivity of the surface (ε) and a surface temperature, which in this case will be the equilibrium temperature, we can determine the flight velocity and altitude necessary for thermal equilibrium. The radiative heat flux, $\varepsilon\sigma T_w^4$, is set equal to the heat flux given by Eq. (27.19), from which a relation between velocity and density (therefore, altitude) is obtained. Under these flight conditions, cooling occurs due to thermal radiation from the heated surface. This so-called radiative cooling plays an important role in the reduction of the net heat flow.

EXAMPLE

Let us determine the heat transfer at the stagnation point of a spherical nose with a radius R_N = 0.25 m for flight at an altitude H = 30 km with a velocity corresponding to M_∞ = 15; the wall temperature is T_w = 1000°K. We will use Eq. (27.15), in which it will be assumed that the Prandtl number is equal to 0.71.

The sequence and the results of the calculations are presented in Table 19, in which part of the data is taken from Table 4. To simplify the calculations, the inviscid parameters at the stagnation point are assumed equal to those behind a normal shock wave. As is evident from Table 19, the heat flux is 1200 kcal/m^2 sec, and the heat transfer coefficient is h = 0.27 kcal/m^2 sec deg.

Now, let us estimate the heat transfer parameters at the stagnation point of a body with a flat nose. The equivalent radius can be determined from Eq. (20.46), and the heating rate at the stagnation point can then be calculated just as at the stagnation point of a sphere with a radius R_{Ne}.

As an example, let us compute the value of q_0 for the conditions given above assuming that the radius of the flat nose is r_N = 0.25 m. From the known density ratio ρ_0'/ρ_∞ = 11 and the curves in Figs. 209 and 212, it can be determined that the radii of curvature of the shocks are $(\bar{R}_{s0})_{sph}$ = 1.14 and $(\bar{R}_{s0})_f$ = 5.25. Therefore, the equivalent nose radius is R_{Ne} = 0.25·5.25/1.14 = 1.15 m, i.e., 4.6 times larger than the radius of the sphere. According to Eq. (20.27a), the value of $\tilde{\lambda}$ for a flat nose will be less than that for a sphere by the same factor. It follows from Eq. (27.15) that the heating rate is reduced by $\sqrt{4.6}$ = 2.15 times and is approximately 560 kcal/m^2 sec.

Calculations using the effective parameters give almost the same result when the effective enthalpy at the stagnation point is calculated from

$$i^* = \frac{1}{2}(i_r + i_w).$$

The more accurate heat flux is only 3 percent larger.

Experimental measurements of the heating rate at the stagnation point of a flat face indicate that

$$(q_0)_f = (0.55 \pm 0.05)(q_0)_{sph},$$

i.e., equal to half the value at the stagnation point of a sphere with the same radius as the flat nose. This corresponds quite well to the calculated value above.

Table 19

CALCULATION OF HEAT TRANSFER AT THE STAGNATION POINT

1	2	3	4	5	6	7	8
M_∞	H km	$\frac{p_{\infty H}}{p_{\infty SL}}$	$\frac{\rho_{\infty H}}{\rho_{\infty SL}}$	$\frac{a_{\infty SL}}{a_{\infty H}} = \sqrt{\frac{T_{\infty SL}}{T_{\infty H}}}$	g m/sec^2	V_∞ m/sec	$T_{\infty H}$ °K
Assumed	Appendix A					$340\frac{M_\infty}{(5)}$	$\frac{288}{(5)^2}$
15	30	0.0118	0.0145	1.11	9.72	$4.61\cdot10^3$	234

9	10	11	12	13	14	15
$i_{\infty H}$ kcal/kgf	$\frac{V_\infty^2}{2}$	i_r kcal/kgf	$\bar{\lambda}$	$\tilde{\lambda}$	$\frac{\rho_0'}{\rho_{\infty H}}$	$\frac{p_0'}{p_{\infty H}}$
0.24·234	$\frac{(7)^2}{2}$	$\frac{(10)^2}{427g} + (9)$	Fig. 201	$\bar{\lambda}\frac{V_\infty}{D_N}$	Eq. (3.46)	Fig. 42
56.2	$10.6\cdot10^6$	2586	1.15	$1.06\cdot10^4$	11	280

16	17	18	19	20
$T_0'/T_{\infty H}$	ρ_0' kgf sec^2/m^4	$T_0'/T_{\infty SL}$	$\mu_0'/\mu_{\infty SL}$	μ_0' kgf sec/m^2
Fig. 40	$0.125\cdot(4)\cdot(14)$	$(16)/(5)^2$	Eq. (2.3) and Fig. 13	$1.82\cdot10^{-6}\cdot(19)$
23	0.02	18.8	7.85	$1.43\cdot10^{-5}$

21	22	23	24	25	26
p_0' kgf/cm^2	T_w °K	i_w kcal/kgf	q_0 kcal/m^2 sec	T_r °K	h kcal/m^2 deg sec
$(3)\cdot(15)$	Assumed	(21), (22), and Fig. 15	Eq. (27.16)	(21), (11), and Fig. 15	$\frac{q_w}{T_r - T_w}$
3.31	1000	250	1200	5430	0.27

NOTE: The italic numbers in parentheses indicate the column of the specified value.

The Effect of Vorticity in the External Flow

The relation presented for the heat flow is obtained on the assumption that the flow in the inviscid layer adjacent to the wall is steady and that there are no velocity gradients across the layer due to vorticity. In reality, the velocity is not constant but increases from its value at the wall, corresponding to stagnation conditions behind a normal shock, to a higher value at the edge of the inviscid layer; thus, vorticity appears in the flow field. The effect of vorticity is apparent at each point on the surface, including the stagnation point, where the ratio of the heating rate including vorticity, q_{0v}, to that with no vorticity depends on a series of factors including the free-stream Mach number and the flight altitude.

For example, calculations showed that the ratio q_{0v}/q_0 was 1.3 and 1.04 at the stagnation point of a hemisphere for $M_\infty = 20$ and altitudes of 90 and 60 km, respectively. Thus, in practice, it is possible to disregard the vortex effect in dense layers of the atmosphere, whereas it is advisable to increase somewhat the calculated heat transfer in a rarefied medium.

The most important parameter determining the effect of vorticity on heat transfer is the Reynolds number calculated from the radius of the sphere and the gasdynamic characteristics at the stagnation point:

$$\mathrm{Re} = \frac{R_N \rho_0' \sqrt{i_r}}{\mu_0'}.$$

In this expression, it should be noted that at high velocities it can be assumed that $i_r \approx V_\infty^2/2$.

Experimental data are presented in Fig. 262 for the ratio q_{0v}/q_0 for Mach numbers of 8 and 20, which can be used to correct the calculated values of the heat flow. It is obvious that the vortex effect is considerably less for $M_\infty = 8$ than for $M_\infty = 20$. The data in Fig. 262 are obtained for a stagnation point temperature of $T_0' = 2000°K$. The effect of vorticity increases with temperature, but even for a considerable temperature increase the effect is not great. Thus, for example, heat transfer due to vorticity increases, in all, by 3 to 4 percent for a temperature increase of 1000°K.

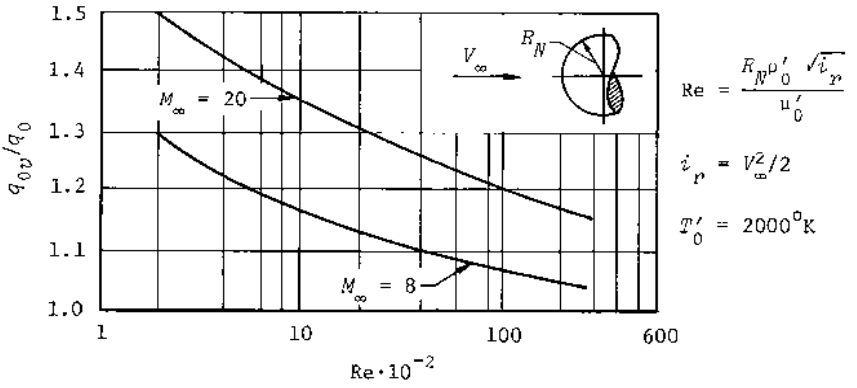

Fig. 262--Effect of vorticity on stagnation point heat transfer

Radiation from a Heated Shock Layer

At very high flight velocities, the significant temperature increase behind the shock wave changes the physical character of the air. In particular, it ceases to be transparent and therefore becomes a source of radiative heat flow to the surface. The opacity of the air results chiefly from a significant increase in the concentration of nitric oxide at high temperatures.

If the optical properties are characterized by a parameter ε representing the emissivity of a unit thickness of the radiative layer, where ε has the dimensions L^{-1}, the quantity εs_0 will be the dimensionless characteristic of the radiation of the gas between the shock and the body, having a thickness s_0. This quantity is called the effective emissivity of the gas. According to the Stefan-Boltzmann law, the heat radiated by a black body is $q = \sigma T^4$. To take transparency into account in this equation, it is necessary to introduce a function, $f(\varepsilon s_0)$, that depends on the effective emissivity. Thus, the general relation for the determination of the radiative heat flow to the wall will have the form

$$q = f(\varepsilon s_0)\sigma(T_0')^4, \qquad (27.20)$$

where T_0' can be assumed equal to the temperature at the stagnation point of the nose. It must be kept in mind that Eq. (27.20) refers to the case

in which the surface does not radiate and its temperature is less than 3000°K.

The curve presented in Fig. 263 shows the variation in the function $f(\varepsilon s_0)$ under real flight conditions at a very high velocity. At sufficiently high values of εs_0, the air practically behaves as an opaque medium and the heat transfer due to radiation can be considerable. Thus,

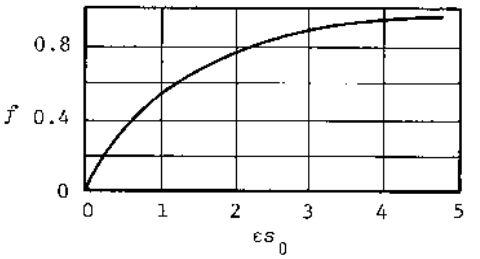

Fig. 263--Variation of $f(\varepsilon s_0)$ for radiative heat flow at the stagnation point

the farther the shock wave is displaced, i.e., the thicker the radiative layer, the larger in value will be the radiative heat flow corresponding to the same flight velocity (ε = const). The curve shown in Fig. 263 can be approximated by the equation

$$f = 1 - \exp(-\varepsilon s_0), \tag{27.21}$$

which gives an error of not more than 20 percent. As one would expect, the function $f = 0$ when $\varepsilon = 0$, i.e., when the air is transparent, which occurs at low flight velocities. At high velocities $f \to 1$; i.e., for practical purposes the gas becomes absolutely black.

The results of physical studies can be used for practical conditions, which show that the parameter ε is a function of the temperature and density of the air. This is evident in Fig. 264, where a family of experimentally determined curves is presented. Each curve represents the dependence of the quantity log (ε) on air temperature for a constant density ratio, where the units of ε are cm^{-1}. In the temperature range

of 8000°K $\leq T \leq$ 16,000°K, this set of curves can be well approximated by the equation

$$\varepsilon = 0.138\left(\frac{\rho}{\rho_{\infty SL}}\right)^{1.28}\left(\frac{T}{10^4}\right)^{6.54} \quad \text{cm}^{-1}. \tag{27.22}$$

If this equation is used to calculate the radiation to the stagnation point of a blunt nose, the density ρ and temperature T of the gas must be assumed equal to their corresponding values ρ_0' and T_0' at this point. The calculation of the temperature T_0' can be simplified if an approximate relation is used:

$$T_0' = 1.34\left(\frac{\rho_0'}{\rho_{\infty SL}}\right)^{0.0667}\left(\frac{V_\infty}{10^4}\right)^{1.333} \quad °\text{K}, \tag{27.23}$$

where V_∞ is in m/sec.

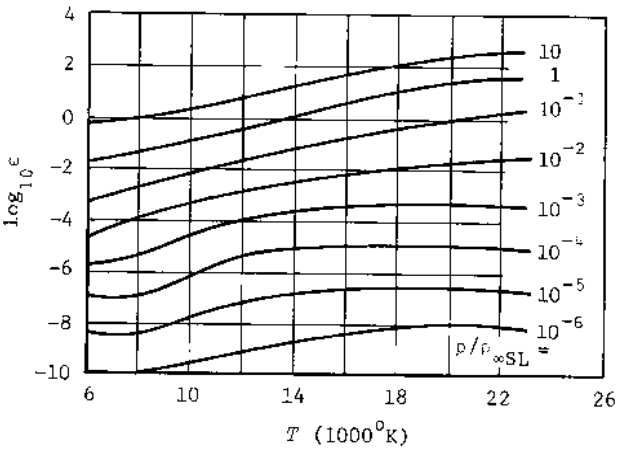

Fig. 264--Experimental data on the emissivity of a gas

On the basis of experimental studies, the following empirical relation was also obtained for the radiative heat flux at the stagnation point:

$$q_{rad} = 2.12 \cdot 10^{7} R_N \left(\frac{V_\infty}{10^4}\right)^{8.5} \left(\frac{\rho_{\infty H}}{\rho_{\infty SL}}\right)^{1.6} \quad \text{kcal/m}^2 \text{ sec}, \qquad (27.24)$$

where R_N is in meters and V_∞ is in meters per second.

A typical distribution of the radiative heat flow q_{rad} and the aerodynamic heat flow q_{aer} for a certain trajectory is presented in Fig. 265. It should be noted that the radiant heat flow has large values at low altitudes. The largest value of q_{rad} corresponds to the maximum aerodynamic heat transfer and is about one-third of that value.

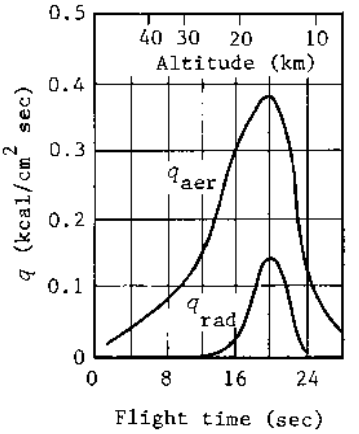

Fig. 265--Convective and radiative heat flow near the stagnation point of a spherically blunt body

THE EFFECT OF DIFFUSION ON HEAT TRANSFER

The Mechanism of Heat Transfer

One of the characteristics of the heat transfer process in the boundary layer for very high flow velocities is based on the fact that atoms and ions, created as the result of dissociation and ionization, take part in the transfer of heat by diffusing into regions with lesser atomic and ionic concentrations.[3] Diffusion, accompanied by the recombination of the atoms and ions, leads to the evolution of additional heat. The total heat flux is increased, because a certain amount of

heat due to recombination of the atoms taking part in the diffusion is added to the heat from ordinary molecular thermal conductivity.

Thus, the total heat flow to the wall will be determined by the expression

$$q = q_T + q_D = -\left[\lambda_w \left(\frac{\partial T}{\partial y}\right)_w + \rho_w \bar{D} i_R \left(\frac{\partial c}{\partial y}\right)_w\right], \tag{27.25}$$

in which $\bar{D}$ is the diffusion coefficient of a binary mixture of air consisting of atoms and molecules, and q_T and q_D are the heat flows due to molecular thermal conductivity and diffusion, respectively. Obviously, it is possible to assume that air can be represented by such a binary mixture since the transfer coefficients, i.e., viscosity, thermal conductivity, and diffusion, as well as the atomic weights of oxygen and nitrogen, are close to one another. Moreover, the concentration of nitric oxide is low and its influence on the transfer of energy is negligible. For the same reason, it is possible to neglect the effects of ionization, which begin to appear only for $M_\infty > 25$.

With the enthalpy of the mixture defined by Eq. (3.40a), the heating rate at the wall can be written

$$q = -\frac{\lambda_w}{\bar{c}_{pw}}\left[\left(\frac{\partial i}{\partial y}\right)_w - i_R \left(\frac{\partial c}{\partial y}\right)_w + \frac{\rho_w \bar{D} \bar{c}_{pw}}{\lambda_w} i_R \left(\frac{\partial c}{\partial y}\right)_w\right]. \tag{27.25a}$$

In the limiting case of local thermodynamic equilibrium, it can be assumed that the degree of dissociation does not vary within the thickness of the boundary layer and is equal to its value at the outer edge, so that the concentration gradient $\partial c/\partial y = 0$. If the enthalpy gradient at the wall is assumed to be of the order of magnitude of

$$\left(\frac{\partial i}{\partial y}\right)_w \sim \frac{i_r - i_w}{\delta},$$

the thermal flux in the equilibrium boundary layer is of the order of

$$q_T \sim \frac{1}{\delta} \frac{\lambda_w}{\bar{c}_{pw}} (i_r - i_w). \tag{27.26}$$

In this case, the heat transfer is due to molecular thermal conductivity involving the transfer of kinetic, vibrational, and rotational energy. Actually, the flow in the boundary layer is not in equilibrium, and a concentration gradient exists. Therefore, in addition to molecular thermal conductivity, heat transfer occurs due to the chemical energy produced by recombination. In general, part of this energy is liberated in the boundary layer and part at the wall as a result of catalytic reaction.

In the limiting case of local equilibrium, the reaction occurs only in the boundary layer. In the other limiting case of frozen flow, recombination occurs only at the catalytic surface.

The total heat flow to the wall can be estimated from Eq. (27.25a) as

$$q \sim q_T[(1 - \bar{i}_w) + \mathrm{Le}_w\, \bar{i}_w], \tag{27.27}$$

where

$$\bar{i}_w = \frac{i_R(c_\delta - c_w)}{i_r - i_w},$$

and $\mathrm{Le}_w = \rho_w \bar{D} \bar{c}_{pw}/\lambda_w$. If the surface temperature is low enough that there is no dissociation at the wall, the concentration of atoms is zero at the wall and the difference $c_\delta - c_w$ should be replaced by c_δ.

The first term in the parentheses in Eq. (27.27) determines the heat transfer due to thermal conductivity and the second gives that due to diffusion. The heat flux caused by thermal conductivity is different from its value for equilibrium flow because of the presence of concentration gradients. It should be noted that the concentration gradient is essentially equivalent to the enthalpy gradient of the atomic component of the binary mixture.

It is evident from Eq. (27.27) that the relative value of each component of the heat flux is determined by the Lewis-Semenov number and by the parameter $\bar{i}_w$. At very high velocities, nonequilibrium becomes the deciding factor in heat transfer. In this case, the relative value of $\bar{i}_w$ is close to unity because practically all of the gas in the boundary layer is dissociated, and the entire heat flow is caused by diffusion.

The magnitude of this flow, as is evident from Eq. (27.27), is of the order of $q \sim q_T \, \mathrm{Le}_w$. If $\mathrm{Le}_w = 1$, the heat flux at any velocity is determined by the value for the case of total thermodynamic equilibrium and is independent of the heat transfer mechanism.

The Frozen Boundary Layer

To obtain a quantitative estimate of the diffusion effect, it is convenient to examine frozen flow when thermodynamic equilibrium exists at the edge of the boundary layer. In this case, the effects of diffusion are contained in a very thin layer next to the catalytic wall. The heat flow due to thermal conductivity can thus be determined separately by solving the equations for the equilibrium boundary layer; e.g., the heat transfer at the stagnation point can be calculated from Eq. (27.15).

The second component of the total heat transfer, resulting from diffusion, must be determined on the basis of the diffusion equation, Eq. (3.29). As a result of its solution, the concentration gradient of the atomic component at the wall can be found, which then determines the diffusional flow of matter by Eq. (2.34). For the required solution, let us convert Eq. (3.29) to the new variables ξ and η to obtain[6]

$$2\xi \frac{\partial z}{\partial \xi} f' - f z' - \left(\frac{C}{\mathrm{Sc}} z'\right)' = 0, \qquad (27.28)$$

where the variable z represents the dimensionless concentration of atoms, $z = c/c_\delta$, the prime indicates differentiation with respect to η, and the Schmidt number is defined as $\mathrm{Sc} = \mu/\rho\bar{D} = \mathrm{Pr}/\mathrm{Le}$. The remaining notation is the same as that in Eqs. (27.8) and (27.9).

Equation (27.28) is to be solved for specified boundary conditions at the wall. For the function f, the condition $f(0) = f'(0) = 0$ must be satisfied. At the outer edge of the boundary layer ($\eta \sim \infty$), the concentration ratio $z(\infty) = 1$, and the boundary condition at the wall is obtained from Eq. (2.35a). Assuming that $m = 1$ in Eq. (2.35a), we can write this condition in terms of the new variables ξ and η as

$$z'(0) = \left(\frac{\partial z}{\partial \eta}\right)_w = \frac{\sqrt{2\xi}}{rV_\delta} \frac{k_w}{\rho_w \bar{D}} z(0).$$

Close to the stagnation point, we can compute ξ from Eq. (27.2) assuming that $r \approx x$, $V_\delta = \tilde{\lambda} x$, and $\rho_\delta \mu_\delta = \text{const}$. Furthermore, assuming that $\rho_\delta \mu_\delta = c_0' \mu_0'$, we find the boundary condition

$$z'(0) = \sqrt{\frac{\rho_0' \mu_0'}{2\tilde{\lambda}}} \frac{k_w}{\rho_w \bar{D}} z(0). \tag{27.29}$$

For this same region, it can be assumed that the concentration profile is independent of x. Furthermore, a good approximation for C is given by $C \approx 1$. This assumption is accurate for a low-temperature boundary layer but is worse at high temperatures. However, it has been established that the heat transfer is almost independent of the parameter C because of the weak dependence of the enthalpy gradient on this parameter at the wall. The parameter C has exactly the same minor influence on the concentration gradient and, therefore, on the heat transfer due to diffusion. In view of this discussion, Eq. (27.28) can be simplified and written in the form

$$\mathrm{Sc}\, f z' + z'' = 0. \tag{27.28a}$$

Integrating this equation twice, we obtain

$$z(\eta) - z(0) = z'(0) \int_0^\eta \exp\left[-\int_0^\eta \mathrm{Sc}\, f(\eta)\, d\eta\right] d\eta. \tag{27.30}$$

Numerical calculations have shown that for $\eta \sim \infty$ the value of the integral is approximately $1/0.47\ \mathrm{Sc}^{\frac{1}{3}}$. Thus, we can write

$$z'(0) = 0.47\ \mathrm{Sc}^{\frac{1}{3}} [1 - z(0)]. \tag{27.31}$$

Introducing the quantity $z'(0)$ from Eq. (27.29), we obtain the dimensionless concentration at the wall:

$$z(0) = \frac{c_w}{c_\delta} \left[\left(\frac{\rho_0' \mu_0'}{2\tilde{\lambda}}\right)^{\frac{1}{2}} \frac{k_w}{0.47\ \mathrm{Sc}^{\frac{1}{3}} \rho_w \bar{D}} + 1\right]^{-1}. \tag{27.32}$$

It follows from Eqs. (27.29) and (27.32) that for the case of infinitely rapid catalysis ($k_w \sim \infty$), the dimensionless concentration at the wall

$z(0) = 0$ and the derivative $z'(0) = 0.4/\,\mathrm{Sc}^{\frac{1}{3}}$. In the other limiting case of infinitely slow catalytic reaction ($k_w = 0$), the concentration at the wall remains the same as that at the outside edge of the layer, i.e., $z(0) = 1$, and the derivative is $z'(0) = 0$.

The heat flux generated by recombination at the wall can be obtained if we substitute the concentration gradient from Eq. (27.31) into Eq. (2.34), using Eq. (27.32) for $z(0)$. This results in

$$q_D = 0.664(\rho_0'\mu_0'\tilde{\lambda})^{\frac{1}{2}}\,\mathrm{Sc}^{-\frac{2}{3}}\,i_R c_\delta \varphi, \tag{27.33}$$

where the so-called catalytic coefficient is

$$\varphi = \left[1 + \frac{0.664\,\mathrm{Sc}^{-\frac{2}{3}}\,(\rho_0'\mu_0'\tilde{\lambda})^{\frac{1}{2}}}{\rho_w k_w}\right]^{-1}. \tag{27.34}$$

This coefficient takes into account the influence of the finite recombination rate, because the parameter k_w enters into the expression. In the limiting case of $k_w \sim \infty$, the coefficient $\varphi = 1$, which corresponds to the release of the maximum amount of heat in recombination. In the other limiting case of an infinitely slow reaction ($k_w = 0$), the catalytic coefficient is $\varphi = 0$, corresponding to the liberation of no additional heat.

The total heat flux to the wall can be determined if the diffusional heat is added to the heat due to thermal conductivity. As a result, we obtain

$$q = q_T\left[1 + (\mathrm{Le}^{\frac{2}{3}}\,\varphi - 1)\,\frac{i_D}{i_r}\right], \tag{27.35}$$

where q_T is the heat transfer without diffusion, and $i_D = i_R c_\delta$ is the dissociation enthalpy.

Introducing the Nusselt and Reynolds numbers

$$\mathrm{Nu}_w = \frac{q\bar{c}_{pw}x}{\lambda_w(i_r - i_w)}, \qquad \mathrm{Re}_w = \frac{V_\delta \rho_w x}{\mu_w},$$

and determining the thermal heat transfer rate from Eq. (27.16), we find

the expression for the heat transfer parameter:†

$$\frac{\mathrm{Nu}_w}{\sqrt{\mathrm{Re}_w}} = \frac{0.763\ \mathrm{Pr}^{\frac{1}{3}}}{(\bar{\rho}_w \bar{\mu}_w)^{0.4}} \left[1 + (\mathrm{Le}^{\frac{2}{3}} \varphi - 1)\frac{i_D}{i_r}\right]. \qquad (27.36)$$

For a more detailed study of the effect of recombination, we can examine the ratio of the heat transfer with a finite recombination rate to that with infinitely rapid catalysis ($k_w \to \infty$). This ratio is

$$\bar{q} = \frac{q}{q(k_w \to \infty)} = 1 - \frac{\mathrm{Le}^{\frac{2}{3}}\ \tilde{i}_D}{1 + (\mathrm{Le}^{\frac{2}{3}} - 1)\tilde{i}_D}(1 - \varphi), \qquad (27.37)$$

where $\tilde{i}_D = i_D/i_r$. It is evident from Eq. (27.34) that the catalytic coefficient φ is a function not only of the recombination rate but also of the flow velocity. Therefore, the heat transfer ratio $\bar{q}$ from Eq. (27.37) is plotted in Fig. 266 with the variables k_w and V_∞. For conditions of thermodynamic equilibrium at the edge of the boundary layer, these data

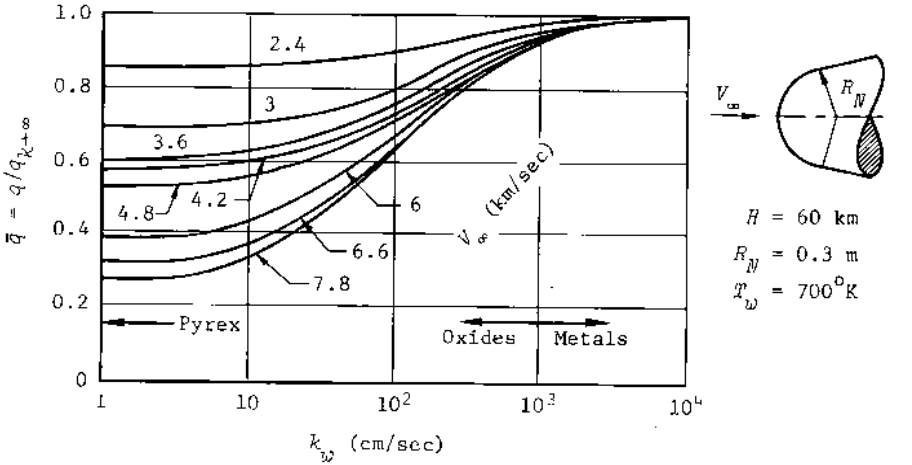

Fig. 266--Variation of heat transfer with flight velocity and recombination rate

†Editor's note: The equation in the Russian text is in error and has been corrected.

reveal how important it is to take into account the finite recombination rate. In addition, the results indicate the possibility of decreasing the heat transfer at the stagnation point through use of a nonmetallic skin, since recombination does not occur close to this type of surface. The net heat flow is decreased since nonequilibrium dissociation absorbs a significant amount of thermal energy. In the limiting case of $\varphi = 0$, the heat transfer is determined from

$$q = q_T\left(1 - \frac{i_D}{i_r}\right). \tag{27.38}$$

The values of $\bar{q} = q/q_T$ calculated from Eq. (27.35) are shown in Fig. 267 as a function of the catalytic parameter

$$\chi = \frac{\rho_w k_w}{0.664\ \mathrm{Sc}^{-\frac{2}{3}}\ (\rho_0'\mu_0'\tilde{\lambda})^{\frac{1}{2}}} \tag{27.39}$$

for various Lewis-Semenov numbers. It is obvious that the parameter χ is related to the coefficient φ by $\chi = \varphi/(1 - \varphi)$.

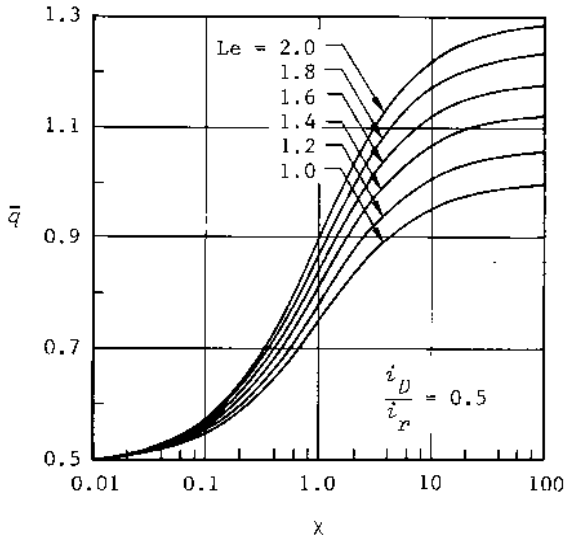

Fig. 267--Heat transfer as a function of the Lewis-Semenov number and the recombination parameter at the wall

The calculations shown in Fig. 267 pertain to the case in which the ratio $i_D/i_r = 0.5$ at the stagnation point and the nose surface is strongly cooled in the vicinity of that point, so that the concentration $c_w = 0$. If the wall remains sufficiently heated, chemical reactions will occur until the establishment of thermodynamic equilibrium with a finite final concentration $c_w \neq 0$, leading to a decrease in the heat flux. The corresponding value of the catalytic coefficient in Eq. (27.35) is determined by

$$\varphi = \frac{\chi}{1 + \chi + c_w}\left(1 - \frac{c_w}{c_\delta}\right). \tag{27.40}$$

The quantity i_D in Eq. (27.35) must then be calculated from the expression

$$i = i_R(c_\delta - c_w),$$

where, for a binary mixture, it can be assumed that $c_\delta = \alpha_\delta$ and $c_w = \alpha_w$. In addition, in the case of a heated wall, it is necessary to replace i_r by $i_r - i_w$ in Eq. (27.35).

Factors That Decrease Diffusional Heat Transfer

In addition to the catalytic recombination rate k_w, a number of other factors tend to decrease diffusional heat transfer.

1. The velocity gradient $\tilde{\lambda} = V_\delta/x$ appears in Eq. (27.33) and varies inversely with the radius of the spherical nose. Therefore, a decrease in the nose radius will reduce the catalytic coefficient and thereby lower the heat transfer.†

2. With an increase in flight velocity, the total heat transfer increases, but that due to diffusion is decreased in the actual case of a finite recombination rate. As the total heat transfer increases, the portion of heat expended on dissociation is increased, and the part of

†Editor's note: This statement is in agreement with the original reference(6) but is incorrect. It is true that an increase in $\tilde{\lambda}$ reduces the catalytic coefficient φ. But $\tilde{\lambda}$ also enters directly into the expression for q_D (see Eq. (27.33)), and the net result is an increase in diffusional heat transfer with increasing $\tilde{\lambda}$. Thus, a large nose radius is desirable to decrease the heating rate.

the energy released as a result of chemical reaction at the wall is decreased.

3. The wall temperature also has an effect on the diffusional heat transfer. It is evident from Eq. (27.34) that the catalytic coefficient φ is a function of the product $\rho_w k_w$, which in turn is determined by T_w. The recombination rate may be a strong function of wall temperature (e.g., for some types of glass $k_w \sim T_w^{\frac{3}{2}}$), but the density variation is less pronounced. Thus, the quantity $\rho_w k_w$ will be approximately proportional to the wall temperature in this case, and it follows that the coefficient φ will decrease with a decrease in T_w. This means that low surface temperatures prevent the release of a large amount of chemical energy. However, it should be noted that other effects appear, e.g., a large heat flow to the wall due to convection.

The Quasi-equilibrium Boundary Layer

To determine the heat transfer in the case of local equilibrium in the boundary layer from Eq. (27.25a), it is necessary to know the concentration gradient and the enthalpy gradient at the wall. The first quantity is calculated from the condition of an equilibrium value of concentration near the wall using the tables or graphs of thermodynamic functions. To calculate the enthalpy gradient, it is necessary to solve the energy equation, Eq. (3.41), including the diffusion term. Converting this equation to the variables ξ and η, we obtain

$$\frac{\partial}{\partial \eta}\left[\frac{C}{\mathrm{Pr}}(1+d)\frac{\partial g}{\partial \eta}\right] + f\frac{\partial g}{\partial \eta} = 0, \tag{27.41}$$

where the parameter d is defined as

$$d = (\mathrm{Le} - 1)(i_A + i_M)\left(\frac{\partial c_A}{\partial i}\right)_p. \tag{27.42}$$

The Lewis-Semenov number is assumed to be identical for all components, and the subscript p designates differentiation at constant pressure.

Equation (27.41) is to be solved with boundary conditions as given in the following expressions:

$$f(0) = 0, \quad \frac{\partial f(0)}{\partial \eta} = 0, \quad \frac{\partial f(\infty)}{\partial \eta} = 1, \quad g(0) = g_w, \quad g(\infty) = 1.$$

The parameters C and d are determined with the aid of the thermodynamic tables or graphs for air in thermodynamic equilibrium.

Using the solution of this equation and assuming that Le = 1, we can find the heat rate without diffusion, q_T. The effect of a Lewis-Semenov number different from unity can be taken into account by the approximate equation

$$q = q_T\left[1 + (\mathrm{Le}^{0.52} - 1)\frac{i_D}{i_r}\right]. \tag{27.43}$$

The somewhat larger exponent of the Lewis-Semenov number in Eq. (27.35), compared with that in the present case of an equilibrium boundary layer, is explained physically by the fact that diffusion through the thickness of the frozen layer has a more important influence on heat transfer. Despite the difference indicated in the values of the exponents, the total heat flux differs little.

The Effect of the Recombination Rate

The case of a finite recombination rate in the boundary layer is the most realistic, because actually there are neither frozen nor equilibrium flows.

The results of calculations[4] are presented in Fig. 268 for the heat transfer parameter

$$\frac{\mathrm{Nu}_w}{\sqrt{\mathrm{Re}_w}} = \frac{0.71q}{(i_r - i_w)(\tilde{\lambda}\rho_w\mu_w)^{\frac{1}{2}}} \tag{27.44}$$

as a function of the recombination rate parameter C given by Eq. (2.29). In one case the wall was catalytic; in the other, noncatalytic.

Curve 1 in Fig. 268 shows the total heat transfer parameter to a catalytic surface, which is practically independent of the recombination rate parameter. This equality of the heat flow is due to the catalytic effect of the wall at small recombination rates (frozen flow) and by the small catalytic effect of the surface in the equilibrium boundary layer

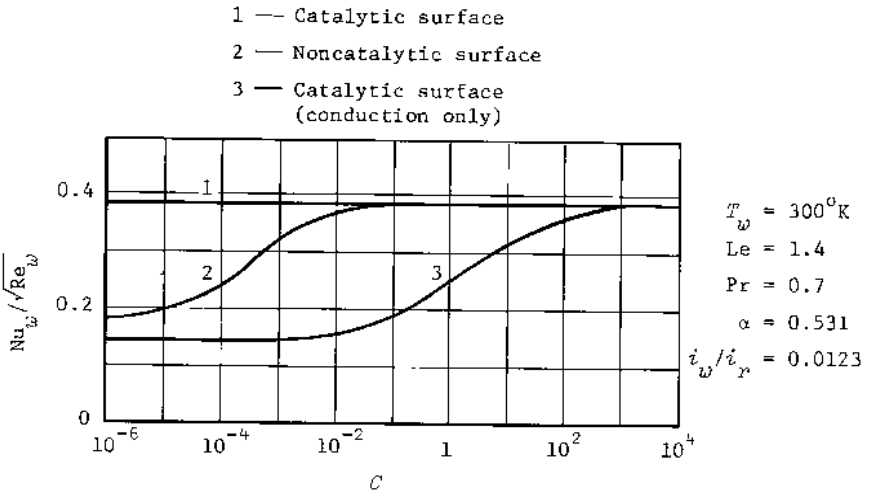

Fig. 268--Heat transfer as a function of the recombination rate

for large recombination rates. In the latter case, the atoms do not succeed in reaching the wall by diffusion but recombine in the boundary layer itself. Thus, as already noted, the calculation of the heat transfer to a catalytic wall can be carried out in practice without considering dissociation.

By comparing curve 1 in Fig. 268 with curve 3, which represents the heat transfer to a catalytic wall due to thermal conductivity alone, we can determine the fraction of the heat flow to a catalytic surface that is caused by diffusion. For large values of the parameter C, corresponding to high recombination rates, the process in the boundary layer is close to equilibrium, and the effect of diffusion toward the wall decreases. In this case, the major part of the heat is supplied by thermal conductivity.

Curve 2 represents the heat transfer parameter to a noncatalytic wall. It is evident that a much smaller value of C is required to produce a frozen boundary layer than for the catalytic wall. This is due to the fact that a much greater number of atoms accumulates near the noncatalytic wall, and a low value of C is required to create frozen flow.

The parameter C varies with the square of the density for a given temperature T_0'. Thus, if the flow in the boundary layer is in equilibrium for atmospheric conditions near sea level where the parameter C is relatively large, it is in a frozen state at high altitudes. If we assume that these two limiting conditions represent a range of values of C approximately equal to 10^4, we must reduce the density 100 times for transition to the frozen state.

The heat transfer at the stagnation point for the flow of a dissociable gas can be calculated from Eq. (27.43) for an equilibrium layer and from Eq. (27.35) for a frozen layer. The heat transfer depends mainly on the product $\rho_0'\mu_0'$ at the outer edge of the boundary layer, where the values of ρ_0' and μ_0' are those for the inviscid parameters at the stagnation point. If the wall is catalytic, the variation in $\rho_0'\mu_0'$ across the boundary layer due to dissociation has no effect on the heat flux, which remains practically the same as in an undissociated boundary layer. If the wall is not catalytic, the total heat transfer can be reduced when the importance of the recombination rate is less than that of the diffusion rate in the boundary layer.

The Enthalpy of Equilibrium Dissociation

If air is examined as a mixture of two components, nitrogen and oxygen, the dissociation enthalpy of the mixture is

$$i_D = c_\delta \frac{\sum_{k=N,O} (ci_R)_k}{\sum_{k=N,O} c_k} = (i_R c)_{O_2} + (i_R c)_{N_2}, \qquad (27.45)$$

where the dissociation enthalpy of the kth component is given by Eq. (2.11) as $i_{Rk} = D_k/2m_k = u_{dk}$. The values of i_{Rk} are given in Tables 2 and 3 and the concentrations are plotted in Fig. 14. For a diatomic gas, $i_D = \alpha u_d = \alpha i_R$, where α is the degree of dissociation of the gas, and $u_d = i_R$ is the characteristic energy of dissociation.

In practical calculations, it is possible to assume that all the oxygen is dissociated by the beginning of the nitrogen dissociation. In this case, the atomic concentration is caused only by the dissociation of oxygen and, therefore, $c = \alpha = 0.2346$. Thus,

$$i_D = 0.2346(i_R)_{O_2}.$$

If the conditions are such that the dissociation of the oxygen is incomplete, $i_D < 0.2346(i_R)_{O_2}$ and the concentration (the degree of dissociation of the mixture) is $c = \alpha < 0.2346$.

At high temperatures and low pressures, the nitrogen dissociates after the oxygen. The enthalpy of the dissociation of the mixture is

$$i_R c = i_R \alpha = i_D = 0.2346(i_R)_{O_2} + (c - 0.2346)(i_R)_{N_2}. \qquad (27.46)$$

Tables or graphs of the thermodynamic functions can be used for rough estimates of the magnitude of i_D. In this case, the enthalpy i_r at the stagnation point is found from the temperature T and the pressure p, and i_D is determined from

$$i_D = i_r - i_{\alpha=0},$$

where $i_{\alpha=0}$ is the enthalpy at the same temperature but without dissociation. For approximate calculations of the enthalpy, the equation

$$i_{\alpha=0} = c_{p0} T \left(\frac{T}{T_0}\right)^{\varphi}$$

can be used, in which the exponent $\varphi = 0.1$ for $T > 1000°K$, and the specific heat c_{p0} is assumed equal to 0.24 kcal/kgf deg for $T_0 = 273°K$.

As an example, let us estimate the maximum value of the heat transfer for infinitely rapid catalysis and for $M_\infty = 15$ and $p_\infty = 0.1$ kgf/cm^2, which corresponds to an altitude of approximately 16 km. The stagnation pressure for these conditions is

$$p_0' = C_{p0} p_\infty \frac{\gamma M_\infty^2}{2} = 30 \text{ kgf/cm}^2.$$

The value of the enthalpy at this point is

$$i_r = \frac{AV_\infty^2}{2g} = \frac{a_\infty^2 M_\infty^2 A}{2g} = 2430 \text{ kcal/kgf}$$

for $A = 1/427$ kcal/kgf m. For these values of i_r and p_0', the temperature is obtained from Fig. 15 as $T_r = 5500°K$. The enthalpy of an undissociated gas at this temperature is $i_{\alpha=0} = 1780$ kcal/kgf. Therefore, the dissociation enthalpy is $i_D = 2430 - 1780 = 650$ kcal/kgf, and the ratio $i_D/i_r = 0.267$.

If it is assumed that Le = 1.45, the effect of diffusion is given by Eq. (27.35) (with the catalytic reaction coefficient equal to unity) as $q/q_T = 1.075$. In this case, the heat flux due to diffusion amounts to 7.5 percent of the total.

The effect of diffusion increases with an increase in velocity, and at very large velocities the ratio i_D/i_r is very close to unity. If it is assumed that $i_D/i_r = 1$, the maximum value of the heat transfer ratio is

$$\frac{q}{q_T} = \mathrm{Le}^{\frac{2}{3}}.$$

For a Lewis-Semenov number of 1.45, this ratio is 1.28, so that the greatest possible increase in heat flux is only 28 percent.

CURVED SURFACES

Thermodynamic Equilibrium

Let us examine some of the relations for calculating the heat transfer at an arbitrary point on a curved surface under conditions of thermodynamic equilibrium.[3] The general form of the function that determines the ratio of the heat flow q at an arbitrary point to its value q_0 at the stagnation point is

$$\frac{q}{q_0} = \frac{F}{F_0} = \frac{(p/p_0')V_\delta r}{2\sqrt{\lambda}\left[\int_0^x (p/p_0')V_\delta r^2\, dx\right]^{\frac{1}{2}}}. \qquad (27.47)$$

Hemispheres. Studies have shown that the distribution of heat transfer over a spherical surface calculated by Eq. (27.47) with a Newtonian pressure distribution, $C_p = C_{p0}\cos^2\varphi$, agrees satisfactorily with experimental data even for $M_\infty < 2$.

To calculate the heat flow, it should be recalled that the velocity

varies almost linearly with the central angle φ for values of φ up to 75° or 80°. Therefore, it can be assumed that the velocity at the outer edge of the boundary layer is $V_\delta = \tilde{\lambda} R_N \varphi$. Furthermore, since

$$dx = R_N\, d\varphi, \qquad r = R_N \sin\varphi,$$

and the pressure ratio for high velocities is given by the Newtonian equation

$$\frac{p}{p_0'} = \cos^2\varphi + \frac{p_\infty}{p_0'} \sin^2\varphi = \cos^2\varphi + \frac{1}{\gamma_\infty M_\infty^2} \sin^2\varphi,$$

Eq. (27.47) can be written in a form more suitable for calculation:

$$\frac{q}{q_0} = \frac{2\varphi \sin\varphi}{\sqrt{D(\varphi)}} \left[\left(1 - \frac{1}{\gamma_\infty M_\infty^2} \right) \cos^2\varphi + \frac{1}{\gamma_\infty M_\infty^2} \right], \tag{27.48}$$

where the function $D(\varphi)$ is defined as

$$D(\varphi) = \left(1 - \frac{1}{\gamma_\infty M_\infty^2} \right) \left(\varphi^2 - \frac{\varphi \sin 4\varphi}{2} + \frac{1 - \cos 4\varphi}{8} \right)$$

$$+ \frac{4}{\gamma_\infty M_\infty^2} \left(\varphi^2 - \varphi \sin 2\varphi + \frac{1 - \cos 2\varphi}{2} \right). \tag{27.49}$$

When $1/\gamma_\infty M_\infty^2 \ll 1$, a simpler expression can be used to estimate the distribution of the heating rate:

$$\frac{q}{q_0} = \frac{2\varphi \sin\varphi \cos^2\varphi}{\left(\varphi^2 - \frac{\varphi \sin 4\varphi}{2} + \frac{1 - \cos 4\varphi}{8} \right)^{\frac{1}{2}}}. \tag{27.50}$$

It is apparent that this expression determines the heat transfer exactly in the limiting case of $M_\infty = \infty$. Furthermore, Eq. (27.50) can probably be used for $M_\infty > 10$, as is shown in Fig. 269, which gives curves calculated from Eqs. (27.48) and (27.50). It was assumed in the calculations that the wall temperature was constant and that $T_w/T_\delta \ll 1$. The heat transfer is a maximum at the stagnation point and decreases with distance,

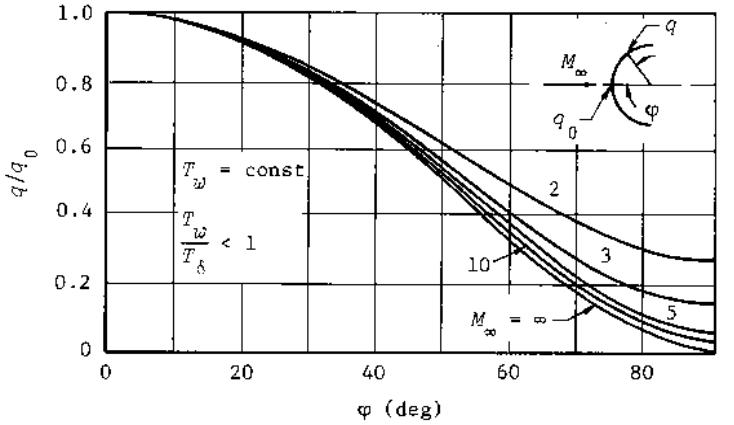

Fig. 269--Heat transfer distribution on a sphere with a laminar boundary layer

because the pressure decreases, and thus the product $\rho_\delta \mu_\delta$ decreases.

Equation (27.48) represents very well the actual distribution of heat transfer. However, this applies for high Mach numbers, for which $p_\infty/p_0' = 1/\gamma_\infty M_\infty^2$. Moreover, for the portion of the surface near $\varphi = 90°$, the actual value of the heat transfer is larger than that obtained theoretically from Eq. (27.48). This is because the static pressure is somewhat higher there than the free-stream pressure, which is the value predicted by the approximate Newtonian equation.

To refine Eq. (27.48), let us assume the following pressure distribution for the sphere:

$$\frac{p}{p_0'} = 1 - \left(1 - \frac{p'}{p_0'}\right) \sin^2\varphi, \tag{27.51}$$

where p' is the pressure at $\varphi = 90°$. Then Eq. (27.48) takes the form

$$\frac{q}{q_0} = \frac{(1 - \zeta \sin^2\varphi)\varphi \sin\varphi}{\left[F_1(\varphi) - \zeta F_2(\varphi)\right]^{\frac{1}{2}}}. \tag{27.52}$$

The following notation is introduced into this equation:

$$\zeta = 1 - \frac{p'}{p'_0},$$

$$F_1(\varphi) = \varphi^2 - \varphi \sin 2\varphi + \sin^2\varphi, \qquad (27.53)$$

$$F_2(\varphi) = \frac{1}{2}\left[\frac{3}{2}\varphi^2 - \varphi \sin 2\varphi\left(\frac{3}{2} + \sin^2\varphi\right) + \frac{3}{2}\sin^2\varphi + \frac{1}{2}\sin^4\varphi\right].$$

The experimental dependence of ζ on M_∞ is presented in Fig. 270. It is evident that for $M_\infty \gg 6$, ζ is practically constant, and the greatest variation is observed for $M_\infty < 3$. Therefore, the ratio q/q_0 also varies considerably at these velocities.

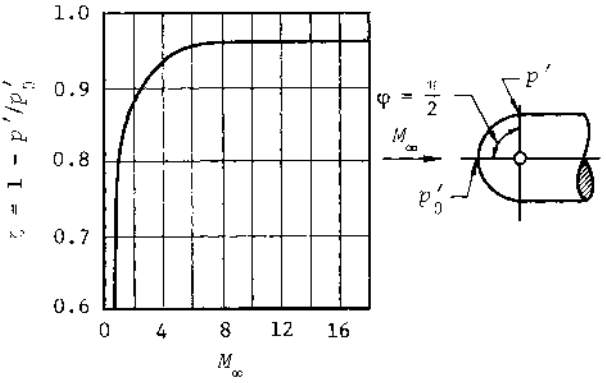

Fig. 270--Relation between the pressure parameter ζ and the Mach number

Comparison with experimental data shows that Eq. (27.52), with the values for ζ presented in Fig. 270, gives satisfactory results for $M_\infty \geq 1$. These results are presented in the form of curves in Fig. 271, where the curve for $M_\infty = 7$ represents the practical limiting value for q/q_0 at very high velocities. The limiting values are independent of Mach number.

The average values of q_{sph}/q_0 for blunting can be computed from the heat transfer distribution around a sphere and are shown as a function of M_∞ in Fig. 272.

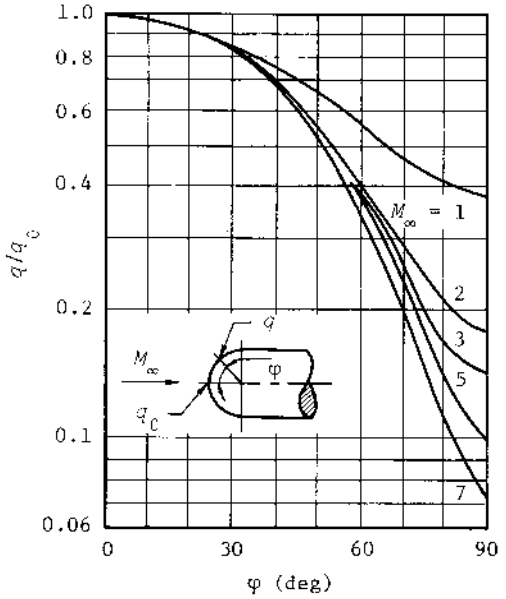

Fig. 271--Distribution of laminar heat flow on a sphere for various Mach numbers

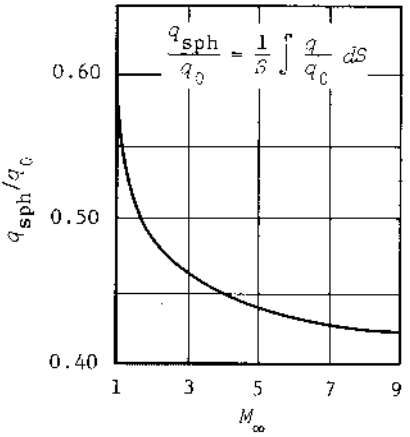

Fig. 272--Average value of heat transfer for laminar flow over a hemisphere

Let us compute the total heat transfer to a sphere with a radius R_N = 0.25 m at M_∞ = 15 and a flight altitude of 30 km. The temperature of the wall is constant and equal to T_w = 1000°K. On the spherical nose, the total thermal flux is determined from the equation

$$Q = \pi^2 R_N^2 q_0 \int_0^{\bar{\varphi}} \frac{q}{q_0} \sin \varphi \, d\bar{\varphi}, \qquad (27.54)$$

in which the variable is $\bar{\varphi} = 2\varphi/\pi$, and q/q_0 is calculated from one of the equations presented above or from the curves in Fig. 271. The integral in Eq. (27.54) can be calculated numerically or graphically. For example, the upper limit for a hemisphere is $\bar{\varphi}$ = 1, and for the given conditions the value of the integral is 0.248. For these conditions, the heat transfer per unit area at the stagnation point was calculated above as q_0 = 1200 kcal/m^2 sec. Thus, the total heat transfer to the surface of a hemispherical nose is given by Eq. (27.54) as 182 kcal/sec.

Flat Noses. The heat transfer on a flat face can be assumed to be constant and equal to its value at the stagnation point. If we use the conditions for the preceding example, q_0 = 560 kcal/m^2 sec and the total heat rate is $Q = \pi R_N^2 q_0$ = 110 kcal/sec. As is evident, the heat flow to a flat surface is considerably less than that to a spherical surface. This is explained not only by the smaller surface area of a flat face but also by the greater deceleration of the flow, which leads to a considerable decrease in velocity at the outer edge of the boundary layer. In addition, there is a reduction in heat flow at the stagnation point of the flat nose because of the decrease in the velocity gradient $\tilde{\lambda}$ compared with that on a sphere.

An accurate analysis shows that the reduction of the total heat flow is less than that indicated in this example, because on a large part of the peripheral surface of the flat face the heat transfer is higher than at the stagnation point. This phenomenon is due to the fact that the pressure decreases more slowly than the velocity increases, moving away from the stagnation point. If the distribution of these parameters is known, the approximate character of the variation in the ratio q/q_0 can be determined from Eq. (27.47), in which it must be assumed

that $r = x$. In Fig. 273, the results of the calculation of this variation are presented for several values of ρ_∞/ρ_0'. The pressure decrease can have a decisive influence near the sharp corner at comparatively small flow velocities and, in spite of a velocity increase, the heat transfer begins to decrease after reaching a maximum value.

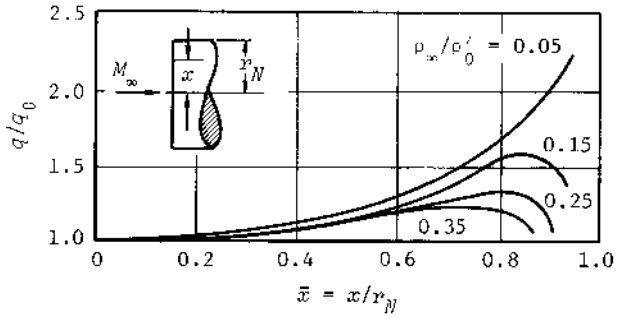

Fig. 273--Distribution of laminar heat flow on a flat face

Equation (27.47) enables us to estimate, approximately, the heat flow distribution around an arbitrary blunt surface. In Fig. 274, the results of such a calculation[7] are compared with experimental data for a flat nose with a beveled edge having a radius of $r = 0.25r_N$. As is evident, the curved surface modified the distribution of the heat transfer somewhat compared with that of a flat nose, although an increase in heating rate with distance from the stagnation point can be noted, as is characteristic for a flat nose.

Ellipsoids of Revolution. Equation (27.47) can be used to calculate the laminar heat transfer around other bodies of revolution. For example, Fig. 275 shows the results of calculations[8] of the variation in q/q_0 as a function of the pressure ratio on ellipsoids with different ratios of the semiaxes a/b. Small values of the ratio a/b correspond to blunt noses with increased drag, whereas the large values refer to bodies with decreased drag.

The heat flux at the stagnation point of an ellipsoid can be computed, for example, from Eq. (27.19) in which $\sqrt{R_N}$ is replaced by $\sqrt{b^2/a}$.

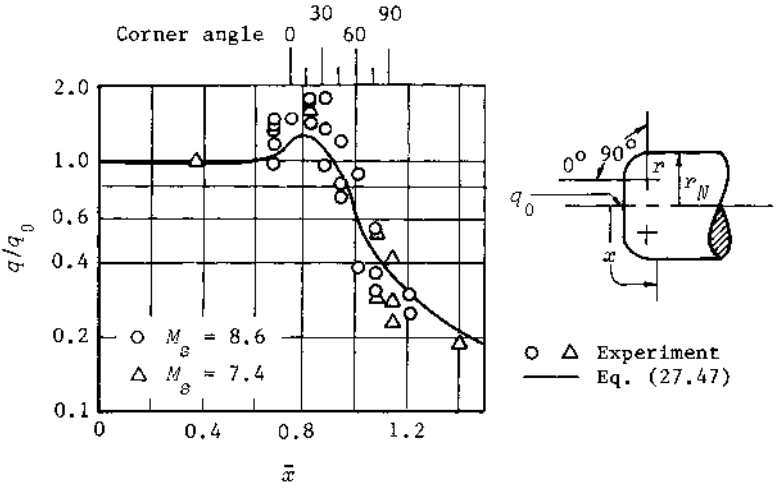

Fig. 274--Distribution of laminar heat flow on a flat face with beveled edges

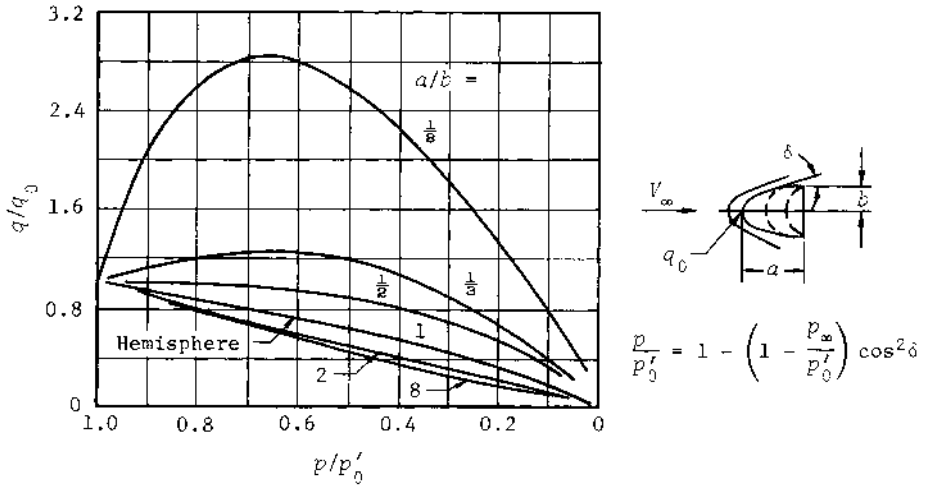

Fig. 275--Heat transfer on an ellipsoid of revolution

Then the heat transfer at an arbitrary point on the surface can be found from Fig. 275. The pressure ratio at this point is determined from Newtonian theory or from experimental data.

Conical Surfaces. Let us examine the calculation of the thermal flow on the surface of a spherically blunted cone.[3] It will be assumed that the inviscid gas parameters on the conical surface are constant and equal to their corresponding values at the end of the sphere. For example, the velocity is

$$V_\delta = \tilde{\lambda} R_N \varphi_c = \tilde{\lambda} R_N \left(\frac{\pi}{2} - \delta_c \right),$$

and the pressure ratio is

$$\frac{p}{p_0'} = \cos^2 \varphi_c + \frac{1}{\gamma_\infty M_\infty^2} \sin^2 \varphi_c .$$

The radial coordinate of an arbitrary point on the cone surface is $r = x_c \sin \delta_c$, in which x_c is the distance along the surface from the imaginary apex of a pointed cone. This distance can be determined from

$$\frac{x_c}{R_N} = \cot \delta_c + \frac{x}{R_N} - \left(\frac{\pi}{2} - \delta_c \right).$$

These relations for V_δ, p/p_0', and r can now be substituted into Eq. (27.47). The integral in the denominator is computed as the sum of two integrals: one with limits of 0 to $x = R_N \varphi_c$ (or for angles from 0 to φ_c) and the other with limits from $R_N \cot \delta_c$ to x_c. The first integral corresponds to the value of the heat transfer at the end of the spherical section (i.e., at the beginning of the conical surface). Of course, the distribution of heat transfer on the spherical tip is the same as that previously obtained for a sphere. The second integral is

$$\int_{R_N \cot \delta_c}^{x_c} G w_c^2 \, dx_c = \frac{G}{3} \left(x_c^3 - R_N^3 \cot^3 \delta_c \right),$$

where the function is

$$G = \tilde{\lambda} R_N \varphi_c \sin^2\varphi_c \left(\cos^2\varphi_c + \frac{1}{\gamma_\infty M_\infty^2} \sin^2\varphi_c\right),$$

and $\varphi_c = \pi/2 - \delta_c$. This angle (or the cone angle δ_c) is the characteristic parameter on which the value and distribution of the heat flux on a conical surface depend.

After the necessary transformations, we obtain the equation

$$\frac{q}{q_0} = \frac{A\bar{x}_c}{\sqrt{B + \bar{x}_c^3}}, \tag{27.55}$$

in which

$$A(\delta_c) = \frac{\sqrt{3}}{2}\left\{\left[\left(1 - \frac{1}{\gamma_\infty M_\infty^2}\right)\sin^2\delta_c + \frac{1}{\gamma_\infty M_\infty^2}\right]\left(\frac{\pi}{2} - \delta_c\right)\right\}^{\frac{1}{2}}, \tag{27.56}$$

$$B(\delta_c) = \frac{(3/16)D(\varphi_c)/\varphi_c}{\left(1 - \frac{1}{\gamma_\infty M_\infty^2}\right)\sin^4\delta_c + \frac{\sin^2\delta_c}{\gamma_\infty M_\infty^2}} - \cot^3\delta_c. \tag{27.57}$$

The function $D(\varphi_c)$ in the last equation is determined from Eq. (27.49) for $\varphi = \varphi_c$. The dimensionless quantity $\bar{x}_c$ in the basic equation, Eq. (27.55), is defined as x_c/R_N. It should be noted that this relation is valid only on the cone, i.e., for values of $\bar{x}_c \geq \cot\delta_c$.

On the basis of these equations, it is possible to calculate the distribution of the heat transfer in the limiting case of $M_\infty \to \infty$. The relations corresponding to this case for the functions $A(\delta_c)$ and $B(\delta_c)$ take the form

$$A(\delta_c) = \frac{\sqrt{3}}{2}\sqrt{\pi/2 - \delta_c}\,\sin\delta_c, \tag{27.56a}$$

$$B(\delta_c) = \frac{3}{16\sin^4\delta_c}\left[\frac{D(\varphi_c)}{\varphi_c}\right] - \cot^3\delta_c. \tag{27.57a}$$

In actual cases, these equations can be used for $M_\infty \sin\delta_c \gg 1$.

In Fig. 276, results are plotted of calculations[3] based on Eqs. (27.55) through (27.57) for a strongly cooled surface ($T_w \ll T_\delta$). The same figure presents results of the calculation from the equation

$$q_c = \frac{0.608 i_r}{\mathrm{Pr}^{\frac{2}{3}}} \left(\frac{\rho_c \mu_c V_c}{x_c}\right)^{\frac{1}{2}}, \qquad (27.58)$$

which is obtained from Eq. (27.55) for $\bar{x}_c \gg 1$. Equation (27.58) gives the value of the heat flow on the surface of the so-called equivalent pointed cone, for which the surface velocity is determined by the expression $V_c = \tilde{\lambda} R_N \varphi_c$. It is evident from Fig. 276 that the heat transfer

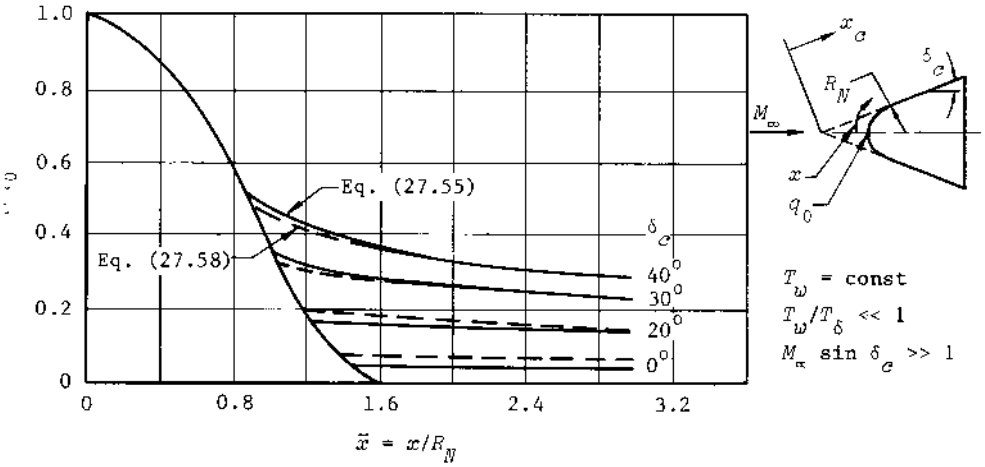

Fig. 276--Laminar heat transfer on the surface of a blunt cone

distribution is almost the same on the blunt and on the equivalent pointed cones for the 30° and 40° cone angles, whereas the heat flow to the slender blunt bodies is less than that for the corresponding equivalent cones.

Equation (27.55) shows that the heat flux far downstream of the stagnation point is approximately proportional to $1/\sqrt{\bar{x}_c}$. Therefore, it is possible to present the heat transfer in a form that is independent of x and R_N by introducing the parameter $(q/q_0)\sqrt{x/R_N}$. This parameter is a function of the local inclination of the surface δ and the free-stream

Mach number. Using the curves presented in Fig. 277, we can determine very simply the heat transfer both on the surface of the blunt nose and on the conical afterbody. Comparison with experimental data and more exact calculations shows that the results obtained from Fig. 277 are better for regions far from the nose on thick bodies. For example, satisfactory results were obtained for cone angles of $\delta_c > 30°$ if the stations were located at a distance of the order $x > 20R_N$ from the nose.

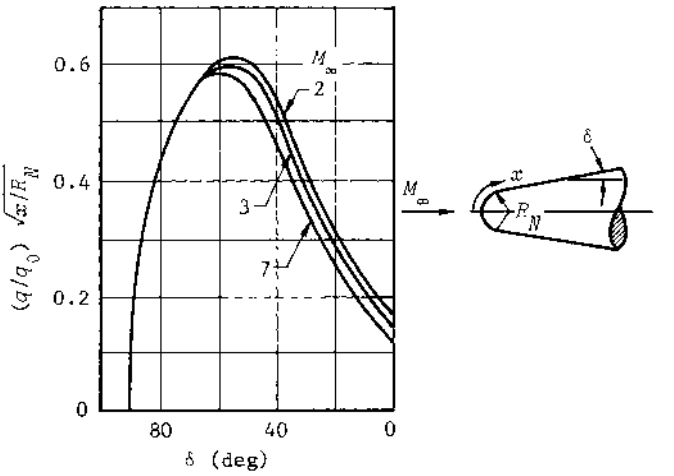

Fig. 277--Laminar heat transfer parameter

The relations presented above, as well as the conclusions, apply to the case in which dissipation in the low-velocity inviscid layer can be neglected. Actually, dissipation does occur and, as indicated earlier, it reduces the effect of blunting. Therefore, the local heat flow will be higher than the calculated value.

The effects of dissipation are a function of the velocity variation at the outer edge of the boundary layer. Thus, the heat flow equals the calculated flux near the nose but increases with distance downstream, approaching the value on a pointed cone. The calculations can be corrected by computing the parameters at the outer edge of the boundary layer including the effect of curvature of the shock wave.

The effect of dissipation can be determined approximately if the heat transfer calculated for a blunt body close to the nose and for a pointed body at a distance from the nose are plotted on a sketch, and then, after assigning a certain length, an interpolation curve is drawn. A longer length must be chosen for dense atmospheres than for rarefied atmospheres.

Cylindrical Surfaces. If a spherical nose has a cylindrical afterbody, the heat transfer distribution can be calculated from Eq. (27.47) for $p/p_0' = 1/\gamma_\infty M_\infty^2$ and $V_\delta = \pi\widetilde{\lambda}R_N/2$; i.e., the parameters are assumed to be the same as at the end of the sphere, where $\varphi = \pi/2$.

Since $r = R_N$ on the cylinder, Eq. (27.47) for the heat transfer takes the form

$$\frac{q}{q_0} = \frac{\pi/\gamma_\infty M_\infty^2}{\left[D\left(\frac{\pi}{2}\right) + \frac{4\pi}{\gamma_\infty M_\infty^2}\bar{x}'_{cyl}\right]^{\frac{1}{2}}}, \tag{27.59}$$

where $\bar{x}'_{cyl} = x'_{cyl}/R_N$ and x'_{cyl} is measured from the beginning of the cylindrical section. The function $D(\pi/2)$ is determined from Eq. (27.49) for $\varphi = \pi/2$:

$$D\left(\frac{\pi}{2}\right) = \frac{\pi^2}{4} + \frac{1}{\gamma_\infty M_\infty^2}\left(\frac{3\pi^2}{4} + 4\right). \tag{27.60}$$

If it is assumed that $p/p_0' = \rho_\delta\mu_\delta/\rho_0'\mu_0'$ and that the heat transfer at the stagnation point (q_0) is given by Eq. (27.16), then for sufficiently distant points on the cylinder (for which $\bar{x}_{cyl} \gg 1$) the heating rate is

$$q = \frac{0.27\dot{c}_p}{\mathrm{Pr}^{\frac{2}{3}}}\sqrt{\frac{\rho_\delta\mu_\delta u_\delta}{x'}}, \tag{27.61}$$

which agrees with the equation for the heat transfer on a flat plate for an equivalent velocity of $u_\delta = \pi\widetilde{\lambda}R_N/2$. Experimental research shows that the heat transfer on a cylinder approaches that on a flat plate somewhat sooner than theory predicts, in fact as far forward as the corner point. If it is assumed that Pr = 0.71 and $u_\delta \approx V_\delta$, then according to Eq. (27.61)

the heat transfer parameter is

$$\mathrm{St}\ \sqrt{\mathrm{Re}} = 0.34,$$

which agrees with the value for incompressible flow.

Calculation of the Heat Flux from the Effective Enthalpy

It was indicated that to obtain Eq. (27.15) we assumed that the product $\rho\mu$ remained constant across the boundary layer. This assumption is valid if the wall is strongly cooled, but in other cases it is necessary to assume that $\rho\mu$ is variable. Such a complication can be avoided if the product of the density and the dynamic viscosity coefficient is assumed equal to the product of the corresponding effective parameters, i.e., to the quantity $\rho^*\mu^*$, where ρ^* and μ^* are functions of the effective enthalpy (Eq. (5.21)). The corresponding expression for heat flow can be obtained from Eq. (27.13), in which the function $F(x)$ is found from the effective parameters; i.e., it is assumed that $F(x) = F^*(x)$. If i_r is replaced by $i_r - i_w$, the heat transfer at an arbitrary point on the surface is given by

$$q^* = \frac{(i_r - i_w)F^*(x)}{2\ \mathrm{Pr}^{\frac{2}{3}}}\ \sqrt{V_\infty \rho'_0 \mu'_0}. \tag{27.62}$$

In this equation, the function $F^*(x)$ is determined from Eq. (27.14), in which p/p'_0 is replaced by $\rho^*\mu^*/\rho'_0\mu'_0$:

$$F^*(x) = \frac{\sqrt{2}}{2}\ \frac{(\rho^*\mu^*/\rho'_0\mu'_0)(V_\delta/V_\infty)r}{\left[\int_0^x (\rho^*\mu^*/\rho'_0\mu'_0)(V_\delta/V_\infty)r^2\ dx\right]^{\frac{1}{2}}}. \tag{27.63}$$

Relating Eqs. (27.62) and (27.63) to stagnation conditions and denoting the corresponding parameters by the subscript 0, we obtain the ratio of the heat flux at an arbitrary point to that at the stagnation point:

$$\frac{q^*}{q_0^*} = \frac{F^*}{F_0^*}. \tag{27.64}$$

The Effect of Vorticity

In the study of heat transfer at the stagnation point, it was established that the effect of vorticity resulted in increased heat transfer. The same result is observed at an arbitrary point on the surface. The results of a study of the effect of vorticity under various conditions are presented in Fig. 278. Using these curves and values for the heat transfer at the stagnation point, we can construct a preliminary curve for the estimation of the heat flow at an arbitrary surface point, accounting for the effect of vorticity.

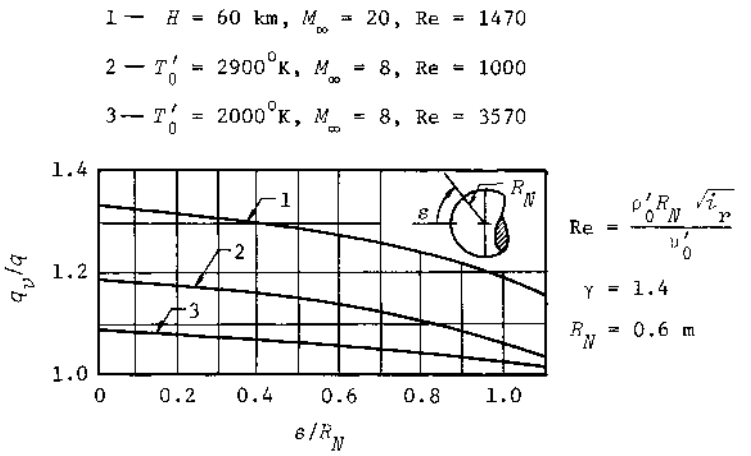

Fig. 278--Effects of vorticity on the local heat transfer to a spherical surface

The Effect of Diffusion

So far, we have presented equations for the calculation of heat transfer on the afterbody of blunt bodies neglecting the effect of diffusion. To correct the calculations for the effect of diffusion, a relation can be used similar to that used in the analysis of heat transfer at the stagnation point. One such equation is

$$q = q_T\left[1 + (\mathrm{Le}^{\beta} - 1)\frac{i_D}{i_r - i_w}\right], \tag{27.65}$$

in which q_T is the heat transfer without diffusion, and the superscript β depends on the flow conditions in the boundary layer. It was shown earlier that at the stagnation point $\beta = \frac{2}{3}$ for frozen dissociation and $\beta = 0.52$ for equilibrium. There are no exact data for the value of β for downstream regions of the surface. Rough calculations show that, in the case of frozen flow, it can be assumed that $\beta = \frac{2}{3}$ for a strongly cooled flat plate. If the data for the stagnation point and a flat plate are compared, it appears that $\beta = \frac{2}{3}$ can be used for an approximate estimate of the effect of diffusion on heat transfer for all parts of the surface of a body.

The expression in the square brackets of Eq. (27.65) can also be interpreted as a correction to the friction coefficient for the effect of diffusion. Therefore,

$$c_f = c_{f0}\left[1 + (\mathrm{Le}^{\beta} - 1)\frac{i_D}{i_r - i_w}\right], \tag{27.66}$$

where c_{f_0} is the friction coefficient without diffusion.

HEAT TRANSFER FOR A TURBULENT BOUNDARY LAYER

Method of Calculation

In practice, some part of the aft surface of a blunt body is covered by a turbulent boundary layer. As a result, the heat transfer from the gas to the body increases considerably in this region. Experimental results are presented in Fig. 279 for a cylinder with a spherical nose.(9) It is evident that the flow becomes turbulent in the Reynolds number range from $4 \cdot 10^5$ to $6 \cdot 10^5$ and the heat transfer is increased by a factor of five.

Measurements have shown that Eq. (5.34a) can be used for the calculation of turbulent heat transfer. In using this equation, we can assume that the Prandtl number is the same as for a laminar boundary layer, although it actually will be different in turbulent flow. For the case of a strongly cooled surface, we can assume that the skin friction coefficient in Eq. (5.34a) is the same as that for an incompressible fluid, using the parameters at the outer edge of the boundary layer. If the wall is cooled only slightly, it is better to use the effective parameters in calculating the skin friction and heat transfer. Nevertheless,

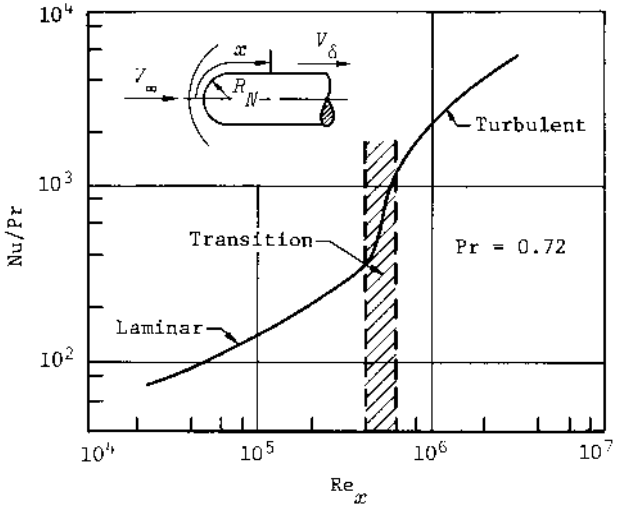

Fig. 279--Heat transfer on a cylinder with a spherical nose

the forms of the applicable relations remain the same as those for incompressible flow.

This method was tested for the laminar boundary layer and gave satisfactory results, and can be assumed to be effective in the case of the turbulent boundary layer. In fact, in such a boundary layer, there is always a thin laminar sublayer in which occur the most important changes in density and other gas parameters. These changes have a decisive influence on the friction and heat transfer. Thus, for calculating turbulent friction and heat transfer it is justifiable to use relations that are similar in external form to those used for calculating the laminar boundary layer.

The Effects of Diffusion

For a dissociated boundary layer, the presence of a concentration profile causes the diffusion of atoms toward the wall, which can be represented by a concentration of atoms at the edge of the laminar sublayer. Therefore, it can be expected that the heat transfer mechanism due to diffusion will be similar to that in a completely laminar layer, and

Eq. (27.65) can be used. However, if this equation is used for the turbulent boundary layer, a correction should be introduced to account for changes in the Lewis-Semenov number and in the exponent β. This correction would only be reliable if it were tested experimentally, but, unfortunately, there are few experimental data at the present time. Some were obtained as a result of heat transfer studies on a cylinder with a spherical nose. It was established that the quantity $(\mathrm{Le}^{\beta} - 1)$ can be assumed approximately equal to 0.4, which then accounts for changes in both the Lewis-Semenov number and in β. Thus, the relation for calculating the turbulent heat transfer on a blunt surface takes the form

$$q = q_T\left(1 + 0.4\,\frac{i_D}{i_r - i_w}\right). \tag{27.67}$$

This relation can be used as a basis for an equation to determine the turbulent skin friction coefficient with diffusion:

$$c_f = c_{f0}\left(1 + 0.4\,\frac{i_D}{i_r - i_w}\right), \tag{27.68}$$

where c_{f0} is the skin friction coefficient without diffusion.

Useful information concerning heat transfer on a blunt surface with a small longitudinal pressure gradient (blunt cones and cylinders) can be obtained from the theory of flow over a flat plate. One of the relations for a plate that can be extended to a surface of revolution takes the form

$$q = A\rho_\delta V_\delta \,\mathrm{Pr}^{-\frac{2}{3}}\,\frac{c_{f0}}{2}\left[2\left(\frac{1 + \alpha_w}{1 + \alpha_\delta}\right)^{\frac{1}{7}} - 1\right]\left[1 + (\mathrm{Le}^{\beta} - 1)\,\frac{i_D}{i_r - i_w}\right](i_r - i_w), \tag{27.69}$$

where the coefficient $A = 1.17$ for a cone.

From Eq. (27.65), it follows that the value of q_T is obtained from the expression

$$q_T = A\rho_\delta V_\delta \,\mathrm{Pr}^{-\frac{2}{3}}\,\frac{c_{f0}}{2}\left[2\left(\frac{1 + \alpha_w}{1 + \alpha_\delta}\right)^{\frac{1}{7}} - 1\right](i_r - i_w). \tag{27.70}$$

If the dissociation at the wall is not zero, the dissociation energy i_D in Eq. (27.69) is calculated for an atom-molecule mixture of nitrogen and oxygen:

$$i_D = (\alpha_\delta - \alpha_w) \frac{\sum_{k=0,N} \left[(c_k)_\delta - (c_k)_w\right](i_R)_k}{\sum_{k=0,N} \left[(c_k)_\delta - (c_k)_w\right]}. \qquad (27.71)$$

The calculations are simplified for a strongly cooled surface because α_w and $(c_k)_w$ are zero. In addition, since $i_w \ll i_r$, the influence of the enthalpy of the gas at the wall can be neglected.

Heat Transfer on a Blunt Nose

A turbulent boundary layer forms on the surface of a blunt nose under certain conditions. If we know the transition Reynolds number, we can find the transition point from laminar to turbulent flow. For blunt bodies, the transition Reynolds number is usually predicted in the form of a Reynolds number based on the momentum thickness δ^{**}; i.e.,

$$\mathrm{Re}_{\delta^{**}} = \frac{V_\delta \rho_\delta \delta^{**}}{\mu_\delta}.$$

The momentum-thickness Reynolds number can be obtained from a correlation[8] of numerical solutions for the laminar boundary layer on a series of ellipsoids of revolution (including a hemisphere), resulting in the expression

$$\mathrm{Re}_{\delta^{**}} = 11.2 \sqrt{b} \left(\frac{\rho_{\infty H}}{\rho_{\infty SL}}\right)^{0.51} \left(\frac{V_\infty}{10^3}\right)^{0.48} \psi, \qquad (27.72)$$

where b, the semiaxis of the ellipse, is in meters, and V_∞ is in meters per second. The function ψ in Eq. (27.72) depends on the location of the point on the surface of the body and on the shape of the surface. Values of ψ for an ellipsoid are presented graphically in Fig. 280 as a function of p/p_0'.

The momentum thickness corresponding to Eq. (27.72) is determined from

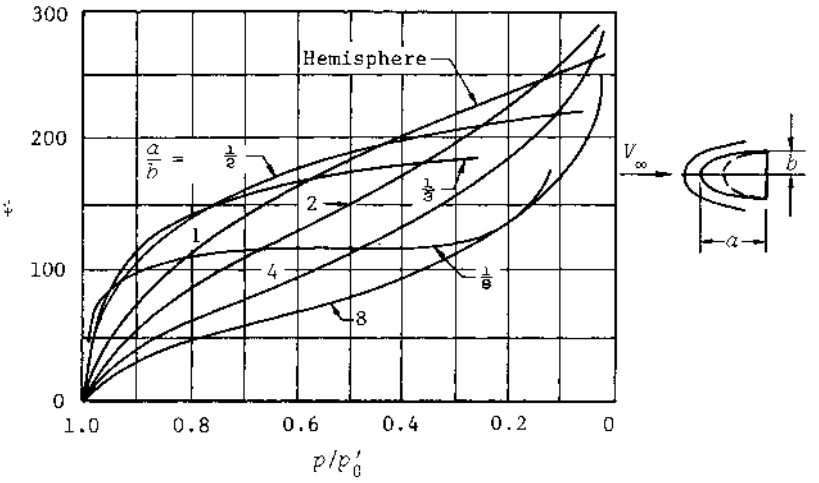

Fig. 280--Parameter for the effects of local pressure gradient and geometric shape on the transition Reynolds number

$$\delta^{**} = \frac{\sqrt{2\xi}}{\rho_\delta V_\delta r}\left[0.491(1 - 0.09\bar{\beta}^{0.4})\left(\frac{\rho_\delta \mu_\delta}{\rho_w \mu_w}\right)^{0.39}\right], \qquad (27.73)$$

where ξ is given by Eq. (27.2). The coefficient $\bar{\beta}$ is a function of the longitudinal velocity gradient and is defined as

$$\bar{\beta} = 2\,\frac{d \log V_\delta}{d \log \xi}.$$

From Eq. (27.73), it is evident that the momentum thickness depends on the degree of cooling of the wall. This is also confirmed by experimental results obtained on a cylindrical body with a hemispherical nose (Fig. 281).

The location of the transition point can be determined by comparing the variation of $Re_{\delta^{**}}$ along the body with experimental values for the transition Reynolds number based on momentum thickness. Experimental data for Re_{tr} on a spherically blunted 30° cone are shown in Fig. 282. These results correspond to a strongly cooled wall. In general, it should be stressed that the transition Reynolds number depends considerably on the wall temperature. The effect of cooling on Re_{tr} can be

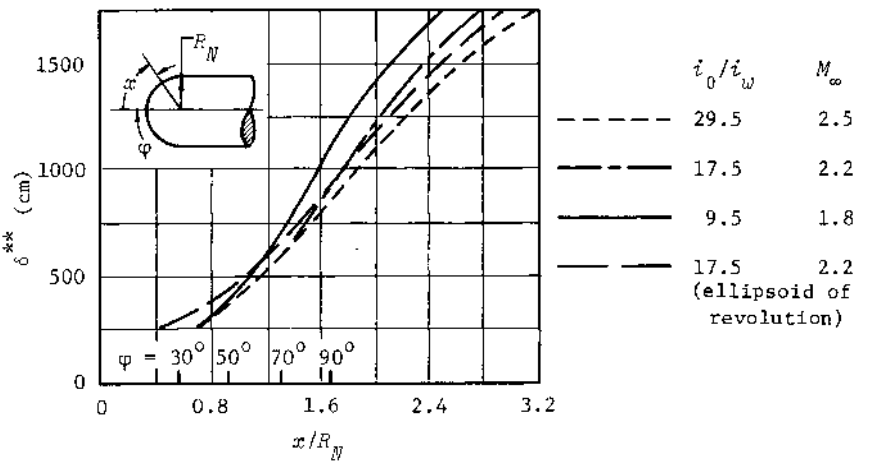

Fig. 281--Momentum thickness on a blunt body with various degrees of cooling

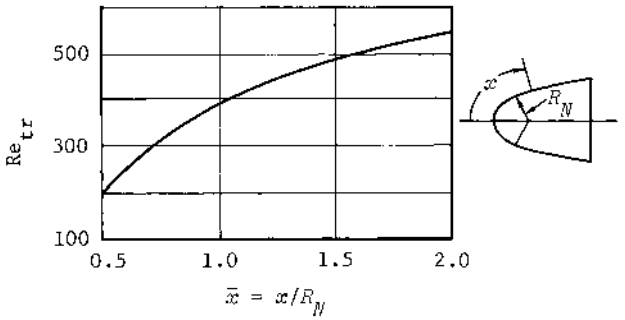

Fig. 282--Transition Reynolds number based on momentum thickness

estimated from Fig. 283, where experimental data are presented for a cylinder with a hemispherical nose. The curves in the figure can be used not only for the curved surface on the nose but also for the afterbody.

Analysis of the curves in Fig. 283 shows that the more intense the cooling of the wall, the larger the transition Reynolds number and the later transition occurs. The relation between Re_{tr} and the cooling parameter i_0/i_w is presented in another form in Fig. 284.

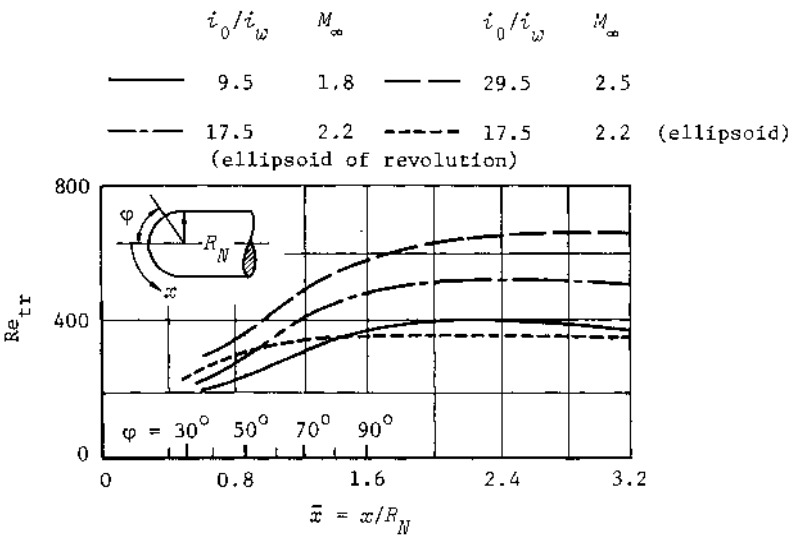

Fig. 283--Transition Reynolds number on a cooled surface

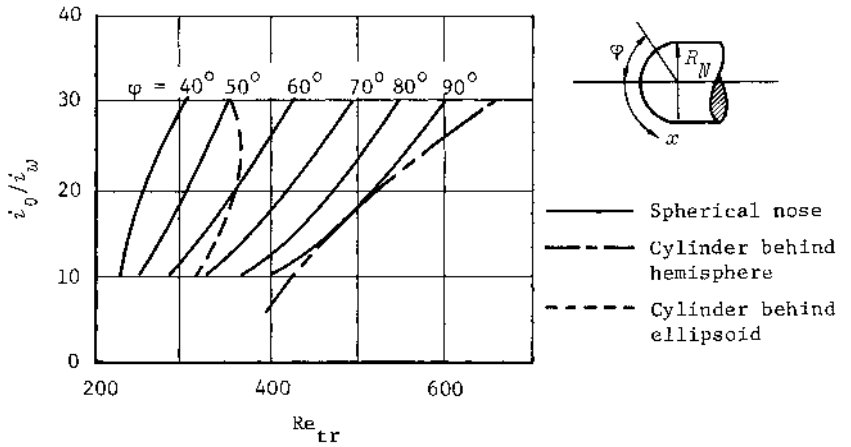

Fig. 284--Variation in transition Reynolds number with degree of cooling

It should be noted that the transition Reynolds number depends not only on the degree of wall cooling but also on the location of the point in question on the surface, i.e., on the history of the boundary layer. Indeed, the history of the boundary layer on the curved surface of the nose is the dominating influence. In the portion located on the cylindrical surface of the body, this influence is unimportant, which is evident from the fact that the transition Reynolds number for a cylinder is almost independent of the distance to the section in question, or, more accurately, of the value of x/R_N (see Fig. 283).

The calculation of the turbulent heat transfer behind the transition point must also account for the history of the boundary layer, i.e., account for the processes that occur upstream. The turbulent heat transfer equation corresponding to Eq. (27.13) for laminar heat transfer is[10]

$$\frac{\widetilde{\mathrm{Nu}}}{\widetilde{\mathrm{Re}}^{\frac{4}{5}}} = \frac{0.029\ \mathrm{Pr}^{\frac{1}{3}}\ \bar{\rho}_\delta \bar{V}_\delta \bar{\mu}_\delta^{\frac{1}{4}} \bar{r}^{\frac{1}{4}}}{\varphi_r^{\frac{2}{5}} \left[\int_0^{\bar{x}} \bar{\rho}_\delta \bar{V}_\delta (\bar{r}\bar{\nu}_\delta)^{\frac{5}{4}}\, d\bar{x}\right]^{\frac{1}{5}}}, \tag{27.74}$$

where the Nusselt number is determined from the expression

$$\widetilde{\mathrm{Nu}} = \frac{q(c_p)_r R_N}{\lambda_r (i_r - i_w)},$$

and the parameter $\widetilde{\mathrm{Re}}$ is given by

$$\widetilde{\mathrm{Re}} = \mathrm{Re}\ \varphi_r^{\frac{1}{2}}, \qquad \mathrm{Re} = \frac{\rho_r R_N \sqrt{i_r}}{\mu_r}.$$

The dimensionless densities, viscosities, and velocities are defined as

$$\bar{\rho}_\delta = \frac{\rho_\delta}{\rho_r}, \qquad \bar{\mu}_\delta = \frac{\mu_\delta}{\mu_r}, \qquad \bar{V}_\delta = \frac{V_\delta}{\sqrt{i_r}},$$

and the parameter φ_r in Eq. (27.74) is

$$\varphi_r = \frac{p_0'}{\rho_r i_r}.$$

All quantities with the subscript r correspond to the recovery enthalpy and can be calculated approximately for stagnation conditions. The dimensionless linear parameters in this equation are based on the radius of the sphere R_N.

As is evident from Eq. (27.74), the integration begins from the conditions at the stagnation point where $\bar{x} = 0$. The solution will be valid only for those sections of the surface (or values of $\bar{x}$) located beyond the transition point from laminar to turbulent flow, the coordinate of which is known approximately. Results of a calculation of the turbulent heat transfer parameter from Eq. (27.74) are compared with experimental data[10] in Fig. 285. With the exception of the transition region, the theoretical results agree satisfactorily with the experimental data.

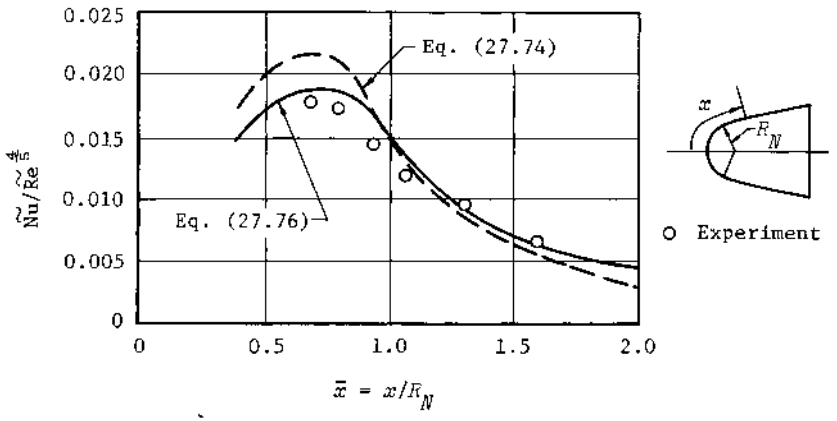

Fig. 285--Turbulent heat transfer parameter

After the heat flow is determined, the local turbulent friction coefficient can be calculated by using the Reynolds analogy:

$$q = \frac{\rho_\delta V_\delta}{\mathrm{Pr}^{\frac{2}{3}}} (i_r - i_w) \frac{c_{fT}}{2}. \qquad (27.75)$$

Studies have shown that approximate heat transfer calculations can be made if we use the relations for a flat plate and neglect the effect

of the longitudinal pressure gradient. If diffusion in the boundary layer is also neglected, the equation for the heat transfer parameter can be written as

$$\frac{\widetilde{Nu}}{\widetilde{Re}_{\delta}^{\frac{4}{5}}} = \frac{0.029\ Pr^{\frac{1}{3}}}{\varphi_{p}^{\frac{8}{5}}} \left(\frac{\bar{\rho}_{\delta}\bar{V}_{\delta}\bar{x}}{\bar{\mu}_{\delta}}\right)^{\frac{4}{5}} \frac{\bar{\mu}_{\delta}}{\bar{x}} \tag{27.76}$$

or

$$Nu^{o} \equiv (Nu)_{Le=1,G=1} = 0.029\ Re_{x}^{\frac{4}{5}}\ Pr^{\frac{1}{3}}. \tag{27.77}^{\dagger}$$

Somewhat better results are obtained if the calculations are made with an effective enthalpy determined by a modified form of Eq. (5.21) that includes the Prandtl number:

$$i^{*} = 0.5i_{w} + 0.22\ Pr^{\frac{1}{3}}\ i_{r} + (0.5 - 0.22\ Pr^{\frac{1}{3}})i_{\delta}. \tag{27.78}$$

The effective parameters corresponding to this enthalpy enter into the Reynolds and Nusselt numbers:

$$Re_{x} = \frac{\rho^{*}V_{\delta}x}{\mu^{*}}, \qquad Nu = \frac{qc_{p}^{*}x}{\lambda^{*}(i_{r} - i_{w})}.$$

The use of the effective parameters in Eq. (27.76) is compared with Eq. (27.74) and the experimental data in Fig. 285.

Further refinement of these equations can be made by accounting for the effects of the longitudinal pressure gradient and diffusion. To do this, a semiempirical relation must be used:

$$\frac{(Nu)_{Le\neq1,G\neq1}}{Nu^{o}} = \frac{(q)_{Le\neq1,G\neq1}}{q^{o}} = 1.037G(\bar{x})\left[1 + (Le^{\beta} - 1)\ \frac{i_{D}}{i_{r} - i_{w}}\right]. \tag{27.79}$$

The function $G(\bar{x})$ determines the effect of the local pressure gradient. As is evident from Fig. 286,[8] the parameter $G(\bar{x})$ depends on the pressure

---

†Editor's note: The function G in the subscript in this equation is a pressure gradient parameter defined on the next page.

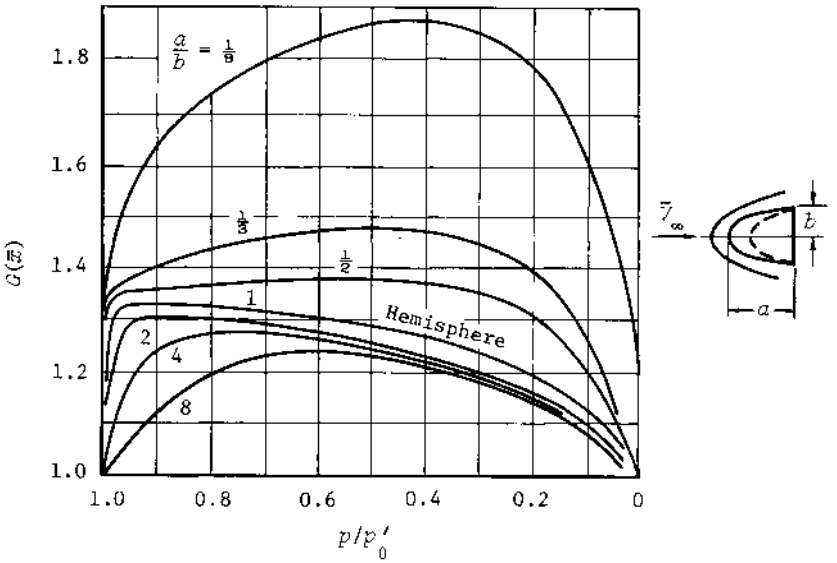

Fig. 286--Parameter for effects of pressure gradient and geometric shape on heat transfer

ratio at a given point on the surface and on the shape of the surface.† The quantity in the square brackets in Eq. (27.79) accounts for the effect of diffusion from the dissociating boundary layer to the wall. The quantity $Le^{\beta} - 1$ can be assumed equal to 0.58, based on experimental results.

†Editor's note: The function $G(\bar{x})$ can be determined from Eq. (27.74):

$$G(\bar{x}) = \left[\frac{\bar{\rho}_\delta \bar{V}_\delta (\bar{\mu}_\delta \bar{r})^{5/4} \bar{x}}{\int_0^{\bar{x}} \bar{\rho}_\delta \bar{V}_\delta (\bar{\mu}_\delta \bar{r})^{5/4} \, d\bar{x}} \right]^{1/5} . \qquad (27.79a)$$

However, Fig. 286 was obtained from Detra and Hidalgo,[8] and their results were based on the formulas of Probstein, Adams, and Rose.[11] For $G(\bar{x})$, the latter authors give

$$G(\bar{x}) = \left(\frac{\bar{\rho}_\delta \bar{V}_\delta^{9/4} \bar{\mu}_\delta^{1/4} \bar{r}^{5/4} \bar{x}}{\int_0^{\bar{x}} \bar{\rho}_\delta \bar{V}_\delta^{9/4} \bar{\mu}_\delta^{1/4} \bar{r}^{5/4} \, d\bar{x}} \right)^{1/5} . \qquad (27.79b)$$

COMPARISON OF HEAT FLOW ON POINTED AND BLUNT CONES

Conical and Spherical Noses

To estimate the effect of blunting on the total heat transfer to a body, it is of interest to first determine the difference in the heat transfer on a pointed cone and on a corresponding spherical nose (Fig. 287). The total heat transfer on a pointed cone is

$$Q_c = 2\pi \int_0^{x_c} q_c r \, dx,$$

which we can evaluate by using Eq. (27.58) for the local heat flow q_c to the surface of the nose. Assuming that Pr is constant, we find

$$Q_c = \frac{0.812 S_c i_r}{\mathrm{Pr}^{\frac{2}{3}}} \sqrt{\frac{\rho_c \mu_c V_c}{x_c}}, \tag{27.80}$$

where the surface area of the cone is given by $S_c = \pi x_c^2 \sin \delta_c$.

The total heat transfer to the surface of an inscribed spherical segment can be calculated from

$$Q_{\mathrm{sph}} = \tfrac{1}{2} S_{\mathrm{sph}} q_0 \int_0^{\varphi_c} \left(\frac{q}{q_0}\right) \sin \varphi \, d\varphi,$$

in which the ratio q/q_0 can be obtained from Eqs. (27.48) or (27.52),

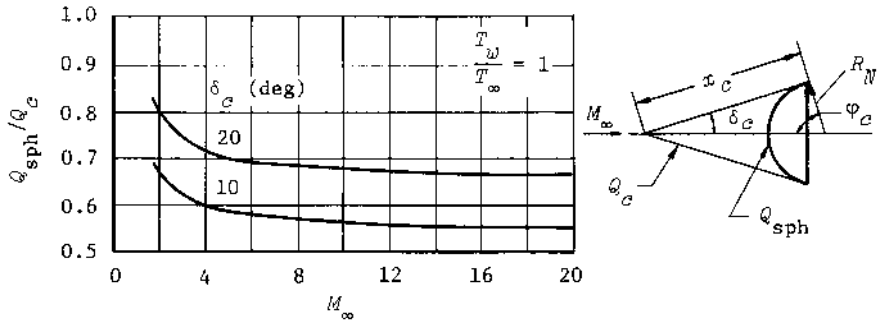

Fig. 287--Comparison of laminar heat transfer on spherically blunted and sharp conical noses

and the surface area of the sphere is

$$S_{\text{sph}} = 4\pi R_N^2 = 4\pi x_c^2 \tan^2\delta_c.$$

The upper limit of the integral is $\varphi_c = \pi/2 - \delta_c$.

The ratio of the total heat flows for the sphere and the cone, i.e., Q_{sph}/Q_c, can be determined for various flow conditions defined by the parameters M_∞, T_w/T_δ, and δ_c. Part of the results of such calculations[1] is presented in Fig. 287 for cones with half angles of 10° and 20° and for a surface cooled to the free-stream temperature. From these data, it is evident that the total heat transfer to the inscribed spherical nose is less than for the conical nose.

Conical Bodies with Pointed and Blunt Noses

We can estimate the variation in the heat transfer on a conical surface as a result of blunting by comparing the local heat flow at corresponding points on the surface of a pointed and a blunt cone. Equation (27.58) can be used, where, as before, the parameters for the blunt and the pointed cones are designated by the subscripts b and c, respectively. Assuming that, in both cases, the Prandtl numbers are identical and that $x_c \approx x_b$ for points far downstream, we obtain from Eq. (27.58)

$$\frac{q_b}{q_c} = \left(\frac{\rho_b \mu_b V_b}{\rho_c \mu_c V_c}\right)^{\frac{1}{2}} \frac{(i_r)_b}{(i_r)_c} = \left(\frac{\text{Re}_b}{\text{Re}_c}\right)^{\frac{1}{2}} \frac{\mu_b}{\mu_c} \frac{(i_r)_b}{(i_r)_c}, \tag{27.81}$$

where the ratio of the Reynolds numbers can be calculated from Eq. (26.10).

If Eq. (2.3) is used to compute the viscosity and the recovery enthalpy is calculated from the expression

$$i_r = c_p T\left(1 + r\,\frac{\gamma - 1}{2} M^2\right),$$

then, assuming $c_p \approx$ const, we can write Eq. (27.81) in the form

$$\frac{q_b}{q_c} = \left(\frac{M_b}{M_c}\right)^{\frac{1}{2}} \frac{1 + r\,\frac{\gamma - 1}{2} M_b^2}{1 + r\,\frac{\gamma - 1}{2} M_c^2} \left(\frac{1 + \frac{\gamma - 1}{2} M_c^2}{1 + \frac{\gamma - 1}{2} M_b^2}\right)^{\frac{1}{2}(n+\frac{3}{2})}. \tag{27.81a}$$

This equation applies to a strongly cooled surface. It indicates that, despite the increase in the local static temperature and in the recovery enthalpy for the blunt cone, the reduction in the Reynolds number leads to a decrease in heat flux on the blunt cone, although the decrease is small. For example, at $M_\infty = 20$, $r = \sqrt{0.71} = 0.845$, $\gamma = 1.4$, and $n = 1$, the decrease is only approximately 5 percent. Thus, there is little need for blunting a pointed cone if it is covered by a laminar boundary layer. The main advantage of blunting appears when a large part of the blunt cone is covered by a laminar layer, but the boundary layer is mostly turbulent on the pointed cone. To illustrate this, let us examine the relation between the friction and heat transfer coefficients for pointed and blunt cones when turbulent and laminar boundary layers, respectively, exist on their surfaces.

The ratio of the local friction coefficients is

$$\frac{(c_f)_b}{(c_f)_c} = \frac{A_b}{A_c}\frac{(c_f^{\mathrm{pl}})_b}{(c_f^{\mathrm{pl}})_c},$$

where $A_b = \sqrt{3}$, $A_c = 1.17$. The coefficients $(c_f^{\mathrm{pl}})_b$ and $(c_f^{\mathrm{pl}})_c$ can be determined from Eq. (5.5), for example, in which it is necessary to convert to the effective parameters in the more general case. If a strongly cooled surface ($i_w \ll i_r$) is considered, this transformation need not be made. However, the calculation must be made from the inviscid parameters on the cone surface. Then, we get

$$\frac{(c_f)_b}{(c_f)_c} = 16.65\left(\frac{\mathrm{Re}_c}{\mathrm{Re}_b}\right)^{1/2}\frac{1}{\mathrm{Re}_c^{3/10}}. \tag{27.82}$$

To estimate the influence of blunting on the average friction coefficient, it is necessary to replace the coefficient 16.65 by 20.4 in Eq. (27.82).

Obviously, to use this equation we must first find the Reynolds numbers for the given points on the blunt and pointed conical surfaces. We can obtain some idea of the order of magnitude of the reduction in friction by assigning anticipated values to these numbers. For example,

if it is assumed that $\mathrm{Re}_c = 10^{10}$ on the pointed cone and $\mathrm{Re}_b = \mathrm{Re}_c/25$ on the blunt cone, the local and average friction coefficients on the blunt surface decrease in comparison with their values on the pointed cone by factors of 12 and 10, respectively.

Equation (27.82) can also be used with the Reynolds analogy for the estimation of the decrease in heat transfer to the blunt surface. For simplicity, it can be assumed that the Prandtl numbers for both bodies are identical. Then, if $i_w \ll i_r$, the ratio of the heating rates is

$$\frac{q_b}{q_c} = 16.65\left(\frac{\mathrm{Re}_b}{\mathrm{Re}_c}\right)^{1/2} \frac{1}{\mathrm{Re}_c^{3/10}} \frac{\mu_b}{\mu_c} \frac{(c_p)_b}{(c_p)_c} \frac{(T_r)_b}{(T_r)_c}.$$

If we assume that the last two ratios on the right side vary little, compute the coefficient of viscosity from Eq. (2.3) and $\mathrm{Re}_b/\mathrm{Re}_c$ from Eq. (26.10), and choose $n = \frac{3}{4}$, we can obtain a simpler relation for the ratio of the local heat flows on the blunt and pointed cones:

$$\frac{q_b}{q_c} = 16.65\left(\frac{M_b}{M_c}\right)^{4/5} \frac{1}{\mathrm{Re}_b^{3/10}} \left(\frac{1 + \frac{\gamma - 1}{2} M_b^2}{1 + \frac{\gamma - 1}{2} M_c^2}\right)^{1/4}. \tag{27.83}$$

The coefficient 20.4 must be substituted for 16.65 to estimate the ratio of the average values of heat transfer.

According to Eq. (27.83), the heat transfer on the blunt body can decrease considerably. For example, for a 10° cone at $M_\infty = 20$, $M_b = 3$, and $\mathrm{Re}_b = 10^6$, the local heat transfer is reduced by a factor of 20 and the average heat transfer by a factor of 16. Experimental research shows that these estimates are very approximate. Actually, the reduction in heat transfer is significantly less, because turbulence occurs on the blunt body before the calculated transition Reynolds number is reached. Thus, a turbulent boundary layer covers a considerable part of the surface, and the heat flow is the same in that region as it is on the pointed cone.

§ 28. VISCOSITY EFFECTS ON THE EXTERNAL FLOW AROUND A BLUNT BODY

ESTIMATE OF THE EFFECT OF VISCOSITY

IN A STUDY of viscosity effects on the external (inviscid) flow parameters, in particular on the static pressure distribution, it is necessary to consider the role of blunting in the formation of the boundary layer. If the free-stream Reynolds number based on the nose diameter is sufficiently large, the influence of the pressure distribution around the blunt nose dominates, i.e., the magnitude and character of the pressure distribution determine the development of the boundary layer. The reciprocal influence of the boundary layer on the external flow is unimportant in the region of the nose. However, this influence increases with distance from the nose and with a thickening of the boundary layer. Therefore, in the calculation of the flow parameters at the outer edge of the boundary layer, it is necessary to take into account the interactions caused by viscous forces.

Studies have shown that, for a body of revolution, the distance L from the blunt nose at which the additional drag (due to viscous effects on the pressure distribution) is equivalent to the drag due to blunting is given by the equation

$$\frac{L}{D_N} = b\,\frac{\mathrm{Re}_{DN}}{M_\infty^2}, \tag{28.1}$$

where b is a coefficient dependent on the flow conditions. For example, it has been found from wind-tunnel tests on a thermally insulated cylindrical surface ($T_w = T_r$) at $M_\infty = 15$ that b is approximately equal to two.

The effects of viscous interaction are decreased considerably for cases in which the surface temperature is much lower than the recovery

temperature, and therefore the boundary layer is thinner than that on an insulated wall. For example, in air at $T_w = 5T_\infty$ and $M_\infty = 15$, the coefficient $b \approx 20$. Thus, viscous interaction is a function of the thermal conditions at the wall, the free-stream Mach number, and Re_{DN}. As an example, let us estimate the interaction on the surface of a sphere-cylinder with $D_N = 1$ m for flight conditions at an altitude of 82 km and a velocity corresponding to $M_\infty = 15$. For these conditions, the Reynolds number is $\mathrm{Re}_{DN} \approx 2640$. If Eq. (28.1) is used, the ratio $L/D_N = 23$ for an insulated wall, while for a cold wall with $T_w = 5T_\infty$ and $b = 20$, the length will be 10 times larger, i.e., $L/D_N = 230$.

For this value of the Reynolds number, it is evident that the effects of viscosity on the pressure distribution can be neglected for bodies having lengths shorter than those calculated above. However, with a decrease in Reynolds number or with an increase in Mach number, the calculated value of L/D_N may be less than the relative length of the actual body, and viscous interaction will be important. For example, at $\mathrm{Re}_{DN} = 225$, $M_\infty = 15$, and $T_r = T_w$, the additional drag due to viscous interaction becomes commensurate with the basic nose drag at a length $L = 2D_N$.

These results are valid only for large Re_{DN} and are of doubtful accuracy for small Reynolds numbers. At the moment, it is difficult to say exactly where the boundary of applicability of the interaction theory is located, i.e., as characterized by some specific value of Re_{DN}. Some data show that a preliminary estimate of the lower limit is probably $\mathrm{Re}_{DN} \approx 100$.

THE EFFECTIVE SHAPE OF THE BODY

The computation of viscous interaction effects on the external flow parameters is based on the calculation of the inviscid flow around an effective body, which is obtained by shifting the given body contour by a quantity equal to the displacement thickness of the boundary layer. The displacement thickness can be calculated approximately on the basis of the theory of an incompressible boundary layer on a flat plate. The displacement thickness is related to the boundary layer thickness by $\delta^* = 3\delta/8$. In turn, δ can be obtained from Eqs. (5.2) and (5.5).

$$\delta = 7.2xc_{fx}.$$

Therefore,

$$\delta^* = 2.7xc_{fx}. \tag{28.2}$$

To determine the local skin friction coefficient c_{fx}, we must take into account the surface shape (cone, sphere, or plate) and also the effects of bluntness on the boundary layer flow.

Since the calculation is of an approximate nature, let us use Eq. (6.28) to estimate c_{fx}. The Stanton number in this equation can be found from the corresponding heat flow equation. Then the relation for the displacement thickness takes the form

$$\delta^* = \frac{5.4qx}{(i_r - i_w)\rho_\delta V_\delta} \mathrm{Pr}^{\frac{2}{3}}. \tag{28.3}$$

To use this equation, the heat flow must be determined. At an arbitrary point on the surface, the heat flow can be defined as $q = \bar{q}q_0$, where the ratio $\bar{q}$ is determined from Eq. (27.50) for a sphere, from Eq. (27.55) for a conical surface, and from Eq. (27.59) for a cylindrical surface. In addition, the corresponding graphs can be used for the calculation.

Using Eq. (27.16) for the heat transfer at the stagnation point and assuming that the Prandtl number is constant, we can write Eq. (28.3) as

$$\delta^* = 4.14(\tilde{\lambda}\rho_0' u_0')^{\frac{1}{2}} \frac{x\bar{q}}{\rho^* V_\delta} \frac{(i_r - i_w)_0}{i_r - i_w}, \tag{28.4}$$

which contains the effective parameters. If the wall is uniformly cooled and $i_w \ll i_r$, then

$$\frac{(i_r - i_w)_0}{i_r - i_w} \approx 1.$$

Furthermore, if it is assumed that $V_\delta = \tilde{\lambda}x$, Eq. (28.4) can be simplified further:

$$\delta^* = 4.14\left(\frac{\rho_0' \mu_0'}{\tilde{\lambda}}\right)^{\frac{1}{2}} \frac{\bar{q}}{\rho^*}. \tag{28.4a}$$

From this equation it follows that, at the stagnation point ($\bar{q} = 1$, $\rho^* = \rho_0'$), the displacement thickness has the finite value

$$\delta^* = 4.14\left(\frac{\mu_0'}{\widetilde{\lambda\rho}_0'}\right)^{\frac{1}{2}}.$$

For the conditions considered in the earlier example ($M_\infty = 15$, $H = 30$ km, and $R_N = 0.25$ m, Table 19), the value of $\delta^*/R_N = 4.32 \cdot 10^{-3}$, i.e., an order of magnitude less than for a thermally insulated surface. If the value of δ^* is estimated for the same free-stream conditions at a point on a sphere corresponding to $\varphi = 80°$, it turns out that the same value of δ^*/R_N is obtained as at the stagnation point. Consequently, viscous interaction on a sphere is negligible for the example in question.

The displacement thickness for points far downstream on a cone and a cylinder (for a cooled surface) can be determined from Eqs. (27.58), (27.61), and (28.3) with the general form

$$\delta^* = \frac{Ax}{\sqrt{\mathrm{Re}_x}}, \tag{28.5}$$

where the coefficient A for a cone and a cylinder is 3.3 and 1.47, respectively. The Reynolds number is $\mathrm{Re}_x = V_\delta \rho_\delta x/\mu_\delta$, where the velocity equals its value at the end of the spherical nose. In practical calculations, the Reynolds number can be computed from Eq. (26.10) or found from Fig. 255.

As an illustration of the application of Eq. (28.5), let us consider the calculation of the displacement thickness for a blunt 10° cone and for a cylinder, each 10 m long. It is assumed that the same flight conditions apply as in the example presented above ($M_\infty = 15$, $H = 30$ m), and that the spherical blunting has the same dimension ($R_N = 0.25$ m). The Reynolds number for these conditions is $9 \cdot 10^7$ for a sharp 10° cone of a length of 10 m. The corresponding Reynolds number for an unblunted cylinder is $5.28 \cdot 10^7$, where an unblunted cylinder can be considered a pointed cone with zero slope. The Reynolds numbers obtained are larger than the transition Reynolds number and, therefore, the boundary layer will be turbulent on the pointed bodies. Since blunting reduces the

Reynolds numbers on a cone by a factor of 30 and on a cylinder by a factor of 48, the boundary layer will be laminar over practically the entire length and, therefore, it is possible to use Eq. (28.5). Substituting the reduced values of the Reynolds numbers, we obtain $\delta^* = 19.2$ mm at the end of the cone and $\delta^* = 14.4$ mm at the end of the cylinder.

The viscous interaction will be greater in turbulent flow. To estimate the displacement thickness in this case, we can use the equation

$$\delta^* = \frac{Bx}{\mathrm{Re}_x^{\frac{1}{5}}}, \tag{28.6}$$

in which the coefficient B for a cone and a cylinder is 0.054 and 0.046, respectively.

It should be noted that this equation gives only limiting values. One of these values corresponds to the case of a thermally insulated wall, for which the Reynolds number must be computed from the effective parameters for $T_w = T_r$. The other limiting value corresponds to the case of a highly cooled wall for which $T_w \ll T_r$. In this case, the Reynolds number must be calculated from the parameters at the external edge of the boundary layer. For the condition $T_w \ll T_r$, and if the reductions in Reynolds number due to bluntness given above are considered, the displacement thickness at the end of a cone and a cylinder is 27 and 28 mm, respectively. Hence, it can be seen that if the thickening for a cone is approximately 2 percent of the base radius, it is significantly greater for a cylinder, approximately 11 percent.

It is interesting to estimate the variation in δ^* for an insulated wall. Calculations show that the effective wall temperature will be approximately 10 times greater than that at the outer edge of the boundary layer. If the variation of ρ and μ with temperature is taken into account, the Reynolds number found from the effective parameters is decreased by 50 times. Thus, the displacement thickness of the laminar boundary layer is increased by a factor of 7, and that of the turbulent boundary layer by a factor of 2.2. The considerable increase in the displacement thickness is related to the decrease in local Reynolds numbers. Thus, the blunting of a body, an increase in flight altitude, or

an increase in the average temperature of the boundary layer, all promote changes in the effective shape of the body.

The results of the calculation of the displacement thickness on a blunt cylinder by another method are presented in Fig. 288 for a thermally insulated body. The displacement thickness parameter

$$\frac{\delta^*}{R_N}(\mathrm{Re})_{R_N}^{\frac{1}{2}}$$

has a value of 0.53 at the stagnation point and at the beginning of the cylindrical section is increased by a factor of 10.

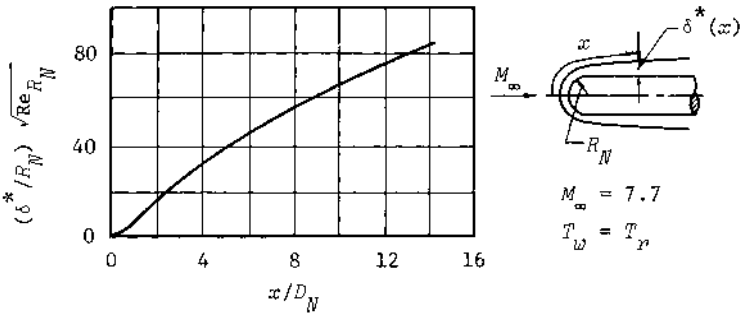

Fig. 288--Variation of the displacement thickness parameter with length on a cylindrical body

After determining the effective shape of the body by shifting the contour in a normal direction by the quantity δ^*, we can compute the pressure distribution and other inviscid parameters for this new shape. One of the characteristics of this new shape (e.g., for a cone) is its effective angle, which can be found approximately from the equation

$$\delta_c^e = \delta_c + \frac{\delta^*}{L},$$

where δ^* is the displacement thickness at a given length L. If a cylinder is considered, its effective shape can be assumed to be a cone

with an angle δ^*/L. However, the determination of the effective shape of a cone or a cylinder is more accurate if it is taken to be a modified surface of revolution with a curved profile. The effective curved shape is obtained, obviously, in all cases when the initial body shape has a curved profile. For the effective curved surfaces, the pressure calculation can be made from the Newtonian equation $C_p = C_{p_0} \sin^2\delta^e$, in which the angle δ^e is determined by the slope of the effective profile relative to the free-stream flow velocity. It is often convenient to construct the body profile to a suitable scale and to establish the required new angle δ^e graphically. In addition, Eqs. (28.5) and (28.6) can be used to compute the increment in slope of the contour, $\Delta\delta$, due to the influence of the displacement thickness for parts of the body sufficiently distant from the blunt nose. Differentiating with respect to x, we obtain

$$\Delta\delta = \frac{d\delta^*}{dx} = \frac{A}{2}\,(\mathrm{Re}_x)^{-\frac{1}{2}}, \tag{28.7}$$

$$\Delta\delta = \frac{d\delta^*}{dx} = \frac{4B}{5}\,(\mathrm{Re}_x)^{-\frac{1}{5}}. \tag{28.8}$$

From these values it is possible to compute the effective slope of the contour $\delta^e = \delta + \Delta\delta$.

The effect of the boundary layer on the pressure distribution is shown in Fig. 289 for the example of a power law body in helium flow. The rather considerable pressure increase due to viscous interaction (on the average approximately 20 percent) is due to the very high Mach number, the comparatively small Reynolds number, and the insulated surface.

In Fig. 290, the effect of Reynolds number on the pressure is reproduced for three points on a cylindrical surface with a spherical nose, where $\mathrm{Re}_\infty = \rho_\infty V_\infty D_N/\mu_\infty$. The boundary layer thickness on this surface depends on the viscous flow conditions over the nose and is larger at a given section for smaller values of Re_∞. It must be kept in mind that for sections of the cylinder far downstream this viscosity effect essentially disappears. It is practically impossible to define a thickness

for the boundary layer under these conditions, since considerable dissipation of the viscous layer occurs in the external flow, and the pressure approaches its value in the unperturbed flow.

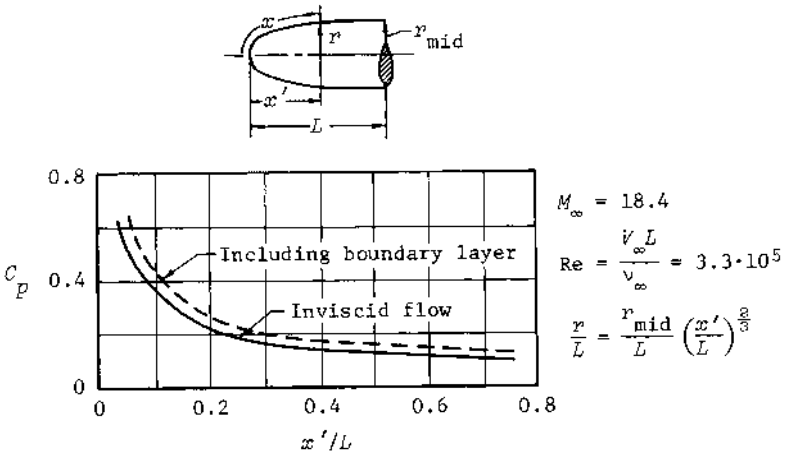

Fig. 289--Effect of the boundary layer on the pressure distribution

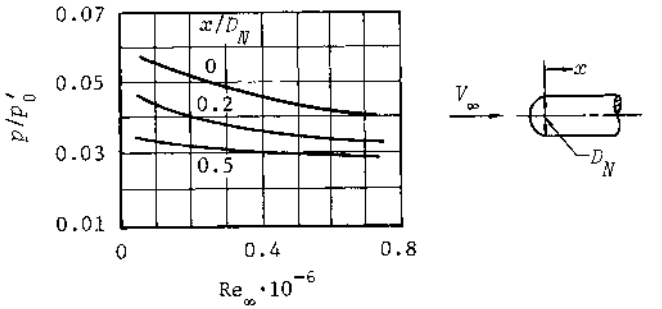

Fig. 290--Effect of Reynolds number on the pressure distribution

Chapter IX

HEAT AND MASS TRANSFER FROM THE SURFACE OF A VEHICLE

Editor's Introduction

THIS CHAPTER PRESENTS *a basic treatment of the process of ablation by melting, vaporization, and sublimation. Although charring ablators have emerged in recent years as attractive materials for providing an efficient thermal protection shield, they are not discussed in the text. Swann* (NASA TR R-195, *June 1964) derives the equations that govern the performance of charring ablators, subject to a diffusion-controlled oxidation mechanism of char removal. A solution is presented for the case of a constant-enthalpy level, and the effects of various material properties and environmental parameters are discussed. Swann, Pittman, and Smith* (NASA TN D-2976, *September 1965) present an analysis of charring ablators consisting of differential equations that are expanded into finite-difference equations and are thus suitable for computerized numerical solutions. The equations provide for three layers of different materials, the first two of which may have moving boundaries.*

Because of the complexity of analyzing theoretically the performance of charring ablators, digital computer programs are usually used for this purpose. Curry (NASA TN D-3150, *December 1965) describes a typical program that predicts the transient thermal response of a charring ablator. The numerical results from this program are in good agreement with exact solutions and test data.*

Lundell, Dickey, and Jones (AIAA J., *June 1968) show that the physical model for analyzing the performance of charring ablative materials in the diffusion-controlled surface combustion regime becomes particularly simple when the surface and char-interface velocities are equal. These velocities, as well as the mass degradation rates, then depend solely upon the ratio of the surface pressure to the nose radius. The surface temperature is a function of this ratio and the enthalpy potential across the boundary layer.*

An important mechanism of ablation may be the failure of a solid surface as a result of loading by aerodynamic shear or by the rapid loss of surface liquid due to the action of both shear and surface pressure gradients on a body in hypersonic flow. Graves (AIAA J., *May 1966) discusses an analytical and experimental investigation of the behavior of ablation materials (pyrex, quartz, phenolic refrasil, and teflon) under conditions that are representative of hypersonic velocity at low altitude. An analysis by Schneider, Dolton, and Reed* (AIAA J.,

January 1968) of elastic/plastic thermal stresses in a carbon/phenolic heat shield during reentry shows that high tangential stresses exist in the char, accompanied by high-frequency char spallation through the peak heating period. In this example, mechanical erosion accounted for two-thirds of the total reentry surface recession.

*A brief discussion is given on page 776 of the desirability of low heat absorption and low heat conduction to the interior of surfaces protected by ablation materials. Gazley (*Handbook of Astronautical Engineering, *1961, Chapter 10) includes the effect of conduction to the interior by defining an effective heat absorption parameter that is more general than the usual effective heat of ablation given in the text. The effective heat absorption of an ablation system is presented as a function of the fractions of heat transferred by radiation, vaporization, and conduction.*

Design techniques, procedures, and example solutions for ablative heat shields are given in the Ablation Handbook, Entry Materials Data and Design, *AFML-TR-66-262, November 1966. The handbook illustrates the important parameters, the problems involved, and the necessary information and sequential steps required in the design process, including mission definition, materials selection, heat shield sizing, and fabrication. Thermal, mechanical, chemical, and ablation data are also presented for a large number of ablative materials.*

§ 29. *GENERAL DEFINITIONS*

ABLATION (MASS TRANSFER)

ON ENTRY INTO THE DENSE LAYERS of the atmosphere, part of the material of a satellite or of the nose section of a ballistic missile is destroyed and carried away due to the fact that the surface is exposed to extreme heating. As a result, the temperature can reach the melting point and, at very high velocities, the vaporization or sublimation temperature. The processes caused by fusion, vaporization, and sublimation are combined under the general term ablation.

Mass transfer must be considered as the most important means of thermal shielding of the remaining part of a vehicle, since a large amount of the energy arriving at its surface is absorbed and dispersed by the mass loss.

THE TWO-PHASE BOUNDARY LAYER

For the majority of usable materials, particularly vitreous materials, the ablation process begins with fusion of the surface into a thin film of molten material, which can be called the liquid phase of the boundary layer. The other phase of the boundary layer is represented by the gas stream next to the molten surface (Fig. 291). When there is insufficient heat to vaporize the liquid, there is negligible interaction between the two phases. Furthermore, since the viscosity of the molten material is much greater than that of the gas, the liquid layer flows with a very small tangential velocity compared with the gas.

For example, calculations show that the ratio of local velocities at the outer edges of the liquid and gas layers under the usual conditions of very high velocity flow is of the order of $V_{x\ell}/V_{x\delta} \approx 5 \cdot 10^{-4}$.

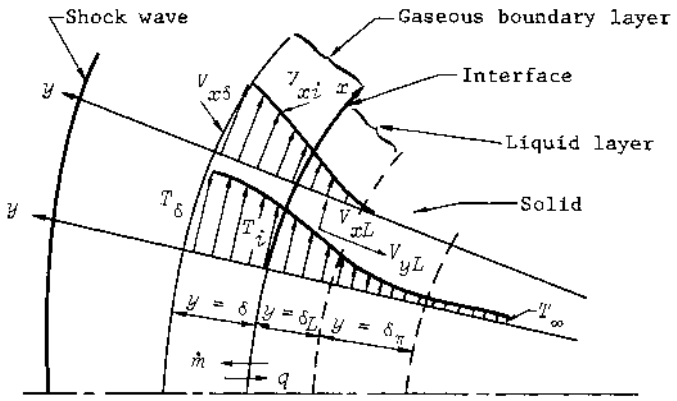

Fig. 291--The two-phase boundary layer on a blunt surface with fusion

Therefore, it can be assumed that the flow in the gaseous phase is practically independent of the liquid layer. In other words, the gas phase behaves as an ordinary boundary layer.

With an increase in heat transfer and temperature, a certain amount of the flowing liquid evaporates, and the vapor penetrates into the gas layer. As a result of this injection of vapor, an interaction occurs between the liquid film and the gaseous boundary layer that leads to a decrease in the aerodynamic heating rate and thus to a reduction in heating. If the temperature of the surface approaches the boiling point, practically the entire liquid layer vaporizes and the maximum amount of vapor enters into the gas phase.

Such is the physical mechanism of the ablation process. Since its basic effect involves the absorption of energy by mass loss, it is very important to know what this energy (heat) of ablation is. As we shall see subsequently, the amount of material lost can be calculated from the value of the heat of ablation.

THE HEAT OF ABLATION FOR VAPORIZATION (OR SUBLIMATION)

To obtain a general expression for the heat of ablation when the molten material is completely vaporized or in the case of sublimation

(for material not having a liquid phase), let us consider the heat balance equation for steady ablation.[1] The heat balance equation for an ablating material expresses the condition that the aerodynamic heat flow (q_i) is expended on heating and vaporization of the material and is partially radiated (q_r). Therefore,

$$q_i = m_v(c_p T_i + i_v) + q_r, \tag{29.1}$$

where m_v is the flow of mass of vaporized material, defined as the rate of mass loss or ablation; i_v is the vaporization enthalpy (latent heat of vaporization); T_i is the surface temperature; and c_p is the specific heat of the material.

The aerodynamic heat flow (q_i) absorbed during ablation is less than the amount of heat (q_0) supplied to the surface in the absence of ablation because of the injection of vaporized material into the boundary layer. The so-called transpiration cooling effect is involved in this phenomenon. The reduced heating rate can be given by $q_i = q_0 - \Delta q$, where Δq is the decrease in heat flow to the wall due to vapor injection and can be represented in the form $\Delta q = q_0(1 - \psi)$. The quantity ψ in this expression is a function of the character of the boundary layer (i.e., whether it is laminar or turbulent) of the mass loss m_v, of the velocity of the body M_∞, and of the molecular weight of the vapor $\bar{\mu}_v$.†

It has been established experimentally that the function ψ has the form[1]

$$\psi = 1 - \frac{\beta m_v}{q_0}(i_0 - i_w), \tag{29.2}$$

where β is called the transpiration coefficient. For laminar and turbulent flows, respectively, the value of β can be determined from

$$\beta_L = N\left(\frac{29}{\bar{\mu}_v}\right)^{\bar{a}}, \qquad \beta_T = \frac{1}{3}\beta_L. \tag{29.3}$$

Equation (29.2) gives satisfactory results for $0.24 \leq \beta \leq 4.0$. From

†Editor's note: It should be noted that $\psi = q_i/q_0$.

experimental data, N and $\bar{\alpha}$ lie in the ranges

$$0.67 \leq N \leq 0.72, \qquad 0.25 \leq \bar{\alpha} \leq 0.4.$$

In particular, for glassy materials it can be assumed that $N = 0.68$ and $\bar{\alpha} = 0.26$.

The molecular weight of the vapors ($\bar{\mu}_v$) of the more common materials such as plastic and glass coincide approximately with the molecular weight of air. If it is assumed that $\bar{\mu}_v = 29$ and $N = 0.7$, the coefficients determined from Eq. (29.3) will be $\beta_L = 0.7$ and $\beta_T = 0.23$.

The surface temperature T_i is approximately equal to the vaporization temperature. The term in parentheses in Eq. (29.1) represents the heat of ablation, and consists of the heat capacity of the material and the heat of vaporization. If it can be determined, the mass loss rate m_v can be computed. In practice, it is convenient to introduce the concept of the effective heat of ablation, defined as

$$q^* = \frac{q_0}{m_v} \quad \text{kcal/kgf}. \tag{29.4}$$

For steady heating, the amount of heat ($q_0 t$) supplied by the ordinary boundary layer in a certain time t is equal to the energy $q^* m_v t$ involved in the loss of mass.

From the expression for w and Eq. (29.1), the effective heat of ablation is given by

$$q^* = \frac{c_p T_i + i_v + \beta(i_0 - i_w)}{1 - q_r/q_0}, \tag{29.5}$$

where the heat flux per unit area due to radiation is $q_r = \varepsilon\sigma T_i^4$. If radiation and the wall enthalpy i_w are neglected, the effective heat of ablation is

$$(q^*)^0 = c_p T_i + i_v + \beta i_0. \tag{29.6}$$

As can be seen, this quantity is a function of the stagnation enthalpy. It should be noted that Eq. (29.6) is not valid when the radiative energy

becomes commensurate with the aerodynamic heating rate. Based on Eq. (29.5), radiative cooling increases the effective heat of ablation according to the relation

$$q^* = \frac{(q^*)^\circ}{1 - q_r/q_0}. \tag{29.7}$$

For some materials, the heat flow to the surface will be increased due to the combustion of the vapors with the oxygen of the air diffusing into the gaseous layer. The amount of heat due to combustion in the laminar layer has been determined to be[2]

$$\Delta q_i = \frac{0.21 i_c}{i_0 - i_w} q_i \tag{29.8}$$

where i_c is the heat of combustion per unit mass of oxygen. Thus, the term q_i in Eq. (29.1) should be modified to the form

$$q_i + \Delta q_i = q_i(1 + \bar{q}_c),$$

where $\bar{q}_c = \Delta q_i/q_i$. Therefore, instead of Eq. (29.5) for calculating the effective heat of ablation, we have

$$q^* = \frac{\beta(i_0 - i_w) + (c_p T_i + i_v)/(1 + \bar{q}_c)}{1 - (q_r/q_0)/(1 + \bar{q}_c)}. \tag{29.9}$$

If radiation and i_w are neglected, this relation is simplified:

$$(q^*)^\circ = \frac{c_p T_i + i_v}{1 + \bar{q}_c} + \beta i_0. \tag{29.10}$$

SIMULTANEOUS FUSION AND VAPORIZATION

The demands associated with the necessity for materials possessing a high effective heat of ablation and a low thermal conductivity result in the use of combinations of heat resistant coatings. For example, one type of coating involves the use of a plastic in conjunction with glass, which has a high viscosity and a low thermal conductivity. A special

feature of these vitreous-plastics or, in general, of similar combination materials is that, under strong thermal action, they behave first as heat absorbers. Then, due to the low coefficient of thermal conductivity, their surface temperature rapidly increases to the level at which simultaneous melting and vaporization is possible. Observations show that in the use of fiber glass the glass component melts and flows without vaporizing, while the plastic component vaporizes.

At high surface temperatures exceeding the melting point, vaporization of part of the molten mass is characteristic for the majority of materials, among them the glassy materials. Furthermore, pyrolysis of the surface layer of the molten material precedes vaporization, as a result of which an additional amount of gas diffuses into the boundary layer. Thus, ablation in the most general case is characterized by simultaneous fusion and vaporization. This feature should be taken into account in determining the effective heat of ablation.

If the total mass loss rate is designated by m, the degree of vaporization (or the vaporization coefficient) can be defined as $\bar{m} = m_v/m$. Therefore, the quantity m_v can be replaced by $m\bar{m}$ in the term in Eq. (29.1) that depends on only the vaporized mass. The effective heat of ablation becomes[1]

$$q^* = \frac{c_p T_i + \bar{m}[i_v + \beta(i_0 - i_w)]}{1 - q_r/q_0}, \tag{29.11}$$

in which the unknowns are the ablation temperature and the coefficient $\bar{m}$. The value of $\bar{m}$ is chiefly a function of the vapor pressure and viscosity of the molten component, factors that depend, in turn, on the temperature as well as on the flow conditions. Some data are available concerning the nature of the variation in $\bar{m}$. For example, with an increase in pressure or a decrease in the stagnation enthalpy, $\bar{m}$ will decrease. For a rough estimate, this coefficient can be defined as the ratio of the mass of the vaporized material to the entire mass.

Equation (29.11) takes radiation into account. If radiation is neglected, the effective heat of ablation is

$$(q^*)^\circ = c_p T_i + \bar{m}[i_v + \beta(i_0 - i_w)], \tag{29.12}$$

and we can consider the influence of radiation later using Eq. (29.7).

FUSION

Fusion represents a limiting case of ablation in the same way as does vaporization. The material melts but it does not evaporate; therefore, the boundary layer is not affected by mass losses of the ablating material.

We can determine the effective heat of ablation by assuming that the vaporization coefficient $\bar{m} = 0$ in Eq. (29.12), resulting in

$$(q^*)^\circ = c_p T_t. \tag{29.13}$$

If this expression is compared with Eqs. (29.6) and (29.12), it is evident that the effective heat for fusion is less than that for simultaneous fusion and vaporization, and also less than that for total vaporization (or sublimation).

In the case of fusion alone, the net heat flux $(q_0 - q_r)$ must be completely absorbed by the liquid. This energy balance is expressed in the form

$$q_0 - q_r = m c_{pL} T_t = m q^*, \tag{29.14}$$

where c_{pL} is the specific heat of the liquid material. As already noted, it is possible to neglect the radiation in a first approximation.

THE FUSION TIME

In practical cases, it is of interest to estimate the time, t_1, required for fusion to begin on the surface of the nose of a body with steady state heating. The equation that determines t_1 is written as

$$t_1 = \frac{1}{4} \frac{\pi \rho c \lambda}{q_{ave}^2} (T_m - T_0)^2. \tag{29.15}$$

In this equation, the average heat rate is

$$q_{ave} = \frac{1}{\pi r_N^2} \int q \, dS, \tag{29.16}$$

where S is the area of the blunt surface. In addition, the temperatures in Eq. (29.15) are defined as T_m, the fusion temperature, and T_0, the initial temperature of the material.

In the derivation of Eq. (29.15), it is assumed that a longitudinal strip of the body is insulated with respect to the lateral surfaces, so that the heat flow is zero at the sides of the strip, and the depth of penetration of the heat in the time t_1 is considerably less than the radius of the nose r_N. Equation (29.15) enables us to compare the time t_1 of the beginning of fusion of bodies with various shapes of blunt noses and indicates that in order of magnitude $t_1 \sim 1/q_{ave}^2$. If the shape of the nose is such that the heat flow is decreased, the time t_1 will be greater. Thus, t_1 will be greater for a flat-faced cylindrical body than for a hemispherical nose.

The accuracy of the calculation from Eq. (29.15) is confirmed by the experimental data presented in Fig. 292. The rapid melting of slender bodies is explained by the increase in the average heating rate, as indicated by Eq. (29.15).

HEAT TRANSFER TO A WALL WITH ABLATION

The general expression for the calculation of heat transfer with ablation has the following form:

$$q = \mathrm{St}\, \rho_\delta V_\delta (i_r - i_w) = mL + q_r. \tag{29.17}$$

The symbol L is the total variation in enthalpy of the ablating material from the solid to the vaporized state. The value of L can be determined from

$$L = c_{pS}(T_L - T_0) + i_L + c_{pL}(T_v - T_L) + i_v, \tag{29.18}$$

where i_L is the heat of fusion. The subscripts S and L designate parameters of the solid and liquid phases of the material, respectively.

Without ablation, the heat transfer is

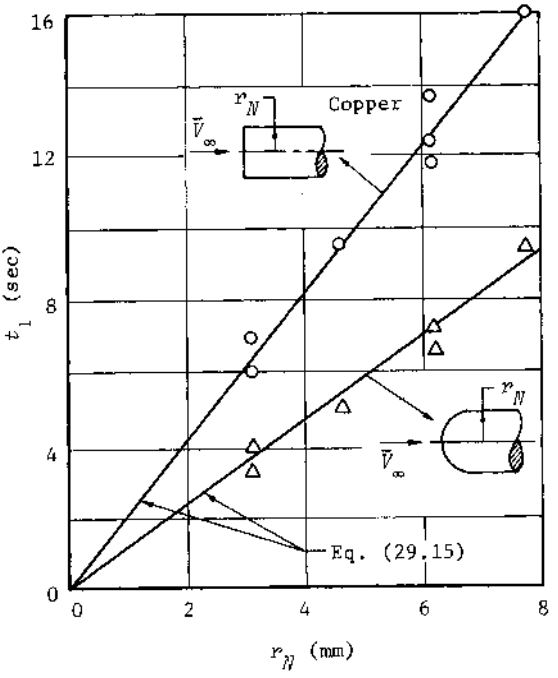

Fig. 292--Time to begin fusion as a function of the type of bluntness

$$q_0 = \mathrm{St}_0 \rho_\delta V_\delta (i_r - i_w).$$

Combining this expression with Eq. (29.17), we obtain for the ratio of the Stanton numbers

$$\frac{\mathrm{St}}{\mathrm{St}_0} = m \frac{L}{q_0} + \frac{q_r}{q_0} = \frac{m}{\rho_\delta V_\delta \mathrm{St}_0 A} + \frac{q_r}{q_0}, \qquad (29.19)$$

in which the parameter $A = (i_r - i_w)/L$.

Since q_0/m represents the effective heat of ablation, Eq. (29.19) can be written as

$$\frac{\mathrm{St}}{\mathrm{St}_0} = \frac{L}{q^*} + \frac{q_r}{q_0}. \qquad (29.19a)$$

The magnitude of this ratio depends on the Reynolds number and Mach number, on the form of ablation, on the properties of the material, as well as on the type of boundary layer, i.e., on whether it is laminar or turbulent. In the case of vaporization, for example, the Stanton number ratio is determined by the function ψ, the relation for which is given in Eq. (29.2).

The graph in Fig. 293 gives an idea of the character of the variation in the heat transfer parameter. The curve determines the relation

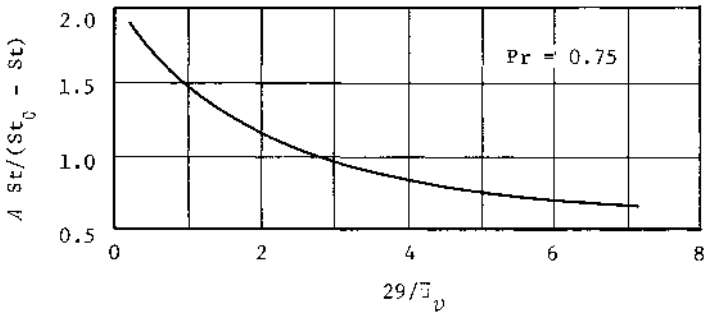

Fig. 293--Laminar heat transfer parameter with vaporization

for $A\ St/(St_0 - St)$ calculated from Eq. (29.19) as a function of the ratio of the molecular weights of the air and the vapor. This curve is approximated by the equation

$$\frac{A\ St}{St_0 - St} = \frac{3.84}{(2 + 29/\bar{\mu}_v)^{0.84}}. \tag{29.20}$$

The ratio of molecular weights has a strong influence on the heat transfer. It is possible to decrease the heat flux considerably by reducing the molecular weight of the vapor, thus causing an increase in the ratio $29/\bar{\mu}_v$.

MASS LOSS

If the effective heat of ablation is known, the rate of mass loss per unit area is given by the equation

$$m = \frac{q_0}{q^*} = \frac{q_0}{(q^*)^0}\left(1 - \frac{q_r}{q_0}\right) \quad \text{kgf/m}^2 \text{ sec.} \tag{29.21}$$

§ 30. *CALCULATION OF THE HEAT OF ABLATION*

THE SYSTEM OF EQUATIONS

THE DETERMINATION OF THE HEAT of ablation consists of the study of the motion of a two-phase fluid over a body, i.e., a fluid having liquid and gaseous phases. If it is assumed that the motion of the liquid layer is independent of the gaseous layer, it is possible to study the liquid boundary layer separately, provided that the heat flow and friction at the liquid-gas interface are given.[3]

The motion of the molten layer is assumed to be steady in a coordinate system located on the liquid-gas interface. Therefore, in a study of this motion, it is possible to use the steady state boundary layer equations in the same form as for an incompressible fluid, with the difference that the viscosity in these equations must be considered a variable depending on the temperature.

The basic system of equations for the laminar layer (the liquid layer is assumed to be laminar) includes the equations of continuity, energy, and motion, Eqs. (3.19a), (3.43), and (3.33), respectively. In the last two equations, it is assumed that the thermal conductivity, the density, and the specific heat are constant, and that the coordinate r is constant and equal to its value for an unmelted surface. The last approximation is possible because the liquid layer is thin.

THE ABLATION RATE

The ablation rate will be considered only in a region close to the stagnation point, since this region experiences the strongest heating, and the problem of heat shielding is of special importance there. We can integrate the continuity equation, Eq. (3.19a), across the thickness of the liquid layer (assuming an infinitely thick liquid layer) to give

$$V_{yi} - V_{yw} = -\frac{1}{r}\int_{-\infty}^{0} \frac{\partial(rV_x)}{\partial x}\,dy, \tag{30.1}$$

where V_{yi} is the normal velocity component of the liquid at the liquid-gas interface and represents the rate of vaporization, and V_{yw} is the normal velocity component of the molten material, i.e., the ablation rate. The latter velocity is assumed to be constant across the thickness of the liquid layer, since the thickness itself is very small.

The process of steady ablation can be represented in such a way that the surface of the melting and vaporizing material is motionless, but the solid body is moving away with the velocity of ablation V_{yw}. This velocity determines the total mass loss rate $m = \rho V_{yw}$, and the velocity V_{yi} determines the rate of mass loss by vaporization, equal to $m_v = \rho V_{yi}$. The velocity ratio $V_{yi}/V_{yw} = \bar{m} = m_v/m$ represents the degree of vaporization.

To determine the ablation rate from Eq. (30.1), it is necessary to find the tangential velocity component V_x of the liquid layer from the equation of motion, Eq. (3.33). Taking into account that the velocities are small due to the high viscosity of the liquid, we can neglect the inertial terms in this equation, and, assuming that $\tau = \mu\partial V_x/\partial y$, we can write Eq. (3.33) in the form

$$\frac{\partial}{\partial y}\left(\mu \frac{\partial V_x}{\partial y}\right) - \frac{\partial p}{\partial x} = 0.$$

If this equation is integrated twice with respect to y, with limits from 0 to y and from $-\infty$ to y, the tangential velocity component is

$$V_x = \left(\mu \frac{\partial V_x}{\partial y}\right)_i \int_{-\infty}^{y} \frac{dy}{\mu} + \frac{\partial p}{\partial x}\int_{-\infty}^{y} \frac{y}{\mu}\,dy, \tag{30.2}$$

where

$$\left(\mu \frac{\partial V_x}{\partial y}\right)_i = \tau_i$$

represents the shear stress at the liquid-gas interface.

The viscosity μ is a strong function of the temperature of the liquid layer and varies, therefore, across its thickness. To find the connection between μ and the coordinate y of an arbitrary point in the layer, it is first necessary to establish the temperature distribution across the thickness of the material. The energy equation, Eq. (3.43), can be simplified for stagnation conditions, because the longitudinal temperature gradient can be assumed to be zero, i.e., $\partial T/\partial x = 0$. Assuming that the ablation velocity V_y is constant and equal to V_{yw} across the thickness of the layer, neglecting the variation in r, and assuming that λ, ρ, and c_p are also constant, we obtain the equation

$$V_{yw} \frac{\partial T}{\partial y} = \frac{\lambda_L}{g\rho_L c_{pL}} \frac{\partial^2 T}{\partial y^2}.$$

Integrating this equation twice with respect to y with limits from 0 to y and from $-\infty$ to y, we obtain the relation for the temperature of the liquid layer:

$$T(y) = \left(\frac{\partial T}{\partial y}\right)_i \delta_\pi \exp\left(\frac{y}{\delta_\pi}\right).$$

Here $(\partial T/\partial y)_i$ is the temperature gradient at the liquid-gas interface and

$$\delta_\pi = \frac{\lambda_L}{g\rho_L V_{yw} c_{pL}}$$

is the thickness of the so-called superheated layer (see Fig. 291); the parameters of the liquid material are designated by the subscript L. Studies have shown that the product $(\partial T/\partial y)_i \delta_\pi$ is approximately equal to the temperature T_i at the interface. Therefore,

$$T(y) = T_i \exp\left(\frac{y}{\delta_\pi}\right). \tag{30.3}$$

The variation of viscosity as a function of temperature is usually established experimentally. For example, for glassy materials, the viscosity varies with the temperature according to the exponential relation

$$\mu = \exp\left(\frac{a}{T} - b\right), \tag{30.4}$$

in which a and b are constants. Equation (30.4) can be approximately represented in a power form:

$$\frac{\mu}{\mu_i} = \left(\frac{T}{T_i}\right)^{-n}, \tag{30.4a}$$

where $n = a/T_i$. Introducing Eq. (30.4a) into Eq. (30.3), we obtain the expression relating the viscosity to the coordinate y:

$$\mu = \mu_i \exp\left(\frac{-y}{\delta_L}\right), \tag{30.5}$$

in which $\delta_L = \delta_\pi/n$ is the thickness of the liquid layer. Thus, the viscosity at the inner edge of the liquid layer, where $y = -\delta_L$, is increased by the factor e.

Substituting Eq. (30.5) for μ under the integral of Eq. (30.2), we can find the relation for the velocity V_x as a function of y. This relation, in turn, enables us to compute the integral in Eq. (30.1). As a result, we obtain the relation for the rate of ablation:

$$V_{yw} = V_{yi} + \frac{2\delta_L^2}{\mu_{Li}}\left[\left(\frac{\partial\tau}{\partial x}\right)_i - 2\delta_L \frac{\partial^2 p}{\partial x^2}\right], \tag{30.6}$$

which is the basic equation in the theory of the motion of a liquid layer. In this equation, the derivative $(\partial\tau/\partial x)_i = \tau_i'$ is a function of the vapor injection into the gaseous boundary layer in the general case, and $\partial^2 p/\partial x^2 = p''$ is, in agreement with Newtonian theory, constant and equal to $-2p_0'/R_N^2$.

ABLATION BY FUSION ALONE (NO VAPORIZATION)

In the case of fusion alone, it can be assumed that $V_{yi} = 0$ in Eq. (30.6), because vapor injection into the gas layer does not occur. Therefore, the liquid film has practically no influence on the gaseous boundary layer, and the ordinary boundary layer relation can be used to calculate the shear stress gradient τ_i'.

If it is assumed that the local skin friction coefficient c_{fx} is given by Reynolds analogy, the friction is

$$\tau_i = c_{fx} \frac{\rho_\delta V_\delta^2}{2} = \mathrm{St}\, \rho_\delta V_\delta^2 \mathrm{Pr}^{\frac{2}{3}} = \frac{q_0 x}{i_0 - i_i} \frac{dV_\delta}{dx} \mathrm{Pr}^{\frac{2}{3}}. \qquad (30.7)$$

In this equation, the heating rate q_0 and the longitudinal velocity gradient dV_δ/dx at the stagnation point are determined from Eqs. (27.16) and (20.27a), respectively. The quantity $i_0 - i_i$ is used in Eq. (30.7) instead of the difference $i_r - i_i$ because it can be assumed that $i_r \approx i_0$ at high velocities.

Using these relations, we can rewrite Eq. (30.6) as

$$4 \frac{\rho_L \mu}{\rho_0' \mu_{Li}} \left(\frac{c_p \lambda_L}{n c_{pL} \lambda} \right)^2 \left[\frac{(q^*)^\circ}{i_0 - i_i} \right]^3 \left\{ 1 + \frac{4}{\mathrm{Pr}^{\frac{1}{3}}} \frac{c_p \lambda_L}{n c_{pL} \lambda} \left[\frac{(q^*)^\circ}{i_0 - i_i} \right] \right\} = 1, \qquad (30.8)$$

where the parameters without the subscript L correspond to conditions for the gas at the stagnation point.

Using Eq. (30.4) for the viscosity, we can determine the effective heat of ablation $(q^*)^\circ$ from Eq. (30.8) and compute the rate of mass loss from Eq. (29.21). The temperature of the interface T_i can be found from Eq. (29.13) if $(q^*)^\circ$ is replaced by q^*, as given by Eq. (29.7).

It is also necessary to know the physical and thermodynamic characteristics of the material for the calculations. One of the materials used for protective coatings, for example, is pyrex. Its composition is 81 percent SiO_2; 12 percent B_2O_3; and small amounts of aluminum (2 percent), sodium (4 percent), and potassium (1 percent). For liquid pyrex, the specific heat is $c_{pL} = 0.25$ to 0.29 kcal/kgf deg, the thermal conductivity coefficient is $\lambda_L = 7.0 \cdot 10^{-4}$ to $9.7 \cdot 10^{-4}$ kcal/m sec deg, and the specific weight is $g\rho_L = 2100$ to 2250 kgf/m^3. The coefficient of dynamic viscosity μ_{Li} is determined from Eq. (30.4) for $b = 17$, $a = 38{,}000$, and a temperature equal to T_i; the viscosity has the dimensions of g/cm sec. In addition to Eq. (30.4), another relation can be used in the calculation of the viscosity of glass:

$$\mu_{Li} = 0.017 \exp \left[\frac{4230}{T_i} \right]^{2.064} \quad \text{kgf sec/m}^2, \qquad (30.9)$$

where T_i is in °K. Having the physical and thermodynamic characteristics

of the material, we can determine the effective heat of ablation from Eq. (30.8).

An analysis of this equation shows that, in order of magnitude, the heat of ablation is

$$(q^*)^\circ \sim \frac{\mu^{\frac{1}{3}} i}{\lambda^{\frac{2}{3}} L}.$$

It is evident that the heat of ablation will be greater, the higher the viscosity and the less the thermal conductivity of the protective coating. However, the stagnation enthalpy of the flow, i_0, is the principal factor.

Using Eq. (30.8) for the heat of ablation of pyrex at the stagnation point, we can obtain the following simple equation:[1]

$$(q^*)^\circ = 178\left(\frac{\rho_{\infty H}}{\rho_{\infty SL}}\right)^{1/(3+n)} \left(\frac{i_0}{RT_{\infty SL}}\right)^{3.64/(3+n)} \text{ kcal/kgf}, \qquad (30.10)$$

where $RT_{\infty SL}$ = 18.8 kcal/kgf, and the value of n can be assumed to be equal to 10 in approximate calculations for very high velocities.

Besides glass, metals also ablate by melting. Experimental data obtained for steel and aluminum give an estimate of the magnitude of the heat of ablation. Those interested in these data should consult the specialized literature.

SIMULTANEOUS FUSION AND VAPORIZATION

The expression for the effective heat of ablation in the case of melting and vaporization can be obtained with Eq. (30.6), which contains both the rate of vaporization V_{yi} and the rate of ablation V_{yw}. We can eliminate the velocity V_{yi} by using Eq. (30.1) and then replace the ablation rate V_{yw} by

$$V_{yw} \approx \frac{q_0}{\rho_L (q^*)^\circ}.$$

We obtain the gradient of the shear stress by differentiating the relation

$\tau_i = \tau_0 \psi$ with respect to x. The latter expression results from the fact that

$$\frac{q_i}{q_0} = \frac{\tau_i}{\tau_0} = \psi.$$

From this relation, the effective heat of ablation can be determined:

$$4\frac{\rho_L \mu}{c_0' \mu_{L0}}\left(\frac{c_p{}^{\lambda}{}_L}{n c_{pL}{}^{\lambda}}\right)^2\left[\frac{(q^*)^0}{i_0 - i_i}\right]^3\Bigg\}\psi + \frac{4}{\mathrm{Pr}^{\frac{1}{3}}}\frac{c_p{}^{\lambda}{}_L}{n c_{pL}{}^{\lambda}}\left[\frac{(q^*)^0}{i_0 - i_i}\right]\Bigg\}\frac{\mu_{L0}}{\mu_{Li}}$$

$$+ \frac{(q^*)^0 - c_{pL}T_i}{i_v + B(i_0 - i_i)} = 1. \qquad (30.11)$$

The parameter ψ is determined from Eq. (29.2), in which the mass loss rate is, in turn, found from Eq. (29.1). The ratio μ_{L0}/μ_{Li} is introduced into Eq. (30.11), in which μ_{L0} is the viscosity corresponding to the temperature at which the vaporization pressure of the material is equal to the stagnation pressure p_0', and μ_{Li} is the viscosity of the material at a vaporization pressure of p_{vi}. Studies show that this ratio is a function of the vapor pressure ratio according to the equation

$$\frac{\mu_{L0}}{\mu_{Li}} = \left(\frac{p_0'}{p_{vi}}\right)^{-\alpha}, \qquad (30.12)$$

in which α is a constant that can be determined by experiment. For example, for silicon gas, $\alpha = 0.825$. The vapor pressure p_{vi} is related to the concentration c_{vi} of the injected vapor by

$$\frac{1}{c_{vi}} = 1 + \frac{29}{\bar{\mu}_v}\left(\frac{p_0'}{p_{vi}} - 1\right). \qquad (30.13)$$

On the other hand, the concentration depends on the vaporization rate, as given by the equation

$$\rho_L V_{yi} = \frac{\psi q_0}{i_0 - i_i}\frac{c_{vi}}{1 - c_{vi}}. \qquad (30.14)$$

Eliminating the concentrations from the last two expressions and substituting V_{yi} from Eq. (30.6), we find for the vapor pressure

$$\frac{p_0'}{p_{vi}} = 1 + \frac{\bar{\mu}_v}{29} \frac{(q^*)^\circ}{(q^*)^\circ - c_{pL}T_i} \left[\frac{i_v}{i_0 - i_i} + \beta \frac{c_{pL}T_i}{(q^*)^\circ} \right], \qquad (30.15)$$

where β is given by Eq. (29.3). In the case of very strong vaporization, $c_{pL}T_i \ll (q^*)^\circ$, and Eq. (30.15) reduces to

$$\frac{p_0'}{p_{vi}} = 1 + \frac{\bar{\mu}_v i_v}{29(i_0 - i_i)}. \qquad (30.16)$$

For approximate computations of the vapor pressure, it is also possible to use an empirical relation obtained for gaseous silica:[3]

$$p_{vi} = \exp\left(-\frac{46{,}000}{T_i} + 14.5\right) \quad \text{kgf/cm}^2. \qquad (30.17)$$

It is also useful to give the equation for the vapor pressure of pure gaseous quartz:†

$$p_{vi} = \exp\left(\frac{130{,}000}{T_i - 273} + 18.48\right) \quad \text{kgf/cm}^2. \qquad (30.18)$$

The viscosity is determined approximately from the vapor pressure:

$$\mu_{Li} = \frac{7 \cdot 10^{-3}}{(p_{vi})^{0.825}} \quad \text{g/cm sec}. \qquad (30.19)$$

Thus, it is possible to determine all the necessary parameters and compute the effective heat of ablation from Eq. (30.11).

The calculations can be simplified by assuming that the temperature of the interface T_i is equal to the temperature of fusion T_f, a value that is known and constant. For example, the fusion temperature

†Editor's note: This expression is incorrect, but the original source cannot be located. With respect to Eq. (30.17), the Russian text reads silicon, but the basic reference states silica.

of glass is approximately equal to 1700°K, and the enthalpy is calculated directly from

$$c_{pL}T_i = c_{pL}T_f.$$

The energy of vaporization is usually determined by experiment. For approximate calculations of the ablation of vitreous materials, it is possible to use, for example, the value i_v = 2470 kcal/kgf obtained for silicon. For pure quartz, the heat of vaporization is i_v = 3000 kcal/kgf.

In practical calculations, it is convenient to use an experimentally obtained relation for the effective heat of ablation of different materials. For example, data have been obtained for fiber glass, consisting of 30 percent plastic and 70 percent glass. From these data, for conditions at the stagnation point in laminar flow, the effective heat of ablation is[1]

$$(q^*)^0 = 125 + 2.7\frac{i_0}{RT_{\infty H}} + 178\left(\frac{\rho_{\infty H}}{\rho_{\infty SL}}\right)^{1/13}\left(\frac{i_0}{RT_{\infty H}}\right)^{7/25} \quad \text{kcal/kgf.} \quad (30.20)$$

Along with this equation, a more general relation can be used:

$$(q^*)^0 = (q^*)^0_{\bar{m}=1} - (1 - \bar{m})\tilde{q} \quad \text{kcal/kgf,} \quad (30.21)$$

which indicates a linear variation of the effective heat of ablation with the vaporization coefficient. The function $\tilde{q}$ in this relation is given by

$$\tilde{q} = 0.554(7430 + 5.38\cdot10^{-5}V_\infty^2) \quad \text{kcal/kgf.} \quad (30.22)$$

The quantity $(q^*)^0_{\bar{m}=1}$ represents the effective heat of sublimation and can be determined by the equation

$$(q^*)^0_{\bar{m}=1} = 0.554(8580 + 5.38\cdot10^{-5}V_\infty^2) \quad \text{kcal/kgf.} \quad (30.23)$$

The velocity in Eqs. (30.22) and (30.23) is in meters per second. The case of sublimation to which Eq. (30.23) corresponds is unrealistic

for refractory and noncombustible materials like quartz; i.e., it is practically impossible to obtain the conditions for which $\bar{m} = 1$. For an estimate of the process that occurs, a series of values of $\bar{m} \leq 1$ can be chosen and the ablation rate and mass loss determined at various points of the trajectory. For example, values of $\bar{m} = 1$ and 0.25 can be assumed.

A special feature of quartz as a refractory material is the high surface temperature, approximately 2200° to 2300°K. Therefore, the correction for radiation in the computation of the effective heat will be more essential here. The radiative flux increases, making the material less liquid. Then, according to Eq. (29.7), the effective enthalpy reaches so great a value that the mass loss due to ablation will be negligibly small. In this case, the surface undergoes intense cooling by radiation, and the heat transfer will be close to that for radiative equilibrium. Under these conditions, the material practically behaves as a heat sink.

The phenomenon of total radiative equilibrium can occur for smooth variations of a small heat input (e.g., for a gradually descending satellite) when it is possible to establish a balance between the radiation and the heat input. For this limiting case, $q^* \to 0$, and the mass loss approaches zero. Thus, under conditions of radiation equilibrium characteristic of gliding vehicles, the material plays the role of a heat-insulating covering.

The noses of rockets are subject to a considerably higher heating rate for short periods of time, and the temperatures do not reach their equilibrium values; thus, the coating provides more protection as an ablating material than as ordinary thermal insulation.

In the special cases considered below, Eq. (30.11) gives comparatively simple results. Let us assume that for certain flight conditions

$$(i_0 - i_i) \gg c_{pL}T_i, \qquad i_v \gg c_{pL}T_i,$$

and, therefore, $(q^*)^0 \gg c_{pL}T_i$ so that the vaporization coefficient will also be considerably less than unity. The first term in Eq. (30.11), which contains the major effects of viscosity, will be greater than

the second term when the viscosity is moderate and when the effects of vaporization are large. Consequently, it is possible to neglect the second term, and Eq. (30.11) reduces to

$$\widetilde{q}^3(A + B\widetilde{q}) = \rho'_0 u_{L0}, \tag{30.24}$$

where $\widetilde{q} = (q^*)^\circ/(i_0 - i_i)$, and A and B are coefficients that can be derived from Eq. (30.11). For the assumptions stated above, A and B are weak functions of the temperature T_i.

The second limiting case is that of small viscosity and negligible vaporization. Hence,

$$[(q^*)^\circ - c_{pL}T_i] \ll c_{pL}T_i.$$

Under these conditions, the second term of Eq. (30.11), which indicates the influence of vaporization, is negligibly small. It is apparent that, without the second term, the simplified equation is similar to Eq. (30.8) for determining the effective heat of ablation for fusion.

THE CASE OF VAPORIZATION ALONE (OR SUBLIMATION)

Another limiting case results from a very large viscosity. The first term in Eq. (30.11) will be small and can be neglected, and the equation transforms into Eq. (29.12) with $\bar{m} = 1$. This corresponds to that process of ablation in which the effective heat of ablation is maximum and independent of viscosity.

Experimental data are available for a number of materials from which one can evaluate certain characteristics and estimate the effective heat of ablation for sublimation. For example, data are known for polymer materials such as teflon $(C_2F_4)_n$. This polymer is subject to pyrolysis under the effect of heat, as a result of which the solid is vaporized into a monomer, C_2F_2. The basic physical and thermodynamic parameters for teflon are the following. The ablation temperature for laminar heating is $T_i = 445°K$, the sublimation enthalpy is $i_v = 416$ kcal/kgf, the molecular weight of the vapor is $\bar{\mu}_v = 100$, the heat of combustion of the vapor in oxygen is $i_c = 5550$ kcal/kgf, and the specific

heat of the material is $c_p = 0.25$ kcal/kgf deg. For these data, Eq. (29.6) gives

$$(q^*)^\circ = 527 + 0.5i_0 \quad \text{kcal/kgf}. \tag{30.25}$$

Research shows that the ablation of teflon is accompanied by the burning of part of the vapor in the boundary layer, as a result of which the C_2F_2 is transformed into the compound COF_2. This decreases the effective heat of ablation. Taking into account the effect of burning by using Eq. (29.10), we obtain

$$(q^*)^\circ = \frac{527i_0}{i_0 + 1165} + 05i_0. \tag{30.26}$$

A comparison of Eqs. (30.25) and (30.26) shows that the influence of burning on the effective heat of ablation is small for values of i_0 of the order of 1500 kcal/kgf and higher. In addition, radiation has an influence on the heat of ablation. However, the equations presented do not account for this effect because radiative cooling is negligibly small at the ablation temperature indicated above.

It should be added that Eqs. (30.25) and (30.26) were obtained in wind tunnels where the flow conditions corresponded to altitudes of 80 to 90 km. The effects of altitude can be considerable, especially at very high flight velocities and for significant changes in altitude. The effective heat of ablation increases with an increase in altitude. For example, as is evident from Fig. 294, for an enthalpy difference of $i_0 - i_w = 4420$ kcal/kgf, an altitude change from 3 to 75 km causes an increase in the effective heat of ablation of teflon of approximately 30 percent.

For plastics consisting of a mixture of phenolic resin and nylon, the equation for the effective heat of ablation, analogous to the corresponding equation for teflon, has the form

$$(q^*)^\circ = 832 + 0.5i_0 \quad \text{kcal/kgf}. \tag{30.27}$$

The special feature of this plastic is that the carbon residue that

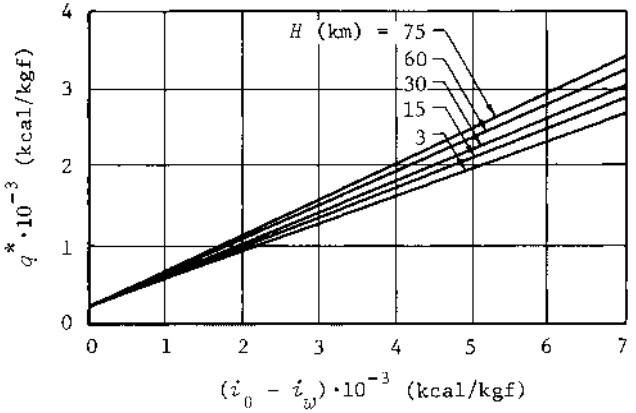

Fig. 294--The effective heat of ablation of teflon

remains after its vaporization is superheated and consequently can radiate intensely.

EVALUATION OF THE EFFECTIVENESS OF THE COATING MATERIAL

It is evident from Eq. (29.21) that the heat of ablation must be large to decrease the mass loss. However, for effective heat protective coatings, it is not enough that the heat of ablation be high. It is also necessary that the material absorb as little heat as possible from thermal conduction. In other words, it is necessary that the ratio of the heat conducted to the interior,

$$q_c = g\rho c_p T_i \delta_{\text{п}} = \lambda \frac{T_i}{V_{yw}},$$

to the total energy $Q = q_0 t$, i.e., the quantity

$$\frac{q_c}{Q} = \frac{\lambda T_i}{q_0 t V_{yw}} = \frac{\lambda \rho T_i q^*}{q_0^2 t} \tag{30.28}$$

be significantly less than unity. Thus, in addition to the requirement for a large value of q^*, it is necessary that the product $\lambda T_i q^*$ be small. For this reason, the material must have as small a coefficient of thermal

conductivity as possible. The required value of the coefficient of thermal conductivity can be estimated if it is assumed that the ratio q_c/Q must be less than unity.

AN EXAMPLE OF THE CALCULATION OF ABLATION

As an illustration, let us calculate the mass loss from the nose section of a vehicle for the conditions of the example presented with Table 19 on page 693 (M_∞ = 15, H = 30 km). The stagnation enthalpy is given in the table as i_0 = 2586 kcal/kgf. For convenience, we shall consider a flat-face surface and assume the heating rate per unit area over the entire flat nose to be equal to that at the stagnation point. In the example, it was shown that at R_N = 0.24 m, the heating rate q_0 = 560 kcal/m^2 sec. In addition, it is necessary to know the duration of heating, which will be assumed to be 100 sec. The results of the calculation according to the foreign literature are presented in Table 20. The materials were chosen in order to present three different types of local ablation: fusion (pyrex glass), simultaneous fusion and vaporization (fiber glass and quartz), and sublimation (teflon).

Table 20

EXAMPLE CALCULATION OF MASS LOSS

Parameter	Material			
	Pyrex	Teflon	Fiber glass	Quartz
	Equation for $(q^*)^\circ$			
	(30.10)	(30.26)	(30.27)	(30.21)
	Important results			
$(q^*)^\circ$ kcal/kgf	510	1820	1007	939
T_a °K (given) kcal/m^2 sec	1300	445	2200	2200
$q_{rad} = \varepsilon\sigma T_a^4$ (assuming ε = 1)	39.2	0.54	323	323
q_{rad}/q_0	0.07	0.001	0.577	0.577
q^* kcal/kgf (Eq. (29.7))	548	1820	2376	2214
m = 560/q^* kgf/m^2 sec (Eq. (29.21))	1.02	0.307	0.236	0.253
Mass loss (kgf) $(\pi R_N^2 t)m$ = 19.6m	20	6.02	4.63	4.96

In practice, this type of analysis of coating materials should take into account the variation with time of the heat transfer to the surface. If the variation is rapid and the ablation process is assumed to be steady then, due to the small coefficient of thermal conductivity, the rate of penetration of heat to the interior of the refractory material will be small compared with the rate of ablation. Thus, interior insulation of the ablating material may not be important. In the other case, when heating occurs over a long period of time and ablation is less important, an additional amount of protective refractory material may be required as insulation.

In the final choice of material, attention must be paid to its deformation, the depth of disintegration of the structure of the surface layer, the resistivity to thermal loads, etc.

If necessary, we can extend the calculation to the case of a blunt nose of arbitrary shape by determining the average heating rate from Eq. (29.16). We can then determine the mass loss by calculating the ablation of the material from the surface of a flat face with a heat flow per unit area equal to this average value.

It is evident from Table 20 that the mass loss due to ablation is not identical for the different materials; it is the least for fiber glass and quartz. However, to reach a final conclusion concerning the effectiveness of the coatings, it is necessary to compute, in addition, the weight of the heat-insulating layer and then determine the total amount of the shielding material. The heat-insulating layer is analyzed by the theory of thermal conductivity, with given conditions of the assumed temperature at the inside of the insulation and the temperature of the outer surface, T_i. The mass of fiber glass or quartz required for insulation will be larger, as a result of their high external temperatures, than of teflon or pyrex. Therefore, the total weight of the heat protection material will also be larger, and pyrex and teflon are preferable.

Chapter X

AERODYNAMICS OF RAREFIED GASES

Editor's Introduction

THIS CHAPTER PRESENTS *a short summary of rarefied gas dynamics and application of the results to bodies of revolution. In general the material in the chapter is disappointing, and the interested reader must refer to other sources to obtain a basic understanding of the theory of rarefied gas dynamics or to find summaries of the plentiful analytical and experimental results for aerodynamic forces.*

*The introductory material in Section 31 contains a discussion of the flow regimes in rarefied gas flow, but little attention is given to the large and important region between slip flow and free molecule flow called the intermediate or transition region. A good summary of theoretical work on the transition regime is given by Patterson in his Wright Brothers Lecture (*AIAA J., *April 1965).*

*There is very little discussion in Section 31 of the importance of interactions between the molecules and the surface as discussed by Schaaf and by Schamberg (*RAND R-339, *1959), among many others. Excellent summaries of the magnitude of the thermal accommodation coefficient with various surface conditions have been published by Hartnett (*Rarefied Gas Dynamics, *1961) and by Wachman (*ARS J., *January 1962). A survey of current developments in the study of gas-surface interactions is presented by Hurlbut (*Rarefied Gas Dynamics, *1967); the volume also contains many papers dealing with specific results. Patterson's Wright Brothers Lecture (op. cit.) also contains a good summary of the effects of surface interaction.*

Section 32 on free molecule flow is based largely on material from Patterson's book.[2] *The only explicit formula given for the force coefficients on a specific body shape is that for the sharp cone in Eqs. (32.42) through (32.44). Formulas for the lift and drag of other shapes are given by Ashley (*J. Aero. Sci., *February 1949) and by Schaaf and Chambre (*Fundamentals of Gas Dynamics, *1958).*

Many theoretical and experimental results have been published in recent years on the gas dynamics of the slip flow and transition regimes; these supplement the discussion in Section 33. A good source for these results, as well as for other recent advances in the study of rarefied gas flow, is the series of volumes titled Rarefied Gas Dynamics, *published biannually by the Academic Press, which represent the published proceedings of International Symposia on Rarefied Gas Dynamics initiated*

in 1960. The proceedings of the Sixth Symposium, held in 1968, appear as Rarefied Gas Dynamics, *Supplement 5, published in 1969.*

§ 31. *THE LIMITS OF APPLICABILITY OF CONTINUUM FLOW THEORY*

THE EXPERIMENTAL DATA for flow around bodies in a rarefied gas differ considerably from the values of the force and moment characteristics (as well as the friction and heat transfer parameters) when these values are calculated from the relations presented for a continuous medium. The mechanics of rarefied gases must be studied by the kinetic theory of gases, accounting for the fact that the fluid actually consists of discrete molecules. The average distance traveled between collisions of molecules is called the mean free path, and for a rarefied gas this distance is comparable to a significant body dimension.

THE MEAN FREE PATH OF MOLECULES

First, let us examine the applicability of the theoretical relations based on the assumption of a continuum. It should be noted that the limits of applicability are of a conditional nature since, for example, it is impossible to indicate an atmospheric altitude above which only molecular theory must be used. Hence, all the relations pertaining to the limits of applicability are in the form of inequalities.

To establish these limits, the mean free path of the molecules must be determined. It is clear from physical considerations that the smaller the mean free path, the closer the medium is to a continuum. The flow of a dense medium is characterized by a large number of collisions between molecules, which implies that the time of establishment of equilibrium in the energy levels of the colliding molecules (the relaxation time) will be very short.

Air in the troposphere (0 to 16 km) and stratosphere (16 to 64 km) and probably in the lower part of the ionosphere (64 to 100 km) can be assumed to be a continuous medium in the sense indicated. The concept

of a continuous (or dense) medium represents a limiting case. Another limiting case originates with ascent to the upper layer of the ionosphere (to 640 km) and to the exosphere (above 640 km). Because the air in these layers is highly rarefied, collisions between the molecules are not important, and the air can be considered as a medium consisting of independent particles. When disturbances occur, the relaxation time is long, because for a period of time the particles do not encounter other molecules in their path.

The methods of statistical mechanics establish a certain mean distance traveled by a molecule between collisions. The distance is called the mean free path and its length is

$$l = \bar{c}t, \tag{31.1}$$

where $\bar{c}$ is the average velocity of the random motion of the molecules and t is the time between two molecular collisions. In turn, this time is determined from the expression $t = 1/n$, in which n is the number of collisions in a unit time, given by $n = NA\bar{c}$ (where N is the number of molecules per unit volume and A is the cross-sectional area of a molecule). Thus,

$$l = \frac{1}{NA}. \tag{31.1a}$$

For example, for air under normal conditions, $N = 2.69 \cdot 10^{19}$ cm^{-3}, $A = 10^{-15}$ cm^2, and the length of the mean free path is $l = 4 \cdot 10^{-5}$ cm.

It follows from Eq. (31.1a) that the mean free path increases with a decrease in density. In addition, temperature has an influence on the mean free path; however, the temperature relation is more complex and is caused by its influence on both of the parameters N and A.

The influence of density on the mean free path is paramount. Therefore, this length increases with ascent in altitude (see Appendix A). At altitudes greater than 150 km the mean free path can be significantly larger than the dimensions of an aircraft.

Along with Eq. (31.1a), the following relation has been established by the kinetic theory of gases:

$$l = 1.225 \frac{\nu \sqrt{\gamma}}{a}, \tag{31.2}$$

where γ is the adiabatic index, a is the speed of sound, and ν is the kinematic viscosity coefficient. This relation makes it possible to estimate the mean free path.

THE FLOW REGIONS OF A GAS

The characteristic parameter for determining the rarefaction of gas and establishing the limits of applicability of continuum theory is the mean free path. To estimate the degree of rarefaction, this length is compared with some characteristic linear dimension of the body.

Let us assume that the gas is located between two plates separated from one another by a small distance δ, with one of the plates moving parallel to the other at a velocity V. In this case, the characteristic parameter indicating the degree of rarefaction can be written as

$$\frac{l}{\delta} = 1.225\,\frac{\nu\sqrt{\gamma}}{V\delta}\,\frac{V}{a} = 1.225\,\sqrt{\gamma}\,\frac{M}{\mathrm{Re}}. \qquad (31.3)$$

The parameter l/δ is called the Knudsen number and is denoted by Kn. If $\mathrm{Kn} \leq 0.01$, the gas can be considered dense. The disturbances from collisions with the wall are transmitted at the speed of sound to all the molecules due to the relative smallness of the mean free path, and continuum theory can be used. If the mean free path of the molecules is larger than the distance between the walls, such that the Knudsen number is $\mathrm{Kn} \geq 10$, the gas must be considered highly rarefied and continuum theory is inapplicable.

It should be kept in mind that, in the latter case, the usual concept of the Reynolds number as a parameter reflecting the ratio of the inertial forces to the viscous forces has no meaning, since the collision of the particles is unimportant and, therefore, viscosity does not develop. Thus, we must consider the impacts of individual particles on the body instead of a continuous flow in determining the effective forces and heat rates. The two cases mentioned represent limits to the characteristic regions of flow. The first of these is the region of continuum flow, the second the region of free molecule flow.

It is commonly assumed that, despite the strong rarefaction and the negligibly small number of collisions per unit volume in free molecule

flow, the number of molecules per unit volume is sufficient to define the macroscopic properties of the gas. For example, the mean free path of the molecules is 3 m at an altitude of approximately 155 km, which indicates high rarefaction of the air. At the same time, the number of molecules per cubic centimeter remains rather large, approximately $1.5 \cdot 10^{-7}$. For such a rarefied medium, the pressure and mass density can be calculated as an average for a given volume, and the flow characteristics are determined on the basis of the Maxwellian distribution of molecular velocities.

The intermediate regime ($1 \leq Kn \leq 10$) and the slip flow regime ($0.1 \leq Kn \leq 1$) are located between the two regimes of continuum and free molecule flows. The intermediate regime is characterized by the fact that the numbers of collisions of the molecules with the wall and with each other are of the same magnitude. Conditions corresponding to this regime occur in flight at altitudes of approximately 100 km. In the slip flow regime, occurring at altitudes somewhat less than 100 km, the collisions between molecules play a more important role. But despite the fact that the mean free path is small compared with the linear dimension δ, it cannot be neglected.

The difference between the various flow regimes is evident from the different velocity profiles between the parallel plates. In continuum flow, after collision with the moving plate, the gas particles acquire the velocity of the plate and the corresponding momentum. The momentum given up to the adjacent particles decreases due to friction, and as a result the velocity also decreases across the thickness δ, reaching the surface of the motionless plate with a zero value. The velocity profile that occurs will be similar to that in the boundary layer on the surface of a body in continuum flow.

In free molecule flow, the particles colliding with the wall do not change the momentum across the thickness of the layer because they do not collide with other molecules after rebounding from the surface. As a result, a velocity profile does not develop, and the gas between the plates is completely undisturbed by the motion of one plate relative to the other. Thus, it is clear that in free molecule flow around any body, the boundary layer concept loses its meaning, since the flow

on the surface has the same velocity as has the flow at some distance from it.

The velocity profile in slip flow occupies an intermediate position. In this case, the moving plate, just as in continuum flow, transmits momentum to the particles. However, after collision the molecule of gas does not acquire the velocity of the plate but, as it were, slips relative to it with a certain velocity v, so that the velocity of the particles relative to the moving plate will be the difference $V - v$. Hence, this type of flow is commonly called "slip flow"; the gas does not "adhere" to the surface of the body but acquires a velocity different from zero but less than that at the outer edge of the boundary layer.

Thus, a velocity discontinuity exists between the gas and the wall, and a velocity gradient will exist near the wall. The latter fact indicates that a boundary layer still exists in a less rarefied gas moving with slip. For this reason, the motion near the surface does not conform to the Maxwellian equilibrium distribution, and the general equations for a viscous, heat conducting, compressible gas must be used. However, we need to revise these equations, taking into account the more general boundary conditions that provide for a possible discontinuity of velocity, temperature, and pressure at the surface.

The boundaries of the flow regimes in question, in agreement with Eq. (31.3), are determined by the relation between the local Reynolds and Mach numbers. If the distance between the plates is the same as the boundary layer thickness in laminar flow, it is possible to convert from $\mathrm{Re} = V\delta/\nu$ to the parameter $\mathrm{Re}_L = \mathrm{Re}\,(L/\delta)$. After substituting the ratio δ/L from Eq. (5.2) into Eq. (31.3), we obtain the relation for the Knudsen parameter:

$$\mathrm{Kn} = \frac{l}{\delta} = 0.21\sqrt{\gamma}\,\frac{M}{\sqrt{\mathrm{Re}_L}}. \qquad (31.4)$$

Equations (31.3) and (31.4) are represented graphically in Fig. 295 for the different flow regimes,[1] where the curves have been calculated without considering the effect on the mean free path of possible physical-chemical changes in the air, particularly without the influence of dissociation of the air. Dissociation is accompanied by an increase in the number of particles, decreasing their mean free path.

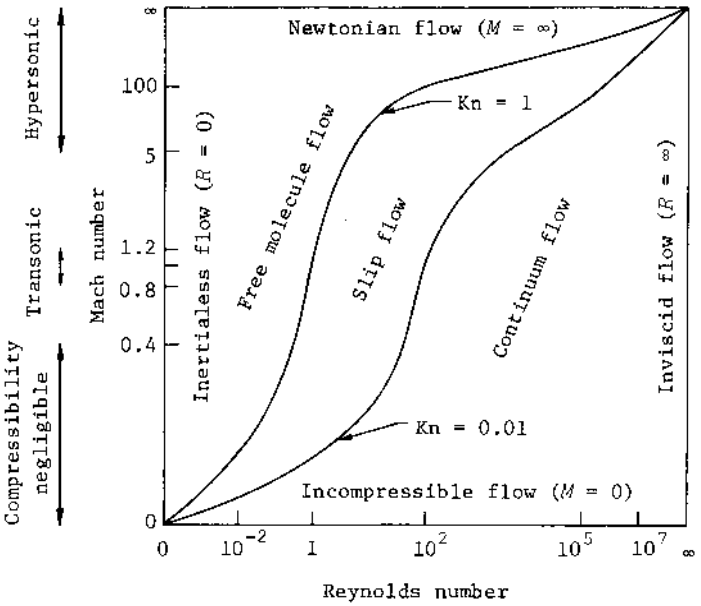

Fig. 295--Gas flow regimes

The curves in Fig. 295 pertain to the flow of an undisturbed gas. However, research shows that it is possible to use the curves for estimating the flow regime near the body if they are based on the local values of M and Re. Furthermore, it can be shown that, far from the nose of a body where the influence of the bow shock is small because of expansion of the flow, regions of slip and free molecule flow can arise even for flight at low altitudes. On the other hand, the compression behind the shock wave near the nose can lead to a region of continuum flow even in those cases when the flight is performed at high altitudes. This can be seen by calculating the Knudsen number from Eq. (31.4) using the local gas parameters.

The characteristic dimension δ must be selected in order to determine the Knudsen number. Since the estimate of the required flow regime is of an approximate nature, the boundary layer thickness can often be selected as the value of δ and can be calculated from the equations for continuum flow.

§ 32. *FREE MOLECULE FLOW*

MECHANISM OF INTERACTION OF MOLECULES WITH THE WALL

A SERIES OF HYPOTHETICAL SCHEMES have been advanced because of the lack of research on the mechanism of the interaction of gas particles with the surface in free molecule flow.

Specular Reflection

Specular molecular reflection can occur when the surface is very smooth and inclined at a small angle of attack. Particles approaching the wall are reflected after impact at an angle equal to the angle of attack (Fig. 296b). Thus, the molecules behave like perfectly elastic spheres. The absolute values of the velocity components do not change, and the tangential component to the surface retains its sign, whereas the normal component reverses its sign. The friction force is absent

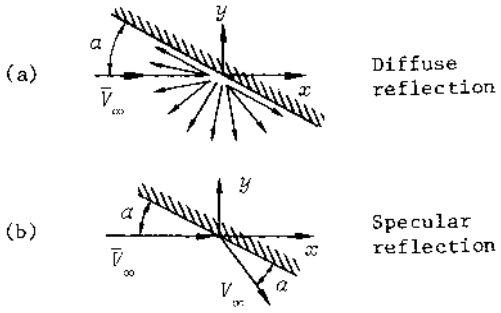

Fig. 296--Types of interaction of molecules with the wall

in the usual sense, and the heat transfer is zero. Therefore, the motion near the wall is isentropic and the temperature of the flow is independent of the thermal state of the surface.

Research has shown that even a carefully polished surface is not sufficiently smooth to achieve the mechanism of specular reflection. In practice, only an insignificant part of the molecules, of the order of several percent, interacts with the wall in this way.

Diffuse Reflection

A large fraction of the molecules interact with the wall by diffuse reflection (Fig. 296a). The gas molecules transfer all their kinetic energy to the body at the collision, diffuse into the wall and, after a lapse of time, are reflected from it in an arbitrary direction at some velocity. While the molecules are in contact with the wall, their temperature approaches that of the wall. The reflected particles do not necessarily have exactly the same temperature as the surface, but in the general case their temperature is different from that of the incident gas. Henceforth, we shall assume that the molecular motion of the incident and reflected molecules conforms to the Maxwellian law of velocity distribution, since the collisions of the impacting and reflecting molecules do not cause important deviations from this law.

FORCES ON THE WALL AND ENERGY TRANSFER FOR TRANSLATIONAL MOTION IN FREE MOLECULE FLOW

Mass Transfer

Let us consider some of the characteristics of free molecule flow around a body.[2] It will be assumed that the molecules, rebounding diffusely, obey the Maxwellian law of velocity distribution and the temperature of the reflected particles equals some value T_r that differs, in the general case, from the surface temperature T_w and the initial gas temperature T_i.

First, we will develop the expression for mass transfer. The velocity components of a molecule can be written as

$$u = \bar{u} + U, \qquad v = \bar{v} + V, \qquad w = \bar{w} + W.$$

The first terms in these expressions are the components of the velocity $\bar{V}_\infty$ of the gas with respect to the surface. The velocity $\bar{V}_\infty$ is the velocity of the mass (or ordered) motion and is determined from the following expression:

$$\bar{V}_\infty^2 = \bar{u}^2 + \bar{v}^2 + \bar{w}^2.$$

The second terms are the velocity components from the thermal motion, where

$$c^2 = U^2 + V^2 + W^2.$$

Let us assume that the y-axis, which corresponds to the component v, is directed normal to the surface at a given point.

We are interested in the transfer of molecules to the surface of the body, which depends on the number of incident molecules. The number of incident molecules per unit volume having velocity components in the intervals

$$u,\ u + du, \qquad v,\ v + dv, \qquad w,\ w + dw$$

is given by the product $n_i f\, du\, dv\, dw$, in which n_i is the number of incident molecules per unit volume, and f is the Maxwellian distribution function. In kinetic theory, the distribution function is determined by the exponential relation

$$f = \frac{1}{(\pi c_m^2)^{\frac{3}{2}}}\, e^{-c^2/c_m^2}, \tag{32.1}$$

where c_m is related to the average speed of the random motion $\bar{c}$ by the equation

$$c_m = \sqrt{\pi \bar{c}^2/4}$$

and is called the most probable speed of the molecules. The average speed is

$$\bar{c} = 2\sqrt{2RT/\pi}.$$

The number of these incident molecules per unit volume colliding

with a unit area of surface in one second is

$$n_i v f \, du \, dv \, dw,$$

which is the number of molecules that reach the surface and are located in a volume with a unit area for the base and with a height equal to the vertical velocity component v.

We can obtain the total number of molecules N_i colliding with a unit surface area in one second by integrating over all possible values of u, v, and w; i.e.,

$$N_i = \frac{n_i}{(\pi c_{mi}^2)^{\frac{3}{2}}} \int_{-\infty}^{\infty} e^{-H_1^2/2} \, du \int_0^{\infty} v e^{-H_2^2/2} \, dv \int_{-\infty}^{\infty} e^{-H_3^2/2} \, dw, \qquad (32.2)$$

where

$$\frac{H_1}{\sqrt{2}} = \frac{U}{c_{mi}}, \qquad \frac{H_2}{\sqrt{2}} = \frac{V}{c_{mi}}, \qquad \frac{H_3}{\sqrt{2}} = \frac{W}{c_{mi}}.$$

Since $du = dU$ and $dw = dW$, the first and third integrals in Eq. (32.2) will be identical and equal to $\sqrt{\pi c_{mi}^2}$. The second integral can be written in the form

$$\int_{-\bar{v}}^{\infty} (\bar{v} + V) e^{-H_2^2/2} \, dV = \frac{c_{mi}^2}{2} \left[e^{-\bar{x}^2} + \bar{x} \sqrt{\pi} \, (1 + \operatorname{erf} \bar{x}) \right], \qquad (32.3)$$

where the probability integral is

$$\operatorname{erf} \bar{x} = \frac{2}{\sqrt{\pi}} \int_0^{\bar{x}} e^{-\bar{x}^2} \, d\bar{x}, \qquad (32.4)$$

and $\bar{x} = \bar{v}/c_{mi}$. As is evident, $\bar{x}$ represents the ratio between the mass velocity component normal to the surface and the most probable velocity of the incident molecules.

The total number of molecules N_i is given by

$$N_i = n_i \sqrt{RT_i/2\pi} \left[e^{-\bar{x}^2} \pm \bar{x} \sqrt{\pi} \, (1 \pm \operatorname{erf} \bar{x}) \right]. \qquad (32.5)$$

It should be noted that

$$c_{mi}^2 = \frac{\pi}{4} \bar{c}_i^2 = 2RT_i$$

and that the product RT_i in Eq. (32.5) is related to the velocity of sound by

$$a_i = \sqrt{\gamma RT_i}.$$

If c_{mi} is replaced by the velocity of sound in the dimensionless parameter $\bar{x}$, the latter can be written in the form

$$\bar{x} = \sqrt{\gamma/2} \, \frac{\bar{v}}{a_i} .$$

In addition, taking into account that δ is the angle between the direction of the vector $\bar{V}_\infty$ and the tangent to the surface at a given point, we can write the relation for $\bar{x}$ as

$$\bar{x} = \sqrt{\gamma/2} \, \frac{V_\infty}{a_i} \sin \delta = \bar{x}_\infty \sin \delta,$$

$$\bar{x}_\infty = \sqrt{\gamma/2} \, \frac{V_\infty}{a_i} = \sqrt{\gamma/2} \, M_\infty.$$

Since the area in question is located on the forward part of the body where $\delta > 0$ (Fig. 297), the upper (plus) sign must be selected in Eq. (32.5). If the area is located on the afterbody where $\delta < 0$, the relation for N_i is obtained by changing the limits of integration for v from $0 \leq v \leq \infty$ to $-\infty \leq v \leq 0$. In this case, we determine the number of molecules N_i by selecting the lower (minus) signs in Eq. (32.5).

Now let us consider the transfer of the reflected molecules. Since diffuse reflection obeys the Maxwellian distribution, it is possible to use Eq. (32.5), but it is assumed that $\bar{x} = 0$, since the particles lose

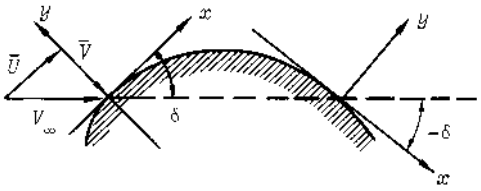

Fig. 297--Flow over a curved surface

all of their mass velocity on collision. On the basis that the reflected particles have a different temperature T_r, we obtain for their number

$$N_r = n_r \sqrt{RT_r/2\pi}, \tag{32.6}$$

where n_r is the number of reflected molecules per unit volume. If it is assumed that the total number of incident particles is equal to the number of reflected particles, i.e., $N_i = N_r$, we can find the relation between the concentrations n_r and n_i by equating the right sides of Eqs. (32.5) and (32.6).

Equation (32.5) can be simplified at sufficiently high velocities. For $\bar{x} \geq 2$, the quantity $\exp(-\bar{x}^2)$ differs little from zero, and the probability integral erf $\bar{x}$ differs little from unity. For example, for $\bar{x} = 2$, the value of $\exp(-\bar{x}^2)$ is 0.018 and erf $\bar{x} = 0.995$. For $\bar{x} \geq 2$, we get

$$M_\infty \geq \sqrt{2/\gamma}\,\frac{\bar{x}}{\sin\delta}.$$

For $\sin\delta = 0.2$ and $\gamma = 1.4$, the Mach number must be greater than 12. For $\delta = 90°$, the smallest possible Mach number is reduced to 2.4. Thus, in the case of large velocities, Eq. (32.5) can be written in the form

$$(N_i)_f = \bar{x} n_i \sqrt{2RT_i}. \tag{32.7}$$

The subscript f indicates that the forward side of a curved surface ($\delta > 0$) is under consideration. If, however, the back side of the surface ($\delta < 0$) is considered, it is apparent that Eq. (32.5) results in $(N_i)_b = 0$ for the stated assumptions. This is because the molecules do not reach the rear surface of a body with a high flight velocity.

Pressure

The pressure is determined from the total loss of momentum normal to the surface by the molecules colliding with the wall. The pressure due to one molecule is mv, and the pressure of a group of molecules colliding in unit time with unit surface area is

$$mn_i v^2 f \, du \, dv \, dw.$$

Therefore, the pressure due to all of the molecules impacting on the forward surface is

$$p_i = \frac{\rho_i}{(\pi c_{mi}^2)^{\frac{3}{2}}} \int_{-\infty}^{\infty} e^{-H_1^2/2} \, du \int_0^{\infty} v^2 e^{-H_2^2/2} \, dv \int_{-\infty}^{\infty} e^{-H_3^2/2} \, dw, \qquad (32.8)$$

where the density is $\rho_i = mn_i$.

If the pressure on the rear surface is determined, for which $\delta < 0$, the limits on v in the second integral of Eq. (32.8) must be changed to correspond to the interval $-\infty \leq v \leq 0$. Carrying out an integration similar to that for the mass transfer equation, we obtain the following expression for the pressure coefficient:

$$C_{pi} = \frac{2p_i}{\rho_i \bar{v}_\infty^2} = \sin^2\delta \left[\frac{1}{\bar{x}\sqrt{\pi}} e^{-\bar{x}^2} \pm \left(1 + \frac{1}{2\bar{x}^2}\right)(1 \pm \operatorname{erf} \bar{x}) \right], \qquad (32.9)$$

in which the upper sign (plus) determines the pressure on the forward surface and the lower sign (minus) on the rear surface.

In addition to the incident particles, the reflected particles create a pressure equal to the sum of the momentum (normal to the surface) of the molecules leaving the wall. Since the reflected particles obey Maxwell's law, we can use Eq. (32.8) by substituting $\bar{v} = 0$ and converting to parameters with the subscript r. Then, we get

$$p_r = \frac{\rho_r}{(\pi c_{mr}^2)^{\frac{3}{2}}} \int_{-\infty}^{\infty} e^{-H_1^2/2} \, dU \int_{-\infty}^{0} V^2 e^{-H_2^2/2} \, dV \int_{-\infty}^{\infty} e^{-H_3^2/2} \, dW,$$

which gives, after integrating,

$$p_r = \frac{1}{2}\rho_r R T_r. \tag{32.10}$$

Since the density of the reflected particles is $\rho_r = mn_r$, and their concentration n_r is determined from the condition $N_r = N_i$, the expression for the pressure coefficient due to the reflected molecules is

$$C_{pr} = \frac{2p_r}{\rho_i V_\infty^2} = \frac{\sin^2\delta}{2\bar{x}^2}\sqrt{T_r/T_i}\left[e^{-\bar{x}^2} \pm \bar{x}\sqrt{\pi}\,(1 \pm \operatorname{erf}\bar{x})\right], \tag{32.11}$$

in which, as before, the upper sign (plus) relates to the forward surface and the lower (minus) to the rear surface.

Therefore, the total value of the pressure coefficient is

$$C_p = \frac{2(p_i + p_r)}{\rho_i V_\infty^2} = \sin^2\delta\left[\frac{1}{\bar{x}}\left(\frac{1}{\sqrt{\tau}} + \frac{1}{2\bar{x}}\sqrt{T_r/T_i}\right)e^{-\bar{x}^2}\right.$$

$$\left. \pm \left(1 + \frac{1}{2\bar{x}^2} + \frac{\sqrt{\pi}}{2\bar{x}}\sqrt{T_r/T_i}\right)(1 \pm \operatorname{erf}\bar{x})\right]. \tag{32.12}$$

As is evident from this expression, the total value of the pressure coefficient depends on the orientation of the surface relative to the velocity vector $\bar{V}_\infty$ (i.e., on the angle δ), on M_∞, and on the temperature ratio T_r/T_i. It can be seen from Eq. (32.12) that the pressure on a motionless surface is

$$p = p_i + p_r = \frac{R}{2}(\rho_i T_i + \rho_r T_r). \tag{32.13}$$

If it is assumed that the temperature does not change in the reflection process, the pressure on the surface of a stationary body is determined by the equation of state $p = \rho_i R T_i$.

At high velocities, for which $\bar{x} \geq 2$, Eqs. (32.9) and (32.11) can be simplified. For the incident particles, the simplified relations will be

$$(C_{pi})_f = 2\sin^2\delta\left(1 + \frac{1}{2\bar{x}^2}\right), \qquad (C_{pi})_b = 0. \tag{32.14}$$

The corresponding equations for the reflected particles are

$$(C_{pr})_f = \frac{\sin^2\delta}{\bar{x}} \sqrt{\pi T_r/T_i}, \qquad (C_{pr})_b = 0. \tag{32.15}$$

With Eqs. (32.14) and (32.15), the total values of the pressure coefficients are

$$C_{pf} = 2 \sin^2\delta \left(1 + \frac{1}{2\bar{x}^2} + \frac{\sqrt{\pi}}{2\bar{x}} \sqrt{T_r/T_i}\right), \qquad C_{pb} = 0. \tag{32.16}$$

Friction

A shear stress occurs because the tangential component of momentum is totally lost on molecular impact. This loss is mu for one molecule and for a number of molecules (per unit area per unit time) is

$$n_i m f u v \, du \, dv \, dw.$$

Therefore, the friction caused by the incidence of all the molecules on the forward surface is

$$\tau_i = \frac{\rho_i}{(\pi c_{mi}^2)^{\frac{3}{2}}} \int_{-\infty}^{\infty} u e^{-H_1^2/2} \, du \int_0^{\infty} v e^{-H_2^2/2} \, dv \int_{-\infty}^{\infty} e^{-H_3^2/2} \, dw. \tag{32.17}$$

The friction on the rear surface is determined from the same expression with the substitution of $-\infty$ and 0 for the limits in the second integral. Noting that $u = V_\infty \cos\delta$ (see Fig. 297), we find the following equation for the friction coefficient:

$$c_f = \frac{2\tau_i}{\rho_i V_\infty^2} = \sin\delta \cos\delta \left[\frac{1}{\bar{x}\sqrt{\pi}} e^{-\bar{x}^2} \pm (1 \pm \operatorname{erf} \bar{x})\right]. \tag{32.18}$$

The reflected molecules do not contribute to the shear stress since all directions of motion are equally probable, and $\tau_r = 0$.

For an uninclined surface ($\delta = 0$), $\bar{x}$ can be replaced by $\bar{x}_\infty \sin\delta$ and the friction coefficient is represented in a simpler form:

$$c_f = \frac{1}{\bar{x}_\infty \sqrt{\eta}} = \sqrt{2/\gamma\pi}\,\frac{1}{M_\infty}. \tag{32.19}$$

The equations are also simplified for $\bar{x} \geq 2$. For conditions on the forward and rear surfaces, respectively, they have the following form:

$$(c_f)_f = 2 \sin \delta \cos \delta, \qquad (c_f)_b = 0. \tag{32.20}$$

The Transfer of Kinetic Energy

We have seen that it is necessary to know the temperature ratio T_r/T_i to determine the normal pressure. The computation of this ratio, in turn, is related to the calculation of the energy of translational motion of the molecules on impact and reflection. On impact, each of the molecules transmits to the surface an energy equal to

$$\frac{1}{2} mc^2 = \frac{1}{2} m(U^2 + V^2 + W^2).$$

The energy supplied by a number of incident molecules arriving on a unit area in a unit time is determined by

$$\frac{1}{2} mn_i c^2 f v \, du \, dv \, dw.$$

As a result of integrating this expression within the same limits as before, we obtain the total amount of energy transmitted on impact:

$$E_i = \frac{1}{2} mN_i \left[V_\infty^2 + RT_i \left(4 \pm \frac{1}{\varphi \pm 1} \right) \right], \tag{32.21}$$

where N_i is determined from Eq. (32.5) and the function φ from

$$\varphi = \frac{e^{-\bar{x}^2}}{\bar{x} \sqrt{\pi} \, (1 \pm \operatorname{erf} \bar{x})}. \tag{32.22}$$

The reflected particles remove from a unit surface an element of energy equal to

$$\frac{1}{2} mn_r c^2 fU\, dU\, dV\, dW.$$

The total energy removed is obtained by integration:

$$E_r = \sqrt{2/\pi}\, \rho_r (RT_r)^{\frac{3}{2}}. \tag{32.23}$$

The density is given by $\rho_r = mn_r$, and the concentration of the reflected particles can be replaced by n_i with $N_r = N_i$. Carrying out the required integration, we obtain the following relation for the kinetic energy removed as a result of reflection from the forward (plus sign) or from the rear (minus sign) surfaces:

$$E_r = 2mN_i RT_r = \sqrt{2/\pi}\, c_i RT_r \sqrt{RT_i} \left[e^{-\bar{x}^2} \pm \bar{x}\sqrt{\pi}\,(1 \pm \operatorname{erf} \bar{x}) \right]. \tag{32.23a}$$

The net kinetic energy transferred by the molecules is equal to the difference between the incoming and outgoing energies, i.e.,

$$E = E_i - E_r.$$

At high velocities ($\bar{x} \geq 2$), the determination of the energy of the translational motion is simplified. From Eq. (32.22), it can be assumed that φ_f and φ_b are approximately zero for the forward and rear surfaces. If the necessary simplifications in Eq. (32.21) are made, the energy of the impacting particles is

$$\begin{aligned} (E_i)_f &= \frac{1}{2}\, \bar{x} o_i \sqrt{2RT_i}\, (V_\infty^2 + 5RT_i), \\ (E_i)_b &= 0. \end{aligned} \tag{32.24}$$

The corresponding equation for the energy of the reflected particles, Eq. (32.23a), can be written as

$$(E_r)_f = 2\sqrt{2}\, \rho_i RT_r \sqrt{RT_i}\, \bar{x}, \qquad (E_r)_b = 0. \tag{32.25}$$

HEAT TRANSFER IN FREE MOLECULE FLOW

Accommodation

It is assumed in Eq. (32.25) that the temperature of the reflected particles differs from the wall temperature and that the energy of the molecules, due to the short time of contact, is not the same as the average energy corresponding to the temperature of the surface. This average energy is

$$E_w = 2mN_i RT_w = \sqrt{2/\pi}\ \rho_i RT_w \sqrt{RT_i}\ \left[e^{-\bar{x}^2} \pm \bar{x}\sqrt{\pi}\ (1 \pm \operatorname{erf}\bar{x})\right]. \quad (32.26)$$

This type of reflection is the most general and is characterized by the absence of total adjustment, or what is called total accommodation, between the solid surface and the molecules. In the general case, the accommodation coefficient η differs from unity, where η is defined as

$$\eta = \frac{E_i - E_r}{E_i - E_w}. \quad (32.27)$$

The presence of the energy discontinuity appears as an abrupt change in temperature, i.e., the difference betweeen T_r and T_w.

The accommodation coefficient plays an important role in the calculation of heat transfer, and it is of great practical value to establish quantitative estimates for this coefficient. At present, this can only be done experimentally, although there are few reliable measurements. Observations show that the nature of the change in the accommodation coefficient is extremely complex. For example, it has been established that η increases with increases in the molecular weight and the surface temperature. In addition, it can be assumed that the accommodation coefficient varies with the velocity of the body, the incidence angle of the surface, the properties of the material, the surface state, etc. In preliminary calculations, it can be assumed that $\eta = 1$, which implies that the temperature of the reflected molecules succeeds in reaching the wall temperature. In this case, the molecules totally adapt, as it were, to the wall conditions.

The Temperature of the Reflected Molecules and the Heat Transfer

Since the pressure depends on the value of T_r, so do the aerodynamic forces developed in free molecule flow. To determine this temperature, it is necessary to use the equation for the balance of energy between the body and the gas. The translational energy transported to a unit area of the surface by the incoming molecules is E_i. The corresponding energy of the reflected molecules is

$$E_r = (1 - \eta)E_i + \eta E_w = (1 - \eta)E_i + 2\eta m N_i R T_w. \tag{32.28}$$

If the heat due to external radiation, q_{rad}, is taken into account (e.g., that supplied by solar radiation), the incident energy will be equal to the sum, $E_i + q_{rad}$. Assuming that the outflow of energy is equal to the heat transported by the reflected molecules plus that radiated from the surface, and including cooling or heating from the interior (corresponding to plus or minus q_c), the heat balance equation for steady heat transfer per unit area is

$$\eta E_i + q_{rad} = 2\eta m N_i R T_w + \varepsilon \sigma T_w^4 \pm q_c. \tag{32.29}$$

The wall temperature is obtained from Eq. (32.29) for given values of ε, q_{rad}, q_c, and T_i by the substitution of Eq. (32.21) for N_i and Eq. (32.5) for N_i. The temperature of the reflected molecules can be found from Eq. (32.28) in the form

$$\frac{T_r}{T_i} = \frac{T_w}{T_i}\left[\frac{(1 - \eta)E_i}{2m N_i R T_w} + \eta\right]. \tag{32.30}$$

Of special interest is the case of adiabatic conditions at the surface. If there is no radiation to or from the surface and no internal heat exchange, the wall is heated only by the transport of translational energy to and from the surface. In this case, Eq. (32.29) is reduced to

$$E_i = 2m N_i R T_w = E_w, \tag{32.31}$$

which corresponds to the condition that the net heat flow is zero. It is evident from Eq. (32.30) that the temperature of the reflected molecules is equal to the wall temperature. Thus, the temperature of an insulated surface is determined from

$$\frac{T_w}{T_i} = \frac{T_r}{T_i} = \frac{1}{4RT_i}\left[V_\infty^2 + RT_i\left(4 \pm \frac{1}{\varphi \pm 1}\right)\right]. \tag{32.32}$$

This equation can be simplified if RT_i is replaced by a_i^2/γ:

$$\frac{T_w}{T_i} = \frac{T_r}{T_i} = 1 + \frac{\gamma M_\infty^2}{4} \pm \frac{1}{4(\varphi \pm 1)}. \tag{32.32a}$$

It is evident from these equations that the wall temperature for adiabatic conditions is somewhat analogous to the stagnation temperature in continuous flow.

Flight conditions at high altitudes can be related to the maintenance of some constant wall temperature. In this case, the wall temperature is given and the temperature of the reflected particles can be determined from Eq. (32.30), which temperature is then used for the pressure calculation.

In addition, the heat transfer to each point can be calculated. It is equal (in corresponding thermal units) to the net flow of energy due to the translational motion of the molecules:

$$q = E = E_i - E_r.$$

The local heat transfer is not constant and, for given flight conditions, varies with the slope of the local surface relative to the incident velocity vector, being largest at the stagnation point. Experimental research has shown that the local heating rate at the stagnation point can be determined by the approximate equation

$$q = 7.35 \cdot 10^7 \eta \frac{\rho_{\infty H}}{\rho_{\infty SL}} \left(\frac{V_\infty}{V_c}\right)^3 \quad \text{kcal/m}^2 \text{ sec.} \tag{32.33}$$

Using this equation in the heat balance equation for steady heat transfer, we obtain the temperature at the stagnation point:

$$T_w = \left(\frac{q + q_{rad} \pm q_c}{\varepsilon\sigma}\right)^{\frac{1}{4}}. \tag{32.34}$$

If the wall is insulated on the inside ($q_c = 0$) and solar radiation is disregarded ($q_{rad} = 0$), the equilibrium wall temperature is given by

$$T_w = 4.83\cdot10^4\left(\frac{\eta}{\varepsilon}\right)^{\frac{1}{4}}\left(\frac{\rho_{\infty H}}{\rho_{\infty SL}}\right)^{\frac{1}{4}}\left(\frac{V_\infty}{V_c}\right)^{\frac{3}{4}}. \tag{32.35}$$

For example, if it is assumed that the density ratio $\rho_{\infty H}/\rho_{\infty SL} = 10^{-8}$ (H = 150 km), that the accommodation coefficient $\eta = 1$, that the surface emissivity $\varepsilon = 1$, and that the body is moving with orbital velocity ($V_\infty = V_c$), the equilibrium temperature at the stagnation point is $T_w = 483°K$.

In the case of very high velocities and a cooled surface, a simple equation can be derived to estimate the heat flow:

$$q = (E_i)_f - (E_r)_f, \tag{32.36}$$

where the values for energy on the right side are determined from Eqs. (32.24) and (32.25), respectively. Since $a_i = a_\infty = \sqrt{\gamma RT_i} \ll V_\infty$, the term $5RT_i$ in Eq. (32.24) can be neglected. In addition, the second term in Eq. (32.36) can be neglected in comparison with the first term, because the energy carried away by the reflected particles is very small due to the cooling of the surface.

After making these simplifications, we obtain

$$\begin{aligned} q &= \frac{1}{2}\rho_i V_\infty^3 \sin\delta \quad \text{kgf m/m}^2\,\text{sec} \\ &= 1.17\cdot10^{-3}\,\rho_i V_\infty^3 \sin\delta \quad \text{kcal/m}^2\,\text{sec}, \end{aligned} \tag{32.37}$$

where ρ_i is in units of kgf sec^2/m^4, and V_∞ is in m/sec.

CALCULATION OF THE AERODYNAMIC FORCES

The General Expression for the Drag Force

As a result of collisions with a local unit area on the forward side of a body ($\delta > 0$), the axial force due to the normal pressure and friction is

$$(F_i)_f = p_i \sin\delta + \tau_i \cos\delta = \frac{\rho_i V_\infty^2}{2} \sin\delta \left[\frac{e^{-\bar{x}^2}}{\bar{x}\sqrt{\pi}} + \left(1 + \frac{\sin^2\delta}{2\bar{x}^2}\right)(1 + \operatorname{erf}\bar{x}) \right]. \tag{32.38}$$

The relation for the forces on the rear side results from choosing the lower signs in Eqs. (32.9) and (32.18):

$$(F_i)_b = \frac{\rho_i V_\infty^2}{2} \sin\delta \left[\frac{e^{-\bar{x}^2}}{\bar{x}\sqrt{\pi}} - \left(1 + \frac{\sin^2\delta}{2\bar{x}^2}\right)(1 - \operatorname{erf}\bar{x}) \right]. \tag{32.39}$$

The reflected particles create an additional force. Rebounding from the forward surface, they act on it with a force expressed as

$$(F_r)_f = p_r \sin\delta = \frac{\rho_i V_\infty^2}{2} \frac{\sin^3\delta}{2\bar{x}^2} \sqrt{T_r/T_i} \left[e^{-\bar{x}^2} + \bar{x}\sqrt{\pi}\,(1 + \operatorname{erf}\bar{x}) \right]. \tag{32.40}$$

The corresponding expression for the forces caused by the action of the reflected molecules on the rear surface is

$$(F_r)_b = \frac{\rho_i V_\infty^2}{2} \frac{\sin^3\delta}{2\bar{x}^2} \sqrt{T_r/T_i} \left[e^{-\bar{x}^2} - \bar{x}\sqrt{\pi}\,(1 - \operatorname{erf}\bar{x}) \right]. \tag{32.41}$$

For cases where $\bar{x} \geq 2$, these equations can be simplified as before. Instead of Eqs. (32.38) and (32.39), we have the corresponding relations

$$(F_i)_f = \rho_i V_\infty^2 \sin\delta \left(1 + \frac{\sin^2\delta}{2\bar{x}^2}\right), \tag{32.38a}$$

$$(F_i)_b = 0, \tag{32.39a}$$

and, instead of Eqs. (32.40) and (32.41), we have

$$(F_r)_f = \frac{\rho_i V_\infty^2}{2} \frac{\sin^3\delta}{\bar{x}} \sqrt{\pi T_r/T_i}, \tag{32.40a}$$

$$(F_r)_b = 0. \tag{32.41a}$$

Pointed Cones

The elementary area of a cone is $2\pi r\, dr$. Therefore, in symmetric flow the drag acting on this area is

$$[(F_i)_f + (F_r)_f] \frac{2\pi r\, dr}{\sin \delta_c}.$$

Integrating from 0 to r_{mid}, we obtain the nose drag coefficient:

$$C_{Dp} = \left(\frac{1}{\sqrt{\pi}} + \frac{\sin \delta_c}{2\bar{x}_\infty} \sqrt{T_r/T_i}\right) \frac{e^{-\bar{x}^2}}{\bar{x}} + \left(1 + \frac{1}{2\bar{x}_\infty^2} + \frac{\sin \delta_c}{2\bar{x}_\infty} \sqrt{\pi T_r/T_i}\right)(1 + \operatorname{erf} \bar{x}). \tag{32.42}$$

The interaction of the molecules with the base area results in an accelerating force rather than in a drag force. The magnitude of the accelerating force is

$$[(F_i)_b + (F_r)_b]\pi r_{mid}^2.$$

The accelerating force coefficient is

$$C_{DB} = \left(\frac{1}{\sqrt{\pi}} + \frac{1}{2\bar{x}_\infty} \sqrt{T_r/T_i}\right) \frac{e^{-\bar{x}_\infty^2}}{\bar{x}_\infty} - \left(1 + \frac{1}{2\bar{x}_\infty^2} + \frac{1}{2\bar{x}_\infty} \sqrt{T_r/T_i}\right)(1 - \operatorname{erf} \bar{x}_\infty). \tag{32.43}$$

Therefore, the total drag coefficient acting on a cone is given by the difference

$$C_D = C_{Dp} - C_{DB}. \tag{32.44}$$

As an example, let us calculate C_D for the flight conditions for

which the wall temperature was determined to be $T_w = 483°K$. The speed of sound at an altitude of 150 km is approximately 400 m/sec and $M_i = 7900/400 \approx 19.7$; therefore, $\bar{x}_\infty \approx 19.7\sqrt{1.4/2} = 16.5$. If a cone angle of 60° is assumed, $\bar{x} = 16.5 \cdot 0.866 = 14.3$. The values of the probability integrals can be found from standard mathematical tables, but they differ so little from unity that it can be assumed that $\operatorname{erf} \bar{x} \approx \operatorname{erf} \bar{x}_\infty \approx 1$ and that the exponentials $e^{-\bar{x}^2}$ and $e^{-\bar{x}_\infty^2}$ are equal to zero.

As a result, the base force coefficient is equal to zero and the nose drag coefficient is approximately equal to 2, so that the total drag coefficient of the cone is

$$C_D = 2. \tag{32.45}$$

It is apparent that this result will apply for very high velocities, corresponding to large values of $\bar{x}$ and $\bar{x}_\infty$. Actually, for $\bar{x} \gg 1$, Eqs. (32.42) and (32.43) indicate that $C_{DB} \approx 0$ and $C_{Dp} \approx 2$. For small velocities for which $\bar{x}$ is small, the value of C_D increases due to the influence of the reflected molecules, as is evident from Fig. 298.

It is noteworthy that the value $C_D = 2$ corresponds to the results of Newtonian theory, where the drag is determined by the total momentum loss of the particles corresponding to the largest cross-sectional area

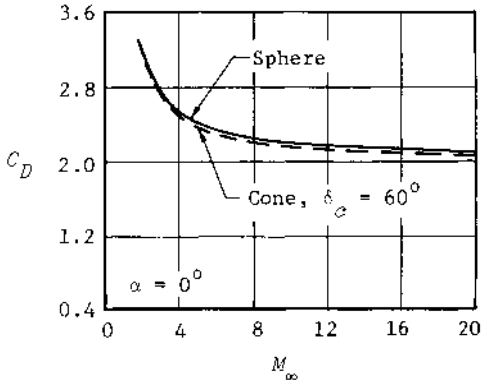

Fig. 298--Drag coefficient of a sphere and a cone in free molecule flow

of the body; at zero angle of attack, the drag force is $\rho_\infty V_\infty^2 \pi r_{mid}^2$, and the drag coefficient is $C_D = 2$. The same formula applies to a body at an angle of attack. The force must be computed as the product of the coefficient $C_D = 2$, the dynamic pressure, and the projection of the body on a plane normal to the direction of the velocity vector $\bar{V}_\infty$.

It is evident that the impact theory discussed above differs in principle from the Newtonian theory of § 18. According to Newtonian theory, the particles are deflected at the incident angle and continue their motion along the wall. The normal component is absorbed and the tangential component remains unvaried. According to impact theory, both components are absorbed and therefore a tangential stress must exist along with the normal pressure.

It can be seen in Fig. 298 that the results of the exact calculation for $M_\infty > 4$ differ little from the value of 2 found from Newtonian theory. Therefore, calculations can be made according to the diffuse reflection theory for comparatively small Mach numbers, and from Newtonian theory for large Mach numbers.

Arbitrary Body Shapes

In the example of the pointed cone, we indicated the possibility of calculating the drag at very large velocities on the basis of the simplified conclusions of the theory of diffuse reflection. This result can be used to calculate free molecule flow around bodies of arbitrary shape and to compute the axial and normal components of the total force and the pitching moment. We can base these calculations on computed values of the local coefficients of normal pressure and friction derived from the theory of free molecule flow, neglecting the influence of diffuse reflection and also excluding all effects in the shadow zone. For example, the equation for the pressure coefficient can be obtained from Eq. (32.16), in which the second and third terms in the parentheses are neglected:

$$C_p = 2 \sin^2 \delta. \tag{32.46}$$

Equations (32.20) can be used for the local skin friction coefficient. Equations (1.6) and (1.9a) give the axial force coefficients due to normal

pressure and shear stress, respectively. Their sum is the total axial force coefficient for a given axisymmetric body.

Let us consider a sphere, for example. The axial force coefficient (or drag coefficient) is

$$C_D = 4\int_0^{\pi/2} \sin^3\delta \cos\delta \, d\delta + 4\int_0^{\pi/2} \sin\delta \cos^3\delta \, d\delta = 2,$$

which is the same result as for a cone. It is evident in Fig. 298 that, as for a cone, the value of $C_D = 2$ at high Mach numbers practically coincides with that obtained from the exact computation. A flat face has exactly the same drag coefficient ($C_D = 2$), as follows from Eqs. (32.46) and (32.20).

If the flat face or hemisphere is followed by a cylinder with length l_{cyl}, the equation for the drag coefficient of the combined body is obtained from Eqs. (32.45) and (32.19) and has the form

$$C_D = 2\left(1 + \frac{2\sqrt{2/\gamma\pi}}{M_\infty}\frac{l_{cyl}}{d_N}\right). \qquad (32.47)$$

It is apparent that the drag is a linear function of the cylinder length.

Asymmetric Flow

The expressions obtained above for the local pressure and friction coefficients can be used as a basis for the calculation of the axial force, normal force, and moment coefficients at angle of attack. It should be noted that the angle δ must be replaced by θ_c, which is the angle between the direction of the flow velocity and the local area and is computed from Eq. (7.1) or Eq. (7.14a). Once the distributions of the local pressure and friction coefficients are known, the aerodynamic coefficients can be calculated from the general expressions presented in § 1. The results of this type of calculation are presented in Fig. 299 for a cylinder with a truncated nose cone, with $M_\infty = 7$ and the temperature ratio $T_w/T_t = 0.18$. The moment coefficient in the figure is calculated with respect to a center of gravity located at a distance of one cylinder diameter from the large end of the cone. It

is necessary to know the atmospheric density to calculate the actual forces and moment from the coefficients. The density up to 700 km can be determined from Appendix A.

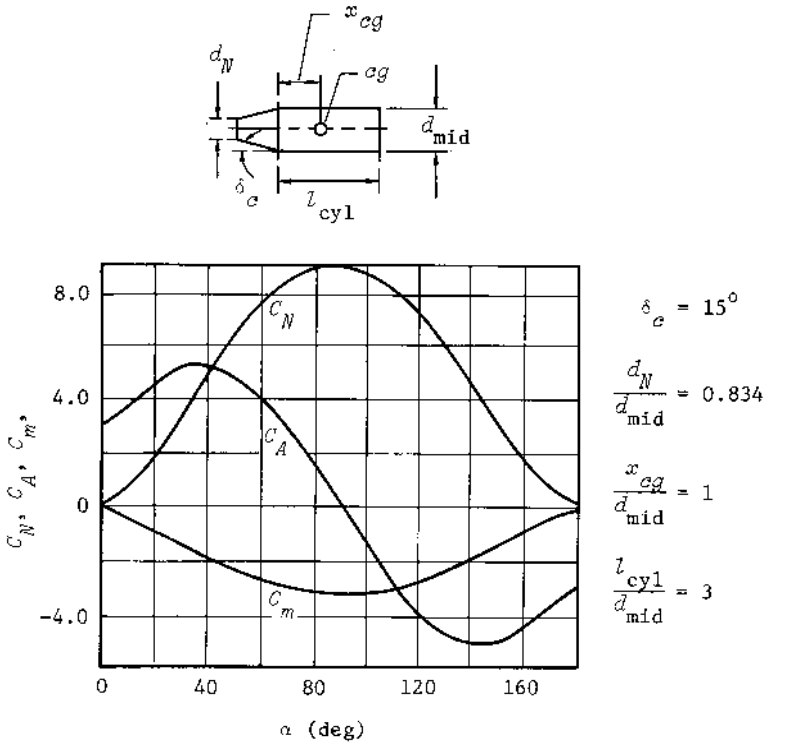

Fig. 299--Aerodynamic coefficients for a truncated cone-cylinder in free molecule flow

§ 33. *FRICTION AND HEAT TRANSFER IN SLIP FLOW*

SHEAR STRESS DUE TO FRICTION

The Slip Velocity and the Slip Coefficient

AS ALREADY INDICATED, a special feature of slip flow is the development of a velocity discontinuity at the surface of the body. The fluid does not adhere to the wall but slips along it with a relative velocity v. Because of slip, the difference between the gas velocity at the outer edge of the boundary layer and at the wall is $V_\delta - v$, and the deceleration will be less than that of a nonslipping denser flow. Therefore, the friction is decreased and, according to Newton's law, can be written approximately in the form

$$\tau = \mu \frac{V_\delta - v}{\delta}.$$

We can estimate the slip velocity v by relating the shear force to the change in momentum for the random transfer of molecules with velocity $\bar{c}$ across the boundary layer. If the mass of molecules that cross a unit area is $m = k\rho\bar{c}$ (k is a proportionality factor), the change in momentum of the gas across a small layer is $m\,\Delta v$ and is equal to the shear stress between two adjacent layers:

$$\tau = k\rho\bar{c}\,\Delta v. \tag{33.1}$$

At the wall, where $\Delta v = v$, Eq. (33.1) can be written as

$$\tau = k\rho\bar{c}v.$$

Equating this relation to the original expression for τ, we obtain

$$k\rho\bar{c}v = \mu \frac{V_\delta - v}{\delta}. \tag{33.2}$$

To eliminate the viscosity from this equation, we can make use of Newton's relation, $\tau = \mu(\Delta v/\Delta y)$, in which Δy is the distance between the layers. This gives the force that causes the deceleration of one layer with respect to the other. Physically, the deceleration is explained by the change in momentum of the molecules that are moving up and down with the velocity of the thermal motion $\bar{c}$. In turn, this change occurs due to the collision of molecules over the mean free path l. Therefore, $\tau = \mu(\Delta v/l)$, and we obtain a relation for μ from Eq. (33.1):

$$\mu = k\rho\bar{c}l. \tag{33.3}$$

If μ is eliminated from Eq. (33.2) with the help of Eq. (33.3) and the ratio V_δ/δ is replaced by the derivative $\partial V_x/\partial y$, the equation for the slip velocity becomes

$$v = \xi \frac{\partial V_x}{\partial y}, \tag{33.4}$$

in which the factor ξ is called the slip coefficient and is given by

$$\xi = \frac{l}{1 + l/\delta}.$$

For slip flow, $l/\delta \ll 1$, so that $\xi = l$ approximately, and the slip coefficient is equal to the mean free path of the molecules.

Friction on a Plate and a Cone

The method of solving the problem of determining the viscous slip flow parameters can be illustrated by the example of a flat plate.[2] The results of this example must be considered approximate, and are useful for quick estimates of the possible effects of slip in the study of bodies of revolution. For convenience, let us consider an unsteady, viscous, compressible, slip flow over a flat plate, which will be converted to steady flow. We shall not dwell in detail on the mathematical methods of solving the equations but shall present only the final results.

Since an infinitely long plate is considered, all the derivatives with respect to x will be zero, and the equations of continuity and momentum for unsteady flow become

$$\frac{\partial \rho}{\partial t} + \frac{\partial}{\partial y}(\rho V_y) = 0, \tag{33.5}$$

$$\frac{\partial V_x}{\partial t} + V_y \frac{\partial V_x}{\partial y} = \frac{1}{\rho}\frac{\partial}{\partial y}\left(\mu \frac{\partial V_x}{\partial y}\right). \tag{33.6}$$

Let us introduce the dimensionless variables

$$\bar{V}_x = \frac{V_x}{V_\delta}, \qquad \bar{V}_y = \frac{V_y}{V_\delta}, \qquad \bar{\rho} = \frac{\rho}{\rho_\delta}, \qquad \bar{\mu} = \frac{\mu}{\mu_\delta}, \qquad \bar{y} = \frac{y}{l}, \qquad \bar{t} = \frac{t}{t_\delta},$$

where t_δ is a characteristic time equal, for example, to l/V_δ. Equations (33.5) and (33.6) can now be written as

$$\frac{\partial \bar{\rho}}{\partial \bar{t}} + \frac{\partial(\bar{\rho}\bar{V}_y)}{\partial \bar{y}} = 0, \tag{33.5a}$$

$$\frac{\partial \bar{V}_x}{\partial \bar{t}} + \bar{V}_y \frac{\partial \bar{V}_x}{\partial \bar{y}} = \frac{1}{\bar{\rho}\mathrm{Re}_l}\frac{\partial}{\partial \bar{y}}\left(\bar{\mu}\frac{\partial \bar{V}_x}{\partial \bar{y}}\right). \tag{33.6a}$$

The Reynolds number in Eq. (33.6a) is based on the mean free path:

$$\mathrm{Re}_l = \frac{\rho_\delta V_\delta l}{\mu_\delta}.$$

Let us introduce the function $\psi(\bar{t}, \bar{y})$, which is related to the dimensionless gasdynamic parameters by

$$\frac{\partial \psi}{\partial \bar{y}} = \bar{\rho}, \qquad \frac{\partial \psi}{\partial \bar{t}} = -\bar{\rho}\bar{V}_y. \tag{33.7}$$

If Eq. (33.7) is introduced into Eq. (33.5a), it becomes clear that the

continuity equation is satisfied identically, which demonstrates that the function defined by Eq. (33.7) actually exists. Using ψ and the operators

$$\left(\frac{\partial}{\partial \bar{t}}\right)_{\bar{y}} = \frac{\partial}{\partial \bar{t}} - \bar{\rho}\bar{V}_y \frac{\partial}{\partial \psi}, \qquad \left(\frac{\partial}{\partial \bar{y}}\right)_{\bar{t}} = \bar{\rho} \frac{\partial}{\partial \psi}, \tag{33.8}$$

we can convert the equation of motion, Eq. (33.6a) to the form

$$\frac{\partial \bar{V}_x}{\partial \bar{t}} = \frac{\sigma}{\mathrm{Re}_l} \frac{\partial^2 \bar{V}_x}{\partial \psi^2}, \tag{33.9}$$

where $\sigma = \bar{\rho}\bar{\mu}$ is assumed to be constant.

Equation (33.9) is solved for the following conditions. At the initial moment of time $\bar{t} = 0$, the flow over the plate is everywhere uniform and $\bar{V}_x = 1$ for $\psi > 0$. For $t \geq 0$ ($\bar{t} \geq 0$), a slip velocity occurs at the surface:

$$(\bar{V}_x)_w = \frac{v}{V_\delta} = \left(\frac{\partial \bar{V}_x}{\partial \bar{y}}\right)_w.$$

At great distances from the plate, for which $\psi \to \infty$, the velocity tends toward its value for undisturbed flow, i.e., $\bar{V}_x \to 1$.

Equation (33.9) is similar to the equation for heat conduction in a solid body, and the solution for the conditions indicated can be obtained with the help of Laplace transforms (see § 16). This solution gives the velocity as a function of t and y. At the wall, the dimensionless slip velocity is

$$(\bar{V}_x)_w = \frac{v}{V_\delta} = \exp(\chi^2)\ \mathrm{erfc}\ \chi, \tag{33.10}$$

where the new parameter is

$$\chi = \sqrt{\sigma \bar{t}/\mathrm{Re}_l},$$

and erfc χ is the so-called complementary probability integral, given by

$$\operatorname{erfc} \chi = 1 - \operatorname{erf} \chi = \frac{2}{\sqrt{\pi}} \int_{\chi}^{\infty} e^{-y^2}\, dy. \tag{33.11}$$

The local skin friction coefficient on the surface of the plate is determined from

$$c_{fx} = \frac{2\tau_w}{\rho_\delta V_\delta^2} = \frac{2\sigma}{\mathrm{Re}_l} \exp(\chi^2) \operatorname{erfc} \chi. \tag{33.12}$$

To convert this result to steady flow, it is first necessary to examine the solutions for steady and unsteady flows without slip, i.e., with zero velocity at the wall. The solutions for these cases are

$$c_{fx} = 0.664\left(\frac{\sigma}{\mathrm{Re}_l \bar{x}}\right)^{\frac{1}{2}}, \qquad c_{fx} = 1.13\left(\frac{\sigma}{\mathrm{Re}_l \bar{t}}\right)^{\frac{1}{2}}, \tag{33.13}$$

where $\bar{x} = x/l$. An interesting feature of the solution of the steady and unsteady problems is observed in these expressions, since it is possible to transfer from one solution to the other by assuming that $\bar{t} = 2.89\bar{x}$. This feature can also be used in the study of slip flow. In particular, we can find the local friction coefficient in steady flow from Eq. (33.12) by making this substitution and assuming that $\sigma = 1$,

$$c_{fx} = \frac{2}{\mathrm{Re}_l} e^{\bar{\chi}} \operatorname{erfc} \bar{\chi}^{\frac{1}{2}}, \tag{33.14}$$

where[†]

$$\bar{\chi} = \frac{2.89\bar{x}}{\mathrm{Re}_l}.$$

It must be kept in mind that in converting from the unsteady to the steady solution in the case of slip, based on the available analogy for continuous flow, it is necessary to assume a small difference in these

[†]Editor's note: There is some confusion in the original text regarding the presence of a square root in the definitions of χ and $\bar{\chi}$. Equation (33.14) and all later relations have been made consistent with the definition of $\bar{\chi}$ appearing here.

flows, i.e., small slip velocities. For these conditions, $\bar{\chi}$ will be large, and Eq. (33.10) for the slip velocity can be approximated by

$$(\bar{V}_x)_w = \frac{0.56}{\bar{\chi}^{\frac{1}{2}}}. \tag{33.15}$$

Large values of $\bar{\chi}$ correspond to large values of $\bar{x}$, since the mean free path l is small compared with the length x.

Equation (33.14) can also be expanded for large values of $\bar{\chi}$, resulting in the following expression for the local friction coefficient:

$$c_{fx} = \frac{0.664}{\sqrt{\mathrm{Re}_\delta}} \left(1 - \frac{1}{2}\frac{1}{\bar{\chi}} + \frac{3}{4}\frac{1}{\bar{\chi}^2} - \ldots\right), \tag{33.16}$$

where $\mathrm{Re}_\delta = V_\delta \rho_\delta x/\mu_\delta$. It follows from Eq. (33.16) that slip decreases the friction coefficient.

Equation (33.14) can also be transformed by using the relation $\mu_\delta = k\rho_\delta \bar{c} l$ and assuming that $k = 0.5$ for air. Then the Reynolds number Re_l in this equation can be replaced by $\mathrm{Re}_l = 1.46 M_\delta$. As a result we obtain

$$M_\delta c_{fx} = 1.37 e^{\bar{\chi}} \operatorname{erfc} \bar{\chi}^{\frac{1}{2}}, \tag{33.17}$$

where $\bar{\chi}$ is now defined as

$$\bar{\chi} = \frac{1.98\bar{x}}{M_\delta}.$$

Thus, $\bar{\chi}$ is the similarity parameter for the function $M_\delta c_{fx}$, which determines the friction in slip flow. Near the leading edge where x is small, $\bar{\chi}$ is also small. Therefore, the greatest influence of slip on the flow can be expected in this region.

The Knudsen number, defined as $\mathrm{Kn} = l/\delta$, can be used instead of $\bar{\chi}$ for the analysis of slip flow. The curve presented in Fig. 300 shows the variation in the theoretical values of the ratio of skin friction coefficients c_f/c_{fo} (where c_{fo} is the friction coefficient in continuum flow) as a function of Knudsen number. These results, which were obtained by assuming a cubic variation of velocity in the boundary layer,

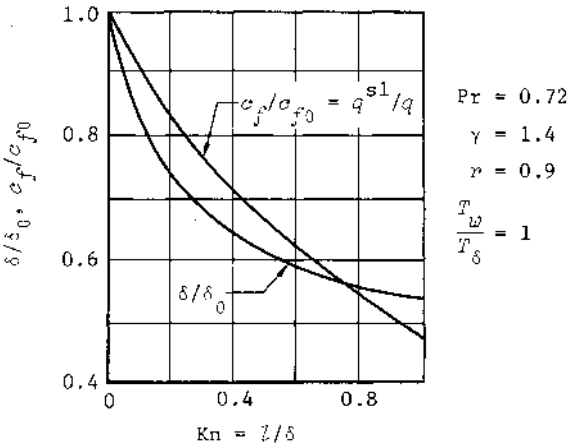

Fig. 300--Slip effects on friction and heat transfer on a flat plate

indicate that slip can considerably decrease the friction coefficient. In the same figure, a theoretical curve is shown illustrating that slip also decreases the boundary layer thickness even more significantly than the friction coefficient.

Equation (33.17) can be used to estimate the limits on $\bar{\chi}$ for the slip regime, but, unfortunately, these estimates can be given only very tentatively at the present time. Observations show that for $\bar{x}/M_\delta > 10$, slip flow changes into continuum flow, and for $\bar{x}/M_\delta < 0.1$, it changes into free molecule flow. Then the expected range of variation in $\bar{x}/M_\delta$ for the slip flow regime will be $0.1 < \bar{x}/M_\delta < 10$, corresponding to $0.2 < \bar{\chi} < 20$. Therefore, Eq. (33.17) should give better results for large values of $\bar{\chi}$, because it is based on the condition that the slip flow differs little from the flow in the continuum regime.

With these limits in mind, Eq. (33.17) can be used for estimating slip flow around a cone. Assuming that we also use the conversion coefficient $\sqrt{3}$ (for converting from a flat plate to a cone in laminar continuum flow) for slip flow close to continuum, we obtain for a cone

$$M_\delta c_{fx} = 2.37 e^{\bar{\chi}} \operatorname{erfc} \bar{\chi}^{\frac{1}{2}}. \tag{33.18}$$

The range of variation of $\bar{\chi}$ for actual calculations will be the same as that for a plate, i.e., $0.2 < \bar{\chi} < 20$.

The skin friction coefficient on a cone surface in viscous continuum flow without slip can be calculated from a convenient equation for c_{fx} as a function of $\bar{\chi}$. Assuming, in the first expression of Eq. (33.13), that $\sigma = 1$ and using the relation $\mathrm{Re}_{\xi} = 1.46 M_{\delta}$, we find for a cone

$$M_{\delta} c_{fx} = \frac{1.34}{\sqrt{\bar{\chi}}}, \tag{33.19}$$

which is applicable for values of $\bar{\chi} > 20$.

Finally, if we consider the other limiting case of free molecule flow around a cone or any other inclined surface, we can determine the magnitude of $M_{\delta} c_{fx}$ from Eq. (32.20) in the form

$$M_{\delta} c_{fx} = 2 M_{\delta} \sin \delta \cos \delta. \tag{33.20}$$

This expression is applicable only for $\bar{\chi} < 0.2$ (or for $\bar{x}/M_{\delta} < 0.1$), for which it is evident that the product $M_{\delta} c_{fx}$ remains constant if M_{δ} does not change.

Equations (33.18) to (33.20) enable us to calculate a curve for the variation in the function $M_{\delta} c_{fx}$ with $\bar{\chi}$ for all three flow regimes. The elements of the curves between the continuum and slip flow regimes and between slip flow and free molecule flow can be constructed by fairing the separate curves. A rough estimate of the friction coefficient can be obtained in the following manner. Instead of Eq. (33.18), computations can be made with only Eqs. (33.19) and (33.20), and in the slip region, $0.2 < \bar{\chi} < 20$, the straight line of Eq. (33.20) and the curve of Eq. (33.19) can be joined by a smooth line.

In determining the parameter $\bar{\chi}$, we must know the mean free path of the molecules. For a cooled surface, this can be calculated from the inviscid flow parameters around a cone in Eq. (31.2):

$$\bar{l} = 1.225 \sqrt{\gamma_{\delta}} \frac{\mu_{\delta}}{\rho_{\delta} a_{\delta}}, \tag{33.21}$$

in which μ_{δ}, ρ_{δ}, and a_{δ} are the viscosity, density, and velocity of

sound at the outer edge of the boundary layer, respectively, and γ_δ is the adiabatic exponent.

HEAT TRANSFER

Slip flow with a velocity discontinuity is also accompanied by a discontinuity between the gas temperature and the surface temperature. The heating rate with slip is related to that for continuum flow by

$$q^{sl} = q\left(1 - \frac{1.89}{\bar{\chi}} + \frac{10.7}{\bar{\chi}^2} - \ldots\right), \tag{33.22}$$

which is obtained for low velocity flow with small slip. Equation (33.22) can be used to estimate the decrease in heat transfer when $\bar{\chi}$ is sufficiently large. The Reynolds analogy can also be used for estimates in engineering calculations of heat transfer including slip (Fig. 300):†

$$\frac{q^{sl}}{q} \approx \frac{c_f}{c_{fc}}. \tag{33.23}$$

To simplify the calculations for arbitrary values of $\bar{\chi}$, estimates of the magnitude of the heat transfer in slip flow can be obtained by sketching a smooth transition between the curve for heat transfer in continuum flow and that for free molecule flow. An approximate construction of this type for heat transfer at the stagnation point is shown in Fig. 301. The curve for continuum flow was obtained for a cooled surface; i.e., it was assumed that $i_w = 0$ in Eq. (27.16), since the wall enthalpy introduces only a small correction. The results for free molecule flow in Fig. 301 were found from Eq. (32.33), in which the accommodation coefficient η was assumed to be unity. A similar method can be applied to an arbitrary point on the surface.

Although this method is very convenient for preliminary estimates, it must be kept in mind that it gives values of shear stress and heat transfer somewhat less than the real values. For confirmation, let us

†Editor's note: Comparison of Eqs. (33.16) and (33.22) shows that this is a poor approximation.

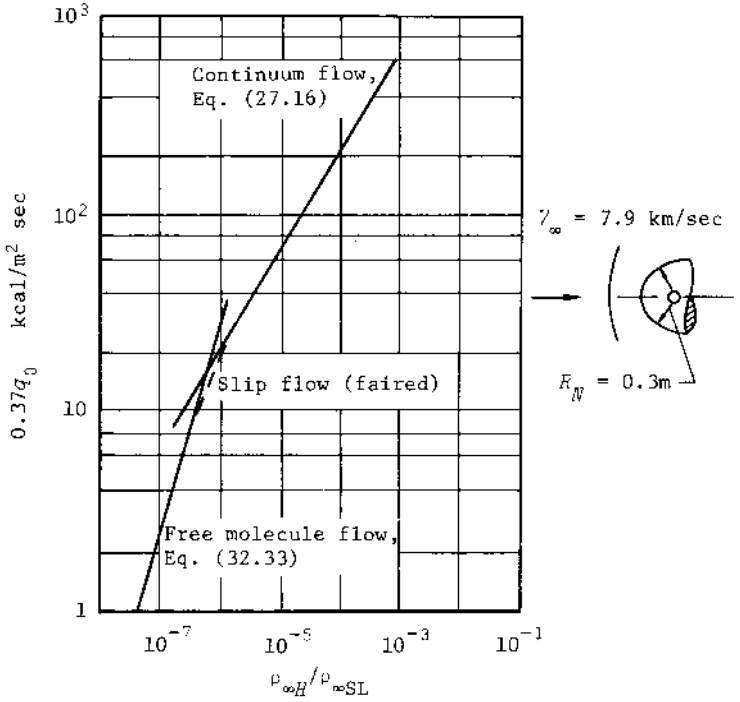

Fig. 301--Heat transfer at the stagnation point of a cooled surface as a function of atmospheric density

examine some theoretical results for viscous flow in the vicinity of the stagnation point at small Reynolds numbers.

VISCOUS RAREFIED FLOW AROUND A BLUNT NOSE

An essential question in research on flow around blunt bodies at high altitudes involves the estimate of the flow regime of a rarefied gas. It was mentioned above that a general criterion for such an estimate is provided by the Knudsen number Kn = l/δ, which depends on a characteristic length δ. It must be emphasized that the choice of the characteristic length is related to the phenomenon being studied; a particular characteristic dimension δ corresponds to each phenomenon. For example, the length of the plate x was chosen as the dimension in the study of flow over a flat plate. In the study of flow around a

blunt nose, it is usual to choose the thickness of the shock layer ε_0 as the characteristic length. Therefore, in an estimate of the limits of applicability of continuum flow theory, it is necessary to assume that the local mean free path must be small compared with the quantity ε_0; i.e., the condition $l/\varepsilon_0 \ll 1$ must be fulfilled.

According to the theory of supersonic flow, the dimensionless thickness ε_0/R_N is of the order of the density ratio across a normal shock wave, i.e., $\varepsilon_0/R_N \sim \bar{\rho} = \rho_{\infty H}/\rho_2$. Thus, the condition for continuum flow is written in the form $l/R_N \ll \bar{\rho}$. If the Reynolds number

$$\mathrm{Re}_\infty = \frac{V_\infty \rho_{\infty H} R_N}{\mu_{\infty H}}$$

is introduced, and the local value of the mean free path is replaced by its free stream value, we can write

$$\frac{l}{R_N} \sim \frac{l_{\infty H}}{R_N} = \frac{M_\infty}{\mathrm{Re}_\infty}.$$

Therefore, the condition indicated above will take the form

$$\frac{M_\infty}{\mathrm{Re}_\infty} \ll \bar{\rho}. \tag{33.24}$$

For example, at Mach numbers from 10 to 20, the density ratio lies between 0.1 and 0.07. Thus, it follows that continuum flow will be maintained for $\mathrm{Re}_\infty > 1000$. If this condition is fulfilled, the continuum flow regime between the body and the shock will be divided into a thin boundary layer and an inviscid zone adjacent to the shock.

As the Reynolds number decreases, the boundary layer will grow thicker, until the shock layer consists of a completely viscous continuous medium. The process of shock transition with time still can be considered to be instantaneous and, therefore, the shock thickness can be considered as infinitesimal. Approximate estimates show that the shock layer must be considered completely viscous when

$$\frac{M_\infty}{\mathrm{Re}_\infty} \ll \tilde{\rho}^{\frac{1}{2}}. \tag{33.25}$$

It is evident that the Reynolds number, approximately 100, is less by an order of magnitude than in the previous case.

As the rarefaction increases, viscosity and thermal conductivity have continually more influence on the formation of the shock wave, which gradually "erodes" and increases in thickness. This regime, sometimes called the merged layer regime, is limited by the condition

$$\frac{M_\infty}{\mathrm{Re}_\infty} < 1. \tag{33.26}$$

For example, at $M_\infty = 20$, the Reynolds number should be in the range $20 < \mathrm{Re}_\infty < 100$. In this regime, the shock wave is not thin and the flow behind it differs somewhat from continuum flow; moreover, the flow on the surface is accompanied by the beginning of slip.

As the degree of rarefaction increases further, the flow deviates increasingly from continuum flow, and slip becomes the deciding factor in the formation of flow behind the shock wave, the thickness of which can be very large. For

$$\frac{M_\infty}{\mathrm{Re}_\infty} > 1, \tag{33.27}$$

the flow is called transitional flow. It is characterized by a large mean free path (by a large value of the Knudsen number $\mathrm{Kn} = l/s_0$), but not large enough for free molecule flow to be assumed.

For free molecule flow, the parameter $M_\infty/\mathrm{Re}_\infty$ must be larger by an order of magnitude, i.e.,

$$\frac{M_\infty}{\mathrm{Re}_\infty} \gg 1. \tag{33.28}$$

For example, for $M_\infty = 20$, the Reynolds number must satisfy the inequality $\mathrm{Re}_\infty \ll 20$.

At the present time, the problems of continuum and free molecule

flows around blunt noses have received the most attention. The results for the intermediate regimes are less complete. In a number of cases, they are of a qualitative nature and can be used only for rough estimates. This is because of lack of study of the process of transition from continuum to free molecule flow.

In this intermediate regime, a rigorous formulation of the flow of the rarefied gas is required, and, in general, the treatment of the problem depends on the use of the kinetic theory of gases. The derivation by such means of the aerodynamic characteristics (e.g., friction and heat transfer) is extremely complicated and in many cases is as yet an unsolved problem. In this connection, attempts have been made to obtain these characteristics fom the most general equations of gas dynamics developed for continuum flow conditions, such as the Navier-Stokes relations. For finding approximate solutions, it is assumed that these equations represent satisfactorily the flow in both the viscous layer and the merged layer between the shock wave and the body. Thus, instead of Prandtl's equations, which are themselves simplified Navier-Stokes equations suitable for the study of the thin viscous boundary layer, the Navier-Stokes equations in their full form are used in the intermediate regime, since the effects of viscosity are important throughout the region of flow. The solution must satisfy the given conditions at the outer edge of the layer. For a viscous layer, the conditions are determined by the flow parameters behind the shock wave and for the merged layer by the unperturbed flow parameters, since the shock wave is so "smeared" that its thickness can be considered to be infinitely large analytically. It is understood that the solutions must also satisfy the boundary conditions on the body surface.

As a result of the solution of the viscous layer problem, the parameters in this layer can be completely determined, including those at the surface of the body near the stagnation point, and the distance to the shock wave can be calculated. The standoff distance and the friction and heat transfer rate at the stagnation point are represented graphically in Figs. 302 to 304. The calculations were made for $\tilde{\rho} = 0.1$ and for a strongly cooled surface, so that the enthalpy at the wall would not be of importance. The Reynolds number based on the nose radius was

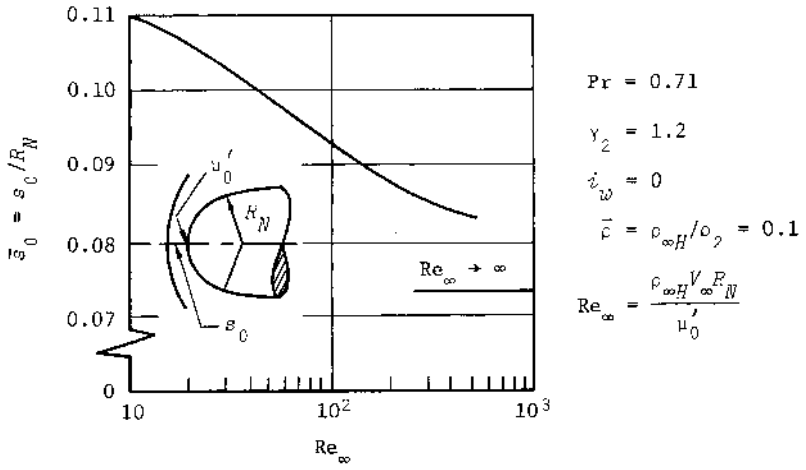

Fig. 302--Shock standoff distance for small Reynolds number

1 — Free molecule flow

2 — Viscous layer (infinitesimal shock thickness)

3 — Incipient merged layer (thick shock)

4 — Boundary layer theory

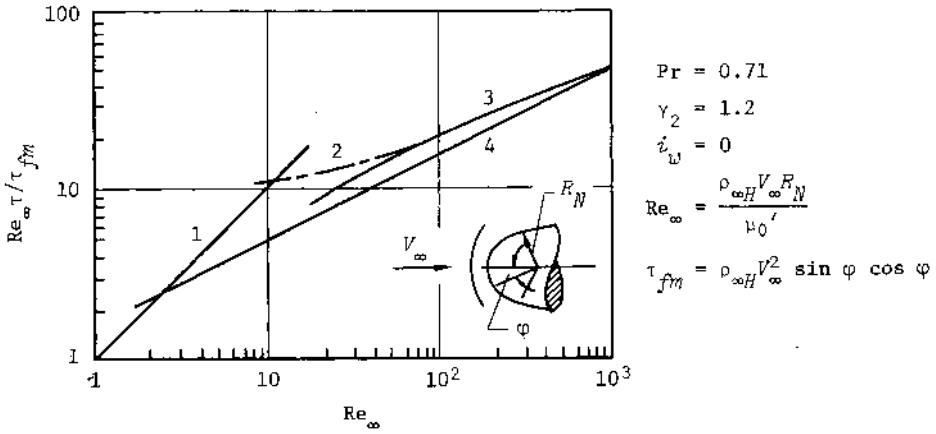

Fig. 303--Shear stress on a cooled sphere

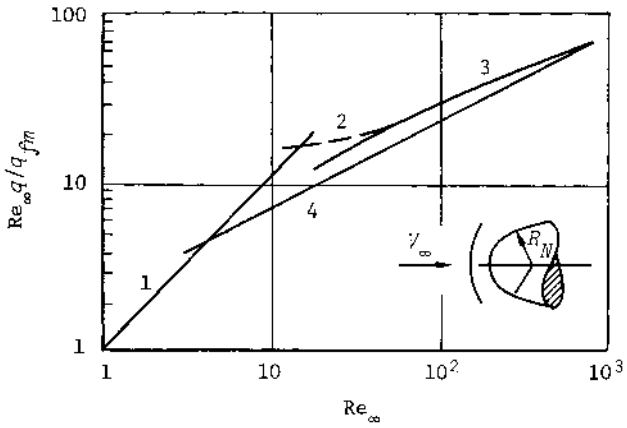

Fig. 304--Stagnation point heat transfer on an insulated sphere

assumed to be the independent variable in the calculations, and the viscosity coefficient μ_0' was based on stagnation conditions. The upper limit for the Reynolds number was chosen as 1000, which corresponds to the usual boundary layer, and the lower limit was chosen as 10, at which the existence of a viscous layer is doubtful and it is normal to assume a merged layer.

It is evident from Fig. 302 that the distance to the shock wave is a function of Reynolds number. Included in this functional relation is the effect of viscosity on the formation of the shock wave in front of a blunt nose in rarefied gas flow. Therefore, the greater the degree of rarefaction and the less the Reynolds number, the greater in magnitude is the displacement of the shock wave from the body compared with its value for continuum (inviscid) flow (in Fig. 302 this value is indicated for $Re_\infty \to \infty$).

The results obtained for friction and heat transfer at the stagnation point (Figs. 303 and 304) indicate that a decrease in Reynolds number leads to some increase in friction and heat transfer compared with continuum (inviscid) flow in the shock layer, i.e., the results of ordinary boundary layer thoery. This is caused by the additional effect of viscous stresses.

The model of the viscous layer for which these results were obtained becomes unsuitable at small Reynolds numbers, and at $Re_\infty < 100$ it is necessary to transfer to a model of a merged layer.

To obtain a solution for the merged layer using the Navier-Stokes equations, it is helpful to examine the initial stage of development of a merged layer, which corresponds to Reynolds numbers from 100 down to 20 or 30. The properties of this layer are still specified by continuum flow. The shock wave has an inner boundary with a radius of curvature R_{s0} on the axis, but the leading edge of the shock is smeared out. The undisturbed flow parameters are the boundary conditions, together with the additional condition that at infinity the gradients of the flow parameters are zero. Thus, it is impossible to examine the shock wave on the basis of the ordinary equations corresponding to an infinitely thin shock. The boundary conditions for the formation of a diffuse shock wave are obtained from the conservation equations; the latter are derived in integral form taking into account the shock thickness, which depends on the viscosity and thermal conductivity.

The calculations carried out by this method (see Figs. 303 and 304) enable us to refine the results obtained for the viscous layer regime. The friction and heat transfer parameters are less than those given by the viscous layer analysis for Reynolds numbers less than about 100 because of an increase in the degree of rarefaction, as a result of which the flow becomes closer in character to free molecular flow.

The merged layer theory has been used to determine the effects of changes in Reynolds number on the density and pressure behind the shock wave. It was shown that, contrary to the usual picture of flow, the parameters behind a normal shock depend on the conditions at the surface of the body, particularly on whether the wall is cooled or insulated. For example, as the Reynolds number decreases the density increases for a cooled surface and decreases for an insulated surface, but the pressure is reduced in both cases.(Fig. 305).

The graph in Fig. 306 is an illustration of the effect of small Reynolds numbers on the heat transfer at the stagnation point. The ordinate is the ratio of the heating rate q_w (including real gas effects behind the shock wave) to the heating rate q_0 from ordinary boundary

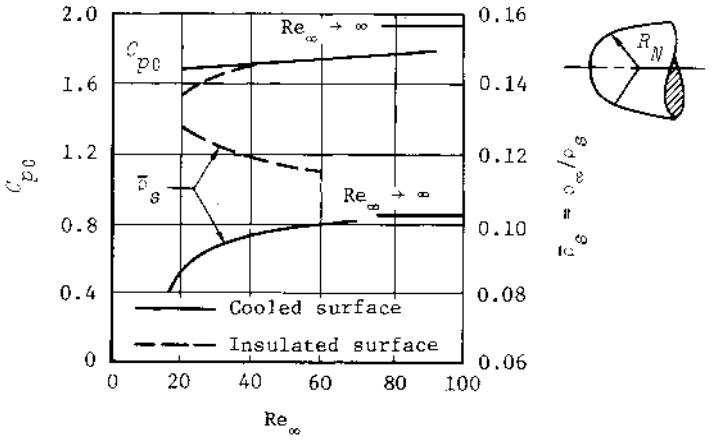

Fig. 305--Pressure and density near the stagnation point of cooled and insulated surfaces at low Reynolds numbers

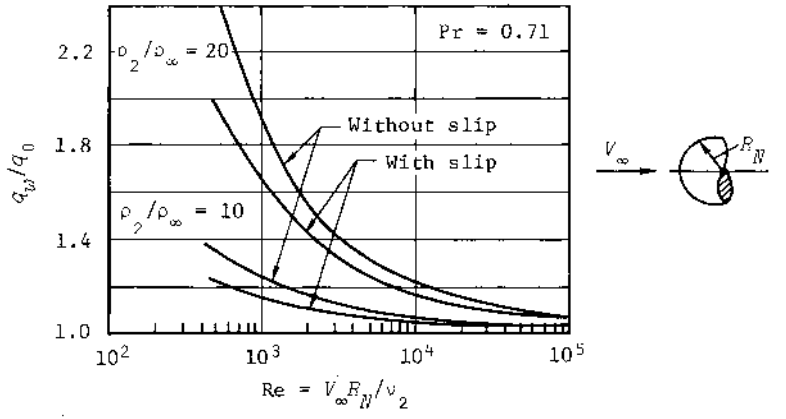

Fig. 306--Effects of vorticity and slip on heat transfer at the stagnation point for low Reynolds numbers

layer theory. The influence of vorticity caused by the curved shape of the shock wave is especially large at small Reynolds numbers. It leads to a considerable increase in heat transfer, because the boundary layer thickness includes almost the entire region between the body and the

shock. Since the vorticity increases with an increase in the strength of the shock wave, its influence will be stronger at high velocities and, accordingly, at large values of the density ratio ρ_2/ρ_∞.

Slip flow is observed on the surface at small Reynolds numbers. Therefore, the heat transfer is reduced somewhat, compensating in some measure for the influence of vorticity. This is evident from Fig. 306, where theoretical results are presented for density ratios of 20 and 10. The curve q_w/q_0 for the lower density ratio is approximated satisfactorily by the equation

$$\frac{q_w}{q_0} = 1 + \frac{14.8}{\mathrm{Re}^{0.6}}\left(1 - \frac{0.98}{\mathrm{Re}^{0.17}}\right), \tag{33.29}$$

in which Re is computed from the velocity V_∞, the radius of the spherical nose R_N, and the kinematic viscosity ν_2 behind the shock, i.e., $\mathrm{Re} = V_\infty R_N/\nu_2$. If the right side of Eq. (33.29) is expanded, the second term represents the increase in heat transfer due to the effect of vorticity, and the third term indicates the decrease in heat transfer caused by the slip effect.

Chapter XI

SIMILARITY LAWS AND AERODYNAMIC CHARACTERISTICS AT TRANSONIC VELOCITIES

Editor's Introduction

THE DEVELOPMENT OF THE SMALL DISTURBANCE THEORY *and the similarity laws for transonic flow in Section 34 follows the original analysis of von Kármán.*[1] *Reference is also made in the text to the work of Spreiter and Alksne,*[2] *and the reader is referred to their report for additional details on the application of transonic flow theory to slender bodies of revolution. Several books on the theory of transonic flow have appeared in the last ten years, and these are excellent sources for those interested in the basic theory. They include Guderley (*The Theory of Transonic Flow, *1962), Oswatitsch (editor,* Symposium Transsonicum, *1964), and Ferrari and Tricomi (*Transonic Aerodynamics, *1968). Unfortunately, the texts by Guderley and by Ferrari and Tricomi contain only a few pages on axisymmetric transonic flow; the book by Oswatitsch is a collection of papers presented at a 1962 symposium, and the major portion of the section related to axisymmetric flow is a paper by Spreiter summarizing the results of Ref. 2.*

*The first half of Section 35 consists of a qualitative discussion of the gross characteristics of transonic flow over bodies of revolution, based largely on German wartime experimental data. Very little has been done in recent years in the way of experiments on the drag-rise Mach number for axisymmetric bodies. A comprehensive collection of free-flight data on bodies of revolution (at both transonic and supersonic speeds) has been published by Stoney (*NASA TR R-100, *1961), but the details of the drag-rise region are not easily identified.*

*The pressure distribution on a flat-nosed cylinder at transonic speeds (Fig. 317) has been carefully measured and analyzed by Stanbrook (*Aeronautical Research Council R&M 3425, *1966). In connection with this, Graff (*Union Carbide Research Institute TR C-24, *October 1964) has obtained an analytical expression for the velocity distribution in compressible flow over a flat face, using the Rayleigh-Janzen method. This result is useful in calculating the pressure distribution and pressure drag of blunt-nosed bodies at high subsonic speeds.*

*The drag of a pointed cone at Mach numbers near that for shock detachment is discussed on pages 858-860. South (*NASA TN D-4563, *May 1968) has successfully applied the Belotserkovskii integral method to the calculation of the flow about pointed cones with detached shock waves. The*

limits of applicability of the method to this problem have not been completely defined, but it appears that there is a minimum Mach number for a given body shape below which solutions do not exist.

Equation (35.7) for the pressure drag coefficient of sharp-nosed bodies at Mach numbers near unity was obtained from a paper by the editor.[9] *The application of this equation to cones and ogive noses is illustrated in the figures given in the Introduction to Chapter III.*

§ 34. *THE TRANSONIC SIMILARITY LAWS*

THE EQUATIONS OF SYMMETRIC FLOW

General Observations

THUS FAR, THE AERODYNAMICS of bodies of revolution have been investigated under conditions of supersonic velocities considerably larger than the velocity of sound. The study of some of the aerodynamic problems at low supersonic speed around slender pointed bodies was carried out using the linear equations of motion of a gas. However, these equations are inapplicable in the case of transonic (near sonic) velocities of flow around a body of revolution, even if it is slender. In the linearized equations, the difference between the squares of the local velocities, $a^2 - V_x^2$, was replaced by the corresponding free-stream quantity $a_\infty^2 - V_\infty^2$. Since $a^2 - V_x^2$ is equal to $a_\infty^2 - V_\infty^2 - (\gamma + 1)V_\infty V_x'$ when expanded, the approximation is acceptable when the term $(\gamma + 1)V_\infty V_x'$ is small compared with the difference $a_\infty^2 - V_\infty^2$. Under transonic flow conditions when the flow velocity is close to sonic, $(\gamma + 1)V_\infty V_x'$ is of the same order of magnitude as $a_\infty^2 - V_\infty^2$, and linearization of the equation is impossible. However, the basic equations can be simplified somewhat, although not linearized; the simplified equations considerably facilitate the study of transonic symmetric flow.[1]

The Equation for the Velocity Potential

The equation for the velocity potential can be derived from Eq. (3.22) for steady symmetric motion. A perturbation potential φ is defined by

$$\frac{\partial \varphi}{\partial x} = V_x - a^*, \qquad \frac{\partial \varphi}{\partial r} = V_r, \tag{34.1}$$

where φ corresponds to the flow around a slender body of revolution when the local velocity differs little from the critical velocity a^*; therefore, $\partial\varphi/\partial x$ is very small. The potential φ must satisfy the conditions at infinity:

$$\left(\frac{\partial\varphi}{\partial x}\right)_\infty = V_\infty - a^*, \qquad \left(\frac{\partial\varphi}{\partial r}\right)_\infty = 0. \tag{34.2}$$

After the introduction of φ into Eq. (3.22), the equation takes the form

$$\left(1 - \frac{V_x^2}{a^2}\right)\varphi_{xx} + \left(1 - \frac{V_r^2}{a^2}\right)\varphi_{rr} - \frac{2V_xV_r}{a^2}\varphi_{rx} + \frac{V_r}{r} = 0. \tag{34.3}$$

If V_r^2 is neglected in comparison with V_x^2, the expression for the velocity of sound can be written as

$$a^2 = \frac{\gamma + 1}{2}a^{*2} - \frac{\gamma - 1}{2}V_x^2. \tag{34.4}$$

Since the flow velocity around the body is close to the speed of sound, we can obtain the following relations from Eqs. (34.1) and (34.4) by neglecting terms containing $(\varphi_x/a)^2$:

$$\frac{V_x^2}{a^2} = 1 + \frac{\gamma + 1}{a^*}\frac{\partial\varphi}{\partial x}, \tag{34.5}$$

$$\frac{V_r^2}{a^2} = \frac{\varphi_r^2}{a^{*2}}, \tag{34.6}$$

$$\frac{V_xV_r}{a^2} = \frac{\varphi_r}{a^*}. \tag{34.7}$$

Introducing Eqs. (34.5) through (34.7) into Eq. (34.3) and neglecting higher-order terms, the differential equation for steady transonic flow becomes

$$\frac{\gamma + 1}{a^*}\varphi_x\varphi_{xx} + \frac{2}{a^*}\varphi_r\varphi_{rx} = \varphi_{rr} + \frac{\varphi_r}{r}. \tag{34.8}$$

This equation is nonlinear with respect to φ; it is more complicated than the linearized equation but is simpler than the general equation (Eq. (3.20)) for the velocity potential.

THE LAW OF FLOW SIMILARITY

The Affine Transformation

The similarity law for transonic flow around bodies of revolution with different fineness ratios but with similar thickness distributions (e.g., conical and parabolic bodies) is obtained by combining the boundary conditions, Eq. (34.2), with Eq. (34.8). The condition of continuous flow at the surface of the body must be satisfied:

$$\frac{dr}{dx} = \frac{V_r}{V_x} \approx \frac{\varphi_r}{a^*}. \tag{34.9}$$

The derivative dr/dx can be written in the form $dr/dx = s(x/l)/\lambda_l$, where $\lambda_l = l/d_{mid}$ is the fineness ratio of the body, and $s(x/l)$ is a function representing the slope of the body profile. Then, from Eq. (34.9), we obtain

$$\varphi_r = \frac{a^*}{\lambda_l} s\left(\frac{x}{l}\right). \tag{34.10}$$

Equation (34.10) shows that the magnitude of the potential on the body surface is of the order of $\varphi \sim ra^*/\lambda_l$ since $s(x/l) \sim 1$. Introducing the affine variables ξ and η, which are related to the coordinates x and r by

$$x = l\xi, \qquad r = \frac{l\lambda_l}{\sqrt{\Gamma}}\eta,$$

we can write an expression for φ:

$$\varphi = la^* \frac{1 - M_\infty}{\Gamma} F(\xi, \eta), \tag{34.11}$$

where $\Gamma = (\gamma + 1)/2$ and $M_\infty = V_\infty/a_\infty$ is the free-stream Mach number. The coefficient $1 - M_\infty$ has been introduced into Eq. (34.11) to satisfy the boundary conditions at infinity, and $F(\xi, \eta)$ is the unknown function to be determined.

Equation (34.8), converted to these variables, has the form

$$\frac{2\lambda_l^2}{\Gamma}(1 - M_\infty)\frac{\partial F}{\partial \xi}\frac{\partial^2 F}{\partial \xi^2} + \frac{2}{\Gamma}(1 - M_\infty)\frac{\partial F}{\partial \eta}\frac{\partial^2 F}{\partial \eta \partial \xi} = \frac{\partial^2 F}{\partial \eta^2} + \frac{1}{\eta}\frac{\partial F}{\partial \eta}. \tag{34.12}$$

The second term on the left can be neglected because it is less than the first term by at least a factor λ_l^2. Introducing the designation

$$K = \frac{1 - M_\infty}{\Gamma}\lambda_l^2, \tag{34.13}$$

Eq. (34.12) is simplified to

$$2K\frac{\partial F}{\partial \xi}\frac{\partial^2 F}{\partial \xi^2} = \frac{\partial^2 F}{\partial \eta^2} + \frac{1}{\eta}\frac{\partial F}{\partial \eta}. \tag{34.14}$$

Replacing $F(\xi, \eta)$ by a function $f(\xi, \eta)$, where

$$F(\xi, \eta) = \frac{1}{K} f(\xi, \eta), \tag{34.15}$$

we obtain

$$2\frac{\partial f}{\partial \xi}\frac{\partial^2 f}{\partial \xi^2} = \frac{\partial^2 f}{\partial \eta^2} + \frac{1}{\eta}\frac{\partial f}{\partial \eta}. \tag{34.16}$$

The boundary conditions that the solution of Eq. (34.16) must satisfy are written in the following manner. The conditions at infinity are

$$\left(\frac{\partial \varphi}{\partial x}\right)_\infty = \frac{\alpha^*(M_\infty - 1)}{\Gamma}, \qquad \left(\frac{\partial \varphi}{\partial r}\right)_\infty = 0.$$

If φ is replaced by $f(\xi, \eta)$, these become

$$\left(\frac{\partial f}{\partial \xi}\right)_\infty = -K, \qquad \left(\frac{\partial f}{\partial \eta}\right)_\infty = 0. \tag{34.17}$$

The condition at the surface of the body is obtained from Eq. (34.9) as

$$2\eta \frac{\partial f}{\partial \eta} = t(\xi), \tag{34.18}$$

where $t(\xi) = t(x/l)$ depends on the geometric shape of the body.

Obviously, for identical values of K, Eq. (34.16) with the boundary conditions of Eqs. (34.17) and (34.18) will give a unique solution that describes a whole class of flows around bodies of revolution with large fineness ratios and with an identical law of thickness distribution; the parameter K represents the similarity parameter for flows at transonic velocity.

The Pressure and Drag Coefficients

The general equation for the pressure coefficient can be found from Eq. (3.58),

$$p = p_0\left(1 - \frac{V_x^2 + V_r^2}{V_{\max}^2}\right)^{\gamma/(\gamma-1)},$$

by replacing V_x^2 by the approximate expression $V_x^2 = V_\infty^2 + 2V_\infty(\varphi_x - \varphi_{x\infty})$, which can be derived from Eqs. (34.1) and (34.2). Noting that

$$V_{\max}^2 = \left(M_\infty^2 + \frac{2}{\gamma - 1}\right)a_\infty^2,$$

and

$$p_0 = p_\infty\left(1 + \frac{\gamma - 1}{2} M_\infty^2\right)^{\gamma/(\gamma-1)},$$

we can write the expression for the static pressure as

$$p = p_\infty\left[1 - \frac{\gamma - 1}{2} \frac{2V_\infty(\varphi_x - \varphi_{x\infty}) + \varphi_r^2}{a_\infty^2}\right]^{\gamma/(\gamma-1)}.$$

Expanding in a series and retaining only two terms in the expansion,

we get

$$p - p_\infty = -\frac{\gamma p_\infty}{2a_\infty^2}\left[2V_\infty(\varphi_x - \varphi_{x\infty}) + \varphi_r^2\right] = -\rho_\infty(\varphi_x - \varphi_{x\infty})V_\infty - \frac{1}{2}\rho_\infty\varphi_r^2.$$

Hence the pressure coefficient is

$$C_p = -\frac{2(\varphi_x - \varphi_{x\infty})}{V_\infty} - \frac{\varphi_r^2}{V_\infty^2} = -\frac{2(V_x - V_\infty)}{V_\infty} - \frac{V_r^2}{V_\infty^2}. \tag{34.19}$$

The axial velocity component is obtained from Eqs. (34.1), (34.11), and (34.15):

$$V_x = a^*\left(1 + \frac{1 - M_\infty}{\Gamma K}\frac{\partial f}{\partial \xi}\right). \tag{34.20}$$

Using Eqs. (34.10) and (34.20) and the approximate relation

$$1 - \frac{V_\infty}{a^*} = \frac{1 - \lambda_\infty}{\Gamma},$$

Eq. (34.19) can be written in the form

$$C_p = \frac{1}{\lambda_l^2}P(K, \xi), \tag{34.21}$$

where the function is

$$P(K, \xi) = -2K\left(1 + \frac{1}{K}\frac{\partial f}{\partial \xi}\right) - s^2(\xi). \tag{34.22}$$

For a given point with the dimensionless coordinate ξ, $P(K, \xi)$ varies only with the similarity parameter K.

The general expression for the pressure drag coefficient can be found by substituting C_p into Eq. (1.6) to obtain

$$C_{Dp} = \frac{1}{\lambda_l^2}D(K), \tag{34.23}$$

where $D(K)$ is determined from the expression

$$D(K) = 4\int_0^1 \lambda_l P(K, \bar{x})\bar{r}\tan\delta\, d\bar{x}. \tag{34.24}$$

The relations for C_p and C_{Dp} indicate that, for identical values of K, the transonic flows around affine-similar bodies of revolution are similar in the sense that the quantities $\lambda_l^2 C_p$ and $\lambda_l^2 C_{Dp}$ remain identical. Thus, K is the basic parameter characterizing the flow in the study of transonic flow, and the law of similarity of flows in terms of K can be used as the basis for experimental and theoretical studies of aerodynamic characteristics.

A relation differing somewhat from Eq. (34.13) can be used for K:

$$K = \frac{(M_\infty^2 - 1)\lambda_l^2}{(\gamma + 1)M_\infty^2}, \tag{34.25}$$

which represents the similarity more exactly.[2] The more detailed study in Ref. (2) leads to the conclusion that the similarity laws are more complicated than those given by Eqs. (34.21) and (34.23); that is,

$$C_p = \frac{B(K, \xi)}{\lambda_l^2} + E(M_\infty, \lambda_l, \gamma, \xi), \tag{34.26}$$

$$C_{Dp} = \frac{C(K)}{\lambda_l^2} + G(M_\infty, \lambda_l, \gamma), \tag{34.27}$$

where B, C, E, and G are certain functions depending on the variables indicated in Eqs. (34.26) and (34.27). According to these equations, the similarity pertains not to the functions $\lambda_l^2 C_p$ and $\lambda_l^2 C_{Dp}$ but to the parameters $\lambda_l^2(C_p - E)$ and $\lambda_l^2(C_{Dp} - G)$, respectively.

The Slender Pointed Body with a Curved Profile

Research has shown that for families of affine-similar slender pointed bodies of revolution the second term in Eq. (34.26) has the form[2,3]

$$E = -\frac{1}{\pi} S''(x) \log\left(\frac{M_\infty}{\lambda_l^2}\sqrt{\gamma + 1}\right). \tag{34.28}$$

Equations (34.28) and (34.26) can be used to generalize experimental data for a given Mach number and for a specific model of a given fineness ratio. An experimental pressure distribution is shown in Fig. 307

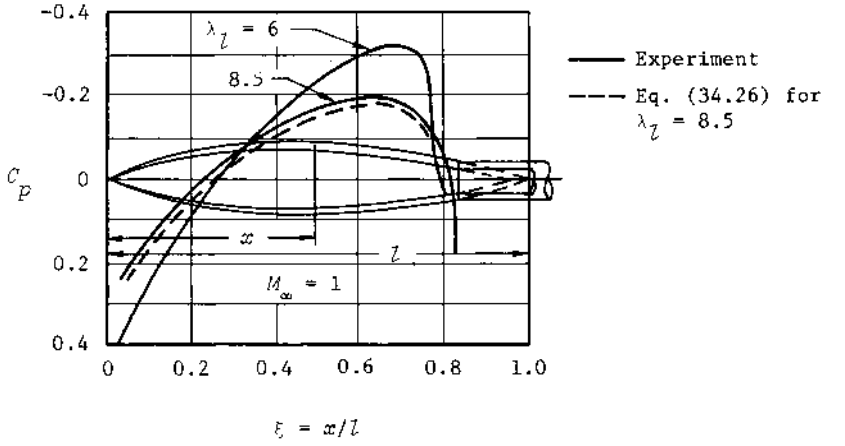

Fig. 307--Application of the similarity law to the calculation of the pressure distribution over a slender body at sonic speed

for $M_\infty = 1$ around a parabolic body of revolution with a fineness ratio $\lambda_l = 6$. The values of $B(\xi)$ were calculated as a function of ξ from these experimental values and Eq. (34.26), and then the pressure coefficients were computed at the corresponding points of a more slender body of revolution with a fineness ratio of 8.5. The results agreed well with experimental data for the more slender body.

Introducing Eq. (34.26) for C_p into Eq. (1.6), we obtain the following similarity law for the drag coefficient:

$$C_{Dp} = \frac{4}{\pi}\frac{C(K)}{\lambda_l^2} - \frac{1}{2\pi}\frac{[S'(l)]^2}{S_{\text{mid}}}\log\left[\frac{M_\infty}{\lambda_l^2}\sqrt{\gamma+1}\right], \qquad (34.29)$$

from which the function C in Eq. (34.27) can be found.

The similarity law of Eq. (34.29) is simplified if the base of the body lies at the maximum cross section or if the afterbody is pointed;

in both cases, the derivative of the cross-sectional area $S'(x_l) = 0$. The relations presented for the similarity law are applicable in the vicinity of $M_\infty = 1$, and the results of calculations agree well with the data obtained for sonic or slightly supersonic flows.

The Slender Pointed Cone with a Cylindrical Afterbody

The peculiarity of transonic or sonic flow around a conical body is that sonic velocity is always obtained at the shoulder. Therefore, the pressure at this point can be calculated beforehand. The flow parameters at the other points of the cone can be found either experimentally or by solving Eq. (34.16). This solution leads to the following relation for the pressure coefficient at $M_\infty = 1$:[2]

$$\frac{C_p}{\delta_c^2} = -2 \log (\delta_c \xi) + \log A - B, \tag{34.30}$$

in which

$$A = \frac{8.96\xi(1 - \xi)}{(\gamma + 1)\delta_c^2}, \qquad B = \frac{1}{2}\frac{1 + \xi}{1 - \xi} \quad \text{for} \quad 0 < \xi \leq \frac{1}{3}$$

$$A = \delta_c^2 + \frac{2.24(1 - \xi^2)}{(\gamma + 1)\delta_c^2}, \qquad B = 1 \quad \text{for} \quad \frac{1}{3} < \xi \leq 1. \tag{34.31}$$

The curve calculated from Eq. (34.30) is presented in Fig. 308 for a cone with $\delta_c = 7°$. These results agree well with experiment.

A similarity law analogous to Eq. (34.30) can be obtained for $M_\infty \neq 1$ by combining Eqs. (34.26) and (34.28). Since $S(x) = \pi x^2 \delta_c^2$, $S''(x) = 2\pi\delta_c^2$, and $\lambda_l = \frac{1}{2}\delta_c$ for a cone, Eq. (34.26) can be written as

$$C_p = 4\delta_c^2 B(K, \xi) - 2\delta_c^2 \log (4\delta_c^2 M_\infty \sqrt{\gamma + 1}). \tag{34.32}$$

The expression for the drag coefficient corresponding to Eq. (34.29) is written in the form

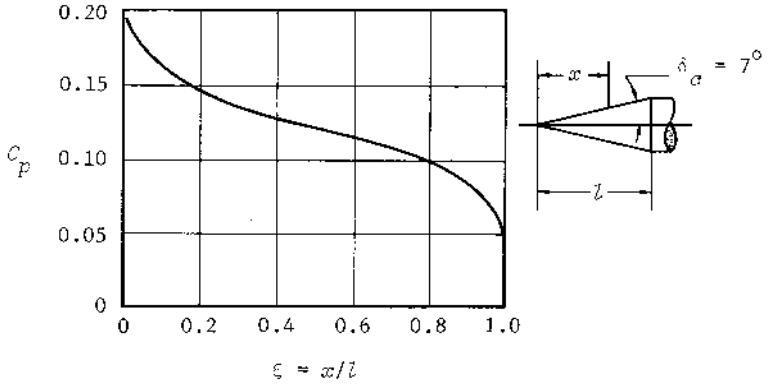

Fig. 308--The pressure distribution on a cone-cylinder at $M_\infty = 1$

$$C_{Dp} = \frac{8\delta_c^2}{\pi} C(K) - 2\delta_c^2 \log (4\delta_c^2 M_\infty \sqrt{\gamma + 1}). \qquad (34.33)^\dagger$$

For $M_\infty = 1$, Eqs. (34.32) and (34.33) are simplified since in this case $K = 0$. For example, the expression for the drag coefficient is

$$(C_{Dp})_{M_\infty = 1} = -\delta_c^2 (1.09 + 4 \log \delta_c). \qquad (34.34)$$

In the case of a Mach number differing from unity, we can use a specific relation for a slender cone instead of the general Eq. (34.33):

---

†Editor's note: Spreiter and Alksne[2] give explicit expressions for C_p and C_{Dp} for $M_\infty \neq 1$ that can be written in the same format as Eq. (34.30); the expression for A is modified from that in Eq. (34.31) by replacing $(\gamma + 1)$ with $(\gamma + 1)M_\infty^2$. The equations are

$$C_p/\delta_c^2 = 8K - 2 \log (\delta_c \xi) + \log A - B, \qquad (34.32a)$$

$$C_{Dp}/\delta_c^2 = 8K - \frac{1}{2} + \log [1.33/(\gamma + 1)M_\infty^2 \delta_c^4], \qquad (34.33a)$$

where K is defined in Eq. (34.25). Equation (34.33a) leads directly to the later equations for C_{Dp} (Eqs. (34.34) and (34.35)).

$$C_{Dp} = -\delta_c^2(1.09 - 8K + 4 \log \delta_c). \tag{34.35}$$

It follows from this equation that for a slender conical body the quantity $(C_{Dp}/\delta_c^2) + 4 \log \delta_c$ depends only on the similarity parameter K. The application of Eq. (34.35) is limited to values of K that satisfy the inequality

$$K = \frac{M_\infty^2 - 1}{4(\gamma + 1)M_\infty^2\delta_c^2} \ll 1. \tag{34.36}$$

This condition corresponds to a weak shock wave located a rather large distance from the body. The distance of the shock from the apex (Fig. 309) is determined by

$$0.125 \log\left(\frac{l_N}{x_s} + 1\right) - \left(1 + \frac{x_s}{l_N}\right) = K. \tag{34.37}$$

This equation serves as another illustration of the similarity law with respect to the parameter K.†

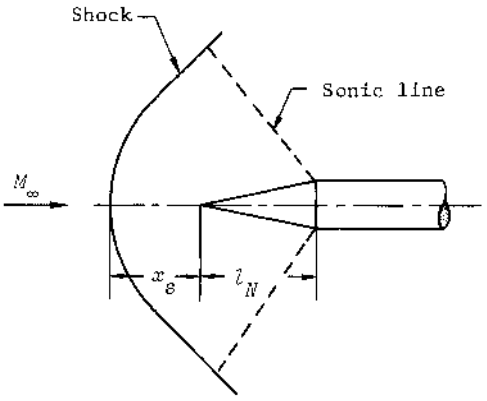

Fig. 309--The detached shock wave for M_∞ slightly greater than one

†Editor's note: This equation is clearly incorrect, but the reference is unknown.

§ 35. *SOME DATA ON TRANSONIC FLOW AROUND BODIES OF REVOLUTION*

THE PHENOMENON OF SHOCK STALL

The Shock Wave on the Body at Subsonic Speeds

ON THE BASIS OF EXPERIMENTAL DATA, it is possible to explain a number of physical phenomena related to shock stall, among which is the formation of a shock wave at subsonic flight velocities. Schlieren photographs of a body of revolution are shown in Fig. 310. Analysis of the photographs shows that at $M_\infty = 0.67$ the local velocity does not exceed sonic velocity (see Fig. 310a) at any point on the body. The drag at this velocity is due only to skin friction and is very small.

The flow at a somewhat larger Mach number, $M_\infty = 0.78$, is shown in Fig. 310b, and it is evident that the velocity is sonic not far from the nose section of the body and then exceeds the velocity of sound somewhat downstream. As a result, a local supersonic zone occurs on the surface of the body. Behind this zone, at approximately half the length of the body, the velocity is decreased by a shock wave and the flow again becomes subsonic. A series of normal shocks is evident in the schlieren photograph, but their strength is small and the velocity is almost unchanged. A sharp change in velocity occurs when the strength of the shock wave increases. A similar phenomenon is observed more clearly in the case of flow around the body at $M_\infty = 0.89$ (Fig. 310c). In this case, the shaded streak in the schlieren represents a strong shock wave.

With the occurrence of shock waves, the kinetic energy of the flow is dissipated by the formation of the shocks, resulting in a considerable increase in drag. In Fig. 310, the relative magnitude of the wave drag coefficient is shown by the light vertical lines on the right, and it is evident that the wave drag coefficient increases sharply with an increase

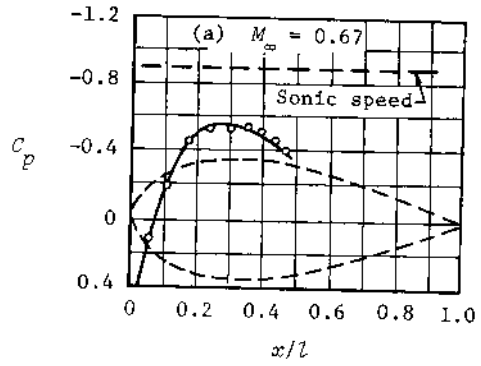

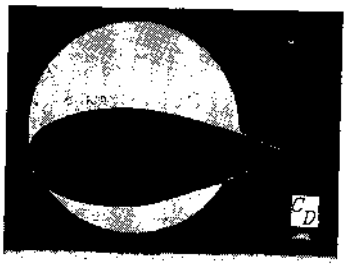

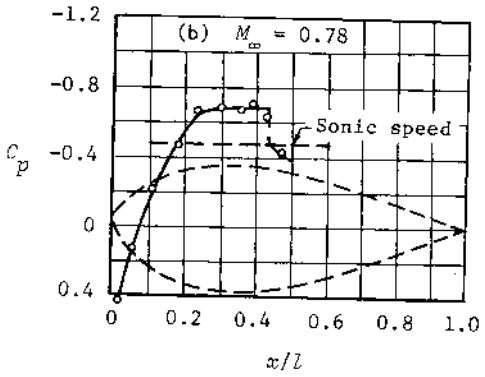

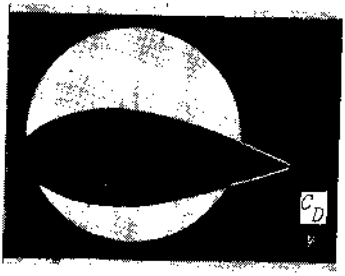

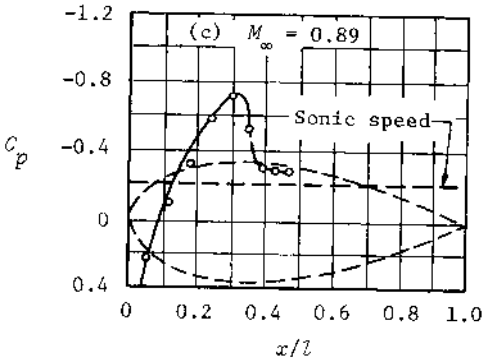

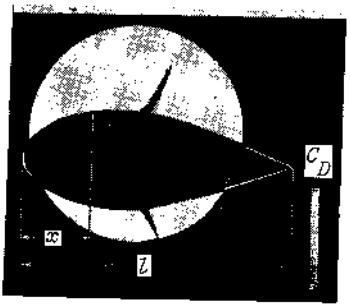

Fig. 310--Schlieren photographs and pressure distributions on bodies of revolution at high subsonic speeds

in M_∞. Thus, the drag coefficient at $M_\infty = 0.89$ is more than ten times greater than that at $M_\infty = 0.78$. The sharp increase in drag and the changes in the other aerodynamic characteristics at transonic speeds is connected with the general concept of shock stall.

The Effect of the Shape of the Body

Experimental research has shown that the phenomenon of shock stall depends essentially on the shape of the body of revolution. Data are presented in Fig. 311 indicating the effects of the shape of the nose, the fineness ratio, and the location of the maximum cross section of the body on the nose drag coefficient and the critical Mach number M_{cr}

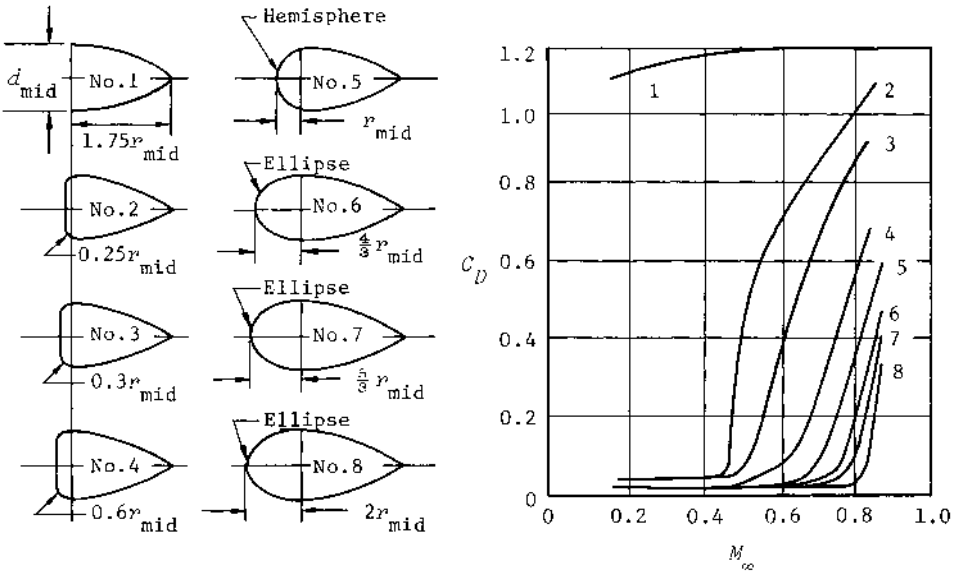

Fig. 311--Drag of different bodies of revolution at subsonic speeds

(the value of M_∞ at which the velocity becomes sonic at some point on the body). The absolute thickness of all bodies under investigation is the same. It is evident from the figure that an increase in the total fineness ratio of the body, in the nose fineness ratio, and in

the curvature of the nose all affect the drag rise and also the general level of the drag. Different local curvatures have an especially strong effect in reducing the drag level, as can be seen from the comparison of the curves for models 1 and 2.

Curves are presented in Fig. 312 for the minimum pressure coefficient in subsonic flow around models 5 to 8 of the bodies shown in Fig. 311. As the nose fineness ratio is increased, the flow needs to expand less and the shock stall is delayed to higher Mach numbers.

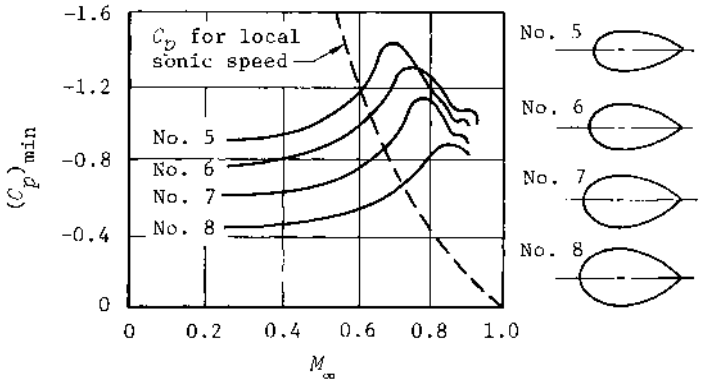

Fig. 312--Minimum pressure coefficients for subsonic flow over bodies of revolution

The critical Mach number for each model can be determined from Fig. 312 as the point of intersection of the curves of $(C_p)_{min}$ with the curve corresponding to local sonic velocity (dashed curve). However, the critical Mach number does not correspond with the beginning of the sharp increase in drag (see Fig. 311), because only the necessary conditions for the development of the stall regime have been reached.

The rapid increase in drag begins at Mach numbers larger than critical, equal approximately to the values corresponding to the points of greatest expansion in the curves in Fig. 312. This indicates that a significant region of supersonic velocities must be developed on the surface of the body as a condition for the formation of strong shock waves and the rapid increase in drag associated with them.

The drag increases to some extent as the result of the interaction of the shock waves with the boundary layer. This interaction promotes the separation of the boundary layer from the surface of the body and necessitates a redistribution of pressure. Moreover, premature turbulence develops in the boundary layer, also increasing the drag of the body.

It is evident from the data presented that transonic flow around rather thick bodies is accompanied by the development of shock waves. This picture of transonic flow changes when slender bodies are considered. In this connection, let us examine some experimental results[4] obtained on a model of a pointed body of revolution with a parabolic shape, having a nose fineness ratio of 3 (Fig. 313). The pressures at

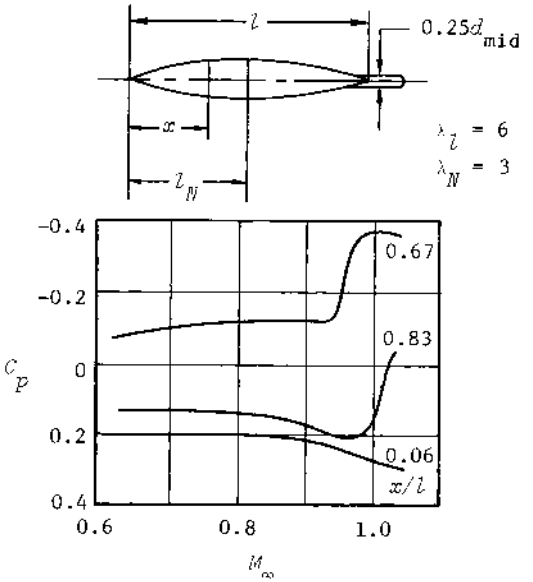

Fig. 313--Pressure coefficient at three stations on a pointed body at high subsonic and transonic speeds

three different stations of this model (x/l = 0.06, 0.67, 0.83) were measured in flight. As is apparent, the effects of compressibility are insignificant and can, in practice, be neglected up to M_∞ = 0.90.

Curves are presented in Fig. 314 for the pressure distribution along the body for different free-stream Mach numbers, from which it can be seen that the critical Mach number (M_{cr}) is equal to approximately 0.90. These data show that the velocity field changes character as it progresses back

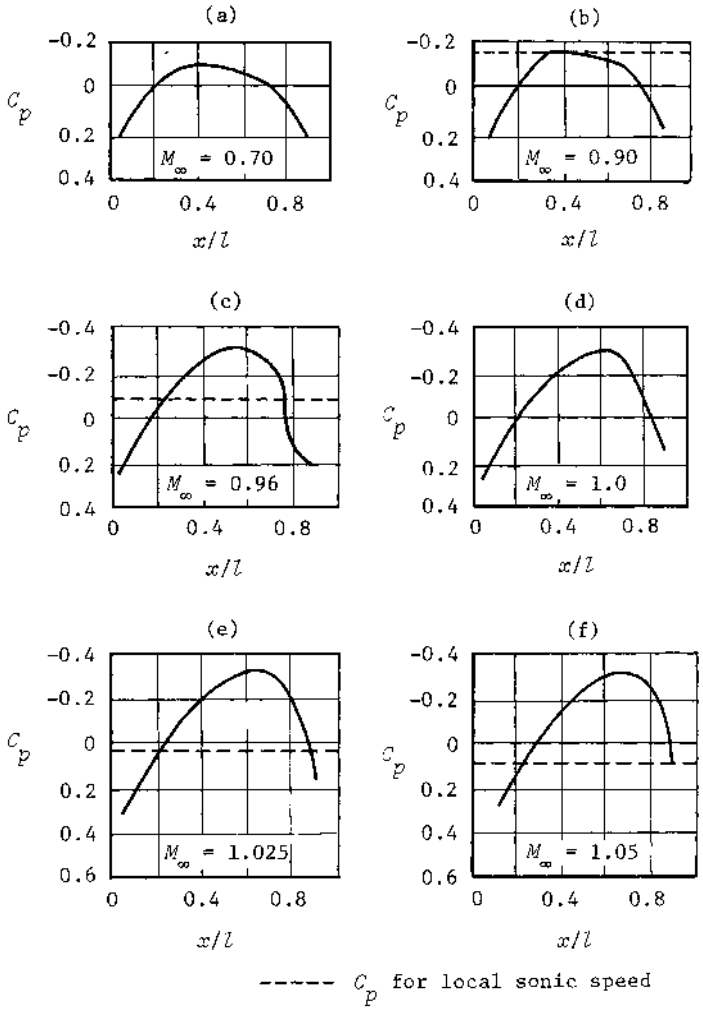

Fig. 314--Pressure distribution on a slender pointed body of revolution at high subsonic and transonic speeds

along the body, as indicated by the fact that the supersonic regions on the body become larger and the region of the negative pressure coefficient is shifted backward. From the physical point of view, an expanding supersonic flow is accompanied by a reduction in pressure, whereas an expanding subsonic flow is associated with a pressure increase. The increase in and the backward shift of the region of negative pressure coefficient leads to a rapid increase in the drag coefficient.

Even in the case of a significant supersonic region on the surface of the body, the transition from supersonic to subsonic flow at the rear, rapid though it is, is accomplished very smoothly. Obviously, it is accomplished through a system of very weak shocks and can, in practice, be considered an isentropic compression.

Using the pressure distributions in Fig. 314, we can compute by graphical integration the drag coefficient for different Mach numbers from Eq. (1.6). As an illustration of this method, Fig. 315 shows the variation in the pressure coefficient with $\bar{r}^2$ for $M_\infty = 0.70$ and 1.05. The pressure drag coefficient can be determined by measuring the net area under the curves, taking into account the signs shown on the graph (measured in a counterclockwise direction around the contour of the body).

Figure 315b shows the variation of the pressure drag coefficient C_{Dp} with Mach number for the body under consideration. The drag coefficient is very small, less than 0.01, up to $M_\infty = 0.9$, because the pressure is distributed practically symmetrically fore and aft in subsonic flow (if the small asymmetry caused by the model support is neglected), and therefore the pressure drag is negligibly small. The almost symmetrical pressure distribution indicates that the boundary layer has little effect on the pressure distribution and that there is no noticeable flow separation. Additional research has shown a tendency toward separation of flow near the support due to a small compression from it. However, this separation does not have much influence on the pressure drag, since the cross section of the body at the aft end is small.

Beginning with a Mach number of 0.94, the drag coefficient increases sharply, reaching 0.21 at $M_\infty = 1$. This sharp increase is associated with the rapid backward shift of the region of negative pressure coefficients

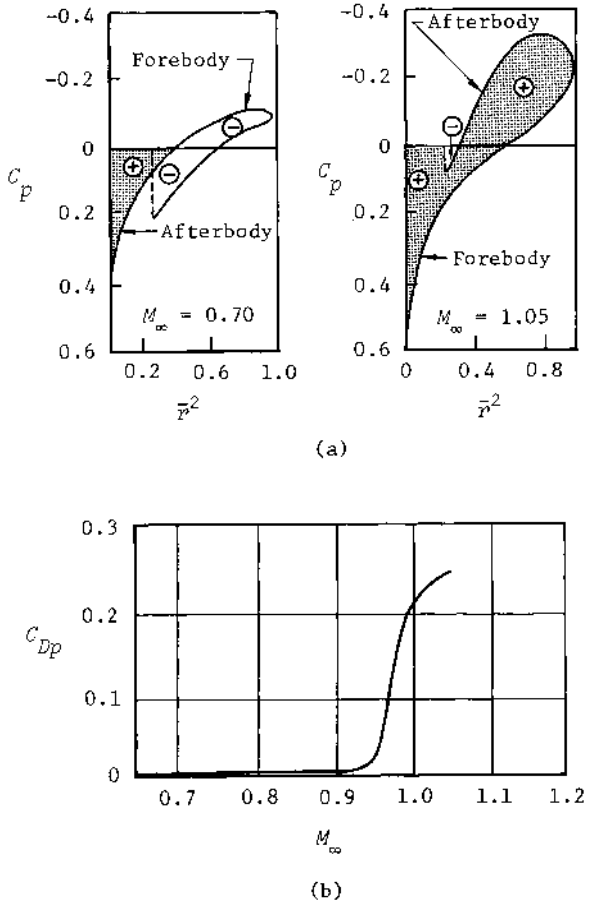

Fig. 315--Method of graphical integration for the pressure drag coefficient

as sonic speed is approached. Flow separation in the transonic regime does not occur in practice due to the smooth shape of the slender body, so that it is not necessary to consider the effects of separation on the drag.

After the free-stream Mach number reaches unity, a rather extended region of supersonic velocities is formed on the body surface, the backward shift of the point of minimum pressure slows down, and the overall

pressure level decreases. In the range of Mach numbers from 1 to 1.05, all these phenomena are accompanied by a more gradual increase in the pressure drag coefficient.

The Total Drag of Various Bodies of Revolution at Transonic Speeds

The transonic regime for slender bodies of revolution lies approximately within the range M_∞ = 0.9 to 1.3. Artillery shells were the first axisymmetric bodies for which the drag was studied at transonic speeds. The experimental data obtained for one of these projectiles, consisting of a cylindrical body with a nose cone, show that the drag coefficient increases rapidly beginning at M_∞ = 0.9 and reaches a maximum at approximately M_∞ = 1.1. The magnitude of the maximum drag coefficient is almost three times larger than that at subsonic velocities.

The experimental curve for C_D as a function of M_∞ for a bomb is presented in Fig. 316.[5] Due to the fact that the afterbody of the bomb is tapered, the drag in the subsonic regime is less than that for a body without a boattail. The shape of the nose section has an increasingly greater influence on the drag at transonic and supersonic speeds. The difference in the drag of the bomb and the shell is due to the different shape of their noses. The drag of the bomb is almost twice as large as that of the shell because its nose is less pointed.

The experimental data in Fig. 317 were obtained for a cylindrical

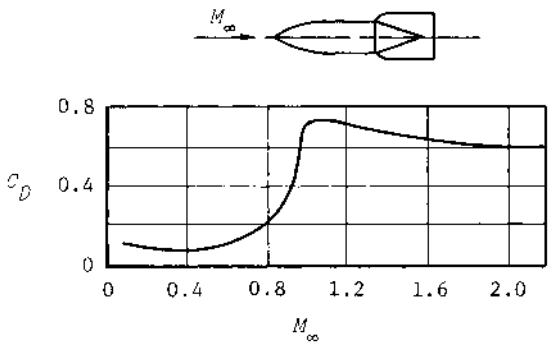

Fig. 316--Experimental drag curve for a bomb

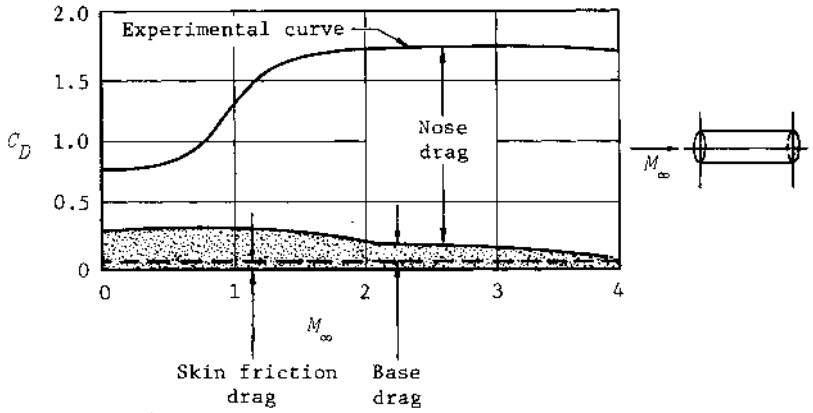

Fig. 317--Drag coefficient for a blunt cylinder

body with a blunt nose.[5] The comparatively rapid increase in drag at $M_\infty = 1$ is in agreement with that predicted by Eq. (20.40).

The drag of a body with a rounded nose is considerably less, particularly a spherical body. An experimental curve for the drag of a sphere at transonic speeds is shown in Fig. 318, and it is evident that the sphere has about two-thirds the drag of a blunt cylinder at $M_\infty = 1$.

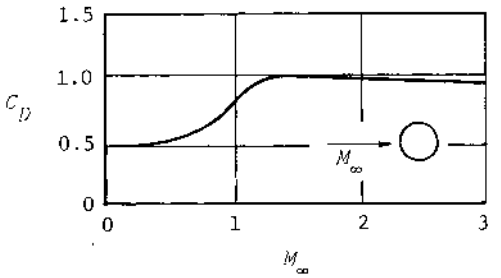

Fig. 318--Experimental drag curve for a sphere

The drag coefficient of the sphere reaches about twice its value at low speeds and then stays approximately constant at $C_D = 1$. The magnitude and character of the variation in drag at supersonic speeds differ from

that presented in Fig. 207 (page 570). The cause of the difference is that the curve in Fig. 318 represents the total drag, whereas that in Fig. 207 represents only the drag due to the pressure acting on the front hemisphere. In addition to pressure drag, the total drag consists also of the drag components caused by skin friction and by expansion over the rear of the body. The influence of these components causes a leveling out of the drag curve at supersonic speeds rather than the increased indicated in Fig. 207.

The following conclusions can be drawn from a summary of the data presented here and other experimental data:

1. The nose drag coefficient reaches a maximum value $C_{D\max}$ at a Mach number somewhat larger than unity and located in a range between $M_\infty = 1.1$ and 1.5.
2. The dominating influence on the magnitude of $C_{D\max}$ is the shape of the nose of the body.

In practice, we can be guided by these conclusions in estimating the maximum value of the nose drag coefficient. It is also possible to use curves based on experimental data, such as shown in Fig. 319, which give the relation between $C_{D\max}$ and the fineness ratio of the nose.[5] This relation can be given by the following empirical equation:

$$C_{D\max} = \frac{0.8}{\lambda_N} + 0.01\lambda_N. \tag{35.1}$$

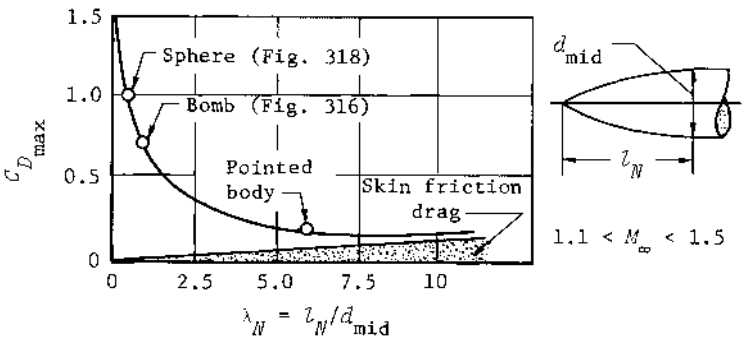

Fig. 319--Maximum drag coefficient of bodies of revolution as a function of nose fineness ratio

The second term on the right in Eq. (35.1) approximates the magnitude of the friction drag coefficient. The minimum value of $C_{D\max}$ according to Eq. (35.1) occurs at a nose fineness ratio of about 9, which corresponds to a very slender body. The friction drag for such a body represents a large proportion of the total drag.

The Normal Force Coefficient and Center of Pressure of Bodies of Revolution at Transonic Speeds

The normal force coefficient and the center of pressure in transonic flow are as difficult to treat in theoretical and experimental research as are the other aerodynamic characteristics. The difficulty in experimental research results chiefly from the instability of the flow in transonic wind tunnels. Only after the development and introduction into the technology of special tunnels with flow stability at Mach numbers of approximately 0.9 to 1.3 did it become possible to obtain reliable information on aerodynamic forces and their coefficients under transonic flow conditions. As a result, much of the aerodynamic data accumulated on bodies of revolution is obtained by means of flight tests. Some of these data relating to nose drag were presented above.

It has been established experimentally that, for slender bodies of revolution, the normal force coefficient at near sonic speeds can attain a maximum value exceeding that for subsonic speeds by 25 to 35 percent. The curve in Fig. 320 shows C_N/α as a function of M_∞ for a

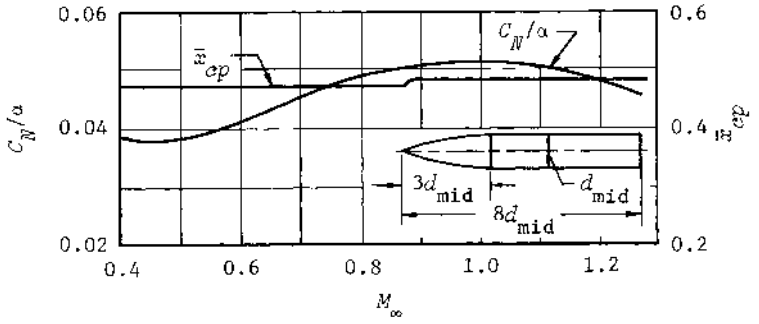

Fig. 320--Variation of C_N/α and the center-of-pressure coefficient at transonic speeds

typical body at angles of attack of 3° and less. The ratio C_N/α attains a maximum value at $M_\infty = 1.0$, where it is approximately 35 percent larger than C_N/α for $M_\infty = 0.4$. The pitching moment also increases with an increase in the normal force. As a result, the location of the center of pressure may not change in practice. This is evident in Fig. 320, where results are presented for the center-of-pressure coefficient of a cylindrical body with a parabolic nose. The variation in this coefficient is only 2 percent for the entire speed range shown.

A similar result is also observed in experimental studies of flow around cones. It is known that the center-of-pressure coefficient of a cone at supersonic speeds is approximately 0.667. Experiments at subsonic speeds show that, for example, for a cone with a semiapex angle of 15°, the center-of-pressure coefficient is less by 4 percent, i.e., the center of pressure is closer to the tip. At transonic speeds, the center-of-pressure coefficient increases slightly, reaching about 0.65 at $M_\infty = 1.0$.

Experimental data indicate that the center of pressure of a cone shifts toward the base of the cone when a cylindrical afterbody is attached to the cone. This occurs both at subsonic and transonic speeds, with the amount of the shift depending on the length of the cylinder. The center of pressure of the cone moves aft because the cylindrical part of the body introduces additional disturbances into the flow, which in subsonic flow are propagated upstream on the surface of the body. The greatest influence of these disturbances is in the region at the base of the cone, causing an increase in pressure. Consequently, an additional normal pressure develops that leads to a displacement in the center of pressure. The longer the afterbody, the larger the disturbances, and the more the center of pressure is displaced.

For slender cones with cylindrical afterbodies whose length is about a half a diameter, the increase in the center-of-pressure coefficient is 5 to 7 percent in the Mach number range from 0.7 to 1.2. For a cylinder length of $0.75d_{\text{mid}}$, this increase reaches 7 to 13 percent, and $\bar{x}_{cp}$ is close to its maximum value. The location of the center of pressure does not change appreciably for a further increase in the length of the cylinder because the perturbations from the lengthened section of

the cylinder do not reach the cone. To have some idea of the variation in the center-of-pressure coefficient of the entire body (consisting of a cone and a cylinder), it is necessary to take into account the normal force on the cylinder as well as that on the cone. The presence of a normal load on the cylinder leads to an additional backward shift in the center of pressure.

The center of pressure does not change noticeably for bodies with parabolic noses at transonic speeds.

FLOW IN THE NEAR-CRITICAL REGIME

The Velocity Field

Let us examine a few of the results of experimental research on flow around conical bodies. Some of these results are related to the case of a shock wave still attached to the apex but distorted from its conical shape, and some are related to the formation of a detached shock. These types of flow occur when the cone angle is close (or equal) to the critical value, and a subsonic region occurs between the shock and the cone surface.

In this connection, a question arises concerning the limit of applicability of the theory of conical flow to the calculation of the flow around a cone. Sketches from schlieren photographs of conical models in wind tunnels are presented in Fig. 321 for M_∞ = 1.415 and 1.328.[6] An analysis of these photographs shows that the shock wave is still

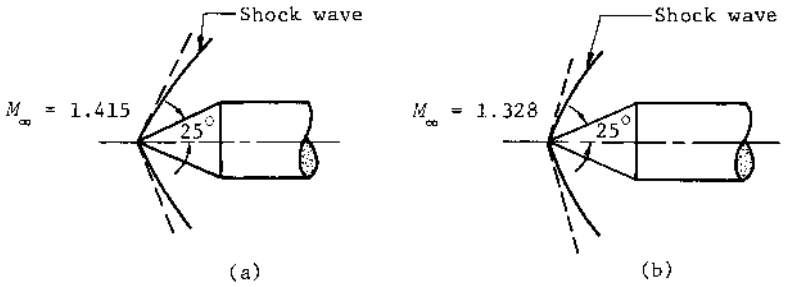

Fig. 321--Shock waves on a cone-cylinder for near-critical flow conditions

attached to the apex of the cone. In Fig. 321a, the shock is straight near the apex but is curved at some distance from it; in Fig. 321b, the shock wave at the lower Mach number is already curved at the apex. The curvature of the shock indicates that the flow is nonconical and that the junction of the cone with the cylinder influences the flow close to the apex of the cone, causing the development of a subsonic region extending from the shoulder to the apex. Figure 322 shows the location

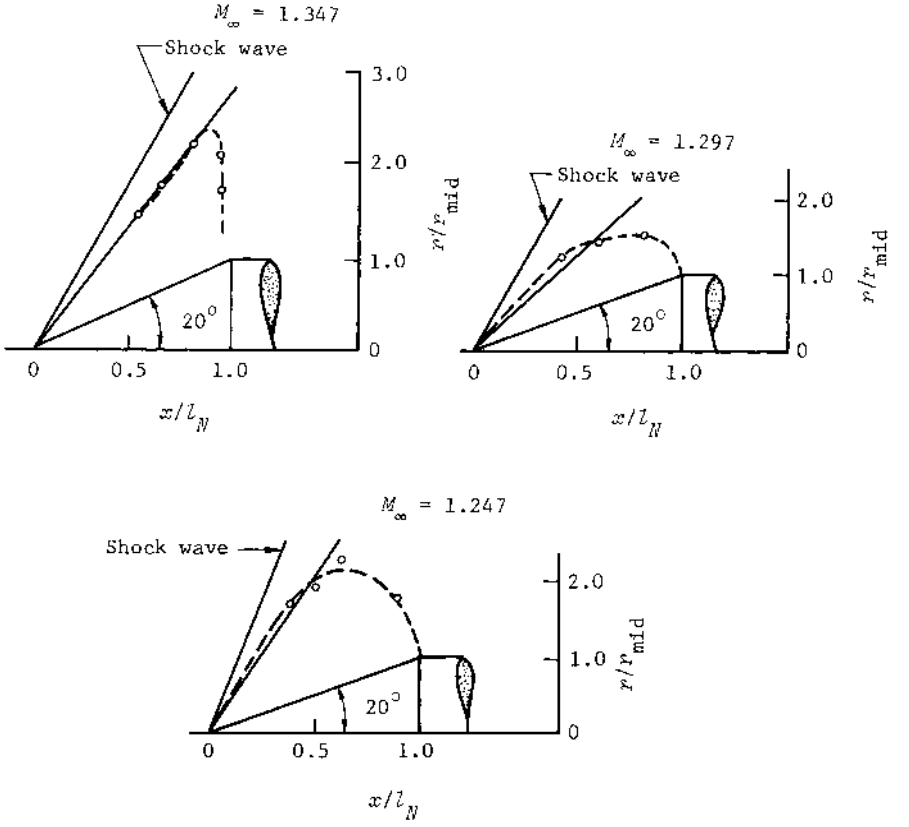

Fig. 322--Location of the sonic line for a cone-cylinder at near-critical flow conditions

of the sonic line separating the subsonic from the supersonic region. The sonic lines begin at the cone-cylinder junction and go in the direction of the apex, where they become straight. Their location in the region adjacent to the apex agrees well with the conical theory. In this connection, it can be assumed that the flow in the vicinity of the apex probably remains conical.

A more detailed study of the flow around a cone cylinder is possible with the help of an interferometer.[6,7] Some of the results of these interferograms are presented in Fig. 323, where the velocity field between the surface of a 25° cone cylinder and a shock wave is shown for three decreasing Mach numbers, M_∞ = 1.401, 1.273, and 1.229. The theoretical Mach number at which the flow on the surface becomes sonic for this body is 1.5, and the experiments show a significant subsonic region on the cone at M_∞ = 1.401 (Fig. 323a). Therefore, the sonic line originating at the shoulder becomes straight close to the apex (similar to the shock wave). The agreement between the pressures calculated according to exact theory and those measured on the cone surface near the apex confirms the assumption concerning the existence of local conical flow near the apex. The subsonic region increases with a decrease in Mach number, and the sonic line (as is evident in Fig. 323b) intersects the shock wave, which is already considerably curved at the apex. The influence of a further decrease in Mach number on the location of the sonic line can be seen in Fig. 323c.

It is possible to give some explanation of the flow processes observed using transonic shock polars and the apple curves shown in Fig. 324. In this figure, the magnitude of u (representing the difference between the velocity of the perturbed flow and the critical velocity a^*) is plotted on the abscissa and the radial velocity component is plotted on the ordinate. From these values, curves I to IV are constructed, the points of which specify the velocities on an intermediate conical surface, i.e., along the ray R. The geometric positions of the lower ends of curves I to IV on the shock polar also represent an apple curve. Every point C on the apple curve corresponds to a conical surface in the physical plane, and the coordinates of these points specify the velocity. The point S on the shock polar corresponds to the shock wave, and the coordinates of this point give the velocity directly behind the shock.

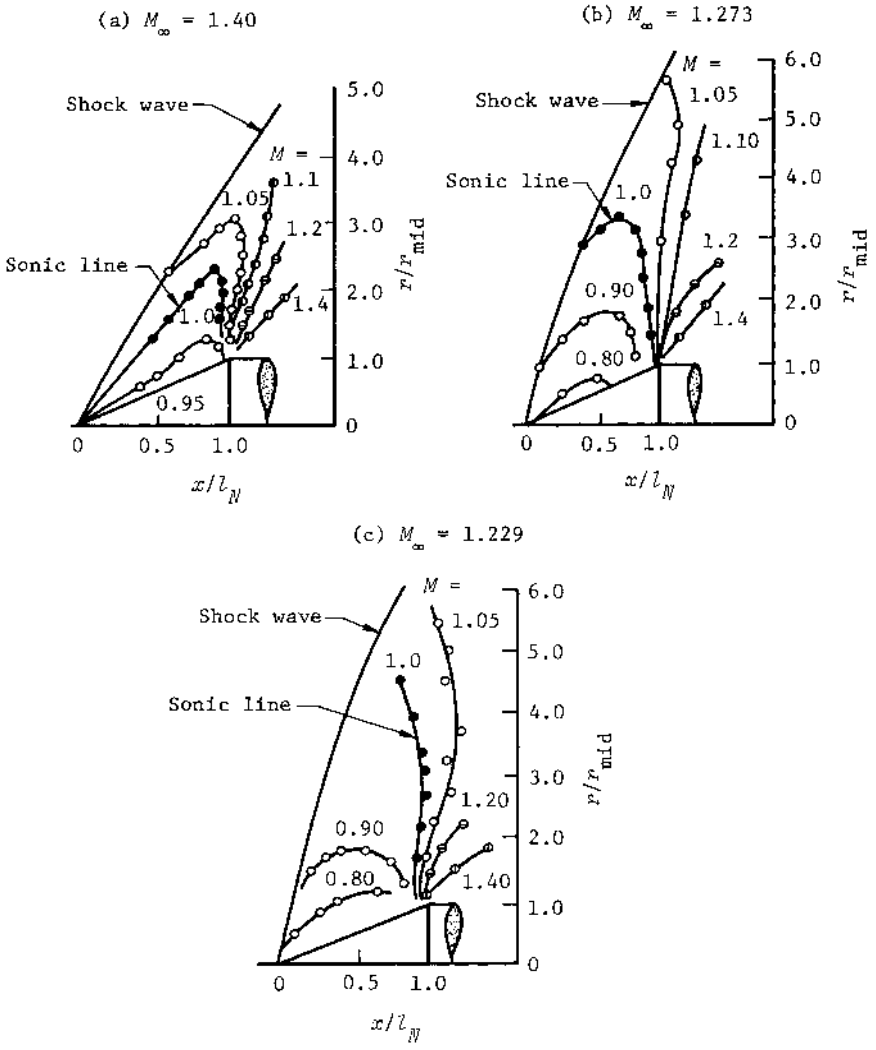

Fig. 323--Velocity field about a 25° cone-cylinder

It is apparent that the vertical axis corresponds to the sonic line in the physical plane, which is also called the sonic line in the hodograph line.

Curve I is located entirely to the right of the sonic line and corresponds to completely supersonic flow between the cone and the shock

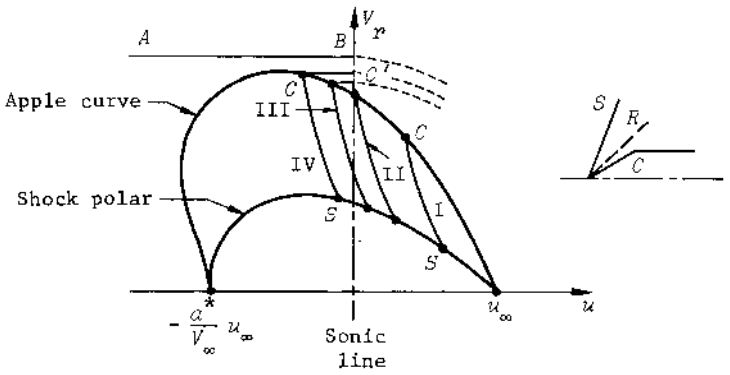

Fig. 324--Hodograph for near-critical flow over a cone

wave. For an increase in the cone angle and a fixed Mach number, curve I will be shifted to the left toward curve II. The terminal point of curve II lies on the sonic line, indicating that the velocity of sound has been attained. A subsonic region occurs near the surface as δ_c continues to increase and it becomes impossible to maintain conical flow in the entire region between the shock wave and the body. As the cone angle is increased still more, corresponding to transition from curve II to curve III, the velocity at the shoulder remains sonic (point C') and the velocity near the apex (point C of curve III) is subsonic. In other words, the velocity does not remain constant along the conical surface, represented in Fig. 324 by the horizontal line CC', but increases from subsonic near the apex to sonic at the junction line.

The sonic line that begins at the shoulder approaches the apex for specific values of δ_c and M_∞, as is evident from Fig. 323a. In Fig. 324, the point G on curve III corresponds to this sonic line.

Curve IV is developed for a further increase in the cone angle; it corresponds to a completely subsonic velocity and does not intersect the sonic line in the hodograph plane. Thus, the sonic line in the physical plane, as is evident from Fig. 323b, passes directly from the shoulder to the shock wave.

When the cone angle reaches supercritical values, the conical surface is no longer specified by a point on the apple curve (in Fig. 324,

this corresponds to the fact that the horizontal line AB does not intersect the apple curve). Therefore, the shock wave must have detached from the apex of the cone. Experimental data show that the shock wave detaches from the apex at values of δ_c somewhat larger than those specified by exact theory. For example, for $M_\infty = 2.45$ it was found experimentally that shock detachment occurred at $\delta_c = 46°$, whereas this angle is 45°40′ according to exact theory.

The Drag of a Cone

The experimental pressure distribution around various cones at $M_\infty = 2.45$ indicates that the conical flow corresponding to constant pressure on the cone is maintained as long as the speed of sound is not attained on its surface.[8] This occurs at $\delta_c = 42°30'$ (Fig. 325). For cone angles exceeding this value, the structure of the flow in the region of the shoulder and the finite dimensions of the model have an

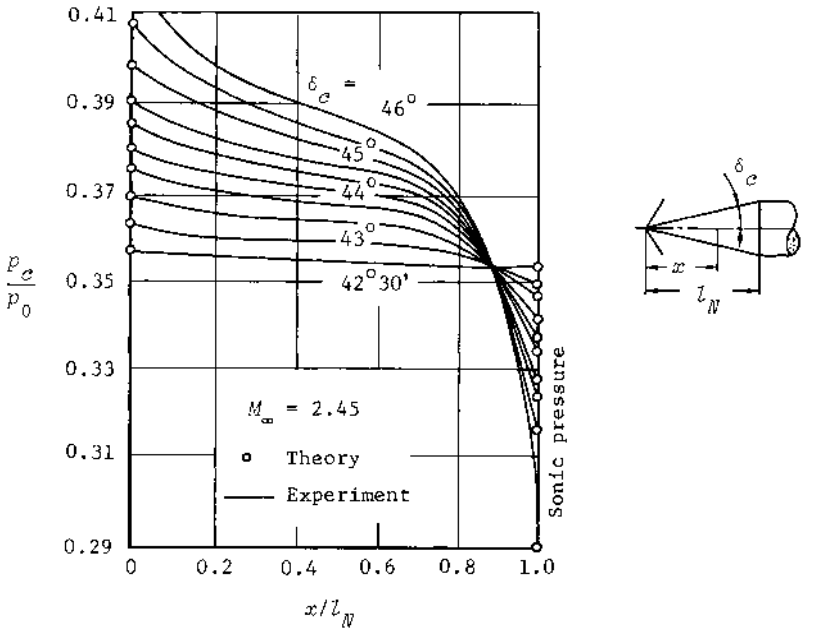

Fig. 325--Pressure ratio on a cone in near-critical flow

effect on the character of the flow. As a result, the pressure along the body varies, as is evident from Fig. 325. In this figure, the theoretical pressure ratios at the terminal points of all the curves are obtained on the basis of the following assumptions:

1. The pressure on the nose of the model is assumed equal to the pressure for an infinitely long cone; i.e., it is assumed that the expansion of the flow at the cone-cylinder junction does not change the pressure at the apex.
2. The pressure at the tip can be calculated from conical theory, provided the shock wave still has not detached from the apex of the cone.
3. The pressure at the shoulder of the body is determined by assuming that the speed of sound is attained at this point.

A comparison of the pressures calculated on the basis of these assumptions with the pressures obtained experimentally shows good agreement for all terminal points. It should be noted that the pressure at the cone-cylinder junction begins to decrease with a further increase in the cone angle because the strength of the shock wave is increasing. The pressure increases slightly on the surface of the cone forward of the corner as the cone angle approaches the value for shock detachment. The deviation from the conical character of the flow along the cone becomes increasingly greater with the increase in the subsonic region between the shock wave and the body surface.

Experimental research has also shown that the boundary layer on the model surface has almost no influence on the pressures on the cone but can play a decisive role in the formation of flow in the vicinity of the cone-cylinder junction, especially in those cases where the cone angle is less than critical and a favorable (negative) pressure gradient is absent. When the cone angle reaches the critical value or exceeds it (in the latter case, the shock wave detaches from the apex), the pressure at the corner is very close to the theoretical value corresponding to sonic velocity.

The variation of the pressure drag coefficient with cone angle at $M_\infty = 2.45$ is shown in Fig. 326. The coefficient C_{Dp} was calculated from the pressure distributions given in Fig. 325. It will be noted that C_{Dp} increases continuously as the cone angle passes through the value

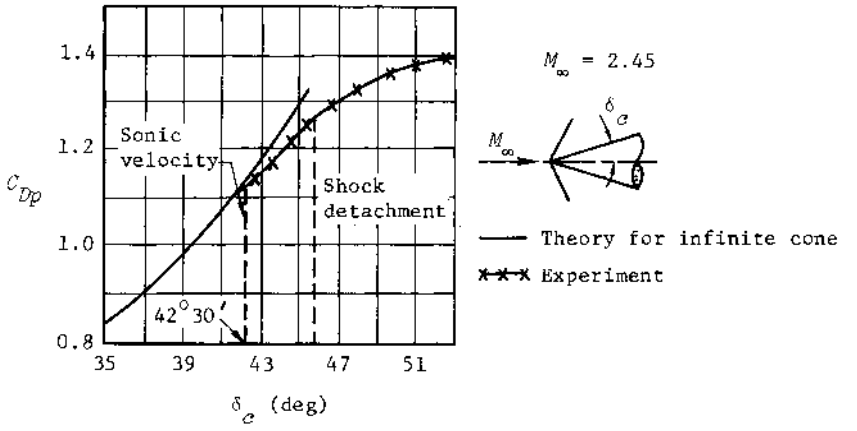

Fig. 326--Pressure drag coefficient on a cone at near-critical velocity

for shock detachment. There is no sudden change in drag as the shock detaches, but this angle corresponds more to a point of inflection in the drag curve. The region of high pressures developed at the apex of the cone is limited to so small a section of the body that it does not cause an abrupt increase in drag.

As soon as conical flow is destroyed, the drag of the body becomes somewhat less than the values calculated theoretically for an infinitely long cone. This is also confirmed by the experimental data presented in Fig. 327,[7] which agree well with the theory of conical flow for supersonic Mach numbers. With a decrease in Mach number, conical theory becomes invalid when the local Mach number on the surface is equal to unity. A further decrease in Mach number leads to an increase in pressure in the vicinity of the cone apex, but the pressure remains sonic near the shoulder. Therefore, as already noted, the actual drag curve is lower than the drag values determined by conical theory. The nose drag for subsonic velocities (see Fig. 327) increases as the Mach number approaches one.

The slope of the drag curves at $M_\infty = 1$ can be obtained by a method based on the principle of stationarity of the local Mach number, formulated and tested first for two-dimensional flows. According to this principle, it is assumed that the derivative $(\partial M/\partial M_\infty)_{M_\infty=1} = 0$; i.e., the

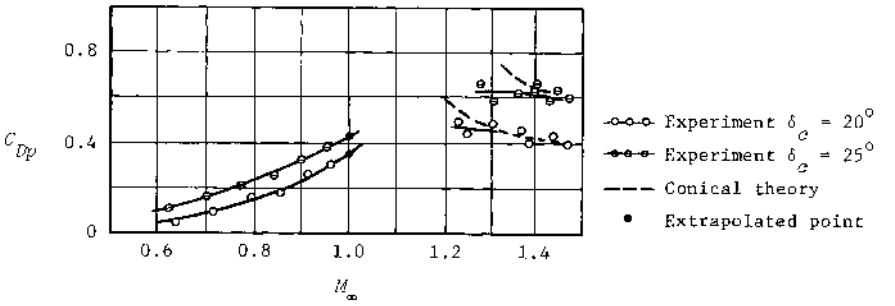

Fig. 327--Pressure drag coefficients of cone-cylinders

local Mach number M does not vary while the Mach number of the incident flow passes through unity. The constancy of the local Mach number for a cone was also tested experimentally.[7] The results of this test are presented in Fig. 328, where the curves show the change in M with M_∞. Each of the curves pertains to a specific station on the cone. The range of free-stream Mach numbers for which the distribution of the local Mach number is constant is comparatively narrow. For example,

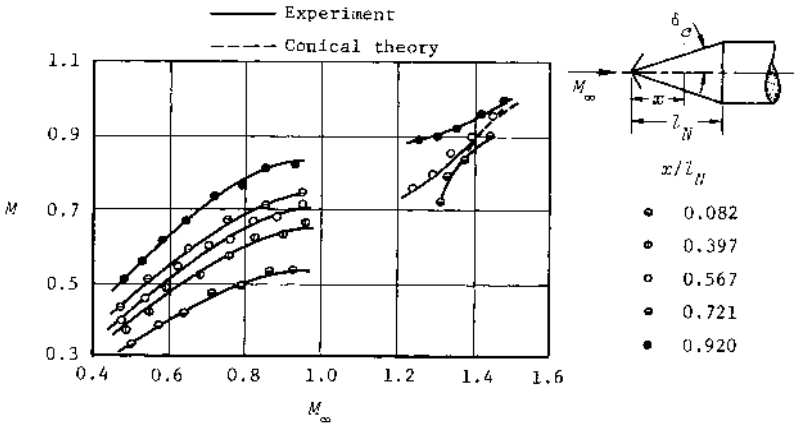

Fig. 328--Surface Mach number on a cone-cylinder

for a 25° cone, this range is specified by the values $M_\infty = 0.9$ to 1.1, and for $\delta_c = 7°$ by $M_\infty = 0.99$ to 1.01.

Using the principle of stationarity of the local Mach number, we can obtain a relation for the drag of a cone at transonic speeds.[9] If the distribution of local Mach numbers on the surface of a cone is assumed to be known, the corresponding velocities are found from

$$\frac{V^2}{V_\infty^2} = \left(\frac{M}{M_\infty}\right)^2 \frac{2 + (\gamma - 1)M_\infty^2}{2 + (\gamma - 1)M^2}, \tag{35.2}$$

and the pressure coefficients from the equation

$$C_p = \frac{2}{\gamma M_\infty^2}\left\{\left[1 + \frac{\gamma - 1}{2} M_\infty^2\left(1 - \frac{V^2}{V_\infty^2}\right)\right]^{\gamma/(\gamma-1)} - 1\right\}. \tag{35.3}$$

If Eqs. (35.2) and (35.3) are substituted into Eq. (1.6) (with $\tan \delta\, dx$ replaced by dr), the relation for the drag coefficient is

$$C_{Dp} = \frac{2}{\gamma M_\infty^2}\left\{\int_0^1 \left[\frac{2 + (\gamma - 1)M_\infty^2}{2 + (\gamma - 1)M^2}\right]^{\gamma/(\gamma-1)} d\bar{r}^2 - 1\right\}. \tag{35.4}$$

Expanding the expression in the square brackets into a series in $(M_\infty^2 - 1)$ and neglecting terms of the second or higher power, we get

$$C_{Dp} = \frac{2}{\gamma M_\infty^2}\left\{\left[1 + \frac{\gamma}{\gamma + 1}(M_\infty^2 - 1)\right]\int_0^1 \left[\frac{\gamma + 1}{2 + (\gamma - 1)M^2}\right]^{\gamma/(\gamma-1)} d\bar{r}^2 - 1\right\}. \tag{35.5}$$

Assuming $M_\infty = 1$ in this expression, the equation that determines the drag at sonic speed is obtained:

$$\left(C_{Dp}\right)_{M_\infty = 1} = \frac{2}{\gamma}\left\{\int_0^1 \left[\frac{\gamma + 1}{2 + (\gamma - 1)M^2}\right]^{\gamma/(\gamma-1)} d\bar{r}^2 - 1\right\}. \tag{35.6}$$

According to the stationarity principle, the local Mach number M is

invariant with respect to M_∞ (close to unity), and the integral in Eq. (35.6) can be substituted for that in Eq. (35.5). We thus obtain

$$C_{Dp} = \frac{\gamma M_\infty^2 + 1}{(\gamma + 1)M_\infty^2} (C_{Dp})_{M_\infty = 1} + \frac{2(M_\infty^2 - 1)}{(\gamma + 1)M_\infty^2}. \qquad (35.7)$$

The experimental curve for $(C_{Dp})_{M_\infty = 1}$ is presented in Fig. 329. Using this curve and Eq. (35.7), values of C_{Dp} can be calculated for other transonic velocities. It is evident in Fig. 329 that the drag coefficient at $M_\infty = 1$ depends strongly on the bluntness of the cone; the value corresponding to a cone half-angle of $\delta_c = 90°$ actually represents the drag of a flat face at sonic speed.

Equation (35.7) can be written in a different form:

$$C_{Dp} = \left[1 - \frac{2}{\gamma + 1} m + f_1(\gamma)m^2\right](C_{Dp})_{M_\infty = 1} + \frac{4}{\gamma + 1} m - f_2(\gamma)m^2, \qquad (35.8)$$

in which $m = M_\infty - 1$ and $f_1(\gamma)$ and $f_2(\gamma)$ are functions of the ratio of specific heats. For $\gamma = 1.4$, $f_1(\gamma) = 125/72$ and $f_2(\gamma) = 65/36$. The equations presented for C_{Dp} can be used to find the slope of the drag

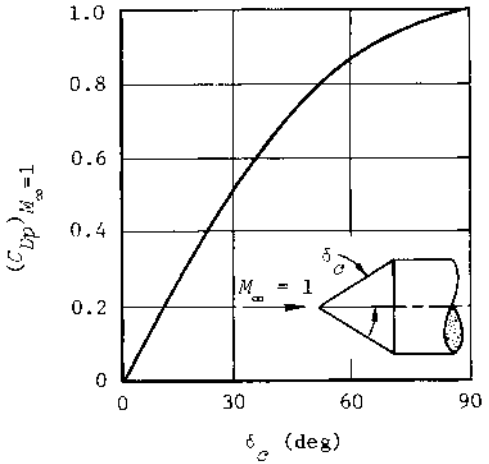

Fig. 329--Drag coefficients of cones at sonic velocity

curve at $M_\infty = 1$. Differentiating C_{Dp} with respect to M_∞ and substituting $M_\infty = 1$, we obtain

$$\left(\frac{\partial C_{Dp}}{\partial M_\infty}\right)_{M_\infty=1} = \frac{4}{\gamma + 1}\left[1 - \frac{1}{2}\,(C_{Dp})_{M_\infty=1}\right]. \qquad (35.9)$$

It has been established experimentally that a rough estimate based on interpolation for $(C_{Dp})_{M_\infty=1}$ for a cone will give good results in Eq. (35.9) for determining the slope of the curve of C_{Dp} at $M_\infty = 1$. For example, for a cone with an angle $\delta_c = 20°$, we find $C_{Dp} = 0.363$ at $M_\infty = 1$ from Fig. 327. The derivative from Eq. (35.9) is

$$\left(\frac{\partial C_{Dp}}{\partial M_\infty}\right)_{M_\infty=1} = \frac{4}{1.4 + 1}\left(1 - \frac{0.363}{2}\right) = 1.365,$$

which corresponds well to the correct value.

Experimental results are presented in Fig. 330 for the drag of a

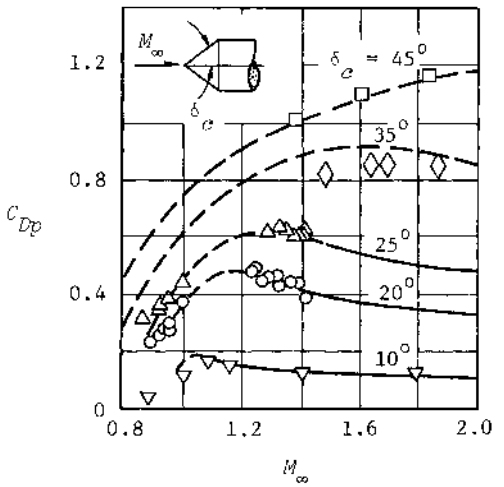

Fig. 330--Drag coefficients of cones at transonic speeds

cone at transonic velocities. These data agree satisfactorily with the results of the calculation of the drag coefficient in the transonic regime and the slope of the curve at $M_\infty \approx 1$.

The Ogive Nose

Research shows that the principle of stationarity of the local Mach number can also be used for calculating the drag of ogive bodies at transonic speeds, so that Eqs. (35.7) and (35.8) can be used.[9] The values of $(C_{Dp})_{M_\infty=1}$ in these equations can be determined from the graph in Fig. 331, which gives the drag at $M_\infty = 1$ for an ogive nose as a function

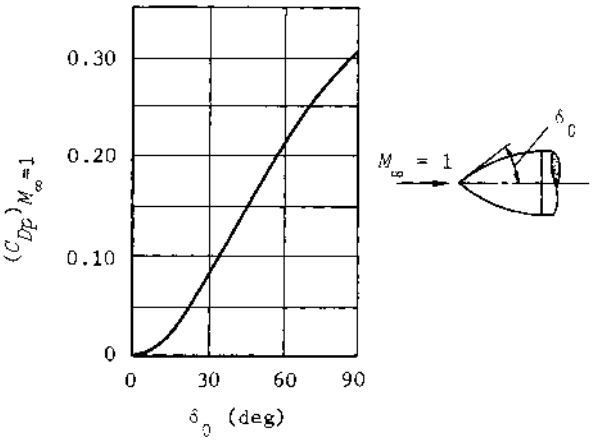

Fig. 331--Drag coefficients of ogive noses at sonic velocity

of the initial half-angle δ_0. The point on the curve corresponding to $\delta_0 = 90°$ is the pressure drag on a hemisphere.

From these values of $(C_{Dp})_{M_\infty=1}$, the slope of the drag curve at $M_\infty = 1$ can be calculated from Eq. (35.9), and the drag coefficient in the vicinity of this point from Eqs. (35.7) or (35.8). Comparison shows that the theoretical and experimental results agree satisfactorily. The general form of the drag curves for a series of ogive noses is shown in Fig. 332.

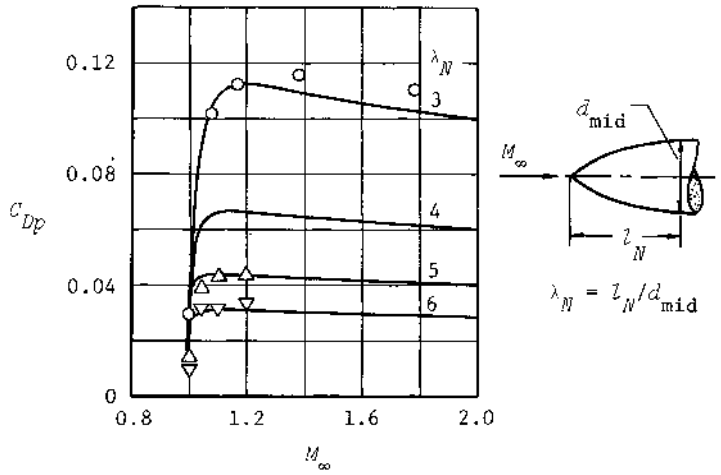

Fig. 332--Drag coefficients of ogive noses at transonic speeds

The Hemispherical Nose

The point on the curve of Fig. 331 corresponding to an angle of 90° determines the drag coefficient of a hemispherical nose at $M_\infty = 1$, as was indicated above. For a Mach number differing from but close to unity, i.e., corresponding to transonic speeds, the drag coefficient can be determined from the empirical equation[10]

$$C_{Dp} = 0.46 - \frac{1}{\pi} \text{ arc tan } [1.61(1.20 - M_\infty)]. \qquad (35.10)$$

This "arc tangent" law can also be used to calculate the pressure coefficient at the stagnation point of a sphere in a transonic flow:

$$C_{p0} = 1.35 - \frac{1}{\pi} \text{ arc tan } [1.96(1 - M_\infty)]. \qquad (35.11)$$

It is evident from Fig. 333 that Eqs. (35.10) and (35.11) give satisfactory results not only in the transonic range of velocities but also for a wide range of Mach numbers from $M_\infty = 0$ to 7 or 8.

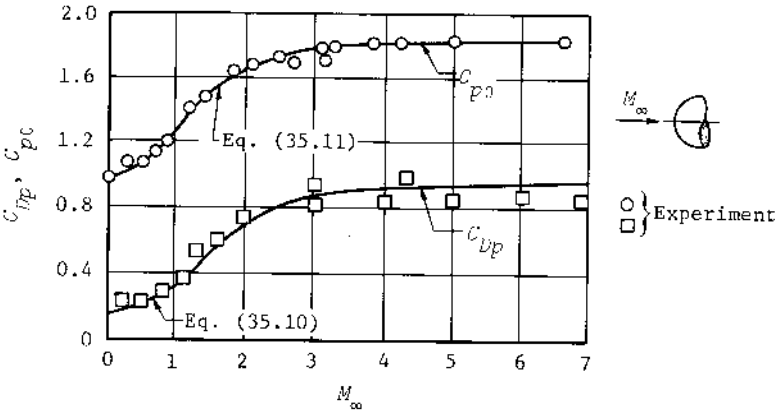

Fig. 333--Stagnation pressure coefficient and pressure drag coefficient for a hemisphere

APPENDIXES

Appendix A

PARAMETERS OF AIR AT VARIOUS ALTITUDES (Standard Atmosphere)

Altitude, H (km)	Pressure, $p \cdot 10^{-3}$ (dynes/cm^2)	Density, ρ (kgm/m^3)	Speed of Sound, a (m/sec)	Average Particle Speed, $\bar{c}$ (m/sec)	Acceleration of Gravity, g (m/sec^2)	Kinematic Viscosity Coefficient, ν (m^2/sec)	Temperature, T (°K)	Thermal Conductivity Coefficient, λ (kcal/m sec °K)	Average Molecular Weight, L_{avg}
Troposphere									
0	1013	1.225	340.3	458.9	9.807	$1.461 \cdot 10^{-5}$	288.2	$6.053 \cdot 10^{-6}$	28.97
2	$7950 \cdot 10^{-1}$	1.007	332.5	448.5	9.800	1.715	275.2	5.808	28.97
4	6166	$8.194 \cdot 10^{-1}$	324.6	437.8	9.794	2.028	262.2	5.559	28.97
6	4722	6.601	316.4	426.8	9.788	2.416	249.2	5.307	28.97
8	3565	5.258	308.1	415.6	9.782	2.905	236.2	5.052	28.97
10	2650	4.135	299.5	404.0	9.776	3.525	223.3	4.794	28.97
12	1940	3.119	295.1	398.0	9.770	4.558	216.7	4.662	28.97
Stratosphere									
14	1417	2.278	295.1	398.0	9.764	6.239	216.7	4.662	28.97
16	$1035 \cdot 10^{-1}$	1.665	295.1	398.0	9.758	$8.540 \cdot 10^{-5}$	216.7	4.662	28.97
18	$7565 \cdot 10^{-2}$	$1.216 \cdot 10^{-1}$	295.1	398.0	9.751	$1.169 \cdot 10^{-4}$	216.7	4.662	28.97
20	5529	$8.891 \cdot 10^{-2}$	295.1	398.0	9.745	1.599	216.7	4.662	28.97
22	4042	6.500	295.1	398.0	9.739	2.187	216.7	4.662	28.97
24	2955	4.752	295.1	398.0	9.733	2.992	216.7	4.662	28.97
Mesosphere									
28	1595	2.466	300.9	405.8	9.721	5.955	225.3	4.835	28.97
30	$1186 \cdot 10^{-2}$	1.786	304.8	411.1	9.715	$8.402 \cdot 10^{-5}$	231.2	4.953	28.97
32	$8880 \cdot 10^{-3}$	$1.304 \cdot 10^{-2}$	308.7	416.4	9.709	$1.175 \cdot 10^{-4}$	237.2	5.071	28.97
34	6701	$9.602 \cdot 10^{-3}$	312.6	421.6	9.703	1.628	243.1	5.188	28.97
36	5091	7.122	316.4	426.7	9.696	2.238	249.0	5.304	28.97
38	3894	5.321	320.2	431.7	9.690	3.053	255.0	5.420	28.97
40	2998	4.003	323.8	436.7	9.684	4.134	260.9	5.534	28.97
42	2322	3.031	327.5	441.6	9.678	5.558	266.8	5.648	28.97
44	1808	2.310	331.1	446.5	9.672	7.422	272.8	5.762	28.97
46	1416	1.770	334.6	451.3	9.666	$9.846 \cdot 10^{-3}$	278.7	5.874	28.97
48	$1115 \cdot 10^{-3}$	1.374	337.0	454.5	9.660	$1.283 \cdot 10^{-4}$	282.7	5.950	28.97
50	$8786 \cdot 10^{-4}$	$1.083 \cdot 10^{-3}$	337.0	454.5	9.654	1.628	282.7	5.950	28.97
52	6926	$8.536 \cdot 10^{-4}$	337.0	454.5	9.648	2.065	282.7	5.950	28.97
54	5459	6.787	335.6	452.6	9.642	2.580	280.2	5.903	28.97
56	4279	4.593	330.2	445.4	9.636	3.108	271.4	5.735	28.97
58	3327	4.416	324.8	438.0	9.630	3.766	262.5	5.565	28.97
60	$2566 \cdot 10^{-4}$	3.524	319.3	430.6	9.624	$4.592 \cdot 10^{-2}$	257.7	5.394	28.97
70	$6021 \cdot 10^{-5}$	$1.001 \cdot 10^{-4}$	290.2	391.4	9.594	$1.382 \cdot 10^{-1}$	209.6	4.519	28.97
80	$1008 \cdot 10^{-5}$	$2.120 \cdot 10^{-5}$	258.0	348.0	9.564	5.311	165.7	3.612	28.97

PARAMETERS OF AIR AT VARIOUS ALTITUDES--*continued*

Altitude, H (km)	Pressure, $p \cdot 10^{-3}$ (dynes/cm^2)	Density, ρ (kgm/m^3)	Speed of Sound, a (m/sec)	Average Particle Speed, $\bar{c}$ (m/sec)	Acceleration of Gravity, g (m/sec^2)	Kinematic Viscosity Coefficient, ν (m^2/sec)	Temperature, T (°K)	Thermal Conductivity Coefficient, λ (kcal/m sec °K)	Average Molecular Weight, μ_{avg}
				Thermosphere					
90	$1353 \cdot 10^{-6}$	$2.846 \cdot 10^{-6}$	258.0	348.0	9.505	$3.957 \cdot 10^{-1}$	165.7	$3.612 \cdot 10^{-6}$	28.97
100	$2138 \cdot 10^{-7}$	$3.734 \cdot 10^{-7}$	--	381.8	9.505	--	199.0	--	28.90
120	$2044 \cdot 10^{-8}$	$1.480 \cdot 10^{-8}$	--	593.1	9.447	--	477.0	--	28.71
140	$7502 \cdot 10^{-9}$	$3.020 \cdot 10^{-9}$	--	795.3	9.389	--	849.9	--	28.45
160	$4018 \cdot 10^{-9}$	$1.123 \cdot 10^{-9}$	--	954.7	9.331	--	1207	--	28.04
180	$2505 \cdot 10^{-9}$	$6.015 \cdot 10^{-10}$	--	1030	9.274	--	1371	--	27.36
200	$1629 \cdot 10^{-9}$	$3.673 \cdot 10^{-10}$	--	1063	9.217	--	1404	--	26.32
300	$3565 \cdot 10^{-10}$	$4.757 \cdot 10^{-11}$	--	1172	9.942	--	1423	--	21.95
400	$9661 \cdot 10^{-11}$	$8.994 \cdot 10^{-12}$	--	1266	8.680	--	1480	--	19.56
500	$1586 \cdot 10^{-11}$	$2.212 \cdot 10^{-12}$	--	1351	8.428	--	1576	--	18.28
600	$5308 \cdot 10^{-12}$	$6.617 \cdot 10^{-13}$	--	1429	8.187	--	1691	--	17.52
700	$2037 \cdot 10^{-12}$	$2.302 \cdot 10^{-13}$	--	1501	7.957	--	1812	--	17.03

Appendix B

CONVERSION TABLE TO INTERNATIONAL UNIT SYSTEM (SI)

Quantity	Dimensional Units in Book	Units in SI System
Force	1 kgf	9.80665 N (newton)
	1 dyne	10^{-5} N
Pressure (stress)	1 kgf/cm^2	98066.5 N/m^2
		0.980665 bar
	1 mm mercury	133.322 N/m^2
		$1.33322 \cdot 10^{-3}$ bar
Dynamic viscosity	1 kgf sec/m^2	9.80665 N sec/m^2
		9.80665 kgm/m sec
	1 poise	0.1 N sec/m^2
Kinematic viscosity	m^2/sec	m^2/sec
Density	1 kgf sec^2/m^4 (mass)	9.80665 kgm/m^3
	1 kgf/m^3 (weight)	9.80665 N/m^3
Work, energy, heat	1 kgf m	9.80665 J (joule)
	1 hp hr†	$2.65 \cdot 10^6$ J
	1 kW hr	$3.6 \cdot 10^6$ J
	1 eV (electron-volt)	$1.60207 \cdot 10^{-16}$ J
	1 cal	4.1868 J
	1 erg	10^{-7} J
Power	1 hp†	735.499 W
	1 cal/sec	4.1868 W
	1 erg/sec	10^{-7} W

†Editor's note: This is metric horsepower, equal to 0.986 hp in British units.

REFERENCES

Chapter I

1. Predvoditelev, A. S., et al., *Tables of Thermodynamic Functions of Air for the Temperature Range 6000-12,000°K and Pressure Range 0.001-1000 Atm*, Infosearch Limited, London, 1958.

2. Ehricke, K. A., "Aero-Thermodynamics of Descending Orbital Vehicles," *Astronautica Acta*, Vol. 2, No. 1, 1956, pp. 1-19.

3. Predvoditelev, A. S., et al., *Tables of Thermodynamic Functions of Air for Temperatures of 12,000 to 20,000°K and Pressures of 0.001 to 1000 Atm*, Associated Technical Services, Inc., Glen Ridge, New Jersey, 1962.

4. Predvoditelev, A. S. (ed.), *Physical Gas Dynamics*, Pergamon Press, New York, 1961.

5. Kibardin, Iu. A., et al., *Atlas of Gasdynamic Functions for High Velocity and High Temperature Air Flow* (in Russian), Gosenergoizdat, Moscow, 1961.

6. Lighthill, M. J., "Dynamics of a Dissociating Gas: Part 1: Equilibrium Flow," *J. Fluid Mech.*, Vol. 2, Part 1, January 1957, pp. 1-32.

7. Goulard, R., "On Catalytic Recombination Rates in Hypersonic Stagnation Heat Transfer," *Jet Propulsion*, Vol. 28, No. 11, November 1958, pp. 737-745.

8. Liepmann, H. W., and A. Roshko, *Elements of Gasdynamics*, John Wiley & Sons, Inc., New York, 1957.

9. Hilsenrath, J., et al., *Tables of Thermal Properties of Gases*, National Bureau of Standards, Circular 564, Washington, D. C., 1955.

10. Dorrance, W. H., "On the Approach to Chemical and Vibrational Equilibrium behind a Strong Normal Shock Wave," *J. Aero. Sci.*, Vol. 28, No. 1, January 1961, pp. 43-50.

11. Schlichting, H., *Boundary Layer Theory*, Pergamon Press, New York, 1955.

12. Luther, M. L., "Comments on 'Turbulent Boundary-Layer Characteristics...,'" *J. Aero. Sci.*, Vol. 19, No. 5, May 1952, p. 357.

13. Saelman, B., "An Additional Note on Equilibrium Skin Temperatures," *J. Aero. Sci.*, Vol. 27, No. 4, April 1960, p. 320.

Chapter II

1. Kopal, Z., *Tables of Supersonic Flow around Cones*, MIT Dept. of Electrical Engineering, Center of Analysis, Technical Report No. 1, Cambridge, Mass., 1947.

2. Neice, S. E., and D. M. Ehret, "Similarity Laws for Slender Bodies of Revolution in Hypersonic Flows," *J. Aero. Sci.*, Vol. 18, No. 8, August 1951, pp. 527-530.

3. Kuznetsov, S. I., *Graphs and Tables for the Flow of Dissociating Air over Wedges, Cones, and Convex Surfaces*, Moscow, Oborongiz, 1962.

4. Kopal, Z., *Tables of Supersonic Flow around Yawing Cones*, MIT Dept. of Electrical Engineering, Center of Analysis, Technical Report No. 3, Cambridge, Mass., 1947.

5. Kopal, Z., *Tables of Supersonic Flow around Cones of Large Yaw*, MIT Dept. of Electrical Engineering, Center of Analysis, Technical Report No. 5, Cambridge, Mass., 1949.

6. Young, G.B.W., and C. P. Siska, "Supersonic Flow around Cones at Large Yaw," *J. Aero. Sci.*, Vol. 19, No. 2, February 1952, pp. 111-119.

7. Gonor, A. L., "Location of Frontal Wave in Asymmetrical Flow of Gas at High Supersonic Speed over a Pointed Body," *ARS J.*, (Russian Supplement), Vol. 30, No. 9, September 1960, pp. 841-842.

Chapter III

1. Frankl, F. I., "Supersonic Flow with Axial Symmetry" (in Russian), *Izv. artill. akad.*, Vol. 1, No. 6, Leningrad, 1934.

2. Ferri, Antonio, *Elements of Aerodynamics of Supersonic Flows*, The Macmillan Co., New York, 1949.

3. Miles, E.R.C., *Semi-empirical Formulas for Ogives*, Applied Physics Laboratory, CM-505, Johns Hopkins University, Baltimore, Md., 1948.

4. Vallander, S. V., unpublished doctoral thesis, Leningrad University, 1949, as cited in G. G. Chernyi, *Introduction to Hypersonic Flow*, Academic Press, New York, 1961.

5. Neice, S. E., and D. M. Ehret, "Similarity Laws for Slender Bodies of Revolution in Hypersonic Flows," *J. Aero. Sci.*, Vol. 18, No. 8, August 1951, pp. 527-530.

6. Resler, E. L., Jr., "Characteristics and Sound Speed in Nonisentropic Gas Flows with Nonequilibrium Thermodynamic States," *J. Aero. Sci.*, Vol. 24, No. 11, November 1957, pp. 785-790.

7. Kuptsov, V. M., "Method of Characteristics for Equilibrium Axisymmetric Flow of a Real Gas" (in Russian), *AN SSSR. Izv. Otd. tekh. nauk. mekh. i mash.*, No. 2, 1960, pp. 138-140.

8. Eggers, A. J., Jr., R. C. Savin, and C. A. Syvertson, "The Generalized Shock-expansion Method and Its Application to Bodies Traveling at High Supersonic Air Speeds," *J. Aero. Sci.*, Vol. 22, No. 4, April 1955, pp. 231-238.

Chapter IV

1. Van Dyke, M. D., "First- and Second-order Theory of Supersonic Flow past Bodies of Revolution," *J. Aero. Sci.*, Vol. 18, No. 3, March 1951, pp. 161-178.

2. Broderick, J. B., "Supersonic Flow round Pointed Bodies of Revolution," *Quart. J. Mech. Appl. Math.*, Vol. 2, Part 1, March 1949, pp. 98-120.

3. Frankl, F. I., and E. A. Karpovich, *Gas Dynamics of Thin Bodies*, Interscience Publishers Inc., New York, 1953.

4. Hoerner, S. F., *Fluid-dynamic Drag*, published by the author, Midland Park, New Jersey, 1958.

Chapter V

1. Syvertson, C. A., and D. H. Dennis, *A Second-order Shock-expansion Method Applicable to Bodies of Revolution Near Zero Lift*, National Advisory Committee for Aeronautics, Report 1328, Washington, D.C., 1957.

2. Mello, J. F., "Investigation of Normal Force Distributions and Wake Vortex Characteristics of Bodies of Revolution at Supersonic Speeds," *J. Aero. Sci.*, Vol. 26, No. 3, March 1959, pp. 155-168.

3. Van Dyke, M. D., "First- and Second-order Theory of Supersonic Flow past Bodies of Revolution," *J. Aero. Sci.*, Vol. 18, No. 3, March 1951, pp. 161-178.

4. Dorrance, W. H., "Nonsteady Supersonic Flow about Pointed Bodies of Revolution," *J. Aero. Sci.*, Vol. 18, No. 8, August 1951, pp. 505-511.

Chapter VI

1. Lees, L., "Note on the Hypersonic Similarity Law for an Unyawed Cone," *J. Aero. Sci.*, Vol. 18, No. 10, October 1951, pp. 700-702.

2. Van Dyke, M. D., "Applications of Hypersonic Small-disturbance Theory," *J. Aero. Sci.*, Vol. 21, No. 3, March 1954, pp. 179-186.

3. Van Dyke, M. D., *A Study of Hypersonic Small-disturbance Theory*, National Advisory Committee for Aeronautics, Report 1194, Washington, D. C., 1954.

4. Grimminger, G., E. P. Williams, and G.B.W. Young, "Lift on Inclined Bodies of Revolution in Hypersonic Flow," *J. Aero. Sci.*, Vol. 17, No. 11, November 1950, pp. 675-690.

5. Large, E., "Nose Shape for Minimum Drag in Hypersonic Flow," *J. Aero. Sci.*, Vol. 29, No. 1, January 1962, pp. 98-99.

Chapter VII

1. Dorodnitsyn, A. A., "The Method of Integral Relations for the Numerical Solution of Partial Differential Equations" (in Russian), in *Trudy instituta tochnoi mekhaniki i vychislitelnoi tekhnik*, AN SSSR, 1958.

2. Belotserkovskii, O. M., "On the Calculation of Flow past Axisymmetric Bodies with Detached Shock Waves Using an Electronic Computing Machine," *J. Appl. Math. Mech.*, Vol. 24, No. 3, 1960, pp. 745-755.

3. Li, T.-Y., and R. E. Geiger, "Stagnation Point of a Blunt Body in

Hypersonic Flow," *J. Aero. Sci.*, Vol. 24, No. 1, January 1957, pp. 25-32.

4. Oliver, R. E., "An Experimental Investigation of Flow about Simple Blunt Bodies at a Nominal Mach Number of 5.8," *J. Aero. Sci.*, Vol. 23, No. 2, February 1956, pp. 177-179.

5. Serbin, H., "Supersonic Flow Around Blunt Bodies," *J. Aero. Sci.*, Vol. 25, No. 1, January 1958, pp. 58-59.

6. Inouye, M., *Blunt Body Solutions for Spheres and Ellipsoids in Equilibrium Gas Mixtures*, National Aeronautics and Space Administration, Technical Note TN D-2780, Washington, D. C., May 1965.

7. Hayes, W. D., and R. F. Probstein, *Hypersonic Flow Theory*, Academic Press, New York, 1959.

8. Seiff, A., *Recent Information on Hypersonic Flow Fields in Gas Dynamics in Space Exploration*, National Aeronautics and Space Administration, SP-24, Washington, D. C., 1962.

9. Holt, M., "Direct Calculation of Pressure Distribution on Blunt Hypersonic Nose Shapes with Sharp Corners," *J. Aero. Sci.*, Vol. 28, No. 11, November 1961, pp. 872-876.

10. Chernyi, G. G., *Introduction to Hypersonic Flow*, R. F. Probstein (trans. and ed.), Academic Press, New York, 1961.

11. Lees, L., and T. Kubota, "Inviscid Hypersonic Flow over Blunt-nosed Slender Bodies," *J. Aero. Sci.*, Vol. 24, No. 3, March 1957, pp. 195-202.

12. Swigart, R. J., "Third-order Blast Wave Theory and Its Application to Hypersonic Flow past Blunt-nosed Cylinders," *J. Fluid Mech.*, Vol. 9, Part 4, December 1960, pp. 613-620.

13. Bertram, M. H., "Tip-bluntness Effects on Cone Pressures at M = 6.85," *J. Aero. Sci.*, Vol. 23, No. 9, September 1956, pp. 898-900.

14. O'Bryant, W. T., and R. M. Machell, "An Experimental Investigation of Flow over Blunt Nosed Cones at a Mach Number of 5.8," *J. Aero. Sci.*, Vol. 23, No. 11, November 1956, pp. 1054-1055.

15. Chushkin, P. I., "Supersonic Flows around Blunted Bodies of Simple Shape," *J. Appl. Math. Mech.*, Vol. 24, No. 5, 1960, pp. 1397-1403.

16. Cole, J. D., "Newtonian Flow Theory for Slender Bodies," *J. Aero. Sci.*, Vol. 24, No. 6, June 1957, pp. 448-455.

17. Bloom, M. H., and M. H. Steiger, "Inviscid Flow with Nonequilibrium Molecular Dissociation for Pressure Distributions Encountered in Hypersonic Flight," *J. Aero. Sci.*, Vol. 27, No. 11, November 1960, pp. 821-835.

Chapter VIII

1. Moeckel, W. E., *Some Effects of Bluntness on Boundary-Layer Transition and Heat Transfer at Supersonic Speeds*, National Advisory Committee for Aeronautics, Report 1312, Washington, D.C., 1957.

2. Van Driest, E. R., and J. C. Boison, "Experiments on Boundary Layer Transition at Supersonic Speeds," *J. Aero. Sci.*, Vol. 24, No. 12, December 1957, pp. 885-899.

3. Lees, L., "Laminar Heat Transfer Over Blunt-nosed Bodies at Hypersonic Flight Speeds," *Jet Propulsion*, Vol. 26, No. 4, April 1956, pp. 259-269.

4. Fay, J. A., and F. R. Riddell, "Theory of Stagnation Point Heat Transfer in Dissociated Air," *J. Aero. Sci.*, Vol. 25, No. 2, February 1958, pp. 73-85.

5. Kemp, N. H., and F. R. Riddell, "Heat Transfer to Satellite Vehicles Re-entering the Atmosphere," *Jet Propulsion*, Vol. 27, No. 2, Part 1, February 1957, pp. 132-137.

6. Goulard, R., "On Catalytic Recombination Rates in Hypersonic Stagnation Heat Transfer," *Jet Propulsion*, Vol. 28, No. 11, November 1958, pp. 737-745.

7. Kemp, N. H., P. H. Rose, and R. W. Detra, "Laminar Heat Transfer around Blunt Bodies in Dissociated Air," *J. Aero. Sci.*, Vol. 26, No. 7, July 1959, pp. 421-430.

8. Detra, R. W., and H. Hidalgo, "Generalized Heat Transfer Formulas and Graphs for Nose Cone Re-entry into the Atmosphere," *ARS J.*, Vol. 31, No. 3, March 1961, pp. 318-321.

9. Rose, P. H., R. F. Probstein, and M. C. Adams, "Turbulent Heat Transfer Through a Highly Cooled, Partially Dissociated Boundary Layer," *J. Aero. Sci.*, Vol. 25, No. 12, December 1958, pp. 751-760.

10. Cresci, R. J., D. A. Mackenzie, and P. A. Libby, "An Investigation of Laminar, Transitional, and Turbulent Heat Transfer on Blunt-nosed Bodies in Hypersonic Flow," *J. Aero. Sci.*, Vol. 27, No. 6, June 1960, pp. 401-414.

11. Probstein, R. F., M. C. Adams, and P. H. Rose, "On Turbulent Heat Transfer Through a Highly Cooled Partially Dissociated Boundary Layer," *Jet Propulsion*, Vol. 28, No. 1, January 1958, pp. 56-58.

Chapter IX

1. Adams, M. C., "Recent Advances in Ablation," *ARS J.*, Vol. 29, No. 9, September 1959, pp. 625-632.

2. Hartnett, J. P., and E.R.G. Eckert, "Mass Transfer Cooling with Combustion in a Laminar Boundary Layer," *1958 Heat Transfer and Fluid Mechanics Institute*, June 1958, pp. 54-68.

3. Bethe, H. A., and M. C. Adams, "A Theory for the Ablation of Glassy Materials," *J. Aero. Sci.*, Vol. 26, No. 6, June 1959, pp. 321-328.

Chapter X

1. Warren, C.H.E., and A. D. Young, *Some Proposals Regarding the Definitions of Terms Relating to Various Flow Regimes of a Gas*, Ministry of Supply, Aeronautical Research Council Current Papers, C. P. No. 368, London, 1958.

2. Patterson, G. N., *Molecular Flow of Gases*, John Wiley & Sons, Inc., New York, 1956.

Chapter XI

1. von Kármán, T., "The Similarity Law of Transonic Flow," *J. of Math. and Physics*, Vol. 26, No. 3, October 1947, pp. 182-190.

2. Spreiter, J. R., and A. Y. Alksne, *Slender-Body Theory Based on Approximate Solution of the Transonic Flow Equation*, NASA Technical Report R-2, 1959.

3. Oswatitsch, K., and S. B. Berndt, *Aerodynamic Similarity at Axisymmetric Transonic Flow Around Slender Bodies*, KTH Stockholm Aeronautics Div., Technical Note 15, 1950.

4. Danforth, E.C.B., and J. F. Johnston, *Pressure Distribution Over a Sharp-Nose Body of Revolution at Transonic Speeds by the NACA Wing-Flow Method*, NACA RM L7K12, 1948.

5. Hoerner, S. F., *Aerodynamic Drag*, published by the author, 1951. (Note: Hoerner's revised and expanded edition, *Fluid-Dynamic Drag*, published in 1958, does not contain some of the figures used by Krasnov.)

6. Solomon, G. E., *Transonic Flow Past Cone Cylinders*, NACA Technical Note 3213, 1954.

7. Cole, J. D., G. E. Solomon, and W. W. Willmarth, "Transonic Flow Past Simple Bodies," *J. Aero. Sci.*, Vol. 20, No. 9, September 1953, pp. 627-634.

8. Johnston, G. W., "An Investigation of the Flow About Cones and Wedges at and Beyond the Critical Angle," *J. Aero. Sci.*, Vol. 20, No. 6, June 1953, pp. 378-382.

9. Morris, D. N., "A Summary of the Supersonic Pressure Drag of Bodies of Revolution," *J. Aero. Sci.*, Vol. 28, No. 7, July 1961, pp. 563-572.

10. Li, T., "Arc-Tangent Fits for Pressure and Pressure-Drag Coefficients of Axisymmetric Blunt Bodies at All Speeds," *J. Aero. Sci.*, Vol. 27, No. 4, April 1960, pp. 309-311.

BIBLIOGRAPHY FOR THE SECOND EDITION

1. Chernyi, G. G., *Techeniia gaza s bol'shoi sverkhzvukovoi skorost'iu* [Gas Flows at High Supersonic Velocities], Fizmatgiz, 1959.

2. Arzhanikov, N. S., and V. N. Mal'tsev, *Aerodinamika* [Aerodynamics], Oborongiz, 1956.

3. Landau, L. D., and E. M. Lifshits, *Mekhanika sploshnykh sred* [Mechanics of Continuous Media], Gostekhizdat, 1954.

4. Ferri, A., *Aerodinamika sverkhzvukovykh techenii* [Aerodynamics of Supersonic Flows], Gostekhizdat, 1953.

5. Zel'dovich, Ia. B., and Iu. P. Raizer, *Fizika udarnykh voln i vysokotemperaturnykh gidrodinamicheskikh iavlenii* [The Physics of Shock Waves and High-temperature Hydrodynamic Phenomena], Fizmatgiz, 1963.

6. Krasnov, N. F., *Aerodinamika* [Aerodynamics], Oborongiz, 1958.

7. Loitsianskii, L. G., *Mekhanika zhidkosti i gaza* [The Mechanics of Liquids and Gases], Gostekhizdat, 1950.

8. Kochin, N. E., I. A. Kibel', and N. V. Roze, *Teoreticheskaia gidromekhanika* [Theoretical Hydromechanics], Parts 1 and 2, Gostekhizdat, 1948.

9. Vallander, S. V. (ed.), *Aerodinamika razrezhennykh gazov; sb. statei* [Aerodynamics of Rarefied Gases; a collection of articles], Izd. Leningradskogo universiteta, 1963.

10. Rosliakov, G. S., and L. A. Chudov (eds.), *Chislennye metody v gazovoi dinamike; sb. statei* [Numerical Methods in Gas Dynamics; a collection of articles], Izd. Moskovskogo universiteta, 1963.

11. *Gazodinamika razrezhennykh gazov; sb. statei* [Rarefied Gas Dynamics; a collection of articles], Inogiz, 1963.

12. Kuznetsov, S. I., *Diagrammy i tablitsy techeniia dissotsiiruiushchego vozdukha okolo klina, konusa i vypukloi poverkhnosti* [Diagrams and Tables of the Flow of Dissociating Air around a Wedge, a Cone, and a Convex Surface], Oborongiz, 1962.

13. Nielsen, J., *Aerodinamika upravliaemykh snariadov* [Missile Aerodynamics], Oborongiz, 1962.

14. Kibardin, Iu. A., S. I. Kuznetsov, A. N. Liubimov, and B. Ia. Shumiatskii, *Atlas gazodinamicheskikh funktsii pri bol'shikh skorostiakh i vysokikh temperaturakh vozdushnogo potoka* [Atlas of Gas Dynamic Functions for High-velocity and High-temperature Air Flow], Gosenergoizdat, 1961.

15. *Problemy vysokikh temperatur v aviatsionnykh konstruktsiiakh; sb. statei* [High-temperature Problems in Airplane Construction; a collection of articles], Inogiz, 1961.

16. Drakin, I. I., *Aerodinamicheskii i luchistyi nagrev v polete* [Aerodynamic and Radiative Heating in Flight], Oborongiz, 1961.

17. Predvoditelev, A. S., E. V. Stupochenko, V. P. Ionov, A. S. Pleshanov, I. B. Rozhdestvenskii, and E. V. Samuilov, *Termodinamicheskie funktsii vozdukha dlia temperatur ot 1000 do 12000°K i davlenii ot 0,001 do 1000 at (grafiki funktsii)* [The Thermodynamic Functions of Air for Temperatures from 1000 to 12,000°K and Pressures from 0.001 to 1000 Atmospheres, (graphs of functions)], Izd. AN SSSR, 1960.

18. Liepmann, H. W., and A. Roshko, *Elementy gazovoi dinamiki*, [Elements of Gas Dynamics], Inogiz, 1960.

19. Patterson, G. N., *Molekuliarnoe techenie gazov*, [Molecular Flow of Gases], Fizmatgiz, 1960.

20. Guderley, K. G., *Teoriia okolozvukovykh techenii* [The Theory of Transonic Flow], 1960.

21. Koshkin, V. K. (ed.), *Osnovy teploperedachi v aviatsionnoi tekhnike* [The Bases of Heat Transfer in Aviation Technology], Oborongiz, 1960.

22. *Fizicheskaia gazodinamika; sb. statei* [Physical Gas Dynamics; a collection of articles], Izd. AN SSSR, 1959.

23. *Problemy dvizheniia golovnoi chasti raket dal'nego deistviia* [Problems of the Motion of the Nose Cone of Long Range Rockets], Inogiz, 1959.

24. *Nauchnye problemy iskusstvennykh sputnikov zemli* [Scientific Problems of Artificial Earth Satellites], Inogiz, 1959.

25. *Aerodinamika chastei samoleta pri bol'shikh skorostiakh* [Aerodynamic Components of Aircraft at High Speeds], Inogiz, 1959.

26. Dorodnitsyn, A. A., *Metod integral'nykh sootnoshenii dlia chislennogo resheniia differentsial'nykh uravnenii v chastnykh proizvodnykh* [The Method of Integral Relations for the Numerical Solution of Partial Differential Equations], Trudy Instituta tochnoi mekhaniki i vychislitel'noi tekhniki [Transactions of the Institute of Precision Mechanics and Computer Technology], AN SSSR, 1958.

27. Ostoslavskii, I. V., *Aerodinamika samoleta* [Aircraft Aerodynamics], Oborongiz, 1957.

28. Predvoditelev, A. S., E. V. Stupochenko, E. V. Samuilov, I. P. Stakhanov, A. S. Pleshanov, and I. B. Rozhdestvenskii, *Tablitsy termodinamicheskikh funktsii vozdukha (dlia temperatur ot 6000 do 12000°K i davlenii ot 0,001 do 1000 atmosfer)* [Tables of the Thermodynamic Functions of Air (for Temperatures from 6000 to 12,000°K and Pressures from 0.001 to 1000 Atmospheres)], Izd. AN SSSR, 1957.

29. Sedov, L. I., *Metody podobiia i razmernosti v mekhanike* [Methods of Similarity and Dimensionality in Mechanics], Gostekhizdat, 1957.

30. Kalikhman, L. E., *Turbulentnyi pogranichnyi sloi na krivolineinoi poverkhnosti, obtekaemoi gazom* [The Turbulent Boundary Layer on a Streamlined Curved Surface], Oborongiz, 1956.

31. Staniukovich, K. P., *Neustanovivshiesia dvizheniia sploshnoi sredy* [Unsteady Motion of a Continuous Medium], Gostekhizdat, 1955.

32. *Sovremennoe sostoianie aerodinamiki bol'shikh skorostei* [The Present State of High-Speed Aerodynamics], 2 vols., Inogiz, 1955-1956.

33. Hilton, W. F., *Aerodinamika bol'shikh skorostei* [High-Speed Aerodynamics], Inogiz, 1955.

34. Sauer, R., *Techeniia sshimaemoi zhidkosti* [Flow of Compressible Fluids), Inogiz, 1954.

35. Vukalovich, M. P., V. A. Kirillin, S. A. Remizov, V. S. Siletskii, and V. N. Timofeev, *Termodinamicheskie svoistva gazov* [The Thermodynamic Properties of Gases], Gostekhizdat, 1953.

36. Hoerner, Sigard F., *Aerodynamic Drag*, Dayton, Ohio, 1951.

37. *Gazovaia dinamika; sb. statei* [Gas Dynamics; a collection of articles], Inogiz, 1950.

38. Courant, R., and K. Friedrichs, *Sverkhzvukovoe techenie i udarnye volny* [Supersonic Flow and Shock Waves], Inogiz, 1950.

39. Frankl', F. I., and E. A. Karpovich, *Gazodinamika tonkikh tel* [The Gas Dynamics of Thin Bodies], Gostekhizdat, 1948.

40. Kopal, Z., *Tables of Supersonic Flow Around Cones of Large Yaw*, Technical Report 5, Massachusetts Institute of Technology, 1949.

41. Kopal, Z., *Tables of Supersonic Flow Around Yawing Cones*, Technical Report 3, Massachusetts Institute of Technology, 1947.

42. Kopal, Z., *Tables of Supersonic Flow Around Cones*, Technical Report 1, Massachusetts Institute of Technology, 1947.

43. *Izvestiia AN SSSR, Mekhanika i mashinostroenie* [Bulletin of the Academy of Sciences of the USSR, Mechanics and Mechanical Engineering], No. 4, 1959; Nos. 2, 3, 1960; No. 11, 1961.

44. *Prikladnaia matematika i mekhanika AN SSSR* [Journal of Applied Mathematics and Mechanics, Academy of Sciences of the USSR], Vol. 24, Nos. 3, 5, 1960; No. 6, 1961.

45. *Journal of the Aeronautical Sciences* [Journal of the Aerospace Sciences], No. 7, 1949; Nos. 11, 12, 1950; Nos. 2, 3, 8, 10, 1951; Nos. 2, 5, 10, 1952; No. 9, 1953; No. 3, 1954; Nos. 1, 2, 3, 4, 6, 1955; No. 2, 1956; Nos. 1, 3, 11, 1957; Nos. 1, 2, 8, 11, 12, 1958; Nos. 2, 3, 5, 6, 8, 9, 10, 1959; Nos. 2, 4, 5, 6, 10, 11, 1960; Nos. 1, 4, 5, 7, 10, 11, 12, 1961; Nos. 1, 2, 7, 11, 12, 1961; Nos. 1, 2, 4, 12, 1962.

46. *Jet Propulsion* [ARS Journal], No. 11, 1957; Nos. 11, 12, 1958; Nos. 2, 4, 6, 1960; Nos. 2, 3, 5, 7, 8, 11, 1961.

47. National Advisory Committee for Aeronautics (NACA), [TR] No. 835, 1946; No. 1194, 1947; [TN] Nos. 2726, 2744, 2579, 2811, 1952.

48. *Journal of Fluid Mechanics*, No. 1, 1957; No. 4, 1958.

Ablation, charring ablators,751
definition,753
effective heat of,756-759
fusion time,759-761
heat transfer,760
mass loss,763
rate of,764-767
transpiration coefficient,755
two-phase boundary layer,753-754
vapor pressure,770-771
Ablative materials, physical properties,752,774
Adiabatic exponent, definition, 30
Affine-similar bodies,23
Angle of attack, definition,4
Arbitrary body, Newtonian flow, axial force coefficient, 505-511
center-of-pressure coefficient,531-532
normal force coefficient, 516,519
pitching moment coefficient,527
pressure distribution, hypersonic flow,487-495
linearized flow,345-359, 372,407-414
Newtonian flow,500-504,640-641
supersonic flow,263-268, 322-328
Axial force, definition,4
Axial force coefficient,6-9
Newtonian flow,498-515
unsteady flow,450
see also Pressure drag coefficient

Base drag,387-397
Base drag coefficient, definition,7
Base pressure coefficient,334, 388-397
definition,7
free molecule flow,803
Beveled flat nose, geometry of, 28-29
laminar heat transfer,718-719
pressure distribution,580-581
pressure drag coefficient,582
Blast wave theory,586-600
piston analogy,586-588,597-600
Blunt cone, center-of-pressure coefficient,624-626
laminar heat transfer,720-724, 738-741
local Reynolds number,670-671
normal force coefficient,544
piston analogy,597-611
pitching moment coefficient, 544
pressure distribution,599-609
universal curve,544,606,623
pressure drag coefficient,602 609-611
shock wave shape,599-604
similarity law,603-606
surface Mach number,666
Blunt curved bodies, piston analogy,627-631
Blunt cylinder, piston analogy, 590-597
pressure distribution,596
shock wave shape,596
Blunt nose, at angle of attack, 621-626
degree of dissociation,644-646,655
equivalent radius,579-580,585
frozen flow,646,658
geometry of,24
inviscid flow,549-554
heat transfer, laminar,683-727
turbulent,727-737
method of integral relations, 550-554
nonequilibrium flow,642-660
piston analogy,586-588,597-600
shock wave curvature,543
stagnation point flow,554-565
velocity gradient at stagnation point,543
viscosity effects on external flow,742-749

Boattail, center-of-pressure coefficient,439
pressure distribution, hypersonic flow,496
linearized flow,372
pressure drag coefficient, hypersonic flow,496
linearized flow,363-375
Body coordinates, definition,4
Boundary layer, displacement thickness,8,298-302,678-679,743-747
effect of compressibility, 143-144
effects on inviscid flow,297-302
effective enthalpy,147,150, 725,736
effective temperature,145
frozen flow,701
incompressible,140
laminar, blunt cone,661
equilibrium dissociation, 683-687
heat transfer,683-727
nonequilibrium,662
momentum thickness,81,730-732
quasi-equilibrium707-708
recovery temperature,151
thickness,141
laminar,145
turbulent,146
turbulent, heat transfer,727-737
velocity profile,140
Boundary layer transition,670-676
effect of blunting,672
effect of pressure gradient, 675
effect of surface temperature, 673-674,732-734

Catalytic coefficient, definition,703
Catalytic parameter, definition, 705
Catalytic recombination,59-62, 700-710
Center-of-pressure coefficient, arbitrary body, Newtonian flow,531-532
blunt cone,624-626
boattail,439
cone, Newtonian flow,533
supersonic flow,232
cone-cylinder,403,436,438
conical flare,435
definition,14-15
hypersonic flow,534-535
linearized flow,430-439
Newtonian flow,531-533
ogive-cylinder,403
ogive nose, linearized flow, 431
Newtonian flow,532
parabolic nose, linearized flow,431
Newtonian flow,532
parabolic nose with cylinder, 438
transonic flow,851-853
viscous crossflow,439
Cone, at angle of attack,207-236
axial force coefficient, Newtonian flow,509
supersonic flow,230-231
blunt, *see* Blunt cone
center-of-pressure coefficient, Newtonian flow,533
supersonic flow,232
drag coefficient,232
in free molecule flow,803-805
dynamic stability derivatives, 458-459
enthalpy on surface,162
flow around, hypersonic speed, 463-470
piston analogy,631-634
heat transfer,198-204
lift coefficient,232
normal force coefficient, supersonic flow,212-213, 230-231
linearized flow,424
Newtonian flow,518-521
pitching moment coefficient, linearized flow,426-427
Newtonian flow,530
supersonic flow,232
pressure coefficient, hypersonic flow,162,466-467
linearized flow,361
Newtonian flow,498-500

piston analogy,633
supersonic flow,182-184
transonic flow,837-838
pressure distribution, transonic,858
pressure drag coefficient, hypersonic flow,466-467
linearized flow,359-361
supersonic flow,230-231, 238
transonic flow,838-839,858-865
shear stress,196
shock wave angle,179
piston analogy,633
similarity law,180,184
skin friction,194-198,200-202
stagnation pressure ratio,181
transonic flow,853-858
velocity on surface,162,178
Cone-cylinder, center-of-pressure coefficient,403,436-438
normal force slope,403
Conical boattail, pressure drag coefficient,365
Conical flare, center-of-pressure coefficient,435
pressure drag coefficient,366-367
Conical flow, angle of attack, 207-236
apple curves,171,176
critical cone angle,171,177
dissociation and ionization, 186-192
equations,164-170
nonequilibrium effects,193-194
tables of,171-175
variable specific heats,185-186
Continuity equation,72-78
cylindrical coordinates,73
curvilinear coordinates,74
normal coordinates,73
spherical coordinates,73
Critical cone angle,171,177
Cylinder, drag coefficient,404, 422
Cylindrical afterbody, drag coefficient, free molecule flow,806
laminar heat transfer,724-725
normal force coefficient,404, 418,421-423

Damping moment,16-18
Damping moment coefficient,16, 453
Diffusion in boundary layer,57-62
catalytic recombination,59-62
diffusional heat transfer,58
diffusion time,60
frozen flow,59-61
Diffusion equation,78
Dissociating diatomic gas, relations for,41-48
Dissociation of air,32,41
characteristic density,42
characteristic energy,43
characteristic pressure,45
characteristic temperature,42
characteristic velocity,45
equation of state,44,46,89
equilibrium enthalpy,710-711
Dissociation parameter, nonequilibrium flow,646-648
Drag coefficient, *see* Pressure drag coefficient
Drag force, definition,4
Drag rise at transonic speed, 840-851
Dynamic stability,18-19
Dynamic stability derivatives, 453-459
cone,458-459
parabolic body,455-458

Effective enthalpy,147,150,725, 736
Effective heat of ablation, definition,756
fusion,759,768-769,774-776
fusion and vaporization,758, 769-774
phenolic nylon,775
teflon,775-776
vaporization,756
Effective temperature,145
Elliptical nose, geometry of,27
laminar heat transfer,718-719
Emissivity, effective,695
of air,697
Energy equation,82-88

boundary layer,83-88
laminar,84-87
turbulent,88
isentropic flow,83
Enthalpy-entropy diagram,34
Entropy, conservation of,90
Entropy layer,663
Epicycloid,251-253
Equations of motion,64
boundary conditions,91-95
boundary layer,70-72
curvilinear coordinates,70
cylindrical coordinates,65-67
normal coordinates,69
spherical coordinates,67-68
Equation of state,44-46,88-90

Fineness ratio, definition,8,20
Flat nose, geometry of,27
laminar heat transfer,717-718
pressure coefficient at shoulder,578
pressure distribution,573-575
pressure drag coefficient,574-575
shock detachment distance,576-577
shock wave curvature,543,576-577
velocity gradient at stagnation point,543,578-580
Flow separation,385-387
Fore drag coefficient,379-387
Free molecule flow,783,787-807
accommodation coefficient,798
adiabatic wall temperature, 800
average molecular speed,789
base pressure,803
diffuse reflection,788
drag force,802
effect of angle of attack, 806-807
equilibrium wall temperature, 801
drag coefficient, cone,803-805
cylindrical afterbody,806
sphere,804-806
friction coefficient,795-796
heat transfer,798-801
Maxwellian distribution function,789
most probable molecular speed,789
pressure coefficient,793-795
specular reflection,787-788
transfer of kinetic energy, 796-797
transfer of mass,788-792
Friction drag coefficient,380-385
see also Skin friction coefficient

Geometry of bodies,19-29

Heat transfer, blunt cone,738-741
catalytic surface,661,700-710
equilibrium temperature,153-155
free molecule flow,798-801
hemisphere cylinder,728
laminar,beveled flat nose, 718-719
blunt cone,720-724
cylindrical afterbody,724-725
effect of diffusion,698-712,726-727
effect of recombination rate,661,704-710
effect of vorticity,726
ellipsoid,718-719
equilibrium dissociation, 686,712-725
flat nose,717-718
spherical nose,712-717
skin temperature,204-206
slip flow,816-817,822-825
stagnation point, effect of vorticity,694-695
equilibrium dissociation, 687-693
nonequilibrium,661,690-691
radiation,661-662,695-698
turbulent,727-737
blunt nose,730
effect of diffusion,728-730
effect of pressure gradient, 736-737
with ablation,760
Heat transfer coefficient, definition,156

Hemisphere cylinder, heat transfer,728
pressure distribution,592-596
shock wave shape,594-597
Hemispherical nose, pressure drag coefficient, transonic, 866-867
Hodograph of velocity,113-115
Hypersonic flow, similarity law, 279,538-541
similarity parameter,116,464
small disturbance theory,470-478
arbitrary body,481-491
cones,478-480

Impulse equation,80
Inviscid high-entropy layer, definition,663
flow in,661,663-667,679-682
thickness,663-667
Isentropic flow,82-83
constant specific heats,95-97
dissociating and ionizing gas, 100
variable specific heats,97-100
Isentropic flow parameters,99

Knudsen number,783,785

Lateral force, definition,4
Law of plane sections,472-474
Lewis-Semenov number,85,700
Lift force, definition,4
Linearized flow, asymmetric pressure coefficient,407-409
axial force coefficient,342
center-of-pressure coefficient,430-439
method of doublets,407-412
method of sources,343-355
minimum drag body,376-378
normal force coefficient,405, 414-425
perturbation potential,336-345,405-407
pitching moment coefficient, 425-429
pressure coefficient,340-342
source distribution,345-346
unsteady flow,443-459
velocity potential,336
Local cones, method of,234,264-269,327-329,491-494

Mach angle,254
Mass transfer, *see* Ablation
Mean free path,781-783,815
Method of characteristics, at angle of attack,303-322
blunt bodies,612-620
pointed bodies,239-296
characteristic curves,244
compatibility conditions,245, 305-313
epicycloids,251-253
hodograph plane,247,271
irrotational dissociable flow, 292-293
rotational flow,270-282,293-296
Method of integral relations, 550-554
Minimum drag body, linearized flow,376-378
Newtonian flow,511-515
Momentum equation,79-82
boundary layer,80
integral form,81
one-dimensional flow,80

Newtonian flow theory,461,498-541
effect of centrifugal force, 535-538
minimum drag body,511-515
modified,515
shadow zone,502,505-506,519-521
Nonequilibrium flow,48-57
behind shock wave,135-139
blunt nose,642-650
characteristic dwell time,652
chemical reaction rate,50-53
dissociation parameter,646θ 648
recombination rate of air,53
recombination rate parameter, 658
relaxation,49
relaxation length,650-651
relaxation time,54-56,651,658
Normal force, definition,4
Normal force coefficient,9-12

arbitrary body, Newtonian flow,516,519-520
blunt cone,544
cone, linearized flow,424
Newtonian flow,518-520
cylindrical afterbody, linearized flow,404,418,421-423
Newtonian flow,517,521-524
effect of boattail,526-527
linearized flow,405-425
longitudinal distribution,11
Newtonian flow,516-527
nonlinear variation,524-526
parabolic nose, Newtonian flow,516-517
slender body theory,416-417
transonic flow,851-852
unsteady flow,450-459
viscous crossflow,403-404, 420-422
Normal force slope, cone-cylinder,403
ogive-cylinder,403
Nusselt number, definition,157

Oblique shock wave, at hypersonic speed,115-117
density ratio,131
dissociable gas,132-134
entropy change,112
equations for,101-134
flow deflection,108-111,122-124,129
Mach number behind,111,117, 129
pressure ratio,131
shock wave angle,107-111
temperature ratio,130
total pressure ratio,112,121-122
velocity behind,111
with constant specific heats, 106-119
with dissociation and ionization,124-134
with variable specific heats, 119-124
Ogive-cylinders, center-of-pressure coefficient,403
normal force slope,403
pressure distribution,283
Ogive nose, center-of-pressure coefficient, linearized flow,431
Newtonian flow,532
geometry of,20-22
pressure drag coefficient, supersonic flow,238,264,269
Newtonian flow,508-509
transonic flow,865-866

Parabolic boattail, pressure drag coefficient,373-374
Parabolic body, dynamic stability derivatives,455-458
Parabolic nose, center-of-pressure coefficient, linearized flow,431
Newtonian flow,532
geometry of,22-24
normal force coefficient,516-517
pitching moment coefficient, 528
pressure distribution, hypersonic flow,492-493
linearized flow,349-353,369
pressure drag coefficient, hypersonic flow,494
linearized flow,369
Newtonian flow,508
supersonic flow,269
universal curve,370
Piston analogy,472-474,586-588, 597-600
Pitching moment, definition,4
Pitching moment coefficient,12-14
arbitrary body, Newtonian flow,527-530
blunt cone,544
cone, linearized flow,426-427
Newtonian flow,530-531
cylindrical afterbody, Newtonian flow,529
linearized flow,425-429
Newtonian flow,527-531
parabolic nose, Newtonian flow,528
slender body theory,427
unsteady flow,450-452
viscous crossflow,428-429
Power law nose, flow around,634-640
geometry of,24
Prandtl number, definition,85
Prandtl-Meyer angle,254

Pressure coefficient, cone, hypersonic flow,466-467
linearized flow,361
Newtonian flow,498-500
piston analogy,633
supersonic flow,182-183
transonic flow,837-838
stagnation point, transonic flow,866-867
supersonic flow,567
Pressure distribution, arbitrary body, hypersonic flow,487-495
linearized flow,345-359,372,407-414
Newtonian flow,500-504,640-641
supersonic flow,263-268,322-328
beveled flat nose,580-581
blunt cone,544,599-609
universal curve,544,606,623
blunt cylinder,596
boattail, hypersonic flow,496
linearized flow,372
flat nose,573-575
hemisphere cylinder,592-596
parabolic body, hypersonic flow,492-493
linearized flow,349-353,369
power law body,637
sphere cone,605-608,611,619
at angle of attack,621-624
spherical nose,566-569
spherical segment nose,580-582
Pressure drag coefficient, arbitrary body, Newtonian flow, 507
at angle of attack,329-332
beveled flat nose,582
blunt cone,602,609-611
boattail,364-366,373-374,496
cone, hypersonic flow,466-468
linearized flow,359-361
Newtonian flow,498-500
supersonic flow,182-184,238
transonic flow,838-839,858-865
conical flare,366
flat nose,574-575
ogive nose, method of local cones,269
Newtonian flow,508-509
supersonic flow,238,264
transonic flow,865-866
parabolic nose, hypersonic flow,494
linearized flow,369
method of local cones,269
Newtonian flow,508
supersonic flow,370
power law body,637-640
sphere cone,609-611
spherical nose,238,569-570,866-867
spherical segment nose,582
transonic flow,848
Pyrex, physical properties,768

Rankine-Hugoniot equation,107
Rarefied gas flow, accommodation coefficient,779
free molecule flow,783,787-807
intermediate regime,779,784,819-820
Knudsen number,783
mean free path,781-783,815
merged layer regime,819-823
slip coefficient,809
slip flow regime,784,808-825
slip velocity,809
surface interaction,779,787-788
transition regime,779,819
Recovery factor,151
Reynolds analogy,155-159,735
Rolling moment, definition,4

Schmidt number, definition,85
Shock detachment distance, beveled flat nose,583
flat nose,576-577
low Reynolds number,821
nonequilibrium flow,654-656
spherical nose,560,570-572
spherical segment nose,584
Shock expansion theory,322-327,494-497
Shock layer radiation,695-698
Shock polar,113-115
Shock wave, nonequilibrium flow behind,134-139
Shock wave angle, cone,161,179,463-465,633

Shock wave curvature, beveled flat nose,584-585
blunt nose,543
flat nose,543,576-577
sharp nose,485-486
spherical nose,570-572
spherical segment nose,585
Shock wave shape, blunt cone, 599-604
blunt cylinder,596
hemisphere cylinder,594-597
power law body,636
Side force, definition,4
Side slip angle, definition,4
Similarity law, blunt cone,603-606
cone,180
hypersonic,464-480
supersonic,355-359,412-414
transonic,829-839
Skin friction and heat transfer, relation between,155-159,735
Skin friction coefficient, average value,141
cone,194-198,200-202
cylindrical afterbody,384
definition,9
effect of diffusion,727-729
laminar,2,141-143,197-202, 379-385
local,141
slip flow,812-816
turbulent,2,141-144,148-149, 198-202,379-385
Slender body theory,353-355,411
normal force coefficient,416-417
pitching moment coefficient, 427
pressure drag coefficient,375-376
unsteady flow,448-449
Slip flow,808-825
skin friction coefficient,812-816
heat transfer,816-817,822,824-825
Small disturbance theory, hypersonic flow,470-478
Specific heat, average for a mixture,84
variation with temperature, 30-31
Sphere, drag coefficient in free molecule flow,804-806
Sphere cone, laminar heat transfer,720-724
pressure distribution,605-608, 611,619
at angle of attack,621-624
pressure drag coefficient,609-611
Spherical nose, flow near stagnation point,554-565
laminar heat transfer,712-717
location of sonic point,565
pressure distribution,566-569
pressure drag coefficient, 569-570
shock detachment distance, 560,570-572
shock wave curvature,570-572
velocity gradient at stagnation point,560-564
Spherical segment nose, geometry of,26-27
Spherically blunted nose, geometry of,24-27
Stabilization of bodies,432-442
effect of flare,441-442
effect of tail surface,439-441
Stagnation point, heat transfer, equilibrium dissociation, 687-693
nonequilibrium,661,690-691
radiation,661-662,695-698
pressure coefficient, hypersonic flow,567
transonic flow,866-867
velocity gradient, blunt nose, 543
flat nose,543,578-580
spherical nose,560-564
Stanton number, definition,157
Static margin,432-435
Static stability,15
Stefan-Boltzmann law,152-153
Stream function,77

Teflon, physical properties,774
Thermodynamic properties of air, 32-40
atomic and molecular concentrations,33
average molecular weight,36

enthalpy-entropy diagram,33-34
speed of sound,37
thermal conductivity,39-40
Transition Reynolds number,381, 399,670-676,730-734
Transonic similarity law,829-839
pressure coefficient,834-835
similarity parameter,832,835

Vaporization coefficient, definition,758
Velocity potential, cylindrical coordinates,74
spherical coordinates,75
Viscosity, glassy materials, 766-768
Viscosity of air,37-39
Sutherland equation,38
Viscous crossflow, center-of-pressure coefficient,439
normal force coefficient,403-404,420-423
pitching moment coefficient, 403-404,428-429

Wind coordinates, definition,4

Yawing moment, definition,4

SELECTED RAND BOOKS

Shanley, F. R. *Weight-Strength Analysis of Aircraft Structures.* New York: McGraw-Hill Book Company, Inc., October 1952.

Williams, J. D. *The Compleat Strategyst: Being a Primer on the Theory of Games of Strategy.* New York: McGraw-Hill Book Company, Inc., June 1954.

The RAND Corporation. *A Million Random Digits with 100,000 Normal Deviates.* Glencoe, Illinois: The Free Press, March 1955.

Bellman, Richard. *Dynamic Programming.* Princeton, New Jersey: Princeton University Press, November 1957.

Krieger, F. J. *Behind the Sputniks: A Survey of Soviet Space Science.* Washington, D. C.: Public Affairs Press, July 1958.

Buchheim, Robert W. and the Staff of The RAND Corporation. *Space Handbook: Astronautics and Its Applications.* New York: Random House, Inc., August 1959.

Brodie, Bernard. *Strategy in the Missile Age.* Princeton, New Jersey, Princeton University Press, September 1959.

Hitch, Charles J., and Roland McKean. *The Economics of Defense in the Nuclear Age.* Cambridge, Massachusetts: Harvard University Press, September 1960.

Hirshleifer, Jack, James C. DeHaven, and Jerome W. Milliman. *Water Supply: Economics, Technology, and Policy.* Chicago, Illinois: The University of Chicago, October 1960.

Dresher, Melvin. *Games of Strategy: Theory and Applications.* Englewood Cliffs, New Jersey: Prentice-Hall, Inc., June 1961.

Dubyago, A. D. *The Determination of Orbits.* New York: The Macmillan Company, November 1961.

Gouré, Leon. *The Siege of Leningrad.* Stanford, California: Stanford University Press, June 1962.

Bellman, Richard E., and Stuart E. Dreyfus. *Applied Dynamic Programming.* Princeton, New Jersey: Princeton University Press, July 1962.

Ford, L. R., Jr., and D. R. Fulkerson. *Flows in Networks.* Princeton, New Jersey: Princeton University Press, September 1962.

Sokolovskii, V. D. (ed.). *Soviet Military Strategy.* Englewood Cliffs, New Jersey: Prentice-Hall, Inc., April 1963.

Bellman, R. E., R. E. Kalaba, and M. C. Prestrud. *Invariant Imbedding and Radiative Transfer in Slabs of Finite Thickness* (Volume 1). New York: American Elsevier Publishing Company, Inc., July 1963.

Boehm, Barry W. *Rocket: Rand's Omnibus Calculator of the Kinematics of Earth Trajectories*. Englewood Cliffs, New Jersey: Prentice-Hall, Inc., February 1964.

Dole, Stephan H. *Habitable Planets for Man*. New York: Blaisdell Publishing Company, March 1964..

Bellman, R. E., H. H. Kagiwada, R. E. Kalaba, and M. C. Prestrud. *Invariant Imbedding and Time-dependent Transport Processes* (Volume 2). New York: American Elsevier Publishing Company, Inc., April 1964.

Judd, William R. (ed.). *State of Stress in the Earth's Crust*. New York: American Elsevier Publishing Company, Inc., September 1964.

Selin, Ivan. *Detection Theory*. Princeton, New Jersey: Princeton University Press, July 1965.

Bellman, Richard E., and Robert E. Kalaba. *Quasilinearization and Nonlinear Boundary-Value Problems* (Volume 3). New York: American Elsevier Publishing Company, Inc., August 1965.

Meyer, John R., Martin Wohl, and John F. Kain. *The Urban Transportation Problem*. Cambridge, Massachusetts: Harvard University Press, September 1965.

Novick, David (ed.). *Program Budgeting: Program Analysis and the Federal Budget*. Cambridge, Massachusetts: Harvard University Press, December 1965.

Horelick, Arnold L., and Nyron Rush. *Strategic Power and Soviet Foreign Policy*. Chicago, Illinois: University of Chicago Press, April 1966.

Bellman, R. E., R. E. Kalaba, and J. Lockett. *Numerical Inversion of the Laplace Transform* (Volume 4). New York: American Elsevier Publishing Company, Inc., December 1966.

Gazley, Jr., Hartnett, and Eckert. *Proceedings of the Second All-Soviet Union Conference on Heat and Mass Transfer* (Volumes 1-7). Ann Arbor, Michigan: University Microfilms, February 1968.

Sheppard, J. J. *Human Color Perception*. New York: American Elsevier Publishing Company, Inc., May 1968.

Quade, E. S., and W. I. Boucher. *Systems Analysis and Policy Planning Applications in Defense*. New York: American Elsevier Publishing Company, Inc., June 1968.

Deirmendjian, D. *Electromagnetic Scattering on Spherical Polydispersions*. New York: American Elsevier Publishing Company, Inc., April 1969.